frontiers | Research Topics

Biomechanics, sensing and bio-inspired control in rehabilitation and wearable robotics

Edited by
Wujing Cao, Zirui Lan, Ningbo Yu, Keyi Wang and Wenwei Yu

Published in
Frontiers in Bioengineering and Biotechnology

ISSN 1664-8714
ISBN 978-2-8325-5728-0
DOI 10.3389/978-2-8325-5728-0

About Frontiers

Frontiers is more than just an open access publisher of scholarly articles: it is a pioneering approach to the world of academia, radically improving the way scholarly research is managed. The grand vision of Frontiers is a world where all people have an equal opportunity to seek, share and generate knowledge. Frontiers provides immediate and permanent online open access to all its publications, but this alone is not enough to realize our grand goals.

Frontiers journal series

The Frontiers journal series is a multi-tier and interdisciplinary set of open-access, online journals, promising a paradigm shift from the current review, selection and dissemination processes in academic publishing. All Frontiers journals are driven by researchers for researchers; therefore, they constitute a service to the scholarly community. At the same time, the *Frontiers journal series* operates on a revolutionary invention, the tiered publishing system, initially addressing specific communities of scholars, and gradually climbing up to broader public understanding, thus serving the interests of the lay society, too.

Dedication to quality

Each Frontiers article is a landmark of the highest quality, thanks to genuinely collaborative interactions between authors and review editors, who include some of the world's best academicians. Research must be certified by peers before entering a stream of knowledge that may eventually reach the public - and shape society; therefore, Frontiers only applies the most rigorous and unbiased reviews. Frontiers revolutionizes research publishing by freely delivering the most outstanding research, evaluated with no bias from both the academic and social point of view. By applying the most advanced information technologies, Frontiers is catapulting scholarly publishing into a new generation.

What are Frontiers Research Topics?

Frontiers Research Topics are very popular trademarks of the *Frontiers journals series*: they are collections of at least ten articles, all centered on a particular subject. With their unique mix of varied contributions from Original Research to Review Articles, Frontiers Research Topics unify the most influential researchers, the latest key findings and historical advances in a hot research area.

Find out more on how to host your own Frontiers Research Topic or contribute to one as an author by contacting the Frontiers editorial office: frontiersin.org/about/contact

Biomechanics, sensing and bio-inspired control in rehabilitation and wearable robotics

Topic editors

Wujing Cao — Shenzhen Institute of Advanced Technology, Chinese Academy of Sciences (CAS), China

Zirui Lan — Fraunhofer, Singapore

Ningbo Yu — Nankai University, China

Keyi Wang — Harbin Engineering University, China

Wenwei Yu — Chiba University, Japan

Citation

Cao, W., Lan, Z., Yu, N., Wang, K., Yu, W., eds. (2024). *Biomechanics, sensing and bio-inspired control in rehabilitation and wearable robotics*.

Lausanne: Frontiers Media SA. doi: 10.3389/978-2-8325-5728-0

Table of contents

frontiers | Frontiers in Bioengineering and Biotechnology

TYPE Editorial
PUBLISHED 23 October 2024
DOI 10.3389/fbioe.2024.1487075

OPEN ACCESS

EDITED AND REVIEWED BY
Markus O. Heller,
University of Southampton, United Kingdom

*CORRESPONDENCE
Wujing Cao,
caowujing414@126.com

RECEIVED 27 August 2024
ACCEPTED 18 October 2024
PUBLISHED 23 October 2024

CITATION
Luo M, Wu X, Yu N, Wang K and Cao W (2024) Editorial: Biomechanics, sensing and bio-inspired control in rehabilitation and wearable robotics.
Front. Bioeng. Biotechnol. 12:1487075.
doi: 10.3389/fbioe.2024.1487075

Editorial: Biomechanics, sensing and bio-inspired control in rehabilitation and wearable robotics

Mingxiang Luo[1], Xinyu Wu[2], Ningbo Yu[3], Keyi Wang[4] and Wujing Cao[2]*

[1]College of Engineering, Southern University of Science and Technology, Shenzhen, China, [2]Guangdong Provincial Key Lab of Robotics and Intelligent System, Shenzhen Institute of Advanced Technology, Chinese Academy of Sciences, Shenzhen, China, [3]College of Artificial Intelligence, Nankai University, Tianjin, China, [4]College of Mechanical and Electrical Engineering, Harbin Engineering University, Harbin, China

KEYWORDS

exoskeleton, control, biomechanics, signal, rehabilitation

Editorial on the Research Topic
Biomechanics, sensing and bio-inspired control in rehabilitation and wearable robotics

Introduction

The integration of biomechanics, sensing technology, and bio-inspired control is transforming rehabilitation and wearable robotics by enhancing human mobility and recovery. Biomechanics informs the design of systems that replicate or support natural movement, while advanced sensors monitor physiological and biomechanical data in real time, enabling personalized assistance. Wearable robotics, such as exoskeletons and prosthetics, benefit from technologies like electromyography (EMG) and inertial measurement units (IMUs), which provide feedback for dynamic control adjustments. Bio-inspired control strategies further enhance these systems by mimicking the adaptability of biological systems, ensuring natural and efficient movement. This Research Topic documents recent advancements in these areas, emphasizing their role in improving mobility and rehabilitation outcomes for individuals with physical impairments. The 25 contributions can be organised into 6 main focus areas: (1) development and evaluation of wearable robotics; (2) control strategy studies; (3) signal and feature recognition; (4) biomechanical analysis; (5) literature review and statistical analysis; (6) rehabilitation training evaluation.

Development and evaluation of wearable robotics

Xiang et al. conducted a study on back-support exoskeletons during manual material handling tasks, focusing on their biomechanical impact using Functional Data Analysis

(FDA) and Functional ANOVA (FANOVA). The goal was to optimize exoskeleton design for safer reduction of lower back load. Participants performed tasks with and without the exoskeleton, while researchers collected data on lumbar load and trunk angle. FANOVA revealed that the exoskeleton significantly reduced lumbar load, particularly in lifting tasks, highlighting its effectiveness. The study also demonstrated FANOVA's advantage in handling time-series data, providing valuable insights for designing better exoskeletal devices. Wang et al. developed a bedside cable-driven lower-limb rehabilitation robot for bedridden patients with neurological or limb disorders. This robot, based on sling exercise therapy, uses flexible cables to drive hip and knee motions at the bedside. A human-cable coupling controller dynamically adjusts the cable's impedance in response to the patient's joint impedance, stabilizing movement during rehabilitation. Experiments showed significant improvements in joint flexibility and stability, proving the robot's effectiveness. Meng et al. designed a multi-degree-of-freedom, reconfigurable ankle rehabilitation robot with an adjustable workspace for post-stroke rehabilitation. The robot can be customized to meet individual needs, providing personalized and effective rehabilitation exercises. The study included finite element simulations to ensure structural integrity and safety, along with practical tests to validate its performance. Zha et al. developed a robot-assisted system for the reduction and rehabilitation of distal radius fractures, equipped with a robotic arm and integrated biplane radiographic imaging. This system enhances the accuracy and efficacy of closed reduction treatments by overcoming manual traction limitations and offering real-time radiographic assessment. Experiments confirmed that the system effectively achieves required traction forces and maintains wrist alignment, improving treatment protocols by making them less invasive, reducing recovery time, and minimizing radiation exposure. Liu et al. explored a knee exoskeleton driven by a series elastic actuator (SEA) for gait rehabilitation in stroke patients. They introduced a synergetic gait prediction model using an attention-based CNN-LSTM network to generate personalized gait trajectories, improving prediction accuracy and rehabilitation outcomes. Additionally, they proposed a compliant control scheme using an artificial potential field (APF) method to tune impedance parameters, ensuring safe and effective interaction between the robot and the patient. Jiao et al. developed a Reconfigurable Multi-Terrain Adaptive Casualty Transport Aid (RMTACTA) for industrial environments, enhancing pre-hospital casualty transport. The device uses a Watt II 6-bar linkage mechanism to transition between multiple modes, facilitating navigation across various terrains. A single remote rope controls the system, ensuring adaptability and ease of operation. A prototype verified the design's functionality, demonstrating significant improvements in casualty transport efficiency and safety. Liu et al. presented a novel non-back-drivable clutch-based self-locking mechanism to improve stability in prosthetic joints. This mechanism allows precise positioning without changing the transmission ratio, which is critical for prosthetic wrists requiring reliable performance. The design minimizes friction during operation and ensures that the prosthetic limb remains fixed even during power failures, enhancing safety and comfort. The study included detailed mechanical design, kinematic analysis, and extensive testing, proving the mechanism's effectiveness and durability.

Control strategy study

Zhang et al. studied adaptive impedance control for an upper limb rehabilitation robot, focusing on dynamically adjusting training parameters based on patient status. Using a two-degree-of-freedom flexible drive joint and a forgetting factor recursive least squares method, they successfully estimated and optimized impedance parameters, significantly improving rehabilitation effectiveness by tailoring assistance to real-time patient needs. Tian et al. proposed a force/position-based velocity control (FPVC) strategy for a lower limb rehabilitation robot, enhancing trajectory tracking and patient participation. Their extensive experiments demonstrated that this approach improves interaction and rehabilitation outcomes. Li et al. introduced an "Orbit Energy" (OE) metric to enhance lower limb exoskeleton stability during standing. This metric helps select balance recovery strategies, such as adjusting ankle and hip torque, significantly improving balance and reducing muscle activation during disturbances. Liang et al. developed a multi-mode adaptive control strategy for lower limb rehabilitation robots, including robot-dominant, patient-dominant, and safety-stop modes. This strategy dynamically adjusts assistance based on patient abilities, improving rehabilitation outcomes and ensuring safety, as validated through simulations.

Signal and feature recognition

Gong et al. explored multimodal fusion and human-robot interaction control in an intelligent robotic walker for gait rehabilitation, aiming to improve support and guidance for stroke patients. By integrating sensors like force sensors, joysticks, and depth-sensing cameras, the walker dynamically adjusts to the user's motion intentions, enhancing walking assistance and potentially improving rehabilitation outcomes. Sarasola-Sanz et al. studied a hybrid brain-muscle-machine interface (hBMI) for stroke rehabilitation, involving six severely paralyzed patients. The hBMI, which combines EMG with brain signals to control an upper limb exoskeleton, showed significant improvements in arm function and neural engagement, demonstrating its potential for effective motor recovery. Feng et al. developed a method using surface electromyography (sEMG) signals to identify coordinated movement intentions in a multi-posture rehabilitation robot. By optimizing features with genetic algorithms, their model accurately recognized movement intentions, enhancing interactive rehabilitation training. Zhou et al. addressed the Sim2Real challenge in soft robotics by introducing the ImbalSim2Real scheme, which optimizes model transition from simulation to real-world data using techniques like discriminator-enhanced samples. Their approach improved bio-signal estimation in medical applications, particularly in soft robot-assisted rehabilitation. Yi et al. developed TGANet, a deep learning model that integrates an attention mechanism into VGG16 to improve the classification of tongue features in Traditional Chinese Medicine. TGANet outperformed traditional models in accuracy, precision, F1 score, and AUC, demonstrating its effectiveness in enhancing diagnostic accuracy and rehabilitation outcomes in TCM.

Biomechanical analysis

Kang et al. studied the biomechanical impact of material anisotropy in 3D printed vertebral body implants for spinal reconstruction. They compared linear elastic isotropy and nonlinear anisotropy models using finite element analysis under various load conditions. Their findings show that the anisotropic model better represents the spinal system's mechanical behavior, with lower stress levels and displacement, suggesting higher safety and stability in spinal reconstructions when anisotropic properties are considered. This research offers valuable insights for improving spinal implant design and clinical outcomes. Shakourisalim et al. conducted a comparative study on the biomechanical impact of manual material handling tasks using back support exoskeletons and assistive tools in both laboratory and real-world settings. They found significant differences in muscle activation between the two environments, highlighting the importance of real-world assessments for accurately evaluating the ergonomic benefits of exoskeletons. Despite these differences, ergonomic risk, measured by REBA scores, remained consistent across settings. This study underscores the need for field assessments to fully understand the impact of ergonomic interventions.

Literature review and statistical analysis

Li et al. reviewed the use of extended reality (XR) technologies, including virtual reality (VR), augmented reality (AR), and mixed reality (MR), in training for myoelectric prostheses. They found that XR enhances training by providing immersive, interactive environments that increase user motivation and skill acquisition. However, challenges remain in translating virtual skills to real-world prosthesis control and improving training protocols. The authors suggest that XR holds promise for advancing prosthetic training and improving clinical outcomes. Zheng et al. examined the challenges in anthropomorphic motion planning for multi-degree-of-freedom robotic arms, focusing on creating humanoid robots with natural, human-like movements. They identified three key areas—motion redundancy, Research Topic, and coordination—as essential for improving robot interactions in various environments, including service, industrial, and healthcare settings. The research emphasizes integrating biomechanics, neurophysiology, and advanced computational models to mimic human movement effectively. Wen et al. conducted a bibliometric and visual analysis of research trends in robotic exoskeleton-assisted walking rehabilitation for stroke patients. Using data from the Web of Science Core Research Topic, they identified a rise in publication volume over the past decade, highlighting key research areas such as exoskeleton technology development, machine learning applications, and the impact on patient quality of life. This analysis offers insights into the current state and future directions of robotic exoskeleton research in stroke rehabilitation.

Rehabilitation training evaluation

Hu et al. studied how walking speed affects gait stability using multi-scale entropy analysis and plantar pressure measurements. They found that slower walking speeds offer greater stability, particularly in elderly populations, providing insights for designing safer walking practices and rehabilitation strategies. Liu et al. evaluated motion compensation in post-stroke rehabilitation using muscle synergy indicators and surface electromyography. Their study, involving stroke patients and healthy subjects performing hand-cycling tasks, showed that synergy symmetry and fusion effectively measure motion compensation, suggesting ways to optimize rehabilitation strategies. Wang et al. developed a finite element model to assess the impact of various rehabilitation methods on urinary and defecation control in elderly men. Their study found that targeted exercises for the levator ani, external anal sphincter, and pelvic floor muscles were particularly effective, emphasizing the importance of personalized rehabilitation programs. Another study by Wang et al. examined the effectiveness of combining diaphragmatic breathing with limb coordination training for treating lower limb lymphedema after gynecologic cancer surgery. They found that combining these exercises with complex decongestive therapy significantly improved symptoms, reduced limb circumference, and alleviated anxiety and depression, suggesting enhanced rehabilitation outcomes for these patients.

Summary

This Research Topic integrates the latest advancements in biomechanics, sensing technology, and bio-inspired control in the fields of rehabilitation and wearable robotics, demonstrating how these technologies can enhance human mobility and rehabilitation outcomes. The research findings are categorized into six main areas: development and evaluation of wearable robotics, control strategy studies, signal and feature recognition, biomechanical analysis, literature review and statistical analysis, and rehabilitation training evaluation. These studies not only expand our understanding of rehabilitation technologies but also provide new approaches for personalized rehabilitation interventions. Future research could delve deeper into several key questions: How can bio-inspired control be combined with real-time sensing data to achieve more precise personalized rehabilitation? How can signal recognition technology enhance devices "ability to perceive patients" intentions, thereby improving human-machine interaction? Additionally, with the application of virtual reality and mixed reality technologies in rehabilitation, exploring their potential to boost motivation and effectiveness in rehabilitation training is of great importance. These directions could not only deepen the understanding of current research findings but also provide strong support for the development of future rehabilitation devices and control strategies, paving the way for future research topics.

Author contributions

ML: Writing–original draft. XW: Writing–review and editing. NY: Writing–review and editing. KW: Writing–review and editing. WC: Conceptualization, Data curation, Formal Analysis, Funding acquisition, Investigation, Methodology, Project administration, Resources, Software, Supervision, Validation, Visualization, Writing–original draft, Writing–review and editing.

Funding

The author(s) declare that financial support was received for the research, authorship, and/or publication of this article. This work was supported in part by the National Key R&D (research and development) Program of China (2022YFB4703300), in part by the Guangdong Basic and Applied Basic Research Foundation (2024A1515030055), in part by the Shenzhen Science and Technology Program (JCYJ20220531100808018), in part by the Shenzhen Medical Research Fund (D2404006), in part by the National Natural Science Foundation of China (62473358), in part by the Key Program of Chinese Academy of Sciences (RCJJ-145-24-18), and in part by the Shenzhen Science and Technology Program (JCYJ20220818101602005).

Conflict of interest

The authors declare that the research was conducted in the absence of any commercial or financial relationships that could be construed as a potential conflict of interest.

Publisher's note

All claims expressed in this article are solely those of the authors and do not necessarily represent those of their affiliated organizations, or those of the publisher, the editors and the reviewers. Any product that may be evaluated in this article, or claim that may be made by its manufacturer, is not guaranteed or endorsed by the publisher.

frontiers | Frontiers in Bioengineering and Biotechnology

TYPE Original Research
PUBLISHED 10 November 2023
DOI 10.3389/fbioe.2023.1289686

OPEN ACCESS

EDITED BY
Wujing Cao,
Chinese Academy of Sciences (CAS), China

REVIEWED BY
Bingshan Hu,
University of Shanghai for Science and Technology, China
Yuquan Leng,
Southern University of Science and Technology, China
Muye Pang,
Wuhan University of Technology, China

*CORRESPONDENCE
Xiaohan Xiang,
shans281@affrc.go.jp

RECEIVED 06 September 2023
ACCEPTED 01 November 2023
PUBLISHED 10 November 2023

CITATION
Xiang X, Tanaka M, Umeno S, Kikuchi Y and Kobayashi Y (2023), Dynamic assessment for low back-support exoskeletons during manual handling tasks.
Front. Bioeng. Biotechnol. 11:1289686.
doi: 10.3389/fbioe.2023.1289686

Dynamic assessment for low back-support exoskeletons during manual handling tasks

Xiaohan Xiang*, Masahiro Tanaka, Satoru Umeno, Yutaka Kikuchi and Yoshihiko Kobayashi

Institute of Agricultural Machinery, National Agriculture and Food Research Organization (NARO), Saitama, Japan

Exoskeletons can protect users' lumbar spine and reduce the risk of low back injury during manual lifting tasks. Although many exoskeletons have been developed, their adoptability is limited by their task- and movement-specific effects on reducing burden. Many studies have evaluated the safety and effectiveness of an exoskeleton using the peak/mean values of biomechanical variables, whereas the performance of the exoskeleton at other time points of the movement has not been investigated in detail. A functional analysis, which presents discrete time-series data as continuous functions, makes it possible to highlight the features of the movement waveform and determine the difference in each variable at each time point. This study investigated an assessment method for exoskeletons based on functional ANOVA, which made it possible to quantify the differences in the biomechanical variables throughout the movement when using an exoskeleton. Additionally, we developed a method based on the interpolation technique to estimate the assistive torque of an exoskeleton. Ten men lifted a 10-kg box under symmetric and asymmetric conditions five times each. Lumbar load was significantly reduced during all phases (flexion, lifting, and laying) under both conditions. Additionally, reductions in kinematic variables were observed, indicating the exoskeleton's impact on motion restrictions. Moreover, the overlap F-ratio curves of the lumbar load and kinematic variables imply that exoskeletons reduce the lumbar load by restricting the kinematic variables. The results suggested that at smaller trunk angles (<25°), an exoskeleton neither significantly reduces the lumbar load nor restricts trunk movement. Our findings will help increasing exoskeleton safety and designing effective products for reducing lumbar injury risks.

KEYWORDS

ergonomics assessment, lumbar load, manual handling task, dynamic simulation, low back pain

1 Introduction

Back-support exoskeletons help farmers, nurses, and industrial workers reduce lumbar burden and improve working efficiency (Kobayashi et al., 2009; Hasegawa and Muramatsu, 2013; Upasani et al., 2019). As one of the specific human-robot collaboration solutions for manual handling tasks, back-support exoskeleton should satisfy the safety requirement for both robot and humans (De Looze et al., 2016; Ajodani et al., 2018). Thus, developing safe and effective exoskeletons will enable a broad range of applications that could benefit users.

ISO 13482 states that the purpose of exoskeletons is to reduce physical workload (ISO, 2014). The safe limit for human lumbar workload averages 3.4 kN (Water et al., 1993). However, accurately evaluating exoskeleton safety is difficult owing to the complexity of human–robot interactions and the unpredictability in user movements. Moreover, exoskeletons can constrain human movement, leading to discomfort (Baltrusch et al., 2018). Performance variations at actual rehabilitation, industrial, and agriculture work sites highlight the need for a standardized and dynamic assessment method for exoskeletons (De looze et al., 2016; Omoniyi et al., 2020; Zheng et al., 2022).

Exoskeleton assessment requires obtaining lumbar load and human movement data. Human movement can be measured by optical or inertial measurement unit (IMU) motion capture systems. Several methods have been used to measure exoskeletons' lumbar load, including directly recording the assistive force by inserting additional load cells into the exoskeleton (Abdoli-Eramaki et al., 2007; Abdoli-Eramaki et al., 2008); assuming a relationship between the magnitude of electromyographic signals and assistive forces, and then estimating the assistive forces by recording trunk muscles' activities (Marras et al., 2000; Lamers et al., 2018; Weston et al., 2018; Koopman et al., 2019b); and establishing an exoskeleton by testing its characteristic performance beforehand (Koopman et al., 2019a). Nabeshima et al. (2018) developed a non-human testing framework to obtain lumbar torque. These methods, which estimate assistive forces, can be used with an inverse dynamic human model to calculate the actual lumbar load when using exoskeletons.

Further, several statistical methods have been employed to examine lumbar load and other key variables. These methods can be flexibly employed to scrutinize data across various temporal frames—individually, collectively, or even utilizing time-weighted averages—based on the specific demands of their research objectives. For instance, the effect of using exoskeleton on a biomechanical variable can be easily examined using the *t*-test (Abdoli-Eramaki et al., 2007; Whitfield et al., 2014; Lamer et al., 2018). Analysis of variance (ANOVA) would be suitable for evaluating the mixed effect between the testing conditions and exoskeleton modes on users (Marras et al., 2000; Abdoli-Eramaki et al., 2008; Ulrey and Fathallah, 2013; Weston et al., 2018; Koopman et al., 2019a; Koopman et al., 2019b; Poliero et al., 2020). Principle component analysis was used to select the important features and identify the differences of using exoskeletons (Sadler et al., 2011).

Except peak burden, when it is effective to use exoskeletons, and when motion is restricted are also concerned and can contribute to the risk of lumbar injury (Upasani et al., 2019; Omoniyi et al., 2020). Thus it is necessary to consider the effect of the exoskeletons not only on the timing when peak lumbar burden occurs but on the lumbar burden across the whole task. In addition it is also found the phase shift.

To the author's knowledge, the effect of exoskeleton at the time other than the peak value in manual handling tasks has not been well-investigated. Therefore, we employed a time-series analysis method Functional data analysis (FDA), specifically functional ANOVA (FANOVA), which is designed to handle functional data such as biomechanical data, accounting for their continuous nature and temporal dependencies (Ramsey and Silverman, 2005). The FANOVA could be separated into a few steps. First, time-series biomechanical data such as the lumbar load and flexion angle were collected (Section 2.3 and Section 2.4). Second, functions were used to present the waveforms of the biomechanical variables, with B-spline the most commonly used (Ramsey and Siverman, 2005) (Section 2.5.1). Third, the obtained functions were aligned at identical timing points to obtain a representative comparison using a data registration (or data alignment) technique (Godwin et al., 2010) (Section 2.5.1). Finally, the FANOVA model was used to calculate the F-ratio between using and not using the exoskeleton (Section 2.5.2). In agriculture, FANOVA has been used to accurately estimate continuous growth trends (Xu et al., 2018) and demonstrate significant differences in various biomechanical contexts, such as lip kinematics and fatigue-induced kinematics changes (Ramsay et al., 1996; Godwin et al., 2010).

Compared to the traditional *t*-test, ANOVA, and PCA methods, FDA is better at dealing with the time-series dataset. The traditional methods usually identify vital features related to the performance of motions and injury mechanisms from the waveforms of the biomechanical data by referring to some individual points and reducing the dimensionality of the waveforms (Moudy et al., 2018). These methods are limited in that the important features are identified before the data have been analyzed. In contrast, FDA can be applied to multidimensional signals and eliminates the need for the prior identification of the relevant features (Donoghue et al., 2008). In addition, the traditional methods have difficulty finding the differences between groups, and individual differences may produce conditions that will cause timing/phase variability in the waveform (Moudy et al., 2018). For example, in different trials, the subject may not be able to reach the maximal flexions at the same time, while the FDA can help us to minimize the time difference (data alignment) among the maximal flexions, and to maintain the shape and amplitude of each curve. Using this technique, FDA can highlight the features of waveforms to reduce the timing/phase variability so that we can analyze the effect of exoskeletons on the magnitude at all timings, and it is not necessary to identify the peak value or mean value (Moudy et al., 2018). Thus, using FDA to assess the performance of an exoskeleton makes it possible to determine when the exoskeleton can significantly reduce the lumbar load or restrict human motion during a task.

Industrial exoskeleton usage requires safety considerations in high-risk scenarios, such as dynamic symmetrical and asymmetrical lifting tasks (De Looze et al., 2016; Huysamen et al., 2018). FANVOA can be a suitable method for revealing exoskeletons' effect on key variables in each phase of these tasks, thus promoting their standardization.

Although important discrete peak and mean values of the lumbar load and kinematics factors have been studied in exoskeleton evaluations, no method is available to evaluate the effectiveness of various postures during lifting-flexion movement of the exoskeleton. Thus, this study was novel because it not only evaluated the performance of the exoskeleton when variables reached their peak values but also at all other times. This made it possible to identify the variability when using the exoskeleton throughout the entire lifting-flexion motion and assess its applicability to the entire manual handling movement.

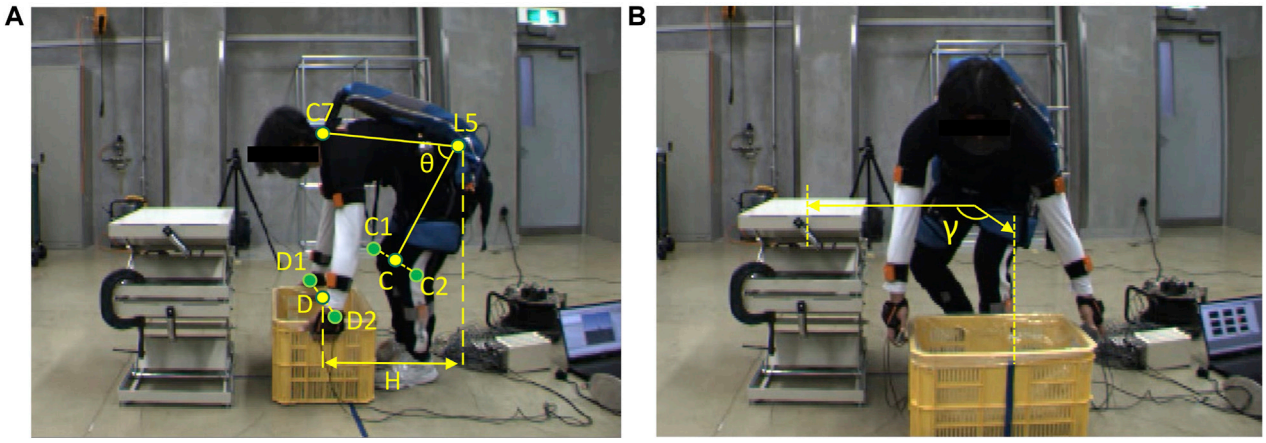

FIGURE 1
Manual handling task of a 10 kg box with an exoskeleton under **(A)** symmetrical and **(B)** asymmetrical conditions.

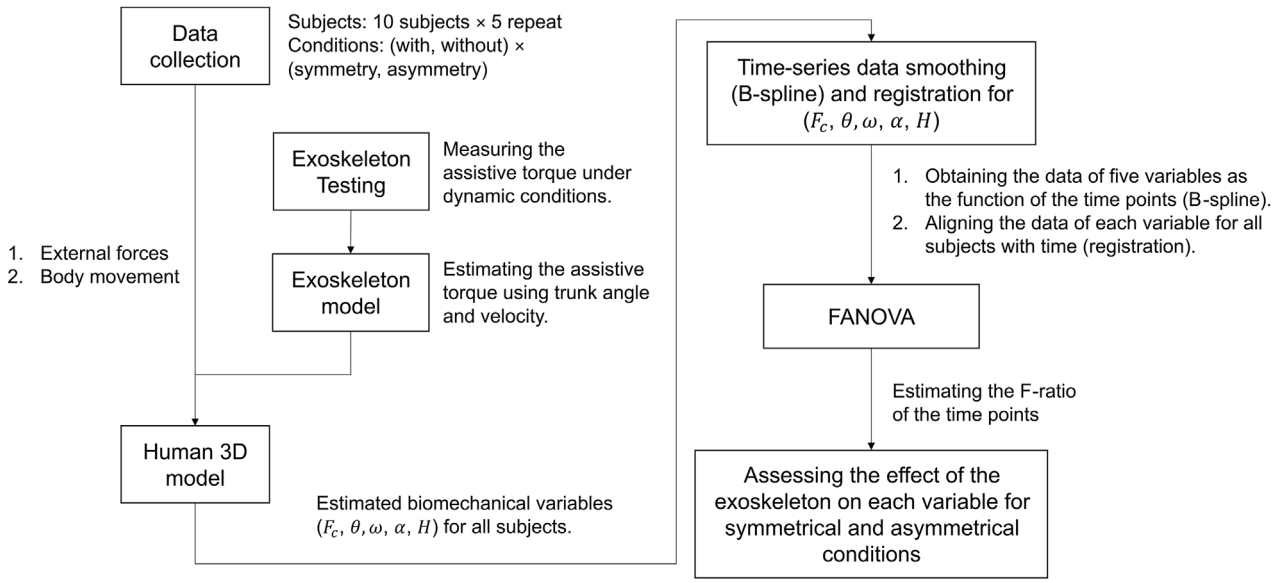

FIGURE 2
The procedure for assessing the effectiveness of the exoskeleton using FANOVA; the movement data are imported into an exoskeleton-human model to estimate the biomechanical variables, which are defined in Section 2.3; then smoothing and registration ensures the data can be presented as functions and aligned with each other; finally, conducting FANOVA and estimate F-ratio to assess the exoskeleton's effect at the time points.

In this study, we mainly focus on developing a FANOVA-based method to evaluate the effects of an exoskeleton on the biomechanical variables at every time point during the manual handling tasks. This analysis allows us to examine when exoskeletons can significantly reduce lumbar load and restrict motions during the task. In addition, we also proposed an exoskeleton–human model to estimate the dynamic lumbar load with the exoskeleton's assistance. It was hypothesized that the FANOVA would demonstrate the exoskeleton, and significantly affect not only the peak biomechanical variables but also that at the other period.

2 Materials and methods

In this study, we used the FANOVA to investigate the effect of the exoskeleton. In this section, 2.1 and 2.2 show the tasks (Figure 1), and instrumentation of this experiment. In the assessment of the exoskeleton, the details are developed as two steps: estimation of biomechanical variables (Section 2.3 and Section 2.4) and FANOVA assessment (Section 2.5 and Section 2.6). As shown in Figure 2, in the first step, using a 3D human model and exoskeleton model to estimate the biomechanical variables, which will be analyzed in the second step using FANOVA after data smoothing and registration,

and finally, the effect of the exoskeleton on each variable can be assessed using F-ratio of time points.

2.1 Participants and tasks

Ten male participants (height: 1.72 ± 0.08 m, body mass: 68.1 ± 8.8 kg, age: 30.9 ± 7.7 years) were recruited and all of them consented to join this experiment. This study was approved by the institutional review board of the Institute of Agricultural Machinery, National Agriculture and Food Research Organization (approval no. Kakushin-ken_Rinri_R03-02). Participants aged 20–40 years were selected because manual handling tasks pose a high risk of low back pain, and young individuals can tolerate relatively high lumbar loads (Kudo et al., 2019).

The manual handling tasks comprised three phases: free-flexion, box-lifting, and box-laying. Figures 1A, B show the beginning of symmetrical and asymmetrical lifting, respectively. The participants performed 2 × 2 non-repetitive tasks (asymmetrical/symmetrical condition with/without the exoskeleton) five times each, the time interval between two trials was around 30 s to reduce the effect of muscle fatigue. The participants' feet were always pointing forward. Prior to the experiment, participants were instructed to perform manual handling tasks at their preferred speed to test their strength.

2.2 Instrumentation

A motion capture system (Xsens MVN Analyze, Xsens, Inc., Enschede, Netherlands) was used to reconstruct motion using IMUs. As shown in Figure 1, 15 IMUs were attached to the participants' heads, shoulders, L5/S1, upper arms, forearms, thighs, shanks, and feet. Two identical force-measuring devices recorded external forces on the hands, each consisting of two three-axis force sensors (USL08-H6, Tec Gihan Co., Ltd., Kyoto, Japan). The box size was 57 cm × 28 cm × 10 cm, with a total mass of 10 kg, which is the limit mass for a normal adult in a one-time lift (ISO 11228-1, 2021). Data recorded at 60 Hz were filtered using a low-pass filter with a 4 Hz cut-off frequency.

2.3 Exoskeleton's effect on biomechanical variables

Lumbar load reduction is the biomechanical criterion for relieving the lumbar burden (Waters et al., 1993). The kinematics variables such as trunk angle, trunk angular velocity, trunk angular acceleration, and the horizontal displacement between the wrist and the lumbar represent the effect of the exoskeleton on the motion restrictions (Potvin, 1997; Marras et al., 2000).

The five representative biomechanical variables are presented as lumbar load (F_c), trunk angle (θ), trunk angular velocity (ω), trunk angular acceleration (α), and horizontal displacement between the wrist and lumbar (H). The trunk angle $\theta = \angle$C7·L5·C is shown in Figure 1A, and the trunk angular velocity and acceleration are the derivatives of the trunk angle and angular velocity, respectively. In Figure 1A, the C7 and L5 positions are determined by virtual markers generated by the motion reconstructed using Xsens MVN Analyze. The wrist (D) and knee (C) positions were determined on the basis of the center of the virtual markers of the left and right wrist (D1, D2), as well as the left and right knee (C1, C2), respectively. During the asymmetrical task, the angle (γ) between the box and the table (65 cm height) in the horizontal plane was 90°, as shown in Figure 1B.

2.4 Lumbar load estimation

2.4.1 Exoskeleton model

The "Muscle Suit Every" (Innophys, Inc., Tokyo, Japan) exoskeleton was used in this study. This exoskeleton uses artificial muscle to provide assistive torque at different trunk angles. In addition, angular velocity influences assistive torque by altering artificial muscle extension speed, which affects the friction force of the artificial muscle and assistive torque generation (Sugimoto et al., 2011; Tondu, 2012). Thus, we used the thin-plate spline (TPS) model for estimating assistive torque based on trunk angle and angular velocity. TPS can provide a robust estimation for spatial data interpolation and surface fitting (Bookstein, 1989; Donato Belongie, 2002).

To establish the TPS model, we used a testing machine to record the assistive torque of the exoskeleton when the trunk angle rotated from 0° to 90° at five speeds (10, 30, 45, 60, and 90°/s) at a sampling rate of 1 kHz (Tanaka et al., 2020). In every test, air pressure of the exoskeleton was set to 0.1 MPa. The tests were repeated at each speed 10 times. Subsequently, the recorded data were processed with a low-pass filter of 10 Hz. The results, shown in Figure 3A, are the relationships between the extension angle and average assistive torque in the 10 trials under each speed condition. Finally, utilizing the TPS method, which was established using MATLAB (version 2022a), the estimated assistive torque could be presented in terms of trunk angle and angular velocity, as shown in Figure 3B. The TPS model's R2 was 0.955 with a root mean square error of 3.70 for all testing data.

2.4.2 Actual lumbar load estimation

As shown in Figure 4, A link-chain human three-dimensional (3D) model was established. The coordinate, movement and center of mass for each segment, and motion reconstruction were recorded using the IMU motion capture system attached to the subject body (data collection). The dynamic link-chain model had nine segments, involving the forearms, upper arms, head, shoulder, thoracic spine, lumbar spine, and pelvis (the lower limbs are not included in the dynamic calculation). The mass of each segment was a proportion of the total body mass, as estimated by a previous study (Winter et al., 2009; Hof, 1992). In addition, the mass of the exoskeleton was added to the center mass at the lumbar segment.

To calculate the lumbar torque, we initially estimated the non-assisted lumbar torque using the top–down inverse dynamic method based on the link-chain human model. Given that the assistive torque only acts in the flexion plane (plane C7L5C in Figure 1A), we subtracted the assistive torque in this plane from the non-assisted torque to obtain the actual torque at the lumbar joint. The geometric model of the trunk muscles was determined using previously reported data (Schultz et al., 1982; Granata and Marras, 1993;

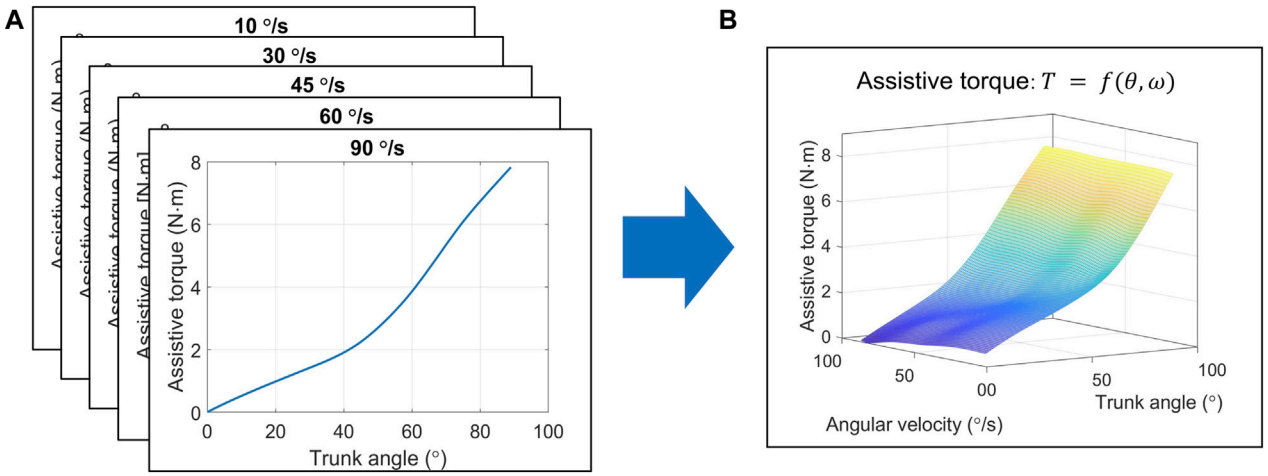

FIGURE 3
Procedure to estimate exoskeleton's assistive torque based on the TPS method. **(A)** The measured assistive torque and trunk angle at different speeds. **(B)** The TPS model estimation of assistive torque using trunk angle and angular velocity. Abbreviations: TPS, thin-plate spline.

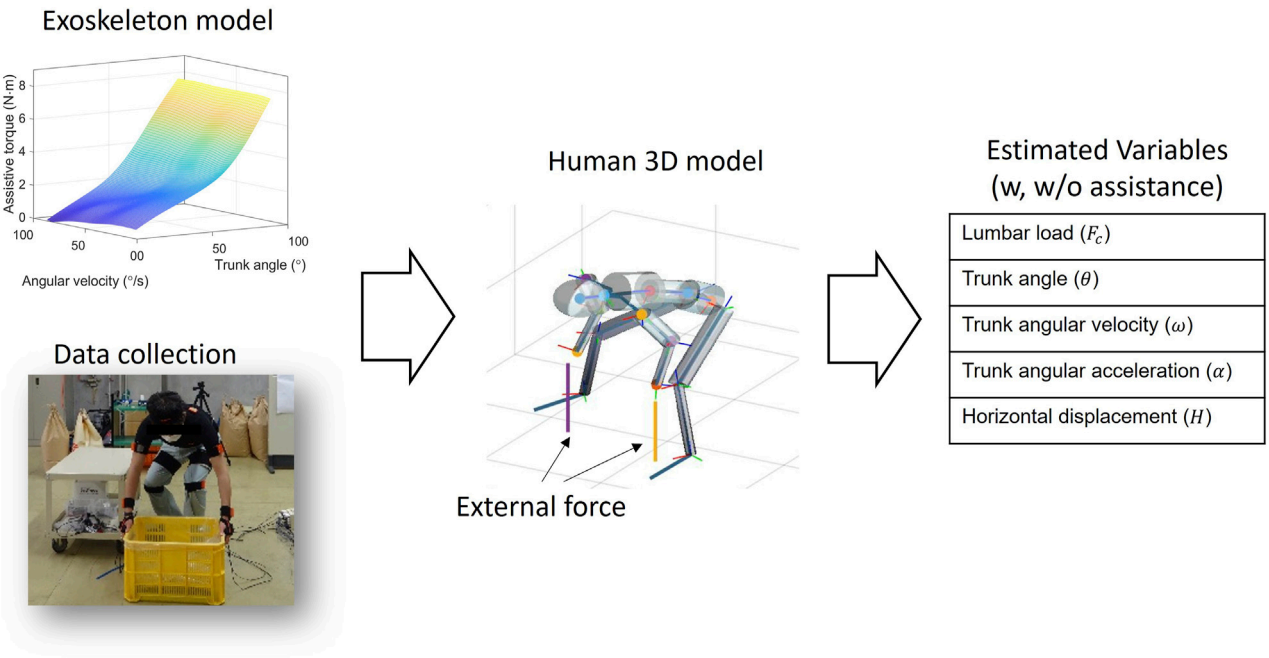

FIGURE 4
Schematic of estimating biomechanical variables using the human 3D model. After obtaining the exoskeleton model, the motion and the external force data are imported into the human 3D model, and then the biomechanical variables are estimated.

Gagnon et al., 2001), and the muscular forces were estimated by minimizing the sum of the trunk muscles' stress square (Anderson and Pandy, 2001). Finally, the lumbar load was obtained by the force resulting from the muscular forces and the upper body load in the direction perpendicular to the lumbar vertebra. The inverse dynamic computation was completed in MATLAB (version 2022a), and the optimization procedure was completed by the quadratic programming algorithm (Stellato et al., 2020).

In order to investigate the accuracy of the 3D human model, we compared the estimated lumbar load from this 3D human model with the *in vivo* data reported by Wilke (Wilke et al., 1999; Wilke et al., 2001) under several body conditions. The estimated lumbar load for each posture was obtained from the average estimation among eight volunteers with a mean body height of 1.72 m and mean body mass of 69 kg, similar to the participant (1.68 m, 70 kg) in Wilke's study.

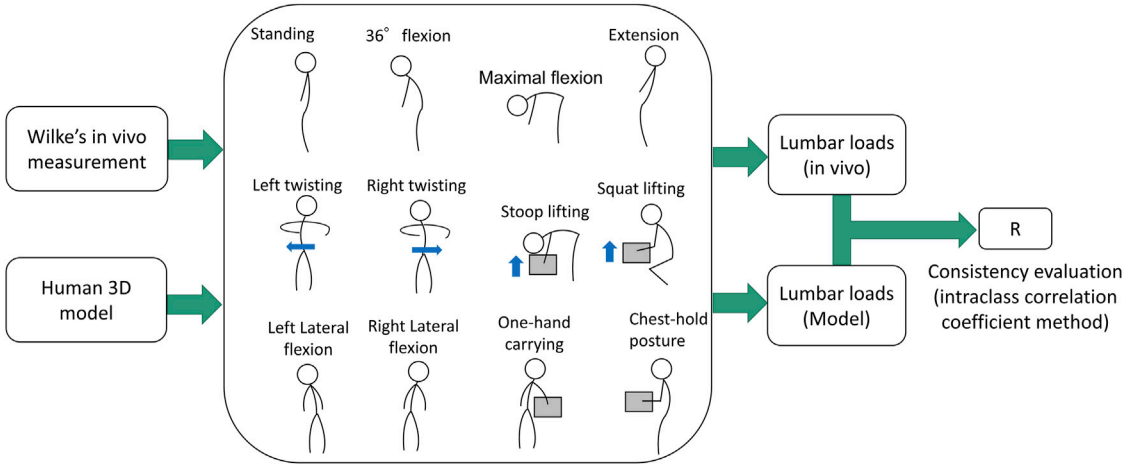

FIGURE 5
Comparison between reported the *in vivo* data and the estimated lumbar load using the 3D human model. The mass of the box is simulated as 20 kg.

The accuracy estimation procedure was presented in Figure 5, where the lumbar loads estimated by the human model at 12 postures including standing, 36° flexion, maximal flexion, extension, lateral flexion, twisting, stoop lifting, squat lifting, one-hand carrying, and close-to-chest handling were compared with these obtained from the reported *in vivo* experiments. The *in vivo* lumbar intradiscal pressure (MPa) estimated by Wilke was converted to lumbar load (N) using the correction factor proposed by Dreischarf et al. (2013). Finally, calculating the R of Intraclass Correlation Coefficient (ICC) between the estimated lumbar loads of the human model and the invasive data for the postures [type of ICC (1,1), and on the 95% confidence interval]. The estimated R is 0.93, which can be explained as excellent reliability (>0.9) (Koo and Li, 2016). The result indicates that the lumbar load estimated by the human model has a high consistency with the *in vivo* data.

2.5 Functional data analysis

2.5.1 Smoothing and processing

This study's biomechanical time-series discrete data, including tracks, angles, and lumbar moment, were converted to functional data in the FDA. In this step, we use a series of the basis functions to fit the recorded biomechanical data and one advantage of this step is to reduce the influence of noise. Since non-repetitive tasks were conducted in this experiment, B-spline is used as the basis function system. Each obtained function can be presented as follows (Ramsay and Silverman, 2005):

$$x_i(t) = \sum_{k=1}^{K} c_{ik}\varphi_k(t) \tag{1}$$

where $x_i(t)$ represents the function converted from the i-th observed data series; t represents the number of time points; c_{ik} represents the coefficients; and $\varphi_k(t)$ are B-spline basis functions with the number, K.

The B-spline fitting functions for the recorded data can be determined using the least square method. The residual sum of squares and a penalty term based on the second derivative of the fitted curve were minimized. The following equation expresses the minimized penalized least squares problem (Ramsay and Siverman, 2005):

$$G = \sum_{i=1}^{N}[X(t_i) - x(t_i)]^2 + \lambda\int_a^b [D^2x(t)]^2 dt \tag{2}$$

where $X(t_i)$ represents the observed data points at the i-th time point (i = 1, 2,. . ., N); $x(t_i)$ represents the estimated data at the i-th time point using the function obtained with Eq. 1; λ is the smoothing variable, which is a non-negative constant that controls the smoothness of the function, with a larger value leading to a smoother function; and $D^2x(t)$ represents the second derivative of the fitted function in time-series. The first part measures goodness of fit between the data points and the fitted function, and its objective is to minimize the residuals. The second part is the penalty term that encourages smoothness in the fitted function by penalizing abrupt changes in curvature; the penalty term is proportional to the integral of the squared second derivative of the function $x(t)$ over the domain (a, b). Thus, this objective function allows us to control the trade-off between the goodness of fit and the smoothness of the function.

Data registration is a technique that aligns generated functional data that might be misaligned. This can improve the ANOVA before estimating the main effects and interactions. We applied data registration to all observed data for each condition and variable using continuous registration (Ramsay and Silverman, 2005).

2.5.2 FANOVA

After obtaining the functional data, we performed FANOVA to investigate the effect of exoskeletons on each variable under symmetrical and asymmetrical conditions. The model for each variable, $f(t)$, with time history can be presented as follows:

$$f(t) = \mu(t) + \alpha_i(t) + \varepsilon(t) \quad (3)$$

where $\mu(t)$ is the mean function indicating the average value of all trials under the symmetrical or asymmetrical condition; $\alpha_i(t)$ represents the effect of using (i = 1) and not (i = 2) exoskeletons on the variable; and $\varepsilon(t)$ is the unexplained variation. We identified the specific effects of using exoskeletons; the constraint added for all t, as $\alpha_1(t) + \alpha_2(t) = 0$.

Then, the model for each variable for each t can be rewritten as a matrix form $\boldsymbol{f}(t)$ as follows:

$$\boldsymbol{f}(t) = \boldsymbol{Z}\boldsymbol{\beta}(t) + \boldsymbol{\varepsilon}(t) \quad (4)$$

where $\boldsymbol{f}(t)$ is the 20 × 1 function vector and $\boldsymbol{Z}$ is the 20 × 3 design matrix, with the 20 rows corresponding to the 10 participants, each contributing with two curves: one when using exoskeletons, and the other when not using them. The first column has ones; the second column has zeros in the first 10 rows, followed by ones; and the final column has ones in the first 10 rows, followed by zeros. $\boldsymbol{\beta}(t)$ is the 3 × 1 vector of parameter functions, with $\boldsymbol{\beta}(t) = [\mu(t), \alpha_1(t), \alpha_2(t)]'$; $\boldsymbol{\varepsilon}(t)$ is the 20 × 1 vector of residual functions.

The vector $\boldsymbol{\beta}(t)$ can be estimated by minimizing the linear minimum mean square error (LMSSE):

$$\mathrm{LMSSE}(\boldsymbol{\beta}) = \int [\boldsymbol{f}(t) - \boldsymbol{Z}\boldsymbol{\beta}(t)]'[\boldsymbol{f}(t) - \boldsymbol{Z}\boldsymbol{\beta}(t)]dt \quad (5)$$

$\mathrm{LMSSE}(\boldsymbol{\beta})$ should be minimized under the condition $\alpha_1(t) + \alpha_2(t) = 0$.

As with traditional ANOVA, the error sum of squares for the residual function and the mean curve were evaluated as a function for each time point in (t) with the following. SSE (sum of squared errors) and SSY (sum of squared in a total) of the model at time t can be calculated as:

$$\mathrm{SSE}(t) = \sum \left[\boldsymbol{f}(t) - \boldsymbol{Z}\hat{\boldsymbol{\beta}}(t)\right]^2 \quad (6)$$

$$\mathrm{SSY}(t) = \sum \left[\boldsymbol{f}(t) - \hat{\mu}(t)\right]^2 \quad (7)$$

where $\hat{\boldsymbol{\beta}}(t)$ is the 20 × 1 vector of the predicted parameters function; $\hat{\boldsymbol{\mu}}(t)$ is the 20 × 1 vector of the predicted mean function of all trials.

The F-ratio determines whether the variance between two data sets is equal, and the FANOVA can evaluate the F-ratio across time t. The F-ratio can be presented as follows:

$$\text{F–ratio}(t) = \frac{[\mathrm{SSY}(t) - \mathrm{SSE}(t)]/\mathrm{df}(\text{error})}{\mathrm{SSE}(t)/\mathrm{df}(\text{regression})} \quad (8)$$

where df(error) is the degree of freedom for error [df(error) = 1], and the df(regression) is the difference in degrees of freedom [df(regression) = 18]. Based on the F-criterion is 4.41. Any time the functional curve F-ratio > F-criterion, the effect of time had reached significance at the chosen α level of 0.05.

2.6 Statistical analysis

For all tasks, the paired t-test (at an α level of 0.05) was used to compare the peak values of the lumbar load, trunk angle, angular velocity, angular acceleration, and horizontal distance between the wrist and lumbar spine under symmetrical and asymmetrical conditions. Subsequently, the result of t-test was compared to that of FANOVA, which was utilized to examine the continuous effect of the exoskeletons on these variables throughout the normalized manual handling tasks. The F-ratio, obtained as time history, was compared to the F-criterion at an α level of 0.05.

The functional analysis for time-series data was performed using the package developed by Ramsey and Silverman, available at https://www.psych.mcgill.ca/misc/fda/downloads/FDAfuns/. All the statistical analyses were conducted using MATLAB (version 2022a).

3 Results

3.1 T-test analysis: effect on peak values of each variable

The estimated peak variables of lumbar load, trunk angle, angular velocity, angular acceleration, and horizontal displacement between the wrist and lumbar are shown in Figure 6, which shows the average peak variables and standard deviations for all participants. Peak lumbar load and angular velocity were significantly lower ($p < 0.05$) when using the exoskeleton during both tasks; however, peak horizontal displacement was significantly lower only during asymmetrical tasks ($p < 0.01$). Compared with not using exoskeletons, using them reduced peak lumbar load by 388 N (14%) and 427 N (17%) during both tasks, respectively. Similarly, the peak trunk angular velocity reduction was 23°/s (24%) and 25°/s (24%) under both conditions. During asymmetrical tasks, the peak horizontal displacement was reduced by 0.02 m (5%). No significant difference was observed in peak trunk angles and angular acceleration variables for both tasks.

3.2 FANOVA: effect on time-series values of each variable

The results of the functional analysis, as presented in Figures 7–9, demonstrate the effect of using exoskeletons on different variables during asymmetrical and symmetrical tasks.

During asymmetrical tasks (Figure 7), the exoskeleton reduced lumbar load by 412, 393, and 383 N with the greatest significant differences during the flexion, lifting, and laying phases, respectively. In addition, the most significant lumbar load reduction (412 N, F-ratio = 33.8) for all phases occurred during the flexion phase (31.7%), as shown in Figure 9. Reductions in the kinematic variables of trunk angle, angular velocity, and angular acceleration were observed in all phases (Figure 7), indicating the exoskeletons' impact on posture and movement restrictions during asymmetrical tasks. As shown in Figure 9, the most significant reduction (5.5°, F-ratio = 18.6) in trunk angle occurred during the laying phase (86.1%); for trunk angular velocity, the reduction (20.0°/s, F-ratio = 18.1) occurred during the flexion phase (14.1%); and for trunk angular acceleration, the reduction (61.5°/s^2, F-ratio = 18.6) occurred during the flexion phase (20.0%). Horizontal displacement was only significantly reduced during the lifting phase (61.9%), by 0.02 m (F-ratio = 11.1).

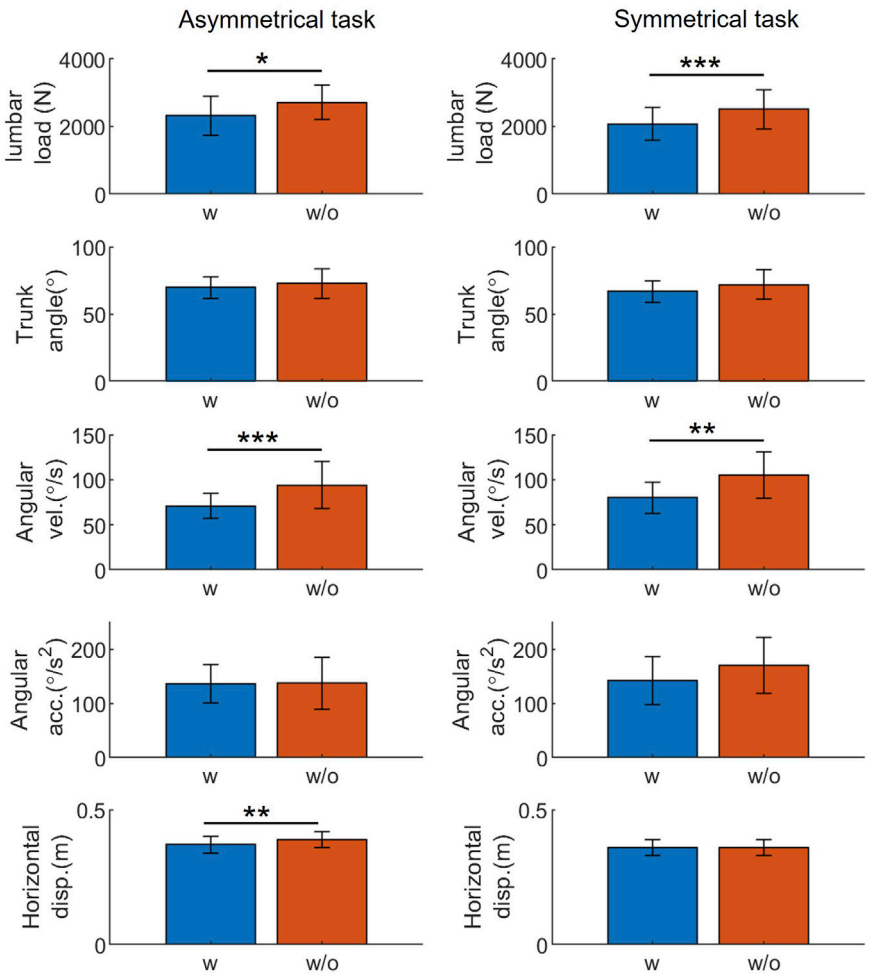

FIGURE 6
The *t*-test result: exoskeletons' influence on the peak value of representative variables during manual handling tasks. Abbreviations: acc., acceleration; disp., displacement; vel., velocity; w, with; w/o, without (*$p < 0.05$; **$p < 0.01$; ***$p < 0.005$).

During symmetrical tasks (Figure 8), the exoskeleton reduced lumbar load by 300, 672, and 280 N with the greatest significant differences during the flexion, lifting, and laying phases, respectively. The most significant lumbar load reduction (300 N, F-ratio = 35.9) for all phases occurred during the flexion phase (26.7%) (Figure 9). Similarly, in asymmetrical tasks, reductions in the kinematic variables such as trunk angle, angular velocity, and angular acceleration were observed in all phases (Figure 8). As shown in Figure 9, the most significant reduction in trunk angle (5.9°, F-ratio = 20.6) occurred during the laying phase (83.2%) and that in trunk angular velocity (22.5°/s, F-ratio = 24.1) during the flexion phase (13.4%). For trunk angular acceleration, the reduction (79.4°/s^2, F-ratio = 16.8) occurred during the flexion phase (10.6%). The patterns of the above kinematic variables were also similar to those in asymmetrical tasks. Horizontal displacement was significantly reduced during the lifting (15.8%) and flexion (42.6%) phases by 0.02 m with similar F-ratios (5.3 vs. 4.8).

Except for providing assistive torque, exoskeletons can reduce the lumbar load by restricting movements. As shown in Figures 7, 8, some significant overlaps were observed between the F-ratio of the lumbar load and the kinematic variables in each phase. During the flexion phase, these overlaps of the significant F-ratios were as follows: lumbar load: 13%–31%; trunk angle: 13%–24%; angular velocity: 13%–18%, 25%–31% (in the flexion phase, both periods were where F-ratios of angular velocity were significant); angular acceleration: 15%–30%; and horizontal displacement: 14%–17%. During the lifting phase, lumbar load: 35%–45%; trunk angle: 39%–49%; angular velocity: 41%–45%; and horizontal displacement: 41%–43%. During the laying phase, lumbar load: 56%–100%; trunk angle: 73%–100%; angular velocity: 56%–58%; and angular acceleration: 79%–82%. These overlaps show the consistency between the reduction of lumbar load and that of kinematic variables, which indicate that the lumbar load reduction is not only affected by lumbar moment reduction but also by restricting the kinematic variables when using the exoskeletons.

4 Discussion

4.1 T-test analysis: effect on peak values of each variable

The findings presented in Figure 6 show that exoskeletons significantly affect the representative biomechanical variables

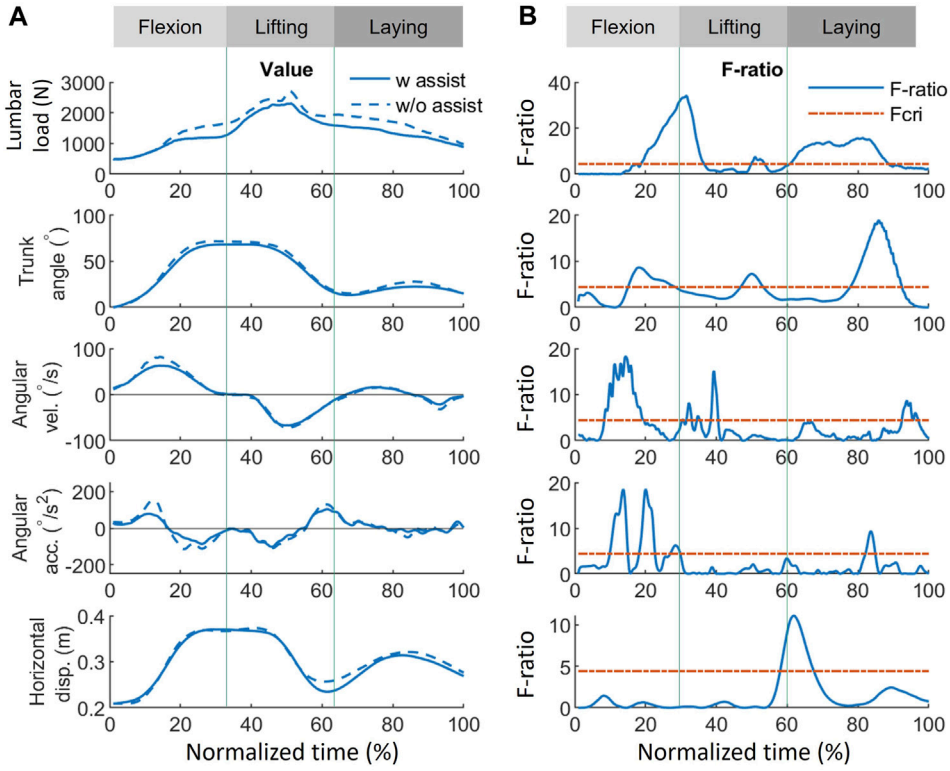

FIGURE 7
Effect of using exoskeletons on the variables during asymmetrical tasks. **(A)** Absolute values of the variables when using (solid line) and not using (dash line) exoskeletons, where positive (+) and negative (−) for angular velocity and acceleration represent flexion and lifting, respectively. **(B)** The corresponding F-ratio generated by FANOVA (solid line) and Fcri = 4.41 with statistical significance at an α level of 0.05 (red dash line). The whole normalized time is separated into flexion (0%–33%), lifting (33%–67%), and laying (67%–100%) phases. Abbreviations: FANOVA, functional analysis of variance; Fcri, F-criterion; acc., acceleration; disp., displacement; vel., velocity; w, with; w/o, without.

during symmetrical and asymmetrical tasks. Exoskeleton use substantially reduced peak lumbar load and motion speed, consistent with previous findings (Koopman et al., 2019b). Increasing trunk angular velocity requires greater trunk muscle activation (Dolan and Adams, 1993). This result aligns with those of previous studies, suggesting that exoskeletons help reduce lumbar load and muscle activation (Huysamen et al., 2018; Lamer et al., 2018), thus, lowering the risk of musculoskeletal disorders and enhancing worker comfort.

No significant differences were detected in peak trunk angles and angular accelerations, in contrast to angular velocity, for both tasks. Thus, it results difficult to infer from peak values whether exoskeletons limit the range of motion or hinder human movement while providing support and reducing lumbar load. Previous studies have yielded mixed results on the exoskeletons' influence on trunk angle: reduction was observed on the nylon elastic support, while no reduction was shown for another passive exoskeleton (Laevo V2.4 Delft, Netherlands) (Marras et al., 2000; Koopman et al., 2019a). The differing results from our experiment and previous studies regarding the influence of exoskeleton on trunk angle can be attributed to variations in design.

The lumbar reduction of the current exoskeleton can meet the 3.4 kN average lumbar load criterion recommended by the National Institute of Occupational Safety and Health (Waters et al., 1993), as shown in Figure 6. However, the lumbar load limit will vary across age groups and sexes (Genaidy et al., 1993). Aging societies have a growing population of older workers, whose lumbar load limit is 1.69 kN lower than that of younger workers (Kudo et al., 2019). Women have lower lumbar load limits than men (Genaidy et al., 1993; Kudo et al., 2019). Thus, deterministic assistive forces should consider lumbar load limits for different age groups and sexes.

4.2 FANOVA: effect on time-series values of each variable

FANOVA enables a more comprehensive examination of the effects of exoskeletons on variables throughout an entire task rather than focusing solely on peak values. The FANOVA results suggested that exoskeletons can alleviate lumbar burden at peak load timings and throughout all task phases (Figure 9). The lumbar load reduction in Figures 7, 8 implies that exoskeletons are probably effective in reducing the lumbar load in all phases during asymmetrical tasks while being much more effective in the lifting phase during symmetrical tasks. Asymmetrical lifting reportedly results in a higher lumbar load than symmetrical lifting, implying that workers are more easily prone to getting lumbar injuries during asymmetrical lifting (Kim and Zhang, 2017). Therefore, improving exoskeletons' performance during asymmetrical lifting can reduce users' lumbar injury risks.

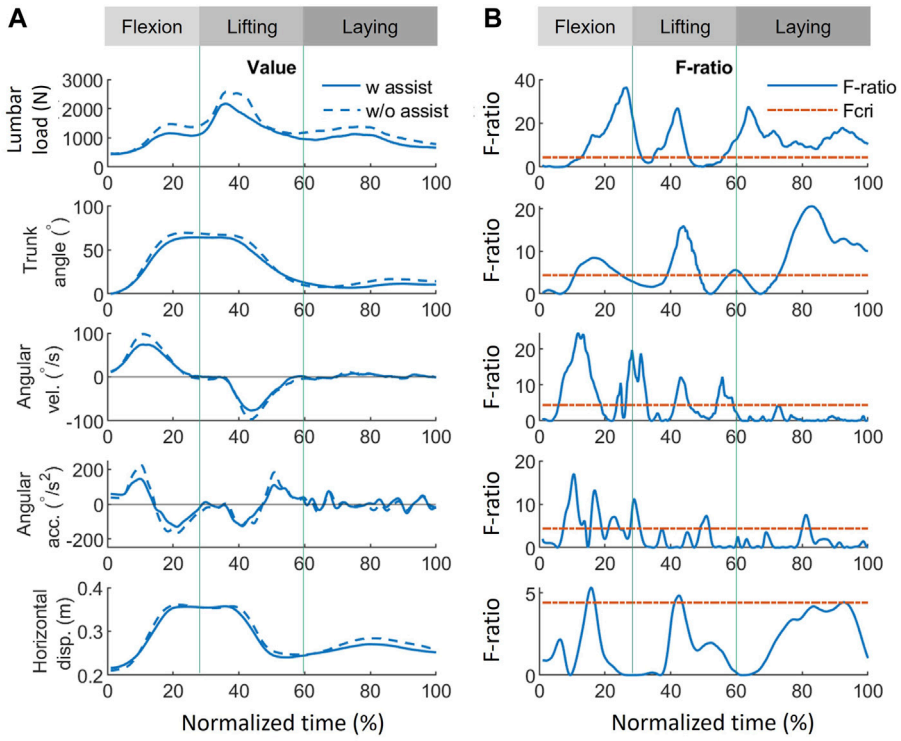

FIGURE 8
Effect of using exoskeletons on the variables during symmetrical tasks. **(A)** Absolute values of the variables when using (solid line) and not using (dash line) exoskeletons, where positive (+) and negative (–) for angular velocity and acceleration represent flexion and lifting, respectively. **(B)** The corresponding F-ratio obtained by FANOVA (solid line) and Fcri = 4.41 (red dash line). The whole normalized time is separated into flexion (0%–30%), lifting (30%–60%), and laying (60%–100%) phases. Abbreviations: FANOVA, functional analysis of variance; Fcri, F-criterion; acc., acceleration; disp., displacement; vel., velocity; w, with; w/o, without.

The reduced trunk angle, angular velocity, and acceleration during both manual handling tasks suggest a similar tendency when exoskeletons assist participants. The results indicated that using the exoskeleton imposes significant restrictions on body movement at larger flexion postures (>25°), in the vicinity of peak lumbar load occurrence, and throughout most of the box-laying movements in both tasks. The most significant reduction in angular velocity and acceleration occurred in the middle of flexion, implying that the human body may experience greater kinematic restrictions from exoskeleton use when not under loading conditions. This could be a reason for exoskeletons not supporting the lumbar load in a small trunk angle, which will be discussed subsequently. However, the restrictions on horizontal displacement differ between symmetrical and asymmetrical conditions. Under asymmetrical conditions, a significant reduction occurred at the end of lifting. In contrast, in symmetrical tasks, restrictions occurred in the middle of flexion and the vicinity of peak lumbar load occurrence. Determining the relationship between these changes using other variables in this study was challenging. This discrepancy in horizontal displacement restrictions may originate from the interaction between the trunk and upper limbs.

Comparing lumbar load and trunk angle in Figures 7, 8, significant reductions when using the exoskeletons were difficult to observe when the trunk angle was less than 25°. The only exception was during the asymmetrical lifting phase, when a significant lumbar load reduction occurred even with a trunk angle smaller than 25°. This lumbar load reduction was likely the result of reduced horizontal displacement rather than trunk angle changes. These results suggest that exoskeletons at smaller trunk angles (<25°) neither significantly reduce lumbar load nor restrict trunk movement. Since the greatest lumbar load typically occurs at larger trunk angles, this design approach may prioritize allowing users a greater range of motion and, consequently, sacrifice effectiveness at smaller trunk angles. This trade-off between range of motion and lumbar load reduction at smaller trunk angles may be a deliberate design choice to improve user comfort and task efficiency while offering lumbar support when needed.

Although restricting body movement may lead to inconvenience, adopting a low-speed or small-inclination posture will lead to lower lumbar injury risk (Marras et al., 1993; Waters et al., 1993). In addition, the lumbar load can also be reduced by decreasing the kinematic variables. The overlap of F-ratios with significance (F-ratio > 4.41) suggests that the reduction in lumbar load is affected by the kinematic variables in all phases. Significant trunk angle and horizontal displacement reductions were observed near peak lumbar load during symmetrical tasks. During asymmetrical tasks, only trunk angle reduction was noted. Quantitatively evaluating the impact of each kinematic factor on lumbar load reduction using FANOVA in conjunction with established ergonomic equations is possible (Potvin, 1997; Merryweather et al., 2009; Arjmand et al., 2011; Arjmand et al.,

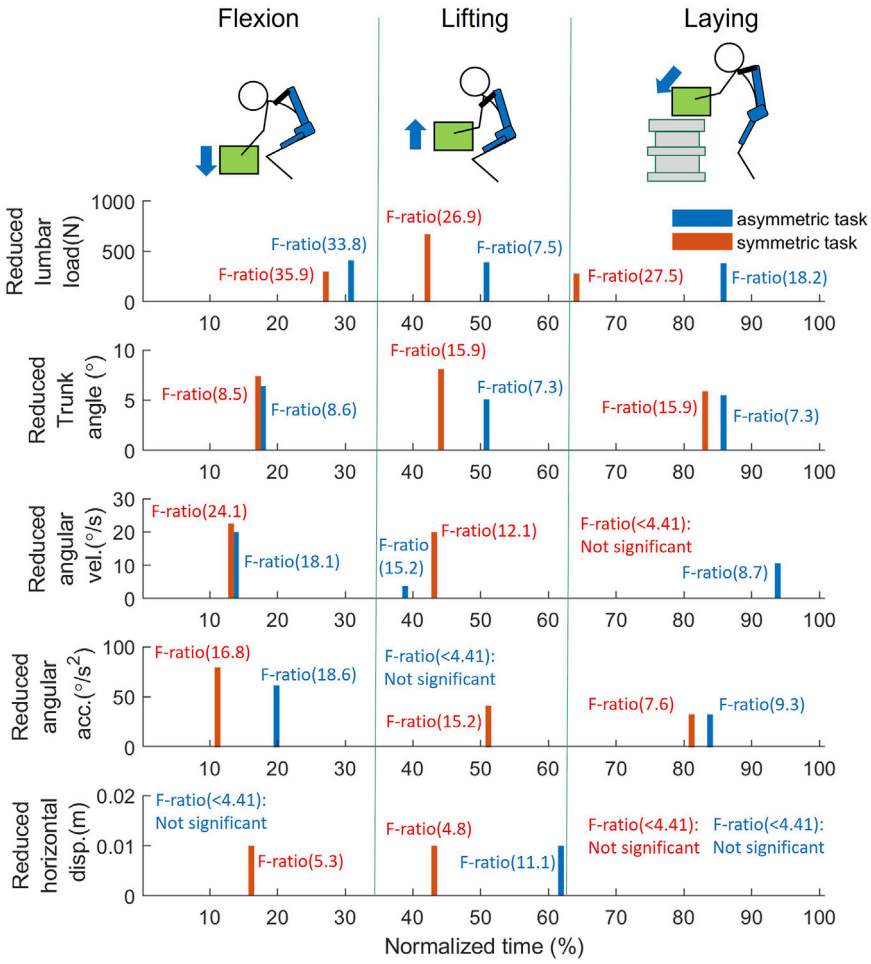

FIGURE 9
FANOVA result: The reduced variables at the peak F-ratio timing for each phase during the manual handling task between w, and w/o assistance; The bar values, representing the reduction of each variable (blue: asymmetrical task; red: symmetrical task), and are obtained at the peak F-ratio of flexion, lifting, and laying phase, respectively. As F-ratio is smaller than 4.41, it is considered no significant difference is found between w, and w/o assistance. Abbreviations: acc., acceleration; disp., displacement; vel., velocity.

2012). Although quantitative assessment methods for the inconvenience of exoskeletons are lacking, the discomfort in kinematic restrictions probably results from contact pressure and friction (Baltrusch et al., 2018; Huysamen et al., 2018). Further investigation into the complex interplay between the various biomechanical variables and the different conditions could improve the understanding of the effects of exoskeleton use on human kinematics.

4.3 Exoskeleton simulation method

Direct measurement methods, such as electromyography or extension force, may introduce errors due to individual differences (Marras et al., 2000; Abdoli-Eramaki et al., 2007; Lamers et al., 2018). To address this, we employed a 3D interpolation method, the TPS, to represent the relationship between extension angle, angular velocity, and assistive torque. Comparing to torque–angle relationship (Koopman et al., 2019a), our approach accounts for certain dynamic factors affecting assistive torque. The advantages of TPS include efficient overfitting reduction through regularization, reduced computational complexity once the analytical form of the TPS model can be obtained, and adaptability to multidimensional datasets (Bookstein, 1989; Donato and Belongie, 2002), making it suitable for modeling various exoskeletons whose assistive torques may be influenced by different factors. Consequently, TPS is expected to contribute to exoskeleton standardization. By incorporating TPS in exoskeleton testing and refining FANOVA assessment methods, researchers can develop more effective, comfortable, and efficient exoskeletons that cater to workers' diverse needs in various industries.

4.4 Comparison between FANOVA and other methods

Compared to the traditional methods such as a *t*-test or ANOVA, FANOVA includes a smoothing and data registration procedure that reduces the noise and variability of the timing/phases. Therefore, the biomechanical variables can be analyzed at each time point.

In this study, we conducted a *t*-test and determined how the peak value was affected by the dynamic movement of an exoskeleton. However, it was difficult to investigate the significant differences in the variables at the other time points because of the variability of the timing/phases of subjects. To reduce this variability, previous studies usually had subjects maintain specific postures before applying a *t*-test or ANOVA (Lamers et al., 2018; Koopman et al., 2019a). For example, Lamers et al. (2018) found that using an exoskeleton could significantly reduce a user's lumbar load under flexion angles of 30°, 60°, and 90°. However, the static assumption may cause the lumbar load to be underestimated compared with those of actual tasks, which are usually dynamic (van Dieën et al., 2010). Moreover, it is a significant task to evaluate the effectiveness of an exoskeleton at all flexion angles, users are normally concerned about how to best use it (Upasani et al., 2019). In contrast, FANOVA makes it possible to evaluate the reduction in the dynamic lumbar load resulting from the use of an exoskeleton, and we found that the lumbar load was reduced at the majority of the flexion angles, with the exception of small angles (<25°) or during a flexion-lifting shift. Thus, compared to the traditional *t*-test and ANOVA, FANOVA can find the most effective conditions for using an exoskeleton.

FANOVA can also find the difference in the flexion angle at times other than under peak or specific conditions. Using a *t*-test, no significant difference can be found in the peak flexion angle under either a dynamic movement (Figure 6) or in static postures (Lamers et al., 2018). However, FANOVA shows that a significant restriction of the trunk angle can be found in all phases when an exoskeleton is used (Figures 7, 8). This could be because the exoskeleton mainly affects the flexion angle not at the beginning or end of lifting or flexion, but during the middle of the task.

The results of this study are expected to contribute to safety standards for exoskeletons. The safety requirements set forth in the international standard for wearable robots, ISO 13482, are limited only to conceptual design guidelines. This study investigated a method that is expected to assist manufacturers in quantitatively evaluating their products throughout the entire movement process and guide users in the appropriate use of an exoskeleton in lifting-flexion tasks.

4.5 Limitations

This study had a few limitations. First, this study relied on a single type of exoskeleton, although design can significantly influence an exoskeleton's effectiveness in reducing lumbar load and modifying kinematic variables (Baltrusch et al., 2018; Kozinc et al., 2020; Luger et al., 2021). Second, the complex and time-intensive computations involved in FDA, such as the data registration procedure, may present challenges as the curves involve a considerable amount of data from lengthy experiments.

Furthermore, multiple comparisons may pose limitations. As the number of exoskeleton modes increases and significant differences are assessed at each time point, methods such as the Bonferroni adjustment, which may reduce the statistical power of the analysis, can be used (Khalaf et al., 1999). An alternative approach is establishing a critical number of simultaneous F-ratios that must exceed the F-crit to be considered significant for that period. However, the optimal number of F-ratios for this method remains unestablished (Godwin et al., 2010).

Other than the criteria mentioned, cumulative load can also contribute to low back pain. However, the lack of a safety criterion for cumulative load makes evaluating the safety of exoskeletons' assistance on this variable difficult, and the value of the safety criterion will affect the evaluation of the exoskeletons' assistance.

This experiment took an interval of around 30 s between two tasks. However, considering individual differences, taking a maximal voluntary contraction (MVC) test after resting would be a better way to confirm whether the rest time was sufficient to reduce muscle fatigue, which was a limitation of our work.

Despite these limitations, the study demonstrates the potential of using FANOVA to assess the effectiveness of exoskeletons in various manual handling tasks. Future research could focus on refining measurement techniques, developing more accessible tools for FANOVA, and exploring alternative statistical approaches for handling multiple comparisons.

5 Conclusion

A dynamic assessment method based on FANOVA was used to investigate the effect of utilizing exoskeletons on five representative biomechanical variables. The result implied that exoskeletons could reduce the lumbar load during manual handling tasks, particularly under symmetrical lifting conditions. The significant reductions in lumbar load and kinematic variables indicate that exoskeletons are crucial in protecting users' lumbar spine and reducing the risk of low back injury. Furthermore, the exoskeletons achieve this reduction by restricting movement, which helps to maintain proper posture during handling tasks. The results also showed how exoskeletons indirectly affect the lumbar load, influencing other kinematic variables in time history. These findings contribute to developing safer and more effective exoskeleton designs, ultimately enhancing the practical adoption of exoskeletons in various scenarios involving manual handling tasks such as in agriculture, industry, and physical rehabilitation.

Data availability statement

The raw data supporting the conclusion of this article will be made available by the authors, without undue reservation.

Ethics statement

The studies involving humans were approved by the institutional review board of the Institute of Agricultural Machinery, National Agriculture and Food Research Organization. The studies were conducted in accordance with the local legislation and institutional requirements. The participants provided their written informed consent to participate in this study.

Author contributions

XX: Conceptualization, Data curation, Formal Analysis, Methodology, Validation, Writing–original draft. MT:

Conceptualization, Data curation, Funding acquisition, Methodology, Writing–original draft. SU: Methodology, Resources, Writing–review and editing. YuK: Conceptualization, Funding acquisition, Writing–review and editing. YoK: Resources, Writing–original draft.

Funding

The author(s) declare financial support was received for the research, authorship, and/or publication of this article. This research was supported by the Japan Society for the Promotion of Science (JSPS) KAKENHI (Grant Number JP21K05865).

Conflict of interest

The authors declare that the research was conducted in the absence of any commercial or financial relationships that could be construed as a potential conflict of interest.

Publisher's note

References

Abdoli-E, M., and Stevenson, J. M. (2008). The effect of on-body lift assistive device on the lumbar 3D dynamic moments and EMG during asymmetric freestyle lifting. Clin. Biomech. *(Bristol, Avon)* 23 (3), 372–380. doi:10.1016/j.clinbiomech.2007.10.012

Abdoli-Eramaki, M., Stevenson, J. M., Reid, S. A., and Bryant, T. J. (2007). Mathematical and empirical proof of principle for an on-body personal lift augmentation device (PLAD). *J. Biomech.* 40 (8), 1694–1700. doi:10.1016/j.jbiomech.2006.09.006

Ajoudani, A., Zanchettin, A. M., Ivaldi, S., Albu-Schäffer, A., Kosuge, K., and Khatib, O. (2018). Progress and prospects of the human–robot collaboration. *Aut. Robots* 42, 957–975. doi:10.1007/s10514-017-9677-2

Anderson, F. C., and Pandy, M. G. (2001). Static and dynamic optimization solutions for gait are practically equivalent. *J. Biomech.* 34 (2), 153–161. doi:10.1016/s0021-9290(00)00155-x

Arjmand, N., Plamondon, A., Shirazi-Adl, A., Larivière, C., and Parnianpour, M. (2011). Predictive equations to estimate spinal loads in symmetric lifting tasks. *J. Biomech.* 44 (1), 84–91. doi:10.1016/j.jbiomech.2010.08.028

Arjmand, N., Plamondon, A., Shirazi-Adl, A., Parnianpour, M., and Larivière, C. (2012). Predictive equations for lumbar spine loads in load-dependent asymmetric one- and two-handed lifting activities. Clin. Biomech. *(Bristol, Avon)* 27 (6), 537–544. doi:10.1016/j.clinbiomech.2011.12.015

Baltrusch, S. J., van Dieën, J. H., van Bennekom, C. A. M., and Houdijk, H. (2018). The effect of a passive trunk exoskeleton on functional performance in healthy individuals. *Appl. Ergon.* 72, 94–106. doi:10.1016/j.apergo.2018.04.007

Bookstein, F. L. (1989). Principal warps: thin-plate splines and the decomposition of deformations. *IEEE Trans. Pattern Anal. Mach. Intell.* 11 (6), 567–585. doi:10.1109/34.24792

De Looze, M. P., Bosch, T., Krause, F., Stadler, K. S., and O'Sullivan, L. W. (2016). Exoskeletons for industrial application and their potential effects on physical work load. *Ergonomics* 59 (5), 671–681. doi:10.1080/00140139.2015.1081988

Dolan, P., and Adams, M. A. (1993). The relationship between EMG activity and extensor moment generation in the erector spinae muscles during bending and lifting activities. *J. Biomech.* 26 (4–5), 513–522. doi:10.1016/0021-9290(93)90013-5

Donato, G., and Belongie, S. (2002). Approximate thin plate spline mappings. *Comput. Vision—ECCV 2002. Proc. Part Iii 7th Eur. Conf. Comput. Vis. Cph.* 7, 21–31. doi:10.1007/3-540-47977-5_2

Donoghue, O. A., Harrison, A. J., Coffey, N., and Hayes, K. (2008). Functional data analysis of running kinematics in chronic Achilles tendon injury. *Med. Sci. sports Exerc.* 40 (7), 1323–1335. doi:10.1249/mss.0b013e31816c4807

Dreischarf, M., Rohlmann, A., Zhu, R., Schmidt, H., and Zander, T. (2013). Is it possible to estimate the compressive force in the lumbar spine from intradiscal pressure measurements? A finite element evaluation. *Med. Eng. Phys.* 35 (9), 1385–1390. doi:10.1016/j.medengphy.2013.03.007

Gagnon, D., Larivière, C., and Loisel, P. (2001). Comparative ability of EMG, optimization, and hybrid modelling approaches to predict trunk muscle forces and lumbar spine loading during dynamic sagittal plane lifting. Clin. Biomech. *(Bristol, Avon)* 16 (5), 359–372. doi:10.1016/s0268-0033(01)00016-x

Genaidy, A. M., Waly, S. M., Khalil, T. M., and Hidalgo, J. (1993). Spinal compression tolerance limits for the design of manual material handling operations in the workplace. *Ergonomics* 36 (4), 415–434. doi:10.1080/00140139308967899

Godwin, A., Takahara, G., Agnew, M., and Stevenson, J. (2010). Functional data analysis as a means of evaluating kinematic and kinetic waveforms. *Theor. Issues Ergon. Sci.* 11 (6), 489–503. doi:10.1080/14639220903023368

Granata, K. P., and Marras, W. S. (1993). An EMG-assisted model of loads on the lumbar spine during asymmetric trunk extensions. *J. Biomech.* 26 (12), 1429–1438. doi:10.1016/0021-9290(93)90093-t

Hasegawa, Y., and Muramatsu, M. (2013). "Wearable lower-limb assistive device for physical load reduction of caregiver on transferring support," in *IEEE/ASME international conference on advanced intelligent mechatronics*, 1027–1032. doi:10.1109/AIM.2013.6584229

Hof, A. L. (1992). An explicit expression for the moment in multibody systems. *J. Biomech.* 25 (10), 1209–1211. doi:10.1016/0021-9290(92)90076-d

Huysamen, K., de Looze, M., Bosch, T., Ortiz, J., Toxiri, S., and O'Sullivan, L. W. (2018). Assessment of an active industrial exoskeleton to aid dynamic lifting and lowering manual handling tasks. *Appl. Ergon.* 68, 125–131. doi:10.1016/j.apergo.2017.11.004

ISO (2014). *Robots and robotic devices – safety requirements for personal care robots*.

ISO 11228-1:2021 (2021). *Ergonomics — manual handling — Part 1: lifting, lowering and carrying*.

Khalaf, K. A., Parnianpour, M., Sparto, P. J., and Barin, K. (1999). Feature extraction and quantification of the variability of dynamic performance profiles due to the different sagittal lift characteristics. *IEEE Trans. Rehabil. Eng.* 7 (3), 278–288. doi:10.1109/86.788465

Kim, H. K., and Zhang, Y. (2017). Estimation of lumbar spinal loading and trunk muscle forces during asymmetric lifting tasks: application of whole-body musculoskeletal modelling in OpenSim. *Ergonomics* 60 (4), 563–576. doi:10.1080/00140139.2016.1191679

Kobayashi, H., Aida, T., and Hashimoto, T. (2009). Muscle suit development and factory application. *Int. J. Autom. Technol.* 3 (6), 709–715. doi:10.20965/ijat.2009.p0709

Koo, T. K., and Li, M. Y. (2016). A guideline of selecting and reporting intraclass correlation coefficients for reliability research. *J. Chiropr. Med.* 15 (2), 155–163. doi:10.1016/j.jcm.2016.02.012

Koopman, A. S., Kingma, I., Faber, G. S., De Looze, M. P., and van Dieën, J. H. (2019a). Effects of a passive exoskeleton on the mechanical loading of the low back in static holding tasks. *J. Biomech.* 83, 97–103. doi:10.1016/j.jbiomech.2018.11.033

Koopman, A. S., Toxiri, S., Power, V., Kingma, I., van Dieën, J. H., Ortiz, J., et al. (2019b). The effect of control strategies for an active back-support exoskeleton on spine loading and kinematics during lifting. *J. Biomech.* 91, 14–22. doi:10.1016/j.jbiomech.2019.04.044

Kozinc, Ž., Baltrusch, S., Houdijk, H., and Šarabon, N. (2020). Reliability of a battery of tests for functional evaluation of trunk exoskeletons. *Appl. Ergon.* 86, 103117. doi:10.1016/j.apergo.2020.103117

Kudo, N., Yamada, Y., and Ito, D. (2019). Age-related injury risk curves for the lumbar spine for use in low-back-pain prevention in manual handling tasks. *ROBOMECH J.* 6, 12. doi:10.1186/s40648-019-0139-9

Lamers, E. P., Yang, A. J., and Zelik, K. E. (2018). Feasibility of a biomechanically-assistive garment to reduce low back loading during leaning and lifting. *IEEE Trans. Biomed. Eng.* 65 (8), 1674–1680. doi:10.1109/TBME.2017.2761455

Luger, T., Bär, M., Seibt, R., Rimmele, P., Rieger, M. A., and Steinhilber, B. (2021). A passive back exoskeleton supporting symmetric and asymmetric lifting in stoop and squat posture reduces trunk and hip extensor muscle activity and adjusts body posture–A laboratory study. *Appl. Ergon.* 97, 103530. doi:10.1016/j.apergo.2021.103530

Marras, W. S., Jorgensen, M. J., and Davis, K. G. (2000). Effect of foot movement and an elastic lumbar back support on spinal loading during free-dynamic symmetric and asymmetric lifting exertions. *Ergonomics* 43 (5), 653–668. doi:10.1080/001401300184314

Marras, W. S., Lavender, S. A., Leurgans, S. E., Rajulu, S. L., Allread, W. G., Fathallah, F. A., et al. (1993). The role of dynamic three-dimensional trunk motion in occupationally-related low back disorders. The effects of workplace factors, trunk position, and trunk motion characteristics on risk of injury. Spine *(Phila Pa 1976)* 18 (5), 617–628. doi:10.1097/00007632-199304000-00015

Merryweather, A. S., Loertscher, M. C., and Bloswick, D. S. (2009). A revised back compressive force estimation model for ergonomic evaluation of lifting tasks. *Work* 34 (3), 263–272. doi:10.3233/WOR-2009-0924

Moudy, S., Richter, C., and Strike, S. (2018). Landmark registering waveform data improves the ability to predict performance measures. *J. biomechanics* 78, 109–117. doi:10.1016/j.jbiomech.2018.07.027

Nabeshima, C., Ayusawa, K., Hochberg, C., and Yoshida, E. (2018). Standard performance test of wearable robots for lumbar support. *IEEE Robot. Autom. Lett.* 3 (3), 2182–2189. doi:10.1109/LRA.2018.2810860

Norman, R., Wells, R., Neumann, P., Frank, J., Shannon, H., Kerr, M., et al. (1998). A comparison of peak vs cumulative physical work exposure risk factors for the reporting of low back pain in the automotive industry. *Clin. Biomech.* 13 (8), 561–573. doi:10.1016/S0268-0033(98)00020-5

Omoniyi, A., Trask, C., Milosavljevic, S., and Thamsuwan, O. (2020). Farmers' perceptions of exoskeleton use on farms: finding the right tool for the work(er). *Int. J. Ind. Ergon.* 80, 103036. doi:10.1016/j.ergon.2020.103036

Poliero, T., Lazzaroni, M., Toxiri, S., Di Natali, C., Caldwell, D. G., and Ortiz, J. (2020). Applicability of an active back-support exoskeleton to carrying activities. *Front. Robot. Ai.* 7, 579963. doi:10.3389/frobt.2020.579963

Potvin, J. R. (1997). Use of NIOSH equation inputs to calculate lumbosacral compression forces. *Ergonomics* 40 (7), 691–707. doi:10.1080/001401397187847

Ramsay, J. O., Munhall, K. G., Gracco, V. L., and Ostry, D. J. (1996). Functional data analyses of lip motion. *J. Acoust. Soc. Am.* 99, 3718–3727. doi:10.1121/1.414986

Ramsay, J. O., and Silverman, B. W. (2005). "Fitting differential equations to functional data: principal differential analysis," in *Functional data analysis* (New York: Springer), 327–348. doi:10.1007/0-387-22751-2_19

Sadler, E. M., Graham, R. B., and Stevenson, J. M. (2011). The personal lift-assist device and lifting technique: a principal component analysis. *Ergonomics* 54 (4), 392–402. doi:10.1080/00140139.2011.556259

Schultz, A., Andersson, G., Ortengren, R., Haderspeck, K., and Nachemson, A. (1982). Loads on the lumbar spine. Validation of a biomechanical analysis by measurements of intradiscal pressures and myoelectric signals. *J. Bone Jt. Surg. Am.* 64 (5), 713–720. doi:10.2106/00004623-198264050-00008

Stellato, B., Banjac, G., Goulart, P., Bemporad, A., and Boyd, S. (2020). OSQP: an operator splitting solver for quadratic programs. *Math. Prog. Comp.* 12 (4), 637–672. doi:10.1007/s12532-020-00179-2

Sugimoto, Y., Naniwa, K., and Osuka, K. (2011). "Static and dynamic characteristics of McKibben pneumatic actuator for realization of stable robot motions," in *Conference on intelligent robots and systems*. Editor R. S. J. International (IEEE Publications), 1817–1822. doi:10.1109/IROS.2011.6094792

Tanaka, M., Umeno, S., and Kikuchi, Y. (2020). Development of a performance-testing method for a power assist suit designed for agricultural work. *J. Jpn. Soc. Agric. Mach.* 82, 196–198. doi:10.11357/jsamfe.82.2_196

Tondu, B. (2012). Modelling of the McKibben artificial muscle: a review. *J. Intell. Mater. Syst. Struct.* 23, 225–253. doi:10.1177/1045389X11435435

Ulrey, B. L., and Fathallah, F. A. (2013). Effect of a personal weight transfer device on muscle activities and joint flexions in the stooped posture. *J. Electromyogr. Kinesiol.* 23 (3), 195–205. doi:10.1016/j.jelekin.2012.08.014

Upasani, S., Franco, R., Niewolny, K., and Srinivasan, D. (2019). The potential for exoskeletons to improve health and safety in agriculture—perspectives from service providers. *IISE Trans. Occup. Ergon. Hum. Factors.* 7 (3–4), 222–229. doi:10.1080/24725838.2019.1575930

van Dieën, J. H., Faber, G. S., Loos, R. C., Kuijer, P. P. F., Kingma, I., van der Molen, H. F., et al. (2010). Validity of estimates of spinal compression forces obtained from worksite measurements. *Ergonomics* 53 (6), 792–800. doi:10.1080/00140131003675091

Waters, T. R., Putz-Anderson, V., Garg, A., and Fine, L. J. (1993). Revised NIOSH equation for the design and evaluation of manual lifting tasks. *Ergonomics* 36 (7), 749–776. doi:10.1080/00140139308967940

Weston, E. B., Alizadeh, M., Knapik, G. G., Wang, X., and Marras, W. S. (2018). Biomechanical evaluation of exoskeleton use on loading of the lumbar spine. *Appl. Ergon.* 68, 101–108. doi:10.1016/j.apergo.2017.11.006

Whitfield, B. H., Costigan, P. A., Stevenson, J. M., and Smallman, C. L. (2014). Effect of an on-body ergonomic aid on oxygen consumption during a repetitive lifting task. *Int. J. Ind. Ergon.* 44 (1), 39–44. doi:10.1016/j.ergon.2013.10.002

Wilke, H. J., Neef, P., Caimi, M., Hoogland, T., and Claes, L. E. (1999). New *in vivo* measurements of pressures in the intervertebral disc in daily life. *Spine* 24 (8), 755–762. doi:10.1097/00007632-199904150-00005

Wilke, H. J., Neef, P., Hinz, B., Seidel, H., and Claes, L. (2001). Intradiscal pressure together with anthropometric data–a data set for the validation of models. *Clin. Biomech.* 16, 111–126. doi:10.1016/S0268-0033(00)00103-0

Winter, D. A. (2009). *Biomechanics and motor control of human movement*. New Jersey: John Wiley & Sons.

Xu, Y., Qiu, Y., and Schnable, J. C. (2018). Functional modeling of plant growth dynamics. *Plant Phenome J.* 1 (1), 1–10. doi:10.2135/tppj2017.09.0007

Zheng, L., Hawke, A. L., and Evans, K. (2022). Critical review on applications and roles of exoskeletons in patient handling. *Int. J. industrial ergonomics* 89, 103290. doi:10.1016/j.ergon.2022.103290

frontiers | Frontiers in Bioengineering and Biotechnology

TYPE Original Research
PUBLISHED 23 November 2023
DOI 10.3389/fbioe.2023.1321905

OPEN ACCESS

EDITED BY
Wujing Cao,
Chinese Academy of Sciences (CAS), China

REVIEWED BY
Peng Xu,
University of Shanghai for Science and Technology, China
Bingze He,
Shanghai Jiao Tong University, China

*CORRESPONDENCE
Hongbo Wang,
Wanghongbo@fudan.edu.cn
Fanfu Fang,
fangfanfu@126.com

RECEIVED 15 October 2023
ACCEPTED 08 November 2023
PUBLISHED 23 November 2023

CITATION
Wang D, Li J, Jian Z, Su H, Wang H and Fang F (2023), Modeling and control of a bedside cable-driven lower-limb rehabilitation robot for bedridden individuals.
Front. Bioeng. Biotechnol. 11:1321905.
doi: 10.3389/fbioe.2023.1321905

Modeling and control of a bedside cable-driven lower-limb rehabilitation robot for bedridden individuals

Daoyu Wang[1], Jicai Li[2], Zhuo Jian[2], Hao Su[3,4,5], Hongbo Wang[1]* and Fanfu Fang[6]*

[1]Academy for Engineering and Technology, Fudan University, Shanghai, China, [2]Shanghai ZD Medical Technology Co., Ltd., Shanghai, China, [3]Department of Mechanical and Aerospace Engineering, North Carolina State University, Raleigh, NC, United States, [4]Joint NCSU/UNC Department of Biomedical Engineering, North Carolina State University, Raleigh, NC, United States, [5]University of North Carolina at Chapel Hill, Chapel Hill, NC, United States, [6]Department of Rehabilitation Medicine, Changhai Hospital, Shanghai, China

Individuals with acute neurological or limb-related disorders may be temporarily bedridden and unable to go to the physical therapy departments. The rehabilitation training of these patients in the ward can only be performed manually by therapists because the space in inpatient wards is limited. This paper proposes a bedside cable-driven lower-limb rehabilitation robot based on the sling exercise therapy theory. The robot can actively drive the hip and knee motions at the bedside using flexible cables linking the knee and ankle joints. A human–cable coupling controller was designed to improve the stability of the human–machine coupling system. The controller dynamically adjusts the impedance coefficient of the cable driving force based on the impedance identification of the human lower-limb joints, thus realizing the stable motion of the human body. The experiments with five participants showed that the cable-driven rehabilitation robot effectively improved the maximum flexion of the hip and knee joints, reaching 85° and 90°, respectively. The mean annulus width of the knee joint trajectory was reduced by 63.84%, and the mean oscillation of the ankle joint was decreased by 56.47%, which demonstrated that human joint impedance identification for cable-driven control can effectively stabilize the motion of the human–cable coupling system.

KEYWORDS

cable-driven, lower-limb rehabilitation, human–machine coupling, impedance identification, sling exercise therapy

1 Introduction

Flaccidity after a stroke is the first stage in the Brunnstrom stages of stroke recovery, also known as flaccid paralysis (Cruz-Almeida et al., 2005; Baer et al., 2014). In flaccid paralysis after cerebral hemorrhage for 2–3 weeks, the patients are conscious or have mildly impaired consciousness, and the vital signs are stable (Dunkerley et al., 2000; Hendricks et al., 2002; Kvorning et al., 2006). However, the muscle strength and tone of the affected limbs and the tendon reflexes are low (Meythaler et al., 2001; Cao et al., 2023). Rehabilitation nursing measures should be undertaken early so as not to interfere with clinical resuscitation and not cause deterioration of the condition. The objective is to prevent complications and secondary

injury while preparing for the next step of functional rehabilitation training (Singer and Mochizuki, 2015; Yang et al., 2023). Sling training effectively improves joint movement and reduces muscle tissue damage in the post-stroke period of flaccid paralysis (Lee and Lee, 2014). Sling exercise therapy (SET) is an unstable chain movement performed with a suspension aid to improve the stability of the core muscles (Oh and Kwon, 2017). Some rehabilitation treatments use the SET to enhance the proprioception, balance, neuromuscular control, and walking ability of individuals with flaccidity (Coote et al., 2008; Jung and Choi, 2019). There are two kinds of kinetic chain exercises: open-chain and closed-chain (Jung and Choi, 2019). In open-chain training, the segment furthest from the body is free and not fixed to an object. In closed-chain training, the segment furthest away from the body is fixed. SET emphasizes the active participation of the patient in training and has both diagnostic and therapeutic functions (Charles et al., 2006). It is useful for detecting the weakest muscles in the human kinetic chain and strengthening them by performing closed-chain and open-chain exercises.

Previously, sling therapists assisted inpatients in moving the upper and lower extremities using elastic cables in a suspension frame (Park and Hwangbo, 2014). A clinical experiment with 50 stroke inpatients showed that upper limb motor dysfunction and shoulder pain are more effectively relieved with SET than with routine training within 2 months after stroke (Liu et al., 2020). Oh and Kwon (2017) applied the methods of sling exercises under the provision of vibrations for people with myelopathy and verified the effectiveness of a muscle function improvement program by sling exercise training (Oh and Kwon, 2017). Traditional sling exercise training has two major deficiencies, lack of feedback on human–machine interaction and non-intelligent training data feedback. Lower-limb rehabilitation sling training mainly depended on the assistance of therapists due to the loss of joint control function in patients in the early stage of stroke (Park and Hwangbo, 2014). Moving such patients from wards to treatment zones added to the trainers' workload (Burtin et al., 2009). A bedside lower-limb rehabilitation training robot can reduce the work intensity of the therapists if it can easily move in the limited space of the ward (Barrett et al., 2006; Jackson et al., 1998). Several industrial and medical robotic manufacturers developed rehabilitation robots for bedridden patients, although there is no SET implemented by bedside rehabilitation robots for flaccid patients. Focusing on mobilizing bedridden patients to a new level, KUKA helps bedridden patients with early and efficient mobilization and relieves the healthcare professionals from heavy lifting and inconvenient working postures with a seven-axis manipulator (LBR Med) (KUKA, 2008). Yaskawa Electric Corporation proposed a bedside therapeutic device for the lower extremity therapy in cerebrovascular patients, which made it possible to repeat lower-limb joint training at varying speed settings and range of motion (Tsuda, 2006). Bedside rehabilitation robots are characterized by three main features: compact size, ease of mobility, and clear functionality. During passive rehabilitation training, the two bedside robots perform with high position accuracy in the workspace. However, both rely on a rigid human–machine coupling, with safety risks, while SET is based on a flexible human–cable coupling system.

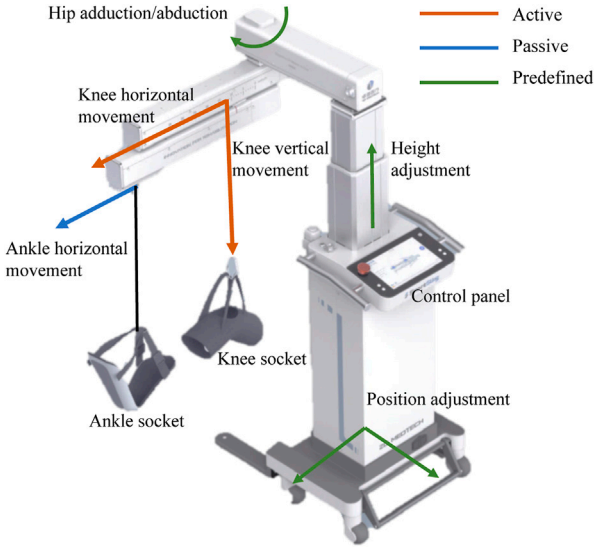

FIGURE 1
Caption system overview of the bedside cable-driven lower-limb rehabilitation robot, SmartSling. It consists of nine parts: knee horizontal movement module, knee vertical movement module, ankle horizontal movement module, knee socket, ankle socket, hip abduction and abduction module, height adjustment module, position adjustment module, and control panel. The knee vertical and horizontal movements are active (red), and the ankle horizontal movement is passive (passive). In addition, with the predefined modules, i.e., hip position and height adjustment modules (green), the rehabilitation robot can assist patients with bedside rehabilitation in most space-limited wards.

Sling exercise training is an interactive process between the cables and the patient's extremities. Research on substituting therapists with robots in sling exercise training is a helpful direction. Cable-driven robots are mechanisms in which the end-effector is moved by controlling the length of the cables connected to it (Zanotto et al., 2014; Li et al., 2021; Vashista et al., 2016; Xie et al., 2021). Cable-driven robots are appealing due to their structural simplicity, high torque-to-weight ratio, and flexibility (Liu et al., 2022; Rosati et al., 2007; Zarebidoki et al., 2021). Sophia-3 is a planar cable-driven device with a tilting working plane featuring a moving pulley block that allows the robot to achieve excellent force capabilities, despite the low number of cables (Zanotto et al., 2014). Its implemented force field could significantly improve users' performance in terms of movement accuracy and execution time. NeReBot is a device used for the treatment of post-stroke upper-limb impairments based on cable transmission and direct-drive actuation (Masiero and Boschetti, 2017; Cao et al., 2022). These cable-driven rehabilitation robots can provide many benefits compared with devices characterized by a rigid structure, such as lower costs, reduced complexity, compliance by design, and a higher degree of reliability and safety. They can effectively move the patient's upper and lower extremities within the training space (Lambert et al., 2020; Li and Zanotto, 2019). However, these robots take up a lot of space, which is unsuitable for application in patient wards. In addition, cable-driven robots are continuously unstable. Currently, there is no research on open- and closed-chain

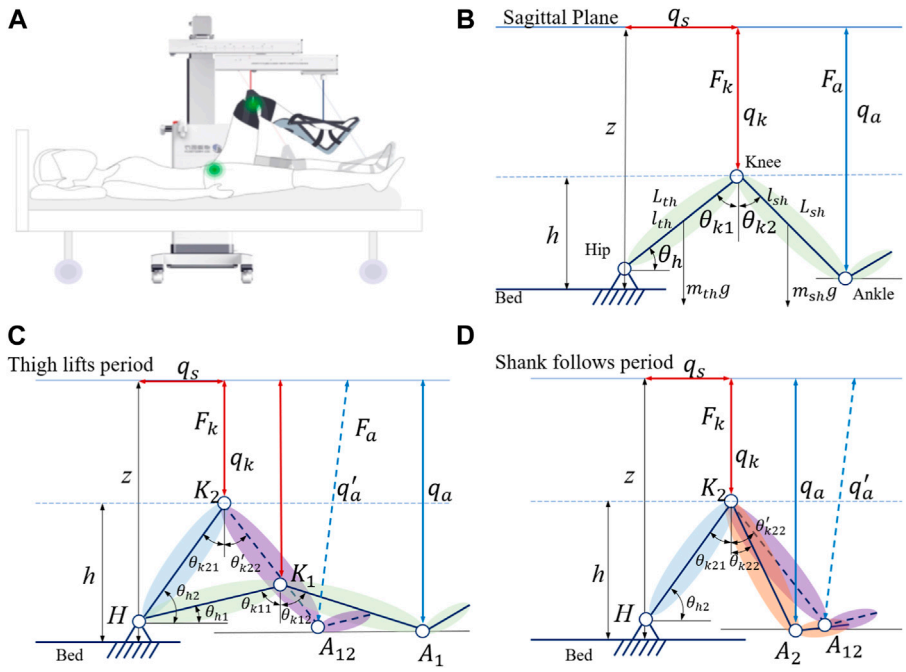

FIGURE 2
Modeling of the leg–machine coupling system in the sagittal plane. **(A)** General view of the human–machine coupling system. **(B)** Kinematic model of the leg–machine coupling system in the sagittal plane. q_s and q_k represent active actuation in the horizontal and vertical modules, respectively, which connect with the knee socket by a non-elastic cable. **(C)** Kinetic model of the leg–machine coupling system in the thigh lifting period. **(D)** Kinetic model of the leg–machine coupling system in the shank following period.

techniques to improve patients' joint motion stability and neuromuscular control.

In this paper, we proposed a cable-driven lower-limb rehabilitation robot (SmartSling) for sling exercise therapy, especially aimed at inpatients in the phase of flaccid paralysis after stroke. As described previously, the contribution seems to be the design, and then it is described as the modeling and control. The contribution of this work is twofold: first, we modeled closed-chain kinematics and kinetics for the human–machine coupled system, and second, we proposed a human–cable impedance controller to minimize the hysteresis of knee movement and stabilize the interaction force for active sling training.

2 Modeling and control of SmartSling

2.1 Mechatronic system of SmartSling

The design of the SmartSling lower-limb rehabilitation training system is shown in Figure 1. SmartSling comprises five components: a height adjustment module, a module for hip adduction–abduction, a module for horizontal–vertical movement in the sagittal plane with suspension cables, a knee–ankle socket, and a control panel for therapists. The modules for hip adduction–abduction and for horizontal–vertical movement are actuated by two DC servo motors (PD4-CB59M024035-E, Nanotec Electronic GmbH & Co. KG) via ball screw mechanisms. The cable connected to the knee joint has two active degrees of freedom in the sagittal plane. The cable connected to the ankle joint has only one passive degree of freedom, and its robotic side is constrained in a linear chute. The two cables are connected with six-axis force/torque sensors (M3715A, Sunrise Instruments). SmartSling can train the bedside inpatients in most space-limited wards, and its position can be adjusted thanks to a wheeled chassis and the height adjustment module.

2.2 Equilibrium state of basic kinematics

Synchronous flexion of the hip and knee in the sagittal plane (Figure 2A) is basic training for individuals with flaccidity after stroke. Thigh and shank lengths (L_{th} and L_{sh}) of the subjects can be set as predefined parameters in SmartSling. As shown in Figure 2B, at equilibrium, the human hip joint angle θ_h is

$$\theta_h = \sin^{-1}\frac{h}{L_{th}}, \tag{1}$$

where the height of the knee joint $h = z - q_k$, h is the height of the knee, z is the distance between the hip and vertical movement module, q_k is the sling movement of the vertical movement module, and L_{th} is the length of the thigh. The knee joint angle θ_k is divided into two parts by the drive cable as

$$\theta_k = \theta_{k1} + \theta_{k2} \tag{2}$$

where θ_{k1} is the complementary angle of the hip joint angle, θ_h, and L_{sh} is the length of the shank. Therefore, θ_{k2} can be calculated by the height of the knee joint as

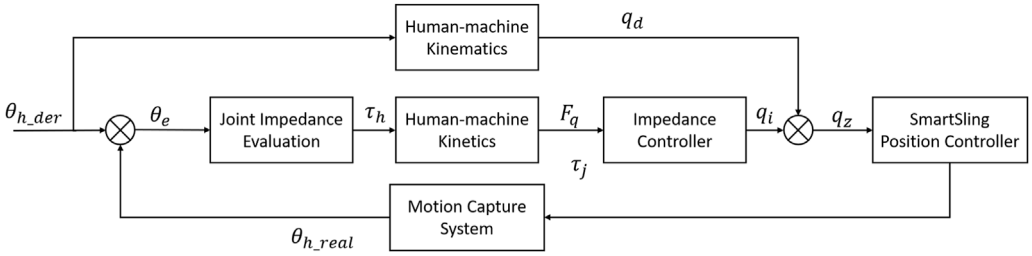

FIGURE 3
Impedance control diagram of the human–machine coupling system for SmartSling.

$$\theta_{k2} = \sin^{-1}\frac{h}{L_{sh}} \tag{3}$$

Therefore, according to the active motion parameters (q_s and q_k) of SmartSling, we can directly calculate the ideal kinematic state of the lower limb joints in real-time.

However, the cables can only be controlled under tension, and the inertia in the human body and the limb of the cable coupling system need to be taken into account. We found that the motion of the trained limb and machine is not completely synchronized when analyzing the position control. This phenomenon can be understood as follows: when starting, the cables are not fully tensioned and move, while the human body has not yet been stressed to move, and when braking, the cables are slack due to the inertia of human body movement. We need to consider the inertial motion of human extremities in the human–machine coupling system and establish dynamic equations to analyze the starting motion and braking motion process. The single-direction training cycle is divided into two states; in the first state, the machine actively slings the hip joint by lifting the thigh, while in the second state, the knee joint passively flexes, as shown in Figure 2D.

2.3 State 1: hip joint active slings

For the inpatients who cannot exert active hip joint torque, the thigh-related torque to the hip joint, τ_{hip}, in the equilibrium state can be expressed as

$$\tau_{hip} = J_{th}\alpha_h + F_k L_{th}\cos\theta_h + m_{th} g l_{th}\cos\theta_h \tag{4}$$

where L_{th} is the length of the thigh, l_{th} is the length from the hip joint to the center of mass of the thigh, m_{th} is the mass of the thigh, J_{th} is the moments of inertia of the thigh, and F_k is the tension force of the cable connected to the knee joint. The shank-related torque of the knee joint, τ_{knee}, in the equilibrium state can be expressed as

$$\begin{aligned}\tau_{knee} = {} & F_a\left(L_{th}\cos\theta_h + L_{sh}\sin\theta_{k2}\right) \\ & + m_{sh} g\left(L_{th}\cos\theta_h + l_{sh}\sin\theta_{k2}\right) + J_{sh}\alpha_k\end{aligned} \tag{5}$$

where l_{sh} is the length from the knee joint to the center of mass of the shank and foot and L_{sh} is the overall length of the shank and foot. Since the ankle socket binds to the shank and foot as a rigid connection, m_{sh} is the mass of the shank and foot, J_{sh} is the moment of inertia of the thigh and foot, and F_a is the tension force of the cable connected to the ankle joint.

From the equilibrium, the hip joint acceleration, α_h, can be expressed as a function of the joint angle θ_h,

$$\alpha_h = \frac{d^2\theta_h}{dt^2} = f(\theta_h) \tag{6}$$

By solving differential equations of $f(\theta_h)$, we can get the relationship between the hip joint angle, θ_h, and time, t, as

$$\theta_h(t) = F_h(t) \tag{7}$$

and the duration of hip rotation, Δt_h, can be written as

$$\Delta t_h = F_h^{-1}(\theta_{h2}) - F_h^{-1}(\theta_{h1}) \tag{8}$$

where F_h^{-1} is the inverse function of $F_h(t)$ and θ_{h1} and θ_{h2} are the initial and terminal positions of the hip joint, respectively.

2.4 State 2: knee joint flex accompanies movement

In the second state, the knee joint flexes passively, which leads to its movement that is not as synchronous as that of the hip joint. The knee joint angle θ_{k2} has a hysteretic movement due to the fact that the cable connected to the ankle has a passive degree of freedom in a horizontal slide joint. The equilibrium condition at low speed during θ_{k2} movement can be written as

$$J_{sh}\alpha_k + F_a L_{sh}\cos(\theta_{k2} + \theta_3) + m_{sh} g l_{sh}\sin\theta_{k2} = 0 \tag{9}$$

where θ_3 can be defined as

$$\theta_3 = \cos^{-1}\left(\frac{q_k + L_{sh}\cos\theta_{k2}}{q_a}\right) \tag{10}$$

From the equilibrium, the knee joint acceleration, α_k, can be expressed as a function of the joint angle θ_{k2},

$$\alpha_k = \frac{d^2\theta_{k2}}{dt^2} = r(\theta_{k2}) \tag{11}$$

By solving differential equations of $r(\theta_{k2})$, we can obtain the relationship between the second part of the knee joint angle, θ_{k2}, and time, t, as

$$\theta_{k2}(t) = R_{k2}(t) \tag{12}$$

and the duration of the knee rotation, Δt_{k2}, can be written as

TABLE 1 Anthropometric data.

Segment	Segment length, l (%BH)	Mass, m (%BM)	l_{CoM} (from the distal joint)	Radius of gyration k_{CoM}
Thigh	25.4	9.9	56.7	0.3
Shank	23.3	4.6	57	0.3
Foot	11.7	1.4	50	0.48

BH, body height; BM, body mass; moment of Inertia, $I = m(k_{CoM} + l_{CoM})^2$

TABLE 2 Subject information.

Subject number	Gender	Age (years)	BH (m)	BM (kg)	Thigh length (cm)	Shank length (cm)	Thigh mass (kg)	Shank mass (kg)	Thigh moment of inertia (kgm^2)	Shank moment of inertia (kgm^2)
1	M	27	1.783	73.9	45.2882	41.5439	7.3161	3.3994	253.2025	97.6329
2	F	25	1.611	58.4	40.9194	37.5363	5.7816	2.6864	163.3522	62.9827
3	M	25	1.855	90.2	47.117	43.2215	8.9298	4.1492	334.5148	128.9863
4	F	26	1.649	61.3	41.8846	38.4217	6.0687	2.8198	179.6481	69.2709
5	M	30	1.712	62.7	43.4848	39.8896	6.2073	2.8842	198.0596	76.3702

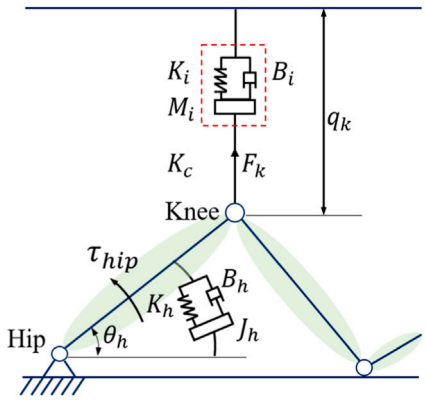

FIGURE 4
Bionic impedance model: the active sling force characterized by the human hip joint.

$$\Delta t_{k2} = R_{k2}^{-1}(\theta'_{k22}) - R_{k2}^{-1}(\theta_{k22}) \tag{13}$$

where R_{k2}^{-1} is the inverse function of $R_{k2}(t)$ and θ'_{k22} and θ_{k22} are the initial and terminal positions of the second part of the knee joint in the shank following period, respectively.

The analysis of thigh lifting and shank following with position control of cables can illustrate the kinematic and kinetic aspects of the human–cable interaction during a single-sling process. The initialization hysteresis of the shank following the active sling procedure demonstrates that the human–cable interaction is unstable without force control.

2.5 Human–cable impedance controller

Here, we design a human–cable impedance controller (HCIC) to minimize the hysteresis of the shank following movement. The diagram of impedance control in the human–machine coupling system for SmartSling is shown in Figure 3. In the first state of active sling force, the kinetic equation can be established as

$$M(\theta)\ddot{\theta} + C\left(\theta, \dot{\theta}\right)\dot{\theta} + G(\theta) = F_k + f_d \tag{14}$$

where θ is the vector containing hip and knee joint angles, $M(\theta)$ is the inertia matrix, $C(\theta, \dot{\theta})\dot{\theta}$ is the Coriolis matrix and centrifugal terms, $G(\theta)$ represents the gravity terms, F_k denotes the two cable tension forces, and f_d represents the lateral disturbances.

The active sling force is influenced by the human hip joint estimated impedance, as shown in Figure 4. During the impedance estimation process, the knee joint is kept in the state of maximum and the hip impedance in the sagittal plane can be identified from

$$\tau_{hip} = J_h\ddot{\theta}_h + B_h\dot{\theta}_h + K_h\theta_h \tag{15}$$

where J_h, B_h, and K_h are the lower-limb intrinsic impedance parameters to be identified, while the joint angle θ_h and torque τ_{hip} are measurable or computable during the whole moving process.

With the identified lower-limb impedance parameters, the interaction force can be defined as

$$F_k = M_i\ddot{q}_k + B_i\dot{q}_k + K_iq_k \tag{16}$$

and the impedance parameters are defined as follows

$$\begin{bmatrix} M_i \\ B_i \\ K_i \end{bmatrix} = \delta \begin{bmatrix} J_h \\ B_h \\ K_h \end{bmatrix} \Big/ L_{th}\cos\theta_h \tag{17}$$

where δ is the impedance gain and q_k can be traced back to θ_h, as expressed in Eq. 1.

The hip joint error, θ_e, can be defined as

$$\theta_e = \theta_{h\_der} - \theta_{h\_real} \tag{18}$$

where θ_{h_der} is the desired and θ_{h_real} is the real-time hip angle measured from a wearable motion capture system (MTI-1, Xsens, Netherlands). The error can be used to calculate the hip joint

FIGURE 5
Training cycle schematics for SmartSling with the trained subject. The arrows indicate the directions of limb movement in the sagittal plane.

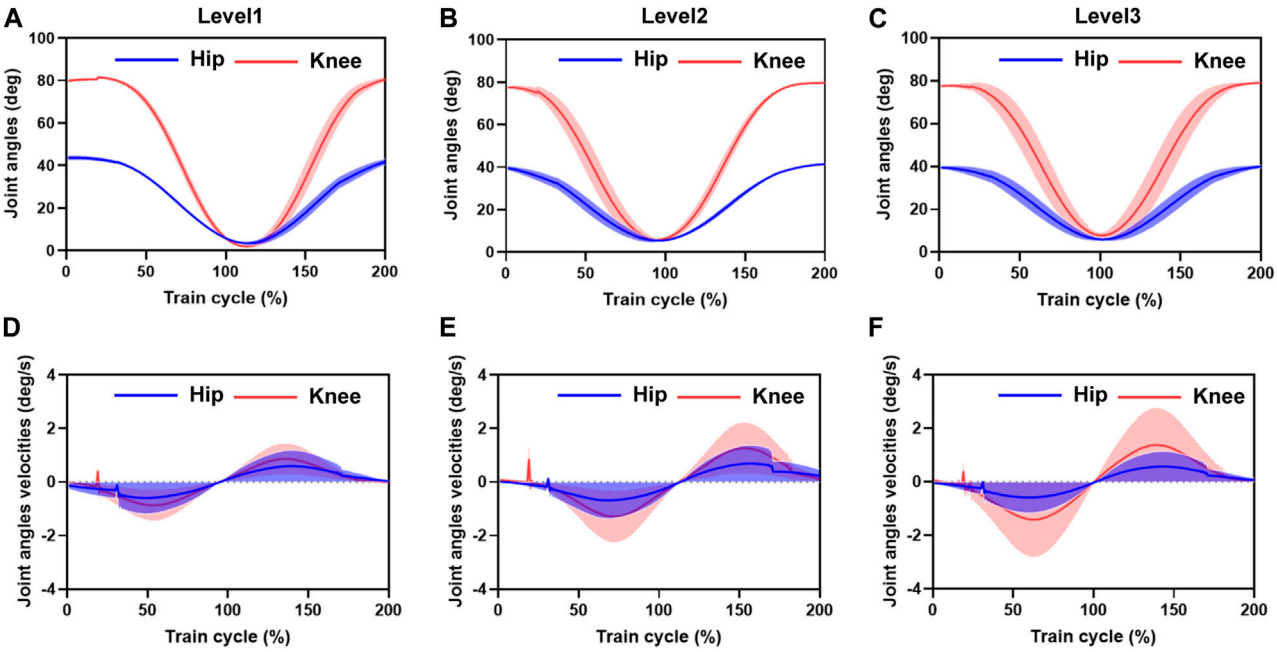

FIGURE 6
Mean and standard deviation of hip and knee motion for different training speed levels under position control without active force. **(A–C)** are the hip range of motion. The hip and knee motion data of the subjects revealed no significant differences in the joint range of motion. However, the RMSE of the hip and knee range of motion angles differed significantly with the increasing speed in motion. The distinct instability of the angular velocities can be observed with the increasing training velocity. **(D–F)** are the RMSE of the angular velocities of hip and knee motion varied with increasing training speed. Hip RMSE and the error bands increased significantly with increasing training speed. Knee RMSE and the error band increased with increasing training speed.

residential impedance parameters, as shown by Eq. 18. The impedance gain, q_i, can be calculated with the impedance controller, as shown in Eq. 19. Finally, the output of the HCIC for the active cable length is the superposition of the desired length from human–machine kinematics, q_d, and the impedance gain, q_i, as

$$q_k = q_d + q_i \tag{19}$$

3 Experiments

The experiments had two objectives: first, observing the kinematics and kinetic performance of the subjects using SmartSling under the position control mode, and second, validating the impedance controller designed in this study to adjust and minimize the hysteresis of the shank following movement. Healthy patients were recruited and asked to be passive during the motion validation experiments to emulate bedridden patients with joint weakness. Overall, five healthy subjects (three males and two females, with mean age 26.6 years with a standard deviation (SD) of 2.07, height 1.72 m with SD 0.09, and weight 69.3 kg with SD 13.07) with no history of neurological impairments were tested. The segment value calculation referred to an anthropometric data distribution rule proposed by Kirtley (2004), as shown in Table 1. The subjects' detailed information is given in Table 2. The Ethics Committee of the Changhai Hospital (Shanghai) approved this study. Written informed consent was obtained from all subjects.

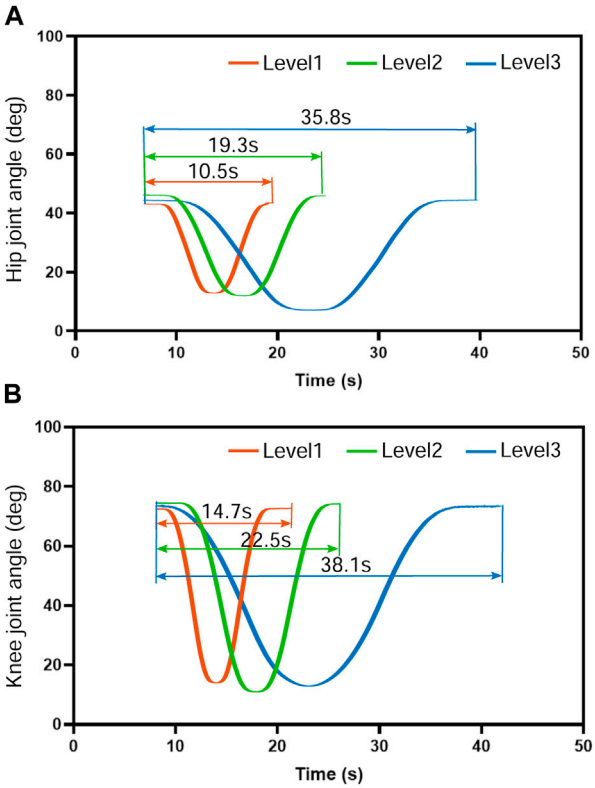

FIGURE 7
Movement duration of the five subjects' hip and knee joints over 10 training cycles under the position control mode for the three training speed levels. The knee joint moved at an average speed of 4.2 s, 3.2 s, and 2.6 s, respectively, slower than the hip joint. The knee hysteresis decreased with increasing training speed with no significant association (p >0.1) between the training level and knee hysteresis. As the training speed level increased, the hip and knee movement time remained consistent. The hip movement time decreased by 8.8 s and 16.5 s, respectively, and the knee movement time decreased by 7.8 s and 15.6 s, respectively.

The experiments are divided into two main processes. 1) Under the position control mode, the robotic system is operated using three velocity levels for the vertical movement of the drive cable at the knee joint, corresponding to 0.05 m/s, 0.1 m/s, and 0.15 m/s, respectively. The time required for a complete set of hip and knee suspension training at different speeds was not synchronized with the position control mode. The average interval time was 5% training cycle time for the three training speeds. 2) In the HCIC mode, the active motion of SmartSling is adjusted in real-time according to the subject's force because of the presence of human–robot interaction. The hip joint torque can be estimated by the HCIC as shown in Eq. 18, which can be a reference parameter for the functional movement evaluation. The speed of motion at a certain position is not determined for different subjects due to the differences in limb characteristics. We fixed only the lowest and highest positions of the drive cable. The obtained experimental results were mainly used to verify the synchronization enhancement of the HCIC for hip and knee joint linkage. The five subjects were asked to perform suspension training with and without active force, respectively, and each training session was carried out three times for each velocity level.

All experimental data exported from the SmartSling system were collected at a sampling rate of 100 Hz. The root mean square error (RMSE) of the experimental results was calculated for analysis. We calculated the active moments of the subjects in real-time through the human–machine coupled kinetic model. The kinetic data could not be temporarily compared and tested using third-party human motion analysis instruments. The normalized comparative analysis of the calculated active motion in humans was performed using SmartSling without making specific numerical comparisons due to the human moment calibration and reference data during sling training. The data of five stable sling training cycles are processed to verify the relationship between the calculation results of the locomotion identification system and the reference values. The RMSE $E(q)$ is obtained as $E(q) = \sqrt{\frac{1}{n}\sum_{i=1}^{n}(q - mean(q))^2}$ where q are the joint angles calculated by the locomotion identification system and $mean(q)$ are the mean values of q. One-way analysis of variance (ANOVA) was conducted to compare the differences in the kinematic performance and estimated joint kinetics, with significance set at $p \leq 0.05$.

4 Results

4.1 Kinematics under position control

The entire training cycle was divided into joint flexion and extension movements, and each part was time-normalized into cycle percentage, as shown in Figure 5. The mean and standard deviation curves of hip and knee motion for different training levels under position control without active force are shown in Figures 6A–F. The hip range of motion was 5.3°–40.7°, 5.1°–42.9°, and 7.3°–40.0°, respectively, and no significant differences were found in the joint range of motion at different training speeds (p = 0.23). The knee range of motion was 4.3°–83.6°, 6.1°–81.2°, and 5.5°–82.5°, respectively, and no significant differences were found in the joint range of motion at different training speeds (p = 0.15). The hip and knee motion data of the subjects revealed no significant differences in the joint range of motion. However, the RMSE of hip and knee angles differed significantly with the increasing speed of training. The hip RMSE at the three training speeds was 2.7°, 3.5°, and 5.4°, respectively, significantly increasing by 29.63% (p = 0.029) and 44.35% (p = 0.013) with increasing training speed, respectively. The knee RMSE was 3.3°, 6.9°, and 12.4°, respectively, significantly increasing with increasing training speed by 52.17% (p = 0.015) and 44.35% (p = 0.008), respectively. The speed of motion in a defined human–machine motion chain is negligible for the joint range of motion, but the distinct instability of the angular velocities can be observed with the increase in training speed.

The angular velocities were obtained by the joint position differences. The sampling time interval was 0.01 s. The hip and knee joint angle results showed that the joint angle error bands caused by the increased training speed are amplified in the velocity calculation. A 5% training cycle time was reserved for the joint flexion and extension limits of each training cycle to mitigate the knee joint hysteresis problem before initiating the motion direction switch. The RMSE of the angular velocities of hip and knee motion varied significantly with increasing training speed, with a hip RMSE of 1.2 deg/s, 1.6 deg/s, and 1.7 deg/s for the three training speeds,

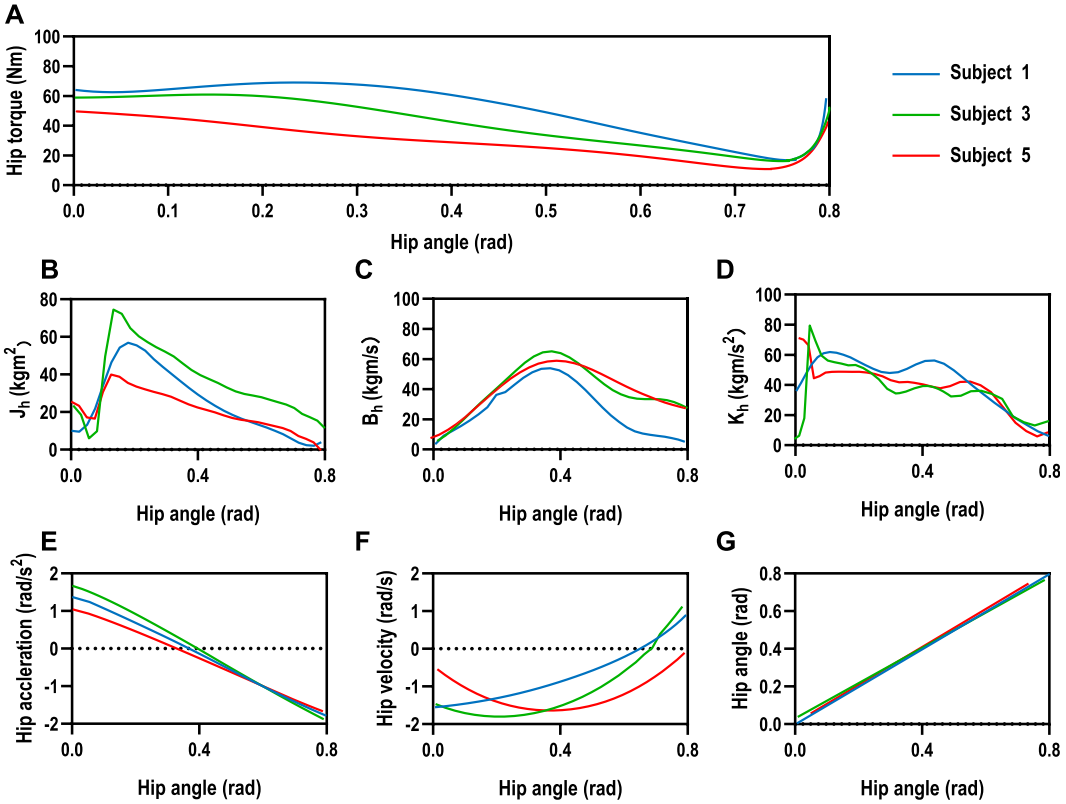

FIGURE 8
Human hip joint impedance estimation. **(A)** The mean joint torques of the three subjects were 22.35*Nm*, 31.99*Nm*, and 27.64*Nm*, respectively, which were positively correlated with their body weight. The range of motion of the hip joint was controlled from 0 to 45° during the estimation progress to facilitate experimental data comparison between different subjects. **(E–G)** The human kinematic performances of the three subjects are relatively stable. However, intrinsic differences existed in body weight and lower-limb proportions among the three subjects. **(B–D)** The lower-limb rotational inertia showed significant differences due to the consequential differences in weight and lower limb dimensions among the three subjects, while the trend and range of hip damping and stiffness coefficients were similar for the three subjects, with an average joint damping of 37±2.3 *kgm/s*, and the average stiffness was 40±1.6 *kgm/s*^{2}.

respectively, and the error bands increasing significantly by 33.49% (p = 0.013) and 6.25% (p = 0.028) with increasing training speed, respectively. The knee RMSE was 1.3 deg/s, 1.8 deg/s, and 2.1 deg/s, respectively, and the error band significantly expanded with increasing training speed by 38.46% (p = 0.021) and 14.28% (p = 0.017), respectively. At the beginning of the draft training, we noticed some oscillations in the joint motion speed, with maximum oscillation of 0.72 deg/s, 1.13 deg/s, and 0.37 deg/s in the hip joint and 0.21 deg/s, 0.26 deg/s, and 0.41 deg/s in the knee joint, respectively. The source of these oscillations was mainly due to the unstable motion caused by the human-driven cable interaction force, which was not considered in the human–machine coupling system.

Figure 7 demonstrates the mean movement duration of the five subjects' hip and knee joints over 10 training cycles under the position control mode for the three training speed levels. The knee joint lagged with an average of 4.2 s, 3.2 s, and 2.6 s, respectively, after the hip joint completed the movement, which means that the hip and knee joints steadily experienced asynchrony problems during the suspension training. This knee hysteresis decreased with increasing training speed, but we did not find a significant association between the training level and knee hysteresis in the one-way ANOVA. However, as the training speed level increased, the hip movement time decreased by 8.8 s and 16.5 s, respectively (Figure 7A), and the knee movement time decreased by 7.8 s and 15.6 s, respectively (Figure 7B), while the hip and knee movement time remained consistent. This trend was consistent with the change time of the human–machine coupled hip motion by calculating the vertical motion time of the active cable at different speed levels. Therefore, the motion trajectory control and time planning under the position control mode are stable.

4.2 Human hip joint impedance estimation

The hip joint impedance coefficients of the subjects are estimated for the human–machine coupling system controller with Eq. 14. The mean values of the relevant parameters were estimated in real-time for 10 sets of hip tests on three male subjects, as shown in Figure 8. The subjects were asked not to exert moment on the hip joint during the test but to rely only on the driven force of SmartSling to measure the passive impedance coefficients of the hip joints. The mean joint torques of the three

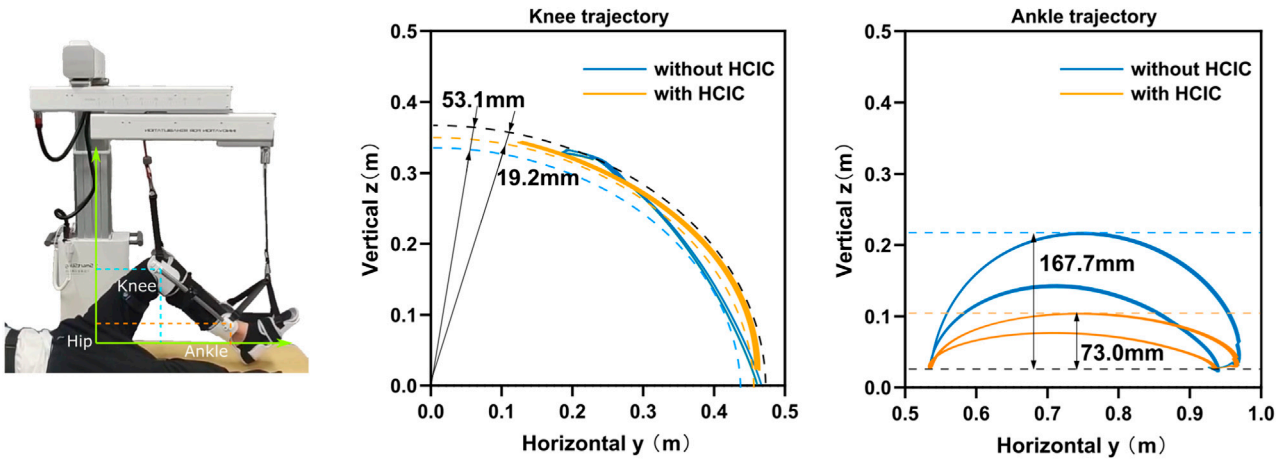

FIGURE 9
The motion trajectories of the knee and ankle joints within the Cartesian space can be utilized for movement assessment. The knee and ankle joint trajectories of subject 1 in the sagittal plane under position control and HCIC training modes are denoted by blue and orange curves. The knee motion has radial oscillation in addition to the circular arc motion around the hip joint due to the instability of the human–machine coupled motion. We use the two circles shown by dashed lines to envelop the knee trajectory under two training modes. The width of the knee oscillation annulus under position control is 53.1 *mm*, and the width of the oscillation annulus under HCIC control is 19.2 *mm*. The whole trajectory profile is closer to a circular arc with a decrease of 63.84% in the knee radial oscillation. The ankle range of motion in the vertical direction was 167.7 *mm* under position control and 73.0 *mm* under HCIC control, and the ankle jump range was reduced by 56.47% under the same horizontal motion start point condition.

subjects were 22.35*Nm*, 31.99*Nm*, and 27.64*Nm*, respectively, which were positively correlated with their body weight (Figure 8A). The range of motion of the hip joint was controlled from 0 to 45° during the estimation progress to facilitate experimental data comparison between different subjects. Thus, the kinematic performances of the three subjects are relatively stable, as shown in Figures 8E–G. However, due to the intrinsic differences in body weight and lower-limb proportions among the three subjects, the lower-limb rotational inertia shown in Figures 8B–D exhibited consequential differences. The lower-limb rotational inertia of subject 3 was $0.21 Nms^2/kg$ larger than that of subject 1 when the body weight is the reference index. The trend and range of hip damping and stiffness coefficients were similar for the three subjects, with an average joint damping of 37 ± 2.3 *kgm/s*, and the average stiffness was 40 ± 1.6 kgm/s^2.

4.3 Knee and ankle trajectory optimization

The motion trajectories of the knee and ankle joints within the Cartesian space can be utilized for movement assessment in addition to the aforementioned kinematic and dynamic parameters of the lower limb joints. The hip joint was used as the origin in the sagittal plane, with the horizontal direction as the horizontal coordinate and vertical direction as the vertical coordinate, as shown in Figure 9. We set the impedance gain δ = 0.8 for the HCIC of subject 1. The knee and ankle joint trajectories of subject 1 in the sagittal plane under position control and HCIC training modes are denoted by blue and orange curves, respectively. The knee joint is theoretically an arc of a circle. Still, the knee motion has radial oscillation in addition to the circular arc motion around the hip joint due to the instability of the human–machine coupled motion. We use the two circles shown by dashed lines to envelop the knee trajectory under two training modes. The width of the knee oscillation annulus under position control is 53.1 *mm*, and the width of the oscillation annulus under HCIC control is 19.2 *mm*. The whole trajectory profile is closer to a circular arc with a decrease of 63.84% in the knee radial oscillation. The ankle joint cannot continuously extend the horizontal movement since the ankle joint-connected cable of SmartSling is a follower joint and moves only in the horizontal direction. As the follower joint of the knee joint, the oscillation effect of the knee joint is amplified at the ankle joint. The horizontal start and end positions are determined and are, therefore, not affected by the control strategy. However, the ankle joint trajectory during the motion shows different effects in the vertical direction of cable traction due to the limb oscillation in the continuous motion because of the different sling control strategies. The ankle range of motion was 167.7 *mm* under position control and 73.0 *mm* under HCIC control, and the ankle jump range was reduced by 56.47% under the same horizontal motion start point condition. The ankle and knee joint trajectory results demonstrated that the lower-limb rehabilitation training of bedridden individuals could be performed using SmartSling stably and smoothly.

4.4 Kinematics optimization with HCIC

One of the objectives of the experiments is to observe the kinematic performance of the subjects to compare the effectiveness of SmartSling under the position control mode and HCIC. Healthy patients with no active joint movement can perform the same function at this experimental stage as bedridden patients with joint weakness. The kinematic performance of subject 1

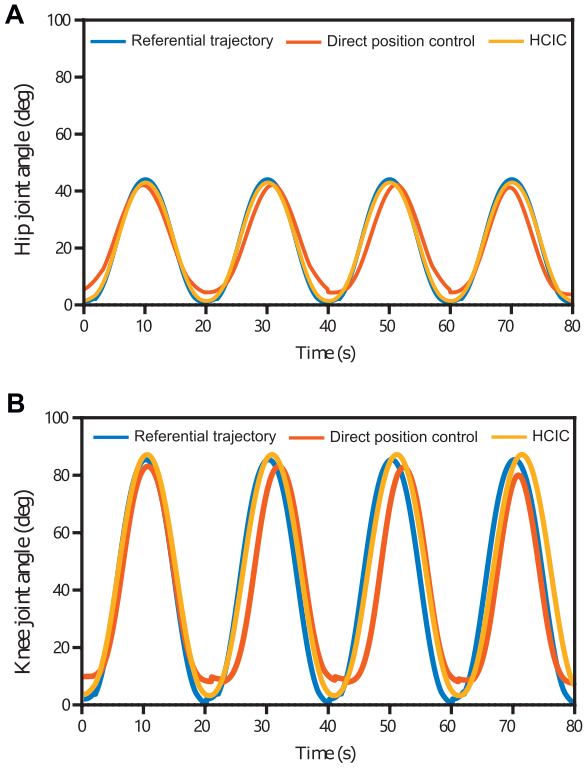

FIGURE 10
Hip and knee joints' kinematic performance in four training cycles (subject 1) under position control and HCIC. The target range of motion of the hip joint was from 0 to 45.0°, and the corresponding motion calculation could yield a knee range of motion from 0 to 84.3°. The ultimate range of motion of the hip and knee joints under position control was close to 95.3% and 92.7% of the reference trajectories, respectively. Under position control, the hip extension was incomplete (the average ultimate extension was 3.5°±0.7°), and the knee extension was incomplete (the average ultimate extension was 10.9°±1.3°). The HCIC effectively restored the hip and knee range of motion to 98.4% and 96.5% of the reference range, respectively. The HCIC reduced knee hysteresis by an average of 2.1 s per training cycle compared to position control.

(Figure 10) was analyzed to demonstrate the superiority of the HCIC compared to direct positional control. The hip and knee joints of the five subjects were analogous. The target range of motion of the hip joint was from 0 to 45.0°, and the corresponding calculation of motion could yield a knee range of motion from 0 to 84.3°. In addition, the theoretical motion states of the two joints were synchronized during the sling training. The ultimate range of motion of the hip and knee joints under position control was close to 95.3% and 92.7% of the reference trajectories, respectively. However, the hip extension was incomplete (the average ultimate extension was 3.5° ± 0.7°), and the knee extension was incomplete (the average ultimate extension was 10.9° ± 1.3°). The HCIC effectively restored the hip and knee range of motion to 98.4% and 96.5% of the reference range, respectively. In addition, in terms of correcting hip and knee synchronization, as shown in Figure 10B, the HCIC reduced motor knee hysteresis by an average of 2.1 s per training cycle compared to position control, which accounts for 10.3% of a single training cycle.

5 Discussion

We designed, built, and tested a cable-driven bedside lower-limb rehabilitation robot to assist patients in patient wards who cannot be transferred over a wide range but are in urgent need of lower-extremity rehabilitation training. The kinematics of the proposed bedside rehabilitation robot under position control was verified with healthy subjects. The lower-limb multi-joint motion has the problem of motion asynchrony due to the limitation of the cable drive itself. Although cable driving is a flexible human–machine interaction method, the human–machine coupled system tended to be unstable under position control in the actual operation process without considering the human joint impedance. Therefore, we added force sensors at one end of the driven cables and proposed a human–machine coupling kinetic model to dynamically identify the impedance coefficients of human lower limbs in the joint space. We designed a human–cable impedance controller based on the identified human joint impedance coefficients. Subject-training experimental tests demonstrated that the proposed human–computer coupled impedance controller improved the synchronization of the lower limbs over the joints and the stability of the human–cable coupled system and restored the range of motion of lower limb joints.

Compared with previous cable-driven rehabilitation robots, the force interaction of the human–cable coupled system proposed in this study can improve the system stability. Cable-driven rehabilitation is inherently flexible as a particular human–machine interaction. Still, the application of force-open loop makes it challenging to avoid inertial movement because of the mismatch between human and robot system impedance characteristics. SET is an unstable, open-chain, and closed-chain movement performed using a suspension aid to improve the stability of the body's core muscles (Oh and Kwon, 2017). The stability of human motion with SmartSling was analyzed in two aspects: end-joint trajectory and joint angle. Analysis of the knee and ankle joint trajectories of the tested subject in the sagittal plane under position control and HCIC training modes showed that the knee motion has radial oscillation in addition to the circular arc motion around the hip joint due to the instability of the human–machine coupled motion. The trajectory profile is closer to a circular arc with a decrease of 63.84% of the knee radial oscillation. The ankle joint cannot continuously extend the horizontal movement since the ankle joint-connected cable of SmartSling is a follower joint and moves only in the horizontal direction. The oscillation effect of the knee joint is amplified at the ankle joint as the knee joint follows the hip joint. The horizontal start and end positions are determined and are, therefore, not affected by the control strategy. However, the ankle joint trajectory during the motion shows different effects in the vertical direction of cable traction due to the limb oscillation in the continuous motion because of the different sling control strategies.

For a bedside rehabilitation robot, rigid driving is not safe enough for a patient in the bedside stage. The existing direct drive of distal joints, such as the ankle joint through the end of the robot arm, is dangerous for the patient without real-time feedback on the torque and angle of the intermediate joints for rehabilitation training (Tsuda, 2006; KUKA, 2008). In contrast, our proposed robot's coordinated drive for each joint is based on flexible

force interaction. The closed-loop human–machine dynamic model calculates the human joint torque in real-time. The experimental results show that this rehabilitation training strategy is safe and effective.

The coupled modeling method of the robotic system proposed in this study provides technical references for other cable-driven robotic designs in human–machine interaction force perception, human static characteristic measurement, and joint motion capability assessment. Currently, SmartSling has limitations for multi-posture lower-extremity training (lying and lateral postures) and standing balance training, according to SET. SmartSling mainly targets lower-extremity limb movement training in the flaccid paralysis phase but is considered from the perspective of flexible human–machine interaction features and easily replaceable wearable accessories. It is expandable to upper-extremity training and even to whole-body training through multi-robot formation, which shows great potential for rehabilitation training in narrow patient wards. In addition, the stability of the human–machine coupling system through the dynamic identification of human–machine interaction force is a potential theoretical research and application scenario in the direction of cable-driven robots, especially for neural rehabilitation robots.

6 Conclusion

This cable-driven lower-limb rehabilitation robot is designed with closed-chain kinematics and kinetics for the human–machine coupled system. It can provide professional and efficient lower-limb rehabilitation training at the bedside for stroke patients. The recognized human joint active parameters from the kinematic and kinetic models will be the clinical references for the next stage of rehabilitation training. We are currently planning on using the rehabilitation robot to investigate the clinical research with cooperated rehabilitation departments, especially for bedside SET training research. In the next research stage, the proposed impedance matching algorithm will be extended to upper-limb rehabilitation training. The flexible human–machine interaction method in this paper is being investigated for application to training scenarios in physical therapy and occupational therapy, more than just the bedside.

Data availability statement

The original contributions presented in the study are included in the article/Supplementary Material; further inquiries can be directed to the corresponding authors.

Ethics statement

The studies involving humans were approved by the Institution Animal Ethics Committee of Changhai Hospital. The studies were conducted in accordance with the local legislation and institutional requirements. Written informed consent for participation in this study was provided by the participants' legal guardians/next of kin. Written informed consent was obtained from the individual(s) for the publication of any potentially identifiable images or data included in this article.

Author contributions

DW: writing–original draft. JL: methodology and writing–original draft. ZJ: methodology and writing–original draft. HS: writing–review and editing. HW: supervision and writing–review and editing. FF: conceptualization, formal analysis, funding acquisition, and writing–review and editing.

Funding

The author(s) declare financial support was received for the research, authorship, and/or publication of this article. This work was supported in part by the Three-year Action Plan for Promoting Clinical Skills and Clinical Innovation in Municipal Hospitals, which is a training project for the innovation and transformation ability of research-oriented physicians (SHDC2022CRD004); the Biomedical Technology Support Special Project of the Shanghai Science and Technology Innovation Action Plan (19441908100); and the Youth Science and Technology Talents Scheme (NQ06128).

Conflict of interest

Authors JL and ZJ were employed by Shanghai ZD Medical Technology Co., Ltd.

The remaining authors declare that the research was conducted in the absence of any commercial or financial relationships that could be construed as a potential conflict of interest.

Publisher's note

References

Baer, P., Choo, C., Langhorne, M., Forster, A., Morris, J., Langhorne, P., et al. (2014). Physical rehabilitation approaches for the recovery of function and mobility following stroke. *Cochrane Database Syst. Rev.* 2023, CD001920. doi:10.1002/14651858.cd001920.pub3

Barrett, A. M., Buxbaum, L. J., Coslett, H. B., Edwards, E., Heilman, K. M., Hillis, A. E., et al. (2006). Cognitive rehabilitation interventions for neglect and related disorders: moving from bench to bedside in stroke patients. *J. Cognitive Neurosci.* 18, 1223–1236. doi:10.1162/jocn.2006.18.7.1223

Burtin, C., Clerckx, B., Robbeets, C., Ferdinande, P., Langer, D., Troosters, T., et al. (2009). Early exercise in critically ill patients enhances short-term functional recovery. *Crit. care Med.* 37, 2499–2505. doi:10.1097/ccm.0b013e3181a38937

Cao, W., Chen, C., Wang, D., Wu, X., Chen, L., Xu, T., et al. (2022). A lower limb exoskeleton with rigid and soft structure for loaded walking assistance. *IEEE Robotics Automation Lett.* 7, 454–461. doi:10.1109/lra.2021.3125723

Cao, W., Shang, D., Yin, M., Li, X., Xu, T., Zhang, L., et al. (2023). Development and evaluation of a hip exoskeleton for lateral resistance walk exercise. *IEEE/ASME Trans. Mechatronics* 28, 1966–1974. doi:10.1109/TMECH.2023.3273717

Charles, J. R., Wolf, S. L., Schneider, J. A., and Gordon, A. M. (2006). Efficacy of a child friendly form of constraint induced movement therapy in hemiplegic cerebral palsy a randomized control trial. *Dev. Med. Child Neurology* 48, 635–642. doi:10.1017/s0012162206001356

Coote, S., Murphy, B., Harwin, W., and Stokes, E. (2008). The effect of the gentle/s robot-mediated therapy system on arm function after stroke. *Clin. Rehabil.* 22, 395–405. doi:10.1177/0269215507085060

Cruz-Almeida, Y., Martinez-Arizala, A., and Widerström-Noga, E. G. (2005). Chronicity of pain associated with spinal cord injury: a longitudinal analysis. *J. rehabilitation Res. Dev.* 42, 585. doi:10.1682/jrrd.2005.02.0045

Dunkerley, A., Ashburn, A., and Stack, E. (2000). Deltoid triceps transfer and functional independence of people with tetraplegia. *Spinal Cord.* 38, 435–441. doi:10.1038/sj.sc.3101025

Hendricks, H. T., van Limbeek, J., Geurts, A. C., and Zwarts, M. J. (2002). Motor recovery after stroke: a systematic review of the literature. *Archives Phys. Med. Rehabilitation* 83, 1629–1637. doi:10.1053/apmr.2002.35473

Jackson, W., Novack, T., and Dowler, R. (1998). Effective serial measurement of cognitive orientation in rehabilitation: the orientation log. *Archives Phys. Med. Rehabilitation* 79, 718–721. doi:10.1016/s0003-9993(98)90051-x

Jung, K. M., and Choi, J. D. (2019). The effects of active shoulder exercise with a sling suspension system on shoulder subluxation, proprioception, and upper extremity function in patients with acute stroke. *Med. Sci. Monit.* 25, 4849–4855. doi:10.12659/msm.915277

Kirtley, C. (2004). *Clinical gait analysis: joint moment*. Milano: Springer Milan, 121.

KUKA (2008). Robert the robot helps patients get out of bed faster. Available at: https://www.kuka.com/en-ca/industries/health-care (Accessed April 24, 2022).

Kvorning, T., Bagger, M., Caserotti, P., and Madsen, K. (2006). Effects of vibration and resistance training on neuromuscular and hormonal measures. *Eur. J. Appl. physiology* 96, 615–625. doi:10.1007/s00421-006-0139-3

Lambert, P., Da Cruz, L., and Bergeles, C. (2020). Design, modeling, and implementation of a 7-dof cable-driven haptic device with a configurable cable platform. *IEEE Robotics Automation Lett.* 5, 5764–5771. doi:10.1109/lra.2020.3010748

Lee, J. S., and Lee, H. G. (2014). Effects of sling exercise therapy on trunk muscle activation and balance in chronic hemiplegic patients. *J. Phys. Ther. Sci.* 26, 655–659. doi:10.1589/jpts.26.655

Li, S., and Zanotto, D. (2019). "Tracking control of fully-constrained cable-driven parallel robots using adaptive dynamic programming," in 2019 IEEE/RSJ International Conference on Intelligent Robots and Systems (IROS), Macau, China, 03-08 November 2019 (IEEE), 6781–6787.

Li, X., Yang, Q., and Song, R. (2021). Performance-based hybrid control of a cable-driven upper-limb rehabilitation robot. *IEEE Trans. Biomed. Eng.* 68, 1351–1359. doi:10.1109/TBME.2020.3027823

Liu, J., Feng, W., Zhou, J., Huang, F., Long, L., Wang, Y., et al. (2020). Effects of sling exercise therapy on balance, mobility, activities of daily living, quality of life and shoulder pain in stroke patients: a randomized controlled trial. *Eur. J. Integr. Med.* 35, 101077. doi:10.1016/j.eujim.2020.101077

Liu, Q., Zuo, J., Zhu, C., Meng, W., Ai, Q., and Xie, S. Q. (2022). Design and hierarchical force-position control of redundant pneumatic muscles-cable-driven ankle rehabilitation robot. *IEEE Robotics Automation Lett.* 7, 502–509. doi:10.1109/LRA.2021.3123747

Masiero, R., and Boschetti, R. (2017). "On the use of cable-driven robots in early inpatient stroke rehabilitation," in *Advances in Italian mechanism science*. Editors G. Boschetti, and A. Gasparetto (Cham: Springer International Publishing), 551–558.

Meythaler, J. M., Guin-Renfroe, S., Brunner, R. C., and Hadley, M. N. (2001). Intrathecal baclofen for spastic hypertonia from stroke. *Stroke* 32, 2099–2109. doi:10.1161/hs0901.095682

Oh, J., and Kwon, T. (2017). "A study on the effect of complex rehabilitation exericise methods through short-term active sling exercises and vibration balls on the upper limb muscle activity of people with myelopathy," in 2017 European Conference on Electrical Engineering and Computer Science (EECS), Bern, Switzerland, 17-19 November 2017, 484–488.

Park, J. H., and Hwangbo, G. (2014). The effect of trunk stabilization exercises using a sling on the balance of patients with hemiplegia. *J. Phys. Ther. Sci.* 26, 219–221. doi:10.1589/jpts.26.219

Rosati, G., Gallina, P., and Masiero, S. (2007). Design, implementation and clinical tests of a wire-based robot for neurorehabilitation. *IEEE Trans. Neural Syst. Rehabilitation Eng.* 15, 560–569. doi:10.1109/TNSRE.2007.908560

Singer, J. C., and Mochizuki, G. (2015). Post-stroke lower limb spasticity alters the interlimb temporal synchronization of centre of pressure displacements across multiple timescales. *IEEE Trans. Neural Syst. Rehabilitation Eng.* 23, 786–795. doi:10.1109/TNSRE.2014.2353636

Tsuda, J. (2006). Yaskawa develops a physical therapy robot for the lower extremities. Available at: https://www.yaskawa-global.com/newsrelease/technology/4260 (Accessed May 10, 2022).

Vashista, V., Martelli, D., and Agrawal, S. K. (2016). Locomotor adaptation to an asymmetric force on the human pelvis directed along the right leg. *IEEE Trans. Neural Syst. Rehabilitation Eng.* 24, 872–881. doi:10.1109/TNSRE.2015.2474303

Xie, C., Zhou, J., Song, R., and Xu, T. (2021). "Deep reinforcement learning based cable tension distribution optimization for cable-driven rehabilitation robot," in 2021 6th IEEE International Conference on Advanced Robotics and Mechatronics (ICARM), Chongqing, China, 03-05 July 2021, 318–322.

Yang, L., Xiang, K., Pang, M., Yin, M., Wu, X., and Cao, W. (2023). Inertial sensing for lateral walking gait detection and application in lateral resistance exoskeleton. *IEEE Trans. Instrum. Meas.* 72, 1–14. doi:10.1109/TIM.2023.3265105

Zanotto, D., Rosati, G., Minto, S., and Rossi, A. (2014). Sophia-3: a semiadaptive cable-driven rehabilitation device with a tilting working plane. *IEEE Trans. Robotics* 30, 974–979. doi:10.1109/TRO.2014.2301532

Zarebidoki, M., Dhupia, J., and Xu, W. (2021). "Dynamics modelling and robust passivity-based control of cable-suspended parallel robots in fluidic environment," in 2021 7th International Conference on Mechatronics and Robotics Engineering (ICMRE), Budapest, Hungary, 03-05 February 2021, 48–53.

frontiers | Frontiers in Bioengineering and Biotechnology

TYPE Original Research
PUBLISHED 24 November 2023
DOI 10.3389/fbioe.2023.1323645

OPEN ACCESS

EDITED BY
Wujing Cao,
Chinese Academy of Sciences (CAS), China

REVIEWED BY
Jinke Li,
Chinese Academy of Sciences (CAS), China
Dongyang Shang,
Northeastern University, China

*CORRESPONDENCE
Qiaoling Meng,
mql@usst.edu.cn

†These authors have contributed equally to this work and share first authorship

RECEIVED 18 October 2023
ACCEPTED 13 November 2023
PUBLISHED 24 November 2023

CITATION
Meng Q, Liu G, Xu X, Meng Q, Qin L and Yu H (2023), A multi-degree-of-freedom reconfigurable ankle rehabilitation robot with adjustable workspace for post-stroke lower limb ankle rehabilitation. *Front. Bioeng. Biotechnol.* 11:1323645. doi: 10.3389/fbioe.2023.1323645

A multi-degree-of-freedom reconfigurable ankle rehabilitation robot with adjustable workspace for post-stroke lower limb ankle rehabilitation

Qingyun Meng[1,2,3†], Guanxin Liu[1,2,3†], Xin Xu[1,2,3], Qiaoling Meng[2,3*], Liang Qin[1,3] and Hongliu Yu[2,3]

[1]College of Medical Instruments, Shanghai University of Medicine and Health Sciences, Shanghai, China, [2]Institute of Rehabilitation Engineering and Technology, University of Shanghai for Science and Technology, Shanghai, China, [3]Shanghai Engineering Research Center of Assistive Devices, Shanghai, China

Introduction: A multi-degree-of-freedom ankle rehabilitation robot with an adjustable workspace has been designed to facilitate ankle joint rehabilitation training. It features a rotation center adapted to the human body, making it suitable for patients with ankle dysfunction following a stroke.

Method: In this study, a multi-degree-of-freedom reconfigurable ankle rehabilitation robot (RARR) with adaptable features, based on the principles of ergonomics, has been proposed to cater to the varying needs of patients. This robot offers an adjustable workspace, allowing for different types of ankle joint rehabilitation exercises to be performed. By adjusting the assembly of the RARR, personalized and targeted training can be provided to patients, circumventing issues of redundancy in degrees of freedom during its use. A kinematic model of the robot has been established, and finite element simulation has been employed to analyze the strength of critical components, ensuring the safety of the robot. An experimental platform has been set up to assess the smoothness of the rehabilitation process with RARR, with angle measurements conducted using an Inertial Measurement Unit (IMU).

Results and discussion: In conclusion, both simulation and experimental results demonstrate that the robot offers an adjustable workspace and exhibits relatively smooth motion, thereby confirming the safety and effectiveness of the robot. These outcomes align with the intended design goals, facilitating ankle joint rehabilitation and advancing the field of reconfigurable robotics. The RARR boasts a compact structure and portability, making it suitable for various usage scenarios. It is easily deployable for at-home use by patients and holds practical application value for wider adoption in rehabilitation settings.

KEYWORDS

rehabilitation robot, rehabilitation training, reconfigurable mechanism, ankle rehabilitation, variable workspace

1 Introduction

Stroke is an acute cerebrovascular disorder characterized by a high incidence rate, elevated mortality, and a range of complications (Feigin et al., 2021; Markus, 2022). In recent years, the issue of post-stroke motor dysfunction has become increasingly pressing due to the growing number of stroke patients, with data indicating that approximately 65% of survivors require rehabilitation (Miao et al., 2023). Traditional rehabilitation is labor-intensive, and associated with limitations such as the inability to quantify rehabilitation data, strained medical resources, inconsistent training, and high costs (Gittler and Davis, 2018; Gao et al., 2023). Robot-assisted therapy has emerged as a solution to address these challenges. As the fields of rehabilitation medicine and robotics continue to integrate, various models of ankle rehabilitation robots have been designed to address ankle joint dysfunction resulting from strokes (Dao et al., 2022; Meng et al., 2023a). These diverse rehabilitation robots possess unique potential, offering the promise of more effective and consistent rehabilitation solutions for these patients, thereby positively impacting their quality of life and rehabilitation outcomes.

Ankle rehabilitation robots have extensive applications in the field of rehabilitation medicine, including but not limited to ankle injury rehabilitation, athlete rehabilitation, and elderly population rehabilitation, among other application contexts. Traditionally, ankle rehabilitation robots can be categorized into two main types: wearable and platform-based systems (Jiang et al., 2019; Li et al., 2020). Platform-based ankle rehabilitation robots are fixed devices consisting of a base and a footplate. The base incorporates control and power systems, while the patient places their foot on the footplate. The robot then moves the footplate within predefined parameters, assisting patients in recovering ankle joint strength and flexibility. Zou et al. (2022) proposed a 3-RRS (where R and S denote revolute and spherical joints, respectively) parallel ankle rehabilitation robot (PARR) with low mobility parallel mechanisms. Tsoi et al. (2009) presented an approach that aligns the rotation center by using the patient's ankle as a part of the robot's kinematic constraints, including the selection of four linear actuators to control platform tilt. However, this approach may inadvertently impose unexpected loads, leading to discomfort and safety concerns. Zhang et al. (2019) developed a parallel ankle rehabilitation robot (PARR) with three rotational degrees of freedom around the virtual stationary center of the ankle joint. They also established a comprehensive information acquisition system to enhance human-machine interaction among the robots, patients, and healthcare providers. These studies emphasize the importance of considering compatibility, convenience, and safety in the design process. Nonetheless, the mentioned rehabilitation devices are often unable to provide targeted treatment solutions to users, leading to unnecessary movements during the rehabilitation process, resulting in redundancy of degrees of freedom. Additionally, their complex structures increase the cost of robot design. To address these issues, Zhang et al. (2017) introduced a redundant-driven reconfigurable robot structure called the Compliance Ankle Rehabilitation Robot (CARR). This robot is powered by four Festo pneumatic muscles, offering an adjustable workspace and actuator torque to meet the range of motion and muscle strengthening requirements for training. However, this rehabilitation equipment is relatively large in size, involves complex setup and adjustments, and has limited applicability in various environments. Furthermore, rehabilitation devices developed using flexible actuators and materials are still in the experimental stage and are primarily found in laboratories (Meng et al., 2023b). Wang et al. (2022) designed a novel reconfigurable ankle rehabilitation exoskeleton capable of static and dynamic rehabilitation exercises and real-time adaptation to the rotation center of the human ankle-foot complex. Yoon and Ryu (2005) developed a reconfigurable ankle rehabilitation robot with multiple rehabilitation modes. This robot can be reconfigured from a range of motion (ROM) or strengthening exercise device by simply adding extra boards to a balance or proprioceptive exercise device.

When developing ankle rehabilitation devices, it is essential to prioritize user needs, such as device adjustability and adaptability, the capability for personalized rehabilitation plans, a comfortable user experience, and low usage costs, among other aspects. However, this presents several challenges: 1. Precision and Safety: Precision and safety are fundamental prerequisites for designing such devices. The robot must ensure the effectiveness and safety of the equipment. 2. Cost and Accessibility: The manufacturing cost of the robot and the accessibility of the equipment pose a challenge. Rehabilitation robots need to be produced within a reasonable price range to ensure widespread availability to medical institutions and patients. 3. Software Development and Algorithm Design: Complex control algorithms need to be developed to enable the robot to provide personalized rehabilitation plans. The causes of ankle injuries in patients are diverse, and each patient may require different rehabilitation approaches. Therefore, the development of a personalized and reconfigurable ankle rehabilitation robot tailored to individual patient needs holds significant importance.

This study presents a multi-degree-of-freedom ankle rehabilitation robot with an adjustable workspace for post-stroke lower limb ankle rehabilitation. The key feature of this robot is its ability to be personalized and assembled according to the specific rehabilitation needs of different users, involving the selection of varying numbers of actuators and assembly modes to achieve different workspaces for the robot. This customization aims to provide personalized treatment, avoid redundancy of degrees of freedom, and alleviate the financial burden on users. The organization of the remainder of this study is as follows: Section 2 provides an overview of the robot's design, including different assembly modes. Section 3 conducts a theoretical analysis of the robot, including the establishment of the robot's kinematic model, the construction of the robot's workspaces in various modes, and finite element simulation analysis to verify the strength of critical robot components, ensuring the robot's safety and effectiveness. Section 4 establishes an experimental platform and conducts passive control rehabilitation motion experiments with the robot prototype, analyzing the experimental results to validate the feasibility of the robot. Finally, in Section 5, a summary and outlook for this study are provided.

2 RARR system design

This section provides a detailed account of the design process for the RARR system, comprising two main aspects: the mechanical structure of RARR and the control system. The mechanical structure

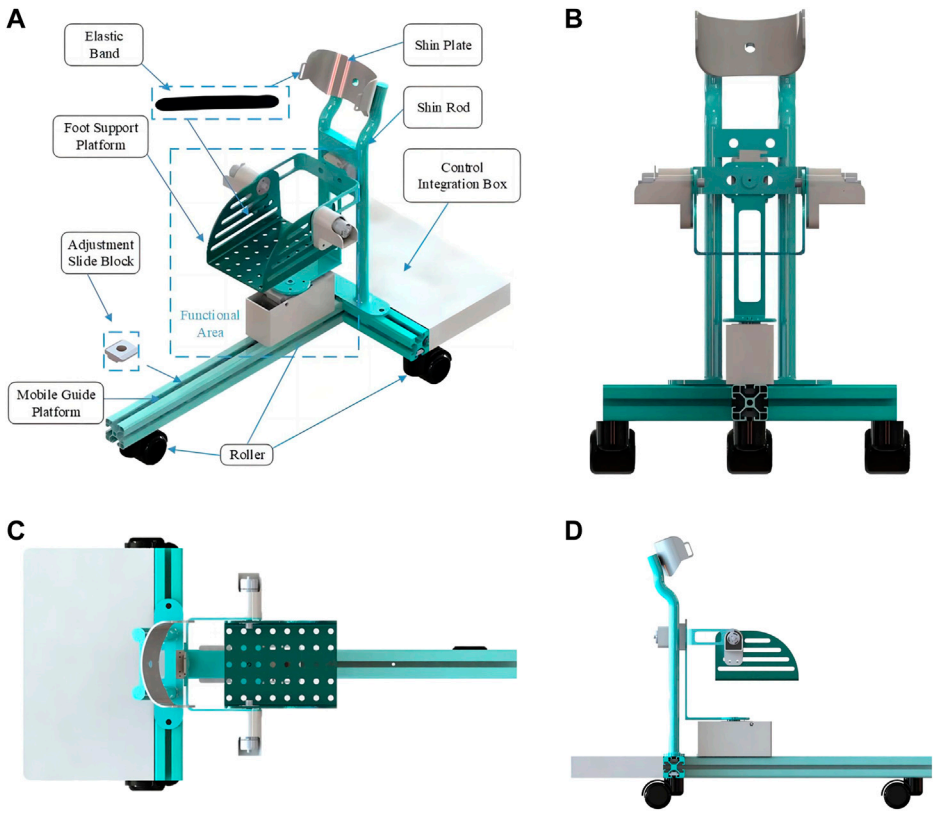

FIGURE 1
RARR model diagram. **(A)** Installation schematic. **(B)** Front view. **(C)** Top view. **(D)** left view.

can be further subdivided into three key components: reconfigurable design, adjustable design, and rotation center matching design. The RARR's mechanical structure encompasses three degrees of freedom, and its adaptability is achieved by selecting different numbers of actuators and diverse assembly configurations to accommodate adjustable robot workspaces. These configurations can be set to enable three single-axis motion modes: dorsiflexion/plantarflexion, inversion/eversion, and internal/external rotation; three dual-axis motion modes: dorsiflexion/plantarflexion with inversion/eversion, dorsiflexion/plantarflexion with internal/external rotation, and inversion/eversion with internal/external rotation; and one three-axis motion mode. The adjustable design allows for user-specific adaptability, facilitating both left and right foot interchangeability and catering to users of varying heights. The rotation center matching design is implemented to prevent patients from incurring secondary injuries while using the system. The control architecture of RARR is composed of four main modules: the central control module, sensing module, selection module, and actuation module.

2.1 Mechanical design

The RARR model is illustrated in Figure 1. The structure of RARR comprises several components, including a mobile guide rail platform, adjustable sliders, a shin rod, a shin support plate, a foot support platform, elastic bands, a control integration box, transmission mechanisms, and three non-powered rollers. The three rollers are situated beneath the mobile guide rail platform and facilitate the robot's movement. These rollers can also be locked to prevent unintended movements during use. During rehabilitation training, the user's lower leg is secured with elastic bands, isolating the ankle from other lower limb joints to prevent compensatory movements and reduce the load on the robot. The functional sections of RARR are fixed to the mobile guide rail platform using sliders and are driven by motors to facilitate user foot movement during rehabilitation. Mechanical limit structures are designed at each rotational joint to ensure user safety. The control integration box houses the necessary components for the control system. Table 1 provides the mechanical specifications of RARR, detailing the range of motion for each joint (Sun et al., 2019).

2.1.1 Reconfigurable design

In the process of rehabilitation training, multifunctional or reconfigurable robots are more appealing to patients as they can reduce healthcare costs and improve the effectiveness of rehabilitation training (Wang et al., 2022). To cater to the diverse rehabilitation needs of different users, RARR has been designed with reconfigurability, offering an adjustable workspace. By choosing varying numbers of actuators and different configurations for the functional sections, RARR can

TABLE 1 Range of motion for RARR.

Motion	Angle range (°)
Internal	0–20
External	0–30
Dorsiflexion	0–30
Plantarflexion	0–50
Inversion	0–40
Eversion	0–30

be reconfigured into 7 different modes, corresponding to 3 single-degree-of-freedom motions, 3 dual-degree-of-freedom motions, and 1 three-degree-of-freedom motion, as depicted in Figure 2.

2.1.2 Adjustable design

To accommodate users with varying lower leg lengths, the robot can be adjusted. By changing the position of the sliders, the functional sections of the robot can be adjusted forward and backwards along the guide rail to suit users of different heights. In RARR, adjustable limit structures are employed at the internal/external rotation and inversion/eversion rotational joints, allowing patients to switch between left and right foot rehabilitation training, as depicted in Figure 3. During left foot rehabilitation training, the user depresses Rod A, pushing its lower end into the limit slot. Simultaneously, Rod C is pushed to the left, securing Rod A. When right foot rehabilitation training is required, Rod B is depressed, pushing its lower end into the limit slot. Rod C is also pushed to the left, securing Rod B. This action simultaneously releases Rod A, which, under the force of a spring, pops out of the limit slot. This adjustment allows for different robot workspaces, facilitating the transition between left and right foot rehabilitation training.

2.1.3 Rotation center matching design

An important consideration in the design of rehabilitation robots is ensuring that the robot's rotation center aligns with the ankle joint's rotation center. Mismatched rotation centers can lead to patient discomfort or even secondary injuries, it is significant to figure out the issue of axis alignment of human-robot coupling (Wang et al., 2022; Cao et al., 2023). Ensuring that the mechanical rotation center of the rehabilitation robot coincides with the ankle joint's rotation center is a crucial issue in the design process. We achieve this objective through the following methods: 1. Anatomical Research: Anatomical studies and measurements of the human ankle joint are conducted to determine the ankle joint's axis of rotation and the location of its rotation center, as depicted in Figure 4. This data serves as a reference for robot design to ensure that the robot's rotation center closely matches or coincides with the ankle joint's rotation center. 2. Software Simulation: Using relevant software, a human body model is imported, and simulations are conducted to represent the robot's operation. By comparing the position of the robot's rotation center with that of the human ankle joint's rotation center, adjustments are made to optimize the robot's design parameters to achieve a matching rotation center, as illustrated in Figure 5.

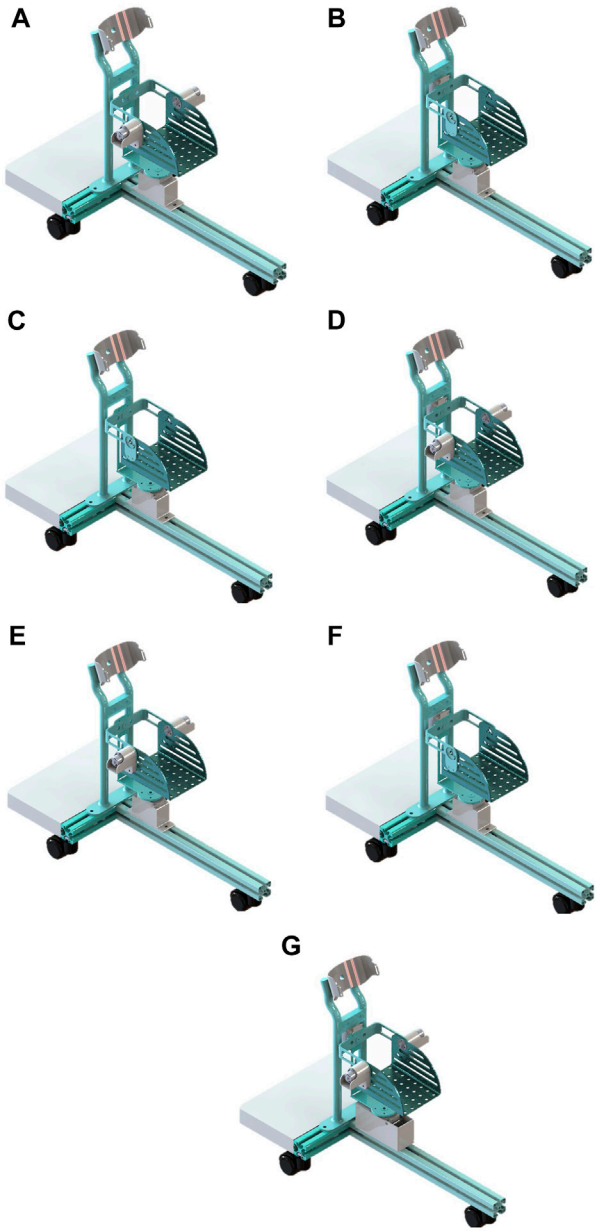

FIGURE 2
Different modes of RARR. **(A)** Dorsiflexion/plantarflexion. **(B)** Inversion/eversion. **(C)** Internal/external rotation. **(D)** dorsiflexion/plantarflexion with inversion/eversion. **(E)** dorsiflexion/plantarflexion with internal/external rotation. **(F)** Inversion/eversion with internal/external rotation. **(G)** 3-degree-of-Freedom.

2.2 Control design

The RARR control system consists of four main modules: the central control module, sensing module, selection module, and actuation module, as depicted in Figure 6. The central control module utilizes an STM32 controller as the control core,

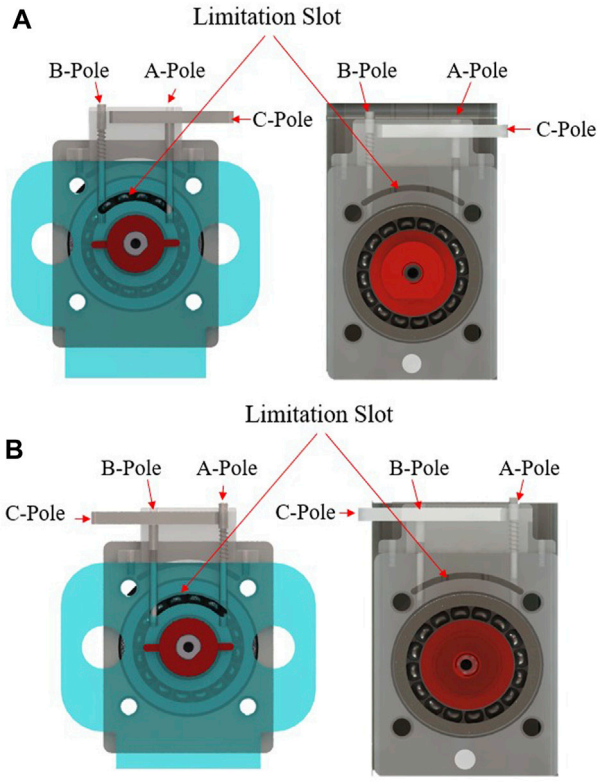

FIGURE 3
Mechanical limitation at rotational joints. **(A)** Limitation device for left foot rehabilitation training. **(B)** Mechanical limitation device for right foot rehabilitation training.

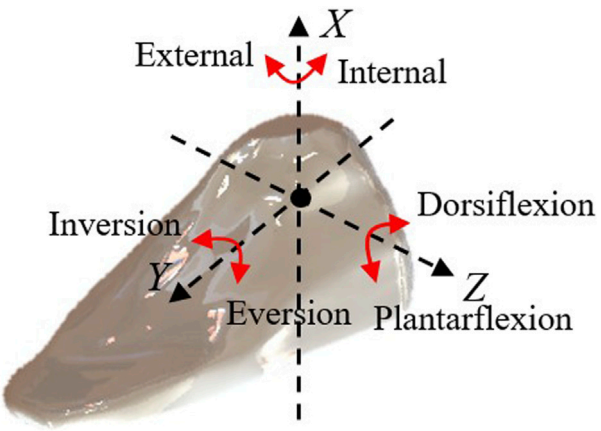

FIGURE 4
Different directions of ankle joint movement.

receiving commands and translating them into corresponding signals. The sensing module comprises a nine-axis IMU sensor (N100, WHEELTEC, Dongguan, China, with an angular accuracy of 0.1RMS) and thin-film pressure sensors. This module collects user foot angle information and pressure data, forming the basis for force feedback and position feedback. The selection module is

FIGURE 5
Matching rotation centers.

primarily implemented through USART HMI, model TJC4827T043_011, which provides users with a graphical interface. It uses different key values to set motion parameters, achieve the desired goals and complete various training tasks. The actuation module is composed of four brushless DC gear motors and encoders. The controller controls the motion of these four brushless DC motors via the CAN bus, enabling rehabilitation training actions. Simultaneously, the encoders and the sensing module continuously monitor the user's condition to observe the user's current information, as shown in Figure 7.

In the course of a patient's rehabilitation exercise, the controller governs the motion based on received signals and control algorithms. Subsequently, the actual joint angles of the robot are fed back to the central control module through motor encoders and posture sensors, forming a closed-loop control system. This system enables real-time and continuous monitoring and adjustment of the patient's rehabilitation status.

3 Theoretical analysis

3.1 Kinematic model

The kinematic analysis of rehabilitation robots is of significant importance for workspace analysis, motion trajectory planning, and the determination of the robot's feasibility. Therefore, it is necessary to establish a kinematic model for the analysis of relevant kinematics (Meng et al., 2023a). In the robot's motion, a Cartesian coordinate system is established using ***RPY*** angles. Initially, a stationary coordinate system {**A**} is set at the robot's virtual rest center as a reference frame. Its *Z*-axis is parallel to the

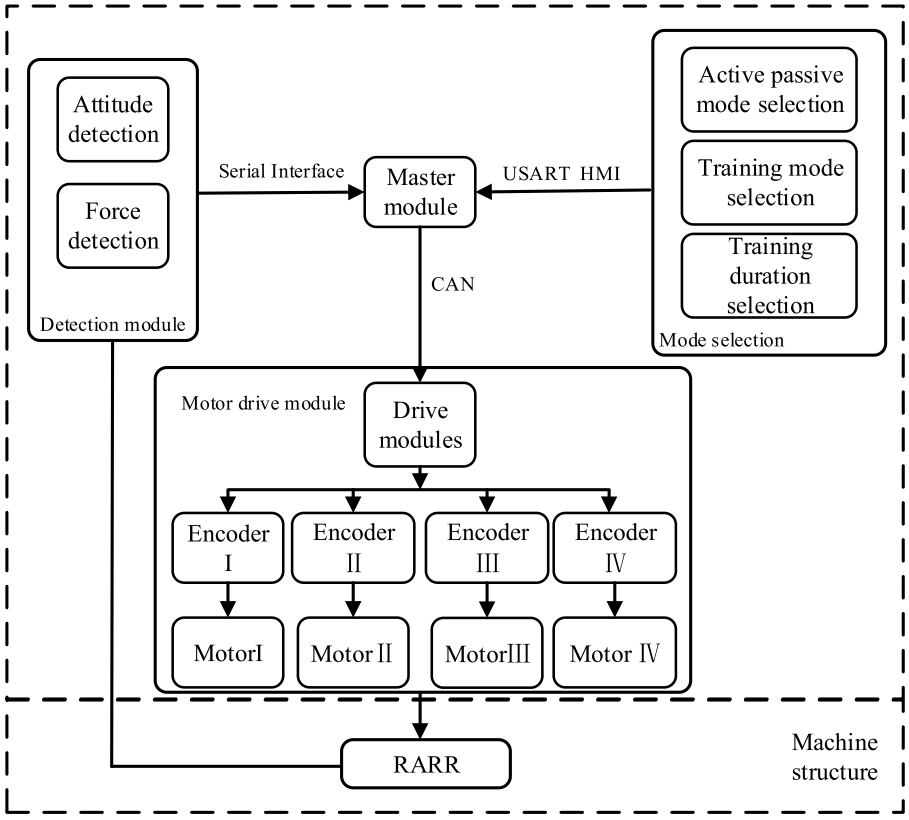

FIGURE 6
Overall control design of the RARR system.

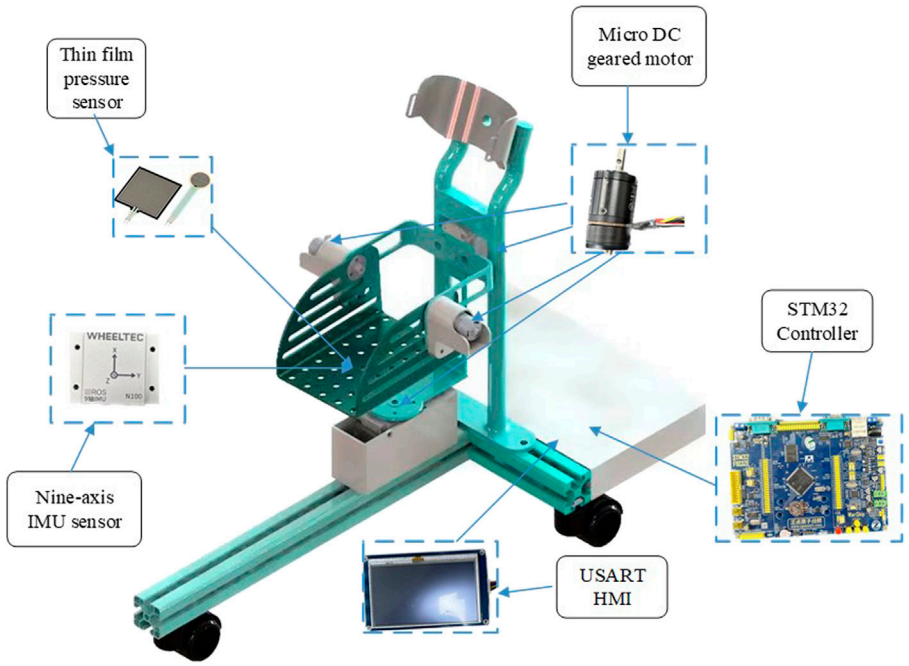

FIGURE 7
Hardware installation model of RARR.

10.3389/fbioe.2023.1323645

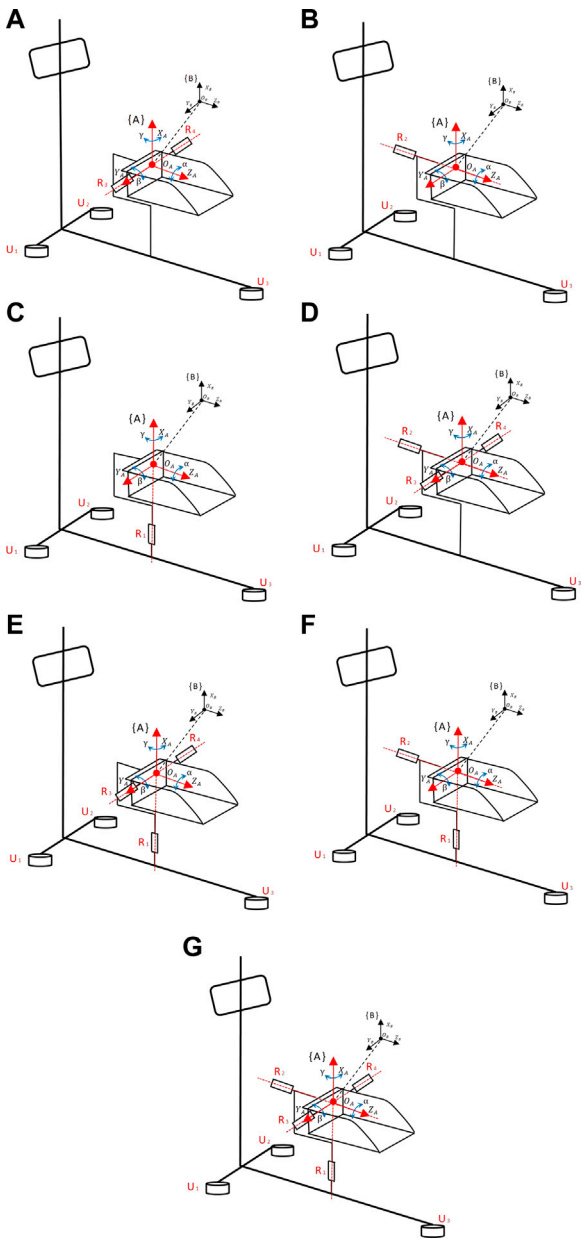

FIGURE 8
Coordinate diagram of RARR motion structure. **(A)** Dorsiflexion/plantarflexion. **(B)** Inversion/eversion. **(C)** Internal/external rotation. **(D)** dorsiflexion/plantarflexion with inversion/eversion. **(E)** dorsiflexion/plantarflexion with internal/external rotation. **(F)** Inversion/eversion with internal/external rotation. **(G)** 3-degree-of-Freedom.

footplate plane, pointing toward the far end of the footplate, the *X*-axis is perpendicular to the footplate plane, pointing upward, and the *Y*-axis is parallel to the footplate plane, pointing to the right of the footplate. Simultaneously, a moving coordinate system {**B**} is established at the same origin, moving with the platform, with its axes oriented similarly to coordinate system {**A**}, representing the post-motion footplate plane, as shown in

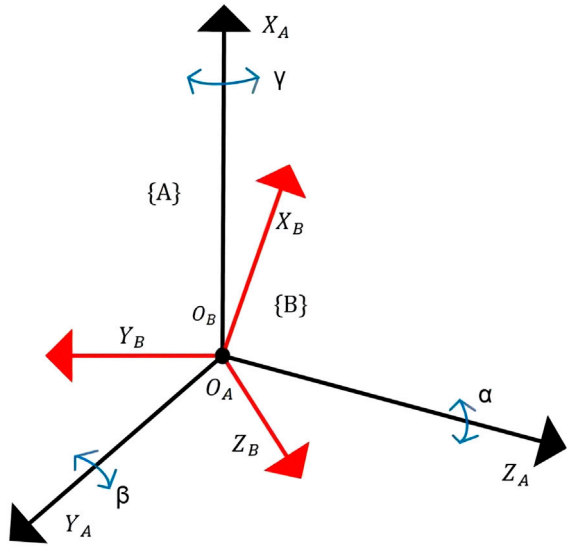

FIGURE 9
Simplified coordinate diagram of RARR.

Figure 8 and simplified in Figure 9. The relationship between coordinate system **B** relative to coordinate system **A** can describe the state of an object.

3.1.1 Forward kinematic analysis

Here, γ, β and α represent the rotation angles of coordinate system **B** around X_A, Y_A and Z_A, respectively. The rotation matrix represented using ***RPY*** angles is as follows:

$$
\begin{aligned}
{}^{A}_{B}R_{XYZ}(\gamma,\beta,\alpha) &= R_Z(\alpha)R_Y(\beta)R_X(\gamma)\\
&= \begin{bmatrix} c\alpha & -s\alpha & 0\\ s\alpha & c\alpha & 0\\ 0 & 0 & 1 \end{bmatrix}\begin{bmatrix} c\beta & 0 & s\beta\\ 0 & 1 & 0\\ -s\beta & 0 & c\beta \end{bmatrix}\begin{bmatrix} 1 & 0 & 0\\ 0 & c\gamma & -s\gamma\\ 0 & s\gamma & c\gamma \end{bmatrix}\\
&= \begin{bmatrix} c\alpha c\beta & c\alpha s\beta s\gamma - s\alpha c\gamma & c\alpha s\beta c\gamma + s\alpha s\gamma\\ s\alpha c\beta & s\alpha s\beta s\gamma + c\alpha c\gamma & s\alpha s\beta c\gamma - c\alpha s\gamma\\ -s\beta & c\beta s\gamma & c\beta c\gamma \end{bmatrix}
\end{aligned}
\tag{1}
$$

When performing dorsiflexion/plantarflexion motion, coordinate system {**B**} rotates around X_A and Z_A angles are 0, which means $\alpha = 0$ and $\gamma = 0$. Therefore, its kinematic equation is as follows:

$$
\begin{aligned}
{}^{A}_{B}R_{XYZ}(\gamma,\beta,\alpha) &= R_Z(\alpha)R_Y(\beta)R_X(\gamma)\\
&= \begin{bmatrix} 1 & 0 & 0\\ 0 & 1 & 0\\ 0 & 0 & 1 \end{bmatrix}\begin{bmatrix} c\beta & 0 & s\beta\\ 0 & 1 & 0\\ -s\beta & 0 & c\beta \end{bmatrix}\begin{bmatrix} 1 & 0 & 0\\ 0 & 1 & 0\\ 0 & 0 & 1 \end{bmatrix} = \begin{bmatrix} c\beta & 0 & s\beta\\ 0 & 1 & 0\\ -s\beta & 0 & c\beta \end{bmatrix}
\end{aligned}
\tag{2}
$$

Similarly, we can derive the kinematic models for the other modes as follows:

Inversion/Eversion Motion Mode:

$$
{}^{A}_{B}R_{XYZ}(\gamma,\beta,\alpha) = \begin{bmatrix} c\alpha & -s\alpha & 0\\ s\alpha & c\alpha & 0\\ 0 & 0 & 1 \end{bmatrix} \tag{3}
$$

10.3389/fbioe.2023.1323645

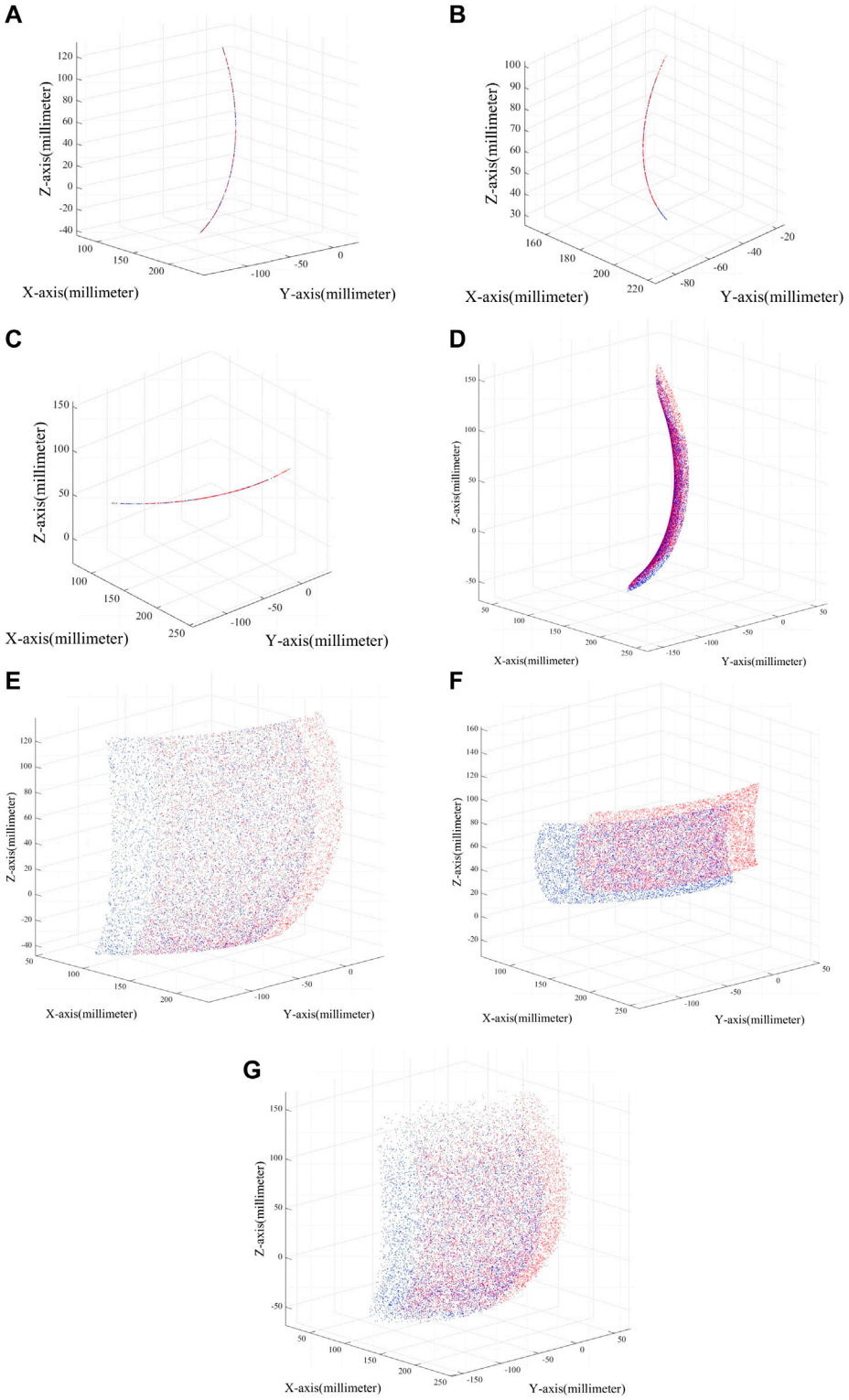

FIGURE 10
Robot workspace in different modes. **(A)** Dorsiflexion/plantarflexion. **(B)** Inversion/eversion. **(C)** Internal/external rotation. **(D)** dorsiflexion/plantarflexion with inversion/eversion. **(E)** dorsiflexion/plantarflexion with internal/external rotation. **(F)** Inversion/eversion with internal/external rotation. **(G)** 3-degree-of-Freedom.

TABLE 2 Material properties of 6,061 aluminum alloy.

Yield Strength (N/m^2)	Tensile Strength (N/m^2)	Young's Modulus (N/m^2)	Poisson's ratio	Mass density (kg/m^3)	Shear modulus (N/m^2)
5.51485e+007	1.24084e+008	6.9e+010	0.33	2,700	2.6e+010

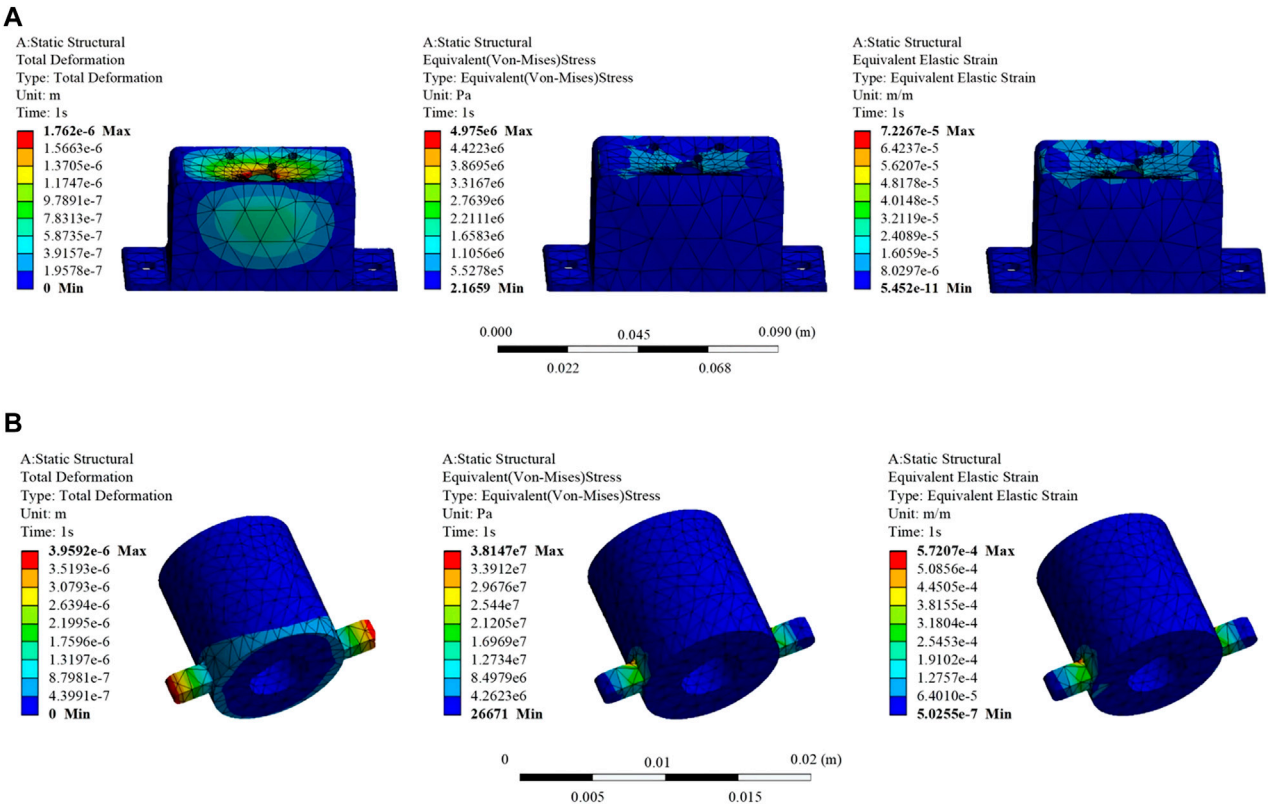

FIGURE 11
Finite element analysis results of selected key components. **(A)** Part 1: Total deformation, equivalent stress, and equivalent elastic strain results. **(B)** Part 2: Total deformation, equivalent stress, and equivalent elastic strain results.

Internal/External Rotation Motion Mode:

$$ {}^{A}_{B}\boldsymbol{R}_{XYZ}(\gamma,\beta,\alpha) = \begin{bmatrix} 1 & 0 & 0 \\ 0 & c\gamma & -s\gamma \\ 0 & s\gamma & c\gamma \end{bmatrix} \tag{4} $$

Dorsiflexion/Plantarflexion and Inversion/Eversion Motion Mode:

$$ {}^{A}_{B}\boldsymbol{R}_{XYZ}(\gamma,\beta,\alpha) = \begin{bmatrix} c\alpha c\beta & -s\alpha & c\alpha s\beta \\ s\alpha c\beta & c\alpha & s\alpha s\beta \\ -s\beta & 0 & c\beta \end{bmatrix} \tag{5} $$

Dorsiflexion/Plantarflexion and Internal/External Rotation Motion Mode:

$$ {}^{A}_{B}\boldsymbol{R}_{XYZ}(\gamma,\beta,\alpha) = \begin{bmatrix} c\beta & s\beta s\gamma & s\beta c\gamma \\ 0 & c\gamma & -s\gamma \\ -s\beta & c\beta s\gamma & c\beta c\gamma \end{bmatrix} \tag{6} $$

Inversion/Eversion and Internal/External Rotation Motion Mode:

$$ {}^{A}_{B}\boldsymbol{R}_{XYZ}(\gamma,\beta,\alpha) = \begin{bmatrix} c\alpha & -s\alpha c\gamma & s\alpha s\gamma \\ s\alpha & c\alpha c\gamma & -c\alpha s\gamma \\ 0 & s\gamma & c\gamma \end{bmatrix} \tag{7} $$

Three Degrees of Freedom Motion Mode:

$$ {}^{A}_{B}\boldsymbol{R}_{XYZ}(\gamma,\beta,\alpha) = \begin{bmatrix} c\alpha c\beta & c\alpha s\beta s\gamma - s\alpha c\gamma & c\alpha s\beta c\gamma + s\alpha s\gamma \\ s\alpha c\beta & s\alpha s\beta s\gamma + c\alpha c\gamma & s\alpha s\beta c\gamma - c\alpha s\gamma \\ -s\beta & c\beta s\gamma & c\beta c\gamma \end{bmatrix} \tag{8} $$

3.1.2 Inverse kinematic analysis

Given the rotation matrix, we can deduce the **XYZ** fixed-angle representation in ***RPY***. Let:

$$ {}^{A}_{B}\boldsymbol{R}_{XYZ}(\gamma,\beta,\alpha) = \begin{bmatrix} r_{11} & r_{12} & r_{13} \\ r_{21} & r_{22} & r_{23} \\ r_{31} & r_{32} & r_{33} \end{bmatrix} = \begin{bmatrix} c\alpha c\beta & c\alpha s\beta s\gamma - s\alpha c\gamma & c\alpha s\beta c\gamma + s\alpha s\gamma \\ s\alpha c\beta & s\alpha s\beta s\gamma + c\alpha c\gamma & s\alpha s\beta c\gamma - c\alpha s\gamma \\ -s\beta & c\beta s\gamma & c\beta c\gamma \end{bmatrix} \tag{9} $$

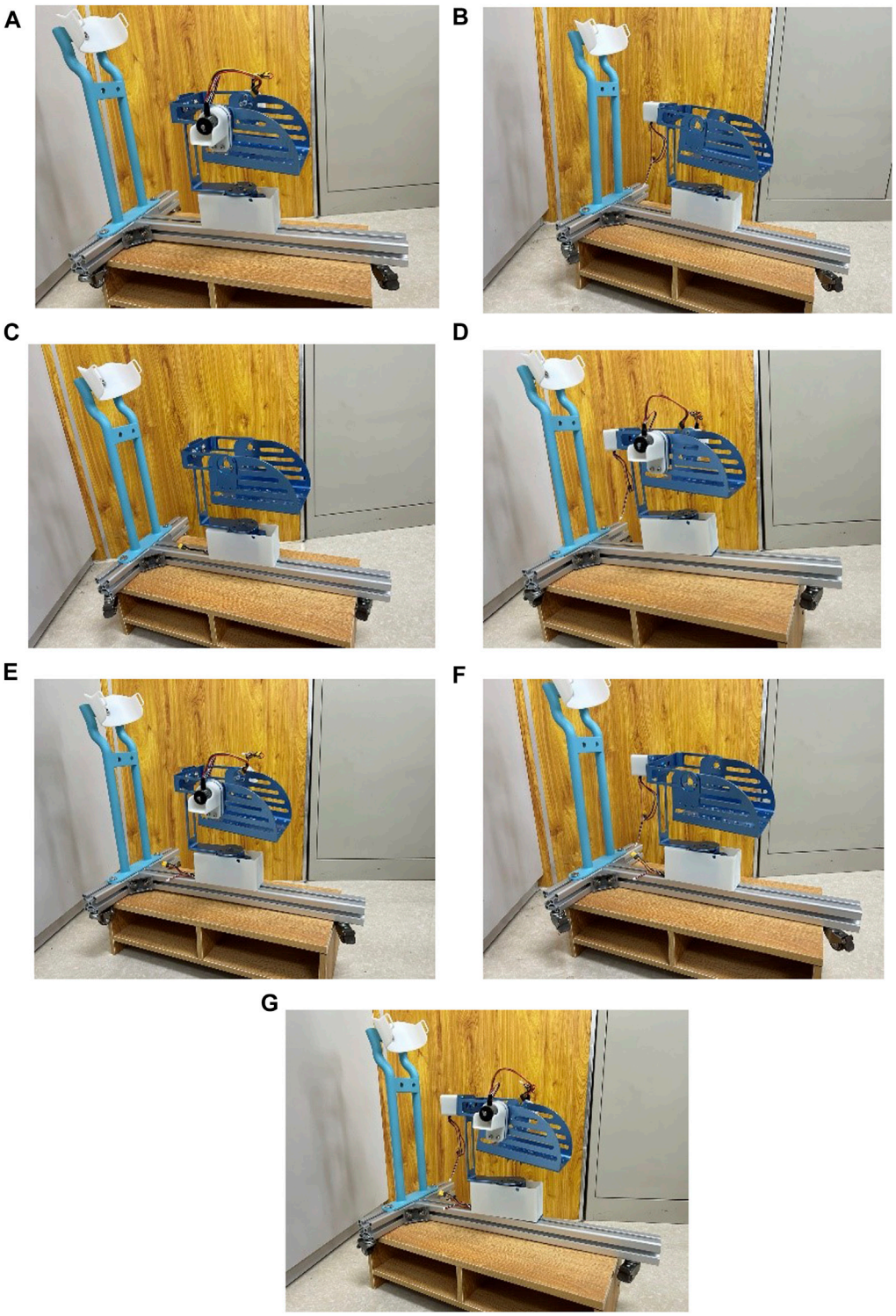

FIGURE 12
Robot prototype in various assembly modes. **(A)** Dorsiflexion/plantarflexion. **(B)** Inversion/eversion. **(C)** Internal/external rotation. **(D)** dorsiflexion/plantarflexion with inversion/eversion. **(E)** dorsiflexion/plantarflexion with internal/external rotation. **(F)** Inversion/eversion with internal/external rotation. **(G)** 3-degree-of-Freedom.

Through derivation, we can obtain:

$$\mathbf{c\beta} = \pm \sqrt{r_{11}^2 + r_{21}^2} \tag{10}$$

By dividing $-r_{31}$ by $c\beta$, we obtain $\tan\beta$, and finally, taking the arctan will give us:

$$\beta = \mathbf{A\tan 2}\left(-r_{31}, \sqrt{r_{11}^2 + r_{21}^2}\right) \tag{11}$$

Based on the normal range of motion of the human ankle joint and the mechanical limit design of the robot, we can determine that $-50^\circ \le \beta \le 30^\circ$ and $c\beta \neq 0$, thus:

$$\alpha = \mathbf{A}\tan 2(r_{21}, r_{11}), \beta = \mathbf{A}\tan 2\left(-r_{31}, \sqrt{r_{11}^2 + r_{21}^2}\right), \gamma = A\tan 2(r_{32}, r_{33}) \quad (12)$$

Where $A\tan 2(y, x)$ is the two-argument arctangent function, with a range of values in $[-\pi, \pi]$.

3.2 Workspace analysis

The workspace of the robot is a crucial metric for evaluating its feasibility, as it reflects the robot's performance and directly impacts its practical application value (Meng et al., 2023b). To visually represent the variability of RARR's workspace, based on the kinematic model of the ankle rehabilitation robot, a Monte Carlo random sampling method was used to plot a large number of end-effector positions to achieve visualization of the robot's workspace, as shown in Figure 10.

Figure 10 displays the variation in the robot's workspace under different modes. From the figure, it is evident that the robot's workspace varies with different configurations, and adjustments within the same mode can also lead to different workspaces. Additionally, the robot's workspace aligns with the physiological parameters of the human ankle joint, making RARR suitable for assisting ankle joint rehabilitation training. The blue area in the figure represents the workspace when using the right foot, while the red area represents the workspace when using the left foot.

3.3 Finite element strength verification of key components

One of the primary objectives of this study is to reduce the volume and overall weight of the ankle rehabilitation robot by simplifying the mechanical structure and optimizing materials. This approach aims to minimize psychological stress on patients during the training process and reduce energy consumption. Considering factors such as material yield strength and mass density, 6,061 aluminum alloy was chosen as the primary material for key components of the RARR. The main material properties of 6,061 aluminum alloy are outlined in Table 2. The remaining components are manufactured using 3D printing with photosensitive resin as the material.

To validate the reliability and rationality of the mechanical design and material selection in this study, finite element analysis was conducted on selected key components of the designed mechanism, as illustrated in Figure 11.

From the information presented in the figures, it is evident that the maximum stresses locally experienced by Part 1 and Part 2 are 4.975e+006N/m^2 and 3.8147e+007N/m^2, respectively. These values are significantly below the material's yield strength of 5.51485e+007N/m^2. The maximum strains are 7.2267e-005 m/m and 5.7207e-004 m/m for Part 1 and Part 2, respectively. Additionally, the maximum displacement values are 1.762e-006 and 3.9592e-006 m for Part 1 and Part 2, respectively, indicating minimal deformation. These results suggest that the chosen materials for Key Components 1 and 2 are appropriate, and the dimensional design of the components meets the design requirements.

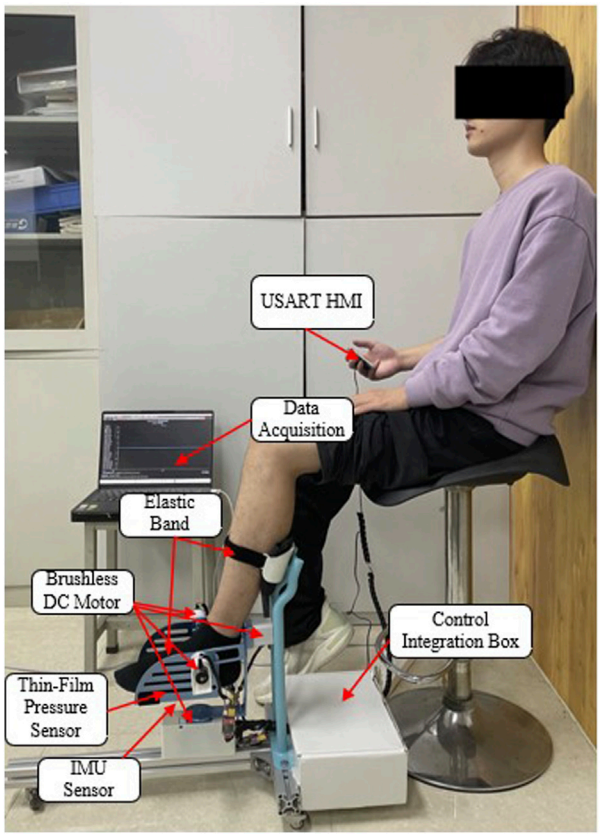

FIGURE 13
Passive control rehabilitation training experiment.

4 Experimental findings

4.1 Manufacturing of the prototype and verification of reconfigurability

In accordance with the design plan, the prototype was successfully manufactured, and seven different assembly modes were realized through various assembly methods, as illustrated in Figure 12. Importantly, there were no interferences during the robot assembly process. The successful manufacturing of the experimental prototype validates the rationality and reconfigurability of the robot design.

4.2 Passive control rehabilitation training experiment

One healthy subject (male, 26 years old, height 178 cm, weight 60 kg) was recruited to undergo passive rehabilitation training. This

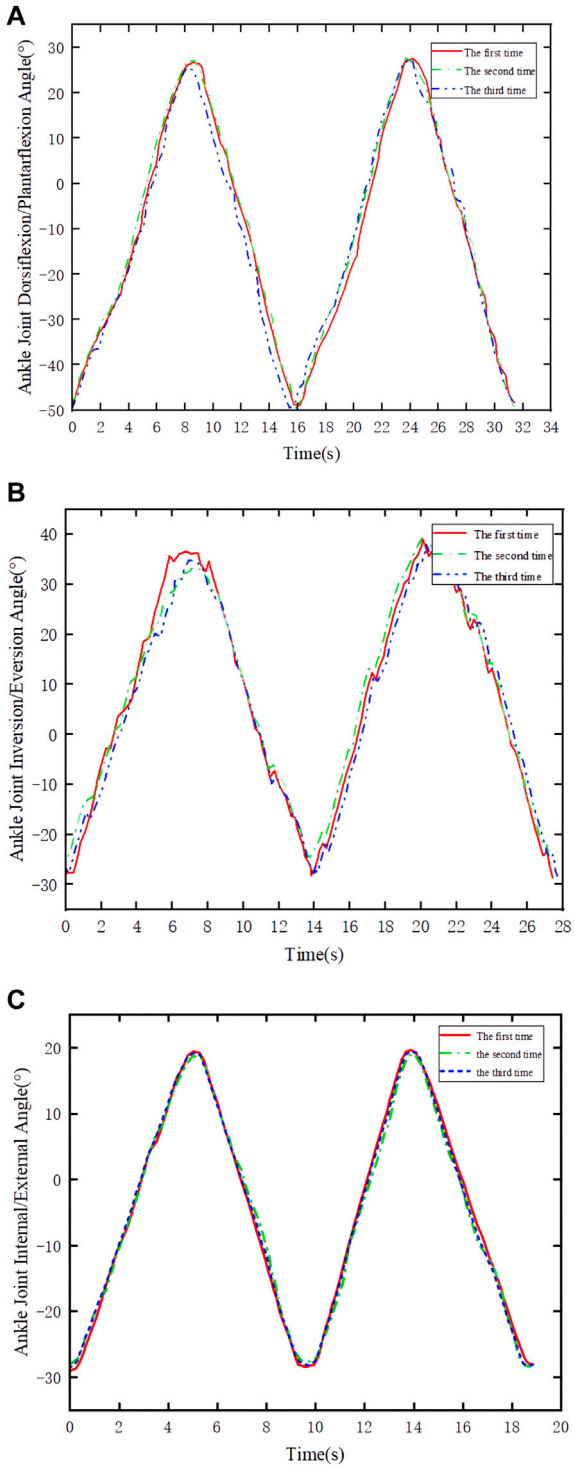

FIGURE 14
Joint angle variations in passive control experiments. **(A)** Dorsiflexion/plantarflexion. **(B)** Inversion/eversion. **(C)** Internal rotation/external rotation.

study was conducted with the approval of the Ethics Review Committee of Shanghai University of Medicine and Health Sciences (Approval Number: 2022-zyxm2-04--420300197109053525), and all procedures adhered to the standards outlined in the Helsinki Declaration.

Passive rehabilitation training is suitable for early rehabilitation of ankle joint dysfunction patients who may exhibit symptoms of muscle weakness, low muscle strength, or high muscle tone. Hence, the experimental setup involved lower joint operating speeds to ensure system safety. After donning the experimental prototype, the subject underwent passive control rehabilitation training to verify the effectiveness and stability of joint motion during the testing, as shown in Figure 13.

During the training process, first, zeroing the IMU device was performed to address errors caused by the installation of the IMU by the experimenter (Yang et al., 2023). Subsequently, a nine-axis IMU sensor was utilized to monitor the patient's posture and acquire the robot's motion performance. Three experiments were conducted with the same motion, as depicted in Figure 14. The experimental results indicate that the training trajectory during passive rehabilitation is smooth, without abrupt angle changes. However, due to interference errors during operation, some angles exhibit fluctuations. In summary, the RARR, driven by direct motor control, moves the footplate to enable ankle rehabilitation training, thereby meeting the user's needs for strengthening ankle muscle, restoring joint mobility, and enhancing ankle joint stability. This robot fulfills its design purpose for assisting in rehabilitation training.

5 Conclusion and future prospects

This study has successfully developed and evaluated a multi-degree-of-freedom, reconfigurable ankle rehabilitation robot with a variable working space to assist in the rehabilitation training of patients with ankle dysfunction following a stroke. The robot's variable working space and reconfigurable characteristics allow it to adapt to seven different modes, catering to the diverse rehabilitation needs of users. The mechanism incorporates three rotational degrees of freedom around the human ankle's rotation center, reducing discomfort for users during operation. Theoretical analysis was conducted to determine the relevant parameters of the robot and validate its performance. Subsequent experiments demonstrated the robot's reconfigurability and the smoothness of training trajectories, aligning with the design objectives. Designed with principles of human factors engineering, the robot features a compact structure, portability, and cost-effectiveness, making it suitable for home use by patients. The modular design helps reduce equipment usage and maintenance costs, depending on the robot's assembly mode, its manufacturing cost ranges from $800 to $1200. As a result, the developed Reconfigurable Ankle Rehabilitation Robot (RARR) holds practical application value in ankle rehabilitation and is primed for widespread use. Furthermore, we believe that the design methods/principles of this device can provide valuable insights for the design of devices for other body parts. For example, in the design of upper limb exoskeleton robots, the interchangeable and adjustable design can facilitate patients in performing rehabilitation exercises for different limbs. Additionally, the adjustability of robot mechanism lengths can accommodate various patients. The application of a simple, compact, and portable design concept not only reduces the production cost of the robot but also allows patients to use it in different settings. In the future, we will continue to enhance the device's practicality and aesthetics,

integrating various human-machine interaction modes such as voice control and a plantar electrostimulation system to increase its utility. Clinical trials will also be conducted to further enhance the rehabilitation effectiveness in clinical practice.

Data availability statement

The raw data supporting the conclusion of this article will be made available by the authors, without undue reservation.

Ethics statement

The studies involving humans were approved by Ethics Review Committee of Shanghai University of Medicine and Health Sciences. The studies were conducted in accordance with the local legislation and institutional requirements. Written informed consent for participation was not required from the participants or the participants' legal guardians/next of kin in accordance with the national legislation and institutional requirements. Written informed consent was obtained from the individual(s) for the publication of any potentially identifiable images or data included in this article.

Author contributions

QnM: Conceptualization, Resources, Validation, Writing–review and editing. GL: Methodology, Software, Writing–original draft. XX: Data curation, Formal Analysis, Writing–original draft. QaM: Funding acquisition, Investigation, Project administration, Writing–review and editing. LQ: Investigation, Supervision, Writing–review and editing. HY: Project administration, Supervision, Writing–review and editing.

Funding

The author(s) declare financial support was received for the research, authorship, and/or publication of this article. This work was funded by the National Key R&D Program of China (2020YFC2007501) and the National Key R&D Program of China (2022YFC3601403).

Conflict of interest

The authors declare that the research was conducted in the absence of any commercial or financial relationships that could be construed as a potential conflict of interest.

Publisher's note

References

Cao, W., Shang, D., Yin, M., Li, X., Xu, T., Zhang, L., et al. (2023). Development and evaluation of a hip exoskeleton for lateral resistance walk exercise. *IEEE ASME Trans. Mechatron.* 28 (4), 1966–1974. doi:10.1109/TMECH.2023.3273717

Dao, M. D., Tran, X. T., Pham, D. P., Ngo, Q. A., and Le, T. T. T. (2022). Study on the ankle rehabilitation device. *Arch. Mech. Eng.* 69, 147–163. doi:10.24425/ame.2021.139803

Feigin, V. L., Stark, B. A., Johnson, C. O., Roth, G. A., Bisignano, C., Abady, G. G., et al. (2021). Global, regional, and national burden of stroke and its risk factors, 1990–2019: a systematic analysis for the Global Burden of Disease Study 2019. *Lancet Neurol.* 20, 795–820. doi:10.1016/S1474-4422(21)00252-0

Gao, X., Zhang, P., Peng, X., Zhao, J., Liu, K., Miao, M., et al. (2023). Autonomous motion and control of lower limb exoskeleton rehabilitation robot. *Front. Bioeng. Biotechnol.* 11, 1223831. doi:10.3389/fbioe.2023.1223831

Gittler, M., and Davis, A. M. (2018). Guidelines for adult stroke rehabilitation and recovery. *Jama* 319, 820–821. doi:10.1001/jama.2017.22036

Jiang, J., Min, Z., Huang, Z., Ma, X., Chen, Y., and Yu, X. (2019). Research status on ankle rehabilitation robot. *Recent Pat. Mech. Eng.* 12, 104–124. doi:10.2174/2212797612666190524104033

Li, J., Zuo, S., Zhang, L., Zhang, L., Dong, M., Zhang, Z., et al. (2020). Mechanical design and performance analysis of a novel parallel robot for ankle rehabilitation. *J. Mech. Robot.* 12, 051007. doi:10.1115/1.4046511

Markus, H. S. (2022). Reducing disability after stroke. *Int. J. Stroke* 17, 249–250. doi:10.1177/17474930221080904

Meng, Q., Liu, G., Meng, Q., Xu, X., Qin, L., and Yu, H. (2023b). Bionic design of a novel portable hand-elbow coordinate exoskeleton for activities of daily living. *Electronics* 12 (15), 3326. doi:10.3390/electronics12153326

Meng, Q., Liu, G., Meng, Q., Xu, X., and Yu, H. (2023a). Design and analysis of a supine ankle rehabilitation robot for early stroke recovery. *Machines* 11 (8), 787. doi:10.3390/machines11080787

Miao, M. d., Gao, X. s., Zhao, J., and Zhao, P. (2023). Rehabilitation robot following motion control algorithm based on human behavior intention. *Appl. Intell.* 53, 6324–6343. doi:10.1007/s10489-022-03823-7

Sun, Z., Wang, C., Wei, J., Xia, J., Wang, T., Liu, Q., et al. (2019). "Kinematics and dynamics analysis of a novel ankle rehabilitation robot," in 2019 IEEE 9th Annual International Conference on CYBER Technology in Automation, Control, and Intelligent Systems (CYBER), Suzhou, China, 29 July 2019 - 02 August 2019, 1404–1409. doi:10.1109/CYBER46603.2019.9066767

Tsoi, Y. H., Xie, S. Q., and Graham, A. E. (2009). "Design, modeling and control of an ankle rehabilitation robot," in *Design and control of intelligent robotic systems*. Editors D. Liu, L. Wang, and K. C. Tan (Berlin, Heidelberg: Springer). Studies in Computational Intelligence. doi:10.1007/978-3-540-89933-4_18

Wang, T., Spyrakos-Papastavridis, E., and Dai, J. S. (2022). Design and analysis of a novel reconfigurable ankle rehabilitation exoskeleton capable of matching the mobile biological joint center in real-time. *ASME. J. Mech. Robot.* 15 (1), 011011. doi:10.1115/1.4054313

Yang, L., Xiang, K., Pang, M., Yin, M., Wu, X., and Cao, W. (2023). Inertial sensing for lateral walking gait detection and application in lateral resistance exoskeleton. *IEEE Trans. Instrum. Meas.* 72 (4004014), 1–14. doi:10.1109/TIM.2023.3265105

Yoon, J., and Ryu, J. (2005). "A novel reconfigurable ankle/foot rehabilitation robot," in Proceedings of the 2005 IEEE International Conference on Robotics and Automation, Barcelona, Spain, 18-22 April 2005, 2290–2295. doi:10.1109/ROBOT.2005.1570454

Zhang, L., Li, J., Dong, M., Fang, B., Cui, Y., Zuo, S., et al. (2019). Design and workspace analysis of a parallel ankle rehabilitation robot (PARR). *J. Healthc. Eng.* 2019, 1–10. doi:10.1155/2019/4164790

Zhang, M., Cao, J., Zhu, G., Miao, Q., Zeng, X., and Xie, S. Q. (2017). Reconfigurable workspace and torque capacity of a compliant ankle rehabilitation robot (CARR). *Rob. Auton. Syst.* 98, 213–221. doi:10.1016/j.robot.2017.06.006

Zou, Y., Zhang, A., Zhang, Q., Zhang, B., Wu, X., and Qin, T. (2022). Design and experimental research of 3-RRS parallel ankle rehabilitation robot. *Micromachines (Basel)* 13 (6), 950. doi:10.3390/mi13060950

frontiers | Frontiers in Bioengineering and Biotechnology

TYPE Original Research
PUBLISHED 03 January 2024
DOI 10.3389/fbioe.2023.1332689

OPEN ACCESS

EDITED BY
Wujing Cao,
Chinese Academy of Sciences (CAS), China

REVIEWED BY
Dongyang Shang,
Northeastern University, China
Yue Ma,
Chinese Academy of Sciences (CAS), China

*CORRESPONDENCE
Minghui Wu,
wuminghui@sues.edu.cn
Hongliu Yu,
yhl_usst@outlook.com

RECEIVED 03 November 2023
ACCEPTED 08 December 2023
PUBLISHED 03 January 2024

CITATION
Zhang Y, Li T, Tao H, Liu F, Hu B, Wu M and Yu H (2024), Research on adaptive impedance control technology of upper limb rehabilitation robot based on impedance parameter prediction. *Front. Bioeng. Biotechnol.* 11:1332689. doi: 10.3389/fbioe.2023.1332689

Research on adaptive impedance control technology of upper limb rehabilitation robot based on impedance parameter prediction

Yuling Zhang[1,2], Tong Li[1,2], Haoran Tao[1,2], Fengchen Liu[1,2], Bingshan Hu[1,2], Minghui Wu[3]* and Hongliu Yu[1,2]*

[1]School of Health Science and Engineering, University of Shanghai for Science and Technology, Shanghai, China, [2]Shanghai Engineering Research Center of Assistive Devices, Shanghai, China, [3]School of Mechanical and Automotive Engineering, Shanghai University of Engineering Science, Shanghai, China

Introduction: With the aggravation of aging and the growing number of stroke patients suffering from hemiplegia in China, rehabilitation robots have become an integral part of rehabilitation training. However, traditional rehabilitation robots cannot modify the training parameters adaptively to match the upper limbs' rehabilitation status automatically and apply them in rehabilitation training effectively, which will improve the efficacy of rehabilitation training.

Methods: In this study, a two-degree-of-freedom flexible drive joint rehabilitation robot platform was built. The forgetting factor recursive least squares method (FFRLS) was utilized to estimate the impedance parameters of human upper limb end. A reward function was established to select the optimal stiffness parameters of the rehabilitation robot.

Results: The results confirmed the effectiveness of the adaptive impedance control strategy. The findings of the adaptive impedance control studies showed that the adaptive impedance control had a significantly greater reward than the constant impedance control, which was in line with the simulation results of the variable impedance control. Moreover, it was observed that the levels of robot assistance could be suitably modified based on the subject's different participation.

Discussion: The results facilitated stroke patients' upper limb rehabilitation by enabling the rehabilitation robot to adaptively change the impedance parameters according to the functional status of the affected limb. In clinic therapy, the proposed control strategy may help to adjust the reward function for different patients to improve the rehabilitation efficacy eventually.

KEYWORDS

rehabilitation robot, upper limb, impedance identification, adaptive impedance control, optimal stiffness

1 Introduction

Stroke is globally recognized as the second leading cause of both disability and mortality (Sun et al., 2022). The incidence of stroke worldwide reached 13.7 million new cases, with China alone accounting for 3.94 million new cases (Ma et al., 2021; Vasu et al., 2021). The severity of stroke affects the probability of hemiplegia, as well as the changes in gait speed, balance, spasticity, and range of motion (Hong et al., 2018). With the aggravation of aging and the growing number of

stroke patients suffering from hemiplegia in China, the impact of stroke is becoming increasingly noticeable (Honghai et al., 2022). The current number of rehabilitation physicians and therapists is hard to meet the needs of rehabilitation training for the numerous hemiplegic patients. The rehabilitation robot is the outcome of the fusion between robot technology and rehabilitation engineering, which may assist patients with rehabilitation training to a great extent by replacing rehabilitation physicians. Fabio *et al.* proved the feasibility and effectiveness of hand rehabilitation assisted by rehabilitation robot (Vanoglio et al., 2016). Rehabilitation robot offers several advantages over traditional therapy performed by therapists, including consistent delivery of therapy, objective and quantitative assessment, and virtual reality interfaces to enhance the rehabilitation experience (Wang et al., 2019). The traditional upper limb rehabilitation robot can only perform the programmed rehabilitation movements repeatedly, lacking the ability to adaptively adjust the training parameters based on the affected limb's participation during active rehabilitation training. Therefore, robot-assisted rehabilitation can more effectively motivate patients to complete their rehabilitation training (Islam et al., 2021).

The impedance parameter of the upper limb is a useful method to evaluate the extent of the affected limb's engagement in rehabilitation exercises, and impedance control is a widely-used technique for regulating the levels of assistance provided by robotic systems during rehabilitation training (Perez-Ibarra et al., 2015). In order to provide appropriate assistant force in training, different control strategies have been proposed by relevant studies. Perez Ibarra *et al.* conducted two adaptive impedance control strategies and indicated that incorporating the damping parameters of patients into the patient impedance model could enhance the velocity correlation (Perez-Ibarra et al., 2019). Krebs *et al.* developed an impedance control algorithm based on performance metrics such as speed, time, or EMG signals to adaptively adjust the duration and levels of assistance provided by the robot during movement (Krebs et al., 2003). In order to adjust the interaction change between the human-machine system, Wolbrecht combined the model-based adaptive impedance control with real-time torque calculation as feed-forward for the affected limb (Wolbrecht et al., 2008). Losey *et al.* proposed a sensorless force estimation component to evaluate the patient's ability state and subsequently modified the training mode of the rehabilitation platform (Pehlivan et al., 2016). Although the resistance training for stroke patients has become a popular method to facilitate rehabilitation, most rehabilitation robots' resistance training offers constant resistance, which lacks adaptability to the patients' variable status.

Some studies considered the adaptation of resistance in robot-assisted rehabilitation. Guozheng Xu used the biological damping and stiffness parameters identified online to monitor the changes of muscle strength of the subjects automatically and modified the required resistance to be aligned with the changes in the muscle strength of the subjects (Xu et al., 2017). OttC proposed a control framework for passive flexible joint rehabilitation robot and designed the impedance controller which was verified on the DLR lightweight robots and was only suitable for the cases of constant impedance parameters (Albu-Schaffer et al., 2007). Researchers from the Chinese University of Hong Kong suggested an iterative learning impedance controller for rehabilitation robots, providing a theoretical basis to ensure dynamic stability in variable impedance control driven by compliance-driven rehabilitation robots (Li et al., 2018). A nonlinear model relating to an adaptive bilateral impedance controller was proposed by Mojtaba Sharifi's group, which was suitable for various collaborative tele-rehabilitation of patient-rehabilitation physician interaction in a multi-degree of freedom tele-robotics system (Sharifi et al., 2017). Adaptive impedance control also played a role in exoskeleton rehabilitation robots, using a nonlinear time-delay disturbance observer (Brahmi et al., 2021). In the current rehabilitation robotics studies, the existing human impedance parameter identification methods can hardly identify the impedance parameters of human upper limb in real time and apply them in rehabilitation training dynamically and effectively.

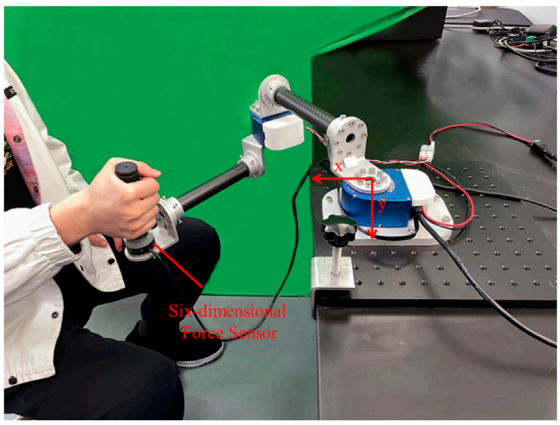

FIGURE 1
The flexible upper limb rehabilitation robot.

In the process of rehabilitation training, more and more people consider the importance of variable impedance for rehabilitation training, and the interaction force between human-machine system to make accurate evaluation of the patient's state. However, the present training model still cannot mobilize the participation of patients. If the rehabilitation robot can identify the impedance parameters of the upper limb end and modify the rehabilitation strategy by adjusting the impedance parameters of the rehabilitation robot adaptively according to the patient's status, the rehabilitation efficiency can be improved significantly, which is more conducive to the rehabilitation of the affected limb.

In this study, aiming to increase the effectiveness of upper limb rehabilitation robot, a robot rehabilitation platform was established and an adaptive impedance control strategy was proposed, which could adaptively change the impedance parameters according to the subject's participation. The paper is organized as follows: Section II describes a mechanical platform of rehabilitation robot built for the following study and the adaptive impedance control strategy. Section III demonstrates the simulation verification and the experiment results. Section IV conducts the discussion about the results, and Section V draws the conclusion of the study.

2 Materials and methods

2.1 Rehabilitation robot system

2.1.1 Mechanical platform and control system

As shown in Figure 1, the flexible joint rehabilitation robot platform was constructed. Based on the two-degree-of-freedom

TABLE 1 XGA key joint parameters.

Configuration	XGA
Maximum torque	19Nm
Maximum speed	28.5RPM
weight	550g
Transmission ratio	766.222:1
communication	Ethernet
sensor	Detect torque, acceleration, temperature and current

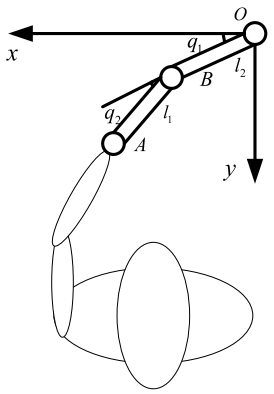

FIGURE 2
The training diagram of the two-degree-of-freedom flexible joint upper limb rehabilitation robot.

flexible joint upper limb rehabilitation robot, two connecting rods were coupled in series using a flexible driver. Tube A and B were made of carbon fiber tubes, which had the advantages of lightweight and strong material. The end force sensor adopted the SRI's six-axis (force and moment) force sensor M3714A, which could simultaneously measure the force and moment in the end of Cartesian coordinate system. The robotic joint was one of Seenpin's XGA series. The joint integrated the motor, reducer, elastomer, controller, and a variety of sensors. The joint was characterized by high power density, high speed, and a high torque output.

The external bus control was applied on the platform. The host and the joint were connected by a network cable. The signal transmission between the two joints and the host was achieved by Ethernet communication. The control system supported MATLAB one-stop development environment, which reduced the time cost of debugging the underlying hardware and network construction for the experiment. Key joint parameters were shown in the following Table 1. The stiffness of the joint adopted in the experiment was 170 Nm/rad.

2.1.2 Robot kinematics model

The training diagram of the two-degree-of-freedom flexible joint upper limb rehabilitation robot could be simplified as Figure 2. The upper limb rehabilitation robot was composed of two rods (rod A and rod B), m_1 = 1 kg, m_2 = 0.7 kg, $l_1 = l_2 = 0.4$, $l_{c1} = l_{c2}$= 0.2. l_{c1} *and* l_{c2} were the centroids of the two rods respectively. l_1 and l_2 were the lengths of the two rods respectively. Assuming the two rods had the same mass, the midpoints of rods A and B served as the mass centers of the two rods respectively, and q_1, q_2 represented the joint angles of rod A and rod B. With point O as the center, the forward kinematics formula of the upper limb rehabilitation robot with two degrees of freedom was established as follows.

$$x_p = l_1 \cos q_1 + l_2 \cos(q_1 + q_2) \tag{1}$$

$$y_p = l_1 \sin q_1 + l_2 \sin(q_1 + q_2) \tag{2}$$

x_p and y_p were the horizontal and vertical coordinates of the Cartesian space of the robot end.

The inverse kinematics formula was derived from the forward kinematics:

$$q_1 = \operatorname{atan2}(-l_2 s_2 x_e + (l_1 + l_2 c_2) y_e, (l_1 + l_2 c_2) x_e + l_2 s_2 y_e) \tag{3}$$

$$q_2 = \pm \operatorname{acos}\left(\frac{x_p^2 + y_p^2 + l_1^2 - l_2^2}{2 l_1 l_2}\right) \tag{4}$$

2.2 Adaptive impedance control strategy

The adaptive impedance control diagram based on human impedance parameter identification was shown in Figure 3, which mainly included impedance parameter estimation of the affected limb, stiffness optimization, impedance controller, trajectory planning, inverse kinematics, and robot controller, etc. The robot first determined the rehabilitation task, chose the task node, carried out trajectory planning for the rehabilitation robot through quintic polynomial interpolation to get the expected end trajectory X_d, and then calculated the joint expected trajectory through inverse kinematics q_d as the controller input. The position of the joint controller was regulated by PD control. Next, the impedance parameters K_h of the affected limb were identified online using the FFRLS. The impedance parameters of the upper limb end were also acquired. The optimal impedance K_r was calculated by equations (14) and (15), and the terminal position correction Δx was obtained by inputting K_r into the impedance controller, correcting the expected trajectory X_d to the reference trajectory X_r. The above process was the adaptive impedance control procedure.

2.2.1 Identification of upper limb impedance parameters

Some studies have considered mechanical impedance control as an important method of human motion control. The complex human arm model was simplified as a Cartesian impedance model. The internal model of the arm was transferred to the end of the human arm in the horizontal plane. Therefore, stiffness, damping, and mass became the three components of the mechanical impedance at the end of the human upper limb, relating to force, position, speed, and acceleration respectively. In order to use this model to assume human-computer interaction in the rehabilitation system, it was necessary to estimate the impedance at the end of the human arm. In this section, a model of human upper limb was established and the impedance at the end of human upper limb was estimated by FFRLS.

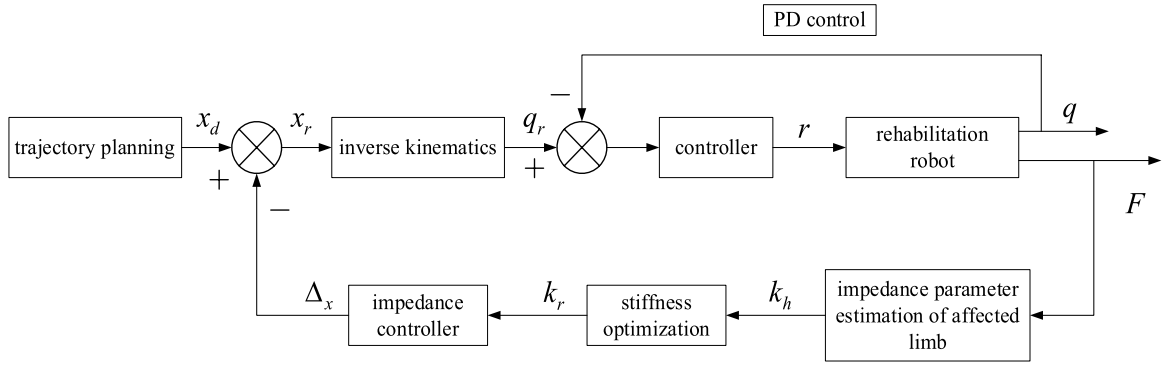

FIGURE 3
The adaptive impedance control diagram based on human impedance parameter identification.

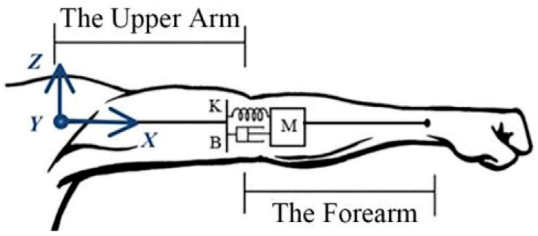

FIGURE 4
The impedance model of the human upper limb.

Since the musculoskeletal system was assumed to be a mass-spring-damping system, the dynamic motion equation of the mass-spring-damper system was used as a mathematical model to measure the dynamic impedance of the upper limb. The impedance model of the upper limb was depicted in Figure 4, which could be used to measure the dynamic impedance of the upper limb under during movement. When the upper limb was in the stable state, the impedance model of the human upper limb end in the Cartesian coordinate system could be displayed as follows:

$$M\ddot{X} + B\dot{X} + KX = F \tag{5}$$

M, B, $K \in \mathbb{R}^{3\times3}$ respectively represented the inertial parameters, damping parameters and stiffness parameters of the human upper limb end, $X \in \mathbb{R}^3$ and $F \in \mathbb{R}^3$ respectively represented the position and force of the upper limb end in the Cartesian coordinate system. The position of the upper limb end was measured by the joint encoder. The joint position was calculated by the kinematic equation, and the end force was measured by the six-dimensional force sensor.

In the process of rehabilitation training, the impedance parameters of human upper limb were variable. With the changes in the rehabilitation cycle, the impedance parameters of human upper limb modified slowly. For the slow time-varying system, the recursive least square (RLS) method had its limitations. As k increased, the values of $P(k)$ and $K(k)$ decreased, resulting in declining corrections for $\hat{\theta}_k$,, the smaller and smaller correction effect of $\hat{\theta}_k$ from new input and output data pairs. Additionally, the accuracy of parameter estimation error decreased and the RLS method was unable to track the changes in system parameters online constantly. To overcome this shortcoming, FFRLS was carried out (Long et al., 2023).

Take the cost function:

$$J = \sum_{k=1}^{L} \lambda^{L-K} \left[y(k) - \varphi^T(k)\hat{\theta} \right]^2 \tag{6}$$

λ was the forgetting factor ($0 < \lambda \leq 1$), which meant that the input and output data were added with a time-varying weight coefficient. The weight of the latest input and output data of the k group was 1, and the weight coefficient of all the previous n groups was λ^n. The smaller the weight coefficient of the original data was, the greater the degree of forgetting was. The values of $P(k)$ and $K(k)$ would not lose their ability to correct $\hat{\theta}_k$ with the increase of k, that is, the influence on the system parameter identification would not decrease.

The RLS derivation formula of forgetting factor was as follows:

$$\begin{cases} \hat{\theta}(k) = \hat{\theta}(k-1) + K(k)\left[y(k) - \varphi^T(k)\hat{\theta}(k-1) \right] \\ K(k) = \dfrac{P(k-1)\varphi(k)}{\lambda + \varphi^T(k)P(k-1)\varphi(k)} \\ P(k) = \dfrac{1}{\lambda}\left[I - K(k)\varphi^T(k) \right] P(k-1) \end{cases} \tag{7}$$

The method of selecting initial values $P(0), \hat{\theta}(0)$ was the same as RLS. The value of forgetting factor λ was generally a positive real number which was close to 1, usually greater than 0.9. In the linear system, the forgetting factor was generally $0.95 \leq \lambda \leq 1$. When $\lambda = 1$, the FFRLS degraded into the ordinary RLS.

2.2.2 Optimal stiffness selection

At different stages of their rehabilitation, patients need different training modalities, requiring a specific stiffness from the rehabilitation robot (Zou et al., 2022). In order to increase the effectiveness of rehabilitation therapy assisted by rehabilitation robot, patients' active participation must be encouraged by the robot controller (Luo et al., 2017; Guo et al., 2022a). At the same time, if the patient's movement deviated from the expected movement, it should be restrained. Therefore, the reward function was set to balance patients' participation and trajectory shift error. The reward function was defined as:

$$r = a_1 F_h V - \|a_2\, e\|^2 = \left(a_1 F_x V_x - a_2^2 e_x^2\right) + \left(a_1 F_y V_y - a_2^2 e_y^2\right) \tag{8}$$

$F_h V$ was the output power of the patient, which was used to measure the effort of the patient; e_x and e_y were the trajectory error at the end of Cartesian space; a_1 and a_2 were the parameters which struck a balance between the patient's effort and the trajectory deviation. When the reward value was higher, the higher the patient's participation in rehabilitation training was higher and the deviation of the expected trajectory was less.

$$\begin{aligned} F_x &= K_{hx}(x_d - x) - B_{hx} V_x \\ F_y &= K_{hy}(y_d - y) - B_{hy} V_y \end{aligned} \tag{9}$$

Eq. 9 was substituted into Eq. 8,

$$r = \left(K_{hx} e_x V_x - a_1 B_{hx} V_x^2 - a_2^2 e_x^2\right) + \left(K_{hy} e_y V_y - a_1 B_{hy} V_y^2 - a_2^2 e_y^2\right) \tag{10}$$

The reward function r took the partial derivative with respect to e_x and e_y respectively.

$$\begin{aligned} \frac{\delta r}{\delta e_x} &= a_1 K_{hx} V_x - 2a_2^2 e_x \\ \frac{\delta r}{\delta e_y} &= a_1 K_{hy} V_y - 2a_2^2 e_y \end{aligned} \tag{11}$$

In order to maximize the reward function, $\frac{\delta r}{\delta e_x} = 0, \frac{\delta r}{\delta e_y} = 0$,

$$\begin{aligned} \hat{e}_x &= \frac{a_1 K_{hx} V_x}{2a_2^2} \\ \hat{e}_y &= \frac{a_1 K_{hy} V_y}{2a_2^2} \end{aligned} \tag{12}$$

During rehabilitation training, the inertia, motion acceleration, and speed of the rehabilitation robot were very small. The inertia force and Coriolis force could be safely disregarded. In addition, compared with the joint torque of the rehabilitation robot, friction was also found to be negligible. Assuming that the affected limb end achieved a stable state within a short time, the force of the rehabilitation robot was equal to that exerted by the patient:

$$\begin{aligned} F_{rx} + F_x &= 0 \\ F_{ry} + F_y &= 0 \end{aligned} \tag{13}$$

$$\begin{aligned} (K_{rx} + K_{hx}) e_x - (B_{rx} + B_{hx}) V_x &= 0 \\ \left(K_{ry} + K_{hy}\right) e_y - \left(B_{ry} + B_{hy}\right) V_y &= 0 \end{aligned} \tag{14}$$

Eq. 12 was substituted into Eq. 14 to obtain the optimal stiffness of impedance control of rehabilitation robot:

$$\begin{aligned} \hat{K}_{rx} &= \frac{2a_2^2 (B_{rx} + B_{hx})}{a_1 K_{hx}} - K_{hx} \\ \hat{K}_{ry} &= \frac{2a_2^2 \left(B_{ry} + B_{hy}\right)}{a_1 K_{hy}} - K_{hy} \end{aligned} \tag{15}$$

$\hat{K}_{rx}$ and $\hat{K}_{ry}$ were the optimal stiffness of the impedance control of the rehabilitation robot, which maximized the reward function during rehabilitation training of the affected limb. As demonstrated by Eq. 15, the optimal stiffness of the robot's impedance control was inversely proportional to the stiffness of the affected limb, which was conducive to providing corresponding feedback and parameter changes according to the different needs and actual state of patients during rehabilitation training. When the capacity of the affected limb decreased, the assisting force of the rehabilitation robot increased. The larger the value of the parameter a_1 was, the smaller the optimal stiffness value of the rehabilitation robot was. In other words, more attention should be paid to the effort of the affected limb during rehabilitation training to satisfy the definition of the reward function. The size of the stiffness parameter was definitely associated with the level of assistance of the rehabilitation robot (Honghai et al., 2022).

When the affected limb had minimal participation ($K_{hx} \approx 0, K_{hy} \approx 0$), the stiffness of the rehabilitation robot tended to be infinity. The following limits were set for the stiffness of the impedance control to avoid this situation. $K_{\min}$ and $K_{\max}$ were the minimum and maximum stiffness that the rehabilitation robot controller could provide.

$$K_r = \max\left\{K_{\min}, \min\left\{K_{\max}, \hat{K}_r\right\}\right\} \tag{16}$$

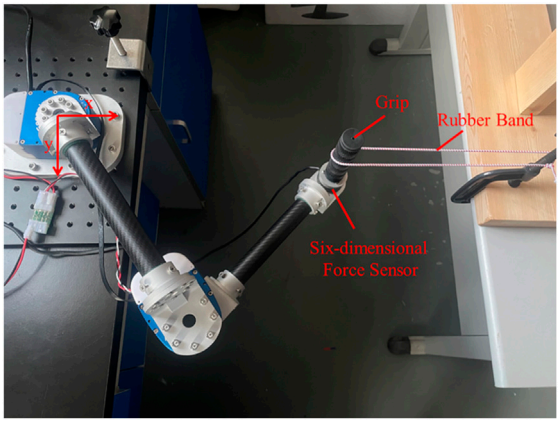

FIGURE 5
The impedance identification experiment platform.

3 Experiment results

In order to verify the impedance identification algorithm and the adaptive impedance control technology proposed in this study, three sets of experiments were carried out in this section: impedance parameter identification verification and variable impedance control simulation experiment, as well as the adaptive impedance control verification.

3.1 Impedance parameter identification verification

As shown in Figure 5, the platform for impedance identification experiment was set up. The end handle of the rehabilitation robot was connected to the elastic body (rubber band). The other end of the elastic body was fixed, and the elastic body was fixed stiffness within a certain range. The six-dimensional force sensor with the end connected to the grip could measure the force and the torque in

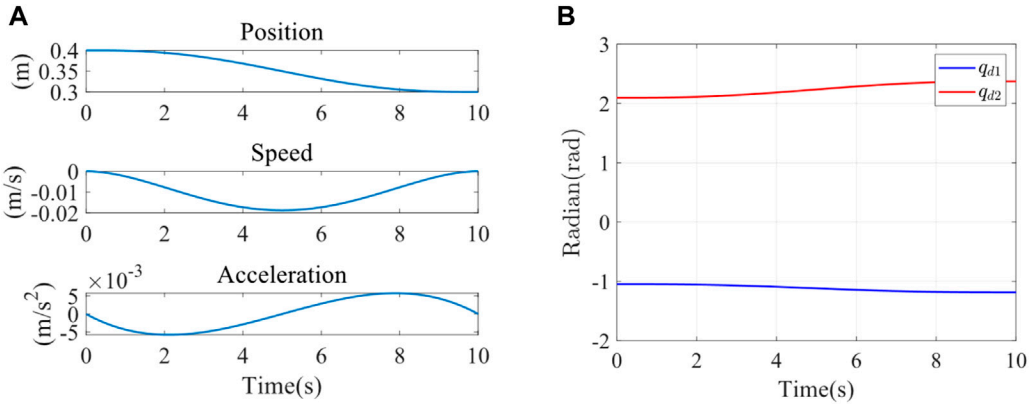

FIGURE 6
(A) *X*-direction trajectory planning in Cartesian space. **(B)** Joint 1 and joint 2 expected trajectory.

three directions in Cartesian space. The Cartesian coordinate system was installed at the rotation center of the first joint. Since the experiment platform belonged to the tabletop upper limb rehabilitation robot, only coordinate systems in the x and y directions were established.

Since the peak moment of the joint was 19 Nm, a spring with excessive stiffness could not be used for the impedance parameter identification experiment. Therefore, a rubber band chosen for the experiment had an elastic stiffness of 25 N/m. The end stiffness parameters were varied by changing the number of strands, stiffness, and position of the rubber bands. Firstly, two strands of rubber bands were selected for the impedance parameter identification experiment. The initial point of the end was (0.4 m, 0), and the movement was planned to (0.3 m, 0). The trajectory planning adopted the quintic polynomial interpolation method. Under the initial condition of the experiment, the elastic band was just taut, and the force sensor could detect the tension of the elastomer at the end, which was in the same plane as the elastomer at the other fixed end. It was planned to move from point A (0.4 m, 0) to point B (0.3 m, 0). The trajectory planning results in the x direction were shown in the following figure using quintic polynomials. The position, speed, and acceleration of the end from top to bottom were illustrated in Figure 6A. It could be observed that the speed and acceleration in the initial and terminal states were 0. This method could successfully avoid the impact of the rehabilitation robot on the motor during the process of starting and stopping. Meanwhile, the smooth trajectory also made the rehabilitation process more steady, which was beneficial to the rehabilitation of the affected limb. The expected trajectories of the two joints were obtained by inverse kinematics, as shown in Figure 6B, q_{d1} and q_{d2} were input to the joint servo controller of the robot as the position control of the two joints controller.

The interaction force F between the end of the elastomer and the rehabilitation robot was detected by the force sensor. The real-time joint angle q was obtained by the encoder of the rehabilitation robot. The real-time angles of two joints q acquired terminal position through the forward kinematics. The terminal speed was obtained by the differential. Inputting the terminal position, terminal speed, and terminal interaction force, the terminal impedance parameters are estimated by the least square method (LS), RLS, and FFRLS. The input parameters of the impedance identification experiment were displayed in Figure 7A. The terminal impedance parameters estimated by LS, RLS, and FFRLS were shown in Figure 7B The blue, red, and yellow lines represented the estimated end stiffness of the LS, RLS, and FFRLS, respectively, while the purple line represented the actual stiffness value. It illustrated that RLS and LS began to converge after 3s, much slower than FFRLS.

Impedance parameter identification errors were shown in Table 2. Since the stiffness estimation of the first few seconds by RLS and LS was divergent, it did not have statistical significance. All data in Table 2 were calculated after the stiffness identification curves of FFRLS, RLS, and LS. The root-mean-square errors of stiffness identification by FFRLS (λ = 0.95), RLS, and LS were 1.5900 N/m, 1.6075 N/m and 2.0703 N/m, respectively. The maximum stiffness identification errors were 1.5900 N/m, 1.6859 N/m, and 2.6888 N/m, respectively. The results showed that the root-mean-square error and maximum error of the FFRLS (λ = 0.95) stiffness estimation were smaller than those of RLS and LS. Therefore, the stiffness estimation from FFRLS had the best result.

3.2 Variable impedance control simulation verification

The feasibility of the above impedance control was verified by simulation in Matlab 2023a. To verify the system's ability of control stiffness under the external disturbances, we simulated the stiffness of the upper limb end of the healthy participants by modifying impedance parameters, thereby altering the system's stiffness behavior. This demonstrated its control capability over impedance characteristics. The simulation platform was set up based on actual platform parameters. The parameters of kinematic model were set as follows: m_1 = 1 kg, m_2 = 0.7 kg, I_1 = 0.25, I_2 = 0.1, $l_1 = l_2 = 0.4$, $l_{c1} = l_{c2} = 0.2$; m_1 and m_2 were the masses of rods A and B respectively. l_1 and l_2 were the lengths of rods A and B respectively. l_{c1} and l_{c2} were the distances from the center of mass of rods A and B to the rotation center, respectively. I_1 and I_2 were the

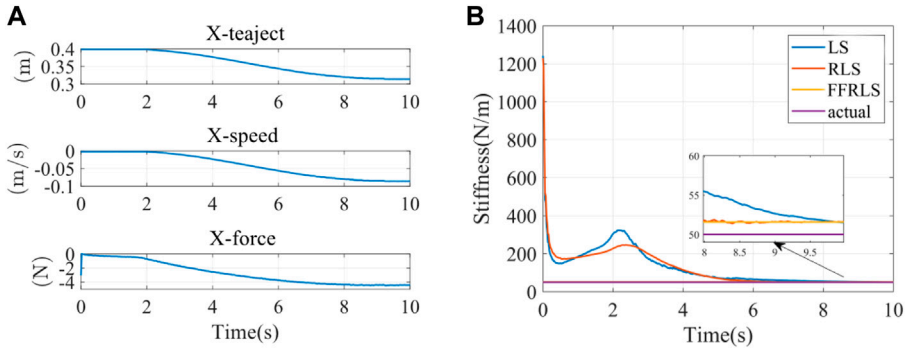

FIGURE 7
(A) The input parameters of impedance identification experiment **(B)** Impedance parameter identification results.

TABLE 2 Impedance parameter identification errors.

Identification stiffness	RMS(N/m)	MAX (N/m)
FFRLS (λ = 0.95)	1.5900	1.5900
RLS	1.6075	1.6859
LS	2.0703	2.6888

moments of inertia of rods A and B, respectively. Parameter g represented the gravitational acceleration and was taken as 9.8 m/s. The control stiffness parameter was established as follows:

$$K_d(t) = diag\{10 + 10\sin(2t), 10 + 10\cos(2t)\} \quad (17)$$

The end load of Cartesian coordinate system was established as follows:

$$f_{e1} = 2\sin(2t), f_{e2} = 2\cos(2t) \quad (18)$$

That is, the stiffness changed at a fixed frequency within a certain range, which was reflected in the varying stiffness of the manipulator's end in different directions on the plane. As shown in Figure 8, the solid and dashed lines were the curves of the stiffness of the two different joints of the robot over time.

Under the above external conditions, the corresponding load force was applied to it. And it was expected that the resulting torque output and error performance could reflect the stiffness control performance. Figures 9A,B were the position tracking error and the derivative change curve caused by the impedance control of the two joints of the robot, respectively. As observed in Figure 9A, in the face of the load imposed by the external environment, the tracking error e_1 of the reference position converged in a small neighborhood where the equilibrium point was 0 and the steady-state error did not exceed 0.06. This result indicated the effectiveness of the adaptive impedance control strategy when the platform faced the variable impedance. As shown in Figure 9B, the first derivative of the reference position tracking error $\dot{e}_1$ gradually converged to 0, which indicated that the position error of the platform gradually stabilized under the variable load force.

Figure 10 was the graph of the output torque of the two joints changing over time, and it displayed that the joint itself output the corresponding output torque to counteract the external input torque.

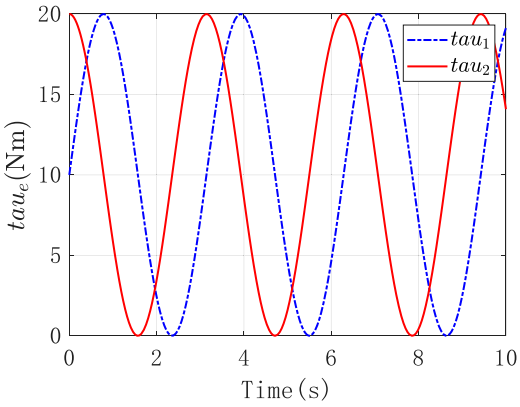

FIGURE 8
The stiffness of two different joints of the robot.

3.3 Adaptive impedance control verification

To verify the adaptive impedance control system in this study, a healthy male participant (24 years old, 1.88 m in height, 84 kg in weight) was recruited in the experiments, as shown in Figure 1, The study was reviewed by Shanghai University of Medicine and Health Sciences ethics, batch number 2022-ZYXM4-04-420300197109053525. The experiment was designed as follows: the rehabilitation task required the subject to move the end of the upper limb from A (0.5 m, 0) to C (0.2 m, 0), and each training time was 10s. Under the condition of constant impedance control and adaptive impedance control, the experiments were carried out with varying participation of the affected limb (i.e., different impedance parameters). The trajectory planning results of x direction using quintic polynomials were reported in Figure 11A, including the position, speed, and acceleration of the end from top to bottom. At the starting point A and the end point C, there was no

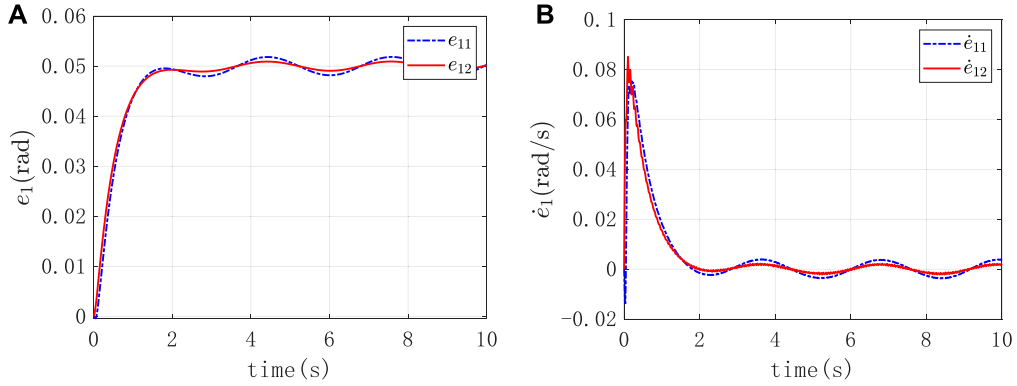

FIGURE 9
(A) The position tracking error caused by the impedance control **(B)** The derivative change curve caused by the impedance control.

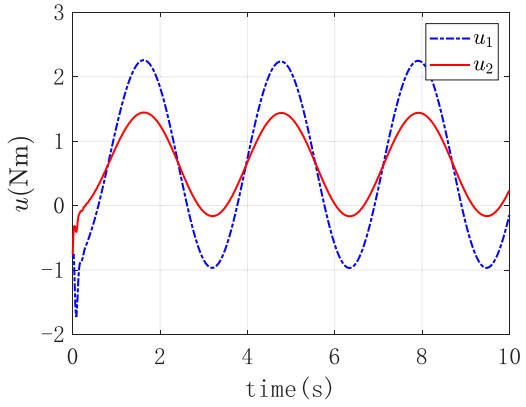

FIGURE 10
The output torque of the two joints.

speed or acceleration. This approach effectively reduced the impact of the rehabilitation robot on the motor during the phases of starting and stopping. Furthermore, the well-executed trajectory enhanced the overall stability of the rehabilitation process, thereby promoting the recovery of the affected limb. The expected trajectories of both joints were determined by inverse kinematics, as illustrated in Figure 11B. q_{d1} and q_{d2} were input to the joint servo controller of the rehabilitation robot as the position control of the two joints controller.

The parameters $a_1 = 10, a_2 = 2$ were set to make the weight of the work performed by the human upper limb higher in the rehabilitation strategy. The upper limit of the optimal stiffness was $K_{max} = 400$ N/m, while the lower limit was $K_{min} = 10$ N/m. The impedance limit could protect the affected limb and improve the safety of the rehabilitation training better. The experiment results under different participation conditions were illustrated in Figure 12, including the end-trajectory, human-computer interaction force, the identified end-damping, end-stiffness of the upper limb, and the robot's optimal stiffness. Figures 12A,B was the result of the subject's high and low participation. When there is a high level of the subject's participation in upper limb rehabilitation training, the stiffness at the upper limb's end is high, and the optimal robot stiffness is low, indicating a lower degree of robot assistance. As a result, a larger degree of robot assistance was indicated when there was a low participation level in upper limb rehabilitation training, low stiffness at the upper limb's end, and high optimal robot stiffness.

The terminal trajectories and interaction forces for both the constant impedance control (Kd = 100 N/m) and the adaptive impedance control were shown in Figure 13A. In both experiments, the interactive forces of adaptive impedance and constant impedance consistently showed high participation levels for the affected limb. Demonstrating that The reward obtained from the adaptive impedance control during the rehabilitation training was significantly higher than that of the constant impedance control with Kd = 100 N/m, as illustrated by the reward functionsin Figure 13B. This confirmed the effectiveness and robustness of the adaptive impedance control strategy proposed in this study.

The analysis of the reward function was shown in Table 3. The average rewards of constant impedance control (Kd = 100 N/m) and adaptive impedance control were 0.0152 and 0.8514, and the maximum rewards were 0.0471 and 13.3437, respectively.

4 Discussion

In this study, we constructed a mechanical platform and developed a novel adaptive impedance control strategy for the upper limb rehabilitation robot. We utilized a mass-spring-damping system to simulate the musculoskeletal system. With the changes in rehabilitation cycle, we used FFRLS to improve the accuracy of parameter estimation error. This method, in contrast to earlier LS or RLS, could constantly track changes in the impedance parameters online and did not decrease system parameter identification due to increased stiffness. We employed the reward function to strike a balance between the subject's participation and the trajectory deviation error, further achieving the optimal stiffness of impedance control of the rehabilitation robot.

Various techniques were employed in some studies to estimate and adjust participants' optimal stiffness. An algorithm that could

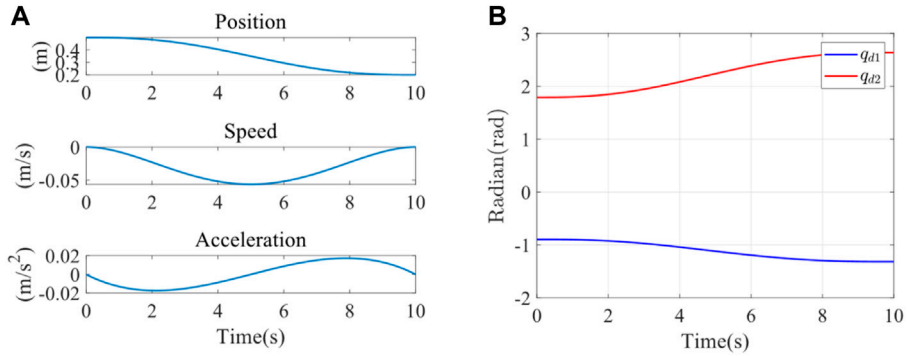

FIGURE 11
(A) *X*-direction trajectory planning **(B)** Expected trajectory of joint 1 and joint 2.

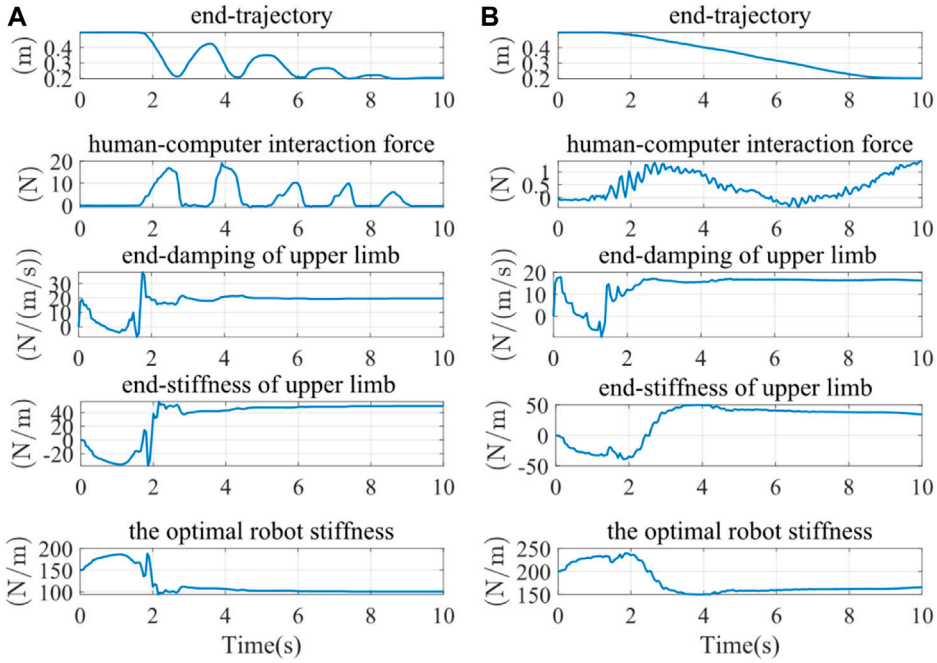

FIGURE 12
The results of experiments under different conditions of the participation. **(A)** High participation experiment results **(B)** Low participation experiment results.

adaptively change the impedance control's stiffness parameters in response to the observed values of the interaction force between patients and robots was proposed by Riener *et al.* Through the linear adaptive law, when the workload of the patient was detected to increase, the stiffness value was reduced (Riener et al., 2005). Ground on the evaluation of human active torque, Shahid *et al.* employed a similar method to control the stiffness of the manipulator (Hussain et al., 2013). Although their methods achieved control results, this study fully considered the levels of the subject's participation and enthusiasm in rehabilitation training in the form of a reward function. Patients' active participation awareness played a significant role in promoting the effect of rehabilitation training (Pawlak et al., 2022).

Moreover, this study designed the experiments under different participation to get the different parameters from the robot. When patients showed the signs of fatigue or reduced movement ability, the robot could increase the assistance level to maintain training continuity and efficacy, avoiding potential secondary injuries or training outcomes (Yang et al., 2023). Conversely, when patients exhibited a high level of participation, the robot might reduce its assistance to encourage patients to make more use of their own muscle, which supported neural plasticity and the rehabilitation of motor functions (Kawahira et al., 2010). Further studies via this approach enables more personalized rehabilitation training, satisfying the specific needs of different patients, thereby improving the efficiency of rehabilitation and accelerating the patient's return to normal life and work.

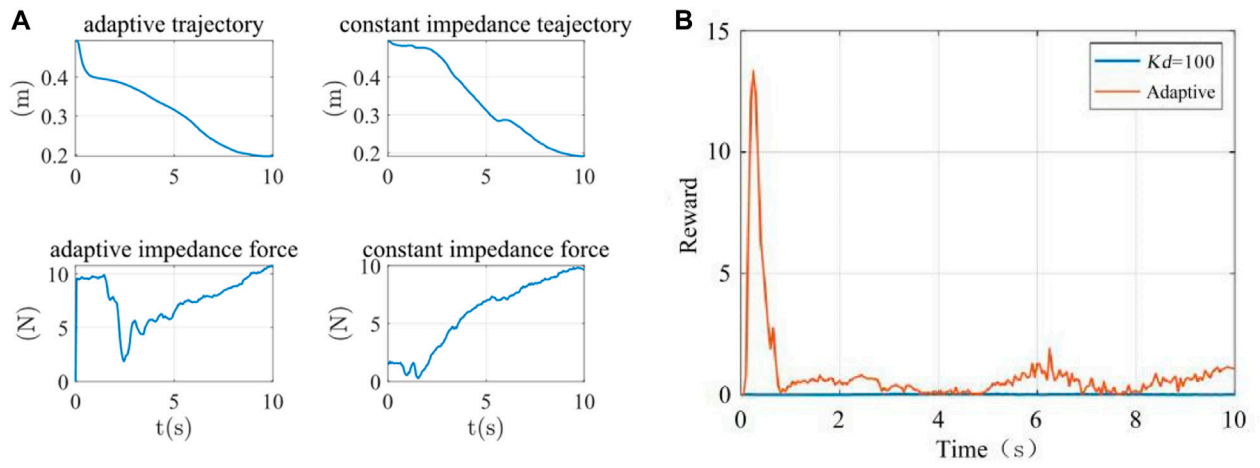

FIGURE 13
(A) The terminal trajectory and interaction force **(B)** Reward function.

TABLE 3 The analysis of reward function.

Control strategy	The average reward	The maximum reward
Constant impedance control (K_d = 100 N/m)	0.0152	0.0471
Adaptive impedance control	0.8514	13.3437

In the simulation experiment, it was observed that the corresponding torque output at the end of the robotic arm could resist the corresponding load force when the platform was facing variable external load force and the error was controlled within a narrow range, proving the effectiveness of the adaptive impedance control strategy. The limit of the simulation was that the stiffness change law was set by ourselves to simulate the actual situation. However, the output stiffness value of the assist-as-needed strategy was optimized according to the stiffness of the affected limb. We will optimize the experimental settings by taking assist-as-needed rehabilitation procedures into account in subsequent studies.

Since impedance control achieved regulation and stabilization of robot motion by establishing a mathematical relationship between the interaction forces and the reference trajectories (Al-Shuka et al., 2018), we compared adaptive impedance control and constant impedance control for experimental verification. By setting different parameters to simulate varying levels of participant engagement, the results obtained were consistent with the experiment in which a healthy subject was involved. We also obtained that the average and maximum rewards of adaptive impedance control were higher than those of constant impedance control at K_d = 100 N/m. Luo, Duan, and Berenice conducted comparative simulation experiments on constant impedance control and variable impedance control (Luo et al., 2017; Maldonado et al., 2015; Duan et al., 2018). In these researches, Luo used different levels of simulated stiffness values, Duan compared the two methods in different environments, and Berenice simulated the situations of subjects under different task modes. Their research findings indicated that adaptive impedance control had better force tracking performance and potential for facilitating rewards compared to constant impedance control. Adaptive impedance control technology can be utilized in robot-assisted rehabilitation systems under various conditions which further prove the effectiveness of adaptive impedance control in rehabilitation training. Ibarra and Wang also suggested adaptive impedance control strategies, considering the influence of patients on the ankle rehabilitation robot and adjusting the robot aids in real time (Perez-Ibarra et al., 2015; Wang et al., 2019). The intervention of the exoskeleton was considered in the process of training (Guo et al., 2022b).

This control strategy offered significant potential for achieving the best active training effect and creating a controllable impedance environment for the patient. The adaptive control strategy can improve the performance of the human-robot interaction and the effectiveness of the control system for upper limb rehabilitation robot. In addition, the proposed strategy could also be applied to the different rehabilitation robots. In our follow-up studies, we will test the proposed method with more healthy subjects and patients to accurately identify the differences based on the different participation, and we will also apply this control system for the wearing assistive devices to test its effectiveness, improving the rehabilitation efficacy eventually.

5 Conclusion

In this study, an novel adaptive impedance strategy for upper-limb rehabilitation robots was proposed. The efficacy of optimal stiffness control was confirmed through a comparison of

performance across various levels of upper limb participation during the rehabilitation process. A comparison of rehabilitation performance between adaptive impedance control and consant impedance control was also conducted. The simulation and the experiments fully verified the effectiveness of this adaptive impedance control strategy.

Data availability statement

The original contributions presented in the study are included in the article/Supplementary Material, further inquiries can be directed to the corresponding author.

Ethics statement

The studies involving humans were approved by Shanghai University of Medicine and Health Sciences ethics. The studies were conducted in accordance with the local legislation and institutional requirements. Written informed consent for participation in this study was provided by the participants' legal guardians/next of kin. Written informed consent was obtained from the individual(s) for the publication of any potentially identifiable images or data included in this article.

Author contributions

YZ: Project administration, Supervision, Writing–review and editing. TL: Data curation, Formal Analysis, Validation, Writing–original draft. HT: Data curation, Formal Analysis, Methodology, Writing–original draft. FL: Formal Analysis, Writing–review and editing. BH: Funding acquisition, Project administration, Writing–review and editing. MW: Supervision, Writing–review and editing. HY: Project administration, Resources, Supervision, Writing–review and editing.

Funding

The author(s) declare financial support was received for the research, authorship, and/or publication of this article.

Acknowledgments

The authors appreciatively acknowledge the financial support from the National Key Research and Development Program of China under Grant 2022YFC3601400 and the Biomedical Science and Technology Support Project of Shanghai under Grant 22S31901400.

Conflict of interest

The authors declare that the research was conducted in the absence of any commercial or financial relationships that could be construed as a potential conflict of interest.

Publisher's note

All claims expressed in this article are solely those of the authors and do not necessarily represent those of their affiliated organizations, or those of the publisher, the editors and the reviewers. Any product that may be evaluated in this article, or claim that may be made by its manufacturer, is not guaranteed or endorsed by the publisher.

Supplementary material

The Supplementary Material for this article can be found online at: https://www.frontiersin.org/articles/10.3389/fbioe.2023.1332689/full#supplementary-material

References

Albu-Schaffer, A., Ott, C., and Hirzinger, G. (2007). A unified passivity based control framework for position, torque and impedance control of flexible joint robots. *Springer Trac. Adv. Ro* 28, 5–21. doi:10.1177/0278364907073776

Al-Shuka, H. F. N., Leonhardt, S., Zhu, W.-H., Song, R., Ding, C., and Li, Y. (2018). Active impedance control of bioinspired motion robotic manipulators: an overview. *Appl. Bionics Biomechanics* 2018, 1–19. doi:10.1155/2018/8203054

Brahmi, B., Driscoll, M., El Bojairami, I. K., Saad, M., and Brahmi, A. (2021). Novel adaptive impedance control for exoskeleton robot for rehabilitation using a nonlinear time-delay disturbance observer. *Isa T* 108, 381–392. doi:10.1016/j.isatra.2020.08.036

Duan, J., Gan, Y., Chen, M., and Dai, X. (2018). Adaptive variable impedance control for dynamic contact force tracking in uncertain environment. *Robotics Aut. Syst.* 102, 54–65. doi:10.1016/j.robot.2018.01.009

Guo, Y. D., Wang, H. P., Tian, Y., and Caldwell, D. G. (2022a). Task performance-based adaptive velocity assist-as-needed control for an upper limb exoskeleton. *Biomed. Signal Proces.*, 73. doi:10.1016/j.bspc.2021.103474

Guo, Y. D., Wang, H. P., Tian, Y., and Xu, J. Z. (2022b). Position/force evaluation-based assist-as-needed control strategy design for upper limb rehabilitation exoskeleton. *Neural Comput. Appl.* 34 (15), 13075–13090. doi:10.1007/s00521-022-07180-x

Hong, Z., Sui, M., Zhuang, Z., Liu, H., Zheng, X., Cai, C., et al. (2018). Effectiveness of neuromuscular electrical stimulation on lower limbs of patients with hemiplegia after chronic stroke: a systematic review. *Archivees Phys. Med. rehabilitation*, 1532–1821. doi:10.1016/j.apmr.2017.12.019

Honghai, L., Zhouping, Y., and Lianqing, L. (2022). "Intelligent robotics and applications," in 15th International Conference, ICIRA 2022, Harbin, China, August, 2022.

Hussain, S., Xie, S. Q., and Jamwal, P. K. (2013). Adaptive impedance control of a robotic orthosis for gait rehabilitation. *Ieee T Cybern.* 43 (3), 1025–1034. doi:10.1109/tsmcb.2012.2222374

Islam, M. R., Assad-Uz-Zaman, M., Brahmi, B., Bouteraa, Y., Wang, I., and Rahman, M. H. (2021). Design and development of an upper limb rehabilitative robot with dual functionality. *Micromachines* 12, 870. doi:10.3390/mi12080870

Kawahira, K., Shimodozono, M., Etoh, S., Kamada, K., Noma, T., and Tanaka, N. (2010). Effects of intensive repetition of a new facilitation technique on motor functional recovery of the hemiplegic upper limb and hand. *Brain Inj.* 24 (10), 1202–1213. doi:10.3109/02699052.2010.506855

Krebs, H. I., Palazzolo, J. J., Dipietro, L., Volpe, B. T., Hogan, N., Rannekleiv, K., et al. (2003). Rehabilitation robotics: performance-based progressive robot-assisted therapy. *Auton. Robot.* 15 (1), 7–20. doi:10.1023/a:1024494031121

Li, X., Liu, Y. H., and Yu, H. Y. (2018). Iterative learning impedance control for rehabilitation robots driven by series elastic actuators. *Automatica* 90, 1–7. doi:10.1016/j.automatica.2017.12.031

Long, T., Wang, S. L., Cao, W., Zhou, H., and Fernandez, C. (2023). An improved variable forgetting factor recursive least square-double extend Kalman filtering based on global mean particle swarm optimization algorithm for collaborative state of energy and

state of health estimation of lithium-ion batteries. *Electrochim Acta*, 450. doi:10.1016/j.electacta.2023.142270

Luo, L., Peng, L., Hou, Z., and Wang, W. (2017). "An adaptive impedance controller for upper limb rehabilitation based on estimation of patients' stiffness," in 2017 IEEE International Conference on Robotics and Biomimetics (ROBIO), Macau, Macao, December, 2017, 532–537.

Ma, Q., Li, R., Wang, L., Yin, P., Wang, Y., Yan, C., et al. (2021). Temporal trend and attributable risk factors of stroke burden in China, 1990-2019: an analysis for the Global Burden of Disease Study 2019. *Lancet Public Health* 6 (12), e897–e906. doi:10.1016/s2468-2667(21)00228-0

Maldonado, B., Mendoza, M., Bonilla, I., and Reyna-Gutiérrez, I. (2015). "Stiffness-based tuning of an adaptive impedance controller for robot-assisted rehabilitation of upper limbs," in 2015 37th Annual International Conference of the IEEE Engineering in Medicine and Biology Society (EMBC), Milan, Italy, August 2015, 3578–3581.

Pawlak, N. D., Serafin, L., and Czarkowska-Pączek, B. (2022). Relationship between patients' subjective involvement in postoperative rehabilitation and quality of life after arthroscopic treatment for osteoarthritic knee – cross-sectional study. *Med. Og. Nauk. Zdr.* 28 (1), 63–69. doi:10.26444/monz/143835

Pehlivan, A. U., Losey, D. P., and O'Malley, M. K. (2016). Minimal assist-as-needed controller for upper limb robotic rehabilitation. *Ieee T Robot.* 32 (1), 113–124. doi:10.1109/tro.2015.2503726

Perez-Ibarra, J. C., Siqueira, A. A. G., and Krebs, H. I. (2015). Assist-as-needed ankle rehabilitation based on adaptive impedance control. *Int. C Rehab Robot.*, 723–728. doi:10.1109/ICORR.2015.7281287

Perez-Ibarra, J. C., Siqueira, A. A. G., Silva-Couto, M. A., de Russo, T. L., and Krebs, H. I. (2019). Adaptive impedance control applied to robot-aided neuro-rehabilitation of the ankle. *Ieee Robot. Autom. Let.* 4 (2), 185–192. doi:10.1109/lra.2018.2885165

Riener, R., Lunenburger, L., Jezernik, S., Anderschitz, M., Colombo, G., and Dietz, V. (2005). Patient-cooperative strategies for robot-aided treadmill training: first experimental results. *Ieee Trans. Neural Syst. Rehabilitation Eng.* 13 (3), 380–394. doi:10.1109/tnsre.2005.848628

Sharifi, M., Behzadipour, S., Salarieh, H., and Tavakoli, M. (2017). Cooperative modalities in robotic tele-rehabilitation using nonlinear bilateral impedance control. *Control Eng. Pract.* 67, 52–63. doi:10.1016/j.conengprac.2017.07.002

Sun, T., Wang, Z., He, C., and Yang, L. (2022). Adaptive robust admittance control of robots using duality principle-based impedance selection. *Appl. Sci.* 12, 12222. doi:10.3390/app122312222

Vanoglio, F., Bernocchi, P., Mulè, C., Garofali, F., Mora, C., Taveggia, G., et al. (2016). Feasibility and efficacy of a robotic device for hand rehabilitation in hemiplegic stroke patients: a randomized pilot controlled study. *Clin. Rehabil.* 31 (3), 351–360. doi:10.1177/0269215516642606

Vasu, S., Luis, G., and Dileep, R. Y. (2021). Global epidemiology of stroke and access to acute ischemic stroke interventions. *Neurology* 97 (20 Suppl. 2), S6–S16. doi:10.1212/wnl.0000000000012781

Wang, C., Peng, L., Hou, Z. G., Wang, W. Q., and Su, T. T. (2019). "A novel assist-as-needed controller based on fuzzy-logic inference and human impedance identification for upper-limb rehabilitation," in 2019 Ieee Symposium Series on Computational Intelligence, Xiamen, China, December 2019, 1133–1139.

Wolbrecht, E. T., Chan, V., Reinkensmeyer, D. J., and Bobrow, J. E. (2008). Optimizing compliant, model-based robotic assistance to promote neurorehabilitation. *IEEE Trans. Neural Syst. Rehabilitation Eng.* 16 (3), 286–297. doi:10.1109/tnsre.2008.918389

Xu, G. Z., Gao, X., Chen, S., Wang, Q., Zhu, B., and Li, J. F. (2017). A novel approach for robot-assisted upper-limb rehabilitation: progressive resistance training as a paradigm. *Int. J. Adv. Robot. Syst.* 14 (6), 172988141773667. doi:10.1177/1729881417736670

Yang, R., Shen, Z., Lyu, Y., Zhuang, Y., Li, L., and Song, R. (2023). Voluntary assist-as-needed controller for an ankle power-assist rehabilitation robot. *IEEE Trans. Biomed. Eng.* 70 (6), 1795–1803. doi:10.1109/tbme.2022.3228070

Zou, Y., Wu, X., Zhang, B., Zhang, Q., Zhang, A., and Qin, T. (2022). Stiffness analysis of parallel cable-driven upper limb rehabilitation robot. *Micromachines* 13, 253. doi:10.3390/mi13020253

frontiers | Frontiers in Bioengineering and Biotechnology

TYPE Original Research
PUBLISHED 04 January 2024
DOI 10.3389/fbioe.2023.1310247

OPEN ACCESS

EDITED BY
Wujing Cao,
Chinese Academy of Sciences (CAS), China

REVIEWED BY
Chengjie Zhang,
Shanghai Jiao Tong University, China
Liu Ying,
East China Jiaotong University, China

*CORRESPONDENCE
Jiancheng Charles Ji,
jcji20@szpt.edu.cn

†These authors share first authorship

‡These authors share last authorship

RECEIVED 09 October 2023
ACCEPTED 13 December 2023
PUBLISHED 04 January 2024

CITATION
Gong T, Chen D, Wang G, Zhang W, Zhang J, Ouyang Z, Zhang F, Sun R, Ji JC and Chen W (2024), Multimodal fusion and human-robot interaction control of an intelligent robot.
Front. Bioeng. Biotechnol. 11:1310247.
doi: 10.3389/fbioe.2023.1310247

Multimodal fusion and human-robot interaction control of an intelligent robot

Tao Gong[1†], Dan Chen[1†], Guangping Wang[2], Weicai Zhang[2], Junqi Zhang[2], Zhongchuan Ouyang[2], Fan Zhang[2], Ruifeng Sun[2], Jiancheng Charles Ji[1*] and Wei Chen[1‡]

[1]Institute of Intelligent Manufacturing, Shenzhen Polytechnic University, Shenzhen, China, [2]AVIC Changhe Aircraft Industry (Group) Corporation Ltd., Jingdezhen, China

Introduction: Small-scaled robotic walkers play an increasingly important role in Activity of Daily Living (ADL) assistance in the face of ever-increasing rehab requirements and existing equipment drawbacks. This paper proposes a Rehabilitation Robotic Walker (RRW) for walking assistance and body weight support (BWS) during gait rehabilitation.

Methods: The walker provides the patients with weight offloading and guiding force to mimic a series of the physiotherapist's (PT's) movements, and creates a natural, comfortable, and safe environment. This system consists of an omnidirectional mobile platform, a BWS mechanism, and a pelvic brace to smooth the motions of the pelvis. To recognize the human intentions, four force sensors, two joysticks, and one depth-sensing camera were used to monitor the human-machine information, and a multimodal fusion algorithm for intention recognition was proposed to improve the accuracy. Then the system obtained the heading angle E, the pelvic pose F, and the motion vector H via the camera, the force sensors, and the joysticks respectively, classified the intentions with feature extraction and information fusion, and finally outputted the motor speed control through the robot's kinematics.

Results: To validate the validity of the algorithm above, a preliminary test with three volunteers was conducted to study the motion control. The results showed that the average error of the integral square error (ISE) was 2.90 and the minimum error was 1.96.

Discussion: The results demonstrated the efficiency of the proposed method, and that the system is capable of providing walking assistance.

KEYWORDS

kinematic modeling, robotic walker, multimodal fusion, human-robot interaction control, stroke

1 Introduction

In 2019, there were an estimated 12.2 million cases of apoplexy (95% uncertainty interval (UI) 11–13.6 million) in the world, with an estimated 101 million sufferers according to the Global Burden of Disease Study (GBD et al., 2021). The increase in stroke patients has resulted in 143 million cases of disability-adjusted life-years (DALYs), and there are currently around 1.3 billion people with disabilities according to data from the World Health Organization (Feigin et al., 2022). Under this tough situation, the present healthcare system, lack of bridle-wise

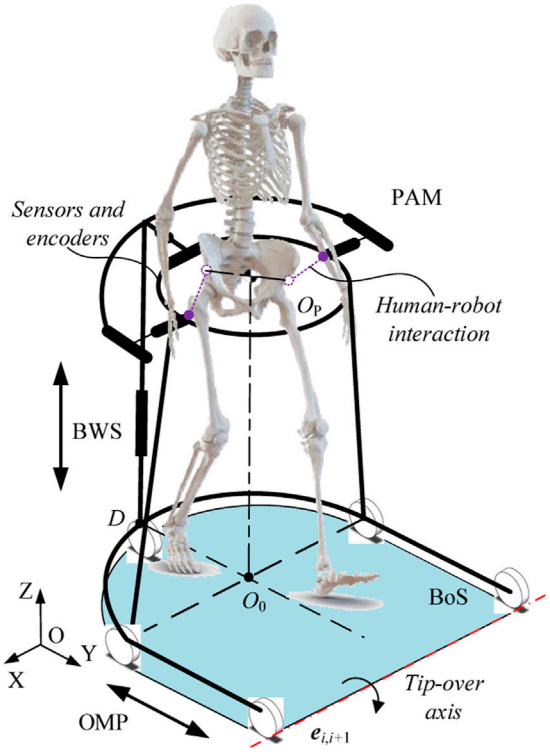

FIGURE 1
Conceptual model of system.

physiotherapists (PT), assistive technology, and effective rehabilitation equipment cannot meet the increasing demand for rehab training, and disability of the lower extremities limits functional independence in activities of daily living and significantly deteriorates the quality of life of the affected individual (Chen et al., 2020; Jarva et al., 2021; Lesaine et al., 2022). Studies have shown that robot-assisted rehabilitation training is more effective than traditional gait training in improving walking ability and balance functions in stroke patients (Nam et al., 2017; Capecci et al., 2019; Calabrò et al., 2021). Furthermore, rehab training using gait assistance could help in providing intensive therapeutic exercises while also allowing for a quantitative assessment of the recovery (Mirelman et al., 2019). However, the trial-and-error learning hypothesis in motor control research suggests that position-control-based movement might decrease motor learning for some tasks, and the human-robot interaction control is the main pain point of training aiding (Reisman et al., 2010; Mojadidi et al., 2017).

During normal walking with the robotic walker, the control system usually recognizes the human intentions via the interactive sensors, then outputs the actuating speed of the wheels based on the classification and interactions. In the literature focused on human-robot interaction (HRI) strategy for human mobility assistance, the cognitive Human-Robot Interaction (*c*HRI) and the physical Human-Robot Interaction (*p*HRI) with humans applied in wearable robotics are explained by Pons et al. (2008). The *c*HRI is explicitly developed to obtain the data acquired by a set of sensors to measure bioelectrical and biomechanical variables. Takanori O. et al. developed an assist robotic walker (JARoW-II) for elderly people, and proposed a pelvic-based walking-support control technique without the use of specific manual controls or additional equipment, via two laser range finders (LRFs) to obtain coordinate data for the surface of the user's lower limbs (Ohnuma et al., 2017). The pHRI is based on a set of actuators and a rigid structure that is used to transmit forces to the human musculoskeletal system. For example, Sierra M. et al. developed Smart Walkers to improve physical stability and sensory support for people with lower limb weakness via a haptic joystick with three operational modes (Sierra M. et al., 2019), after that they proposed the AGoRA Smart Walker with a human detection system and a user interaction system, and the walker can estimate the intentions via thehuman–robot–environment interface (Sierra et al., 2019). However, the integration of classic Human-Computer interfaces (HCi) with newer types of interfaces facilitates effective interaction (Sharma et al., 1998), such as speech or visual interfaces, tactile sensors, the LRF, the IMU, and force/torque sensors. The ASBGO system proposed by the University of Minho is a typical example, the walker was equipped with load cells, an infrared sensor, the Inertial Measurement Unit (IMU), and a real sense camera to detect the postural and gait parameters of the user (Moreira et al., 2019). To improve the accuracy of the task, a new multimodal interface for walker-assisted gait is proposed, which involves the integration of different modalities (Frizera et al., 2011). The UFES's smart walker combined force sensing and lower limbs monitoring to detect the user's legs and showed accurate performance in all experiments (Valadão et al., 2016). However, multi-modality information fusion facilitates better use of the relationships between multiple types of data, which can improve the model matching accuracy and effectiveness (Cifuentes and Anselmo, 2016; Horii and Nagai, 2021; Su et al., 2023). Therefore, this paper proposed a method for the multimodal fusion and the HRI control, the video image from the real sense camera, the interaction forces from the load sensors, and the motion vector from the joysticks were employed to detect the interaction information, based on the multimodal fusion method, a new interactive controller was designed to assist the patients.

The remainder of this brief is organized as follows. Section 2 contains a description of the RRW system. Section 3 describes the modeling of the system, and formulation of the control problem as well as the design and implementation of the desired controller. Section 4 presents the setup and results of the preliminary test with three volunteers. Finally, Section 5 concludes the brief.

2 System description

Generally, a human-robot interaction system works in conjunction with a mobile platform to achieve gait assistance, the robotic walker provides the user with a safe environment via balance maintenance, meanwhile, sensors and encoders are employed to detect the motion intention of the user and calculate the control output (Zhao et al., 2020; Wang et al., 2023). Therefore, as shown in Figure 1, we designed a robotic walker consisting of three main parts: i) an omnidirectional mobile platform (OMP); ii) a body weight support system (BWS), and iii) a pelvic assist mechanism (PAM), the design details will be described.

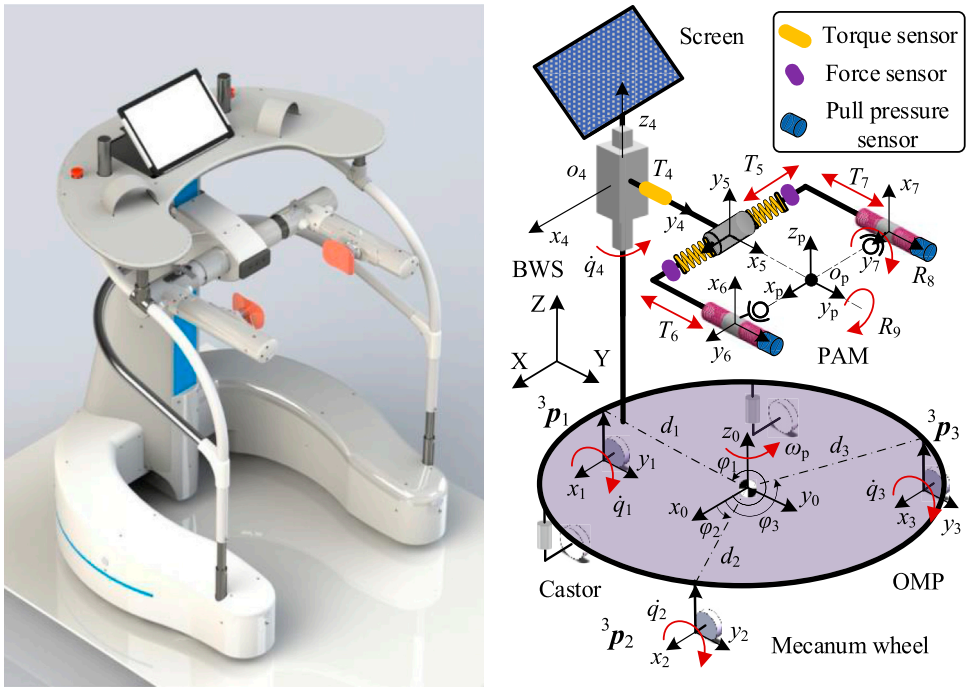

FIGURE 2
The CAD model of the walker and coordinate system.

2.1 Hardware description

In this paper, we present a walking assist system facilitating pelvic movements for several reasons. First, based on the walking characteristics of the patients and the problem definition, pelvic movement abnormalities lead to an increase in the double support phase and abnormal gait. Second, pelvic obliquity and pelvic rotation are the key parameters for lower extremity motor function. And third, the pelvic motions are associated with the gait. Therefore, we proposed the PAM to smooth the pelvic motions and install the force/torque sensors, as shown in Figure 2, so we can detect the middle-lateral and vertical displacement of the pelvis, as well as pelvic obliquity and pelvic rotation. Based on the range of pelvic motions during normal gait, the user can achieve normal gait with the help of the PAM. The T_5 corresponds to the middle-lateral displacement, which consists of a set of ball splines and two springs, and the displacement is monitored by the force sensors at the end of the spring. Similarly, T_6 and T_7 are coupled and correspond to the forward-back displacement and pelvic rotation, as the pelvis is connected to the walker by the sliders of the two ball splines. The pose information of the pelvis is given through calculating sensor data. Then there is a revolute pair to achieve pelvic obliquity and tilt, labeled as R_8 and R_9 respectively. Furthermore, one torque sensor is installed on the joint pontes between the BWS and the PAM to detect the vertical motion.

For weight offloading and reduction of the cardiopulmonary burden, a servo motor is designed to realize the approximately 0.5 m vertical displacement of the pelvis and provide subjects with appropriate body weight support via a guide screw and a set of linear guideways. The error between the offloading value and sensor signal is used to trace the pelvic motion, and the system control is implemented in TwinCAT2 using a controller (Beckhoff PLC CX5130). On the top of the BWS, the control platform is installed to support the upper body weight and implement the interaction control. Two joysticks and one depth-sensing camera (Surface Go 2) were used to monitor the human-machine information, the user manipulated the walker via the left or right joystick according to the actual condition. The depth-sensing camera is used to obtain the facial features, as the heading angle can reveal the motion intention.

The primary aim of the OMP is to provide over-ground mobility, and thus achieve gait assistance. The OMP consists of three active wheels to provide power, two passive castors to maintain balance, and a U-shaped rigid steel frame to provide an installation base. According to the motions of lower limbs, a U-shaped rigid steel frame is designed to satisfy approximately 0.5 m of free space in the medio/lateral direction, and 0.8 m of free space in the anterior/posterior direction. For the active omnidirectional wheels, the walker is capable of rotation with arbitrary radius.

As described above, the multimodal Human-Robot Interaction (*m*HRI) is used to estimate the motion intention: the video image from the real sense camera, which belongs to the *c*HRI. the interaction forces from the load sensors and the motion vector from the joysticks were employed to detect the interaction information, which belongs to the *p*HRI.

2.2 Problem statement

In the interactive control process of lower limb rehabilitation robot, it is easy to produce more interference signals for the abnormal walking characteristics of the hemiplegic patients, which leads to the indisposed control performance, and then the

FIGURE 3
The physical prototype of the robotic walker.

robotic walkers cannot assist the users to finish the Activity of Daily Living (ADL) tasks. For the problem at hand, mobile rehab robots need to perceive the motion intentions via the *c*HRI or the *p*HRI. For passive walkers, the problem is to detect the safety of the user and brake at the right moment. For the active walkers, the HRI is more important for that the system needs to identify the gait pattern accurately and output appropriate velocity to trace the user. According to the above analysis, the two major issues are: 1) estimating the motion intentions; and 2) calculating output velocity.

For estimating the motion intentions, the JARoW-II active robotic walker obtained the coordinate data for the surface of the user's lower limbs via the two LRFs (Hokuyo Automatic Co. Ltd. model URG-04LX), the advantage of the scheme is capable of the gait information acquisition, but the drawback is large amounts of computation; the KineAssist rehab robot estimated the interaction forces via two ATI force/torque sensors at both side of the pelvis, the advantage of the scheme is capable of the pelvic information acquisition, but the drawback is exorbitant price (Hurt et al., 2015). To sum up, there exist some problems with the current solution, such as high cost, poor intelligence, and inaccurate intention recognition.

For calculating output velocity, the mobile robots following behind a user is a common approach in walker-assisted locomotion (Seo and Lee, 2009), and it is more natural and comfortable for the person to control the walker if the robot is placed in front of the user (Haoyong et al., 2003). But the control problem is the position error between the mobile robots and humans, for the signal delay from the *c*HRI or the *p*HRI. The potential solution is to control the system to minimize the tracking error between humans and the mobile robot locomotion. A virtual spring model is used to absorb the gap between the human and the mobile robot motion via the input velocity generated on the basis of an elastic force (Morioka et al., 2004). But for *p*HRI, this solution can lead to a radical change in the interaction force.

Therefore, we present a method to obtain the heading angle E, the pelvic pose F, and the motion vector H via the camera, the force sensors, and the joysticks respectively, as shown in Figure 3, and go through several steps to get the classification of gait pattern, then output the velocity to minimize the tracking error, the methods are detailed in the next chapter.

3 Modeling and control

In order to improve the movement performance and the controllability of the robotic walker, the robot movement control model was produced in this chapter based on the robot kinematics, the active and passive joints were involved. The relation between the tacking velocity and the output of the servo motors was derived. On this basis, the control method was presented, which is two stages of control: the first step performed the *m*HRI detection via the camera, the force sensors, and the joysticks; while the second step corresponded to an inverse kinematic controller.

3.1 Kinematic model

The human-robot interaction model is shown in Figure 2, The variables and parameters used in this paper are defined as follows: the $OXYZ$ is a global coordinate system, point o_0 is the center of the circle of the OMP, $o_0x_0y_0z_0$ is a local coordinate system attached to the robotic walker, three omnidirectional wheels are uniformly distributed along the circumference frame, with the center $o_i\,(i = 1, 2, 3)$, and $\varphi_i\,(i = 1, 2, 3)$ represents the position angle of the three wheels. The BWS system is located at point D, through the pelvic assistance mechanism connecting to the pelvic center o_p, point C is the mass center of the robotic walker. Using the position, orientation, and velocity of point o_0 to indicate the position, orientation, and velocity of the robotic walker, θ is the heading angle of the mobile platform relative to the X-axis. r is the radius of the driving wheel, s is the screw lead of the BWS's precision ball screw, $\varphi_i\,(i = 1, 2, 3)$ is the distance from the mass center C to the three omnidirectional wheels.

Defining the velocity matrix of the OMP relative to the global coordinate system as $\dot{\boldsymbol{q}} = [\,\dot{x}\ \ \dot{y}\ \ \dot{\theta}\,]^T$, the angular velocity of the three driving wheels as $\boldsymbol{\omega} = \left[\,\dot{\theta}_1\ \ \dot{\theta}_2\ \ \dot{\theta}_3\,\right]^T$, and the velocity matrix relative to the local coordinate system as $\dot{\boldsymbol{q}}_R = [\,\dot{x}_R\ \ \dot{y}_R\ \ \dot{\theta}_R\,]^T$. Under the circumstances that the kinestate of driving wheels is pure rolling without slide, and the mobile platform is able to do instantaneous motion along the heading direction of the driving wheels. Defining the velocity of the PAM, i.e., T_4 relative to the global coordinate system as $\dot{z}$. The angular velocity of the screw as $\dot{\theta}_4$.

According to robot kinematics and the earlier paper (Ji et al., 2021), deducing the mapping relation $\mathcal{H}(\boldsymbol{q})$ between the tracking velocity and angular velocity of the joints:

$$\mathcal{H}(\boldsymbol{q})\colon \mathbb{R}^n \rightarrow \mathbb{R}^l \tag{1}$$

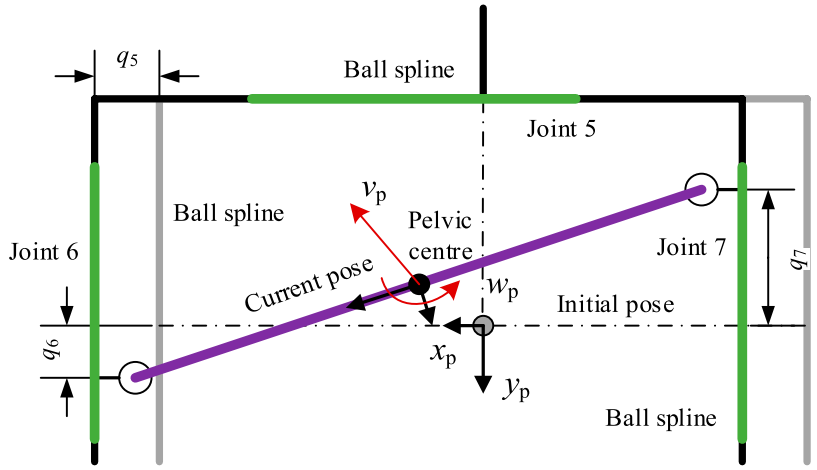

FIGURE 4
Mechanical construction of the PAM.

where $\mathbb{R}^n$ represents the set of the joint angle $\boldsymbol{q}$, velocity $\dot{\boldsymbol{q}}$ and accelerated velocity $\ddot{\boldsymbol{q}}$, and $\mathbb{R}^l$ represents the set of the generalized position and posture vector $\boldsymbol{x}$ in the local coordinate system as defined in Eqs 2, 3:

$$\boldsymbol{x} \in \mathbb{R}^l \tag{2}$$

$$\boldsymbol{q}, \dot{\boldsymbol{q}}, \ddot{\boldsymbol{q}} \in \mathbb{R}^n \tag{3}$$

Then, the velocity vector $\dot{\boldsymbol{x}}$ in the local coordinate system can be obtained by the partial derivative about the mapping relation $\mathcal{H}(\boldsymbol{q})$, as:

$$\dot{\boldsymbol{x}} = (\partial \mathcal{H}(\boldsymbol{q})/\partial \boldsymbol{q})\dot{\boldsymbol{q}} = \mathbf{J}(\boldsymbol{q})\dot{\boldsymbol{q}} \tag{4}$$

where $\mathbf{J}(\boldsymbol{q})$ of Eq. 5 is the Jacobian matrix, which belongs to the set $\mathbb{R}^{l\times n}$,

$$\mathbf{J}(\boldsymbol{q}) \in \mathbb{R}^{l\times n} \tag{5}$$

According to the derivation of the earlier paper, for the active joints, the inverse Jacobian matrix can be obtained as Eq. 6,

$$\mathbf{J}^{-1} = \frac{1}{r}\begin{bmatrix} -1 & 0 & 0 & d_1\cos(\pi/2-\varphi_1) \\ 0.5 & -0.866 & 0 & d_2\cos(\pi/6-\varphi_2) \\ 0.5 & 0.866 & 0 & d_3\cos(\pi/6+\varphi_3) \\ 0 & 0 & 2\pi r/s & 0 \end{bmatrix} \tag{6}$$

Through the matrix inverse in the MATLAB, the explicit expression of the Jacobian matrix can be written as Eq. 7:

$$\mathbf{J}(\boldsymbol{q}) = r\begin{bmatrix} -2/3 & 1/3 & 1/3 & 0 \\ 0 & -\sqrt{3}/3 & \sqrt{3}/3 & 0 \\ 0 & 0 & 0 & 3s/2\pi r \\ \dfrac{1}{3d_1\cos(\pi/2-\varphi_1)} & \dfrac{1}{3d_2\cos(\pi/6-\varphi_2)} & \dfrac{1}{3d_3\cos(\pi/6+\varphi_3)} & 0 \end{bmatrix} \tag{7}$$

For the passive part of the robotic walker, as shown in Figure 4, the pelvic motions can lead to a change of position, so the D-H method is used to calculate the relation between the current pelvic pose and the passive joints, then we can obtain the current pelvic pose through the inverse kinematics and sensor data.

For the passive joint i, the rotation matrix ${}^{i-1}\boldsymbol{R}_i$ and displacement vector $\boldsymbol{b}_i'$ contain the static joint structure (${}^{i-1}\boldsymbol{R}_{si}$ and $\boldsymbol{b}_{si}'$) and dynamic rigid motion ($\boldsymbol{R}_{mi}$ and $\boldsymbol{b}_{mi}'$), which can be expressed as Eqs 8, 9:

$${}^{i-1}\boldsymbol{R}_i = {}^{i-1}\boldsymbol{R}_{si}\boldsymbol{R}_{mi} \tag{8}$$

$$\boldsymbol{b}_i' = \boldsymbol{b}_{si}' + \boldsymbol{b}_{mi}' \tag{9}$$

According to Eq. 1, the position vector and rotation matrix of the joint can be obtained as Eqs 10, 11:

$${}^0\mathbf{P}_{n+1} = \sum_{i=0}^{n} {}^0\boldsymbol{R}_i\boldsymbol{b}_i' \tag{10}$$

$${}^0\boldsymbol{R}_n = \prod_{i=1}^{n} {}^{i-1}\boldsymbol{R}_i \tag{11}$$

Via Eq. 4, a velocity vector in the local coordinate system can be obtained. To translate into the velocity vector in the global coordinate system, taking point o_0 as a reference point, Eq. 4 premultiplies rotation matrix and $\boldsymbol{t}_R = [\,\boldsymbol{v}_R \;\; \boldsymbol{\omega}_R\,]^T$ translates to robot velocity in the global coordinate system $\boldsymbol{t}_M$:

$$\boldsymbol{t}_M = \boldsymbol{J}_G\boldsymbol{t}_R \tag{12}$$

where $\boldsymbol{t}_M = [\,\boldsymbol{v}_M \;\; \boldsymbol{\omega}_M\,]^T$, $\boldsymbol{J}_G$ is the rotation matrix. Then we can obtain the velocity and angular velocity of the robotic walker in the global coordinate system, which is used for error tracking.

3.2 Intention prediction

The multimodal human-robot interaction model is shown in Figure 5, the facial recognition is the *c*HRI, which is used to detect the Yaw, Roll, and Pitch angle of the head via a real sense camera, then we can predict the direction the user wants to go and extract the angle feature E. The force sensors and control levers are the *p*HRI, which are used to interact with users. The force sensors installed on the PAM can not only able to obtain the interaction force and torque but also detect the current pelvic pose. By the signal combination of the sensors and the principles of human motion, the motion intentions of the lower limbs can be obtained as $\boldsymbol{F}$. Secondly, the

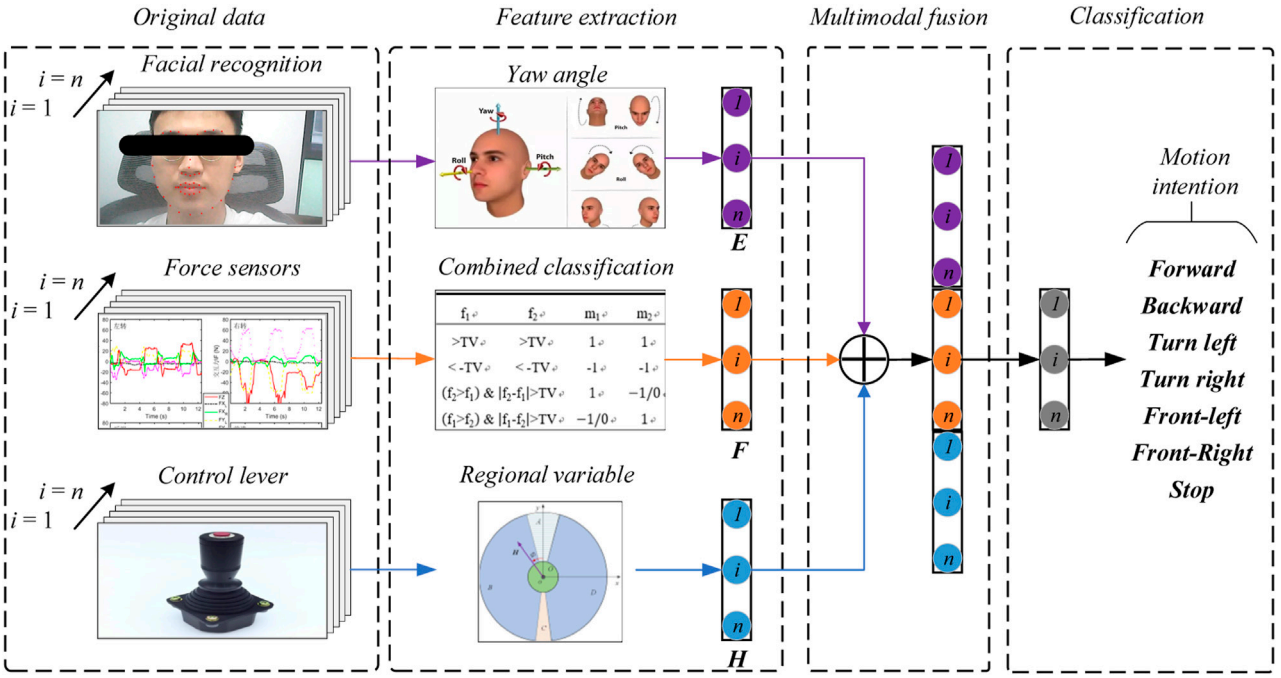

FIGURE 5
The multimodal human-robot interaction model of the robotic walker.

control levers are used to interact with the hands, and we can obtain the motion intentions by the information vector, defined as H. After the feature extraction, we combine the feature via multimodal fusion, which classifies the motion intention into seven types: forward, backward, turn left, turn right, front-left, front-right, and stop.

For the control levers, we can control the walker with two levers as described in the previous paper (Ji et al., 2021). This paper addressed the prediction pattern with a single control lever, defining the lever vector as **H**, the magnitude of the vector as |**H**|, the direction of the vector as Φ, and the method to obtain the motion intentions is as follows:

1) Classify the workspace of the lever into five regions OABCD, defined as Eqs 12a–16:

$$O \in |\mathbf{H}| \le t, -\pi < \Phi \le \pi \tag{12a}$$

$$A \in t < |\mathbf{H}| \le m, -\pi/12 \le \Phi \le \pi/12 \tag{13}$$

$$B \in t < |\mathbf{H}| \le m, -17\pi/18 < \Phi < -\pi/12 \tag{14}$$

$$C \in t < |\mathbf{H}| \le m, 17\pi/18 \le \Phi \le -17\pi/18 \tag{15}$$

$$D \in t < |\mathbf{H}| \le m, \pi/12 < \Phi < 17\pi/18 \tag{16}$$

where t is the threshold value, m is the maximum value.

2) signal collection of the lever vector, as shown in Figure 6, obtain the direction and magnitude of the vector, save the data in time order;

3) predict the motion intention via the current region and change of the region, the relation between the change rule and the motion intention is shown in Table 1.

The basic movement pattern of the robotic walker is shown in Table 1, forward, backward, turn left, turn right, front-left, front-right, and stop respectively. When the change rule is of the O-A, B-A, or D-A, the system predicts the human intends to move forward; when the change rule is of the O-C, the system predicts the human intends to move backward; when the change rule is of the O-B, the system predicts the human intends to turn left; when the change rule is of the O-D, the system predicts the human intends to turn right; when the change rule is of the A-B, the system predicts the human intends to move to front-left; when the change rule is of the A-D, the system predicts the human intend to move to front-right; and the walker will stop with other conditions. Besides, when the interaction forces show abnormal values or rapid change, or the real sense camera detects a dangerous

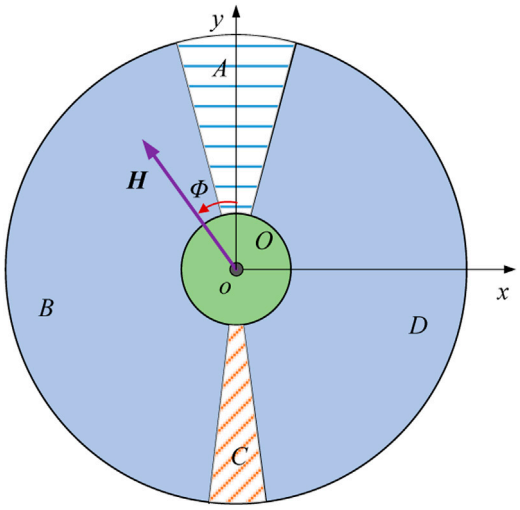

FIGURE 6
Definition of the five regions OABCD.

TABLE 1 Basic movement pattern of the robotic walker.

Region	O	A	B	C	D
O	—	Forward	Turn left	Backward	Turn right
A	Stop	—	Front-left	—	Front-right
B	Stop	Forward	—	Stop	—
C	Stop	—	Stop	—	Stop
D	Stop	Forward	—	Stop	—

expression, or the emergency stop button is pressed, the walker performs the Stop action.

The decision rule by the interaction forces has been discussed in the previous paper (Ji et al., 2020). For facial recognition, we use a real sense camera to detect the Yaw, Roll, and Pitch angle of the head, the angle feature E is used to assist the prediction. When the angle feature $E \in [-\pi/12 \ \ \pi/12]$, the system predicts the human intends to move forward, and we define that $E = 1$; when the angle feature $E \in [-\pi/2 \ \ -\pi/12]$, the system predicts the human intends to turn left, and we define that $E = 2$; when the angle feature $E \in [\pi/12 \ \ \pi/2]$, the system predicts the human intends to turn right, and we define that $E = 3$; we define that $E = 0$ with other conditions. In practice, apply the comprehensive methods to improve the recognition precision, and classify the move patterns via the multimodal fusion.

Then the controller calculates the output based on the classification results and interaction single, the function relationship can be expressed as Eq. 17:

$$f(\boldsymbol{v}_R, \boldsymbol{\omega}_R, \boldsymbol{r}_R) = g(\mathbf{H}, \boldsymbol{F}, \boldsymbol{E}) \tag{17}$$

After the signal has been processed, we define the dead zone to improve stability, then the robot velocity in the local coordinate system can be expressed as Eqs 18, 19:

$$\boldsymbol{v}_R = \begin{cases} k_p \mathrm{H} + k_d \dot{\mathrm{H}} + k_F \sum_{i=1}^{2} \boldsymbol{F_i}, E > 0 \\ 0, \ E \le 0 \end{cases} \tag{18}$$

$$\boldsymbol{\omega}_R = \begin{cases} k_p \mathrm{H} \sin\Phi + k_d \dot{\mathrm{H}} \sin\Phi + k_F \Delta \boldsymbol{F_i}, E > 0 \\ 0, \ E \le 0 \end{cases} \tag{19}$$

$$\boldsymbol{r}_R = \frac{m}{|\mathrm{H} \sin\Phi|} - 1, \in (0, +\infty) \tag{20}$$

where k_p and k_d are the PD gain coefficient, and k_F is the gain coefficient of the interaction force.

Then by Eq. 12 to calculate the robot velocity in the global coordinate system $\boldsymbol{t}_M$, which is used to obtain the motion trail in the plane OXY, so we can compare the reference path and the actual path, and evaluate the effectiveness of the control method.

4 Experiment and verification

To prove the effectiveness of the proposed control method, a preliminary experiment with three healthy volunteers was carried out in this study. In the preliminary experiment, three healthy volunteers were asked to finish a task within the required time. Three kinds of trajectories were chosen to simulate the ADL task which were printed on the ground, and then the actual path data was recorded by the Programmable Logic Controller (PLC).

4.1 Experimental setup

The robotic walker was tested with the proposed control method and three health volunteers. The "∞" path, "○" path, and "□" path were used to test if the robotic walker could allow the volunteers to walk naturally. The experiment was carried out to evaluate the control performance by asking the three healthy volunteers to walk along the three given paths respectively. Three healthy adults were selected for the experiment study, and three men with an average age of 30.7, height of 173.3 cm, and weight of 71.7 kg were involved. Before the experiment, the volunteer wore a harness to connect with the robotic walker and adjusted the pelvic width. Inclusion criteria are no abnormalities in the nervous system, muscle-bone system, or found during physical examination, and having had no special balance training previously. A commonly used "∞" curve was firstly painted in black on the ground as the target path that the volunteers were asked to follow, and then the "∞" curve was replaced with a "○" and "□" curve, respectively. Each person had one chance to try the three paths and the experiment results were recorded by the encoders of the three

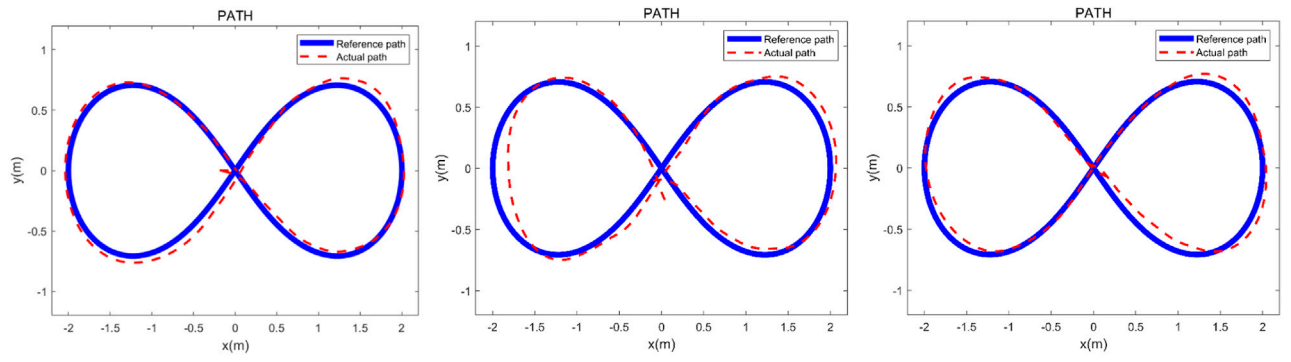

FIGURE 7
Verification experiment to finish the "∞" curve with three healthy adults. The heavy line is the reference path and the dashed line represents the actual path.

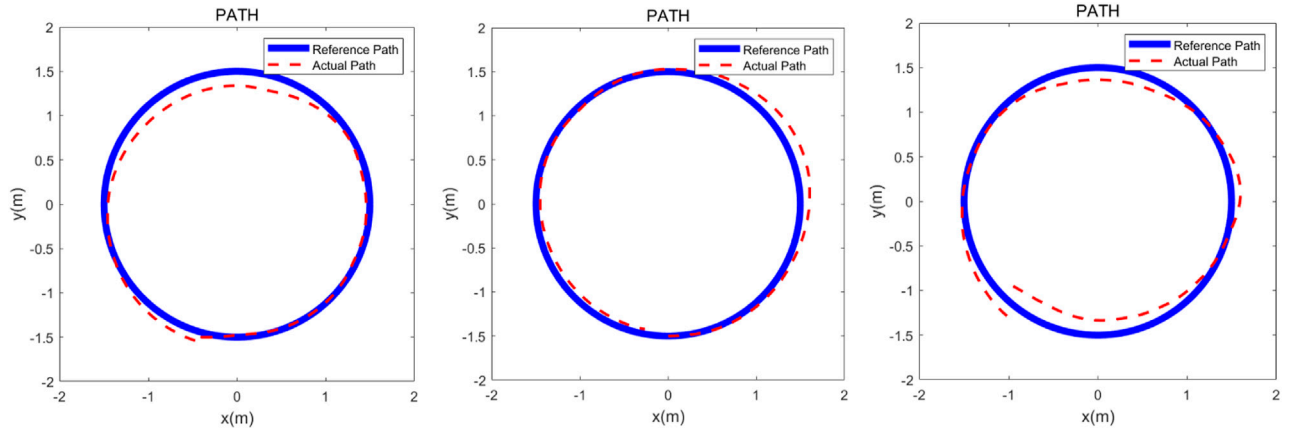

FIGURE 8
Verification experiment to finish the "O" curve with three healthy adults. The heavy line is the reference path and the dashed line represents the actual path.

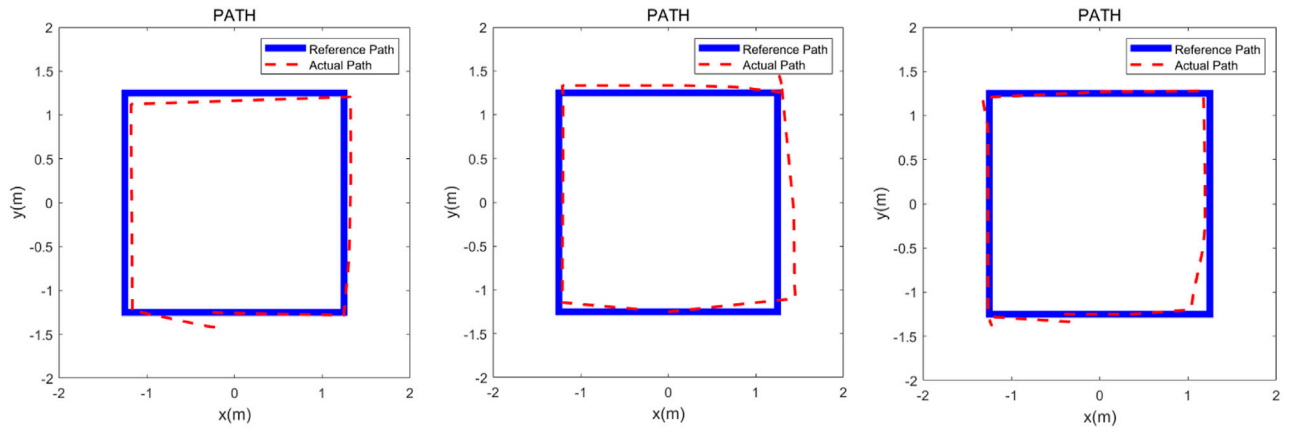

FIGURE 9
Verification experiment to finish the "□" curve with three healthy adults. The heavy line is the reference path and the dashed line represents the actual path.

omni wheels. In the experiment, the volunteers were asked to familiarize the operation of the robotic walker for 5 min and then finish the task within 60 s.

4.2 Data processing

For the tracking error analysis, the three target paths were mathematized in MATLAB to ensure the consistency between the painted curve and the mathematized curve. The actual position and orientation of the robotic walker were calculated by the three encoders of the driving wheel, which were calculated by the previously derived formulas. Then calculating the error between the actual path and reference pose samples, for comparison, the amount of the discrete point was processed into consistent. The normalized integral square error (ISE) cost function was used to evaluate the path-tracking error.

Descriptive and analytical statistics were performed by the SPSS 22.0 and MATLAB 2016b. The actual paths were time normalized to 100% reference path. The error mean and standard deviation of position and orientation is defined by the difference between the target path and the reference path. The experimental results are shown in Figures 7–9.

5 Discussion

The three experimental results are shown in Figures 7–9, the volunteers finished the task within the prescribed time, it can be seen that the volunteers can follow the three given paths within an acceptable error range, and the "∞" curve is the most difficult task, indicating that the robotic walker allows the person to walk naturally under the *m*HRI and control with very minimal effort. As shown in Figure 7, the initial point and the endpoint are in the center

of the curve, and volunteer 1 and volunteer 2 showed relatively big errors, and the ISE results are 2.69, 3.84, and 3.43 respectively, compared with the previous experimental results, the proposed method has a significant improvement. For the verification experiment to finish the "○" curve, the volunteers easily finished the task within the prescribed time, and the ISE results are 2.85, 2.15, and 3.76 respectively. For the "□" curve experiment, the volunteers easily finished the task within the prescribed time, and the ISE results are 2.44, 2.96, and 1.98 respectively. The results show that subjects can operate the walker to follow the prescribed curve, and it is evident that the walker can recognize the motion intent accurately and the volunteers can control the walker to fulfill the given task. This tracking experiment paves the way for the clinical application.

6 Conclusion

The present work demonstrates that the robotic walker is capable of intent recognition with the proposed *m*HRI system, in the ADL assistance, the robotic walker has the potential to reduce the stress on relatives of the patient. The proposed control algorithm for the motion control is derived via the robot kinematics and multimodal fusion human-robot interaction and proved to be effective in the pursuit movement by the preliminary experiment with three health volunteers. The experiment result shows that the robotic walker can effectively predict the user's movement intention and provide appropriate output velocity to track. The RRW system may be used to improve the gait function of stroke survivors which is crucial to their quality of life.

Data availability statement

The original contributions presented in the study are included in the article/supplementary material, further inquiries can be directed to the corresponding authors.

Author contributions

TG: Funding acquisition, Resources, Writing–review and editing. DC: Investigation, Writing–review and editing. GW: Supervision, Writing–review and editing. WZ: Data curation, Writing–original draft. JZ: Formal Analysis, Writing–original draft. ZO: Validation, Writing–review and editing. FZ: Resources, Writing–review and editing. RS: Writing–original draft, Software. JJ: Conceptualization, Writing–original draft. WC: Funding acquisition, Project administration, Writing–review and editing.

Funding

The author(s) declare that no financial support was received for the research, authorship, and/or publication of this article.

Conflict of interest

Authors GW, WZ, JZ, ZQ, FZ, and RS were employed by AVIC Changhe Aircraft Industry (Group) Corporation Ltd.

The remaining authors declare that the research was conducted in the absence of any commercial or financial relationships that could be construed as a potential conflict of interest.

Publisher's note

All claims expressed in this article are solely those of the authors and do not necessarily represent those of their affiliated organizations, or those of the publisher, the editors and the reviewers. Any product that may be evaluated in this article, or claim that may be made by its manufacturer, is not guaranteed or endorsed by the publisher.

References

Calabrò, R. S., Sorrentino, G., Cassio, A., Mazzoli, D., Andrenelli, E., Bizzarini, E., et al. (2021). Robotic-assisted gait rehabilitation following stroke: a systematic review of current guidelines and practical clinical recommendations. *Eur. J. Phys. Rehabil. Med.* 57 (3), 460–471. doi:10.23736/s1973-9087.21.06887-8

Capecci, M., Pournajaf, S., Galafate, D., Sale, P., Le Pera, D., Goffredo, M., et al. (2019). Clinical effects of robot-assisted gait training and treadmill training for Parkinson's disease. A randomized controlled trial. *Ann. Phys. Rehabil. Med.* 62 (5), 303–312. doi:10.1016/j.rehab.2019.06.016

Chen, Y., Chen, Y., Zheng, K., Dodakian, L., See, J., Zhou, R., et al. (2020). A qualitative study on user acceptance of a home-based stroke telerehabilitation system. *Top. Stroke Rehabil.* 27 (2), 81–92. doi:10.1080/10749357.2019.1683792

Cifuentes, C. A., and Anselmo, F. (2016). *Human-robot interaction strategies for walker-assisted locomotion*.

Feigin, V. L., Brainin, M., Norrving, B., Martins, S., Sacco, R. L., Hacke, W., et al. (2022). World stroke organization (WSO): global stroke fact sheet 2022. *Int. J. Stroke* 17 (1), 18–29. doi:10.1177/17474930211065917

Frizera, A., Ceres, R., Frizera-Neto, A., Ceres, R., Rocon, E., and Pons, J. L. (2011). Empowering and assisting natural human mobility: the simbiosis walker. *Int. J. Adv. Robot. Syst.* 80 (3), 29–50. doi:10.5772/10666

GBDStark, B. A., Johnson, C. O., Roth, G. A., Bisignano, C., Abady, G. G., et al. (2021). Global, regional, and national burden of stroke and its risk factors, 1990–2019: a systematic analysis for the Global Burden of Disease Study 2019. *Lancet Neurol.* 20 (10), 795–820. doi:10.1016/s1474-4422(21)00252-0

Haoyong, Yu., Spenko, M., and Dubowsky, S. (2003). An adaptive shared control system for an intelligent mobility aid for the elderly. *Auton. Robots* 15 (1), 53–66. doi:10.1023/a:1024488717009

Horii, T., and Nagai, Y. (2021). Active inference through energy minimization in multimodal affective human-robot interaction. *Front. Robot. AI* 8, 684401. doi:10.3389/frobt.2021.684401

Hurt, C. P., Burgess, J. K., and Brown, D. A. (2015). Limb contribution to increased self-selected walking speeds during body weight support in individuals poststroke. *Gait Posture* 41 (3), 857–859. doi:10.1016/j.gaitpost.2015.02.004

Jarva, E., Mikkonen, K., Tuomikoski, A. M., Kääriäinen, M., Meriläinen, M., Karsikas, E., et al. (2021). Healthcare professionals' competence in stroke care pathways: a mixed-methods systematic review. *J. Clin. Nurs.* 30 (9-10), 1206–1235. doi:10.1111/jocn.15612

Ji, J., Chen, W., Wang, W., and Xi, J. (2021). Design and control of an omni-directional robotic walker based on human–machine interaction. *IEEE Access* 9, 111358–111367. doi:10.1109/ACCESS.2021.3103202

Ji, J., Guo, S., Xi, F., and Zhang, L. (2020). Design and analysis of a smart rehabilitation walker with passive pelvic mechanism. *J. Mech. Robotics* 12 (3). doi:10.1115/1.4045509

Lesaine, E., Francis-Oliviero, F., Domecq, S., Bijon, M., Cetran, L., Coste, P., et al. (2022). Effects of healthcare system transformations spurred by the COVID-19 pandemic on management of stroke and STEMI: a registry-based cohort study in France. *BMJ Open* 12 (9), e061025. doi:10.1136/bmjopen-2022-061025

Mirelman, A., Bonato, P., Camicioli, R., Ellis, T. D., Giladi, N., Hamilton, J. L., et al. (2019). Gait impairments in Parkinson's disease. *Lancet Neurol.* 18 (7), 697–708. doi:10.1016/s1474-4422(19)30044-4

Mojadidi, M. K., Mahmoud, A. N., and Elgendy, I. Y. (2017). Percutaneous patent foramen ovale closure for cryptogenic stroke: learning from clinical trial and error. *J. Thorac. Dis.* 9 (11), 4222–4225. doi:10.21037/jtd.2017.09.153

Moreira, R., Alves, J., Matias, A., and Santos, C. (2019). Smart and assistive walker - ASBGo: rehabilitation robotics: a smart-walker to assist ataxic patients. *Adv. Exp. Med. Biol.* 1170, 37–68. doi:10.1007/978-3-030-24230-5_2

Morioka, K., Lee, J. H., and Hashimoto, H. (2004). Human-following mobile robot in a distributed intelligent sensor network. *IEEE Trans. Ind. Electron.* 51 (1), 229–237. doi:10.1109/tie.2003.821894

Nam, K. Y., Kim, H. J., Kwon, B. S., Park, J. W., Lee, H. J., and Yoo, A. (2017). Robot-assisted gait training (Lokomat) improves walking function and activity in people with spinal cord injury: a systematic review. *J. Neuroeng Rehabil.* 14 (1), 24. doi:10.1186/s12984-017-0232-3

Ohnuma, T., Lee, G., and Chong, N. Y. (2017). Development of JARoW-II active robotic walker reflecting pelvic movements while walking. *Intell. Serv. Robot.* 10, 95–107. doi:10.1007/s11370-016-0212-7

Pons, J., Ceres, R., and Calderón, L. (2008). "Chapter introduction to wearable robots and exoskeletons," in *Wearable robots: biomechatronic exoskeletons* (Wiley), 1–5.

Reisman, D. S., Bastian, A. J., and Morton, S. M. (2010). Neurophysiologic and rehabilitation insights from the split-belt and other locomotor adaptation paradigms. *Phys. Ther.* 90 (2), 187–195. doi:10.2522/ptj.20090073

Seo, K. H., and Lee, J. J. (2009). The development of two mobile gait rehabilitation systems. *IEEE Trans. Neural Syst. Rehabil. Eng.* 17 (2), 156–166. doi:10.1109/tnsre.2009.2015179

Sharma, R., Pavlovic, V. I., and Huang, T. S. (1998). Toward multimodal human-computer interface, in *Proc. IEEE*, 860(5): 853–869. doi:10.1109/5.664275

Sierra, M., Sergio, D., Garzón, M., and Cifuentes, C. A. (2019). Human–robot–environment interaction interface for smart walker assisted gait: AGoRA walker. *Sensors* 19 (13), 2897. doi:10.3390/s19132897

Sierra M., S. D., Jimenez, M. F., Múnera, M. C., Bastos, T., Frizera-Neto, A., and Cifuentes, C. A. (2019). *A therapist helping hand for walker-assisted gait rehabilitation: a pre-clinical assessment," 2019 ieee 4th Colombian conference on automatic control*. Medellin, Colombia: CCAC, 1–6.

Su, H., Qi, W., Chen, J., Yang, C., Sandoval, J., and Laribi, M. A. (2023). Recent advancements in multimodal human-robot interaction. *Front. Neurorobot* 17, 1084000. doi:10.3389/fnbot.2023.1084000

Valadão, C., Caldeira, E., Bastos-Filho, T., Frizera-Neto, A., and Carelli, R. (2016). A new controller for a smart walker based on human-robot formation. *Sensors* 16, 1116. doi:10.3390/s16071116

Wang, W., Gong, T., Song, Z., Wang, Z., and Ji, J. (2023). Simulation study on assist-as-needed control of a rehabilitation robotic walker. *Technol. Health Care* 31 (S1), 293–302. doi:10.3233/thc-236025

Zhao, X., Zhu, Z., Liu, M., Zhao, C., Zhao, Y., Pan, J., et al. (2020). A smart robotic walker with intelligent close-proximity interaction capabilities for elderly mobility safety. *Front. Neurorobot* 14, 575889. doi:10.3389/fnbot.2020.575889

frontiers | Frontiers in Bioengineering and Biotechnology

TYPE Original Research
PUBLISHED 08 January 2024
DOI 10.3389/fbioe.2023.1335071

OPEN ACCESS

EDITED BY
Wujing Cao,
Chinese Academy of Sciences (CAS), China

REVIEWED BY
Jianfeng Li,
Beijing University of Technology, China
Jiaxin Wang,
Hebei University of Technology, China

*CORRESPONDENCE
Jianye Niu,
jyniu@ysu.edu.cn
Bo Cheng,
barrycb@163.com

RECEIVED 08 November 2023
ACCEPTED 20 December 2023
PUBLISHED 08 January 2024

CITATION
Tian J, Wang H, Lu H, Yang Y, Li L, Niu J and Cheng B (2024), Force/position-based velocity control strategy for the lower limb rehabilitation robot during active training: design and validation.
Front. Bioeng. Biotechnol. 11:1335071.
doi: 10.3389/fbioe.2023.1335071

Force/position-based velocity control strategy for the lower limb rehabilitation robot during active training: design and validation

Junjie Tian[1,2], Hongbo Wang[1,2,3], Hao Lu[3], Yang Yang[1,2], Lianqing Li[1,2], Jianye Niu[1,2]* and Bo Cheng[4]*

[1]Hebei Provincial Key Laboratory of Parallel Robot and Mechatronic System, Yanshan University, Qinhuangdao, China, [2]School of Mechanical Engineering, Yanshan University, Qinhuangdao, China, [3]Academy for Engineering and Technology, Fudan University, Shanghai, China, [4]Qinhuangdao Hospital of Traditional Chinese Medicine, Qinhuangdao, China

Aiming at the shortcomings of most existing control strategies for lower limb rehabilitation robots that are difficult to guarantee trajectory tracking effect and active participation of the patient, this paper proposes a force/position-based velocity control (FPVC) strategy for the hybrid end-effector lower limb rehabilitation robot (HE-LRR) during active training. The configuration of HE-LRR is described and the inverse Jacobian analysis is carried out. Then, the FPVC strategy design is introduced in detail, including normal velocity planning and tangential velocity planning. The experimental platform for the HE-LRR system is presented. A series of experiments are conducted to validate the FPVC strategy's performance, including trajectory measurement experiments, force and velocity measurement experiments, and active participation experiments. Experimental studies show that the end effector possesses good following performance with the reference trajectory and the desired velocity, and the active participation of subjects can be adjusted by the control strategy parameters. The experiments have verified the rationality of the FPVC strategy, which can meet the requirements of trajectory tracking effect and active participation, indicating its good application prospects in the patient's robot-assisted active training.

KEYWORDS

active training, rehabilitation robot, trajectory tracking, velocity control, active participation

1 Introduction

Stroke is a cerebrovascular disease that seriously endangers human health (Langhorne et al., 2011; Singh et al., 2018). Its high incidence rate and high disability rate have brought heavy burdens to individuals, families and society (Feigin et al., 2009). Epidemiological investigation shows that motor dysfunction is the leading cause of disability after stroke (Zhang et al., 2016; Dulyan et al., 2022). In recent years, many studies have been dedicated to developing rehabilitation robot systems to assist stroke patients in limb rehabilitation training, and a series of research achievements have been made (Krebs et al., 2007; Zhou et al., 2021; Cao et al., 2023).

According to patients' degree of active participation, training methods are mainly divided into two types: passive training and active training (Shi et al., 2019). The robot guides the patient's limbs along the required reference trajectory in passive training. It aims to prevent

muscle atrophy through repetitive movement (Wu et al., 2022). Passive training is suitable for improving proprioceptive sensitivity around limb joints in the early rehabilitation stage (Chiyohara et al., 2020). In active training, patients are required to complete corresponding tasks within a certain period based on verbal or visual instructions (Sun et al., 2023). Clinical research shows that the patient's active participation is conducive to motor-related cortical activation and limb rehabilitation (Zheng et al., 2021). The control strategies involved in active training are primarily based on bioelectrical signals and force/torque signals (Zhang et al., 2017).

Two active control strategies utilizing sEMG signals are available for rehabilitation robots: continuous control and triggered control (Meng et al., 2015; Cao et al., 2022). With the continuous control, sEMG signals are used to recognize the limb motion intention, and torque assistance based on this intention is provided for generating the desired motion (Lu et al., 2019). Xie et al. have combined sEMG signals with interaction force to optimize trajectory planning for the rehabilitation robot and planned different periodic trajectories (Xie et al., 2016). Khoshdel et al. developed a neural impedance control strategy to estimate the exerted force using sEMG signals for a single-DOF rehabilitation robot (Khoshdel et al., 2018). Shi et al. proposed a model for predicting the continuous motion of lower limbs for rehabilitation robots (Shi et al., 2020). Their study examined the influence of different muscle types on joint angles as well as the robustness of their prediction model. With the triggered control, the robot begins to provide the assistance when the sEMG signals reach a certain threshold (Artz, 2015). Using the support vector machine classification model, Meng et al. developed a control strategy capable of predicting limb motion intention and triggering robot assistance based on sEMG signals (Meng et al., 2014). Ma et al. used sEMG signals to predict the angles of the hip and knee joints. When the predicted angle values reached the set thresholds, the lower limb rehabilitation robot was triggered to complete the corresponding gait (Ma et al., 2019). An sEMG-based trigger was proposed by Kawamoto et al. for the HAL rehabilitation robot. By providing the patient with motion support, HAL could move the joints in accordance with the movement intention and improve the lower limb's joint mobility (Kawamoto et al., 2010). Nevertheless, bioelectrical signals used for active control are susceptible to interference and consume considerable time. Implementation and interpretation of this approach are highly dependent on the individual (Taffese, 2017).

Compared with bioelectrical signals, force/torque signals have the advantages of stable performance (Lotti et al., 2022). The active training control strategies based on force/torque information mainly include the impedance control and the hybrid force/position control strategies (Tsoi et al., 2009). The impedance control aims to synchronously adjust motion and force by establishing an appropriate interaction relationship (Zhou et al., 2021). Huo et al. developed an impedance modulation method for the exoskeleton robot, which can provide balance assistance during the switch between sitting and standing (Huo et al., 2022). Mokhtari et al. proposed a hybrid optimal sliding mode impedance control method and compared the performance with that of the traditional sliding mode controller in the lower limb exoskeleton system (Mokhtari et al., 2021). Tran et al. designed a fuzzy rule-based impedance control strategy that can adjust the impedance coefficients between the robot and the lower limb under various walking speeds (Tran et al., 2016). The hybrid position/force controller is intended for both position and force trajectory tracking

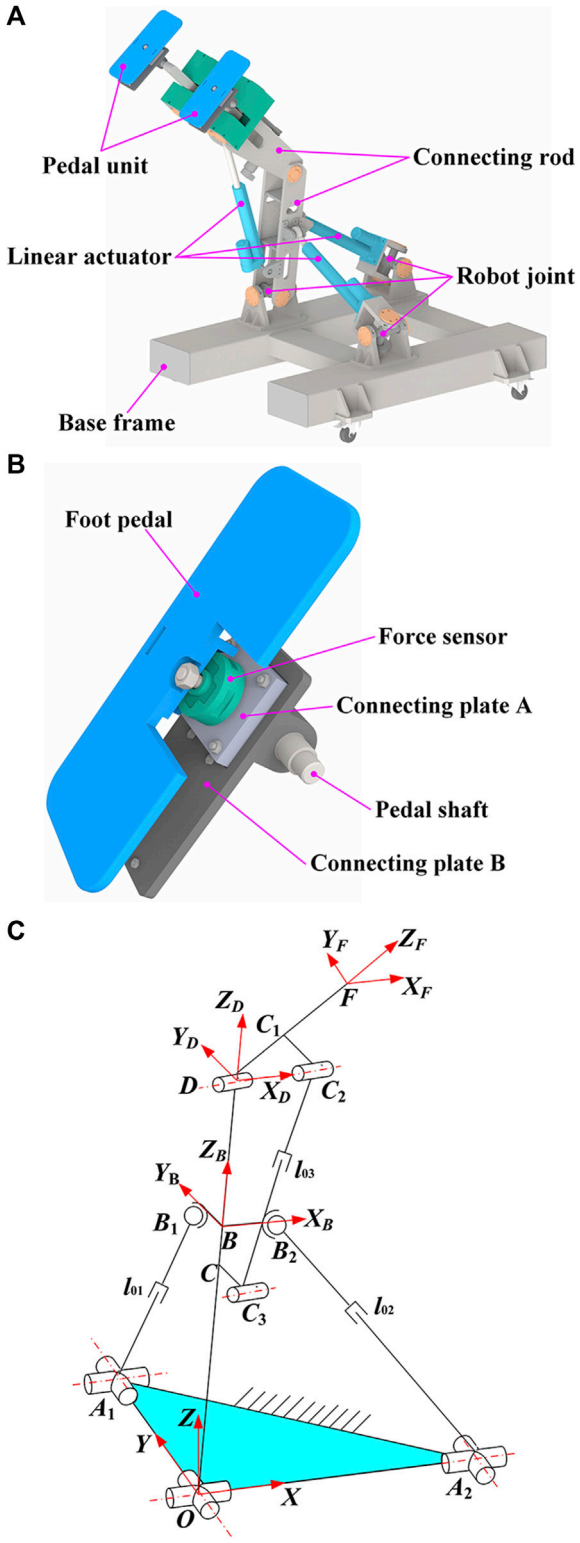

FIGURE 1
Configuration of HE-LRR. **(A)** Overall structure of the robot. **(B)** Detailed structure of the pedal unit. **(C)** Schematic diagram of robot configuration.

(Navvabi and Markazi, 2019). Bernhardt et al. proposed a hybrid control strategy for the rehabilitation robot Lokomat. In the swing phase, the rehabilitation robot was controlled by force so the patient

TABLE 1 Parameter symbols and descriptions of the robot configuration.

Symbol	Description
l_1	Length of OD
l_2	Length of DF
l_{01}	Length of A_1B_1
l_{02}	Length of A_2B_2
l_{03}	Length of C_2C_3
a_1	Length of OA_1
a_2	Length of OA_2
b_1	Length of BB_1
b_2	Length of BB_2
a_3	Length of CC_3
b_3	Length of C_1C_2
l_{OB}	Length of OB
m_1	Length of CD
m_2	Length of C_1D
α	The angle of $\{D\text{-}X_DY_DZ_D\}$ relative to $\{O\text{-}XYZ\}$ around the X-axis
β	The angle of $\{D\text{-}X_DY_DZ_D\}$ relative to $\{O\text{-}XYZ\}$ around the Y-axis
γ	The angle of $\{F\text{-}X_FY_FZ_F\}$ relative to $\{D\text{-}X_DY_DZ_D\}$ around the X_D axis

could walk independently. In the stance phase, the control software switched to position control to guide the limb to move (Bernhardt et al., 2005). Ju et al. developed a hybrid position/force controller for the rehabilitation robot combined with fuzzy logic to track the desired force along the preset motion direction (Ju et al., 2005). Valera et al. developed a hybrid control scheme based on the position/force information, which makes it possible to perform different lower limb rehabilitation exercises (Valera et al., 2017). However, due to the position/force dynamic relationship being adjusted to increase robot compliance in impedance control, it increases the difficulty of guaranteeing the trajectory tracking effect of the robot in lower limb rehabilitation training (Lv et al., 2017). The common position/force hybrid control strategy allows patients to bear a certain amount of resistance close to the preset trajectory, which limits the active participation of patients (Rivas-Blanco et al., 2013).

Aiming at the shortcomings of most existing control strategies for lower limb rehabilitation robots that are difficult to guarantee trajectory tracking effect and active participation of the patient, a force/position-based velocity control (FPVC) strategy is proposed for the hybrid end-effector lower limb rehabilitation robot (HE-LRR) in this paper. On one hand, HE-LRR has the advantages of a large workspace and strong bearing capacity and is also suitable for experimental verification on subjects with different body dimensions. On the other hand, HE-LRR can guide the lower limbs to perform three-dimensional spatial movements, achieving various typical lower limb rehabilitation exercises such as MOTOmed therapy and continuous passive motion (CPM) therapy. Experimental studies have been conducted to verify the rationality of the FPVC strategy under MOTOmed and CPM modes. This paper is organized as follows. In the Materials and Methods section, the configuration of HE-LRR is introduced and the FPVC strategy design is proposed. Then the experimental platform is described. In the Results section, the validation experiments are conducted, including trajectory measurement experiments, force and velocity measurement experiments, and active participation experiments. In the Conclusions and Discussion section, the summary and prospect of the FPVC strategy are presented.

2 Materials and methods

2.1 Configuration of HE-LRR

HE-LRR consists of a base frame, connecting rods, linear actuators, robot joints, and pedal units, as shown in Figure 1A. The pedal unit is the end effector of HE-LRR, consisting of a foot pedal, a force sensor, connecting plates, and a pedal shaft, as shown in Figure 1B.

Figure 1C shows the robot configuration diagram. The origin of the fixed coordinate system $\{O\text{-}XYZ\}$ lies at the intersection of the two rotational auxiliary axes of the universal joint. The X-axis coincides with one axis of the universal joint and along the OA_2 direction. The Y-axis coincides with another axis of the universal joint and along the OA_1 direction. The direction of the Z-axis is determined by the right-hand screw rule. Moving coordinate system $\{B\text{-}X_BY_BZ_B\}$ has its origin at the OD rod, X_B axis along the BB_2 direction, and Y_B axis along the BB_1 direction. The moving coordinate system $\{D\text{-}X_DY_DZ_D\}$ is established with the X_D axis along the axis of the revolute joint D and the Z_D axis along the OD direction. Point F represents the midpoint of the robot end effectors (pedal units). The X_F axis of the moving coordinate system $\{F\text{-}X_FY_FZ_F\}$ is parallel to the X_D direction, and the Z_F axis is along the DF direction.

2.2 Inverse Jacobian analysis

In this subsection, the parameter symbols and descriptions of the robot configuration are shown in Table 1. According to the geometric relationships in Figure 1C, the coordinates of point F can be expressed as follows:

$$\begin{cases} F_x = l_2 \sin\beta \cos(\alpha+\gamma) + l_1 \cos\alpha \sin\beta \\ F_y = -l_2 \sin(\alpha+\gamma) - l_1 \sin\alpha \\ F_z = l_2 \cos\beta \cos(\alpha+\gamma) + l_1 \cos\alpha \cos\beta \end{cases} \tag{1}$$

According to Eq. 1, the rotation angles α, β and γ can be expressed as:

$$\begin{cases} \alpha = -\arccos\left(\dfrac{l_1^2 + F_x^2 + F_y^2 + F_z^2 - l_2^2}{2l_1\sqrt{F_x^2 + F_y^2 + F_z^2}}\right) - \arctan\left(\dfrac{F_y}{F_z}\cos\beta\right) \\ \beta = \arctan\left(\dfrac{F_x}{F_z}\right) \\ \gamma = \arccos\dfrac{F_x^2 + F_y^2 + F_z^2 - l_2^2 - l_1^2}{2l_1l_2} \end{cases} \tag{2}$$

Taking the derivative of time on both sides of Eq. 2, the mapping relationship between the angular velocities and the velocity components of the robot end effector can be expressed in the following matrix form:

10.3389/fbioe.2023.1335071

$$\begin{bmatrix} \dot{\alpha} \\ \dot{\beta} \\ \dot{\gamma} \end{bmatrix} = \boldsymbol{J}_1 \begin{bmatrix} \dot{F}_x \\ \dot{F}_y \\ \dot{F}_z \end{bmatrix} = \begin{bmatrix} \frac{\partial \alpha}{\partial F_x} & \frac{\partial \alpha}{\partial F_y} & \frac{\partial \alpha}{\partial F_z} \\ \frac{\partial \beta}{\partial F_x} & \frac{\partial \beta}{\partial F_y} & \frac{\partial \beta}{\partial F_z} \\ \frac{\partial \gamma}{\partial F_x} & \frac{\partial \gamma}{\partial F_y} & \frac{\partial \gamma}{\partial F_z} \end{bmatrix} \begin{bmatrix} \dot{F}_x \\ \dot{F}_y \\ \dot{F}_z \end{bmatrix} \tag{3}$$

where $\boldsymbol{J}_1$ is the velocity Jacobian matrix between the angular velocities and velocity components of the robot end effector.

Establish the following closed-loop vector equation in the fixed coordinate system $\{O\text{-}XYZ\}$

$$\boldsymbol{l}_{OB} + {}^{O}_{B}\boldsymbol{R}\boldsymbol{n}_i = \boldsymbol{m}_i + \boldsymbol{A}_i\boldsymbol{B}_i \, (i = 1, 2) \tag{4}$$

where ${}^{O}_{B}\boldsymbol{R}$ is the rotation matrix from $\{B\text{-}X_BY_BZ_B\}$ to $\{O\text{-}XYZ\}$, $\boldsymbol{n}_i$ is the position vector of B_i in the coordinate system $\{B\text{-}X_BY_BZ_B\}$, $\boldsymbol{m}_i$ is the position vector of A_i in the coordinate system $\{O\text{-}XYZ\}$, $\boldsymbol{l}_{OB}$ and $\boldsymbol{A}_i\boldsymbol{B}_i$ are the vectors of OB and A_iB_i in the fixed coordinate system.

Substituting mechanical parameters into Eq. 4 and simplifying to get expressions of the linear actuator lengths l_{01} and l_{02}

$$\begin{cases} l_{01} = \sqrt{a_1^2 + b_1^2 + l_{OB}^2 - 1a_1b_1\cos\alpha + 2l_{OB}a_1\sin\alpha} \\ l_{02} = \sqrt{a_2^2 + b_2^2 + l_{OB}^2 - 1a_2b_2\cos\beta + 2l_{OB}a_1\sin\beta} \end{cases} \tag{5}$$

According to the Cosine Theorem, we can get Eq. 6

$$\cos\angle C_2DC_3 = \frac{b_3^2 + m_2^2 + m_1^2 + a_3^2 - l_{03}^2}{2\sqrt{b_3^2 + m_2^2}\sqrt{m_1^2 + a_3^2}} \tag{6}$$

γ angle can be solved as Eq. 7

$$\gamma = \pi - \arccos\frac{b_3^2 + m_2^2 + a_3^2 + m_1^2 - l_{03}^2}{2\sqrt{b_3^2 + m_2^2}\sqrt{a_3^2 + m_1^2}} \tag{7}$$

Hence, the linear actuator length l_{03} can be expressed as

$$l_{03} = \sqrt{a_3^2 + b_3^2 + m_1^2 + m_2^2 + 2\sqrt{m_1^2 + a_3^2}\sqrt{m_2^2 + b_3^2}\cos\left(\gamma + \arctan\frac{b_3}{m_2} + \arctan\frac{a_3}{m_1}\right)} \tag{8}$$

The relationship between linear actuator velocities and angular velocities can be obtained by taking the derivative of time on both sides of Eqs 5, 8:

$$\begin{cases} \dot{l}_{01} = \dfrac{a_1l_{OB}\cos\alpha + a_1b_1\sin\alpha}{l_{01}}\dot{\alpha} \\ \dot{l}_{02} = \dfrac{a_2l_{OB}\sin\alpha\sin\beta}{l_{02}}\dot{\alpha} \\ \quad + \dfrac{a_2b_2\sin\beta - a_2l_{OB}\cos\alpha\cos\beta}{l_{02}}\dot{\beta} \\ \dot{l}_{03} = -\dfrac{\sin\left(\gamma + \arctan\dfrac{b_3}{m_2} + \arctan\dfrac{a_3}{m_1}\right)\sqrt{a_3{}^2 + m_1{}^2}\sqrt{b_3{}^2 + m_2{}^2}}{l_{03}}\dot{\gamma} \end{cases} \tag{9}$$

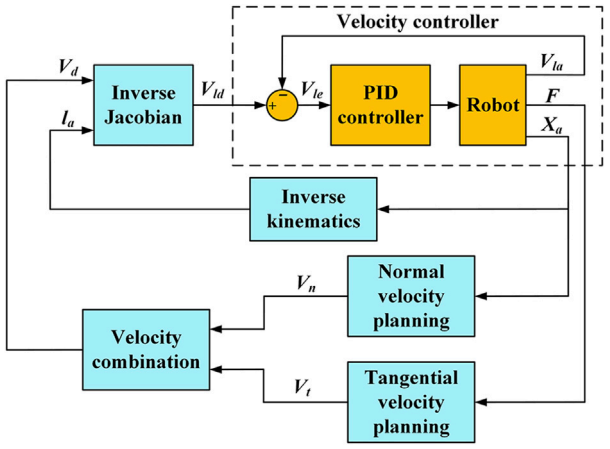

FIGURE 2
FPVC strategy diagram for HE-LRR.

$\boldsymbol{J}_2$ is used to represent the Jacobian matrix between the linear actuator velocities and angular velocities. Eq. 9 can be written in the following matrix form:

$$\begin{bmatrix} \dot{l}_{01} \\ \dot{l}_{02} \\ \dot{l}_{03} \end{bmatrix} = \boldsymbol{J}_2 \begin{bmatrix} \dot{\alpha} \\ \dot{\beta} \\ \dot{\gamma} \end{bmatrix} = \begin{bmatrix} J_{11} & 0 & 0 \\ J_{21} & J_{22} & 0 \\ 0 & 0 & J_{33} \end{bmatrix} \begin{bmatrix} \dot{\alpha} \\ \dot{\beta} \\ \dot{\gamma} \end{bmatrix} \tag{10}$$

where

$$\begin{cases} J_{11} = \dfrac{a_1l_{OB}\cos\alpha + a_1b_1\sin\alpha}{l_{01}} \\ J_{21} = \dfrac{a_2l_{OB}\sin\alpha\sin\beta}{l_{02}} \\ J_{22} = \dfrac{a_2b_2\sin\beta - a_2l_{OB}\cos\alpha\cos\beta}{l_{02}} \\ J_{33} = -\dfrac{\sin\left(\gamma + \arctan\dfrac{b_3}{m_2} + \arctan\dfrac{a_3}{m_1}\right)\sqrt{a_3{}^2 + m_1{}^2}\sqrt{b_3{}^2 + m_2{}^2}}{l_{03}} \end{cases}$$

The inverse Jacobian matrix $\boldsymbol{J}_i$ can be used to represent the mapping relationship between the linear actuator velocities and the velocity components of the robot end effector. Combined with Eqs 3, 10, we can obtain Eq. 11:

$$\begin{bmatrix} \dot{l}_{01} \\ \dot{l}_{02} \\ \dot{l}_{03} \end{bmatrix} = \boldsymbol{J}_i \begin{bmatrix} \dot{F}_x \\ \dot{F}_y \\ \dot{F}_z \end{bmatrix}, \boldsymbol{J}_i = \boldsymbol{J}_1\boldsymbol{J}_2 \tag{11}$$

2.3 FPVC strategy design

Figure 2 shows the FPVC strategy diagram for HE-LRR. The end effector's actual three-dimensional position coordinate information X_a is used to plan the normal velocity (NV) V_n of HE-LRR, and man-machine contact force (MCF) F is used to plan the tangential velocity (TV) V_t of HE-LRR. The NV and TV are combined as the

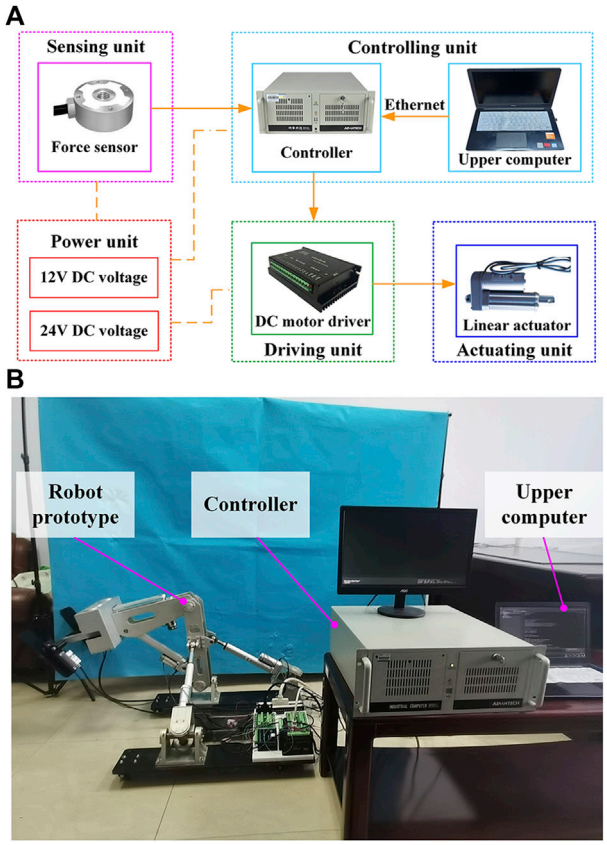

FIGURE 3
Experimental platform. **(A)** Block diagram of the robot control system. **(B)** Physical picture of the robot prototype and the control system.

end effector's desired velocity V_d. The actual position of each linear actuator l_a is calculated by inverse kinematics. Combined with the desired velocity V_d and the actual linear actuator position l_a, the desired velocity of each linear actuator V_{ld} is calculated by inverse Jacobian and is sent to the velocity controller of the FPVC strategy. The calculation process of inverse kinematics is shown in the literature (Wang et al., 2022). NV planning and TV planning are introduced in this subsection in detail.

HE-LRR assists the patient's lower limbs in performing rehabilitation exercises under the constraint trajectory through end traction, so it is essential that the end effector can move along the reference trajectory in space. When the end effector deviates from the reference trajectory, the desired NV is planned to reduce the deviation. P_1 is the actual end point of the end effector of HE-LRR, and P_2 is the closest point on the reference trajectory to point P_1. The desired NV direction is along the direction of P_1P_2 and points towards P_2.

The end effector's desired NV can be calculated by Eq. 12:

$$V_n = k_n d \tag{12}$$

where k_n is the NV coefficient, and d is the shortest distance from point P_1 to the reference trajectory.

The mapping function between TV and MCF is planned as a piecewise function, including the initial segment sub-function, linear segment sub-function and parabolic segment sub-function. When MCF is less than the initial threshold F_i, it is considered that MCF is caused by random factors such as mechanical jitter, and cannot represent the patient's active intention, and the desired TV is equal to zero. When the MCF exceeds the initial threshold F_i and falls below the linear threshold F_b it is considered that MCF can reflect the patient's movement intention. The mapping function is planned as a linear correlation between the desired TV and MCF. When MCF exceeds the linear threshold F_b the slope of the mapping function needs to decrease based on safety consideration, and the mapping relationship between TV and MCF is planned as a parabolic sub-function.

According to the above parameters and settings, the initial segment sub-function is:

$$V_t = 0 \left(F \le F_i\right) \tag{13}$$

The linear segment sub-function is:

$$V_t = k_l F - k_l F_i \left(F_i < F \le F_l\right) \tag{14}$$

where k_l represents the linear segment slope.

The linear threshold F_l can be expressed as follows:

$$F_l = \frac{V_{lm} + k_l F_i}{k_l} \tag{15}$$

where V_{lm} represents the maximum linear velocity.

The parabolic equation whose focus is on the F-axis is chosen for the planning of the third segment sub-function. The parabolic sub-function can be written as:

$$V_t = \sqrt{2p\left(F - q\right)} \tag{16}$$

where q is the F-axis translation distance, and p represents the distance from the focus to the directrix of the parabola.

To meet the piecewise function's continuity requirement, the point (F_b, V_{lm}) is the intersection point of the linear segment and the parabolic segment, thus:

$$V_{lm} = \sqrt{2p\left(F_l - q\right)} \tag{17}$$

The parabolic slope at the point (F_b, V_{lm}) is set to half the linear slope, thus:

$$\frac{k_l}{2} = \frac{p}{\sqrt{2p\left(F_l - q\right)}} \tag{18}$$

Combined with Eqs 15–18, the parabolic segment sub-function can be expressed as:

$$V_t = \sqrt{k_l V_{lm} \left(F - F_i\right)} \ \left(F > F_l\right) \tag{19}$$

Combined with Eqs 13, 14, 19, the piecewise function can be expressed as:

$$V_t = \begin{cases} 0 & F \le F_i \\ k_l F - k_l F_i & F_i < F \le \dfrac{V_{lm} + k_l F_i}{k_l} \\ \sqrt{k_l V_{lm} \left(F - F_i\right)} & F > \dfrac{V_{lm} + k_l F_i}{k_l} \end{cases} \tag{20}$$

It can be seen from Eq. 20 that the mapping function between TV and MCF can be determined by three parameters, including the initial threshold F_i, the linear segment slope k_l, and the maximum linear velocity V_{lm}.

TABLE 2 Basic information on healthy subjects.

Number	Height (mm)	Weight (kg)	Thigh length (mm)	Calf length (mm)
1	1720	75	430	400
2	1670	78	405	385
3	1690	72	415	400

2.4 Experimental platform

Figure 3A illustrates the block diagram of the lower limb rehabilitation robot's control system, which includes the controlling, sensing, driving, actuating, and power units. A personal computer (Advantech, IPC610, CN) serves as the controller. In addition to receiving commands from the upper computer (Dell, Vostro 5370, USA), the IPC can also receive signals from force sensors (HUILIZHI, LZ-SWF40, 0–300 N, ±0.3%F.S., CN) and encoders. The motor drivers (Magicon Intelligent, MC-FBLD-6600, 9–36 V, 12 A, CN) receive commands from the controller to accomplish the telescopic movement of the linear actuators (YCMC, LEC606, 210 mm, 0–450 N, CN). An incremental encoder records the DC motor's actual position as it moves to facilitate the linear actuator's velocity closed-loop control. The angle sensors, encoders, and motor drivers are powered by the power unit that supplies 12 V or 24 V DC voltage.

As shown in Figure 3B, the prototype of HE-LRR has been manufactured, and the control system has been built. The robot's base frame is equipped with casters with brakes to facilitate robot movement and improve stability. Rehabilitation training is performed with the patient's feet on the pedal units. According to the procedure (CRRC-IEC-RF-SC-005-01) approved by the China Rehabilitation Research Center, three healthy subjects were recruited to participate in the experiments. Basic information about the subjects is presented in Table 2. During the experiments, none of the subjects reported discomfort.

3 Results

To validate the feasibility of the FPVC strategy, trajectory measurement experiments, force and velocity measurement experiments, and active participation experiments are carried out in this section.

3.1 Trajectory measurement experiments

The active training based on the FPVC strategy is carried out under the constraint trajectory, which makes it possible for patients to obtain a large range of joint activities. The trajectory measurement experiments of HE-LRR are carried out under MOTOmed mode (Figure 4A) and CPM mode (Figure 4B). The constraint trajectories for the above two modes are a circular trajectory and a linear trajectory, respectively. The subject's feet are connected with the end effector through Velcro tapes. During the experiment, the actual positions of the linear actuators are recorded, and the actual end position of HE-LRR can be calculated through the forward kinematics of the robot. Each group of experiments was conducted for 10 min. In subsections 3.1 and 3.2, 10 s of data were displayed to more clearly represent the results.

The trajectory measurement experimental results of HE-LRR in MOTOmed mode are shown in Figure 5. The reference trajectory parameters are set as shown in Figure 5A: the center coordinates (x_0, y_0, z_0)=(0, −670, 470), the radius is 100.00 mm. When the initial position is outside the circular trajectory, the initial point is set to (x_0, y_0, z_0)=(0, −670, 620). When the initial position is inside the circular trajectory, the initial point is set to (x_0, y_0, z_0)=(0, −670, 520). It can be seen that during the experiment, the end position of the robot quickly approaches the reference trajectory first, and then the approaching velocity slows down. Finally, the end effector's actual trajectory has a good coincidence degree with the reference trajectory. The minimum distance between the end effector's actual position and the reference trajectory is defined as the actual position error of the robot. Figure 5B shows the robot's actual position errors under MOTOmed mode. The position errors of the robot are different due to the difference in the starting point. The initial position errors of experimental Group A and Group B are 50 mm and −50 mm, respectively. The positive error value indicates that the initial point is outside the circular trajectory, and the negative value indicates that the initial point is inside the circular trajectory. At about 2.91 s, the position error of experimental Group A decreases to 5.00 mm. At about 1.70 s, the position error of experimental Group B becomes −5.00 mm. After about 4 s, the end error of the robot decreases to a small range, which suggests that the trajectory tracking effect of the end effector shows good accuracy and stability under different initial position errors.

The trajectory measurement experimental results of HE-LRR in CPM mode are shown in Figure 6. The reference trajectory parameters are set as shown in Figure 6A: the linear trajectory passes through (x_0, y_0, z_0)=(0, −810, 290), and the inclination angle is 10°. When the starting point is above the linear trajectory, the initial point is set as (x_0, y_0, z_0)=(0, −725, 400). When the starting point is below the linear trajectory, the initial point is set as (x_0, y_0, z_0) =(0, −720, 215). It can be seen that the end position of the robot approaches the reference trajectory quickly initially. After the switch from forward motion to backward motion, the end position of the robot still gets close to the reference trajectory. Finally, the actual trajectory has a good coincidence with the reference trajectory. According to Figure 6B, when the starting point is above the linear trajectory, the initial position error is −93.57 mm, and after 2.35 s, the position error becomes −9.36 mm (approximately 10% of the initial position error), and the final position error is in a small range. When the starting point is below the linear trajectory, the initial position error is 89.48 mm. After 2.31 s, the position error

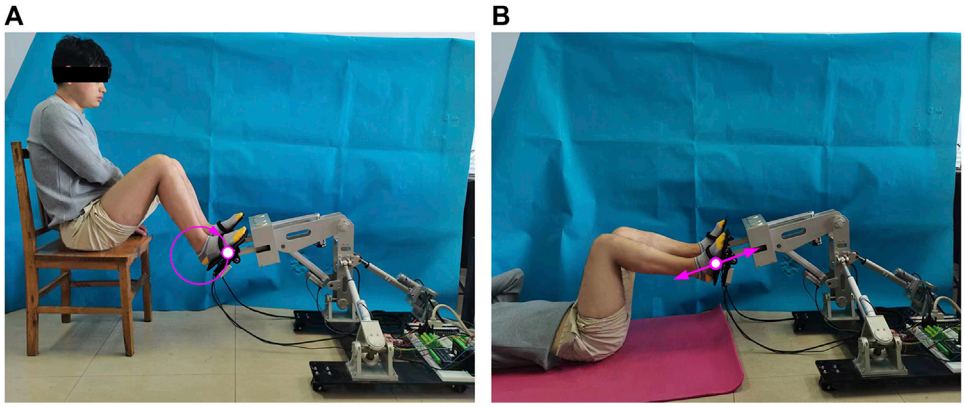

FIGURE 4
Field diagram of trajectory measurement experiments of HE-LRR. **(A)** MOTOmed mode. **(B)** CPM mode.

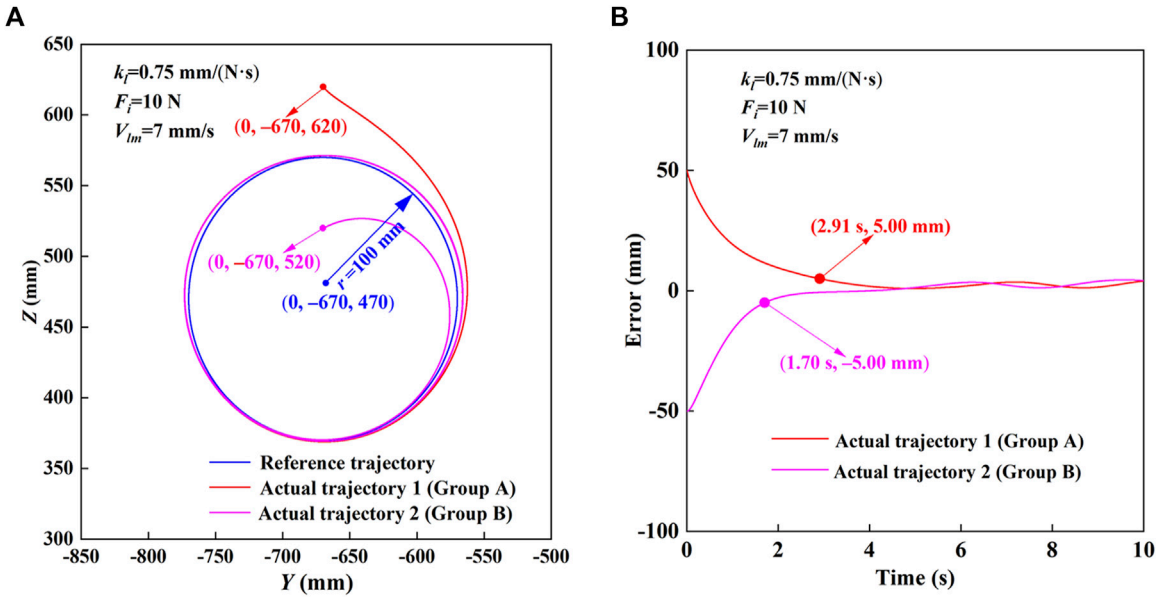

FIGURE 5
Trajectory measurement experimental results of HE-LRR in MOTOmed mode. **(A)** Comparison of the reference trajectory and actual trajectory. **(B)** Actual position errors.

decreases to 8.95 mm (approximately 10% of the initial position error), and the final position error is in a small range. In conclusion, the robot based on the FPVC strategy can realize the rehabilitation training of the predetermined trajectory with good accuracy and stability under the MOTOmed and CPM modes.

3.2 Force and velocity measurement experiments

In active training, the robot system recognizes the motion intention of the patient by detecting the force applied at the end effector, and assists the lower limb in realizing the rehabilitation training through the actuating unit. The parameter settings of the circular trajectory and the linear trajectory are consistent with those in Section 5.1. The control strategy parameters are set as follows: the initial threshold F_i = 10 N, the maximum linear velocity V_{lm} = 7 mm/s, and the linear segment slope k_l = 0.75 mm/(N·s). Based on the forward kinematics of the robot, the end effector's actual position can be calculated from the actual positions of linear actuators. After the differential calculation, the end effector's actual velocity can be obtained.

Figure 7 shows the experimental results of the force and velocity of the robot in MOTOmed mode. In MOTOmed mode, clockwise and counterclockwise motions are studied, respectively. In the clockwise motion (Figure 7A), when the MCF value is positive, the desired velocity is also non-negative and the fluctuation trend of

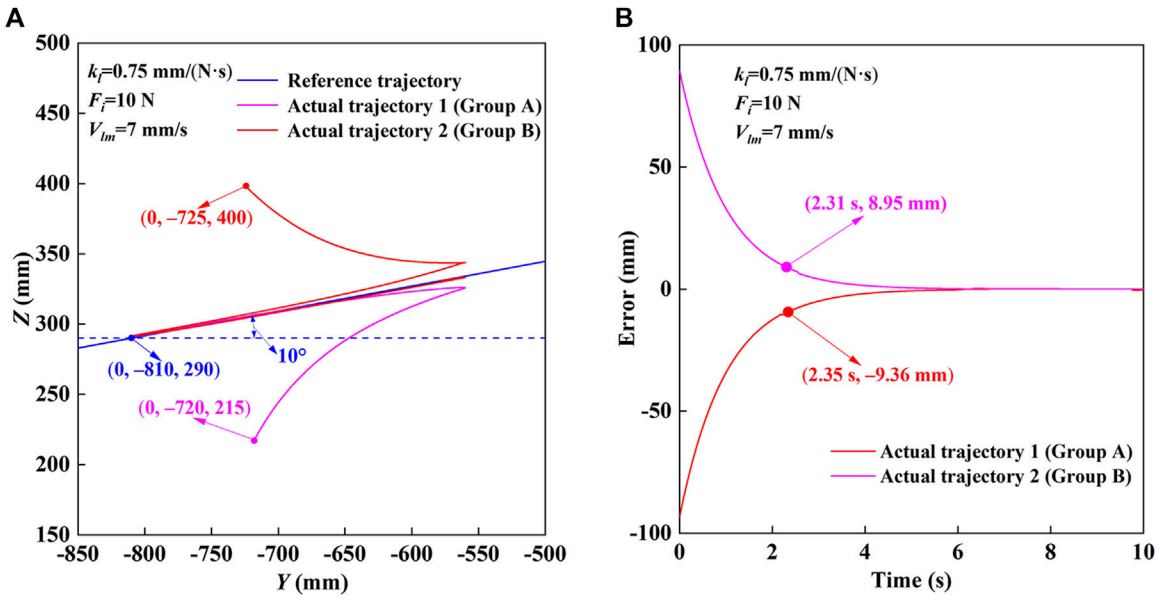

FIGURE 6
Trajectory measurement experimental results of HE-LRR in CPM mode. **(A)** Comparison of the reference trajectory and actual trajectory. **(B)** Actual position errors.

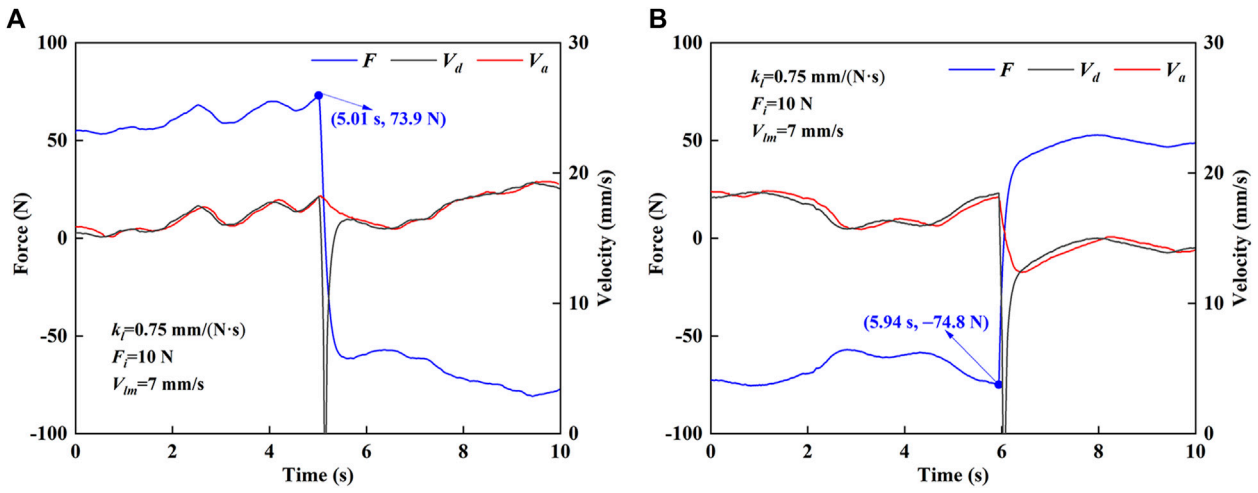

FIGURE 7
Force and velocity results of HE-LRR in MOTOmed mode. **(A)** Clockwise motion. **(B)** Counterclockwise motion.

the desired velocity is consistent with MCF. When the MCF value is negative, the desired velocity is non-negative and the fluctuation trend of the desired velocity is opposite to that of MCF. After 5.01 s, the MCF rapidly changes from compression force (73.9 N) to tension force. At this time, the desired velocity rapidly decreases to 0 mm/s and then rapidly increases. In the counterclockwise motion (Figure 7B), when the MCF value is negative, the desired velocity is non-negative and the fluctuation trend of the desired velocity is opposite to that of the MCF. When the MCF value is positive, the desired velocity is non-negative and the desired velocity and MCF have the same fluctuation trend. From 5.94 s, the MCF quickly changes from tension force (−74.8 N) to compression force, and the desired velocity shows a changing law of rapid decrease and rapid increase. When the desired velocity change rate is low, the end effector's actual velocity can better follow the desired velocity. When the desired velocity curve has a significant mutation, the changing trend of the actual velocity is quite different and the velocity change is relatively slow. Since it is expected to avoid the velocity mutation during the rehabilitation training, it is beneficial that the actual velocity of the robot can keep relatively stable.

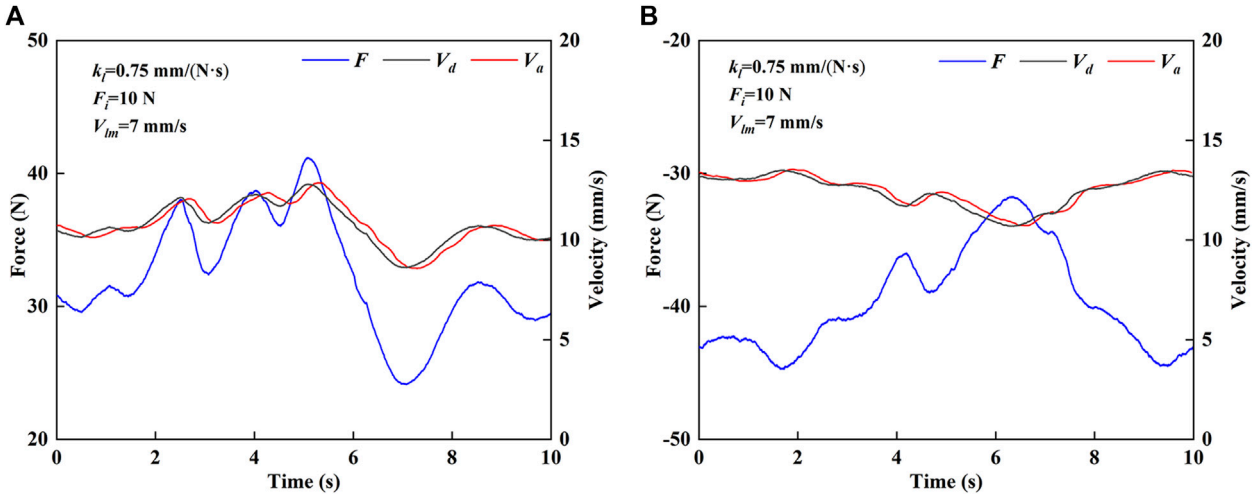

FIGURE 8
Force and velocity results of HE-LRR in CPM mode. **(A)** Forward motion. **(B)** Backward motion.

Figure 8 shows the experimental results of the force and velocity of the robot in CPM mode. In CPM mode, it is divided into forward motion and backward motion for research. As shown in Figure 8A, in the forward motion, the value of MCF is positive, and the desired velocity is non-negative. The desired velocity and the MCF show similar fluctuation trends. As shown in Figure 8B, in the backward motion, the MCF value is negative, and the desired velocity is non-negative. The desired velocity and the MCF show opposite fluctuation trends. It can be seen that the end effector's actual velocity has good following ability to the desired velocity in both forward and backward motions, which indicates that the robot motion is very sensitive to the change of the MCF, and can adapt to the active movement intention of the subject.

3.3 Active participation experiments

In order to study the FPVC strategy parameters' effects on the active participation of subjects, this section conducts experimental research on active participation. We recruited three healthy subjects to participate in the MOTOmed and CPM modes. All subjects agreed to include personal data in the study before the experiments. Each subject participated in 30 active training tasks under different control strategy parameters.

During active participation experiments, subjects were required to complete a certain number of tasks in 10 minutes. For the MOTOmed mode, eight cycles of training needed to be completed per minute; For the CPM mode, it was required to complete ten cycles of training per minute, and each subject could have a rest and physical recovery after completing each task. After completing the training task, the subject was asked to take a questionnaire on the subjective feeling and the participation score. When the subject's subjective feeling was boredom, relaxation, excitement, stress, or frustration, the corresponding participation score was 1, 2, 3, 4, or 5, respectively.

During the experiment, the MCF signal collected by the force sensor was filtered by the Kalman filter, and the objective feature values of root mean square (RMS), mean absolute value (MAV), variance (VAR), and zero crossing (ZC) were extracted from the processed MCF signal. RMS and MAV are statistics which can reflect the MCF signal's effective value and average strength. VAR can provide information regarding the signal's power. ZC represents the number of times the signal crosses the zero line, reflecting the number of times the MCF signal switches between tension force and compression force and can be used to calculate the number of training cycles. The additional threshold judgment is introduced to reduce the impact of signal noise on the ZC. The feature values can be calculated according to Eq. 21:

$$\begin{cases} \mathrm{MAV} = \dfrac{1}{N}\sum_{i=1}^{N}|x_i| \\ \mathrm{RMS} = \sqrt{\dfrac{\sum_{i=1}^{N}x_i^2}{N}} \\ \mathrm{VAR} = \dfrac{1}{N-1}\sum_{i=1}^{N}x_i^2 \\ \mathrm{ZC} = \sum_{i=1}^{N-1} f(i) \\ f(i) = \begin{cases} 1 & x_i x_{i+1} < 0, \text{and } |x_i - x_{i+1}| > \text{threshold} \\ 0 & \text{otherwise} \end{cases} \end{cases} \tag{21}$$

where x_i represents the ith value of the MCF signal, and N represents the number of the data values.

Figure 9 shows the MCF's feature values and the participation score of Subject No. 1 in the MOTOmed mode under different FPVC strategy parameters. When F_i and V_{lm} are constant: F_i = 10 N and V_{lm} = 7 mm/s (Figure 9A), ZC values are 160, indicating that the subject has completed 80 cycles of MOTOmed training. MAV, RMS and VAR increase with the

10.3389/fbioe.2023.1335071

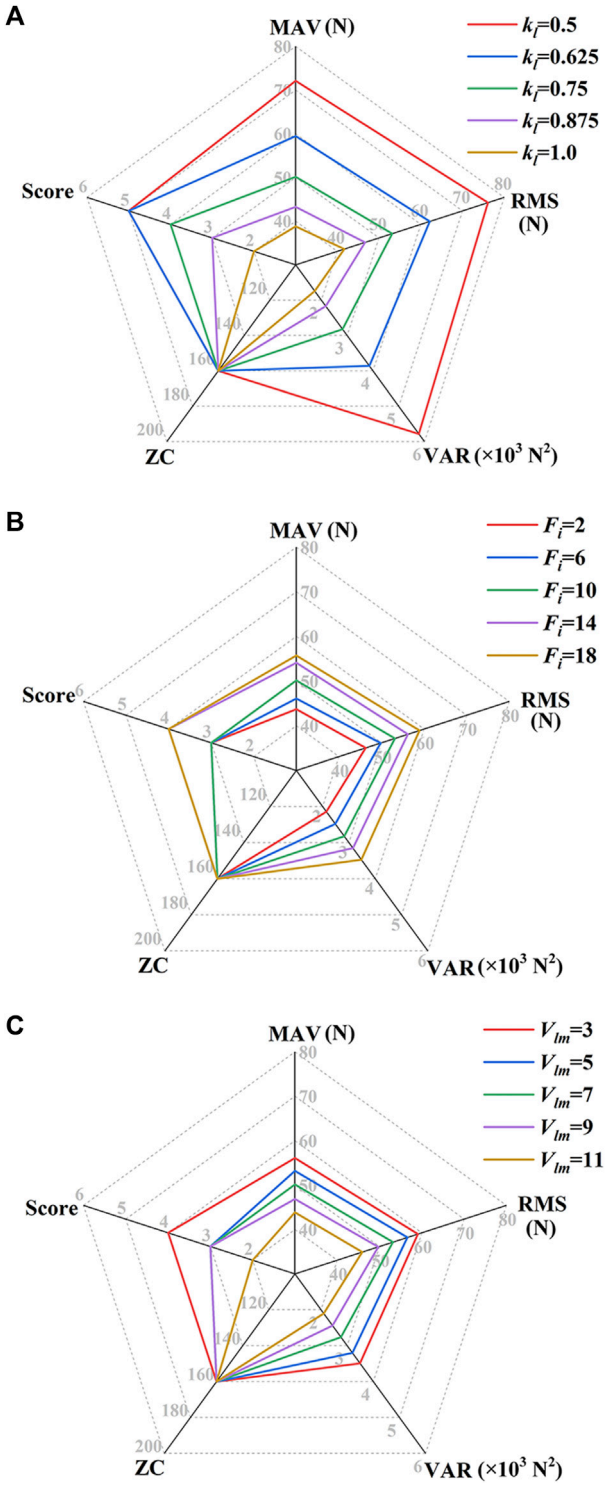

FIGURE 9
MCF's feature values and the participation score of Subject No. 1 in the MOTOmed mode under different FPVC strategy parameters. **(A)** F_i = 10 N, V_{lm} = 7 mm/s; **(B)** k_l = 0.75 mm/(N·s), V_{lm} = 7 mm/s; **(C)** k_l = 0.75 mm/(N·s), F_i = 10 N [F_i, unit: N; V_{lm}, unit: mm/s; k_l, unit: mm/(N·s)].

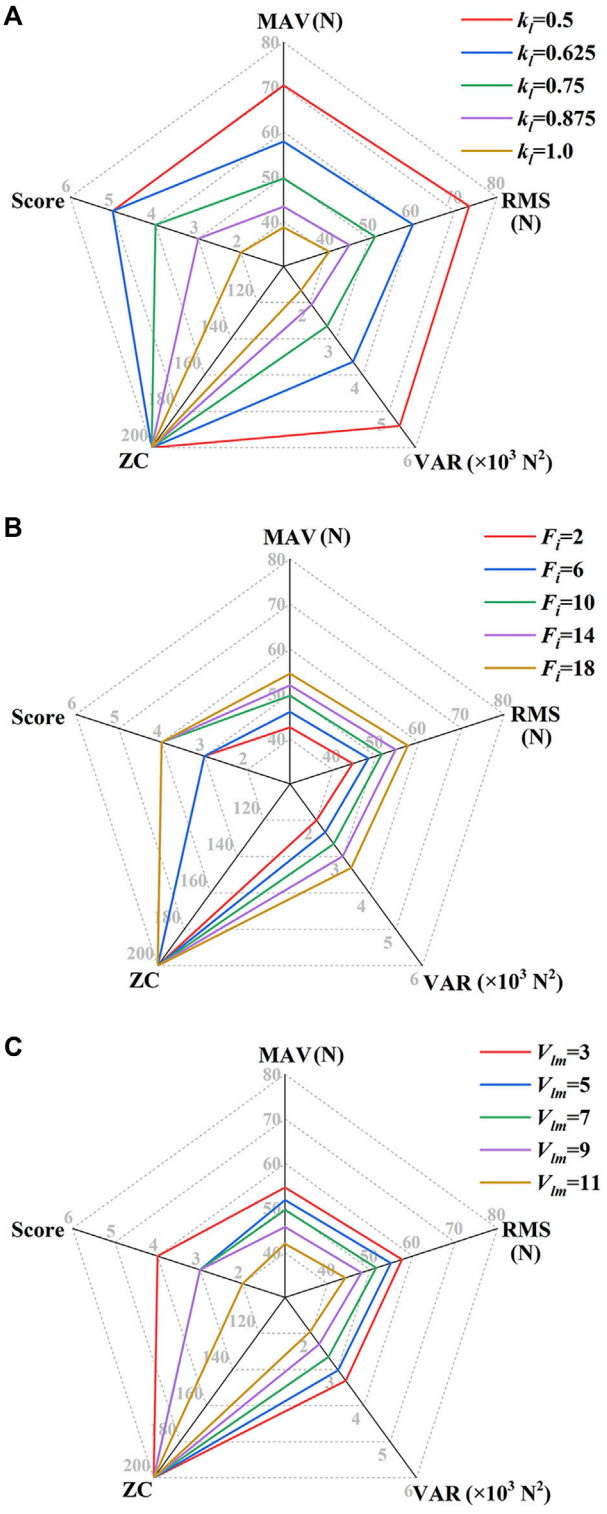

FIGURE 10
MCF's feature values and the participation score of Subject No. 1 in the CPM mode under different FPVC strategy parameters. **(A)** F_i = 10 N, V_{lm} = 7 mm/s; **(B)** k_l = 0.75 mm/(N·s), V_{lm} = 7 mm/s; **(C)** k_l = 0.75 mm/(N·s), F_i = 10 N [F_i, unit: N; V_{lm}, unit: mm/s; k_l, unit: mm/(N·s)].

decrease of k_l; When k_l = 0.5 mm/(N·s), MAV, RMS and VAR achieve maximum values, and the participation score is 5, indicating that the subjective feeling is frustration. When k_l and V_{lm} are constant: k_l = 0.75 mm/(N·s) and V_{lm} = 7 mm/s (Figure 9B), MAV, RMS, VAR increase with the increase of F_i, and ZC value remains unchanged. When F_i = 18 N, the objective

TABLE 3 PSO-BP algorithm parameter setting.

Parameter	Parameter value
Training number	1000
Learning rate	0.01
Minimum error	1×10^{-5}
Momentum factor	0.01
Minimum gradient	1×10^{-6}
Swarm size	30
Space dimension	82
Maximal number of iterations	100
Inertia weight	0.9
Acceleration coefficients (c_1, c_2)	(2, 2)

indicators achieve the maximum values, and the participation score is 4. When k_l and F_i are constant: k_l = 0.75 mm/(N·s) and F_i = 10 N (Figure 9C), MAV, RMS and VAR increase with the decrease of V_{lm}. When V_{lm} = 3 m/s, MAV, RMS and VAR achieve maximum values, and the participation score is 4. When V_{lm} = 11 m/s, MAV, RMS and VAR achieve minimum values, and the participation score is 2.

Figure 10 shows the MCF's feature values and the participation score of Subject No. 1 in the CPM mode under different FPVC strategy parameters. When F_i and V_{lm} are fixed: F_i = 10 N and V_{lm} = 7 mm/s (Figure 10A), the ZC value is 200, indicating that the subject has completed 100 cycles of CPM training. MAV, RMS and VAR have similar change laws as in the MOTOmed mode. When k_l and V_{lm} are constant: k_l = 0.75 mm/(N·s) and V_{lm} = 7 mm/s (Figure 10B), the ZC value is 200. When F_i = 18 N, MAV, RMS and VAR achieve maximum values, and the participation score is 4. When k_l and F_i are constant: k_l = 0.75 mm/(N·s) and F_i = 10 N (Figure 10C), the ZC value is also 200. When V_{lm} = 3 mm/s, the objective indicators achieve maximum values, and the participation score is 4.

Based on the above experimental results, the mapping relationship between the objective indicators (the feature values of the MCF signal) and the subjective indicators (participation scores given by the subjects) was studied to realize the prediction from the objective indicators to the subjective indicators. The particle swarm optimization-backpropagation (PSO-BP) algorithm was selected for the regression prediction of active participation. The algorithm parameter setting is shown in Table 3. Three subjects participated in the active training of the MOTOmed and CPM modes under different control strategy parameters. The feature values of MCF were taken as the training set's input parameters $\boldsymbol{X_s}$, and the questionnaire scores of subjects for different training tasks were taken as the output parameters $\boldsymbol{Y_s}$ of the training set.

Each subject participated in 10 groups of training under different control strategy parameters. After the experiments, they took the questionnaire survey. The feature values of MCF were taken as input parameters $\boldsymbol{X_I}$ of the testing set, and the active participation scores of the questionnaire were taken as the actual output parameters $\boldsymbol{Y_I}$ of the testing set. Using the trained prediction model of active participation, the predicted values $\boldsymbol{Y_p}$ were predicted from the input parameters $\boldsymbol{X_I}$. The comparison between the actual value and the predicted value of the testing sets for different subjects is shown in Figure 11.

The participation score of the subject in the testing set is an integer score of "1, 2, 3, 4, 5". Because the subjects have different evaluation criteria for participation, the dynamic trends of training data are also different. The experimental results show that the active participation scores predicted by the PSO-BO algorithm are close to the actual values. If the absolute error value between the actual value and the predicted value is less than 0.25, it is regarded as accurate; Otherwise, it is regarded as inaccurate. Then the prediction accuracy rate for Subject No. 1 is 60% (Figure 11A), that for Subject No. 2 is 80% (Figure 11B), and that for Subject No. 3 is 70% (Figure 11C). If the absolute error value between the actual value and the predicted value is less than 0.5, it is regarded as accurate; Otherwise, it is regarded as inaccurate. Then the prediction accuracy for three subjects can reach 100%. The above results show that subjects' active participation in training tasks can be predicted from the MCF's feature values, and the prediction accuracy can meet the prediction requirements from objective feature values to subjective indicators.

4 Conclusion and discussion

In this paper, a force/position-based velocity control strategy was proposed for HE-LRR to meet the demands of trajectory tracking effect and active participation of lower limb rehabilitation robots. The end effector's velocity planning was introduced in detail. Experimental studies were carried out on the control strategy with the following conclusions:

(1) The trajectory measurement experiments of HE-LRR were carried out under two training modes. The results showed that the end effector could approach the reference trajectory in a short time when the starting points of the end effector were different (inside the circular trajectory, outside the circular trajectory, above the linear trajectory, below the linear trajectory), which proved that the FPVC strategy is beneficial for subjects to achieve active rehabilitation training under accurate trajectories.
(2) The force and velocity measurement experiments of HE-LRR were carried out in two training modes. The results showed that the actual velocity of the end effector possessed good following performance compared with the desired velocity, which reflected that the robot could adapt to the changes of MCF, and proved the rationality of velocity planning in the FPVC strategy.
(3) Active participation experiments were conducted under different control strategy parameters, and the prediction of the active participation was performed using the PSO-BP algorithm. The results showed that the active participation of subjects could be adjusted by the control strategy parameters, and the active participation score could be predicted accurately from the MCF's feature values.

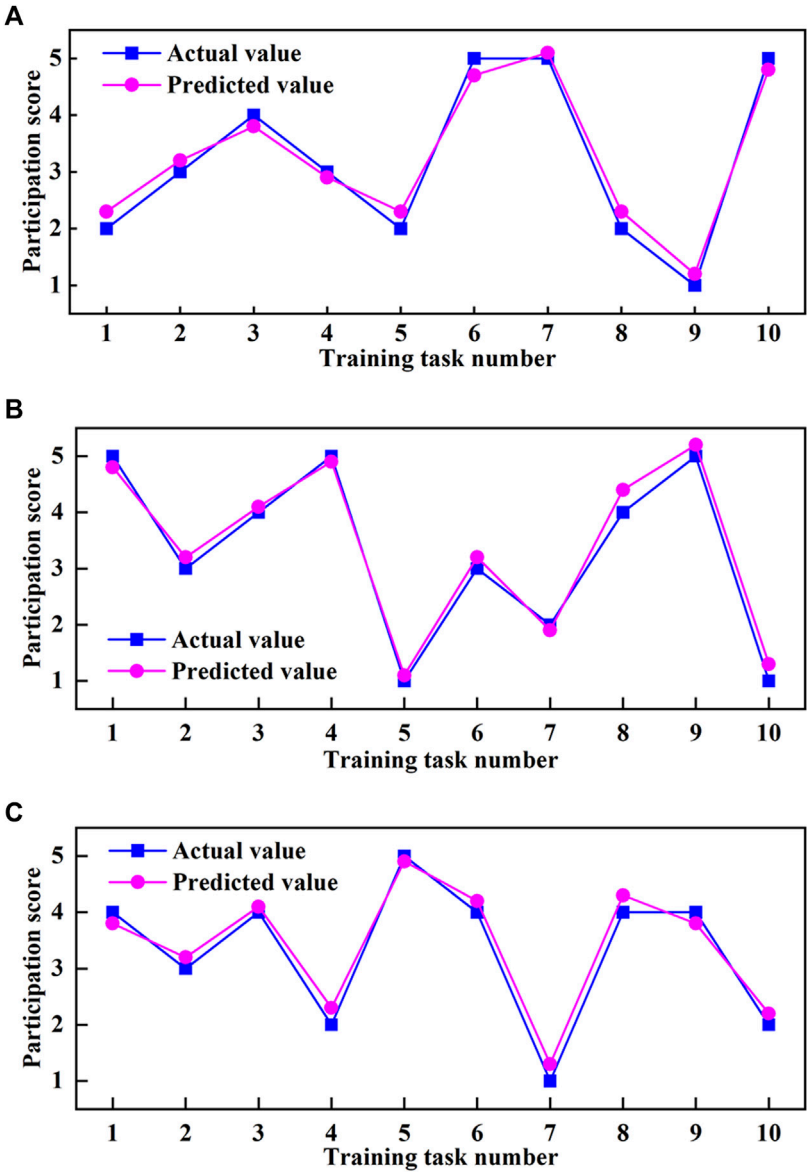

FIGURE 11
Comparison between the actual value and the predicted value of active participation score. **(A)** Subject No. 1. **(B)** Subject No. 2. **(C)** Subject No. 3.

Although the rationality and feasibility of the FPVC strategy have been experimentally verified on the HE-LRR system, there are still some things that could be improved in the research work. For example, the FPVC strategy was mainly validated on the end-effector lower limb rehabilitation robot under MOTOmed and CPM modes, which are training modes in the sagittal plane, and the experimental validation of the FPVC strategy was conducted by recruiting a series of healthy subjects. Our future research work will mainly focus on carrying out three-dimensional spatial trajectory verification and on the exoskeleton-type lower limb rehabilitation robot to improve the robot's functionality and practicality, and conducting clinical experiments to study patients' experience and active participation under the FPVC strategy.

Data availability statement

The raw data supporting the conclusion of this article will be made available by the authors, without undue reservation.

Ethics statement

The studies involving humans were approved by the China Rehabilitation Research Center. The studies were conducted in accordance with the local legislation and institutional requirements. The participants provided their written informed consent to participate in this study.

Author contributions

JT: Methodology, Software, Validation, Writing–original draft. HW: Funding acquisition, Project administration, Writing–review and editing. HL: Investigation, Methodology, Writing–review and editing. YY: Validation, Writing–review and editing. LL: Validation, Writing–review and editing. JN: Funding acquisition, Project administration, Writing–review and editing. BC: Funding acquisition, Project administration, Writing–review and editing.

Funding

The author(s) declare financial support was received for the research, authorship, and/or publication of this article. This research was supported by the Science and Technology (S&T) Program of Hebei under Grant 216Z1803G and the National Key Science and Technology Project Undertaken by Shenzhen under Grant CJGJZD20220517142405013.

Conflict of interest

The authors declare that the research was conducted in the absence of any commercial or financial relationships that could be construed as a potential conflict of interest.

Publisher's note

All claims expressed in this article are solely those of the authors and do not necessarily represent those of their affiliated organizations, or those of the publisher, the editors and the reviewers. Any product that may be evaluated in this article, or claim that may be made by its manufacturer, is not guaranteed or endorsed by the publisher.

References

Artz, E. J. (2015). Myoelectric control of a robotic exoskeleton for rehabilitation. *Master's Thesis*. Houston, Texas, USA: Rice University.

Bernhardt, M., Frey, M., Colombo, G., and Riener, R. (2005). "Hybrid force-position control yields cooperative behaviour of the rehabilitation robot Lokomat," in *9th international Conference on rehabilitation robotics (ICORR)* (Chicago, IL, USA: IEEE), 536–539. doi:10.1109/ICORR.2005.1501159

Cao, W., Ma, Y., Chen, C., Zhang, J., and Wu, X. (2022). Hardware circuits design and performance evaluation of a soft lower limb exoskeleton. *IEEE Trans. Biomed. Circuits Syst.* 16 (3), 384–394. doi:10.1109/TBCAS.2022.3173965

Cao, W., Shang, D., Yin, M., Li, X., Xu, T., Zhang, L., et al. (2023). Development and evaluation of a hip exoskeleton for lateral resistance walk exercise. *IEEE/ASME Trans. Mechatronics* 28 (4), 1966–1974. doi:10.1109/TMECH.2023.3273717

Chiyohara, S., Furukawa, J., Noda, T., Morimoto, J., and Imamizu, H. (2020). Passive training with upper extremity exoskeleton robot affects proprioceptive acuity and performance of motor learning. *Sci. Rep.* 10 (1), 11820. doi:10.1038/s41598-020-68711-x

Dulyan, L., Talozzi, L., Pacella, V., Corbetta, M., Forkel, S. J., and Thiebaut de Schotten, M. (2022). Longitudinal prediction of motor dysfunction after stroke: a disconnectome study. *Brain Struct. Funct.* 227 (9), 3085–3098. doi:10.1007/s00429-022-02589-5

Feigin, V. L., Lawes, C. M., Bennett, D. A., Barker-Collo, S. L., and Parag, V. (2009). Worldwide stroke incidence and early case fatality reported in 56 population-based studies: a systematic review. *Lancet Neurology* 8 (4), 355–369. doi:10.1016/S1474-4422(09)70025-0

Huo, W., Moon, H., Alouane, M. A., Bonnet, V., Huang, J., Amirat, Y., et al. (2022). Impedance modulation control of a lower-limb exoskeleton to assist sit-to-stand movements. *IEEE Trans. Robotics* 38 (2), 1230–1249. doi:10.1109/TRO.2021.3104244

Ju, M.-S., Lin, C.-C. K., Lin, D.-H., Hwang, I.-S., and Chen, S.-M. (2005). A rehabilitation robot with force-position hybrid fuzzy controller: hybrid fuzzy control of rehabilitation robot. *IEEE Trans. Neural Syst. Rehabilitation Eng.* 13 (3), 349–358. doi:10.1109/TNSRE.2005.847354

Kawamoto, H., Taal, S., Niniss, H., Hayashi, T., Kamibayashi, K., Eguchi, K., et al. (2010). "Voluntary motion support control of Robot Suit HAL triggered by bioelectrical signal for hemiplegia," in *2010 annual international conference of the IEEE engineering in medicine and biology* (Buenos Aires, Argentina: IEEE), 462–466. doi:10.1109/IEMBS.2010.5626191

Khoshdel, V., Akbarzadeh, A., Naghavi, N., Sharifnezhad, A., and Souzanchi-Kashani, M. (2018). sEMG-based impedance control for lower-limb rehabilitation robot. *Intell. Serv. Robot.* 11 (1), 97–108. doi:10.1007/s11370-017-0239-4

Krebs, H. I., Volpe, B. T., Williams, D., Celestino, J., Charles, S. K., Lynch, D., et al. (2007). Robot-aided neurorehabilitation: a robot for wrist rehabilitation. *IEEE Trans. Neural Syst. Rehabilitation Eng.* 15 (3), 327–335. doi:10.1109/TNSRE.2007.903899

Langhorne, P., Bernhardt, J., and Kwakkel, G. (2011). Stroke rehabilitation. *Lancet* 377 (9778), 1693–1702. doi:10.1016/S0140-6736(11)60325-5

Lotti, N., Xiloyannis, M., Missiroli, F., Bokranz, C., Chiaradia, D., Frisoli, A., et al. (2022). Myoelectric or force control? A comparative study on a soft arm exosuit. *IEEE Trans. Robotics* 38 (3), 1363–1379. doi:10.1109/TRO.2021.3137748

Lu, L., Wu, Q., Chen, X., Shao, Z., Chen, B., and Wu, H. (2019). Development of a sEMG-based torque estimation control strategy for a soft elbow exoskeleton. *Robotics Aut. Syst.* 111, 88–98. doi:10.1016/j.robot.2018.10.017

Lv, X., Han, J., Yang, C., and Cong, D. (2017). "Model reference adaptive impedance control in lower limbs rehabilitation robot," in 2017 IEEE international Conference on Information and automation (ICIA). *2017 Macao, China* (IEEE), 254–259. doi:10.1109/ICInfA.2017.8078915

Ma, X., Long, X., Yan, Z., Wang, C., Guo, Z., and Wu, X. (2019). "Real-time active control of a lower limb exoskeleton based on sEMG," in *2019 IEEE/ASME international conference on advanced intelligent mechatronics (AIM)* (IEEE), 589–594. doi:10.1109/AIM.2019.8868817

Meng, W., Liu, Q., Zhou, Z., Ai, Q., Sheng, B., Xie, S., et al. (2015). Recent development of mechanisms and control strategies for robot-assisted lower limb rehabilitation. *Mechatronics* 31, 132–145. doi:10.1016/j.mechatronics.2015.04.005

Meng, W., Zhu, Y., Zhou, Z., Chen, K., and Ai, Q. (2014). "Active interaction control of a rehabilitation robot based on motion recognition and adaptive impedance control," in *2014 IEEE international Conference on fuzzy systems (FUZZ-IEEE)* (Beijing, China: IEEE), 1436–1441. doi:10.1109/FUZZ-IEEE.2014.6891705

Mokhtari, M., Taghizadeh, M., and Mazare, M. (2021). Impedance control based on optimal adaptive high order super twisting sliding mode for a 7-DOF lower limb exoskeleton. *Meccanica* 56, 535–548. doi:10.1007/s11012-021-01308-4

Navvabi, H., and Markazi, A. H. D. (2019). Hybrid position/force control of Stewart manipulator using extended adaptive fuzzy sliding mode controller (E-AFSMC). *ISA Trans.* 88, 280–295. doi:10.1016/j.isatra.2018.11.037

Rivas-Blanco, I., Bauzano, E., Cuevas-Rodriguez, M., del Saz-Orozco, P., and Munoz, V. F. (2013). "Force-position control for a miniature camera robotic system for single-site surgery," in *2013 IEEE/RSJ international Conference on intelligent Robots and systems* (Tokyo, Japan: IEEE), 3065–3070. doi:10.1109/IROS.2013.6696790

Shi, D., Zhang, W., Zhang, W., and Ding, X. (2019). A review on lower limb rehabilitation exoskeleton robots. *Chin. J. Mech. Eng.* 32 (1), 74. doi:10.1186/s10033-019-0389-8

Shi, Y., Wang, S., Li, J., Gao, X., Lv, J., Lv, P., et al. (2020). "Prediction of continuous motion for lower limb joints based on sEMG signal," in *2020 IEEE international Conference on Mechatronics and automation (ICMA)* (Beijing, China: IEEE), 383–388. doi:10.1109/ICMA49215.2020.9233813

Singh, R.-J., Chen, S., Ganesh, A., and Hill, M. D. (2018). Long-term neurological, vascular, and mortality outcomes after stroke. *Int. J. Stroke* 13 (8), 787–796. doi:10.1177/1747493018798526

Sun, P., Shan, R., and Wang, S. (2023). An intelligent rehabilitation robot with passive and active direct switching training: improving intelligence and security of human–robot interaction systems. *IEEE Robotics Automation Mag.* 30 (1), 72–83. doi:10.1109/MRA.2022.3228490

Taffese, T. B. (2017). *A review of using EEG and EMG psychophysiological measurements in user experience research*. Oulu, Finland: University of Oulu. Master's Thesis.

Tran, H. T., Cheng, H., Rui, H., Lin, X., Duong, M. K., and Chen, Q. (2016). Evaluation of a fuzzy-based impedance control strategy on a powered lower exoskeleton. *Int. J. Soc. Robotics* 8, 103–123. doi:10.1007/s12369-015-0324-9

Tsoi, Y. H., Xie, S. Q., and Mallinson, G. D. (2009). "Joint force control of parallel robot for ankle rehabilitation," in *2009 IEEE international Conference on Control and automation* (Christchurch, New Zealand: IEEE), 1856–1861. doi:10.1109/ICCA.2009.5410377

Valera, A., Díaz-Rodríguez, M., Valles, M., Oliver, E., Mata, V., and Page, A. (2017). Controller–observer design and dynamic parameter identification for model-based control of an electromechanical lower-limb rehabilitation system. *Int. J. Control* 90 (4), 702–714. doi:10.1080/00207179.2016.1215529

Wang, L., Tian, J., Du, J., Zheng, S., Niu, J., Zhang, Z., et al. (2022). A hybrid mechanism-based robot for end-traction lower limb rehabilitation: design, analysis and experimental evaluation. *Machines* 10 (2), 99. doi:10.3390/machines10020099

Wu, X., Cao, W., Yu, H., Zhang, Z., Leng, Y., and Zhang, M. (2022). Generating electricity during locomotion modes dominated by negative work via a knee energy-harvesting exoskeleton. *IEEE/ASME Trans. Mechatronics* 27 (6), 4451–4461. doi:10.1109/TMECH.2022.3157848

Xie, P., Qiu, S., Li, X., Du, Y., Wu, X., and Guo, Z. (2016). "Adaptive trajectory planning of lower limb rehabilitation robot based on EMG and human-robot interaction," in *2016 IEEE international Conference on Information and automation (ICIA)* (Ningbo, China: IEEE), 1273–1277. doi:10.1109/ICInfA.2016.7832015

Zhang, X., Yue, Z., and Wang, J. (2017). Robotics in lower-limb rehabilitation after stroke. *Behav. Neurol.* 2017, 1–13. doi:10.1155/2017/3731802

Zhang, Y., Cai, J., Zhang, Y., Ren, T., Zhao, M., and Zhao, Q. (2016). Improvement in stroke-induced motor dysfunction by music-supported therapy: a systematic review and meta-analysis. *Sci. Rep.* 6, 38521. doi:10.1038/srep38521

Zheng, J., Shi, P., Fan, M., Liang, S., Li, S., and Yu, H. (2021). Effects of passive and active training modes of upper-limb rehabilitation robot on cortical activation: a functional near-infrared spectroscopy study. *NeuroReport* 32 (6), 479–488. doi:10.1097/WNR.0000000000001615

Zhou, J., Li, Z., Li, X., Wang, X., and Song, R. (2021a). Human–robot cooperation control based on trajectory deformation algorithm for a lower limb rehabilitation robot. *IEEE/ASME Trans. Mechatronics* 26 (6), 3128–3138. doi:10.1109/TMECH.2021.3053562

Zhou, Y., She, J., Liu, Z.-T., Xu, C., and Yang, Z. (2021b). "Implementation of impedance control for lower-limb rehabilitation robots," in *2021 4th IEEE international Conference on industrial cyber-physical systems (ICPS)* (Victoria, BC, Canada: IEEE), 700–704. doi:10.1109/ICPS49255.2021.9468210

frontiers | Frontiers in Bioengineering and Biotechnology

TYPE Review
PUBLISHED 08 January 2024
DOI 10.3389/fbioe.2023.1334771

OPEN ACCESS

EDITED BY
Wujing Cao,
Chinese Academy of Sciences (CAS), China

REVIEWED BY
Xiangxin Li,
Chinese Academy of Sciences (CAS), China
Dan Chen,
Shenzhen Polytechnic University, China

*CORRESPONDENCE
Hongliu Yu,
yhl98@hotmail.com

RECEIVED 07 November 2023
ACCEPTED 13 December 2023
PUBLISHED 08 January 2024

CITATION
Li W, Shi P, Li S and Yu H (2024), Current status and clinical perspectives of extended reality for myoelectric prostheses: review.
Front. Bioeng. Biotechnol. 11:1334771.
doi: 10.3389/fbioe.2023.1334771

Current status and clinical perspectives of extended reality for myoelectric prostheses: review

Wei Li[1,2,3], Ping Shi[1,2,3], Sujiao Li[1,2,3] and Hongliu Yu[1,2,3]*

[1]Institute of Rehabilitation Engineering and Technology, University of Shanghai for Science and Technology, Shanghai, China, [2]Shanghai Engineering Research Center of Assistive Devices, Shanghai, China, [3]Key Laboratory of Neural-Functional Information and Rehabilitation Engineering of the Ministry of Civil Affairs, Shanghai, China

Training with "Extended Reality" or X-Reality (XR) systems can undoubtedly enhance the control of the myoelectric prostheses. However, there is no consensus on which factors improve the efficiency of skill transfer from virtual training to actual prosthesis abilities. This review examines the current status and clinical applications of XR in the field of myoelectric prosthesis training and analyses possible influences on skill migration. We have conducted a thorough search on databases in the field of prostheses using keywords such as extended reality, virtual reality and serious gaming. Our scoping review encompassed relevant applications, control methods, performance evaluation and assessment metrics. Our findings indicate that the implementation of XR technology for myoelectric rehabilitative training on prostheses provides considerable benefits. Additionally, there are numerous standardised methods available for evaluating training effectiveness. Recently, there has been a surge in the number of XR-based training tools for myoelectric prostheses, with an emphasis on user engagement and virtual training evaluation. Insufficient attention has been paid to significant limitations in the behaviour, functionality, and usage patterns of XR and myoelectric prostheses, potentially obstructing the transfer of skills and prospects for clinical application. Improvements are recommended in four critical areas: activities of daily living, training strategies, feedback, and the alignment of the virtual environment with the physical devices.

KEYWORDS

myoelectric prostheses, extended reality prosthetic systems, virtual reality, augmented reality, mixed reality, serious games

1 Introduction

The loss of the upper extremity is one of the most significant and destructive injuries after central nervous system damage, including spinal cord injury, stroke, and traumatic brain injury, which would cause a drastic sensory-motor deficiency, serious physical disorders, and limited daily life. Myoelectric prostheses are valuable tools for meeting the demand for functional recovery improvement of amputees, and the establishment of advanced rehabilitation techniques for upper extremity loss holds great promise for improving the quality of life of patients (Pasquina et al., 2015). However, using myoelectric prostheses in daily activities necessitates the user's ability to produce precise and synchronized electromyography (EMG) signals, which requires extensive training and

prolonged practice to achieve even minimum levels of dexterity (Resnik et al., 2012; Johnson and Mansfield, 2014). Although these prostheses have begun to implement sophisticated artificial intelligence algorithms and control schemes, the lack of appropriate training and limited integration into the activities of daily living (ADL) has contributed to high rejection rates (19%–61%) (Biddiss and Chau, 2007a; Biddiss and Chau, 2007c; Østlie et al., 2012; Salminger et al., 2022). Consequently, the efficiency of myoelectric prostheses remains a challenging problem (Biddiss and Chau, 2007b). The average waiting period from amputation to the initial prosthesis fitting is around 6 months, with no associated training provided during this time (Pezzin et al., 2004; Østlie et al., 2012; Salminger et al., 2022). Research has shown that fitting the prosthesis earlier improves compliance (Roeschlein and Domholdt, 1989). Delaying fitting would only exacerbate the user's feelings of discomfort and hassle, highlighting the necessity for advanced pre-prosthetic training tools (McFarland et al., 2010).

Neural plasticity plays a crucial role in the utilization of myoelectric prostheses, facilitating a novel mode of coordination, which reduces phantom limb pain caused by amputation, whilst supporting long-term skill retention and transfer (Rogers et al., 2016; Preißler et al., 2017; Snow et al., 2017; Akbulut et al., 2019; Kulkarni et al., 2020). Nonetheless, it necessitates intensive muscle training to achieve control. Conventional physical therapy (CPT) is a highly repetitive exercise rehabilitation training under the supervision of doctors or therapists, which stimulates the motor nerve paths through mobilization, stretching and strengthening to enhances the control ability of the muscles of the stump (O'Keeffe, 2011; Cerritelli et al., 2021; Cao et al., 2023). This training method lacks accurate quantitative evaluation criteria for amputees. And the whole process is very arduous and monotonous. Many participants become fatigued and lose motivation, and some even completely abandon myoelectric prostheses (Resnik et al., 2012). Consequently, traditional rehabilitation training methods are difficult to help amputees to complete the target task (Stucki, 2021). There is an urgent need for a personalized, high-quality and attractive prosthetic rehabilitation training program to constantly improve equipment control, both prior to use and during the operation of the prostheses. Better training results will stem from more comprehensive, more clinical, more rewarding and entertaining myoelectric training for amputees, making rehabilitation feel less like rehabilitation. Previous studies indicate that "Extended Reality" or X-Reality (XR) systems, utilizing gamification and edutainment, can provide superior outcomes in comparison to CPT exercises. XR is a virtual environment capable of generating precise control over numerous physical factors and has been widely used in education, brain-computer interfaces and human-computer collaboration and other fields. For the training of myoelectric prostheses, XR systems have become popular tools for physical rehabilitation and motor learning, as XR helps to increase amputees' willingness and motivation to participate in training, while also allowing for improved assessment and evaluation of progress (Radianti et al., 2020). It is a valuable resource for those seeking prostheses training, and its impact on the field is significant.

In this paper, the term XR in prostheses training refers to a very broad concept, which encompasses all reproduced real environments and generated virtual digital environments by computer technology and wearable devices, along with novel methods of human-computer interaction, which includes virtual reality (VR), augmented reality (AR), and mixed reality system (MR) (Figure 1). The major feature of this technology is immersion, which refers to any solution capable of delivering more immersive and captivating training experiences to patients. Apart from visual stimulus conveyed by images or videos, it may also entail other sensory stimuli, such as touch and sound. Among these technologies, VR system utilizes computer simulation to create a three-dimensional space and create a sense illusion for users, increasing the user's sense of presence, allowing for greater interactivity within the virtual world. However, the VR system necessitates users to wear a head-mounted display with a binocular omni-orientation monitor to completely occlude the natural physical space of the surroundings, which may induce a series of problems, such as dizziness, motion sickness and other health issues. The AR system uses computer simulation to create virtual information based on physical data that is challenging to experience in real-world conditions. This virtual information is then superimposed onto the real space to generate a new picture or space that enhances the user's visual experience and provides a sense of interaction that extends beyond reality (Hugues et al., 2011). The MR can mix virtual object information in the real space, and realize the interaction between users and virtual objects. It establishes an interactive feedback information loop between the real world, virtual space and users, enhancing realism and creating a richer experience (Flavián et al., 2019). The distinction between AR and MR is opaquer; both mix real and virtual elements and augment reality with virtual elements. The only essential difference between VR and AR (MR) is that while the former confronts the user solely in the digitally created world, the latter mixes digital with the real world (where the real world can be given either directly through transparent lenses (e.g., Microsoft HoloLens) or indirectly, through displays that stream the camera feed (e.g., Apple XR)). The XR prosthesis system refers to a virtual version of a prosthesis, built in XR environment, which does not necessarily have a control object as the prosthesis, but rather is programmed and calibrated in a manner similar to a physical prosthesis and uses simulated objects to map control commands of the EMG, allowing amputees to practice the control scheme in a well-practiced environment. XR-based rehabilitation has been proved to have some positive effects on behavior and physiology, and is very popular with elderly, Stroke, and Parkinson's disease patients (Murray et al., 2007; Saposnik and Levin, 2011; Cao et al., 2022; Wu et al., 2022). This technology has gradually become a popular tool for clinical prostheses training, rehabilitation, and motor learning.

Compared to CPT, the XR prosthesis training have precise control over various physical factors in the environment and positively impacts the user's physiological, psychological, and rehabilitation outcomes, thereby increasing patient motivation during therapy. Systematic data analysis can effectively record the training process and effect, provide more accurate performance evaluation methods and reduce human interpretation errors. This training approach will decrease expenses and enhance the patient's innate drive, thus augmenting their commitment towards neuromuscular rehabilitation training. (Garske et al., 2021). shows that there are a large number of prosthetic training software based on serious games, which focus more on improving engagement and muscle training, without paying

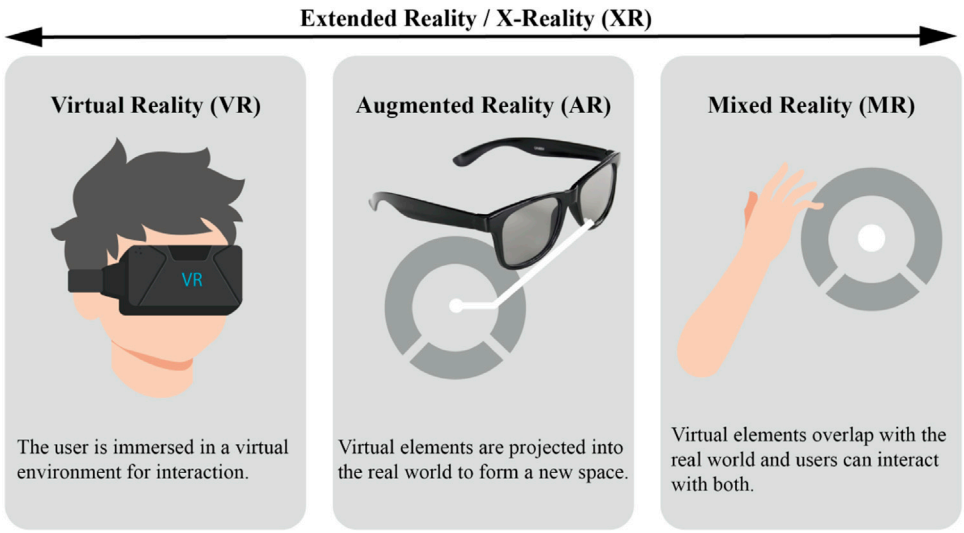

FIGURE 1
Illustrations showing the relationships and definitions between the most common realities (extended reality, virtual reality, augmented reality and mixed reality).

attention to the importance of skill transfer. (Gaballa et al., 2022). introduces the existing virtual prosthetic training technology and the user evaluation procedure to ensure the practicability in the clinical environment, and identify obstacles in technology, human factors, clinical and management levels, economy, and suggest possible pathways to deployment for successful clinical adoption in the future. (Toledo-Peral et al., 2022). analyzed the application of VR/AR in motor neurorehabilitation after stroke/amputation, including the scope of application, characteristics, target anatomical region, how to use, signal processing methods and hardware. Prosthesis training using XR techniques for upper limb amputees has the potential to enhance competency or speed up the learning process for acquiring the skill; however, there is no consensus on which factors are crucial in the transfer of skills from virtual training to actual prosthetic competence. In light of the above, the current review focus on four critical areas:

- Components and available cases of the XR prosthetic system,
- Training methods and evaluation metrics of the XR Prosthetic System compared to other rehabilitation protocols,
- What are the technical limitations and barriers in the process of skills transfer?
- Possible deployment pathways for future successful clinical applications.

We surveyed papers dealing with upper limb prosthesis training or assessment with the assistance of the XR environment and using EMG signals as input. Relevant papers were identified during the literature survey and enhanced by systematic searches using PubMed, Web of Science, Science Direct, IEEE Xplore, Google Scholar and SCOPUS databases. Based on a summary of existing XR prosthetic systems, with associated control methods, assessment methods and evaluation metrics, and comparing the application of prosthetic hands, this review analyses the characteristics and shortcomings of the existing systems in the process of skill transfer from virtual training to actual prosthetic ability in four aspects: ADL, training methods, feedback, the relationship between the virtual environment and the physical device.

2 The existing XR systems for upper extremity prostheses

The two most important aspects of XR for myoelectric prosthetic hand are the user interface and myoelectric control.

2.1 User interface

The XR prosthesis system offers an interactive environment that enables users to repeat various actions. Most of the time, this type of interface works to immerse users in a virtual environment and perform virtual actions using electromyography control, which gives users the sensation of experiencing a similar movement in reality (Woodward et al., 2017). According to the immersion level applied to XR, it can be categorized as nonimmersive XR and immersive XR (Sveistrup, 2004). Nonimmersive XR involves interactions between an environment and players via a computer monitor or non-HMD display, maintaining a safe distance between participants and the game (Bevilacqua et al., 2019). Immersive refers to the utilization of various head-mounted displays (such as Occulus Rift Headset, HTC VIVE Pro, Google Glass, Meta Glass, and Microsoft Hololens), which are connected to the human body to interact with the game (Narayanasamy et al., 2006; Lu et al., 2012) clarify that the user interface of XR systems can be categorized into two types: serious games and simulation tasks. Serious games replace prostheses with gamification elements in fictional scenarios, maps EMG control commands with specific game goals, which is able to provide a variety of challenges, increase the enjoyment of training, and optimize the learning process. Conversely, simulation tasks

TABLE 1 Detailed categorization of the serious game.

Program (Genre)	Task	Feedback mechanism	Control strategy	Performance metrics	Skill transfer
Myoboy	Abstact task	Traditional Media	DC		No
Air-Guitar Hero (rhythm game)	Abstact task	Traditional Media	ML	score	No
WiiEMG (sports game)	Abstact task	Traditional Media	ML	Time, accuracy	No
Sonic Racing (racing game)	Abstact task	Traditional Media	DC	Time	No
MyoBox (dexterity game)	Abstact task	Traditional Media	ML	Separability, consistency, variability	Yes
MyoBeatz (rhythm game)	Abstact task	Traditional Media	DC	SUS, proportional muscle activation	No
Falling of Momo (vertical scroller)	Abstact task	Traditional Media	DC	UES, IMI, SUS	No
Volcanic Crush (reaction game)	Abstact task	Traditional Media	DC	UES, IMI, SUS	No
Dino Sprint (endless runner)	Abstact task	Traditional Media	DC	UES, IMI, SUS	No
ino Feast (dexterity game)	Abstact task	Traditional Media	DC	UES, IMI, SUS	No
Breakout-EMG (arcade game)	Abstact task	Traditional Media	DC	Accuracy	Yes
Crossbow Game	Posture reproduction	VR	ML	Postures completed score	No
UpBeat (rhythm game)	Posture reproduction	AR	ML	Gesture completion, muscle activation	No
MyoTrain	Posture reproduction	Traditional Media	ML	Accuracy	No

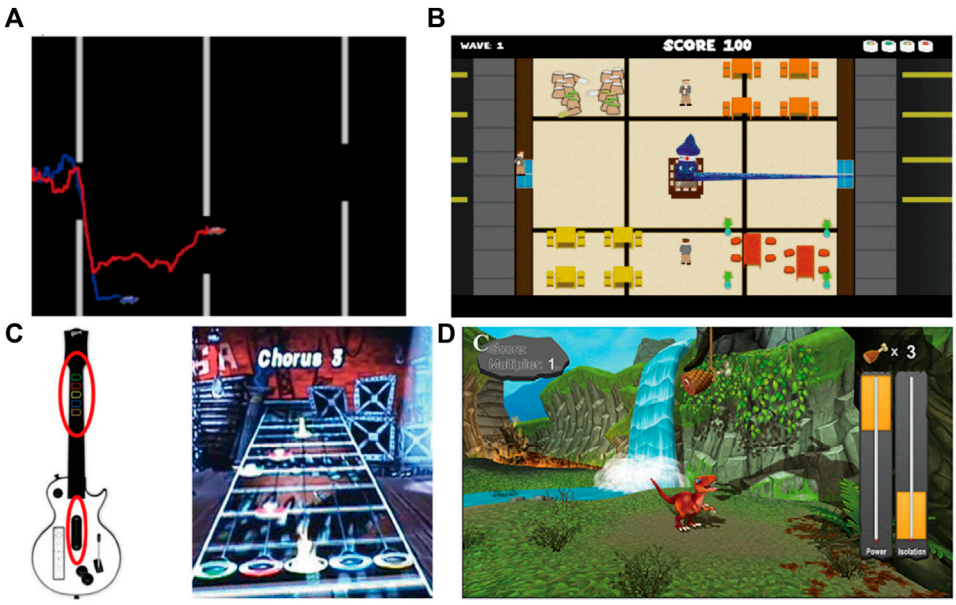

FIGURE 2
Serious game: **(A)** MyoBoy; **(B)** Sushi Slap; **(C)** Air Guitar Hero; and **(D)** Dino-Feast.

generally involve recreating a prosthetic-like control object and duplicate the controls in real-world scenarios, requiring standard operating procedures and lacking in entertainment.

Since the early 1990s, serious games have been researched for prostheses control training (Lovely et al., 1990), which is a video game with an explicit and carefully thought-out educational purpose and intended to impart certain knowledge or skills to users (Graafland et al., 2012; Laamarti et al., 2014). As a virtual training system, serious games can increase patients' motivation, improve muscle coordination, and ultimately augment

electromyography control ability (see Table 1) (Clingman and Pidcoe, 2014). MyoBoy (Figure 2A) and PAULA or Virtu Limb™ are mature computer-based electromyography training systems. These systems use the subject's flexor and extensor muscles to improve electromyography control. Patient feedback has indicated that the current commercial method, which depends on basic graphic representations of EMG, is less motivating and satisfying than the training system that is reliant on serious games (Prahm et al., 2017a). Several serious games based on traditional game design, such as Pong (de la Rosa et al., 2008), Flappy Bird (Radhakrishnan et al., 2019), Space Invaders (Radhakrishnan et al., 2019), SuperTuxKart (Prahm et al., 2017b), Sushi Slap (Smith et al., 2018b; Smith et al., 2018a) (Figure 2B), Crazy Meteor (Smith et al., 2018b; Smith et al., 2018a), Dog Jump/Beeline Border Collie (Smith et al., 2018b; Smith et al., 2018a), Crate Whacke (Hashim et al., 2021a), Race the Sun (Hashim et al., 2021a), Fruit Ninja (Hashim et al., 2021a), and Kaiju Carnag (Hashim et al., 2021a), employ a method similar to the user's control of a physical prosthetic hand, which not only repeatedly activates the flexor and extensor muscles, but also instigates the random training of joint or continuous muscle contraction. This approach provides an ideal training method for direct control (DC), while also enhancing the motivation and adherence of the amputation rehabilitation plan. Rhythm games and car racing games, such as Air Guitar Hero (Armiger and Vogelstein, 2008) (Figure 2C), MyoBeatz (Prahm et al., 2019a,8), UpBeat(Melero et al., 2019), and Sonic Racing (Martinez-Luna et al., 2020), incorporate sound feedback into traditional gameplay, which are valuable for early-stage rehabilitation and provide solid starting points for the inclusion of feedback (Prahm et al., 2018). Mobile phone games, such as such as Volcanic Crush incorporate based dual-site muscle activation, Dino Spirit and Dino Feast (Figure 2D) involving sequential and proportional movement control, and Dino Claw with 3-D movement control, create more opportunities for myoelectric training outside the clinical environment, which overcome logistical, financial and geographical barriers to users, and increase training motivation (Winslow et al., 2018). For improving the training performance, serious games have the following characteristics: 1) The subjects focus on the screen and can find the best training scheme to the challenge through implicit learning without clear prompts (Kristoffersen et al., 2021); 2) Tasks of varying difficulty levels can be provided to enhance the interest and motivation of the subjects as well as extend their training time (Rahmani and Boren, 2012); 3) Remote personalized guidance can be provided by therapists or doctors (Holden, 2005); 4) Real-time feedback can be incorporated to optimize the training effect (van Diest et al., 2013). Serious games offer a simplified myoelectric control interface displayed on a computer screen. While unable to display quantitative results, it provides direct control of a limited set of muscles with intuitive functionality. Its usefulness is limited to early-stage rehabilitation and does not induce changes in muscle performance.

Simulation tasks are typically presented in either the third-person perspective or the first-person perspective. The former aids the user's spatial perception, while the latter can enhance the user's sense of interaction with the virtual object. Both perspectives offer distinct benefits, and align with the desired functionality of myoelectric rehabilitation systems. Generally, simulation tasks involve posture reproduction tasks, which necessitate following typical operating procedures and assessment indicators but lack entertainment value (see Table 2). XR systems based on simple simulation tasks, such as UVa-NTS platform (de la Rosa et al., 2009), Virtual training environment (Cavalcante et al., 2021), VRd testing environment (Blana et al., 2016) (Figure 3A), Training environment (Al-Jumaily and Olivares, 2009), and Virtual model (Muri et al., 2013), provide a solid research foundation for making virtual prosthetic systems and training amputees. Simulation tasks combined with standard training schemes, such as Virtual box and beans test (Prahm et al., 2019b), Virtual box and blocks test (Hashim et al., 2021b), Virtual rehabilitation training tool (Dhawan et al., 2019,8), Virtual Therapy Arm (VITA) (Nissler et al., 2019), AR prostheses simulator (Kenedy Lopes, 2012), Virtual training system (Nakamura et al., 2017), Performance assessment (Hargrove et al., 2007), Prostheses simulator (Lambrecht et al., 2011) (Figure 3B), and Virtual reality environment System (Resnik et al., 2011), have shown promise as a tool for developing and evaluating control methods by enhancing and refining particular skills. XR systems based on complex environment, such as Exploration (Phelan et al., 2015) (Figure 3C), Virtual simulation (Soares et al., 2003), and HoloPHAM (Sharma et al., 2019), have created virtual environments that are more suitable for daily life, which can satisfy users' sense of immersiveness. These systems are being studied how to best assess the impact and accuracy of such environment. Open source systems, such as VIE (Perry et al., 2018) (Figure 3D) and Musculoskeletal Modelling Software (MSMS) (Davoodi and Loeb, 2012), prove that amputees can effectively learn the EMG contraction mode, provide effective training platforms based on machine learning (ML) control, and make it possible for different research groups to develop effective and unified training methods. Systems based on virtual prosthetics, including Catching simulator (van Dijk et al., 2016b), Catching simulator Prostheses Gripper (Kristoffersen et al., 2021) (Figure 3E), and MSMS, have demonstrated the transfer effect and existing deficiencies from virtual prosthetics to physical prosthetics. Imitation-oriented XR exercises can produce lower practice variability, and assist with movement learning by promoting consistent movements through accurate repetition. ADL-oriented XR could elicite stronger muscle activity and movement variations. The combined design appears to yield superior training outcomes. Several XR prosthetic systems, such as ARlimb (Boschmann et al., 2016; Boschmann et al., 2021), AR prostheses simulator, and Mixed reality training (Sharma et al., 2018) (Figure 3F), illustrate the differences between AR/MR and VR. However, the systems are not compared to one another.

2.2 Myoelectric control

Currently, the mainstream myoelectric control methods ARE DC and ML. The DC primarily employs EMG signals from two muscle groups to control all possible grasping modes, including on/off control, sequence control, and mode switching control. This control requires users to actively switch among multiple degrees of freedom (DoFs). Due to its ease and implementation, DC is the most cfrequently utilized control approach in commercial prostheses and XR systems. Unlike DC, ML uses electrodes with more than two to

TABLE 2 Detailed categorization of the simulation tasks.

Program (Genre)	Task	Feedback mechanism	Control strategy	Evaluation procedure	Performance metrics	Skill transfer
UVa-NTS platform	Abstact task	Traditional Media	DC		Success rate, time	No
PAULA	Abstact task	Traditional Media	DC		Velocity, error	No
Virtual training environment	ADL	VR	ML	BBT	Score	No
Mixed reality training	ADL	MR	ML	PHAM	time	No
Virtual box and blocks test	ADL	VR	DC	BBT	Score	Yes
Virtual box and beans test	ADL	Traditional Media	ML	BBT	IMI	No
Virtual Therapy Arm	ADL	VR	ML	BBT	Score	No
Exploration	ADL	VR	ML		Score	No
Catching simulator	ADL	Traditional Media	DC, ML		Score	Yes
Performance assessment	ADL	Traditional Media	ML	CRT	Accuracy, pin time, Classification errors	No
VR evaluation environment	Posture reproduction	VR	ML		Accuracy	No
ARlimb	Posture reproduction	AR	ML	CRT	Accuracy	Yes
Training platform	Posture reproduction	Traditional Media	ML		Accuracy	Yes
HoloPHAM	ADL	MR		CRT, PHAM		No

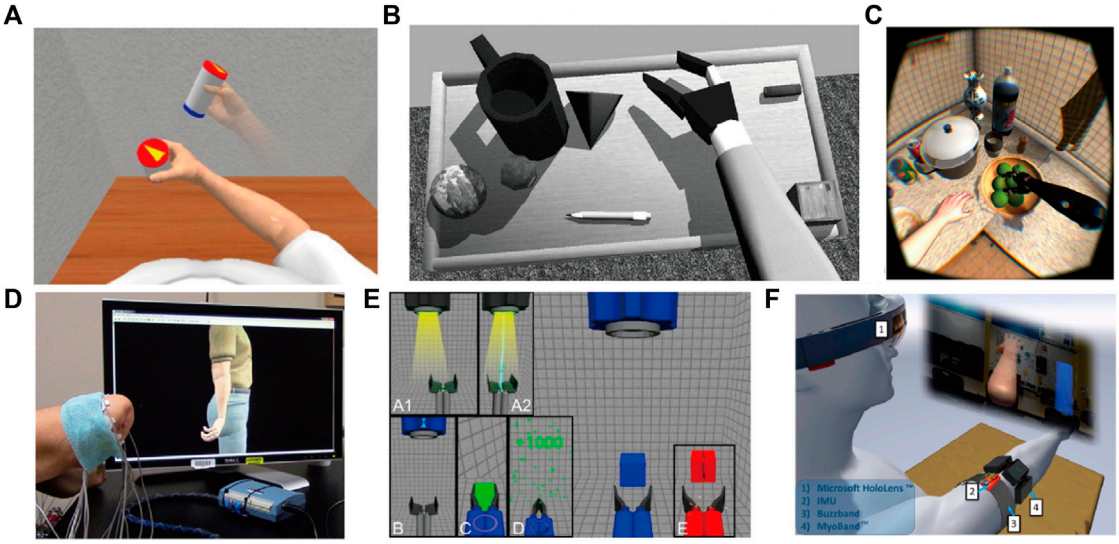

FIGURE 3
Simulation tasks: **(A)** VRd testing environment; **(B)** Prostheses simulator; **(C)** Exploration; **(D)** VIE; **(E)** Catching simulator Prostheses Gripper; and **(F)** Mixed reality training.

measure EMG on multiple muscles in the stump, and calculates EMG features that can be mapped to the input of the learning algorithm for prosthetic control commands. This in turn enables users to generate a potentially larger range of control commands. ML can realize simultaneous control of multiple DoFs by using muscle contraction mode, which aligns more closely with the neural pathway of natural human control and can also minimize compensatory movements of the trunk and shoulder. ML control

can reveal the full potential of prostheses, potentially improving prosthesis function and reducing the burden on upper extremity amputees.

Unlike the DC based XR system, games using ML control, like Crossbow Game, are not designed specifically for training users. In these systems, users cannot distinguish which type of muscle contraction corresponds to which type of motion. Thus, they can explore every possible muscle contraction that can be performed throughout training, resulting in both muscle contraction and algorithm adapting to one another to achieve better myoelectric control (Kristoffersen et al., 2021; P, 2016). The Rehabilitation Institute of Chicago proposed that the XR system based on ML entails a sophisticated training process comprising of four distinct stages: Conceptual Training (teaching the principle of system and determining which movements would be used to achieve better control), Control training (providing guidance when learning to use the system), Function use training (testing prostheses used in daily life activities), Prostheses recalibration training (teaching how to maintain system performance in daily use) (Simon et al., 2012). Systems based on adaptive algorithms, such as VR evaluation environment and Virtual box and blocks test, can successfully prevent XR system performance decline during extended training session (Lambrecht et al., 2011). Most papers surprisingly lack detailed descriptions of processing algorithms. Presently, the utilization and processing of EMG signals in the realm of upper extremity prostheses remain scattered and heterogeneous, lacking consensus on the selection methods of signal processing, classification algorithms, and performance evaluation. We suggest it is crucial to elucidate these concepts as one of the technical guidelines for fostering consistency within the proposed protocols.

3 Clinical outcome assessments and performance metrics

Effective evaluation methods can enhance the assessment of muscle control ability and the efficacy of the XR prosthetic system, thereby facilitating amputee rehabilitation training. The clinical assessment of prosthetic user outcomes are typically assessed through subjective patient-report outcome measures and objective performance-based outcome tests (Wang et al., 2018). The use of subjective patient-report outcome measures allows for the disclosure of subjective details regarding improvements in daily activities, an assessment of user satisfaction with the device, and the evaluation of impacts on life quality. This measurement is preferred because it provides insight into the subjective information regarding the training effect's improvement and the evaluation of the user's satisfaction with the system. Meanwhile, the objective performance based measurement utilizing standardized procedures is able to evaluate system performance, provide quantitative results that are objective, unbiased, and repeatable, and effectively aid both the therapist and user in improving training. While the subjective patient-report test offers a detailed understanding of the patient's experience with the device, it may be biased and influenced by their memory of past events and perspectives. An objective, performance-based measure accounts for these issues but does not address the user's attitude towards the device. In other words, a testing methodology that relies solely on performance-based measures disregards the patient experience, potentially overlooking long-term concerns. Therefore, to ensure effectiveness and suitability upon deployment, clinical rehabilitation tools must undergo comprehensive testing using both objective performance-based measures and subjective patient reports.

3.1 Subjective patient-report outcome measures

Intrinsic Motivation Inventory (IMI), System Usability Scale (SUS), User Evaluation Survey (UES), and NASA Task Load Index are four prominent measures in subjective patient-report outcome measures. IMI is composed of several subscales, which mainly rate the enjoyment, perceived choice, perceived competence and immersion of XR system to evaluate the experience of playing video games (Anderson and Bischof, 2014; Hashim et al., 2021a). SUS is a questionnaire with 10 items, involving the stations, overall game experience, virtual reality experience and all session experience, which is used for quick usability evaluation across multiple domains (Bangor et al., 2008; Dawson et al., 2012). UES mainly scores the game input, control, motivation and fun, including 1) rating the game, 2) rating the input 3) rating the control methods, 4) rating the EMG assessment, and 5) determining the attractive elements (Prahm et al., 2017b; Prahm et al., 2017c). The NASA Task Load Index has been utilized multiple times with upper extremity prostheses, which contains various questions to evaluate mental and physical demand, temporal demand, task performance, effort, and frustration (Osborn et al., 2021; Chappell et al., 2022; Parr et al., 2023).

3.2 Objective performance-based outcome measures

In the designing of XR prostheses training system, therapists utilize various training tools to restore control of the residual limb during daily activities. Some of these tools have undergone clinical verification while others are mentioned in literature (Lindner et al., 2010). Clinical outcome assessments (COAs) are employed to assess the progress of individual rehabilitation or training through XR system. Research has demonstrated that motor control learning is highly specific. Effective evaluation methods can provide more accurate assessments of muscle control ability and the effectiveness of XR system, and can promote the rehabilitation training for amputees (Giboin et al., 2015; van Dijk et al., 2016b). Consequently, selecting appropriate training activities to assist prosthetic users in returning to their regular routines is critical. While physical prosthetic devices form the basis of most of these methods, training in virtual environments has emerged as an effective means of assessing patients' performance during daily living tasks. After reviewing the available literature, this paper outlines 14 frequently utilized clinical outcome measures for the performance-based assessment of residual limb training (Table 3).

For Motion Test (Figure 4A), participants received instructions to follow the motion prompts while observing the virtual prostheses that decoded their movements. This test aimed to investigate changes in EMG levels, but it oversimplified the study by not

TABLE 3 Commonly used clinical outcome indicators.

Performance metrics	Procedure	Properties	Deficiencies
Motion test	Execute the appropriate movement following the virtual prostheses	Investigated changes in EMG levels	Oversimplified
TAC test	Control the virtual prostheses to move to the target posture	Adjust the speed of the virtual prostheses according to the muscle contraction	Interaction space is a virtual environment rather than a physical environment
BBT	Move the block from one side of the box to the other	Allows continuous estimation of single-finger activation and incremental learning	Focus on a limited number of DoFs only
NHPT	Pick up the pegs, put them into the hole on the board, and remove it	Ability to perform flexibility testing	Relatively simple and short
CRT	Move the clothespins from the horizontal bar to the vertical bar	Perform repetitive coordinated stretching and grasping movements	Results scoring without corresponding compensatory movement
Task tests	Simulation of prosthetic gripping tasks	Improved performance of transfer from virtual space to prostheses	Differences between virtual space and actual tasks lead to errors
JHFT	7 ADL tasks	Simulate ADL corresponding to prostheses use in daily life	Training differences between the virtual and real environment
AM-ULA	18 ADL tasks that can be divided into subtasks	Assessment of awkwardness and compensatory exercise	Training differences between the virtual and real environment
CAPPFUL	11 ADL tasks	Assesses the ability, time and quality to complete activities	Training differences between the virtual and real environment
ACMC	30 functional hand movements that can be categorized into 4 hand use	Measuring the ability to operate prostheses while performing ordinary life activities	Influenced by a relatively large subjective component
ARAT	19 arm function assessment tasks	Objects to be moved to shelves of different heights	Influenced by subjective components
SHAP	14 ADLs and 12 additional object transfer tasks	Assesses ability to execute specific grips	lengthy and tiring
AHAP	26 grasping tasks	Replicability using publicly available Yale-CMU-Berkeley objects	Converts complex tasks into simple grasping tasks
PHAM	Manipulate a group of objects by grasping them and changing their position	Ability to monitor gesture completion rates and consider compensatory movements	Lack of comprehensive quantitative assessment methods

examining changes in muscle function levels (Kuiken, 2009; Kristoffersen et al., 2020; Portnova-Fahreeva et al., 2023).

Unlike the Motion Test, the Target Achievement Control (TAC) (Figure 4B) test enables subjects to move the virtual prostheses at a slow or fast pace based on their muscle contraction intensity (Simon et al., 2011). Assessment criteria consist of Test Complexity, Movement Distance, Target Width, Dwell Time and Trial Timeout. Misclassification may aid in completing the motion gradually. One limitation of TAC testing is the absence of interaction between the subjects and the virtual environment (Boschmann et al., 2016; Hargrove et al., 2018; Woodward and Hargrove, 2019).

The Box And Block Test (BBT) (Figure 4C) instructs subjects to move blocks from one compartment of the box to another as much as possible within 60 s (Mathiowetz et al., 1985a). This assessment evaluates the user's capability to perform fundamental actions using a prosthetic device. However, there is not an evaluation test for proportional force control (Hebert and Lewicke, 2012; Kontson et al., 2017). To enhance the system's modular features, the BBT incorporates everyday virtual daily-living activities scenes, such as the living room and kitchen (Nissler et al., 2019). In this setting, it can cause alterations in other areas of the participant's body and handle items of varying elevations.

Similar to BBT, the Nine-Hole Peg Test (NHPT) (Figure 4E) requires subjects to insert and remove wooden pegs into and out of holes on a board, with scoring based on the time and speed required to complete the task (Mathiowetz et al., 1985b; Oxford Grice et al., 2003; Kristoffersen et al., 2021).

The Clothespin-Relocation Test (CRT) (Figure 4D) is an established tool for testing upper limb flexibility, by assessing the time required to reposition the three pins of the Rolyan Graded Pinch Exerciser system from the horizontal bar to the vertical bar (Hussaini and Kyberd, 2017; Kyberd et al., 2018; Hussaini et al., 2019). It realizes precise myoelectric control and coordinated movement of the upper limb joint through repeated coordinated reaching and grasping movements, and repositioning the clothespin in space.

Task Tests refers to task-specific tests such as grasping, interception, tracking, matching, and object recognition (Bouwsema et al., 2014; van Dijk et al., 2016b; Manero et al., 2019). This test can enhance the information related to ADL in a game-relevant way, and improve the performance of XR transfer to the prostheses. The limitation of this test lies in the design of

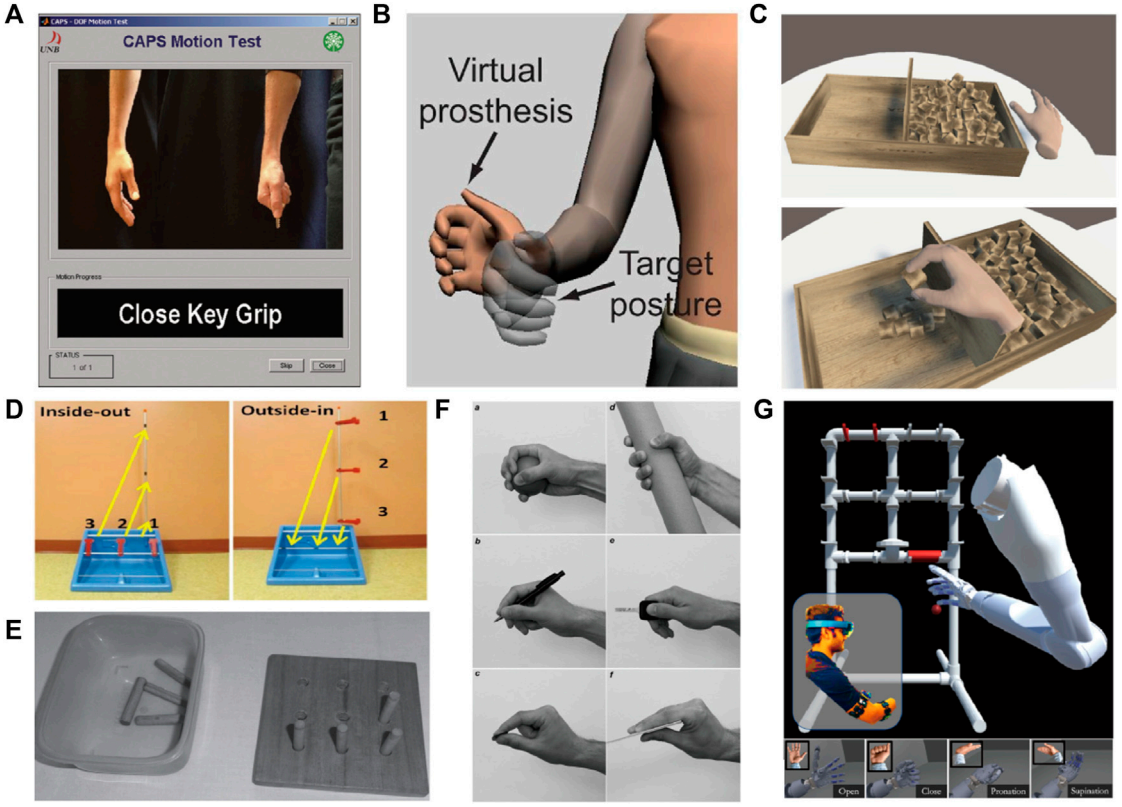

FIGURE 4
Objective performance-based outcome tests: **(A)** Motion Test; **(B)** TAC; **(C)** BBT; **(D)** CRT; **(E)** NHPT; **(F)** SHAP; and **(G)** PHAM.

virtual tasks, and it is impossible to calculate the error amount and solution space related to each goal.

The Jebsen-Taylor Test of Hand Function (JHFT) (Davis Sears and Chung, 2010; Wang et al., 2018), the Activities Measure for Upper Limb Amputees (AM-ULA) (Resnik et al., 2013) and the Capacity Assessment of Prosthetic Performance for the Upper Limb (CAPPFUL) (Kearns et al., 2018) are designed to train or assess various unimanual hand functions required for ADLs with corresponding objects. These three COAs consist of 7, 18, and 11 ADLs, respectively, which are used to assess the ability to perform activities, completion time and movement quality. JHFT is a series of standardized activities, including writing a sentence, page turning, stacking checkers, simulated feeding, picking up/lifting large objects, picking up/lifting heavy objects and picking up/lifting small objects. During training, the completion of these activities is graded by time, with a maximum time limit of 120 s. AM-ULA tasks include combing hair, putting on and taking off clothes, buttoning a shirt, zipping a jacket, tying socks, tying shoes, pouring soda, turning a doorknob, hammering, folding a towel, using a cup, fork, spoon, scissors, and telephone, writing a word, reaching overhead, etc. Each task is further divided into subtasks according to the steps required to complete the task. Task scoring is based on the extent of subtask completion, speed of completion, quality of movement, grip control and prosthetic skills, and independence.

The Assessment for Capacity of Myoelectric Control (ACMC) is an observational assessment designed to measure prosthetic control of ADLs (Hermansson et al., 2004). It consists of 32 functional hand movements, which are divided into 4 categories of hand use: gripping, holding, releasing, and coordinating. In addition, it uses a 4-category scale to identify and evaluate hand movements and judge the ability of subjects to perform spontaneous movements. In all evaluations, only ACMC has been clinically shown to have good test-retest reliability for upper extremity prostheses (Hermansson et al., 2006).

The Action Research Arm Test (ARAT) consists of 19 tasks, which are divided into 4 categories: grasp, grip, pinch, and gross movement (Fitts, 1954). Meanwhile, the test requires the subjects to move objects to different heights of shelves, manipulate common objects, such as washers and blocks, and perform ADLs, such as pouring water into a glass. Some tasks also assess the arm range of motion.

Southampton Hand Assessment Protocol (SHAP) (Figure 4F) is one of the most detailed hand function assessment tools available. It consists of 26 separate tasks, including six grip types (spherical, tripod, tip, power, lateral, and extension), which can be divided into abstract object processing (light/heavy sphere, tripod, power, lateral, tip and extension) and ADLs (pick up coins, undo buttons, food cutting, page turning, remove jar lid, pour water from jug and carton, move a full jar, an empty tin, and a tray, rotate a key, screw, and door handle, open/close a zip) (Bouwsema et al., 2012; Burgerhof et al., 2017). It mainly quantifies the time required to perform the task, regardless of how the task is performed. It is tedious and

exhausting for amputees with limited abilities (Vasluian et al., 2014; Kyberd, 2017; Kristoffersen et al., 2021).

The Anthropomorphic Hand Assessment Protocol (AHAP) is a digital standard to quantify the ability of prostheses to perform daily grasping, which is divided into 26 tasks (Llop-Harillo et al., 2019). According to the kinematic structure of the hand and grasp frequency of ADLs, these tasks are divided into eight grasp types [pulp pinch (PP), lateral pinch (LP), diagonal volar grip (DVG), cylindrical grip (CG), extension grip (EG), tripod pinch (TP), spherical grip (SG) and hook grip (H)] and two non-grasping postures [platform (P) and index pointing/pressing (IP)]. To account for changes in object size, shape, weight, texture, and stiffness during human-environment interaction, each grip type selects three different objects from the YCB suite to achieve reproducibility (Llop-Harillo et al., 2022).

Prosthetic Hand Assessment Measure (PHAM) (Figure 4G) is a standard for upper limb amputees to quantitatively evaluate a series of operational tasks related to object manipulation (e.g., water, pencil, coin, and power), focusing on monitoring gesture completion rates and compensatory movements (Hunt et al., 2017; Sharma et al., 2019). In PHAM protocol, users need to grasp objects with specific gestures and change their position in the frame to manipulate a group of objects within the physical frame (Melero et al., 2019).

3.3 Performance metrics

For DC, the training focuses on two muscles that are independent of each other in terms of contraction function, as well as execution of the mode switching command. For ML, the key point is to adapt several muscle groups to produce EMG patterns that can separate different actions and repeat the same action. Myoelectric control depends on each muscle playing its role during training, so using XR system for EMG training should enable subjects to produce consistent and distinguishable muscle patterns. It is not possible to design a long-term ML algorithm for each subject because it requires a lot of time and resources. Therefore, if users do not perform tests in the laboratory, they may encounter limitations in control flexibility or incorrect movements, which is also considered a common reason for abandoning the use of prostheses (Biddiss and Chau, 2007c; Scheme and Englehart, 2011; Chadwell et al., 2016). If users can understand that their training program may lead to poor actual use, they can immediately adjust the training system to reduce unnecessary frustration and help achieve better electromyographic control. Some studies have established more comprehensive offline training metrics before real-time experiments, including classification measures, variability measures, separability measures, complexity measures, and neighborhood measures (Ortiz-Catalan et al., 2014; Franzke et al., 2021; Nawfel et al., 2021). The classification index is a measure that describes the correctly computed prediction score of the system. The variability metrics is a measure of the reproducibility of EMG patterns between repetitions, which quantifies intra-class characteristics and feedback on the consistency of EMG patterns. The separability metrics is a measure of the reproducibility of EMG patterns between classes, which assesses inter-class characteristics.

To more comprehensively measure training effect and task difficulty in real-time testing, previous research has proposed many online performance metrics. Most clinical assessments test the ability to perform specific movements using time-related parameters (Joyner et al., 2021), as illustrated in Figure 5. Motion completion time is defined as the time from movement initiation to task completion, which includes the full range of motion of each movement. Motion selection time is the time required to correctly select the target motion, which is used to quantitatively measure the speed at which the motion command is converted into a correct motion prediction. Motion completion rate is the percentage of the total motion attempts that are successfully completed within the time limit. Task attempt is defined as the number of times the subject initiates interaction with the object and moves toward task completion (Bangor et al., 2008). Motion quality is defined as the number of awkward and compensatory movements used by the subject in the process of completing the task.

Based on the fact that users must respond to and correct the system's misclassifications to successfully complete the task, Fitts' law, which can be used to demonstrate that any movement task exhibits a trade-off between speed and accuracy, has also been widely used to evaluate online myoelectric control (Fitts, 1954). Fitts' Law typically uses completion rate, path efficiency, overshoot or throughput, and other parameters to evaluate the online performance of XR systems (Park et al., 2008; Scheme and Englehart, 2013; Gusman et al., 2017; Nawfel et al., 2021). The completion rate was mentioned above. Throughput (TP) is the most important metric in Fitts' law, which is defined as the transfer of information in the results of repeated tests over different target distances and widths. Path efficiency is defined as the ratio of the shortest path to the actual path to the target. Overshoot is used to count the number of times the target is lost before reaching the stop position during each movement, and to measure the stability of the users' task performance. The TAC test is very similar to a test based on Fitts' law, which uses the virtual prostheses on the screen to evaluate the control and positioning ability of the prostheses.

4 Existing challenges and future development

The positive results of the XR prosthetic system involve many aspects of the virtual environment. In this section, we will analyze the current status and possible trends of the system in terms of ADL, training modalities, feedback and the relationship between the virtual environment and the physical device to support the implementation of future systems with more effective training capabilities.

4.1 ADL

XR prostheses training should focus on two core themes: user engagement and skill transfer from virtual prosthetics to physical prosthetics. A critical element in using XR as a training and rehabilitation tool is the authenticity of the virtual space created. Obviously, XR system can effectively enhance user participation, but for skill transfer, most studies only verify the performance

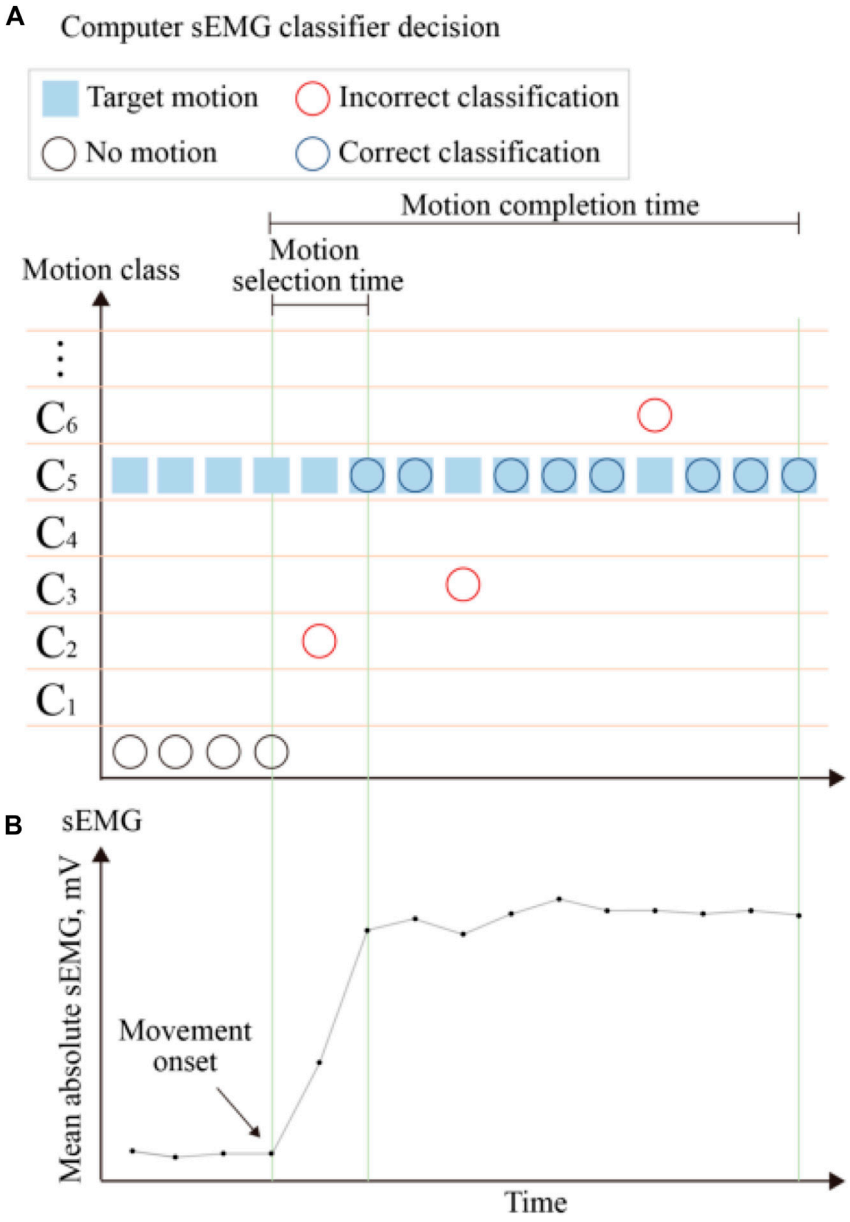

FIGURE 5
Definition of the real-time performance metrics. The mean absolute values of the sEMG signals used to generate control commands are shown at the **(B)**. The **(A)** present the control decisions generated in response to the sEMG signal classifier and corresponding performance metrics. The blue boxes indicate the target motion. The control decisions are represented by three circles, with black circles indicating decisions with no motion, blue circles indicating decisions with correct classification, and red circles indicating decisions with incorrect classification. The performance metrics shown include motion selection time and motion completion time.

improvement or abstract control in XR system. It seems to be tacitly assumed that the XR system, which uses the same muscle tissue and corresponding EMG signal as the prosthetic task, which can easily be translated into the improvement of prosthetic control. However, previous studies have shown that the emergence of migration phenomenon requires virtual space to be as close as possible to the target of physical prosthetic tasks, that is, more ADL training (Belter et al., 2013; Woodward and Hargrove, 2019).

Virtual space has many potential benefits, including task automation, movement scalability, exercise gamification, environmental security and performance tracking. XR prosthesis system is a powerful tool that can generate or present the properties of all virtual models in interactive tasks, including shape, texture, compliance, and interactive features. Using virtual space to simulate ADL-oriented training is a natural extension of the "real world." (van Dijk et al., 2016b; van Dijk et al., 2016a). have developed a game to simulate grasping tasks, which augments ADL-relevant information and incorporates the proportional relationship between EMG amplitude and end-effector. This study proved for the first time the transfer effect of using ADL-related information on tasks from XR to myoelectric prostheses, but only when the game was designed to encourage behaviors specific to controlling

prostheses. The design of XR prostheses system should pay attention to the balance between game motivation and task functionality (Kristoffersen et al., 2021).

The research on ADL-oriented virtual prosthetic training to improve the daily life performance of amputees has begun to appear. Next, ADL-oriented interventions in virtual space should be close to the real world, including a home-like scenario. Specifically, when designing a virtual system, it is necessary to establish the relationship between ADL tasks and virtual tasks, to specify the information about the relationship between ADL goals and user actions that allows adaptive coordination of these actions, because virtual tasks cannot completely simulate ADL in daily life. It seems that the transfer effect is best evaluated by measuring the performance of ADL tasks, such as the timing of closing or opening the hand, which is also a direction to be improved. The ADL-related training based on actual activities raises an interesting point. In this case, the user would be naturally induced to move and manipulate objects at different heights. This exercise and training performed/exerted by muscles other than the missing ones could form a new physical therapy, which is more conducive to the rehabilitation of users.

4.2 Train modalities

The feature of EMG signal are easily affected by external factors, such as muscle fatigue, electrode displacement, limb position change, contraction force change and individual differences. This type of influence cannot be suppressed, and it is also unpredictable. However, it is impractical to account for all the confounding factors in a single training session. Therefore, when myoelectric control is introduced into clinical practice, it is very necessary to have an effective, unified and easy-to-implement training protocol. Putting users' daily life in the center of research and formulating research objectives, and improving the clinical application performance of the system with clinically relevant results as the goal. The existing research shows that the XR prostheses training system is far behind the new dexterous prosthetic hand and the advanced functional evaluation model. The XR prosthetic training system should be designed by integrating the prosthetic hand control mechanism, such as switch, threshold, proportion, pattern switch and pattern recognition. At the same time, it can integrate multiple functional elements, including training intensity, training times and training level, and even the training level and program required by users (Winslow et al., 2018; Prahm et al., 2019a,8; Prahm et al., 2017c).

Due to technical limitations, XR prostheses system usually only describes the virtual hand on the screen or in a two-dimensional environment, excluding multi-DOF depth of field control and the joint environment with joint drive as the goal, and has no connection with the user's body. We believe that the future XR prosthetic system should adopt the AR/MR technology combined with IMU, where virtual reconstruction is carried out with the help of IMU tags attached to the user's body, so the virtual hand or virtual prosthetic will cover the user's residual limb. The system predicts or tracks the trajectory of the virtual hand through IMU, and controls the virtual hand through the user's muscle contraction. More realistic virtual hand models, interactive objects and rich scenes would not only provide a unique personalized training interface, but also create a more attractive, more immersive and realistic user experience. Adding game function design, task type, scoring mechanism, type of control scheme used by the program, and feedback can effectively attract users to focus on the results of the game (external focus of attention) rather than on muscle changes (internal focus of attention) during training, which can improve cognitive effort and lead to faster, more accurate, and more effective virtual hand movements.

The game elements are alternated to adapt to the specific needs and development of users at different times or training stages. The virtual system should have a built-in logging capabilities to record the movement status of each component in the virtual space during training and to evaluate the overall rehabilitation performance. The XR prostheses system with rich elements can be used by users to create or select more specific training scenarios. In addition, when combined with accurate rehabilitation methods, it can also provide a higher level of personalized training programs. A better training effect for users would result from a more comprehensive, more clinical and more entertaining virtual prosthesis training.

4.3 Feedback

To improve user participation, the existing XR prosthetic system tends to pay more attention to aesthetic design, but ignores functionality. The virtual hand is usually represented by a game element or visualisation. Interacting with objects in the XR environment typically involves attaching them to the hand through programming, rather than controlling the virtual hand using a myoelectric controller that mimics the functionality of the prosthetic hand (Hargrove et al., 2018; Nissler et al., 2019; Phelan et al., 2021) compared the virtual TAC test with a set of outcome measures for physical prostheses, including SHAP, JTHF, BBT, and CRT. Their findings showed a correlation between virtual test measurement and physical performance, but no causal relationship was found. (Boschmann et al., 2021). proposed an AR system that enables users to practice pattern classification control, modulate grasping force with feedback, and adjust wrist rotation via a tilted bar. Through testing, the system can transfer the skills needed to control actual prosthetics. Judging the effectiveness of the training is primarily based on the subjective feedback from the therapist and user, which poses challenges to the objective assessment of the outcomes. The study indicates that the provision of force feedback can enhance the level of realism in the virtual environment and the user's sensation of embodiment with the virtual hand. Additionally, it can augment the performance of the virtual system and effectively enhance the user's training outcome (Dosen et al., 2015).

In the straightforward task of grasping, the objective is to lift a cylindrical object with uncertain measurements of diameter, hardness, and friction. The prosthetic hand user must regulate the aperture of the prosthetic hand to correspond with the size of the object, which is essential for skillful utilization of the prosthetic hand. To prevent any breakage of the object, the user must also have the capability to adjust the virtual hand's force in response to the object's hardness. Force feedback is essential in virtual environments because users are unable to sense grip force directly. To assist users, a virtual strength can be applied to the object, enabling them to proficiently regulate the force the virtual

hand exerts after numerous training sessions. Additionally, friction feedback can be incorporated to simulate objects slipping, providing users with an opportunity to practice all feasible object manipulation strategies.

The development of XR systems would not eradicate work, but rather redistribute and reshape existing activities. Although XR has several advantages over CPT, physiotherapists still play an important role (Almeida and Nunes, 2020). We consider the suggestions of physiotherapists to be a special kind of feedback. The XR prosthetic system and CPT have a mutually advantageous relationship and the program promotes patient engagement while ensuring scientifically-sound training methods. The physical therapist creates a training plan that encompasses a preliminary diagnosis and follow-up assessments. The therapist informs the patient about their condition, adjusts the system, recommends exercises, and assesses the outcomes to attain the anticipated advantages of participation and intervention. Additionally, physical therapists can aid individuals in choosing suitable training methods, difficulty and intensity levels, and tools based on individual traits and interests, creating a personalized training experience. Even when training at home, physical therapists can monitor an individual's progress through the Internet of Things and take part in their training. Furthermore, it is crucial for physical therapists to be part of the design process of XR systems to ensure their optimization.

4.4 Virtual environment and physical devices

The XR prostheses system serves two primary purposes: neuromotor rehabilitation and prosthetic control training. However, the system currently prioritizes neuromotor rehabilitation and virtual prostheses training, disregarding the crucial process of amputees adapting to new prostheses devices (P, 2016). It is necessary to consider these variances when implementing and interpreting results. During clinical practice, XR is mainly used for EMG signal control training to restore muscle function and encourage voluntary muscle contraction. During this time frame, participants practiced grasping objects of different shapes and sizes and performing daily tasks. Subsequently, they received training on how to perform these tasks using a myoelectric prosthetic hand. However, amputees who have achieved voluntary control of EMG signals could potentially face challenges while performing tasks as intended. The impact of prosthetic weight and arm posture on EMG signals, the inconsistencies between XR tasks and actual grasping tasks, and differences in virtual versus real prosthetic hand models contribute to these findings. While some studies suggest that training with virtual prostheses is equivalent to training with physical ones, the extent to which skills acquired in the simulated environment are transferable to the actual task remains unclear.

The virtual prostheses can be programmed and calibrated to replicate the physical prosthetic system, allowing users to practice controlling the system using virtual objects (Lambrecht et al., 2011; Kluger et al., 2019; Elor and Kurniawan, 2020; Chappell et al., 2022) proposed a pre-prosthetic hand training system that integrates virtual reality with a robot arm. This system employs the robot arm to simulate the actions and forces of the virtual arm through precise physical simulation. The study reveals that implementation of robot arms can significantly improve training outcomes. However, a gap between the real and virtual environment increases user frustration. Migrating XR prosthetic systems effectively requires consistency and similarity in their function and training with physical prosthetic systems. While relevant guidelines have been proposed for training, scoring, and clinical interpretation, differences still exist in the selection and completion time of movements, task attempts, task quality, and tolerance required to achieve the target posture.

The use of the XR prostheses system in neuromotor rehabilitation training could lead to more complex and distinguishable EMG patterns compared to movements typically used in activating a prosthetic hand. To optimize training effectiveness, it may be beneficial to limit movements that mimic prosthetic control (Na et al., 2017; Kristoffersen et al., 2020). The virtual reality programming engines, such as Unity and Unreal Engine, have precise physics calculation engines that simulate prosthetic hand movements, mechatronic models, delays, and limitations. This enables the implementation of the same model for virtual space control and physical prosthetics. Thus, virtual prosthetics training can lead to direct transfer for physical prosthetics control. During training, advanced prosthetic technology is utilized to create an intuitive and easily manageable system that combines both virtual and real simulations of prosthetic hands. Furthermore, the XR prostheses system and desktop prosthetic hand or prostheses simulators are combined in order to optimize the training process. The user has the ability to adjust the level of control required for training, thereby facilitating gradual improvement in rehabilitation progress. The system design would provide users with a realistic simulation of a future prostheses, enabling them to perform rehabilitation tasks quickly, similar to their experience with physical prosthetics during the early stages of amputation. Additionally, this feature would empower developers to test and assess the structural design and control performance of the prosthetic hand based on personalized user problems, thereby improving the hands' adaptability.

5 Conclusion

This review presents recent advances in XR systems applied to myoelectric prostheses, including existing XR prosthetic systems, virtual control methods, performance evaluation methods, and performance metrics. Our analysis of XR prosthetic systems indicates that serious games can increase user engagement, while simulated tasks improve training outcomes. Existing systems have achieved satisfactory training outcomes, while performance evaluation methods and metrics are continually undergoing refinement. In addition to enhancing user engagement, the XR prosthetic system can serve as a pre-training tool during the wait for a new prosthesis. There are limited direct strategies for transferring performance from virtual environments to physical devices in current systems. However, the emergence of AR/MR technology seems to address this issue. To achieve this objective, this paper compares prosthetic applications, identifies gaps in virtual control methods, performance assessment methods, and physical prosthetic systems, and analyzes the limitations of existing systems while examining proposed development prospects in four areas: ADL,

training modalities, feedback, and the relationship between the virtual environment and the physical device. The application of XR technology for myoelectric prosthetic hand training and rehabilitation undoubtedly holds great promise. Establishing a patient-centered XR prosthetic system that is aimed at and inspired by real-world use cases is essential for surmounting hurdles to adoption.

Author contributions

WL: Writing–original draft. PS: Writing–review and editing. SL: Writing–review and editing. HY: Project administration, Supervision.

Funding

The author(s) declare financial support was received for the research, authorship, and/or publication of this article. This work was supported by the National Key Research and Development Program of China (2020YFC2007902).

Conflict of interest

The authors declare that the research was conducted in the absence of any commercial or financial relationships that could be construed as a potential conflict of interest.

Publisher's note

All claims expressed in this article are solely those of the authors and do not necessarily represent those of their affiliated organizations, or those of the publisher, the editors and the reviewers. Any product that may be evaluated in this article, or claim that may be made by its manufacturer, is not guaranteed or endorsed by the publisher.

References

Akbulut, A., Güngör, F., Tarakcı, E., Çabuk, A., and Aydin, M. A. (2019). "Immersive virtual reality games for rehabilitation of phantom limb pain," in *2019 medical technologies congress (TIPTEKNO)*, 1–4. doi:10.1109/TIPTEKNO.2019.8895177

Al-Jumaily, A., and Olivares, R. A. (2009). "Electromyogram (EMG) driven system based virtual reality for prosthetic and rehabilitation devices," in Proceedings of the 11th International Conference on Information Integration and Web-based Applications and Services - iiWAS '09, 582–586. doi:10.1145/1806338.1806448

Almeida, J., and Nunes, F. (2020). The practical work of ensuring effective use of serious games in a rehabilitation clinic: a qualitative study. *JMIR Rehabilitation Assistive Technol.* 7, e15428. doi:10.2196/15428

Anderson, F., and Bischof, W. F. (2014). Augmented reality improves myoelectric prosthesis training. *Int. J. Disabil. Hum. Dev.* 13, 349–354. doi:10.1515/ijdhd-2014-0327

Armiger, R. S., and Vogelstein, R. J. (2008). "Air-Guitar Hero: a real-time video game interface for training and evaluation of dexterous upper-extremity neuroprosthetic control algorithms," in 2008 IEEE Biomedical Circuits and Systems Conference, 121–124. doi:10.1109/biocas.2008.4696889

Bangor, A., Kortum, P. T., and Miller, J. T. (2008). An empirical evaluation of the system usability scale. *Int. J. Human-Computer Interact.* 24, 574–594. doi:10.1080/10447310802205776

Belter, J. T., Segil, J. L., Dollar, A. M., and Weir, R. F. (2013). Mechanical design and performance specifications of anthropomorphic prosthetic hands: a review. *J. Rehabilitation Res. Dev.* 50, 599. doi:10.1682/JRRD.2011.10.0188

Bevilacqua, R., Maranesi, E., Riccardi, G. R., Donna, V. D., Pelliccioni, P., Luzi, R., et al. (2019). Non-immersive virtual reality for rehabilitation of the older people: a systematic review into efficacy and effectiveness. *J. Clin. Med.* 8, 1882. doi:10.3390/jcm8111882

Biddiss, E., and Chau, T. (2007a). The roles of predisposing characteristics, established need, and enabling resources on upper extremity prosthesis use and abandonment. *Disabil. Rehabilitation Assistive Technol.* 2, 71–84. doi:10.1080/17483100601138959

Biddiss, E., and Chau, T. (2007b). Upper-limb prosthetics: critical factors in device abandonment. *Am. J. Phys. Med. Rehabilitation* 86, 977–987. doi:10.1097/PHM.0b013e3181587f6c

Biddiss, E. A., and Chau, T. T. (2007c). Upper limb prosthesis use and abandonment: a survey of the last 25 years. *Prosthetics Orthot. Int.* 31, 236–257. doi:10.1080/03093640600994581

Blana, D., Kyriacou, T., Lambrecht, J. M., and Chadwick, E. K. (2016). Feasibility of using combined EMG and kinematic signals for prosthesis control: a simulation study using a virtual reality environment. *J. Electromyogr. Kinesiol.* 29, 21–27. doi:10.1016/j.jelekin.2015.06.010

Boschmann, A., Dosen, S., Werner, A., Raies, A., and Farina, D. (2016). "A novel immersive augmented reality system for prosthesis training and assessment," in 2016 IEEE-EMBS International Conference on Biomedical and Health Informatics (BHI), 280–283. doi:10.1109/BHI.2016.7455889

Boschmann, A., Neuhaus, D., Vogt, S., Kaltschmidt, C., Platzner, M., and Dosen, S. (2021). Immersive augmented reality system for the training of pattern classification control with a myoelectric prosthesis. *J. NeuroEngineering Rehabilitation* 18, 25. doi:10.1186/s12984-021-00822-6

Bouwsema, H., Kyberd, P. J., Hill, W., van der Sluis, C. K., and Bongers, R. M. (2012). Determining skill level in myoelectric prosthesis use with multiple outcome measures. *J. Rehabilitation Res. Dev.* 49, 1331. doi:10.1682/JRRD.2011.09.0179

Bouwsema, H., van der Sluis, C. K., and Bongers, R. M. (2014). Effect of feedback during virtual training of grip force control with a myoelectric prosthesis. *PLoS ONE* 9, e98301. doi:10.1371/journal.pone.0098301

Burgerhof, J. G., Vasluian, E., Dijkstra, P. U., Bongers, R. M., and van der Sluis, C. K. (2017). The Southampton Hand Assessment Procedure revisited: a transparent linear scoring system, applied to data of experienced prosthetic users. *J. Hand Ther.* 30, 49–57. doi:10.1016/j.jht.2016.05.001

Cao, W., Ma, Y., Chen, C., Zhang, J., and Wu, X. (2022). Hardware circuits design and performance evaluation of a soft lower limb exoskeleton. *IEEE Trans. Biomed. Circuits Syst.* 16, 384–394. doi:10.1109/TBCAS.2022.3173965

Cao, W., Shang, D., Yin, M., Li, X., Xu, T., Zhang, L., et al. (2023). Development and evaluation of a hip exoskeleton for lateral resistance walk exercise. *IEEE/ASME Trans. Mechatronics* 28, 1966–1974. doi:10.1109/TMECH.2023.3273717

Cavalcante, R., Gaballa, A., Cabibihan, J.-J., Soares, A., and Lamounier, E. (2021). "The importance of sensory feedback to enhance embodiment during virtual training of myoelectric prostheses users," in 2021 IEEE Conference on Virtual Reality and 3D User Interfaces Abstracts and Workshops (VRW), 558. doi:10.1109/VRW52623.2021.00161

Cerritelli, F., Chiera, M., Abbro, M., Megale, V., Esteves, J., Gallace, A., et al. (2021). The challenges and perspectives of the integration between virtual and augmented reality and manual therapies. *Front. Neurology* 12, 700211. doi:10.3389/fneur.2021.700211

Chadwell, A., Kenney, L., Thies, S., Galpin, A., and Head, J. (2016). The reality of myoelectric prostheses: understanding what makes these devices difficult for some users to control. *Front. Neurorobotics* 10, 7. doi:10.3389/fnbot.2016.00007

Chappell, D., Son, H. W., Clark, A. B., Yang, Z., Bello, F., Kormushev, P., et al. (2022). Virtual reality pre-prosthetic hand training with physics simulation and robotic force interaction. *IEEE Robotics Automation Lett.* 7, 4550–4557. doi:10.1109/LRA.2022.3151569

Clingman, R., and Pidcoe, P. (2014). A novel myoelectric training device for upper limb prostheses. *IEEE Trans. Neural Syst. Rehabilitation Eng.* 22, 879–885. doi:10.1109/TNSRE.2014.2315046

Davis Sears, E., and Chung, K. C. (2010). Validity and responsiveness of the jebsen–taylor hand function test. *J. Hand Surg.* 35, 30–37. doi:10.1016/j.jhsa.2009.09.008

Davoodi, R., and Loeb, G. E. (2012). Development of a physics-based target shooting game to train amputee users of multijoint upper limb prostheses. *Presence Teleoperators Virtual Environ.* 21, 85–95. doi:10.1162/PRES_a_00091

Dawson, M. R., Fahimi, F., and Carey, J. P. (2012). The development of a myoelectric training tool for above-elbow amputees. *Open Biomed. Eng. J.* 6, 5–15. doi:10.2174/1874120701206010005

de la Rosa, R., Alonso, A., de la Rosa, S., and Abasolo, D. (2008). "Myo-Pong: a neuromuscular game for the UVa-Neuromuscular Training System platform," in 2008 Virtual Rehabilitation, 61. doi:10.1109/ICVR.2008.4625124

de la Rosa, R., de la Rosa, S., Alonso, A., and del Val, L. (2009). "The UVa-neuromuscular training system platform," in *Distributed computing, artificial intelligence, bioinformatics, soft computing, and ambient assisted living*. Editors S. Omatu, M. P. Rocha, J. Bravo, F. Fernández, E. Corchado, A. Bustillo, et al. (Berlin, Heidelberg: Springer), 863–869. Lecture Notes in Computer Science. doi:10.1007/978-3-642-02481-8_131

Dhawan, D., Barlow, M., and Lakshika, E. (2019). "Prosthetic rehabilitation training in virtual reality," in 2019 IEEE 7th International Conference on Serious Games and Applications for Health (SeGAH), 1–8. doi:10.1109/SeGAH.2019.8882455

Dosen, S., Markovic, M., Somer, K., Graimann, B., and Farina, D. (2015). EMG Biofeedback for online predictive control of grasping force in a myoelectric prosthesis. *J. NeuroEngineering Rehabilitation* 12, 55. doi:10.1186/s12984-015-0047-z

Elor, A., and Kurniawan, S. (2020). The ultimate display for physical rehabilitation: a bridging review on immersive virtual reality. *Front. Virtual Real.* 1. doi:10.3389/frvir.2020.585993

Fitts, P. M. (1954). The information capacity of the human motor system in controlling the amplitude of movement. *J. Exp. Psychol.* 47, 381–391. doi:10.1037/h0055392

Flavián, C., Ibáñez-Sánchez, S., and Orús, C. (2019). The impact of virtual, augmented and mixed reality technologies on the customer experience. *J. Bus. Res.* 100, 547–560. doi:10.1016/j.jbusres.2018.10.050

Franzke, A. W., Kristoffersen, M. B., Jayaram, V., van der Sluis, C. K., Murgia, A., and Bongers, R. M. (2021). Exploring the relationship between EMG feature space characteristics and control performance in machine learning myoelectric control. *IEEE Trans. Neural Syst. Rehabilitation Eng.* 29, 21–30. doi:10.1109/tnsre.2020.3029873

Gaballa, A., Cavalcante, R. S., Lamounier, E., Soares, A., and Cabibihan, J.-J. (2022). Extended reality "X-reality" for prosthesis training of upper-limb amputees: a review on current and future clinical potential. *IEEE Trans. Neural Syst. Rehabilitation Eng.* 30, 1652–1663. doi:10.1109/TNSRE.2022.3179327

Garske, C. A., Dyson, M., Dupan, S., Morgan, G., and Nazarpour, K. (2021). Serious games are not serious enough for myoelectric prosthetics. *JMIR Serious Games* 9, e28079. doi:10.2196/28079

Geethanjali, P. (2016). Myoelectric control of prosthetic hands: state-of-the-art review. *Med. devices Auckl. N.Z.)* 9, 247–255. doi:10.2147/MDER.S91102

Giboin, L.-S., Gruber, M., and Kramer, A. (2015). Task-specificity of balance training. *Hum. Mov. Sci.* 44, 22–31. doi:10.1016/j.humov.2015.08.012

Graafland, M., Schraagen, J. M., and Schijven, M. P. (2012). Systematic review of serious games for medical education and surgical skills training. *Br. J. Surg.* 99, 1322–1330. doi:10.1002/bjs.8819

Gusman, J., Mastinu, E., and Ortiz-Catalan, M. (2017). Evaluation of computer-based target achievement tests for myoelectric control. *IEEE J. Transl. Eng. health Med.* 5, 1–10. doi:10.1109/JTEHM.2017.2776925

Hargrove, L., Losier, Y., Lock, B., Englehart, K., and Hudgins, B. (2007). "A real-time pattern recognition based myoelectric control usability study implemented in a virtual environment," in 2007 29th Annual International Conference of the IEEE Engineering in Medicine and Biology Society, 4842–4845. doi:10.1109/iembs.2007.4353424

Hargrove, L., Miller, L., Turner, K., and Kuiken, T. (2018). Control within a virtual environment is correlated to functional outcomes when using a physical prosthesis. *J. NeuroEngineering Rehabilitation* 15, 60. doi:10.1186/s12984-018-0402-y

Hashim, N. A., Abd Razak, N. A., Gholizadeh, H., and Abu Osman, N. A. (2021a). Video game–based rehabilitation approach for individuals who have undergone upper limb amputation: case-control study. *JMIR Serious Games* 9, e17017. doi:10.2196/17017

Hashim, N. A., Razak, N. A. A., and Osman, N. A. A. (2021b). Comparison of conventional and virtual reality box and blocks tests in upper limb amputees: a case-control study. *IEEE Access* 9, 76983–76990. doi:10.1109/access.2021.3072988

Hebert, J. S., and Lewicke, J. (2012). Case report of modified Box and Blocks test with motion capture to measure prosthetic function. *J. Rehabilitation Res. Dev.* 49, 1163. doi:10.1682/JRRD.2011.10.0207

Hermansson, L., Fisher, A., Bernspång, B., and Eliasson, A.-C. (2004). Assessment of Capacity for Myoelectric Control: a new rasch-built measure of prosthetic hand control. J. Rehabilitation Med. - 1, 1. doi:10.1080/16501970410024280

Hermansson, L. M., Bodin, L., and Eliasson, A.-C. (2006). Intra- and inter-rater reliability of the assessment of capacity for myoelectric control. *J. Rehabilitation Med.* 38, 118–123. doi:10.1080/16501970500312222

Holden, M. K. (2005). Virtual environments for motor rehabilitation: review. *CyberPsychology Behav.* 8, 187–211. doi:10.1089/cpb.2005.8.187

Hugues, O., Fuchs, P., and Nannipieri, O. (2011). "New augmented reality taxonomy: technologies and features of augmented environment," in *Handbook of augmented reality*. Editor B. Furht (New York, NY: Springer), 47–63.

Hunt, C., Yerrabelli, R., Clancy, C., Osborn, L., Kaliki, R., and Thakor, N. (2017). *PHAM: prosthetic hand assessment measure*.

Hussaini, A., Hill, W., and Kyberd, P. (2019). Clinical evaluation of the refined clothespin relocation test. *Prosthetics Orthot. Int.* 43, 485–491. doi:10.1177/0309364619843779

Hussaini, A., and Kyberd, P. (2017). Refined clothespin relocation test and assessment of motion. *Prosthetics Orthot. Int.* 41, 294–302. doi:10.1177/0309364616660250

Johnson, S. S., and Mansfield, E. (2014). Prosthetic training: upper limb. *Phys. Med. Rehabilitation Clin. N. Am.* 25, 133–151. doi:10.1016/j.pmr.2013.09.012

Joyner, J. S., Vaughn-Cooke, M., and Benz, H. L. (2021). Comparison of dexterous task performance in virtual reality and real-world environments. *Front. Virtual Real.* 2. doi:10.3389/frvir.2021.599274

Kearns, N. T., Peterson, J. K., Smurr Walters, L., Jackson, W. T., Miguelez, J. M., and Ryan, T. (2018). Development and psychometric validation of capacity assessment of prosthetic performance for the upper limb (CAPPFUL). *Archives Phys. Med. Rehabilitation* 99, 1789–1797. doi:10.1016/j.apmr.2018.04.021

Kenedy Lopes, E. A. L. (2012). Using augmented reality techniques to simulate myoelectric upper limb prostheses. *J. Bioeng. Biomed. Sci.*, 010. doi:10.4172/2155-9538.S1-010

Kluger, D. T., Joyner, J. S., Wendelken, S. M., Davis, T. S., George, J. A., Page, D. M., et al. (2019). Virtual reality provides an effective platform for functional evaluations of closed-loop neuromyoelectric control. *IEEE Trans. Neural Syst. Rehabilitation Eng.* 27, 876–886. doi:10.1109/TNSRE.2019.2908817

Kontson, K., Marcus, I., Myklebust, B., and Civillico, E. (2017). Targeted box and blocks test: normative data and comparison to standard tests. *PLOS ONE* 12, e0177965. doi:10.1371/journal.pone.0177965

Kristoffersen, M. B., Franzke, A. W., Bongers, R. M., Wand, M., Murgia, A., and van der Sluis, C. K. (2021). User training for machine learning controlled upper limb prostheses: a serious game approach. *J. NeuroEngineering Rehabilitation* 18, 32–15. doi:10.1186/s12984-021-00831-5

Kristoffersen, M. B., Franzke, A. W., van der Sluis, C. K., Murgia, A., and Bongers, R. M. (2020). Serious gaming to generate separated and consistent EMG patterns in pattern-recognition prosthesis control. *Biomed. Signal Process. Control* 62, 102140. doi:10.1016/j.bspc.2020.102140

Kuiken, T. A. (2009). Targeted muscle reinnervation for real-time myoelectric control of multifunction artificial arms. *JAMA* 301, 619. doi:10.1001/jama.2009.116

Kulkarni, J., Pettifer, S., Turner, S., and Richardson, C. (2020). An investigation into the effects of a virtual reality system on phantom limb pain: a pilot study. *Br. J. Pain* 14, 92–97. doi:10.1177/2049463719859913

Kyberd, P., Hussaini, A., and Maillet, G. (2018). Characterisation of the clothespin relocation test as a functional assessment tool. *J. Rehabilitation Assistive Technol. Eng.* 5, 205566831775081. doi:10.1177/2055668317750810

Kyberd, P. J. (2017). Assessment of functionality of multifunction prosthetic hands. *JPO J. Prosthetics Orthot.* 29, 103–111. doi:10.1097/JPO.0000000000000139

Laamarti, F., Eid, M., and El Saddik, A. (2014). An overview of serious games. *Int. J. Comput. Games Technol.* 2014, 1–15. doi:10.1155/2014/358152

Lambrecht, J. M., Pulliam, C. L., and Kirsch, R. F. (2011). Virtual reality environment for simulating tasks with a myoelectric prosthesis: an assessment and training tool. *JPO J. Prosthetics Orthot.* 23, 89–94. doi:10.1097/jpo.0b013e318217a30c

Lindner, H. Y. N., Nätterlund, B. S., and Hermansson, L. M. N. (2010). Upper limb prosthetic outcome measures. *Prosthetics Orthot. Int.* 34, 109–128. doi:10.3109/03093641003776976

Llop-Harillo, I., Iserte, J. L., and Pérez-González, A. (2022). Benchmarking anthropomorphic hands through grasping simulations. *J. Comput. Des. Eng.* 9, 330–342. doi:10.1093/jcde/qwac002

Llop-Harillo, I., Pérez-González, A., Starke, J., and Asfour, T. (2019). The anthropomorphic hand assessment protocol (AHAP). *Robotics Aut. Syst.* 121, 103259. doi:10.1016/j.robot.2019.103259

Lovely, D., Stocker, D., and Scott, R. (1990). A computer-aided myoelectric training system for young upper limb amputees. *J. Microcomput. Appl.* 13, 245–259. doi:10.1016/0745-7138(90)90026-4

Lu, A. S., Baranowski, T., Thompson, D., and Buday, R. (2012). Story immersion of videogames for youth health promotion: a review of literature. *Games Health J.* 1, 199–204. doi:10.1089/g4h.2011.0012

Manero, A., Smith, P., Sparkman, J., Dombrowski, M., Courbin, D., Barclay, P., et al. (2019). Utilizing additive manufacturing and gamified virtual simulation in the design of neuroprosthetics to improve pediatric outcomes. *MRS Commun.* 9, 941–947. doi:10.1557/mrc.2019.99

Martinez-Luna, C., Kelly, C., Rozell, B., and Farrell, T. (2020). A Myoelectric video game training pilot study: changes in control signal properties. MEC20 Symposium

Mathiowetz, V., Volland, G., Kashman, N., and Weber, K. (1985a). Adult norms for the box and block test of manual dexterity. *Am. J. Occup. Ther.* 39, 386–391. doi:10.5014/ajot.39.6.386

Mathiowetz, V., Weber, K., Kashman, N., and Volland, G. (1985b). Adult norms for the nine hole peg test of finger dexterity. *Occup. Ther. J. Res.* 5, 24–38. doi:10.1177/153944928500500102

McFarland, L. V., Hubbard Winkler, S. L., Heinemann, A. W., Jones, M., and Esquenazi, A. (2010). Unilateral upper-limb loss: satisfaction and prosthetic-device use in veterans and servicemembers from Vietnam and OIF/OEF conflicts. *J. Rehabilitation Res. Dev.* 47, 299–316. doi:10.1682/jrrd.2009.03.0027

Melero, M., Hou, A., Cheng, E. H., Tayade, A., Lee, C.-S., Lee, S. C., et al. (2019). Upbeat: augmented reality-guided dancing for prosthetic rehabilitation of upper limb amputees. *J. Healthc. Eng.* 2019, 1–9. doi:10.1155/2019/2163705

Muri, F., Carbajal, C., Echenique, A. M., Fernández, H., and López, N. M. (2013). Virtual reality upper limb model controlled by EMG signals. *J. Phys. Conf. Ser.* 477, 012041. doi:10.1088/1742-6596/477/1/012041

Murray, C. D., Pettifer, S., Howard, T., Patchick, E. L., Caillette, F., Kulkarni, J., et al. (2007). The treatment of phantom limb pain using immersive virtual reality: three case studies. *Disabil. Rehabilitation* 29, 1465–1469. doi:10.1080/09638280601107385

Na, Y., Kim, S. J., Jo, S., and Kim, J. (2017). Ranking hand movements for myoelectric pattern recognition considering forearm muscle structure. *Med. Biol. Eng. Comput.* 55, 1507–1518. doi:10.1007/s11517-016-1608-4

Nakamura, G., Shibanoki, T., Kurita, Y., Honda, Y., Masuda, A., Mizobe, F., et al. (2017). A virtual myoelectric prosthesis training system capable of providing instructions on hand operations. *Int. J. Adv. Robotic Syst.* 14, 172988141772845. doi:10.1177/1729881417728452

Narayanasamy, V., Wong, K. W., Fung, C. C., and Rai, S. (2006). Distinguishing games and simulation games from simulators. *Comput. Entertain.* 4, 9. doi:10.1145/1129006.1129021

Nawfel, J. L., Englehart, K. B., and Scheme, E. J. (2021). A multi-variate approach to predicting myoelectric control usability. *IEEE Trans. Neural Syst. Rehabilitation Eng.* 29, 1312–1327. doi:10.1109/TNSRE.2021.3094324

Nissler, C., Nowak, M., Connan, M., Büttner, S., Vogel, J., Kossyk, I., et al. (2019). VITA—an everyday virtual reality setup for prosthetics and upper-limb rehabilitation. *J. Neural Eng.* 16, 026039. doi:10.1088/1741-2552/aaf35f

O'Keeffe, B. (2011). Prosthetic rehabilitation of the upper limb amputee. *Indian J. Plastic Surg.* 44, 246–252. doi:10.4103/0970-0358.85346

Ortiz-Catalan, M., Hakansson, B., and Branemark, R. (2014). Real-time and simultaneous control of artificial limbs based on pattern recognition algorithms. *IEEE Trans. Neural Syst. Rehabilitation Eng.* 22, 756–764. doi:10.1109/TNSRE.2014.2305097

Osborn, L. E., Moran, C. W., Johannes, M. S., Sutton, E. E., Wormley, J. M., Dohopolski, C., et al. (2021). Extended home use of an advanced osseointegrated prosthetic arm improves function, performance, and control efficiency. *J. Neural Eng.* 18, 026020. doi:10.1088/1741-2552/abe20d

Østlie, K., Lesjø, I. M., Franklin, R. J., Garfelt, B., Skjeldal, O. H., and Magnus, P. (2012). Prosthesis rejection in acquired major upper-limb amputees: a population-based survey. *Disabil. Rehabilitation Assistive Technol.* 7, 294–303. doi:10.3109/17483107.2011.635405

Oxford Grice, K., Vogel, K. A., Le, V., Mitchell, A., Muniz, S., and Vollmer, M. A. (2003). Adult norms for a commercially available nine hole peg test for finger dexterity. *Am. J. Occup. Ther.* 57, 570–573. doi:10.5014/ajot.57.5.570

Park, J., Bae, W., Kim, H., and Park, S. (2008). "EMG —force correlation considering Fitts' law," in 2008 IEEE International Conference on Multisensor Fusion and Integration for Intelligent Systems, 644–649. doi:10.1109/MFI.2008.4648017

Parr, J. V. V., Galpin, A., Uiga, L., Marshall, B., Wright, D. J., Franklin, Z. C., et al. (2023). A tool for measuring mental workload during prosthesis use: the Prosthesis Task Load Index (PROS-TLX). *PLOS ONE* 18, e0285382. doi:10.1371/journal.pone.0285382

Pasquina, P. F., Perry, B. N., Miller, M. E., Ling, G. S., and Tsao, J. W. (2015). Recent advances in bioelectric prostheses. *Neurol. Clin. Pract.* 5, 164–170. doi:10.1212/CPJ.0000000000000132

Perry, B. N., Armiger, R. S., Yu, K. E., Alattar, A. A., Moran, C. W., Wolde, M., et al. (2018). Virtual integration environment as an advanced prosthetic limb training platform. *Front. Neurology* 9, 785. doi:10.3389/fneur.2018.00785

Pezzin, L. E., Dillingham, T. R., Mackenzie, E. J., Ephraim, P., and Rossbach, P. (2004). Use and satisfaction with prosthetic limb devices and related services 11No commercial party having a direct financial interest in the results of the research supporting this article has or will confer a benefit on the author(s) or on any organization with which the author(s) is/are associated. *Archives Phys. Med. Rehabilitation* 85, 723–729. doi:10.1016/j.apmr.2003.06.002

Phelan, I., Arden, M., Garcia, C., and Roast, C. (2015). "Exploring virtual reality and prosthetic training," in 2015 IEEE Virtual Reality (VR), 353–354. doi:10.1109/vr.2015.7223441

Phelan, I., Arden, M., Matsangidou, M., Carrion-Plaza, A., and Lindley, S. (2021). "Designing a virtual reality myoelectric prosthesis training system for amputees," in CHI EA '21 Extended Abstracts of the 2021 CHI Conference on Human Factors in Computing Systems (New York, NY, USA: Association for Computing Machinery). doi:10.1145/3411763.3443454

Portnova-Fahreeva, A. A., Rizzoglio, F., Casadio, M., Mussa-Ivaldi, F. A., and Rombokas, E. (2023). Learning to operate a high-dimensional hand via a low-dimensional controller. *Front. Bioeng. Biotechnol.* 11, 1139405. doi:10.3389/fbioe.2023.1139405

Prahm, C., Kayali, F., and Aszmann, O. (2019a). "MyoBeatz: using music and rhythm to improve prosthetic control in a mobile game for health," in 2019 IEEE 7th International Conference on Serious Games and Applications for Health (SeGAH), 1–6. doi:10.1109/SeGAH.2019.8882432

Prahm, C., Kayali, F., Sturma, A., and Aszmann, O. (2017a). Recommendations for games to increase patient motivation during upper limb amputee rehabilitation. *Biosyst. Biorobotics* 1157, 1157–1161. doi:10.1007/978-3-319-46669-9_188

Prahm, C., Kayali, F., Sturma, A., and Aszmann, O. (2018). PlayBionic: game-based interventions to encourage patient engagement and performance in prosthetic motor rehabilitation. *PM&R* 10, 1252–1260. doi:10.1016/j.pmrj.2018.09.027

Prahm, C., Kayali, F., Vujaklija, I., Sturma, A., and Aszmann, O. (2017b). Increasing motivation, effort and performance through game-based rehabilitation for upper limb myoelectric prosthesis control. 2017 International Conference on Virtual Rehabilitation (ICVR), 1–6. doi:10.1109/icvr.2017.8007517

Prahm, C., Schulz, A., Paaben, B., Schoisswohl, J., Kaniusas, E., Dorffner, G., et al. (2019b). Counteracting electrode shifts in upper-limb prosthesis control via transfer learning. *IEEE Trans. Neural Syst. Rehabilitation Eng.* 27, 956–962. doi:10.1109/tnsre.2019.2907200

Prahm, C., Vujaklija, I., Kayali, F., Purgathofer, P., and Aszmann, O. C. (2017c). Game-based rehabilitation for myoelectric prosthesis control. *JMIR Serious Games* 5, e3. doi:10.2196/games.6026

Preißler, S., Thielemann, D., Dietrich, C., Hofmann, G. O., Miltner, W. H. R., and Weiss, T. (2017). Preliminary evidence for training-induced changes of morphology and phantom limb pain. *Front. Hum. Neurosci.* 11, 319. doi:10.3389/fnhum.2017.00319

Radhakrishnan, M., Smailagic, A., French, B., Siewiorek, D. P., and Balan, R. K. (2019). "Design and assessment of myoelectric games for prosthesis training of upper limb amputees," in 2019 IEEE International Conference on Pervasive Computing and Communications Workshops Kyoto, Japan: (PerCom Workshops), 151–157. doi:10.1109/PERCOMW.2019.8730824

Radianti, J., Majchrzak, T. A., Fromm, J., and Wohlgenannt, I. (2020). A systematic review of immersive virtual reality applications for higher education: design elements, lessons learned, and research agenda. *Comput. Educ.* 147, 103778. doi:10.1016/j.compedu.2019.103778

Rahmani, E., and Boren, S. A. (2012). Videogames and health improvement: a literature review of randomized controlled trials. *Games Health J.* 1, 331–341. doi:10.1089/g4h.2012.0031

Resnik, L., Adams, L., Borgia, M., Delikat, J., Disla, R., Ebner, C., et al. (2013). Development and evaluation of the activities measure for upper limb amputees. *Archives Phys. Med. Rehabilitation* 94, 488–494.e4. doi:10.1016/j.apmr.2012.10.004

Resnik, L., Etter, K., Klinger, S. L., and Kambe, C. (2011). Using virtual reality environment to facilitate training with advanced upper-limb prosthesis. *J. Rehabilitation Res. Dev.* 48, 707. doi:10.1682/jrrd.2010.07.0127

Resnik, L., Meucci, M. R., Lieberman-Klinger, S., Fantini, C., Kelty, D. L., Disla, R., et al. (2012). Advanced upper limb prosthetic devices: implications for upper limb prosthetic rehabilitation. *Archives Phys. Med. Rehabilitation* 93, 710–717. doi:10.1016/j.apmr.2011.11.010

Roeschlein, R. A., and Domholdt, E. (1989). Factors related to successful upper extremity prosthetic use. *Prosthetics Orthot. Int.* 13, 14–18. doi:10.3109/03093648909079404

Rogers, C., Lau, J., Huynh, D., Albertson, S., Beem, J., and Qian, E. (2016). Capturing the perceived phantom limb through virtual reality. *Adv. Human-Computer Interact.* 2, 1–6. doi:10.1155/2016/8608972

Salminger, S., Stino, H., Pichler, L. H., Gstoettner, C., Sturma, A., Mayer, J. A., et al. (2022). Current rates of prosthetic usage in upper-limb amputees – have innovations had an impact on device acceptance? *Disabil. Rehabilitation* 44, 3708–3713. doi:10.1080/09638288.2020.1866684

Saposnik, G., Levin, M., and Outcome Research Canada (SORCan) Working Group (2011). Virtual reality in stroke rehabilitation: a meta-analysis and implications for clinicians. *Stroke* 42, 1380–1386. doi:10.1161/STROKEAHA.110.605451

Scheme, E., and Englehart, K. (2011). Electromyogram pattern recognition for control of powered upper-limb prostheses: state of the art and challenges for clinical use. *J. Rehabilitation Res. Dev.* 48, 643–659. doi:10.1682/JRRD.2010.09.0177

Scheme, E. J., and Englehart, K. B. (2013). Validation of a selective ensemble-based classification scheme for myoelectric control using a three-dimensional Fitts' law test. *IEEE Trans. Neural Syst. Rehabilitation Eng.* 21, 616–623. doi:10.1109/TNSRE.2012.2226189

Sharma, A., Hunt, C. L., Maheshwari, A., Osborn, L., Levay, G., Kaliki, R. R., et al. (2018). "A mixed-reality training environment for upper limb prosthesis control," in 2018 IEEE Biomedical Circuits and Systems Conference (BioCAS), 1–4. doi:10.1109/BIOCAS.2018.8584739

Sharma, A., Sharma, A., Niu, W., Hunt, C. L., Levay, G., Kaliki, R. R., et al. (2019). Augmented reality prosthesis training setup for motor skill enhancement. *arXiv: Human-Computer Interaction*

Simon, A. M., Hargrove, L. J., Lock, B. A., and Kuiken, T. A. (2011). Target Achievement Control Test: evaluating real-time myoelectric pattern-recognition control of multifunctional upper-limb prostheses. *J. rehabilitation Res. Dev.* 48, 619–627. doi:10.1682/jrrd.2010.08.0149

Simon, A. M., Lock, B. A., and Stubblefield, K. A. (2012). Patient training for functional use of pattern recognition–controlled prostheses. *JPO J. Prosthetics Orthot.* 24, 56–64. doi:10.1097/JPO.0b013e3182515437

Smith, P. A., Dombrowski, M., Buyssens, R., and Barclay, P. (2018a). The impact of a custom electromyograph (EMG) controller on player enjoyment of games designed to teach the use of prosthetic arms. *Comput. Games J.* 7, 131–147. doi:10.1007/s40869-018-0060-0

Smith, P. A., Dombrowski, M., Buyssens, R., and Barclay, P. (2018b). "Usability testing games for prosthetic training," in 2018 IEEE 6th International Conference on Serious Games and Applications for Health (SeGAH), 1–7. doi:10.1109/segah.2018.8401376

Snow, P. W., Sedki, I., Sinisi, M., Comley, R., and Loureiro, R. C. (2017). "Robotic therapy for phantom limb pain in upper limb amputees," in 2017 International Conference on Rehabilitation Robotics (ICORR), 1019–1024. doi:10.1109/ICORR.2017.8009383

Soares, A., Andrade, A., Lamounier, E., and Carrijo, R. (2003). The development of a virtual myoelectric prosthesis controlled by an EMG pattern recognition system based on neural networks. *J. Intelligent Inf. Syst.* 21, 127–141. doi:10.1023/A:1024758415877

Stucki, G. (2021). Advancing the rehabilitation Sciences. *Front. Rehabilitation Sci.* 1, 617749. doi:10.3389/fresc.2020.617749

Sveistrup, H. (2004). Motor rehabilitation using virtual reality. *J. NeuroEngineering Rehabilitation* 1, 10. doi:10.1186/1743-0003-1-10

Toledo-Peral, C. L., Vega-Martínez, G., Mercado-Gutiérrez, J. A., Rodríguez-Reyes, G., Vera-Hernández, A., Leija-Salas, L., et al. (2022). Virtual/augmented reality for rehabilitation applications using electromyography as control/biofeedback: systematic literature review. *Electronics* 11, 2271. doi:10.3390/electronics11142271

van Diest, M., Lamoth, C. J., Stegenga, J., Verkerke, G. J., and Postema, K. (2013). Exergaming for balance training of elderly: state of the art and future developments. *J. NeuroEngineering Rehabilitation* 10, 101. doi:10.1186/1743-0003-10-101

van Dijk, L., van der Sluis, C. K., van Dijk, H. W., and Bongers, R. M. (2016a). Learning an EMG controlled game: task-specific adaptations and transfer. *PLOS ONE* 11, e0160817. doi:10.1371/journal.pone.0160817

van Dijk, L., van der Sluis, C. K., van Dijk, H. W., and Bongers, R. M. (2016b). Task-oriented gaming for transfer to prosthesis use. *IEEE Trans. Neural Syst. Rehabilitation Eng.* 24, 1384–1394. doi:10.1109/tnsre.2015.2502424

Vasluian, E., Bongers, R., Reinders-Messelink, H., Burgerhof, J., Dijkstra, P., and Sluis, C. (2014). Learning effects of repetitive administration of the Southampton Hand Assessment Procedure in novice prosthetic users. *J. Rehabilitation Med.* 46, 788–797. doi:10.2340/16501977-1827

Wang, S., Hsu, C. J., Trent, L., Ryan, T., Kearns, N. T., Civillico, E. F., et al. (2018). Evaluation of performance-based outcome measures for the upper limb: a comprehensive narrative review. *PM&R* 10, 951–962.e3. doi:10.1016/j.pmrj.2018.02.008

Winslow, B. D., Ruble, M., and Huber, Z. (2018). Mobile, game-based training for myoelectric prosthesis control. *Front. Bioeng. Biotechnol.* 6, 94. doi:10.3389/fbioe.2018.00094

Woodward, R. B., Cancio, J. M., Fisher, R., Hargrove, L. J., Rábago, C. A., Siewiorek, D., et al. (2017). "A virtual coach for upper-extremity myoelectric prosthetic rehabilitation," in 2017 International Conference on Virtual Rehabilitation (ICVR), 1–2. doi:10.1109/ICVR.2017.8007495

Woodward, R. B., and Hargrove, L. J. (2019). Adapting myoelectric control in real-time using a virtual environment. *J. NeuroEngineering Rehabilitation* 16, 11. doi:10.1186/s12984-019-0480-5

Wu, X., Cao, W., Yu, H., Zhang, Z., Leng, Y., and Zhang, M. (2022). Generating electricity during locomotion modes dominated by negative work via a knee energy-harvesting exoskeleton. *IEEE/ASME Trans. Mechatronics* 27, 4451–4461. doi:10.1109/TMECH.2022.3157848

frontiers | Frontiers in Bioengineering and Biotechnology

TYPE Original Research
PUBLISHED 10 January 2024
DOI 10.3389/fbioe.2023.1349372

OPEN ACCESS

EDITED BY
Wujing Cao,
Chinese Academy of Sciences (CAS), China

REVIEWED BY
Jinzhu Zhang,
Taiyuan University of Technology, China
Xu Liang,
North China University of Technology, China

*CORRESPONDENCE
Fangyan Dong,
dongfangyan@nbu.edu.cn
Min Tang,
tangmin8493491@163.com

RECEIVED 04 December 2023
ACCEPTED 26 December 2023
PUBLISHED 10 January 2024

CITATION
Feng Y, Yu L, Dong F, Zhong M, Pop AA, Tang M and Vladareanu L (2024), Research on the method of identifying upper and lower limb coordinated movement intentions based on surface EMG signals.
Front. Bioeng. Biotechnol. 11:1349372.
doi: 10.3389/fbioe.2023.1349372

Research on the method of identifying upper and lower limb coordinated movement intentions based on surface EMG signals

Yongfei Feng[1,2], Long Yu[1], Fangyan Dong[1]*, Mingwei Zhong[1], Abigail Alexa Pop[3], Min Tang[4]* and Luigi Vladareanu[3]

[1]Faculty of Mechanical Engineering and Mechanics, Ningbo University, Ningbo, China, [2]Academy for Engineering and Technology, Fudan University, Shanghai, China, [3]Robotics and Mechatronics Department, Institute of Solid Mechanics of the Romanian Academy, Bucharest, Romania, [4]Department of Neurological Rehabilitation, Ningbo Rehabilitation Hospital, Ningbo, China

Rehabilitation robots have gained considerable focus in recent years, aiming to assist immobilized patients in regaining motor capabilities in their limbs. However, most current rehabilitation robots are designed specifically for either upper or lower limbs. This limits their ability to facilitate coordinated movement between upper and lower limbs and poses challenges in accurately identifying patients' intentions for multi-limbs coordinated movement. This research presents a multi-postures upper and lower limb cooperative rehabilitation robot (U-LLCRR) to address this gap. Additionally, the study proposes a method that can be adjusted to accommodate multi-channel surface electromyographic (sEMG) signals. This method aims to accurately identify upper and lower limb coordinated movement intentions during rehabilitation training. By using genetic algorithms and dissimilarity evaluation, various features are optimized. The Sine-BWOA-LSSVM (SBL) classification model is developed using the improved Black Widow Optimization Algorithm (BWOA) to enhance the performance of the Least Squares Support Vector Machine (LSSVM) classifier. Discrete movement recognition studies are conducted to validate the exceptional precision of the SBL classification model in limb movement recognition, achieving an average accuracy of 92.87%. Ultimately, the U-LLCRR undergoes online testing to evaluate continuous motion, specifically the movements of "Marching in place with arm swinging". The results show that the SBL classification model maintains high accuracy in recognizing continuous motion intentions, with an average identification rate of 89.25%. This indicates its potential usefulness in future rehabilitation robot-active training methods, which will be a promising tool for a wide range of applications in the fields of healthcare, sports, and beyond.

KEYWORDS

upper and lower limb coordinated movement, rehabilitation robot, motion intention recognition, SEMG signal, pattern classification

1 Introduction

According to statistics from the World Health Organization, approximately 15 million individuals worldwide suffer strokes annually, with over 80% of survivors experiencing motor function disorders (World Health Organization, 2023). Leveraging the human brain's plasticity, precise and timely rehabilitation training facilitates patients in neural reorganization or compensation. This process stimulates the creation of new neural cells related to motor function, thus significantly enhancing the chances of survival and recovery of motor abilities (Rossini et al., 2003). Traditional hemiplegia rehabilitation, mainly conducted by physicians providing manual training assistance, presents challenges such as increased workload, reduced efficiency, and an unbalanced physician-to-patient ratio (Rossini et al., 2003). The incorporation of rehabilitation robots in limb motor function rehabilitation training emerges as a newfound prospect for individuals afflicted with paralysis (Zhang et al., 2017).

In the past decade, there has been continuous development of intelligent robots for limb rehabilitation, attracting extensive attention from scholars (Pérez-Bahena et al., 2023). However, the current focus of rehabilitation robots primarily centers on the limbs most affected in patients, with relatively less research dedicated to rehabilitation robots that address multi-limbs coordination and balance training systems (Mu et al., 2019). Recent research on upper limb rehabilitation robots has concentrated on the joint rehabilitation of upper limbs but lacks attention to lower limb rehabilitation needs (Durand et al., 2019; Xie et al., 2022; Wu et al., 2023). Similarly, recently developed lower limb rehabilitation robots can only provide training for the patients' lower limbs (Han et al., 2019; Gao et al., 2022; Tian et al., 2022). However, relevant studies have shown that the movements of the upper and lower limbs are coupled and mutually influential during normal walking, with the normal swing of the upper limbs playing a crucial role in an individual's walking (Dietz et al., 2002; Arya et al., 2019). Rehabilitation robots that can coordinate upper and lower limb training consider the comprehensive recovery of limb function. By applying theories of motor neuron coupling, these robots enhance the strength and coordination of both upper and lower limbs through specific task training (Fang et al., 2017; Huo et al., 2019) integrated coordinated upper limb swing functions into the Rowas rehabilitation robot, ensuring synchronous movement between the lower limbs and the upper limb shoulder joint, thereby achieving coordinated rehabilitation of both upper and lower limbs in patients (Huang et al., 2023). designed an exoskeleton-based upper and lower limb rehabilitation robot system, planning training trajectories for the hip, knee, and shoulder joints. Therefore, it is necessary to design a robot that coordinates upper and lower limb rehabilitation. This approach aims to induce and reorganize abnormal coupling symptoms in the motor nerves of stroke patients, thereby enhancing rehabilitation treatment for the balance and coordination of the patient's limbs.

Clinical rehabilitation research suggests that tailoring rehabilitation training to the patient's limb movement patterns enhances rehabilitation efficiency (Pichiorri et al., 2015; Song et al., 2023). sEMG signals, known for their non-invasiveness and operational simplicity, serve as a common tool to reflect human muscle activity, facilitating research in human motion classification (Wu et al., 2016). employed a LLE model to streamline algorithm complexity and utilized the ELM for the swift classification of upper limb movements involving the shoulder, elbow, and wrist (Shao et al., 2020). accurately identified movements of the shoulder, elbow, and wrist joints using a combined SVD-WDBN classification model (Hu et al., 2021). used a sEMG array sensor to collect electrical signals from the muscles of the wrist and successfully recognized discrete gestures and continuous movements. However, the current stage of sEMG signal pattern recognition primarily focuses on single areas such as the upper limbs or hands, lacking research on the recognition of coordinated movement intentions between upper and lower limbs. Therefore, there is a need to develop an algorithm for multi-limbs movement intention recognition based on multi-channel sEMG signals. This algorithm would adapt to training movements of U-LLCRR, to achieve the goal of human-machine interaction.

In this study, the research mainly focuses on developing a human upper and lower limb coordinated movement intention recognition method based on the developed U-LLCRR and sEMG signals. The meachnical structure and hardware control system of the U-LLCRR are designed. Based on the robot's training mode, the study designs a recognition scheme for continuous motion, specifically the movements of 'Marching in place with arm swinging'. The SBL classification model is developed, integrating various classification models to enhance the classification of the extracted features. This study establishes a foundation for subsequent research in human-machine interaction control.

2 Materials and methods

2.1 Mechanical structure design of U-LLCRR

Figure 1A depicts the structure and key components of the proposed U-LLCRR, including lower limb rehabilitation module, upper limb rehabilitation module, multi-postures support module. As depicted in Figure 1B, the upper limb rehabilitation module, comprising of the shoulder joint servo motor, linear motor, and handle, transmits the driving force from the shoulder joint motor to the patient's whole upper limbs. The screw slider in the upper limb rehabilitation module adjusts the position of the shoulder joint servor motor to accommodate patients of varying heights. The linear motor induces linear motion at the wrist joint, enabling flexion and extension of bilateral shoulder-elbow-wrist joints in the human sagittal plane. In Figure 1C, the lower limb rehabilitation module adjusts the position of the ankle's foot pedal by modifying the linear motor, accommodating patients of varying heights. The lower limb rehabilitation module connects to the patient's thigh using velcro. The hip joint servo motor, leg drive rod, and foot pedal collaborate to transmit power from the servo motor to the patient's thigh, This enables flexion and extension of bilateral hip-knee-ankle joints in the human sagittal plane. In Figure 1D, the multi-postures support module enables rehabilitation training for bedridden patients in different posture, including lying posture, inclined lying posture, and standing posture. The omni-directional wheels offer mobility and stability to the multi-postures U-LLCRR. The extension and retraction of the electric push rod could raise and lower the movable support frame, thereby altering the robot's training postures' height.

Based on the mechanism design of the proposed U-LLCRR, it can achieve 8 types of inter-limb coordinated movements, including bilateral upper limbs symmetry/asymmetry movement, bilateral lower limbs symmetry/asymmetry movement, limbs symmetry/asymmetry in the same direction movement, and limbs symmetry/asymmetry in the opposite direction movement (Figure 2). Among these, the same

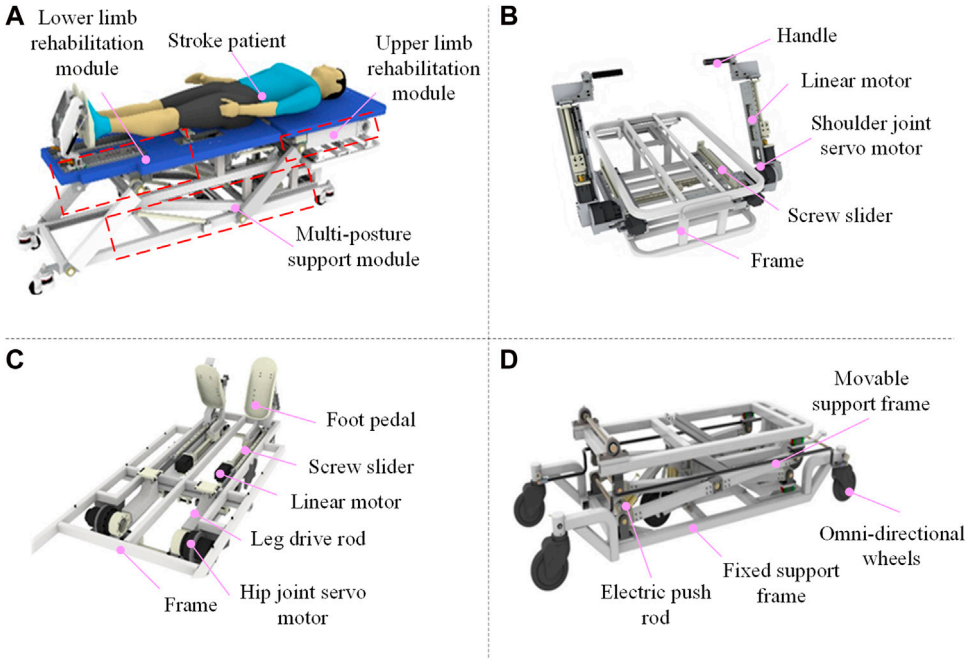

FIGURE 1
Structural diagram of the U-LLCRR. **(A)** Virtual overall prototype model. **(B)** Upper limb rehabilitation module. **(C)** Lower limb rehabilitation module. **(D)** Multi-posture support module.

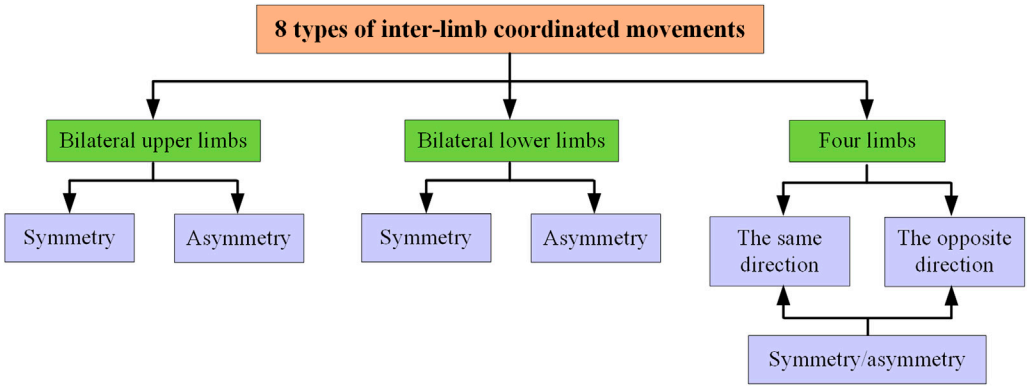

FIGURE 2
Eight types of inter-limb coordinated movements.

direction denotes that the upper and lower limbs on the same side move in the same direction, while symmetry implies that the left and right limbs move in the same direction. The proposed U-LLCRR overcomes the challenge of not being able to give patients synchronous upper and lower limb movements with current rehabilitation robots.

2.2 Hardware control system design of U-LLCRR

The hardware control system of U-LLCRR utilises a distributed control structure, as seen in Figure 3. This hardware control system features a high-level medical serial screen coupled with a low-level STM32. The whole hardware control system comprises a serial screen, an embedded microcontroller, drivers, servo motors, and supplementary components. The STM32 development board establishes communication with the upper-level medical serial screen using a serial port operating at a baud rate of 115,200 bits per second. Additionally, it communicates with the motor driver using CAN protocol at a frequency of 1,000 Hz. Upon receiving inputs from the higher echelons, the STM32 employs motion decoding to produce control signals for the servo motors. This approach streamlines periodic rehabilitation training by guiding the patient's limbs in continuous movements to predefined positions and velocities.

The study employs the BCIduino amplifier, developed by the Navigation Biology Company, for collecting sEMG data from

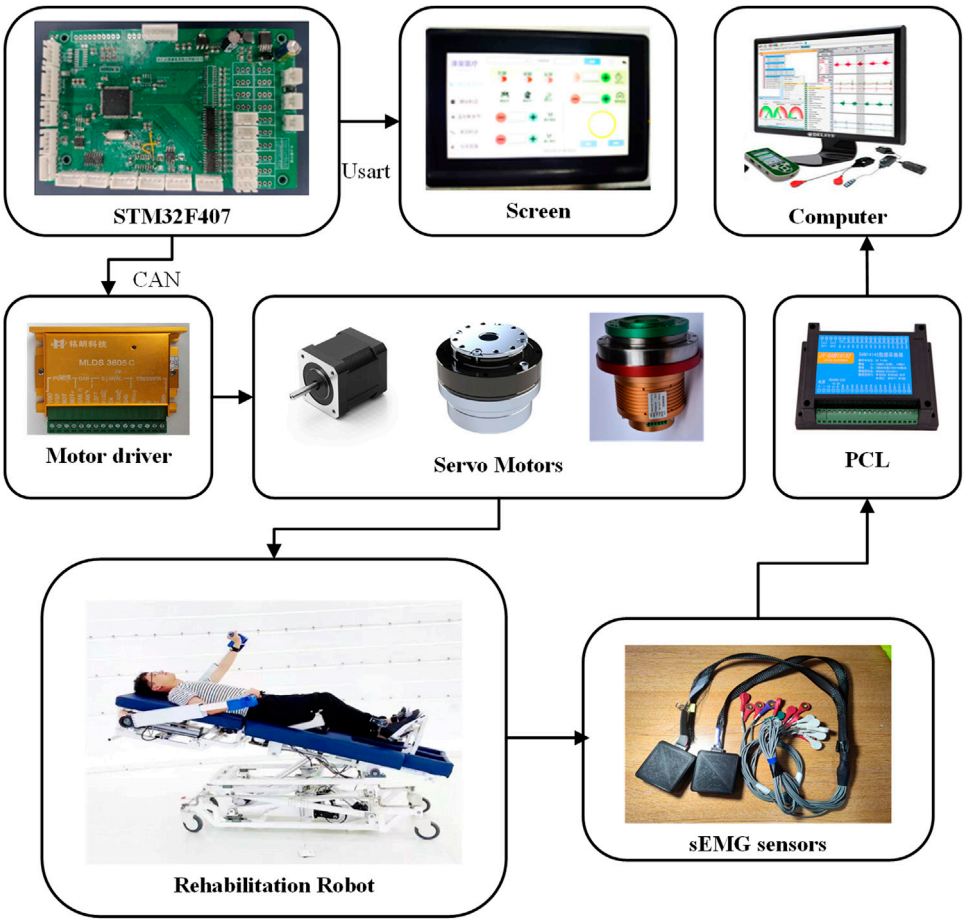

FIGURE 3
Electrical control and sEMG signal acquisition diagram for U-LLCRR.

specific muscle groups in the patient's upper and lower limbs. The hardware of BCIduino amplifier is composed of 16-channel wireless sensors designed for the capture of sEMG signals. The system uses OpenBCI software to carry out real-time filtering and visualisation of the sEMG data. During rehabilitation robot training, electromyographic information is consistently collected from the patient and transmitted to the PC (ISK, Lenovo Inc.) for real-time analysis.

2.3 Selection of classification movements

This study defines a six particular limb movements which includes upper and lower limb movements of marching in place with arm swinging. And the defined movements could be realized through the proposed U-LLCRR. The activities mentioned relate to movements in the sagittal plane, specifically including the shoulder and elbow for the upper limbs, and the hip, knee and ankle for the lower limbs. The six types of limb movements consist of left arm shoulder joint flexion/extension (LS-FLX), left arm elbow joint flexion/extension (LE-FLX), right arm shoulder joint flexion/extension (RS-FLX), right arm elbow joint flexion/extension (RE-FLX), left leg hip joint flexion/extension (LH-FLX), and right leg hip joint flexion/extension (RH-FLX). Different limb motions are associated with different muscle groups, necessitating precise sensor positioning to capture signals. The process of associating various types of limb movements with specific muscle groups, while considering factors like ease of measurement, signals diversity, and accurate differentiation (Feng et al., 2021), led to decision to specifically target certain muscles in the upper and lower limbs as shown in Figure 4. The muscle groups highlighted in red font represent the specific muscles targeted for sEMG signal acquisition. For the upper limbs, the selected muscles are the deltoid, biceps brachii, triceps brachii, and brachioradialis. For the lower limbs, the chosen muscles are the biceps femoris, semitendinosus, adductor magnus, and tensor fasciae latae.

2.4 Evaluation of feature separability

Feature extraction is necessary for the 16-channel sEMG signals once they have been collected and preprocessed. The chosen features consist of four time-domain measures, like mean absolute value (MAV), root mean square (RMS), variance (VAR), and integrated EMG (iEMG), as well as two frequency-domain measures, like mean frequency (MF) and median power frequency (MPF). The prolonged and detrimental use of sEMG characteristics, which includes extraneous noise and interference from sensor cables, can result in reduced in computational speed and accuracy (Hu et al., 2021).

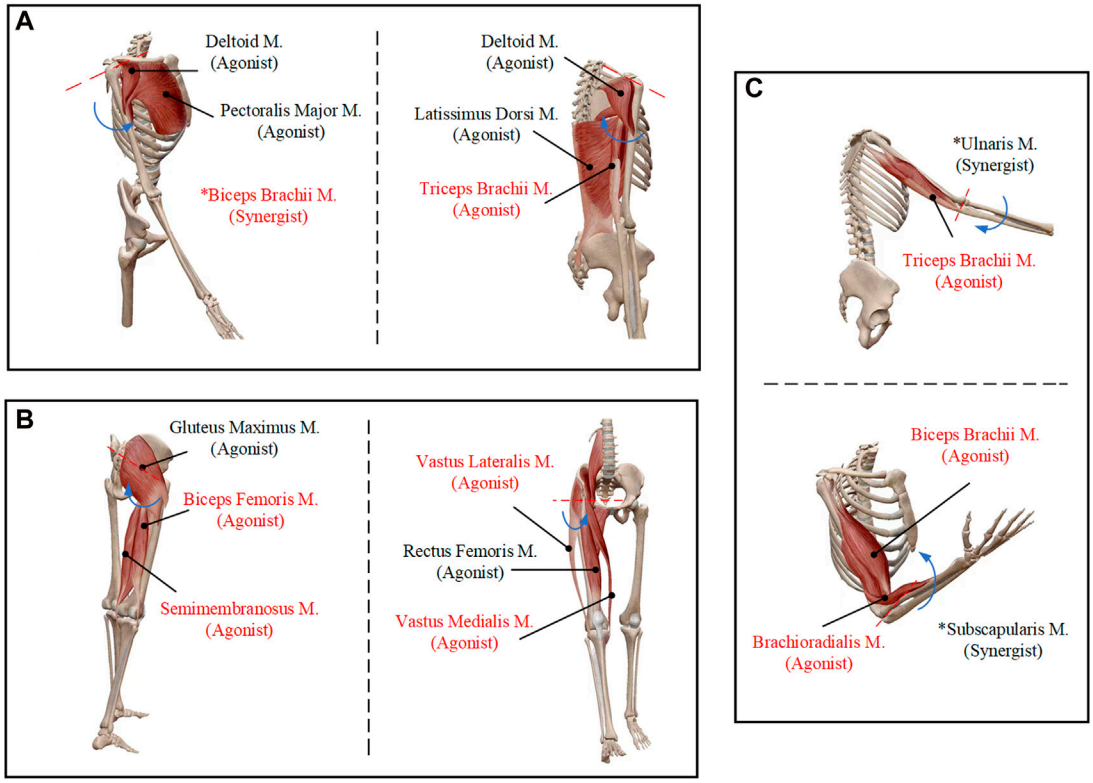

FIGURE 4
Six types of movements and the selected muscles. **(A)** Shoulder joint flexion/extension. **(B)** Elbow joint flexion/extension. **(C)** Hip joint flexion/extension.

This diminishes the system's ability to recognise intentions in real-time. This study introduces a novel approach to selecting features in sEMG differing from existing methods. It presents a method for evaluating feature discriminability based on dispersion calculation.

For various limb movement classes, the separability of intra-class and inter-class distances is evaluated using the Fisher function as a discriminant criterion (Zhang et al., 2012). This method calculates the average separations between different feature vectors across various combinations. Initially, samples from various categories are projected onto a single dimension. Subsequently, the average separations between samples inside and between classes are computed. Following this, the ideal projection direction of the function is determined. The underlying concept is to maximize the average distance between classes while minimizing the average distance within them. This serves as the separability discriminant for different limb movement categories. In this study, the approach is further expanded to provide average distances between multiple classes.

$$\begin{cases} J_d(x) = \sum_{i=1}^{c} P_i \left[\frac{1}{n_i} \sum_{k=1}^{n_i} \left(x_k^{(i)} - m_i \right)^T \left(x_k^{(i)} - m_i \right) + (m_i - m)^T (m_i - m) \right] \\ \boldsymbol{m}_i = \frac{1}{n_i} \sum_{k=1}^{n_i} \boldsymbol{x}_k^{(i)} \\ \boldsymbol{m} = \sum_{i=1}^{c} P_i \boldsymbol{m}_i \end{cases} \tag{1}$$

In Eq. 1, $J_d(x)$ represents the distance between the D-dimensional sample of class i and samples from other classes. A larger value indicates better separability of the feature (Liu et al., 2013). $\boldsymbol{m}_i$ is the mean vector of the $i-th$ class sample set, $\boldsymbol{m}$ is the overall mean vector of all class sample sets, $x_k{}^{(i)}$ is the D-dimensional feature vector within class i, and P_i is the prior probability of class i.

The Fisher fitness function, used in conjunction with the genetic algorithm, identifies the optimal combination of feature values. The algorithm iteratively determines the feature with the greatest dispersion among all features. The selected features form the input feature vector for the classification model.

2.5 Movement intention classification model

2.5.1 Least Squares Support Vector Machine (LSSVM)

The LSSVM classification model is employed to classify the features that were extracted. LSSVM, an enhanced SVM algorithm (Mellit et al., 2012), is known for its rapid convergence, accuracy, and solution speed. To prevent the classifier from getting trapped in a local optimum and to enhance the predicted performance of the classification model, adjusting the parameters '*gam*' and '*sig2*' in LSSVM is crucial. Traditional methods for determining LSSVM settings often depend on historical performance data (Ahmad et al.,

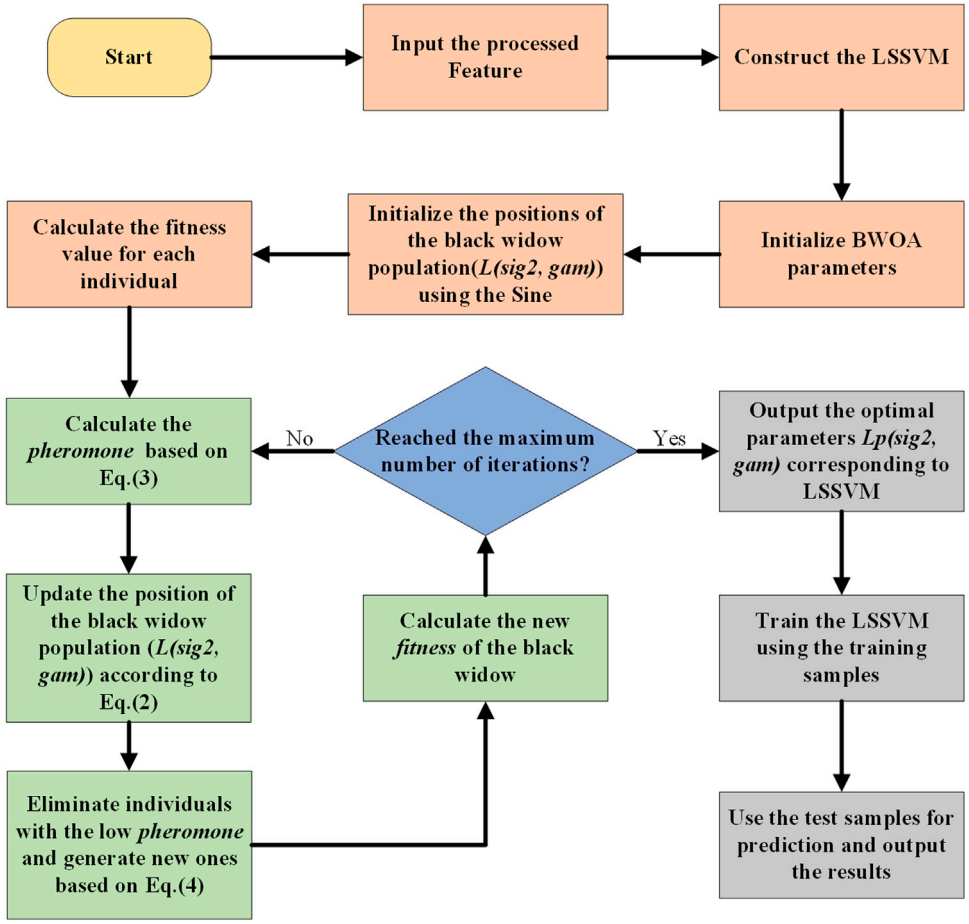

FIGURE 5
The SBL classification algorithm flow.

TABLE 1 Details of experimental protocol.

Experiment	Movement	Subject	Assistance	Data
I. Discrete test	Six types of limb movements	9	No	Online collection
II. Continuous decoding	'Marching in place with arm swinging' task	2	U-LLCRR	Online collection

2014). This study enhances the classification performance of LSSVM by fine-tuning the parameters '*gam*' and '*sig2*' within predefined ranges using intelligent optimization algorithms (Xue and Shen, 2020).

2.5.2 Improved BWOA based on sine chaotic mapping

Inspired by the hunting behavior of black widow spiders, characterized by both linear and spiral movements within their webs, the BWOA offers advantages in both local exploitation and global exploration (Hayyolalam and Pourhaji Kazem, 2019; Peña-Delgado et al., 2020). Population initialization, reproduction, intraspecific predation, mutation, and population update are its five stages. The remaining four stages, apart from the initial population stage, involve iteration until the termination criteria are met. This method employs LSSVM for classifying limb movements and determines the most fit "black widow" in the process.

The mathematical model is represented by Eq. 2:

$$\vec{x}_i(t+1) = \begin{cases} \vec{x}_*(t) - m\vec{x}_{r_1}(t), & \text{if rand}() \le 0.3 \\ \vec{x}_*(t) - \cos(2\pi\beta)\vec{x}_i(t), & \text{in other case} \end{cases} \quad (2)$$

In Eq. 2, $\vec{x}_i(t+1)$ denotes the updated individual position, $\vec{x}_*(t)$ represents the current optimal individual position, m is a random floating-point number generated between [0.4, 0.9], β is a random floating-point number within the range [-1, 1], r_1 is a random integer 1~npop, $\vec{x}_{r_1}(t)$ signifies the randomly selected position at index r_1, where $i \neq r_1$, and $\vec{x}_i(t)$ is the current individual's position.

The pheromone has a significant impact on the courtship behavior of black widow spiders. The pheromone deposition rate is defined as follows:

10.3389/fbioe.2023.1349372

TABLE 2 Movement sequences in the 'Marching in place with arm swinging' task.

Order	Sub-movements	Time(s)	Order	Sub-movements	Time(s)
Phase 1			Phase 3		
1	LS-FLX	1–3	12	LE-FLX	34–36
2	LE-FLX	4–6	13	RS-FLX	37–39
3	RS-FLX	7–9	14	RE-FLX	40–42
4	RE-FLX	10–12	15	LH-FLX	43–45
5	LH-FLX	13–15	16	RH-FLX	46–48
6	RH-FLX	16–18	Phase 4		
Phase 2			17	LH-FLX	49–51
7	LH-FLX	19–21	18	RE-FLX	52–54
8	RE-FLX	22–24	19	RS-FLX	55–57
9	RS-FLX	25–27			
10	LE-FLX	28–30			
11	LS-FLX	31–33			

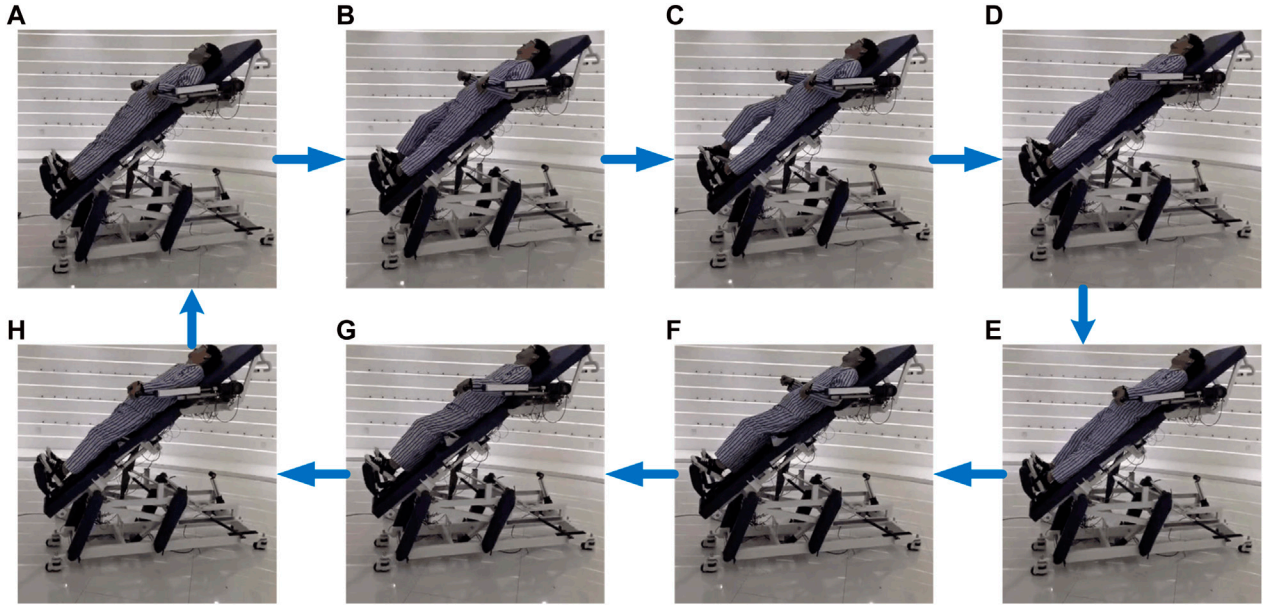

FIGURE 6
Actual upper and lower limbs coordinated movement process for subjects.

$$pheromone(i) = \frac{fitness_{\max} - fitness(i)}{fitness_{\max} - fitness_{\min}} \tag{3}$$

where, $fitness_{\max}$ and $fitness_{\min}$ denote the worst and best fitness values in the current population, respectively. $fitness(i)$ represents the fitness value of the $i-th$ individual. And the pheromone vector contains fitness values normalized within [0,1].

Black widow spiders with low pheromone levels often resort to cannibalizing the female spiders of the same species. These individuals face collective rejection by the population and may be abandoned by the group (Houssein et al., 2020). During the iterative process, when an individual with low pheromone is abandoned, it becomes imperative to promptly replenish the population count. When *pheromone* is less than or equal to 0.3, the individual's position is updated using Eq. 4:

$$\vec{x}_i(t) = \vec{x}_\star(t) + \frac{1}{2}\left[\vec{x}_{r_1}(t) - (-1)^\sigma \vec{x}_{r_2}(t)\right] \tag{4}$$

where, $\vec{x}_i(t)$ represents the position of the black widow with low pheromone levels within the female's body. r_1 and r_2 are random

FIGURE 7
Frequency and time domain features for 16 channels.

integers between 1~npop, with $r_1 \neq r_2$ $\vec{x}_{r_1}$ and $\vec{x}_{r_2}$ denote the positions of the black widow spiders at indices r_1 and r_2, and $\sigma \in \{0, 1\}$ is a random binary number.

Given that the initial positions of the black widow population are randomly generated, the study employs chaotic initialization using the Sine function from the chaos mapping strategy (Wu et al., 2021). This improves the quality of initial solutions, ensuring a more uniform distribution of the population within the search space. The expression is as follows:

$$x_{k+1} = \frac{a}{n}\sin(\pi x_k), a \in (0, n] \tag{5}$$

Where k is the iteration count, x_k is the $k-th$ chaotic number, and a is a random number.

2.5.3 Sine-BWOA-LSSVM classification model

Each prediction model has its own set of advantages and disadvantages. By logically combining multiple single models, the shortcomings of each individual prediction model can be significantly mitigated, thereby enhancing forecast accuracy. To optimize the LSSVM classification method in Figure 5, this research presents a hybrid classification recognition model based on the improved BWOA with chaotic mapping, namely, the SBL classification model. The following are the precise steps:

- Step 1, Initialize basic parameters for BWOA, including the maximum number of iterations, procreating rate (PP), cannibalism rate (CR), and mutation rate (PM).
- Step 2, Initialize the positions of the black widow population using Sine chaotic mapping. The initial population is selected from fitness-sorted black widow individuals.
- Step 3, Use Sine-BWOA to optimize '*gam*' and '*sig2*' in LSSVM. Optimal parameters '*gam*' and '*sig2*' for LSSVM are obtained by iteratively updating the positions of black widow spiders.
- Step 4, Update LSSVM model, and conduct training and testing to obtain recognition results for feature output.

3 Experiments and results

Discrete limb combination experiments without robot assistance, and online decoding experiments based on the U-LLCRR are conducted as detailed in Table 1.

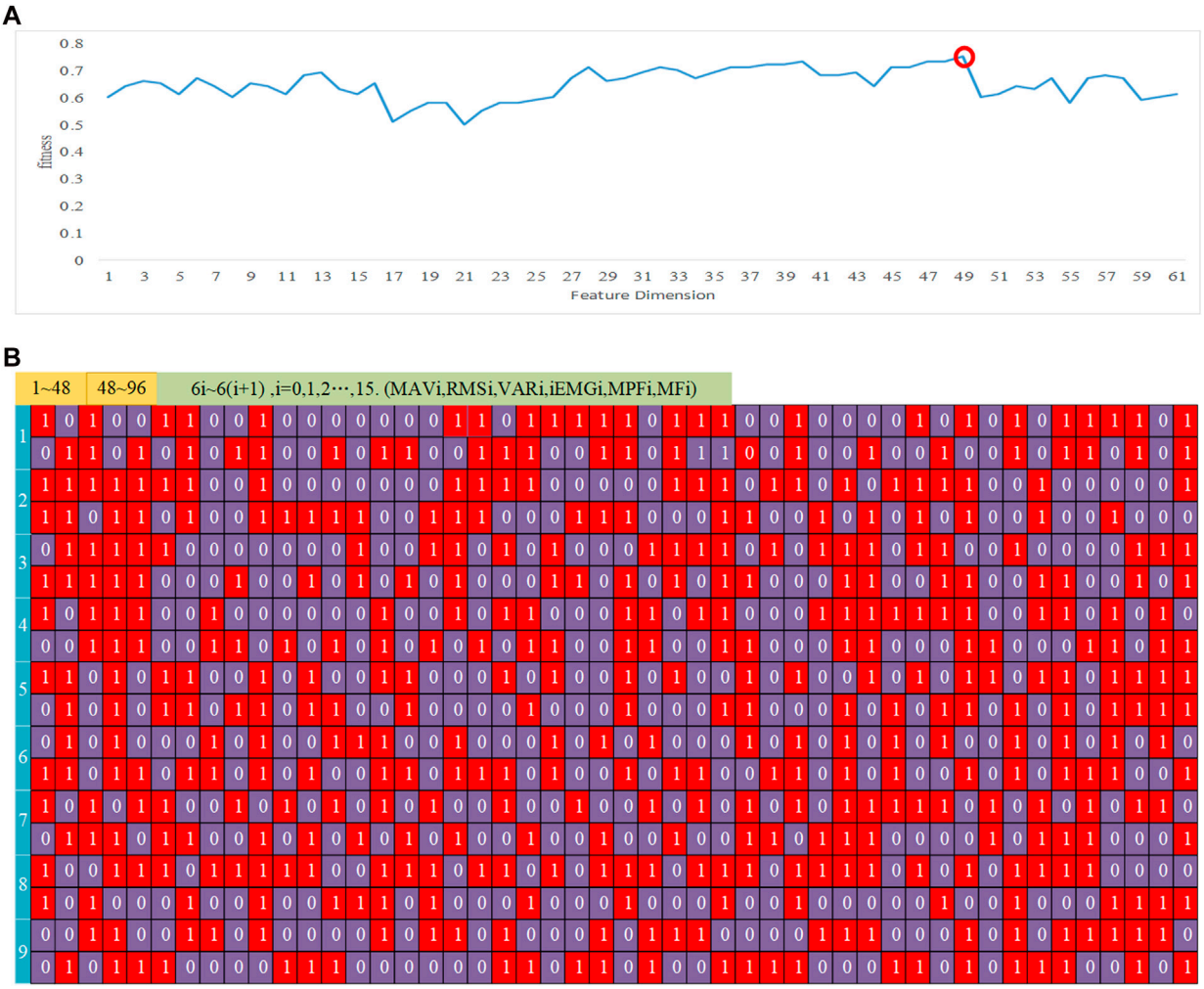

FIGURE 8
Optimal feature vector combinations. **(A)** Dissimilarity iteration curves across various dimensions and features. **(B)** The selection of optimal feature vectors.

3.1 Training and discrete testing of the SBL classifier

In this experiment, discrete data on six types of limb movements were collected from 9 healthy participants using a 16-channel sEMG signal capture device. Preprocessing procedures, such as noise reduction and bias removal, were applied to the collected sEMG signals. A **D** (96) feature vector, comprising six different types of features, was created from the extracted sEMG signal. In the feature selection process, a genetic algorithm and a discreteness computation were employed, resulting in **d** (48) feature vector. The data was split into a 30% test set and a 70% training set. Subsequently, the SBL classification model was trained offline using the training set. The trained model was subsequently applied for the recognition of online movements. To validate the robustness of the proposed categorization model, its experimental findings were compared with those from other models.

The subjects executed the aforementioned six types of limb movement combinations, performing each in 3 experimental sets. Each set consisted of 10 repetitions, with completion of each combination movement lasting approximately 4–5 s. The time interval between successive collections of the same combination movement was 6–8 s, and there was a 1–5 min interval between each set of experiments. Before each subsequent sEMG data collection session, it was confirmed that each subject was free from muscle fatigue. During the data collection process, the sensors continuously transmitted the acquired sEMG signals in real-time to a computer. This process yielded 180 data points for each type of limb movement per subject, resulting in a total of 2,880 data samples.

3.2 Continuous motion decoding

In order to verify the classification model's ability to make accurate generalizations, a continuous motion recognition experiment is conducted, with the "Marching in place with arm swinging" assignment from the ADL training (Kwakkel et al., 2004). The experiment consists of four phases and fully includes the six types of selected limb movements mentioned above. The movement

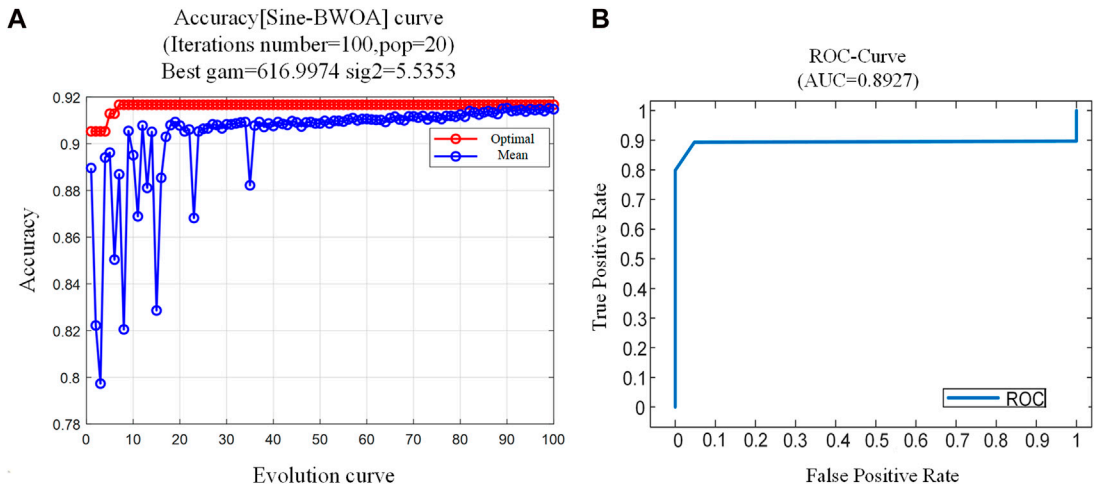

FIGURE 9
Training results of the SBL model. **(A)** Sine-BWOA fitness curve. **(B)** the ROC curve of the SBL model.

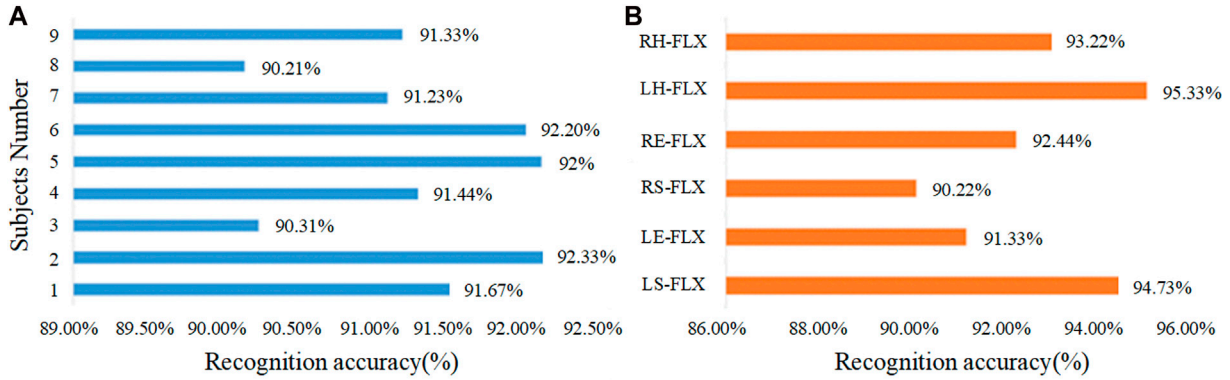

FIGURE 10
Accuracy of motion recognition **(A)** Subject body movements. **(B)** Discrete movements.

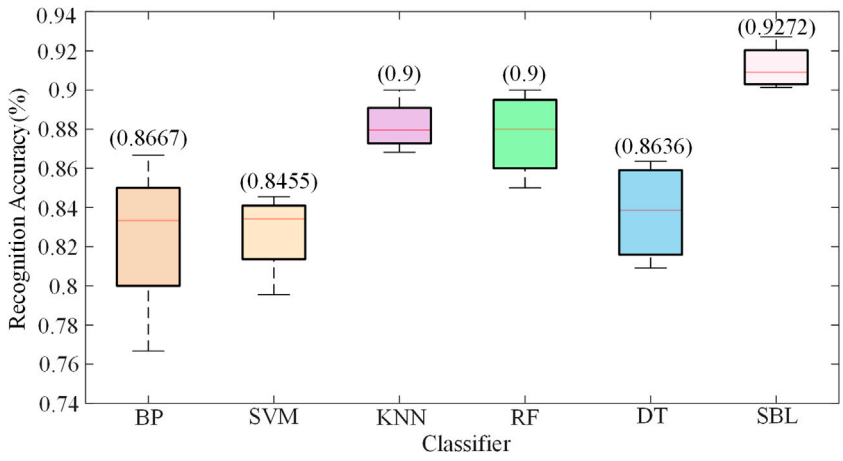

FIGURE 11
Recognition accuracy based on different classifiers.

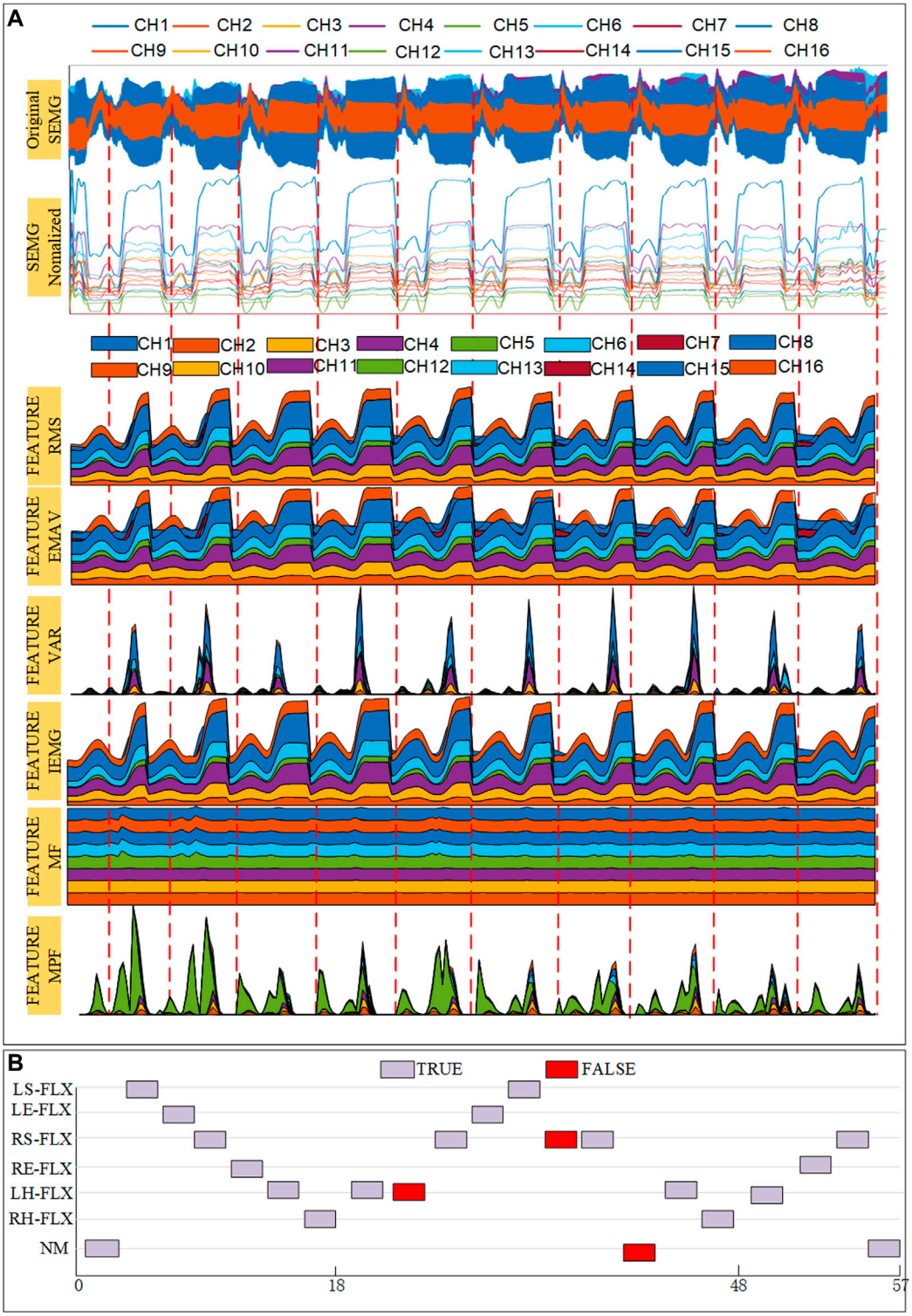

FIGURE 12
Experimental results of subject No. I in continuous movement. **(A)** Signal acquisition and feature value results **(B)** Continuous movement classification results.

sequence is outlined in Table 2. Using the U-LLCRR, 2 subjects are selected to participate in the experiment. They perform the "Marching in place with arm swinging" continuously on the U-LLCRR, ensuring consistent and uninterrupted movement. Figure 6 illustrates the real-time identification of subjects' sEMG data.

TABLE 3 Confusion matrix of recognition results.

movements to be recognized	Movements Recognition Results								Accuracy
		LS-FLX	LE-FLX	RS-FLX	RE-FLX	LH-FLX	RH-FLX	NM	
	LS-FLX	2	3						80.7%
	LE-FLX	1	20						95.2%
	RS-FLX			25		2			90.6%
	RE-FLX	1	1		17			1	89.47%
	LH-FLX					21	1		95.45%
	RH-FLX					1	26		95.29%
	NM	1		3		1		10	76.92%
Accuracy		87.5%	80%	94.6%	100%	87.5%	95.3%	90.9%	89.25%

Each limb movement lasts for 3 s. Every subject performs four sets of continuous movements, following a specific motion sequence. Each set consists of 5 repetitions, totaling 20 repetitions per subject. The sEMG signals collected from subjects undergo the previously mentioned feature selection and SBL classification model method training. The training data is then input into the optimization algorithm for continuous limbs movement intention recognition, maintaining a 3:1 ratio for training and testing datasets, respectively. This process aims to validate the model's accuracy in recognizing continuous movements and establishes a foundation for future research into the application of rehabilitation robots in active training.

3.3 Result of discrete test of the sine-BWOA-LSSVM classifier

3.3.1 Feature processing

After preprocessing the sEMG data obtained from 16 channels across 9 subjects, feature analysis was conducted in both the time and frequency domains. Figure 7 depicts the mean values of the six types of limb movements. The four time-domain features (MAV, RMS, VAR, iEMG) are somewhat effective in distinguishing between the movements. Some aspects demonstrated noticeable overlap, especially in movements involving the shoulder joint. Frequency-domain signals (MPF, MF) showed reduced variability and greater stability compared to the time-domain signals.

Constructing larger-dimensional feature vectors by utilizing disparities among features enables more effective information extraction and improves movements differentiation. The calculated features were combined to form a 16 × 6 dimensional feature matrix encompassing various categories. To select a suitable multi-dimensional feature dimension, designated as $\mathbf{d}$ (n), dissimilarity was estimated using inter-class evaluation metrics from the above. Figure 8A illustrates the variations in dissimilarity across different dimensions and features after 100 cycles. Dissimilarity peaked at a feature dimension of 48, reaching a value of 0.75. Consequently, a total of 48 dimensions were selected. The 96-dimensional feature values were consolidated into $\mathbf{d}$ (48) composite feature vectors, and GA were repeatedly employed to assess dissimilarity using the Fisher function. Figure 8B displays the most favorable feature combinations of for the 9 subjects following iterative combination. The blue marks in Figure 8B represent the topic numbers, while the yellow on the right side indicates the layout. The red squares indicate a value of 1, representing the selected feature vectors, while the blue squares with a value of 0, represent the non-selected feature vectors.

3.3.2 SBL classification model validation

In applying the classification model for recognizing limb movement intentions, the BWOA parameters were initialized with a population size ($Pop = 20$), the iteration index ($i = [0{:}100]$), $PP = 0.8$, $PM = 0.4$, and an infinitesimally small constant ($\varepsilon = 10E - 8$).

The first 15 instances of each movement, collected from the 9 subjects and totaling 1,440 instances, were used as the training dataset. The SBL classifier was trained using the optimal feature vectors obtained from the feature vector selection process (Figure 9), denoted as $\mathbf{d}$ (48) for each subject. Figure 9A shows the Sine-BWOA fitness variation curve, indicating that the population fitness gradually stabilizes after 35 iterations. The iterative results indicated that the optimal parameters for the LSSVM are gam = 616.9974 and $sig2$ = 5.5353. Figure 9B presents the ROC (receiver operating characteristic) curve for the model, with an AUC (area under curve) of 0.8927. Given that 1 > AUC > 0.5, it indicates that the SBL classification model exhibits good classification performance.

The SBL classification model was tested using the most recent 15 instances of each activity from 9 subjects, yielding a total of 1,440 instances. The outcomes of this test are illustrated in Figure 10A. The graph shows minor fluctuations in identification rates across the participants, but the overall results are quite consistent, with an average recognition rate of 91.413%. Subject No.8 has the lowest percentage of limb movement intention recognition rate at 90.21%, while the highest rate is 92.33% in Subject No.2. Figure 10B shows the results of the categorization test for the six types of limb movements, with an average recognition rate of 92.87%. Among the movements, LH-FLX has the highest recognition rate at 95.33%, while RS-FLX has the lowest recognition rate at 90.22%. The primary factor contributing to this variance is the susceptibility of sEMG signals from various muscle groups to interference during these specific actions.

To confirm the reliability of the developed the SBL classifier, the data were tested using five widely utilized classification algorithms, namely, SVM, BPNN (backpropagation neural network), KNN (k-nearest neighbor), RF (random forest), and DT (decision tree). Figure 11 provides a comparative analysis of the categorization performance. This figure clearly shows that the SBL classifier outperforms other classifiers in motion intention recognition, using the same sample data.

3.4 Result of continuous movement intentions decoding

During a specific instance of continuous movement, raw sEMG signals, normalized sEMG data, and an overlaid graph displaying characteristic values were gathered from subject No. I, as depicted in Figure 12A. The figure shows preprocessed data graphs derived from 16 channels of sEMG data, collected from both the upper and lower limbs. The data underwent denoising and normalization procedures. The overlaid graphs illustrate the extent of six characteristics measured from the processed data. The feature combination vectors were then inputted into the SBL classification model, and the resulting classification outcome is depicted in Figure 12B. In this depiction, 'NM' denotes the condition of no movement, grayscale squares represent accurate classifications, and red squares represent incorrect classifications.

Following the test findings, the confusion matrix for continuous limb movement recognition was derived, which was displayed in Table 3. In the table, the blue area indicates the count of accurate classifications, while the orange section indicates the count of incorrect classifications. This matrix presents the results of 240 consecutive movements performed by a single individual, detected using the SBL classifier. Subject No. I's continuous movements achieved an average recognition rate of 89.25%. The recognition rates for the six types of limb movements RS-FLX, RE-FLX, and RH-FLX actions, are the highest, at 94.6%, 100%, and 95.29% respectively, all exceeding 90%. Conversely, LS-FLX, LE-FLX, and LH-FLX have recognition rates of 87.5%, 80%, and 87.5%, respectively. These rates fall within the 80%–90% range. The primary challenge contributing to this issue is the overlapping of movement processes, causing significant interference across muscle groups in different channels. Although continuous movement recognition may show reduced accuracy compared to individual movement intention recognition, the overall findings are still sufficiently reliable and suitable for subsequent active rehabilitation training using the U-LLCRR.

4 Conclusion

A novel multi-postures upper and lower limb cooperative rehabilitation robot has been proposed, enabling the realization of eight distinct coordinated limb movements. This innovation establishes a physical platform for the identification of upper and lower limb coordinated movement intentions based on sEMG signals. Multi-dimensional sEMG signal classification and continuous movement recognition methods have been explored, leading to the proposal of a SBL classification model. It has been demonstrated through experimental results that the model excels in recognizing limb motion intentions, especially in differentiating between various limb movements, with some movement achieving recognition rates above 90%. Although a slight reduction in accuracy for continuous movement recognition has been observed, the overall results have been found to be reliable, rendering the model suitable for active rehabilitation training using the U-LLCRR. This outcome is significant for the development of more effective and personalized rehabilitation training programs. The effectiveness of the SBL model in continuous movement recognition has been validated, providing valuable insights for future advancements in rehabilitation technology. Future research will be directed towards enhancing the model's robustness and exploring a broader range of movement patterns, with the aim of expanding the application scope of rehabilitation robot technology.

Data availability statement

The original contributions presented in the study are included in the article/Supplementary material, further inquiries can be directed to the corresponding authors.

Ethics statement

The studies involving humans were approved by the Medical Ethics Committee of Ningbo University. The studies were conducted in accordance with the local legislation and institutional requirements. Written informed consent for participation in this study was provided by the participants' legal guardians/next of kin.

Author contributions

YF: Conceptualization, Data curation, Methodology, Writing–original draft. LY: Conceptualization, Formal Analysis, Methodology, Writing–original draft. FD: Conceptualization, Funding acquisition, Methodology, Writing–original draft. MZ: Formal Analysis, Methodology, Writing–original draft. AP: Resources, Writing–review and editing. MT: Conceptualization, Funding acquisition, Writing–review and editing. LV: Resources, Writing–review and editing.

Funding

The author(s) declare financial support was received for the research, authorship, and/or publication of this article. This research was funded by the National Natural Science Foundation Youth Science Fund Project of China (52305025), the China Postdoctoral Science Foundation (2023M740662) and the Ningbo International Cooperation Project (2023H014).

Conflict of interest

The authors declare that the research was conducted in the absence of any commercial or financial relationships that could be construed as a potential conflict of interest.

Publisher's note

References

Ahmad, A. S., Hassan, M. Y., Abdullah, M. P., Rahman, H. A., Hussin, F., Abdullah, H., et al. (2014). A review on applications of ANN and SVM for building electrical energy consumption forecasting. *Renew. Sustain. Energy Rev.* 33, 102–109. doi:10.1016/j.rser.2014.01.069

Arya, K. N., Pandian, S., Sharma, A., Kumar, V., and Kashyap, V. K. (2019). Interlimb coupling in poststroke rehabilitation: a pilot randomized controlled trial. *Top. Stroke Rehabil.* 27, 272–289. doi:10.1080/10749357.2019.1682368

Dietz, V., Fouad, K., and Bastiaanse, C. M. (2002). Neuronal coordination of arm and leg movements during human locomotion. *Eur. J. Neurosci.* 14, 1906–1914. doi:10.1046/j.0953-816x.2001.01813.x

Durand, S., Rohan, C. P.-Y., Hamilton, T., Skalli, W., and Krebs, H. I. (2019). Passive wrist stiffness: the influence of handedness. *IEEE Trans. Biomed. Eng.* 66, 656–665. doi:10.1109/tbme.2018.2853591

Fang, J., Xie, Q., Yang, G.-Y., and Xie, L. (2017). Development and feasibility assessment of a rotational orthosis for walking with arm swing. *Front. Neurosci.* 11, 32. doi:10.3389/fnins.2017.00032

Feng, Y., Zhong, M., Wang, X., Lu, H., Wang, H., Liu, P., et al. (2021). Active triggering control of pneumatic rehabilitation gloves based on surface electromyography sensors. *PeerJ Comput. Sci.* 7, e448. doi:10.7717/peerj-cs.448

Gao, M., Wang, Z., Pang, Z., Sun, J., Li, J., Li, S., et al. (2022). Electrically driven lower limb exoskeleton rehabilitation robot based on anthropomorphic design. *Machines* 10, 266. doi:10.3390/machines10040266

Han, Y., Zhu, S., Zhou, Y., and Gao, H. (2019). An admittance controller based on assistive torque estimation for a rehabilitation leg exoskeleton. *Intell. Serv. Robot.* 12, 381–391. doi:10.1007/s11370-019-00289-4

Hayyolalam, V., and Pourhaji Kazem, A. A. (2019). Black Widow Optimization Algorithm: a novel meta-heuristic approach for solving engineering optimization problems. *Eng. Appl. Artif. Intell.* 87, 103249. doi:10.1016/j.engappai.2019.103249

Houssein, E. H., Helmy, B. E., Oliva, D., Elngar, A. A., and Shaban, H. (2020). A novel Black Widow Optimization algorithm for multilevel thresholding image segmentation. *Expert Syst. Appl.* 167, 114159. doi:10.1016/j.eswa.2020.114159

Hu, X., Zeng, H., Song, A., and Chen, D. (2021). Robust continuous hand motion recognition using wearable array Myoelectric sensor. *IEEE Sens. J.* 21, 20596–20605. doi:10.1109/jsen.2021.3098120

Huang, J., Guo, L., Cao, Y., Xue, L., Zhang, J., and Ning, H. (2023). Design of upper-and-lower-limb-coordinated active rehabilitation motion control system for rehabilitation robot. *Chin. Med. Equip. J.* 44, 15–20. doi:10.19745/j.1003-8868.2023087

Huo, C., Xu, G., Li, Z., Lv, Z., Liu, Q., Li, W., et al. (2019). Limb linkage rehabilitation training-related changes in cortical activation and effective connectivity after stroke: a functional near-infrared spectroscopy study. *Sci. Rep.* 9, 6226. doi:10.1038/s41598-019-42674-0

Kwakkel, G., van Peppen, R., Wagenaar, R. C., Wood Dauphinee, S., Richards, C., Ashburn, A., et al. (2004). Effects of augmented exercise therapy time after stroke: a meta-analysis. *Stroke* 35, 2529–2539. doi:10.1161/01.str.0000143153.76460.7d

Liu, Y., Li, Z., Xiong, H., Gao, X., Wu, J., and Wu, S. (2013). Understanding and enhancement of internal clustering validation measures. *IEEE Trans. Cybern.* 43, 982–994. doi:10.1109/tsmcb.2012.2220543

Mellit, A., Pavan, A. M., and Benghanem, M. (2012). Least squares support vector machine for short-term prediction of meteorological time series. *Theor. Appl. Climatol.* 111, 297–307. doi:10.1007/s00704-012-0661-7

Mu, Z., Fang, J., Chen, L., and Zhang, Q. (2019). Design of structure and control system for a rotational orthosis for walking with arm swing. *Chin. J. Eng. Des.* 26, 736–742. doi:10.3785/j.issn.1006-754X.2019.00.005

Peña-Delgado, A. F., Peraza-Vázquez, H., Almazán-Covarrubias, J. H., Torres Cruz, N., García-Vite, P. M., Morales-Cepeda, A. B., et al. (2020). A novel bio-Inspired algorithm applied to selective harmonic elimination in a three-phase eleven-level inverter. *Math. Probl. Eng.* 2020, 1–10. doi:10.1155/2020/8856040

Pérez-Bahena, M. H., Niño-Suarez, P. A., Sánchez, O. F. A., Beleño, R. H., Caldas, O. I., and Pellico-Sánchez, O. I. (2023). Trends in robotic systems for lower limb rehabilitation. *IETE Tech. Rev.*, 1–12. doi:10.1080/02564602.2023.2185691

Pichiorri, F., Morone, G., Petti, M., Toppi, J., Pisotta, I., Molinari, M., et al. (2015). Brain-computer interface boosts motor imagery practice during stroke recovery. *Ann. Neurol.* 77, 851–865. doi:10.1002/ana.24390

Rossini, P. M., Calautti, C., Pauri, F., and Baron, J.-C. (2003). Post-stroke plastic reorganisation in the adult brain. *Lancet Neurol.* 2, 493–502. doi:10.1016/s1474-4422(03)00485-x

Shao, J., Niu, Y., Xue, C., Wu, Q., Zhou, X., Xie, Y., et al. (2020). Single-channel sEMG using wavelet deep belief networks for upper limb motion recognition. *Int. J. Ind. Ergon.* 76, 102905. doi:10.1016/j.ergon.2019.102905

Song, T., Yan, Z., Guo, S., Li, Y., Li, X., and Xi, F. (2023). Review of sEMG for robot control: techniques and applications. *Appl. Sci.* 13, 9546. doi:10.3390/app13179546

Tian, J., Yuan, L., Xiao, W., Ran, T., Zhang, J., and He, L. (2022). Constrained control methods for lower extremity rehabilitation exoskeleton robot considering unknown perturbations. *Nonlinear Dyn.* 108, 1395–1408. doi:10.1007/s11071-022-07272-2

World Health Organization (2023). Stroke, cerebrovascular accident: health topics. Available at: http://www.emro.who.int/health-topics/stroke-cerebrovascular-accident (Accessed January 24, 2023).

Wu, C., Sun, K., and Xiao, Y. (2021). A hyperchaotic map with multi-elliptic cavities based on modulation and coupling. *Eur. Phys. J. Spec. Top.* 230, 2011–2020. doi:10.1140/epjs/s11734-021-00126-9

Wu, Q., Shao, J., Wu, X., Zhou, Y., Liu, F., and Xiao, F. (2016). Upper limb motion recognition based on LLE-ELM method of sEMG. *Intern J. Pattern Recognit. Artif. Intell.* 31, 1750018. doi:10.1142/s0218001417500185

Wu, Q., Wang, Z., and Chen, Y. (2023). sEMG-based adaptive cooperative multi-mode control of a soft elbow exoskeleton using neural network compensation. *IEEE Trans. Neural Syst. Rehabilitation Eng.* 31, 3384–3396. doi:10.1109/tnsre.2023.3306201

Xie, P., Lin, C., Cai, S., and Xie, L. (2022). Learning-based compensation-corrective control strategy for upper limb rehabilitation robots. *Int. J. Soc. Robot.* doi:10.1007/s12369-022-00943-5

Xue, J., and Shen, B. (2020). A novel swarm intelligence optimization approach: sparrow search algorithm. *Syst. Sci. Control Eng.* 8, 22–34. doi:10.1080/21642583.2019.1708830

Zhang, D., Ren, Y., Gui, K., Jia, J., and Xu, W. (2017). Cooperative control for a hybrid rehabilitation system combining functional electrical stimulation and robotic exoskeleton. *Front. Neurosci.* 11, 725. doi:10.3389/fnins.2017.00725

Zhang, Z., Li, J., Li, X., Huang, H., Zhou, L., and Xiong, T. (2012). High efficiency iron removal from quartz sand using phosphoric acid. *Int. J. Min. Process* 114 (117), 30–34. doi:10.1016/j.minpro.2012.09.001

frontiers | Frontiers in Bioengineering and Biotechnology

TYPE Original Research
PUBLISHED 10 January 2024
DOI 10.3389/fbioe.2023.1342229

OPEN ACCESS

EDITED BY
Wujing Cao,
Chinese Academy of Sciences (CAS), China

REVIEWED BY
Wen-Ming Chen,
Fudan University, China
Zhen Geng,
Shanghai University, China

*CORRESPONDENCE
Hongbo Yang,
yanghb@sibet.ac.cn
Xiaofeng Shen,
29240818@qq.com
Yuwei Li,
lyw97538@126.com

RECEIVED 21 November 2023
ACCEPTED 26 December 2023
PUBLISHED 10 January 2024

CITATION
Zha Q, Xu Z, Yang H, Zhang G, Cai X, Zhang W, Liu Y, Shen X and Li Y (2024), Development of a robot-assisted reduction and rehabilitation system for distal radius fractures.
Front. Bioeng. Biotechnol. 11:1342229.
doi: 10.3389/fbioe.2023.1342229

Development of a robot-assisted reduction and rehabilitation system for distal radius fractures

Qing Zha[1,2], Zeou Xu[1,2], Hongbo Yang[1,2]*, Guodong Zhang[3], Xuefeng Cai[3], Wanlin Zhang[3], Yujiang Liu[3], Xiaofeng Shen[3]* and Yuwei Li[3]*

[1]School of Biomedical Engineering (Suzhou), Division of Life Sciences and Medicine, University of Science and Technology of China, Hefei, China, [2]Suzhou Institute of Biomedical Engineering and Technology, Chinese Academy of Science, Suzhou, China, [3]Suzhou TCM Hospital Affiliated to Nanjing University of Chinese Medicine, Suzhou, China

Background: Closed reduction is the preferred treatment for distal radius fractures. However, it requires a multiple experienced medical staff and manually maintaining stable traction is difficult. Additionally, doctors cannot assess the reduction status of a fracture in real-time through radiographic images, which may lead to improper reduction. Furthermore, post-fracture complications such as joint adhesion, stiffness, and impaired mobility pose a challenge for the doctors. So it is necessary to optimize the treatment process of the distal radius fracture through technological means.

Methods: A robot-assisted closed reduction and rehabilitation system, which could assist doctors throughout the entire process of reduction, fixation, and rehabilitation of distal radius fractures, was developed. A mechanical system, composed of two grippers and a cooperative robotic arm, was used to grasp and tract the affected limb. A doctor controlled the robot through a joystick console and Windows application program. A biplane radiographic device was integrated into the system, which is not only convenient for doctors to view radiographic images of the fracture at any time but also for them to select the rotation axis of the wrist on the images before reduction and rehabilitation. Important information including the anteroposterior and lateral radiographic data and force and position parameters during the reduction and rehabilitation process were displayed on a graphic user interface.

Results: Experimental results showed that the proposed robotic system can meet the technical requirements for the reduction and rehabilitation of distal radius fractures, all the rotation angles could be achieved, a maximum force of more than 50 N could be achieved in all traction directions, and the error in selecting the wrist joint rotation axis line using radiographic images was less than 5 mm.

Conclusion: The developed robot-assisted system was shown to be suitable for closed reduction and rehabilitation of distal radius fractures, contributing a potential improvement in the quality of the procedures.

KEYWORDS

distal radius fractures, robot-assisted, reduction, rehabilitation, biplane radiographic

1 Introduction

Reduction, fixation, and rehabilitation are the three basic processes of fracture treatment. Reduction and fixation are the core treatments, and rehabilitation guarantees satisfactory functioning and efficacy of the limb after fracture surgery (Lichtman et al., 2011). Distal radius fracture is common in clinical settings. Displaced fractures are usually reduced using closed reduction methods, which are non-surgical and generally comprise traction and manipulation. The resulting position is then stabilized, typically by plaster cast immobilization (Handoll et al., 1996). The plaster cast immobilizes the wrist in a flexed, pronated, and ulnar deviated position for up to 6 weeks, often resulting in wrist pain and stiffness, especially during supination and extension (Charnley, 2003). Exercise is prescribed for at least 90% of patients after a distal radius fracture (Handoll et al., 2003). Physical therapy of joints, following surgery, focuses on both passive motion to restore mobility and active exercises to restore strength. Although a therapist perform passive motion for patients, continuous passive motion (CPM) devices have also been used. CPM improves recovery by stimulating the healing of articular tissues and circulation of synovial fluid, reducing local edema, and preventing adhesions, joint stiffness or contractures, or cartilage degeneration (Shirzadi et al., 2020). Adding mobilization with movement (MWM) to exercise and advice gives a faster and greater improvement in motion impairments for non-operative management of distal radius fracture (Reid et al., 2020). Thus Multiple experienced medical professionals are involved in the reduction, fixation, and rehabilitation of distal radius fractures. To overcome the drawbacks of traditional fracture reduction surgery, robot-assisted fracture reduction (RAFR) aimed to bring benefits, such as improved accuracy, less invasiveness, less radiation, a short hospital stay and accelerated postoperative rehabilitation (Zhao et al., 2020; Westphal et al., 2008). Therefore, various types of assistive robots have been developed. These robots are structured according to the following: (a) fixed external frame structure, (b) serial structure (such as that of an industrial robot), (c) parallel structure, and (d) serial-parallel hybrid structure (Bai et al., 2019). Machinery has surpassed human hands in terms of accuracy, stability, and repeatability. In fracture management, it can measure the angles, displacement, and force necessary for fracture reduction with precision and achieve perfect alignment of the fracture ends. Utilizing programmed fracture reduction treatment processes results in stable and consistent outcomes, reducing variations in results among doctors with different experience levels and years of service. In orthopedic surgery, robots have been developing rapidly in the past decades and are significantly beneficial to patients and healthcare providers (Zhao et al., 2020).

Regarding fracture reduction robots, research has primarily focused on the long bones of the limbs. Li et al. conducted a preliminarily study of a master and slave remote-controlled robotic system, and the experimental results showed high accuracy for fracture reduction and excellent performance (Li et al., 2016). Alruwaili et al. proposed a Wide-Open 3-armed parallel robot, Robossis, which can reach the boundary points of the workspace with a submillimeter accuracy and provide the required traction forces of up to 432 N to align femur fractures (Alruwaili et al., 2022). Zhu et al. designed and kinematically analyzed a femoral fracture reduction robot, which comprises a six-degree-of-freedom serial-link robot with three prismatic and three rotational joints. The proposed system has the potential for practical application in orthopedic clinical surgery (Zhu et al., 2022). Dagnino et al. designed a six-degree-of-freedom parallel robotic system for fracture manipulation, which allows for remote control in automatic mode and intra-operative adaptation for better reduction accuracy (root mean square error of 1.18 ± 1.14 mm [translations] and 1.85° ± 1.54° [rotations]) (Dagnino et al., 2015). Seide et al. developed a six-degree-of-freedom external fixator based on a hexapod robot, which had high-precision three-dimensional bone movement and could be expanded into a "smart fixator" in the future to automate controlled fracture and deformity treatment (Seide et al., 2004). Westphal et al. developed a robotic system for the reduction of femoral shaft fractures by utilizing modern techniques such as three-dimensional (3D) imaging, navigation, and robotics to overcome the disadvantages of the minimally invasive technique of intramedullary nailing, including malaligned fracture reductions and high radiographic exposure. The authors showed that high reduction accuracies could be achieved with the robotic system and that robot-assisted drill guidance achieves superior results compared with that achieved with the conventional procedure (Westphal et al., 2009). Priya et al. developed a novel method for reducing distal radius fractures using a mechanical device, which decreases the number of surgeons and time required to reduce the distal radius fracture and seeks to improve the accuracy of reduction (Priya et al., 2019). Xie et al. developed a novel fracture reduction device which enables only one doctor to complete the traditional manual reduction easily with precise measurements of all the necessary biomechanics and related parameters (Xie et al., 2016).

Regarding fracture rehabilitation robots, Picelli et al. supported the hypothesis that robot-assisted arm training might be a feasible tool for treating upper limb impairment in adult patients with distal radius fracture treated conservatively or surgically. The treatment of arm impairment consequent to distal radius fractures by means of robot-assisted arm training may allow therapists to focus on functional rehabilitation during occupational (individual) therapy and supervise (more than one) patients simultaneously during robotic training sessions (Picelli et al., 2020). César et al. designed and analyzed a horizontal rehabilitation robot based on a parallel mechanism for the treatment of femoral shaft fractures. Their designed robot helped patients to perform passive exercises of the hip. The system consists of three degrees of freedom actuated with linear actuators (Valdivia et al., 2013). Viriyasaranon designed and built a robot for elbow rehabilitation after elbow fractures, which could measure the limited range of motion of passive and active movements, measure stiffness of the human arm for passive movement, and provide assistive and resistive rehabilitation (Viriyasaranon, 2017). Wang et al. designed and implemented a soft parallel robot for automated wrist rehabilitation, which can assist the wrist to achieve all the required training motions, including abduction-adduction, flexion-extension, and supination-pronation motions (Wang and Xu, 2021). Noviyanto et al. designed a Continuous Passive Motion (CPM) machine for wrist joint therapy to reduce joint stiffness and improve joint mobility after surgery. The machine allows flexion, extension, ulnar, and radial movements of the wrist joint, with adjustable angles and speeds. The testing of the device showed a maximum difference of movement of 2°and a difference in speed of rotation of 0.5 s. The results indicate that the machine can be controlled according to the desired movement settings (Noviyanto et al., 2021). Kleber et al. integrated robotics and electronic games with the objective of producing more motivating and attractive therapeutic activities in distal radius fracture rehabilitation (wrist region) (Andrade et al., 2010). Cao et al. proposed innovative methods for circuit improvement,

damping settings, and energy harvesting for rehabilitation training robots (Cao et al., 2022; Cao et al., 2023).

Closed reduction is the preferred treatment for distal radius fractures, but it requires the participation of multiple healthcare personnel, and maintaining stable traction manually through closed reduction is difficult. Additionally, doctors cannot assess the reduction status of the fracture on radiographic images in real-time, which may lead to improper reduction. Furthermore, post-fracture complications such as joint adhesion, stiffness, and impaired mobility are challenging for doctors. To address these issues, a robot-assisted closed reduction and rehabilitation system, which could assist doctors in completing the entire reduction, fixation, and rehabilitation process for distal radius fractures, was developed. The main contributions of this paper are as follows:

1) A mechanical system composed of two grippers and a cooperative robotic arm is used to grasp and provide traction to the affected limb. The doctor controls the robot through a joystick console and Windows application program.
2) A biplane radiographic device was integrated into the system, which is not only convenient for doctors to view the fracture on radiographic images at any time but also for selecting the rotation axis of the wrist based on the images obtained before reduction and rehabilitation.
3) Important information including the anteroposterior and lateral radiographic images and force and position parameters during the reduction and rehabilitation process were displayed on a graphic user interface (GUI).

2 Materials and methods

2.1 Clinical analysis

To achieve an effective design, it is essential to involve the inputs of primary and secondary stakeholders at the outset of the development process. Their knowledge and input aid in understanding present practices and identifying specific obstacles with current procedures and equipment (Georgilas et al., 2018). It is also important to develop a surgeon- and patient-friendly orthopedic surgical robot by imitating surgeons' manual conduct of fracture reduction surgery and by maintaining surgeons' way of thinking and planning surgeries (Zhu et al., 2021). The fracture reduction assistant robot is a novel medical equipment aimed to assist doctors to complete fracture reduction and rehabilitation more efficiently and accurately. To ensure the robot's effectiveness and safety, it is crucial to design it based on clinical needs that meet the requirements of doctors. Therefore, we conducted a survey of 30 experienced doctors in the Bone and Joint Department of the Suzhou Hospital of Traditional Chinese Medicine who had more than 5 years of experience in distal radius fracture reduction. We gathered feedback and recommendations from different perspectives, and based on the survey results, we summarized the following required technical parameters:

1) Position of the patient's body: Sitting or lying position.
2) Position of the affected limb: Shoulder abduction, 60°–90°; elbow flexion, 90° or 180°; and forearm and wrist in pronation or the neutral position.
3) Position for holding: The distal end is the palm or fingers, and the proximal end is the part of the forearm closer to the elbow joint.
4) Parameters of traction: Along the longitudinal axis of the limb, the traction force is controlled at 40–50 N depending on the specific situation. The traction time is preferably 1–3 min, and the traction displacement is about 5–10 mm. The range of wrist flexion and deflection angles is ±60° and ±30°, respectively
5) Continuous passive motion (CPM): The vertical bending wrist movement known as extension and flexion is shown in Figure 1A. The side-to-side horizontal tilting movement of the wrist, known as radial and ulnar deviation, is shown in Figure 1B. The wrist and forearm rotation movement, known as pronation and supination, is shown in Figure 1C.
6) Mobilization with movement (MWM): Anterior and posterior gliding, clockwise and counterclockwise rotation, longitudinal separation traction, and compression along the palmar axis of the wrist joint. Each action is performed in the functional position, which is palm flexion, ulnar deviation, wrist extension, and end-range radial deviation.

2.2 System configuration

The robot-assisted closed reduction and rehabilitation system for distal radius fractures developed in this article is composed of the following elements: the robot body, lead protective curtain, mobile lead screen (Suzhou Kangshidun Protective Technology Co., Ltd., China), computer host (Advantech Co. Ltd., China), control console, and mobile cart as shown in Figure 2. The robot body consists of a movable base, a collaborative robotic arm (Aubo Intelligent Technology Co., Ltd., China), two sets of radiographic devices (Shanghai Anzhu Optoelectronic Technology Co., Ltd., China), and two gripping jaws (Shenzhen Dahuan Robot Technology Co., Ltd., China) and their parameters are shown in Table 1. The interaction between the doctor, robot, and patient forms a human-machine system, emphasizing the safety of medical personnel and patients in the design. Consequently, emergency stop buttons are present on both the robot body and control console. To ensure protection against radiations from radiography, a specially designed low-dose radiography machine is used for the forearm, effectively minimizing radiation exposure. The doctor is protected by a glass lead screen while the patient is shielded by a movable lead curtain, exposing only the affected limb to the radiation field. The collaborative robotic arm features collision detection and automatically stops when obstacles are encountered. It is equipped with a six-axis force sensor at its end, and the arm and palm clamps offer adjustable gripping force on the limb within an acceptable range. The control system monitors force in real time, and the robotic arm pauses automatically if the force exceeds the limit. The host serves as a relay station for all data and control transmission. The mobile lead curtain and lead screen provide protection for the patient and doctor, respectively. The upper part of the lead screen is a lift-up glass lead screen, enabling the doctor to easily observe the status of the robot and patient. The mobile cart facilitates close-range and long-range operations for the doctor.

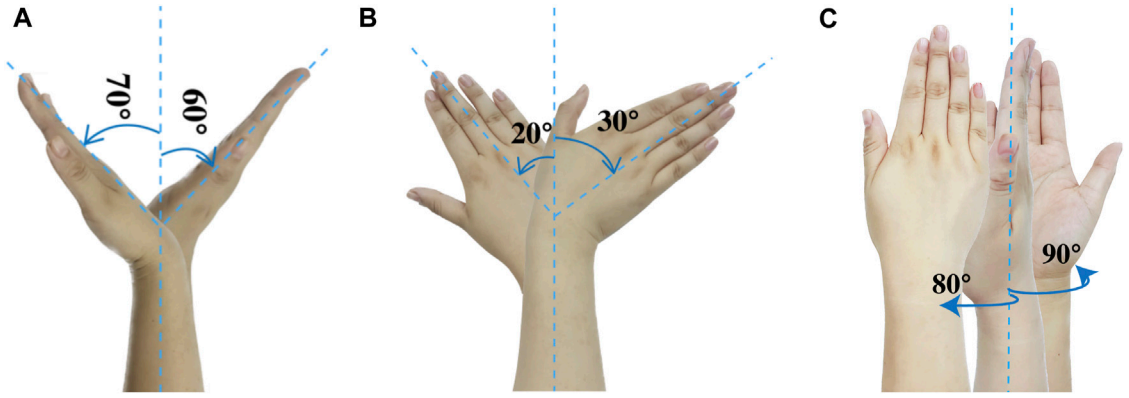

FIGURE 1
The angles of wrist movement. **(A)** Bending. **(B)** Tilting. **(C)** Rotating.

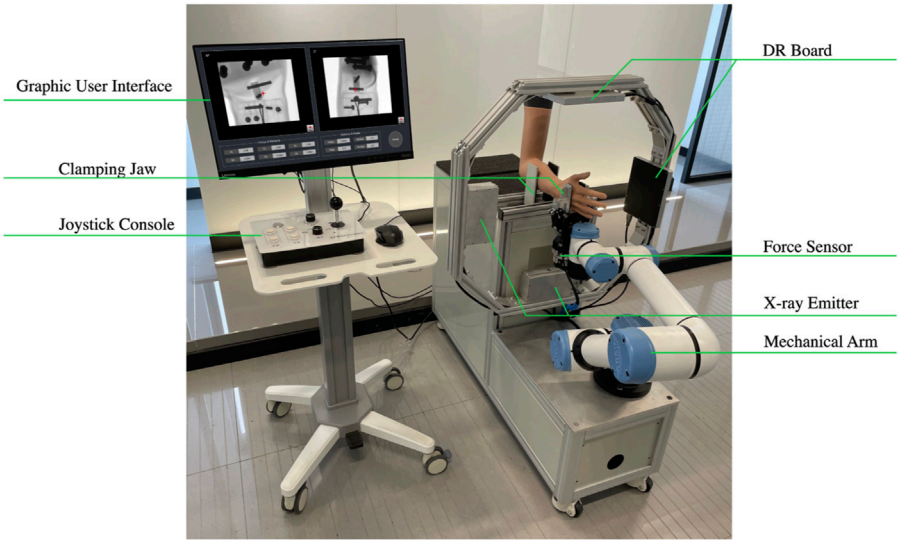

FIGURE 2
The robot-assisted reduction and rehabilitation system for distal radius fractures.

2.3 Joystick console

The console's main functions are to control the opening and closing of arm and palm grippers, adjust the movement speed of the robotic arm, select traction mode (drawing, palmar flexion, dorsal extension, ulnar deviation, and rotation), and implement movement. It controls the arm and palm grippers and adjusts the robotic arm's movement through the host. As shown in Figure 3A, the console has four independent buttons including a four-speed switch, a four-direction joystick switch, and one knob. These components are abstracted into four independent modules that are connected to the main control module. The main control module, shown in Figure 3B, communicates with the upper computer and is based on STM32, the only microcontroller. As shown in Figure 4, the control module exchanges data with the upper computer through the USART serial port. After the upper computer sends specific instructions, the microcontroller returns a byte stream that includes status information of the four console components, such as whether all buttons are pressed, which gear position the switch is in, whether the joystick is being operated, and the position of the knob.

2.4 Biplane radiographic image acquisition system

The large G-arm radiography machines employed in hospitals are costly and unwieldy, which are excessive for distal radius fractures. As shown in Figures 5A, B, by integrating radiography machines into robots, the positional relationship between the limbs in the image and the actual physical space can be determined. As shown in Figures 5C, D, the biplane radiographic image acquisition system comprises three main components including radiography source control, reception panel network layer control, and primary image processing. The base coordinate origin of the robotic system is set at the center of the flange at the base of the

TABLE 1 The parameters of robot-assisted reduction and rehabilitation system.

Parameter	Value
Collaborative robotic arm(AUBO i5)	d1 = 140.5 mm
	a2 = 408 mm
	a3 = 376 mm
Joint dimensions	d4 = 102.5 mm
	d5 = 102.5 mm
	d6 = 94 mm
Repeatability	±0.02 mm
Workspace (spherical)	886.5 mm (radius)
Load capacity	50 N
Clamping jaw for palm(DAHUAN AG95)	
Travel distance	0–95 mm
Clamping force	45–160N
Clamping jaw for palm(DAHUAN PGI-140)	
Travel distance	0–95 mm
Clamping force	40–140N
Six-axis force sensor(KUNWEI KWR75D)	
Force	Fx (500N), Fy (700N), Fz (700N)
Moment	Mx (18Nm), My (18Nm), Mz (18Nm)

collaborating robotic arm. The detection area of the receiving plate is 160 mm × 128 mm, and the pixels of the radiographic images are 640 × 512. As shown in Figure 4, the computer host connects to the microcontroller and two radiography receiving panels through a USB serial port and two RJ45 network interfaces, respectively. The system controls two sets of radiographic emission-reception devices separately in the vertical and horizontal directions based on the set exposure parameters. After image processing, the acquired radiographic images are displayed. A doctor can activate the acquisition of anteroposterior and lateral radiographic images using a foot pedal.

2.5 Graphic user interface

The GUI is used to display the images and parameter data the doctor needs to view during fracture reduction. Meanwhile, in rehabilitation training mode, the doctor can set rehabilitation training parameters and start or stop the training through the GUI. As shown in Figure 6, the anteroposterior and lateral images can be displayed simultaneously, enabling doctors to check the fracture situation in real time. The doctor can set the rotation axis of the end of the robotic arm based on the anteroposterior and lateral radiographic images. The velocity of the robotic arm and the gripping force of the jaws can also be adjusted. The gripping force can be adjusted to 40–50 N for individuals with less muscles and can reach up to 140 N for those with more muscles. The maximum pressure a human body can withstand is 140 N, so the gripper will not cause harm to the body. Furthermore, the six-dimensional force sensor collects data parameters of force and moment, which are displayed on the interface. After the rotation axis is set, the traction force and position parameters are reset to zero. During reduction, parameters of force and position for pulling, bending, tilting, and rotating in real time are displayed on the software interface and parameters such as traction force, speed, range, time, and axis of rotation can be set. The connection status of the robot and radiography machine is displayed on the interface.

2.6 Force and torque compensation

To obtain the force and torque of the robot on the affected limb in real time, a six-dimensional force sensor was installed under the clamp claw. Due to the low-speed robotic movements, the influence of inertial

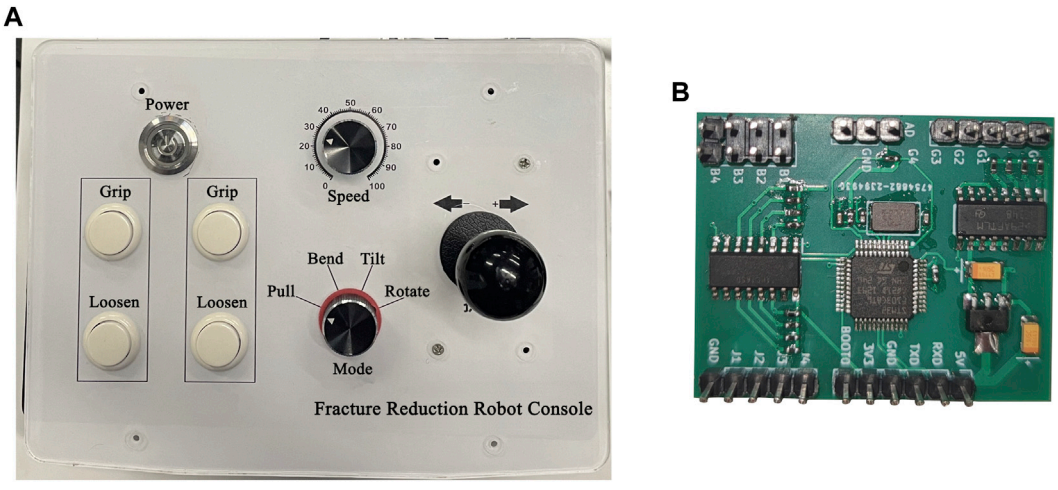

FIGURE 3
The joystick console. **(A)** Operation interface. **(B)** Circuit board.

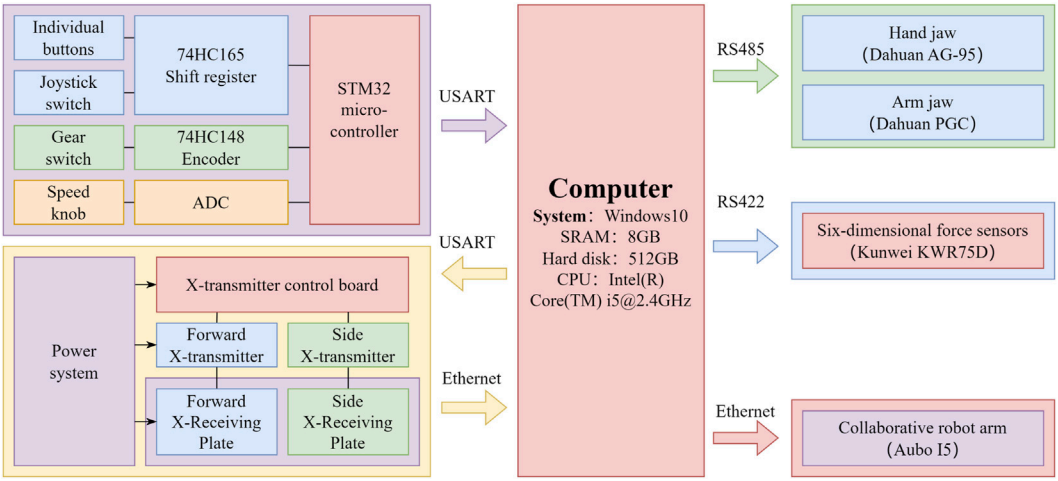

FIGURE 4
The block diagram of the control system.

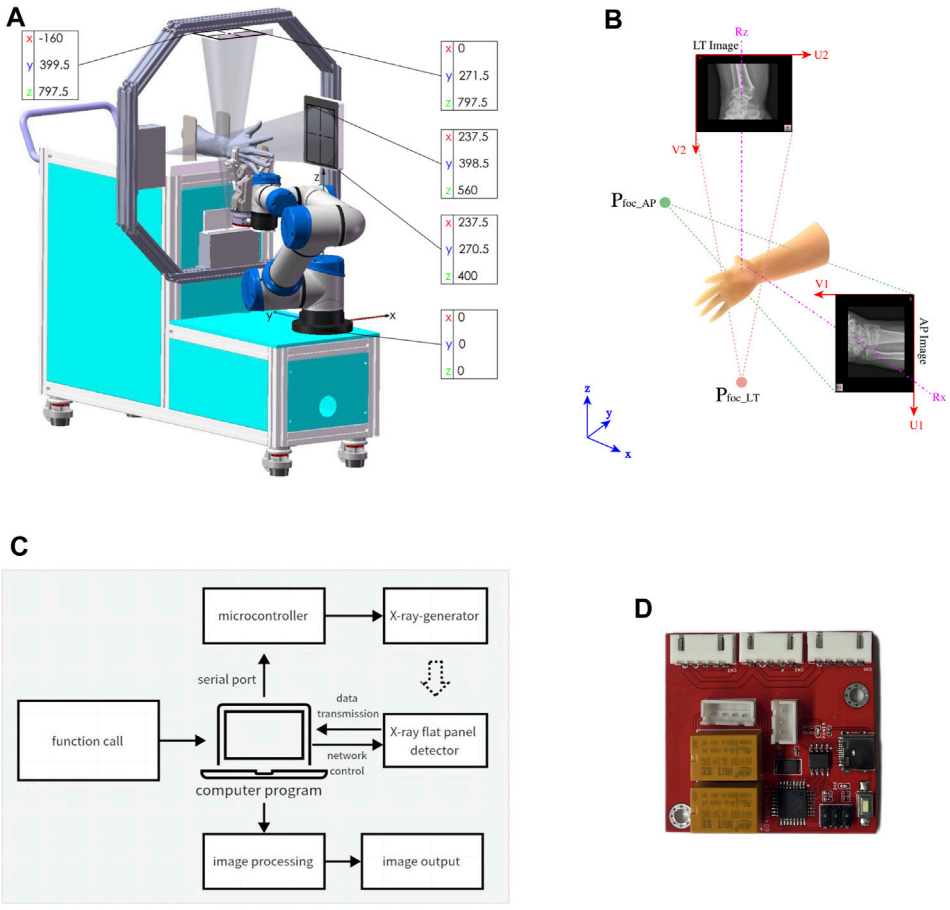

FIGURE 5
The biplane X-ray image acquisition system. **(A)** Block diagram. **(B)** circuit board. **(C)** Size and position. **(D)** Coordinates of image.

force can be neglected. Force sensor data fluctuations are ignored and the end tooling is not replaced. Therefore, the load is subject to external contact force and only needs influence of a sensor system error, and load gravity action should be eliminated. By selecting the six-dimensional force sensor at different poses, the gravity size and the center of gravity position of the load end can be calculated (Kim et al., 2013).

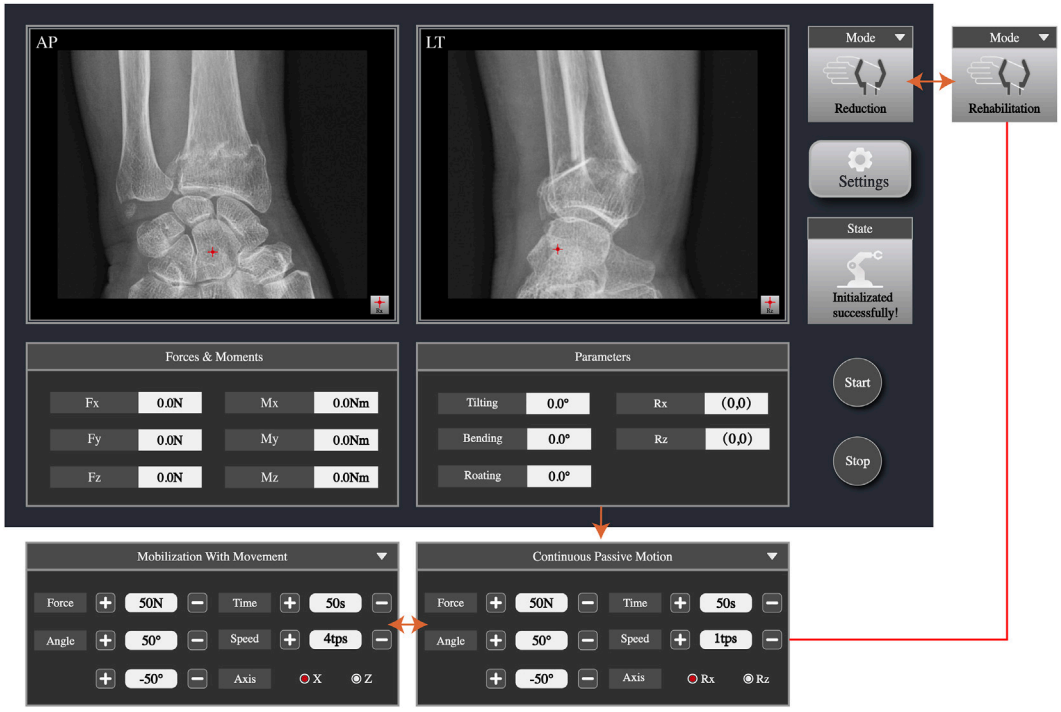

FIGURE 6
The Graphic User Interface (GUI) of the system.

As shown in Figure 7A, the coordinate systems are established, and the mechanical arm base coordinate system is $O_O - X_O Y_O Z_O$ coordinate system {O}. The measurement coordinate system of the six-dimensional force sensor is $O_S - X_S Y_S Z_S$, as coordinate system {S}. The coordinates of the center of mass (p_{xS}, p_{yS}, p_{zS}), the zero value of the force components (F_{x0}, F_{y0}, F_{z0}), and the zero value of the torque components (M_{x0}, M_{y0}, M_{z0}) in the six-dimensional force sensor coordinate system can be calculated from multiple sets of data using the least-squares method by the following equation.

$$\begin{bmatrix} M_{xS} \\ M_{yS} \\ M_{zS} \end{bmatrix} = \begin{bmatrix} 0 & F_{zS} & -F_{yS} & 1 & 0 & 0 \\ -F_{zS} & 0 & F_{xS} & 0 & 1 & 0 \\ F_{yS} & -F_{xS} & 0 & 0 & 0 & 1 \end{bmatrix} \begin{bmatrix} p_{xS} \\ p_{yS} \\ p_{zS} \\ k1 \\ k2 \\ k3 \end{bmatrix}$$

where $\begin{cases} k_1 = M_{x0} + F_{y0} \times p_{zS} - F_{z0} \times p_{yS} \\ k_2 = M_{y0} + F_{z0} \times p_{xS} - F_{x0} \times p_{zS} \\ k_3 = M_{z0} + F_{x0} \times p_{yS} - F_{y0} \times p_{xS} \end{cases}$

Then load-end gravity $\boldsymbol{G}_T = \sqrt{F_{xS}^2 + F_{yS}^2 + F_{zS}^2}$

After the load-related parameters are determined, as shown in Figure 7B, the coordinate system {T} at the center of gravity point, which is $O_T - X_T Y_T Z_T$, is established. The direction of {T}is the same as that at the base coordinate system {O}. The coordinate system is established at the action point of the mechanical arm and the external force, $O_E - X_E Y_E Z_E$, as {E}. The direction of {E} is the same as that of the coordinate system {S}. Map the gravity and torque of the load end under the coordinate system {?} to the coordinate system {?}, and the calculation formula of the gravity and torque value that can represent the load end compensation of the sensor is

$$\begin{bmatrix} \boldsymbol{F}_{SC} \\ \boldsymbol{M}_{SC} \end{bmatrix} = \begin{bmatrix} R_S^T & 0 \\ \ell({}^S\boldsymbol{P}_T)\,{}_S^T R & {}_S^T R \end{bmatrix} \begin{bmatrix} \boldsymbol{F}_T \\ \boldsymbol{M}_T \end{bmatrix}$$

where load-end gravity and torque is $[F_T \quad M_T]^T = [0\,0\,-|G_T|\,0\,0\,0]^T$, $\ell({}^S\boldsymbol{P}_T) = \begin{bmatrix} 0 & -p_{zS} & p_{yS} \\ p_{zS} & 0 & -p_{xS} \\ -p_{yS} & p_{xS} & 0 \end{bmatrix}$ is operator matrix, ${}_S^T\boldsymbol{R} = \begin{bmatrix} -1 & 0 & 0 \\ 0 & -1 & 0 \\ 0 & 0 & 1 \end{bmatrix}$ is the rotation transformation matrix of the coordinate system $\{T\}$ relative to the coordinate system $\{S\}$.

Finally the external force on the end of the robotic arm can be calculated by the following equation.

$$\begin{bmatrix} \boldsymbol{F}_E \\ \boldsymbol{M}_E \end{bmatrix} = \begin{bmatrix} {}_E^S\boldsymbol{R} & 0 \\ \ell({}^S\boldsymbol{P}_E)\,{}_E^S\boldsymbol{R} & {}_E^S\boldsymbol{R} \end{bmatrix}^{-1} \left(\begin{bmatrix} \boldsymbol{F}_S \\ \boldsymbol{M}_S \end{bmatrix} - \begin{bmatrix} \boldsymbol{F}_{SC} \\ \boldsymbol{M}_{SC} \end{bmatrix} - \begin{bmatrix} \boldsymbol{F}_0 \\ \boldsymbol{M}_0 \end{bmatrix} \right)$$

In which $\ell({}^S\boldsymbol{P}_E) = \begin{bmatrix} 0 & -p_{zE} & p_{yE} \\ p_{zE} & 0 & -p_{xE} \\ -p_{yE} & p_{xE} & 0 \end{bmatrix}$ is operator matrix, ${}_E^S\boldsymbol{R} = \begin{bmatrix} 1 & 0 & 0 \\ 0 & 1 & 0 \\ 0 & 0 & 1 \end{bmatrix}$ is the rotation transformation matrix of the coordinate system {S} relative to the coordinate system {E}.

3 Results

3.1 Axis alignment error

The biplane radiograph system is mounted and calibrated according to the parameters of the robotic system, and we use a metric ruler with a square-handled ball and an embedded lead scale to

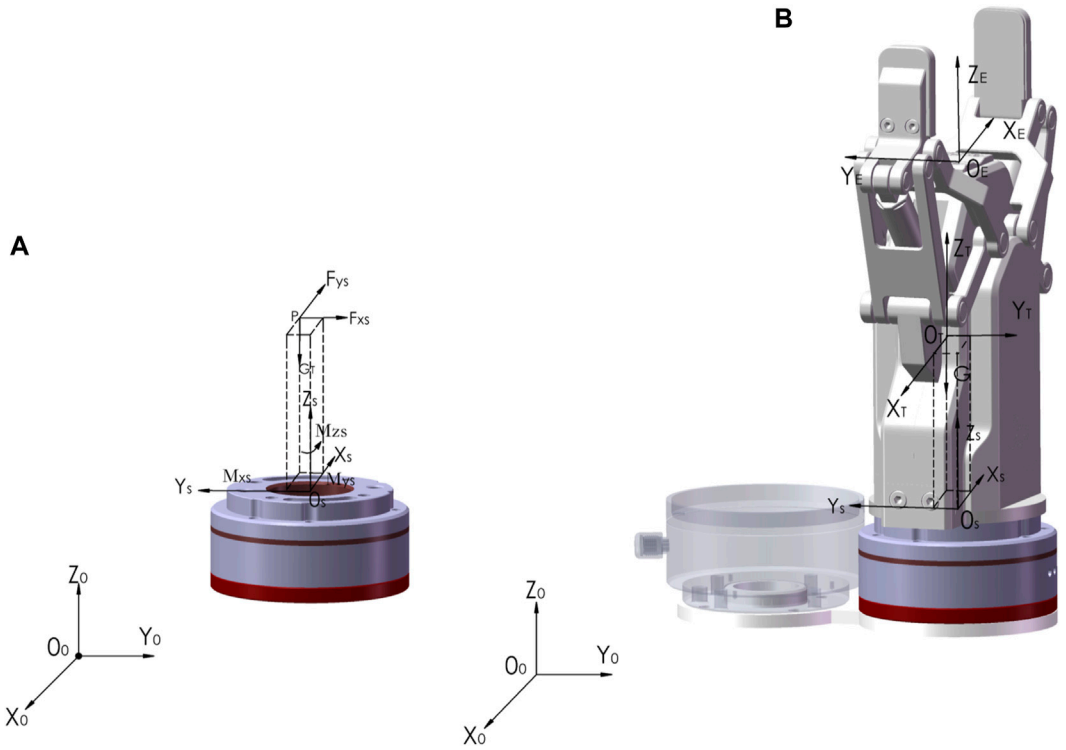

FIGURE 7
The force and torque calibration of six-dimensional force sensor. **(A)** Gravity and center of mass. **(B)** The coordinate systems.

mount, calibrate, and measure error. Sources of error include the aluminum alloy profile material dimensions, mounting, center emission point of the radiographic emitter, and the receiving plate. The flat plate received rays that are similar to the radiograph emission angle of ±19° and greater than the detector receiving angle of 16.3°. The arm could be completely imaged on the receiving plate. According to the principle of radiography, the magnification factor (Magnification Factor) can be calculated by Mf = d/D where d is the distance between object and emission source, D is the distance between emission source and receiving plate. We conducted a positioning accuracy experiment using a 3D printed spherical ball with a handle and the transfer plate on the robotic arm. Three different positions were selected in both the anterior and lateral directions for X-ray imaging, then center points were selected on the acquired images to test positioning accuracy. Table 2 presents the test results, indicating that the coordinate error of the spherical center remains within a 5 mm range.

3.2 Traction parameters

According to Section 2.1, during the fracture reduction and rehabilitation, the robotic arm needs to exert the maximum traction force between 40 and 50 N in each required position. We measured the angle at the end of the robotic arm through the digital display inclinometer (TLL-90S, Dongguan Jingyan Instrument Technology Co., LTD., China) and assessed whether the traction force with the pull pressure gauge (SSMCL-YL-1kN, Shenzhen You Zhongli Technology Co., LTD., China) meets the requirements. The traction force of the robotic arm along the axis of the arm can reach more than 50 N at different angles.

3.3 Simulated reduction

Using the fracture reduction-assisted robot developed in this study, we requested chief physicians from the Suzhou Hospital of Traditional Chinese Medicine to test the auxiliary reduction and rehabilitation training function with a Colles' Fracture Reduction Trainer. The reduction steps are as follows: (1) connect the power supply, open the collaboration mechanical arm control cabinet, start the master control computer, and initialize; (2) place the hand model in the appropriate position on the machine and hold it with the clip claw; (3) step on the radiography machine pedal to obtain the forward side image, observe the fracture situation and select the wrist joint axis on the image; (3) the doctor operates the robotic arm along the axis of the arm through the rocker arm console and positions the robot in the palm flexion deviation; (4) the doctor adjusts the traction and angle during the manual reduction, and (5) adjusts the traction force and angle after the reduction; and (6) the clip claw is released after fixation, and the arm model is removed. The experimental results show that the robot can effectively hold the affected limb and implement the required traction when the doctor implements the manual reduction and external fixation of the fracture model.

TABLE 2 Positioning accuracy from image to space.

Object	Error (mm)					
	Vertical (x,y)			Horizontal (y,z)		
	P1	P2	P3	P1	P2	P3
Sphere	(0.65,2.13)	(0.86,2.87)	(1.06,3.34)	(0.94,2.69)	(1.35,3.47)	(1.91,4.28)
Disk	(0.74,1,85)	(0.93,1.80)	(1.42,3.74)	(0.36,0.50)	(0.64,0.44)	(1.52,0.40)

3.4 Simulated rehabilitation

In the rehabilitation mode, the rehabilitation therapist should first control the mechanical arm through the joystick console to drive the movement of the affected limb to obtain the compression and traction forces a patient's wrist joint can withstand and to obtain achievable training angles. The automatic movement of the mechanical arm is then observed through the software interface. First, the rehabilitation mode, CPM or MWM, is selected. Subsequently, the rotational axis of the wrist is selected on the lateral radiographic image; the traction force, direction, angle, speed, and frequency of joint movements are set, and the start button is pressed. When choosing CPM mode, the arm is held so it can only be achieved bending and tilting. Their axes of rotation were selected on the AP (Rz) and LT (Rx) X-ray images. When choosing MWM mode, the arm is in a semi-restricted position and the wrist motion are faster linear reciprocating motion in the 30 mm range of the XZ directions. Table 3 illustrates the results of experimental tests, indicating that both the robot-assisted CPM and MWM are capable of fulfilling the usage requirements of rehabilitation therapists.

4 Discussion

The development of the robot-assisted system for fracture reduction and rehabilitation is an innovative and potentially game-changing advancement in orthopedic surgery. This technology, which can be challenging and complex, aims to improve the accuracy, precision, and safety of the reduction and rehabilitation procedure. Therefore, all aspects of the robot including the form of the robotic arm (Lin et al., 2013; Wang et al., 2013; Zhu et al., 2017; Georgilas et al., 2019), the connection technology between the bone and the robot (Yang et al., 2021), the force and moment in the reduction process (Zhu et al., 2016; Lei et al., 2020), functional evaluation (Hung and Lee, 2010), accuracy evaluation (Li et al., 2014), and interaction mode (Suero et al., 2018), have been studied. By utilizing a robot, surgeons can enhance their surgical techniques by obtaining real-time imaging guidance, improving their visualization of the fracture site. The robot can assist with the precise manipulation and repositioning of the fractured bone fragments, ensuring optimal alignment and stability during the reduction process. One of the key benefits of using a robot for closed reduction is the potential for decreased tissue trauma and reduced surgical time. By relying on robot-assisted techniques, surgeons can minimize soft tissue damage and achieve more efficient surgeries, which may lead to the quicker recovery of patients. Additionally, the use of robotics in closed reduction procedures can potentially decrease the risk of complications, such as improper alignment or unstable fixation, which are common challenges of traditional manual reduction techniques. The robot's ability to perform repetitive and precise movements may improve overall outcomes and enhance the quality of care provided to patients. However, it is important to note that the development of a robot for closed reduction and rehabilitation of distal radius fractures is still an ongoing area of research and development. The technology is not yet widely available or fully optimized for clinical use. Further studies and trials are necessary to assess its safety, efficacy, and cost-effectiveness before widespread implementation. Nevertheless, the potential benefits of a robot-assisted closed reduction and rehabilitation system for distal radius fractures hold promise for the future of orthopedic surgery, paving the way for advancements in surgical techniques and ultimately improving patient outcomes.

In this study, empirical parameters such as the position of the patient and affected limb, clamping position, direction of traction and reduction, angle, and force required for fracture reduction were obtained through clinical research, guiding the development of the distal radius fracture reduction and rehabilitation robot. The structure, hardware, and software of the reduction and rehabilitation robot were developed, and parameter indexes were tested. Experiments were conducted using a distal radius fracture model. The tests and results demonstrate that the developed closed reduction auxiliary robot for distal radius fractures can effectively assist doctors in completing the reduction, fixation, and rehabilitation process by enabling the binding of the affected limb, multi-degree-of-freedom traction, and real-time display of radiographic images.

The robot-assisted system for distal radius fractures can assist doctors in performing closed manual reduction and assist in rehabilitation. Lead screens and lead curtains are used to protect doctors and patients from radiation. The radiation emitted by small radiography machines is significantly smaller than that of large C-arm or G-arm radiography machines. The mechanical arm is operated using a joystick console to achieve fracture reduction, while the radiography machine only needs to be turned on during fracture analysis and viewing. Mostly, the machine remains in a non-radiation state, allowing doctors to view the images up close. With the help of the radiography device, doctors can monitor a patient's fracture status in real time through the display screen, while maintaining the position of the patient's arm using the robotic arm and gripper system, thereby achieving precise reduction. This eliminates the need for the patient to visit the radiology

TABLE 3 Parameters for reduction and rehabilitation of the robot.

Traction force	Reduction		Rehabilitation			
			CPM(0~2tps)		MWM(0~4tps)	
	Bending	Tilting	Rx	Rz	X (mm)	Z (mm)
0N ~ 50N	−5°~5°	−30°~30°	−5°~5°	−30°–30°	±30	±30
No load	−60°–70°	−30°~30°	−30°~20°	−60°–70°	±30	±30

department multiple times before and after the operation, ultimately reducing medical costs.

The developed closed reduction and rehabilitation auxiliary robot system for distal radius fractures is suitable for outpatient orthopedics and traumatology clinics. It has low radiation dose and includes movable lead curtains and screens. The system is compact in size and easy to install. Patients can directly obtain radiographic images in the clinic using the system. After diagnosis by a doctor, if the patient meets the applicable fracture range of the system, the doctor proceeds with the reduction procedure after obtaining the patient's consent. However, it can only achieve auxiliary traction and rehabilitation functions, cannot directly apply forces to the fractured bones for reduction purposes, such as the technique of manipulating the fracture site. It also lacks intelligent functions such as guidance based on X-ray images and force feedback control. The next step involves adding a top-folding mechanism to directly apply force to the broken bone to better simulate manual reduction, as well as incorporating functions such as artificial intelligence fracture classification and reduction guidance. Further experiments are necessary to verify the influence of muscle strength on various animal bones and cadavers, analyze the performance of the control system, and optimize the mechanism of the robotic system for patient safety and convenience before applying it to clinical environments in the future. Currently, there are no mature commercialized products for a robotic system for distal radius fractures worldwide, and many research institutes and hospitals are still in the exploratory stage of research about this system. Building an auxiliary fracture reduction robotic system based on medical image guidance to assist doctors in completing distal radius fracture reduction and achieving precise minimally invasive surgery hold great medical potential.

Data availability statement

The original contributions presented in the study are included in the article/Supplementary material, further inquiries can be directed to the corresponding authors.

Author contributions

QZ: Writing–original draft, Writing–review and editing. ZX: Data curation, Software, Writing–review and editing. HY: Funding acquisition, Resources, Writing–review and editing. GZ: Methodology, Resources, Writing–review and editing. XC: Data curation, Formal Analysis, Writing–review and editing. WZ: Investigation, Methodology, Validation, Writing–review and editing. YjL: Data curation, Investigation, Validation, Writing–review and editing. XS: Project administration, Supervision, Validation, Writing–review and editing. YwL: Conceptualization, Supervision, Visualization, Writing–review and editing.

Funding

The author(s) declare financial support was received for the research, authorship, and/or publication of this article. This research was funded by the National Key R&D Program of China under Grant 2020YFC2007402, 2020YFC2007404, 2020YFC2007400, 2020YFC2007401, 2020YFC2007403, 2020YFC2007405 and Science and Technology Program of National Administration of Traditional Chinese Medicine and Health Commission of Shandong Province, China (No. GZY-KJS-SD-2023-030) and Science and Technology Program of Jiangsu Province, China (No. BE2021662) and Science and Technology Program of Suzhou, China (No. SYG202019, SKY2023068) and Natural Science Foundation of Nanjing University of Chinese Medicine, China (No. XZR2021040).

Conflict of interest

The authors declare that the research was conducted in the absence of any commercial or financial relationships that could be construed as a potential conflict of interest.

Publisher's note

References

Alruwaili, F., Saeedi-Hosseiny, M. S., Guzman, L., McMillan, S., Iordachita, I. I., and Abedin-Nasab, M. H. (2022). A 3-armed 6-DOF parallel robot for femur fracture reduction: trajectory and force testing, 2022 International Symposium on Medical Robotics (ISMR), GA, USA, April, 2022, 1–6. doi:10.1109/ISMR48347.2022.9807539

Andrade, K. O., Ito, G. G., Joaquim, R. C., Jardim, B., Siqueira, A. A. G., Caurin, G. A. P., et al. (2010). "A robotic system for rehabilitation of distal radius fracture using games," in 2010 Brazilian symposium on games and digital entertainment, Florianopolis, Brazil, November, 2010 (IEEE), 25–32. doi:10.1109/SBGAMES.2010.26

Bai, L., Yang, J., Chen, X., Sun, Y., and Li, X. (2019). Medical robotics in bone fracture reduction surgery: a review. *Sensors* 19 (16), 3593. doi:10.3390/s19163593

Cao, W., Ma, Y., Chen, C., Zhang, J., and Wu, X. (2022). Hardware circuits design and performance evaluation of a soft lower limb exoskeleton. *IEEE Trans. Biomed. Circuits Syst.* 16 (3), 384–394. doi:10.1109/TBCAS.2022.3173965

Cao, W., Shang, D., Yin, M., Li, X., Xu, T., Zhang, L., et al. (2023). Development and evaluation of a hip exoskeleton for lateral resistance walk exercise. *IEEE-ASME Trans. Mechatronics* 28 (4), 1966–1974. doi:10.1109/TMECH.2023.3273717

Charnley, J. (2003). *The closed treatment of common fractures*. Cambridge, United Kingdom: Cambridge University Press.

Dagnino, G., Georgilas, I., Tarassoli, P., Atkins, R., and Dogramadzi, S. (2015). "Design and real-time control of a robotic system for fracture manipulation," in 2015 37th Annual International Conference of the IEEE Engineering in Medicine and Biology Society (EMBC), Milan, Italy, August, 2015 (IEEE), 4865–4868. doi:10.1109/EMBC.2015.7319483

Georgilas, I., Dagnino, G., Martins, B. A., Tarassoli, P., Morad, S., Georgilas, K., et al. (2019). Design and evalation of a percutanous fragment manipulation deviceor minimally invasive fracture surgery. *Front. Robotics AI* 6, 103. doi:10.3389/frobt.2019.00103

Georgilas, I., Dagnino, G., Tarassoli, P., Atkins, R., and Dogramadzi, S. (2018). Robot-assisted fracture surgery: surgical requirements and system design. *Ann. Biomed. Eng.* 46, 1637–1649. doi:10.1007/s10439-018-2005-y

Handoll, H. H. G., Madhok, R., and Cochrane Bone, Joint and Muscle Trauma Group. (1996). Closed reduction methods for treating distal radial fractures in adults. *Cochrane Database Syst. Rev.* 2010(1). doi:10.1002/14651858.CD003763

Handoll, H. H. G., Madhok, R., and Howe, T. E., A systematic review of rehabilitation for distal radial fractures in adults. *Br. J. Hand Ther.*, 2003, 8(1): 16–23. doi:10.1177/175899830300800103

Hung, S.-S., and Lee, M.-Y. (2010). Functional assessment of a surgical robot for reduction of lower limb fractures. *Int. J. Med. Robot. Comput. Assist. Surg.* 6, 413–421. doi:10.1002/rcs.351

Kim, W. Y., Han, S. H., Park, S., Park, J-. O., and Ko, S. Y. (2013). Gravity compensation of a force/torque sensor for a bone fracture reduction system. *Proc. Int. Congr. Soc. Control Robot Syst.*, 1042–1045.

Lei, J., Zheng, G., Hu, L., Zhang, L., and Wang, T. (2020). External force estimation of fracture reduction robot based on force residual method. *Int. J. Adv. Robotic Syst.* 17 (1). doi:10.1177/1729881419897470

Li, C., Wang, T., Hu, L., Tang, P., Wang, L., Zhang, L., et al. (2016). A novel master–slave teleoperation robot system for diaphyseal fracture reduction: a preliminary study. *Comput. Assist. Surg.* 21 (Suppl. 1), 162–167. doi:10.1080/24699322.2016.1240304

Li, C., Wang, T., Hu, L., Zhang, L., Du, H., Wang, L., et al. (2014). Accuracy analysis of a robot system for closed diaphyseal fracture reduction. *Int. J. Adv. Robotic Syst.* 11 (10), 169. doi:10.5772/59184

Lichtman, D. M., Bindra, R. R., Boyer, M. I., Putnam, M. D., Ring, D., et al. (2011). American Academy of Orthopaedic Surgeons clinical practice guideline on: the treatment of distal radius fractures. *JBJS* 93 (8), 775–778. doi:10.2106/JBJS.938ebo

Lin, H., Wang, J. Q., and Han, W. (2013). "Parallel manipulator robot assisted femoral fracture reduction on traction table," in 2013 35th Annual International Conference of the IEEE Engineering in Medicine and Biology Society (EMBC), Osaka, Japan, July, 2013, 4847–4850. doi:10.1109/EMBC.2013.6610633

Noviyanto, A. H., Septilianingtyas, L. D., and Rahmawati, D. (2021). Design of a continuous passive motion (CPM) machine for wrist joint therapy. *J. Robotics Control (JRC)* 2(4): 311–315. doi:10.18196/jrc.2498

Picelli, A., Munari, D., Modenese, A., Filippetti, M., Saggioro, G., Marialuisa, G., et al. Robot-assisted arm training for treating adult patients with distal radius fracture: a proof-of-concept pilot study. *Eur. J. Phys. Rehabilitation Med.*, 2020, 56(4): 444–450. doi:10.23736/S1973-9087.20.06112-2

Priya, L., Kumar, N. V., SanjayBalaji, M., and Revanth, C. V. (2019). A mechanical device for the reduction of distal radius fracture. *Int. J. Innovative Technol. Explor. Eng.* 8 (7). doi:10.1177/0278364909101189

Reid, S. A., Andersen, J. M., and Vicenzino, B. (2020). Adding mobilisation with movement to exercise and advice hastens the improvement in range, pain and function after non-operative cast immobilisation for distal radius fracture: a multicentre, randomised trial. *J. Physiother.* 66(2): 105–112. doi:10.1016/j.jphys.2020.03.010

Seide, K., Faschingbauer, M., Wenzl, M. E., Weinrich, N., and Juergens, C. (2004). A hexapod robot external fixator for computer assisted fracture reduction and deformity correction. *Int. J. Med. Robotics Comput. Assisted Surg.* 1 (1), 64–69. doi:10.1002/rcs.6

Shirzadi, A., Farzad, M., Farhoud, A. R., and Shafiee, E. (2020). Application of continuous passive motion in patients with distal radius fractures: a randomized clinical trial. *Hand Surg. Rehabilitation* 39(6): 522–527. doi:10.1016/j.hansur.2020.08.001

Suero, E. M., Hartung, T., Westphal, R., Hawi, N., Liodakis, E., Citak, M., et al. (2018). Improving the human–robot interface for telemanipulated robotic long bone fracture reduction: joystick device vs. Haptic manipulator. *Int. J. Med. Robot. Comput. Assist. Surg.* 14, e1863. doi:10.1002/rcs.1863

Valdivia, C. H. G., Ortega, A. B., Salazar, M. A. O., and Escobedo, J. L. C. (2013). Design and analysis of a lower limbs horizontal robot for femoral shaft fracture rehabilitation using linear actuators. *Int. J. Adv. Eng. Technol.* 6(2): 583.

Viriyasaranon, T. (2017). *Orthopedic rehabilitation robot for elbow fractures*. Pathum Thani, Thailand: Asian Institute of Technology.

Wang, J., Han, W., and Lin, H. (2013). Femoral fracture reduction with a parallel manipulator robot on a traction table. *Int. J. Med. Robotics Comput. Assisted Surg.* 9(4): 464–471. doi:10.1002/rcs.1550

Wang, Y., and Xu, Q. (2021). Design and testing of a soft parallel robot based on pneumatic artificial muscles for wrist rehabilitation. *Sci. Rep.* 11(1): 1273. doi:10.1038/s41598-020-80411-0

Westphal, R., Winkelbach, S., Gösling, T., Oszwald, M., Hüfner, T., Krettek, C., et al. (2008). *Telemanipulated long bone fracture reduction*. London, UK: INTECH Open Access Publisher.

Westphal, R., Winkelbach, S., Wahl, F., Gösling, T., Oszwald, M., Hüfner, T., et al. (2009). Robot-assisted long bone fracture reduction. *Int. J. Robotics Res.* 28 (10), 1259–1278. doi:10.1177/0278364909101189

Wu, X., Cao, W., Yu, H., Zhang, Z., Leng, Y., and Zhang, M. (2022). Generating electricity during locomotion modes dominated by negative work with a knee energy harvesting exoskeleton. *IEEE-ASME Trans. Mechatronics* 27 (6), 4451–4461. doi:10.1109/TMECH.2022.3157848

Xie, Z., Liang, B., Wang, X., and Tian, M. (2016). Design of fracture reduction device for distal radius. In 2016 23rd International Conference on Mechatronics and Machine Vision in Practice (M2VIP), Nanjing, China, November, 2016, 1–5. doi:10.1109/M2VIP.2016.7827339

Yang, J., Xiong, Y., Chen, X., Sun, Y., Hou, W., Chen, R., et al. (2021). Bone fracture reduction surgery-aimed bone connection robotic hand. *J. Bionic Eng.* 18, 333–345. doi:10.1007/s42235-021-0023-1

Zhao, J. X., Li, C., Ren, H., Hao, M., Zhang, L. C., and Tang, P. F. (2020). Evolution and current applications of robot-assisted fracture reduction: a comprehensive review. *Ann. Biomed. Eng.* 48, 203–224. doi:10.1007/s10439-019-02332-y

Zhu, Q., Liang, B., Wang, X., Sun, X., and Wang, L. (2016). Force–torque intraoperative measurements for femoral shaft fracture reduction. *Comput. Assist. Surg.* 21 (Suppl. 1), 37–44. doi:10.1080/24699322.2016.1240311

Zhu, Q., Liang, B., Wang, X., Sun, X., and Wang, L. (2017). Minimally invasive treatment of displaced femoral shaft fractures with a teleoperated robot-assisted surgical system. *Injury* 48 (10), 2253–2259. doi:10.1016/j.injury.2017.07.014

Zhu, Q., Tian, M., Liu, Q., and Wang, X. (2022). Design, kinematics and manipulability analyses of a serial-link robot for minimally invasive treatment in femoral shaft fractures. *J. Mech. Med. Biol.* 22 (09), 2240060. doi:10.1142/S0219519422400607

Zhu, S., Zhao, Z., Chen, Y., Deng, J., Zhu, J., Pan, Y., et al. (2021). "Development of a surgeon and patient-friendly orthopedic surgical robot," in 2021 International Symposium on Medical Robotics (ISMR), Atlanta, GA, USA, November, 2021, 1–6. doi:10.1109/ISMR48346.2021.9661481

frontiers | Frontiers in Bioengineering and Biotechnology

TYPE Original Research
PUBLISHED 26 January 2024
DOI 10.3389/fbioe.2024.1358022

OPEN ACCESS

EDITED BY
Wujing Cao,
Chinese Academy of Sciences (CAS), China

REVIEWED BY
Zhenhong Li,
The University of Manchester, United Kingdom
Dingguo Zhang,
University of Bath, United Kingdom
Mingjie Dong,
Beijing University of Technology, China

*CORRESPONDENCE
Wei Meng,
weimeng@whut.edu.cn

†These authors have contributed equally to this work

RECEIVED 19 December 2023
ACCEPTED 15 January 2024
PUBLISHED 26 January 2024

CITATION
Liu H, Zhu C, Zhou Z, Dong Y, Meng W and Liu Q (2024), Synergetic gait prediction and compliant control of SEA-driven knee exoskeleton for gait rehabilitation.
Front. Bioeng. Biotechnol. 12:1358022.
doi: 10.3389/fbioe.2024.1358022

Synergetic gait prediction and compliant control of SEA-driven knee exoskeleton for gait rehabilitation

Haojie Liu†, Chang Zhu†, Zude Zhou, Yunfei Dong, Wei Meng* and Quan Liu

The School of Information Engineering, Wuhan University of Technology, Wuhan, China

In recent years, lower limb exoskeletons have achieved satisfactory clinical curative effects in rehabilitating stroke patients. Furthermore, generating individualized trajectories for each patient and avoiding secondary injury in rehabilitation training are important issues. This paper explores the utilization of series elastic actuator (SEA) to deliver compliant force and enhance impact resistance in human-robot interaction, and we present the design of novel knee exoskeleton driven by SEA. Subsequently, the novel gait trajectory prediction method and compliant control method are proposed. The attention-based CNN-LSTM model is established to generate personalized gait trajectories for affected limbs, in which the spatial-temporal attention mechanism is adopted to improve the prediction accuracy. The compliant control strategy is proposed to nonlinearly and adaptively tune impedance parameters based on artificial potential field (APF) method, and active rehabilitation training is carried out in the coordination space to guarantee patient safety. The experimental results based on four healthy subjects demonstrated that synergetic gait prediction model could satisfactorily characterize the coordination movement with higher accuracy. The compliant control could limit the patient's movement in the safe coordination tunnel while considering personalization and flexibility.

KEYWORDS

knee exoskeleton, series elastic actuator, gait prediction, compliant control, personalized trajectory

1 Introduction

According to the Global Burden of Disease Study, stroke remains the primary cause of the second-highest mortality rate and the third-highest disability rate in the world (Feigin et al., 2022). Patients with lower extremity motor dysfunction after stroke usually show weakened lower extremity muscle strength, limited range of motion, and unstable shift of center of gravity, often accompanied by foot drop and varus deformity (Wang et al., 2017). Knee joint is the most complex joint of human body in structure, which can not only support basic locomotion such as walking, running, and standing, but also effectively dampen the impact force generated during walking. Knee dysfunction caused by neurological diseases is the most common factor leading to gait abnormalities, which severely affects patients' activities of daily living. Therefore, it is necessary to carry out rehabilitation training and develop the knee exoskeleton to improve mobility (Yan et al.,

2022). Research shows that rehabilitation training for patients at the early stage of the stroke has a significantly positive effect (Ballester et al., 2022).

The traditional rehabilitation therapy is time-consuming and laborious, and rehabilitation outcome is limited (Zhang et al., 2021). The lower limb rehabilitation robots can not only reduce the burden of rehabilitation therapists, but also customize the gait trajectory and training intensity (Kim et al., 2019; Cao et al., 2023; Yang et al., 2023). However, traditional knee exoskeletons mostly adopt rigid actuators, which can achieve accurate position control, but lack compliance (Chen et al., 2017). Exoskeletons driven by pneumatic muscles possess high compliance, but how to provide power conveniently is a challenge (Sridar et al., 2018). Series elastic actuator (SEA) intentionally introduces an elastic element between the actuator and output, which has many advantages, including lower reflection coefficient, impact resistance, and more accurate stability control in unconstrained environment (Yu and Lan, 2019). Recently, knee exoskeletons driven by SEA have received increasing attention (Kong et al., 2012; Song et al., 2023). Kong et al. designed the knee exoskeleton with compact rotary series elastic actuator (cRSEA), in which worm gears made no noise and were used to amplify the torque produced by the motor (Kong et al., 2012). Song et al. studied a crank-slider series elastic actuator (CS-SEA), in which crank-slider mechanism could improve the torque effect and the level of transparency, and the experimental results showed the precise force control performance of CS-SEA (Song et al., 2023). However, the weight of the knee exoskeleton can be the burden for patients, and patients vary in body shapes, so the knee exoskeleton should be adjustable to accommodate patients with different physical parameters to improve the adaptability of device and limit the range of motion of the knee exoskeleton to prevent secondary injury.

The predefined gait trajectory is suitable for patients who lack the ability to walk independently in the early stage of rehabilitation. However, in the middle and late stages of rehabilitation, the predefined trajectory may conflict with the patient's active intention (Zhu et al., 2022; Na et al., 2023). The continuous estimation of human motion intention through gait prediction method exhibits potential for compliant human-robot interaction (Xiong et al., 2021). Gait prediction is mainly based on motion information and physiological information. Motion information mainly includes joint angle, angular acceleration, and plantar pressure (Liu et al., 2017; Mounir Boudali et al., 2019; Sivakumar et al., 2019), and physiological information includes surface electromyography (sEMG) and electroencephalogram (EEG) (Gautam et al., 2020; Morbidoni et al., 2021; Liu et al., 2022). Meanwhile, multi-sensor fusion and multi-feature fusion can realize better prediction accuracy in gait prediction (Mazumder et al., 2016; Arami et al., 2019). Zou et al. proposed a gait prediction model to generate personalized gait trajectory for different subjects, which took the current joint angle of healthy lower limb and the observed historical joint angle of both lower limbs as input, and predicted the future joint angle of the paralyzed leg (Zou et al., 2021).

Human-robot interaction has requirements for control accuracy and safety, but the two criteria are conflict. Compliant control can provide a compromise between control accuracy and safety (Schumacher et al., 2019). Compliant control can control the position and force simultaneously and purposefully, including impedance/admittance control (Kim et al., 2021), hybrid force/position control (Yang et al., 2020), and parallel force/position control (Wang et al., 2011). Compared to hybrid and parallel force/position control, impedance control focuses more on achieving the target relationship between force and position, but does not necessarily track the expected trajectories (Perez-Ibarra et al., 2019; Chen et al., 2020; Sun et al., 2020). Admittance control, also known as position-based impedance control, adjusts the desired trajectory according to force deviation (Almaghout et al., 2022; Huang et al., 2022). Impedance control with adjustable parameters can respond to changes in the external environment (Liu et al., 2020; Wang et al., 2021). Li et al. proposed an iterative learning impedance control method, in which the control objective was the impedance model. This method achieved the desired control accuracy through iteration, which was suitable for the rehabilitation tasks with repeatability (Li et al., 2018). Spyrakos et al. introduced a variable impedance control scheme performing stable trajectory tracking, which ensured the stability of impedance control for flexible-joint robots (Spyrakos-Papastavridis and Dai, 2021).

Currently, AAN algorithm modifies the intervention of the robot according to the patient's behavior, while adopting virtual walls to guarantee patient safety (Banala et al., 2009; Perez-Ibarra et al., 2019; Asl et al., 2020). Banala et al. developed the force-field controller which applied tangential and normal forces to the ankle, in which the tangential forces moved the ankle along the trajectory, and the normal forces produced virtual tunnel around the desired ankle trajectory (Banala et al., 2009). Asl et al. adopted the force field control term in the velocity field controllers, which acted as the virtual tunnel around the desired trajectory. The forces were applied to the desired trajectory whenever the position of the device deviated more than the safety threshold (Asl et al., 2020). However, the desired trajectory is not individualized for each patient, and the actual trajectory should be modified according to the patient's motion intentions.

In this paper, the flexible knee exoskeleton driven by SEA is designed, and compliant control scheme is proposed for the rehabilitation of stroke patients. The main contributions of this article can be listed as follows.

1) The ball screw drive system, adjustable design, safety mechanism, dual-purpose interface, and support module are adopted in the knee exoskeleton driven by SEA to improve the safety, compatibility, and utilization rate of the device.
2) The attention-based CNN-LSTM network combined with inter-limb synergy is proposed to generate individualized gait trajectory, in which the spatial-temporal attention mechanism is adopted to improve the prediction accuracy.
3) The compliant control scheme based on artificial potential field (APF) method is proposed to nonlinearly and adaptively modify the impedance parameters according to actual conditions, improving the safety and compliance of individualized gait rehabilitation.

The rest of this paper is organized as follows: Section II demonstrates the detailed information of the knee exoskeleton driven by SEA. Section III introduces the proposed individualized gait trajectory prediction model. Section IV shows the compliant control scheme. Experiments and results are conducted in Section V. Section VI is discussion. Conclusion are presented in Section VII.

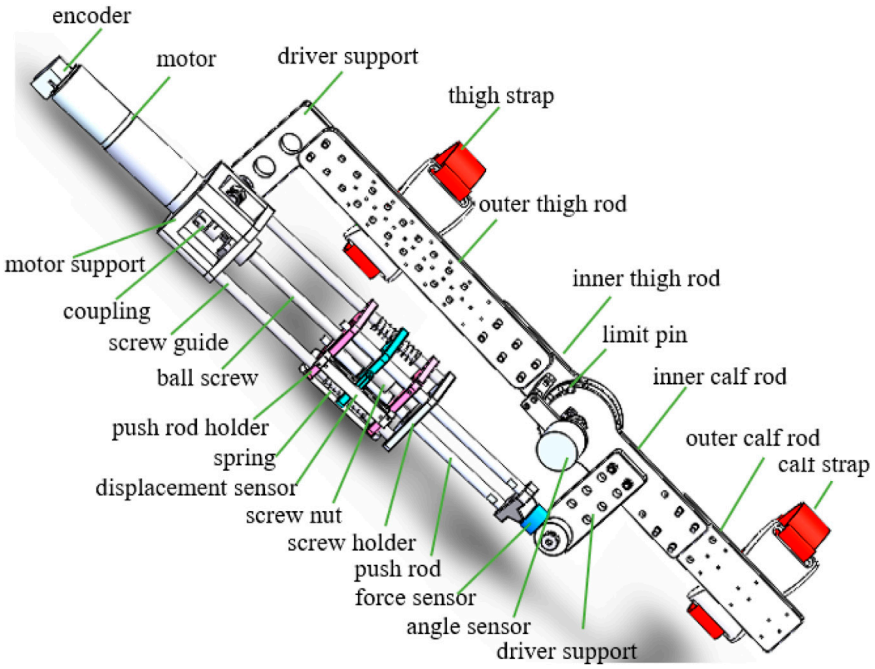

FIGURE 1
Detailed display of knee exoskeleton driven by SEA (Dong et al., 2022).

2 Mechanical design

To enable normal walking, the output torque and angle of the knee exoskeleton in the flexion/extension direction should meet the standards of the human body. The knee angle ranges from −4–66°, and the knee torque ranges from −5–66 $N \cdot m$ (Chen et al., 2019). Meanwhile, the exoskeleton should be designed with an adjustable mechanism to adapt to patients with varying physical parameters.

The knee exoskeleton driven by SEA designed in this paper is used for unilateral lower limb. The main structure of the knee exoskeleton driven by SEA is shown in Figure 1, which mainly includes six modules, namely, thigh module, calf module, knee module, actuator module, support module, and protection module. The length of the thigh module and the calf module can be adjusted to accommodate patients with different physical parameters, which improves the utilization and adaptability of equipment. The inner calf rod and the drive support can also be adjusted, allowing different force arms to be realized to satisfy different rehabilitation needs.

There is a dual-purpose interface at the end of the actuator module, which can realize the normal rotation of the knee joint or calibrate the spring coefficient. The knee module is equipped with safety mechanism to ensure the safety of rehabilitation training. The safety latch can be inserted into the limit hole, and the range of motion of the knee angle can be adjusted by changing the position of the safety latch. The protection module is manufactured through 3D printing technology, and the flexible material enables the protection module to adapt perfectly to the human body. The support module can alleviate the burden on patient, and the patients can wear the knee exoskeleton to achieve gait rehabilitation on the treadmill, as shown in Figure 2A. The support module can also adjust the position of the exoskeleton in three directions. The end of the support module is connected with a bearing, thus promoting unrestricted movement of the hip joint.

The knee exoskeleton adopts SEA as the actuator, as shown in Figure 2B. The SEA is isolated from the load through flexible elements. When the system is impacted, the spring can provide a buffer and absorb energy, which plays a protective role and improve the flexibility of SEA. The angle and displacement sensors are installed at the bottom of the knee module, which can monitor the patient's motion in real time, providing a hardware basis for compliant and intelligent control. When SEA works, the motor drives the ball screw to rotate, and the nut of the ball screw moves linearly, which compresses or stretches the spring. The force of spring makes the push rod of SEA generate thrust or tension, which can realize the flexion or extension movement of the knee joint. At the same time, the actuator module rotates relatively with the thigh and calf driver support module in a small range. The displacement sensor records the deformation of the spring, and the angle sensor records the flexion and extension angle of the knee joint, and the two signal feeds it back to the control system.

3 Individualized gait prediction model

3.1 TASK design and data acquisition

Human motor coordination refers to the ability of the neurobiological motor system to generate complex movements involving multiple limbs or joints. Various types of coordinated movements can be executed by the lower limb, including sitting/standing, squatting/jumping. The most common coordinated

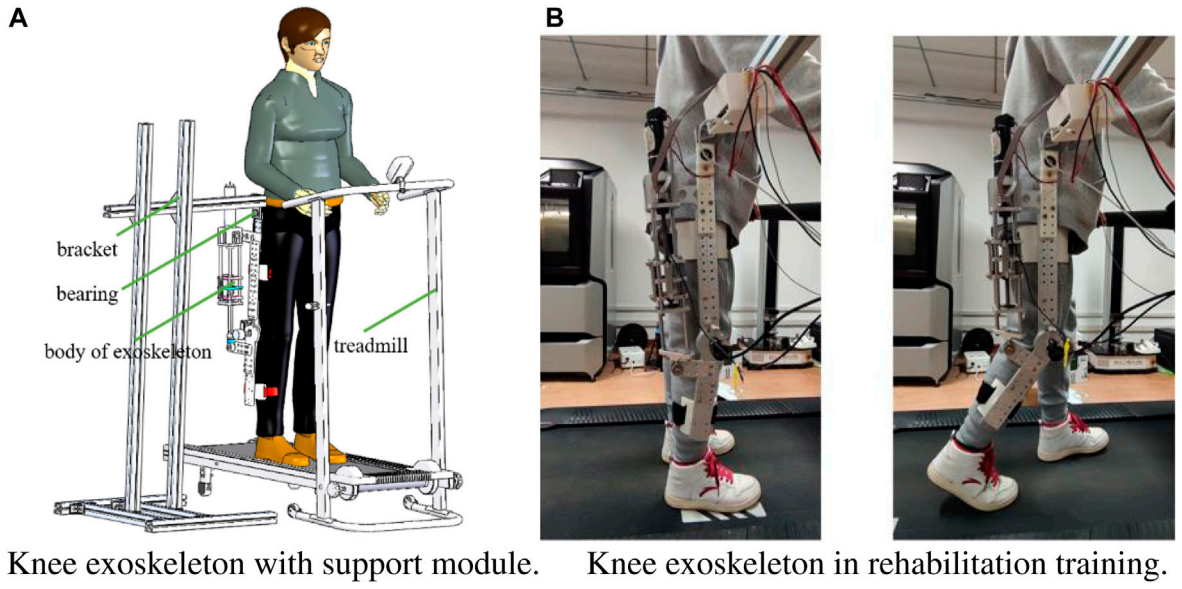

FIGURE 2
The mechanism of knee exoskeleton. **(A)** Knee exoskeleton with support module. **(B)** Knee exoskeleton in rehabilitation training.

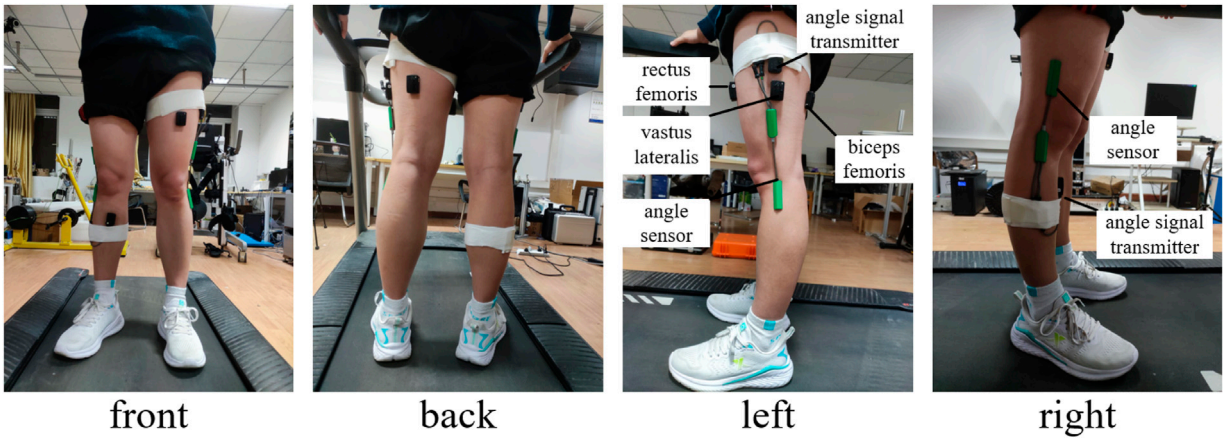

FIGURE 3
Position of the sEMG and angle sensor.

movement is walking, which is a fundamental athletic skill for other activities.

In this paper, a variety of lower limb coordinated movement tasks using the knee joint are designed. The subjects walked on treadmills at different speeds and slopes. The speeds included 0.5 km/h, 1.5 km/h, and 3.0 km/h, and the slopes included 0°, 4°, and 8°. The slope 0° represent that the human walks on flat ground. The subjects initiated a gait cycle with the right heel touching the ground and end the gait cycle with the next right heel touching the ground. The gait trajectory is the knee joint position trajectory during walking in this paper (Tanghe et al., 2020; Challa et al., 2022; Song et al., 2023).

The coordinated movement data of the subjects are collected and recorded by the Delsys sEMG signal acquisition system. The position of the sEMG and angle sensors is displayed in Figure 3. The sEMG sensors are attached with special double-sided adhesive tape to the three muscles closely associated with the movement of knee joint, namely, rectus femoris, vastus lateralis, and biceps femoris. Two angle sensors are attached to the knee joints with ordinary double-sided tape.

Four healthy subjects were invited to participate in the data collection. This trial has been approved by Human Participants Ethics Committee from Wuhan University of Technology, and written informed consent was obtained from each participant. Participants walked while imitating patients with left lower limb injuries, with a reduction in force produced by the left lower limb muscles and an increase in force mainly produced by the right lower limb muscles. The data collected in the experiment were the sEMG

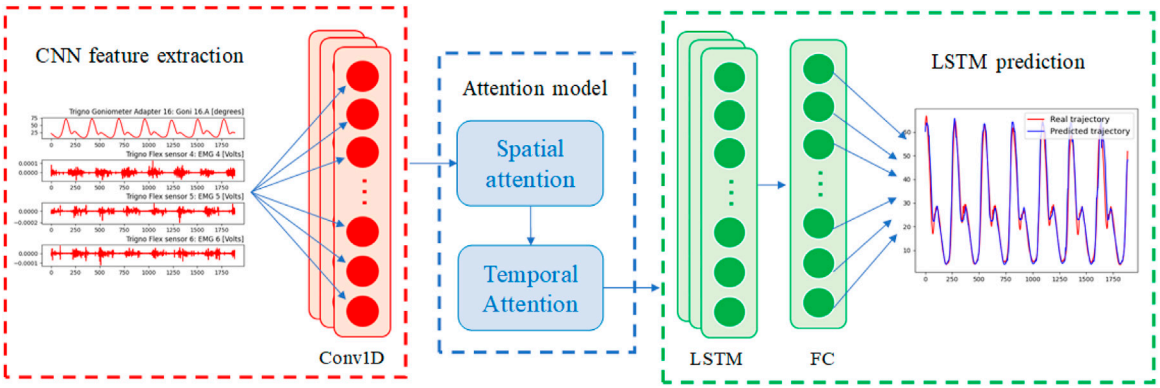

FIGURE 4
Structure of attention-based CNN-LSTM model.

of the three muscles and knee angle signal of the healthy lower limb, as well as knee angle signal of the affected lower limb.

3.2 Attention-based CNN-LSTM model

Synergy mechanism is adopted in statistical regression to extract couplings between limbs in healthy synergetic motion. The synergetic gait prediction model can generate the individualized gait trajectory of the affected lower limb based on the sEMG signal and the knee joint angle of the healthy lower limb. Convolutional neural network (CNN) and long short-term memory (LSTM) neural network are widely applied in gait prediction. Standard CNN model is well suited for handling spatially autocorrelated data, which is unsuitable for dealing with complex and long-term dependencies. In contrast, LSTM model is more suitable in handling temporal autocorrelated data. Therefore, the hybrid CNN-LSTM model can effectively improve forecasting performance. Furthermore, the attention model can assign weights to important features, thus enhancing the prediction accuracy (Thakur and Biswas, 2022; Xu et al., 2022). Individualized gait prediction typically involves the collection and analysis of the data specific to an individual, such as motion capture data, the ground reaction forces, and sEMG data. Machine learning algorithms are adopted to analyze the data and develop personalized models that can accurately predict the individual's gait characteristics.

The structure of attention-based CNN-LSTM model mainly includes four modules, namely, CNN module, spatial attention module, temporal attention module, LSTM module, as shown in Figure 4. The spatial attention module is as shown in Figure 5A, which refers to the Convolutional Block Attention Module (CBAM) (Woo et al., 2018). The input features are respectively subjected to maximum pooling and average pooling to obtain pooled features $\mathbf{F}^{s}_{avg} \in R^{1\times H}$ and $\mathbf{F}^{s}_{max} \in R^{1\times H}$. H represent the number of features. Then, the features pass through a 1D convolutional layer with a filter size of 7, and performs a sigmoid function operation to generate a spatial attention weight vector. The attention weight is multiplied element-by-element with the original feature to output the feature vector $\mathbf{M}_s \in R^{1\times H}$, as shown in Eq. 1.

$$\begin{aligned}\mathbf{M}_s(\mathbf{F}) &= \sigma\left(f^7\left(\left[AvgPool(\mathbf{F}); MaxPool(\mathbf{F})\right]\right)\right)\\ &= \sigma\left(f^7\left(\left[\mathbf{F}^{s}_{avg}; \mathbf{F}^{s}_{max}\right]\right)\right)\end{aligned} \tag{1}$$

where f^7 indicating that the filter size of the convolutional layer is 7, $\mathbf{F}^{s}_{avg}$, $\mathbf{F}^{s}_{max}$ represent pooled features after maximum pooling and average pooling operation, respectively.

$$k = \psi(C) = \left|\frac{\log_2(C)}{\gamma} + \frac{b}{\gamma}\right|_{odd} \tag{2}$$

where the size of the kernel k describes the size of the temporal neighborhood, and γ, b are constants.

The temporal attention module is as shown in Figure 5B, which refers to Squeeze-and-Excitation Network (SENet) (Wang et al., 2020). Firstly, global average pooling is performed on the input features $\mathbf{F} \in R^{C\times H}$, and the dimensions of the input features are mapped from $C \times H$ to $C \times 1$. C represents the number of time steps. Then, 1D convolution is performed on the features, and the sigmoid function operation is performed to generate a temporal attention weight vector. The attention weight is multiplied element-wise with the original feature to output the feature vector $\mathbf{M}_t \in R^{C\times 1}$. k is adaptive to the number of time steps C, determined by Eq. 2, where $\gamma = 2$, $b = 1$. Longer time steps mean longer distance interactions through mapping $\psi(C)$.

4 Adaptive compliant control strategy

4.1 PATH planning

The coordinated gait trajectory of the affected lower limb can be generated based on the information of patient's healthy lower limb, and the data is collected and inputted into the pre-trained synergetic gait prediction model in actual rehabilitation training. However, it is also necessary to consider the safety problems caused by excessive human-robot interaction force on the affected lower limb. The impedance control can modify the expected trajectory of the exoskeleton through the deviation between expected and actual human-robot interaction force, which can realize that the exoskeleton can move under the guidance of the coordinated gait

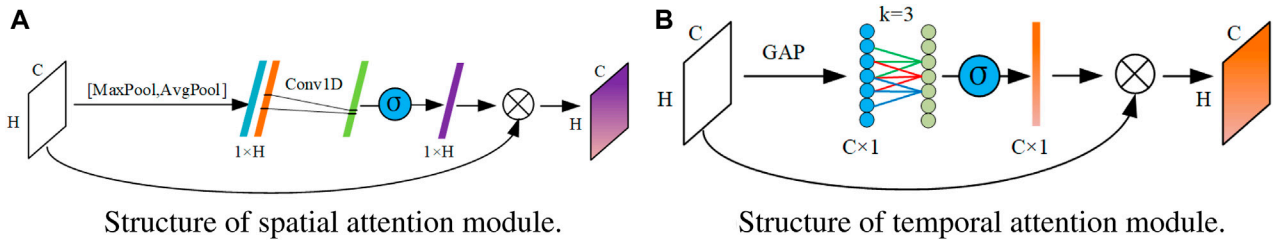

FIGURE 5
Structure of attention module. **(A)** Structure of spatial attention module. **(B)** Structure of temporal attention module.

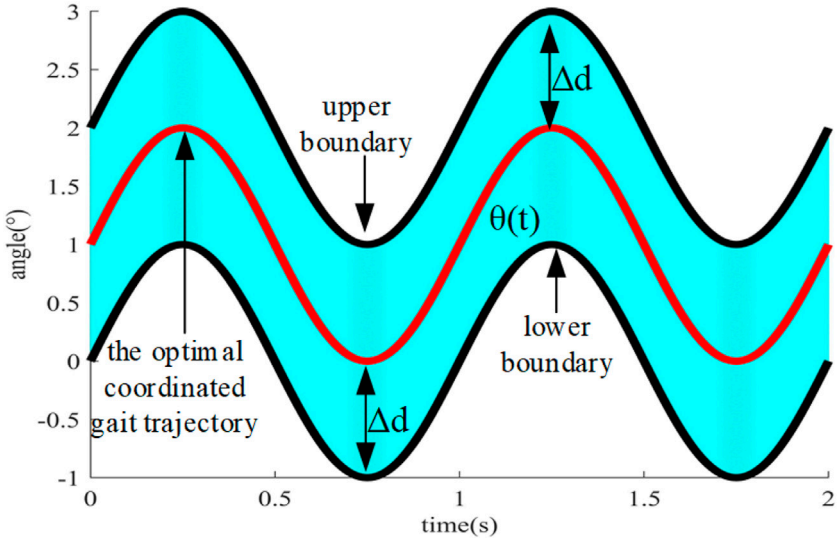

FIGURE 6
Diagram of coordination space.

trajectory as much as possible, while maintaining compliance and reducing the risk of injury.

As shown in Figure 6, the optimal coordinated gait trajectory is defined as the individualized gait of the affected lower limb generated through synergetic gait prediction model in the specific task or scene. Coordination space is defined as the space that extends outwards with the optimal coordinated gait trajectory as the center, and the movements in the coordination space are all in accordance with normal gait pattern. The robot shows the strong compliance near the optimal coordinated trajectory, and the patient's motion intention can correct the expected trajectory. When deviating from the optimal coordinated trajectory, the compliance of the robot gradually decreases, but it still follows the optimal coordinated trajectory and ensures that it always cannot exceed the boundary of the coordination space. Meanwhile, the stiffness coefficient needs to be increased. The trajectory is closer to the boundary of coordination space, the faster the impedance parameter increases, and the inertia coefficient and damping coefficient also need to be increased synchronously to ensure the stability of system.

The APF method is widely adopted in obstacle avoidance in path planning, which can make the robot bypass the obstacle and gradually approach the target by controlling the gravitational field and the repulsive field. Similarly, the optimal coordinated gait trajectory is defined as the target, which is generated by synergetic gait prediction model, and the upper and lower boundaries of coordinated space are defined as the obstacles. The gravitational force near the target increases, and the repulsive force near the obstacle increases. The resultant force at the current position serves as the impedance control parameter, enabling small position corrections near the optimal coordinated gait trajectory and extensive position corrections near the boundary of coordination space.

Define the potential function $U(p)$ of an object at the point p, which is the sum of the gravitational potential function $U_1(p)$ and the repulsive potential function $U_2(p)$, as shown in Eq. 3.

$$U(p) = U_1(p) + U_2(p) \tag{3}$$

$$U_1(p) = \frac{1}{2}\varsigma\rho^2\left(p, p_{target}\right) \tag{4}$$

where ς is the gravitational gain factor, and $\rho(p, p_{obstacle})$ represents the Euclidean distance between the object and the target.

$$U_2(p) = \frac{1}{2}\eta\left(\frac{1}{\rho(p, p_{obstacle})} - \frac{1}{\rho_0}\right)^2 \tag{5}$$

where η is the repulsion gain factor. $\rho(p, p_{obstacle})$ represents the Euclidean distance between the object and the obstacle. ρ_0 represents

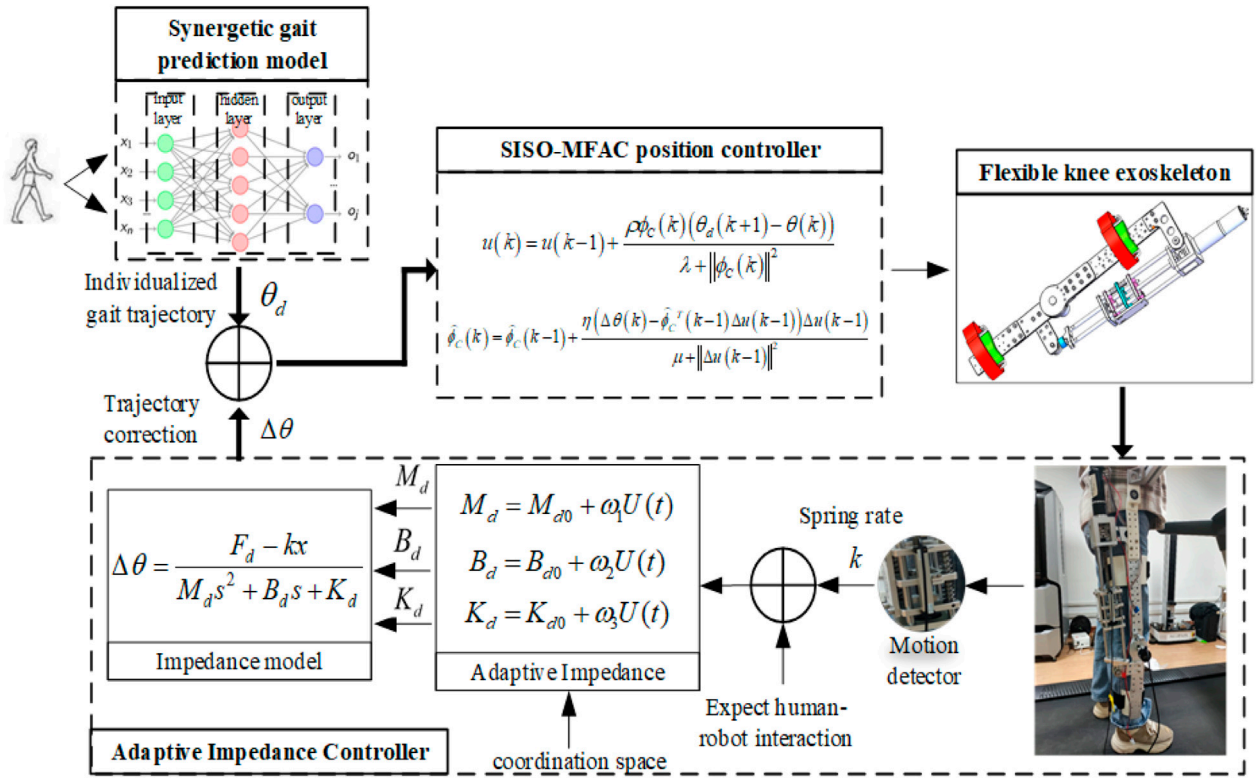

FIGURE 7
Diagram of the proposed compliant controller.

the maximum distance of the repulsion field generated by the obstacle, and $0 \le \rho(p, p_{obstacle}) \le \rho_0$. When $\rho(p, p_{obstacle}) > \rho_0$, $U_2(p) = 0$, and the repulsion field does not work.

When the object is close to the target, the potential function is small and changes slowly, otherwise the potential function is large and changes quickly. When approaching the boundary, the repulsive potential function approaches infinity, which prevents the object from crossing the boundary of coordination space. The potential safety concerns can be raised by infinite impedance. The compliant control gradually increases the impedance as the knee joint approaches the boundary and stops increasing the impedance once the safety threshold has been reached. Therefore, the adaptive impedance control based on the APF is designed as Eq. 6.

$$\begin{cases} M_d = M_{d0} + \omega_1 U(t) \\ B_d = B_{d0} + \omega_2 U(t) \\ K_d = K_{d0} + \omega_3 U(t) \end{cases} \tag{6}$$

where M_{d0}, B_{d0}, and K_{d0} represent the initial values set by inertia coefficient M_d, damping coefficient B_d, and stiffness coefficient K_d, respectively. $U(t)$ represents the potential function at the time t. ω_1, ω_2 and ω_3 represent the positive weights on the potential function.

4.2 Compliant control

The paper employs a single-input single-output model-free adaptive controller (SISO-MFAC) as the position controller to achieve trajectory tracking. SISO-MFAC only adopts the input and output of the controlled system to automatically modify the control signal, which can overcome uncertainty interference and obtain strong robustness against disturbances and unknown model dynamics, as shown in Eq. 7.

$$\begin{cases} u(k) = u(k-1) + \dfrac{\rho\phi_C(k)(\theta_d(k+1)-\theta(k))}{\lambda+\phi_C{}^2(k)} \\ \hat{\phi}_C(k) = \hat{\phi}_C(k-1) \\ \qquad + \dfrac{\eta\left(\Delta\theta(k) - \hat{\phi}_C^T(k-1)\Delta u(k-1)\right)\Delta u(k-1)}{\mu+|\Delta u(k-1)|^2} \\ \hat{\phi}_C(k) = \hat{\phi}_C(1), if\left|\hat{\phi}_C(k)\right| < b or |\Delta u(k-1)| < b \\ \qquad or sign\left(\hat{\phi}_C(k)\right) \ne sign\left(\hat{\phi}_C(1)\right) \end{cases} \tag{7}$$

where $u(k)$ and $\theta(k)$ represent the input and output of the system at time k, respectively. $\phi_C(k) \in R^m$ is the pseudo-gradient of the system. $\hat{\phi_C}(k)$ is an estimate of $\phi_C(k)$ λ and μ are weighting factors. ρ and η are step factors. $\hat{\phi_C}(1)$ is the initial value of $\hat{\phi_C}(k)$.

$$\begin{cases} 0 < 1 - \dfrac{\eta\Delta u^2(k-1)}{\mu+|\Delta u(k-1)|^2} \le d_1 < 1 \\ 0 < 1 - \dfrac{\rho\phi_C(k)\hat{\phi}_C(k)}{\lambda+\hat{\phi}_C^2(k)} \le d_2 < 1 \end{cases} \tag{8}$$

where d_1 and d_2 are constants.

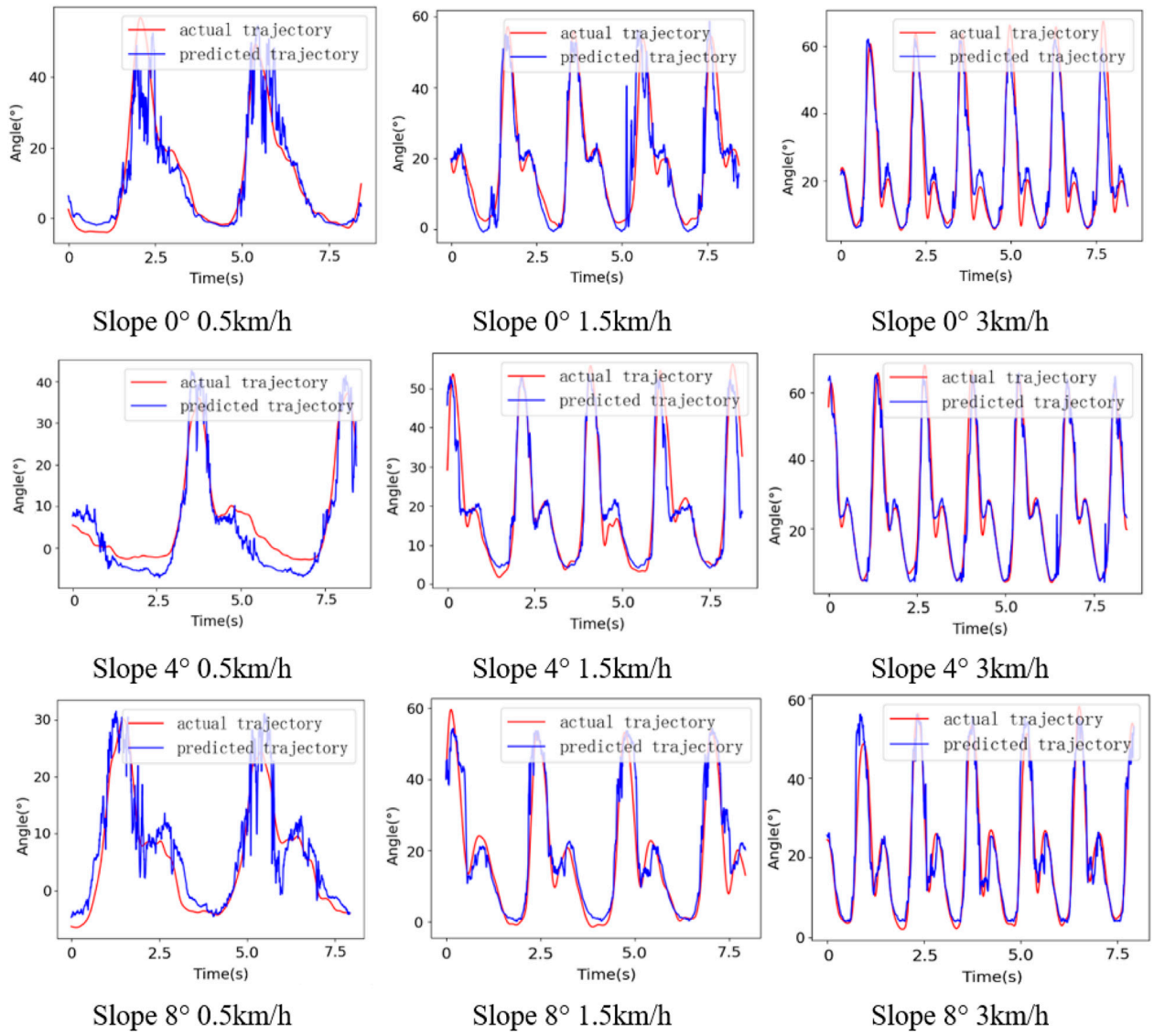

FIGURE 8
Gait prediction results of subject S1.

The diagram of the proposed compliant controller is shown in Figure 7. The compliant controller of knee exoskeleton consists of synergetic gait prediction model, adaptive impedance controller, position controller, and knee exoskeleton. The synergetic gait prediction model is used to generate individualized gait trajectories, and the coordinated gait trajectory of the affected lower limb is generated according to the knee joint angle and sEMG signals of the healthy lower limb. The adaptive impedance controller corrects the expected trajectory in the coordination space according to the deviation between the expected and actual human-robot interaction force. The SISO-MFAC controller can realize the actual trajectory of the exoskeleton to accurately track the expected trajectory. The knee exoskeleton driven by SEA is used as the control object to assist the patient to perform rehabilitation training. Furthermore, the human-robot interaction force between the patient and the exoskeleton is measured by the spring compression at the end of SEA, and the displacement sensor with the range of 50 mm is installed on the spring, which avoids inaccurate measurement due to the relative displacement between the sensor and the human body or the robot. When the actual human-robot interaction force is not equal to the expected human-robot interaction force, the compliant controller generates the correction of expected trajectory, and the position controller controls the exoskeleton to move according to the corrected trajectory. The APF method can ensure that the gait trajectory does not exceed the boundary of coordination space, and the actual trajectory can be guaranteed to be located in the coordination space.

5 Experiments and results

5.1 Individualized gait trajectory prediction

The sampling frequency of the signal acquisition system is 200 Hz, and the time step is 5 ms, and each sample is 50 s. The

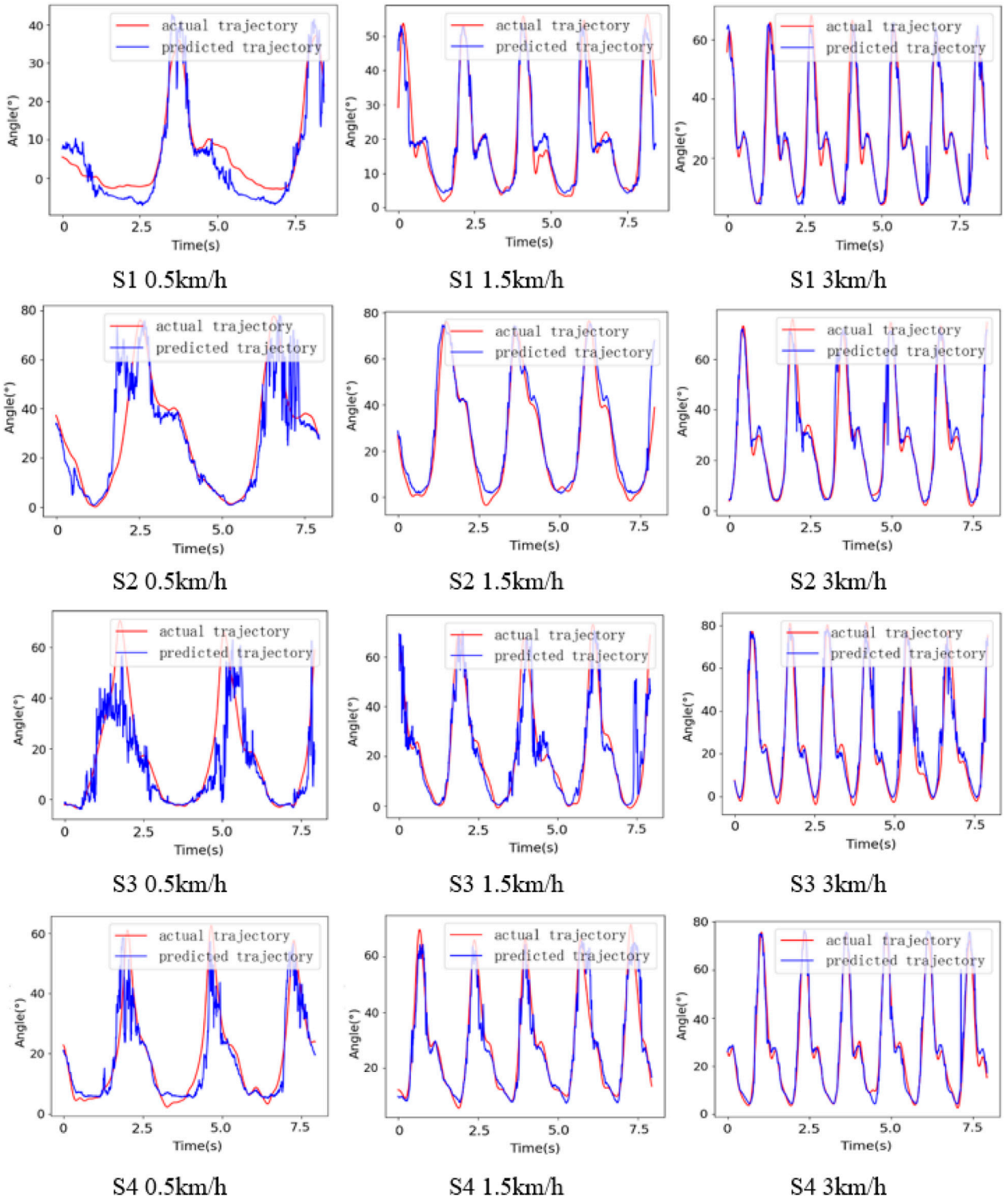

FIGURE 9
Gait prediction results of different subjects.

knee joint data of the affected lower limb at the current moment is influenced by the healthy lower limb at the previous moment, and there is the delay in actual application from gait prediction to data transmission. After comprehensive considerations, the time step is set to 10, and the knee joint angle of the affected lower limb is predicted based on the information of the healthy lower limb in the previous 100 ms. The dimension of dataset under each task is 8980 × 4. The dataset is split into training (60%), validation (20%) and test (20%) subsets. The input dimension of each dataset is 20 × 4 and the output dimension is 1 × 1. The model is trained based on intra-

TABLE 1 Performance of gait trajectory prediction using different networks (slope 4°).

Subject	Speed	MAE (°)				CC(%)			
		0.5	1.5	3	Mean	0.5	1.5	3	Mean
S1	Net1	4.081	3.479	2.910	3.490	**96.64**	94.66	97.08	96.13
	Net2	3.685	3.364	2.757	3.269	96.10	**95.96**	97.26	96.44
	CNN	4.019	3.624	3.253	3.632	92.36	95.18	95.21	94.25
	LSTM	4.617	3.973	3.408	3.999	91.01	94.44	96.37	93.94
	Net	**3.574**	**3.172**	**2.503**	**3.083**	96.22	95.64	**97.80**	**96.55**
S2	Net1	7.327	4.749	4.178	5.418	86.75	**97.07**	95.53	93.12
	Net2	6.403	5.403	3.679	5.162	88.18	96.97	96.67	93.94
	CNN	8.434	5.448	4.344	6.075	80.22	96.37	95.53	90.71
	LSTM	9.194	6.005	4.124	6.441	77.39	95.16	95.94	89.49
	Net	**5.855**	**4.429**	**3.395**	**4.600**	**90.44**	96.92	**96.90**	**94.75**
S3	Net1	10.766	9.400	6.006	8.724	67.94	76.65	93.51	79.37
	Net2	10.054	8.070	6.794	8.306	**75.42**	81.52	93.18	83.37
	CNN	12.001	11.462	6.549	10.004	65.76	79.01	92.49	79.08
	LSTM	12.840	12.485	6.933	10.752	60.80	64.34	92.03	72.39
	Net	**9.508**	**7.838**	**5.598**	**7.648**	73.78	**82.52**	**94.34**	**83.55**
S4	Net1	4.272	3.673	2.854	3.600	90.00	**96.54**	98.20	94.91
	Net2	4.080	3.571	3.158	3.603	91.66	96.18	98.24	95.36
	CNN	5.960	4.608	3.438	4.668	85.62	96.44	97.25	93.10
	LSTM	4.916	4.040	3.452	4.136	88.07	95.83	97.17	93.69
	Net	**3.823**	**3.489**	**2.675**	**3.329**	**92.30**	95.74	**98.46**	**95.50**

The bold values represent the optimal performance of the model for each subject on the metric.

TABLE 2 Performance of gait trajectory prediction using different input (slope 4°).

Subject	Speed	MAE (°)				CC(%)			
		0.5	1.5	3	Mean	0.5	1.5	3	Mean
S1	Net3	3.861	3.932	3.349	3.714	95.72	92.72	96.08	94.84
	Net	**3.574**	**3.172**	**2.503**	**3.083**	**96.22**	**95.64**	**97.80**	**96.55**
S2	Net3	8.911	6.518	5.976	7.135	77.18	91.48	92.02	86.89
	Net	**5.855**	**4.429**	**3.395**	**4.560**	**90.44**	**96.92**	**96.90**	**94.75**
S3	Net3	10.710	9.183	**5.347**	8.413	69.83	78.41	**95.70**	81.31
	Net	**9.508**	**7.838**	5.598	**7.648**	**73.78**	**82.52**	94.34	**83.55**
S4	Net3	5.138	4.823	3.248	4.403	85.12	90.82	97.34	91.09
	Net	**3.823**	**3.489**	**2.675**	**3.329**	**92.30**	**95.74**	**98.46**	**95.50**

The bold values represent the optimal performance of the model for each subject on the metric.

subjects, and the data is obtained from the trained subject with varying speeds and inclines.

Figure 8 shows gait prediction performance of the subject S1 when walking at different speeds on different slopes, in which the red curve represents actual trajectory, and the blue curve represents predicted trajectory. The prediction error is lowest when the speed is 3 km/h, and the prediction performance is worst at the speed of 0.5 km/h. The prediction error at the speed of 0.5 km/h is 42.79% higher than that at the speed of 3 km/h and 12.67% higher than that

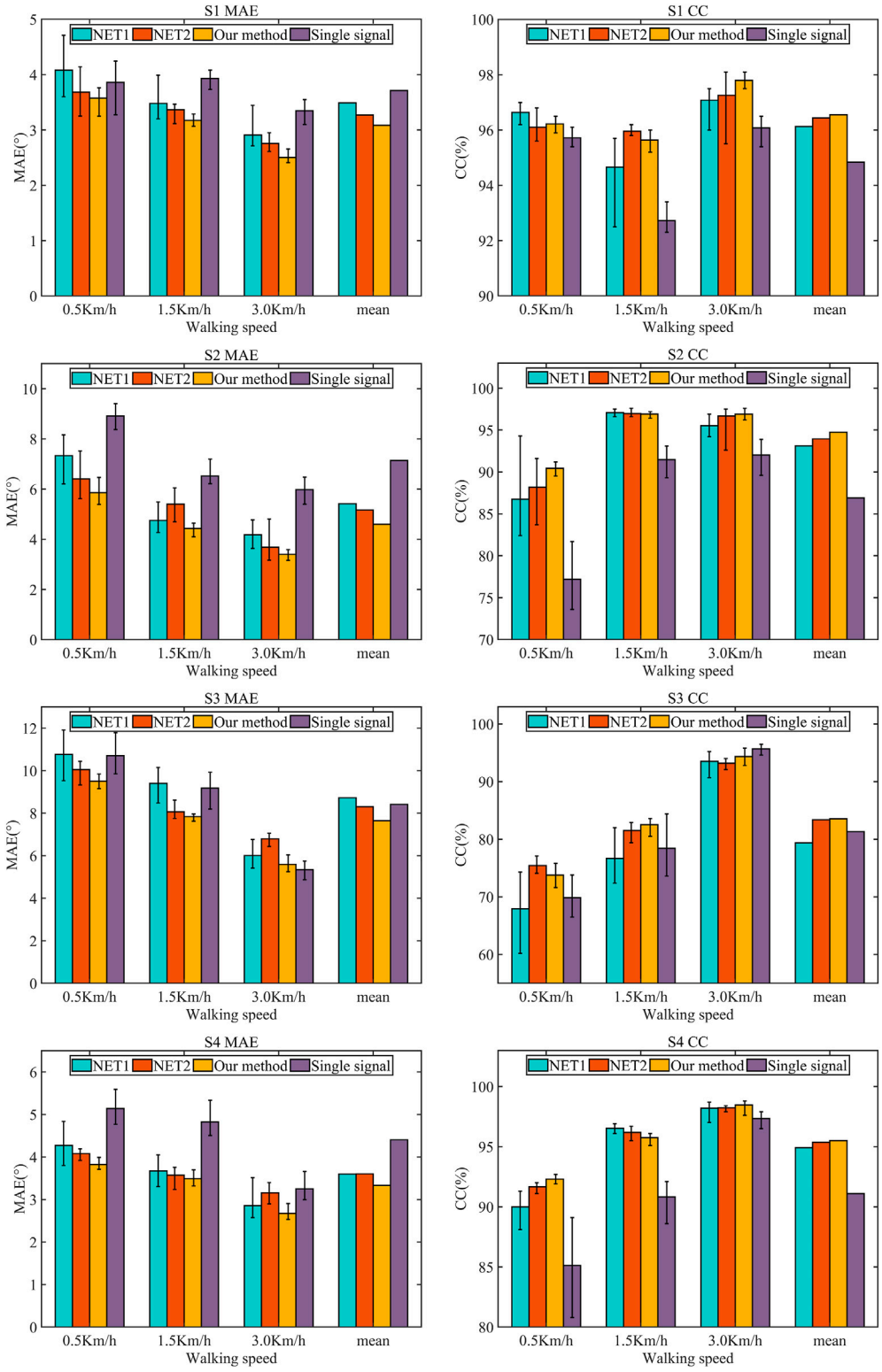

FIGURE 10
Results of different methods for different subjects at different speeds (slope 4°).

at the speed of 1.5 km/h. The muscle activity of the subjects is low when walking at low speed, and the periodicity and amplitude of EMG signals is weaker, so the performance of gait prediction at the speed of 0.5 km/h is worst. Similarly, the prediction performance is best when the slope is 8°, and the prediction error is highest on the slope of 0°. Moreover, although the prediction performance is worst at low speed and flat slope, the trend of angle can still be reflected.

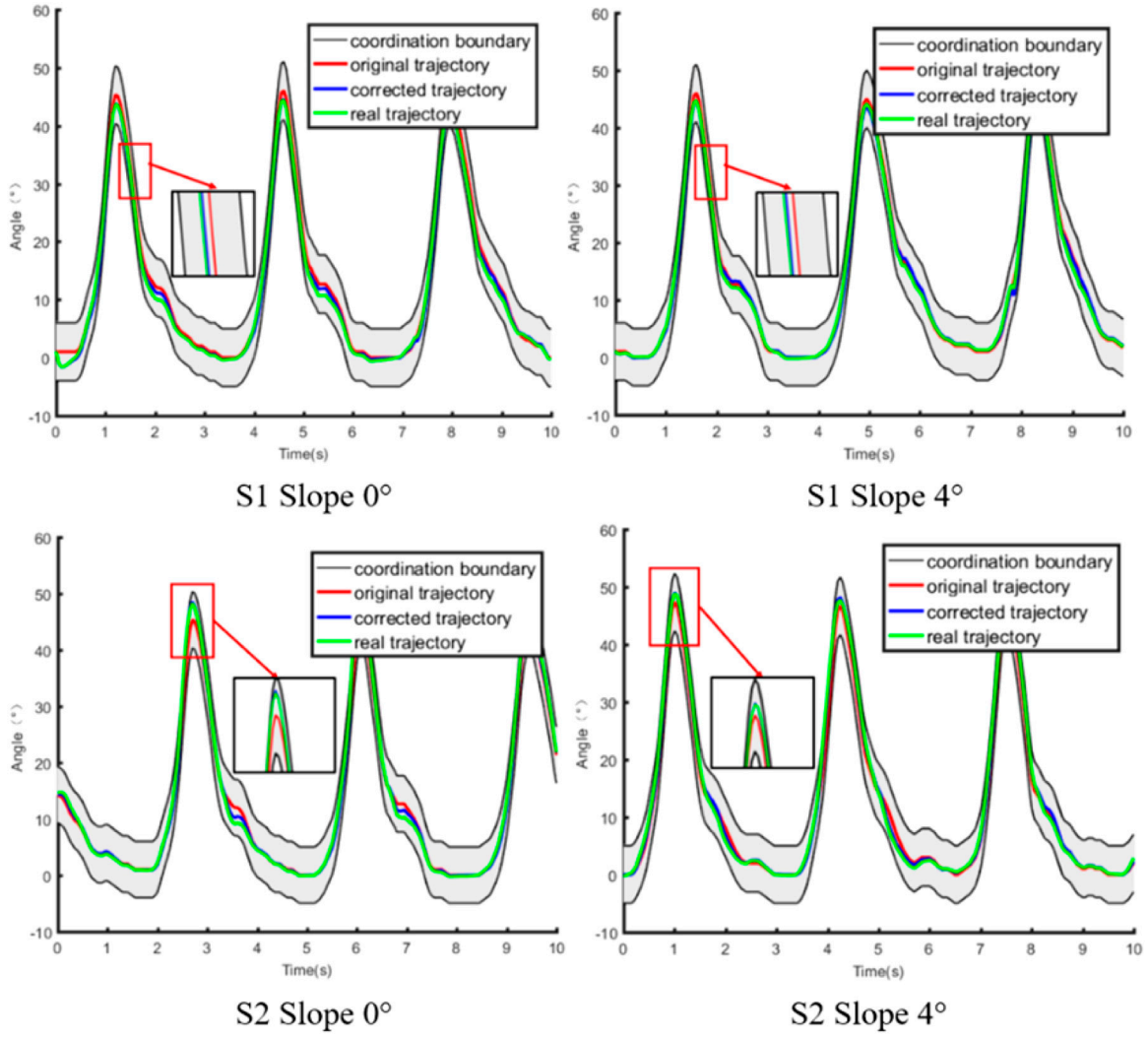

FIGURE 11
Results of compliant control.

To test the applicability of the synergetic gait prediction model, the performance of gait prediction of four subjects at different speeds is analyzed, as shown in Figure 9. The prediction error of S3 is 123.65% higher than that of S1, 64.89% higher than that of S2, and 109.27% higher than that of S4. We have selected five metrics in the time and frequency domains to analyze the sEMG signal, including root mean square (RMS), mean absolute value (MAV), median frequency (MF), mean power frequency (MPF), and signal-to-noise ratio (SNR), and the RMS, MAV, MF, MPF, and SNR metrics show positive correlation with the prediction performance. However, the above metrics are not a dependable basis of prediction performance and can only be adopted as the preliminary reference.

To further quantitatively evaluate the performance, this paper adopts the mean absolute error (MAE) and Pearson correlation coefficient (CC) as the metric. Net1 represents the CNN-LSTM network without attention mechanism, and Net2 refers to the CNN-LSTM network with attention mechanism used in paper (Zhu et al., 2021), and Net is the proposed networks in this paper. The attention mechanism in the Net2 model is the weighted average sum of the output vectors of the LSTM layer. Taking the scene with a slope of 4° as an example, the prediction performance using different model are shown in Table 1. To evaluate the performance of model adopting multi-sensors fusion, the results are shown in Table 2. The Net model adopts the information of the knee joint angle and EMG signal in healthy lower limb as the network input, while the Net3 model only employs the information of the knee joint angle in healthy lower limb.

As shown in Table 1, taking the subject S1 as an example, compared with Net1, the MAE of the model proposed in this paper decrease by 12.42%, 8.82% and 13.99% at 0.5 km/h, 1.5 km/h and 3 km/h, and the CC increase by −0.42% and 0.99%, and 0.72%. Compared with Net2, the MAE of the model proposed in this paper decrease by 3.01%, 5.71% and 9.21%, and the CC increase by 0.12%, −0.32% and 0.18%. The above trend is also reflected in the prediction results of subjects S2, S3 and S4. In summary, the prediction performance of proposed model in this paper is better than Net1 and Net2.

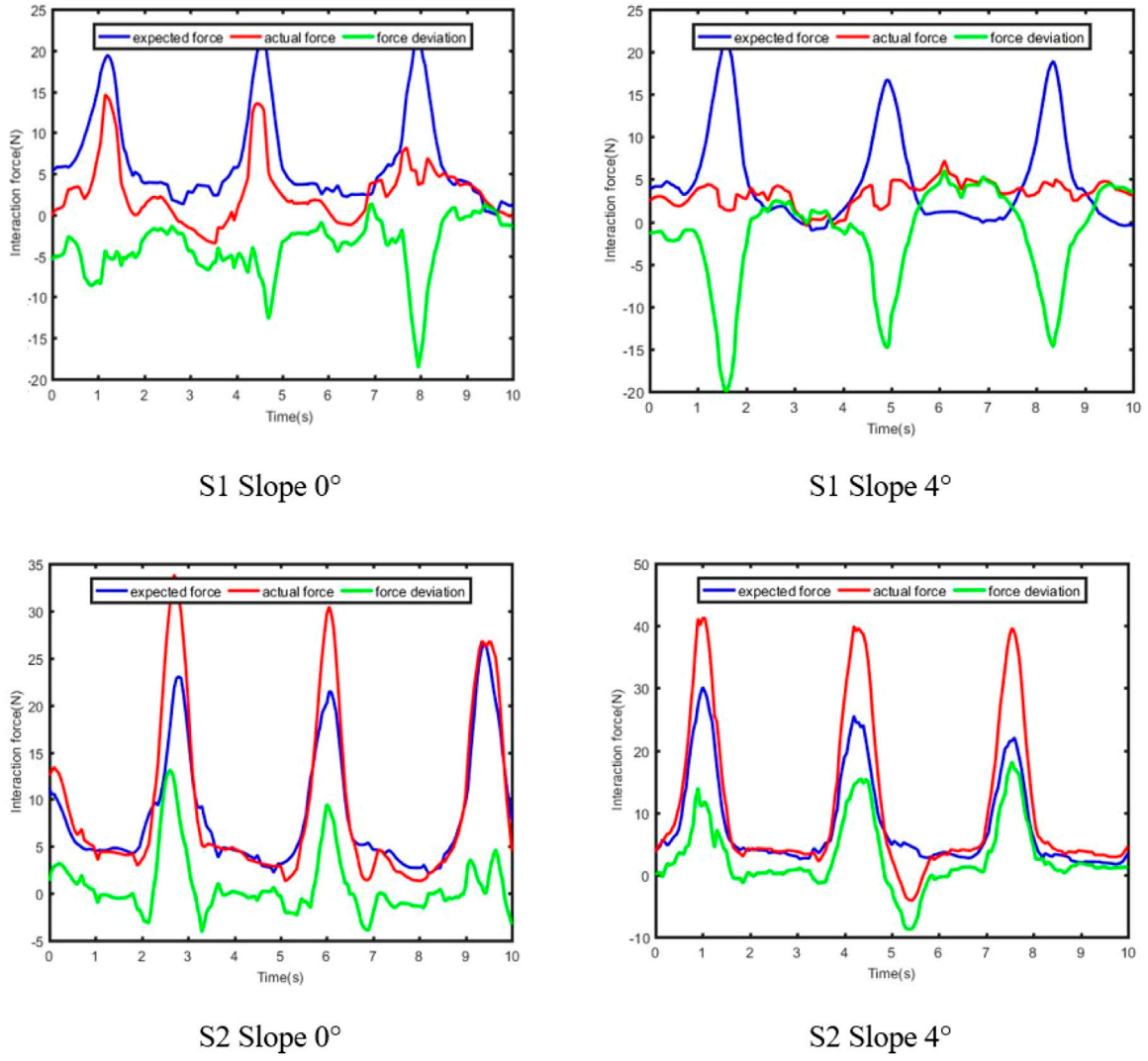

FIGURE 12
Results of human-robot interaction force.

As shown in Table 2, taking the subject S1 as an example, compared with Net3, the MAE of the model adopting multi-sensors input decrease by 7.43%, 19.33%, and 25.26% at 0.5 km/h, 1.5 km/h, and 3 km/h, and CC increase by 0.5%, 2.92% and 1.72%. It is worth noting that although the CC of the model using single input is higher, and the MAE is lower when the subject S3 is at 3 km/h, the mean of CC and MAE at three speeds are still better than Net3. Furthermore, the results of the subjects S1, S2, and S4 are consistent, which shows that multi-sensor fusion can further improve the accuracy of gait prediction. Figure 10 visually shows the prediction results of different methods for different subjects at different speeds on slope 4°. The model using multi-sensors information has smaller MAE and higher CC compared with the model adopting single input. Meanwhile, the mean of MAE at three speeds is smaller than that of the other network, and the mean of CC is higher than that of the other network, which shows that the model proposed in this paper has smaller prediction error and better applicability to different individuals.

5.2 Adaptive compliant control

Experiments are carried out on a SEA-driven knee exoskeleton to assess the effectiveness of the proposed compliant control method. Considering the site conditions and safety factors, the experimental scenes are divided into two types, namely, walking on the slope 0° and 4° at the speed of 0.5 km/h, respectively. The boundary range of the coordination space is set to a constant value $\Delta d = 5°$, and the distance between the upper and lower boundaries of the coordination space is 10°. To guarantee participant safety, the knee exoskeleton's motion angle has been limited to −5°–65° degrees *via* the software.

The results of compliant control of the subjects S1 and S2 in different scenes are shown in Figure 11, in which the red curve represents the optimal coordinated trajectory, and the blue curve represents the corrected trajectory, and the green curve represents the actual trajectory of the exoskeleton. The original trajectory is defined as the gait trajectory generated by the prediction model and filtered to comply with the normal human gait pattern. The

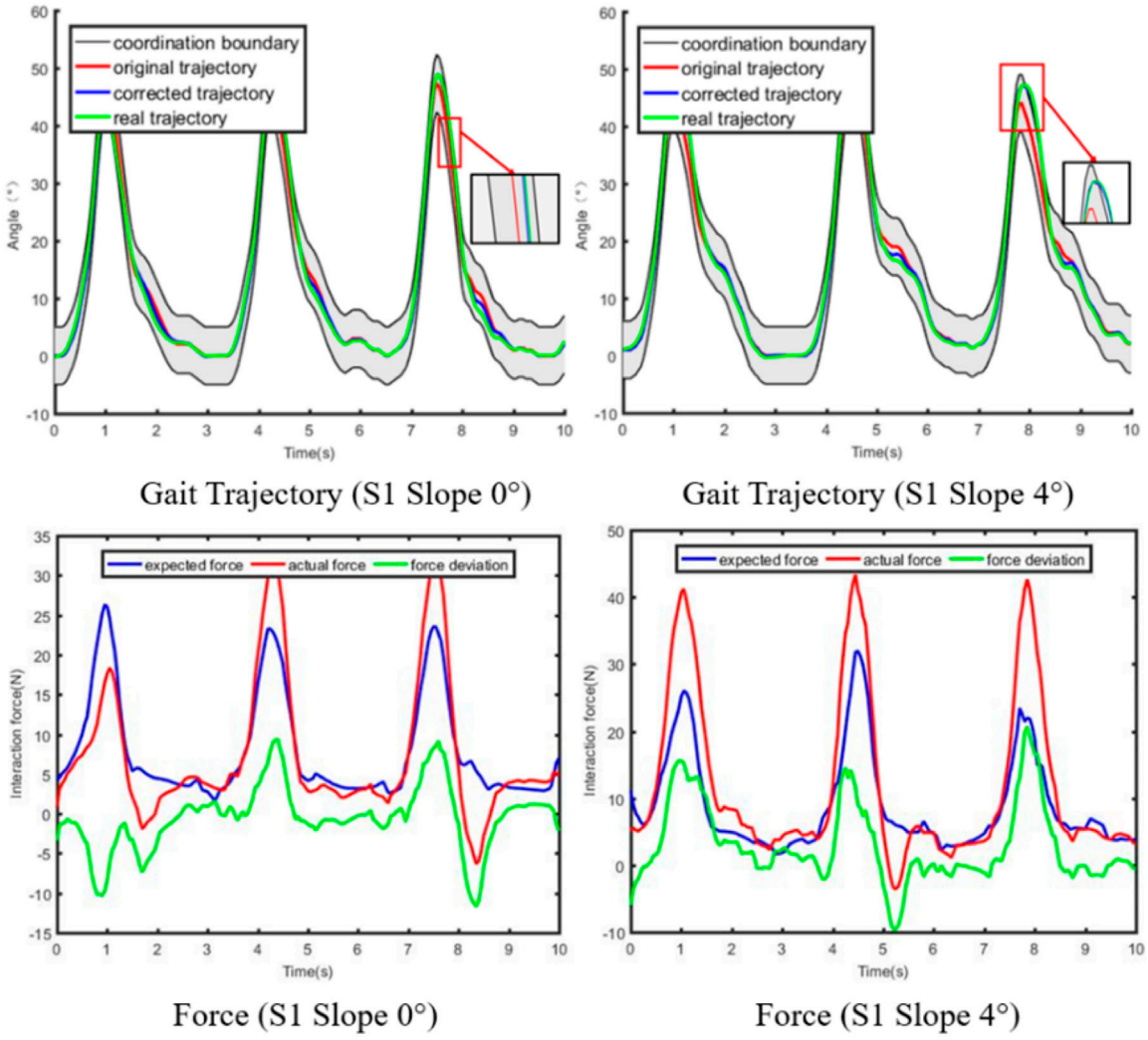

FIGURE 13
Results of Compliant control with fixed impedance parameters.

corrected trajectory represents the trajectory modified by the compliant controller when the actual human-robot interaction force is not equal to the expected human-robot interaction force. The actual trajectory is defined as the angle signal collected by the angle sensor on the knee exoskeleton. Furthermore, the optimal coordinated gait trajectory, the corrected trajectory, and the actual trajectory are all in the coordination space, which proves that the compliant control method can adaptively and nonlinearly modify the impedance parameters according to the actual conditions, and ensure the safety and coordination of rehabilitation training.

The results of the human-robot interaction force is shown in Figure 12, in which the blue curve represents the expected human-robot interaction force, and the red curve represents the actual human-robot interaction force, and the green curve represents the deviation between the expected and actual human-robot interaction force. The expected force is defined as the human-robot interaction force of healthy subjects collected by the force sensor in advance. The actual force is defined as the human-robot interaction force of patients during rehabilitation training. Combining Figures 11, 12, it is evident that the trajectory correction is not proportional to the force deviation. The deviation of force is positive, which indicates that the motion intention of the subject is consistent with the direction of the robot.

The experiment with fixed impedance parameters on the subject S1 are conducted, and the experimental results are shown in Figure 13. When the actual human-robot interaction force deviates from the expected human-robot interaction force, the impedance controller with fixed parameters can also correct the trajectory. However, if the deviation of force is large, the corrected trajectory may exceed the boundary of the coordination space. Consequently, the impedance control system with fixed impedance parameters cannot completely guarantee the safety and coordination of rehabilitation training. The adaptive impedance control proposed in this paper can not only nonlinearly and adaptively modify the expected trajectory according to the human-robot interaction force, but also restrict the actual trajectory to always be in the coordination space.

6 Discussion

As an emerging rehabilitation equipment, exoskeleton can reduce the burden on physicians while ensuring the efficacy of rehabilitation, which has gradually become a research hotspot in the field of rehabilitation. However, the current trajectories for rehabilitation are mostly predefined trajectories, which cannot adapt to speed and slope changes during rehabilitation training in the middle and late stages of rehabilitation. Based on the attention-based CNN-LSTM model, the individualized coordinated trajectory of the affected lower limb under different tasks is obtained. The performance of synergetic gait prediction model of different individuals varied widely. Attention mechanism has been proven to effectively improve the performance of the neural network model. Spatial attention and temporal attention modules can assign attention weights to important features. The combined attention mechanism is introduced into synergetic gait prediction model to further improve the prediction accuracy of individualized gait.

Compliant controller is designed based on the guidance of synergetic gait prediction model. The predicted individualized gait trajectory is inputted into the compliant controller as the expected trajectory. The compliant controller can adaptively and nonlinearly modify the impedance parameters according to the distance from the boundary. The correction of trajectory is larger near the expected trajectory, which shows strong compliance. The APF method can ensure that the actual trajectory does not cross the boundary of coordination space while realizing compliant control. There is no clear evidence that compliant control is superior to pure torque/force control or pure position control for stroke rehabilitation. However, patient-dominated training can enhance rehabilitation outcomes, and compliant control can improve patient participation while ensuring patient safety. In addition, the proposed compliant control is mainly used in the middle and late stages of rehabilitation when the patient obtains some motor abilities. Position control is used to assist patients with repetitive passive training, which is mainly used in the early stages of rehabilitation. The advantage of compliant control compared to pure torque/force control lies in the personalized assistance, including the generation of the personalized trajectory and the adaptive modification of impedance parameters in response to actual conditions (Shi et al., 2022; Cao et al., 2024).

The knee exoskeleton driven by SEA designed in this paper has the function of limit protection and size adjustment, which improves the safety and applicability of the equipment. However, the knee exoskeleton is not lightweight, and it is a little cumbersome and inconvenient for patients to use. We aim to decrease the weight and volume of the knee exoskeleton through optimizing the power transmission mode, selecting lightweight high-strength materials such as carbon fiber as the main materials of knee exoskeleton, and combining 3D printing technology. In addition, the application of inter-limb coordination in knee joint rehabilitation is controversial (Vallery et al., 2009; Liang et al., 2018), because the abnormalities in knee joint may alter the features of other joints, ultimately resulting in the deficient desired trajectory of knee joint. Our proposed method can customize the rehabilitation according to the patient's range of motion and body parameters. Now, we have been actively collaborating with Tongji Hospital, Wuhan, China, to identify eligible patients for the experimental study. Meanwhile, we plan to consider more sensors for multi-level and multi-spatial information complementarity to improve the prediction performance of the subjects with substandard signal quality.

7 Conclusion

In this paper, a synergetic gait prediction model based on attention-based CNN-LSTM network and compliant control method based on APF method are proposed. The experimental results show that the proposed synergetic gait prediction model can generate the coordinated gait trajectory, which can achieve lower MAE and higher CC. The subjects move in the coordination space but never cross the coordination boundary. Coordination, compliance, and safety are simultaneously considered in the rehabilitation. In the future, we will design knee exoskeletons that are more lightweight and patient-friendly, test individualized gait prediction model under more scenes, and further verify the effectiveness of the proposed method on patients.

Data availability statement

The original contributions presented in the study are included in the article/Supplementary Material, further inquiries can be directed to the corresponding author.

Ethics statement

The studies involving humans were approved by the Human Participants Ethics Committee of Wuhan University of Technology. The studies were conducted in accordance with the local legislation and institutional requirements. The participants provided their written informed consent to participate in this study.

Author contributions

HL: Writing–original draft. CZ: Writing–original draft. ZZ: Writing–review and editing. YD: Writing–original draft. WM: Writing–review and editing. QL: Writing–review and editing.

Funding

The author(s) declare financial support was received for the research, authorship, and/or publication of this article. This work was supported in part by the Key Research and Development Program of Hubei Province under Grant 2022BAA066 and in part by the National Natural Science Foundation of China under Grant 52075398 and Grant 52275029.

Conflict of interest

The authors declare that the research was conducted in the absence of any commercial or financial relationships that could be construed as a potential conflict of interest.

Publisher's note

All claims expressed in this article are solely those of the authors and do not necessarily represent those of their affiliated organizations, or those of the publisher, the editors and the reviewers. Any product that may be evaluated in this article, or claim that may be made by its manufacturer, is not guaranteed or endorsed by the publisher.

Supplementary material

The Supplementary Material for this article can be found online at: https://www.frontiersin.org/articles/10.3389/fbioe.2024.1358022/full#supplementary-material

References

Almaghout, K., Tarvirdizadeh, B., Alipour, K., and Hadi, A. (2022). Rbf neural network-based admittance pd control for knee rehabilitation robot. *Robotica* 40, 4512–4534. doi:10.1017/S0263574722001084

Arami, A., Poulakakis-Daktylidis, A., Tai, Y. F., and Burdet, E. (2019). Prediction of gait freezing in parkinsonian patients: a binary classification augmented with time series prediction. *IEEE Trans. Neural Syst. Rehabilitation Eng.* 27, 1909–1919. doi:10.1109/TNSRE.2019.2933626

Asl, H. J., Yamashita, M., Narikiyo, T., and Kawanishi, M. (2020). Field-based assist-as-needed control schemes for rehabilitation robots. *IEEE Trans. Mechatronics* 25, 2100–2111. doi:10.1109/tmech.2020.2992090

Ballester, B. R., Ward, N. S., Brander, F., Maier, M., Kelly, K., and Verschure, P. (2022). Relationship between intensity and recovery in post-stroke rehabilitation: a retrospective analysis. *J. Neurology Neurosurg. Psychiatry* 93, 226–228. doi:10.1136/jnnp-2021-326948

Banala, S. K., Kim, S. H., Agrawal, S. K., and Scholz, J. P. (2009). Robot assisted gait training with active leg exoskeleton (alex). *IEEE Trans. Neural Syst. Rehabilitation Eng.* 17, 2–8. doi:10.1109/tnsre.2008.2008280

Cao, W., Shang, D., Yin, M., Li, X., Xu, T., Zhang, L., et al. (2023). Development and evaluation of a hip exoskeleton for lateral resistance walk exercise. *IEEE Trans. Mechatronics* 28, 1966–1974. doi:10.1109/TMECH.2023.3273717

Cao, Y., Chen, X., Zhang, M., and Huang, J. (2024). Adaptive position constrained assist-as-needed control for rehabilitation robots. *IEEE Trans. Industrial Electron.* 71, 4059–4068. doi:10.1109/tie.2023.3273270

Challa, S. K., Kumar, A., Semwal, V. B., and Dua, N. (2022). An optimized-lstm and rgb-d sensor-based human gait trajectory generator for bipedal robot walking. *IEEE Sensors J.* 22, 24352–24363. doi:10.1109/jsen.2022.3222412

Chen, B., Zhong, C. H., Zhao, X., Ma, H., Guan, X., Li, X., et al. (2017). A wearable exoskeleton suit for motion assistance to paralysed patients. *J. Orthop. Transl.* 11, 7–18. doi:10.1016/j.jot.2017.02.007

Chen, B., Zi, B., Wang, Z., Qin, L., and Liao, W.-H. (2019). Knee exoskeletons for gait rehabilitation and human performance augmentation: a state-of-the-art. *Mech. Mach. Theory* 134, 499–511. doi:10.1016/j.mechmachtheory.2019.01.016

Chen, L., Wang, C., Song, X., Wang, J., Zhang, T., and Li, X. (2020). Dynamic trajectory adjustment of lower limb exoskeleton in swing phase based on impedance control strategy. *Proc. Institution Mech. Eng. Part I J. Syst. Control Eng.* 234, 1120–1132. doi:10.1177/0959651820932026

Dong, Y., Ai, Q., Liu, H., Meng, W., and Cheng, W. (2022). "Design and control of a sea driven knee exoskeleton for walking assistance," in 2022 IEEE/ASME International Conference on Advanced Intelligent Mechatronics (AIM), Hokkaido, Japan, July 11th-15th, 2022, 1243. doi:10.1109/aim52237.2022.9863380

Feigin, V. L., Brainin, M., Norrving, B., Martins, S., Sacco, R. L., Hacke, W., et al. (2022). World stroke organization (wso): global stroke fact sheet 2022. *Int. J. Stroke* 17, 18–29. doi:10.1177/17474930211065917

Gautam, A., Panwar, M., Biswas, D., and Acharyya, A. (2020). Myonet: a transfer-learning-based lrcn for lower limb movement recognition and knee joint angle prediction for remote monitoring of rehabilitation progress from semg. *IEEE J. Transl. Eng. Health Med.* 8, 1–10. doi:10.1109/JTEHM.2020.2972523

Huang, P., Li, Z., Zhou, M., Li, X., and Cheng, M. (2022). Fuzzy enhanced adaptive admittance control of a wearable walking exoskeleton with step trajectory shaping. *IEEE Trans. Fuzzy Syst.* 30, 1541–1552. doi:10.1109/tfuzz.2022.3162700

Kim, J., Lee, G., Heimgartner, R., Revi, D. A., Karavas, N., Nathanson, D., et al. (2019). Reducing the metabolic rate of walking and running with a versatile, portable exosuit. *Sci. Robotics* 365, 668–672. doi:10.1126/science.aav7536

Kim, J., Moon, J. H., and Kim, J. (2021). Impedance control of human ankle joint with electrically stimulated antagonistic muscle co-contraction. *IEEE Trans. Neural Syst. Rehabilitation Eng.* 29, 1593–1603. doi:10.1109/TNSRE.2021.3104091

Kong, K., Bae, J., and Tomizuka, M. (2012). A compact rotary series elastic actuator for human assistive systems. *IEEE Trans. Mechatronics* 17, 288–297. doi:10.1109/tmech.2010.2100046

Li, X., Liu, Y.-H., and Yu, H. (2018). Iterative learning impedance control for rehabilitation robots driven by series elastic actuators. *Automatica* 90, 1–7. doi:10.1016/j.automatica.2017.12.031

Liang, F.-Y., Zhong, C.-H., Zhao, X., Castro, D. L., Chen, B., Gao, F., et al. (2018). "Online adaptive and lstm-based trajectory generation of lower limb exoskeletons for stroke rehabilitation," in IEEE International Conference on Robotics and Biomimetics, Kuala Lumpur, Malaysia, December 12-15, 2018, 27–32. doi:10.1109/ROBIO.2018.8664778

Liu, D.-X., Wu, X., Du, W., Wang, C., Chen, C., and Xu, T. (2017). Deep spatial-temporal model for rehabilitation gait: optimal trajectory generation for knee joint of lower-limb exoskeleton. *Assem. Autom.* 37, 369–378. doi:10.1108/aa-11-2016-155

Liu, J., Wang, C., He, B., Li, P., and Wu, X. (2022). Metric learning for robust gait phase recognition for a lower limb exoskeleton robot based on semg. *IEEE Trans. Med. Robotics Bionics* 4, 472–479. doi:10.1109/tmrb.2022.3166543

Liu, L., Leonhardt, S., Ngo, C., and Misgeld, B. J. E. (2020). Impedance-controlled variable stiffness actuator for lower limb robot applications. *IEEE Trans. Automation Sci. Eng.* 17, 991–1004. doi:10.1109/tase.2019.2954769

Mazumder, O., Kundu, A. S., Lenka, P. K., and Bhaumik, S. (2016). Multi-channel fusion based adaptive gait trajectory generation using wearable sensors. *J. Intelligent Robotic Syst.* 86, 335–351. doi:10.1007/s10846-016-0436-y

Morbidoni, C., Cucchiarelli, A., Agostini, V., Knaflitz, M., Fioretti, S., and Di Nardo, F. (2021). Machine-learning-based prediction of gait events from emg in cerebral palsy children. *IEEE Trans. Neural Syst. Rehabilitation Eng.* 29, 819–830. doi:10.1109/TNSRE.2021.3076366

Mounir Boudali, A., Sinclair, P. J., and Manchester, I. R. (2019). Predicting transitioning walking gaits: hip and knee joint trajectories from the motion of walking canes. *IEEE Trans. Neural Syst. Rehabilitation Eng.* 27, 1791–1800. doi:10.1109/TNSRE.2019.2933896

Na, J., Kim, H., Lee, G., and Nam, W. (2023). Deep domain adaptation, pseudo-labeling, and shallow network for accurate and fast gait prediction of unlabeled datasets. *IEEE Trans. Neural Syst. Rehabilitation Eng.* 31, 2448–2456. doi:10.1109/TNSRE.2023.3272887

Perez-Ibarra, J. C., Siqueira, A. A. G., Silva-Couto, M. A., de Russo, T. L., and Krebs, H. I. (2019). Adaptive impedance control applied to robot-aided neuro-rehabilitation of the ankle. *IEEE Robotics Automation Lett.* 4, 185–192. doi:10.1109/lra.2018.2885165

Schumacher, M., Wojtusch, J., Beckerle, P., and von Stryk, O. (2019). An introductory review of active compliant control. *Robotics Aut. Syst.* 119, 185–200. doi:10.1016/j.robot.2019.06.009

Shi, D., Li, L., Zhang, W., and Ding, X. (2022). Field-based human-centred control on so(3) for assist-as-needed robotic rehabilitation. *IEEE Trans. Med. Robotics Bionics* 4, 785–795. doi:10.1109/tmrb.2022.3194372

Sivakumar, S., Gopalai, A. A., Lim, K. H., and Gouwanda, D. (2019). Artificial neural network based ankle joint angle estimation using instrumented foot insoles. *Biomed. Signal Process. Control* 54, 101614. doi:10.1016/j.bspc.2019.101614

Song, J., Zhu, A., Tu, Y., Zhang, X., and Cao, G. (2023a). Novel design and control of a crank-slider series elastic actuated knee exoskeleton for compliant human–robot interaction. *IEEE Trans. Mechatronics* 28, 531–542. doi:10.1109/tmech.2022.3204921

Song, W., Zhao, P., Li, X., Deng, X., and Zi, B. (2023b). Data-driven design of a six-bar lower-limb rehabilitation mechanism based on gait trajectory prediction. *IEEE Trans. Neural Syst. Rehabilitation Eng.* 31, 109–118. doi:10.1109/TNSRE.2022.3217448

Spyrakos-Papastavridis, E., and Dai, J. S. (2021). Minimally model-based trajectory tracking and variable impedance control of flexible-joint robots. *IEEE Trans. Industrial Electron.* 68, 6031–6041. doi:10.1109/tie.2020.2994886

Sridar, S., Qiao, Z., Muthukrishnan, N., Zhang, W., and Polygerinos, P. (2018). A soft-inflatable exosuit for knee rehabilitation: assisting swing phase during walking. *Front. Robotics AI* 5, 44. doi:10.3389/frobt.2018.00044

Sun, T., Peng, L., Cheng, L., Hou, Z. G., and Pan, Y. (2020). Composite learning enhanced robot impedance control. *IEEE Trans. Neural Netw. Learn. Syst.* 31, 1052–1059. doi:10.1109/TNNLS.2019.2912212

Tanghe, K., De Groote, F., Lefeber, D., De Schutter, J., and Aertbelien, E. (2020). Gait trajectory and event prediction from state estimation for exoskeletons during gait. *IEEE Trans. Neural Syst. Rehabilitation Eng.* 28, 211–220. doi:10.1109/TNSRE.2019.2950309

Thakur, D., and Biswas, S. (2022). Attention-based deep learning framework for hemiplegic gait prediction with smartphone sensors. *IEEE Sensors J.* 22, 11979–11988. doi:10.1109/jsen.2022.3172603

Vallery, H., van Asseldonk, E. H., Buss, M., and van der Kooij, H. (2009). Reference trajectory generation for rehabilitation robots: complementary limb motion estimation. *IEEE Trans. Neural Syst. Rehabilitation Eng.* 17, 23–30. doi:10.1109/TNSRE.2008.2008278

Wang, K. Y., Ma, F. C., Hao, M., Zhang, L. X., and Liu, P. (2011). Experimental research on force/position control of a wire-driven parallel rehabilitative robot. *Appl. Mech. Mater.* 138-139, 68–73. doi:10.4028/www.scientific.net/AMM.138-139.68

Wang, Q., Wu, B., Zhu, P., Li, P., Zuo, W., and Hu, Q. (2020). "Eca-net: efficient channel attention for deep convolutional neural networks," in 2020 IEEE/CVF Conference on Computer Vision and Pattern Recognition (CVPR), Seattle, WA, USA, June 13 2020 to June 19 2020. doi:10.1109/cvpr42600.2020.01155

Wang, Y., Yang, Y., Zhao, B., Qi, X., Hu, Y., Li, B., et al. (2021). Variable admittance control based on trajectory prediction of human hand motion for physical human-robot interaction. *Appl. Sci.* 11, 5651. doi:10.3390/app11125651

Wang, Z., Zhu, M., Su, Z., Guan, B., Wang, A., Wang, Y., et al. (2017). Post-stroke depression: different characteristics based on follow-up stage and gender-a cohort perspective study from mainland China. *Neurological Res.* 39, 996–1005. doi:10.1080/01616412.2017.1364514

Woo, S., Park, J., Lee, J.-Y., and Kweon, I. S. (2018). "Cbam: convolutional block attention module," in European conference on computer vision (ECCV), Munich, Germany, September 8-14, 2018. doi:10.1007/978-3-030-01234-2_1

Xiong, D., Zhang, D., Zhao, X., and Zhao, Y. (2021). Deep learning for emg-based human-machine interaction: a review. *IEEE/CAA J. Automatica Sinica* 8, 512–533. doi:10.1109/jas.2021.1003865

Xu, Y., Yang, W., Chen, M., Chen, S., and Huang, L. (2022). Attention-based gait recognition and walking direction estimation in wi-fi networks. *IEEE Trans. Mob. Comput.* 21, 465–479. doi:10.1109/tmc.2020.3012784

Yan, Y., Liu, G., Zhang, L., Gong, R., Fu, P., Han, B., et al. (2022). Biomechanical effect of valgus knee braces on the treatment of medial gonarthrosis: a systematic review. *Appl. Bionics Biomechanics* 2022, 1–15. doi:10.1155/2022/4194472

Yang, L., Xiang, K., Pang, M., Yin, M., Wu, X., and Cao, W. (2023). Inertial sensing for lateral walking gait detection and application in lateral resistance exoskeleton. *IEEE Trans. Instrum. Meas.* 72, 1–14. doi:10.1109/TIM.2023.3265105

Yang, Q., Xie, C., Tang, R., Liu, H., and Song, R. (2020). Hybrid active control with human intention detection of an upper-limb cable-driven rehabilitation robot. *IEEE Access* 8, 195206–195215. doi:10.1109/access.2020.3033301

Yu, Y.-L., and Lan, C.-C. (2019). Design of a miniature series elastic actuator for bilateral teleoperations requiring accurate torque sensing and control. *IEEE Robotics Automation Lett.* 4, 500–507. doi:10.1109/lra.2019.2891287

Zhang, C., Huang, M. Z., Kehs, G. J., Braun, R. G., Cole, J. W., and Zhang, L. Q. (2021). Intensive in-bed sensorimotor rehabilitation of early subacute stroke survivors with severe hemiplegia using a wearable robot. *IEEE Trans. Neural Syst. Rehabilitation Eng.* 29, 2252–2259. doi:10.1109/TNSRE.2021.3121204

Zhu, C., Liu, Q., Meng, W., Ai, Q., and Xie, S. (2021). "An attentionbased cnn-lstm model with limb synergy for joint angles prediction," in 2021 IEEE/ASME International Conference on Advanced Intelligent Mechatronics (AIM), Delft, Netherlands, 12-16 July 2021, 747–752. doi:10.1109/aim46487.2021.9517544

Zhu, C., Luo, L., Mai, J., and Wang, Q. (2022). Recognizing continuous multiple degrees of freedom foot movements with inertial sensors. *IEEE Trans. Neural Syst. Rehabilitation Eng.* 30, 431–440. doi:10.1109/TNSRE.2022.3149793

Zou, C., Huang, R., Peng, Z., Qiu, J., and Cheng, H. (2021). "Synergetic gait prediction for stroke rehabilitation with varying walking speeds," in 2021 IEEE/RSJ International Conference on Intelligent Robots and Systems (IROS), Prague, Czech Republic, September 27 - Oct. 1, 2021, 7231. doi:10.1109/iros51168.2021.9635860

frontiers | Frontiers in Bioengineering and Biotechnology

TYPE Original Research
PUBLISHED 28 February 2024
DOI 10.3389/fbioe.2024.1328996

OPEN ACCESS

EDITED BY
Ningbo Yu,
Nankai University, China

REVIEWED BY
Bingshan Hu,
University of Shanghai for Science and Technology, China
Jiantao Yang,
University of Shanghai for Science and Technology, China

*CORRESPONDENCE
Haicheng Wei,
wei_hc@nun.edu.cn

RECEIVED 27 October 2023
ACCEPTED 16 February 2024
PUBLISHED 28 February 2024

CITATION
Hu Z, Li M, Wei J, Zhao J, Tang X and Wei H (2024), Assessing the impact of gait speed on gait stability using multi-scale entropy fused with plantar pressure signals.
Front. Bioeng. Biotechnol. 12:1328996.
doi: 10.3389/fbioe.2024.1328996

Assessing the impact of gait speed on gait stability using multi-scale entropy fused with plantar pressure signals

Zilei Hu[1], Miaomiao Li[1], Jiale Wei[1], Jing Zhao[2], Xiaojing Tang[3] and Haicheng Wei[1]*

[1]School of Electrical and Information Engineering, North Minzu University, Yinchuan, China, [2]School of Information Engineering, Ningxia University, Yinchuan, China, [3]School of Science, Ningxia Medical University, Yinchuan, Ningxia, China

Introduction: Walking speed can affect gait stability and increase the risk of falling.

Methods: In this study, we design a device to measure the distribution of the plantar pressure to investigate the impact of the walking speed on the stability of the human gait and movements of the body. We fused the entropy acquired at multiple scales with signals of the plantar pressure to evaluate the effects of the walking speed on the stability of the human gait. We simultaneously collected data on the motion-induced pressure from eight plantar regions to obtain the fused regional pressure. To verify their accuracy, we obtained data on the plantar pressure during walking by using the force table of the Qualisys system. We then extracted the peak points and intervals of the human stride from pressure signals fused over three regions, and analyzed the mechanics of their regional fusion by using the regional amplitude–pressure ratio to obtain the distribution of the plantar pressure at an asynchronous walking speed. Furthermore, we introduced multi-scale entropy to quantify the complexity of the gait and evaluate its stability at different walking speeds.

Results: The results of experiments showed that increasing the speed from 2 to 6 km/h decreased the stability of the gait, with a 26.7% increase in the amplitude of pressure in the region of the forefoot. The hindfoot and forefoot regions were subjected to the minimal pressure at a speed of 2 km/h, while the most consistent stress was observed in regions of the forefoot, midfoot, and hindfoot. Moreover, the curve of entropy at a speed of 2 km/h exhibited a slow decline at a small scale and high stability at a large scale.

Discussion: The multi-scale entropy increased the variation in the stability of the synchronous velocity of walking compared with the sample entropy and the analysis of regional fusion mechanics. Multi-scale entropy can thus be used to qualitatively assess the relationship between the speed and stability of the gait, and to identify the most stable gait speed that can ensure gait stability and posture control.

KEYWORDS

regional fusion pressure, multi-scale entropy, walking speed, gait stability, distribution of the plantar pressure

1 Introduction

Walking exercise is beneficial to health, and appropriate exercise intensity can reduce the risk of chronic complications (Piercy et al., 2018; Liao et al., 2019). A rapid gait may affect a person's stability while they are walking (McAndrew Young and Dingwell, 2012), and can lead to falls among elderly people (Nascimento et al., 2022). It can also damage the plantar soft tissue to cause foot ulcers (Wu et al., 2020). Therefore, it is important to investigate the impact of the walking speed on the plantar pressure and people's gait to avoid injuries among elderly people.

Deep learning algorithms are being used in prevalent research to investigate the link between the plantar pressure and the human gait. A complete gait is generated as one walks with one heel on the ground until the same heel comes into contact with the ground again (Okawara et al., 2022; Caldas et al., 2017). Jeong et al. (2017) used the multi-class support vector machine to identify the plantar pressure of people walking on level ground as well as up and down a flight of stairs, and were able to classify their gait with an accuracy of 95.2%. Luo et al. (2019) measured electromyography signals of the thigh muscle and signals of the plantar pressure, and used a combination of the Long Short Term Memory (LSTM) network and the Multi-Layer Perceptron (MLP) to identify the phases of their gait with an accuracy of 94.10%. Jun et al. (2021) input sequential 3D data on the human skeleton and data on the average plantar pressure into the coding layers of the RNN and CNN, respectively, extracted the relevant features from them, and fed them into the fully connected layer of the network for classification. The two networks were able to identify abnormal gait with accuracies of 68.82% and 93.40%, respectively. Shalin et al. (2021) used data on the plantar pressure of patients with Parkinson's disease as they walked, extracted the relevant features, and used the LSTM to detect the Parkinsonian freezing of gait with an accuracy of 95%.

Previous studies in the area have identified distinct types of gait based on clinical diagnoses, but little research has addressed the effects of the speed of the gait on its stability. Studies have shown that the complex stability of the human gait can be investigated by analyzing the time series of the interval of strides (Prakash et al., 2018). Warlop et al. (2016) found that the variation in the duration of strides affects the stability of gait in patients with Parkinson's disease. Chandrasekaran et al. (2022) used the Lyapunov exponent to analyze the stride intervals, found that it was correlated with variations in the duration of strides, and used this to obtain the threshold of gait stability. Aziz and Arif (2006) claimed that the stride interval of the gait reflects a law of the human gait, and analyzed the complex stability of gait in patients with neurodegenerative diseases based on the symbolic entropy of the stride interval. Yu et al. (2017) proposed that the analysis of the symbolic entropy of the time series of stride intervals can reflect the complex stability of the gait. However, the above studies have used single-scale sign entropy to analyze the complex stability of the gait, where this cannot explain differences in the complex stability of the gait at the multiple time scales that are inherent in the corresponding time series.

In this study, we design a device to acquire the distributed plantar pressure to examine the effects of the speed of walking on the stability of the human gait. We propose a method for the mechanical analysis of the complex stability of the human gait based on regional fusion to this end. This device can simultaneously measure the distribution of the dynamic pressure at eight plantar locations, partition the human gait cycle, and extract the characteristics of the stride intervals by using fused values of the plantar pressure. It represents the heel-to-heel movement, full foot on the floor, the stance of the forefoot, and the toe-off in the support phase as the peaks and valleys of the waves. Following this, we introduce the ratio of the regional amplitude of the fused pressure to examine the difference in the distributions of the plantar pressure under an asynchronous speed of walking. Multi-scale entropy is used to analyze the stride interval, explain the difference in entropy at different speeds of walking at multiple time scales, quantify the complex stability of the human gait, and distinguish between its states of stability. This method can be used to evaluate the stability of the gait and the distribution of the plantar pressure at different walking speeds, and can provide a theoretical basis for determining an appropriate walking speed for rehabilitation exercises.

1.1 Overall structure

The framework design to assess the stability of the human gait based on the distribution of the plantar pressure is shown in Figure 1. Data on the dynamic plantar pressure of healthy people at different walking speeds were first collected by using a hardware acquisition device. The pressure signals from eight plantar regions were then fused to obtain the pressure distributions of regions of the hindfoot, midfoot, and forefoot. The plantar pressure was analyzed by using regional fusion mechanics and complex stability. The distributions of the plantar pressure and multi-scale entropy were estimated to assess the stability of the gait at different walking speeds, and the appropriate walking speed was then chosen to improve gait stability.

2 Methods

2.1 Hardware acquisition device for plantar pressure

Acquiring data on the plantar pressure required choosing an appropriate pressure sensor. Obtaining reliable data required that the normal movement of the human body not be impeded during the measurements. We designed a pressure insole with eight area pressure sensors for the measurements. The flexible thin-film resistive pressure sensor used here was based on the FSR-402 sensor. Its resistance decreased when a large force was applied to the sensing surface. The sensor had an average service life of over one million presses, a thickness of 0.46 mm, a working voltage of 5 V, and a range of accurate weight measurements of 100 to 10 kg. It converted the pressure signals on the applied surface into changes in the electrical resistance to detect the plantar pressure as a person walked. The circuit for voltage conversion transformed the resistance of the sensor into a change in the analog voltage. Data conversion was carried out by using the NI-6001 multi-channel data acquisition card. Its built-in 14-bit ADC, with a rate of sampling of up to 20 kS/s, could provide eight channels each for the analog input and the signal output. After connecting the acquisition card to an upper PC, we set-up the serial communication protocol and the DAQ driver, adjusted the frequency of sampling to 100 Hz, and stored and displayed signals of the plantar pressure as shown in Figure 2.

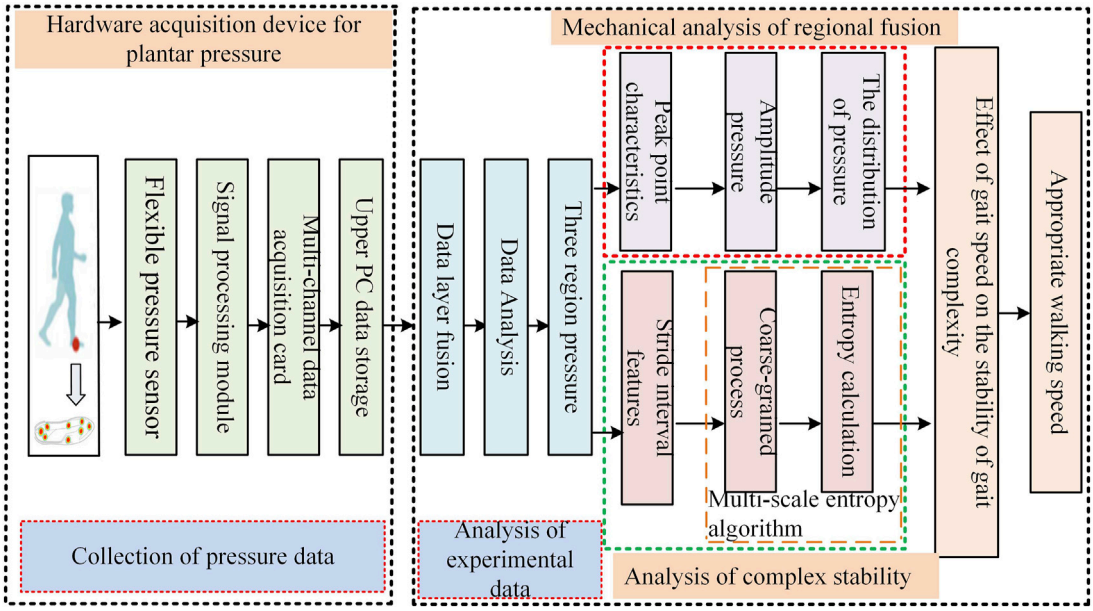

FIGURE 1
Block diagram of the overall framework to assess gait stability.

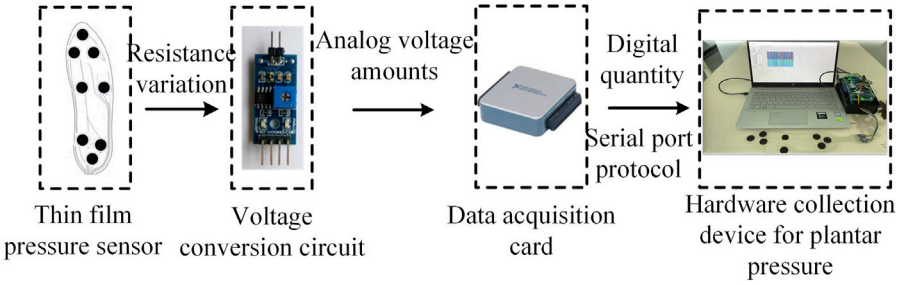

FIGURE 2
Structural composition of device used to acquire the plantar pressure.

2.2 Collection of experimental data

We recruited 32 healthy male subjects, with an average foot size of 40 ± 0.74, average weight of 57.5 ± 2.55 kg, average height of 173 ± 2.45 cm, and average age of 23.5 ± 0.85 years for our experiments. None of the subjects suffered from any walking dysfunction or foot deformity. They were asked to strap the hardware device to acquire plantar pressure signals to their right calves, and wore flat shoes with sensor insoles.

The subjects were asked to walk on a treadmill at speeds of 2, 4, and 6 km/h, respectively. Before each set of measurements, we asked the subjects to walk for 1 min on the treadmill to allow them to become accustomed to its speed, and this was followed by the collection of pressure-related data at various speeds for 3 min. This experimental process was repeated several times to obtain multiple groups of experimental data. We obtained about 160,000 data points on the subjects in each group for experimental analysis, for a total of about 6,040 complete gait cycles.

To validate the accuracy of the data thus obtained, we used the 3D optical motion capture system Qualisys with eight infrared cameras and two Kistler force gauges to collect data on the plantar pressure as the subjects walked on the treadmill. A force table was embedded into the ground in a longitudinal arrangement. A metronome was used during the experiment to guide the subjects to walk at the specified speed. The first step of the standing subject landed on the first force board, followed by the second step landing on the second force board. Figure 3 shows the collection of the experimental data.

2.3 Multi-scale entropy algorithm

The entropy is used in signal analysis to describe the complexity of the signal and represent the degree of chaos in the system. Sample entropy reflects the complexity of the system on a single scale, and cannot be used to fully quantify its complexity. The multi-scale entropy method was proposed by Costa et al. (2002), and offers the

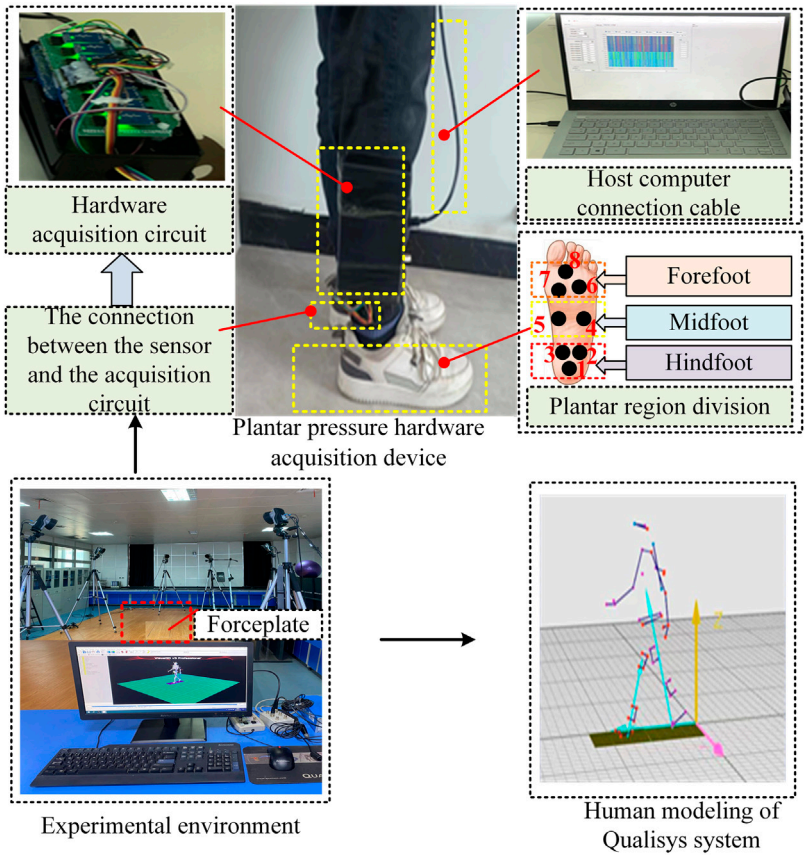

FIGURE 3
Collection of experimental data.

advantages of the sample entropy while avoiding the loss of information caused by the use of a single scale. We used pressure-related data from the sensor for the hindfoot region based on the data on plantar pressure, and then applied mean processing to obtain pressure signals for it. The stride interval used here was based on the interval between adjacent peak points of the pressure signals in the region of the hindfoot. The stride interval was used according to the original time series of the model of multi-scale entropy. Multi-scale entropy (MSE) can be divided into the coarse-graining of the signals and the calculation of a new sequence of entropy values (Busa and van Emmerik, 2016).

Coarse graining process:

(1) The time series of the N original signals X = $[\chi_1, \chi_2, \chi_3, ..., \chi_N]$ is coarse-grained to construct a new time series.
(2) When the scale is $s = 1$, the coarse-grained series is the original time series. When $s = 2$, let the window of length two move forward on the original sequence. Calculate the average of χ_1 and χ_2 to obtain y_1.
(3) Move the window forward by two units. y_2 is obtained by calculating the average of χ_3 and χ_4. Shift the window by two units once again to obtain the average value and use it to form a new sequence. The new sequence at scale $s = 2$ is Y = $[y_1, y_2, y_3, ...y_{N/2}]$.
(4) Similarly, when the scale $s = 3$, let the window of length three move forward on the time series X of the original signals. Start by averaging χ_1, χ_2 and χ_3 to y_1. Move the window by three units, and calculate the mean value of the original sequence in the window to obtain y_1, y_2, and y_3. The new sequence at scale $s = 3$ is then Y = $[y_1, y_2, y_3, ...y_{N/3}]$

Calculating the entropy of the new sequence:

(1) Suppose that the length of the time series X of the original signals is N and the scale factor is s. Then, the coarse-grained sequence is given by:

$$Z_j^{(s)} = \frac{1}{s}\sum_{i=(j-1)s+1}^{js} x(i), 1 \le j \le \frac{N}{S} \quad (1)$$

(2) Under an m-dimensional vector, the data sequence is given by:

$$Z(i) = [z_i, z_{i+1}, z_{i+2}, ...z_{i+m-1}], 1 \le i \le \frac{N}{s} - m + 1 \quad (2)$$

(3) Find the number of distances d_{ij} shorter than r, $d_{ij} < r$. Then, the ratio of the number of such distances to the total number of distances is given by:

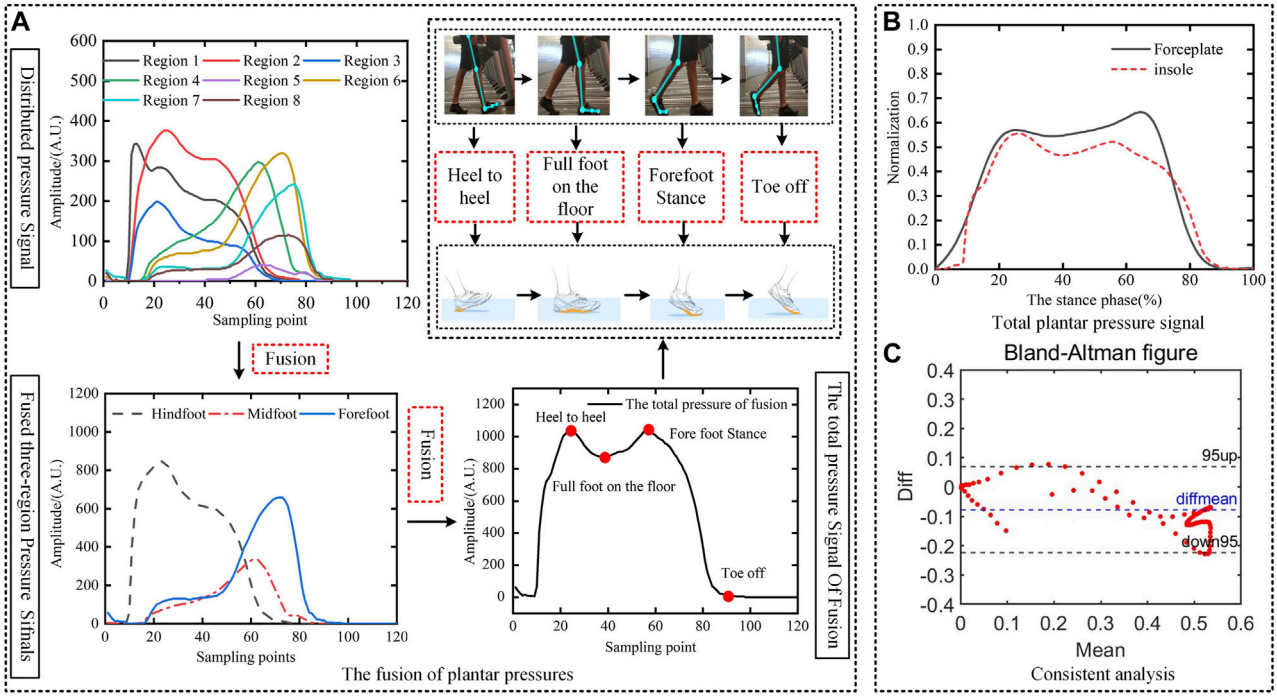

FIGURE 4
Comparative analysis of signals of plantar pressure measured at the pressure plate and the insole. **(A)** The fusion of plantar pressures. **(B)** Total plantar pressure signal. **(C)** Consistent analysis.

$$d_{ij}\left[Z(i), Z(j)\right] = \max_{0<k<m-1}\left[z(i+k) - z(j+k)\right] \quad (3)$$

$$L_i^m(r) = num\left(d_{ij} < r\right) \Big/ (N/s - m), i \neq j, i = 1, ..., \frac{N}{s} - m + 1 \quad (4)$$

where d_{ij} is the maximum distance between vectors $Z(i)$ and $Z(j)$, and r is the range of tolerance for a given time series.

(4) Set the number of dimensions to $m + 1$ and repeat the above steps to obtain the following:

$$L_i^{m+1}(r) = num\left(d_{ij} < r\right) \Big/ (N/s - m), i \neq j, i = 1, ...\frac{N}{s} - m \quad (5)$$

(5) Calculate the average of $L_i^m(r)$ and $L_i^{m+1}(r)$:

$$L_i^m(r) = \frac{1}{N/s - m + 1}\sum_{i=1}^{N/s-m+1} L_i^m(r) \quad (6)$$

$$L_i^{m+1}(r) = \frac{1}{N/s - m + 1}\sum_{i=1}^{N/s-m} L_i^{m+1}(r) \quad (7)$$

(6) The entropy value of the new sequence is that of the MSE, E_{MSE}:

$$E_{MSE} = -\ln\left(L^{m+1}(r) - L^m(r)\right) \quad (8)$$

Some studies have shown that too large a number of dimensions m significantly increases the amount of required computation and leads to a decline in computational efficiency. m is generally set to one or two, while r is set to 0.10–0.25SD, where SD is the standard deviation of the original time series. When m is two, the length of the sequence N is minimally dependent on the accuracy of the calculated results (Zheng et al., 2023). Therefore, we set m = 2 and r = 0.25SD in this study.

3 Results

3.1 Validation of experimental data

A gait cycle is divided into a stance phase and a swinging phase. The stance phase is the process in which the foot makes contact with the ground to generate plantar pressure. The swing phase is defined as the forward movement of the limb without any contact with the ground (Cicirelli et al., 2022).

A comparative analysis of signals of the plantar pressure measured by the pressure plate and the insole is shown in Figure 4. We use a speed of 2 km/h as an example. The pressure signals at eight points in the plantar as the subject walked were obtained and fused. Figure 4A shows that the force at each point exhibited a peak of the wave as the foot came into contact with the ground. The pressure-related data from each sensor in the three regions were averaged and fused. The fused pressure signals showed the changes in pressure in the hindfoot, midfoot, and forefoot throughout the stance phase. The total plantar pressure was obtained by further fusing these three regional signals, and can be used to illustrate the troughs and peaks of the four states in the stance phase.

To verify the accuracy of the pressure-related data obtained from the insole, we eliminated the influence of the subject's weight on the distribution of the plantar pressure. The fused signals of the total pressure obtained from the insole and the pressure plate of the same

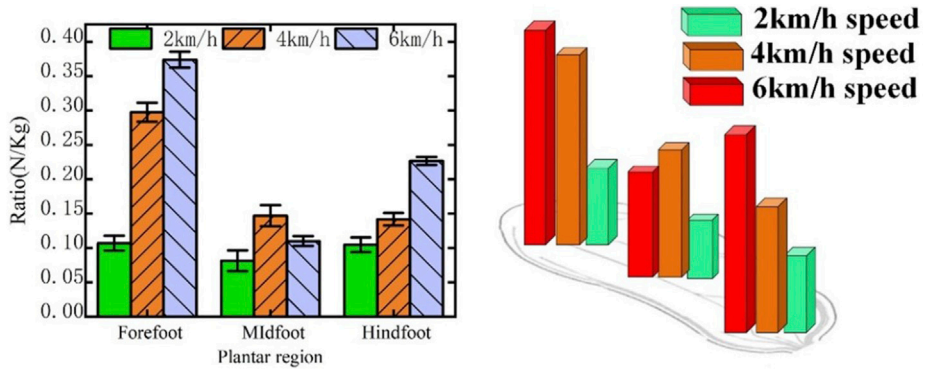

FIGURE 5
Changes in pressure in the three plantar regions at three walking speeds.

TABLE 1 Values of entropy of gaits at three speeds.

Index of complexity	2 km/h	4 km/h	6 km/h
SampEn	0.816 ± 0.04	0.907 ± 0.07	1.088 ± 0.09
MSE_S	0.901 ± 0.03	1.216 ± 0.02	1.480 ± 0.04
MSE_L	0.732 ± 0.02	0.773 ± 0.03	0.89774 ± 0.02

Note: The values are expressed as mean ± SD. "SampEn" is the overall sample entropy of the gait. "MSE_S" is the mean value of scales 1–3. "MSE_L" is the mean value of scales 4–6.

subject were normalized based on their amplitude and the transverse axis, respectively. Figure 4B shows that the trends of changes in the pressure signals of both were consistent with each other. The reaction force from the vertical ground obtained by the pressure plate and the insole had a prominent "double peak" characteristic.

We used the Bland–Altman plot to evaluate the consistency of the two methods of measurement. Figure 4C shows that the difference between the measurements of the pressure plate and the insole was within the 95% confidence interval. $p < 0.05$ and r = 0.9513 for these two methods of measurement. These results show that there was a significant correlation between the data measured from the insole and the pressure plate, which leads us to conclude that they were reliable. The second peak point of measurements of the insole was smaller than that of the force measurement table. This is because when the sole was in the forefoot stance, it made full contact with the ground and there were few pressure sensors in the sole area of the insole. As a result, the pressure distribution in the sole of the foot could not be entirely monitored, and a smaller amount of pressure-related data were obtained from it.

3.2 Mechanical analysis of regional fusion

To eliminate the influence of the subject's weight on the experimental results, we normalized the amplitudes of pressure of the three plantar regions, which were fused in the stance phase of the gait cycle, by weight. We used the ratio of the amplitude of pressure to the weight of the subjects to examine the differences in distributions of the plantar pressure at walking speeds of 2, 4, and 6 km/h.

Figure 5 shows the pressures in the three plantar regions at the three speeds of walking considered here. As the walking speed

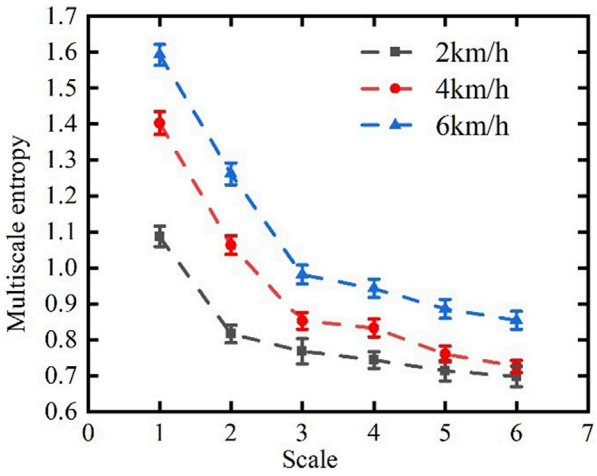

FIGURE 6
Curves of distribution of the multi-scale entropy of the stride interval of the gait.

increased, the ratios of the amplitude of pressure in the hindfoot and forefoot regions of the body increased significantly. When the subject's walking speed was increased from 2 to 6 km/h, the ratio of the amplitude of pressure in the forefoot region increased by 26.7%. The foot bears the weight of the body during normal walking, while balance and movement are controlled through contractions of the plantar muscles. If the plantar pressure is not regularly distributed, the body requires more control to maintain balance and stability during normal walking.

Studies have shown that increased plantar pressure can enhance the risks of soft tissue injury in the plantar and metatarsal stress fracture (Zhang et al., 2018). The forefoot area is responsible for the balance and control of the center of gravity of the body. Nevertheless, the pressure on the forefoot is excessively high such that the body requires greater control to maintain equilibrium (Zheng et al., 2020). When the subjects walked at a speed of 2 km/h, the pressure in the forefoot and hindfoot regions was relatively low, and its distribution in the three regions was the most uniform. When they walked at 4 km/h, the magnitude of force

in the forefoot and hindfoot areas progressively grew, the load on the hindfoot and forefoot gradually increased, and the disparity in the pressure distributions at the three locations became larger. When the subjects walked at 6 km/h, the magnitude of force in the forefoot and hindfoot regions continued to increase, the pressure distributions in the three regions were the largest, and might have led to an increase in gait oscillation to lead to an unstable gait. Thus, the pressure distribution in the three plantar zones was reasonably balanced at a speed of 2 km/h, and the burden on the hindfoot and the forefoot was the smallest. This helped the balance of the body and the health of the feet.

3.3 Analysis of complex stability

The differences in the pressure distributions in the three plantar regions caused by an asynchronous speed of walking cannot directly reflect the corresponding differences in the stability of the gait. Studies have shown that the irregularity of distribution of the plantar pressure can be reflected by the varying degrees of changes in the length and frequency of the stride, which in turn affect the stability of the gait (Biswas et al., 2008). We used MSE to examine the time series of stride intervals of the subjects to measure the complexity of the rhythm of their gait at different time scales, and thus to evaluate the differences in its stability at different speeds of walking.

A system with a larger entropy is more complex and less regular (Kędziorek and Blażkiewicz, 2020). Table 1 shows that walking at 2 km/h yielded the lowest overall sample entropy of the gait, indicating that the sequence of strides had the highest self-similarity, the least complexity, and led to a highly regular gait in this case. However, the differences among the three were not prominent, and the overall difference in entropy was small.

Figure 6 shows curves of the distribution of MSE as the subjects walked at the three speeds considered here, while Table 1 shows the scale of the magnitude of entropy of the gait. MSE can be used to amplify the temporal differences in gait complexity at the three speeds. Compared with those at 4 km/h and 6 km/h, the MSE at a speed of walking of 2 km/h was smaller by 0.315 and 0.579, respectively, and this shows that the differences in entropy among the three speeds was prominent at a small scale but slight at a large scale. MSE was thus able to more clearly identify the differences in stability at various walking speeds, and to amplify the differences in entropy at a small scale in comparison with sample entropy. This may be because the stability and regularity of the gait are impaired over short time scales, but the change in the stride interval is generally smooth and stable over long time scales as the body gradually adapts to the change in the frequency of steps.

Therefore, the curve of entropy at a small scale decreased more slowly at 2 km/h than at 4 km/h and 6 km/h, and was the most stable at a large scale.

4 Discussion

Some studies have shown that the more stable the gait is, the lower are the multi-scale entropy of the sequence of stride intervals and the rate of decline (Hsieh and Abbod, 2021). When one is walking slowly, the frequency of strides is low, the stride interval is relatively long, and the gait is more stable because the difference between steps is relatively small and body control is thus easier (Wu et al., 2019). England and Granata quantified the stability of the gait by using the Lyapunov exponent λ, and found that λ was smaller at lower walking speeds. This indicates that slower walking increases the stability of the gait (England and Granata, 2007). The subjects in our experiments exhibited a more dynamically stable gait at lower speeds, and older adults at risk of falling are advised to reduce their walking speed to improve their stability (Dingwell and Marin, 2006). Walking quickly may result in a less regular gait and a more complex time scale owing to the increased frequency of steps and the shortening of the stride interval, where this reduces the stability of the gait and increases the difficulty of body control. Therefore, walking at a speed of 2 km/h is more conducive to the postural balance and health of the body than walking at speeds of 4 and 6 km/h.

5 Conclusion

The results of this study showed that different walking speeds have significant effects on the distribution of the plantar pressure and the stability of the human gait. Through an analysis of the human gait based on the plantar pressure, we combined the mechanical analysis of regionally fused data with complex stability analysis based on multi-scale entropy to differentiate between the stabilities of the gait at different speeds of walking at multiple time scales. The results of experiments involving subjects walking at speeds of 2, 4, and 6 km/h showed that the differences between gait stability were prominent at small scales but weak at large scales. This shows that the stability of the gait may be compromised at short time scales. A walking speed of 2 km/h yielded a lower complexity than the other two speeds considered here, and the curve of entropy decreased more slowly at a small scale. This curve was the most stable at a large scale, and this reflected a stable gait. By distinguishing between the stabilities of the gait at asynchronous speeds of walking, the proposed method can help clinicians develop training programs to help patients balance their gait and reduce the risk of falls among the elderly.

Data availability statement

The original contributions presented in the study are included in the article/Supplementary Material, further inquiries can be directed to the corresponding author.

Ethics statement

The studies involving humans were approved by Medical Ethics Committee of Ningxia Hui Autonomous Region People's Hospital. The studies were conducted in accordance with the local legislation and institutional requirements. The participants provided their written informed consent to participate in this study. Written informed consent was obtained from the individual(s) for the

publication of any potentially identifiable images or data included in this article.

Author contributions

ZH: Writing–review and editing, Conceptualization, Writing–original draft. ML: Methodology, Writing–review and editing. JW: Conceptualization, Software, Writing–review and editing. JZ: Conceptualization, Data curation, Writing–review and editing. XT: Conceptualization, Resources, Writing–review and editing. HW: Funding acquisition, Supervision, Writing–review and editing.

Funding

The author(s) declare that financial support was received for the research, authorship, and/or publication of this article. This work was supported by the Natural Science Foundation of Ningxia (No. 2022AAC03244, 2022AAC03006), the National Natural Science Foundation of China (No. 62361001), Leading Talent Project Plan of the State Ethnic Affairs Commission, Ningxia Technology Innovative Team of Advanced Intelligent Perception and Control, Leading talents in scientific and technological innovation of Ningxia, and the Graduate Student Innovation Project of North Minzu University (No. YCX23121).

Conflict of interest

The authors declare that the research was conducted in the absence of any commercial or financial relationships that could be construed as a potential conflict of interest.

Publisher's note

References

Aziz, W., and Arif, M. (2006). Complexity analysis of stride interval time series by threshold dependent symbolic entropy. *Eur. J. Appl. Physiol.* 98, 30–40. doi:10.1007/s00421-006-0226-5

Biswas, A., Lemaire, E. D., and Kofman, J. (2008). Dynamic gait stability index based on plantar pressures and fuzzy logic. *J. Biomech.* 41, 1574–1581. doi:10.1016/j.jbiomech.2008.02.009

Busa, M. A., and van Emmerik, R. E. A. (2016). Multiscale entropy: a tool for understanding the complexity of postural control. *J. Sport Health Sci.* 5, 44–51. doi:10.1016/j.jshs.2016.01.018

Caldas, R., Mundt, M., Potthast, W., Buarque de Lima Neto, F. B., and Markert, B. (2017). A systematic review of gait analysis methods based on inertial sensors and adaptive algorithms. *Gait Posture* 57, 204–210. doi:10.1016/j.gaitpost.2017.06.019

Chandrasekaran, S., Ngo, C., Lueken, M., Bollheimer, C., Wolf, A., and Leonhardt, S. (2022). On gait stability: correlations between Lyapunov exponent and stride time variability. *Curr. Dir. Biomed. Eng.* 8, 564–567. doi:10.1515/cdbme-2022-1144

Cicirelli, G., Impedovo, D., Dentamaro, V., Marani, R., Pirlo, G., and D'Orazio, T. R. (2022). Human gait analysis in neurodegenerative diseases: a review. *IEEE J. Biomed. Health Inf.* 26, 229–242. doi:10.1109/JBHI.2021.3092875

Costa, M., Goldberger, A. L., and Peng, C. K. (2002). Multiscale entropy analysis of complex physiologic time series. *Phys. Rev. Lett.* 89, 068102. doi:10.1103/PhysRevLett.89.068102

Dingwell, J. B., and Marin, L. C. (2006). Kinematic variability and local dynamic stability of upper body motions when walking at different speeds. *J. Biomech.* 39, 444–452. doi:10.1016/j.jbiomech.2004.12.014

England, S. A., and Granata, K. P. (2007). The influence of gait speed on local dynamic stability of walking. *Gait Posture* 25, 172–178. doi:10.1016/j.gaitpost.2006.03.003

Hsieh, Y. L., and Abbod, M. F. (2021). Gait analyses of Parkinson's disease patients using multiscale entropy. *Electronics* 10, 2604. doi:10.3390/electronics10212604

Jeong, G. M., Truong, P. H., and Choi, S. I. (2017). Classification of three types of walking activities regarding stairs using plantar pressure sensors. *IEEE Sens. J.* 17, 2638–2639. doi:10.1109/JSEN.2017.2682322

Jun, K., Lee, S., Lee, D. W., and Kim, M. S. (2021). Deep learning-based multimodal abnormal gait classification using a 3D skeleton and plantar foot pressure. *IEEE Access* 9, 161576–161589. doi:10.1109/ACCESS.2021.3131613

Kędziorek, J., and Blażkiewicz, M. (2020). Nonlinear measures to evaluate upright postural stability: a systematic review. *Entropy* 22, 1357. doi:10.3390/e22121357

Liao, F., An, R., Pu, F., Burns, S., Shen, S., and Jan, Y. K. (2019). Effect of exercise on risk factors of diabetic foot ulcers: a systematic review and meta-analysis. *Am. J. Phys. Med. Rehabil.* 98, 103–116. doi:10.1097/PHM.0000000000001002

Luo, R., Sun, S., Zhang, X., Tang, Z., and Wang, W. (2019). A low-cost end-to-end sEMG-based gait sub-phase recognition system. *IEEE Trans. Neural Syst. Rehabil. Eng.* 28, 267–276. doi:10.1109/TNSRE.2019.2950096

McAndrew Young, P. M. M. A., and Dingwell, J. B. (2012). Voluntarily changing step length or step width affects dynamic stability of human walking. *Gait Posture* 35, 472–477. doi:10.1016/j.gaitpost.2011.11.010

Nascimento, M. M., Gouveia, É. R., Gouveia, B. R., Marques, A., Martins, F., Przednowek, K., et al. (2022). Associations of gait speed, cadence, gait stability ratio, and body balance with falls in older adults. *Int. J. Environ. Res. Public Health* 19, 13926. doi:10.3390/ijerph192113926

Okawara, H., Sawada, T., Hakukawa, S., Nishizawa, K., Okuno, M., Nakamura, M., et al. (2022). Footsteps required for reliable and valid in-shoe plantar pressure assessment during gait per foot region in people with hallux valgus. *Gait Posture* 97, 21–27. doi:10.1016/j.gaitpost.2022.07.009

Piercy, K. L., Troiano, R. P., Ballard, R. M., Carlson, S. A., Fulton, J. E., Galuska, D. A., et al. (2018). The physical activity guidelines for Americans. *JAMA* 320, 2020–2028. doi:10.1001/jama.2018.14854

Prakash, C., Kumar, R., and Mittal, N. (2018). Recent developments in human gait research: parameters, approaches, applications, machine learning techniques, datasets and challenges. *Artif. Intell. Rev.* 49, 1–40. doi:10.1007/s10462-016-9514-6

Shalin, G., Pardoel, S., Lemaire, E. D., Nantel, J., and Kofman, J. (2021). Prediction and detection of freezing of gait in Parkinson's disease from plantar pressure data using long short-term memory neural-networks. *J. Neuroeng. Rehabil.* 18, 167. doi:10.1186/s12984-021-00958-5

Warlop, T., Detrembleur, C., Bollens, B., Stoquart, G., Crevecoeur, F., Jeanjean, A., et al. (2016). Temporal organization of stride duration variability as a marker of gait instability in Parkinson's disease. *J. Rehabil. Med.* 48, 865–871. doi:10.2340/16501977-2158

Wu, A. R., Simpson, C. S., van Asseldonk, E. H. F., van der Kooij, H., and Ijspeert, A. J. (2019). Mechanics of very slow human walking. *Sci. Rep.* 9, 18079. doi:10.1038/s41598-019-54271-2

Wu, F. L., Wang, W. T. J., Liao, F., Elliott, J., Jain, S., and Jan, Y. K. (2020). Effects of walking speeds and durations on plantar skin blood flow responses. *Microvasc. Res.* 128, 103936. doi:10.1016/j.mvr.2019.103936

Yu, J., Cao, J., Liao, W. H., Chen, Y., Lin, J., and Liu, R. (2017). Multivariate multiscale symbolic entropy analysis of human gait signals. *Entropy* 19, 557. doi:10.3390/e19100557

Zhang, Y., Awrejcewicz, J., Szymanowska, O., Shen, S., Zhao, X., Baker, J. S., et al. (2018). Effects of severe hallux valgus on metatarsal stress and the metatarsophalangeal loading during balanced standing: a finite element analysis. *Comput. Biol. Med.* 97, 1–7. doi:10.1016/j.compbiomed.2018.04.010

Zheng, J., Li, Y., Zhai, Y., Zhang, N., Yu, H., Tang, C., et al. (2023). Effects of sampling rate on multiscale entropy of electroencephalogram time series. *Biocybern. Biomed. Eng.* 43, 233–245. doi:10.1016/j.bbe.2022.12.007

Zheng, T., Yu, Z., Wang, J., and Lu, G. (2020). A new automatic foot arch index measurement method based on a flexible membrane pressure sensor. *Sensors* 20, 2892. doi:10.3390/s20102892

frontiers | Frontiers in Bioengineering and Biotechnology

TYPE Methods
PUBLISHED 07 March 2024
DOI 10.3389/fbioe.2024.1375277

OPEN ACCESS

EDITED BY
Wujing Cao,
Chinese Academy of Sciences (CAS), China

REVIEWED BY
Xingang Zhao,
Chinese Academy of Sciences (CAS), China
Long Cheng,
Chinese Academy of Sciences (CAS), China

*CORRESPONDENCE
Zan Zhang,
zanzan@zzu.edu.cn

RECEIVED 23 January 2024
ACCEPTED 20 February 2024
PUBLISHED 07 March 2024

CITATION
Liu Y, Li Y, Zhang Z, Huo B and Dong A (2024), Quantitative evaluation of motion compensation in post-stroke rehabilitation training based on muscle synergy.
Front. Bioeng. Biotechnol. 12:1375277.
doi: 10.3389/fbioe.2024.1375277

Quantitative evaluation of motion compensation in post-stroke rehabilitation training based on muscle synergy

Yanhong Liu[1], Yaowei Li[1], Zan Zhang[1]*, Benyan Huo[1] and Anqin Dong[2]

[1]School of Electrical and Informatic Engineering, Zhengzhou University, Zhengzhou, China, [2]The Rehabilitation Department, Fifth Affiliated Hospital of Zhengzhou University, Zhengzhou, China

Introduction: Stroke is the second leading cause of death globally and a primary factor contributing to disability. Unilateral limb motor impairment caused by stroke is the most common scenario. The bilateral movement pattern plays a crucial role in assisting stroke survivors on the affected side to relearn lost skills. However, motion compensation often lead to decreased coordination between the limbs on both sides. Furthermore, muscle fatigue resulting from imbalanced force exertion on both sides of the limbs can also impact the rehabilitation outcomes.

Method: In this study, an assessment method based on muscle synergy indicators was proposed to objectively quantify the impact of motion compensation issues on rehabilitation outcomes. Muscle synergy describes the body's neuromuscular control mechanism, representing the coordinated activation of multiple muscles during movement. 8 post-stroke hemiplegia patients and 8 healthy subjects participated in this study. During hand-cycling tasks with different resistance levels, surface electromyography signals were synchronously collected from these participants before and after fatigue. Additionally, a simulated compensation experiment was set up for healthy participants to mimic various hemiparetic states observed in patients.

Results and discussion: Synergy symmetry and synergy fusion were chosen as potential indicators for assessing motion compensation. The experimental results indicate significant differences in synergy symmetry and fusion levels between the healthy control group and the patient group ($p \leq 0.05$), as well as between the healthy control group and the compensation group. Moreover, the analysis across different resistance levels showed no significant variations in the assessed indicators ($p > 0.05$), suggesting the utility of synergy symmetry and fusion indicators for the quantitative evaluation of compensation behaviors. Although muscle fatigue did not significantly alter the symmetry and fusion levels of bilateral synergies ($p > 0.05$), it did reduce the synergy repeatability across adjacent movement cycles, compromising movement stability and hindering patient recovery. Based on synergy symmetry and fusion indicators,

the degree of bilateral motion compensation in patients can be quantitatively assessed, providing personalized recommendations for rehabilitation training and enhancing its effectiveness.

KEYWORDS

rehabilitation training, motion compensation, surface electromyography, muscle synergy, quantitative assessment

1 Introduction

The Global Burden of Disease (GBD) research data revealed that in 2019, there were over 100 million stroke cases worldwide (Feigin and Stark, 2021). The number of patients in China is as high as 17.8 million (Tu and Wang, 2023). Stroke incidents often result in impairment of the motor cortex and its descending spinal pathways, causing functional limitations in limb movements. Statistics indicate that roughly 80% of stroke survivors experience upper limb motor dysfunction with unilateral limb motor impairment caused by stroke being the most common (Mazzoleni et al., 2018), making rehabilitation crucial for restoring lost functionality (Gauthier et al., 2008; Huang et al., 2022; Xie et al., 2023). Rehabilitation techniques encompass professional therapeutic interventions, the use of rehabilitative exoskeleton robots (Kim et al., 2012; Louie et al., 2020; Singh et al., 2021; Nolan et al., 2023) and active rehabilitation devices (Sugihra et al., 2018). However, the scarcity of rehabilitation physicians and the cumbersome nature of rehabilitative exoskeleton robots hinder their widespread use.

Active rehabilitation devices involve patients utilizing their less affected limb to assist in rehabilitation exercises, such as using hand-crank devices (Kraaijenbrink et al., 2021) and Bobath hand techniques (Pathak et al., 2021). This method promotes the initiative of patients during the training process. Studies have suggested that simultaneous training of both limbs provides additional stimulation to the brain, aiding in rehabilitation (Woldag et al., 2004; Renner et al., 2005). Nonetheless, this training method raises concerns about motion compensation. The affected limb's reduced function leads to continuous reliance on the unaffected limb. Additionally, Calabro and Perez (2016) indicated that simultaneous action on both sides would adversely affect the movement of the affected side by the healthier side, as evidenced by comparisons of several movement indicators. The continuous exertion by the healthier side easily leads to muscle fatigue, while the affected side, due to its functional deficit, is prone to fatigue as well. This imbalanced force exertion on both sides of the limbs caused by compensation can significantly hinder a patient's recovery.

Therefore, timely rehabilitation assessment of rehabilitation training can effectively reduce the impact of motion compensation and muscle fatigue. Presently, upper limb rehabilitation assessment methods, including Brunnstrom Recovery Stage (Meng et al., 2022), Fugl-Meyer Assessment (DJ, 2002), and Modified Ashworth Scale (Ansari et al., 2012), possess comprehensive evaluation criteria. They heavily rely on clinical expertise and possess subjectivity. Li et al. (2022) integrated surface electromyography (sEMG) signals and motion information for the quantitative assessment of hand function. However, these methods face challenges in assessing motion compensation. Therefore, timely rehabilitation assessment of rehabilitation training can effectively reduce the impact of motion compensation and muscle fatigue on rehabilitation training. Timely detection of motion compensation remains challenging in clinical practice, delaying patient recovery and potentially resulting in permanent functional deficits in the affected limb.

The muscle synergy theory describes the inherent neuro-muscular control mechanism in the human body, suggesting that motor neurons do not solely control individual muscles but recruit multiple muscles simultaneously to execute coordinated movements (Aoi and Funato, 2016; Hirashima and Oya, 2016; Zhao et al., 2019). Tang et al. (2014) applied Pearson correlation analysis on muscle synergy among different healthy subjects executing similar tasks revealed a correlation coefficient of up to 0.85. Chen et al. (2023) identified shared and specific synergies in six upper limb actions, forming a basis for the muscle synergy theory. Brambilla and Scano (2022) utilized experimental and simulated data to investigate the influence of the number of muscles on the structure and quantity of synergies. Their conclusions suggest that both a low and high number of muscles can yield relatively high similarity in synergy. Additionally, a lower number of muscles might potentially underestimate the dimensionality of motor control, thereby potentially providing a basis for motor control. Pan et al. (2021) further analyzed that different combinations of the original muscle synergies could achieve complex movements in different planes. The distinct topology of muscle synergy networks among different tasks demonstrates the significant differences, thus affirming the potential of the muscle synergy theory in understanding human motor control mechanisms and their impact on neurorehabilitation. Due to the interpretability of muscle synergy in human movement mechanisms, this theory is often employed for patients' rehabilitation assessments.

Commonly used approaches for applying muscle synergy to rehabilitation assessment involve comparing muscle synergies between healthy individuals and patients to gauge changes in patient synergy indicators. In experiments conducted by Funato et al. (2022), both healthy individuals and stroke patients were tasked with executing the 37-item tasks from the Fugl-Meyer assessment method. The corresponding muscle synergies were analyzed to explore the relationship between synergy characteristics and stroke-related motor impairments. Ultimately, it was deduced that muscle synergy serves as an effective method in stroke assessment. Ma et al. (2021) extracted upper limb muscle synergies from healthy subjects and stroke patients, analyzing the inherent consistency of the patients' multiple experimental outcomes. This analysis revealed lower inherent consistency in stroke patients compared to healthy subjects, accompanied by a higher level of synergy complexity. Sheng et al. (2022) introduced a

novel assessment method known as the Muscle Synergy Space (MSS) model, aimed at evaluating post-stroke motor function. By comparing muscle synergy characteristics between healthy individuals and stroke patients, the model's effectiveness was demonstrated, providing scientific guidance for rehabilitation.

Another approach considers that patients often exhibit better functionality in their unaffected (healthy) side. Therefore, by comparing and analyzing the muscle synergy between the unaffected and affected sides, it is also feasible to assess the motor function of the affected side. This primarily involves an analysis from the perspective of the correlation and integration level of muscle synergy between both sides of the body (Cheung et al., 2012; Pan et al., 2018). However, while the first method uses healthy subjects' synergy as a reference to reflect patient synergy defects, it fails to assess the balance of bilateral muscle coordination during coordinated movements. The second method involves experiments solely focusing on independent movements on both sides, reflecting only some indicators of changes during independent movements. Consequently, the results do not adequately indicate differences in muscle coordination levels due to compensation by the unaffected side.

The innovation of this study lies in not only analyzing the patient's own muscle synergy indicators but also conducting a significance analysis between the results of patients and healthy subjects. This evaluation is based on indicators such as the symmetry and fusion degree of muscle synergy on both sides of the body, aiming to assess the issue of motion compensation. Collecting surface electromyography signals from patients and healthy participants during bilateral movement, will facilitate analysis of indicators variations. This will quantify patients motion compensation through comparative analysis based on muscle synergy indicators. Considering that resistance is often applied during experimental procedures to enhance rehabilitation training, and patients tend to experience muscle fatigue, an analysis of muscle synergy indicators has been conducted under various resistance levels and fatigue statuses. The main contributions of this paper can be summarized as follows.

1. The combined muscle synergy extraction method utilizing Principal Component Analysis (PCA) and Non-negative Matrix Factorization (NMF) ensures the stability of muscle synergy patterns and subsequent analytical results.
2. Designing experimental paradigms sensibly, using synergy symmetry and synergy fusion indicators, validated the feasibility of quantifying motion compensation issues through muscle synergy.
3. By comparing data between the healthy group and the patient group, as well as between the healthy group and the simulated group, the impact of resistance level and fatigue status on motion compensation is analyzed using significance level indicators.

The rest of paper is organized as follows. Section 2 describes the recruited subjects, experimental protocols, and muscle synergy quantification indicators. Section 3 presents the analysis results of the experiments, while Section 4 delves into the discussion of these analytical findings. Conclusion are set out in Section 5.

TABLE 1 Stroke subjects.

Subject	Age	Affected side	Stroke type	Brunnstrom
S1	16	*R*	*Ischemic*	3
S2	60	*R*	*Ischemic*	3
S3	58	*R*	*Ischemic*	4
S4	32	*L*	*Ischemic*	5
S5	37	*R*	*Ischemic*	5
S6	58	*L*	*Ischemic*	3
S7	55	*L*	*Ischemic*	4
S8	45	*L*	*Ischemic*	5

2 Materials and methods

This study primarily analyzes the coordination level between the two sides of the human body from the perspective of muscle synergy. The muscle synergy extraction algorithm was employed to extract muscle synergies and activation coefficient matrices from sEMG signals. Muscle synergy reflects the recruitment pattern of muscles within a muscle group and can also serve as a measure of muscle symmetry, while activation coefficients indicate the degree of involvement of each muscle synergy. The symmetry and fusion indicators of bilateral muscle synergy reflect the coordination of muscles, and the effectiveness of applying this method to detect motion compensation can be determined through a significant difference analysis between healthy subjects and patients.

2.1 Subjects

Eight stroke patients (S1-S8, mean age 45 ± 15 years) and eight healthy subjects (H1-H8, mean age 24 ± 2 years) participated in this experiment. All patients were capable of independently completing a minimum of 20 min of hand-cranked rehabilitation training. All eight healthy subjects were right-handed. The information of stroke patient is available in Table 1. The experiment was in accordance with the declaration of Helsinki and received approval from the Fifth Affiliated Hospital of Zhengzhou University. All subjects provided informed consent before participating in the experiment.

2.2 Experiment protocols

2.2.1 Experimental platform

This study utilized a coordinated bilateral hand-cycling as the experimental apparatus, as shown in Figure 1A, and employed the multi-channel wireless sEMG signals sensor Delsys for data acquisition in Figure 1B.The sEMG sampling rate was 1,926 Hz. Data collection was performed on eight muscle groups on both the left and right sides of the human body, with sensor attachment positions on the right side illustrated in Figure 2, which were mirrored symmetrically on the left side.

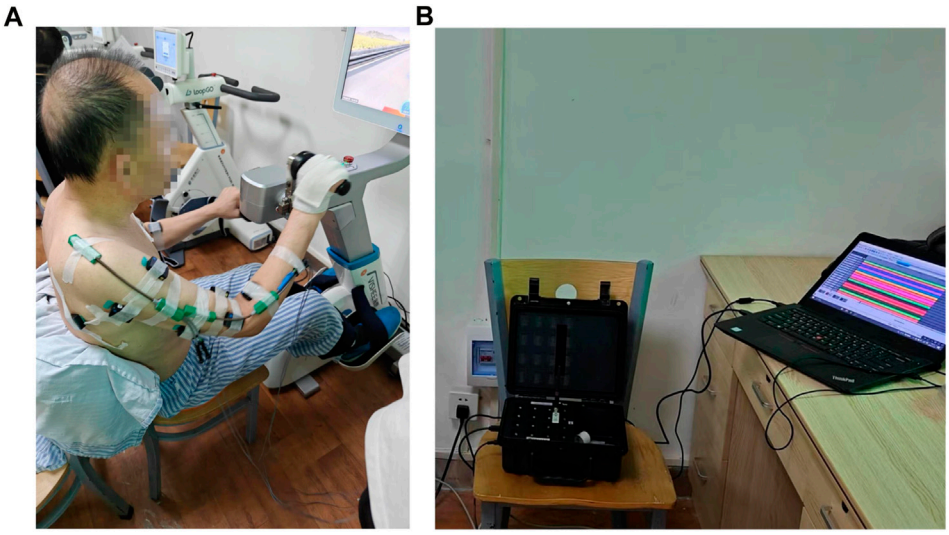

FIGURE 1
(A) Experimental setup and equipment-hand-cycling. The device allows for adjustable training resistance. **(B)** Experimental data acquisition equipment-Delsys. The device can simultaneously collect sEMG signals from up to 16 muscles.

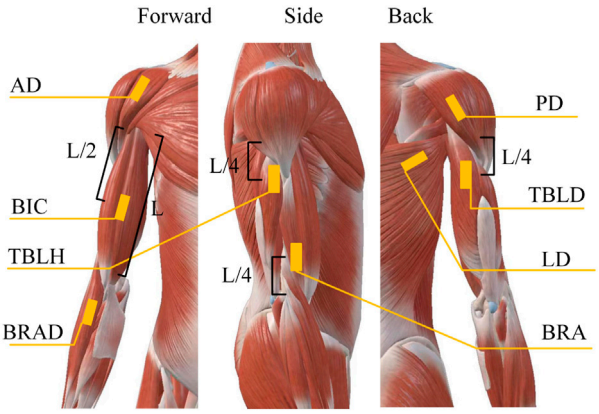

FIGURE 2
Electrode positions for sEMG signals acquisition. The positions of each muscle were predetermined through referencing anatomical charts.

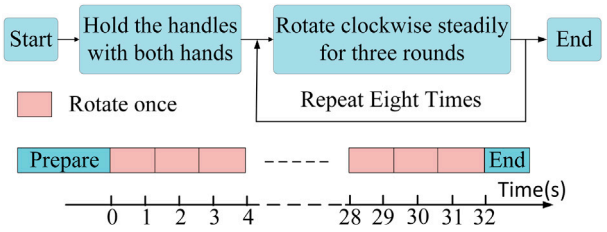

FIGURE 3
Experimental paradigm. Every 3 complete rotational cycles constitute a single large cycle, and at least 8 large cycles (32 s) were collected as one dataset.

The muscles associated with rehabilitation training for hand-operated carts are the Biceps Brachii (BIC), Brachialis (BRA), Anterior Deltoid (AD), Brachioradialis (BRAD), Posterior Deltoid (PD), Triceps Brachii Long Head (TBLD), Triceps Brachii Lateral Head (TBLH), and Latissimus Dorsi (LD), as determined through examination of anatomical charts and experimental analysis. After wiping the skin with alcohol wipes, affixing the sensor to the designated location, and subsequently securing it more firmly with medical tape, this approach aims to diminish noise caused by skin perspiration and artifacts from sensor movement.

2.2.2 Experimental paradigm

The overall experimental paradigm is indicated in Figure 3. The participants were initially briefed on the experimental procedure, where three rotation cycles were considered a complete co-contraction extraction cycle. Most patients completed three full rotation cycles within a 4 s interval, considering this timeframe as a major cycle for coordinated data extraction. Healthy subjects followed a similar pace, leading to a total data collection time of 32 s. To prevent any interference from the initiation and cessation movements at the start and the end, a minimum data collection duration of 36 s was ensured for each participant, with intermittent rest periods. Two distinguishable resistance levels were set, labeled as Resistance level 1 (R 1) and Resistance level 2 (R 2). Once data collection for both resistance levels was completed, patients continued with at least 20 min of rehabilitation training. Subsequently, data were gathered at the R 1 to capture fatigue data.

All healthy subjects underwent the following simulated compensation experiment based on the original experiment, with the resistance set at R 1.

Case 1: Maintain a balanced movement on both sides as much as possible.

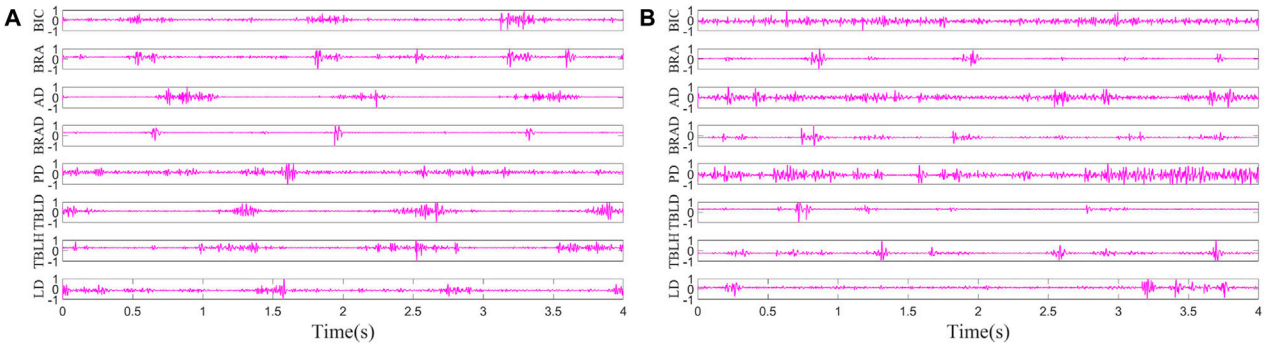

FIGURE 4
(A) sEMG of H1. **(B)** sEMG of S1.

Case 2: Sustain stable force exertion on the right side, with occasional engagement of the left side in movement, simulating a milder degree of motion compensation.

Case 3: The left side exerts no force and is entirely driven by the right side, simulating a more severe form of motion compensation.

2.3 The preprocessing of sEMG

The preprocessing of sEMG signals involved several steps. First, a Butterworth high-pass filter with a cutoff frequency of 40 Hz was applied to the acquired sEMG signals (Chen et al., 2023). Next, a 50 Hz notch filter was used to remove powerline interference. The signals were mean-centered and rectified. Subsequently, Finite Impulse Response (FIR) low-pass filter with a cutoff frequency of 20 Hz was applied to extract the signal envelope (Pan et al., 2018). Root mean square smoothing was employed to further refine the signals, eliminating the aberrant electrical noise and ensuring a smoother envelope. Finally, a normalization process was carried out to ensure that the contribution of smaller muscle groups was adequately represented.

The pre-processing results of sEMG signals from the left side of H1 in Case 1 and the affected side of S1 are shown in Figure 4. The result involves the normalization of sEMG, constraining its range to −1 to 1, and the envelope signals have not yet been extracted. It is evident that the periodicity of data from healthy subjects is more intuitively apparent.

2.4 The extraction of muscle synergies

When controlling limb movements, the human body doesn't individually control each muscle, rather it coordinates the entire muscle group through the spinal cord. Muscle synergy can be extracted from preprocessed sEMG signals using feature extraction algorithms, as described in Eq. 1

$$V^{m\times n} = W^{m\times r} H^{r\times n} + E, \tag{1}$$

where V is the preprocessed surface sEMG signals, with m as the number of sampling channels and n as the number of sampling points, W is the muscle synergy matrix, with r is the number of muscle synergies, H is the activation coefficient matrix, E is the obtained residual error. The extraction of muscle synergies involves two steps.

Step 1: PCA is employed to obtain the feature matrix and principal component matrix. The selection is made for feature vectors and their corresponding principal components equal to the number of muscle synergies.

Step 2: The results obtained in the previous step are taken in absolute values as the initial values for NMF (Lee and Seung, 1999).

The number of muscle synergies is determined by the error between the decomposition results and the original signals. This error is represented by the variance accounted for (VAF) (Cheung et al., 2012), as shown in Eq. 2

$$VAF = 1 - \frac{\|V - V'\|_2}{\|V\|_2}, \tag{2}$$

where V is the preprocessed surface sEMG signals matrix, V' is the reconstruction matrix. When the VAF is excessively high, it fails to achieve effective dimensionality reduction, as redundant information cannot be completely eliminated. Conversely, if the VAF is too low, it may result in the loss of valuable information. Therefore, the minimum number of synergies is chosen when VAF exceeds 80%.

2.5 Synergy symmetry and fusion

In the study, muscle synergies were extracted using the mentioned method from both sides of both healthy subjects and patients. The symmetry of muscle synergy refers to the correlation calculation results of the extracted muscle synergies on both sides of the human body. This indicator can reflect the balance of movement on both sides, thereby indicating the degree of motion compensation. Although the muscle synergy modules were relatively stable, the order in which muscle synergies were extracted exhibited randomness. To establish a more meaningful order of muscle synergies, the muscle synergy order within the synergy matrix was rearranged to optimize the overall synergy

correlation. This was done by calculating synergy correlations between the extracted muscle synergies on both sides. The correlation calculation method employed in the study was the Pearson correlation coefficient (Lalumiere et al., 2022), as shown in Eq. 3

$$\rho = \frac{\sum(X-\bar{X})(Y-\bar{Y})}{\sqrt{\sum(X-\bar{X})^2\sum(Y-\bar{Y})^2}}, \quad (3)$$

where X and Y correspond to two synergy vectors that require correlation determination, and $\bar{X}$ and $\bar{Y}$ represent the respective means. Synergy vector refers to the results of each column in the extracted synergy matrix. In this study, the number of channels in the multi-channel signals is 8, and the number of elements in each synergy vector is also 8.

In cases where one side displays reduced functionality, resulting in abnormal muscle synergy, a phenomenon known as synergy fusion may manifest. The fusion indicator of muscle synergy denotes that the muscle synergy on one side of the subject is formed by the fusion of muscle synergies from the other side. This indicator reflects the variation in the force exerted by individual muscles on both sides during the coordinated movement process in patients, thereby indicating the degree of motion compensation. Specifically, when muscle synergy on the affected side becomes aberrant while that on the unaffected side remains relatively normal, a fusion of synergies may occur as in Eq. 4. In this study, the calculation of synergy fusion on the affected side is carried out utilizing the least squares method (Cheung et al., 2012).

$$W_i^a = \sum_{k=1}^{N^u} m_k^i W_k^u, \quad i = 1 \ \ldots N^a, \quad (4)$$

where W_i^a represents the $i-th$ muscle synergy on the affected side, N^a signifies the number of synergies on the affected side, W_k^u denotes the $k-th$ muscle synergy on the healthy side, fusion coefficient m_k^i denotes the contribution level of the kth healthy side muscle synergy, and N^u represents the number of muscle synergies on the healthy side. When the fusion coefficient exceeds 0.2, it indicates the involvement of one synergy in composing the synergy on the other side. If only one fusion coefficient exceeds 0.2, the presence of fusion is not considered. If more than two fusion coefficients exceed 0.2, it is considered that another synergy exists in fusion on the opposite side.

2.6 Significance analysis

This study conducted experiments with two resistance levels and under fatigue status for both healthy subjects and patients. The determination of significance levels for computed indicators relating to muscle synergy under various conditions involves employing distinct statistical methodologies contingent upon the distribution of the data. Typically, in instances where the data adheres to a normal distribution, significance analysis is carried out using one-way analysis of variance (ANOVA). The Lilliefors test was utilized to assess the normal distribution of characteristics associated with muscle synergy (Abdi and Molin, 2007). This method is deemed appropriate for small sample sizes, and if the data deviates from a normal distribution ($p \leq 0.05$), the Kruskal–Wallis test is subsequently applied to assess the significance of differences (Bala et al., 2023).

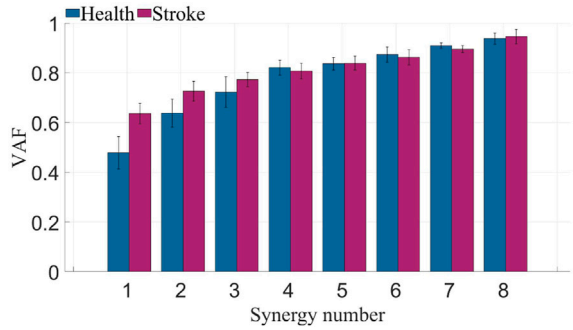

FIGURE 5
VAF of healthy subjects and stroke patients. The blue bars represent the *VAF* across different muscle synergy numbers for healthy subjects, while the purple bars represent the *VAF* across different muscle synergy numbers for patients.

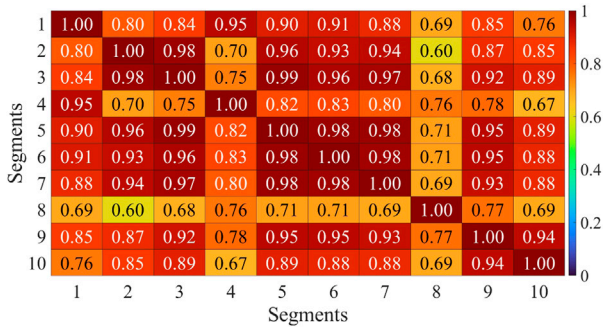

FIGURE 6
Correlation analysis of muscle synergy with equidistant offset of H1. Horizontal axis and vertical axis corresponds to the sequential numbers used for muscle synergy extraction data sets.

3 Results

3.1 The number of muscle synergies

Following preprocessing of multi-channel sEMG from both sides of all participants, a combination of PCA and NMF algorithms was employed to determine different counts of co-activation, aiming to extract muscle synergies. The *VAF* were computed under various co-activation counts. As depicted in Figure 5, muscle synergies on the left side of healthy subjects and the affected side of patients exhibited *VAF* values exceeding 0.8 when the synergies count exceeded 4. Consequently, The number of muscle synergies extracted for both healthy subjects and patients was determined to be 4. This synergy number adequately reconstructs the information of the original data while eliminating some redundant information.

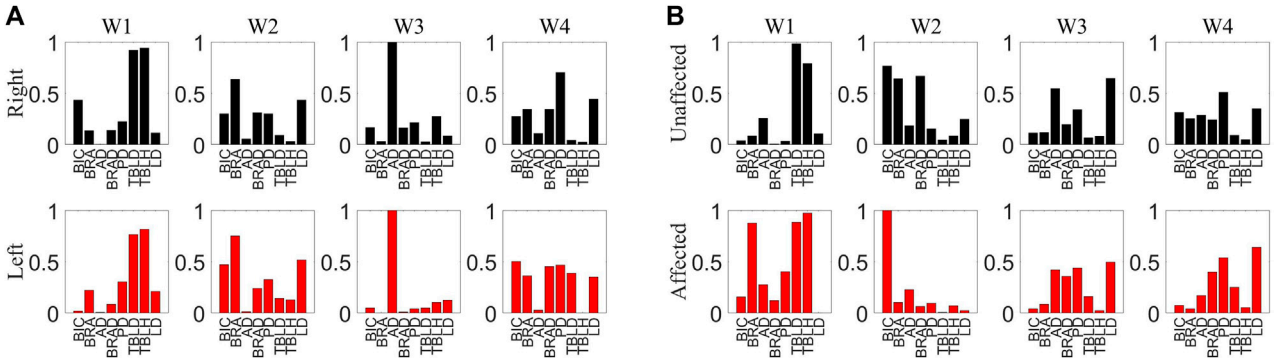

FIGURE 7
(A) Muscle synergy of H1. The upper section representing the synergy of the right side muscles and the lower section depicting the synergy of the left side muscles. **(B)** Muscle synergy of S1. The upper section representing the synergy of the healthy side muscles and the lower section depicting the synergy of the affected side muscles.

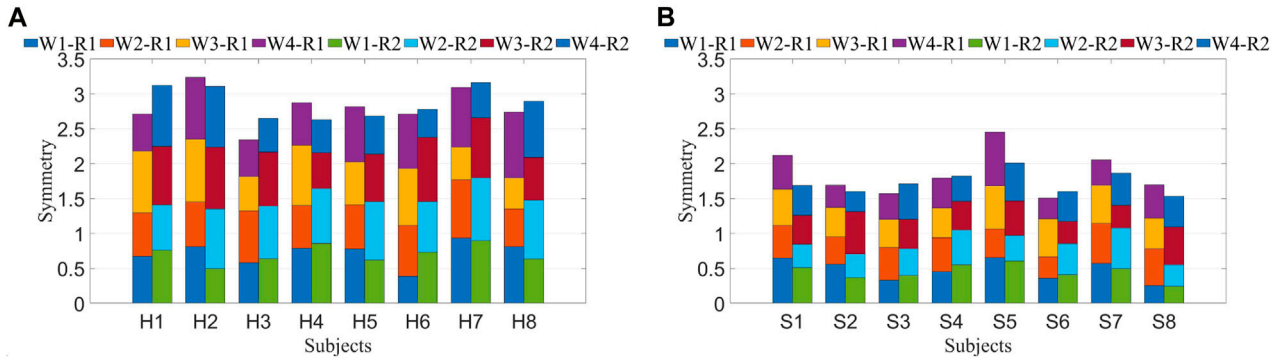

FIGURE 8
(A) Symmetry of synergy in healthy subjects. **(B)** Symmetry of synergy in stroke patients. Each bar consists of four segments, where each segment represents symmetry between both sides for a synergy. W1-W4 denote four synergies, while R 1 and R 2 represent two resistance levels.

3.2 Symmetry of bilateral synergy

Muscle synergies were extracted from 8 channels of sEMG signals on both sides, and the Pearson correlation coefficient was employed to assess the symmetry between bilateral muscle synergies. This study involved the extraction and analysis of sEMG signals during simultaneous movement of the left and right sides. Considering the potential impact of phase deviations between both sides, an initial computation involved evaluating the correlation of muscle synergy extraction results for ten segments with a phase deviation of 200 sampling points. As depicted in Figure 6, the majority of data segments exhibited a symmetry above 0.85, indicating minimal variations in synergy with slight time deviations. Extract muscle synergy from both sides of healthy participants and patients, as illustrated in Figure 7.

To minimize the errors introduced by periodic variations, the average of the symmetry results from eight data segments was calculated to represent the final data, aiming to reduce the impact of small temporal deviations on muscle synergy analysis. The symmetry of muscle synergies for eight patients is shown in Figure 8. Each column consists of 4 segments, representing the symmetry values of each synergy. The overall synergy symmetry for healthy subjects is mostly above 2.5, while for patients, it is predominantly below 2.5.

Similar computations performed on muscle synergies in fatigue status yielded identical outcomes. Under different statuses, the Pearson correlation coefficient was utilized to compute the symmetry of muscle synergies across all healthy subjects and patients, generating mean and standard deviation values. After conducting the Lilliefors test for normality on the data and determining that it does not follow a normal distribution, the Kruskal–Wallis test was applied to determine if there were significant differences in symmetry between R 1 and R 2 for both healthy subjects and patients. Similar computations were conducted for pre-fatigue and post-fatigue conditions, as depicted in Figure 9A.

The symmetry in healthy subjects under R 1 (0.70 ± 0.07) and R 2 (0.72 ± 0.06) did not show significant differences ($p > 0.05$). Additionally, the symmetry before fatigue under R 1 did not significantly differ from the symmetry after fatigue (0.69 ± 0.04, $p > 0.05$). For patients, symmetry under R 1 (0.46 ± 0.08) and R 2 (0.43 ± 0.04) showed no significant differences ($p > 0.05$), and the symmetry before fatigue under R 1 did not significantly differ from

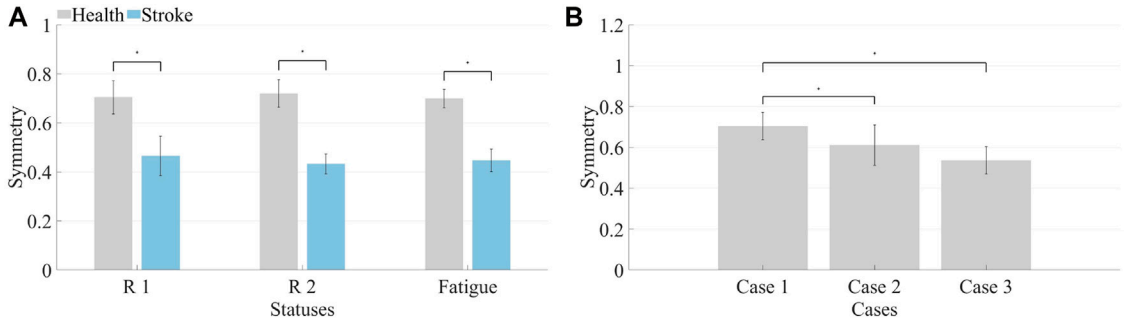

FIGURE 9
(A) Synergy symmetry in different states. The left bars indicate the average symmetry between both sides in three statuses for healthy subjects, while the right bars represent the average symmetry across three conditions for patients. **(B)** Synergy symmetry in simulated compensation cases. Calculate the average synergy symmetry for each case across different healthy subjects.

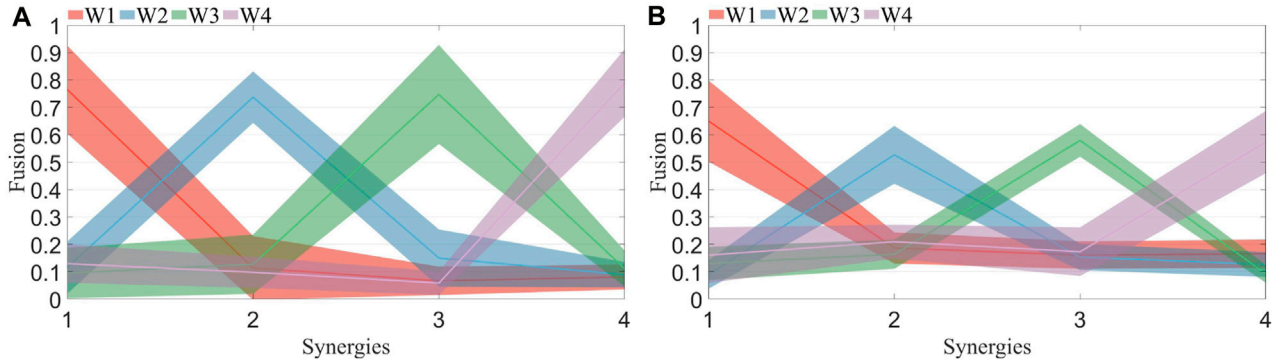

FIGURE 10
(A) Synergy fusion in healthy subjects. Each color corresponds to the four points on the x-axis, representing the fusion of the four synergies from the left side to the right side. The solid line indicates the mean, while the shaded area represents the standard deviation. **(B)** Synergy fusion in patients. Each color corresponds to the four points on the x-axis, representing the fusion of the four synergies from the healthy side to the affected side. The solid line indicates the mean, while the shaded area represents the standard deviation.

the symmetry after fatigue (0.44 ± 0.05, $p > 0.05$). However, healthy subjects exhibited significantly higher synergy symmetry compared to patients ($p \leq 0.05$). Consequently, it is inferred that resistance levels and fatigue statuses do not significantly impact bilateral muscle synergy symmetry in the human body. However, significant differences exist in the symmetry of muscle synergies between patients and healthy subjects.

The average and standard deviation of muscle synergy symmetry across different subjects under the three cases were computed which is shown in Figure 9B. For most subjects, the synergy symmetry was highest in Case 1, lowest in Case 3, and the significance level was determined. The average symmetry for Case 2 was (0.61 ± 0.10), and for Case 3, it was (0.54 ± 0.07). The symmetry in Case 1 was significantly higher than that of Case 3 ($p \leq 0.05$).

3.3 Fusion of bilateral synergy

This study computes the fusion of muscle synergies, considering that all healthy subjects are right-handed. For healthy subjects, the fusion of left-side muscle synergies was calculated from the right-side muscle synergies. For patients, the fusion of affected-side muscle synergies was derived from the unaffected-side muscle synergies.

The fusion levels of muscle synergies were calculated for both healthy subjects and patients under R 1, R 2, and fatigue statuses. H1 represents healthy subject 1. The computed fusion levels among healthy subjects is shown in Figure 10A. The solid line represents the average across all subjects, while the shaded area indicates the standard deviation. Each curve corresponds to four points, representing the reconstruction coefficients of that synergy by four synergies from the other side. A coefficient exceeding 0.2 suggests the involvement of the corresponding synergy in the reconstruction process. When the number of reconstructed synergies exceeds 2, fusion of that synergy is considered to be present. From the graph, it is evident that most curves display a single prominent peak, with other points mostly below 0.2. The synergy fusion status among patients under R 1 is shown in Figure 10B. Each curve not only exhibits a dominant peak but also contains additional points with values exceeding 0.2. This suggests the presence of multiple synergies formed through fusion of synergies from the unaffected side.

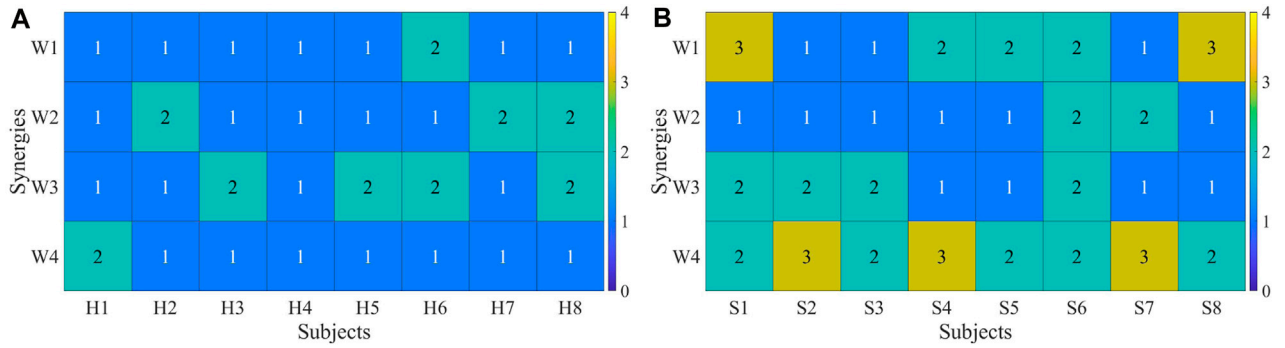

FIGURE 11
(A) Synergy fusion in healthy subjects. **(B)** Synergy fusion in patients. Each column represents a healthy subject **(A)** or a patient **(B)**, and each row depicts the degree of synergy fusion. A value above 2 indicates the presence of fusion.

TABLE 2 Fusion of healthy subjects.

Subject	H1	H2	H3	H4	H5	H6	H7	H8
R 1	1	1	1	0	1	2	1	2
R 2	1	1	1	1	1	2	1	2
Fatigue	2	1	2	1	1	2	1	2
Case 1	1	1	1	0	1	2	1	2
Case 2	0	1	3	1	3	1	3	2
Case 3	1	2	3	2	3	0	3	3

TABLE 3 Fusion of stroke subjects.

Subject	S1	S2	S3	S4	S5	S6	S7	S8
R 1	3	2	2	2	2	4	2	2
R 2	2	4	3	2	2	3	4	2
Fatigue	2	3	3	3	2	4	3	2

Each participant's synergy fusion status was plotted individually. The calculation of synergy fusion among healthy subjects under R 1 is shown in Figure 11A. Each column represents a participant, while the values in each row denote the fusion status of that synergy. Values exceeding 2 indicate the presence of fusion for a given synergy. Most healthy participants exhibit fusion in only one out of the four muscle synergies, except for participants 6 and 8. The calculation of synergy fusion among patients under R 1 is shown in Figure 11B. Healthy subjects typically show fusion in two or fewer muscle synergies, while patients often exhibit fusion in more than two synergies, with some demonstrating fusion in all four synergies.

Both healthy subjects and patients underwent analysis for synergy fusion levels under R 1, R 2, and fatigue statuses, as illustrated in Tables 2, 3. The numbers in the table represent the count of synergistic fusion occurrences among the four muscle synergies for each subject. The average and standard deviation of fused synergies were calculated for healthy subjects and patients, as depicted in Figure 12A. Subsequently, the significance level of differences among various statuses was determined. The outcomes indicate an absence of significant differences in synergy fusion levels between the two resistance levels and pre-fatigue and post-fatigue statuses. The number of fusions for healthy participants under R 1 (1.13 ± 0.64) and R 2 (1.25 ± 0.46) showed no significant difference ($p > 0.05$). Also, there was no significant difference between the pre-fatigue and post-fatigue fusion counts under R 1 (1.5 ± 0.53) among healthy participants ($p > 0.05$). For patients, there was no significant difference in the fusion counts between R 1 (2.37 ± 0.74) and R 2 (2.75 ± 0.89, $p > 0.05$). Similarly, there was no significant difference between pre-fatigue and post-fatigue fusion numbers under R 1 (2.5 ± 0.53) among patients ($p > 0.05$). However, the number of fusions in healthy participants was significantly lower than in patients ($p \leq 0.05$).

It is illustrated that the computation of synergy fusion levels among healthy subjects in simulated compensation scenarios in Table 2. The average results for multiple healthy subjects are depicted in Figure 12B. The results indicate a gradual increase in synergy fusion levels from Case 1 to Case 3. The average fusion count for Case 2 is (1.75 ± 1.17), and for Case 3 is (2.13 ± 1.23). The fusion count in Case 1 is significantly lower than in Case 3 ($p \leq 0.05$).

3.4 Influence of muscle fatigue on synergy

The analysis conducted above indicates that muscle fatigue does not significantly impact the symmetry of coordination and fusion levels during bilateral coordinated movements in the human body. However, an assessment was performed on the correlation of muscle synergies pre and post fatigue. Muscle synergies were extracted from five movement cycles before and after fatigue for each participant, and the correlation between these synergies was computed pairwise. It is presented that the computed results for one of the patients, demonstrating a reduction in synergy correlation post-fatigue in Figure 13. Moreover, a slight decline in correlation was observed in the five sets of post-fatigue muscle synergy data, which was consistent across multiple participants. This suggests that muscle fatigue leads to an increase in the instability of muscle synergies, which could impede effective rehabilitation training and assessment. Therefore, mitigating the occurrence of muscle fatigue should be a priority to ensure optimal conditions for rehabilitation training and evaluation.

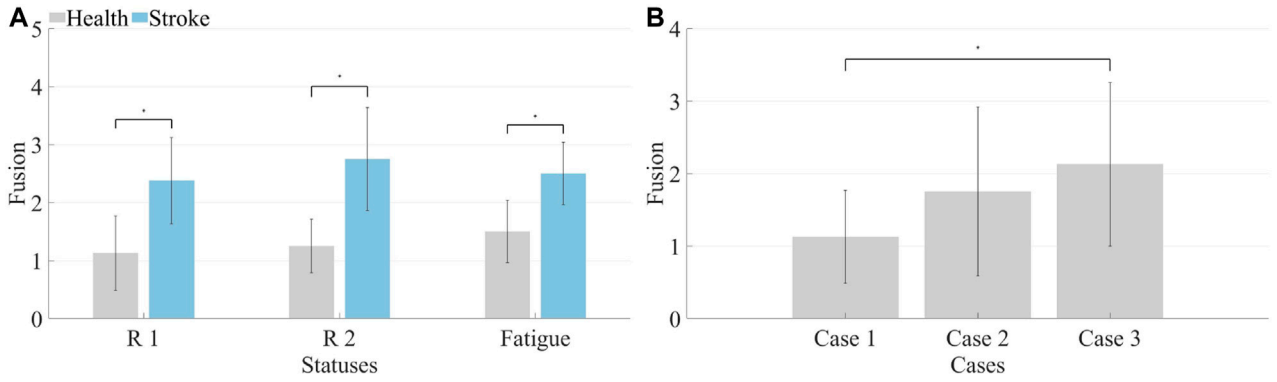

FIGURE 12
(A) Synergy fusion in different states. The left side represents healthy subjects, while the right side represents patients. **(B)** Synergy fusion in simulated compensation status. Calculate the average synergy fusion count for each case across different healthy subjects.

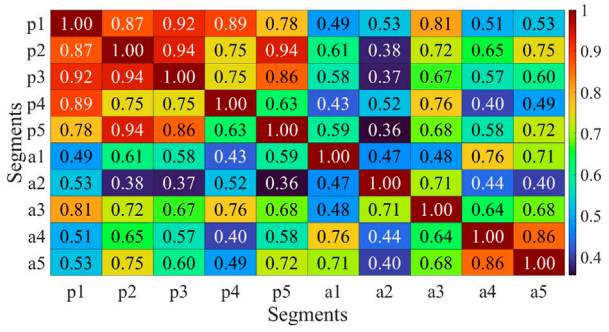

FIGURE 13
Multicycle synergy correlation before and after fatigue of H2. p1-p5 represent the five consecutive cycle data before fatigue, while a1-a5 represent the five consecutive cycle data after fatigue.

4 Discussion

The present study takes into account the compensation phenomenon that occurs during bilateral auxiliary movement. Compensation is the phenomenon of leveraging the function of muscles on both sides due to functional deficiencies. In the process of bilateral auxiliary rehabilitation training, patients tend to excessively rely on the unaffected side due to the functional impairment of the affected side. Current rehabilitation assessment methods often rely heavily on clinical expertise, such as FMA and Fugl-Meyer scales. However, these methods lack the ability to promptly detect the occurrence of compensation behaviors in patients. Prolonged reliance on the unaffected side may lead to muscle atrophy and permanent loss of function on the affected side.

To quantify compensation behaviors on both sides, this study designed experiments using a handcart and incorporated simulated compensation experiments. Healthy subjects' right hand was designated as the unaffected side, while the left side was either completely restrained or occasionally engaged in the handcart's rotational movement. Motion compensation manifests in the coordination of muscle exertion levels. Given that sEMG reflect the degree of muscle exertion in each muscle, bilateral balance handcart experiments were conducted to collect sEMG signals from corresponding areas on both sides of healthy subjects and patients. According to muscle synergy theory, human body movement is achieved through the linear combination of multiple synergy modules. Extracting muscle synergy from multi-channel sEMG signals is essential. Presently, NMF is primarily used for muscle synergy extraction, mainly due to the interpretability of its non-negative results. However, NMF's drawback lies in its multiple solutions, indicating instability as it might yield different outcomes when run multiple times on the same dataset. This variability significantly impacts the application of muscle synergy in rehabilitation assessment, leading to substantial differences between multiple analytical results. Some studies have employed PCA to extract muscle synergy. PCA's advantage lies in its capability to extract stable muscle synergies. However, its results often contain negative values, limiting its application in rehabilitation assessment. Nevertheless, there are studies integrating muscle synergies extracted by PCA into rehabilitation exoskeletons' dimensionality reduction control (Alibeji et al., 2015).

This study analyzes the symmetry of muscle synergy on both sides of the body, demanding high stability in extracted synergies. To obtain stable muscle synergies, sEMG signals underwent filtering and smoothing, followed by normalization for each channel to prevent smaller muscles' participation from being overshadowed by larger muscle groups. Considering that NMF algorithm results are significantly influenced by the initial input matrix, this study employed PCA for preliminary decomposition of multi-channel surface electromyographic signals on each side. The absolute value of the decomposed results was then processed and utilized as the input matrix for the NMF algorithm, resulting in relatively stable muscle synergy outcomes. Symmetry and fusion levels of muscle synergy extracted from both sides of the body were primarily analyzed. Furthermore, variations in muscle synergy indicators during compensation simulated experiments were examined to identify potential indices applicable for quantifying compensation behavior.

4.1 The number of muscle synergy

The determination of the quantity of muscle synergies is not automatically established through an algorithm but involves

selecting various synergy numbers, computing the *VAF* values, and assessing them through plotting. The computed *VAF* values for synergy extraction on the affected side of patients and the left side of healthy subjects is shown in Figure 5. Typically, a threshold is set to determine the number of synergies. Considering the redundancy in sEMG, this study set the threshold at 0.8, which reflects 80% of the original data's information in the obtained synergy results. From the graph, notable differences in *VAF* between patients and healthy subjects are observed when the synergy numbers are small. However, when the synergy numbers exceed 4, most participants in both patient and healthy subject groups exhibit a *VAF* greater than 0.8. Similar results are obtained when analyzing the other side. Consequently, the quantity of muscle synergies was established as 4.

4.2 The symmetry of bilateral muscle synergy

The primary consideration was the phase shift in bilateral movement during the handcart training, which, reflected in sEMG signals, represents a time shift. Approximately 1.3 s are required for a full rotation, resulting in a time offset of roughly half a rotation between the two sides. With a sampling rate of 1,926 Hz, this offset corresponds to 1,251 data points. Therefore, this study employed 8,000 as a data window, ensuring the inclusion of at least three complete rotation cycles, encompassing the initiation, termination, and transitional phases of the movement in the sEMG signals. Muscle selection was performed at intervals of 200 from 10 segments of sEMG signals, followed by muscle synergy extraction.

The assessment of muscle synergy variations across different signal segments, as shown in Figure 6, indicated that the correlation of most muscle synergies exceeded 0.85, suggesting minimal phase shifts and negligible changes in synergy. To minimize errors induced by shifts, the study computed muscle synergy symmetry for eight data segments and averaged them to yield the final results. The extracted results of muscle synergies for healthy subjects and patients are shown in Figure 7. The right panel displays the muscle synergies on both sides for patients. Compared to healthy subjects, there are notable differences in muscle synergies on both sides for patients.

The initial phase involved the calculation of muscle synergy symmetry between both sides of the participants, as depicted in Figure 8. Each bar consists of four segments, representing the symmetry of individual muscle synergies. The bar chart visually illustrates a significant difference in overall synergy symmetry between healthy subjects and patients. The overall synergy symmetry for healthy subjects is mostly above 2.5, whereas for patients, it tends to be below 2.5. The analysis revealed an average synergy symmetry of 0.70 for healthy subjects, contrasting with only 0.46 for patients, as depicted in Figure 9A. Notably, synergy symmetry in healthy subjects was significantly higher than in patients. Analyzing the simulated compensation muscle synergy states of healthy subjects, as illustrated in Figure 9B. The synergy symmetry demonstrated a declining trend across the three cases, with Case 1 exhibiting significantly higher symmetry than Case 2 and Case 3 ($p \leq 0.05$). This stepped pattern across the three cases indicates that muscle synergy symmetry could quantify compensation behaviors. A significant analysis of muscle synergy results under different resistance levels ($p > 0.05$) suggests no significant differences in symmetry outcomes under varying resistance levels. Geng et al. (2020) also suggests high stability in muscle synergy analysis under different resistance Level. Furthermore, a significant analysis of pre- and post-fatigue muscle synergy results revealed ($p > 0.05$), indicating that muscle fatigue does not significantly impact synergy symmetry.

4.3 The fusion of bilateral muscle synergy

The fusion of synergies implies when the muscle synergies on the affected side are composed of contributions from more than two healthy-side muscle synergies. The fusion coefficients were computed using non-negative least squares. Results for healthy subjects are illustrated in Figure 10A, while those for patients are depicted in Figure 10B. A comparison reveals that most maximum fusion coefficients in patients are smaller than those in healthy subjects, whereas most minimum fusion coefficients are larger in patients than in healthy subjects. Subsequently, the fusion status of synergies was computed and plotted in Figure 11, where each column of four numbers corresponds to the fusion status of four synergies for a participant. Values above 2 indicate the presence of fusion in that synergy. The analysis indicates that the synergy fusion counts in healthy subjects are mostly below 2, whereas patients tend to have a synergy fusion count significantly above 2. The average synergy counts among different resistance levels and post-fatigue in various participants was calculated, followed by significant analysis depicted in Figure 12A. The synergy fusion counts in patients is significantly higher than in healthy subjects. After fatigue, there is a slight increase in fusion counts for healthy subjects, which, however, is not significant ($p > 0.05$). Patients show the maximum fusion synergy count after increased resistance levels, but neither resistance levels nor fatigue resulted in significant changes. Regarding the calculation of synergy fusion under simulated compensation cases in Figure 12B, a stair-like increment is observed across the three cases. Notably, the fusion count in Case 1 is significantly lower than in Case 3 ($p \leq 0.05$). Furthermore, the fusion count in Case 3 is more similar to that of the patients, indicating that fusion indicators can quantify compensation evaluation on both sides. The calculation of different cycle synergy correlations pre-and post-fatigue among participants revealed a decrease in synergy correlations for most subjects after fatigue, indicating increased instability in human control due to muscle fatigue in Figure 13. This factor might not favor rehabilitation training and assessment. Thus, efforts should be made to avoid muscle fatigue during rehabilitation training.

5 Conclusion

This study proposed a muscle synergy-based assessment method to objectively quantify motion compensation in post-stroke hemiplegia patients. The results demonstrated that synergy symmetry and synergy fusion indicators effectively assessed motion compensation during hand-cycling tasks. Patients with poorer limb functionality exhibited lower synergy symmetry, indicating decreased coordination. Simulated compensation

experiments of healthy subjects further validated these results. Moreover, neither resistance levels nor fatigue status demonstrates a significant impact on these indicators. However, fatigue led to reduced stability in motor control for both patients and healthy subjects. The study emphasizes the importance of minimizing muscle fatigue during rehabilitation training. Overall, synergy-based indicators provide a quantitative assessment of bilateral motion compensation, offering personalized recommendations for effective rehabilitation.

Data availability statement

The raw data supporting the conclusion of this article will be made available by the authors, without undue reservation.

Ethics statement

The studies involving humans were approved by the Ethics Committee of Zhengzhou University, China (Approval No. ZZURIB 2023-85). The studies were conducted in accordance with the local legislation and institutional requirements. Written informed consent for participation in this study was provided by the participants' legal guardians/next of kin. Written informed consent was obtained from the individual(s) for the publication of any potentially identifiable images or data included in this article.

Author contributions

YnL: Formal Analysis, Investigation, Project administration, Supervision, Writing–original draft, Writing–review and editing, Methodology. YoL: Formal Analysis, Investigation, Methodology, Validation, Writing–original draft. ZZ: Data curation, Formal Analysis, Investigation, Methodology, Writing–original draft, Validation. BH: Data curation, Formal Analysis, Writing–review and editing. AD: Methodology, Resources, Writing–original draft.

Funding

The author(s) declare financial support was received for the research, authorship, and/or publication of this article. This work is supported by the National Key Research and Development Project (No. 2020YFB1313701), the National Natural Science Foundation of China (No. 62103376), the Outstanding Foreign Scientist Support Project in Henan Province (No. GZS2019008) and Science & Technology Research Project in Henan Province of China (212102310253).

Conflict of interest

The authors declare that the research was conducted in the absence of any commercial or financial relationships that could be construed as a potential conflict of interest.

Publisher's note

References

Abdi, H., and Molin, P. (2007). "Lilliefors/Van Soest's test of normality," in *Encyclopedia of measurement and statistics* (SAGE), 540–544.

Alibeji, N. A., Kirsch, N. A., and Sharma, N. (2015). A muscle synergy-inspired adaptive control scheme for a hybrid walking neuroprosthesis. *Front. Bioeng. Biotechnol.* 3, 203. doi:10.3389/fbioe.2015.00203

Ansari, N. N., Naghdi, S., Mashayekhi, M., Hasson, S., Fakhari, Z., and Jalaie, S. (2012). Intra-rater reliability of the Modified Modified Ashworth Scale (MMAS) in the assessment of upper-limb muscle spasticity. *NeuroRehabilitation* 31, 215–222. doi:10.3233/NRE-2012-0791

Aoi, S., and Funato, T. (2016). Neuromusculoskeletal models based on the muscle synergy hypothesis for the investigation of adaptive motor control in locomotion via sensory-motor coordination. *Neurosci. Res.* 104, 88–95. doi:10.1016/j.neures.2015.11.005

Bala, S., Vishnu, V. Y., and Joshi, D. (2023). Muscle synergy-based functional electrical stimulation reduces muscular fatigue in post-stroke patients: a systematic comparison. *IEEE Trans. Neural Syst. Rehabilitation Eng.* 31, 2858–2871. doi:10.1109/TNSRE.2023.3290293

Brambilla, C., and Scano, A. (2022). The number and structure of muscle synergies depend on the number of recorded muscles: a pilot simulation study with opensim. *Sensors* 22, 8584. doi:10.3390/s22228584

Calabro, F. J., and Perez, M. A. (2016). Bilateral reach-to-grasp movement asymmetries after human spinal cord injury. *J. neurophysiology* 115, 157–167. doi:10.1152/jn.00692.2015

Chen, X., Dong, X., Feng, Y., Jiao, Y., Yu, J., Song, Y., et al. (2023). Muscle activation patterns and muscle synergies reflect different modes of coordination during upper extremity movement. *Front. Hum. Neurosci.* 16, 912440. doi:10.3389/fnhum.2022.912440

Cheung, V. C., Turolla, A., Agostini, M., Silvoni, S., Bennis, C., Kasi, P., et al. (2012). Muscle synergy patterns as physiological markers of motor cortical damage. *Proc. Natl. Acad. Sci.* 109, 14652–14656. doi:10.1073/pnas.1212056109

Dj, G., Danells, C. J., and Black, S. E. (2002). The fugl-meyer assessment of motor recovery after stroke: a critical review of its measurement properties. *Neurorehabili Neural Repair* 16, 232–240. doi:10.1177/154596802401105171

Feigin, V. L., Stark, B. A., Johnson, C. O., Roth, G. A., Bisignano, C., Abady, G. G., et al. (2021). Global, regional, and national burden of stroke and its risk factors, 1990–2019: a systematic analysis for the global burden of disease study 2019. *Lancet Neurology* 20, 795–820. doi:10.1016/S1474-4422(21)00252-0

Funato, T., Hattori, N., Yozu, A., An, Q., Oya, T., Shirafuji, S., et al. (2022). Muscle synergy analysis yields an efficient and physiologically relevant method of assessing stroke. *Brain Commun.* 4, fcac200. doi:10.1093/braincomms/fcac200

Gauthier, L. V., Taub, E., Perkins, C., Ortmann, M., Mark, V. W., and Uswatte, G. (2008). Remodeling the brain: plastic structural brain changes produced by different motor therapies after stroke. *Stroke* 39, 1520–1525. doi:10.1161/STROKEAHA.107.502229

Geng, Y., Deng, H., Samuel, O. W., Cheung, V., Xu, L., and Li, G. (2020). Modulation of muscle synergies for multiple forearm movements under variant force and arm position constraints. *J. neural Eng.* 17, 026015. doi:10.1088/1741-2552/ab7c1a

Hirashima, M., and Oya, T. (2016). How does the brain solve muscle redundancy? filling the gap between optimization and muscle synergy hypotheses. *Neurosci. Res.* 104, 80–87. doi:10.1016/j.neures.2015.12.008

Huang, J., Ji, J.-R., Liang, C., Zhang, Y. Z., Sun, H. C., Yan, Y. H., et al. (2022). Effects of physical therapy-based rehabilitation on recovery of upper limb motor function after stroke in adults: a systematic review and meta-analysis of randomized controlled trials. *Ann. Palliat. Med.* 11, 521–531. doi:10.21037/apm-21-3710

Kim, H., Miller, L. M., Fedulow, I., Simkins, M., Abrams, G. M., Byl, N., et al. (2012). Kinematic data analysis for post-stroke patients following bilateral versus unilateral rehabilitation with an upper limb wearable robotic system. *IEEE Trans. neural Syst. rehabilitation Eng.* 21, 153–164. doi:10.1109/TNSRE.2012.2207462

Kraaijenbrink, C., Vegter, R., de Groot, S., Arnet, U., Valent, L., Verellen, J., et al. (2021). Biophysical aspects of handcycling performance in rehabilitation, daily life and recreational sports; a narrative review. *Disabil. rehabilitation* 43, 3461–3475. doi:10.1080/09638288.2020.1815872

Lalumiere, M., Bourbonnais, D., Goyette, M., Perrino, S., Desmeules, F., and Gagnon, D. H. (2022). Unilateral symptomatic achilles tendinopathy has limited effects on bilateral lower limb ground reaction force asymmetries and muscular synergy attributes when walking at natural and fast speeds. *J. Foot Ankle Res.* 15, 66. doi:10.1186/s13047-022-00570-3

Lee, D. D., and Seung, H. S. (1999). Learning the parts of objects by non-negative matrix factorization. *Nature* 401, 788–791. doi:10.1038/44565

Li, C., Yang, H., Cheng, L., Huang, F., Zhao, S., Li, D., et al. (2022). Quantitative assessment of hand motor function for post-stroke rehabilitation based on hagcn and multimodality fusion. *IEEE Trans. Neural Syst. Rehabilitation Eng.* 30, 2032–2041. doi:10.1109/TNSRE.2022.3192479

Louie, D. R., Mortenson, W. B., Durocher, M., Teasell, R., Yao, J., and Eng, J. J. (2020). Exoskeleton for post-stroke recovery of ambulation (ExStRA): study protocol for a mixed-methods study investigating the efficacy and acceptance of an exoskeleton-based physical therapy program during stroke inpatient rehabilitation. *BMC Neurol.* 20, 35–39. doi:10.1186/s12883-020-1617-7

Ma, Y., Shi, C., Xu, J., Ye, S., Zhou, H., and Zuo, G. (2021). A novel muscle synergy extraction method used for motor function evaluation of stroke patients: a pilot study. *Sensors* 21, 3833. doi:10.3390/s21113833

Mazzoleni, S., Battini, E., Crecchi, R., Dario, P., and Posteraro, F. (2018). Upper limb robot-assisted therapy in subacute and chronic stroke patients using an innovative end-effector haptic device: a pilot study. *NeuroRehabilitation* 42, 43–52. doi:10.3233/NRE-172166

Meng, L., Jiang, X., Qin, H., Fan, J., Zeng, Z., Chen, C., et al. (2022). Automatic upper-limb brunnstrom recovery stage evaluation via daily activity monitoring. *IEEE Trans. Neural Syst. Rehabilitation Eng.* 30, 2589–2599. doi:10.1109/TNSRE.2022.3204781

Nolan, K. J., Ames, G. R., and Dandola, C. M. (2023). "Intensity modulated exoskeleton gait training post stroke," in 2023 45th Annual International Conference of the IEEE Engineering in Medicine and Biology Society (EMBC), Sydney, Australia, 24-27 July 2023 (IEEE), 1–4.

Pan, B., Huang, Z., Wu, J., and Shen, Y. (2021). Primitive muscle synergies reflect different modes of coordination in upper limb motions. *Med. Biol. Eng. Comput.* 59, 2153–2163. doi:10.1007/s11517-021-02429-4

Pan, B., Sun, Y., Xie, B., Huang, Z., Wu, J., Hou, J., et al. (2018). Alterations of muscle synergies during voluntary arm reaching movement in subacute stroke survivors at different levels of impairment. *Front. Comput. Neurosci.* 12, 69. doi:10.3389/fncom.2018.00069

Pathak, A., Gyanpuri, V., and Dev, P. (2021). The Bobath Concept (NDT) as rehabilitation in stroke patients: a systematic review. *J. Fam. Med. Prim. Care* 10, 3983. doi:10.4103/jfmpc.jfmpc_528_21

Renner, C. I., Woldag, H., Atanasova, R., and Hummelsheim, H. (2005). Change of facilitation during voluntary bilateral hand activation after stroke. *J. neurological Sci.* 239, 25–30. doi:10.1016/j.jns.2005.07.005

Sheng, Y., Tan, G., Liu, J., Chang, H., Wang, J., Xie, Q., et al. (2022). Upper limb motor function quantification in post-stroke rehabilitation using muscle synergy space model. *IEEE Trans. Biomed. Eng.* 69, 3119–3130. doi:10.1109/TBME.2022.3161726

Singh, N., Saini, M., Kumar, N., Srivastava, M. V. P., and Mehndiratta, A. (2021). Evidence of neuroplasticity with robotic hand exoskeleton for post-stroke rehabilitation: a randomized controlled trial. *J. neuroengineering rehabilitation* 18, 76. doi:10.1186/s12984-021-00867-7

Sugihra, S., Toda, H., and Yamaguchi, T. (2018). "Ankle joint stretching device by using tension rod structure for self rehabilitation," in 2018 IEEE International Conference on Robotics and Biomimetics (ROBIO), Kuala Lumpur, Malaysia, 12-15 December 2018 (IEEE), 680–684.

Tang, L., Li, F., and Cao, S. (2014). "Muscle synergy analysis for similar upper limb motion tasks," in 2014 36th Annual International Conference of the IEEE Engineering in Medicine and Biology Society, Chicago, IL, USA, 26-30 August 2014 (IEEE), 3590–3593.

Tu, W.-J., Wang, L.-D., Yan, F., Peng, B., Hua, Y., Liu, M., et al. (2023). China stroke surveillance report 2021. *Mil. Med. Res.* 10, 33. doi:10.1186/s40779-023-00463-x

Woldag, H., Lukhaup, S., Renner, C., and Hummelsheim, H. (2004). Enhanced motor cortex excitability during ipsilateral voluntary hand activation in healthy subjects and stroke patients. *Stroke* 35, 2556–2559. doi:10.1161/01.STR.0000144651.07122.da

Xie, Q., Wu, J., Zhang, Q., Zhang, Y., Sheng, B., Wang, X., et al. (2023). Neurobiomechanical mechanism of Tai Chi to improve upper limb coordination function in post-stroke patients: a study protocol for a randomized controlled trial. *Trials* 24, 788. doi:10.1186/s13063-023-07743-w

Zhao, K., Zhang, Z., Wen, H., Wang, Z., and Wu, J. (2019). Modular organization of muscle synergies to achieve movement behaviors. *J. Healthc. Eng.* 2019, 1–9. doi:10.1155/2019/8130297

frontiers | Frontiers in Bioengineering and Biotechnology

TYPE Original Research
PUBLISHED 28 March 2024
DOI 10.3389/fbioe.2024.1360902

OPEN ACCESS

EDITED BY
Wujing Cao,
Chinese Academy of Sciences (CAS), China

REVIEWED BY
Jen Rowson,
The University of Sheffield, United Kingdom
Qing Sun,
Shanghai University, China

*CORRESPONDENCE
Xuhua Lu,
xuhualu@hotmail.com
Qiaoling Meng,
qiaoling_meng@126.com

RECEIVED 24 December 2023
ACCEPTED 08 March 2024
PUBLISHED 28 March 2024

CITATION
Jiao Z, Wang H, Fei C, Wang L, Yuan J, Meng Q and Lu X (2024), A reconfigurable multi-terrain adaptive casualty transport aid base on Watt II six-bar linkage for industrial environment. *Front. Bioeng. Biotechnol.* 12:1360902. doi: 10.3389/fbioe.2024.1360902

A reconfigurable multi-terrain adaptive casualty transport aid base on Watt II six-bar linkage for industrial environment

Zongqi Jiao[1,2], Haibin Wang[2], Cuizhi Fei[1,2], Liang Wang[2], Jincan Yuan[2], Qiaoling Meng[1]* and Xuhua Lu[2]*

[1]Institute of Rehabilitation Engineering and Technology, University of Shanghai for Science and Technology, Shanghai, China, [2]Department of Orthopaedic Surgery, Changzheng Hospital, Naval Medical University, Shanghai, China

Introduction: This paper presents the Reconfigurable Multi-Terrain Adaptive Casualty Transport Aid (RMTACTA), an innovative solution addressing the critical need for rapid and safe pre-hospital casualty transport in industrial environments. The RMTACTA, leveraging the Watt II six-bar linkage, offers enhanced adaptability through six modes of motion, overcoming the limitations of traditional stretchers and stretcher vehicles by facilitating navigation across narrow and challenging terrains.

Methods: The RMTACTA's design incorporates two branching four-bar mechanisms to form a compact, reconfigurable Watt II six-bar linkage mechanism. This setup is controlled via a single remote rope, allowing for easy transition between its multiple operational modes, including stretcher, stretcher vehicle, folding, gangway-passing, obstacle-crossing, and upright modes. The mechanical design and kinematics of this innovative linkage are detailed, alongside an analysis of the optimal design and mechanical evaluation of rope control.

Results: A prototype of the RMTACTA was developed, embodying the proposed mechanical and kinematic solutions. Preliminary tests were conducted to verify the prototype's feasibility and operability across different terrains, demonstrating its capability to safely and efficiently transport casualties.

Discussion: The development of the proposed Reconfigurable Multi-Terrain Adaptive Casualty Transport Aid (RMTACTA) introduces a novel perspective on the design of emergency medical transport robots and the enhancement of casualty evacuation strategies. Its innovative application of the Watt II six-bar linkage mechanism not only showcases the RMTACTA's versatility across varied terrains but also illuminates its potential utility in critical scenarios such as earthquake relief, maritime rescue, and battlefield medical support.

KEYWORDS

casualty transport aid, Watt II six-bar linkage, reconfigurable robot, kinematics and statics, parametric study

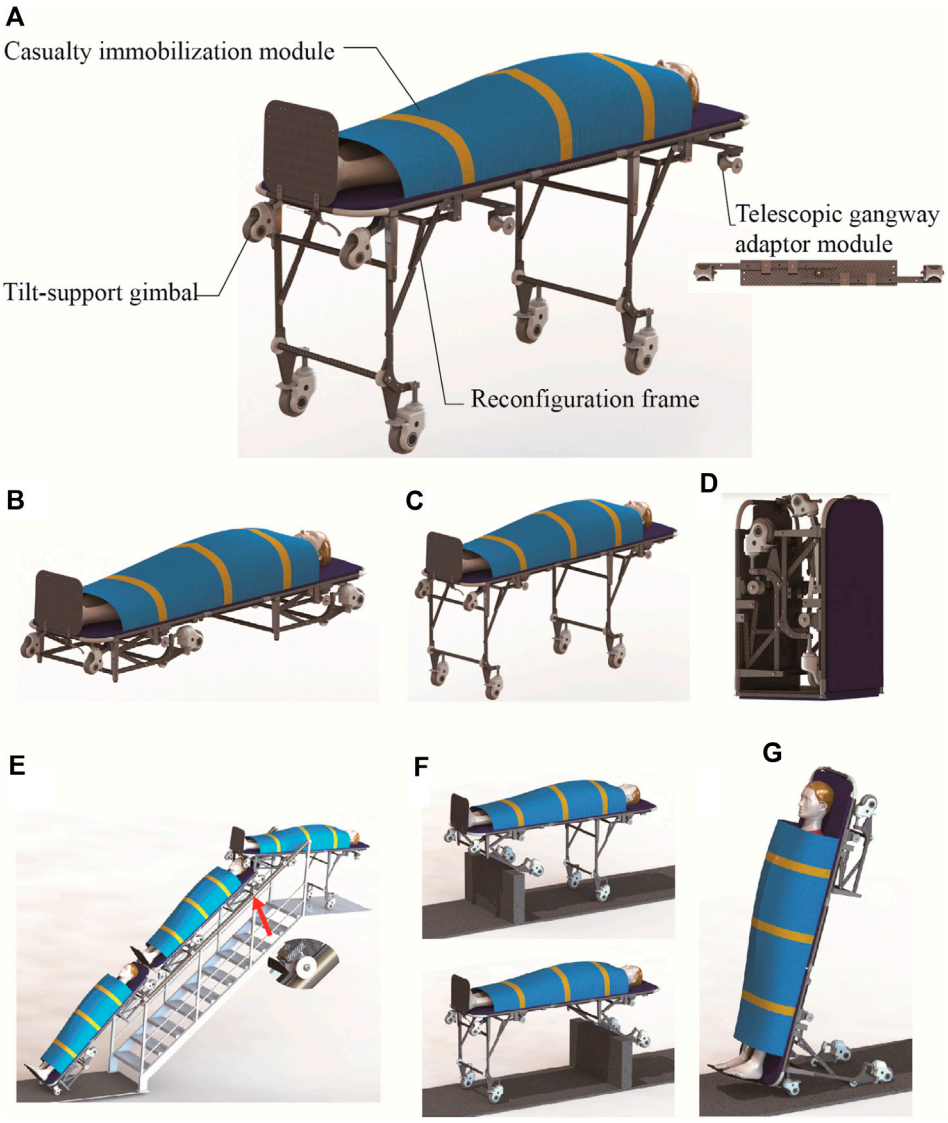

FIGURE 1
Mechanical structure of the RMTACTA and the six modes. **(A)** Mechanical structure of the RMTACTA. **(B)** Stretcher mode. **(C)** Stretcher vehicle mode. **(D)** Folding mode. **(E)** Gangway-passing mode. **(F)** Obstacle-crossing mode. **(G)** Upright mode.

1 Introduction

Pre-hospital casualty transport is particularly critical for injured casualties suffering from limb and spinal fractures, brain injuries and visceral injuries (Wilson et al., 2015). Rapid and safe casualty transfer will allow the injured to receive care as soon as possible, enhancing survival and post-operative recovery rates (Bricknell, 2003; Cao et al., 2023; Yang et al., 2023). The complexity of casualty transfer is increased by the presence of narrow passageways, turns, gangways, and other obstacles in industrial environments like factories and ships (Butler FK et al., 2022). A fast and efficient casualty transport aid can help rescuers overcome these challenges and ensure that the casualty reaches the medical facility without incident. Stretchers and stretcher trucks are the most common casualty transport aid. The stretcher is frequently employed in field ambulances and disaster rescue due to its lightweight, portable structure and excellent environmental compatibility (Lim and Ng, 2021). However, there are safety risks associated with using the stretcher, including as overturning, a heavy load on the rescue team, a poor transfer pace, and other issues (Drobinsky et al., 2020). Stretcher vehicles, such as the Stryker Stretcher Vehicle, can provide more protection for the injured while also increasing transfer efficiency by switching from lifting to pushing. However, the stretcher vehicles' larger size and heavier weight make them more suitable for more spacious areas such as hospitals and neighborhoods, making it difficult to pass easily through narrow environments and terrain with a significant difference in height, such as gangways and high thresholds (Qin and Li, 2023).

Advancements and innovations in casualty transfer aid have yielded significant results. Several researchers, including Xixi Hong (Hong et al., 2020), Lingfeng Sang (Sang et al., 2019), Aguilar-Pérez L A (Aguilar-Pérez et al., 2021) and Jin Rui (Rui and Gao, 2019), have developed equipment based on a multi-link design. This design

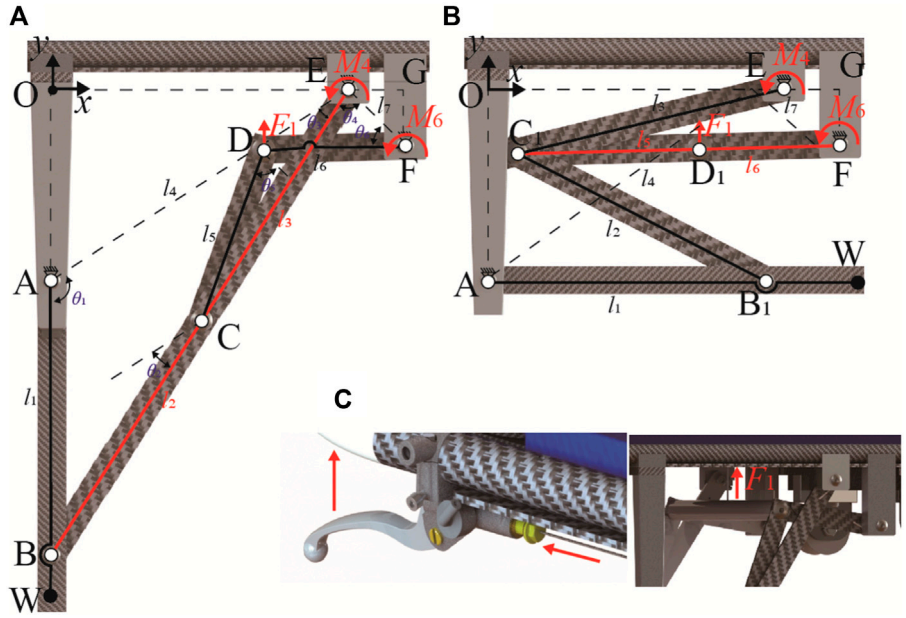

FIGURE 2
Geometry of the Watt II six-bar linkage in the reconfigurable frame. **(A)** Expansion mode. **(B)** Retracted mode. **(C)** Remote cable-driven mechanism.

allows for a seamless transition between a stretcher and a wheelchair, significantly reducing the equipment's turning radius. As a result, it simplifies navigation in confined spaces such as elevators and tight corners. However, changing the stance of the stretcher and wheelchair will cause the casualty's stance to alter, which is undesirable for badly injured people, such as those with spinal injuries. To tackle the difficulty of moving the victim through the stairs, transfer equipment with a range of auxiliary modules such as tracks (Iwano et al., 2011), active gimbals (Verjans et al., 2021a; Verjans et al., 2021b), passive gimbals (Feng et al., 2022), and so on has been devised for stairway terrain. The above research, however, is prone to uncontrolled falls and other problems when utilized on gangways in factories, ships, and other situations where gangways have greater slopes of up to 70° (community stairways have slopes of only 30°).

Inspired by the aforementioned casualty transport aid and the analysis of industrial environment, this paper proposes a reconfigurable multi-terrain adaptive casualty transport aid (RMTACTA) with multiple motion modes as shown in Figure 1. The proposed RMTACTA possesses six different operating modes in total, including stretcher mode, stretcher vehicle mode, folding mode, gangway-passing mode, obstacle-crossing mode, and upright mode. This multipurpose tool can move across any kind of tight terrain quickly and safely, ensuring the relative calm of the victim and lightening the rescuer's load. The reconfigurable frame of the proposed RMTACTA is formed by two branching four-bar mechanisms to form a Watt II six-bar linkage mechanism unit, which is manually controlled by only one remote rope, as shown in Figure 2C. The structure of the proposed casualty transfer robot is much more compact compared to the stretcher truck. Although the Watt II six-bar linkage has been widely used in various engineering applications such as rehabilitation exoskeletons, robotics, etc., this is the first time that it has been developed due to the reconfigurable casualty transport aid. The proposed RMTACTA, which is built on this reconfigurable frame, has numerous capabilities while still ensuring a compact structure. Although the Watt II six-bar linkage has been widely used in various engineering applications (Erdman et al., 2001; Waldorn et al., 2016) such as exoskeleton (Hyun et al., 2019), rehabilitation robot (Gezgin et al., 2016), mobile robot (Luo et al., 2018), etc., this is the first time that it has been developed due to the reconfigurable casualty transport aid.

The mechanical design of the RMTACTA is introduced and the kinematics of the reconfigurable Watt II six-bar linkage is presented. The kinematic mechanism of the Watt II six-bar linkage is revealed, and the optimal design of the linkage and the mechanical analysis of the rope control are performed. A prototype of the proposed RMTACTA is developed leading to the tests verifying its feasibility and operability.

2 Mechanical design of a reconfigurable multi-terrain adaptive casualty transport aid

The reconfigurable multi-terrain adaptive casualty transport aid (RMTACTA) proposed in this paper is a modular multi-locomotion transport aid, as shown in Figure 1A. It consists of two pairs of reconfigurable frames, two sets of telescopic gangway adaptor modules, a casualty immobilization module, and a pair of title-support gimbal.

The aid is designed for portability and can be compactly folded for storage in a rucksack, facilitating rapid transportation to emergency scenes (Figure 1D). It can be swiftly deployed into stretcher mode, facilitating the process of moving a casualty from the ground onto the stretcher and administering first aid (Figure 1B). For enhanced transfer speed on flat terrain, the aid transitions to stretcher trolley mode

(Figure 1C). In the presence of a gangway, the device adapts to gangway passing mode. This is achieved by extending the pulleys of the telescopic gangway adaptor module, which engage with the gangway handrail, allowing smooth maneuvering of the equipment through the gangway (Figure 1E). Upon encountering obstacles such as high thresholds, the aid shifts to obstacle-crossing mode. This involves unlocking the reconfigurable frame, rotating the leg frame upon contact with the obstacle, and allowing it to automatically unfold and lock due to gravity. This feature enables the aid to traverse obstacles while ensuring continuous ground contact with a set of support wheels, thereby reducing the physical strain on the rescuer and maintaining the aid's stability (Figure 1F). In scenarios involving elevators and tight turns, the aid converts to upright mode through the coordinated action of the reconfigurable frame and tilt-support gimbals. In this configuration, the tilt-support gimbals and leg frame wheels form a stable mobile platform, enabling the rescuer to navigate the aid through confined spaces with a minimal turning radius (Figure 1G).

The multifunctional motion modes of this aid are achieved through an innovative reconfigurable system, which includes a wire drive system and symmetrical reconfigurable frames. Each frame utilizes a Watt II six-bar linkage with two double-loop, four-bar configuration. This design employs the dead point states of the two four-bars to lock the wheel leg in both extended and retracted position. Torsion springs maintain the stability of the four-bars at the dead point positions, with the wheel legs serving as the output. The control system for each reconfigurable frame is wire-driven remote control system consisting of a Bowden cable and a handbrake located at the handle, which is used to provide actuation for disengaging the Watt II six-bar linkage from its two dead point states. This reconfigurable frame, in conjunction with the wire-driven remote control system, enables dual-mode switching via a single manual switch. Apart from the operation of extracting the pulleys to align with the gangway, all other functions can be controlled by the rescuer using a single handbrake, and throughout the process, both hands need not leave the device handle. This significantly reduces the operations required by the rescuer, which is of great importance in rescue situations (NAEMT, 2016).

3 Kinematics of Watt II six-bar linkage and configurations of the transport aid

Based on the mechanical design previously mentioned, it can be concluded that the multimodal transformation of the aid is realized through of the reconfigurable frame which is constructed using a Watt II six-bar linkage. In this section, the kinematics of the linkage is investigated, and the configuration of the structure is characterized, in order to expose the relationship between the configuration of the reconfigurable frame and the motion of the transport aid.

3.1 Kinematics of the Watt II six-bar linkage

The schematic diagram of the Watt II six-bar linkage of the reconfigurable frame is given in Figure 2. Where, link AEF is a ternary V-shaped link, and the rest of links are the binary linkages. By using the V-shaped link as a fixed link that is solidly attached to aid's body, a Cartesian coordinate system is established with the origin at point O, which the y-axis being isotropic to the vector AO, and x-axis being isotropic to the vector OE. The geometric parameters are further defined as: (1) For the branching four-link ABCE, AE is the fixed link, and l_1, l_2, l_3, and l_4 refer to the lengths of the links of AB, BC, CE, and AE (2) For the branching four-link ECDF, EF is the fixed link, and l_3, l_5, l_6, and l_7 refer to the lengths of the linkage of CE, CD, DF, and EF. (3) The joint angles θ_1 to θ_6 are defined as the linkage pinch angles, where θ_2 is the angle between the parallel lines of BC and AD, and θ_5 is the angle between the parallel lines of CD and EF for the convenience of kinematic modeling. (4) The input angle of the linkage is θ_1 varying from 180-∠OAE to 90-∠OAE. (5) The Degree of Freedom (DoF) of the mechanism is calculated as $F = 3N\text{-}2F_L\text{-}F_H = 3\times5\text{–}2\times7 = 1$.

During the mode switching process, the motion and locking of the wheel legs predominantly rely on the dead center position of the linkage mechanism, at which point the DoF of the mechanism is F = 3N-2FL-FH = 3×4–2×6 = 0. Consequently, this section investigates the displacements at points C and D, based on the geometric structure of the Watt II six-bar linkage. By decomposing the mechanism, the Watt II six-bar linkage is categorized into two sub-branches of four-bar linkages, namely, ABCE and ECDF. The displacement of point C is determined within the linkage ABCE, while the displacement of point D is deduced within the linkage ECDF.

In four-bar linkage ABCE based on loop equation (Michael McCarthy, 2010), it has

$$\begin{bmatrix} \cos\theta_1 & \cos\theta_2 \\ \sin\theta_1 & \sin\theta_2 \end{bmatrix}\begin{bmatrix} l_1 \\ l_2 \end{bmatrix} = \begin{bmatrix} \cos\theta_3 & \cos\theta_{AE} \\ \sin\theta_3 & \sin\theta_{AE} \end{bmatrix}\begin{bmatrix} l_3 \\ l_4 \end{bmatrix} \tag{1}$$

where θ_1 is the input angle, the angle θ_{AE} of the fixed link AE is defined as 0° for simplicity of calculation and $l_3 = l_{BE}\text{-}l_2$ in Figure 2A.

Solving Eq. 1 leads to the two variables, i.e., angles θ_2 and θ_3 as defined in Eq. 2.

$$\begin{aligned} \theta_2 &= 2\times\arctan\left(\left(-\beta-\sqrt{\beta^2-4\times\delta\times\varepsilon}\right)\Big/(2\times\delta)\right) \\ \theta_3 &= 2\times\arctan\left(\left(-\beta-\sqrt{\beta^2-4\times\alpha\times\gamma}\right)\Big/(2\times\alpha)\right) \end{aligned} \tag{2}$$

where the expression for α, γ, β, δ, and ε are shown as

$$\begin{aligned} \alpha &= -l_4/l_1 + (1-l_4/l_3)\times\cos(\theta_1) + \left(l_4^2+l_1^2-l_2^2+l_3^2\right)/(2\times l_1\times l_3) \\ \beta &= -2\times\sin(\theta_1) \\ \gamma &= l_4/l_1 - (1+l_4/l_3)\times\cos(\theta_1) + \left(l_4^2+l_1^2-l_2^2+l_3^2\right)/(2\times l_1\times l_3) \\ \delta &= -l_4/l_1 + (1+l_4/l_2)\times\cos(\theta_1) + \left(-l_4^2-l_1^2-l_2^2+l_3^2\right)/(2\times l_1\times l_2) \\ \varepsilon &= l_4/l_1 - (1-l_4/l_2)\times\cos(\theta_1) + \left(-l_4^2-l_1^2-l_2^2+l_3^2\right)/(2\times l_1\times l_2) \end{aligned}$$

Thus, position of point C can be presented as

$$P_C = \begin{bmatrix} x_C \\ y_C \end{bmatrix} = \begin{bmatrix} x_E & \cos(\theta_3-\theta_{OEA}) \\ y_E & \sin(\theta_{OEA}-\theta_3) \end{bmatrix}\begin{bmatrix} 1 \\ l_3 \end{bmatrix} \tag{3}$$

Similarly, in the sub-branch four-bar linkage ECDF, position of point D can be deduced as

$$P_D = \begin{bmatrix} x_D \\ y_D \end{bmatrix} = \begin{bmatrix} x_F & \sin(\theta_{GFE}-\theta_6) \\ y_F & -\cos(\theta_{GFE}-\theta_6) \end{bmatrix}\begin{bmatrix} 1 \\ l_6 \end{bmatrix} \tag{4}$$

where $l_6 = l_{C1F}\text{-}\ l_5$ in Figure 2B, and using loop equation it has

$$\theta_6 = 2\times\arctan\left(\left(-\beta'-\sqrt{\beta'^2-4\times\alpha'\times\chi'}\right)\Big/(2\times\alpha')\right) \tag{5}$$

where the expression for α, γ, β, δ, and ε are shown as

10.3389/fbioe.2024.1360902

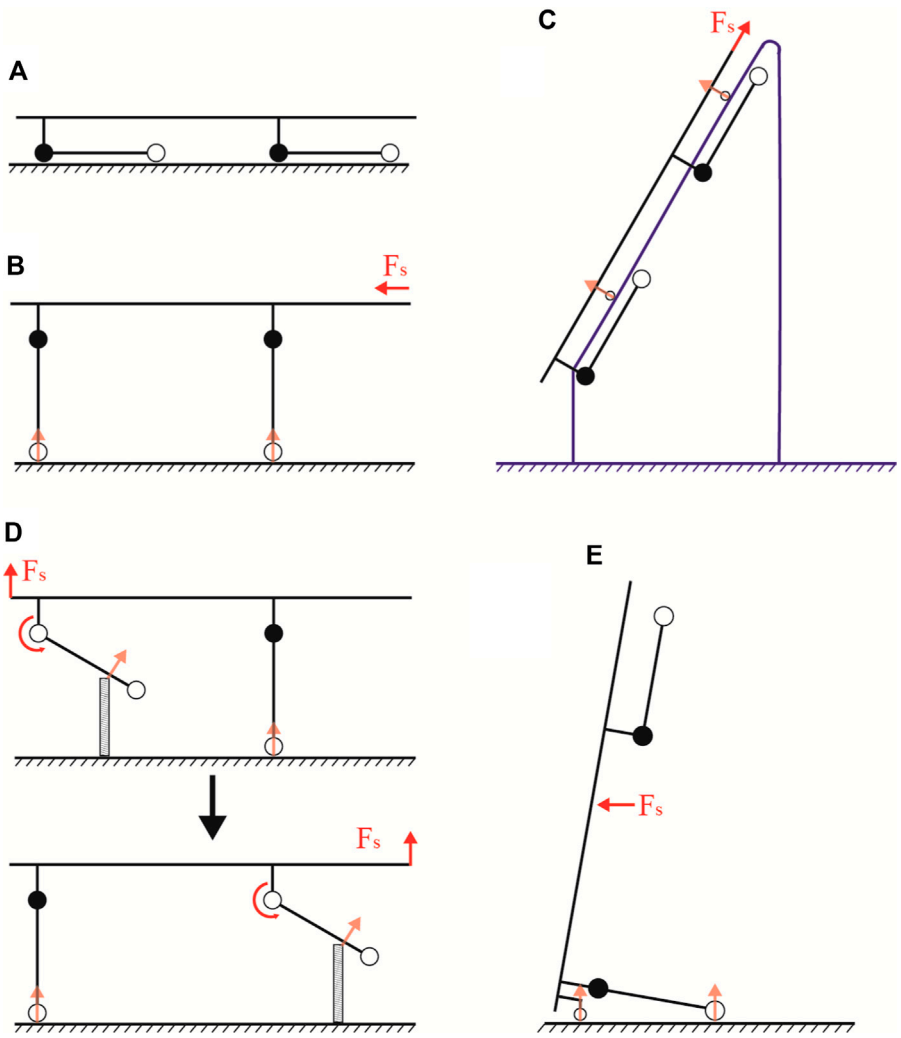

FIGURE 3
Locomotion modes of the transport aid. **(A)** Stretcher mode. **(B)** Stretcher vehicle mode. **(C)** Gangway-passing mode. **(D)** Obstacle-crossing mode. **(E)** Upright mode.

TABLE 1 Structure parameters of the reconfigurable frame in initial design.

Structure parameter	l_{OA}	l_{OE}	l_{EG}	l_{GF}	l_1	l_2	l_5
Length(mm)	150	200	50	0	150	180.3	115

$$\theta_4 = 180 - \theta_3 - \theta_{OEA} - \theta_{GEF}$$
$$\alpha' = -l_7/l_3 + (1 - l_7/l_6) \times cos(\theta_4) + (l_7^2 + l_3^2 - l_5^2 + l_6^2)/(2 \times l_3 \times l_6)$$
$$\beta' = -2 \times sin(\theta_4)$$
$$\chi' = l_7/l_3 - (1 + l_7/l_6) \times cos(\theta_4) + (l_7^2 + l_3^2 - l_5^2 + l_6^2)/(2 \times l_3 \times l_6)$$
$$\delta' = -l_7/l_3 + (1 + l_7/l_5) \times cos(\theta_4) + (-l_7^2 - l_3^2 - l_5^2 + l_6^2)/(2 \times l_3 \times l_5)$$
$$\varepsilon' = l_7/l_3 - (1 - l_7/l_5) \times cos(\theta_4) + (-l_7^2 - l_3^2 - l_5^2 + l_6^2)/(2 \times l_3 \times l_5)$$

In addition, angle θ_5 can be obtained as

$$\theta_5 = 2 \times \arctan\left(\left(-\beta' - \sqrt{\beta'^2 - 4 \times \delta' \times \varepsilon'}\right)/(2 \times \delta')\right) \quad (6)$$

To guarantee that the reconfigurable mechanism achieves two locking positions, the structural parameters of the dual sub-branch four-linkages must fulfill the constraints: $l_{B1E} \leq |l_3 - l_2|$ and $l_{C1F} \leq |l_5 - l_6|$.

3.2 Configurations and locomotion modes of the casualty transport aid

The reconfiguration of the Watt II six-bar linkage permits the wheel legs to lock in both the extended and retracted positions, forming the stretcher mode and the stretcher vehicle mode, respectively (refer to Figures 2A, B). This reconfiguration enables the aid to operate in five modes: stretcher mode, stretcher vehicle mode, obstacle-crossing mode, gangway-passing mode, and upright mode, as depicted in Figure 3.

The stretcher mode is primarily used for transporting casualty short distances from the ground to the stretcher (Figure 3A). The stretcher vehicle mode is particularly suited for rapid movement on flat terrain (Figure 3B). Upon encountering an obstacle, the Watt II six-bar linkage is unlocked, allowing the wheel legs to move freely.

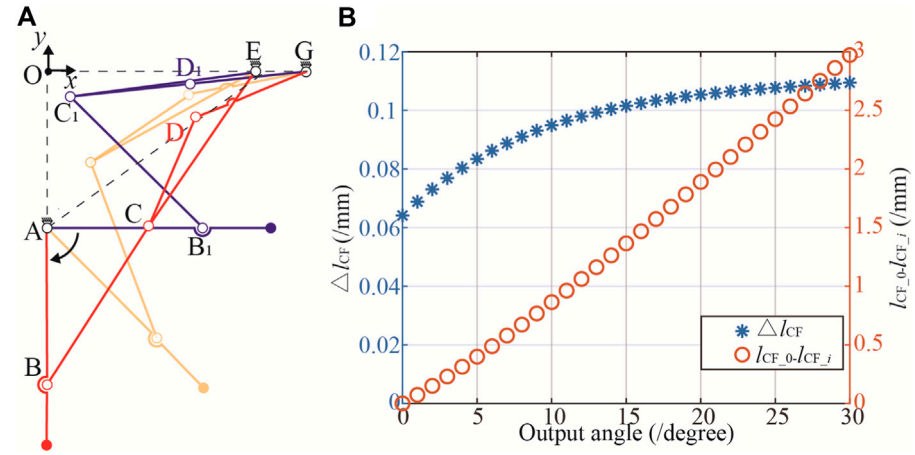

FIGURE 4
Simulation of the transformation process. **(A)** Motion trajectories of the mechanism. **(B)** The change in length of $\triangle l_{CF}$.

TABLE 2 Optimized structure parameters of the reconfigurable frame.

Structure parameter	l_{OA}	l_{OE}	l_{EG}	l_{GF}	l_1	l_2	l_3	l_5	l_6
Length(mm)	137	210	40.1	40.1	197	199.1	195.6	130.1	100.2

This transition transforms the stretcher vehicle mode into the obstacle-crossing mode (Figure 3D). In this mode, the aid ensures the casualty remains horizontal while crossing obstacles and maintains at least one set of support wheels on the ground, significantly reducing the rescuers' effort and enhancing the aid's stability.

Moreover, the stretcher mode, when combined with retractable pulleys, can be transformed into the gangway-passing mode for navigating through gangways (Figure 3C). Similarly, integrating tail casters with the stretcher vehicle mode enables the conversion to upright mode, facilitating maneuvering through narrow turns, elevators, and varied terrain, as shown in (Figure 3E).

4 Numerical simulation and parametric study

4.1 Numerical simulation and position synchronization

In order to validate the operational principle of the reconfigurable mechanism, numerical simulations based on the structural parameters outlined in Table 1 in this section. Here, l_{OE}, l_{EG}, l_{GF}, l_1, l_2, l_5, and l_6 are identified as design variables, while the remaining parameters are determined through equation-based calculations. For clarity, the output angle of the reconfigurable mechanism, transitioning from retracted to extended, is defined as the angular variation when AB shifts from being parallel to the x-axis to parallel to the y-axis, and is established as ranging from 0 to 90°.

Upon substituting the structural parameters into Eqs 3 to 6, and setting the input/driving angles θ_1 from 90-∠OAE to θ_1 = 180-∠OAE, the motion trajectory of the mechanism transitioning from the retracted to the extended position is depicted in Figure 4A. Additionally, the variation in the length of C_1F is illustrated in Figure 4B.

Figure 4A reveals that, within the two operational configurations of the Watt II six-bar linkage mechanism, the positional disparity between points D and D_1 amounts to 34.1 mm. However, the actuation of this six-bar mechanism for positional switching is facilitated by the application of driving force at point D. The displacement of point D in these configurations requires the integration of a position compensation mechanism into the force application system, consequently elevating the structural complexity and compromising the stability of the device.

The collinearity of links CD and DG, i.e., $l_{CD} + l_{DG} = l_{C1G}$, leads to the DoF of the Watt II six-bar linkage is 0 ($F = 3N-2F_L = 3 \times 4-2 \times 6 = 0$), consequently fixing the mechanism in a stationary state. Figure 4B illustrates the relationship between the angle of the output bar AB and the length of l_{C1G} when the mechanism is fixed. The variation in l_{C1G} per degree is remarkably small, less than 0.1 mm before reaching 15°. The cumulative length change, defined as the difference in l_{C1G} 's length at an output angle of 0° and at an angle i (l_{CG_0}- l_{CG_i}), has a maximum value of 2.97 mm, averaging 0.099 mm per degree. Such minute variations pose challenges in ensuring that AB remains in the required horizontal position during practical applications. The existing initial design demands high precision in the machining and assembly of the device. However, the operational environment of the device is often suboptimal, characterized by factors such as collisions and humidity, which lead to part deformation and rust. Consequently, precision cannot be guaranteed, preventing the wheel legs from locking in a horizontal position and causing wobble, which ultimately reduces the overall reliability of the device.

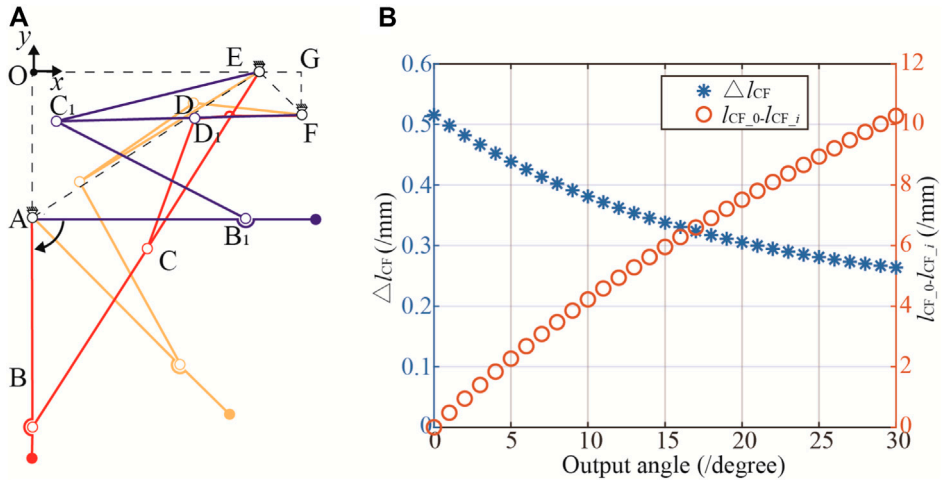

FIGURE 5
Optimized trajectories and $\triangle l_{CF}$. **(A)** Imoproved motion trajectories. **(B)** Optimized result.

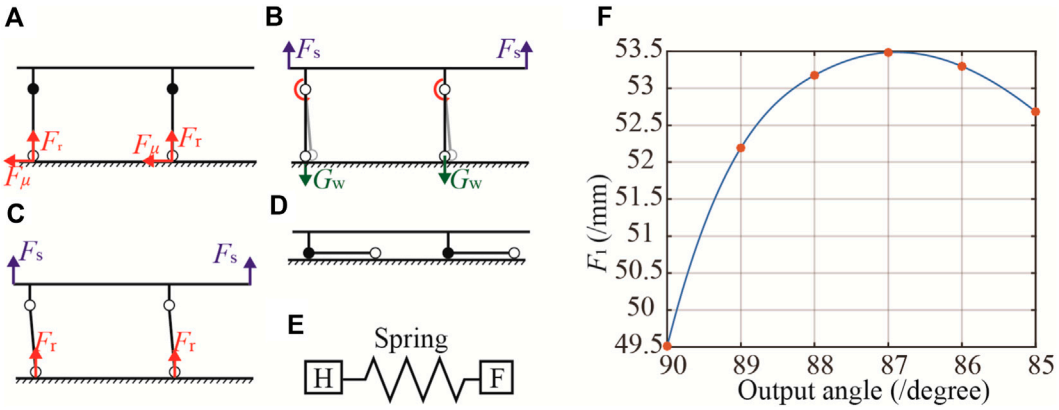

FIGURE 6
The transformation of stretcher vehicle mode to the stretcher mode. **(A)** Distribution of forces on aid in stretcher vehicle mode when bearing a casualty. **(B)** Depicts initial transition step with a 5° wheel leg rotation to increase the ground reaction lever arm. **(C)** Highlights smoother mode transition due to increased lever arm. **(D)** Finalizes the stretcher mode transition. **(E)** The elastic mechanism. **(F)** Force-displacement curve.

This paper addresses the identified deficiencies of the mechanism with its initial dimensions by optimizing the structural parameters through a multivariate constrained nonlinear optimization method (Scales, 1985). The primary objective of this optimization is to maintain the consistency of point D's position in both the extended and retracted position. Consequently, the objective function is formulated as follows:

$$f(\mathrm{x})_{\min} = \left(x_{D_1} - x_D\right)^2 + \left(y_{D_1} - y_D\right)^2 \tag{7}$$

where x = [l_{OA}, l_{OE}, l_{EG}, l_{GF}, l_1, l_2, l_5], (x_D, y_D) is the position of point D in the extended position of the mechanism and (x_{D1}, y_{D1}) is the position of point D in the retracted position of the mechanism.

The two positions of the reconfigurable mechanism are realised by BC-CE and C_1D_1-D_1F covariance respectively, i.e., their constraints can be expressed as follows:

$$g_1(\mathrm{x}) = l_2 + l_3 - l_{BE} = 0 \quad \text{if (AB//y-axis)} \tag{8}$$

$$g_2(\mathrm{x}) = l_5 + l_6 - l_{C_1F} = 0 \text{ if (AB // x-axis)} \tag{9}$$

where l_{BE} and l_{C1F} are derived by extrapolation from the kinematic model of the mechanism.

In order to avoid interference in the mechanism during motion, point C must never be co-linear with OA and OE in the motion of the mechanism, the expression for which is:

$$g_3(\mathrm{x}) = x_O - x_{C_1} \le 0 \tag{10}$$

$$g_4(\mathrm{x}) = x_{C_1} - x_E \le 0 \tag{11}$$

$$g_5(\mathrm{x}) = y_{C_1} - y_O \le 0 \tag{12}$$

$$g_6(\mathrm{x}) = y_A - y_{C_1} \le 0 \tag{13}$$

Applying the cosine theorem, extending GF's length enhances the variation in C_1F's length during motion, thereby resolving the issue of minimal C_1F length change that leads to

mechanism instability. The design adheres to the criteria if C_1F's length variation exceeds 0.2 mm per 1° rotation of the AB, as informed by engineering expertise. This constraint is articulated as follows:

$$g_7(x) = 0.2 - l_{CF\_i} + l_{CF\_i-1} \le 0 \ (0 < i \le 90) \tag{14}$$

Finally, the structural parameter constraints of the linkage mentioned in Section 3.1 can be expressed as:

$$g_8(x) = l_{B_1E} - |l_3 - l_2| \le 0 \tag{15}$$

$$g_9(x) = l_{C_1F} - |l_5 - l_6| \le 0 \tag{16}$$

Based on the constraints from Eq. 8 to Eq. 16, the objective function in Eq. 7 was solved, and the optimized structural parameters were obtained by rounding the results to one decimal place, as shown in Table 2. When these parameters are incorporated into the kinematic equations from Section 3; Figure 5A illustrates the extended and retracted positions of the reconfigurable frame. The positional deviation of point D is a minimal 2.3 mm, a discrepancy arising from the rounding to one decimal place. Such a deviation is deemed entirely acceptable for the design of wire-driven remote control systems. Figure 5B depicts the post-optimization variation in the length of C_1F. The changes in C_1F consistently exceed 0.2 mm/° and reach 0.5 mm when AB is at 0°, ensuring that the output link AB remains fixed in the horizontal position. The differential in l_{CG_0}-l_{CG_i} attains a maximum of 10 mm, with an average variation of 0.3 mm/°. This level of precision allows the mechanism to maintain its fixed position even under deformation during use, thereby enhancing the equipment's stability.

5 Analysis of the driving force of the reconfigurable frame

During stretcher vehicle operations for casualty transport, there is a risk of rescuers accidentally engaging the handbrake or other objects inadvertently triggering it, potentially leading to the unintended unlocking of the reconfigurable frame. Such occurrences could cause the wheel legs to fail and the stretcher vehicle to fall. To avert these situations, the protocol for transferring from the stretcher vehicle to the stretcher requires rescuers to stabilize the weight of the casualty and aid before engaging the handbrake to unlock the reconfigurable frame. Furthermore, an elastic mechanism has been incorporated into the drive system (Figure 6E) to constrain the maximum tensile force applied by the handbrake to point D of the reconfigurable frame, ensuring the frame remains locked even if the handbrake is activated before lifting the stretcher vehicle.

This section applies the principle of virtual work to determine the minimum actuation force required to disengage the locking mechanism at the dead center of the reconfigurable frame (extended and retracted states), thus determining the lower force threshold of the elastic mechanism. In addition, the drive force required to disengage the frame in the extended state during the transportation of a casualty is calculated, thus determining the upper force threshold.

The force-displacement properties of the Watt II six-bar linkage are modeled in this section using the virtual work principle. It should be noted that for simplicity purpose, the weight of the connecting rod is neglected in the modeling process and the torque of the torsion spring and the weight of the universal wheel are taken into account.

The principle of virtual work posits that for a multibody system in equilibrium under external forces, the total work done by these forces for any virtual velocity is zero. By introducing the generalized virtual velocities, denoted as $\delta\theta$, and acknowledging that the work from internal constraint reactions is null, the total virtual work, represented as δW, can be expressed as follows:

$$\delta W = \overrightarrow{F_1}\delta\overrightarrow{Z_1} + M_4 \cdot \delta\overrightarrow{\theta_4} + M_6 \cdot \delta\overrightarrow{\theta_6} + \overrightarrow{F_2}\delta\overrightarrow{Z_2} = 0 \tag{17}$$

where F_1 and F_2 correspond to the tensile force and the force at the caster, respectively. Z_i represents the displacement vector associated with the force, M_i denotes the torque generated by the torsion spring, and θ_i is the angular displacement vector corresponding to the torque.

Using θ_6 as the generalized coordinate, Eq. 17 can be derived:

$$\begin{aligned}\delta W = &-F_1 l_6 \sin(\theta_6 + \theta_{EFG})\delta\theta_6 + k_6(\theta_6 - \theta_{60})\delta\theta_6 \\ &+ k_4(\theta_4 - \theta_{40})\theta'_{46}\delta\theta_6 + F_2 l_1 \theta'_{16}\delta\theta_6 \\ &= 0\end{aligned} \tag{18}$$

where k_i is the torsional spring constant, and $\theta_{i\,0}$ represents the angle of the torsion spring when undeformed. Solving Eq. 18 yields the linear driving force F_1 as follows:

$$F_1 = \frac{k_1(\theta_6 - \theta_{60}) + k_2(\theta_4 - \theta_{40})\theta'_{46} + F_2 l\theta'_{16}}{l_6 \sin(\theta_6 + \theta_{EFG})} \tag{19}$$

where θ'_{46} and θ'_{16} are the linkage motion coefficients (Pennock and Israr, 2009), which will subsequently be determined through the linkage kinematics model.

The loop equations for the four-bar linkage ABCE and ECDF, when written as scalar equations, are as follows:

$$l_1\cos(\theta_1) + l_2\cos(\theta_2) - l_3\cos(\theta_3) - l_4\cos(180°) = 0 \tag{20}$$

$$l_1\sin(\theta_1) + l_2\sin(\theta_2) - l_3\sin(\theta_3) - l_4\sin(180°) = 0 \tag{21}$$

$$l_3\cos(\theta_4) + l_5\cos(\theta_5) - l_6\cos(\theta_6) - l_7\cos(180°) = 0 \tag{22}$$

$$l_3\sin(\theta_4) + l_5\sin(\theta_5) - l_6\sin(\theta_6) - l_7\sin(180°) = 0 \tag{23}$$

Given that $\theta_3 = \theta_4 + \theta_{OEA} + \theta_{GEF} = \theta_4 + \theta_t$, differentiation of Eqs 20, 21 with respect to θ_4 yields:

$$l_1\sin(\theta_1)\theta'_{14} + l_2\sin(\theta_2)\theta'_{24} - l_3\sin(\theta_4 + \theta_t) = 0 \tag{24}$$

$$l_1\cos(\theta_1)\theta'_{14} + l_2\cos(\theta_2)\theta'_{24} - l_3\cos(\theta_4 + \theta_t) = 0 \tag{25}$$

Differentiating Eqs 22, 23 with respect to θ_6 give:

$$l_3\sin(\theta_4)\theta'_{46} + l_5\sin(\theta_5)\theta'_{46} - l_6\sin(\theta_6) = 0 \tag{26}$$

$$l_3\cos(\theta_4)\theta'_{46} + l_5\cos(\theta_5)\theta'_{46} - l_6\cos(\theta_6) = 0 \tag{27}$$

Writing Eqs 24, 25 in matrix form gives:

$$\begin{bmatrix} l_1\sin(\theta_1) & l_2\sin(\theta_2) \\ l_1\cos(\theta_1) & l_2\cos(\theta_2) \end{bmatrix}\begin{bmatrix} \theta'_{14} \\ \theta'_{24} \end{bmatrix} = \begin{bmatrix} l_3\sin(\theta_4 + \theta_t) \\ l_3\cos(\theta_4 + \theta_t) \end{bmatrix} \tag{28}$$

and writing Eqs 26, 27 in matrix form gives:

$$\begin{bmatrix} l_3\sin(\theta_4) & l_5\sin(\theta_5) \\ l_3\cos(\theta_4) & l_5\cos(\theta_5) \end{bmatrix}\begin{bmatrix} \theta'_{46} \\ \theta'_{56} \end{bmatrix} = \begin{bmatrix} l_6\sin(\theta_6) \\ l_6\cos(\theta_6) \end{bmatrix} \tag{29}$$

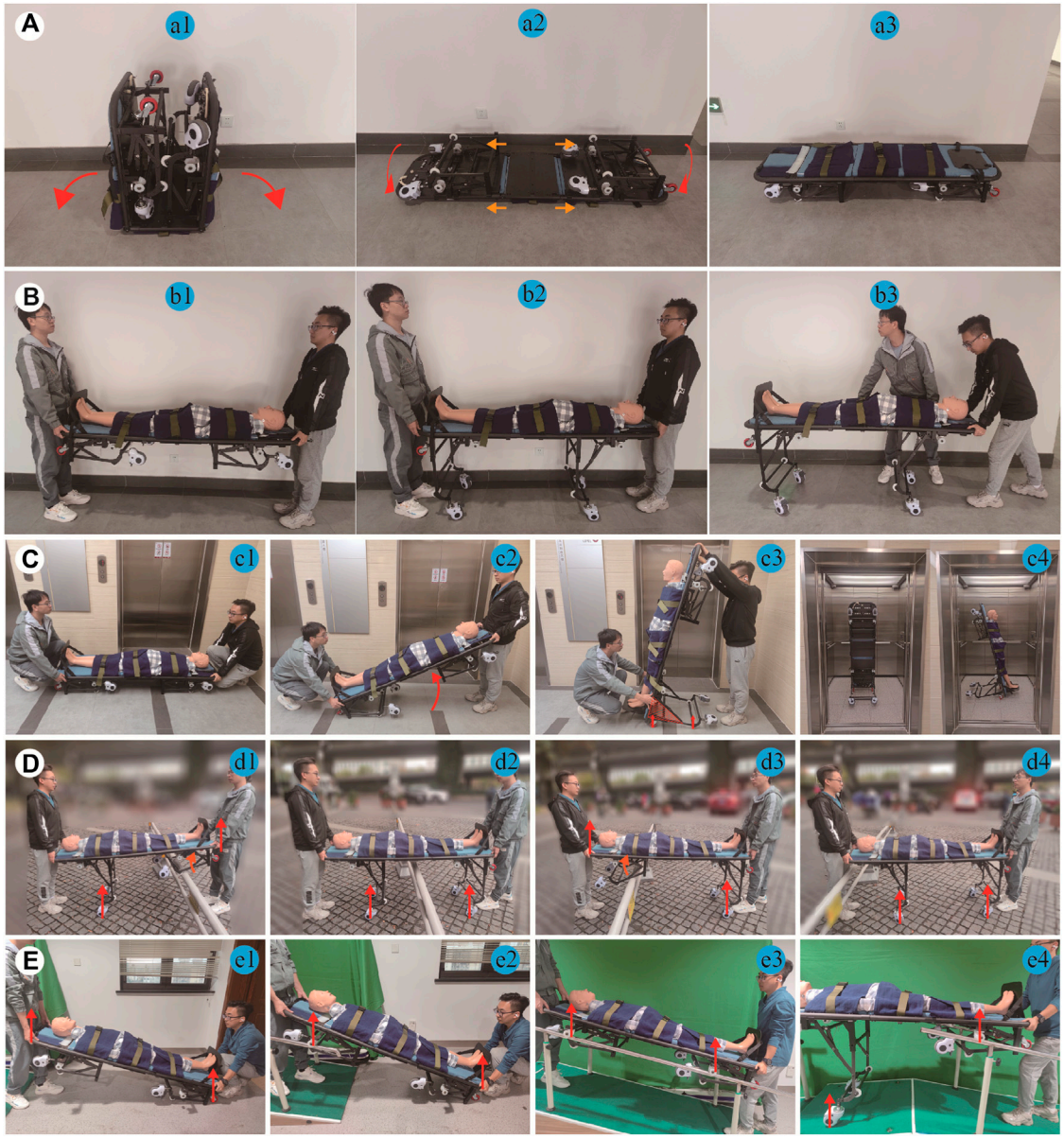

FIGURE 7
RMTACTA's various locomotion modes. **(A)** Procedure for switching from folding mode to stretcher mode. **(B)** Procedure for switching from stretcher mode to stretcher vehicle mode. **(C)** Procedure for switching from stretcher mode to upright mode. **(D)** Demonstration of the workflow of the aid in obstacle-crossing mode. **(E)** Demonstration of the workflow of the aid in gangway-passing mode.

Using Cramer's rule (Wang and Sun, 2004), the first-order kinematic coefficients can be written from Eqs 28, 29 as

$$\theta'_{14} = \frac{l_3 \sin(\theta_4 + \theta_t - \theta_2)}{l_1 \sin(\theta_1 - \theta_2)} \tag{30}$$

$$\theta'_{46} = \frac{l_6 \sin(\theta_6 - \theta_5)}{l_3 \sin(\theta_4 - \theta_5)} \tag{31}$$

$$\theta'_{16} = \theta'_{14} \times \theta'_{46} = \frac{l_3 \sin(\theta_4 + \theta_t - \theta_2)}{l_1 \sin(\theta_1 - \theta_2)} \times \frac{l_6 \sin(\theta_6 - \theta_5)}{l_3 \sin(\theta_4 - \theta_5)} = \frac{l_6 \sin(\theta_4 + \theta_t - \theta_2) \sin(\theta_6 - \theta_5)}{l_1 \sin(\theta_1 - \theta_2) \sin(\theta_4 - \theta_5)} \tag{32}$$

Substitution of Eq. 30 and Eq. 32 into Eq. 19 yields the resultant expression:

$$F_1 = \frac{k_1(\theta_6 - \theta_{60}) + k_2(\theta_4 - \theta_{40}) \frac{l_6 \sin(\theta_6 - \theta_5)}{l_3 \sin(\theta_4 - \theta_5)} + F_2 l \frac{l_6 \sin(\theta_4 + \theta_t - \theta_2) \sin(\theta_6 - \theta_5)}{l_1 \sin(\theta_1 - \theta_2) \sin(\theta_4 - \theta_5)}}{l_6 \sin(\theta_6 + \theta_{EFG})} \tag{33}$$

In the stretcher vehicle mode, when bearing a casualty, the force distribution on the aid is illustrated in Figure 6A. The casters experience a reactive force from the ground, generating friction that impedes movement when the reconfigurable framework is unlocked, described by the equation $F_2 l = F_\mu \times l_{AW}$ in Eq. 33. From this, F_1 is determined to be 107.6 N. To transition from the stretcher vehicle mode to stretcher mode (Figure 6D), the reconfigurable framework is unlocked using a handbrake, and additional force is applied to rotate the wheel leg by 5°, as shown

in Figure 6B, thereby increasing the lever arm of the ground reaction force and facilitating a smoother mode transition, as depicted in Figure 6C. Under this method, in Eq. 33, $F_2 l = G_W \times \sin(\theta_1 + \angle OAE) \times l_{AW}$, and the variation in F_1 is presented in Figure 6F. The maximum force and force-displacement curves obtained from the above can be used as the basis for the design of the spring mechanism.

6 Prototype development and field tests

Based on the aforementioned theoretical analysis, a physical prototype of the proposed RMTACTA is developed using the structural characteristics obtained in Table 2 with some necessary modifications to the mechanical component design, as shown in Figure 7. It consists of two pairs of reconfigurable frames, two sets of telescopic gangway adaptor modules, a casualty immobilization module, and a pair of tilt-support gimbals. The aid can transition into six motion modes: folding mode (a1), stretcher mode (b1), stretcher vehicle mode (b2), upright mode (c), obstacle-crossing mode (d), and gangway-passing mode (e).

The equipment's structural framework is constructed from carbon fiber tubing and panels; connectors are precision-engineered from aluminum alloy through CNC machining and undergo surface oxidation treatment; handrails are produced from nylon via 3D printing techniques. This results in a low production cost for the equipment, which maintains a lightweight profile at merely 20 kg.

Field tests are conducted on the physical prototype to evaluate and verify the performance of the proposed casualty transport aid. These tests utilized a medical mannequin to replicate a casualty, and involved two rescuers. Each rescuer can realize the switching of multiple modes of the casualty transport aid by controlling the handbrake on one side separately.

The transport aid is initially mode in the folding mode for expedited delivery to emergency locations, and it can be quickly converted into the stretcher mode, as shown in Figure 7 a1 to Figure 7 a3. The conversion process entails laying the aid's front and rear ends flat on the ground, shifting the sleeve to secure the hinge, and then inverting the aid. This stretcher mode enables rescuers to effortlessly lift casualties from the ground onto the stretcher for immediate first aid, providing an advantage during short-range transport, as demonstrated in Figure 7 a3. In flat terrain, as shown in Figure 7 b3, the rescuer can convert the aid to stretcher mode by applying the handbrake and lifting the stretcher, thus increasing the efficiency of the transfer, reducing the turning radius, and decreasing the physical burden on the rescuer.

When needing to enter or exit elevators or navigate tight corners, the rescuer can transition the transport aid from stretcher mode to upright mode. Specifically, the rescuer at the device's rear operates the handbrake to unlocking the locked reconfigurable frame, and the rescuer at the device's head raises it to an 80° angle with the ground. Meanwhile, the reconfigurable frame at the rear locks in the extended mode automatically, forming a stable mobile platform with the wheels on the wheel legs and the title-support gimbal, as depicted in Figure 7C. In upright mode, the rescuer can easily maneuver the transport aid, entering and exiting elevators and navigating tight corners.

When the transport aid encounters obstacles such as high thresholds, rescuers utilize a handbrake to unlock the reconfigurable framework, enabling the wheel-legs to rotate upon encountering a reactive force from the obstacle, thus allowing the equipment to pass the obstacle. During this process of passing obstacles, a set of support wheels maintains continuous contact with the ground, thereby reducing the physical strain on rescuer and ensuring the stability of the transport aid, as illustrated in Figure 7D.

When encountering a gangway, rescue personnel can facilitate the passage of the equipment along with the injured by dragging, rather than lifting, through the gangway. This is achieved by engaging the pulleys of the telescopic gangway adaptor module with the handrail of the gangway, as illustrated in Figure 7E. To ensure safety, this experiment was conducted using an indoor staircase instead of a gangway. Furthermore, during the passage, the aid ensures that at least one set of wheels is in contact with the ground or the gangway, thereby assisting rescue personnel in sharing the burden of the casualty's weight.

The tests conducted in this study not only validate the structural design, mathematical model, and optimization approach but also demonstrate the effectiveness of the transfer equipment developed according to the proposed design principles, which exhibits exceptional capability in casualty transfer. When using this equipment, rescuers can use a simpler and safer method for transferring casualties. Subsequent testing of the aid's casualty transportation capabilities will be conducted in a real-world industrial environment.

7 Conclusion

This paper presents the inaugural development of a reconfigurable multi-terrain adaptive casualty transport aid (RMTACTA) for emergency rescue within industrial settings. The device boasts six distinct operational modes: stretcher, stretcher vehicle, folding, gangway-passing, obstacle-crossing, and upright. Reconfigurability of the proposed aid is achieved by the creative design through the combination of a reconfigurable Watt II six-bar linkage framework with various functional modules.

Mechanical design for a casualty transport aid was presented and kinematic and static analysis of the reconfigurable framework. Optimization of the framework's structural parameters was achieved through an investigation into the actuation points' spatial positioning and the framework's fixed orientation conditions. Employing the principle of virtual work, a mechanical analysis was performed on the optimized structural parameters of the reconfigurable framework to establish the upper and lower limits of the driving force required for the mechanism's state transitions. These limits serve as the criteria for designing the elastic elements of the line-driven mechanisms.

The physical prototype of the RMTACTA was developed based on optimized structural parameters and mechanical analysis. Subsequent field trials were conducted to demonstrate the design concept, feasibility, and human-machine interaction of the proposed transport aid. The test results show that the RMTACTA can be reconfigured to meet various terrain and functional requirements. Additionally, the majority of mode changes can be controlled by rescue personnel using a single handbrake, allowing them to keep their hands on

the aid's handles throughout the casualty transport process, significantly reducing the operational effort required.

The novel proposed reconfigurable casualty transportation aid has provided novel insights into the design of robots for emergency medical transport and the improvement of casualty evacuation methods, which has potential applications in earthquake relief, maritime rescue, and battlefield medical support.

Data availability statement

The original contributions presented in the study are included in the article/Supplementary Material, further inquiries can be directed to the corresponding authors.

Ethics Statement

Written informed consent was obtained from the individual(s) for the publication of any potentially identifiable images or data included in this article.

Author contributions

ZJ: Writing–original draft, Writing–review and editing. HW: Writing–review and editing. CF: Writing–review and editing. LW: Writing–review and editing. JY: Writing–review and editing. QM: Writing–review and editing. XL: Funding acquisition, Resources, Supervision, Writing–review and editing.

Funding

The author(s) declare that financial support was received for the research, authorship, and/or publication of this article. The authors gratefully acknowledge the support from Shanghai Changzheng Hospital Pyramid Talent Project (0910) and Shanghai Changzheng Hospital Key Scientific Research Project (BHJ22C018).

Conflict of interest

The authors declare that the research was conducted in the absence of any commercial or financial relationships that could be construed as a potential conflict of interest.

Publisher's note

All claims expressed in this article are solely those of the authors and do not necessarily represent those of their affiliated organizations, or those of the publisher, the editors and the reviewers. Any product that may be evaluated in this article, or claim that may be made by its manufacturer, is not guaranteed or endorsed by the publisher.

References

Aguilar-Pérez, L. A., Paredes-Rojas, J. C., Sanchez-Cruz, J. I., Leal-Naranjo, J. A., Oropeza-Osornio, A., and Torres-SanMiguel, C. R. (2021). Design of an automated multiposition dynamic wheelchair. *Sensors* 21, 7533. doi:10.3390/s21227533

Bricknell, M. (2003). The evolution of casualty evacuation in the 20th century (Part 5) - into the future. *BMJ Mil. Health* 149, 357–363. doi:10.1136/jramc-149-04-19

Butler Fk, B. T., Jr, Chernenko, M., Chimiak, J., Chung, J., Cubano, M., Gurney, J. M., et al. (2022). Tactical combat casualty care maritime scenario: shipboard missile strike. *J. Special Operations Med. a Peer Rev. J. SOF Med. Prof.* 22, 9–28. doi:10.55460/zt9j-ei8z

Cao, W., Shang, D., Yin, M., Li, X., Xu, T., Zhang, L., et al. (2023). Development and evaluation of a hip exoskeleton for lateral resistance walk exercise. *IEEE/ASME Trans. Mechatronics* 28, 1966–1974. doi:10.1109/tmech.2023.3273717

Drobinsky, S., Verjans, M., Schleer, P., Kolk, B., Bensiek, H., Radermacher, K., et al. (2020). Workflow and human-centered risk analysis for novel mechatronic rescue aids I. *Curr. Dir. Biomed. Eng.* 6, 612–615. doi:10.1515/cdbme-2020-3156

Erdman, A. G., Sandor, G. N., and Kota, S. (2001). *Mechanism design: analysis and synthesis*. Upper Saddle River, New Jersey, United States: Prentice Hall.

Feng, Y., Liu, H., Yu, F., Yu, X., Kumar, D., and Li, N. (2022). "Design and analysis of dual purpose tripod wheeled stretcher for Navy and Army," in Second International Conference on Cloud Computing and Mechatronic Engineering (I3CME 2022) (Chengdu, China: SPIE), 135–140.

Gezgin, E., Chang, P.-H., and Akhan, A. F. (2016). Synthesis of a Watt II six-bar linkage in the design of a hand rehabilitation robot. *Mech. Mach. Theory* 104, 177–189. doi:10.1016/j.mechmachtheory.2016.05.023

Hong, X., Sun, L., and Liu, X. (2020). "Optimization design of a multifunctional patient conveying device," in Proceedings of the 2020 3rd International Conference on E-Business. Wuhan, China: Information Management and Computer Science, 437–440.

Hyun, D. J., Bae, K., Kim, K., Nam, S., and Lee, D.-h. (2019). A light-weight passive upper arm assistive exoskeleton based on multi-linkage spring-energy dissipation mechanism for overhead tasks. *Robotics Aut. Syst.* 122, 103309. doi:10.1016/j.robot.2019.103309

Iwano, Y., Koichi, O., and Hisanori, A. (2011). "Development of rescue support stretcher system with stair-climbing," in 2011 IEEE International Symposium on Safety, Security, and Rescue Robotics (IEEE), 245–250.

Lim, S. H., and Ng, P. K. (2021). Synthesisation of design features for multifunctional stretcher concepts. *J. Med. Eng. Technol.* 45, 145–157. doi:10.1080/03091902.2021.1873442

Luo, Z., Shang, J., Wei, G., and Ren, L. (2018). A reconfigurable hybrid wheel-track mobile robot based on Watt II six-bar linkage. *Mech. Mach. Theory* 128, 16–32. doi:10.1016/j.mechmachtheory.2018.04.020

Michael McCarthy, G. S. S. J. (2010). *Geometric design of linkages*. Springer Science & Business Media.

Naemt, PHTLS (2016). *Prehospital trauma life support*. 8th ed. Burlington: Jones & Bartlett Learning.

Pennock, G. R., and Israr, A. (2009). Kinematic analysis and synthesis of an adjustable six-bar linkage. *Mech. Mach. Theory* 44, 306–323. doi:10.1016/j.mechmachtheory.2008.04.007

Qin, X., and Li, B. (2023). "Study on the design of pre-hospital emergency stretcher for the elderly based on scenario construction method," in International Conference on Man-Machine-Environment System Engineering. Singapore, Springer Nature Singapore, 215–224.

Rui, J., and Gao, Q. (2019). Design and analysis of a multifunctional wheelchair, IOP Conference Series: Materials Science and Engineering. Chengdu, China: IOP Publishing, 012045.

Sang, L., Yamamura, M., Dong, F., Gan, Z., Fu, J., Wang, H., et al. (2019). Analysis, design, and experimental research of a novel wheelchair-stretcher assistive robot. *Appl. Sci.* 10, 264. doi:10.3390/app10010264

Scales, L. E. (1985). *Introduction to non-linear optimization*. Springer-Verlag.

Verjans, M., Phlippen, L., Li, Z., Schleer, P., and Radermacher, K. (2021a). Semi-automated stair climbing of a wheel hub-based patient transportation aid for emergency medical services. *A. T. - Autom.* 69, 550–561. doi:10.1515/auto-2020-0160

Verjans, M., Schleer, P., Kinzius, M., Krumholz, P., Phlippen, L., Drobinsky, S., et al. (2021b). Evaluation of a novel stair-climbing transportation aid for emergency medical services. *Biomed. Eng./Biomed. Tech.* 66, 323–333. doi:10.1515/bmt-2020-0166

Waldorn, K. J., Kinzel, L. G., and Agrawal, S. K. (2016). *Kinematics, dynamics, and design of machinery*. John Wiley & Sons.

Wang, G.-r., and Sun, J. (2004). A Cramer rule for solution of the general restricted matrix equation. *Appl. Math. Comput.* 154, 415–422. doi:10.1016/s0096-3003(03)00721-5

Wilson, M. H., Habig, K., Wright, C., Hughes, A., Davies, G., and Imray, C. H. E. (2015). Pre-hospital emergency medicine. *Lancet* 386, 2526–2534. doi:10.1016/s0140-6736(15)00985-x

Yang, L., Xiang, K., Pang, M., Yin, M., Wu, X., and Cao, W. (2023). Inertial sensing for lateral walking gait detection and application in lateral resistance exoskeleton. *IEEE Trans. Instrum. Meas.* 72, 1–14. doi:10.1109/tim.2023.3265105

frontiers | Frontiers in Bioengineering and Biotechnology

TYPE Original Research
PUBLISHED 12 April 2024
DOI 10.3389/fbioe.2024.1330330

OPEN ACCESS

EDITED BY
Ningbo Yu,
Nankai University, China

REVIEWED BY
Hongjun Yang,
Chinese Academy of Sciences (CAS), China
Ning Sun,
Shandong Normal University, China

*CORRESPONDENCE
Andrea Sarasola-Sanz,
andrea.sarasola@tecnalia.com

†These authors have contributed equally to this work

RECEIVED 30 October 2023
ACCEPTED 21 March 2024
PUBLISHED 12 April 2024

CITATION
Sarasola-Sanz A, Ray AM, Insausti-Delgado A, Irastorza-Landa N, Mahmoud WJ, Brötz D, Bibián-Nogueras C, Helmhold F, Zrenner C, Ziemann U, López-Larraz E and Ramos-Murguialday A (2024), A hybrid brain-muscle-machine interface for stroke rehabilitation: Usability and functionality validation in a 2-week intensive intervention. *Front. Bioeng. Biotechnol.* 12:1330330. doi: 10.3389/fbioe.2024.1330330

A hybrid brain-muscle-machine interface for stroke rehabilitation: Usability and functionality validation in a 2-week intensive intervention

Andrea Sarasola-Sanz[1*†], Andreas M. Ray[2†], Ainhoa Insausti-Delgado[1], Nerea Irastorza-Landa[1], Wala Jaser Mahmoud[2], Doris Brötz[2], Carlos Bibián-Nogueras[2], Florian Helmhold[2], Christoph Zrenner[3,4,5,6,7], Ulf Ziemann[3,4], Eduardo López-Larraz[8] and Ander Ramos-Murguialday[1,2]

[1]Health Unit, TECNALIA, Basque Research and Technology Alliance (BRTA), San Sebastian, Spain, [2]Institute of Medical Psychology and Behavioral Neurobiology, University of Tübingen, Tübingen, Germany, [3]Department of Neurology and Stroke, University Tübingen, Tübingen, Germany, [4]Hertie Institute for Clinical Brain Research, University Tübingen, Tübingen, Germany, [5]Temerty Centre for Therapeutic Brain Intervention, Centre for Addiction and Mental Health, Toronto, Canada, [6]Department of Psychiatry, University of Toronto, Toronto, Canada, [7]Institute for Biomedical Engineering, University of Toronto, Toronto, Canada, [8]Bitbrain, Zaragoza, Spain

Introduction: The primary constraint of non-invasive brain-machine interfaces (BMIs) in stroke rehabilitation lies in the poor spatial resolution of motor intention related neural activity capture. To address this limitation, hybrid brain-muscle-machine interfaces (hBMIs) have been suggested as superior alternatives. These hybrid interfaces incorporate supplementary input data from muscle signals to enhance the accuracy, smoothness and dexterity of rehabilitation device control. Nevertheless, determining the distribution of control between the brain and muscles is a complex task, particularly when applied to exoskeletons with multiple degrees of freedom (DoFs). Here we present a feasibility, usability and functionality study of a bio-inspired hybrid brain-muscle machine interface to continuously control an upper limb exoskeleton with 7 DoFs.

Methods: The system implements a hierarchical control strategy that follows the biologically natural motor command pathway from the brain to the muscles. Additionally, it employs an innovative mirror myoelectric decoder, offering patients a reference model to assist them in relearning healthy muscle activation patterns during training. Furthermore, the multi-DoF exoskeleton enables the practice of coordinated arm and hand movements, which may facilitate the early use of the affected arm in daily life activities. In this pilot trial six chronic and severely paralyzed patients controlled the multi-DoF exoskeleton using their brain and muscle activity. The intervention consisted of 2 weeks of hBMI training of functional tasks with the system followed by physiotherapy. Patients' feedback was collected during and after the trial by means of several feedback questionnaires. Assessment sessions comprised clinical scales and neurophysiological measurements, conducted prior to, immediately following the intervention, and at a 2-week follow-up.

Results: Patients' feedback indicates a great adoption of the technology and their confidence in its rehabilitation potential. Half of the patients showed improvements in their arm function and 83% improved their hand function. Furthermore, we found improved patterns of muscle activation as well as increased motor evoked potentials after the intervention.

Discussion: This underscores the significant potential of bio-inspired interfaces that engage the entire nervous system, spanning from the brain to the muscles, for the rehabilitation of stroke patients, even those who are severely paralyzed and in the chronic phase.

KEYWORDS

hybrid brain-muscle-machine interface, stroke, upper limb rehabilitation, multidegree of freedom exoskeleton, bio-inspired motor control, cortico-muscular connection, pilot clinical trial

1 Introduction

After a stroke, cortical and subcortical damage disrupts signals descending from the motor cortex to the spinal cord. The resulting recruitment patterns of muscles are pathological (Roh et al., 2013; Urra et al., 2014). Stroke is among the leading causes of disability and more than 30% of all survivors show limited recovery of their motor abilities (Young and Forster, 2007; Langhorne et al., 2009).

In a rehabilitation intervention, training of functional movements involving multiple degrees of freedom (DoFs) of the upper limb has been shown to facilitate the translation of the regained motor skills to activities of daily living (Takeuchi and Izumi, 2012; Garcia-Cossio et al., 2013). Nonetheless, effectively and proficiently controlling rehabilitation exoskeletons with multiple DoFs using neurophysiological signals remains a challenge. This is due to the dynamics and the mechanical constraints of the exoskeletons, as well as the complexity of modelling human motor control mechanisms (Sartori et al., 2018). This has been reflected in the absence of multi-DoF rehabilitation systems that can offer an accurate method to train functional tasks.

Conventional non-invasive Brain-Machine Interface (BMI) therapies have shown promising results in rehabilitation of the upper limb of stroke patients. However, the poor quality of the signal captured from the brain constitutes a major limitation. Currently, precise control of a rehabilitation robot complex enough to be able to train functional tasks is not possible with such systems.

Hybrid brain-muscle-machine interfaces (hBMI) have been proposed to overcome these limitations. These systems supplement the brain signals used for decoding the patient´s intention by including electromyography (EMG) as a control signal (Leeb et al., 2011; Müller-Putz et al., 2011; Lalitharatne et al., 2013; Kawase et al., 2017; Sarasola-Sanz et al., 2017; Loopez-Larraz et al., 2018; Zhang et al., 2019) or by using features based on the functional connection between the brain and the muscle activity, such as the corticomuscular coherence (Chowdhury et al., 2019; Colamarino et al., 2021; de Seta et al., 2022; Guo et al., 2022; Pichiorri et al., 2023). This, in turn, improves the accuracy of movement intention detection and the feedback given to stroke patients (López-Larraz et al., 2019). Moreover, these types of hBMIs establish a biologically inspired hierarchical control flow, reinforcing the brain-to-muscle connection and thus, acting both at the central and peripheral nervous systems for an integral rehabilitation.

Although the control of these hBMIs and the accuracy of feedback have advanced significantly in recent years, to our knowledge, there is no study that has achieved continuous control of an upper limb exoskeleton with multiple degrees of freedom (DoFs) for post-stroke rehabilitation. Most systems are limited to triggering a predetermined movement of a single degree of freedom at a time. Furthermore, only one researcher group has validated their system in real-time conditions with stroke patients (Guo et al., 2022). In this study we assess the feasibility, usability and functionality of an hBMI system and training protocol for stroke rehabilitation. The system allows the continuous control of a 7-DoF upper limb exoskeleton. This is achieved by combining the continuous output of a binary electroencephalography (EEG)-decoder and a continuous EMG decoder, with a gating control flow that ensures the functional activation of both central and peripheral structures for the movement execution. Six chronic and severely impaired stroke patients without active finger extension trained functional tasks such as grasping, pointing and wrist rotations in combination with reaching movements with the proposed rehabilitation system for 10 days. The usability and functionality of the system and the training protocol were evaluated by means of feedback questionnaires. Furthermore, the outcome of this rehabilitation pilot intervention was assessed with behavioral and electrophysiological signal measurements.

2 Materials and methods

2.1 Patients

Six patients were recruited via advertisements at the University Hospital of Tübingen and physiotherapy clinics in Tübingen, Germany and via public information with stroke associations. All of them gave written consent to the procedures as approved by the ethics committee of the Faculty of Medicine of the University of Tübingen, Germany.

All participants fulfilled the following criteria: 1) paralysis of one hand with no active finger extension; 2) time since stroke of at least

TABLE 1 Summary of demographics and functional data (*combined hand and arm scores (motor part) from the modified upper limb Fugl-Meyer-Assessment (cFMA) (excluding coordination, speed and reflexes scores; Max = 54points. These values are the average of two baseline measurements that were done 2 weeks (Pre1) and right before (Pre2) the intervention) (Ramos-Murguialday et al., 2013).

Patient	Gender	Lesion side	Age	Months since stroke	Initial Fugl-Meyer Assessment (cFMA) score*
1	M	R	65	84	9.0
2	F	R	63	50	9.5
3	M	R	49	92	6.0
4	F	L	40	182	14.0
5	M	L	62	9	15.5
6	M	L	54	34	10.5

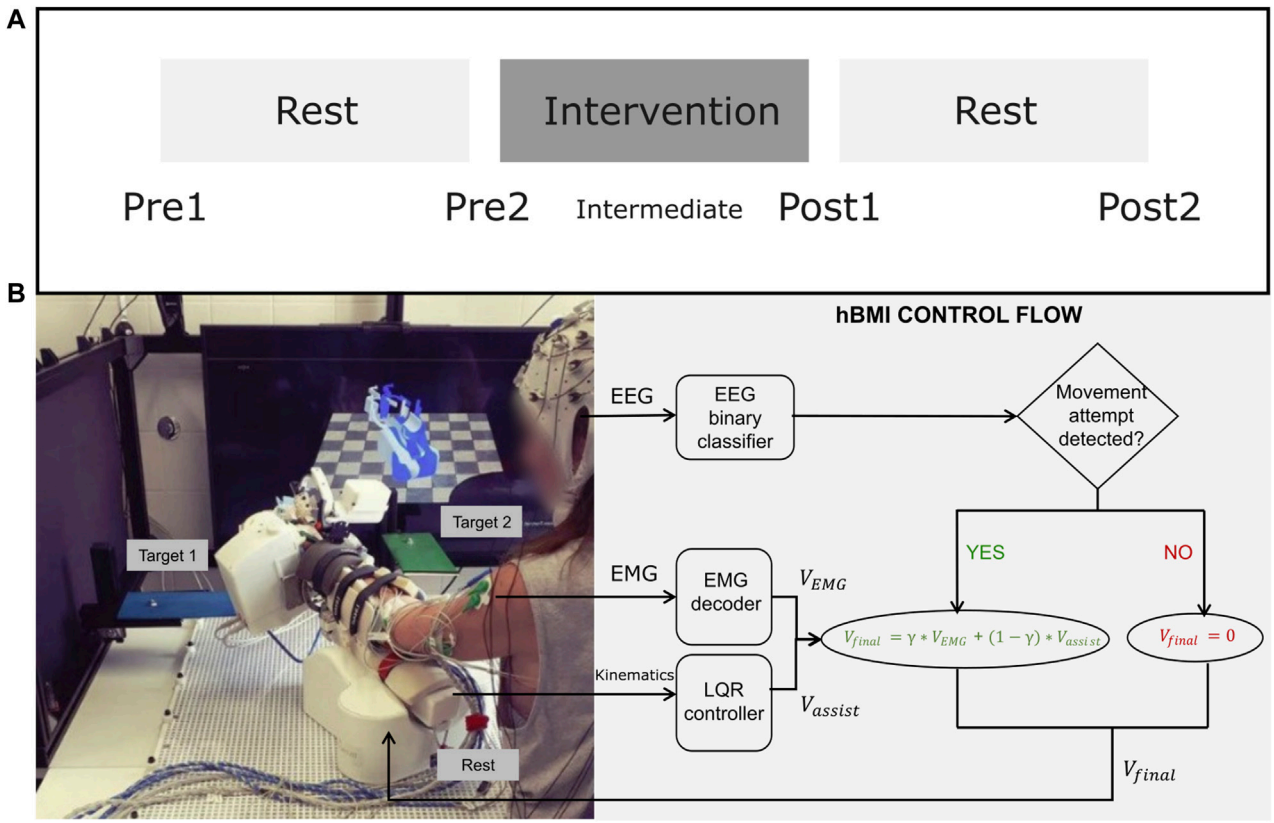

FIGURE 1
(A) Intervention and Assessment Schedule. **(B)**-Left: The experimental setup including EEG, EMG, the exoskeleton, the targets of two task types, and the visual feedback on the screen. An additional target was place to the right of the patient. **(B)**-Right: A diagram explaining the hierarchical control flow of the hybrid BMI.

9 months; 3) age between 18 and 80 years. Psychiatric or neurological conditions other than stroke, cerebellar lesion or bilateral motor deficit, pregnancy and epilepsy constituted exclusion criteria. All patients were able to understand and follow instructions.

None of the patients could extend their fingers or their wrist. According to the sensibility scores of the Fugl-Meyer-Assessment (FMA) all patients felt the arm moving and half of them felt hand movements, too. A summary of the patient's demographics and functional data are presented in Table 1.

2.2 Experimental protocol

The study consisted of 2 weeks of intervention and multiple assessment sessions (Figure 1). Patients trained daily with the rehabilitation hBMI system for 2 consecutive weeks (except Saturdays and Sundays) for 1 h, followed by an individual physiotherapy session of 30 min. Assessments included clinical scales as well as neurophysiological measurements (EMG and EEG recordings and Motor Evoked Potentials induced with Transcranial Magnetic Stimulation). These were carried out four

times in total: 2 weeks before the intervention started (Pre1), once directly before (Pre2) and directly after (Post1) the intervention, and the last one 2 weeks after the end of the intervention (Post2). The two measurements taken before the intervention (Pre1 and Pre2) were averaged to establish a single baseline measurement in order to account for familiarization and test variability effects (Whitall et al., 2011). Patients rested during 2 weeks before and after the intervention. Feedback questionnaires were also administered after the first week of training (Intermediate) and right after the intervention (Post1).

Patients trained functional tasks that included coordinated reaching and hand movements towards three different target positions, which were marked with colors around the workspace. The three task types were the following:

- Forward reaching leftwards, pronation of the wrist and grasping with all fingers (red_grasp)
- Forward reaching to the front and pointing with the index finger (green_point)
- Forward reaching rightwards, supination of the wrist and opening of the fingers (blue_up)

These reaching movements always started and ended at a resting position specifically defined for each patient, in which the patient could rest comfortably.

A training session consisted of between four and six blocks. Within each block, the task types (red_grasp, green_point or blue_up) were presented in random order. Each task type or target was presented once per block. The patients had 10 s to reach each target. If the target was not reached within that time a resting break of between 3 s and 5 s followed before continuing the movement towards the target. Patients had a maximum of 4 attempts to reach the target. As soon as the target or the maximum of attempts were reached a resting break of between 3 s and 5 s followed before going back to the rest position–a movement that the patients also tried to perform actively.

The presentation of the cues indicating the task type was auditory. In addition, a screen in front of the patients showed two virtual models of the exoskeleton, a translucent one in the current position and a colored one in the target position (Figure 1).

2.3 Experimental setup

During the training sessions, patients sat in a chair while having their upper limb attached to a 7-DoF exoskeleton that could move and turn on a table (2D plane, DoFs 1–3), pronate or supinate the forearm (DoF 4) and extend or flex the thumb (DoF 5), the index (DoF 6) and the group of pinky, ring and middle fingers (DoF 7) (Sarasola-Sanz et al., 2015).

EEG was acquired from a 32-channel EEG cap at a sampling rate of 1000 Hz (EasyCap GmbH, BrainProducts GmbH, Germany). EMG signals were registered from surface electrodes (Myotronics-Noromed, United States) over 14 muscles of their paretic upper limb (First dorsal interosseous, Abductor pollicis longus, Extensor carpi ulnaris, Extensor carpi radialis, Extensor digitorum, Flexor digitorum superficialis, Flexor carpi radialis, Pronator teres, Biceps, Triceps, Deltoid anterior, Deltoid medialis, Teres major and Pectoralis major) at 1,000 Hz. Vertical and horizontal EOG was also recorded.

2.4 Hybrid brain-muscle-machine interface control

During the training with the hybrid brain-muscle-machine interface, the exoskeleton moved the patients' upper limb based on the output of a hybrid decoder with a control flow inspired by biological principles (Figure 1) (Sarasola-Sanz et al., 2017). The EEG signal measured over the ipsilesional motor cortex was decoded and whenever the intention to move was detected (i.e., a desynchronization of the sensorimotor rhythm (SMR)), the EMG control was enabled. Then, EMG activity captured from the 14 electrodes placed on the paralyzed upper limb was continuously decoded and translated into velocity commands for each of the 7 DoFs of the exoskeleton (V_{EMG}). To compute the final velocity sent to each of the exoskeleton DoFs (V_{final}), the EMG velocity components were combined (Eq. 1) and weighted ($\gamma = 0.5$) with assistive velocity components ($V_{assistive}$) calculated using an LQR controller, which aided the patient in reaching the target position. Hence, patients received visual and proprioceptive feedback from the movement of the exoskeleton in real-time, establishing a hybrid closed-loop control.

$$V_{final} = \gamma * V_{EMG} + (1 - \gamma) * V_{assistive} \quad (1)$$

The assistive component was introduced to compensate for possible occasional mechanical issues in the exoskeleton (e.g., wheels sliding) and for the complexity that controlling a mirror myoelectric decoder might pose for patients. Our mirror decoder does not aim to achieve the highest possible performance but instead, it provides patients with feedback about their incorrect activation patterns (Sarasola-Sanz et al., 2018). Hence, a certain level of assistance was introduced to avoid frustration, especially at the beginning of therapy when users are not yet accustomed to the system and have not learned the myoelectric mirror map. The assistance level ($\gamma = 0.5$) was chosen based on previous experiments (Sarasola-Sanz et al., 2022) to ensure patients would achieve successful control of the multi-DoF interface while allowing them to learn and adapt to the myoelectric mapping over time.

To achieve a smoother and more stable control experience, the movement of the exoskeleton was not triggered (or stopped) until the EEG-decoder output was classified five consecutive times as "Movement" (or "Rest") (Ramos-Murguialday et al., 2013). Additionally, the exoskeleton remained blocked during the rest and preparation periods, ignoring the outputs of the decoders.

2.5 EEG calibration and decoding methods

To choose the electrodes and frequency bands that could best control the interface, an EEG screening was introduced before the beginning of the hBMI training. During the screening patients were asked to either relax or try to open and close their paretic hand, guided by visual and auditory cues.

EEG signals were bandpass filtered (fourth order Butterworth filter at 5–48 Hz), down-sampled to 100 Hz and spatially filtered with a Surface Laplacian transform. An automated EOG artifact rejection method was applied following the method described by (Schlögl et al., 2007). Spectral estimation was performed by modelling the resulting signals as an autoregressive process of order 20 using 0.5 s-long windows and a step size of 50 ms. To identify the EEG channel and frequency bands showing the largest power difference between rest and movement, the mean power spectral density was computed and a visualization of r-squared values of these power values was created. Two raters visually selected the two most discriminative perilesional electrodes and frequency bands that would be used as input features for the decoder during the real-time hybrid control.

During real-time hybrid control, the EEG decoder was retrained at the end of each trial based upon the last 2 minutes of data collected from each condition ("Rest" and "Movement"). This adaptive strategy helped to mitigate potential effects of impedance changes or other intra-session variabilities.

2.6 EMG calibration and decoding methods

EMG data was filtered (10–500 Hz and 50 Hz comb filter). Five time-domain features (Mean of absolute value, Variance, Waveform Length, Root-mean-square error, and the Logarithm of the Variance) were extracted from the 14 EMG channels and normalized to zero mean and unit variance using the mean and standard deviation computed on the last minute of EMG data during the real-time hBMI operation.

The EMG activity of the patients was decoded using a mirror decoder approach (Sarasola-Sanz et al., 2018). The EMG of the same 14 muscles on the patient´s healthy arm was recorded during an initial calibration session while performing the same type of movements with the exoskeleton. This data was mirrored and processed before training the patient-specific mirror decoder. A ridge regression algorithm with a regularization parameter $\lambda = 10^4$ was utilized to build the mirror decoder, which interpreted the EMG activity from the paretic arm during the real-time hBMI control. Hence, the mirror decoder enabled patients to relearn non-compensatory muscle activation patterns from their healthy arm.

2.7 Physiotherapy

Immediately following the hBMI training session, patients participated in a 30-min behavioral physiotherapy session tailored to their individual abilities and needs. The primary objective of these sessions was training arm and hand movements to facilitate the translation of possible gains from the hBMI training into functional motor benefits. This involved a diverse range of exercises, such as forward reaching to enhance shoulder flexion and extension, forearm supination and pronation, and elbow and wrist flexion and extension. These exercises were integrated into meaningful everyday tasks specific to each patient, such as grasping objects and bringing them closer to the body, practicing hand opening and closing to improve object manipulation skills, holding and releasing different shaped and sized objects and bringing the hand to the mouth for enhanced eating abilities.

2.8 Assessment

2.8.1 Usability and functionality

Three questionnaires (see templates in Supplementary Material) comprising a total of 52 statements were presented to the participants to gather their feedback about the usability and functionality of the system and their expectations of the intervention. Two of them were administered in the middle (Intermediate) and right at the end of the trial (Post1), and the third one was only given right at the end (Post1). Patients were asked to indicate their level of agreement to each statement on a range from 0 (strongly disagree) to 7 (strongly agree). The statements were grouped into the following categories to simplify the analysis:

- *Exoskeleton functioning*: evaluated whether the exoskeleton moved smoothly and at a comfortable speed.
- *Exoskeleton ergonomy*: comprised statements about how comfortable it was to wear the exoskeleton.
- *Exoskeleton control*: assessed how difficult it was for participants to control the movement of the exoskeleton with their EMG and EEG activity.
- *Feedback accuracy*: evaluated the perception of the participants about the feedback provided (i.e., whether they felt that the exoskeleton moved according to or against their will).
- *Protocol design, tasks and instructions*: looked for the opinion of the participants regarding how tired they were after the training, whether the pauses were long enough, whether the tasks trained were adequate and the instructions were clear.
- *Experimenter*: analyzed participants' opinion about the people running the experiment, whether they were experienced, and the treatment received was adequate.
- *Performance perception and expectations of improvement*: evaluated participants' perception of how well they were performing and their expectations for the outcomes they would achieve from the intervention.

First, the answers of the two questionnaires administered in the Intermediate and Post1 measurements were compared to see if the feedback varied along the trial. Additionally, the answers to the three questionnaires at Post1 were studied to evaluate the general perception of the participants about the intervention in the aforementioned categories.

2.8.2 Primary behavioral outcome measure: Fugl-Meyer assessment (cFMA)

The combined hand and arm scores (motor part) from the modified upper limb cFMA (Ramos-Murguialday et al., 2013) were used to measure the behavioral outcome (maximal score = 54 points). Patients could not perform the movements required for the scores related to coordination and speed. The scores related to reflexes add uncertainty to the measurement (Crow and Harmeling-Van Der Wel, 2008). Both types of scores were thus excluded.

2.8.3 Secondary behavioral outcome measures: Broetz scale

The Broetz scale is a validated instrument specifically designed for reliable assessment of hand function in severely paralyzed stroke patients (Broetz et al., 2014). It allows to assess small variations in hand function in this group of patients using seven tasks of daily life with the paralyzed hand. It was applied right after the cFMA score in each assessment session.

2.8.4 Further outcome measures based on neurophysiological data

2.8.4.1 Electromyography during compliant movements

During the assessment sessions, compliant movements were recorded with the exoskeleton on the healthy (2 sessions) and paretic (3 sessions at Pre, Post1 and Post2) limbs, separately, in patients 2–6. The exoskeleton moved the upper limb of the patient towards the three predefined target positions fully automatically. The patients were asked to follow the movement of the robot without applying any counteracting force. Each session comprised five blocks, with approximately 12 trials per block (3 trials per task type). EMG activity from the 14 muscles described in Section 2.3 was acquired. In this manner, we anticipated acquiring consistent EMG recordings during assisted movements on the patients' limbs across all assessments, ensuring comparability.

EMG data was acquired at 1 kHz. Raw data was band-pass filtered between 5and 300 Hz using a zero-phase FIR filter, full wave rectified, and low-pass filtered at 0.3 Hz (second order, Butterworth) to extract a smoothed signal envelope. After visually inspecting the EMG data, the data from the first dorsal interosseous muscle was excluded from this analysis due to high levels of noise observed in the acquired signals from this superficial muscle in most of the sessions and in most patients. The EMG data was segmented into trials from the time of the auditory signal that announced the start of the movement ('go' instruction) to the end of the movement (encompassing both the forward and return to the rest position phases) and aggregated into task-specific datasets. S1 Patient 1 (P1) was not included in this analysis because the motor tasks recorded in the assessment sessions were different, and therefore not comparable between them. Every EMG trial was time-normalized to 1,000 and Z-score-normalized in amplitude. For each patient, session and task, trials displaying EMG activity levels outside the range of the averaged task-specific pattern of activity ±3 units at any timepoint during the trial were excluded. Muscles with fewer than 5 remaining trials after trial rejection were not considered to exhibit a representative and stable EMG pattern associated with the assisted robotic movement. Therefore, they were not evaluated for that specific task, session, and patient. With the remaining trials, the average EMG pattern of each muscle was calculated for every patient, assessment session and task.

The Pearson correlation coefficient (CC) and the variance accounted for (VAF) metrics were utilized to evaluate the degree of similarity between two EMG profiles (Irastorza-Landa et al., 2021). Values close to 1 indicate perfect temporal coactivation for CC and a perfect match in normalized EMG pattern amplitudes for VAF. These metrics were first computed by comparing homologous EMG profiles from the two recording sessions on the healthy limb for each patient, task and muscle. This provided reference mean and standard deviation values of these metrics. Values below 1 might be attributed to inter-session variability, even in healthy datasets.

CC and VAF were subsequently computed between the averaged healthy reference EMG patterns (data from both healthy limb sessions pooled together) and the corresponding measures in the paretic limb for each patient, assessment session, task and muscle. Finally, the mean and standard deviation of CC and VAF were computed across muscles and tasks for each patient and session.

2.8.4.2 Motor evoked potentials

The efficacy of cortico-muscular connections was evaluated through motor evoked potentials (MEPs) using transcranial magnetic stimulation (TMS). Having a metallic implant was an exclusion criterion that resulted in two patients (patients 2 and 3) not being eligible for this measure.

We used a magnetic stimulator (Magstim Rapid2, Magstim Ltd., United Kingdom) equipped with a figure-of-eight coil (D70 Air Film Coil, Magstim Ltd., United Kingdom) to provide single pulse stimuli over the ipsilesional hand-motor cortex of the participants. The scalp of each participant was registered with a neuronavigation system (Localite GmbH, Germany) that allowed accurate tracking of the stimulation coil relative to the hand-motor cortex. Two distal muscles of the forearm, the first dorsal interosseous (FDI) and the abductor pollicis longus (APL)) were defined as target muscles for measuring MEPs, as they allow for the evaluation of the effectiveness of the entire upper limb, from the brain to the muscles that control hand functionality. We adapted the amplitude criteria typically used to define the resting motor threshold (RMT) to prevent potential discomfort or headache (Groppa et al., 2012). The resting RMT was thus defined as the minimum stimulation intensity required to elicit at least 5 evoked potentials in the target muscles larger than 20 μV out of 10 consecutive stimulation pulses.

For the evaluation of the MEPs, we initially identified the spot that produced the largest MEPs in the target muscle (referred to as the "hot spot") and marked this location in the neuronavigation system. Then, in a clockwise direction, we recorded a spiral mapping of the surrounding area, which was divided into a grid with a mesh-density of 1 cm and a size of 10 × 10 cm in the 3D head model. In each assessment session, 10 stimulations were delivered on each point of the grid at 120% of the RMT every 5–5.5 s. The spiral mapping concluded when less than 5 MEP responses out of 10 consecutive stimulations were obtained.

The raw EMG activity of the muscles was initially processed by removing the signal within 10 ms before and after the stimulation artifacts and correcting for any voltage differences at the edges of the merged traces. The resulting signal was band-pass filtered between 10 and 2000 Hz and notch filtered using a second order Butterworth filter. Then, the signal was trimmed down to 200 ms trials from −100 to 100 ms with respect to the stimulation trigger. To avoid a facilitation effect of EMG contraction before the stimulation trigger on the MEPs, we implemented an automatic method for muscular activity detection. The envelopes of the EMG signal of 10 ms sliding windows with 1 sample step were calculated in the interval prior to the stimulation artifact [-100 0]ms. The envelope values of each sliding window were averaged, and the mean and standard deviation between trials recorded in the same stimulation spot and channel were used to calculate the rejection threshold. Those trials containing at least one sliding window value that exceeded 4 standard deviations above the mean were

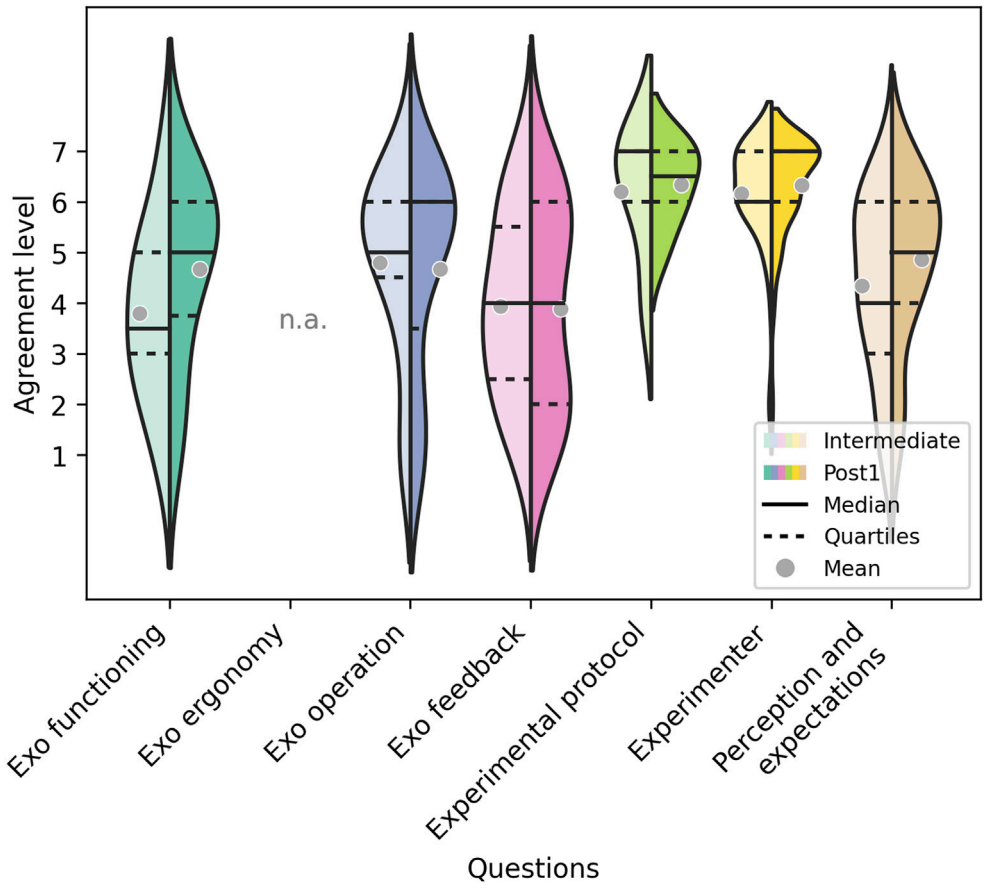

FIGURE 2
Responses of the participants to the questionnaires filled out in the middle (Intermediate) (Left half) and at the end of the intervention (Post1) (Right half) for each of the 7 categories. The horizontal lines define the median values and the gray dots the mean values.

discarded. Clean trials were pooled together and averaged for each patient, channel, and spot in the spiral mapping of the motor cortex. The peak-to-peak amplitude and latency of the resulting potential were computed.

2.8.5 hBMI control performance

Performance of patients controlling the hBMI system were evaluated using the EEG decoder outputs. The EEG decoder computed an output every 25 ms and it was positive if the brain state was classified as movement intention. The EEG performance measure is represented by the percentage of positive outputs out of all decoder outputs. Only the first try to reach each target was considered to evaluate values comparable between patients. This measure serves as an estimation of the ability of the patients to operate the system.

3 Results

3.1 Usability and functionality

3.1.1 Intermediate-Post1 feedback comparison

Figure 2 represents the mean, median and the distribution of the responses of the participants to the questionnaires filled out in the middle (Intermediate) and at the end of the intervention (Post1). It shows satisfactory mean response values (in the range [3.8, 6.2]) in the middle of the intervention, which became even better in most of the categories after the intervention (mean values in the range [3.9, 6.3]). Median values either remained stable or improved in the Post1 measurements. Furthermore, the median values at Post1 fell within the range of [5,7] in all the categories but the "Exo feedback", where the median was 4.

3.1.2 Post1 feedback evaluation

The answers to the three questionnaires at the end of the trial are illustrated in Figure 3, which show positive feedback of the system's usability and functionality as well as of the users' expectations. Mean values lie within [4.24, 6.32], and the distribution of the responses was skewed towards higher values, as reflected by the median values of 5 or higher for all categories but the " Exo feedback".

3.2 Primary behavioral outcome measure: Fugl-Meyer assessment (cFMA)

The changes of the Fugl-Meyer scores of arm and hand combined for the intervention ranged from −0.5 to +3 points

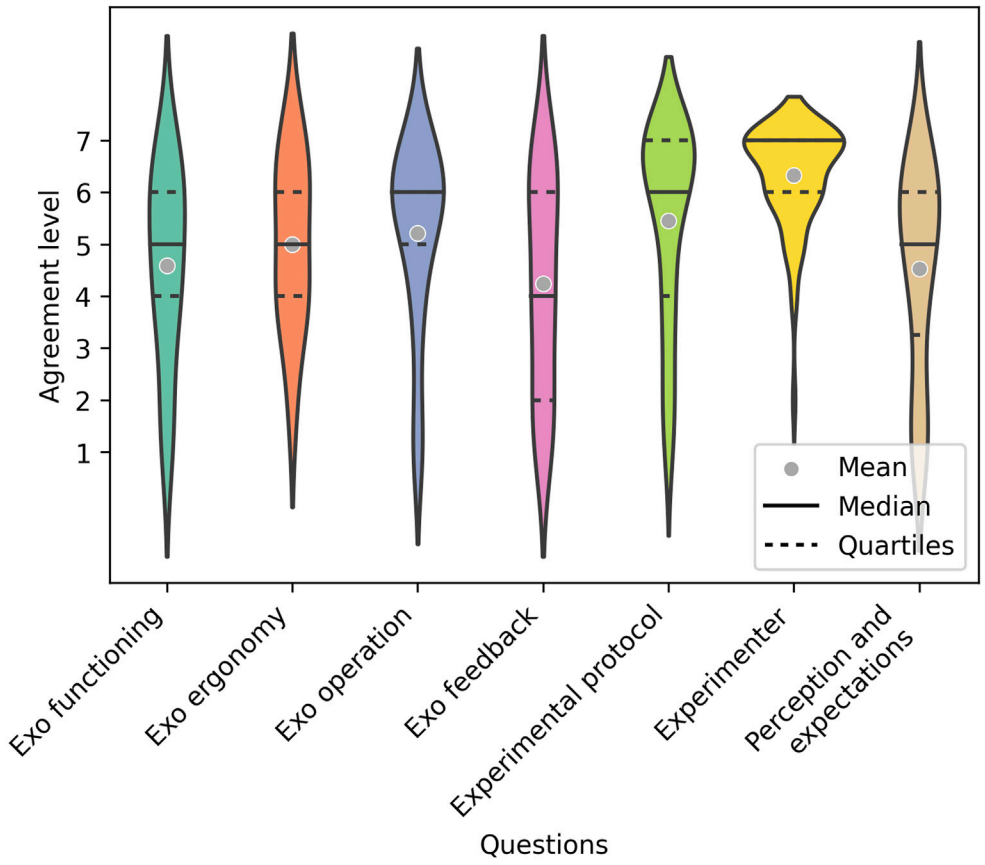

FIGURE 3
Responses of the participants to the questionnaires filled out and at the end of the intervention (Post1) for each of the 7 categories. The horizontal lines define the median values and the gray dots the mean values.

TABLE 2 Changes of the Fugl-Meyer scores (arm and hand combined) and the Broetz scores during the intervention.

Patient	cFMA	Broetz scale
1	0.0	2.5
2	1.0	1
3	−0.5	3
4	0.0	4
5	3.0	12
6	1.5	−2

with mean and standard deviation of 0.83 and 1.3 (Table 2). There was no statistical difference of the scores to 0 (t-test). Remarkably, patient 5 showed a three-point improvement on the scale after only 10 days of training.

3.3 Secondary behavioral outcome measures: Broetz scale

The changes of the Broetz scores ranged from −2 to +12 points with mean and standard deviation of 3.4 and 4.7 (Table 2). There was no statistical difference of the scores to 0. The notable improvement of Patient 5 is also reflected on the Broetz scale, representing an advancement of multiple steps of complexity in the tasks performed during the test.

3.4 Further outcome measures based on neurophysiological data

3.4.1 EMG during compliant movements

The task-specific normalized and averaged EMG profiles of four muscles in Patient 4 are depicted for both the healthy and the paretic limbs in various assessment sessions in Figure 4A (See Supplementary Material for the rest of the patients). In the case of this patient, it can be observed that the task-specific EMG profiles after the intervention (Post1, blue) became more similar to those recorded in the healthy limb (Healthy, black), particularly for certain muscles (e.g., Extensor carpi ulnaris, Flexor carpi radialis, Biceps, and Deltoid Medialis during the green_point task). In some cases, no significant changes in muscle modulation were observed across different time points (e.g., Biceps or Flexor carpi radialis during the red_grasp task).

In general, most patients exhibited CC and VAF values below the average healthy reference for all or some of the tasks, indicating at least a partial mismatch in temporal coactivation and EMG patterns between limbs (see Figure 4B). However, the mean VAF value demonstrates an

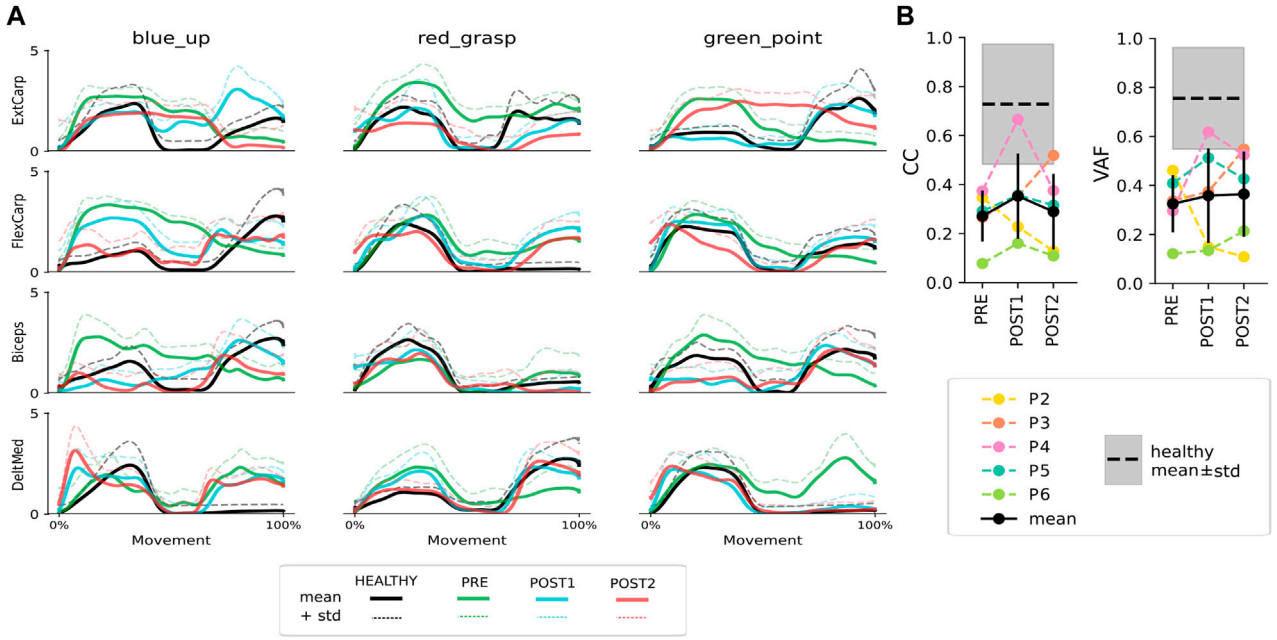

FIGURE 4
(A) Average EMG activations (solid lines) + 1 standard deviation (dashed lines) of a subset of four muscles in the combined healthy reference datasets (black) and in the paretic limb in Pre (green), Post1 (blue) and Post2 (red) assessment measurements in a representative participant. **(B)** Colored lines represent the CC and VAF values averaged among muscles and tasks for each patient in different assessment sessions. The mean and standard deviation values among all patients (P2-P6) are indicated by a black errorbar. The mean and standard deviation of the healthy reference are represented by a dashed black line and a gray shaded area, respectively.

upward trend from Pre to Post2, and the CC values show an increase in Post1. When examining the results for each patient individually, it can be observed that Patient 2 showed the best CC and VAF values at the baseline (Pre), with a significant decrease at both timepoints after the intervention (Post1 and Post2). However, the remaining four patients showed an increase or similar CC and VAF values after the intervention (Post1) compared to the baseline status (Pre).

3.4.2 Motor evoked potentials

Figure 5 shows the results of the hand-mapping around the hot spot of each participant along the different assessment sessions (see Supplementary Material for the stimulation intensity utilized for each participant). No motor evoked potentials were obtained in Patient 4 in any of the measurements.

Patient 1 exhibited a significant increase of MEP amplitude in the FDI muscle right after finishing the intervention (Post1) and continued increasing even 2 weeks after (Post2). Furthermore, the region adjacent to the hot spot presented larger MEP responses, suggesting an improvement of synaptic efficacy of corticospinal tracts (Figure 5, upper row).

For Patient 5, the corticospinal efficacy of the APL increased immediately after completing the intervention (Post1) and continued to rise during the 2 weeks following this phase (Post2) (Figure 5, middle row). The excitatory effect of the intervention was observable not only at the hot spot but also in the surrounding area, as depicted in the heatmaps.

As shown in the heatmaps of Patient 6 (Figure 5, bottom row), the corticospinal tracts projecting to APL from neighboring cortical areas exhibited stronger responses following the intervention (Post1) and this effect persisted for up to 2 weeks (Post2). When focusing on the hot spot, an enhancement of synaptic efficacy was also observed over time.

3.5 hBMI control performance

All the patients, despite being severely impaired could control the hBMI successfully to perform coordinated functional arm and hand tasks. The percentage of positive outputs of the EEG decoder is shown in Figure 6. For most patients, the performance stayed on a similar level throughout the intervention (p-values >0.05 for all linear regressions). Only Patient 5 showed larger variability than the other patients. For a major part of the intervention the performance was in a range of 60%–70% on average. There are only very few sessions for Patients 2, 5 and 6 during which performance dropped below 50%. Patients 1 and 3 achieved the highest performance values with average values between 75% and 95%.

4 Discussion

In this pilot trial we demonstrated the feasibility of an intensive rehabilitation training with a hybrid interface that integrates muscle and brain activity to control an exoskeleton with 7 DoFs. The feedback received from the 6 patients demonstrates the usability and functionality of the system, as well as the confidence of the participants about its operation and its potential for rehabilitation. Furthermore, we showed the therapeutic potential of the system in

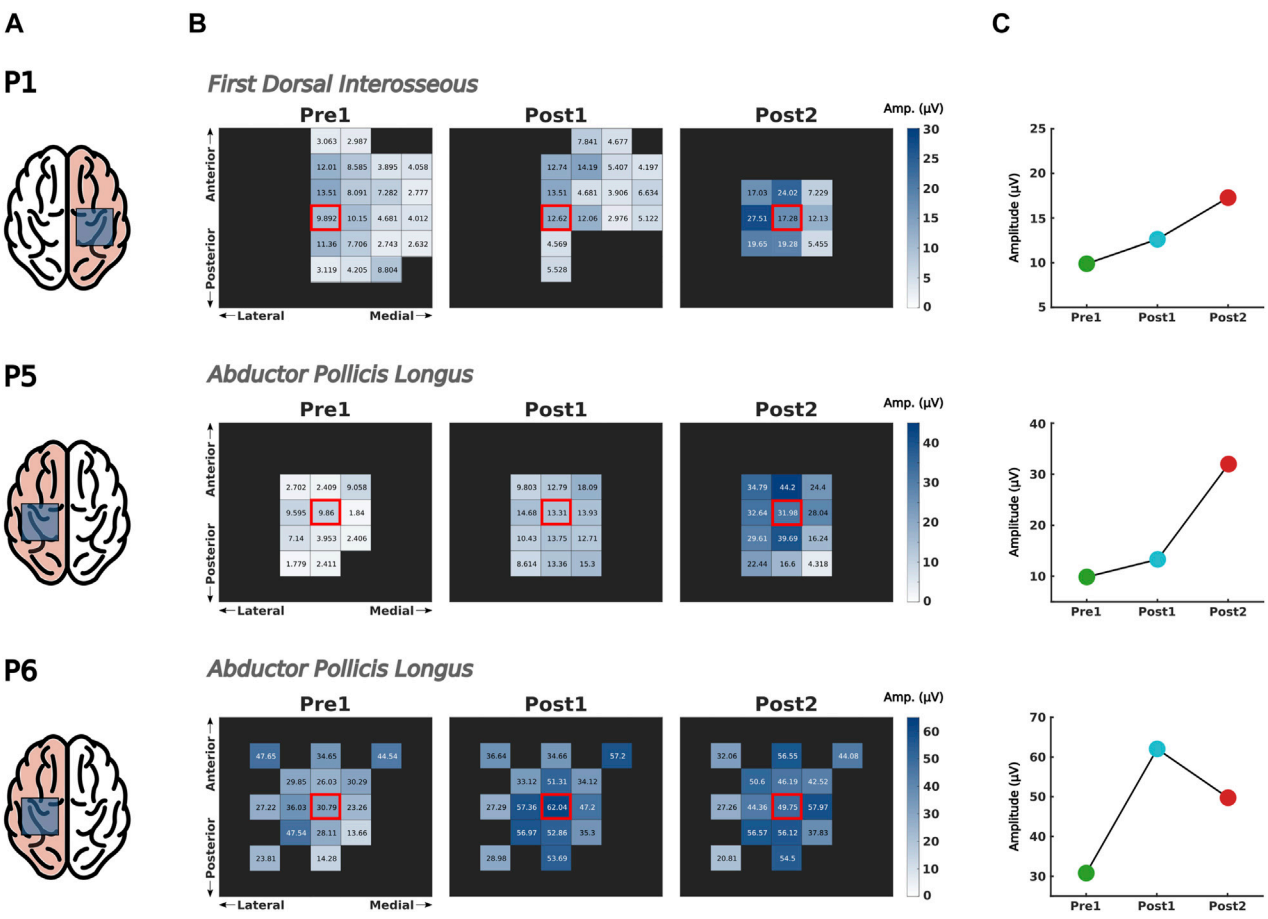

FIGURE 5
Comparison of corticospinal excitability over time. **(A)** Corticospinal excitability was assessed by means of motor evoked potentials (MEPs) over the hand motor cortex of the ipsilesional hemisphere, represented inside the shaded square in the highlighted brain laterality. **(B)** The peak-to-peak amplitude of 10 MEPs elicited in the target muscle were measured in the spot presenting larger muscular response (i.e., hot spot, indicated with a red square) and in the surrounding cortical region. **(C)** Changes in MEP size of the hot spot before and after intervention.

severely paralyzed and chronic patients, who are not eligible for most of the existing and clinically available treatments.

The patients' responses to the questionnaires show that they highly value the system, the protocol and the experimenters. The responses at the Intermediate measurement indicate that even severely affected and chronic patients, after just 5 days of use, can adapt to the hybrid interface and are satisfied with its operation. This is further demonstrated by the brain activity decoding performance values, which range from 60% to 70% on average, showing that from the beginning, patients were able to adapt to the EEG decoder to successfully control the interface, even though it was retrained after each trial. Moreover, the performance remained consistently stable throughout the intervention for all patients except Patient 5, who exhibited a greater degree of variability. However, it is important to note that Patient 5 also demonstrated the most significant improvement on the Fugl-Meyer scale. This suggests that higher variability or a lower percentage of positive outputs from the EEG decoder did not hinder the patient's recovery process, as other variables, such as the myoelectric control of the interface, also influence the rehabilitation outcome. The EMG decoding performance was not included in these analyses as the goal of the mirror myoelectric decoder in our system is not to achieve the highest performance possible, independently of whether patients produce correct or pathological activations. Instead, its purpose is to offer a reference map of healthy EMG activity that could help patients correct their abnormal patterns as a means for rehabilitation. Nevertheless, performance values of the mirror myoelectric decoder method in various configurations can be found in (Sarasola-Sanz et al., 2018).

Comparing the ratings between the Intermediate and Post stages reveals an increase: patients improve their perception of the "Exo functioning" and "Exo operation", as well as their "Performance perception and their expectations of improvement". This implies that patients became more comfortable operating the interface and felt that they were controlling it better over time. Additionally, they gained more confidence in the system's potential to assist in their recovery.

In the responses to the final questionnaires, patients gave a positive evaluation of the ergonomics of the exoskeleton. Extrapolating from these results on a prototypical research tool, we expect this evaluation to be even more positive once the current system is industrialized for use in routine clinical settings.

The values for "Exo feedback" are the lowest among all the question groups. However, they have an average value above 4, which is very positive considering the complexity of the hybrid feedback with the mirror decoder. Furthermore, the system aims to provide patients with feedback about whether they are activating their muscles correctly or not,

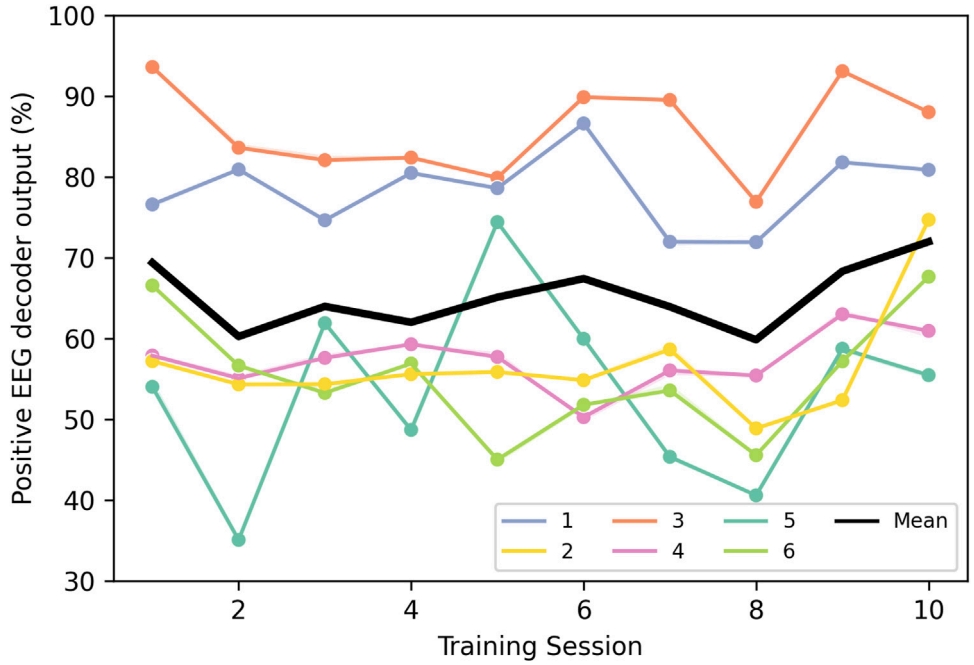

FIGURE 6
Percentage of EEG decoder outputs that were decoded as "Movement" during the trial time for each patient (1–6) and training session, as well as the mean of all of them.

rather than simply translating muscle activations, pathological or not, into a movement towards the target. This means that although patients try to bring the exoskeleton to the target, if the brain and muscle activations were not correct, the exoskeleton would deviate from the trajectory towards the target, and therefore, patients might perceive the feedback as not going in the desired direction. However, this is the foundation on which our system is based, to promote the correction of pathological patterns and thus encourage motor learning. Additionally, it should be mentioned that half of the patients had compromised proprioceptive sensation in the hand, and two of them also in the arm. These patients might not have been able to distinguish the direction in which their limb was being moved without relying on visual feedback. This could have also affected their perception and evaluation of the exoskeleton's movements.

Half of the patients show improvements of arm function after a 2-week training, according to the Fugl-Meyer scale. Even a small enhancement on the Fugl-Meyer scale could lead to significant changes in behavior, particularly for patients who are severely and chronically paralyzed and are not expected to experience any spontaneous improvements in their behavior. Patients who did not exhibit improvement could potentially be classified as hBMI non-responders, a phenomenon documented in previous research (Vidaurre and Blankertz, 2010). Another possibility is that the intervention might have been too short to induce changes capturable by this clinical scale. Nevertheless, it is worth noting that the sensitivity of the scores in this severely paralyzed patient group might be insufficient. The Broetz scale was included to capture finer improvement in the hand joints. This scale was able to capture improvements in hand function in 5 of the 6 patients along the intervention, which were not always reflected in changes in the Fugl-Meyer scale.

Additionally, objective assessment measurements based on neurophysiological parameters were included to evaluate the rehabilitation effects. Despite being severely impaired, these patients exhibit some degree of ability to activate paretic muscles in a task-specific manner with consistent EMG activation profiles during compliant movements. Moreover, the results of the CC and VAF analyses show that the muscle activation patterns become more similar to those in the healthy arm after the intervention in 4 of the 5 patients. This reflects the positive effect of using a mirror decoder of healthy activity as a reference model, upon which the feedback (i.e., exoskeleton movement) provided to the patients is founded (Sarasola-Sanz et al., 2018). The poor results of Patient 2 might be due to the fact that this patient was constantly performing a rocking movement of the trunk during the therapy, which could have affected the consistency of the measurements. The overall CC and VAF levels of patients do not necessarily align with the FMA or Broetz values at those timepoints. However, it is important to consider that these clinical scales assess a broader repertoire of functional and analytical movements, whereas this EMG analysis focuses solely on three specific motor tasks. Lastly, CC values decrease in the follow-up measurement after 2-week of rest, indicating the influence of the training on the way patients recruit their muscles. A longer intervention would likely be necessary to sustain the improvements gained during the training over time and to proof its effect on recovery.

Previous research has demonstrated that EEG and EMG signals provide complementary information (Balasubramanian et al., 2018; López-Larraz et al., 2024). However, the relationship between brain and muscle activations remains challenging to understand and characterize. Significant advancements have been made in utilizing features that capture this relationship for the control of rehabilitation devices (Chowdhury et al., 2019; Colamarino et al., 2021; de Seta et al., 2022; Guo et al., 2022; Pichiorri et al., 2023). However, they are still

limited to decoding movement attempts that trigger predefined movements and do not allow for continuous and skillful control of a multi-DoF interface. Moreover, their real-time application in stroke patients still requires a greater number of validation studies. Alternatively, we designed an hBMI with a gating strategy that follows the biologically natural motor command pathway, ensuring constant activation of both central and peripheral structures throughout the entire movement duration. Our results showed that the MEP amplitude in upper-limb muscles increased, and that the effective area of the hand-motor cortex broadened after the intervention, indicating that the hBMI training could strengthen corticospinal connections. Our hBMI is a neurorehabilitative technology that engages the entire sensorimotor network from the brain to muscles, potentially resulting in stronger muscular responses. The results we observed after the 2-week intervention lend support to the notion of enhanced corticospinal plasticity, which endures over time, due to the hybrid control of the hBMI.

Physiotherapy also influences the recovery, but in this pilot, we did not focus on disentangling physiotherapy from hBMI effects. Instead, we were testing their combined effect, following previous research (Ramos-Murguialday et al., 2013).

Altogether, the current study in severely paralyzed patients validates the feasibility, usability and functionality of this novel hBMI system, which allows the training of complex functional tasks and involves both central and peripheral structures of the nervous system establishing a biologically inspired closed-loop control. This pilot trial also indicates the potential of this hBMI system to potentiate the plasticity of the entire neural system from the brain to the muscles, which could lead to the reconnection of such structures and by extension, to motor recovery. This would have to be validated in subsequent longitudinal rehabilitation interventions with a larger number of patients, and control groups to compare the effects to those achieved with other rehabilitation methods such as physiotherapy and traditional BMIs.

Data availability statement

The raw data supporting the conclusion of this article will be made available by the authors, without undue reservation.

Ethics statement

The studies involving humans were approved by Ethics Committee of the Faculty of Medicine of the University of Tübingen, Germany. The studies were conducted in accordance with the local legislation and institutional requirements. The participants provided their written informed consent to participate in this study. Written informed consent was obtained from the individual(s) for the publication of any potentially identifiable images or data included in this article.

Author contributions

AS-S: Conceptualization, Data curation, Formal Analysis, Investigation, Methodology, Software, Writing–original draft. AMR: Conceptualization, Data curation, Formal Analysis, Investigation, Methodology, Software, Writing–original draft. AI-D: Conceptualization, Data curation, Formal Analysis, Investigation, Methodology, Software, Writing–original draft. NI-L: Conceptualization, Data curation, Formal Analysis, Investigation, Methodology, Software, Writing–original draft. WM: Conceptualization, Data curation, Formal Analysis, Investigation, Methodology, Writing–original draft. DB: Conceptualization, Data curation, Formal Analysis, Investigation, Methodology, Writing–original draft. CB-N: Conceptualization, Data curation, Formal Analysis, Investigation, Methodology, Software, Writing–original draft. FH: Writing–original draft, Conceptualization, Data curation, Formal Analysis, Investigation, Methodology, Software. CZ: Conceptualization, Investigation, Methodology, Software, Writing–review and editing. UZ: Conceptualization, Investigation, Methodology, Writing–review and editing. EL-L: Conceptualization, Data curation, Formal Analysis, Investigation, Methodology, Software, Writing–original draft. AR-M: Conceptualization, Formal Analysis, Investigation, Methodology, Writing–original draft.

Funding

The author(s) declare financial support was received for the research, authorship, and/or publication of this article. This work was supported by the Eurostars Project E! 113928 SubliminalHomeRehab (SHR), the Bundesministerium für Bildung und Forschung (BMBF) (FKZ: SHR 01QE 2023; REHOME 16SV8606 and REHALITY 13GW0213), the Diputación Foral de Gipuzkoa in the frame of Programa "Red guipuzcoana de Ciencia, Tecnología e Innovación 2021" under 2022-CIEN-000038-01 BRAIN2MOVE project., and the European Union H2020-FETPROACT-EIC-2018-2020 (MAIA 951910).

Conflict of interest

Author EL was employed by company Bitbrain.

The authors declare that the research was conducted in the absence of any commercial or financial relationships that could be construed as a potential conflict of interest.

The author(s) CZ declared that they were an editorial board member of Frontiers, at the time of submission. This had no impact on the peer review process and the final decision.

Publisher's note

Supplementary material

The Supplementary Material for this article can be found online at: https://www.frontiersin.org/articles/10.3389/fbioe.2024.1330330/full#supplementary-material

References

Balasubramanian, S., Garcia-Cossio, E., Birbaumer, N., Burdet, E., and Ramos-Murguialday, A. (2018). Is EMG a viable alternative to BCI for detecting movement intention in severe stroke? *IEEE Trans. Biomed. Eng.* 65 (12), 2790–2797. doi:10.1109/TBME.2018.2817688

Broetz, D., Del Grosso, N. A., Rea, M., Ramos-Murguialday, A., Soekadar, S. R., and Birbaumer, N. (2014). A new hand assessment instrument for severely affected stroke patients. *NeuroRehabilitation* 34 (3), 409–427. doi:10.3233/NRE-141063

Chowdhury, A., Raza, H., Kumar Meena, Y., Dutta, A., and Prasad, G. (2019). An EEG-EMG correlation-based brain-computer interface for hand orthosis supported neuro-rehabilitation. *J. Neurosci. Methods* 312, 1–11. doi:10.1016/J.JNEUMETH.2018.11.010

Colamarino, E., De Seta, V., Masciullo, M., Cincotti, F., Mattia, D., Pichiorri, F., et al. (2021). Corticomuscular and intermuscular coupling in simple hand movements to enable a hybrid brain–computer interface. *Int. J. Neural Syst.* 31 (11), 2150052. doi:10.1142/S0129065721500520

Crow, J. L., and Harmeling-Van Der Wel, B. C. (2008). Hierarchical properties of the motor function sections of the fugl-meyer assessment scale for people after stroke: a retrospective study. *Phys. Ther.* 88 (12), 1554–1567. doi:10.2522/PTJ.20070186

de Seta, V., Toppi, J., Colamarino, E., Molle, R., Castellani, F., Cincotti, F., et al. (2022). Cortico-muscular coupling to control a hybrid brain-computer interface for upper limb motor rehabilitation: a pseudo-online study on stroke patients. *Front. Hum. Neurosci.* 16, 1016862. doi:10.3389/fnhum.2022.1016862

Garcia-Cossio, E., Birbaumer, N., and Ramos-Murguialday, A. (2013). "Facilitation of completely paralyzed forearm muscle activity in chronic stroke patients," in 2013 6th International IEEE/EMBS Conference on Neural Engineering (NER), San Diego, CA, USA, 06-08 November 2013, 1545–1548. doi:10.1109/NER.2013.6696241

Groppa, S., Oliviero, A., Eisen, A., Quartarone, A., Cohen, L. G., Mall, V., et al. (2012). A practical guide to diagnostic transcranial magnetic stimulation: report of an IFCN committee. *Clin. Neurophysiol.* 123 (5), 858–882. doi:10.1016/J.CLINPH.2012.01.010

Guo, Z., Zhou, S., Ji, K., Zhuang, Y., Song, J., Nam, C., et al. (2022). Corticomuscular integrated representation of voluntary motor effort in robotic control for wrist-hand rehabilitation after stroke. *J. Neural Eng.* 19 (2), 026004. doi:10.1088/1741-2552/AC5757

Irastorza-Landa, N., García-Cossio, E., Sarasola-Sanz, A., Brötz, D., Birbaumer, N., and Ramos-Murguialday, A. (2021). Functional synergy recruitment index as a reliable biomarker of motor function and recovery in chronic stroke patients. *J. Neural Eng.* 18 (4), 046061. doi:10.1088/1741-2552/ABE244

Kawase, T., Sakurada, T., Koike, Y., and Kansaku, K. (2017). A hybrid BMI-based exoskeleton for paresis: EMG control for assisting arm movements. *J. Neural Eng.* 14 (1), 016015. doi:10.1088/1741-2552/aa525f

Lalitharatne, T., Teramoto, K., Hayashi, Y., and Kiguchi, K. (2013). Towards hybrid EEG-EMG-based control approaches to Be used in bio-robotics applications: current status, challenges and future directions. *PALADYN J. Behav. Robotics Rev. Article* 4 (2), 147–154. doi:10.2478/pjbr-2013-0009

Langhorne, P., Coupar, F., and Pollock, A. (2009). Motor recovery after stroke: a systematic review. *Lancet Neurology* 8 (8), 741–754. doi:10.1016/S1474-4422(09)70150-4

Leeb, R., Sagha, H., Chavarriaga, R., and Millán, J. R. (2011). A hybrid brain–computer interface based on the fusion of electroencephalographic and electromyographic activities. *J. Neural Eng.* 8 (2), 025011. doi:10.1088/1741-2560/8/2/025011

Loopez-Larraz, E., Birbaumer, N., and Ramos-Murguialday, A. (2018). "A hybrid EEG-EMG BMI improves the detection of movement intention in cortical stroke patients with complete hand paralysis," in Proceedings of the Annual International Conference of the IEEE Engineering in Medicine and Biology Society, Honolulu, HI, USA, 18-21 July 2018, 2000–2003. doi:10.1109/EMBC.2018.8512711

López-Larraz, E., Birbaumer, N., and Ramos-Murguialday, A. (2019). Designing hybrid brain-machine interfaces to detect movement attempts in stroke patients. *Biosyst. Biorobotics* 21, 897–901. doi:10.1007/978-3-030-01845-0_180/FIGURES/1

López-Larraz, E., Sarasola-Sanz, A., Birbaumer, N., and Ramos-Murguialday, A. (2024). Unveiling movement intention after stroke: integrating EEG and EMG for motor rehabilitation. bioRxiv. Available at: https://doi.org/10.1101/2024.02.22.581596.

Müller-Putz, G. R., Breitwieser, C., Cincotti, F., Leeb, R., Schreuder, M., Leotta, F., et al. (2011). Tools for brain-computer interaction: a general concept for a hybrid BCI. *Front. Neuroinformatics* 5, 30. doi:10.3389/fninf.2011.00030

Pichiorri, F., Toppi, J., de Seta, V., Colamarino, E., Masciullo, M., Tamburella, F., et al. (2023). Exploring high-density corticomuscular networks after stroke to enable a hybrid brain-computer interface for hand motor rehabilitation. *J. NeuroEngineering Rehabilitation* 20 (1), 5–14. doi:10.1186/s12984-023-01127-6

Ramos-Murguialday, A., Broetz, D., Rea, M., Läer, L., Yilmaz, Ö., Brasil, F. L., et al. (2013). Brain-machine interface in chronic stroke rehabilitation: a controlled study. *Ann. Neurology* 74 (1), 100–108. doi:10.1002/ana.23879

Roh, J., Rymer, W. Z., Perreault, E. J., Yoo, S. B., and Beer, R. F. (2013). Alterations in upper limb muscle synergy structure in chronic stroke survivors. *J. Neurophysiology* 109 (3), 768–781. doi:10.1152/jn.00670.2012

Sarasola-Sanz, A., Irastorza-Landa, N., López-Larraz, E., Bibián, C., Helmhold, F., Broetz, D., et al. (2017). "A hybrid brain-machine interface based on EEG and EMG activity for the motor rehabilitation of stroke patients," in IEEE International Conference on Rehabilitation Robotics, London, UK, 17-20 July 2017, 895–900. doi:10.1109/ICORR.2017.8009362

Sarasola-Sanz, A., Irastorza-Landa, N., López-Larraz, E., Shiman, F., Spüler, M., Birbaumer, N., et al. (2018). Design and effectiveness evaluation of mirror myoelectric interfaces: a novel method to restore movement in hemiplegic patients. *Sci. Rep.* 8 (1), 16688–16713. doi:10.1038/s41598-018-34785-x

Sarasola-Sanz, A., Irastorza-Landa, N., Shiman, F., Lopez-Larraz, E., Spuler, M., Birbaumer, N., et al. (2015). "EMG-based multi-joint kinematics decoding for robot-aided rehabilitation therapies," in 2015 IEEE International Conference on Rehabilitation Robotics (ICORR), Singapore, 11-14 August 2015, 229–234. doi:10.1109/ICORR.2015.7281204

Sarasola-Sanz, A., López-Larraz, E., Irastorza-Landa, N., Rossi, G., Figueiredo, T., McIntyre, J., et al. (2022). Real-time control of a multi-degree-of-freedom mirror myoelectric interface during functional task training. *Front. Neurosci.* 16, 764936. doi:10.3389/fnins.2022.764936

Sartori, M., Durandau, G., Došen, S., and Farina, D. (2018). Robust simultaneous myoelectric control of multiple degrees of freedom in wrist-hand prostheses by real-time neuromusculoskeletal modeling. *J. Neural Eng.* 15 (6), 066026. doi:10.1088/1741-2552/aae26b

Schlögl, A., Keinrath, C., Zimmermann, D., Scherer, R., Leeb, R., and Pfurtscheller, G. (2007). A fully automated correction method of EOG artifacts in EEG recordings. *Clin. Neurophysiol.* 118 (1), 98–104. doi:10.1016/J.CLINPH.2006.09.003

Takeuchi, N., and Izumi, S.-I. (2012). Maladaptive plasticity for motor recovery after stroke: mechanisms and approaches. *Neural Plast.* 2012, 1–9. doi:10.1155/2012/359728

Tortora, S., Tonin, L., Chisari, C., Micera, S., Menegatti, E., and Artoni, F. (2020). Hybrid human-machine interface for gait decoding through bayesian fusion of EEG and EMG classifiers. *Front. Neurorobotics* 14, 582728. doi:10.3389/fnbot.2020.582728

Urra, O., Casals, A., and Jané, R. (2014). "Synergy analysis as a tool to design and assess an effective stroke rehabilitation," in 2014 36th Annual International Conference of the IEEE Engineering in Medicine and Biology Society, Chicago, IL, USA, 26-30 August 2014, 3550–3553. doi:10.1109/EMBC.2014.6944389

Vidaurre, C., and Blankertz, B. (2010). Towards a cure for BCI illiteracy. *Brain Topogr.* 23 (2), 194–198. doi:10.1007/s10548-009-0121-6

Whitall, J., Waller, S. M., Sorkin, J. D., Forrester, L. W., Macko, R. F., Hanley, D. F., et al. (2011). Bilateral and unilateral arm training improve motor function through differing neuroplastic mechanisms: a single-blinded randomized controlled trial. *Neurorehabilitation Neural Repair* 25 (2), 118–129. doi:10.1177/1545968310380685

Young, J., and Forster, A. (2007). Review of stroke rehabilitation. *BMJ. Br. Med. J. Int. Ed.* 334 (7584), 86–90. doi:10.1136/bmj.39059.456794.68

Zhang, J., Wang, B., Zhang, C., Xiao, Y., and Wang, M. Y. (2019). An EEG/EMG/EOG-Based multimodal human-machine interface to real-time control of a soft robot hand. *Front. Neurorobotics* 13, 7. doi:10.3389/fnbot.2019.00007

frontiers | Frontiers in Bioengineering and Biotechnology

TYPE Original Research
PUBLISHED 29 April 2024
DOI 10.3389/fbioe.2024.1389243

OPEN ACCESS

EDITED BY
Wujing Cao,
Chinese Academy of Sciences (CAS), China

REVIEWED BY
Yaonan Zhu,
Nagoya University, Japan
Benyan Huo,
Zhengzhou University, China

*CORRESPONDENCE
Xingang Zhao,
zhaoxingang@sia.cn
Bi Zhang,
zhangbi@sia.cn

RECEIVED 21 February 2024
ACCEPTED 08 April 2024
PUBLISHED 29 April 2024

CITATION
Li M, Zhang B, Liu L, Tan X, Li N and Zhao X (2024), Balance recovery for lower limb exoskeleton in standing posture based on orbit energy analysis.
Front. Bioeng. Biotechnol. 12:1389243.
doi: 10.3389/fbioe.2024.1389243

Balance recovery for lower limb exoskeleton in standing posture based on orbit energy analysis

Mengze Li[1,2,3], Bi Zhang[1,2]*, Ligang Liu[4], Xiaowei Tan[1,2], Ning Li[1,2] and Xingang Zhao[1,2]*

[1]State Key Laboratory of Robotics, Shenyang Institute of Automation, Chinese Academy of Science, Shenyang, China, [2]Institutes for Robotics and Intelligent Manufacturing, Chinese Academy of Sciences, Shenyang, China, [3]Research Center for Frontier Fundamental Studies, Zhejiang Lab, Hangzhou, China, [4]BYD Auto Industry Company Limited, Shenzhen, China

Introduction: The need for effective balance control in lower limb rehabilitation exoskeletons is critical for ensuring stability and safety during rehabilitation training. Current research into specialized balance recovery strategies is limited, highlighting a gap in biomechanics-inspired control methods.

Methods: We introduce a new metric called "Orbit Energy" (OE), which assesses the balance state of the human-exoskeleton system based on the dynamics of the overall center of mass. Our control framework utilizes OE to choose appropriate balance recovery strategies, including torque controls at the ankle and hip joints.

Results: The efficacy of our control algorithm was confirmed through Matlab Simulink simulations, which analyzed the recovery of balance under various disturbance forces and conditions. Further validation came from physical experiments with human subjects wearing the exoskeleton, where a significant reduction in muscle activation was observed during balance maintenance under external disturbances.

Discussion: Our findings underscore the potential of biomechanics-inspired metrics like OE in enhancing exoskeleton functionality for rehabilitation purposes. The introduction of such metrics could lead to more targeted and effective balance recovery strategies, ultimately improving the safety and stability of exoskeleton use in rehabilitation settings.

KEYWORDS

wearable exoskeleton, balance assistance, rehabilitation, bio-inspired control, model predictive control

1 Introduction

Rehabilitation training is crucial for enhancing the quality of life of patients, particularly in restoring capabilities such as standing and walking (Siviy et al., 2023). Standing balance is a core component of rehabilitation training, essential for maintaining independence and safety in daily life activities (Afschrift et al., 2022). Exoskeleton robots, as innovative assistive technologies, have demonstrated unique value in rehabilitation training. Studies have shown that exoskeletons significantly improve the efficacy of standing and walking training, especially for patients with lower limb disabilities, by providing controlled and repetitive training environments (Rodríguez-Fernández et al., 2021; Zhou et al., 2021). Additionally, the use of exoskeletons is associated with multiple health benefits, including improved blood circulation, reflex activities, and bowel and bladder functions (Zhou et al., 2021; Beck et al., 2023). In neurological patients, rehabilitation using exoskeletons has been shown to aid

significantly in advancing standing and walking skills while reducing the risk of falls (Lippi and Mergner, 2020; Postol et al., 2021).

To date, there has been notable progress in the development of control technologies for exoskeleton robots (Su et al., 2023), focusing primarily on compliance and interaction. For instance, Zhou et al. emphasized research progress in Lower Limb Rehabilitation Exoskeleton Robots (LLRER), particularly in mechanical design and control technologies (Zhou et al., 2021). Another study specifically analyzed the application of human gait analysis in the design and control of LLRERs (Shi et al., 2019). Additionally, several studies focused on the latest advancements in exoskeleton technology, especially in lower limb motion assistance (Siviy et al., 2023).

The importance of balance control in exoskeletons has been recognized in some research, but a comprehensive exploration of this vital aspect remains lacking (Baud et al., 2021). For example, a study on spinal cord injury patients explored the application of ground-walking exoskeletons in rehabilitation, mentioning gait speed and pain management, but discussions on balance were not comprehensive (Postol et al., 2021). Another research focusing on LLRERs for stroke patients highlighted the importance of providing support and balance in rehabilitation training tasks, yet specific balance control algorithms were not deeply studied (Farkhatdinov et al., 2019). Furthermore, studies on neurological patients using exoskeletons indicated that despite progress in rehabilitating standing and walking skills, challenges such as postural instability and risk of falls highlight the importance of balance control (Lippi and Mergner, 2020).

Only a limited number of studies have focused on enhancing the balance performance of exoskeletons by adjusting joint stiffness or implementing impedance control strategies. For example, Ugurlu et al. proposed (Ugurlu et al., 2015) ankle joint variable stiffness control, Karavas et al. (2013) and hou et al. proposed (Huo et al., 2021) impedance control, Rajasekaran et al. proposed (Rajasekaran et al., 2015) adaptive balance recovery strategy, focuses on specific joints or aspects of balance, and Sugiura et al. proposed (Sugiura et al., 2023a; Sugiura et al., 2023b) support polygon control that assists balance during actions such as standing, kneeling, and sit-to-stand transfers by expanding the support polygon in accordance with shifts in the center of gravity position. Comprehensive approaches that integrate the influence of the wearer and the entire human-exoskeleton system's dynamics are still evolving (Stegall et al., 2013).

Collectively, these studies suggest that while significant advancements have been made in the application of exoskeleton technology in the field of rehabilitation, especially in enhancing interaction and adapting to human motion, Specialized algorithms designed specifically for standing balance control are relatively scarce. This indicates that ensuring the stability and safety of standing balance remains a key issue to be addressed in the research and application of exoskeleton robots.

Given their structural and functional similarities to bipedal robots, lower limb exoskeletons can benefit from bipedal robots' balance strategies (Peng et al., 2017). In the field of bipedal robots, notable advancements in stability assessment and balance recovery control have been made (Stephens, 2007; Millard et al., 2009; Stephens and Atkeson, 2010; van der Kooij et al., 2016). For example, Stephens and Atkeson (2010) proposed a Push Recovery Model Predictive Control (PR-MPC) for adjusting stride against external forces, while Wieber (2006) developed a linear MPC scheme for dynamic disturbance compensation. Nishiwaki and Kagami (2009) achieved stable walking

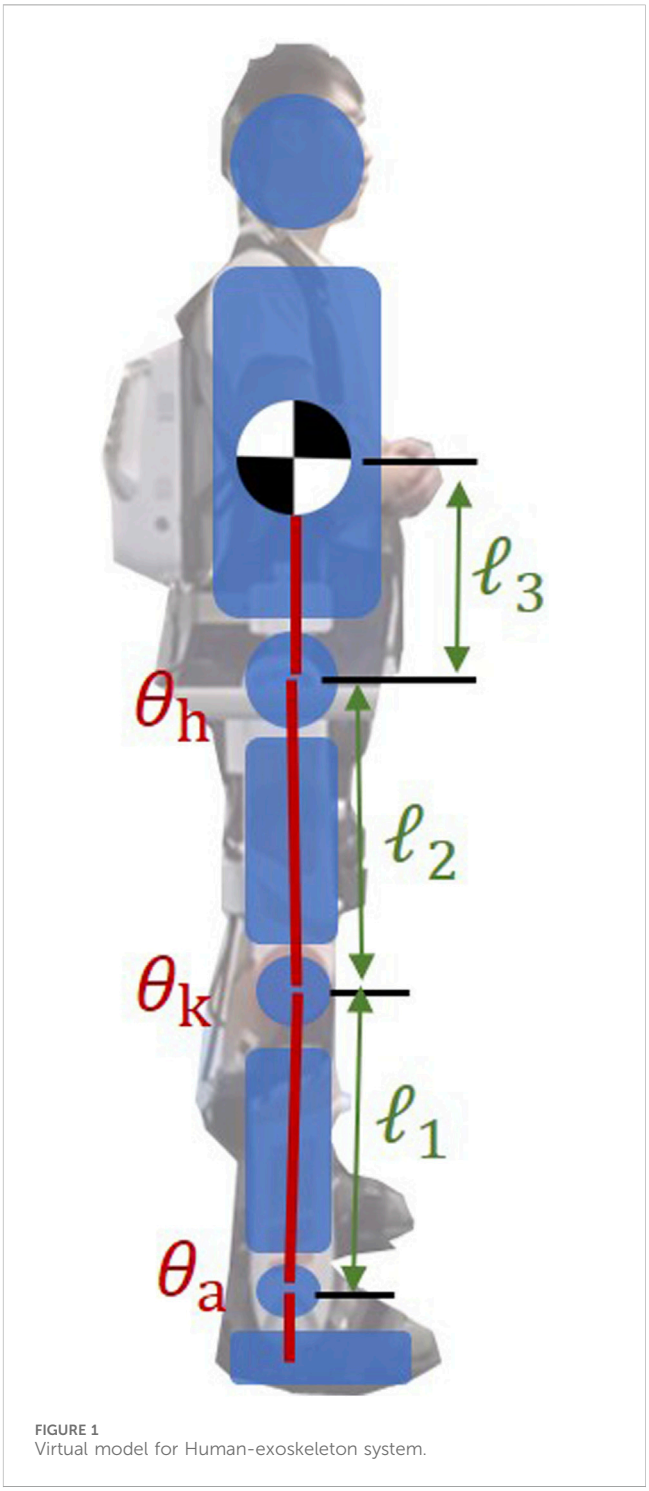

FIGURE 1
Virtual model for Human-exoskeleton system.

with an updateable predictive controller, and Englsberger et al. (2015) introduced subject-time control for three-dimensional DCM trajectories.

The integration of balance strategies from bipedal robots into exoskeleton systems encounters distinct challenges, especially due to the disparities between bipedal robotics and the exoskeleton-human systems. Bipedal robots typically rely on model-based control approaches, necessitating the identification of a model that aptly simulates both bipedal robotics and the exoskeleton-human systems, thereby becoming a pivotal element for the adaptation of successful algorithms. The Flywheel Inverted Pendulum (FIP) model offers a

pivotal solution in bridging these disparities. Employed as a prevalent model for balance control, it utilizes the inertia of the trunk and the torques of the lower limbs to negate external perturbations, a strategy that closely mirrors the balance tactics of the human. This approach not only encapsulates the dynamic balance mechanisms inherent to humans but also provides a foundational basis for advancing balance control technologies within exoskeleton robotics.

In this paper, we present a control framework for standing balance in lower limb exoskeleton robots, with 'Orbit Energy' (OE) serving as a balance evaluation metric. The framework integrates torque controllers for the ankle and hip joints. The control system, based on the OE and Flywheel Inverted Pendulum model, assesses the human-machine system's balance state and selects appropriate control strategies. The effectiveness of the algorithm is verified through Matlab Simulink and tests with a physical exoskeleton robot. By examining changes in muscle activity during push-recovery experiments with subjects, we analyze how the proposed method aids in balance recovery.

2 Model and orbit energy

2.1 Virtual model

The integrated system of a human wearing an exoskeleton robot is effectively represented through a virtual model. This model, initially introduced by Pratt J. and colleagues (Pratt et al., 2001), serves as a computational framework within robotics and control systems to simulate dynamic interactions. It abstractly constructs components such as springs, dampers, and forces, which, although not physically present, are essential for mathematically simulating the system's dynamics. To enhance understanding, Figure 1 now includes detailed annotations and vectors representing the equivalent torques at the hip, knee, and ankle joints, alongside a simplified diagram that maps these virtual components to their respective physical counterparts in the exoskeleton structure. This visualization aids in comprehending how virtual forces and torques are applied within the model to mimic real-world physical interactions between the user and the exoskeleton.

$$\begin{bmatrix} x \\ z \\ \theta \end{bmatrix} = \begin{bmatrix} l_1 S_a + l_2 S_{ak} + l_3 S_{akh} \\ l_1 C_a + l_2 C_{ak} + l_3 C_{akh} \\ \theta_1 + \theta_2 + \theta_3 \end{bmatrix} \tag{1}$$

Here, l_1, l_2 and l_3 stand for the lower leg's length, the thigh's length, and the distance between the hip joint and the body's center of mass. The angles of the hip, knee, and ankle joints are denoted by θ_h, θ_k and θ_a respectively. Additionally, the terms S_{ak} and C_{ak} represent the shorthand for $\sin(\theta_a + \theta_k)$ and $\cos(\theta_a + \theta_k)$.

Taking the derivative of Eq. 1 provides Eq. 2, the Jacobian matrix during a bipedal stance:

$$J = \begin{bmatrix} l_1 C_a + l_2 C_{ak} + l_3 C_{akh} & l_2 C_{ak} + l_3 C_{akh} & l_3 C_{akh} \\ -l_1 S_{a1} - l_2 S_{ak} - l_3 S_{akh} & -l_2 S_{ak} - l_3 S_{akh} & -l_3 S_{akh} \\ 1 & 1 & 1 \end{bmatrix} \tag{2}$$

Using this Jacobian matrix, it is possible to compute the equivalent joint torque from the virtual force and torque at the center of mass, as shown in Eq. 3:

$$\begin{bmatrix} \tau_a \\ \tau_k \\ \tau_h \end{bmatrix} = J^T \begin{bmatrix} F_x \\ F_z \\ \tau \end{bmatrix} \tag{3}$$

In this context, the variables τ_a, τ_k, τ_h represent the torques exerted on the ankle, knee, and hip joints, respectively, while F_x, F_z and τ denote the resultant force and torque acting upon the body's center of mass. Upon expanding the equation, we arrive at the following Eq. 4:

$$\begin{aligned} \tau_a &= (l_1 C_a + l_2 C_{ak} + l_3 C_{akh}) F_x - (l_1 S_{a1} + l_2 S_{ak} + l_3 S_{akh}) F_z + \tau \\ \tau_k &= (l_2 C_{ak} + l_3 C_{akh}) F_x - (l_2 S_{ak} + l_3 S_{akh}) F_z + \tau \\ \tau_h &= l_3 C_{akh} F_x - l_3 S_{akh} F_z + \tau \end{aligned} \tag{4}$$

In the context of human standing, the knee remains unbent, thereby rendering the torque at the knee joint, denoted by τ_k, equal to zero. Consequently, we deduce Eq. 5:

$$\tau = (l_2 S_{ak} + l_3 S_{akh}) F_x - (l_2 C_{ak} + l_3 C_{akh}) F_z \tag{5}$$

Upon substituting Eq. 4 into Eq. 3 with the condition $\theta_k = 0$, and following a process of simplification and reorganization, we obtain the following Eq. 6:

$$\tau_a + \tau_h = (l_1 + l_2) S_a F_x - (l_2 + l_2) C_a + F_z \tag{6}$$

We observe that the forces acting on the Center of Mass (CoM), denoted as F_x and F_z, are independent of the link length l_3 and the angle θ_h. For simplification purposes, the term $(l_1 + l_2)S_a$ is represented as z, and $(l_1 + l_2)C_a$ is represented as x.

Further assuming that the vertical distance between the CoM and the ground remains constant, denoted as $z \equiv z_0$, and considering that $F_x = m\ddot{x}$ and $F_z = mg$, we derive the following Eq. 7:

$$\ddot{x} = \omega^2 x + \frac{\tau_a}{z_0 m} + \frac{\tau_h}{z_0 m} \tag{7}$$

For an exoskeleton in a standing position, to prevent any slip between the exoskeleton footplate and the ground, it is crucial that the virtual force complies with the condition: $F_x/F_z < \mu$, where μ symbolizes the static friction coefficient of the surface. Concurrently, to ensure that both feet remain grounded, the virtual force should also adhere to the condition:$F_z > 0$.

2.2 Simplified model and orbital energy

Based on Eq. 7, and subject to certain constraints, the virtual model can be effectively simplified to a Flywheel Inverted Pendulum (FIP) Model. As depicted in Figure 2, this model consists of a scalable, massless link, denoted as l, a mass flywheel, which is controllable via a torque τ, and a foot with a finite length ranging from $-r_1$ to r_2. The combined center of mass of both the wearer and the exoskeleton system is represented by the center of this mass flywheel.

Pratt et al. (2006) conducted a detailed analysis of the balance recovery theory for the flywheel inverted pendulum model under disturbances, which can be articulated using the energy orbit expression by Kajita et al. (2010). The system can be conceptualized as a spring with unit mass and a stiffness of $-g/z_0$. The orbital energy is expressed as the difference between kinetic and potential energy, as shown in Eq. 8:

$$E_{LIP} = \frac{1}{2}\dot{x}^2 - \frac{g}{2z_0}x^2 \tag{8}$$

'Capture Point' refers to a specific point on the ground where, if the robot steps, it can achieve balance and stop without further

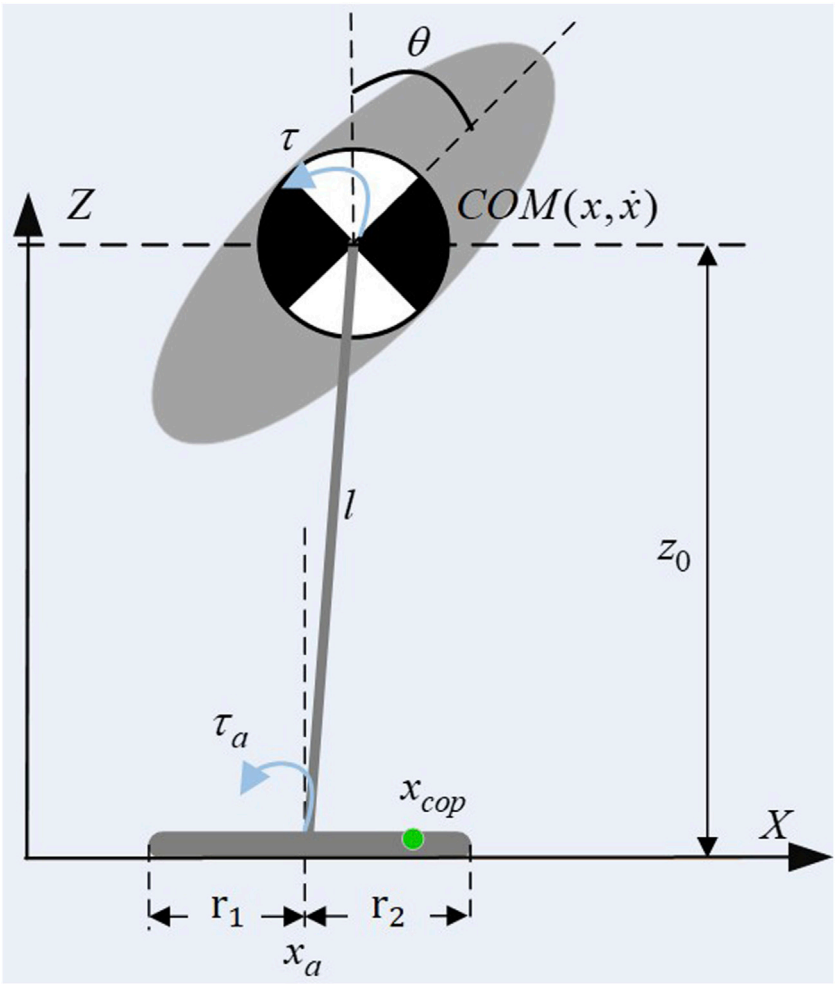

FIGURE 2
Flywheel inverted pendulum with finite feet.

movement. The system's capture point can be determined when $E_{LIP} = 0$, leads us to the following Eq. 9:

$$x_{cp} = \dot{x}\sqrt{\frac{z_0}{g}} \tag{9}$$

where z_0 represents the constant height of the overall center of mass of the human-machine system relative to the ground, g is the gravitational acceleration. The condition $E_{LIP} = 0$ leads to two solutions: $\dot{x} = \pm x\sqrt{g/z_0}$. The negative solution $\dot{x} = -x\sqrt{g/z_0}$ indicates that without external forces, the system will naturally tend to return to the initial balanced state. In contrast, the positive solution $\dot{x} = x\sqrt{g/z_0}$ relates to the capture point, where the robot steps forward to a new equilibrium, stopping further motion.

Figure 3 shows the phase diagram of a FIP, the straight line formed by the position and velocity of the center of mass is called a stable orbit. For a given state, FIP only has one capture point, and its state is transformed into a stable eigenvector.

In order to apply the CP balance evaluation index to exoskeleton robots, we propose the 'Orbit Energy' (OE) to evaluate the stability of the human-exoskeleton system. OE is defined in Eq. 10:

$$S = x + \frac{\dot{x}}{\omega} \tag{10}$$

By inputting the centroid position and velocity of the human-exoskeleton system, the current stable state of the system can be determined. When subjected to external disturbances, substituting the position x and velocity $\dot{x}$ into Eq. 10 yields an orbit energy.

For the FIP system, an OE threshold *Sth* exists. When the orbit offset caused by disturbances is less than this threshold, i.e., $S < Sth$, the system can autonomously recover stability.

3 Balance recovery strategy

Research on human balance mechanisms underscores the importance of the hip and ankle joints in regaining equilibrium after disturbances, as highlighted in studies like (Winter, 1995). Healthy individuals, despite having most of their body mass located far from the ground, can adeptly recover balance due to their flexible joints, developed muscles, and the cerebellum's sophisticated motor control.

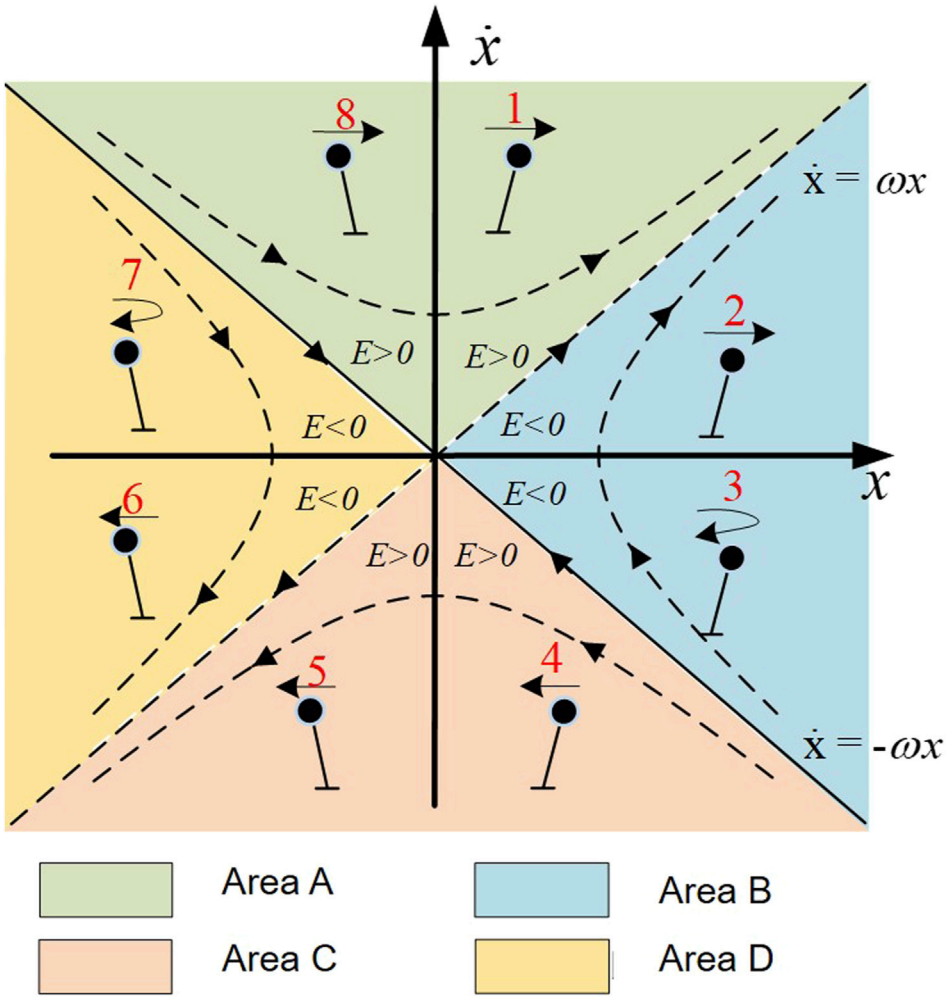

FIGURE 3
Diagram of orbital energy.

However, the engineering technologies, degrees of freedom, flexibility, and control systems in current lower limb exoskeleton robots do not fully match these human balance mechanisms. Insights gained from human balance recovery strategies, as identified in research such as Winter's (Winter, 1995), are crucial. These strategies, specifically the ankle and ankle-hip strategies, are the focus of this paper, while the step strategy is considered out of scope.

3.1 Self-stabilization range

To better analyze the characteristics of FIP using EO, Eq. 8 can be reformulated into a state-space representation as Eq. 11:

$$\begin{bmatrix} \dot{x} \\ \ddot{x} \end{bmatrix} = \begin{bmatrix} 0 & 1 \\ \omega^2 & 0 \end{bmatrix} \begin{bmatrix} x \\ \dot{x} \end{bmatrix} + \begin{bmatrix} 0 & 0 \\ \frac{1}{z_0 m} & \frac{1}{z_0 m} \end{bmatrix} \begin{bmatrix} \tau_a \\ \tau_h \end{bmatrix} \tag{11}$$

In this context, the state vector is defined as $x = [\, x \;\; \dot{x} \,]^T$ representing the position and velocity, while the torques applied by the ankle and hip joints are denoted by $u = [\, \tau_a \;\; \tau_h \,]^T$. The output is represented as Eq. 12:

$$y = \begin{bmatrix} 1 & \frac{1}{\omega} \end{bmatrix} \begin{bmatrix} x \\ \dot{x} \end{bmatrix} \tag{12}$$

The output variable $y(k)$ represents the capture point position, which is also the target variable we want to optimize and control. In the absence of joint torque assistance for balance, that is, when τ_a and τ_h, we can derive the open-loop analytical solution of the state space Eq. 13:

$$\begin{bmatrix} x \\ \dot{x} \end{bmatrix} = \begin{bmatrix} cosh(\omega t) & \frac{1}{\omega} sinh(\omega t) \\ \omega sinh(\omega t) & cosh(\omega t) \end{bmatrix} \begin{bmatrix} x_0 \\ \dot{x}_0 \end{bmatrix} \tag{13}$$

The contact between the exoskeleton robot's foot and the ground is not a single point but rather an area. When the capture point lies within this area, the system can autonomously regain balance without external assistance. This area is denoted as Eq. 14:

$$-r_1 < x + \frac{\dot{x}}{\omega} < r_2 \tag{14}$$

Where r_1 and r_2 denote the boundary of the support polygon. Substituting Eq. 13 into the stable constraint Eq. 14 yields Eq. 15:

$$\begin{aligned} -r_1 < x_0 cosh(\omega t) + \dot{x}_0 \frac{1}{\omega} sinh(\omega t) \\ + x_0 sinh(\omega t) + \dot{x}_0 \frac{1}{\omega} cosh(\omega t) < r_2 \end{aligned} \tag{15}$$

When the system's center of mass, represented by x, meets the aforementioned criteria, the system can autonomously regain stability; however, if these conditions are not met, the ankle strategy must be implemented to avert a fall.

3.2 Ankle strategy

The ankle strategy employs torque around the ankle joint to restore balance, particularly effective against minor disturbances by increasing muscle stiffness near the ankle. Drawing from this reflex mechanism, we counteract small external forces on the human-exoskeleton system by applying reverse torque at the exoskeleton's ankle joint, while other joints remain stationary.

The most impactful torque profile on balance is achieved by applying the maximum possible acceleration to the flywheel in a single direction, followed by a deceleration phase that halts the flywheel at its furthest angular position. The expression for the torque is Eq. 16:

$$\tau(t) = \tau_{max} u(t) - 2\tau_{max} u(t - T_{R1}) + \tau_{max} u(t - T_{R2}) \tag{16}$$

The torque at any given time t, denoted by $\tau(t)$, is modeled as starting from a base value determined by the maximum torque $\tau_{\max}$ that the joint is capable of exerting. This initial torque is then modified by a unit step function initiated at time T, which represents the onset of the torque application.

The torque undergoes a reduction, specifically a subtraction of twice the maximum torque, beginning at time T_{R1} which marks the transition from acceleration to deceleration of the flywheel. Finally, an additional instance of the maximum torque is factored in at time T_{R2}, reflecting the moment when the flywheel ceases movement entirely.

At this juncture, the orbit energy (OE) is equivalent to x_{cp}, necessitating an analysis of the system's zero-state and zero-input responses, followed by the simultaneous solution of equations. Pratt has already conducted a detailed derivation of this, which can be referenced in the paper (Pratt et al., 2006). The calculation result is presented as Eq. 17:

$$x_{cp} = -\frac{1}{\omega}\left(-\dot{x}_0 + \frac{\tau_{a,max}}{mg}\left[\frac{e^{\omega T_{R2}} - 2e^{\omega(T_{R2}-T_{R1})} + 1}{e^{\omega T_{R2}}}\right]\right) \tag{17}$$

The position at which the system can be considered captured is given by the negative of x_0. To determine the opposite limit of the Capture Region, one may replicate the process using the minimum torque $\tau_{\min}$.

If the objective is to ascertain a Capture Point devoid of angular momentum influence, the procedure is the same except that T_{R1} is set to zero. The duration T_{R2} should be sufficient to halt any ongoing rotational motion of the flywheel, and thus, the value of x_0 can be calculated in the same manner as previously described.

Based on the calculated capture point x_{cp} position from the equation, if it falls within the support region (i.e., the foot area, between $-r_1$ and r_2), the ankle torque strategy is used for balance recovery; if beyond that range, the strategy of applying torque simultaneously at the ankle and hip joints is needed.

3.3 Ankle-hip strategy

The ankle-hip strategy, which involves applying torque simultaneously to both the ankle and hip joints to restore balance (Winter, 1995), follows a calculation method similar to that of the capture point in the ankle strategy. The derivation here is omitted for brevity, with the resulting expression presented as Eq. 18:

$$x_{cp} = -\frac{1}{\omega}\left(-\dot{x}_0 + \frac{\tau_{a,max} + \tau_{h,max}}{mg}\left[\frac{e^{\omega T_{R2}} - 2e^{\omega(T_{R2}-T_{R1})} + 1}{e^{\omega T_{R2}}}\right]\right) \tag{18}$$

The calculations based on the above equation indicate that when x_{cp} falls within the support polygon, the range between $-r_1$ and r_2, the ankle-hip strategy can be employed.

3.4 Model predictive controller

MPC, often referred to as receding horizon predictive control, is employed here in its discrete-time variant, which is executed through the employment of discrete-time state space functions. Within this framework, the discrete-time state space equation is expressed as a recursive relation, as shown in Eqs 19, 20, where the state vector at any subsequent instant is determined by the present state and control inputs.

$$x(k+1) = Ax(k) + Bu(k) \tag{19}$$

$$y(k) = Cx(k) \tag{20}$$

The system's dynamic behavior is characterized by a linear relationship defined by a state matrix A, a control matrix B and a output matrix C.

The control objective is to regulate the capture point within the support area, ensuring that the final state of the system converges, with the position returning to the origin and velocity reaching zero. Therefore, we transfer the original state space equation into an augmented Eq. 21:

$$\begin{bmatrix} \delta x(k+1) \\ y(k+1) \end{bmatrix} = \begin{bmatrix} A & 0 \\ CA & 1 \end{bmatrix} \begin{bmatrix} \delta x(k) \\ y(k) \end{bmatrix} + \begin{bmatrix} B \\ CB \end{bmatrix} \delta u(k) \tag{21}$$

In this context, the augmented state vector is defined as $x = [\,\delta x \;\; y\,]^T$ representing the state of the system and capture point. Consequently, the augmented output vector encompasses both the system state and the system output. This integration facilitates the application towards control objectives, as illustrated in Eq. 22:

$$y(k) = \begin{bmatrix} 0 & 1 \end{bmatrix} \begin{bmatrix} \delta x(k) \\ y(k) \end{bmatrix} \tag{22}$$

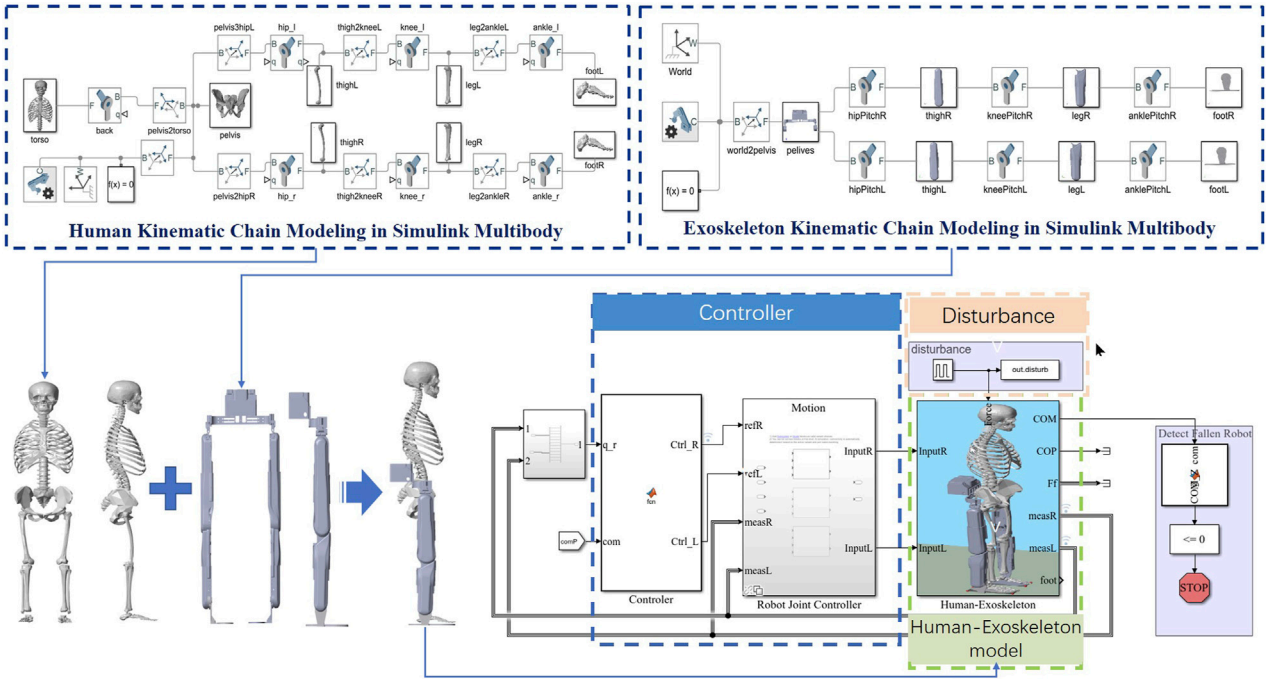

FIGURE 4
Simulation science and MPC control frame.

To effectively implement MPC under the constraint of boundary conditions, it is imperative to define a cost function and constraints across a defined finite horizon.

$$\begin{aligned} \underset{u}{\text{minimize}} \quad & J = \sum_{k=0}^{N} y(k)^T Q y(k) + \delta u(k)^T R \delta u(k) \\ \text{subject to} \quad & -r_1 \le y(k) \le r_2, \ k = 1, \ldots, N, \\ & \tau_{\min} \le u(k) \le \tau_{\max}, \ k = 1, \ldots, N, \\ & \theta_{\min} \le \theta_a(k) \le \theta_{\max}, \ k = 1, \ldots, N, \\ & \theta_{\min} \le \theta_h(k) \le \theta_{\max}, \ k = 1, \ldots, N. \end{aligned} \tag{23}$$

This cost function, Eq. 23, is composed of the cumulative stage costs. Each stage cost is a quadratic function of the state and control input vectors, which are weighted by the matrices Q and R, respectively.

$$\tau_{opt} = \left[\tau_{opt}(0), \tau_{opt}(1), \ldots, \tau_{opt}(N-1)\right] \tag{24}$$

$$x_{opt} = \left[x_{opt}(1), x_{opt}(2), \ldots, x_{opt}(N)\right] \tag{25}$$

Solved via an optimization solver, Eq. 24 and 25, the optimal control sequence τ_{opt} and x_{opt} are obtained. This includes the initial control signal $\tau_{opt}(0)$ applied to the system, consequently generating the actual state $x(1)$.

These actual states, $x(k)$, are measured and may align with or differ from the predicted states $x_{opt}(k)$. At the next time step, these actual states serve as the new starting point for the subsequent optimization problem, occurring at the sample time k. This process is cyclically repeated by the MPC, which consistently recalibrates the control inputs for the system based on the latest observed state. This leads to a continuous observation and adjustment cycle, making the MPC a recursive algorithm for achieving optimal control.

4 Simulation verification

4.1 Simulation environment

In order to verify the effectiveness of the balance recovery control strategy, provide reference data for human-exoskeleton experiments, and ensure the safe and orderly conduct of human-exoskeleton experiments, we built a human-machine system model in Matlab Simulink SimMechanics and conducted simulation verification. The lower limb exoskeleton model is modeled using Solidworks and the model parameters are imported into SimMechanics, as shown in Figure 4.

The exoskeleton robot has a mass of 26 kg, with each leg equipped with hip joint flexion/extension (HFE), hip abduction/adduction (HAA), hip medial and lateral rotation (HMR), knee joint flexion/extension (KFE), ankle joint dorsiflexion/plantar flexion (DF/PF), and ankle inversion/eversion (AIE), totaling 6 degrees of freedom per leg.

4.2 Simulation setup

The mass of the human body model is 75 kg, the mass of the exoskeleton model is 26 kg, and the length of the exoskeleton sole plate is 0.26 m (the connection between the ankle joint and the sole of the foot is in the forward and backward direction). The stiffness of ADP is set to 130 Nm, the damping is set to 5, and the maximum torque is set to 70Nm; The stiffness of HFE and KFE is set to 1000N, and the damping is set to 10; Prohibit movement of HML, HAA, AEI.

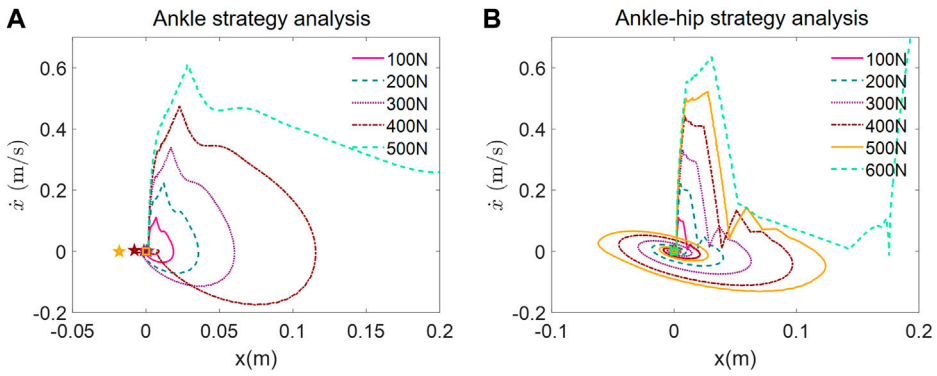

FIGURE 5
Phase portrait of push recovery simulation. **(A)** Ankle strategy analysis. **(B)** Ankle-hip strategy analysis.

Simulation 1: We applied an ankle strategy for balance recovery in an exoskeleton, inducing pulse disturbances ranging from 0 to 500 N on the backpack. Each disturbance was 0.5 s long with a 10-s interval. Disturbances increased by 10 N increments, over 101 simulations. No additional countermeasures were used if the strategy failed.

Simulation 2: The ankle-hip strategy was tested with disturbances from 0 to 600N, also in 10 N increments and with the same duration and interval as Simulation 1. This series included 121 simulations, with no extra measures for failed recoveries.

4.3 Simulation result

Ankle Strategy Analysis: Under the ankle strategy, as shown in Figure 5A, the CoM trajectories exhibit a trend of increasing displacement with higher magnitudes of applied force. The phase plots reveal that for lower disturbances (up to 100 N), the CoM trajectories form tight, closed loops around the origin, indicating effective balance recovery and stability. As the disturbance force increases, the loops become larger and more elongated, suggesting that the ability of the ankle strategy to maintain balance diminishes with greater perturbations.

The trajectories for the highest forces show significant deviation from the origin, indicating that the ankle strategy may not be sufficient to counteract higher levels of disturbance. The absence of additional recovery measures upon strategy failure suggests the importance of implementing multi-joint strategies in exoskeletons for more effective balance recovery.

Ankle-Hip Strategy Analysis: With the implementation of the ankle-hip strategy, as shown in Figure 5B, the CoM trajectories demonstrate a more complex pattern. For disturbances up to 400N, the phase portraits show closed loops, although they appear to be more spread out compared to the ankle strategy, implying a more active and potentially more controlled recovery process. Notably, at disturbances of 500 N and above, the trajectories start to exhibit open loops, indicating instances of failure to recover balance.

The inclusion of the hip strategy appears to enhance the balance recovery capability of the exoskeleton, as evidenced by the ability to withstand higher disturbances before strategy failure. However, similar to the ankle strategy, the ankle-hip strategy also reaches a threshold beyond which it cannot maintain balance, as seen with the 600 N disturbance.

5 Experiment verification

To validate the devised standing balance recovery method for the human-exoskeleton system, we conducted a disturbance experiment utilizing a lower limb exoskeleton robot.

5.1 Milebot exoskeleton BEAR-H1

BEAR-H1, as shown in Figure 6, is a wearable, battery-powered lower-limb exoskeleton developed by Shenzhen Milebot company with the purpose of assisting in gait rehabilitation training. The specification of BEAR-H1 is shown in Table 1. The BEAR-H1 features three actively compliant motor-actuated joints on each leg, facilitating rotations along the hip joint, knee joint, and ankle joint within the sagittal plane. The length of the thigh and calf is adjustable to accommodate individuals with heights ranging from 150 to 190 cm and weighing less than 85 kg. To monitor gait, a touchable screen is integrated beneath the back panel, and a ground reaction force (GRF) sensor is embedded in the sole to detect touchdown events.

5.2 Exoskeleton control framework

The control framework is shown in Figure 7. The depicted control framework for an exoskeleton employs real-time data from an Inertial Measurement Unit (IMU) and sole force sensors to calculate the dynamic state of the system. The system dynamically toggles between ankle and ankle-hip balance strategies, selecting the optimal approach based on the calculated energy state and predefined safety thresholds.

The selected strategy informs an advanced optimization routine within a predictive model that anticipates the exoskeleton's future trajectory, enabling the calculation of ideal control inputs. These inputs modulate the force controller, which drives the motor, and the impedance controller, which fine-tunes the exoskeleton's responsiveness, ensuring the system's stability and congruent assistance with the user's standing.

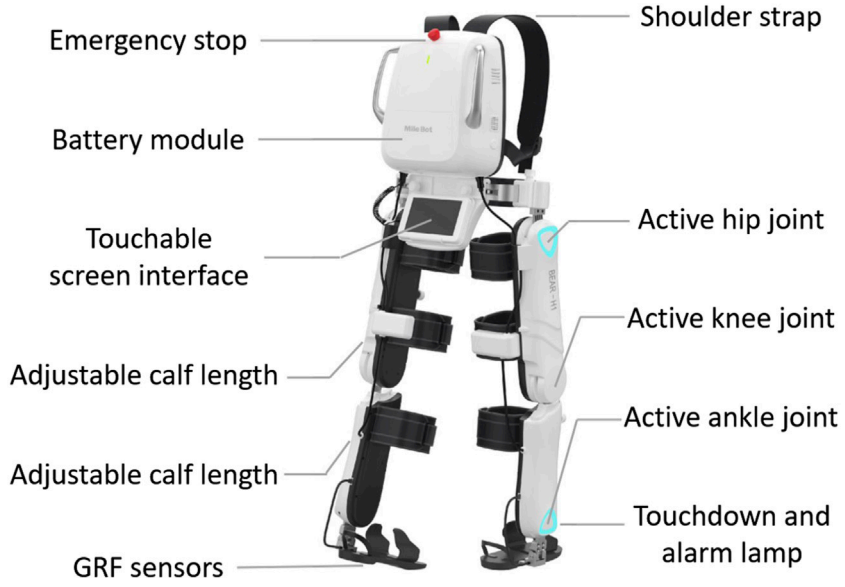

FIGURE 6
Milebot exoskeleton BEAR-H1.

TABLE 1 Specification of Milebot BEAR-H1.

Parts	Parameters
Input Power	21.6 V, 5 A
Equipment mass	26 kg
Maximum patient weight	85 kg
Applicable height range	155 ~ 190 cm
Waist width	290 ~ 420 mm
Thigh length	360 ~ 480 mm
Calf length	345 ~ 450 mm
Signal acquisition frequency	100 Hz

5.3 Experiment setup

Before the experiment started, the participants put on the exoskeleton, and electrodes were affixed to their leg skin for the collection of surface electromyography (sEMG) data. To ensure the safety of the experimental participants, a safety harness was suspended above the treadmill to prevent any unforeseen accidents.

Before each experiment session, participants were explicitly instructed not to engage in proactive balance recovery measures in response to external disturbances. However, it is worth noting that participants with intact limb motor function might exhibit conditioned reflexes leading to the spontaneous adoption of balance recovery strategies.

Research findings have established that the amplitude of sEMG signals reflects the degree of muscle activation and can indirectly indicate muscle strength. To assess the extent of the human body's involvement in the balance recovery process, this study employed EMG acquisition sensors manufactured by NORAXON Company. These sensors were strategically placed on the participant's tibialis anterior (TA), semitendinosus (ST), lateral gastrocnemius muscle (LG), peroneus longus (PL), rectus femoris (RF), vastus medialis (VM), vastus lateralis (VL), and biceps femoris muscle (BF), resulting in a total of 16 channels for sEMG data collection and subsequent calculation of muscle activation.

For this experiment, a group of two healthy male volunteers was selected, with average ages, heights, and weights of 25 ± 2 years old, 1.74 ± 0.08 m, and 69 ± 10.9 kg, respectively. Importantly, none of the participants had a history of neurological disorders.

Experiment 1: Each joint motor of the exoskeleton is configured in zero-torque mode. After each volunteer puts on the exoskeleton, they are given a 3-min period to become acquainted with it. Subsequently, the experiment commences by applying a horizontal forward thrust of 100 N at the position of the exoskeleton backpack. Each thrust lasts approximately 500 milliseconds, with a total of 10 repetitions, and a 5-s interval between each push. Data from the electromyography sensors and the exoskeleton sensors are recorded. The aforementioned procedure is then repeated, but this time with a horizontal backward pulling force of 100 N at the backpack.

Experiment 2: Configure the exoskeleton in ankle strategy mode and replicate the steps outlined in Experiment 1.

Experiment 3: Configure the exoskeleton in ankle-hip strategy mode and replicate the steps outlined in Experiment 1.

5.4 Experiment result and analysis

The experiment scene is shown in Figure 8. The exoskeleton's sensor data is acquired at a frequency of 100Hz, while the sEMG data is sampled at 2000 Hz. The sEMG signal collected by the EMG sensor often contains substantial noise. According to prior research (Chu et al., 2006), the typical frequency range of the sEMG signal falls between 0 and 500 Hz.

10.3389/fbioe.2024.1389243

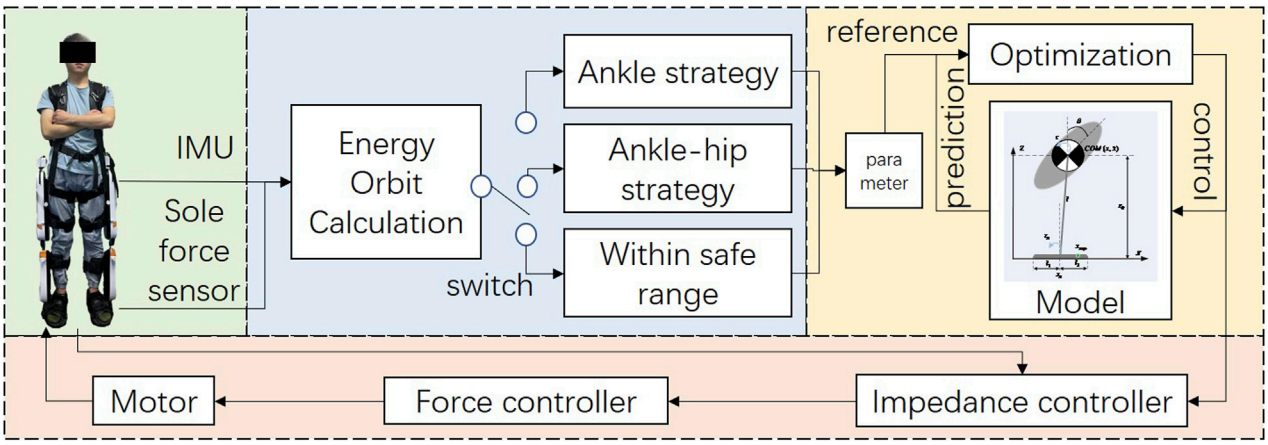

FIGURE 7
Control framework of human-exoskeleton system.

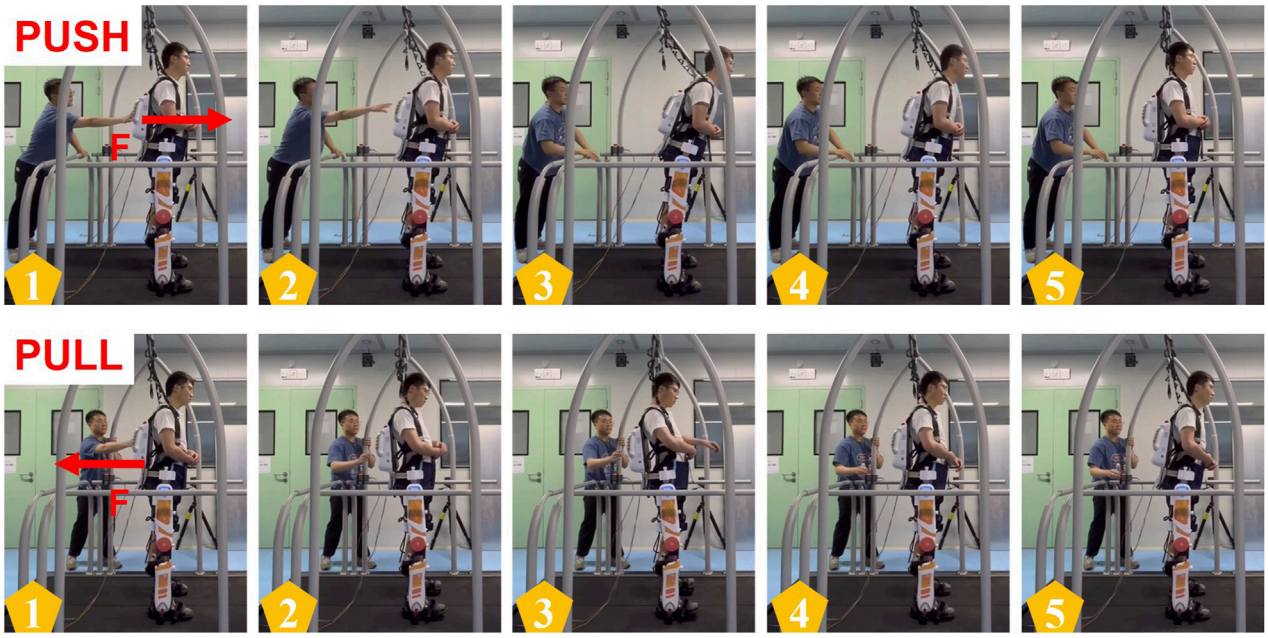

FIGURE 8
Experiment scene of push and pull recovery experiment.

To mitigate the noise present in the EMG signal, we applied pre-processing techniques to the surface sEMG data. This involved a 25 Hz fifth-order Butterworth high-pass filter and rectification, followed by a 5 Hz fifth-order Butterworth low-pass filter, as well as data normalization, as described in previous work (Zhang et al., 2020). The resulting normalized signal was employed for neural activation analysis, utilizing the following Eq. 26:

$$u_j(t) = \alpha e_j(t-d) - \beta_1 u_j(t-1) - \beta_2 u_j(t-2) \tag{26}$$

Where $\beta_1 = C_1 + C_2$, $B_2 = C_1 \cdot C_2$, and $\alpha = \beta_1 + \beta_2 + 1$. The muscle activation a(t) can be denoted as Eq. 27:

$$a_i(t) = \frac{e^{A_i u_i(t)} - 1}{e^{A_I} - 1} \tag{27}$$

Where A is a nonlinear shape coefficient, representing the degree of nonlinearity between nerve activation intensity and muscle activation intensity, and the value range of A is [-3,0] (Mantoan et al., 2015).

5.4.1 Analysis of joint angle responses in exoskeleton-assisted push recovery experiment

Figure 9 depicts data from push recovery Experiment, showing the hip, knee and ankle joint angles over time in

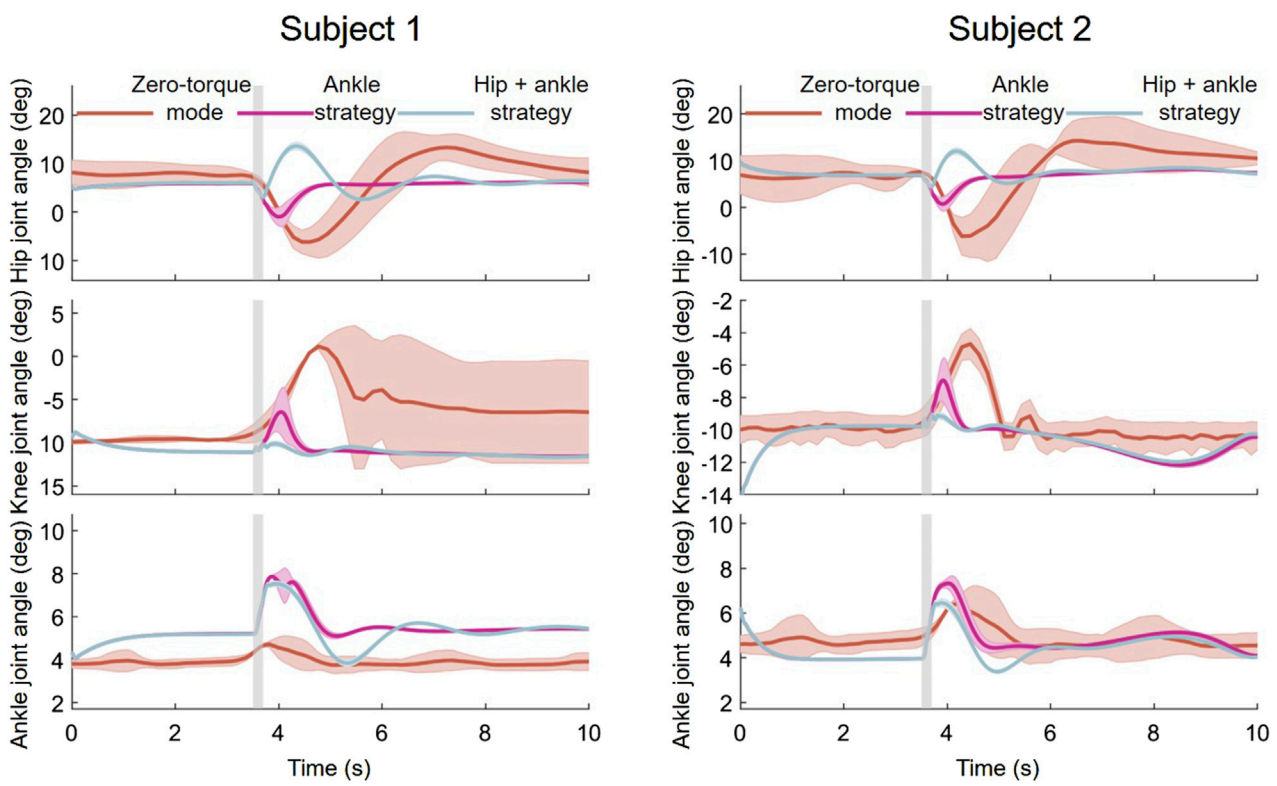

FIGURE 9
Joint angle responses during push recovery experiment.

response to the controlled disturbance. The Figure shows three distinct phases for each joint: Zero-torque mode, Ankle strategy, and Ankle-hip strategy. These phases are likely indicative of different configurations of the exoskeleton used during the experiments.

Zero-torque Mode Analysis: In the zero-torque mode, the exoskeleton does not provide active force assistance, and changes in joint angles are primarily controlled by the subject's autonomous movements. The experimental results indicate that after disturbances, both the hip and ankle joints exhibit certain fluctuations in angles, reflecting the subjects' reliance on their body's innate strategies to regain balance in the absence of exoskeleton assistance.

Ankle Strategy Analysis: When switched to the ankle strategy, the exoskeleton actively adjusts the ankle joint angles to counteract disturbances. In this experiment, the ankle joint's response is more pronounced, suggesting that the ankle strategy plays a key role in maintaining and restoring balance. The hip and knee joints respond less but still make slight adjustments to aid in balancing.

Ankle-Hip Strategy Analysis: In the hip-ankle strategy, the exoskeleton concurrently adjusts both the hip and ankle joints to respond more comprehensively to disturbances. The figures show that the hip joint undergoes more significant dynamic changes, indicating that under this strategy, both the hip and ankle joints work together, providing a more complex mechanism for balance recovery. The knee joint's angle fluctuations also increase, which may accommodate the larger range of motion from the hip and ankle joints.

5.4.2 Analysis of sEMG in exoskeleton-assisted push recovery experiment

The sEMG results depicted in Figure 10 shows the mean and standard deviation of the lower limb muscle activation of the wearer under 10 perturbations in the process of forward and backward pushing, and provides a comparative quantification of muscle activations across three modes of exoskeleton operation, offering insights into the biomechanical implications of each strategy.

Zero-Torque Mode Analysis: In the Zero-torque mode, where the exoskeleton operates without providing active assistance to the wearer, the sEMG data indicates a baseline level of muscle activation. This mode reflects the user's natural muscular response to the perturbations, with moderate activation across all muscle groups. The gastrocnemius muscles display relatively higher activation, which may suggest a natural inclination to utilize the ankle strategy even without exoskeleton assistance.

Ankle Strategy Mode Analysis: Transitioning to the Ankle strategy, there is an apparent shift in the activation pattern. The medial and lateral gastrocnemius muscles exhibit a notable increase in activation, reinforcing their role in the ankle strategy's balance recovery mechanism. This increase suggests that the exoskeleton's ankle strategy enhances the natural response by specifically augmenting the force production in these muscles to stabilize the user following a perturbation.

Ankle-Hip Strategy Mode Analysis: The Hip-ankle strategy mode demonstrates a distributed pattern of muscle activation, with the semitendinosus, and biceps femoris muscles showing significant engagement. This indicates that the hip strategy, when

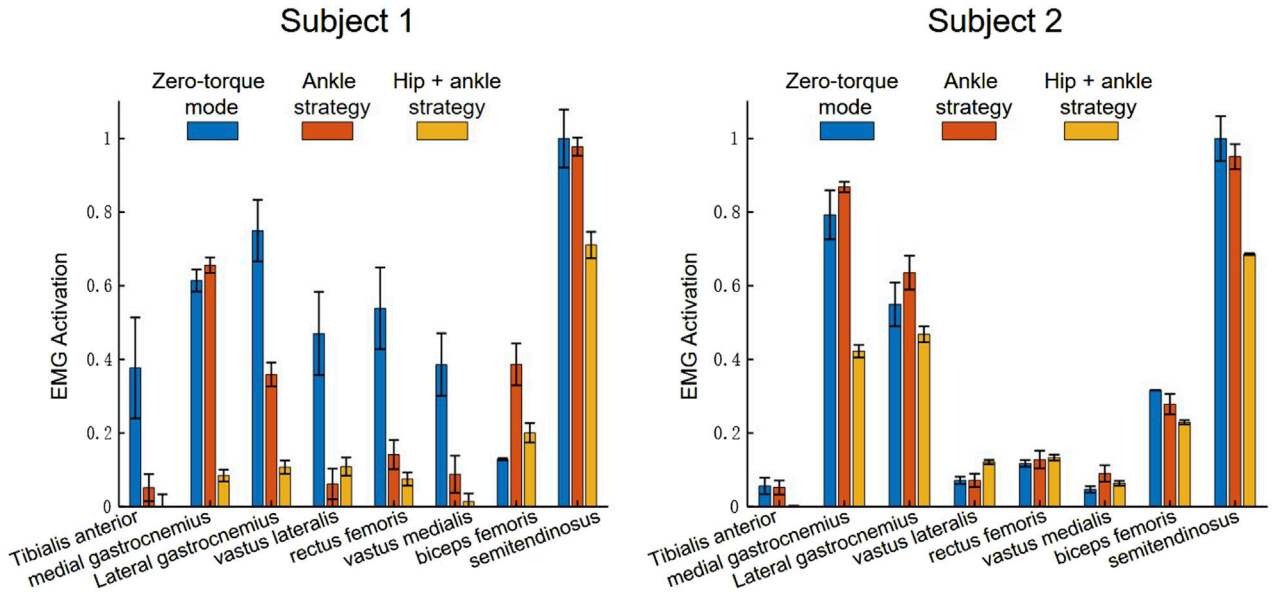

FIGURE 10
sEMG activation during push recovery experiment.

combined with the ankle strategy, does not solely rely on the lower leg muscles but also engages the thigh muscles, likely providing a more robust and comprehensive balance recovery response.

5.4.3 Analysis of muscle activation variability in exoskeleton-assisted push recovery experiment

As shown in Table 2 and Table 3, the mean sEMG activation levels and their associated standard deviations across multiple muscles provide insights into the exoskeleton's effect on muscle engagement.

Muscle Activation Patterns: Across the operational modes, the gastrocnemius muscles (medial gastrocnemius, MG, and lateral gastrocnemius, LG) and the semitendinosus (ST) typically exhibit higher mean activations, indicating their significant role in balance and locomotion tasks. Notably, the mean activation levels for these muscles decrease from Zero-Torque Mode to the Ankle and Hip-Ankle Strategies, suggesting that active assistance by the exoskeleton reduces the muscular effort required by the user. The Ankle Strategy mode often shows a slight increase in muscle activation compared to the Hip-Ankle Strategy, which may reflect the specific demand placed on the ankle muscles to stabilize the posture when the hip is less engaged.

Variability in Activation: The standard deviation percentages reflect the variability in muscle activation within each mode. Generally, a high standard deviation indicates a larger variability in muscle response, which could be attributed to individual differences in muscle control, fatigue levels, or the consistency of the exoskeleton's assistance. A lower standard deviation in the Ankle-Hip Strategy suggests that this mode offers a more consistent level of support, potentially leading to a more predictable and uniform response across different movements and perturbations.

Efficiency of Exoskeleton Assistance: The efficiency of exoskeleton assistance can be inferred from the reduction in mean activation levels from Zero-Torque Mode to the Ankle and Hip-Ankle Strategies. The data indicates that the active control strategies of the exoskeleton likely contribute to a more economical muscle activation, thereby conserving energy for the user.

5.4.4 Summary and discussion

Across all experiments, the mean trajectories of joint angles and their surrounding shaded areas, indicating variability or confidence intervals, provide insight into the consistency of responses among different individuals or repeated trials. In the Ankle and Ankle-Hip strategies, the proximity of the shaded area to the mean trajectory line denotes a higher uniformity in subjects' responses to perturbations, with a reduced variability. These outcomes suggest the efficacy of the "Orbit Energy" metric in conjunction with the MPC controller in dynamically modulating the balance of the human-exoskeleton system, ensuring precise torque control.

The sEMG analysis provides a clear depiction of muscle activation trends across various strategies. The data illustrate a notable refinement in activation patterns and a decrease in the dispersion of muscle responses when employing the Ankle and Ankle-Hip strategies. These strategies, informed by the "Orbit Energy" metric and regulated by the MPC controller, contribute to a more consistent and targeted approach to balance recovery. The resulting reduction in muscle activation variability not only underscores the precision of our control system but also implies a potential decrease in muscular metabolic demand during balance maintenance.

When applied to a wide range of users with different physical characteristics, the current framework presents scalability challenges. This diversity necessitates further research into adaptive algorithms capable of customizing balance recovery strategies to individual user profiles. Additionally, the current study's scope limited the types of disturbances tested; future

TABLE 2 Mean and standard deviation of sEMG activation—subject 1.

Muscle	Zero-torque mode		Ankle strategy		Hip-ankle strategy	
	Mean	SD (%)	Mean	SD (%)	Mean	SD (%)
TA	0.06	2.23%	0.05	1.91%	0.00	0.23%
MG	0.79	6.68%	0.87	1.42%	0.42	1.73%
LG	0.55	5.92%	0.64	4.63%	0.47	2.17%
VL	0.07	1.00%	0.07	1.80%	0.12	0.59%
RF	0.12	0.93%	0.13	2.39%	0.13	0.79%
VM	0.05	0.87%	0.09	2.24%	0.06	0.65%
BF	0.32	0.03%	0.28	2.76%	0.23	0.58%
ST	1.00	6.06%	0.95	3.39%	0.69	0.22%

TABLE 3 Mean and standard deviation of sEMG activation—subject 2.

Muscle	Zero-torque mode		Ankle strategy		Hip-ankle strategy	
	Mean	SD (%)	Mean	SD (%)	Mean	SD (%)
TA	0.38	13.71%	0.05	3.68%	0.00	3.38%
MG	0.61	2.99%	0.66	2.09%	0.08	1.60%
LG	0.75	8.37%	0.36	3.25%	0.11	1.80%
VL	0.47	11.31%	0.06	4.17%	0.11	2.47%
RF	0.54	11.09%	0.14	3.95%	0.08	1.78%
VM	0.39	8.50%	0.09	5.05%	0.01	2.20%
BF	0.13	0.31%	0.39	5.70%	0.20	2.63%
ST	1.00	7.86%	0.98	2.45%	0.71	3.59%

work should explore the system's responsiveness to a wider range of unpredictable real-world scenarios.

6 Conclusion

In this paper, we have presented a control framework for standing balance recovery in lower limb exoskeleton robots. The key innovation lies in using the proposed 'Orbit Energy' (OE) metric to assess balance and trigger appropriate strategies. The OE integrates the position and velocity of the overall center of mass of the human-exoskeleton system. It allows the determination of stable states after disturbances, providing an effective basis for strategy selection. The ankle torque controller recovers balance against minor perturbations. For larger disturbances, the ankle-hip torque controller expands the recovery range. The model predictive control optimizes torque inputs to regulate the capture point within the base of support. Simulations conducted in Simulink verify that the OE threshold successfully distinguishes the self-recovery range from cases needing control assistance. Experiments with human subjects further validate the framework's ability to reduce muscle effort in maintaining balance. This research underscores the significance and innovations of the proposed Orbit Energy metrics, marking a pivotal advancement in managing standing balance control for lower limb exoskeletons.

Our current approach primarily focuses on standing balance, without extending to the complexities of walking balance. Recognizing this limitation, our future research will delve into the fundamental principles of human locomotive balance control. By integrating these principles with the unique characteristics of the human-exoskeleton interface, we aim to develop a comprehensive balance control algorithm tailored for both standing and walking scenarios. This advancement will bridge the current gap in our methodology, offering a more holistic approach to balance management in lower limb exoskeletons.

Data availability statement

The raw data supporting the conclusions of this article will be made available by the authors, without undue reservation.

Ethics statement

The studies involving humans were approved by the Research Ethics Committee of the Shenyang Institute of Automation. The studies were conducted in accordance with the local legislation and institutional requirements. Written informed consent was obtained from the individual(s) for the publication of any potentially identifiable images or data included in this article.

Author contributions

ML: Writing–original draft, Methodology, Writing–review and editing. BZ: Writing–review and editing, Formal Analysis. LL: Validation, Writing–original draft. XT: Data curation, Writing–original draft. NL: Writing–original draft, Investigation. XZ: Writing–review and editing, Supervision.

Funding

The author(s) declare that financial support was received for the research, authorship, and/or publication of this article. This work is supported by the National Key Research and Development Project under Grant Number 2022YFB4703200, and is also supported by the National Natural Science Foundation of China under Grant Number 62333007.

Conflict of interest

Author LL was employed by BYD Auto Industry Company Limited.

The remaining authors declare that the research was conducted in the absence of any commercial or financial relationships that could be construed as a potential conflict of interest.

Publisher's note

All claims expressed in this article are solely those of the authors and do not necessarily represent those of their affiliated organizations, or those of the publisher, the editors and the reviewers. Any product that may be evaluated in this article, or claim that may be made by its manufacturer, is not guaranteed or endorsed by the publisher.

References

Afschrift, M., van Asseldonk, E., van Mierlo, M., Bayon, C., Keemink, A., Van Der Kooij, H., et al. (2022). Assisting walking balance using a bio-inspired exoskeleton controller. *bioRxiv*, 2022–2110. doi:10.1186/s12984-023-01205-9

Baud, R., Manzoori, A. R., Ijspeert, A., and Bouri, M. (2021). Review of control strategies for lower-limb exoskeletons to assist gait. *J. NeuroEngineering Rehabilitation* 18, 119–134. doi:10.1186/s12984-021-00906-3

Beck, O. N., Shepherd, M. K., Rastogi, R., Martino, G., Ting, L. H., and Sawicki, G. S. (2023). Exoskeletons need to react faster than physiological responses to improve standing balance. *Sci. robotics* 8, eadf1080. doi:10.1126/scirobotics.adf1080

Chu, J.-U., Moon, I., and Mun, M.-S. (2006). "A supervised feature projection for real-time multifunction myoelectric hand control," in 2006 International Conference of the IEEE Engineering in Medicine and Biology Society, New York, 3 September 2006 (IEEE), 2417–2420.

Englsberger, J., Ott, C., and Albu-Schäffer, A. (2015). Three-dimensional bipedal walking control based on divergent component of motion. *Ieee Trans. robotics* 31, 355–368. doi:10.1109/tro.2015.2405592

Farkhatdinov, I., Ebert, J., Van Oort, G., Vlutters, M., Van Asseldonk, E., and Burdet, E. (2019). Assisting human balance in standing with a robotic exoskeleton. *IEEE Robotics automation Lett.* 4, 414–421. doi:10.1109/lra.2018.2890671

Huo, W., Moon, H., Alouane, M. A., Bonnet, V., Huang, J., Amirat, Y., et al. (2021). Impedance modulation control of a lower-limb exoskeleton to assist sit-to-stand movements. *IEEE Trans. Robotics* 38, 1230–1249. doi:10.1109/tro.2021.3104244

Kajita, S., Morisawa, M., Miura, K., Nakaoka, S., Harada, K., Kaneko, K., et al. (2010). "Biped walking stabilization based on linear inverted pendulum tracking," in 2010 IEEE/RSJ International Conference on Intelligent Robots and Systems, USA, 18-22 Oct. 2010 (IEEE), 4489–4496.

Karavas, N., Ajoudani, A., Tsagarakis, N., and Caldwell, D. (2013).Human-inspired balancing assistance: application to a knee exoskeleton, 2013 IEEE international conference on robotics and biomimetics (ROBIO), 12-14 Dec. 2013, China. IEEE, 292–297.

Lippi, V., and Mergner, T. (2020). A challenge: support of standing balance in assistive robotic devices. *Appl. Sci.* 10, 5240. doi:10.3390/app10155240

Mantoan, A., Pizzolato, C., Sartori, M., Sawacha, Z., Cobelli, C., and Reggiani, M. (2015). Motonms: a matlab toolbox to process motion data for neuromusculoskeletal modeling and simulation. *Source code Biol. Med.* 10, 12–14. doi:10.1186/s13029-015-0044-4

Millard, M., Wight, D., McPhee, J., Kubica, E., and Wang, D. (2009). *Human foot placement and balance in the sagittal plane*.

Nishiwaki, K., and Kagami, S. (2009). Online walking control system for humanoids with short cycle pattern generation. *Int. J. Robotics Res.* 28, 729–742. doi:10.1177/0278364908097883

Peng, Z., Jiang, S., and Li, J. (2017). "Control strategies for stability recovery of full lower limb exoskeleton robot based on plantar pressure," in 2017 12th IEEE Conference on Industrial Electronics and Applications (ICIEA), USA, 18-20 June 2017 (IEEE), 1218–1223.

Postol, N., Spratt, N. J., Bivard, A., and Marquez, J. (2021). Physiotherapy using a free-standing robotic exoskeleton for patients with spinal cord injury: a feasibility study. *J. NeuroEngineering Rehabilitation* 18, 180–210. doi:10.1186/s12984-021-00967-4

Pratt, J., Carff, J., Drakunov, S., and Goswami, A. (2006). "Capture point: a step toward humanoid push recovery," in 2006 6th IEEE-RAS international conference on humanoid robots (IEEE), Italy, 04-06 December 2006 (IEEE), 200–207.

Pratt, J., Chew, C.-M., Torres, A., Dilworth, P., and Pratt, G. (2001). Virtual model control: an intuitive approach for bipedal locomotion. *Int. J. Robotics Res.* 20, 129–143. doi:10.1177/02783640122067309

Rajasekaran, V., Aranda, J., Casals, A., and Pons, J. L. (2015). An adaptive control strategy for postural stability using a wearable robot. *Robotics Aut. Syst.* 73, 16–23. doi:10.1016/j.robot.2014.11.014

Rodríguez-Fernández, A., Lobo-Prat, J., and Font-Llagunes, J. M. (2021). Systematic review on wearable lower-limb exoskeletons for gait training in neuromuscular impairments. *J. neuroengineering rehabilitation* 18, 22–21. doi:10.1186/s12984-021-00815-5

Shi, D., Zhang, W., Zhang, W., and Ding, X. (2019). A review on lower limb rehabilitation exoskeleton robots. *Chin. J. Mech. Eng.* 32, 74–11. doi:10.1186/s10033-019-0389-8

Siviy, C., Baker, L. M., Quinlivan, B. T., Porciuncula, F., Swaminathan, K., Awad, L. N., et al. (2023). Opportunities and challenges in the development of exoskeletons for locomotor assistance. *Nat. Biomed. Eng.* 7, 456–472. doi:10.1038/s41551-022-00984-1

Stegall, P., Winfree, K., Zanotto, D., and Agrawal, S. K. (2013). Rehabilitation exoskeleton design: exploring the effect of the anterior lunge degree of freedom. *IEEE Trans. Robotics* 29, 838–846. doi:10.1109/tro.2013.2256309

Stephens, B. (2007). "Humanoid push recovery," in 2007 7th IEEE-RAS International Conference on Humanoid Robots (IEEE), USA, December 1, 2007 (IEEE), 589–595.

Stephens, B. J., and Atkeson, C. G. (2010). "Push recovery by stepping for humanoid robots with force controlled joints," in 2010 10th IEEE-RAS International conference on humanoid robots (IEEE), USA, 6-8 Dec. 2010 (IEEE), 52–59.

Su, D., Hu, Z., Wu, J., Shang, P., and Luo, Z. (2023). Review of adaptive control for stroke lower limb exoskeleton rehabilitation robot based on motion intention recognition. *Front. Neurorobotics* 17, 1186175. doi:10.3389/fnbot.2023.1186175

Sugiura, S., Unde, J., Zhu, Y., and Hasegawa, Y. (2023a). Variable grounding flexible limb tracking center of gravity for sit-to-stand transfer assistance. *IEEE Robotics Automation Lett.* 9, 175–182. doi:10.1109/lra.2023.3328449

Sugiura, S., Zhu, Y., Huang, J., and Hasegawa, Y. (2023b). Passive lower limb exoskeleton for kneeling and postural transition assistance with expanded support polygon. *IEEE/ASME Trans. Mechatronics*, 1–12. doi:10.1109/tmech.2023.3294255

Ugurlu, B., Doppmann, C., Hamaya, M., Forni, P., Teramae, T., Noda, T., et al. (2015). Variable ankle stiffness improves balance control: experiments on a bipedal exoskeleton. *IEEE/ASME Trans. mechatronics* 21, 79–87. doi:10.1109/TMECH.2015.2448932

van der Kooij, H., van Asseldonk, E. H., and Vlutters, M. (2016). "Towards exoskeletons with balance capacities," in Wearable Robotics: Challenges and Trends: Proceedings of the 2nd International Symposium on Wearable Robotics, WeRob2016, Segovia, Spain, October 18-21, 2016 (Springer), 175–179.

Wieber, P.-B. (2006). "Trajectory free linear model predictive control for stable walking in the presence of strong perturbations," in 2006 6th IEEE-RAS International Conference on Humanoid Robots (IEEE), Italy, 04-06 December 2006 (IEEE), 137–142.

Winter, D. A. (1995). Human balance and posture control during standing and walking. *Gait posture* 3, 193–214. doi:10.1016/0966-6362(96)82849-9

Zhang, L., Li, Z., Hu, Y., Smith, C., Farewik, E. M. G., and Wang, R. (2020). Ankle joint torque estimation using an emg-driven neuromusculoskeletal model and an artificial neural network model. *IEEE Trans. Automation Sci. Eng.* 18, 564–573. doi:10.1109/tase.2020.3033664

Zhou, J., Yang, S., and Xue, Q. (2021). Lower limb rehabilitation exoskeleton robot: a review. *Adv. Mech. Eng.* 13, 168781402110118. doi:10.1177/16878140211011862

frontiers | Frontiers in Bioengineering and Biotechnology

TYPE Original Research
PUBLISHED 09 May 2024
DOI 10.3389/fbioe.2024.1392513

OPEN ACCESS

EDITED BY
Wujing Cao,
Chinese Academy of Sciences (CAS), China

REVIEWED BY
Dong Wang,
University of Exeter, United Kingdom
Jian Cui,
Institute of Artificial Intelligence, China

*CORRESPONDENCE
Senlin Fang,
✉ D22092100360@cityu.edu.mo

RECEIVED 27 February 2024
ACCEPTED 16 April 2024
PUBLISHED 09 May 2024

CITATION
Yi Z, Lai X, Sun A and Fang S (2024), Tongue feature recognition to monitor rehabilitation: deep neural network with visual attention mechanism.
Front. Bioeng. Biotechnol. 12:1392513.
doi: 10.3389/fbioe.2024.1392513

Tongue feature recognition to monitor rehabilitation: deep neural network with visual attention mechanism

Zhengheng Yi[1,2,3], Xinsheng Lai[2,3], Aining Sun[4] and Senlin Fang[5]*

[1]Shenzhen Fuyong People's Hospital, Shenzhen, China, [2]Guangzhou University of Chinese Medicine, Guangzhou, China, [3]National Famous Traditional Chinese Medicine Expert LAI Xin-sheng Inheritance Studio, Guangzhou, China, [4]Guangdong Zhengyuanchun Traditional Chinese Medicine Clinic Co., Ltd, Guangzhou, China, [5]Faculty of Data Science, City University of Macau, Macau, China

Objective: We endeavor to develop a novel deep learning architecture tailored specifically for the analysis and classification of tongue features, including color, shape, and coating. Unlike conventional methods based on architectures like VGG or ResNet, our proposed method aims to address the challenges arising from their extensive size, thereby mitigating the overfitting problem. Through this research, we aim to contribute to the advancement of techniques in tongue feature recognition, ultimately leading to more precise diagnoses and better patient rehabilitation in Traditional Chinese Medicine (TCM).

Methods: In this study, we introduce TGANet (Tongue Feature Attention Network) to enhance model performance. TGANet utilizes the initial five convolutional blocks of pre-trained VGG16 as the backbone and integrates an attention mechanism into this backbone. The integration of the attention mechanism aims to mimic human cognitive attention, emphasizing model weights on pivotal regions of the image. During the learning process, the allocation of attention weights facilitates the interpretation of causal relationships in the model's decision-making.

Results: Experimental results demonstrate that TGANet outperforms baseline models, including VGG16, ResNet18, and TSC-WNet, in terms of accuracy, precision, F1 score, and AUC metrics. Additionally, TGANet provides a more intuitive and meaningful understanding of tongue feature classification models through the visualization of attention weights.

Conclusion: In conclusion, TGANet presents an effective approach to tongue feature classification, addressing challenges associated with model size and overfitting. By leveraging the attention mechanism and pre-trained VGG16 backbone, TGANet achieves superior performance metrics and enhances the interpretability of the model's decision-making process. The visualization of attention weights contributes to a more intuitive understanding of the classification process, making TGANet a promising tool in tongue diagnosis and rehabilitation.

KEYWORDS

traditional Chinese medicine, tongue feature recognition, deep neural network, attention mechanism, rehabilitation

1 Introduction

Traditional Chinese Medicine (TCM) practitioners monitor the rehabilitation process by carefully observing and analyzing the patient's tongue. This method not only aids in determining the progression of the illness but also provides crucial clues for rehabilitation Du et al. (2024). Tongue diagnosis plays a pivotal role in the rehabilitation process as changes in the tongue can reflect the overall health condition of the patient. By monitoring features such as the color, shape, and moisture of the tongue, TCM practitioners can assess the progress of the patient's rehabilitation and adjust treatment plans accordingly. Tongue features such as color, shape, and coating can be utilized to determine if a patient has an underlying health condition. Traditional Chinese tongue diagnosis Solos and Liang (2018) typically involves observations in the following aspects: 1. Tongue color: Different tongue colors may indicate various health issues. For example, a pale red tongue is often associated with good health, while a deep red tongue may suggest insufficiency of vital energy and blood; 2. Tongue shape: The shape of the tongue can also provide information about the patient's health. For instance, an excessively large tongue, known as a fat and enlarged tongue, often accompanied by tooth imprints, may indicate the insufficiency of both the spleen and the kidney; 3. Tongue coating: The tongue coating, a thin layer of film on the tongue surface, is closely related to the intensity of dampness heat syndrome in TCM theory. Medical studies have shown a correlation between greasy tongue coating and various diseases, such as gastrointestinal disorders, and more recently, the novel coronavirus disease (COVID-19) Pang et al. (2020).

Traditional Chinese tongue diagnosis heavily relies on the subjective judgment and clinical experience of TCM practitioners, resulting in outcomes that lack objective indicators Miao et al. (2023). The adoption of computer-aided tongue feature recognition models allows for an objective and quantitative diagnosis of tongue conditions, establishing a quantifiable relationship between tongue features and diseases Zhang et al. (2006). With significant advancements in computer vision (CV), research on automatic tongue diagnosis systems based on image processing and feature recognition has become more prevalent. For instance, Zhang et al. (2015) extracted 20 color features and 20 texture features from tongue diagnosis images, including energy, entropy, contrast, and correlation, primarily describing tongue color and coating thickness. Qi et al. (2016) classified four different tongue colors, employing the ICC profile method for color correction to enhance image consistency. Subsequently, support vector machine (SVM) and random forest (RF) were employed for classification. Pang et al. (2004) introduced a computerized tongue diagnosis method based on a Bayesian network classifier, focusing on quantitative analysis of tongue color and texture features for diagnostic purposes. Song (2020) proposed a cascade classifier based on Local Binary Pattern (LBP) features to address the issue of irrelevant information interference, such as lips and cheeks in traditional Chinese tongue diagnosis images. This method utilized LBP features to describe tongue texture and employed the AdaBoost algorithm to construct the cascade classifier. Yamamoto et al. (2011) utilized a hyperspectral imaging system to acquire tongue images, identifying the most clinically relevant component vectors through Principal Component Analysis (PCA), offering an alternative approach for tongue diagnosis. Additionally, Gao et al. (2007) employed image processing algorithms to extract quantitative features of the tongue, including color and texture features, and SVM was employed for tongue classification.

However, the complexity of multiple features and variations in tongue image acquisition conditions, such as environmental factors and angles, often render traditional CV algorithms ineffective Xie et al. (2021); Li D. et al. (2022). With the rapid advancement of deep learning (DL), research on automatic tongue diagnosis programs based on DL models has gained prominence. DL methods typically exhibit stronger generalization and higher feature recognition accuracy compared to traditional computer vision algorithms, circumventing the manual feature extraction drawbacks associated with traditional machine learning methods. Most DL automatic tongue diagnosis systems encompass DL models for both tongue segmentation and tongue feature recognition. Segmentation commonly utilizes models based on U-Net Huang et al. (2020), while tongue feature recognition employs pre-trained models such as ResNet or VGG Tammina (2019). For instance, Yan J. et al. (2022) aimed to distinguish different tongue textures, such as the toughness or softness of the tongue body, through the analysis of tongue image textures. They employed the DeepLab v3+ deep learning semantic segmentation model to segment the tongue image, separating the tongue from the background. Subsequently, a ResNet101-based tongue image texture classification model was constructed. Experimental results demonstrated that using ResNet101 achieved better classification performance compared to traditional tongue image texture classification methods. In another study, Yan B. et al. (2022) proposed a convolutional neural network based on semantic modeling for tongue segmentation. Different feature extraction networks (AlexNet, VGG16, ResNet18, and DenseNet101) were compared for their effectiveness in extracting tongue color features. Combining U-Net, Inception, and dilated convolutions, Wei et al. (2022) introduced a new tongue image segmentation method called IAUNet. They designed a network named TCCNet for tongue color classification, incorporating technologies such as ResNet, Inception, and Triplet-Loss. Experimental results showed that TCCNet achieved favorable results in tongue color classification, achieving higher F1-Score and mAP compared to other baselines. Lastly, Li J. et al. (2022) employed UENET for tongue segmentation, using ResNet34 as the backbone network to extract features and perform classification from tongue photos, with overall accuracy surpassing 86%. Wang et al. (2022) develop a GreasyCoatNet model based on ResNet, which can recognize and classify different degrees of tongue greasy coating.

These above researches on tongue feature classification are mostly built based on VGG or ResNet Zhuang et al. (2022); Huang et al. (2023); Li J. et al. (2022); Wang et al. (2020). However, due to its large size, VGG or ResNet demands substantial computational resources and memory. Additionally, training directly with VGG or ResNet may lead to overfitting, especially when tongue images are challenging to collect and training data is limited. Therefore, our proposed TGANet (Togue Feature Attention Network) utilizes the pretrained VGG16's initial five convolutional blocks as the backbone. Furthermore, we integrate an attention mechanism Fukui et al. (2019) into the backbone,

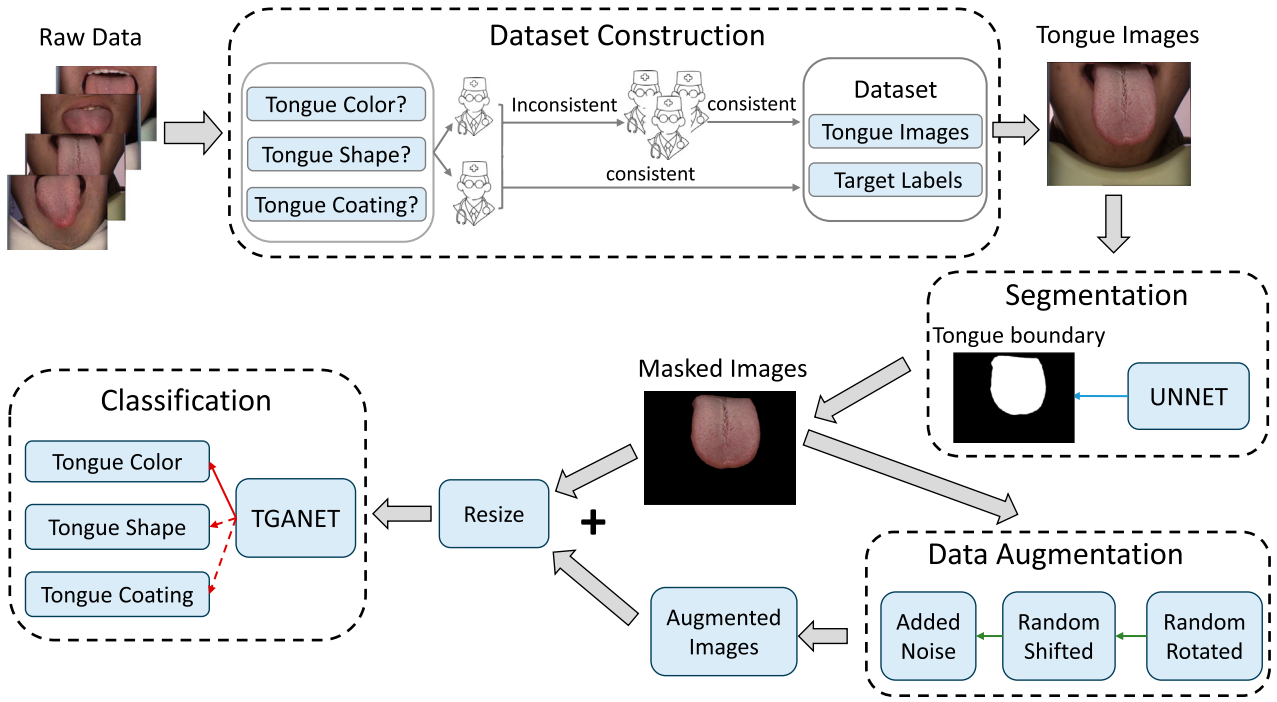

FIGURE 1
The framework for tongue color recognition encompasses four key stages: Dataset Construction, Segmentation, Data Augmentation, and Classification.

aiming to mimic human cognitive attention. The primary objective is to focus model weights on crucial parts of the image. For example, in tongue coating classification, the coating is usually concentrated at the root of the tongue. If the model can prioritize local features related to coating, similar to human attention, it enhances efficiency and accuracy. Moreover, the allocation of attention weights during the learning process aids in interpreting causal relationships in the model's judgments. Our proposed architecture TGANet is primarily based on the foundation of Yan et al. (2019).

2 Methods

The overall framework for classifying tongue features classification is illustrated in Figure 1. Initially, the U-Net is employed to segment the input tongue images to obtain the tongue boundary. Subsequently, the masked image derived from the tongue boundary is followed by a data augmentation process. Specifically, the masked image undergoes sequential random rotation, shifting, and adding noise. Following this augmentation, both the masked images and their augmented counterparts are fed into the TGANet to execute the classification of tongue features. In the classification phrase, three kinds of tongue features are classified: tongue color, tongue shape, and tongue coating.

2.1 Dataset Construction

The publicly available BioHit image dataset comprises 300 tongue images with dimensions of 567 × 768 pixels. We annotated this original dataset with diagnostic labels. The image annotation process involves three steps. Firstly, domain experts engaged in discussions to establish diagnostic criteria for each category within the three types of tongue features. The detail of the three categories and their class labels is shown in Table 1. Subsequently, two well-trained TCM practitioners from the Guangzhou University of Chinese Medicine independently assessed each tongue image to distinguish the class labels for each tongue feature. A third TCM professional with 20 years of expertise joined the deliberations to collectively resolve any disputes and achieve a final consensus. Images with unanimous agreement were then incorporated into the dataset for the development of a deep learning-based tongue feature recognition model.

2.2 Image segmentation

The aim of tongue image segmentation is to enhance the effectiveness of tongue feature classification by eliminating extraneous information in the image, such as interference from the human jaw or background details, which can disrupt the classification process. To achieve this, we employed the deep convolutional neural network U-Net for tongue segmentation. U-Net is widely utilized in image segmentation, drawing inspiration from semantic segmentation tasks and designed to deliver high-resolution, precise segmentation results.The overall architecture of the U-Net dedicated to segmenting the contour images of the tongue is illustrated in Figure 2. U-Net adopts an encoder-decoder structure. The encoder is responsible for sequentially extracting features from the input tongue image

TABLE 1 Tongue feature labels and corresponding descriptions.

Label\Tongue feature	Tongue color	Tongue body	Tongue coating
0	Pale Red	Swollen	White Greasy
1	Red	Non-Swollen	Thin White
2	Dark Red	N/A	Thin Yellow
3	N/A	N/A	Yellow Greasy

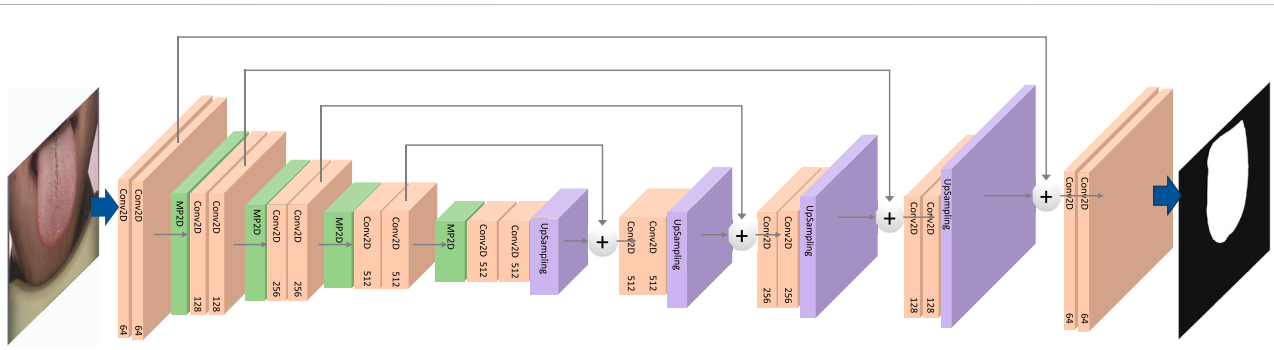

FIGURE 2
The architecture of U-Net for tongue image segmentation.

through convolution and pooling operations, progressively reducing spatial resolution. The decoder gradually restores spatial resolution through upsampling and deconvolution operations. U-Net incorporates skip connections by linking the output of the last convolutional layer of each encoder block to the corresponding layer in the decoder. This helps retain more detailed information at different resolutions, overcoming potential information loss in deep networks. The final segmentation output is generated in the last layer using a 1 × 1 convolutional layer. The training utilizes the cross-entropy loss function to measure the difference between the model's output and the actual segmented image. By leveraging U-Net, we obtain the masked tongue image by acquiring the tongue segmentation contour mask from the input tongue image.

2.3 Image augmentation

Due to the limited number of samples in medical images and the imbalance in the number of samples for each category, data augmentation is applied to the samples before image classification. This ensures that the quantity of each category in tongue feature classification remains consistent, maintaining an equal number of samples for both the training and validation sets. The commonly employed method to balance categories involves setting the upper limit based on the category with the maximum sample count and augmenting samples from categories with fewer samples.

Various data augmentation techniques are typically utilized, including random translation, random rotation, and the addition of Gaussian noise in different combinations to enhance images. As shown in Figure 3, we implemented the augmentation in the order of random translation, followed by random rotation, and then the addition of Gaussian noise. Specifically, random translation involves random shifts in both the x and y-axes within the range from −10 pixels (ps) to 10 ps. Random rotation includes clockwise rotation within the range from −15° to 15°, and Gaussian noise is added with a mean of 0 and a variance of 0.1.

2.4 Tongue feature classification

The overall architecture of the TGANet model for tongue feature classification is illustrated in Figure 4. We employ VGG16 as the model's backbone, removing all fully connected layers. Input images sequentially pass through convolutional blocks $B1$ to $B5$, extracting global features from the input images. Intermediate features (denoted as F) obtained from pooling layers in $B2$ and $B4$ are used to learn attention maps, while the output of the pooling layer after $B5$ (denoted as G) represents global features extracted by all convolutional blocks in the network. Intermediate feature F and global feature G are jointly input into the Attention Module to obtain attention feature F:

$$F' = Attention(F, G). \tag{1}$$

Here, "Attention" represents the operation within the attention module. Specifically, to match the sizes of intermediate and global features, F undergoes a convolutional layer to increase its channel count to 256, and bilinear interpolation aligns its feature size with G. G undergoes a convolutional layer to compress its channel count to 256. The transformed F and G are then added to obtain U:

$$U = W_F * F + UP(W_G * G). \tag{2}$$

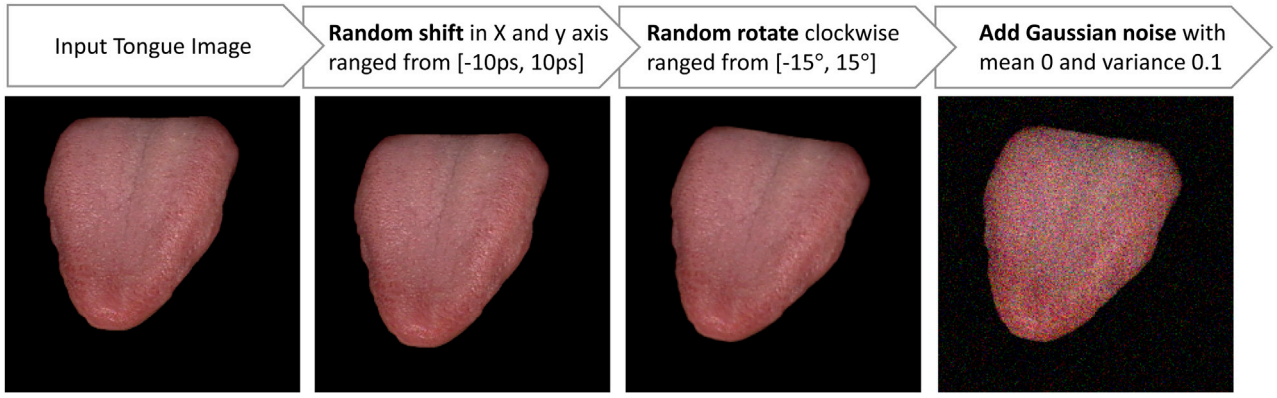

FIGURE 3
The input tongue images undergo augmentation through the following actions: random shift, random rotation, and the addition of Gaussian noise.

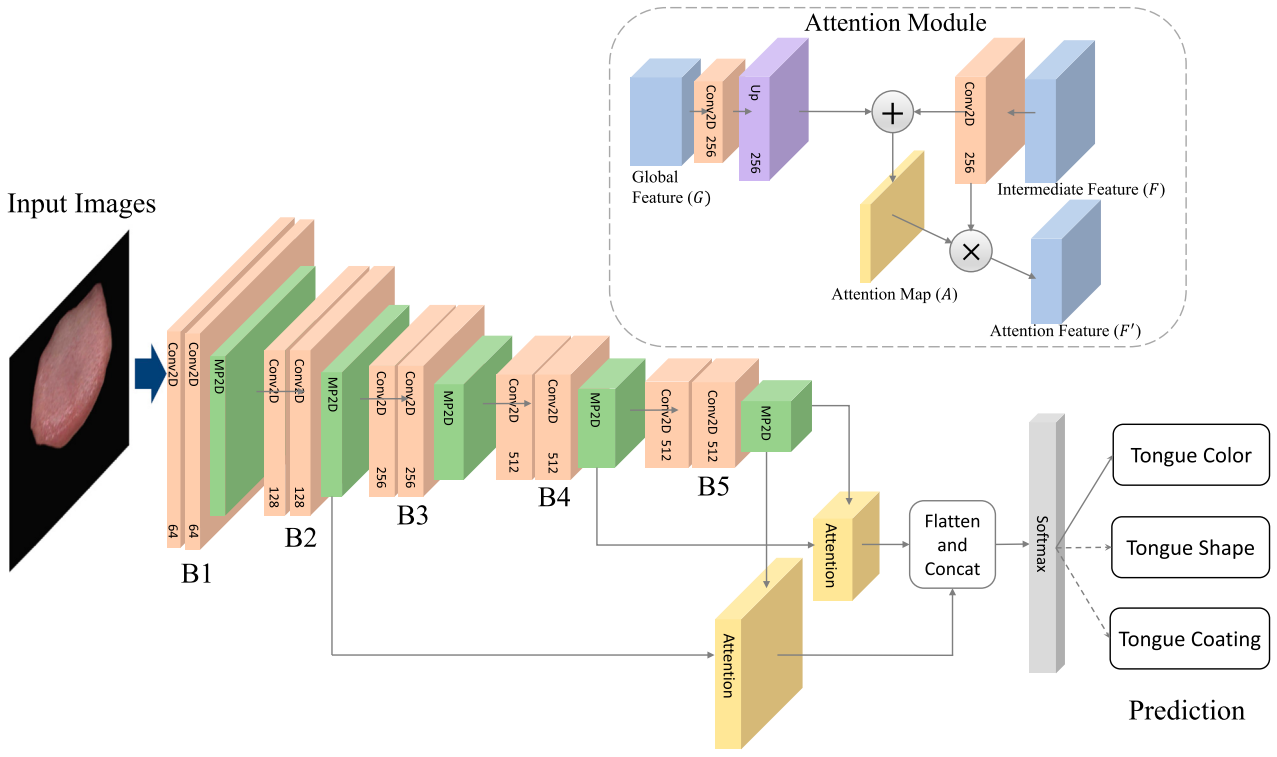

FIGURE 4
The architecture of TGANet.The TGANet employs the VGG16 architecture as its backbone, with all fully connected layers removed. Input images undergo sequential processing through convolutional blocks *B*1 to *B*5, capturing global features from the input data. Intermediate features (denoted as *F*) extracted from pooling layers in *B*2 and *B*4 are utilized for attention map learning. Additionally, the output of the pooling layer following *B*5 (denoted as *G*) represents the global features aggregated by all convolutional blocks within the network.

The * symbol denotes convolutional operation, and *UP* represents bilinear interpolation. W_F and W_G are the convolutional weights for *F* and *G*, respectively. Next, *U* undergoes an operation to transform into an attention map *A*:

$$A = Sigmoid\,(Conv\,(ReLU\,(U))). \tag{3}$$

Subsequently, pixel-wise multiplication of *F* and *A* yields the Attention Feature:

$$F' = A * F. \tag{4}$$

Finally, attention features generated from intermediate features (*B*2 and *B*4) are concatenated with global features. The softmax operation is applied to obtain the final predictions for tongue features. Specifically, predictions are made for three different tongue features: tongue color, tongue shape, and tongue coating. The overall architecture is trained end-to-end.

2.5 Model evaluation

The model training was conducted on a Windows 11 system equipped with an NVIDIA 4090 GPU, utilizing Python and PyTorch. Initial model parameters were initialized with weights pre-trained on the ImageNet dataset. This transfer learning strategy endowed the model with robust prior knowledge, contributing to superior performance. Subsequently, fine-tuning of the model parameters was performed using the tongue dataset. The parameters of the Attention module were initialized using the Kaiming initialization method, and model optimization employed the Adam optimizer with a learning rate of 0.0001. Three distinct tongue feature classifications shared the same model structure, with the only difference lying in the output of the final fully connected classification layer, which was adjusted according to the different categories. During the training process, model parameter updates were achieved by minimizing the cross-entropy loss function. All models underwent 20 training epochs with a batch size of 20, and model parameters were fixed based on the best performance observed on the validation dataset. Training and testing the model on the tongue color, shape, and coating classification respectively with the 5-fold cross-validation.

2.6 Metric

Accuracy is the proportion of correctly classified samples by the model on the entire dataset. In model evaluation, accuracy is a crucial metric for assessing the overall performance of the model. The calculation of accuracy *Acc* is the ratio of the number of samples correctly predicted by the model to the total number of samples:

$$Acc = \frac{N_c}{N_t}, \tag{5}$$

where N_c is the number of correctly predicted samples, and N_t is the total number of samples.

Precision Ashley (2016) refers to the proportion of actual positive samples among all the samples predicted as positive by the model. In some applications, high precision may be a key objective as it indicates the accuracy of the model in positive class predictions. Precision P is calculated as:

$$P = \frac{TP}{TP + FP}, \tag{6}$$

where TP represents true positives, indicating the number of samples correctly predicted as positive by the model, and FP represents false positives, indicating the number of instances where the model incorrectly predicted negative class samples as positive.

F1 Score Goutte and Gaussier (2005) is the harmonic mean of precision and recall, used to comprehensively consider the model's accuracy and recall performance. In some situations, the F1 Score is used as a balance between precision and recall. The calculation of F1 Score $F1$ is given by:

$$F1 = 2 \times \frac{P \times R}{P + R}, \tag{7}$$

where R is recall, also known as sensitivity or true positive rate, is a metric that measures the ability of a model to capture all positive instances in the dataset. It is defined as the ratio of TP to the sum of TP and False Negatives (positive samples incorrectly predicted as negative). The formula for R is given by:

$$R = \frac{TP}{TP + FN}. \tag{8}$$

AUC Wu and Flach (2005) is the area under the ROC curve, where the ROC curve illustrates the trade-off between true positive and false positive rates at different thresholds. A higher AUC value, closer to 1, indicates better model performance. AUC is commonly used for performance evaluation in binary classification problems, especially when dealing with imbalanced datasets. The specific calculation of AUC is not enumerated here but is typically obtained by integrating the ROC curve.

3 Results

3.1 Baseline models

Throughout the experiments, we compare the TGANet with the following models.

1) VGG16: VGG16 Tammina (2019) is a deep convolutional neural network architecture designed for image classification tasks. The "16" in VGG16 refers to the network's depth. VGG16 follows a simple and uniform architecture with small 3 × 3 convolutional filters, which helps maintain a consistent receptive field. It also employs max-pooling layers for spatial down-sampling. The pre-trained VGG16 weights on large datasets ImageNet to initialize their models before fine-tuning for our tongue feature classification tasks.
2) ResNet18 Odusami et al. (2021): short for Residual Network with 18 layers, is a convolutional neural network architecture introduced by Kaiming He et al. It is part of the ResNet family, known for its deep structure and the incorporation of residual learning blocks. The architecture includes a stack of residual blocks, where each block consists of two convolutional layers with batch normalization and rectified linear unit (ReLU) activation functions. The key innovation in ResNet architectures is the use of skip connections or shortcuts that skip one or more layers, allowing the gradient to flow more easily during backpropagation. This facilitates the training of very deep networks and helps alleviate the vanishing gradient problem. ResNet18 architecture serves as a baseline model and is widely used in tongue feature classification tasks due to its effectiveness and efficiency.
3) TSC-WNet Huang et al. (2023): TSC-WNet is a comprehensive neural network architecture designed for the classification of tongue size and shape. TSC-WNet consists of two subnetworks: TSC-UNet and TSC-Net. TSC-Net serves as the classification backbone, while TSC-UNet is responsible for tongue segmentation. TSC-Net employs a simple and efficient architecture with four convolutional layers. By combining both classification and segmentation features, TSC-WNet shows the

TABLE 2 Comparison of the metrics between our proposed TGANet and the baselines on the three tongue feature classifications (Mean ± SEM). The result is the mean and standard deviation of the five folds by using 5-fold cross-validation. The best performance is marked in bold.

Model	Tongue feature	Accuracy (%)	Precision (%)	F1 score (%)	AUC (%)
VGG16	Tongue Color	75.13 ± 4.64	75.43 ± 5.03	69.16 ± 5.96	84.31 ± 3.02
ResNet18		82.37 ± 6.42	82.87 ± 5.40	80.86 ± 5.78	93.49 ± 3.10
TSC-WNet		83.08 ± 4.68	82.76 ± 4.92	79.72 ± 6.45	92.76 ± 3.59
TGANet (our)		**91.88 ± 2.65**	**90.53 ± 3.16**	**89.87 ± 3.17**	**96.45 ± 1.94**
VGG16	Tongue Shape	91.93 ± 1.70	94.15 ± 2.87	93.55 ± 3.16	96.31 ± 3.04
ResNet18		91.43 ± 2.65	91.15 ± 2.69	90.25 ± 2.89	**97.89 ± 1.47**
TSC-WNet		89.83 ± 2.00	90.88 ± 1.84	88.83 ± 2.85	94.74 ± 1.80
TGANet (our)		**92.38 ± 1.43**	**94.93 ± 1.63**	**94.05 ± 2.13**	97.55 ± 1.57
VGG16	Tongue Coating	91.69 ± 1.41	94.16 ± 2.40	93.50 ± 2.61	98.46 ± 0.70
ResNet18		90.16 ± 5.17	93.34 ± 3.67	91.92 ± 5.60	**98.80 ± 0.62**
TSC-WNet		84.62 ± 2.69	87.32 ± 3.47	85.54 ± 3.80	95.87 ± 1.63
TGANet (our)		**94.77 ± 1.02**	**95.59 ± 1.52**	**95.02 ± 1.72**	98.77 ± 1.21

best validation accuracy and steady performance during training. TSC-WNet is a well-designed network architecture that integrates classification and segmentation tasks, showcasing improved accuracy and robust performance in the challenging domain of tongue analysis.

3.2 Tongue feature classification model performance

Table 2 presents a comprehensive performance comparison of various tongue classification models, including ResNet18, TS-WCNet, and our proposed TGANet. The result is the mean and standard deviation of the five folds by using 5-fold cross-validation. The models were evaluated based on different tongue features: Tongue Color, Tongue Shape, and Tongue Coating by using 5-fold cross-validation. For the Tongue Color feature, TGANet outperformed both VGG16, ResNet18, and TSC-WNet with a remarkable accuracy of 91.88%, precision of 90.53%, F1 score of 89.87%, and AUC of 96.45%. These results highlight the superior performance of TGANet in capturing color-related information for tongue classification. Similarly, when focusing on the Tongue Shape feature, TGANet demonstrated a significant improvement in accuracy (92.38%), precision (94.93%), and F1 score (94.05%) compared to VGG16, ResNet18, and TS-WCNet. The robustness of TGANet in extracting shape-related features contributes to its outstanding performance. In the case of Tongue Coating classification, TGANet exhibited outstanding results with an accuracy of 94.77%, precision of 95.59%, and F1 score of 95.02%. This emphasizes the efficacy of TGANet in recognizing and classifying diverse tongue coating patterns. Additionally, the uncertainty in the model's performance is captured through the standard deviation, providing insights into the stability of the results across multiple evaluations. The consistent outperformance of TGANet across different tongue features underscores its robustness and effectiveness in tongue classification tasks.

3.3 Attention visualization

Attention Visualization is designed to add a visualization of attention weights (attention map) to input images. Initially, the input image is transformed from a PyTorch tensor to a NumPy array, with channel dimensions adjusted to the correct order. The attention map's size is adjusted based on an upsampling factor using bilinear interpolation. The grayscale attention map is then converted to a heatmap using the JET color map from OpenCV. Finally, the image and normalized attention map are blended in a certain proportion, creating an overlay of attention visualization on the image. This process visualizes the depth of focus of a deep learning model on the input. This is particularly helpful in understanding the decision-making process of a deep learning model in tongue feature classification, emphasizing regions considered crucial for tongue segmentation tasks.

As depicted in Figure 5, the attention visualization images for tongue color classification show that the model primarily utilizes features from the tip of the tongue in its decision-making process, which is reasonable given that the color of the tongue tip is typically more distinct. As shown in Figure 6, the attention visualization images for tongue coating classification reveal that the model's decision-making relies heavily on features from the root of the tongue, which is sensible as tongue coating is mainly concentrated in the root area. Figure 7 illustrates the attention visualization images for tongue shape classification, demonstrating that the model's decision-making focuses on the contour features of the tongue. This aligns with the common practice among practitioners who assess the thickness and appearance of the tongue's outline to determine its texture.

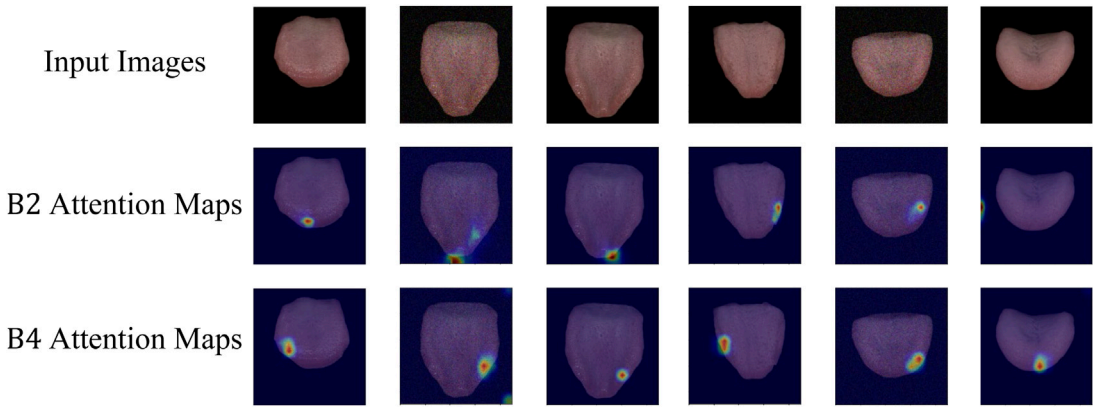

FIGURE 5
Visualization of TGANet attention weights for tongue color classification. B2 Attention Maps are the attention weights learning from the intermediate features of *B2*, and B4 Attention Maps are the attention weights learning from the intermediate features of *B4*.

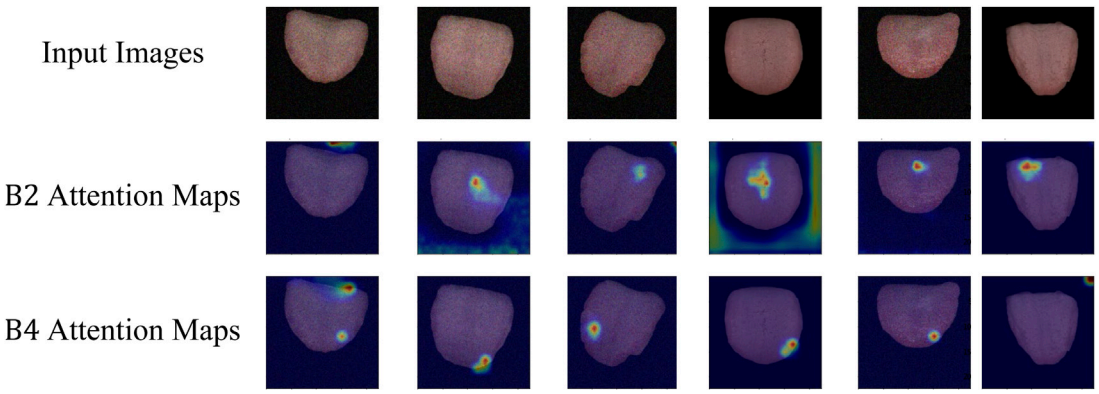

FIGURE 6
Visualization of TGANet attention weights for tongue coating classification.

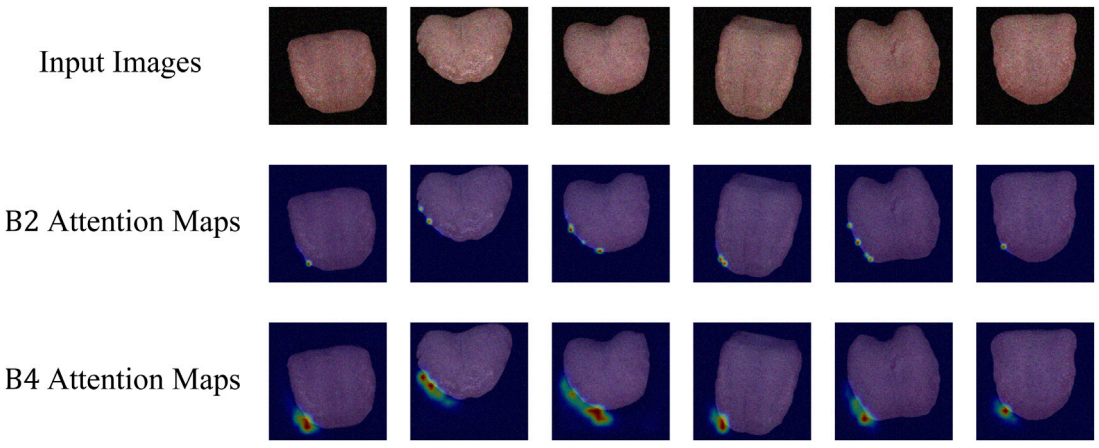

FIGURE 7
Visualization of TGANet attention weights of TGANet for tongue shape classification.

4 Discussion

TCM practitioners can moniter the patient rehabilitation process by carefully observing and analyzing the patient's tongue feature. For instance, a deep red tongue may suggest a deficiency in vital energy and blood, a fat and enlarged tongue may indicate the insufficiency of both the spleen and the kidney, and a thin layer of film on the tongue surface is closely linked to the intensity of dampness-heat syndrome in TCM theory. Here, we propose a framework designed for the classification of three distinct tongue features. Initially, our expert physicians labeled a publicly available dataset, BioHit, based on these three different tongue features. Subsequently, we preprocessed and augmented the images using image segmentation and augmentation techniques. Then, employing the TGANet architecture with an attention mechanism, we classified the three different tongue features. Our TGANet model outperforms baseline models, achieving the highest accuracy, precision, F1 score, and AUC metrics.

Additionally, the TGANet, based on the VGG16 architecture with attention modules, exhibits superior performance. Compared to the VGG16 without attention modules, the attention modules in our TGANet were further visualized. It was observed that for different tongue feature classifications, the neural network's attention weights varied. For tongue color classification, attention weights were concentrated on the tongue tip; for tongue shape classification, attention weights were focused on the tongue contour; for tongue coating classification, attention weights were centered around the tongue base. This alignment with the expertise of physicians emphasizes the effectiveness of the features learned by our model. Furthermore, the visualization of attention modules provides interpretability for deep learning-based tongue diagnostic models.

In practical applications, establishing a universal model applicable to various tongue feature classifications is highly meaningful in tongue diagnosis and rehabilitation. This contributes to mitigating the overfitting problem. As a result, our TGANet demonstrates outstanding performance in different tongue feature classifications compared to baselines, ultimately leading to more precise diagnoses and better patient rehabilitation in TCM.

5 Conclusion

In conclusion, our study introduces TGANet, a novel DL model designed for the classification of crucial tongue features in TCM. Leveraging the initial five convolutional blocks of pre-trained VGG16 as the backbone and integrating an Attention mechanism, TGANet outperforms baseline models in accuracy, precision, F1 score, and AUC metrics for distinguishing tongue color, coating, and shape. The integration of an attention mechanism provides interpretability by emphasizing model weights on significant regions of the tongue image. TGANet exhibits robust performance, and the visualization of attention weight further reveals the model's focus on specific tongue regions for decision-making, aligning with clinical practices. This study contributes to advancing automatic tongue diagnosis systems, providing a foundation for objective and quantitative assessment of tongue conditions in TCM.

Data availability statement

The original contributions presented in the study are included in the article/Supplementary material, further inquiries can be directed to the corresponding author.

Author contributions

ZY: Writing–original draft, Writing–review and editing, Conceptualization, Investigation, Supervision. XL: Data curation, Formal Analysis, Funding acquisition, Project administration, Resources, Supervision, Writing–review and editing. AS: Data curation, Funding acquisition, Methodology, Project administration, Resources, Supervision, Writing–review and editing. SF: Conceptualization, Data curation, Formal Analysis, Methodology, Visualization, Writing–original draft, Writing–review and editing.

Funding

The author(s) declare that no financial support was received for the research, authorship, and/or publication of this article.

Conflict of interest

Author AS was employed by Guangdong Zhengyuanchun Traditional Chinese Medicine Clinic Co., Ltd.

The remaining authors declare that the research was conducted in the absence of any commercial or financial relationships that could be construed as a potential conflict of interest.

Publisher's note

References

Ashley, E. A. (2016). Towards precision medicine. *Nat. Rev. Genet.* 17, 507–522. doi:10.1038/nrg.2016.86

Du, T., Liu, J., Xie, H., Wang, X., Yang, X., Yang, Y., et al. (2024). Multifunctional coatings of nickel-titanium implant toward promote osseointegration after operation of bone tumor and clinical application: a review. *Front. Bioeng. Biotechnol.* 12, 1325707. doi:10.3389/fbioe.2024.1325707

Fukui, H., Hirakawa, T., Yamashita, T., and Fujiyoshi, H. (2019). "Attention branch network: learning of attention mechanism for visual explanation," in Proceedings of the

IEEE/CVF conference on computer vision and pattern recognition (IEEE), 10705–10714.

Gao, Z., Po, L., Jiang, W., Zhao, X., and Dong, H. (2007). "A novel computerized method based on support vector machine for tongue diagnosis," in 2007 third international IEEE conference on signal-image technologies and internet-based system (IEEE), 849–854.

Goutte, C., and Gaussier, E. (2005). "A probabilistic interpretation of precision, recall and f-score, with implication for evaluation," in European conference on information retrieval (Springer), 345–359.

Huang, H., Lin, L., Tong, R., Hu, H., Zhang, Q., Iwamoto, Y., et al. (2020). "Unet 3+: a full-scale connected unet for medical image segmentation," in ICASSP 2020-2020 IEEE international conference on acoustics, speech and signal processing (ICASSP) (IEEE), 1055–1059.

Huang, Y., Li, X., Zheng, S., Li, Z., Li, S., Shen, L., et al. (2023). Tongue size and shape classification fusing segmentation features for traditional Chinese medicine diagnosis. *Neural Comput. Appl.* 35, 7581–7594. doi:10.1007/s00521-022-08054-y

Li, D., Hu, J., Zhang, L., Li, L., Yin, Q., Shi, J., et al. (2022a). Deep learning and machine intelligence: new computational modeling techniques for discovery of the combination rules and pharmacodynamic characteristics of traditional Chinese medicine. *Eur. J. Pharmacol.* 933, 175260. doi:10.1016/j.ejphar.2022.175260

Li, J., Zhang, Z., Zhu, X., Zhao, Y., Ma, Y., Zang, J., et al. (2022b). Automatic classification framework of tongue feature based on convolutional neural networks. *Micromachines* 13, 501. doi:10.3390/mi13040501

Miao, J., Huang, Y., Wang, Z., Wu, Z., and Lv, J. (2023). Image recognition of traditional Chinese medicine based on deep learning. *Front. Bioeng. Biotechnol.* 11, 1199803. doi:10.3389/fbioe.2023.1199803

Odusami, M., Maskeliunas, R., Damaševičius, R., and Krilavičius, T. (2021). Analysis of features of alzheimer's disease: detection of early stage from functional brain changes in magnetic resonance images using a finetuned resnet18 network. *Diagnostics* 11, 1071. doi:10.3390/diagnostics11061071

Pang, B., Zhang, D., Li, N., and Wang, K. (2004). Computerized tongue diagnosis based on bayesian networks. *IEEE Trans. Biomed. Eng.* 51, 1803–1810. doi:10.1109/tbme.2004.831534

Pang, W., Zhang, D., Zhang, J., Li, N., Zheng, W., Wang, H., et al. (2020). Tongue features of patients with coronavirus disease 2019: a retrospective cross-sectional study. *Integr. Med. Res.* 9, 100493. doi:10.1016/j.imr.2020.100493

Qi, Z., Tu, L.-p., Chen, J.-b., Hu, X.-j., Xu, J.-t., Zhang, Z.-f., et al. (2016). The classification of tongue colors with standardized acquisition and icc profile correction in traditional Chinese medicine. *BioMed Res. Int.* 2016, 1–9. doi:10.1155/2016/3510807

Solos, I., and Liang, Y. (2018). A historical evaluation of Chinese tongue diagnosis in the treatment of septicemic plague in the pre-antibiotic era, and as a new direction for revolutionary clinical research applications. *J. Integr. Med.* 16, 141–146. doi:10.1016/j.joim.2018.04.001

Song, C. (2020). Tongue localization method based on cascade classifier. *J. Artif. Intell. Pract.* 3, 13–21. doi:10.23977/jaip.2020.030104

Tammina, S. (2019). Transfer learning using vgg-16 with deep convolutional neural network for classifying images. *Int. J. Sci. Res. Publ. (IJSRP)* 9, 94200–p10150. doi:10.29322/ijsrp.9.10.2019.p9420

Wang, X., Liu, J., Wu, C., Liu, J., Li, Q., Chen, Y., et al. (2020). Artificial intelligence in tongue diagnosis: using deep convolutional neural network for recognizing unhealthy tongue with tooth-mark. *Comput. Struct. Biotechnol. J.* 18, 973–980. doi:10.1016/j.csbj.2020.04.002

Wang, X., Wang, X., Lou, Y., Liu, J., Huo, S., Pang, X., et al. (2022). Constructing tongue coating recognition model using deep transfer learning to assist syndrome diagnosis and its potential in noninvasive ethnopharmacological evaluation. *J. Ethnopharmacol.* 285, 114905. doi:10.1016/j.jep.2021.114905

Wei, L., Jinming, C., Bo, L., Wei, H., Xingjin, W., and Hui, Z. (2022). Tongue image segmentation and tongue color classification based on deep learning. *Digit. Chin. Med.* 5, 253–263. doi:10.1016/j.dcmed.2022.10.002

Wu, S., and Flach, P. (2005). "A scored auc metric for classifier evaluation and selection," in *Second workshop on ROC analysis in ML* (bonn, Germany).

Xie, J., Jing, C., Zhang, Z., Xu, J., Duan, Y., and Xu, D. (2021). Digital tongue image analyses for health assessment. *Med. Rev.* 1, 172–198. doi:10.1515/mr-2021-0018

Yamamoto, S., Tsumura, N., Nakaguchi, T., Namiki, T., Kasahara, Y., Ogawa-Ochiai, K., et al. (2011). Principal component vector rotation of the tongue color spectrum to predict "mibyou"(disease-oriented state). *Int. J. Comput. assisted radiology Surg.* 6, 209–215. doi:10.1007/s11548-010-0506-8

Yan, B., Zhang, S., Yang, Z., Su, H., and Zheng, H. (2022a). Tongue segmentation and color classification using deep convolutional neural networks. *Mathematics* 10, 4286. doi:10.3390/math10224286

Yan, J., Chen, B., Guo, R., Zeng, M., Yan, H., Xu, Z., et al. (2022b). Tongue image texture classification based on image inpainting and convolutional neural network. *Comput. Math. Methods Med.* 2022, 1–11. doi:10.1155/2022/6066640

Yan, Y., Kawahara, J., and Hamarneh, G. (2019). "Melanoma recognition via visual attention," in Information Processing in Medical Imaging: 26th International Conference, IPMI 2019, Hong Kong, China, June 2–7, 2019 (Springer), 793–804.

Zhang, H., Wang, K., Zhang, D., Pang, B., and Huang, B. (2006). "Computer aided tongue diagnosis system," in 2005 IEEE engineering in medicine and biology 27th annual conference (IEEE), 6754–6757.

Zhang, X., Zhang, J., Hu, G., and Wang, Y. (2015). "Preliminary study of tongue image classification based on multi-label learning," in Proceedings, Part III 11 Advanced Intelligent Computing Theories and Applications: 11th International Conference, ICIC 2015, Fuzhou, China, August 20-23, 2015 (Springer), 208–220.

Zhuang, Q., Gan, S., and Zhang, L. (2022). Human-computer interaction based health diagnostics using resnet34 for tongue image classification. *Comput. Methods Programs Biomed.* 226, 107096. doi:10.1016/j.cmpb.2022.107096

frontiers | Frontiers in Bioengineering and Biotechnology

TYPE Original Research
PUBLISHED 16 May 2024
DOI 10.3389/fbioe.2024.1392599

OPEN ACCESS

EDITED BY
Wujing Cao,
Chinese Academy of Sciences (CAS), China

REVIEWED BY
Chong Li,
Tsinghua University, China
Jianlong Hao,
Shanxi University of Finance and Economics, China
Bingshan Hu,
University of Shanghai for Science and Technology, China

*CORRESPONDENCE
Tingting Su,
sutingting@bjut.edu.cn

RECEIVED 27 February 2024
ACCEPTED 10 April 2024
PUBLISHED 16 May 2024

CITATION
Liang X, Yan Y, Dai S, Guo Z, Li Z, Liu S and Su T (2024), Multi-mode adaptive control strategy for a lower limb rehabilitation robot. *Front. Bioeng. Biotechnol.* 12:1392599. doi: 10.3389/fbioe.2024.1392599

Multi-mode adaptive control strategy for a lower limb rehabilitation robot

Xu Liang[1], Yuchen Yan[2], Shenghua Dai[1], Zhao Guo[3], Zheng Li[4], Shengda Liu[5] and Tingting Su[6]*

[1]School of Automation and Intelligence, Beijing Jiaotong University, Beijing, China, [2]Department of Mechanical and Electrical Engineering, North China University of Technology, Beijing, China, [3]School of Power and Mechanical Engineering, Wuhan University, Wuhan, China, [4]Faculty of Medicine, The Chinese University of Hong Kong, Shatin, China, [5]Institute of Automation, Chinese Academy of Sciences, Beijing, China, [6]Faculty of Information Technology, Beijing University of Technology, Beijing, China

Different patients have different rehabilitation requirements. It is essential to ensure the safety and comfort of patients at different recovery stages during rehabilitation training. This study proposes a multi-mode adaptive control method to achieve a safe and compliant rehabilitation training strategy. First, patients' motion intention and motor ability are evaluated based on the average human–robot interaction force per task cycle. Second, three kinds of rehabilitation training modes—robot-dominant, patient-dominant, and safety-stop—are established, and the adaptive controller can dexterously switch between the three training modes. In the robot-dominant mode, based on the motion errors, the patient's motor ability, and motion intention, the controller can adaptively adjust its assistance level and impedance parameters to help patients complete rehabilitation tasks and encourage them to actively participate. In the patient-dominant mode, the controller only adjusts the training speed. When the trajectory error is too large, the controller switches to the safety-stop mode to ensure patient safety. The stabilities of the adaptive controller under three training modes are then proven using Lyapunov theory. Finally, the effectiveness of the multi-mode adaptive controller is verified by simulation results.

KEYWORDS

impedance control, rehabilitation robot, multi-mode adaptive control, human–robot interaction, rehabilitation training strategy

1 Introduction

In recent years, the number of patients with movement disorders caused by stroke and spinal cord injury has increased rapidly, as has the corresponding rehabilitation demand. Traditional rehabilitation strategies rely on therapists to help patients participate in training, and there are some problems such as long rehabilitation cycle and low efficiency of rehabilitation which make it difficult to meet the growing recovery needs (Luo et al., 2019). As a new way of rehabilitation training, rehabilitation robots can effectively save medical resources and improve the efficiency of rehabilitation training. Therefore, this has received wide attention and recognition (Adhikari et al., 2023).

The control method plays a crucial role in the rehabilitation effect (Zhou et al., 2021) as the patient has been interacting with the robot during the training process. Traditional control methods may subject the patient to excessive torque, which increases the risk of

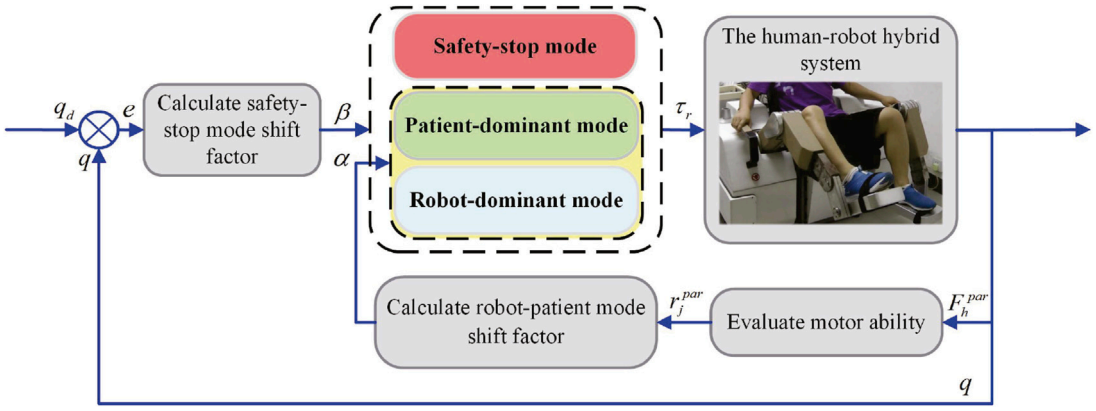

FIGURE 1
Multi-mode adaptive control block diagram.

secondary injury. In contrast, control methods based on human–robot interactive information can have good rehabilitation training effects (Guo et al., 2021). Such methods can not only effectively avoid potential injuries but also help improve recovery. Therefore, it is important to design a safe, natural, and compliant human–robot interaction control method for rehabilitation robot systems (Masengo et al., 2023; Bergmann et al., 2023; Li Z. et al., 2024; Lu et al., 2023).

For patients with weak motor ability, rehabilitation robots should provide enough assistive force to help complete training tasks. However, too much assistance may make patients slack off, and too little assistance will not help patients implement training tasks—both may reduce rehabilitation effects. In order to realize efficient rehabilitation training, human–robot interaction methods need to follow the assisted-as-need (AAN) principle (Li N. et al., 2024). At present, impedance control is usually used to implement the AAN strategy (Han et al., 2023). Mao et al. (2015) established a force field controller which constructs a virtual tunnel with impedance characteristics around the desired trajectory to assist the patient's movement. Jamwal et al. (2016) built an impedance controller for an ankle robot to assist patient compliance. Due to individual differences, it is difficult to obtain optimal impedance parameters. In addition, the interaction force and motion speed change over time, and fixed impedance parameters usually cannot meet the practical needs. The dynamic relationship between motion and interaction force can be adjusted according to the actual task by using time-varying impedance control; thus, good dynamic interaction performance can be achieved (Liang et al., 2022). Asl et al. (2020) constructed an AAN impedance controller which utilizes velocity tracking errors to adjust impedance parameters online. However, only the damping parameter is adjusted in this study, and its adaptive adjustment ability is relatively limited. Han et al. (2023) proposed an AAN control strategy for rehabilitation robots based on patients' motor intention and task performance. The learning efficiency of impedance parameters and the auxiliary level were adaptively adjusted according to the assessment results of interaction force and patient performance. The experimental results show that this method can motivate patients to increase their engagement.

For patients with a partial recovery of motor function or strong motor ability, interference with their movement should be reduced to provide sufficient freedom of movement (Han et al., 2023; Zhang and Cheah, 2015). Higher freedom of movement does not mean that patients can move without restriction. When the position and speed of robots reach a certain level, patients may be exposed to the potential risk of secondary injury (Gao et al., 2023). To ensure patient safety, control methods should have safety features such as emergency stops or motion position limitations.

To meet the needs of patients at different recovery stages and ensure their safety, multi-mode control strategies have been proposed (Zhang and Cheah, 2015; Li et al., 2021; Yang et al., 2023; Xu et al., 2019; Li et al., 2017a,b). Zhang and Cheah (2015) proposed a multi-mode control method for upper limb rehabilitation robots. The training mode is chosen based on the position error to realize safety assistance. Li et al. (2021) and Yang et al. (2023) also designed multi-mode control strategies and switched control modes according to the tracking error. These methods switch control modes according to the position errors, which will partly limit the movement freedom of patients with strong motor ability. To solve this problem, a patient's bioelectrical or interactive force signals can be used as the basis for switching training modes. Xu et al. (2019) proposed a multi-mode adaptive control strategy for a sitting lower limb rehabilitation robot. The human–robot interaction torque is estimated by using an EMG-driven impedance model. Based on the estimated human–robot interaction torque, a smooth transition between the robot-dominant and human-dominant modes can be achieved. Compared with bioelectrical signals, interaction force signals are more reliable. Li et al. (2017a) proposed an adaptive control method to smoothly switch the training modes between robot- and human-dominant modes based on the human–robot interaction force to realize safe interaction between humans and robots. Since this method ignores trajectory errors, the trajectory errors in the human-dominant mode may be large, which will lead to a reduction in the training effect. In the multi-mode control strategy, relying on only a single signal cannot provide the most suitable rehabilitation training mode for patients. Li et al. (2017b) proposed a multi-mode control strategy in which the tracking error and human-robot interaction force are taken as the basis for mode switching. Based on the tracking error, the controller can switch flexibly between human- and robot-dominant modes. When the human–robot interaction force exceeds the safety threshold, the controller will switch to the safety-stop mode to ensure the patient's safety. This method still uses the tracking error as the basis for switching

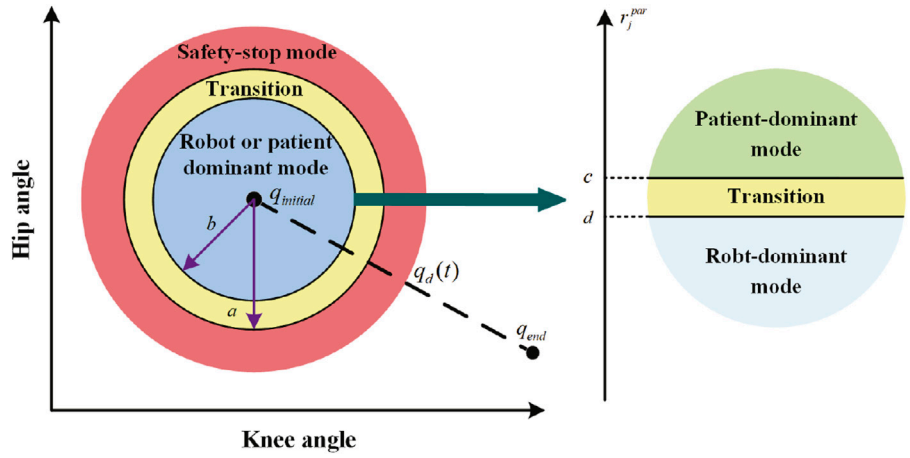

FIGURE 2
Training modes.

between human- and robot-dominated modes, which will also limit the movement freedom of patients with strong motor ability. In addition, the interaction force signals cannot fully indicate the patients' motor ability.

To solve such problems, a multi-mode adaptive control strategy for repetitive rehabilitation tasks is here proposed. The human–robot interaction force evaluation factor is introduced to assess a patient's motor ability and motor intention online (Han et al., 2023). Based on the evaluation result of the patient's motor ability and trajectory errors, the training mode can be freely switched between robot-dominant, patient-dominant, and safety-stop modes. In the robot-dominant mode, the robot's assistance level and the learning efficiency of impedance parameters are periodically adjusted according to the trajectory error, speed error, the assessed motor ability, and the motion intention, so as to provide appropriate assistance for patients with different motor abilities. In the patient-dominant mode, the controller allows the patient to modify the reference speed so that patients with higher motor ability have enough freedom of movement. When the trajectory error exceeds the safe range, it switches to safety-stop mode to ensure patient safety. The proposed method is not only suitable for patients at different stages of recovery and with different motor abilities but can also stimulate their enthusiasm to participate in rehabilitation training, further enhancing the rehabilitation effect.

2 Dynamic model of the human–robot hybrid system

During the rehabilitation training, the lower limb rehabilitation robot is in close contact with the patients' affected limb, forming a human–robot hybrid system. The hybrid system's dynamic model is shown as Eq. 1.

$$M(q)\ddot{q} + C(q,\dot{q})\dot{q} + G(q) = \tau_r + \tau_h, \tag{1}$$

where $q = [q_1 \cdots q_i]^{\mathrm{T}}$ represents the robot's joint angle, and i denotes the number of the robot's joints. $\dot{q}$ and $\ddot{q}$ represent the angular speed and angular acceleration, respectively. $M(q)$, $C(q,\dot{q})$ and $G(q)$ denote the inertia matrix, the Coriolis and centrifugal matrix, and the gravity vector, respectively. τ_r and τ_h respectively represent the actuation torque and interaction torque exerted by patient. In this paper, the interaction force F_h is exerted on the robot end, give by Eq. 2.

$$\tau_h = J^{\mathrm{T}}(q)F_h, \tag{2}$$

where $J(q)$ represents the Jacobian matrix.

3 Multi-mode control method

The functions and designs of the three control modes are briefly introduced in this section. For repetitive tasks, when the patient does not have enough motor ability to independently complete the training task, the robot-dominant mode runs. Adaptive assistance is then provided according to the patient's motor ability and motion intention. For patients with weak motor ability, the assistance level will be periodically increased. For patients with a certain motor ability but who cannot yet complete the task independently, the assistance intensity will reduce appropriately to encourage more active participation in the training task. When the patient has recovered part of the motor function and can complete the training task independently, the patient-dominant mode runs. In this case, only movement speed is adjusted to provide the patient with a high degree of freedom of movement. When the patient's movement is abnormal or the task is too difficult, the robot's trajectory may exceed the safe range. In this case, the safety-stop mode runs to ensure patient safety.

3.1 Design of human–robot interaction force evaluation factor and mode shift factor

According to the functional requirements of the three control modes, a unified control law is established that includes the

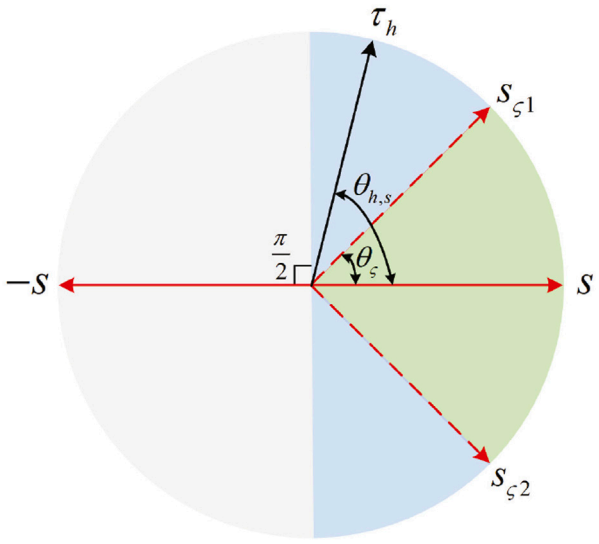

FIGURE 3
Schematic diagram of the compensation principle. When $|\theta_{h,s}| < \theta_\varsigma$, τ_h is retained. When $\theta_\varsigma \le |\theta_{h,s}| \le \frac{\pi}{2}$, τ_h is compensated to $s_{\varsigma 1}$ or $s_{\varsigma 2}$. When $\frac{\pi}{2} \le |\theta_{h,s}|$, τ_c is utilized to neutralize τ_h.

reference term, impedance learning term, sliding term, and compensation term, as shown below.

$$\tau_r = \underbrace{M\ddot{q}_{ref} + C\dot{q}_{ref} + G}_{\text{reference term}} + \underbrace{\alpha(K(t)e + D(t)\dot{e})}_{\text{impedance learning term}} + \underbrace{L(t)s}_{\text{sliding term}} + \underbrace{\tau_c(t)}_{\text{compensation term}} \tag{3}$$

where M, C, and G are abbreviations of $M(q), C(q,\dot{q})$, and $G(q)$, respectively. $K(t)$ and $D(t)$ denote variable stiffness and damping, respectively. $L(t)$ denotes the sliding control gain, while $e = q_d - q$ represents the trajectory error between the desired q_d and actual trajectory q. $s = \dot{q}_{ref} - \dot{q}$ denotes the sliding vector. $\dot{q}_{ref} = (1-\beta)(\dot{q}_d + \alpha A e + (1-\alpha)\dot{q}_h)$ denotes the reference speed, where A is a symmetric positive definite matrix, $\dot{q}_h$ is the modified speed determined by the interaction torque, α is the robot–patient mode shift factor determined by the patients' motor ability, and β is the stop-mode shift factor, determined by the trajectory error. Before analyzing the change pattern of these two mode shift factors, the human–robot interaction force evaluation factors r_j^{par} and r_j^{ort} are introduced to assess the patients' motor ability and motion intention (Han et al., 2023) as shown in Eqs 4, 5.

$$r_j^{par} = \frac{1}{T}\int_{t_{j-1}}^{t_j} F_h^{par}\,dt = \frac{1}{T}\int_{t_{j-1}}^{t_j} F_h^{\mathrm{T}} \frac{[\dot{x}_d, \dot{y}_d]^{\mathrm{T}}}{\sqrt{\dot{x}_d^2 + \dot{y}_d^2}}\,dt, \tag{4}$$

$$r_j^{ort} = \frac{1}{T}\int_{t_{j-1}}^{t_j} F_h^{ort}\,dt = \frac{1}{T}\int_{t_{j-1}}^{t_j} F_h^{\mathrm{T}} \frac{[-\dot{y}_d, \dot{x}_d]^{\mathrm{T}}}{\sqrt{\dot{x}_d^2 + \dot{y}_d^2}}\,dt, \tag{5}$$

where F_h^{par} represents the human–robot interaction force parallel to the desired trajectory. F_h^{ort} represents the human–robot interaction force perpendicular to the desired trajectory. $(\dot{x}_d, \dot{y}_d)$ represents the desired speed at the robot end. F_h can be obtained by the interaction force estimation methods (Lu et al., 2023; Liang et al., 2023). j denotes the jth training task, T denotes the task period. t_j, and t_{j-1} represent the initial moments of the jth and $(j-1)$th task, respectively.

When r_j^{par} is positive, the patient's movement speed is greater than the desired speed, and the robot is driven by the patient along the desired trajectory. On the other hand, when r_j^{par} is negative, the patient is driven by the robot along the desired trajectory. $|r_j^{ort}| > 0$ means that the patient intends to deviate from the desired trajectory. The greater the r_j^{par}, the stronger the patient's motor ability. The larger $|r_j^{ort}|$ is, the stronger the patient's intention to move away from the desired trajectory.

The change pattern of α and β is designed as follows:

$$\beta = \begin{cases} 1, & \|e\| \in (a, +\infty) \\ 0, & \|e\| \in [0, a] \end{cases}, \tag{6}$$

$$\alpha = \begin{cases} 1, & \beta = 0 \text{ and } r_j^{par} \in (-\infty, c] \\ 0, & \beta = 0 \text{ and } r_j^{par} \in (c, +\infty) \\ 0, & \beta = 1 \end{cases}, \tag{7}$$

where a and c are given values. $\|e\|$ denotes the Euclidean norm of e. If $\|e\| > a$, then the task is too difficult or the patient's movement is

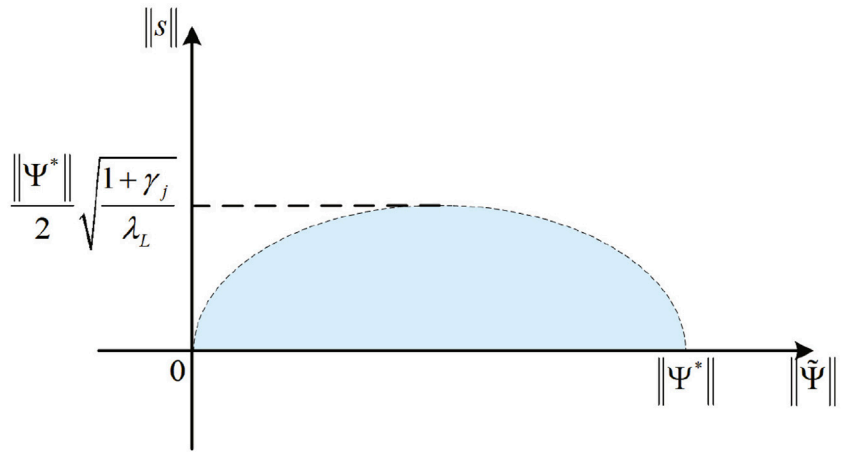

FIGURE 4
Schematic diagram of the boundary set Ω.

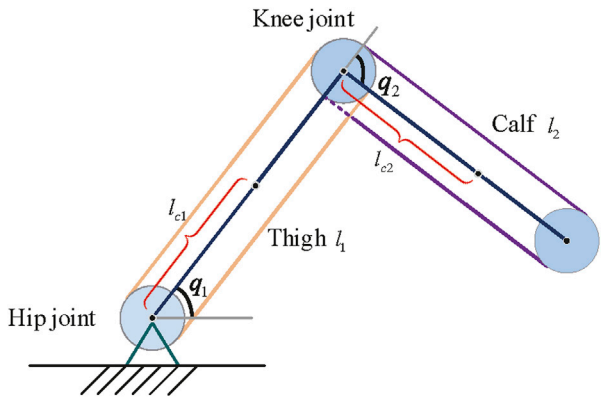

FIGURE 5
Simplified structure of a lower limb rehabilitation robot.

TABLE 1 Initialization parameters in simulation.

Parameter	Value	Parameter	Value
a	$\pi/12$	Q_{τ_c}	[30, 0; 0, 30]
b	$\pi/18$	$s_{\min}$	0.008
c	−0.1	θ_ς	$4\pi/9$
d	−0.4	r_1^{par}	−1
L_0	[4, 0; 0, 4]	r_1^{ort}	0
$r_{\min}^{par}$	−2	A	[10, 0; 0, 10]
$r_{\max}^{par}$	−1	m_1	8
$r_{\min}^{ort}$	0.1	m_2	8
$r_{\max}^{ort}$	0.5	l_1	0.5
Q_K	[50, 0; 0, 50]	l_2	0.6
Q_D	[10, 0; 0, 10]	l_{c1}	0.3
T	10	l_{c2}	0.4
M_{im}	[120, 0; 0, 60]	T_{smo}	1.7
B_{im}	[60, 0; 0, 30]		

abnormal, which will lead to excessive trajectory errors or even secondary injury to the patient. The controller will then switch to safety-stop mode to ensure patient safety. If $\|e\| \le a$, then the patient is able to complete training task either with the robot's assistance or independently. The controller will then switch to either robot-dominant or patient-dominant mode based on the value of α. If $r_j^{par} > c$, then the patient can complete the task independently, and it will switch to patient-dominant mode. If $r_j^{par} \le c$, the patient's motor ability is insufficient to complete the training task, and it will switch to the robot-dominant mode. In practice, c can be set to a constant close to 0. If the patient has good control over the affected limb, c can be slightly reduced, allowing the controller to easily enter and maintain the patient-dominant mode. If the patient has poor control over the affected limb, c can be slightly increased so that the controller is always in robot-dominant mode so that the robot can help the patient complete the training task and correct their wrong movements.

The control diagram is shown in Figure 1. To ensure patient safety, the safety-stop mode has the highest priority among the three modes, which is reasonable in practical applications. To ensure the smoothness of the mode switching process, transition intervals are added to Eqs 6, 7, and then the change pattern of α and β is modified as Eqs 8, 9.

$$\beta = \begin{cases} 1, & \|e\| \in (a, +\infty) \\ \dfrac{\left[\left(\|e\|^2 - a^2\right)^4 - \left(b^2 - a^2\right)^4\right]^4}{\left(b^2 - a^2\right)^{16}}, & \|e\| \in (b, a] \\ 0, & \|e\| \in [0, b], \end{cases} \tag{8}$$

$$\alpha = \begin{cases} 1, & \beta \ne 1 \text{ and } r_j^{par} \in (-\infty, d] \\ 1 - \sin^2\left(\dfrac{\left(r_j^{par} - d\right)\pi}{2(c-d)}\right), & \beta \ne 1 \text{ and } r_j^{par} \in (d, c] \\ 0, & \beta \ne 1 \text{ and } r_j^{par} \in (c, +\infty) \\ 0, & \beta = 1, \end{cases} \tag{9}$$

where b and d are given values. The modified α and β change smoothly as r_j^{par} and e change. According to the patient's motor ability and trajectory error, the controller switches freely between the three modes (Figure 2). However, r_j^{par} is periodically adjusted, and it will cause α to be discontinuous in time. When α changes at t_1, the changed α is expressed as $\alpha_1 = \alpha(t_1)$, and we have

$$\alpha(t) = \alpha_s + (\alpha_1 - \alpha_s)\sin^2\left(\frac{(t - t_1)\pi}{2T_{smo}}\right) t \in [t_1, t_1 + T_{smo}], \tag{10}$$

where $\alpha_s = \alpha(t_1 - t_s)$, t_s is the sampling time, and T_{smo} is the smoothing time. Thus, α is smooth in time.

Although Eq. 10 can ensure the continuity of α, T_{smo} may also cause a lag in mode switching. Therefore, the value of T_{smo} should not be too large in practical applications.

3.2 The Robot-dominant mode

When $\alpha = 1, \beta = 0$, the controller is in the robot-dominant mode. In this mode, the human–robot interaction torque is described as Eq. 11 (Han et al., 2023; Yang et al., 2011):

$$\tau_h(t) = \tau_0(t) + K_h(t)e + D_h(t)\dot{e}, \tag{11}$$

where the stiffness parameters $K_h(t)$, damping parameters $D_h(t)$, and compensating torque $\tau_0(t)$ are assumed to vary with time. The minimum quantities of stiffness, damping, and compensating torque are assumed to be $K_m(t)$, $D_m(t)$, and $\tau_m(t)$, respectively, and

$$\int_{t-T}^{t} -\left[s^{\mathrm{T}}(\sigma)K_m(\sigma)e(\sigma) + s^{\mathrm{T}}(\sigma)D_m(\sigma)\dot{e}(\sigma) + s^{\mathrm{T}}(\sigma)\tau_m(\sigma) + s^{\mathrm{T}}(\sigma)\tau_h(\sigma)\right]d\sigma \le 0. \tag{12}$$

In this mode, Eq. 3 can be written as Eq. 13.

$$\tau_r = M\ddot{q}_{ref} + C\dot{q}_{ref} + G + K(t)e + D(t)\dot{e} + L(t)s + \tau_c(t), \tag{13}$$

where the update rules of $K(t)$, $D(t)$, $L(t)$, and $\tau_c(t)$ adhere to the following principles. 1) When r_j^{par} is negative and its absolute value

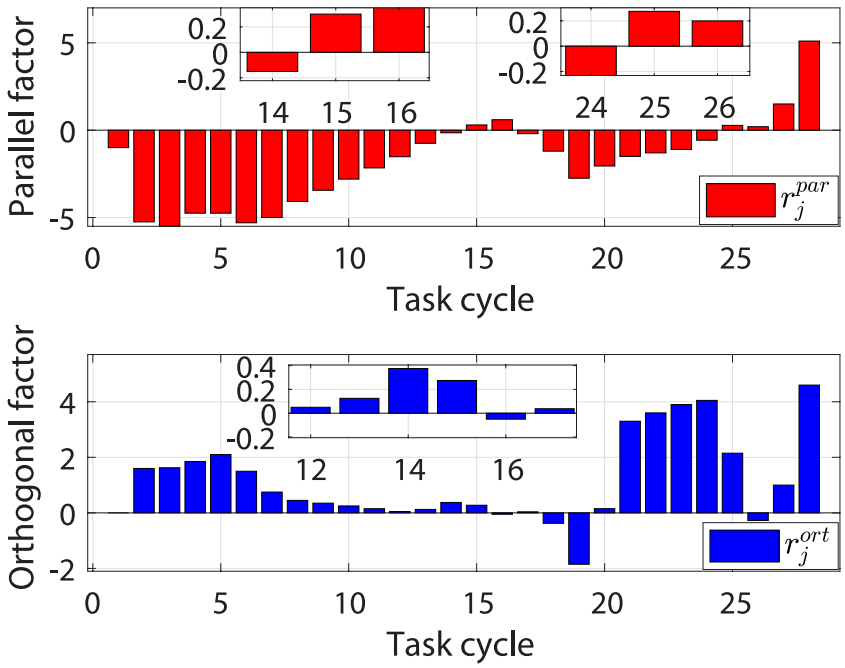

FIGURE 6
Evaluation results of the human–robot interaction force under different task cycles.

is large, the patient's motor ability is insufficient to complete the desired training task. In this case, the robot should increase its assistance level to help the patient complete training task. When r_j^{par} is negative and its absolute value is small, then, although the patient does not have the ability to complete the training task independently, the degree of active participation in the training is relatively high. In this case, the robot should reduce its assistance level to encourage the patient to further improve training enthusiasm. 2) The impedance parameters and torque compensation terms are adjusted adaptively by iterative learning. When the absolute value of r_j^{ort} is large, the learning speed increases to quickly correct the patient's movement. When the absolute value of r_j^{ort} is small, the learning speed slows down.

The update law for $L(t)$ is designed as follows:

$$\begin{aligned} L(t) &= \left(1+\eta_j\right)L_0 \\ \eta_j &= \left(1+\eta\right)\left(1+\eta_{j-1}\right)-1, \end{aligned} \tag{14}$$

where

$$\begin{cases} \eta = 0, & r_{\min}^{par} \le r_j^{par} \le r_{\max}^{par} \\ -1 < \eta < 0, & r_j^{par} > r_{\max}^{par} \\ 0 < \eta < 1, & r_j^{par} < r_{\min}^{par}, \end{cases} \tag{15}$$

where $\eta_0 = 0$. L_0 is a positive definite matrix. In this mode, $L(t)$ is periodically adjusted according to the value of r_j^{par} as shown in Eqs 14, 15. $r_{\min}^{par}$ and $r_{\max}^{par}$ are given constants, and their values are smaller than c and d. In practice, these two parameters can be adjusted according to the patient's motor ability. If their motor ability is weak, $r_{\min}^{par}$ and $r_{\max}^{par}$ can be set to smaller values so that the controller can more easily detect the patient's effort and reduce the robot's assistance level.

The update law for $K(t)$, $D(t)$, and $\tau_c(t)$ are given as follows:

$$\begin{cases} \Delta K(t) = K(t) - K(t-T) = Q_K\left(se^{\mathrm{T}} - \left(1+\gamma_j\right)K(t)\right) \\ \Delta D(t) = D(t) - D(t-T) = Q_D\left(s\dot{e}^{\mathrm{T}} - \left(1+\gamma_j\right)D(t)\right) \\ \Delta\tau_c(t) = \tau_c(t) - \tau_c(t-T) = Q_{\tau_c}\left(s - \left(1+\gamma_j\right)\tau_c(t)\right) \end{cases} \tag{16}$$

where γ_j is updated as shown in Eq. 17.

$$\gamma_j = (1+\zeta)\left(1+\gamma_{j-1}\right)-1, \begin{cases} \zeta = 0, & r_{\min}^{ort} \le \left|r_j^{ort}\right| \le r_{\max}^{ort} \\ -1 < \zeta < 0, & \left|r_j^{ort}\right| > r_{\max}^{ort} \\ 0 < \zeta < 1, & \left|r_j^{ort}\right| < r_{\min}^{ort} \end{cases}, \tag{17}$$

where $\gamma_j \in (-1, 1)$ denotes the iterative learning factor, and ζ denotes the update rate. $\gamma_0 = 0$. Q_K, Q_D, and Q_{τ_c} are symmetric positive definite matrices. During the first task cycle, $K(t) = 0^{i\times i}$, $D(t) = 0^{i\times i}$, and $\tau_c(t) = 0^{i\times 1}$.

In this mode, based on the assessment of motor ability and motor intention, $L(t)$ and γ_j are periodically adjusted to provide adaptive assistance for patients at different recovery stages.

3.3 The patient-dominant mode

When $\alpha = 0$, $\beta = 0$, the controller is in the patient-dominant mode. In this mode, Eq. 3 can be written as Eq. 18.

$$\tau_r = M\ddot{q}_{ref} + C\dot{q}_{ref} + G + L(t)s + \tau_c, \tag{18}$$

where $L(t)$ is given in Eq. 19.

$$L(t) = \begin{cases} L_0, & j = 1 \text{ or } \lambda_{L_{last}} < \lambda_{L_0} \\ L_{last}, & j > 1 \text{ and } \lambda_{L_{last}} \ge \lambda_{L_0} \end{cases}, \tag{19}$$

where L_{last} denotes the last updated value of $L(t)$ before entering this mode. $\lambda_{L_{last}}$ denotes the smallest eigenvalue of L_{last}, and λ_{L_0} denotes the smallest eigenvalue of L_0. From the definition of $\dot{q}_{ref}$ and s, we

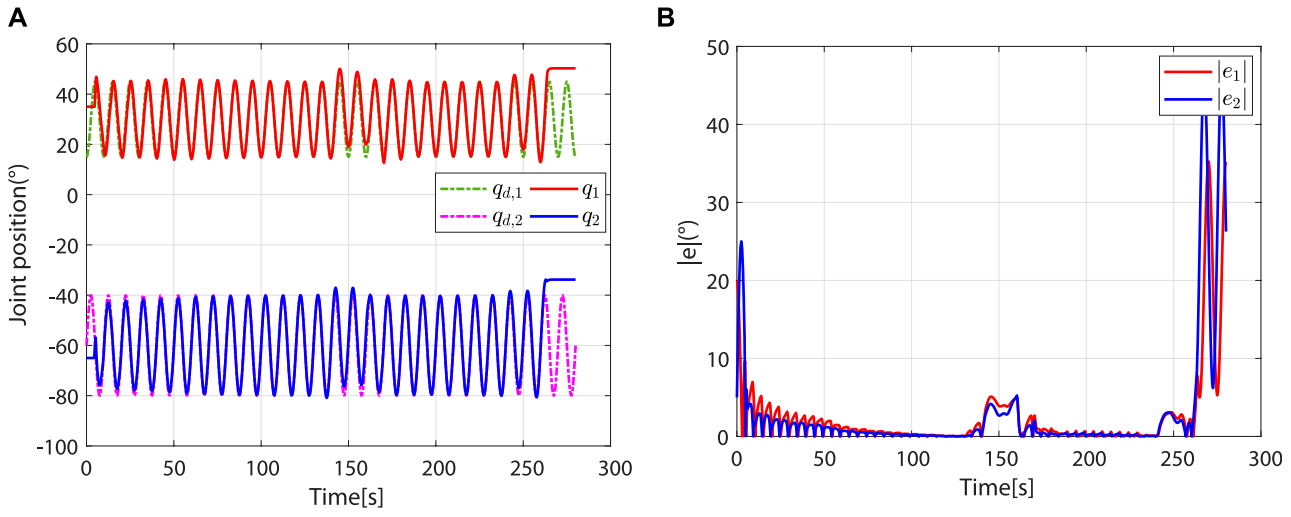

FIGURE 7
Entire simulation results of hip and knee joints. **(A)** Desired and actual trajectories. **(B)** Absolute values of trajectory errors.

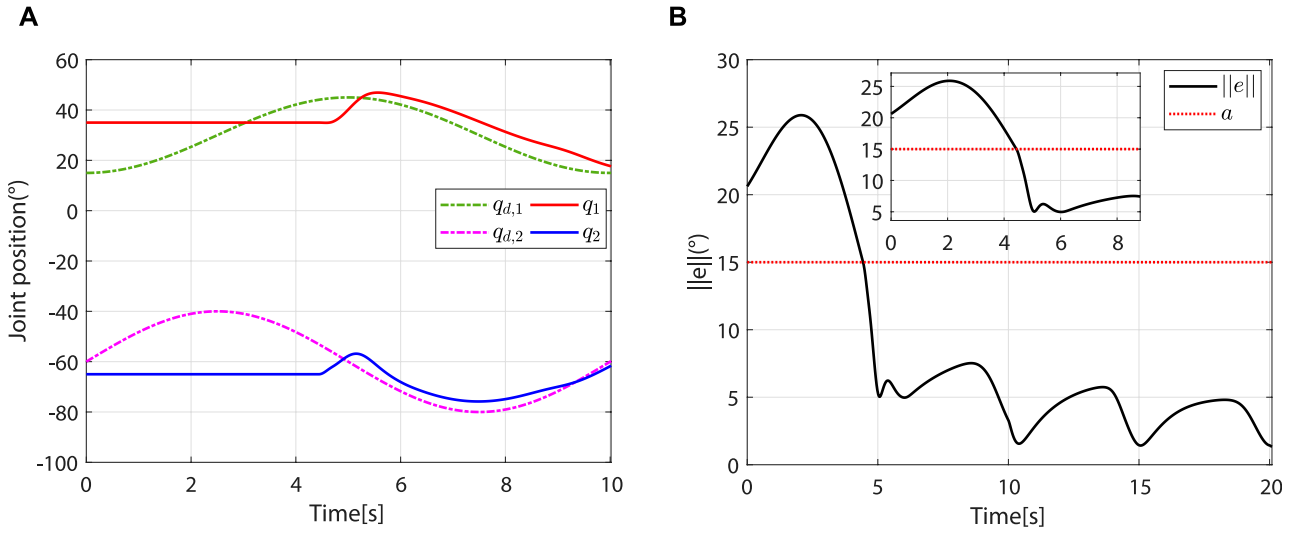

FIGURE 8
The controller leaves the safety-stop mode at approximately 4.44 s. **(A)** Desired and actual trajectories. **(B)** At approximately 4.44 s, $\|e\| < a$.

derive $s = \dot{q}_{ref} - \dot{q} = \dot{q}_d + \dot{q}_h - \dot{q}$. In this mode, $\dot{q}_h$ can be obtained by using the following impedance equation:

$$\tau_h = M_{im}\ddot{q}_h + B_{im}\dot{q}_h \tag{20}$$

where M_{im} and B_{im} denote the inertia and damping parameters, respectively.

To ensure the stability of human–robot interactions and encourage active patient participation, τ_c was utilized to appropriately compensate τ_h (Zhang and Cheah, 2015). When the absolute value of the angle $\theta_{h,s}$ between τ_h and s is smaller than θ_ς and $\theta_\varsigma \in (0, \frac{\pi}{2})$, then the patient exerts an interactive force to drive the robot close to the reference speed—that is, the patient's motion intention can be seen as correct. In this case, τ_h is retained. When $\theta_\varsigma \le |\theta_{h,s}| \le \frac{\pi}{2}$, then the patient's motion intention cannot be seen as quite correct. In this case, τ_h is compensated to its nearest unit vector $s_{\varsigma 1}$ or $s_{\varsigma 2}$ to ensure that the angle between the compensated torque and s is equal to θ_ς. When $|\theta_{h,s}| > \frac{\pi}{2}$, the patient's motion intention cannot be seen as correct. In this case, τ_c is utilized to neutralize τ_h—that is, $\tau_c + \tau_h = 0$. The schematic diagram of the compensation principle is shown in Figure 3. In this mode, $\tau_c + \tau_h$ can be expressed as Eqs 21–23

$$\tau_c + \tau_h = \mu(s)c(\tau_h), \tag{21}$$

where

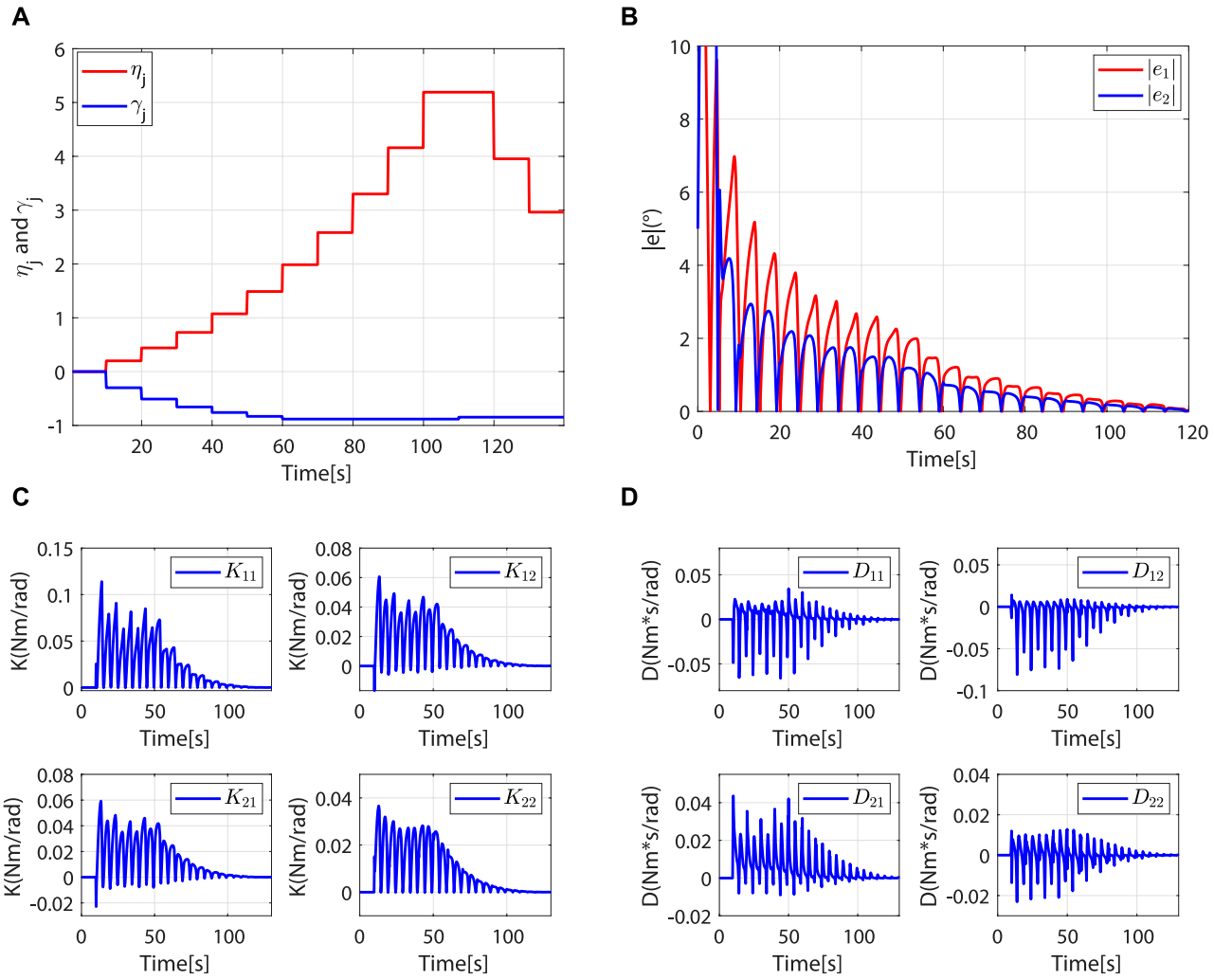

FIGURE 9
The controller is in the robot-dominant mode, and the robot assisted the patient to complete the rehabilitation task. **(A)** η_j and γ_j. **(B)** Absolute values of trajectory errors. **(C)** $K(t)$. **(D)** $D(t)$.

$$\mu(s) = \begin{cases} 1, & \|s\| \geq s_{\min} \\ \sin^2\left(\dfrac{\|s\|\pi}{2s_{\min}}\right), & \|s\| < s_{\min} \end{cases} \tag{22}$$

and

$$c(\tau_h) = \begin{cases} \tau_h, & |\theta_{h,s}| \in [0, \theta_\varsigma) \\ s_\varsigma \|\tau_h\| \cos^2\left(\dfrac{(|\theta_{h,s}| - \theta_\varsigma)\pi}{2\left(\frac{\pi}{2} - \theta_\varsigma\right)}\right), & |\theta_{h,s}| \in \left[\theta_\varsigma, \frac{\pi}{2}\right] \\ 0, & |\theta_{h,s}| \in \left(\frac{\pi}{2}, \pi\right], \end{cases} \tag{23}$$

where $s_{\min}$ is a small positive number. $\mu(s)$ ensures the smoothness of $\tau_c + \tau_h$ at $s = 0$. s_ς equals $s_{\varsigma 1}$ or $s_{\varsigma 2}$.

In this mode, the impedance learning term is removed, and the sliding mode control term is converted to a speed control term. In addition, the patient can modify the reference speed, improving compliance with and the flexibility of rehabilitation training. τ_c is used to compensate τ_h appropriately. Compared with the robot-dominant mode, the patient-dominant mode further improves the patient's freedom of movement.

3.4 The safety-stop mode

When $\alpha = 0$, $\beta = 1$, the controller is in the safety-stop mode. In this mode, Eq. 3 can be written as Eq. 24.

$$\tau_r = M\ddot{q}_{ref} + C\dot{q}_{ref} + G + L(t)s + \tau_c, \tag{24}$$

where $L(t)$ is given as Eq. 25.

$$L(t) = \begin{cases} L_0, & j = 1 \text{ or } \lambda_{L_{last}} < \lambda_{L_0} \\ L_{last}, & j > 1 \text{ and } \lambda_{L_{last}} \geq \lambda_{L_0}. \end{cases} \tag{25}$$

τ_c is utilized to neutralize τ_h—that is, $\tau_c + \tau_h = 0$. From the definition of $\dot{q}_{ref}$ and s, we derive $s = \dot{q}_{ref} - \dot{q} = -\dot{q}$.

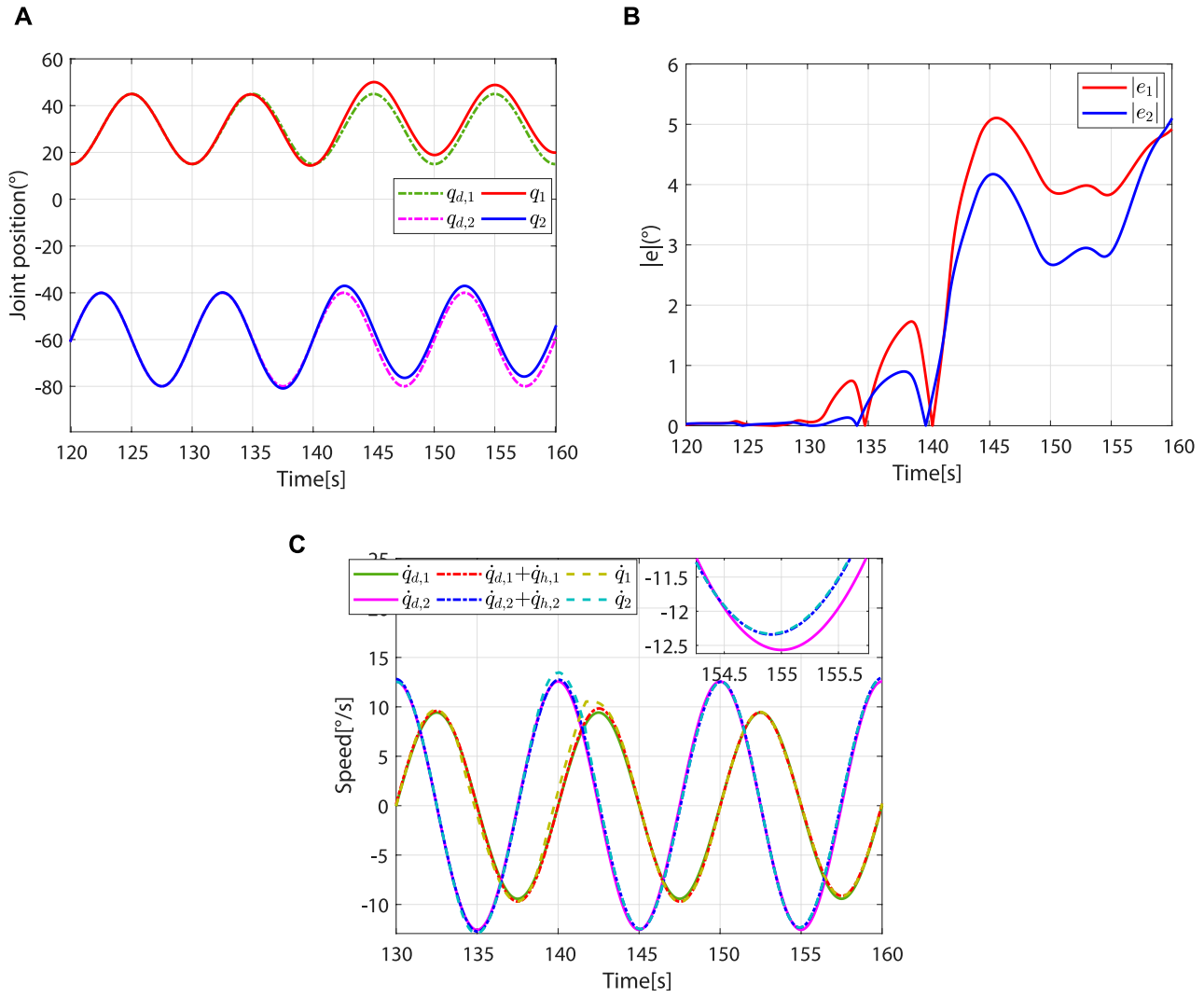

FIGURE 10
Controller switches from robot-dominant to patient-dominant mode and remains in the patient-dominant mode. **(A)** Desired and actual trajectories. **(B)** Absolute values of the trajectory errors. **(C)** Desired angular speed, reference angular speed, and actual angular speed.

In this mode, the impedance learning term is removed, and the sliding mode control term is converted to a damping control term. The robot stops moving to ensure the patient's safety.

4 Stability analysis

In this section, the Lyapunov stability theorem is used to establish the stability of the human–robot interaction process. Specifically, in the robot-dominant mode, s is limited to a certain bound. Under the assumption of Eq. (12), the learning errors of impedance parameters and torque compensation terms are bounded (Han et al., 2023). In the patient-dominant mode, the robot's speed converges to $\dot{q}_d + \dot{q}_h$. When it switches to the safety-stop mode, the robot's speed decreases to zero.

The Lyapunov candidate function is chosen as Eq. 26.

$$V(t) = V_1(t) + V_2(t) = \frac{1}{2}s^{\mathrm{T}}Ms + \frac{1}{2}\int_{t-T}^{t} \alpha\tilde{\Psi}^{\mathrm{T}}(\sigma)Q^{-1}\tilde{\Psi}(\sigma)d\sigma, \quad (26)$$

where

$$\tilde{\Psi}(t) = \Psi(t) - \Psi^{*}(t) = \left[vec\left(\tilde{K}(t)\right)^{\mathrm{T}}, vec\left(\tilde{D}(t)\right)^{\mathrm{T}}, \tilde{\tau}_c(t)^{\mathrm{T}}\right]^{\mathrm{T}}, \quad (27)$$

$$\begin{cases} \tilde{K}(t) = K(t) - K_m(t) \\ \tilde{D}(t) = D(t) - D_m(t) \\ \tilde{\tau}_c(t) = \tau_c(t) - \tau_m(t), \end{cases} \quad (28)$$

$$\begin{cases} \Psi(t) = \left[vec(K(t))^{\mathrm{T}}, vec(D(t))^{\mathrm{T}}, \tau_c(t)^{\mathrm{T}}\right]^{\mathrm{T}} \\ \Psi^{*}(t) = \left[vec(K_m(t))^{\mathrm{T}}, vec(D_m(t))^{\mathrm{T}}, \tau_m(t)^{\mathrm{T}}\right]^{\mathrm{T}} \\ Q = diag\left(I \otimes Q_K, I \otimes Q_D, Q_{\tau_c}\right), \end{cases} \quad (29)$$

where $vec(\cdot)$ represents the column vectorization operator. $\otimes$ represents the Kronecker product.

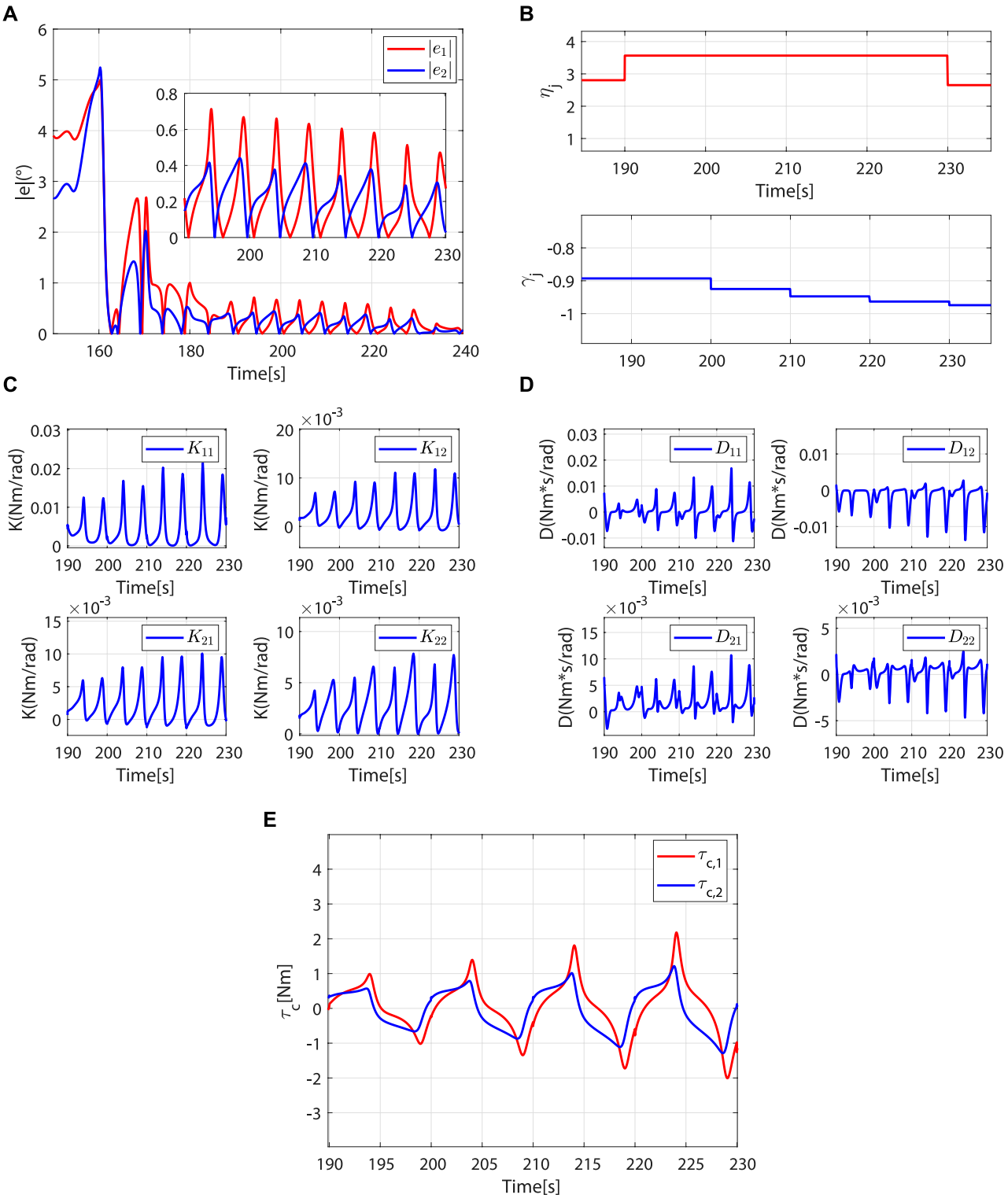

FIGURE 11
Controller switches from patient-dominant to robot-dominant mode and remains in the robot-dominant mode. **(A)** Absolute values of trajectory errors. **(B)** η_j and γ_j. **(C)** $K(t)$. **(D)** $D(t)$. **(E)** $\tau_c(t)$.

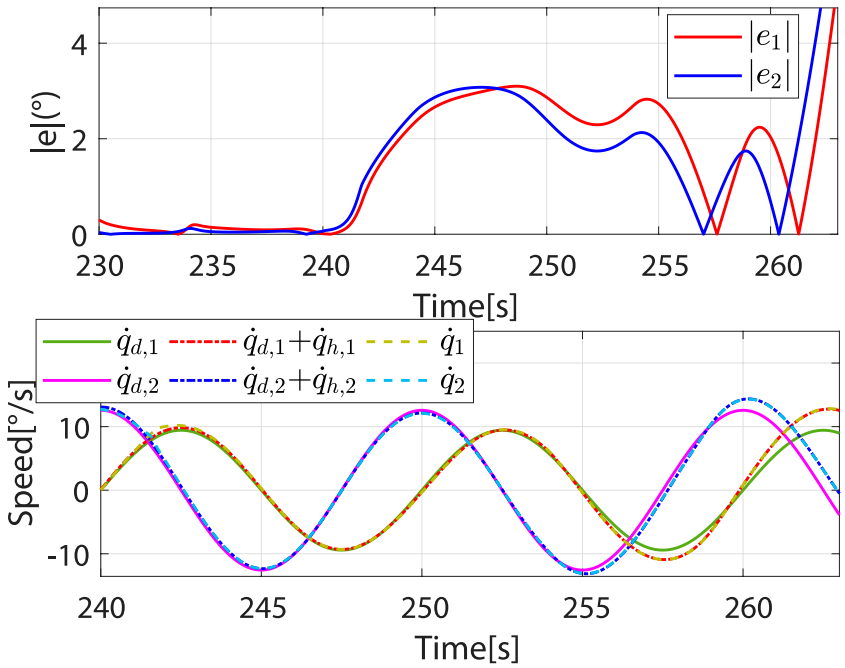

FIGURE 12
Speed and absolute values of trajectory errors when controller switches again from robot-dominant to patient-dominant mode.

4.1 Stability analysis in the robot-dominant mode

In this mode, the system is stable if $V(t)$ is non-growing in each task cycle (Han et al., 2023).

$$\Delta V = V(t) - V(t-T) \le 0. \tag{30}$$

Taking the derivative of $V_1(t)$, we derive

$$\dot{V}_1(t) = s^{\mathrm{T}} M \dot{s} + \frac{1}{2} s^{\mathrm{T}} \dot{M} s. \tag{31}$$

Since $\dot{M} - 2C$ is an antisymmetric matrix, we can obtain Eq. 32.

$$\dot{M}^{\mathrm{T}} + \dot{M} = 2\dot{M} = 2C^{\mathrm{T}} + 2C. \tag{32}$$

Combining Eq. 31 and the definition of s, we then have

$$\begin{aligned} \dot{V}_1(t) &= s^{\mathrm{T}}\left(M\ddot{q}_{ref} - M\ddot{q}\right) + \frac{1}{2} s^{\mathrm{T}}\left(C^{\mathrm{T}} + C\right)s \\ &= -\alpha s^{\mathrm{T}} K(t) e - \alpha s^{\mathrm{T}} D(t)\dot{e} - s^{\mathrm{T}} L(t) s - s^{\mathrm{T}}\tau_c(t) - s^{\mathrm{T}}\tau_h(t). \end{aligned} \tag{33}$$

Since $\alpha = 1$, $\beta = 0$, Eq. 33 can be expressed as Eq. 34.

$$\dot{V}_1(t) = -s^{\mathrm{T}} K(t) e - s^{\mathrm{T}} D(t)\dot{e} - s^{\mathrm{T}} L(t) s - s^{\mathrm{T}}\tau_c(t) - s^{\mathrm{T}}\tau_h(t). \tag{34}$$

Then, we can get Eq. 35

$$\begin{aligned} \Delta V_1 &= \Delta V_1(t) - \Delta V_1(t-T) \\ &= \int_{t-T}^{t} -s^{\mathrm{T}} K(\sigma) e - s^{\mathrm{T}} D(\sigma)\dot{e} - s^{\mathrm{T}} L(\sigma) s - s^{\mathrm{T}}\tau_c(\sigma) - s^{\mathrm{T}}\tau_h(\sigma) d\sigma \end{aligned}. \tag{35}$$

Since $L(t)$ is periodically adjusted, the following inequality can be obtained:

$$\Delta V_1 \le \int_{t-T}^{t} -s^{\mathrm{T}} K(\sigma) e - s^{\mathrm{T}} D(\sigma)\dot{e} - s^{\mathrm{T}}\lambda_L s - s^{\mathrm{T}}\tau_c(\sigma) - s^{\mathrm{T}}\tau_h(\sigma) d\sigma, \tag{36}$$

where λ_L is the smallest eigenvalue of $L(\sigma)$.

According to Eqs 12, 28, 36, we thus obtain Eq. 37

$$\begin{aligned} &\int_{t-T}^{t} -s^{\mathrm{T}} K(\sigma) e - s^{\mathrm{T}} D(\sigma)\dot{e} - s^{\mathrm{T}}\lambda_L s - s^{\mathrm{T}}\tau_c(\sigma) - s^{\mathrm{T}}\tau_h(\sigma) d\sigma \\ &= \int_{t-T}^{t} \left[-s^{\mathrm{T}}\tilde{K}(\sigma) e - s^{\mathrm{T}}\tilde{D}(\sigma)\dot{e} - s^{\mathrm{T}}\lambda_L s - s^{\mathrm{T}}\tilde{\tau}_c(\sigma) \right. \\ &\quad \left. -s^{\mathrm{T}} K_m(\sigma) e - s^{\mathrm{T}} D_m(\sigma)\dot{e} - s^{\mathrm{T}}\tau_m(\sigma) - s^{\mathrm{T}}\tau_h(\sigma)\right] d\sigma \\ &\le \int_{t-T}^{t} \left[-s^{\mathrm{T}}\tilde{K}(\sigma) e - s^{\mathrm{T}}\tilde{D}(\sigma)\dot{e} - s^{\mathrm{T}}\lambda_L s - s^{\mathrm{T}}\tilde{\tau}_c(\sigma)\right] d\sigma, \end{aligned} \tag{37}$$

that is,

$$\Delta V_1 \le \int_{t-T}^{t} \left[-s^{\mathrm{T}}\tilde{K}(\sigma) e - s^{\mathrm{T}}\tilde{D}(\sigma)\dot{e} - s^{\mathrm{T}}\lambda_L s - s^{\mathrm{T}}\tilde{\tau}_c(\sigma)\right] d\sigma. \tag{38}$$

According to Eqs 27–29, we obtain

$$\begin{aligned} \Delta V_2 &= \Delta V_2(t) - \Delta V_2(t-T) \\ &= \frac{1}{2}\int_{t-T}^{t} \underbrace{tr\left\{\tilde{K}^{\mathrm{T}}(\sigma) Q_K^{-1}\tilde{K}(\sigma) - \tilde{K}^{\mathrm{T}}(\sigma-T) Q_K^{-1}\tilde{K}(\sigma-T)\right\}}_{Item\ a} \\ &\quad + \underbrace{tr\left\{\tilde{D}^{\mathrm{T}}(\sigma) Q_D^{-1}\tilde{D}(\sigma) - \tilde{D}^{\mathrm{T}}(\sigma-T) Q_D^{-1}\tilde{D}(\sigma-T)\right\}}_{Item\ b} \\ &\quad + \underbrace{\tilde{\tau}_c^{\mathrm{T}}(\sigma) Q_{\tau_c}^{-1}\tilde{\tau}_c(\sigma) - \tilde{\tau}_c^{\mathrm{T}}(\sigma-T) Q_{\tau_c}^{-1}\tilde{\tau}_c(\sigma-T)}_{Item\ c}\, d\sigma. \end{aligned} \tag{39}$$

Since $K_m(t)$, $D_m(t)$, and $\tau_m(t)$ are periodic, Eq. 16 can be written as Eq. 40.

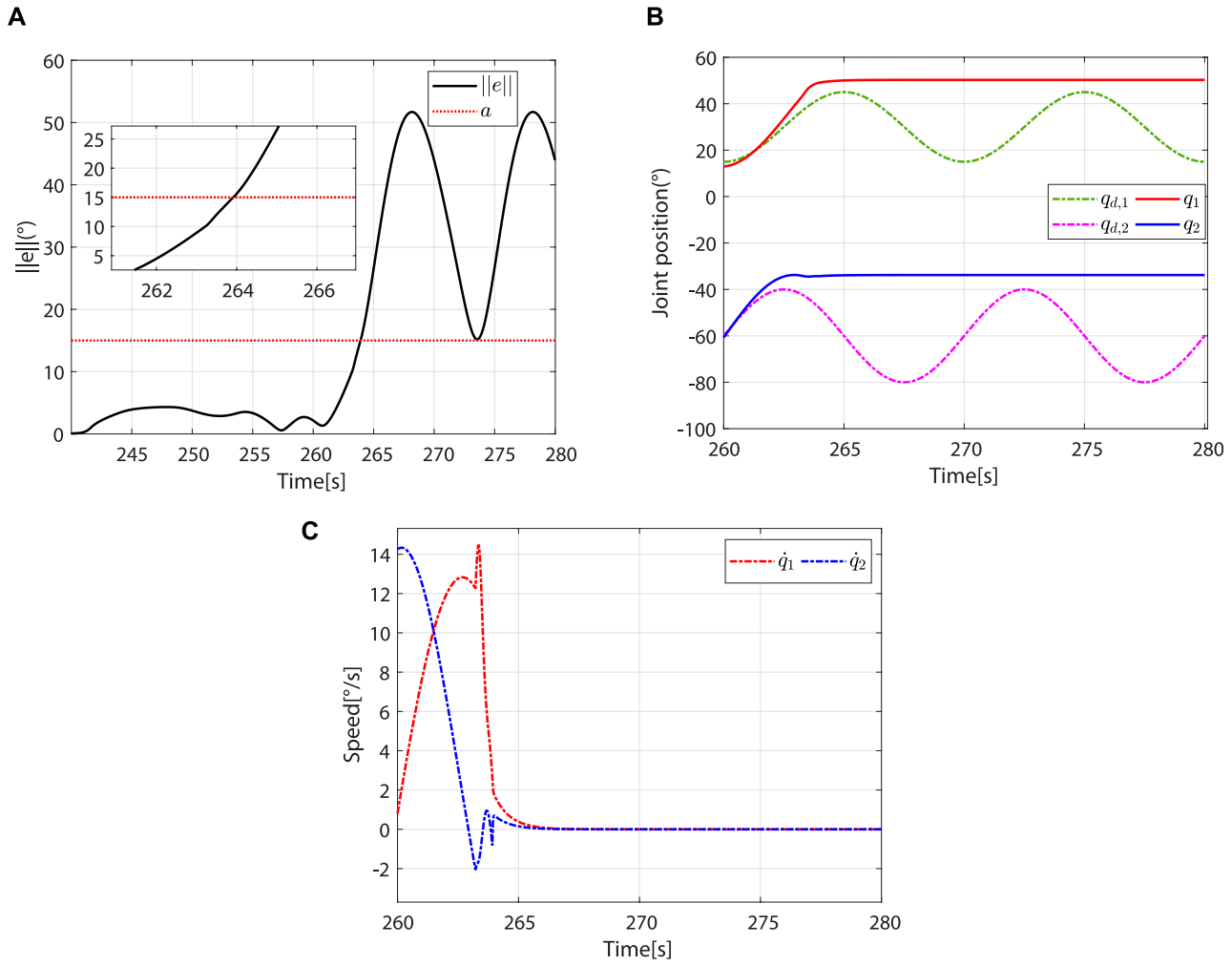

FIGURE 13
The controller switches to the safety-stop mode. **(A)** At approximately 263.92 s, $\|e\| > a$. **(B)** Desired and actual trajectories. **(C)** Actual angular speed.

$$\begin{cases} \Delta K(t) = K(t) - K(t-T) - K_m(t) + K_m(t-T) \\ \quad = \Delta\tilde{K}(t) = Q_K\left(se^{\mathrm{T}} - \left(1+\gamma_j\right)K(t)\right) \\ \Delta D(t) = D(t) - D(t-T) - D_m(t) + D_m(t-T) \\ \quad = \Delta\tilde{D}(t) = Q_D\left(s\dot{e}^{\mathrm{T}} - \left(1+\gamma_j\right)D(t)\right) \\ \Delta\tau_c(t) = \tau_c(t) - \tau_c(t-T) - \tau_m(t) + \tau_m(t-T) \\ \quad = \Delta\tilde{\tau}_c(t) = Q_{\tau_c}\left(s - \left(1+\gamma_j\right)\tau_c(t)\right) \end{cases} \tag{40}$$

Since Q_K^{-1} is symmetric, *Item a* in Eq. 39 can be expressed thus:

$$\begin{aligned} &tr\left\{\tilde{K}^{\mathrm{T}}(\sigma)Q_K^{-1}\tilde{K}(\sigma) - \tilde{K}^{\mathrm{T}}(\sigma-T)Q_K^{-1}\tilde{K}(\sigma-T)\right\} \\ &= tr\left\{\left[\tilde{K}(\sigma) - \tilde{K}(\sigma-T)\right]^{\mathrm{T}}Q_K^{-1}\left[\tilde{K}(\sigma) + \tilde{K}(\sigma-T)\right]\right\} \\ &= tr\left\{\Delta\tilde{K}(\sigma)^{\mathrm{T}}Q_K^{-1}\left[2\tilde{K}(\sigma) - \left(\tilde{K}(\sigma) - \tilde{K}(\sigma-T)\right)\right]\right\} \\ &= tr\left\{-\Delta\tilde{K}(\sigma)^{\mathrm{T}}Q_K^{-1}\Delta\tilde{K}(\sigma) + 2\Delta\tilde{K}(\sigma)^{\mathrm{T}}Q_K^{-1}\tilde{K}(\sigma)\right\} \\ &= -tr\left\{\Delta\tilde{K}(\sigma)^{\mathrm{T}}Q_K^{-1}\Delta\tilde{K}(\sigma)\right\} + 2tr\left\{\left(se^{\mathrm{T}} - \left(1+\gamma_j\right)K(\sigma)\right)^{\mathrm{T}}Q^{\mathrm{T}}{}_KQ_K^{-1}\tilde{K}(\sigma)\right\} \\ &= -tr\left\{\Delta\tilde{K}^{\mathrm{T}}(\sigma)Q_K^{-1}\Delta\tilde{K}(\sigma)\right\} + 2tr\left\{\left(se^{\mathrm{T}} - \left(1+\gamma_j\right)K(\sigma)\right)^{\mathrm{T}}\tilde{K}(\sigma)\right\} \\ &= -tr\left\{\Delta\tilde{K}^{\mathrm{T}}(\sigma)Q_K^{-1}\Delta\tilde{K}(\sigma)\right\} + 2s^{\mathrm{T}}\tilde{K}(\sigma)e - 2\left(1+\gamma_j\right)tr\left\{K^{\mathrm{T}}(\sigma)\tilde{K}(\sigma)\right\}. \end{aligned} \tag{41}$$

Similarly, *Item b* and *Item c* in Eq. 39 can be expressed as follows:

$$\begin{aligned} &tr\left\{\tilde{D}^{\mathrm{T}}(\sigma)Q_D^{-1}\tilde{D}(\sigma) - \tilde{D}^{\mathrm{T}}(\sigma-T)Q_D^{-1}\tilde{D}(\sigma-T)\right\} \\ &\quad = -tr\left\{\Delta\tilde{D}^{\mathrm{T}}(\sigma)Q_D^{-1}\Delta\tilde{D}(\sigma)\right\} + 2s^{\mathrm{T}}\tilde{D}(\sigma)\dot{e} \\ &\quad -2\left(1+\gamma_j\right)tr\left\{D^{\mathrm{T}}(\sigma)\tilde{D}(\sigma)\right\} \end{aligned} \tag{42}$$

and

$$\begin{aligned} &\tilde{\tau}_c{}^{\mathrm{T}}(\sigma)Q_{\tau_c}^{-1}\tilde{\tau}_c(\sigma) - \tilde{\tau}_c{}^{\mathrm{T}}(\sigma-T)Q_{\tau_c}^{-1}\tilde{\tau}_c(\sigma-T) \\ &\quad = -\Delta\tilde{\tau}_c{}^{\mathrm{T}}(\sigma)Q_{\tau_c}^{-1}\Delta\tilde{\tau}_c(\sigma) + 2s^{\mathrm{T}}\tilde{\tau}_c(\sigma) - 2\left(1+\gamma_j\right)\tau_c{}^{\mathrm{T}}(\sigma)\tilde{\tau}_c(\sigma). \end{aligned} \tag{43}$$

By bringing Eqs 41–43 into Eq. 39, we obtain

$$\begin{aligned} \Delta V_2 &= \Delta V_2(t) - \Delta V_2(t-T) \\ &= -\frac{1}{2}\int_{t-T}^{t}\Delta\tilde{\Psi}^{\mathrm{T}}(\sigma)Q^{-1}\Delta\tilde{\Psi}(\sigma)d\sigma + \int_{t-T}^{t}s^{\mathrm{T}}\tilde{K}(\sigma)e + s^{\mathrm{T}}\tilde{D}(\sigma)\dot{e} \\ &\quad + s^{\mathrm{T}}\tilde{\tau}_c(\sigma)d\sigma - \left(1+\gamma_j\right)\int_{t-T}^{t}\tilde{\Psi}^{\mathrm{T}}(\sigma)\Psi(\sigma)d\sigma. \end{aligned} \tag{44}$$

By bringing Eqs 38, 44 into Eq. 30, we obtain Eq. 45.

$$\begin{aligned} \Delta V &= \Delta V_1(t) + \Delta V_2(t) \\ &\le \int_{t-T}^{t} -\frac{1}{2}\Delta\tilde{\Psi}^{\mathrm{T}}(\sigma)Q^{-1}\Delta\tilde{\Psi}(\sigma) - s^{\mathrm{T}}\lambda_L s - \left(1+\gamma_j\right)\tilde{\Psi}^{\mathrm{T}}(\sigma)\Psi(\sigma)d\sigma \end{aligned}. \tag{45}$$

Since $\tilde{\Psi}(\sigma) = \Psi(\sigma) - \Psi^{\star}(\sigma)$, we can obtain Eq. 46

$$\begin{aligned}\Delta V \le \int_{t-T}^{t} &-\frac{1}{2}\Delta\tilde{\Psi}^{\mathrm{T}}(\sigma)Q^{-1}\Delta\tilde{\Psi}(\sigma) - s^{\mathrm{T}}\lambda_L s \\ &-\left(1+\gamma_j\right)\tilde{\Psi}^{\mathrm{T}}(\sigma)\tilde{\Psi}(\sigma) - \left(1+\gamma_j\right)\tilde{\Psi}^{\mathrm{T}}(\sigma)\Psi^{\star}(\sigma)d\sigma.\end{aligned} \tag{46}$$

A sufficient condition for ΔV to be non-positive definite is

$$\begin{aligned}&s^{\mathrm{T}}\lambda_L s + \left(1+\gamma_j\right)\tilde{\Psi}^{\mathrm{T}}(\sigma)\tilde{\Psi}(\sigma) + \left(1+\gamma_j\right)\tilde{\Psi}^{\mathrm{T}}(\sigma)\Psi^{\star}(\sigma) \\ &\ge \underbrace{\lambda_L\|s\|^2 + \left(1+\gamma_j\right)\|\tilde{\Psi}\|^2 - \left(1+\gamma_j\right)\|\tilde{\Psi}\|\|\Psi^{\star}\|}_{Item\ d} \ge 0.\end{aligned} \tag{47}$$

When *Item d* in Eq. 47 is equal to zero, we obtain

$$\frac{\|s\|^2}{\left(1+\gamma_j\right)\|\Psi^{\star}\|^2/4\lambda_L} + \frac{\left(\|\tilde{\Psi}\| - \|\Psi^{\star}\|/2\right)^2}{\|\Psi^{\star}\|^2/4} = 1. \tag{48}$$

According to LaSalle's theorem, $\|s\|$ and $\|\tilde{\Psi}\|$ will converge on the invariant set Ω_i of $\Delta V = 0$. Based on Eq. 48, a boundary set Ω can be designed as Eq. 49:

$$\Omega = \left\{ \left(\|s\|, \|\tilde{\Psi}\|\right), \frac{\|s\|^2}{\left(1+\gamma_j\right)\|\Psi^{\star}\|^2/4\lambda_L} + \frac{\left(\|\tilde{\Psi}\| - \|\Psi^{\star}\|/2\right)^2}{\|\Psi^{\star}\|^2/4} \le 1 \right\}. \tag{49}$$

Since $\|s\|$, $\|\tilde{\Psi}\|$, and $\|\Psi^{\star}\|$ are non-negative and $1+\gamma_j$ and λ_L are positive numbers, the boundary set Ω is in the first quadrant, as shown in Figure 4.

From the inequality (Eq. 47), $\|s\|$ and $\|\tilde{\Psi}\|$ will converge on the invariant set Ω_i of $\Delta V = 0$, and $\Omega_i \subseteq \Omega$. γ_j and $L(t)$ can be used to regulate the boundary set Ω. If λ_L increases, then a smaller $\|s\|$ is allowed, which means an increase in motion accuracy. If λ_L decreases, the system will allow for larger motion errors.

4.2 Stability analysis in the patient-dominant mode

In this mode, $\alpha = 0$, $\beta = 0$. $V(t)$ and its derivative are expressed as follows.

$$V(t) = V_1(t) = \frac{1}{2}s^{\mathrm{T}}Ms \tag{50}$$

and

$$\dot{V}(t) = \dot{V}_1(t) = -s^{\mathrm{T}}L(t)s - s^{\mathrm{T}}(\tau_c + \tau_h) \tag{51}$$

By the definition of $L(t)$, it is positive definite. From the definition of $\tau_c + \tau_h$, the angle between $\tau_c + \tau_h$ and s is less than or equal to $\frac{\pi}{2}$—that is $s^{\mathrm{T}}(\tau_c + \tau_h) \ge 0$. Hence, we can get $\dot{V}(t) \le 0$, and $V(t) \le V(0)$. Since $V(0)$ is bounded, s is bounded.

To determine the consistent continuity of $\dot{V}(t)$, Eq. 51 is derived as Eq. 52:

$$\begin{aligned}\ddot{V}(t) &= \ddot{V}_1(t) \\ &= -s^{\mathrm{T}}L(t)\dot{s} - \dot{s}^{\mathrm{T}}L(t)s - s^{\mathrm{T}}\dot{L}(t)s - \dot{s}^{\mathrm{T}}(\tau_c + \tau_h) - s^{\mathrm{T}}(\dot{\tau}_c + \dot{\tau}_h),\end{aligned} \tag{52}$$

where $\dot{L}(t) = 0$. Due to the human motion ability limitation, τ_h and $\dot{\tau}_h$ can be assumed to be bounded. The boundedness of $\mu(s)$ and $c(\tau_h)$ ensures that $\tau_c + \tau_h$ is bounded. $\dot{\tau}_c + \dot{\tau}_h$ can be expressed as Eq. 53

$$\dot{\tau}_c + \dot{\tau}_h = \dot{\mu}(s)\dot{s}c(\tau_h) + \mu(s)\dot{c}(\tau_h)\dot{\tau}_h. \tag{53}$$

The boundedness of s suggests the boundedness of $\dot{q}_{ref}$ and $\dot{q}$. Since $\dot{q}_{ref}$ is bounded, $\dot{q}_h$ is too. According to Eq. 20, the boundedness of τ_h ensures that $\ddot{q}_h$ is bounded, so that $\ddot{q}_{ref}$ is also bounded. The $\dot{\tau}_c + \dot{\tau}_h$ is bounded due to the boundedness of $\dot{\mu}(s)$, $\dot{s}$, $c(\tau_h)$, $\mu(s)$, $\dot{\tau}_h$, and $\dot{c}(\tau_h)$. Therefore, $\ddot{V}(t)$ is bounded. According to Barbalat's lemma, $\lim_{t\to\infty}\dot{V}(t) \to 0$, which means that if $t \to \infty$, $s \to 0$. From the definition of s, the robot's speed converges to $\dot{q}_{ref}$—that is, $\dot{q}_d + \dot{q}_h$.

4.3 Stability analysis in the safety-stop mode

When the trajectory error is too large, it will switch to the patient-dominant mode—$\alpha = 0, \beta = 1$. $V(t)$ and its derivative are the same as Eqs 50, 51. In this mode, $L(t)$ is positive definite and $\tau_c + \tau_h = 0$; thus, we obtain $\dot{V}(t) \le 0$, and $V(t) \le V(0)$. Since $V(0)$ is bounded, s is bounded. The derivation of $\dot{V}$ is given as Eq. 54

$$\ddot{V}(t) = \ddot{V}_1(t) = -s^{\mathrm{T}}L(t)\dot{s} - \dot{s}^{\mathrm{T}}L(t)s - s^{\mathrm{T}}\dot{L}(t)s, \tag{54}$$

where $\dot{L}(t) = 0$. The boundedness of $\tau_r + \tau_h$ ensures the boundedness of $\ddot{q}$ and $\dot{s}$. Therefore, $\ddot{V}(t)$ is bounded. According to Barbalat's lemma, $\lim_{t\to\infty}\dot{V}(t) \to 0$, so that if $t \to \infty$, $s \to 0$. From the definition of s, the robot will stop moving.

5 Simulations

A two-degree-of-freedom lower limb rehabilitation robot is used to verify the effectiveness of the proposed method. As shown in Figure 5, m_1 and m_2 represent the mass of the thigh and calf, respectively. l_1 and l_2 represent the length of the thigh and calf, respectively. l_{c1} denotes the distance from the hip joint to the center of mass of the thigh. l_{c2} denotes the distance from knee joint to the center of mass of the calf. The dynamic model of this hybrid system is described as Eq. 55

$$\begin{aligned}&\begin{bmatrix} M_{11} & M_{12} \\ M_{21} & M_{22} \end{bmatrix}\begin{bmatrix} \ddot{q}_1 \\ \ddot{q}_2 \end{bmatrix} + \begin{bmatrix} C_{11} & C_{12} \\ C_{21} & C_{22} \end{bmatrix}\begin{bmatrix} \dot{q}_1 \\ \dot{q}_2 \end{bmatrix} + \begin{bmatrix} G_1 \\ G_2 \end{bmatrix} \\ &= \begin{bmatrix} \tau_{r,1} \\ \tau_{r,2} \end{bmatrix} + \begin{bmatrix} \tau_{h,1} \\ \tau_{h,2} \end{bmatrix},\end{aligned} \tag{55}$$

where $M_{11} = I_1 + I_2 + m_2 l_1^2 + 2m_2 l_1 l_{c2} cos(q_2)$. $I_1 = m_1 l_{c1}^2$ and $I_2 = m_2 l_{c2}^2$ represent the inertia of the thigh and calf, respectively. $M_{12} = I_2 + m_2 l_1 l_{c2} cos(q_2)$, $M_{21} = M_{12}$, $M_{22} = I_2$, $C_{11} = -C_0\dot{q}_2$, $C_{12} = -C_0(\dot{q}_1 + \dot{q}_2)$, $C_{21} = C_0\dot{q}_1$, $C_{22} = 0$, and $C_0 = m_2 l_1 l_{c2} sin(q_2)$. $G_1 = (m_1 l_{c1} + m_2 l_1) g cos(q_1) + m_2 l_{c2} g cos(q_1 + q_2)$. $G_2 = m_2 l_{c2} g cos(q_1 + q_2)$. g is the acceleration of gravity. The desired trajectory is designed as Eq. 56.

$$\begin{cases} q_{d,1} = \frac{\pi}{6} - \frac{\pi}{12}cos(0.2\pi t) \\ q_{d,2} = -\frac{\pi}{3} + \frac{\pi}{9}sin(0.2\pi t) \end{cases} \tag{56}$$

The initial angle of the robot is set to $q_0 = [7\pi/36, -13\pi/36]^{\mathrm{T}}$. The initial parameters of the proposed method and lower limb rehabilitation robot are listed in Table 1. The values of η and ζ are given as Eqs 57, 58

$$\begin{cases} \eta = 0, & -2 \le r_j^{par} \le -1 \\ \eta = -0.2, & r_j^{par} > -1 \\ \eta = 0.2, & r_j^{par} < -2, \end{cases} \tag{57}$$

$$\begin{cases} \zeta = 0, & 0.1 \le \left| r_j^{ort} \right| \le 0.5 \\ \zeta = -0.3, & \left| r_j^{ort} \right| > 0.5 \\ \zeta = 0.3, & \left| r_j^{ort} \right| < 0.1. \end{cases} \tag{58}$$

The simulation process consists of 28 task cycles, each lasting 10 s. The results of the human–robot interaction force evaluation for each task cycle are given in Figure 6, which shows the patients' motor ability and motion intention under different task cycles. The simulation results are shown in Figure 7.

At the beginning, the controller is in safety-stop mode due to $\|e\| > a$. In this mode, τ_h is neutralized by τ_c. At approximately 4.44 s, $\|e\| < a$. Meanwhile, due to $r_1^{par} = -1$, the controller leaves the safety-stop mode and gradually transitions to the robot-dominant mode (Figure 8).

In the robot-dominant mode, according to r_j^{par} and r_j^{ort}, the robot's assistance level is adaptively adjusted to help the patient complete the desired task. The change trends of η_j and γ_j are shown in Figure 9A. When $r_j^{par} < r_{\min}^{par}$, $L(t)$ increases periodically with η_j. Although there are fluctuations in the changes of r_j^{par} and r_j^{ort}, the trajectory error decreases periodically (Figure 9B). The increase of the eigenvalue of $L(t)$ improves motion accuracy. When $r_{\min}^{par} < r_j^{par} < r_{\max}^{par}$, η_j remains unchanged. When $r_j^{par} > r_{\max}^{par}$, $L(t)$ decreases periodically with η_j. It can be observed that $|r_j^{ort}|$ is greater than $r_{\max}^{ort}$ in the second to seventh task cycle, which means that the patient intends to move away from the desired trajectory. γ_j will then reduce to a lower value to increase the learning rate of the impedance parameters, thus correcting the patient's motion trajectory (Figure 9A). However, with the gradual reduction of γ_j, the impedance parameters present a tendency to decrease periodically (Figures 9C, D). According to Eq. 16, this phenomenon is attributed to the improvement of motion accuracy.

When $d < r_j^{par} \le c$, the controller breaks away from the robot-dominant mode and transitions to the patient-dominant mode. When $r_j^{par} > c$, the controller is in patient-dominant mode. As the controller switches from robot-dominant to patient-dominant mode, greater trajectory errors are allowed, which provides greater freedom of movement (Figures 10A, B). In addition, the robot's speed gradually converges to $\dot{q}_d + \dot{q}_h$ (Figure 10C). This phenomenon is consistent with theory.

As r_j^{par} decreases, the controller switches again to the robot-dominant mode. Compared to the patient-dominant mode, the trajectory error is significantly reduced at this point (Figure 11A). From 190 to 230 s, η_j does not change. Affected by the vertical interaction force, γ_j decreases periodically (Figure 11B). From Figures 11C–E, the impedance parameter and torque compensation term increase periodically to correct patient motion, and the trajectory error is gradually reduced (Figure 11A).

When $r_j^{par} > c$, the controller switches to the patient-dominant mode again, where the patient's freedom of movement increases and the robot's speed converges to $\dot{q}_d + \dot{q}_h$ (Figure 12). To test the safety stop function of the controller during rehabilitation training, the excessive F_h^{par} and F_h^{ort} are applied, which will cause $\|e\|$ to increase sharply and $\|e\| > a$ (Figure 13A). In this case, the controller switches to the safety-stop mode to ensure patient safety (Figure 13B), and the actual speed of the robot decreases rapidly to zero (Figure 13C).

The effectiveness of the proposed method is demonstrated by the trajectory errors, adaptive change of controller parameters, and joint angular speed during human–robot interaction in three modes. In addition, the simulation includes the transition process between each mode, and the system can still run stably during this transition process.

6 Conclusion

This study proposes a multi-mode adaptive control method, including robot-dominant, patient-dominant, and safety-stop modes. The patient's motor ability and the system's trajectory error are taken as the basis for mode switching. Based on the patients' motor ability, the controller can switch between robot-dominant and patient-dominant modes. Trajectory errors are used to determine whether to switch to the safety-stop mode. The proposed control strategy is not only suitable for patients with different motor abilities and rehabilitation stages but also guarantees safety during rehabilitation training. Since the transition between robot-dominant and patient-dominant modes does not depend on the trajectory errors, the patient-dominant mode allows for greater trajectory errors than the robot-dominated mode, and the reference speed can be modified by the patient, improving their freedom of movement. The stability of the proposed method under three control modes is analyzed using Lyapunov theory. Numerical simulations are carried out on a two-degree-of-freedom lower limb rehabilitation robot to verify the effectiveness of the proposed method. Our future work will focus on clinical applications.

Data availability statement

The original contributions presented in the study are included in the article/supplementary material; further inquiries can be directed to the corresponding author.

Author contributions

XL: conceptualization, formal analysis, and writing–original draft. YY: methodology, software, and writing–original draft. SD: data curation, formal analysis, and writing–review and editing. ZG: conceptualization, validation, and writing–review and editing. ZL: investigation and writing–review and editing. SL: investigation,

validation, and writing–review and editing. TS: formal analysis, project administration, software, and writing–original draft.

Funding

The authors declare that financial support was received for the research, authorship, and/or publication of this article. This work was supported by the National Key R&D Program of China under Grant 2023YFE0202100; the Natural Science Foundation of China under grants 62373013, 62103007, 62203442, and 62003005; the R&D Program of Beijing Municipal Education Commission under grants KM202110009009 and KM202210009010; the Natural Science Foundation of Beijing under grants L202020 and 4204097; and the Talent Fund of Beijing Jiaotong University under grant KAIXKRC24003532.

Conflict of interest

The authors declare that the research was conducted in the absence of any commercial or financial relationships that could be construed as a potential conflict of interest.

Publisher's note

References

Adhikari, B., Bharadwaj, V. R., Miller, B. A., Novak, V. D., and Jiang, C. (2023). Learning skill training schedules from domain experts for a multi-patient multi-robot rehabilitation gym. *IEEE Trans. Neural Syst. Rehabil. Eng.* 31, 4256–4265. doi:10.1109/TNSRE.2023.3326777

Asl, H. J., Yamashita, M., Narikiyo, T., and Kawanishi, M. (2020). Field-based assist-as-needed control schemes for rehabilitation robots. *IEEE ASME Trans. Mechatron.* 25, 2100–2111. doi:10.1109/TMECH.2020.2992090

Bergmann, L., Voss, D., Leonhardt, S., and Ngo, C. (2023). Lower-limb exoskeleton with compliant actuators: human cooperative control. *IEEE Trans. Med. Robot.* 5, 717–729. doi:10.1109/TMRB.2023.3290982

Gao, M., Chen, J., Li, M., and Dai, J. S. (2023). "Design and evaluation of a novel self-adaptive ankle rehabilitation exoskeleton with elastic modules," in *2023 international conference on advanced robotics and mechatronics (ICARM)*, 900–905. doi:10.1109/ICARM58088.2023.10218858

Guo, L., Lu, Z., and Yao, L. (2021). Human-machine interaction sensing technology based on hand gesture recognition: a review. *IEEE Trans. Hum. Mach. Syst.* 51, 300–309. doi:10.1109/THMS.2021.3086003

Han, S., Wang, H., and Yu, H. (2023). Human-robot interaction evaluation-based AAN control for upper limb rehabilitation robots driven by series elastic actuators. *IEEE Trans. Robot.* 39, 3437–3451. doi:10.1109/TRO.2023.3286073

Jamwal, P. K., Hussain, S., Ghayesh, M. H., and Rogozina, S. V. (2016). Impedance control of an intrinsically compliant parallel ankle rehabilitation robot. *IEEE Trans. Ind. Electron.* 63, 3638–3647. doi:10.1109/TIE.2016.2521600

Li, N., Yang, Y., Li, G., Yang, T., Wang, Y., Chen, W., et al. (2024a). Multi-sensor fusion-based mirror adaptive assist-as-needed control strategy of a soft exoskeleton for upper limb rehabilitation. *IEEE Trans. Autom.* 21, 475–487. doi:10.1109/TASE.2022.3225727

Li, X., Pan, Y., Chen, G., and Yu, H. (2017a). Adaptive human-robot interaction control for robots driven by series elastic actuators. *IEEE Trans. Robot.* 33, 169–182. doi:10.1109/TRO.2016.2626479

Li, X., Pan, Y., Chen, G., and Yu, H. (2017b). Multi-modal control scheme for rehabilitation robotic exoskeletons. *Int. J. Robot. Res.* 36, 759–777. doi:10.1177/0278364917691111

Li, X., Yang, Q., and Song, R. (2021). Performance-based hybrid control of a cable-driven upper-limb rehabilitation robot. *IEEE Trans. Biomed. Eng.* 68, 1351–1359. doi:10.1109/TBME.2020.3027823

Li, Z., Zhang, T., Huang, P., and Li, G. (2024b). Human-in-the-loop cooperative control of a walking exoskeleton for following time-variable human intention. *IEEE Trans. Cybern.* 54, 2142–2154. doi:10.1109/TCYB.2022.3211925

Liang, X., Su, T., Zhang, Z., Zhang, J., Liu, S., Zhao, Q., et al. (2022). An adaptive time-varying impedance controller for manipulators. *Front. Neurorobot.* 16, 789842. doi:10.3389/fnbot.2022.789842

Liang, X., Yan, Y., Su, T., Guo, Z., Liu, S., Zhang, H., et al. (2023). "Kalman filter and moving average method based human-robot interaction torque estimation for a lower limb rehabilitation robot," in *2023 international conference on advanced robotics and mechatronics (ICARM)*, 1083–1088. doi:10.1109/ICARM58088.2023.10218932

Lu, Z., He, B., Cai, Y., Chen, B., Yao, L., Huang, H., et al. (2023). Human-machine interaction technology for simultaneous gesture recognition and force assessment: a review. *IEEE Sens. J.* 23, 26981–26996. doi:10.1109/JSEN.2023.3314104

Luo, L., Peng, L., Wang, C., and Hou, Z.-G. (2019). A greedy assist-as-needed controller for upper limb rehabilitation. *IEEE Trans. Neural Netw. Learn. Syst.* 30, 3433–3443. doi:10.1109/TNNLS.2019.2892157

Mao, Y., Jin, X., Gera Dutta, G., Scholz, J. P., and Agrawal, S. K. (2015). Human movement training with a cable driven arm exoskeleton (CAREX). *IEEE Trans. Neural Syst. Rehabil. Eng.* 23, 84–92. doi:10.1109/TNSRE.2014.2329018

Masengo, G., Zhang, X., Dong, R., Alhassan, A. B., Hamza, K., and Mudaheranwa, E. (2023). Lower limb exoskeleton robot and its cooperative control: a review, trends, and challenges for future research. *Front. Neurorobot.* 16, 913748. doi:10.3389/fnbot.2022.913748

Xu, J., Li, Y., Xu, L., Peng, C., Chen, S., Liu, J., et al. (2019). A multi-mode rehabilitation robot with magnetorheological actuators based on human motion intention estimation. *IEEE Trans. Neural Syst. Rehabil. Eng.* 27, 2216–2228. doi:10.1109/TNSRE.2019.2937000

Yang, C., Ganesh, G., Haddadin, S., Parusel, S., Albu-Schaeffer, A., and Burdet, E. (2011). Human-like adaptation of force and impedance in stable and unstable interactions. *IEEE Trans. Robot.* 27, 918–930. doi:10.1109/TRO.2011.2158251

Yang, R., Shen, Z., Lyu, Y., Zhuang, Y., Li, L., and Song, R. (2023). Voluntary assist-as-needed controller for an ankle power-assist rehabilitation robot. *IEEE Trans. Biomed. Eng.* 70, 1795–1803. doi:10.1109/TBME.2022.3228070

Zhang, J., and Cheah, C. C. (2015). Passivity and stability of human-robot interaction control for upper-limb rehabilitation robots. *IEEE Trans. Robot.* 31, 233–245. doi:10.1109/TRO.2015.2392451

Zhou, J., Li, Z., Li, X., Wang, X., and Song, R. (2021). Human-robot cooperation control based on trajectory deformation algorithm for a lower limb rehabilitation robot. *IEEE ASME Trans. Mechatron.* 26, 3128–3138. doi:10.1109/TMECH.2021.3053562

frontiers | Frontiers in Bioengineering and Biotechnology

TYPE Review
PUBLISHED 17 May 2024
DOI 10.3389/fbioe.2024.1391322

OPEN ACCESS

EDITED BY
Wujing Cao,
Chinese Academy of Sciences (CAS), China

REVIEWED BY
Zhirui Fan,
Chongqing University, China
Yihua Dan,
Tsinghua University, China

*CORRESPONDENCE
Hegao Yu,
yuhg3@mail.sysu.edu.cn

RECEIVED 25 February 2024
ACCEPTED 08 April 2024
PUBLISHED 17 May 2024

CITATION
Wen S, Huang R, Liu L, Zheng Y and Yu H (2024), Robotic exoskeleton-assisted walking rehabilitation for stroke patients: a bibliometric and visual analysis.
Front. Bioeng. Biotechnol. 12:1391322.
doi: 10.3389/fbioe.2024.1391322

Robotic exoskeleton-assisted walking rehabilitation for stroke patients: a bibliometric and visual analysis

Shuangshuang Wen[1], Ruina Huang[1], Lu Liu[1], Yan Zheng[2] and Hegao Yu[1]*

[1]The Eighth Affiliated Hospital, Sun Yat-sen University, Shenzhen, China, [2]Shenzhen Health Capacity Building and Continuing Education Center, Shenzhen, China

Objective: This study aimed to conduct a bibliometric analysis of the literature on exoskeleton robot assisted walking rehabilitation for stroke patients in the Web of Science Core Collection over the past decade.

Method: Retrieved literature on exoskeleton robot assisted gait training for stroke hemiplegic patients from the Web of Science Core Collection from 1 January 2014 to 31 January 2024. The search method was topic search, and the types of documents were "article, meeting abstract, review article, early access." CiteSpace was used to analyze the search results from countries, institutions, keywords, cited references and cited authors.

Result: A total of 1,349 articles were retrieved, and 1,034 were ultimately included for visualization analysis. The annual publication volume showed an upward trend, with countries, institutions, and authors from Europe and America in a leading position. The core literature was also published by authors from European and American countries. The keywords were divided into 8 clusters: # 0 soft robotic exit, # 1 robot assisted gain training, # 2 multiple scales, # 3 magnetic rheological brake, # 4 test retest reliability, # 5 electromechanical assisted training, # 6 cerebra salary, and # 7 slow gain. The early research direction focused on the development of exoskeleton robots, verifying their reliability and feasibility. Later, the focus was on the combination of exoskeleton robot with machine learning and other technologies, rehabilitation costs, and patient quality of life.

Conclusion: This study provides a visual display of the research status, development trends, and research hotspots, which helps researchers in this field to grasp the research hotspots and choose future research directions.

KEYWORDS

robotic exoskeleton, rehabilitation, stroke, walking, bibliometric

1 Introduction

Stroke is the third leading cause of disability globally (Feigin et al., 2022). Although the age-standardized mortality rate for stroke is declining (Krishnamurthi et al., 2020), the incidence remains high, with over 12.2 million new cases occurring worldwide annually (Feigin et al., 2021). Hemiplegia is a primary challenge faced by affected individuals and their caregivers, bringing a substantial burden on patients and their families. Post-stroke

patients require rehabilitation to regain ambulatory and balance capabilities, essential for maintaining normal activity levels (Warutkar et al., 2022). However, data indicates that 70% of individuals experience reduced walking speed and capacity post-stroke, with 20% becoming reliant on wheelchairs, which significantly impeding their independence in daily living (Mehrholz et al., 2020; Kim and Kim, 2022). Traditional rehabilitation is delivered by therapists or nurses, but the rising incidence of stroke has led to a shortage of qualified professionals (Mehrholz et al., 2020). The advent of rehabilitation robotics offers a novel solution to this issue, as these devices can assist in performing repetitive and standardized rehabilitation tasks (Riener et al., 2005), thereby alleviating the burden on rehabilitation workers (Yang et al., 2023). In recent years, due to advancements in chemical material sciences, control technologies, and the integration of artificial intelligence, there has been a rapid development of exoskeletal robotic devices (Yi and Yubing, 2024). These devices have emerged as groundbreaking in the adjunctive therapy of post-stroke hemiparesis, facilitating the reclamation of ambulatory abilities and gait balance (Rodríguez-Fernández et al., 2021). Contrasting with end-effectors, robotic exoskeleton (RE) are wearable robotic units that are affixed to an individual's limbs, providing either a substitution or enhancement of limbs movement. In the context of ambulation therapy for patients with hemiparesis, these RE emulate normative walking patterns to aid in the movement of the lower limbs, targeting the correction of gait or assistance in walking (Pons, 2008). This modality not only promotes greater freedom of movement for the patients but also actively engages their motor awareness, fostering a conducive environment for motor learning.

Current research on RE in the context of gait rehabilitation therapy for stroke patients is bifurcated into two main domains: technological development and therapeutic efficacy. Technological investigations are concentrated on the biomimetic design of exoskeletal mechanisms, the detection of movement intention, and the motor control within human-machine hybrid systems. The efficacy dimension focuses on the assessment of patient gait restoration, the consequent effects on neuroplasticity, and the overall impact on the patients' self-care capabilities and quality of life (Koenig et al., 2011; Loro et al., 2023; Pournajaf et al., 2023; Yang et al., 2023). Some scholars have provided comprehensive reviews on the effectiveness of RE in rehabilitative treatments for stroke survivors (Yang et al., 2023). However, traditional reviews or systematic reviews prioritize the synthesis and critical appraisal of literature, aiming to address specific questions within a given field (Yu et al., 2017). Bibliometrics is an interdisciplinary field that employs statistical methods to depict the characteristics and relationships of existing publications, active scholars, research institutions, research topics, or keywords within a research domain, as to as highlighting gaps in the field and predicte hotspots and trends over time (Hu et al., 2020; Donthu et al., 2021; Ninkov et al., 2022).

There has been a significant increase in bibliometric studies on post-stroke patients in the past 2 years, including patient rehabilitation and treatment (Dong et al., 2022; Harjpal et al., 2022; Uivarosan et al., 2022; Zuccon et al., 2022; Ogihara et al., 2023; Wu et al., 2023; Cheng and Yu, 2024), dysphagia (Xu et al., 2023), cognitive impairments (Chi et al., 2023), and pain (Li et al., 2022). However, studies on rehabilitation robots are few and far between. Giacomo Zuccon and other scholars had conducted bibliometric analyses on the technologies of post-stroke rehabilitation robots over the last 20 years, suggesting an increasing focus on the application of robots in the early-stage lower limb training of stroke patients (Zuccon et al., 2022). Diana Uivarosan and others presented relevant data from journals, authors, countries and institutions, and analyzed literature on the application of robots in rehabilitation for stroke patients (Zuccon et al., 2022). There is an increasing amount of research on the technological and application aspects of RE assisting in gait therapy for stroke patients, yet bibliometric studies in this area are still unseen. Therefore, this study conductd a bibliometric analysis on the research of exoskeleton robots in gait rehabilitation of stroke patients over the past decade, which was crucial for understanding the development of this field and selecting future research directions.

2 Data and methods

2.1 Data source and search strategy

A literature search on studies related to exoskeleton robot-assisted gait training after stroke was conducted in the Web of Science Core Collection database. The search strategy was topic search, covering the period from 1 January 2014 to 31 January 2024. The types of documents searched included "article, meeting abstract, review article, early access". The search strategy was as follows:#1 TS = (Exoskeleton robot OR rehabilitation robot OR robotic exoskeleton OR robot-assisted); #2 TS = (stroke OR apoplexy OR cerebrovascular accident OR cerebral hemorrhage OR hematencephalic OR encephalorrhagia OR cerebral ischemia); #3 TS = (walk* OR gait OR ambulation OR locomotion OR leg* OR lower limb* OR lower extremit*); #4 = (#3 AND #2 AND #1).

2.2 Analysis tools

In this study, we utilized the CiteSpace software developed by Professor Chaomei Chen for bibliometric visualization analysis. CiteSpace is among the leading tools for creating knowledge maps, capable of delineating the current state and predicting future research prospects and hotspots in a given field. By employing co-citation analysis and the Path Finder network algorithm, CiteSpace quantitatively analyzes literature. It conducts a complex network analysis that is diversified, time-phased, and dynamic by tracing the formation, accumulation, diffusion, transformation, and evolutionary paths of citation clusters and their knowledge inflection points. CiteSpace explores the current status, development trends, key points, research hotspots, research frontiers, and evolution process of a scientific field, and judge the development trends in the furture.

2.3 Data extraction

We employed CiteSpace 6.3. R1 software for bibliometric analysis of literature retrieved from the Web of Science database.

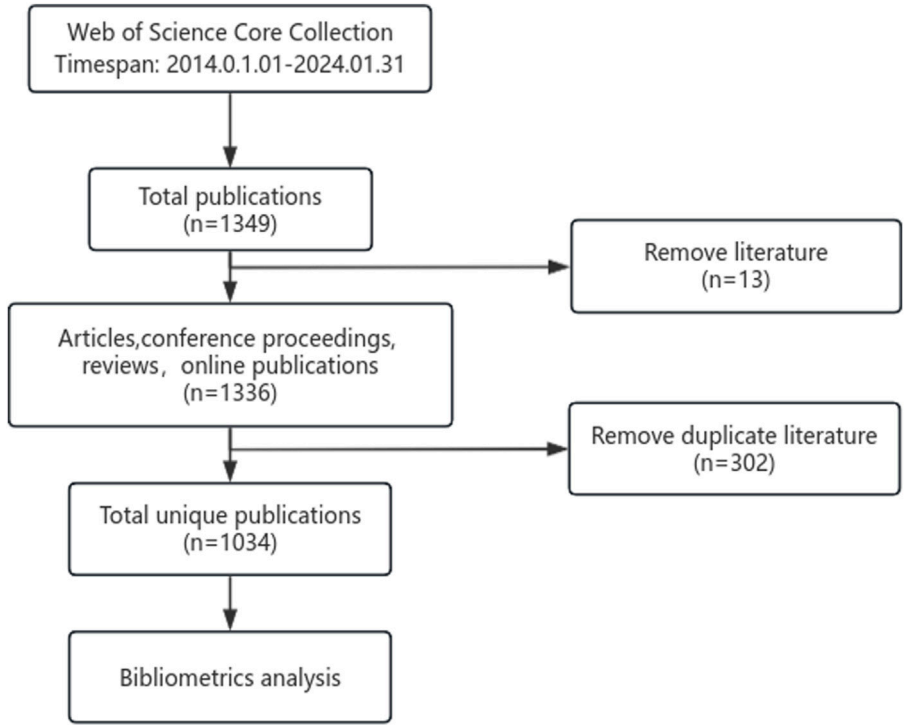

FIGURE 1
Flow chart of literature selection.

Literature from the Web of Science was exported in full record format and named 'download.txt' for compatibility with CiteSpace 6.3. R1, which was then imported into the software. Due to the potential for duplicate records in the database retrieval, the software's built-in deduplication feature was used to eliminate duplicate entries. This facilitated the analysis of countries, institutions, and keywords, as well as the visualization of cited references and cited authors. During the analysis, issues such as synonymic keywords and inconsistent institution name representations were encountered. To address these, data cleaning was performed first, using Notepad to search for and manually merge synonymic keywords and institution names. The flow chart of the literature screening is shown in Figure 1.

3 Result

3.1 Analysis of literature

3.1.1 Annual publications

In a preliminary search, a total of 1,349 documents published over the past decade on post-stroke exoskeleton-assisted gait training were retrieved. This collection includes articles, conference papers, reviews, and online publications, amounting to 1,336 documents. After removing duplicates, the number of papers was narrowed down to 1,034. As illustrated in Figure 2, the annual publication volume has been increasing year by year, with the highest number of publications recorded in 2021 (160 papers).

3.1.2 Analysis of national (regional) cooperation

In the past decade, a total of 67 countries (regions) have published research related to exoskeleton robot-assisted gait training following stroke, as illustrated in the cooperation map in Figure 3. The cooperation map encompasses 67 nodes and 242 connections, indicating strong collaborative relationships among these countries. The top 5 countries in terms of the number of publications are: the United States (United States of America) with 218 articles, China with 217 articles, Italy with 137 articles, South Korea with 107 articles, and Japan with 92 articles. In terms of betweenness centrality, the top 5 countries are: United States of America with 0.43, Spain with 0.22, Japan with 0.21, Italy with 0.19, and China with 0.15. The United States of America ranks first in both publication volume and betweenness centrality, indicating a leading position among Western countries, while Asian countries such as China, South Korea, and Japan also show strong capabilities in this research area. China ranks second globally in publication volume, but its betweenness centrality is relatively low. A possible reason for this could be China's recent significant investment in this field, leading to a rapid increase in publications despite a later start.

3.1.3 Institutional collaboration analysis

In the past decade, a total of 158 institutions have published research related to exoskeleton robot-assisted gait training after stroke, primarily comprising universities from various countries with existing cooperative relationships, as illustrated in the cooperation map shown in Figure 4. The cooperation map features 158 nodes and 268 connections, indicating strong collaborative relationships among these institutions. The top 5 institutions by publication volume are: Swiss Federal Institutes of Technology

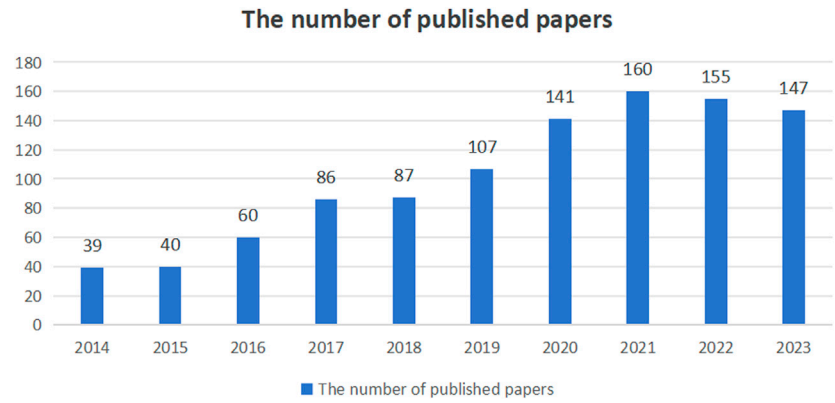

FIGURE 2
The number of published papers.

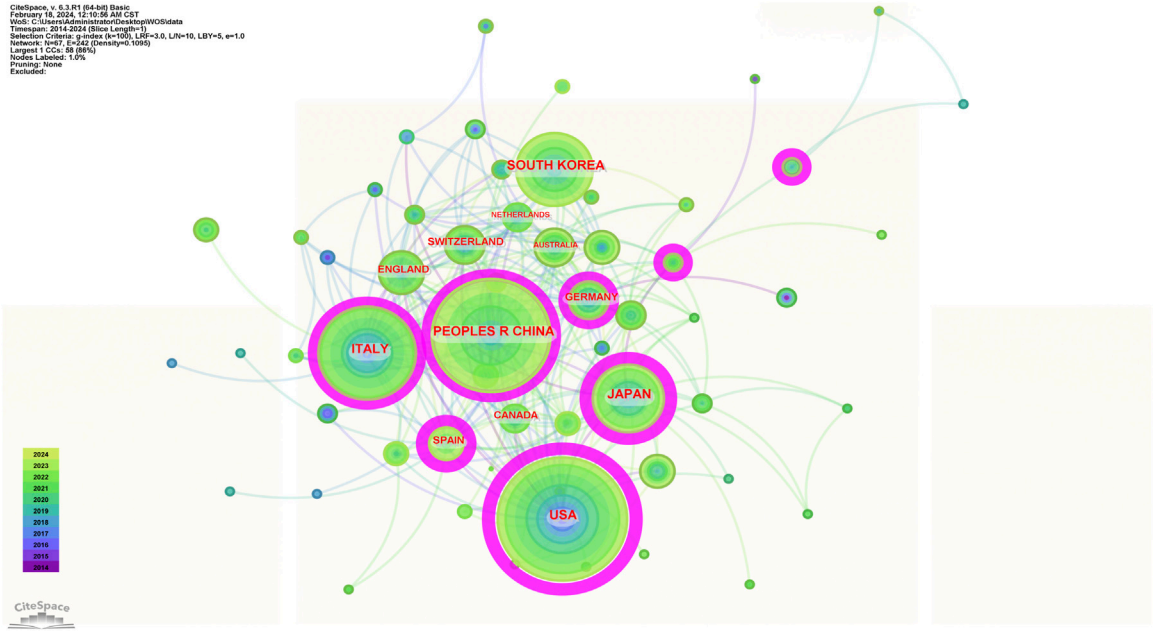

FIGURE 3
National cooperation analysis map.

Domain with 27 articles, Northwestern University (United States of America) with 21 articles, University of Tsukuba (Japan) with 21 articles, Harvard University (United States of America) with 19 articles, and Yonsei University (South Korea) with 18 articles. Regarding betweenness centrality, the top 5 institutions are: Swiss Federal Institutes of Technology Domain (0.19), Shirley Ryan AbilityLab (United States of America) (0.19), Chinese Academy of Sciences (0.13), Yonsei University (South Korea) (0.11), and Harvard University (United States of America) (0.06). Both in terms of publication volume and betweenness centrality, the Swiss Federal Institutes of Technology Domain ranks first, with institutions mainly from Europe and America leading. The Chinese Academy of Sciences ranks third in betweenness centrality.

3.1.4 Co-citation analysis of highly influential authors and cited authors

In the past decade, scholars from around the world have participated in research within this field, with two scholars publishing more than 10 papers each. These are Professor Rocco Salvatore Calabrò from the IRCCS Neurology Center in Italy (18 papers) and Professor Franco Molteni from Valduce Hospital in Italy (10 papers). The top 10 authors in terms of publication volume have relatively low betweenness centrality and citation rates, as shown in Table 1. Over the last 10 years, the top 5 core authors ranked by citation frequency are Mehrholz J from the European Private Scientific Research Institute in Germany (334 citations), Hesse S from the Free University of Berlin in Germany (241 citations), Kwakkel G from the University of

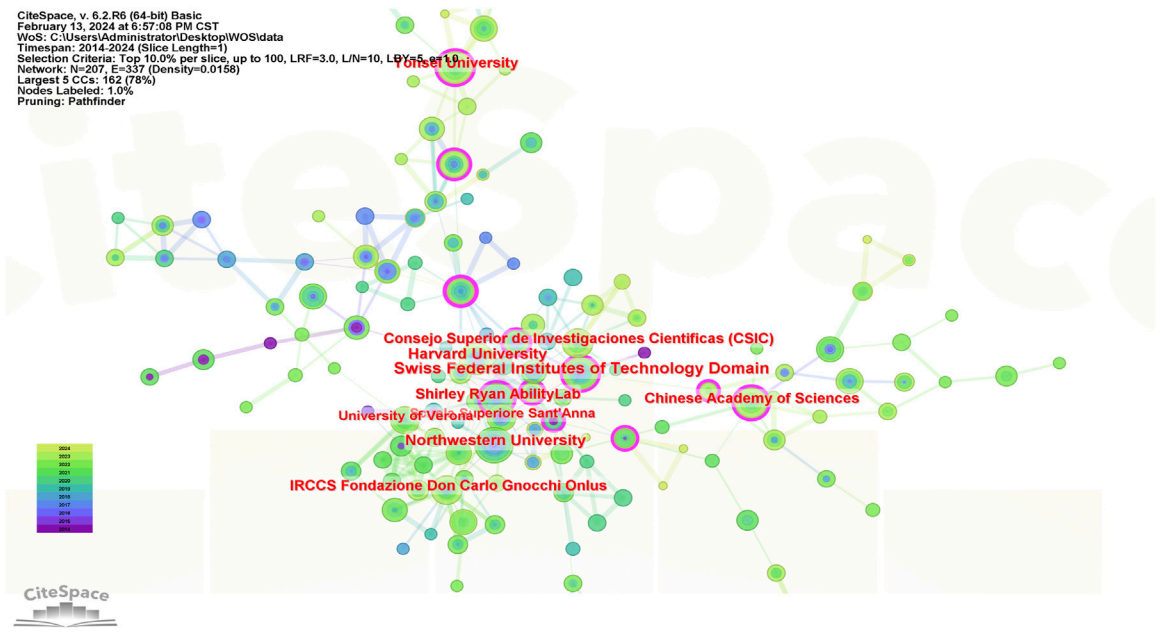

FIGURE 4
Institutional collaboration analysis map.

TABLE 1 Top 10 High-impact Authors and top 10 co-cited Authors in referenced documents.

High-impact author				Co-cited authors of referenced documents			
Author	Country	Number of published papers	Betweenness centrality score	Author	Country	Citation frequency	Betweenness centrality score
Rocco Salvatore Calabro	Italy	18	0.01	Mehrholz J	Germany	334	0.13
Franco Molteni	Italy	10	0	Hesse S	Germany	241	0.06
Yoshiyuki Sankai	Japan	9	0	Kwakkel G	Netherlands	173	0.06
Yasushi Hada	Japan	8	0	Hornby TG	United States of America	152	0.08
Antonino Naro	Italy	8	0	Morone G	Italy	150	0.06
Min Ho Chun	South Korea	8	0	Langhorne P	England	134	0.02
Giovanni Morone	Italy	7	0.01	Hidler J	United States of America	133	0.06
Akira Matsumura	Japan	7	0	Veneman JF	Netherlands	127	0.04
Louis N Awad	United States of America	7	0	Calabrò RS	Italy	126	0.04
Masashi Yamazaki	Japan	7	0	Krebs HI	United States of America	118	0.05

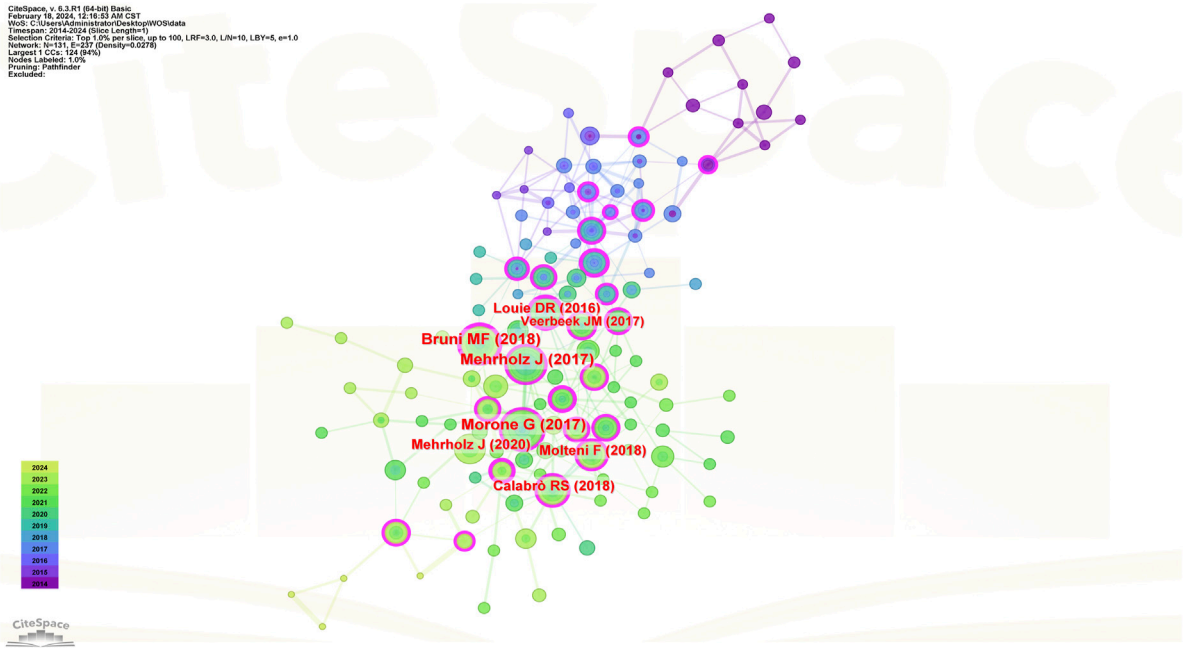

FIGURE 5
Highly cited core literature analysis map.

Amsterdam in the Netherlands (173 citations), Hornby TG from Northwestern University in the United States of America (152 citations), and MORONE G from the Santa Lucia Foundation in Italy (150 citations). The top 5 core cited authors ranked by betweenness centrality are Mehrholz J from the European Private Scientific Research Institute in Germany (0.13), Banala SK from the University of Delaware in the United States of America (0.09), Hornby TG from Northwestern University in the United States of America (0.08), Schwartz I from Hadassah-Hebrew University in Israel (0.07), and Kawamoto H from the University of Tsukuba in Japan (0.07), as shown in Table 1. Among them, Professor Mehrholz J has the highest citation frequency and betweenness centrality.

3.2 Analysis results of research hotspots

3.2.1 Analysis results of core literature citation and co-citation

Figure 5 reveals that research in this field over the past decade involves a total of 131 core referenced documents. The top five most-cited references are as follows: A document published by Morone G et al. from the Santa Lucia Foundation, Italy, in 2017 on *NEUROPSYCH DIS TREAT*, cited 68 times (Morone et al., 2017); a document by Mehrholz J et al. from the European Private Scientific Research Institute, Germany, in 2017 on *COCHRANE DB SYST REV*, cited 65 times (Mehrholz et al., 2020); a document by Bruni MF et al. from the IRCCS Neurology Center, Italy, in 2018 on *J CLIN NEUROSCI*, cited 61 times (Bruni et al., 2018); and a document by Calabrò RS et al. from the IRCCS Neurology Center, Italy, in 2018 on *J NEUROENG REHABIL*, cited 42 times (Calabrò et al., 2018), and a document by Louie DR et al. from the University of British Columbia, Canada, in 2016 on J *NEUROENG REHABIL*, cited 41 times (Louie and Eng, 2016). Among these five studies, four are reviews, and their findings are similar, all affirming the positive role of robotics in the gait rehabilitation of stroke patients, as detailed in Table 2.

The top five publications ranked by centrality in the intermediary network are as follows: A document by Bruni MF et al. from the IRCCS Neurology Center, Italy, published in *J CLIN NEUROSCI* in 2018, with a centrality score of 0.3 (Bruni et al., 2018); a paper by Louie DR et al. from the University of British Columbia, Canada, in *J NEUROENG REHABIL* in 2016, with a centrality score of 0.28 (Louie and Eng, 2016); a publication by Young AJ et al. from the Georgia Institute of Technology in *IEEE T NEUR SYS REH* in 2017, with a centrality score of 0.25 (Young and Ferris, 2016); a study by Molteni F and team from Valduce Hospital, Italy, in *BRAIN SCI* in 2021, with a centrality score of 0.22 (Molteni et al., 2021); and a document by Morone G et al. from the Santa Lucia Foundation, Italy, in *NEUROPSYCH DIS TREAT* in 2017, with a centrality score of 0.2 (Morone et al., 2017), as detailed in Table 3.

3.2.2 Highly cited literature burst intensity ranking

Burst intensity can effectively illustrate the research frontiers within a specific timeframe in a given field, showcasing the areas of concentrated interest and trends. The recent 10-year outlook on the most highly cited publications, ranked by burst intensity in this domain, is presented in Figure 6 (Mehrholz et al., 2020; Louie and Eng, 2016; Duncan et al., 2011; Langhorne et al., 2011; Dobkin and Duncan, 2012; Mehrholz and Pohl, 2012; Pennycott et al., 2012; Kawamoto et al., 2013; Klamroth-Marganska et al., 2014; Nilsson et al., 2014).

3.2.3 Analysis of keyword co-occurrence

In the co-occurrence graph of keywords, the size of a node represents the frequency of occurrence of the keyword; the larger the

TABLE 2 Top 5 cited references of the highest frequency.

Author	Frequency cited	Year	Main content
Morone G (Morone et al., 2017)	68	2017	This paper provides a comprehensive overview of the current advancements and future outlook of robotic technology, encompassing both market-ready systems, in the rehabilitation of post-stroke patients aiming at the restoration of ambulatory functions
Mehrholz J (Mehrholz et al., 2020)	65	2017	The researcher deduced from a meta-analytical approach that post-stroke patients engaging in a regimen of electromechanical-assisted gait training alongside conventional physiotherapy exhibited a higher propensity for regaining autonomous ambulation compared to counterparts abstaining from such technological interventions. This observation was particularly pronounced within the initial 3 months following a cerebrovascular event and was most notable in patients with an initial inability to walk. Future studies are necessitated to ascertain the optimal frequency and length of sessions for electromechanical-assisted gait training to maximize rehabilitative outcomes
Bruni MF (Bruni et al., 2018)	61	2018	The investigator, through a systematic meta-analysis, inferred that the integration of robotic assistance into gait rehabilitation programs could yield favorable results for stroke survivors. Stroke survivors who underwent a combination of robotic device-assisted therapy and conventional physical therapy demonstrated enhanced performance across various measures including the 10-m Walking Test, the 6-Minute Walk Test, the Timed-Up-and-Go, the 5-m Walk Test, and the Functional Ambulation Categories, as compared to those who participated solely in traditional gait training protocols
Calabrò RS (Calabrò et al., 2018)	42	2018	Through a randomized controlled trial, the researcher substantiated that patients with chronic hemiplegia due to stroke exhibited enhanced gait efficacy and neurological plasticity when utilizing the Ekso™ wearable exoskeletons, as opposed to those engaging in conventional terrestrial gait exercises
Louie DR (Louie and Eng, 2016)	41	2016	A scoping review suggested that for individuals with chronic stroke, gait training with exoskeletal support appears to match the efficacy of conventional therapy, whereas those in the sub-acute phase might derive additional advantages from such technologically assisted training

TABLE 3 Top 5 cited core references of the betweenness centrality.

Author	Betweenness centrality score	Year	Main content
Bruni MF (Bruni et al., 2018)	0.3	2018	Table 2 shows
Louie DR (Louie and Eng, 2016)	0.28	2016	Table 2 shows
Young AJ (Young and Ferris, 2016)	0.25	2017	This study focused on the actors, sensors, energy sources, materials, and control strategies in the design of lower limb robotic exoskeletons, and discussed the advantages and disadvantages of the emerging technologies and possible futures for the field
Molteni F (Molteni et al., 2021)	0.22	2021	A multicenter randomized controlled trial demonstrated that the clinical efficacy of ground robot assisted gait training (o-RAGT) in subacute stroke patients was similar to that of traditional gait training
Morone G (Morone et al., 2017)	0.2	2017	Table 2 shows

node, the more frequently the keyword appears, indicating a higher popularity of the research topic. The primary metric for measurement is betweenness centrality (ranging from 0 to 1), where a higher value signifies greater influence. A betweenness centrality of ≥0.1 indicates high centrality. As shown in Table 4; Figure 7, the top 10 keywords by betweenness centrality are: rehabilitation, walking, gait rehabilitation, stroke, therapy, body weight support, stroke patients, individuals, upper limb, recovery.

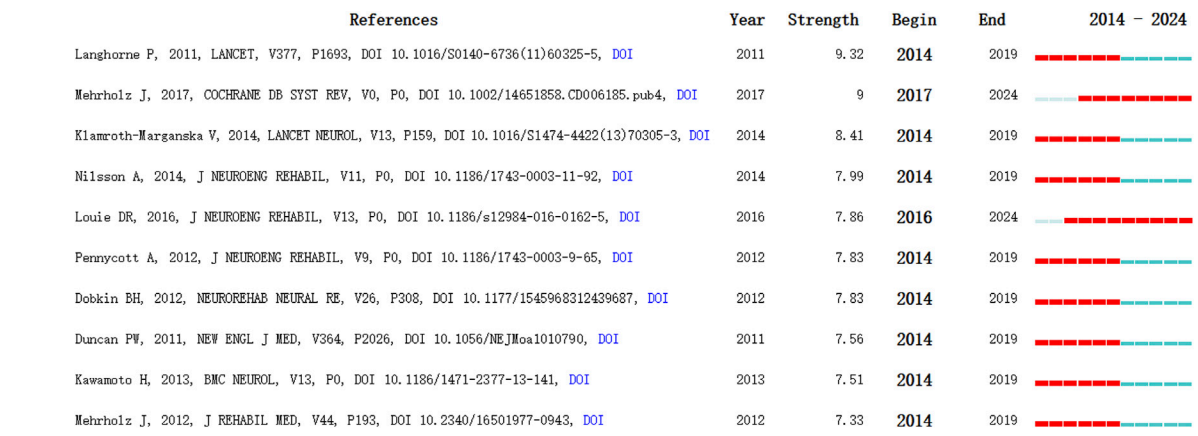

FIGURE 6
Co-cited references of the burst intensity.

TABLE 4 Top 10 keywords of the betweenness centrality and frequency.

Keyword	Betweenness centrality score	Keyword	Frequency
Rehabilitation	0.17	Stroke	318
Walking	0.15	Rehabilitation	301
Gait rehabilitation	0.14	Walking	237
Stroke	0.11	Recovery	205
Therapy	0.1	Gait	156
Body weight support	0.1	Design	128
Stroke patients	0.09	Spinal cord injury	103
Individuals	0.09	Exoskeleton	98
Upper limb	0.09	Therapy	97
Recovery	0.08	Stroke patients	97

The top 10 keywords by frequency of occurrence are: stroke, rehabilitation, walking, recovery, gait, design, spinal cord injury, exoskeleton, therapy, stroke patients.

3.2.4 Analysis of keyword co-occurrence clustering

Keyword co-occurrence clustering analysis is the process of grouping closely related and similar keywords into one category. The greater the number of keywords in a cluster, the smaller the cluster number. The modularity Q represents the clarity of the boundaries between clusters, indicating the significance of the cluster structure. It is generally considered satisfactory if this value is >0.3, indicating clear cluster delineation and significant structure. The Silhouette value measures the degree of closeness between keywords within a cluster, with Silhouette S > 0.5 indicating reasonable clustering. As shown in Figure 8, the cluster modularity Q is 0.3955, and the average silhouette S is 0.7203, suggesting significant cluster structure and high homogeneity. The keywords are divided into 8 clusters: #0 soft robotic exosuit (0.795), #1 robot-assisted gait training (0.717), #2 multiple sclerosis (0.664), #3 magneto-rheological brake (0.619), #4 test-retest reliability (0.673), #5 electromechanical-assisted training (0.77), #6 cerebral palsy (0.754), #7 slow gait (0.891). The keywords of each cluster are listed in Table 5.

3.2.5 Analysis of keyword burst and timeline view

Keyword burst refers to the sudden appearance of keywords within a certain period of time, representing the development trend of research. It can effectively showcase the different research frontiers at various time stages, presenting the hotspots and trends of the field. 'Year' indicates the first year the keyword appeared, 'Begin' and 'End' represent the start and end time of the keyword's occurrence, respectively. 'Strength' denotes the intensity of burst, where a higher value indicates greater burst strength. It is generally considered that only when a keyword's burst strength exceeds 3 can it be termed an emerging keyword. A timeline view, created after generating the co-citation cluster map, uses cluster numbers as the *Y*-axis and the publication years of citations as the *X*-axis to draw a knowledge map. As shown in Figures 9, 10, the burst of keywords in this research field can be roughly divided into two periods: (1) From 2014 to 2020, the research focus was

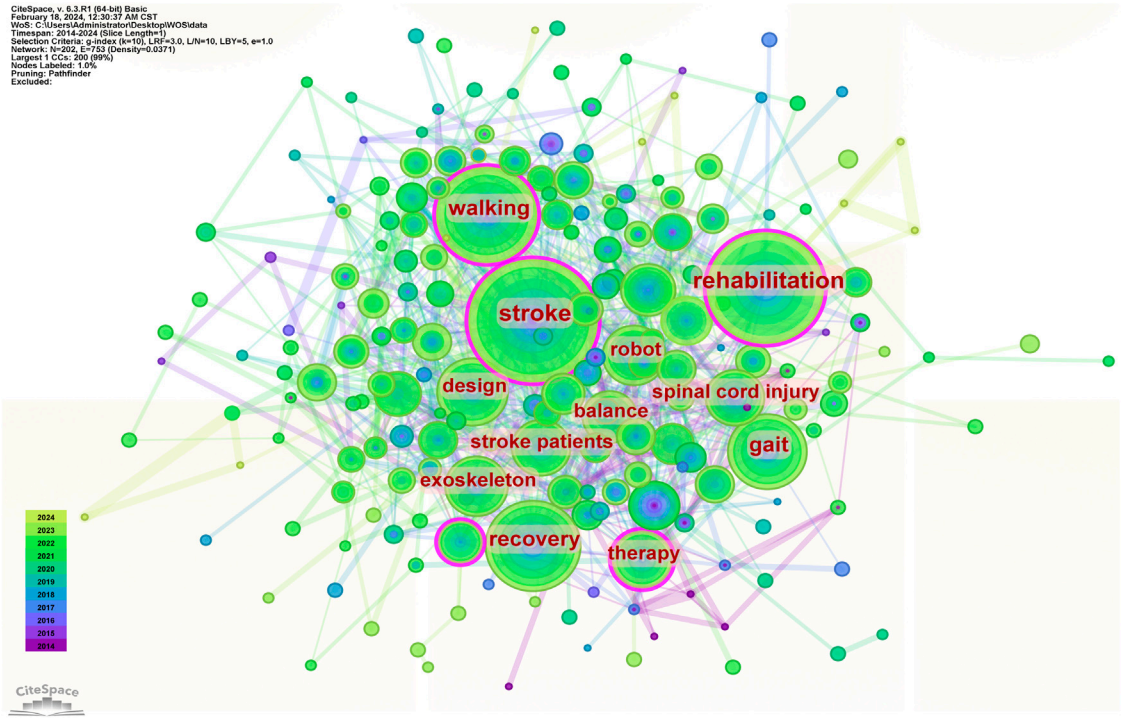

FIGURE 7
Keyword co-occurrence analysis map.

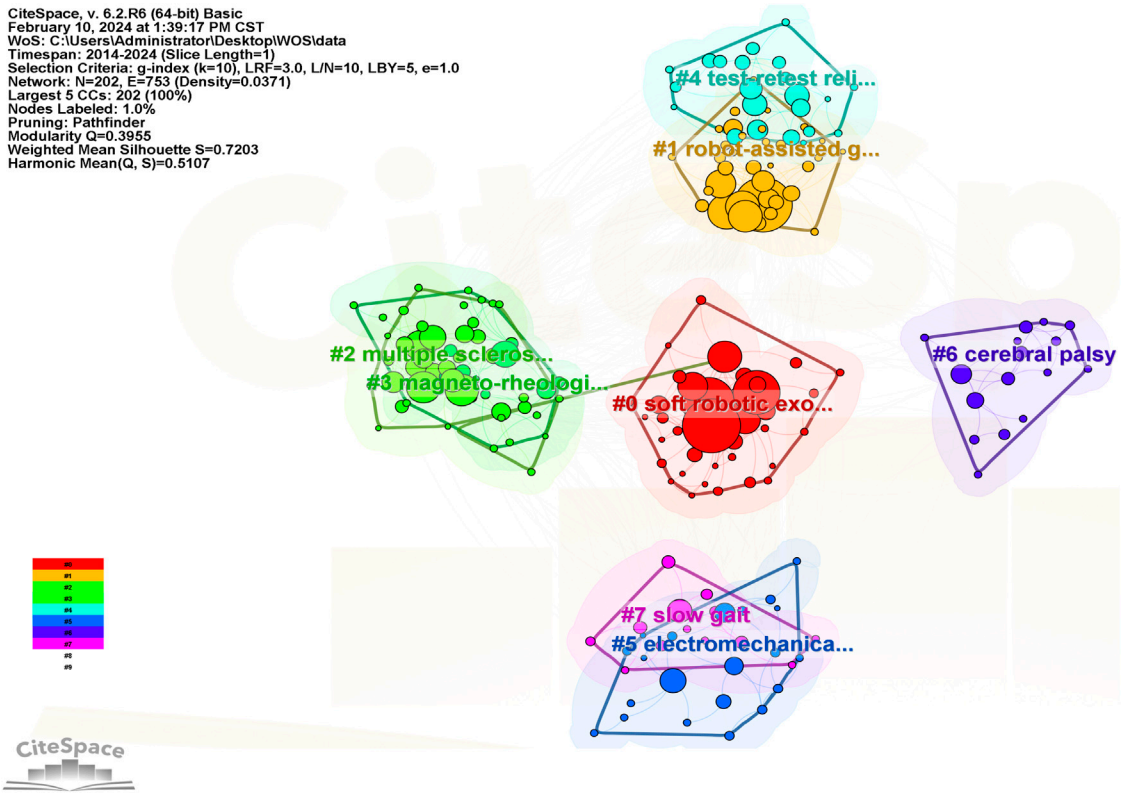

FIGURE 8
Keyword clustering map.

TABLE 5 Main clusters and contained keywords.

ClusterID	Label (LLR)	Silhouette	Year	Keywords
0	Soft robotic exosuit	0.795	2018	robot-assisted gait training; systematic review; stroke patient; gait training; controlled trial | virtual reality; feasibility study; non-ambulatory patient; robot-assisted gait; using welwalk
1	Robot-assisted gait training	0.717	2017	gait rehabilitation; gait training; systematic review; knee exoskeleton; rehabilitation robot | robot-assisted gait training; chronic stroke patient; pneumatic artificial muscle; robotic rehabilitation; feasibility study
2	Multiple sclerosis	0.664	2016	robot-assisted gait training; chronic stroke patient; gait training; multiple sclerosis; spinal cord injury | systematic review; robotic exoskeleton; chronic stroke; subacute stroke; controlled trial
3	Magneto-rheological brake	0.619	2019	systematic review; robot-assisted gait training; controlled trial; gait training; chronic stroke patient | stroke survivor; randomized controlled trial; robotic therapy; physical human-robot interaction force; case study
4	Test-retest reliability	0.673	2017	motor function; stroke survivor; systematic review; test-retest reliability; randomized controlled trial | robot-mediated rehabilitation; observational feasibility study; italian rehabilitation center; new organizational model; robotic exoskeleton device
5	Electromechanical-assisted training	0.77	2016	robot-assisted gait training; systematic review; stroke patient; gait rehabilitation; effective robot | gait training; chronic stroke; chronic stroke patient; subacute stroke; novel gait training device
6	Cerebral palsy	0.754	2018	systematic review; cerebral palsy; robot-assisted gait training; rehabilitation technologies; advanced robotic therapy individualized gait rehabilitation robotics; before-after study; gait training; hemiplegic patient; same person
7	Slow gait	0.891	2020	robot-assisted gait training; systematic review; stroke patient; intended gait speed prediction; slow gait | randomized controlled trial; overground exoskeleton gait training; inpatient rehabilitation; descriptive analysis; 1-year follow-up study

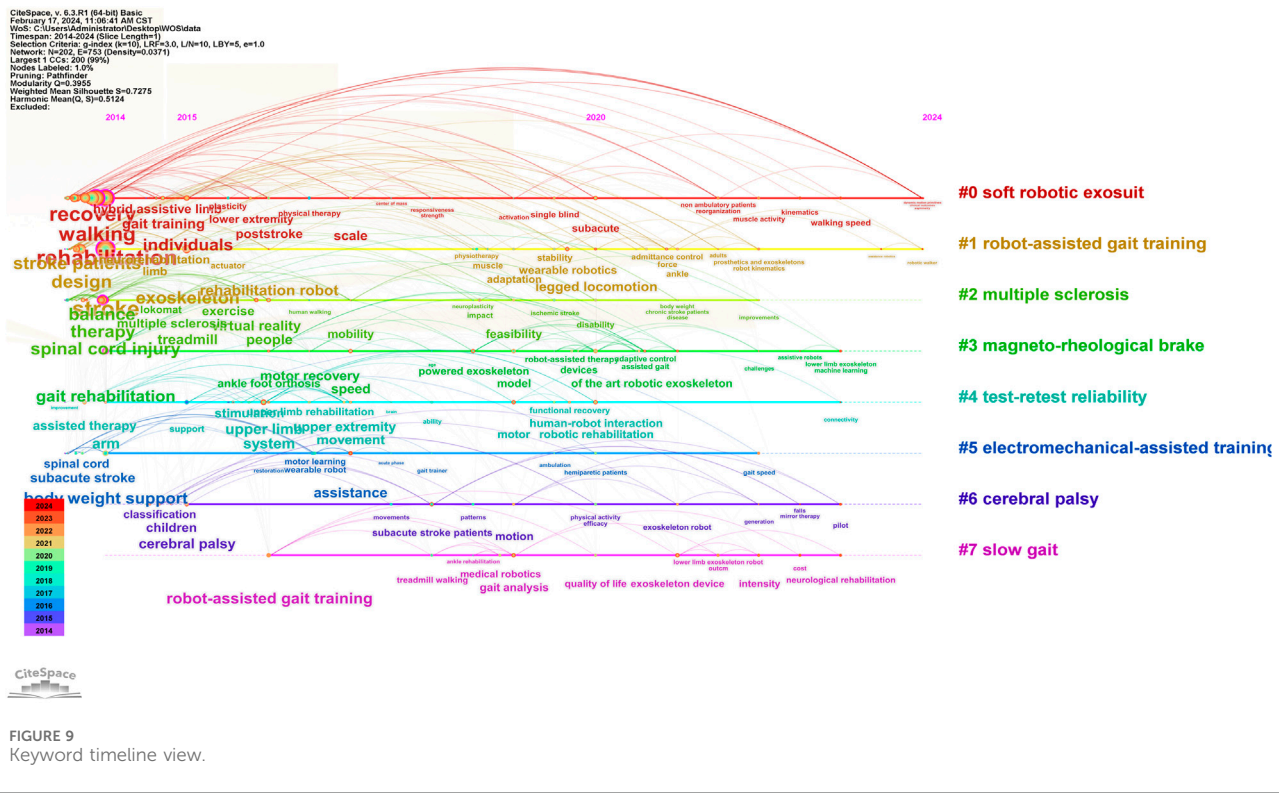

FIGURE 9
Keyword timeline view.

Keywords	Year	Strength	Begin	End	2014 – 2024
body weight support	2014	8.44	2014	2017	
spinal cord	2014	5.34	2014	2019	
support	2015	4.56	2015	2017	
stimulation	2016	5.85	2016	2019	
locomotion	2014	4.1	2016	2017	
subacute stroke	2014	4.15	2017	2019	
adaptation	2019	4.23	2019	2021	
quality of life	2020	4.81	2020	2021	
robotic exoskeleton	2021	4.31	2021	2024	
lower extremity	2016	4.21	2021	2022	

FIGURE 10
Ranking of keywords by burst strength.

on exploring the effectiveness and reliability of RE in assisting stroke patients with gait training. The movement patterns of gait training were continuously adjusted in practice, and the types and functions of RE were constantly optimized and iterated. (2) From 2021 to 2024, the emerging hotspots shifted to quality of life, machine learning, and cost.

4 Discussion

4.1 Distribution of countries, institutions, authors, and co-citation analysis

In terms of publication volume and betweenness centrality, the United States of America ranks first, overall indicating that Western countries lead in this field, while Asian countries such as China, South Korea, and Japan also possess strong capabilities. This may relate to the economic strength of these countries, policy directions, and research funding orientations. The United States has the highest number of publications globally and has always been at the forefront of technological innovation and artificial intelligence. As a populous country, China has seen an increasing incidence and number of stroke patients (Wu et al., 2019), thus prioritizing related research. Being a manufacturing powerhouse, China has rapidly developed in the field of artificial intelligence in recent years, leading to swift advancements and applications of RE. Notably, although China ranks second globally in publication volume, its betweenness centrality is relatively low. This may be due to the country's significant investment in this field in recent years, leading to a rapid increase in publications. However, due to a later start in technology, its performance in academic collaboration appears less favorable. While Switzerland does not dominate in publication volume, the Swiss Federal Institutes of Technology Domain has shown exceptional performance in institutional cooperation, possibly due to its early start in research and technical accumulation in engineering and technology fields.

Overall, authors with a high frequency of citations and betweenness centrality in the cited literature are predominantly scholars in the medical field, with few from engineering disciplines. This might be attributed to the fact that although the development of RE poses a technological challenge, the clinical efficacy of such devices requires long-term and careful observation. Hence, scholars in the medical field tend to have their publications cited more frequently in this area. Among them, the most frequently cited and highest betweenness centrality author is Professor J. Mehrholz from the European Private Scientific Research Institute and the Carl Gustav Carus Faculty of Medicine at Dresden University of Technology in Germany. Professor Mehrholz's research primarily focuses on functional impairments caused by conditions such as stroke, Parkinson's disease, and myasthenia, and is dedicated to evaluating the effectiveness of common rehabilitation methods in the neurology field through evidence-based medicine. His research direction in the field of motor rehabilitation for stroke patients includes electromechanical-assisted training, robotic-assisted therapy, and other means to improve lower limb function (Hesse et al., 2008; Mehrholz and Pohl, 2012; Mehrholz, 2016; Mehrholz et al., 2017; Wu et al., 2019).

Highly cited papers often include reviews and systematic reviews, likely because research related to RE mainly consists of comparative studies. However, due to constraints related to research subjects, intervention measures, ethics, etc., initial studies tend to have smaller sample sizes (Leow et al., 2023). Meta-analyses increase the sample size by pooling study results, thereby offering a more holistic and comprehensive analysis of intervention effects, leading to a higher citation count. However, due to inherent limitations of meta-analyses, such as issues with heterogeneity, publication bias, and significant influence from the quality of original studies (Khan et al., 1996; Hatala et al., 2005), meta-analyses cannot replace original research. The field requires more large-scale, multicenter randomized controlled trials to provide high-quality evidence in the future.

4.2 The research status and hotspots of RE assisting in gait therapy for stroke patients

From the standpoint of publication volume and timing, the application of RE in facilitating gait rehabilitation for patients with

stroke-induced hemiparesis has attracted increasing scholarly interest since the early 21st century, with a significantly growing body of literature observed. Notably, a marked increase in publications has been evident since 2016. This trend can likely be attributed to the advanced maturation of RE technology and its evolution from a phase of technological exploration to broader market and application phases (Calafiore et al., 2022). According to an analysis of keyword co-occurrence and clustering, the past decade's prominent research topics have encompassed the technology of RE, including both hardware and control strategies, alongside their clinical applications. Prior to 2016, technological research predominantly focused on body weight support and motion control within RE systems. Following 2020, machine learning has become a pivotal area of research interest. In the domain of RE applications, the period leading up to 2020 saw intense research focus on evaluating the efficacy and safety outcomes. After 2020, the academic community has increasingly turned its attention towards examining the impact of RE on quality of life and considerations of cost analysis.

4.2.1 RE hardware devices

Currently, there are two types of RE: rigid exoskeletons and soft exoskeletons. Accroding to keyword co-occurrence clustering analysis, "soft exoskeletons" was the hotspots. In the analysis of keyword co-occurrence, the high frequency of occurrence for "weight support" indicates that the weight ratio (the self-weight of the exoskeleton and its maximum load capacity) is a technical research focal point in the hardware configuration of exoskeletons. The average weight of exoskeletons used for stroke patients is 8.90 ± 7.48 kg, with a maximum carrying weight of 100 kg (Rodríguez-Fernández et al., 2021). The more joint drives an RE has, the heavier it becomes, and the overweight exoskeleton becomes a problem for patients to wear and carry (Tefertiller et al., 2018). Soft exoskeletons, due to their different materials, tend to be lighter than rigid exoskeletons (Sanchez-Villamañan et al., 2019), but their load-bearing capacity is less than that of rigid exoskeletons, therefore their use is limited in patients with severe muscle weakness and may increase the risk of falling (Awad et al., 2017). Stroke patients have a higher rate of obesity (Ekker et al., 2018), and although the weight of stroke survivors decreases post-stroke, during the subacute phase of stroke—a critical period for recovery—the patient's weight does not suddenly drop. Therefore, when designing, a broader audience needs to be considered, and engineers need to consider reducing the self-weight of the exoskeleton while increasing its load-bearing capacity.

4.2.2 Control strategies of RE

Scholars such as De Miguel-Fernández, J, in their work (de Miguel-Fernández et al., 2023), focus on the research progress in incorporating fall detection, balance recovery, and stability assurance strategies in the design and application of lower limb exoskeletons. They provide an overview of the current control strategy framework for lower limb exoskeletons and analyze the advantages and disadvantages of common methods used for stable walking with exoskeletons (including zero moment point, center of mass, and extrapolated center of mass). The study finds that the current level of evidence regarding the effectiveness of different machine control strategies on clinical outcomes for patients is not high. This is mainly due to the limited number of studies on RE with different control strategies within the same series and the lack of uniformity in research subjects and clinical outcome indicators, leading to high heterogeneity in clinical results. It is suggested that future research should focus more on standardized comparisons between control strategies, analyze the relationship between control parameters and biomechanical indicators, and reduce biases caused by hardware heterogeneity and patients' own recovery and compensation strategies. David Pinto-Fernandez et al. (Pinto-Fernandez et al., 2020) note that the number of papers assessing robot-assisted motion is growing exponentially, with almost half of the papers focusing on walking on level ground or treadmills. This highlights that the current research hotspot on exoskeleton motion control strategies is still on achieving basic motor skills. However, the study of control strategies should go beyond the achievement of basic motor skills to more extensively focus on how these strategies can be effectively translated into clinical practice, particularly in complex and unpredictable outdoor environments. In the clinical setting, the control strategies for RE require further refinement and personalization to cater to the specific needs and rehabilitation stages of different patients (Tian et al., 2024). As demonstrated in the framework proposed by Hohl et al. (Hohl et al., 2022) clinicians should consider the patient's specific impairments, device characteristics, and the overall goals of the treatment plan when selecting and implementing exoskeleton technology. This includes a detailed matching of the support level provided by the device, assistance/resistance modes, feedback enhancement, and the minimum functionality required.

4.2.3 The efficacy of RE-assisted walking therapy for stroke patients

The effectiveness of RE in stroke patients primarily pertains to the correction of abnormal gait patterns and the enhancement of walking ability. Additional reported benefits include improved cardiopulmonary function, alleviation of lower limb spasticity, enhancement of patients' balance capabilities, promotion of proprioceptive recovery, and increased neural plasticity (Molteni et al., 2020; Herrin et al., 2023; Lee et al., 2023; Rey-Prieto et al., 2023). Currently, most RE on the market offer dual functionalities, as lower limb rehabilitation in clinical settings is predominantly based on gait. Initiating walking training too early in acute stroke patients can lead to abnormal movement patterns due to insufficient leg strength and balance (Plummer et al., 2007). RE can simulate normal gait patterns in a weight-reduced state and adjust the level of assistance based on the patient's gait changes, thus helping patients establish a normal gait while also improving muscle strength and walking distance. Commonly used criteria for assessing the promotion of lower limb rehabilitation by RE include walking ability tests, muscle tone and strength assessments, joint range of motion measurements, balance ability assessments, gait analysis (including kinematic and kinetic analyses, and dynamic electromyography tracking), and surface electromyography. Calabrò et al. conducted a clinical trial on neuroplasticity in stroke patients utilizing powered exoskeletons, finding that the exoskeletons also impact the wearer's neuromuscular control, facilitating the restoration of specific cerebral plasticity mechanisms. Although RE are

generally beneficial for lower limb rehabilitation and social reintegration in hemiplegic stroke patients, the current evidence is insufficient for clinical physicians to select specific treatment plans due to variations in RE types, treatment dosages, stages of stroke patients, and disease severity. This has become one of the barriers to the clinical application of RE. Future research could consider comparing different RE, treatment doses, and stroke populations to provide more detailed and reliable treatment strategies for clinical physicians, guiding the selection and use of RE for patients with different clinical needs.

The effectiveness of RE is of paramount concern for developers and clinical researchers, yet it is important to note that research on user experience is relatively scarce (Louie et al., 2020; Morone et al., 2017). Given that the end users and operators of exoskeletons are patients and professional healthcare personnel, it is essential to thoroughly understand the experiences of these two groups when utilizing RE. Such insights are vital for directing the future development and optimization of RE technology. Researchers like Julie Vaughan-Graham have explored the experiences of stroke patients and physical therapists with the Exo-H2 exoskeleton (a powered exoskeleton) in gait rehabilitation. Physical therapists believe that improvements are necessary in the efficiency of donning and doffing the technology, the convenience of its operation, the diversity of parameter settings, and the real-time output of data. Concurrently, they express concerns regarding the balance of the RE and the potential musculoskeletal damage they may cause. Patients have an optimistic view of the technology, but because the exoskeleton's pre-programmed modes control their movements, it makes them feel as though the exoskeleton is walking for them, rather than assisting. They prefer the exoskeleton to aid in walking, not to replace it. Thus, enhancing the interaction between RE and users, as well as the self-balancing features of exoskeleton are likely challenges that technicians will need to address in the future (Vaughan-Graham et al., 2020).

4.3 Research trends in RE-assisted walking therapy for stroke patients

In the field of RE technology research, RE have evolved from strict gait standardization control towards a shared control with human-machine interaction. While standardization control can correct a patient's gait to match the trajectory of a healthy person's gait, achieving a seemingly corrective objective, it also limits active engagement with the machine, potentially reducing the patient's motivation (Wu, 2021). Shared control addresses this issue more effectively, currently, shared control technology mainly utilizes theories such as adaptive fuzzy control, admittance control, impedance control, and gait trajectory planning as a basis to adjust and optimize leg movements during a patient's walking process (Rajasekaran et al., 2018). However, the application of current technology still seems to fall short of idealized interaction, with patients not being entirely satisfied with the experience. Future research hotspots and trends include exoskeleton human-machine symbiotic design, motion intention detection, human-machine hybrid system motion control, and the integration of technologies such as virtual reality and machine learning (Postol et al., 2021).

Generally, RE exert a positive effects on therapeutic effectiveness and the enhancement of quality of life. However, it is worth noting that current application research is primarily focused on patients in the subacute phase of stroke, which may be attributed to the critical importance of correcting gait and restoring walking ability during this period. Appropriate interventions during this phase can help reduce sequelae and improve long-term outcomes (Calafiore et al., 2022). However, with the decline in mortality rates among stroke patients (Benjamin et al., 2019), the life expectancy of patients in the chronic phase has extended. The capacity for mobility and self-care within this demographic necessitates proactive intervention and enhancement. Consequently, the efficacy of applications amongst such populations must also be duly reported. Additionally, previous studies often selected hospitals or specific rehabilitation treatment site due to easier access to patients and the presence of professional medical staff to prevent injuries. However, with the maturation and expansion of RE technology, future applications in homes and communities might become a trend, considering that most stroke survivors spend a significant amount of their time at home or in the community, rather than in rehabilitation institutions or hospitals.

5 Limitation

In terms of data, this article only retrieved documents from the Web of Science Core Collection, omitting searches in other databases such as PUBMED, Embase, and related databases. This exclusion may lead to the omission of some relevant articles in the field. Secondly, the types of documents included in this study were primarily English-language papers and reviews, thereby potentially overlooking the contributions of high-quality works published in other languages or formats. Finally, since the data of this study, such as citation counts and co-occurrence frequencies, are related to the publication date, it is possible that some high-quality articles that were published more recently may have been overlooked.

6 Conclusion

This study synthesizes a decade of research on robotic exoskeletons for stroke rehabilitation, revealing a surge in publications and technological evolution. The United States, China, and several European countries lead with significant contributions. Initial focus on exoskeleton development has transitioned to integrating AI and optimizing user interaction. High-impact reviews consolidate evidence, yet there's a call for more rigorous trials. Technological strides from rigid to soft exoskeletons address weight and usability, with control strategies advancing for patient comfort and safety. Looking forward, the field is set to focus on human-machine symbiosis, motion intention detection, and the integration of virtual reality and machine learning, with potential for home and community-based rehabilitation. Future research should prioritize investigations within the cohort of chronic stroke patients, while concurrently attending to the experiential accounts of both patients and rehabilitation therapists.

Author contributions

SW: Writing–original draft, Writing–review and editing, Conceptualization, Data curation, Formal Analysis, Methodology. RH: Methodology, Writing–original draft, Writing–review and editing. LL: Data curation, Methodology, Writing–review and editing. YZ: Writing–review and editing, Resources. HY: Resources, Writing–review and editing, Funding acquisition.

Funding

The author(s) declare that financial support was received for the research, authorship, and/or publication of this article. The work was supported in part by the National Natural Science Foundation of China under Grant 62373346.

Conflict of interest

The authors declare that the research was conducted in the absence of any commercial or financial relationships that could be construed as a potential conflict of interest.

Publisher's note

References

Awad, L. N., Bae, J., O'donnell, K., De Rossi, S. M., Hendron, K., Sloot, L. H., et al. (2017). A soft robotic exosuit improves walking in patients after stroke. *Sci. Transl. Med.* 9 (400), eaai9084. doi:10.1126/scitranslmed.aai9084

Benjamin, E. J., Muntner, P., Alonso, A., Bittencourt, M. S., Callaway, C. W., Carson, A. P., et al. (2019). Heart disease and stroke statistics—2019 update: a report from the American Heart Association. *Circulation* 139 (10), e56–e528. doi:10.1161/cir.0000000000000659

Bruni, M. F., Melegari, C., De Cola, M. C., Bramanti, A., Bramanti, P., and Calabrò, R. S. (2018). What does best evidence tell us about robotic gait rehabilitation in stroke patients: a systematic review and meta-analysis. *J. Clin. Neurosci.* 48, 11–17. doi:10.1016/j.jocn.2017.10.048

Calabrò, R. S., Naro, A., Russo, M., Bramanti, P., Carioti, L., Balletta, T., et al. (2018). Sha** neuroplasticity by using powered exoskeletons in patients with stroke: a randomized clinical trial. *J. neuroengineering rehabilitation* 15 (1), 1–16. doi:10.1186/s12984-018-0377-8

Calafiore, D., Negrini, F., Tottoli, N., Ferraro, F., Ozyemisci-Taskiran, O., and de Sire, A. (2022). Efficacy of robotic exoskeleton for gait rehabilitation in patients with subacute stroke: a systematic review. *Eur. J. Phys. Rehabilitation Med.* 58 (1), 1–8. doi:10.23736/s1973-9087.21.06846-5

Cheng, C. J., and Yu, H. B. (2024). Global trends and development of acupuncture for stroke: a review and bibliometric analysis. *Medicine* 103 (3), e36984. doi:10.1097/md.0000000000036984

Chi, X., Fan, X., Fu, G., Liu, Y., Zhang, Y., and Shen, W. (2023). Research trends and hotspots of post-stroke cognitive impairment: a bibliometric analysis. *Front. Pharmacol.* 14, 1184830. doi:10.3389/fphar.2023.1184830

de Miguel-Fernández, J., Lobo-Prat, J., Prinsen, E., Font-Llagunes, J. M., and Marchal-Crespo, L. (2023). Control strategies used in lower limb exoskeletons for gait rehabilitation after brain injury: a systematic review and analysis of clinical effectiveness. *J. neuroengineering rehabilitation* 20 (1), 23. doi:10.1186/s12984-023-01144-5

de Miguel Fernandez, J., Rey-Prieto, M., Rio, M. S., Lopez-Matas, H., Guirao-Cano, L., Font-Llagunes, J. M., and Lobo-Prat, J. (2023). Adapted Assistance and Resistance Training With a Knee Exoskeleton After Stroke. IEEE transactions on neural systems and rehabilitation engineering: a publication of the IEEE Engineering in Medicine and Biology Society, 31, 3265–3274. doi:10.1109/TNSRE.2023.3303777

Dobkin, B. H., and Duncan, P. W. (2012). Should body weight–supported treadmill training and robotic-assistive steppers for locomotor training trot back to the starting gate? *Neurorehabilitation neural repair* 26 (4), 308–317. doi:10.1177/1545968312439687

Dong, Y., Weng, L., Hu, Y., Mao, Y., Zhang, Y., Lu, Z., et al. (2022). Exercise for stroke rehabilitation: a bibliometric analysis of global research from 2001 to 2021. *Front. Aging Neurosci.* 14, 876954. doi:10.3389/fnagi.2022.876954

Donthu, N., Kumar, S., Mukherjee, D., Pandey, N., and Lim, W. M. (2021). How to conduct a bibliometric analysis: an overview and guidelines. *J. Bus. Res.* 133, 285–296. doi:10.1016/j.jbusres.2021.04.070

Duncan, P. W., Sullivan, K. J., Behrman, A. L., Azen, S. P., Wu, S. S., Nadeau, S. E., et al. (2011). Body-weight–supported treadmill rehabilitation after stroke. *N. Engl. J. Med.* 364 (21), 2026–2036. doi:10.1056/nejmoa1010790

Ekker, M. S., Boot, E. M., Singhal, A. B., Tan, K. S., Debette, S., Tuladhar, A. M., et al. (2018). Epidemiology, aetiology, and management of ischaemic stroke in young adults. *Lancet Neurology* 17 (9), 790–801. doi:10.1016/s1474-4422(18)30233-3

Feigin, V. L., Brainin, M., Norrving, B., Martins, S., Sacco, R. L., Hacke, W., et al. (2022). World Stroke Organization (WSO): global stroke fact sheet 2022. *Int. J. Stroke* 17 (1), 18–29. doi:10.1177/17474930211065917

Feigin, V. L., Stark, B. A., Johnson, C. O., Roth, G. A., Bisignano, C., Abady, G. G., et al. (2021). Global, regional, and national burden of stroke and its risk factors, 1990–2019: a systematic analysis for the Global Burden of Disease Study 2019. *Lancet Neurology* 20 (10), 795–820. doi:10.1016/s1474-4422(21)00252-0

Harjpal, P., Kovela, R. K., Jain, M., and Kovela Sr, R. K. (2022). Bilateral lower limb training for post-stroke survivors: a bibliometric analysis. *Cureus* 14 (9), e29615. doi:10.7759/cureus.29615

Hatala, R., Keitz, S., Wyer, P., and Guyatt, G. (2005). Tips for learners of evidence-based medicine: 4. Assessing heterogeneity of primary studies in systematic reviews and whether to combine their results. *Cmaj* 172 (5), 661–665. doi:10.1503/cmaj.1031920

Herrin, K., Upton, E., and Young, A. (2023). Towards meaningful community ambulation in individuals post stroke through use of a smart hip exoskeleton: a preliminary investigation. *Assist. Technol.*, 1–11. doi:10.1080/10400435.2023.2239555

Hesse, S., Mehrholz, J., and Werner, C. (2008). Robot-assisted upper and lower limb rehabilitation after stroke: walking and arm/hand function. *Dtsch. Ärzteblatt Int.* 105 (18), 330–336. doi:10.3238/arztebl.2008.0330

Hohl, K., Giffhorn, M., Jackson, S., and Jayaraman, A. (2022). A framework for clinical utilization of robotic exoskeletons in rehabilitation. *J. neuroengineering rehabilitation* 19 (1), 115. doi:10.1186/s12984-022-01083-7

Hu, Y., Yu, Z., Cheng, X., Luo, Y., and Wen, C. (2020). A bibliometric analysis and visualization of medical data mining research. *Medicine* 99 (22), e20338. doi:10.1097/md.0000000000020338

Kawamoto, H., Kamibayashi, K., Nakata, Y., Yamawaki, K., Ariyasu, R., Sankai, Y., et al. (2013). Pilot study of locomotion improvement using hybrid assistive limb in chronic stroke patients. *BMC Neurol.* 13, 141–148. doi:10.1186/1471-2377-13-141

Khan, K. S., Daya, S., and Jadad, A. R. (1996). The importance of quality of primary studies in producing unbiased systematic reviews. *Archives Intern. Med.* 156 (6), 661–666. doi:10.1001/archinte.156.6.661

Kim, C., and Kim, H. J. (2022). Effect of robot-assisted wearable exoskeleton on gait speed of post-stroke patients: a systematic review and meta-analysis of a randomized controlled trials. *Phys. Ther. Rehabilitation Sci.* 11 (4), 471–477. doi:10.14474/ptrs.2022.11.4.471

Klamroth-Marganska, V., Blanco, J., Campen, K., Curt, A., Dietz, V., Ettlin, T., et al. (2014). Three-dimensional, task-specific robot therapy of the arm after stroke: a multicentre, parallel-group randomised trial. *Lancet Neurology* 13 (2), 159–166. doi:10.1016/s1474-4422(13)70305-3

Koenig, A., Omlin, X., Bergmann, J., Zimmerli, L., Bolliger, M., Müller, F., et al. (2011). Controlling patient participation during robot-assisted gait training. *J. neuroengineering rehabilitation* 8, 14–12. doi:10.1186/1743-0003-8-14

Krishnamurthi, R. V., Ikeda, T., and Feigin, V. L. (2020). Global, regional and country-specific burden of ischaemic stroke, intracerebral haemorrhage and subarachnoid haemorrhage: a systematic analysis of the global burden of disease study 2017. *Neuroepidemiology* 54 (2), 171–179. doi:10.1159/000506396

Langhorne, P., Bernhardt, J., and Kwakkel, G. (2011). Stroke rehabilitation. *Lancet* 377 (9778), 1693–1702. doi:10.1016/s0140-6736(11)60325-5

Lee, Y. H., Ko, L. W., Hsu, C. Y., and Cheng, Y. Y. (2023). Therapeutic effects of robotic-exoskeleton-assisted gait rehabilitation and predictive factors of significant

improvements in stroke patients: a randomized controlled trial. *Bioengineering* 10 (5), 585. doi:10.3390/bioengineering10050585

Leow, X. R. G., Ng, S. L. A., and Lau, Y. (2023). Overground robotic exoskeleton training for patients with stroke on walking-related outcomes: a systematic review and meta-analysis of randomized controlled trials. *Archives Phys. Med. Rehabilitation* 104, 1698–1710. doi:10.1016/j.apmr.2023.03.006

Li, C., Shu, X., and Liu, X. (2022). Research hotspots and frontiers in post stroke pain: a bibliometric analysis study. *Front. Mol. Neurosci.* 15, 905679. doi:10.3389/fnmol.2022.905679

Loro, A., Borg, M. B., Battaglia, M., Amico, A. P., Antenucci, R., Benanti, P., et al. (2023). Balance rehabilitation through robot-assisted gait training in post-stroke patients: a systematic review and meta-analysis. *Brain Sci.* 13 (1), 92. doi:10.3390/brainsci13010092

Louie, D. R., and Eng, J. J. (2016). Powered robotic exoskeletons in post-stroke rehabilitation of gait: a sco** review. *J. neuroengineering rehabilitation* 13, 1–10. doi:10.1186/s12984-016-0162-5

Louie, D. R., Mortenson, W. B., Durocher, M., Teasell, R., Yao, J., and Eng, J. J. (2020). Exoskeleton for post-stroke recovery of ambulation (ExStRA): study protocol for a mixed-methods study investigating the efficacy and acceptance of an exoskeleton-based physical therapy program during stroke inpatient rehabilitation. *BMC Neurol.* 20 (1), 35–39. doi:10.1186/s12883-020-1617-7

Mehrholz, J. (2016). Towards evidence-based practice of technology-based gait rehabilitation after stroke. *Physiother. Res. Int. J. Res. Clin. Phys. Ther.* 21 (4), 201–202. doi:10.1002/pri.1680

Mehrholz, J., and Pohl, M. (2012). Electromechanical-assisted gait training after stroke: a systematic review comparing end-effector and exoskeleton devices. *J. rehabilitation Med.* 44 (3), 193–199. doi:10.2340/16501977-0943

Mehrholz, J., Thomas, S., and Elsner, B. (2017). Treadmill training and body weight support for walking after stroke. *Cochrane database Syst. Rev.* 2017 (8), CD002840. doi:10.1002/14651858.cd002840.pub4

Mehrholz, J., Thomas, S., Kugler, J., Pohl, M., and Elsner, B. (2020). Electromechanical-assisted training for walking after stroke. *Cochrane database Syst. Rev.* 2020 (10), CD006185. doi:10.1002/14651858.cd006185.pub5

Molteni, F., Formaggio, E., Bosco, A., Guanziroli, E., Piccione, F., Masiero, S., et al. (2020). Brain connectivity modulation after exoskeleton-assisted gait in chronic hemiplegic stroke survivors: a pilot study. *Am. J. Phys. Med. rehabilitation* 99 (8), 694–700. doi:10.1097/phm.0000000000001395

Molteni, F., Guanziroli, E., Goffredo, M., Calabrò, R. S., Pournajaf, S., Gaffuri, M., et al. (2021). Gait recovery with an overground powered exoskeleton: a randomized controlled trial on subacute stroke subjects. *Brain Sci.* 11 (1), 104. doi:10.3390/brainsci11010104

Morone, G., Paolucci, S., Cherubini, A., De Angelis, D., Venturiero, V., Coiro, P., et al. (2017). Robot-assisted gait training for stroke patients: current state of the art and perspectives of robotics. *Neuropsychiatric Dis. Treat.* Vol. 13, 1303–1311. doi:10.2147/ndt.s114102

Nilsson, A., Vreede, K. S., Häglund, V., Kawamoto, H., Sankai, Y., and Borg, J. (2014). Gait training early after stroke with a new exoskeleton–the hybrid assistive limb: a study of safety and feasibility. *J. neuroengineering rehabilitation* 11, 92–11. doi:10.1186/1743-0003-11-92

Ninkov, A., Frank, J. R., and Maggio, L. A. (2022). Bibliometrics: methods for studying academic publishing. *Perspect. Med. Educ.* 11 (3), 173–176. doi:10.1007/s40037-021-00695-4

Ogihara, H., Yamamoto, N., Kurasawa, Y., Kamo, T., Hagiyama, A., Hayashi, S., et al. (2023). Characteristics and methodological quality of the top 50 most influential articles on stroke rehabilitation: a bibliometric analysis. *Am. J. Phys. Med. Rehabilitation*, 10–1097. doi:10.1097/PHM.0000000000002412

Pennycott, A., Wyss, D., Vallery, H., Klamroth-Marganska, V., and Riener, R. (2012). Towards more effective robotic gait training for stroke rehabilitation: a review. *J. neuroengineering rehabilitation* 9 (1), 65–13. doi:10.1186/1743-0003-9-65

Pinto-Fernandez, D., Torricelli, D., del Carmen Sanchez-Villamanan, M., Aller, F., Mombaur, K., Conti, R., et al. (2020). Performance evaluation of lower limb exoskeletons: a systematic review. *IEEE Trans. Neural Syst. Rehabilitation Eng.* 28 (7), 1573–1583. doi:10.1109/tnsre.2020.2989481

Plummer, P., Behrman, A. L., Duncan, P. W., Spigel, P., Saracino, D., Martin, J., et al. (2007). Effects of stroke severity and training duration on locomotor recovery after stroke: a pilot study. *Neurorehabilitation neural repair* 21 (2), 137–151. doi:10.1177/1545968306295559

Pons, J. L. (2008). *Wearable robots: biomechatronic exoskeletons*. USA: John Wiley & Sons.

Postol, N., Grissell, J., McHugh, C., Bivard, A., Spratt, N. J., and Marquez, J. (2021). Effects of therapy with a free-standing robotic exoskeleton on motor function and other health indicators in people with severe mobility impairment due to chronic stroke: a quasi-controlled study. *J. Rehabilitation Assistive Technol. Eng.* 8, 205566832110458. doi:10.1177/20556683211045837

Pournajaf, S., Calabrò, R. S., Naro, A., Goffredo, M., Aprile, I., Tamburella, F., et al. (2023). Robotic versus conventional Overground gait training in subacute stroke survivors: a multicenter controlled clinical trial. *J. Clin. Med.* 12 (2), 439. doi:10.3390/jcm12020439

Rajasekaran, V., López-Larraz, E., Trincado-Alonso, F., Aranda, J., Montesano, L., Del-Ama, A. J., et al. (2018). Volition-adaptive control for gait training using wearable exoskeleton: preliminary tests with incomplete spinal cord injury individuals. *J. neuroengineering rehabilitation* 15 (1), 4–15. doi:10.1186/s12984-017-0345-8

Riener, R., Nef, T., and Colombo, G. (2005). Robot-aided neurorehabilitation of the upper extremities. *Med. Biol. Eng. Comput.* 43, 2–10. doi:10.1007/bf02345116

Rodríguez-Fernández, A., Lobo-Prat, J., and Font-Llagunes, J. M. (2021). Systematic review on wearable lower-limb exoskeletons for gait training in neuromuscular impairments. *J. neuroengineering rehabilitation* 18 (1), 22–21. doi:10.1186/s12984-021-00815-5

Sanchez-Villamañan, M. D. C., Gonzalez-Vargas, J., Torricelli, D., Moreno, J. C., and Pons, J. L. (2019). Compliant lower limb exoskeletons: a comprehensive review on mechanical design principles. *J. neuroengineering rehabilitation* 16 (1), 55–16. doi:10.1186/s12984-019-0517-9

Tefertiller, C., Hays, K., Jones, J., Jayaraman, A., Hartigan, C., Bushnik, T., et al. (2018). Initial outcomes from a multicenter study utilizing the indego powered exoskeleton in spinal cord injury. *Top. spinal cord Inj. rehabilitation* 24 (1), 78–85. doi:10.1310/sci17-00014

Tian, D., Li, F., and He, Y. (2024). Data-driven estimation for uphill continuous rehabilitation motion at different slopes using sEMG. *Biomed Signal Processi and Con* 93 (5), 106162.

Uivarosan, D., Bungau, S. G., Nistor-Cseppento, C. D., Negru, P. A., Bungau, A. F., Sabau, A. M., et al. (2022). Application of robotic recovery techniques to stroke survivors—bibliometric analysis. *J. Personalized Med.* 12 (12), 2066. doi:10.3390/jpm12122066

Vaughan-Graham, J., Brooks, D., Rose, L., Nejat, G., Pons, J., and Patterson, K. (2020). Exoskeleton use in post-stroke gait rehabilitation: a qualitative study of the perspectives of persons post-stroke and physiotherapists. *J. neuroengineering rehabilitation* 17 (1), 123–215. doi:10.1186/s12984-020-00750-x

Warutkar, V., Dadgal, R., and Mangulkar, U. R. (2022). Use of robotics in gait rehabilitation following stroke: a review. *Cureus* 14 (11), e31075. doi:10.7759/cureus.31075

Wu, A. R. (2021). Human biomechanics perspective on robotics for gait assistance: challenges and potential solutions. *Proc. R. Soc. B* 288 (1956), 20211197. doi:10.1098/rspb.2021.1197

Wu, D., Zhang, H., Leng, Y., Li, K., Li, S., and Lo, W. L. A. (2023). A bibliometric analysis of telerehabilitation services for patients with stroke. *Front. neurology* 13, 1026867. doi:10.3389/fneur.2022.1026867

Wu, S., Wu, B. O., Liu, M., Chen, Z., Wang, W., Anderson, C. S., et al. (2019). Stroke in China: advances and challenges in epidemiology, prevention, and management. *Lancet Neurology* 18 (4), 394–405. doi:10.1016/s1474-4422(18)30500-3

Xu, F., Bai, L., Dai, Z., and Cheng, H. (2023). Research hotspots and trends in post-stroke dysphagia: a bibliometric analysis. *Front. Neurosci.* 17, 1275748. doi:10.3389/fnins.2023.1275748

Yang, J., Gong, Y., Yu, L., Peng, L., Cui, Y., and Huang, H. (2023). Effect of exoskeleton robot-assisted training on gait function in chronic stroke survivors: a systematic review of randomised controlled trials. *BMJ open* 13 (9), e074481. doi:10.1136/bmjopen-2023-074481

Yi, X., and Yubing, D. (2024). Exoskeleton-assisted walking rehabilitation for spinal cord injury: CiteSpace analysis of research hotspots. *Res. Chin. Organ. Eng.*, 5403–5412. doi:10.12307/2024.674

Young, A. J., and Ferris, D. P. (2016). State of the art and future directions for lower limb robotic exoskeletons. *IEEE Trans. Neural Syst. Rehabilitation Eng.* 25 (2), 171–182. doi:10.1109/tnsre.2016.2521160

Yu, D., Xu, Z., Pedrycz, W., and Wang, W. (2017). Information sciences 1968–2016: a retrospective analysis with text mining and bibliometric. *Inf. Sci.* 418, 619–634. doi:10.1016/j.ins.2017.08.031

Zuccon, G., Lenzo, B., Bottin, M., and Rosati, G. (2022). Rehabilitation robotics after stroke: a bibliometric literature review. *Expert Rev. Med. Devices* 19 (5), 405–421. doi:10.1080/17434440.2022.2096438

frontiers | Frontiers in Bioengineering and Biotechnology

TYPE Brief Research Report
PUBLISHED 20 May 2024
DOI 10.3389/fbioe.2024.1358670

OPEN ACCESS

EDITED BY
Wujing Cao,
Chinese Academy of Sciences (CAS), China

REVIEWED BY
Wenxin Niu,
Tongji University, China
Hassan Sadeghi Naeini,
Iran University of Science and Technology, Iran

*CORRESPONDENCE
Hossein Rouhani,
hrouhani@ualberta.ca

RECEIVED 20 December 2023
ACCEPTED 29 April 2024
PUBLISHED 20 May 2024

CITATION
Shakourisalim M, Wang X, Beltran Martinez K, Golabchi A, Krell S, Tavakoli M and Rouhani H (2024), A comparative study of biomechanical assessments in laboratory and field settings for manual material handling tasks using extractor tools and exoskeletons.
Front. Bioeng. Biotechnol. 12:1358670.
doi: 10.3389/fbioe.2024.1358670

A comparative study of biomechanical assessments in laboratory and field settings for manual material handling tasks using extractor tools and exoskeletons

Maryam Shakourisalim[1], Xun Wang[1], Karla Beltran Martinez[1], Ali Golabchi[2,3], Sarah Krell[4], Mahdi Tavakoli[5] and Hossein Rouhani[1,5]*

[1]Department of Mechanical Engineering, University of Alberta, Edmonton, AB, Canada, [2]Department of Civil and Environmental Engineering, University of Alberta, Edmonton, AB, Canada, [3]EWI Works Inc., Edmonton, AB, Canada, [4]EPCOR Utilities Inc., Edmonton, AB, Canada, [5]Department of Electrical and Computer Engineering, University of Alberta, Edmonton, AB, Canada, [6]Glenrose Rehabilitation Hospital, Edmonton, AB, Canada

To enhance physical capabilities of workers who regularly perform physically demanding tasks involving heavy lifting and awkward postures, various tools and occupational exoskeletons can be used. Most of the studies aiming to explore the efficiency of these tools and exoskeletons have been performed in confined and controlled laboratory spaces, which do not represent the real-world work environment. This study aimed to compare the outcome of biomechanical assessment of using a back support exoskeleton and assistive tools (Lever and Jake) in the procedure of a high demanding manual material handling task versus the results found by performing the same task in a laboratory. Ten able-bodied participants and ten able-bodied utility workers performed the same manhole removal task in-lab and in-field, respectively, with the aid of an exoskeleton and Lever and Jake tools. Muscle activity and Rapid Entire Body Assessment (REBA) scores were recorded using surface electromyography and inertial measurement units, respectively and compared between in-lab and in-field trials. The field experiments indicated significant differences ($p < 0.05$) in normalized muscle activity across most muscles when compared to laboratory data. These results revealed how muscle activity is affected by the controlled lab setting compared to real-world field conditions. However, REBA scores indicate similar ergonomic implications regardless of the utilization of exoskeletons or tools. These findings underscore that real-world field assessments are crucial for evaluating ergonomic risks and effects of occupational exoskeletons and tools to account for environmental factors and workers' skills in ergonomic evaluations of this nature.

KEYWORDS

low back pain, ergonomic risk assessment, inertial measurement unit, occupational exoskeleton, electromyography

1 Introduction

To reduce the prevalence of work-related musculoskeletal disorders (WMSDs), employers are increasingly investing in equipment, tools, and training initiatives designed to minimize the physical strain associated with physically demanding tasks, and subsequently improve the wellbeing of the workers, enhance workplace productivity, and reduce the economic burden of injuries (Coenen et al., 2014). For example, occupational exoskeletons are proposed to reduce the risk of fatigue and chronic WMSDs. Exoskeletons are wearable devices constructed from lightweight materials and integrate mechanical components to enhance the physical capabilities of workers, addressing challenges like lifting heavy objects, performing repetitive tasks, or enduring extended periods of standing or kneeling (Kim et al., 2019; Andrade and Nathan-Roberts, 2022).

Numerous studies have focused on ergonomic risk analysis and the effect of physical assistance devices, such as occupational exoskeletons. However, these studies are mostly conducted in laboratory settings (Baltrusch et al., 2019; Theurel and Desbrosses, 2019; De Bock et al., 2022). Laboratory assessments provide controlled environments for detailed biomechanical and physiological measurements, isolating the exoskeleton's effects from other variables and allow for precise and repeatable measurements (Baltrusch et al., 2019). These controlled conditions may not accurately represent the complexities and variability of real-world tasks, which can limit the generalizability of findings and impact ecological validity of assessments (Hoogendoorn et al., 2000; Wami et al., 2019). In contrast, field evaluations conducted in actual work environments allow researchers to observe and evaluate workers in their natural settings, which ensures that the assessments are contextually relevant and offer crucial insights into the exoskeleton's real-world performance, usability, and user acceptance (De Bock et al., 2020; Gull et al., 2020; Bennett et al., 2023). In-field ergonomic risk assessments are also subject to limitations such as the influence of uncontrolled environmental variables and limited measuring equipment (Crea et al., 2021; Khandan et al., 2022).

This study critically examines the discrepancies in biomechanical assessments of manual material handling tasks in laboratory versus field settings, focusing on the potential for varied interpretations of ergonomic risks and the effectiveness of assistive devices, including exoskeletons. An experimental approach was adopted by evaluating measurements of muscle activities and body posture, for a manhole cover removal task. This task is a representative high-demand, frequent manual handling activity, commonly performed by utility workers. Experiments were conducted in both lab and field environments, utilizing assistive tools and a passive back-support exoskeleton. Our objectives were to compare biomechanical outcomes in laboratory and field conditions, to evaluate the effectiveness of back support exoskeletons in mitigating ergonomic risks in varied settings, and to contribute to the development of more effective ergonomic assessments and tools in real-world work environments. We hypothesize significant variances in biomechanical assessments between lab and field environments and expect the exoskeleton's effectiveness in reducing ergonomic risks to differ across these settings. The anticipated results are expected to deepen our understanding of ergonomic risk factors across different environments.

2 Methods

2.1 Study design and participants

For the in-field assessment, ten able-bodied male workers from drainage and construction (body mass: 73 ± 18 kg, body height: 180 ± 5 cm, age: 33 ± 7 years) volunteered to perform the manhole removal task on their jobsite. The in-lab data was recorded from ten able-bodied participants (6 males, 4 females, body mass: 63 ± 13 kg, body height: 170 ± 7 cm, age: 26 ± 1 years) among university students. The in-lab setup was designed to replicate the tasks performed by workers on the job site. Participants had no clinical history of lower back pain up to 6 months prior to the study, and written consent was collected from the participants after they were informed of the experimental procedures. The study was approved by the research ethics board of the University of Alberta, ID: Pro00109264.

2.2 Experimental procedure

Surface electromyography (EMG) data was captured bilaterally from the Brachioradialis, Biceps Brachii, Triceps Brachii, middle branch of the Trapezius, Latissimus Dorsi, Thoracolumbar Fascia, Rectus Femoris, and Bicep Femoris muscles using 16 Trigno Avanti sensors provided by Delsys Inc., United States (Figure 1). In addition to this, a Rapid Entire Body Assessment (REBA) was conducted to evaluate ergonomic risks, with body joint angles being measured using 11 inertial measurement units (IMUs) from Xsens Technologies, NL. These units were attached to the head, upper trunk (over the sternum), upper arms, forearms, lower back, thighs, and shanks (Figure 1).

The activity being assessed involved moving a manhole cover using either a sledgehammer and a pick bar tool called the "Jake" tool or an in-house lever-based tool called the "Lever" tool. Each participant engaged in two repetitions of the task, with a resting period of five seconds of standing still between each repetition, as illustrated in Figure 2. To explore the effectiveness of an exoskeleton in minimizing ergonomic risks, the participants repeated the trials while wearing a passive back-support exoskeleton, the BackX from SuitX, United States. The BackX exoskeleton incorporates passive torque-generating mechanisms around the hip to support the trunk extensor muscles during activities that involve bending and lifting. BackX offers a significant reduction in the load on the lower back, with maximum net torques of 24.8 Nm during flexion, thereby enhancing ergonomic safety (Madinei et al., 2022). Its design features adjustable support settings, including two modes (instant vs. standard) and two levels of support (low vs. high). The instant mode delivers assistive torque immediately upon forward bending, while the standard mode activates supportive torque when trunk flexion reaches approximately 35°. This exoskeleton uses passive mechanisms, including springs, to generate assistive torque only when the user bends forward, without hindering other movements like walking. In the present study, we assessed the exoskeleton's

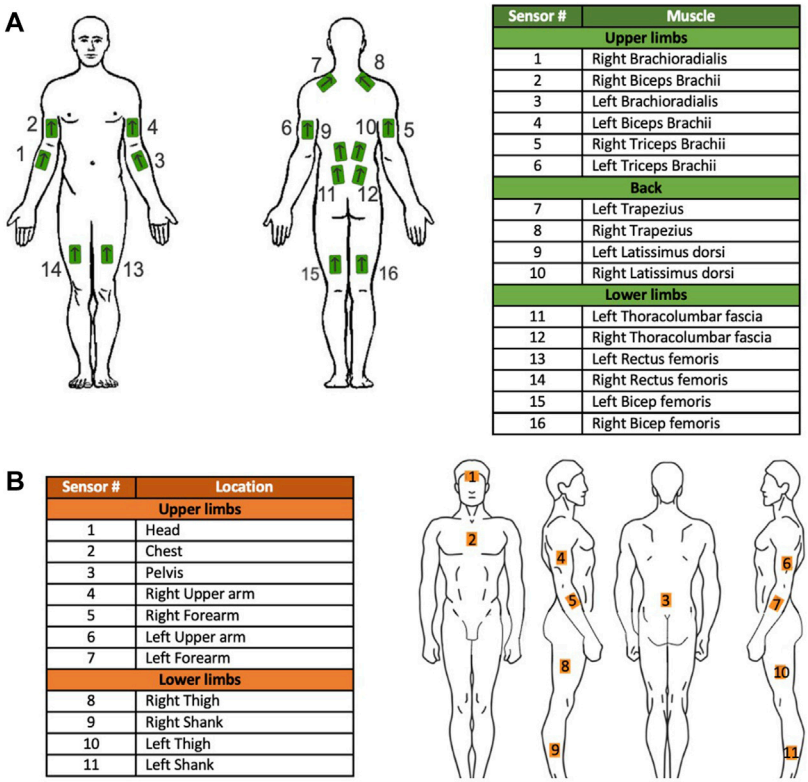

Sensor #	Muscle
Upper limbs	
1	Right Brachioradialis
2	Right Biceps Brachii
3	Left Brachioradialis
4	Left Biceps Brachii
5	Right Triceps Brachii
6	Left Triceps Brachii
Back	
7	Left Trapezius
8	Right Trapezius
9	Left Latissimus dorsi
10	Right Latissimus dorsi
Lower limbs	
11	Left Thoracolumbar fascia
12	Right Thoracolumbar fascia
13	Left Rectus femoris
14	Right Rectus femoris
15	Left Bicep femoris
16	Right Bicep femoris

Sensor #	Location
Upper limbs	
1	Head
2	Chest
3	Pelvis
4	Right Upper arm
5	Right Forearm
6	Left Upper arm
7	Left Forearm
Lower limbs	
8	Right Thigh
9	Right Shank
10	Left Thigh
11	Left Shank

FIGURE 1
Sensor placement of **(A)** EMG sensors and **(B)** IMU sensors on the participants.

performance in only instant and its effect on participants' posture and muscle activities. Each task was performed twice with and without the exoskeleton.

In-field data was collected from utility workers removing manhole covers on the job site. The in-lab trial was designed to duplicate the in-field trials by employing a total of 60 lbs weight plates within the laboratory environment, aiming to replicate the 60 lbs manhole cover used in-field. Furthermore, we maintained consistency by utilizing identical Jake and Lever tools for both the in-field and in-lab tests, ensuring a seamless comparison between the two scenarios. This approach allowed us to assess the performance of the tools and the exoskeleton in a controlled setting, mirroring real-world conditions as accurately as possible. However, there were inconsistencies, such as differences in the experience level between actual workers and student participants. In addition, the in-field manhole covers are flush with the ground which was not possible to exactly replicate in-lab.

2.3 Data analysis

The analysis of muscle activities while removing a manhole cover was conducted using EMG sensors. The EMG data was gathered at a rate of 2,000 Hz and then subjected to a band-pass filter, isolating frequencies in the range of 10–500 Hz. Subsequently, the signal was rectified and smoothed using a moving average filter with a window size of 500 data points. In order to standardize the amplitude of the EMG signal, a Maximum Voluntary Contraction (MVC) technique was applied to each of the muscles under observation (Konrad, 2005; Wang et al., 2023). Finally, we determined the Root Mean Square (RMS) value for the normalized amplitude of the EMG signal across the duration of the activity.

The data recorded by IMU, underwent a low-pass filtering process using a 2nd order Butterworth filter set at a 6 Hz cut-off frequency. This filtered data was then used to ascertain the sensor orientations through the application of a sensor fusion algorithm, as described in Nazarahari and Rouhani (2020) and (2021). In addition to this, the orientation of the sensor relative to the body was determined through a functional calibration procedure, as outlined in (Nazarahari et al., 2019). Following these initial steps, the orientations of different body segments were calculated and the angles of various joints during the trials were computed and expressed within the Joint Coordinate System (JCS), as referenced in (Grood and Suntay, 1983).

The calculated joint angles were used to obtain a Rapid Entire Body Assessment (REBA) based on the participants' body posture and joint angles. REBA is an evaluation tool employed to assess the risk of WMSDs linked to specific job activities. REBA score is used to assess ergonomic risk through the observation of body postures, using the measured joint angle. Each body region is scored separately, and these scores are combined in a two-step table, leading to a single REBA score (Martinez et al., 2022). The accuracy of the REBA score calculated by IMUs was previously validated for manual handling tasks (Humadi et al., 2020; Martinez et al., 2022).

FIGURE 2
Experimental procedures in-field **(A,C)**, in-lab **(B,D)** using Jake tool **(C,D)**, and Lever tool **(A,B)**.

The REBA scores measured using IMU data, and the RMS values of normalized EMG amplitudes for each task were compared between in-field and in-lab experiments. These comparisons were performed with both Lever and Jake tools with and without the exoskeleton. The data did not exhibit a normal distribution, as determined by the Shapiro-Wilk test. Therefore, we chose to employ the Wilcoxon rank-sum test with a significance level of 5% to investigate whether there were any significant differences in the dependent variables among the paired comparisons (Wilcoxon, 1992).

3 Results

The analysis of normalized muscle activity during in-field experiments revealed significant differences ($p < 0.05$) when compared to the in-lab data for most of the muscle groups. Specifically, when participants used the Jake and Lever tools with and without the exoskeleton, the muscle activity levels were notably different in the field compared to the laboratory settings (Figures 3, 4). This suggests that the muscle engagement required for the same task can vary considerably depending on the environment in which the task is performed and participants' level of experience. Interestingly, despite these differences in muscle activity levels, the REBA scores, which are used to assess posture-related ergonomic risk, showed no statistically significant difference between in-field workers and their in-lab counterparts. This was consistent across scenarios, whether the workers were using the Jake and Lever tools with or without the exoskeleton (Figure 5). This aspect of the results indicates that while the ergonomic posture risk remained consistent across both environments, the actual muscle exertion and patterns of activity differed.

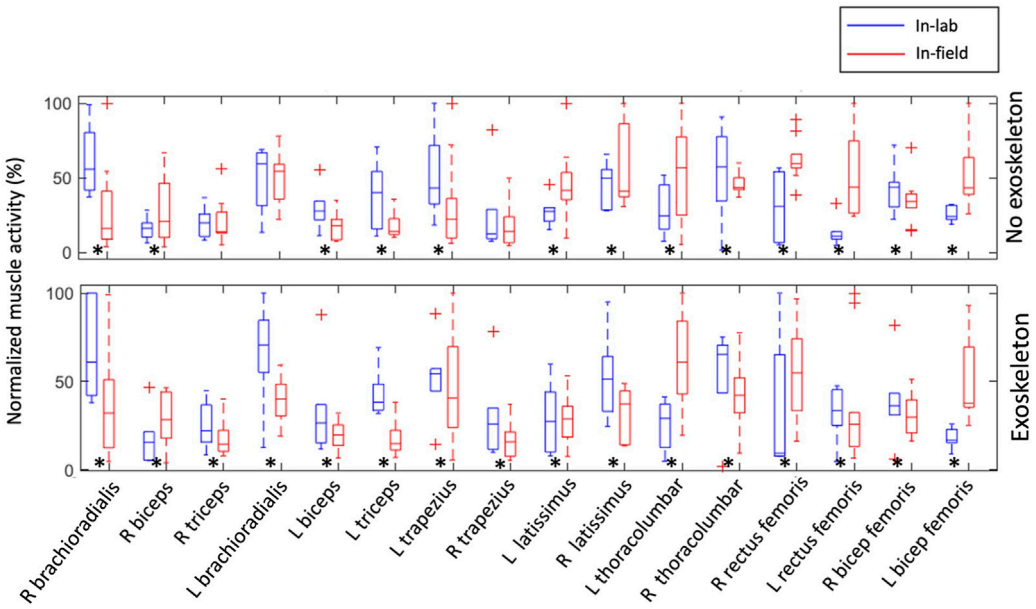

FIGURE 3
Comparison between normalized muscle activation amplitudes during in-field and in-lab experiments with and without the exoskeleton while using the Jake tool. The results for all participants are presented as boxplots. Crosses indicate an outlier. Black asterisks indicate a significant difference with zero with p-values < 0.05.

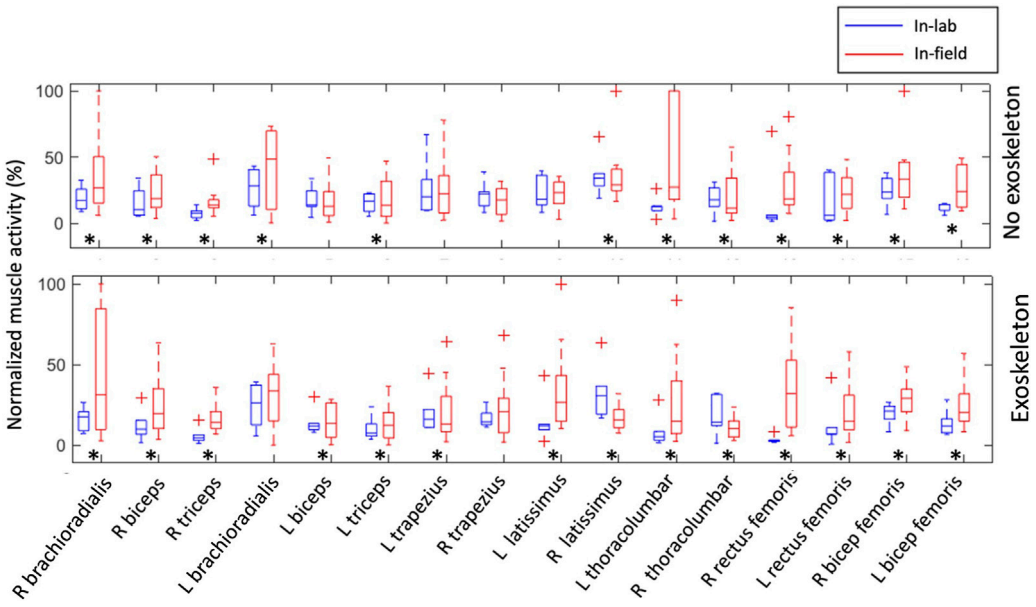

FIGURE 4
Comparison between normalized muscle activation amplitudes during in-field and in-lab experiments with and without the exoskeleton while using the Lever tool. The results for all participants are presented as boxplots. Crosses indicate an outlier. Black asterisks indicate a significant difference with zero with p-values < 0.05.

4 Discussions

This study aimed to investigate if in-lab experiments with non-workers as participants for ergonomic risk assessment in various tasks and using various tools and exoskeletons can be a reliable surrogate for in-field experiments with actual workers. The findings highlighted that the body postures (assessed by REBA Score) were comparable between the in-lab experiments with non-workers as

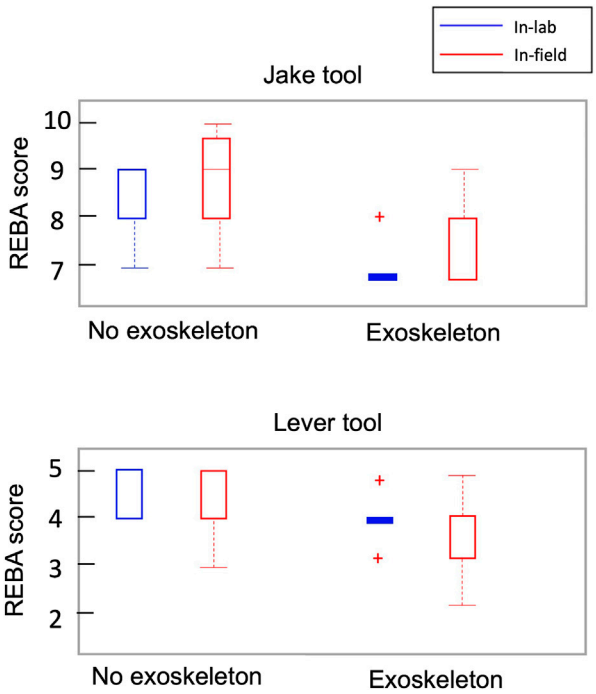

FIGURE 5
Comparison between REBA scores during in-field and in-lab manhole cover removal experiments using different tools and with and without Exoskeleton. The results for all participants are presented as boxplots. Red crosses indicate an outlier, and there are no significant differences with zero.

participants and the in-field experiments with actual experienced workers regardless of the use of exoskeletons or tools. Yet, the muscle activity levels significantly differed between these two conditions showcasing a variance in muscle engagement patterns when tasks were performed with and without the aid of tools and exoskeletons. These differences suggest that the controlled laboratory environment with the use of weights instead of the actual manhole and non-workers as participants instead of actual workers does not fully capture the complexity of real-world tasks, leading to potential discrepancies in ergonomic assessment. This raises intriguing questions about the interpretation of muscle activity data in isolation and highlights the importance of a holistic approach to ergonomic assessment, considering both muscle activity and body posture to gain a comprehensive understanding of the impacts on worker health and safety.

Notably, the observed muscle activities were not higher or lower across all muscle groups in lab experiments compared to the real-world experiments. When using tools and exoskeleton in both modes, the activity level of some muscles increased in lab compared to the real world and decreased for other muscles. This may indicate that actual workers in field employed different muscle recruitment strategy and synergy compared to non-workers in the lab while both participant groups had comparable body postures and performed similar tasks. This might partially be due to demographic differences (such as body height, body mass, age, and sex) between the two participant groups and their different physical fitness and experience level for manual handling task execution. This experience might have led to more efficient movement patterns and muscle use in the field, which were not replicated in the lab setting. Future research should thus aim at deeper understanding of these patterns and their implications for ergonomic interventions. Given that occupational exoskeletons are ultimately intended for use in field environments, it becomes evident that a detailed field analysis with actual workers is essential and likely to yield more insightful results compared to the controlled in-lab studies. In addition, due to the observed different outcomes or exoskeletons among users of different demographics, it is recommended to consider a diverse population in the design and validation of occupational exoskeletons, to ensure that the findings are broadly applicable and inclusive. This diversity should encompass not just gender and age but also physical conditioning and professional experience, as these factors contribute to the efficiency of movement patterns and muscle use.

Besides the difference between the study participants, the differences between experimental conditions can contribute to the observed difference in muscle activities. In a real-world context, numerous uncontrollable variables come into play, such as the varied layers of clothing worn by participants, which can affect movement and muscle engagement. Beyond these, environmental conditions like weather, temperature, and even the time of day may impact the results, which are often unaccounted for in laboratory settings. Moreover, the psychological state of participants, influenced by real-world stressors or the artificial environment of a lab, can also alter performance and outcomes. These discrepancies highlight the need for future studies to perform comprehensive evaluations to understand how each of these factors might influence results differently across various measurement conditions.

In our study, we utilized circular weights with central holes to simulate the lifting of manhole covers, different from manhole covers that often have holes at the edge. In addition, the circular weight were not flush with the ground similar to the real-world manhole cover. This design choice may affect the torque dynamics experienced during actual lifting operations, potentially influencing the ergonomic assessment outcomes. This limitation of our experimental design highlights the importance of designing future studies with closer alignment to real-world conditions to fully understand the ergonomic implications of lifting tasks in utility work.

In this study, we focused on a single material handling task: the removal of utility manhole covers. This task was selected due to its relevance and demand in manual material handling. However, we recognize this as a limitation, as our findings may not fully extend to other types of material handling tasks. Future research could benefit from including a diverse range of scenarios, allowing for a broader understanding of biomechanical and ergonomic impacts across different tasks and enhancing the applicability and generalizability of our findings. In addition, in our study, each participant was tested only twice in each scenario. While this was sufficient to gain preliminary insights, it may impact the overall data reliability and generalizability of the findings. Future studies should consider increasing the number of repetitions to enhance data robustness.

This study focused on comparing the muscle activities and body posture while a back-support exoskeleton was used in a laboratory

and in the field. Comparing other factors such as energy consumption (Madinei et al., 2020) between these two experimental conditions should be targeted in the future.

In summary, our study design introduced multiple variables, such as differing environments, experimental setup and participant demographics, which may influence the research outcomes. While this approach provides valuable insights into the real-world application of exoskeletons and tools, it complicates the isolation of single variables to understand their specific impacts. For future research, we recommend controlled studies that isolate and examine an individual factor that may affect the efficacy of exoskeletons and tools in real-world settings. Such studies would complement our findings by providing a deeper understanding of how each variable contributes to the overall effectiveness of tool and exoskeleton interventions in improving worker safety and productivity.

5 Conclusion

This study emphasizes the need to evaluate occupational exoskeletons and assistive tools in real-world settings, as muscle activity differs significantly between controlled lab environments and actual field conditions. These insights contribute to a more comprehensive understanding of the practical implications of various tools and exoskeletons employed for physically demanding tasks, such as manhole cover removal and emphasize the importance of considering environmental factors in such ergonomic assessments.

Data availability statement

The raw data supporting the conclusion of this article will be made available by the authors, without undue reservation.

Ethics statement

The study was approved by the research ethics board of the University of Alberta, ID: Pro00109264. The studies were conducted in accordance with the local legislation and institutional requirements. The participants provided their written informed consent to participate in this study. Written informed consent was obtained from the individual(s) for the publication of any potentially identifiable images or data included in this article.

Author contributions

MS: Writing–original draft, Writing–review and editing, Conceptualization, Data curation, Investigation, Methodology, Visualization. XW: Writing–review and editing, Data curation, Investigation, Methodology. KB: Writing–review and editing, Data curation, Formal Analysis, Investigation, Methodology. AG: Writing–review and editing, Conceptualization, Funding acquisition, Project administration, Resources. SK: Writing–review and editing, Investigation, Resources. MT: Writing–review and editing, Conceptualization, Funding acquisition, Project administration, Resources, Supervision. HR: Writing–review and editing, Conceptualization, Funding acquisition, Investigation, Project administration, Resources, Supervision.

Funding

The author(s) declare that financial support was received for the research, authorship, and/or publication of this article. This project was funded by the Natural Sciences and Engineering Research Council of Canada in partnership with Alberta Innovates (Grant # ALLRP 567348–21).

Conflict of interest

Author AG was employed by EWI Works Inc. Author SK was employed by EPCOR Utilities Inc.

The remaining authors declare that the research was conducted in the absence of any commercial or financial relationships that could be construed as a potential conflict of interest.

The author(s) declared that they were an editorial board member of Frontiers, at the time of submission. This had no impact on the peer review process and the final decision.

Publisher's note

References

Andrade, C., and Nathan-Roberts, D. (2022) *Occupational exoskeleton adoption and acceptance in construction and industrial work: a scoping review*. Los Angeles, CA: SAGE Publications Sage CA, 1325–1329.

Baltrusch, S., Van Dieën, J., Bruijn, S., Koopman, A., Van Bennekom, C., and Houdijk, H. (2019). The effect of a passive trunk exoskeleton on metabolic costs during lifting and walking. *Ergonomics* 62, 903–916. doi:10.1080/00140139.2019.1602288

Bennett, S. T., Han, W., Mahmud, D., Adamczyk, P. G., Dai, F., Wehner, M., et al. (2023). Usability and biomechanical testing of passive exoskeletons for construction workers: a field-based pilot study. *Buildings* 13 (3), 822. doi:10.3390/buildings13030822

Coenen, P., Gouttebarge, V., van der Burght, A. S., van Dieën, J. H., Frings-Dresen, M. H., van der Beek, A. J., et al. (2014). The effect of lifting during work on low back pain: a health impact assessment based on a meta-analysis. *Occup. Environ. Med.* 71 (12), 871–877. doi:10.1136/oemed-2014-102346

Crea, S., Beckerle, P., De Looze, M., De Pauw, K., Grazi, L., Kermavnar, T., et al. (2021). Occupational exoskeletons: a roadmap toward large-scale adoption. Methodology and challenges of bringing exoskeletons to workplaces. *Wearable Technol.* 2, e11. doi:10.1017/wtc.2021.11

De Bock, S., Ghillebert, J., Govaerts, R., Elprama, S. A., Marusic, U., Serrien, B., et al. (2020). Passive shoulder exoskeletons: more effective in the lab than in the field? *IEEE Trans. Neural Syst. Rehabilitation Eng.* 29, 173–183. doi:10.1109/tnsre.2020.3041906

De Bock, S., Rossini, M., Lefeber, D., Rodriguez-Guerrero, C., Geeroms, J., Meeusen, R., et al. (2022). An occupational shoulder exoskeleton reduces muscle activity and fatigue during overhead work. *IEEE Trans. Biomed. Eng.* 69 (10), 3008–3020. doi:10.1109/tbme.2022.3159094

Grood, E. S., and Suntay, W. J. (1983) *A joint coordinate system for the clinical description of three-dimensional motions: application to the knee*.

Gull, M. A., Bai, S., and Bak, T. (2020). A review on design of upper limb exoskeletons. *Robotics* 9 (1), 16. doi:10.3390/robotics9010016

Hoogendoorn, W. E., Bongers, P. M., De Vet, H. C., Douwes, M., Koes, B. W., Miedema, M. C., et al. (2000). Flexion and rotation of the trunk and lifting at work are risk factors for low back pain: results of a prospective cohort study. *Spine* 25 (23), 3087–3092. doi:10.1097/00007632-200012010-00018

Humadi, A., Nazarahari, M., Ahmad, R., and Rouhani, H. (2020). Instrumented ergonomic risk assessment using wearable inertial measurement units: impact of joint angle convention. *IEEE Access* 9, 7293–7305. doi:10.1109/access.2020.3048645

Khandan, A., Fathian, R., Carey, J. P., and Rouhani, H. (2022). Assessment of three-dimensional kinematics of high-and low-calibre hockey skaters on synthetic ice using wearable sensors. *Sensors* 23 (1), 334. doi:10.3390/s23010334

Kim, S., Moore, A., Srinivasan, D., Akanmu, A., Barr, A., Harris-Adamson, C., et al. (2019). Potential of exoskeleton technologies to enhance safety, health, and performance in construction: industry perspectives and future research directions. *IISE Trans. Occup. Ergonomics Hum. Factors* 7 (3–4), 185–191. doi:10.1080/24725838.2018.1561557

Konrad, P. (2005) *The ABC of EMG, A practical introduction to kinesiological electromyography*. USA: Noraxon INC.

Madinei, S., Alemi, M. M., Kim, S., Srinivasan, D., and Nussbaum, M. A. (2020). Biomechanical assessment of two back-support exoskeletons in symmetric and asymmetric repetitive lifting with moderate postural demands. *Appl. Ergon.* 88, 103156. doi:10.1016/j.apergo.2020.103156

Madinei, S., Kim, S., Park, J. H., Srinivasan, D., and Nussbaum, M. A. (2022). A novel approach to quantify the assistive torque profiles generated by passive back-support exoskeletons. *J. Biomechanics* 145, 111363. doi:10.1016/j.jbiomech.2022.111363

Martinez, K. B., Nazarahari, M., and Rouhani, H. (2022). K-score: a novel scoring system to quantify fatigue-related ergonomic risk based on joint angle measurements via wearable inertial measurement units. *Appl. Ergon.* 102, 103757. doi:10.1016/j.apergo.2022.103757

Nazarahari, M., Noamani, A., Ahmadian, N., and Rouhani, H. (2019). Sensor-to-body calibration procedure for clinical motion analysis of lower limb using magnetic and inertial measurement units. *J. Biomechanics* 85, 224–229. doi:10.1016/j.jbiomech.2019.01.027

Nazarahari, M., and Rouhani, H. (2020). Adaptive gain regulation of sensor fusion algorithms for orientation estimation with magnetic and inertial measurement units. *IEEE Trans. Instrum. Meas.* 70, 1–13. doi:10.1109/tim.2020.3033077

Nazarahari, M., and Rouhani, H. (2021). A full-state robust extended Kalman filter for orientation tracking during long-duration dynamic tasks using magnetic and inertial measurement units. *IEEE Trans. Neural Syst. Rehabilitation Eng.* 29, 1280–1289. doi:10.1109/tnsre.2021.3093006

Theurel, J., and Desbrosses, K. (2019). Occupational exoskeletons: overview of their benefits and limitations in preventing work-related musculoskeletal disorders. *IISE Trans. Occup. Ergonomics Hum. Factors* 7 (3–4), 264–280. doi:10.1080/24725838.2019.1638331

Wami, S. D., Abere, G., Dessie, A., and Getachew, D. (2019). Work-related risk factors and the prevalence of low back pain among low wage workers: results from a cross-sectional study. *BMC Public Health* 19 (1), 1072–1079. doi:10.1186/s12889-019-7430-9

Wang, X., Beltran Martinez, K., Golabchi, A., Tavakoli, M., and Rouhani, H. (2023). A dynamic procedure to detect maximum voluntary contractions in low back. *Sensors* 23 (11), 4999. doi:10.3390/s23114999

Wilcoxon, F. (1992). "Individual comparisons by ranking methods," in *Breakthroughs in statistics: methodology and distribution* (Germany: Springer), 196–202.

frontiers | Frontiers in Bioengineering and Biotechnology

TYPE Review
PUBLISHED 28 May 2024
DOI 10.3389/fbioe.2024.1388609

OPEN ACCESS

EDITED BY
Wujing Cao,
Chinese Academy of Sciences (CAS), China

REVIEWED BY
Bingshan Hu,
University of Shanghai for Science and Technology, China
Chunjie Chen,
Chinese Academy of Sciences (CAS), China

*CORRESPONDENCE
Jiejunyi Liang,
jiejunyiliang@gmail.com
Yunyun Han,
yhan@hust.edu.cn

RECEIVED 20 February 2024
ACCEPTED 13 May 2024
PUBLISHED 28 May 2024

CITATION
Zheng X, Han Y and Liang J (2024), Anthropomorphic motion planning for multi-degree-of-freedom arms.
Front. Bioeng. Biotechnol. 12:1388609.
doi: 10.3389/fbioe.2024.1388609

Anthropomorphic motion planning for multi-degree-of-freedom arms

Xiongfei Zheng[1], Yunyun Han[2]* and Jiejunyi Liang[1]*

[1]State Key Laboratory of Intelligent Manufacturing Equipment and Technology, Huazhong University of Science and Technology, Wuhan, China, [2]Department of Neurobiology, School of Basic Medicine, Tongji Medical College, Huazhong University of Science and Technology, Wuhan, China

With the development of technology, the humanoid robot is no longer a concept, but a practical partner with the potential to assist people in industry, healthcare and other daily scenarios. The basis for the success of humanoid robots is not only their appearance, but more importantly their anthropomorphic behaviors, which is crucial for the human-robot interaction. Conventionally, robots are designed to follow meticulously calculated and planned trajectories, which typically rely on predefined algorithms and models, resulting in the inadaptability to unknown environments. Especially when faced with the increasing demand for personalized and customized services, predefined motion planning cannot be adapted in time to adapt to personal behavior. To solve this problem, anthropomorphic motion planning has become the focus of recent research with advances in biomechanics, neurophysiology, and exercise physiology which deepened the understanding of the body for generating and controlling movement. However, there is still no consensus on the criteria by which anthropomorphic motion is accurately generated and how to generate anthropomorphic motion. Although there are articles that provide an overview of anthropomorphic motion planning such as sampling-based, optimization-based, mimicry-based, and other methods, these methods differ only in the nature of the planning algorithms and have not yet been systematically discussed in terms of the basis for extracting upper limb motion characteristics. To better address the problem of anthropomorphic motion planning, the key milestones and most recent literature have been collated and summarized, and three crucial topics are proposed to achieve anthropomorphic motion, which are motion redundancy, motion variation, and motion coordination. The three characteristics are interrelated and interdependent, posing the challenge for anthropomorphic motion planning system. To provide some insights for the research on anthropomorphic motion planning, and improve the anthropomorphic motion ability, this article proposes a new taxonomy based on physiology, and a more complete system of anthropomorphic motion planning by providing a detailed overview of the existing methods and their contributions.

KEYWORDS

anthropomorphic, motion planning, arms, motion redundancy, motion variation, motion coordination

1 Introduction

Robots, following meticulously calculated and planned trajectories, have been providing safer and more efficient working environments for humans with superior quality in many scenarios. Especially in industrial manufacturing, robotic arms can even independently perform various tasks such as handling, machining, and assembling in specified conditions, which dramatically improves the productivity.

However, conventional motion planning techniques typically rely on predefined algorithms and models that may not be adaptable to new environments. Especially when faced with the increasing demand for personalized and customized services, predefined motion planning cannot be adjusted in time to adapt to personal behavior, which will seriously affect the efficiency of task completion. In this case, robots need to establish a stronger connection with humans by increasing interaction and expanding the human-robot sharing space in order to develop algorithms and models that could adapt to the individual preferences, habits, and needs.

Recent researches demonstrated that humans are more inclined to accept actions similar to themselves during human-robot interactions (Arkin and Moshkina, 2014; Dragan and Srinivasa, 2014). To meet this requirement, researches across the world have been initiated to improve human-robot interaction by enhancing the anthropomorphism of robot motion (Kiesler et al., 2008; Kühnlenz et al., 2013). There are three main scenarios, service robots, new industrial robots, and wearable robots (exoskeletons), where anthropomorphism of robot arm motion is highly demanding and the robots need to interact and collaborate with humans in a shared human-robot interaction space. For anthropomorphic service robots, adopting anthropomorphic motion can significantly enhance the robot's similarity to humans, foster a greater sense of familiarity, and thus increase the robot's acceptance among users. For new industrial robots, anthropomorphic motion can enhance not only the synchronicity between the workers and the robots during collaborative process, but also the efficiency and overall safety of the human-robot interaction. During the interaction, the workers can accurately and promptly comprehend the robots' behavior, which enables them to make rational assumptions about the robots' motion patterns. When there is a risk of collision between a robot and a worker or the environment, the worker can take prompt action to avoid collisions and increase the safety. In addition, anthropomorphic motion provides a better way to interact, which greatly reduces the training time of the worker. For wearable robots, anthropomorphic motion has a more direct impact on the therapeutic performance of rehabilitation training. For exoskeletons used to enhance human function, if the motion does not match the way that the patients move, the rehabilitation training will not only fail to enable the patient to regain movement ability, but may cause secondary damage to the patient.

How to achieve anthropomorphic motion in robots? An analysis of human movement shows that the process of human movement at the physiological level can be represented by the process chain: neural commands-muscle activation-joint motion-hand movement-task goal (Flash et al., 2013). Inspired by this chain, current researches on anthropomorphic motion mainly focus on three directions: anthropomorphic structural design, anthropomorphic trajectory generation, and anthropomorphic motion control (Kulic et al., 2016).

In anthropomorphic structural design, researchers have developed humanoid robots that closely resemble humans in appearance, joint structure, and motion by modeling the human musculoskeletal system. This kind of design is inspired by biology and based on research in human anatomy, kinesiology, and biomechanics (Ogawa et al., 2011; Paik et al., 2012; Lenzi et al., 2016), which has contributed to an increased acceptance and trust among users. However, these robots are still challenged in mimicking the flexibility, elasticity and stability of the human limbs.

In anthropomorphic trajectory generation, researchers tried to explore the human upper limb movement laws from the motion posture and trajectory, combine it with human kinematics and physiology, and determine the optimal motion trajectories and movement sequences through simulation and experimental validation, so as to make the robot's motion more natural, smooth, and match the physiological characteristics of the human. Specifically, by studying the correlations and variations between the rotation angles of certain joints (e.g., elbow elevation angle (Kim et al., 2006)) and hand postures, researchers have generated anthropomorphic motion for robotic arms (Zanchettin et al., 2013; Su et al., 2018). In addition, the researchers found some motion characteristics, such as bell-shaped velocity curve (Ferrer et al., 2023), sinusoidal acceleration curve (Morasso, 1981), bell-shaped positional variance (Taniai et al., 2022), Fitts's Law (Fitts, 1954), and temporal distribution (Young et al., 2009), for analyzing physical quantities, such as joint velocities, accelerations, and trajectories during the natural movement of the upper limbs, and used them as criteria for generating anthropomorphic trajectories for robotic arms. However, these studies only focus on the kinematic nature of upper limb movement, and have not tapped into the cornerstones of upper limb movement laws that underlie anthropomorphic motion generation in robotic arms. Guigon et al. (2007) assumed that the motor control is governed by four principles (separation principle, optimal feedback control principle, maximum efficiency principle, constant effort principle) by building a computational model, and attempted to provide a unified explanation of biological motor behavior. von Zitzewitz et al. (2013) argued that robot perception plays a crucial role in human-robot interaction, and anthropomorphism as a factor of interaction efficiency should not be considered as a single parameter, but as a variable influenced by other parameters. They proposed to divide the network of parameter fields describing anthropomorphism into two categories: appearance and behavior (Minato et al., 2012) to describe the static and dynamic states of the robot, respectively. However, these motion parameters only describe possible similar aspects of robots and humans from multiple perspectives, but do not provide quantitative anthropomorphic metrics that can be directly used as criteria for generating anthropomorphic motion.

In anthropomorphic motion control, researchers are trying to explore how to achieve precise control and adaptive regulation of robot motion by mimicking human movement styles and behavioral characteristics, so that robot motion will have similar motor capabilities to those of humans, which includes accurate collection and processing of sensor data, as well as real-time

adjustment and optimization of control algorithms. Most approaches rely on high-gain control and fast control loops that enable robots to perform specific tasks in structured environments, but are unable to deal with unexpected disturbances or system variations, and do not simulate the flexibility, versatility, and robustness of human movement control.

Among the three research directions, anthropomorphic trajectory generation can provide input for anthropomorphic motion planning based on human motion characteristics, which is crucial for robots to realize anthropomorphic motion. It enables robots with natural and smooth motion, enhances their adaptability and safety, and improves the performance of human-robot interaction so that robots have more anthropomorphic motion and behavior characteristics. Overall, current studies have made some progress in improving the anthropomorphism of robot motion, but there is still no consensus on the criteria by which anthropomorphic motion is accurately generated. The main reason is the criteria derived from existing research may not be able to fully cover the most important aspects concerning the similarity between robots and humans.

In recent years, researchers have gradually deepened the study of anthropomorphic motion planning and applied it to humanoid robots, which has made considerable progress. Service robots have gradually been a part of people's daily lives, cooperating with them in a friendly way (Potkonjak et al., 2001). New industrial robots can not only work closely with human workers to perform complex manufacturing and assembly tasks, but can also operate independently in harsh environments such as high temperatures and pressures, increasing the efficiency of industrial production and ensuring worker safety (Zacharias et al., 2011). Wearable robots enhance or reconstruct the natural movement of disabled limbs (Soltani Zarrin et al., 2021). These products dramatically improve efficiency and deliver better care and services that not only improve quality of life, but also drive technological advancement and innovation. At the same time, biomechanics, neurophysiology, and exercise physiology have advanced our understanding of the body's mechanisms for generating and controlling movement, and upper limb motion patterns were progressively resolved, which provides a physiological basis for motion characteristic extraction. With the help of tools in statistics and computer graphics, researchers can discover the laws embedded in the upper limb movement data (or movement sequences), extract the motion characteristics, describe them intuitively and quantitatively, realistically show the upper limb movement status and motion characteristics, build models to describe human movement behaviors, so as to replicate human movement on a humanoid robot as closely as possible through motion planning. In addition, the increasing computational capability of motion models has facilitated the continuous improvement of motion control schemes, which in turn has promoted in-depth exploration of the nature of motion. At the same time, concepts such as the "spatiotemporal characteristics" inherent in the movement process have been proposed as new anthropomorphic evaluation criteria. With the development of virtual reality, machine learning, intent recognition, semantic grasping, and other related technologies, motion accuracy has been significantly improved, which has driven the emerge of new anthropomorphic motion planning methods to some extent.

However, the current anthropomorphic motion planning algorithms still have some problems in practical applications, that need to be further improved and solved. First, the modeling of the biomechanical characteristics of the human movement is not investigated enough. Anthropomorphic motion planning algorithms are often based on simplified models of human biomechanics, ignoring many details and complexities, which can result in the differences between the movements of robots and human, and the lack of biomechanical naturalness. As a result, biomechanical characteristics such as human bones, muscles, and joints must be more accurately and meticulously modeled to improve the realism and fidelity of robotic motion. Second, there is a lack of understanding of human movement variation. Human upper limb movement has some individual variation and can vary considerably from person to person. Moreover, unlike the lower limbs, the upper limbs do not have a single, periodic functional activity, which makes it difficult to establish a standardized experimental paradigm for the upper limbs. However, current anthropomorphic motion planning algorithms are typically modeled based on average motion data or data from a small number of subjects, ignoring the individual variation, which leads to a lack of personalization and diversity in robot motion. Third, there is a lack of in-depth research on neurophysiology and exercise physiology. Human upper limb movement involves the coordination of multiple neuromuscular systems and complex neural signaling control processes. However, current anthropomorphic motion planning algorithms have an insufficient understanding of these neurophysiological and exercise physiological mechanisms and lack detailed modeling and simulation of neuromuscular models and motor control signals. Therefore, further in-depth studies of neurophysiology and exercise physiology are needed to incorporate these physiological characteristics into anthropomorphic motion planning algorithms to improve the biomimicry and realism of motion. Fourth, the problem of motion planning and obstacle avoidance in complex environments has not been fully solved. In practical applications, robots often need to plan their motion and avoid obstacles in complex, dynamic environments. The potential failures coming from the unpredictability of robot-human interactions still troubles the users, which seriously hinders the large-scale application of humanoid robots. Further research is needed on how to generate adaptive and flexible anthropomorphic motion that take into account environmental constraints. This may involve the integration of perception, planning, and control, as well as accurate modeling and real-time updating of environmental information. Fifth, current humanoid robots still have limited autonomy and adaptability. Most anthropomorphic motion planning algorithms (including inverse kinematics methods (Li G. et al., 2019; Li et al., 2022), visual teaching (Kuniyoshi et al., 1994), reference path generation for upper limb rehabilitation exoskeletons (Soltani-Zarrin et al., 2017), optimal control methods (Taïx et al., 2013; Geoffroy et al., 2014), etc.) rely on offline planning and must be pre-programmed or rely on external commands to perform the task, and are simply not capable of continuously performing complex tasks outside of a specific work environment. Sixth, the complexity of the human body's own movement laws leads to the fact that a single (or several) anthropomorphic criterion is still unable to describe most of the

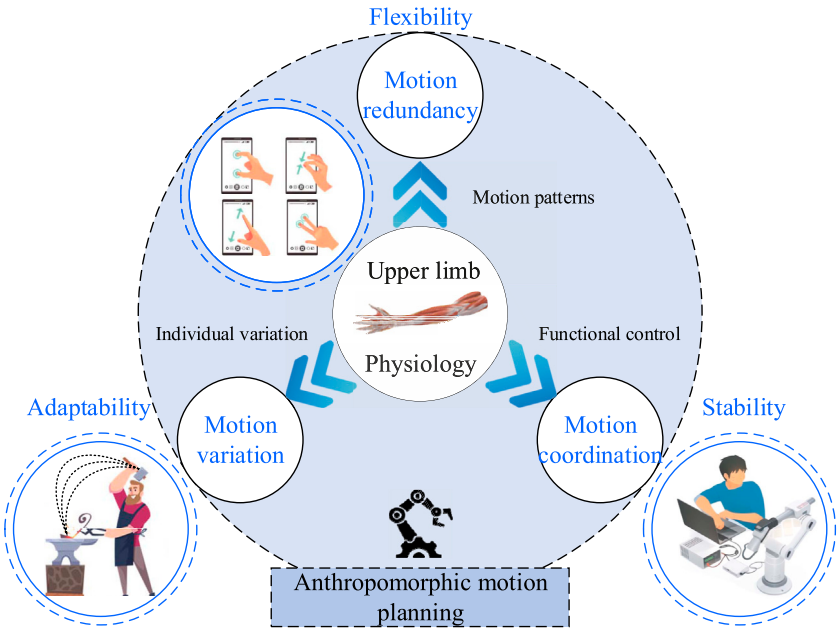

FIGURE 1
A frame of anthropomorphic motion planning system composed of three components.

human movements, resulting in a lack of anthropomorphism in robot motion, which is far from natural human movement behavior. Therefore, the existing anthropomorphic motion planning methods are still not sufficient for practical applications.

Despite the existence of articles that provide a cursory overview of classification methods for anthropomorphic motion planning of robotic arms, including sampling-based (random search), optimization-based (constrained optimization), and imitation-based (demonstration learning) approaches, these overviews typically rely on simple distinctions based on the nature of the planning algorithms. However, they lack a systematic examination of the rationale behind the extraction of upper limb motion characteristics using these methods. Furthermore, these characteristics do not comprehensively capture the full range of upper limb motion patterns and fail to elaborate on their specific roles in the development of an anthropomorphic motion planning framework. Some research has revealed the existence of invariant motion characteristics in the natural movement of human upper limbs (Soechting and Lacquaniti, 1981; Atkeson and Hollerbach, 1985), which contribute to the uniqueness of human motion behavior and its difficulty to emulate or replicate. Despite the general similarity in morphological structure and motion patterns between current humanoid robotic arms and human upper limbs, the lack of comprehensive guidance from human upper limb movement laws prevents the achievement of highly anthropomorphic motion.

To facilitate the realization of more natural anthropomorphic motion in humanoid robotic arms, the key milestones and most recent literature have been collated and summarized, and three essential conditions have been identified. These are: 1) Motion redundancy. It is crucial for achieving the flexibility and accuracy of human upper limb movement through different motion patterns, serving as the foundation for humans' robust motion capabilities and interactive abilities. 2) Motion variation. It accounts for the diversity and individual variation in human upper limb movement, representing a unique capacity for adaptation, self-learning, and continuous evolution. 3) Motion coordination. It ensures the efficiency and stability of human upper limb movement by functional control, providing a safeguard for generating and controlling motion while maintaining inertia. These three characteristics are interrelated and interdependent, as shown in Figure 1, posing a challenge for the anthropomorphic motion planning framework. Therefore, this article systematically analyzes the anthropomorphic motion planning methods in recent years, with a particular focus on the concepts of motion redundancy, motion variation and motion coordination, and discusses the limitations and challenges.

2 Motion redundancy

Humans can adjust the posture of the upper limbs according to the position of the target to perform the task with appropriate movements, such as surgeons operating on small wounds according to different circumstances, "cutting", "suturing", "knotting" and others to ensure the success of the operation, all of which rely on the flexibility provided by the redundancy of the upper limbs. The redundancy of the upper limbs provides humans with a wealth of motor skills, adaptations, and means of perceptual communication that enhance their ability to interact and adapt with others and the environment.

In practical scenarios, robotic arms not only have to interact with humans, but also have to take into account obstacle avoidance and joint limitations. A common method for generating anthropomorphic motion trajectories is to preplan the collision-free waypoints of the end-effector in Cartesian space using path

planning algorithms such as PRM (Kavraki et al., 1996), RRT (Kuffner and LaValle, 2000), and CHOMP (Zucker et al., 2013), and then establish a mapping relationship between Cartesian space and joint space, and solve for the joint angles of the robotic arm at different moments by inverse kinematics. The trajectories of each joint are generated by interpolation. Commonly used interpolation methods are cubic polynomials, quintic polynomials, and spline curves (Xie et al., 2011; Hu et al., 2023; Li et al., 2019; Wang et al., 2020). The key to this approach is to develop an appropriate kinematic/dynamical model for the upper limbs to solve the inverse kinematics.

In studies, human upper limbs are often regarded as an articulated structure composed of connecting rods (bones) and joints with a high degree of redundancy, where different joints cooperate in a variety of combinations to perform complex tasks according to different needs (Kulic et al., 2016; Wei and Zhao, 2019). It is generally accepted that the human upper limbs have 10 DoFs, while the 10-DoFs robotic arm is too flexible to control (Liu and Xiong, 2013). For simplicity, a simplified 7-DoFs robotic arm with only three joints: shoulder, elbow, and wrist, was as a sphere-revolute-sphere structure (Xia et al., 2021), which was roughly the same as the human upper limb in shape and motion style, and has become the mainstream approach. This kind of anthropomorphic design is the basis for realizing human-like behaviors (Fang et al., 2019). Meanwhile, a study proposed the use of Rapid Upper Limb Assessment (RULA) to evaluate the naturalness of the humanoid robotic arm configuration (Zacharias et al., 2011). However, the human-like appearance and configuration of a robotic arm alone is not enough to generate anthropomorphic motion. The reason is the generation mechanism of natural human movement is still not fully revealed, that is, how humans deal with redundancy in the upper limbs during complex motion. From a physiological perspective, the redundancy of the human upper limbs is primarily attributable to the central nervous system's ability to control the contraction and relaxation of muscle groups through intricate neural networks and signaling pathways. This control mechanism enables the precise control of multiple muscles corresponding to multiple joints, thereby facilitating the precise control of multiple joints in the upper limbs. The problem of redundancy in humanoid robotic arms exists at the level of kinematics and dynamics, which leads to an infinite number of inverse kinematics solutions. How to solve the inverse kinematics problem and find the best solution that fits the configuration of the robotic arm among countless solutions is one of the difficulties in anthropomorphic motion planning.

Overall, there are three typical redundancy problems in the human upper limbs: 1) Trajectory redundancy in Cartesian space. That is, for a given task, the hand has multiple realization paths with non-unique trajectories. 2) Trajectory redundancy in joint space. That is, given a time-varying motion trajectory of the hand, it is still not possible to uniquely determine the kinematic parameters such as direction, angle, and velocity of each joint over time. 3) Redundancy in joint muscle forces and moments. Even after the trajectories of the joints over time are determined, it is still not possible to uniquely determine the forces and moments exerted on the joints by each muscle. A plethora of studies have been conducted to investigate these issues. Based on the laws presented during the natural movement of the human upper limbs for classification, the prevailing methodologies can be broadly categorized into two main categories. The first category involves constraining the optimization of a cost function representing the natural motion characteristics. The second category leverages the unique relationship between the joints of the upper limbs presented in natural motion.

2.1 Constrained optimization

A robotic arm may face multiple constraints, such as environmental constraints, task constraints, and coordination constraints, as it performs various operational tasks in an unstructured scenario. These constraints increase the difficulty of solving inverse kinematics. There is an argument that the redundancy problem can be viewed as a constrained optimization problem (Tommasino and Campolo, 2017). Solving inverse kinematics is essentially solving a nonlinear optimization problem where the optimal solution can be obtained by minimizing the cost function as follows

$$\begin{cases} \min\ f(x) \text{ over } x \\ \text{s.t. } g_i(x) \le 0 \\ h_j(x) = 0 \end{cases} \tag{1}$$

where f is a nonlinear function/cost function, x is the state vector of the robotic arm, that is, the values for all joint space. In motion planning, x is not a single state at a given moment, but all states along the entire planning path, that is, $x = [x_0, \cdots, x_t, \cdots, x_T]$. g is an inequality constraint, including linear and nonlinear constraints, which aims to strictly control the feasibility of the trajectory of the robotic arm and ensure that the robotic arm does not collide with objects. h is the equation constraint, that is, the target assigned to the robotic arm.

The cost function is mainly derived from the laws of natural movement of upper limbs. The study of point-to-point reaching movement of the human upper limbs revealed two of the most important motion characteristics, straight paths and bell-shaped speed profiles (Flash and Hogan, 1985; Todorov, 2004). In (Arimoto and Sekimoto, 2006), these two characteristics were used as criteria to determine the degree of anthropomorphism of the robotic arm's trajectories. However, the criteria may not be sufficient for complex upper limb movement such as manual dexterity tasks like writing with a pen, threading a needle, or carving with a knife (Shin and Kim, 2015). To solve this problem, by thoroughly studying the smoothness of the upper limb trajectories, Todorov and Jordan (1998) found that a significant acceleration can cause a shock or jolt in the movement process, and that the human body maintains a very small acceleration during movement to prevent self-injury of the musculoskeletal system, which led to the proposal of an optimization criterion that used the minimum acceleration as a cost function. Li et al. (2020) used the minimum potential energy as an optimization criterion to achieve precise control of the motion to reduce the magnitude of the potential energy change of the upper limb exoskeleton and ensure the smoothness of the motion trajectory. In addition, many studies also used other laws of motion as cost functions, such as minimum torque (Kang et al., 2003), minimum time (Tangpattanakul and Artrit, 2009), and minimum joint torque change (Wada et al., 2001). These cost

TABLE 1 Approaches of constrained optimization.

Study	Task	Anthropomorphic criterion	Approach	Contribution
Todorov and Jordan (1998)	Complex arm movements	Maximum smoothness	Constrained minimum-jerk model	Stronger relationship between the path and the speed profile
Wada et al. (2001)	Point-to-point movements	Minimum commanded torque change	A prediction algorithm using the Euler-Poisson equation	Obtain the converged solution in a very short time
Kang et al. (2003)	Reaching movements	Minimum joint torque	Minimum-torque model	Determine arm configurations during normal and natural movements
Arimoto and Sekimoto (2006)	Reaching movements	Straight paths, bell-shaped speed profiles	Virtual spring-damper hypothesis	Resolve the ill-posedness of inverse kinematics
Tangpattanakul and Artrit (2009)	Simulation of consecutive via-points	Minimum time	Harmony search algorithm	Obtain the optimal interval time and reduce complication and time consuming
Albrecht et al. (2011)	Reaching-to-a-bar tasks	mechanical energy, joint smoothness	Inverse optimal control	Support the cost combination hypothesis
Shin and Kim (2015)	Reaching, grasping, moving an object	Compare the hand and elbow trajectories through the simulations and experiments	Lagrangian multiplier optimization method	Human-likeness depends on the purpose of given tasks
Li et al. (2020)	Path tracking	Minimal potential energy	Zeroing dynamics method	Track the desired motion path accurately
Wochner et al. (2020)	Point-to-manifold reaching movements	Smoothness, energy, internal force	Bayesian optimization	A mixed cost function replicates the behavior much better than single criterion

functions were used to explain the principles of how humans generate natural movement, that is, the existence of invariant motion characteristics in the upper limbs that are independent of factors such as target, motion magnitude and direction, initial position, and external loads. These criteria chosen for the cost function were derived from the regular analysis of human upper limb trajectories, which represent the common characteristics of most upper limb movement, and were used in most studies to evaluate whether the trajectory is anthropomorphic or not.

However, the application scenarios of the above methods are limited to point-to-point movement (where the shoulder is assumed to be stationary during movement) and are not suitable for activities of daily living (scenarios where the center of the shoulder is moving in real time). Therefore, it has been suggested that a single cost function can only partially explain the anthropomorphism of the upper limb movement, which only works under special movement and cannot be applied to most scenarios. As a result, it does not provide enough flexibility to the robotic arm. The combination of several cost functions may be the solution to this problem (Berret et al., 2011).

By investigating the interaction between nonlinear muscle dynamics and control principles based on previous work, Wochner et al. (2020) argued that the human body follows a combination of independent and recognized criteria for optimality when controlling the upper limbs to generate optimal trajectories. They used the combined cost function of smoothness (to prevent damage to the musculoskeletal system itself), energy (to reduce energy consumption during movement), and internal force (necessary for human movement) as a new optimization criterion to reveal the contribution of human muscle dynamics in point-to-manifold motion, which in turn generates anthropomorphic trajectories. Based on this research, Albrecht et al. (2011) assigned weighting factors to different optimization criteria to combine them into a new cost function, and simplified the multi-objective optimization problem by adjusting the weight factors to balance the relationship between multiple objectives, thus finding the optimal anthropomorphic trajectory that matches the configuration of the robotic arm. For conciseness, a brief summary of constrained optimization methods is shown in Table 1.

These approaches can accurately identify the optimal solution that satisfies the constraints through mathematical optimization techniques. However, they entail a significant computational burden, particularly when searching for the optimal solution in a high-dimensional space, which may result in high computational costs.

2.2 Special relationships between joints

In addition to optimization methods, dimensionality reduction is another idea for dealing with redundancy: explore the special relationships between the shoulder, elbow, and wrist in the natural motion of the upper limbs to reduce redundant DoFs so as to obtain optimal inverse kinematic solutions.

The complete movement process of the upper limbs can be regarded as a process quantity. Each moment in the process corresponds to the posture of the upper limb and can be considered as a state quantity. The solution of the inverse kinematics of redundant arms can be decomposed into a finite number of state quantities. In order to find a suitable state quantity to describe the upper limb posture, the concept of arm triangle was introduced in (Berman et al., 2008). In (Seraji, 1989), a plane consisting of the shoulder, elbow, and wrist joints is used to describe the posture of the upper limbs, and the upper limbs are free to rotate around the shoulder and elbow joints, respectively. Liu

TABLE 2 Approaches of special relationships between joints.

Study	Task	Anthropomorphic criterion	Approach	Contribution
Kim et al. (2006)	Point-to-point hand motion	Elbow elevation angle	Response surface methodology	First propose a mathematical representation for characterizing human arm motion
Zanchettin et al. (2011)	Hand motion along a sphere	Swivel angle	Cluster and weighted least-square approach	Provide a repeatable and identifiable kinematic constraint
Kim et al. (2012)	Natural human arm movement	Swivel angle	Kinematic and dynamic constraint	Reproduces natural human arm movement with less than five degrees of estimation error
Liu et al. (2016)	Self-motion	Self-motion angle	Wrist-elbow-in-line method	Validated in practice and extended for obstacle avoidance
Su et al. (2019)	Swivel motion	Elbow angle	Deep convolutional neural network	Reduce online prediction time, noise robustness

et al. (2016) proposed a wrist-elbow-in-line method based on the similarity of the kinematic structures of the human upper limb and the humanoid robotic arm. The method introduced the elbow and wrist joint positions as key positions and reduced redundancy by using them as end-effector orientation constraints of the robotic arm. The positions of elbow and wrist joints in Cartesian space were used as configuration parameters of the robotic arm, and the anthropomorphic configuration was obtained by inverse kinematic analysis. However, due to the different lengths and joint limitations of the human upper limb and the robotic arm, the robotic arm is unable to create an anthropomorphic configuration at all times, which makes it difficult to perform fully anthropomorphic motion throughout the workspace. Artemiadis et al. (2010) realized that the shoulder and elbow joints are more flexible than the wrist joint by observing human writing movements. They also found that the three joints of the shoulder, elbow, and wrist are highly interconnected to form a specific plane, and this plane is deflected during movement. The angle of rotation formed by the deflection is unique, and is defined as the elbow elevation angle (Kim et al., 2006). Then they used the constraint equation formed by the elbow elevation angle to reduce the redundancy to obtain the kinematic inverse solution, and then obtain the best anthropomorphic motion trajectory that meets the human posture. However, this method ignores the effect of wrist posture on upper limb movement. Zanchettin et al. (2011) improved this method by taking wrist posture into account and using least-squares cluster analysis to derive the relationship with elbow elevation. Kim et al. (2012) proposed an inverse kinematics-based rotation angle estimation algorithm by linearly combining two different rotation angles resulting from kinematic and dynamic constraints. The algorithm successfully reproduced the natural motion of the human upper limbs with an error of less than 5° compared to real human movement and can be applied to wearable exoskeleton robots. Su et al. (2019) used a new deep convolutional neural network to establish the mapping relationship between rotation angle and hand pose, which improves the accuracy and iteration speed of motion reconstruction with strong robustness. A brief summary of using special relationships between joints to solve motion redundancy listed in Table 2.

In comparison to complex mathematical optimization methods, these methods may exhibit higher computational efficiency and be suitable for application scenarios with high real-time requirements. However, due to the complexity of human motion, a single natural motion relation may not be applicable to all types of redundancy problems, thus requiring customized designs for different problems.

The motion redundancy in the upper limbs is of great importance as a primary solution in anthropomorphic motion planning. A variety of inverse kinematics methods proposed by the researchers provide ideas for solving the redundancy problem, which greatly advance the development of anthropomorphic motion planning. However, there are still some problems with current methods: inverse kinematics solution methods in the joint space lack sufficient physiological basis and it is inadequate to ensure the variations in the motion process and vulnerable to interference.

3 Motion variation

Humans can accomplish the same task in different ways, for example, when a blacksmith repeatedly strikes an iron block, the trajectory of the strike is different each time, which suggests that there is no rigidly fixed pattern of repetitive movements. We call this phenomenon motion variation. A large number of studies have confirmed that kinematic variation is considered to be a control strategy for the human motor system and also an intrinsic characteristic of multi-degree-of-freedom limb motion (Latash et al., 2002).

Motion variation represents the diversity of human movement, which is the difference in control, motion patterns, and experience habits of different individuals. These differences include the pattern of muscle activity, the variation of joint angles, and the way of force application, which are indispensable for humanoid robots to realize anthropomorphic motion planning. How do humanoid robots exploit these differences in motion? Imitating and learning human movement may solve this problem.

It is a great idea to accurately reproduce human movement on a robot. A motion capture system can be utilized to gather data on natural human movement and construct a motion database. By comparing the end-effector trajectory with the database, the robot joint configuration and motion trajectories can be predicted (Yamane, 2020). The approach not only avoids the joint redundant, but also controls the grasping force and posture, and predicts the position and time of grasping. However, the large dataset may reduce the prediction efficiency. The human position is collected by the motion capture system in advance and then converted into joint angle information offline, then sent to the robot

controller for execution, so that the robot's movements are modeled after human movements, which is only applicable in weak interaction scenarios (Liu et al., 2012; Zuher and Romero, 2012). However, the limitation of these approaches is that they rely exclusively on pre-collected data that do not cover all possible human-robot interaction situations. Consequently, the robot's responses may not be sufficiently flexible. Furthermore, since the robots' movements are entirely derived from pre-existing human movements, they can only move in a repetitive manner, which greatly limits their use in humanoid robots that require frequent interaction with the outside world.

To address this issue, it is necessary to adopt a more flexible and adaptable approach to the movement of humanoid robots. In addition to replicating human movements, the robot must also learn the motion patterns of the human upper limbs, which enables robots to transfer human motor skills into their own systems in a straightforward manner and employ appropriate methods to replicate anthropomorphic motor trajectories. These trajectories exhibit similar or comparable motor characteristics to humans, making them suitable for practical applications.

The motion patterns of the human upper limbs are unique and rely on a strong learning capacity, which enables humans to adapt to complex and changing environments based on previous experience (Huang and Zhang, 2020). Even without prior knowledge, humans are still able to interact correctly with objects in the surrounding environment. (Nagahama et al., 2021). The variation and adaptability of humans are crucial in achieving effective motion in various situations. It has been a challenging problem to equip robots with learning and motor skills of humans. Researchers attempt to understand the laws governing upper limb movement at the physiological level and map human behavior patterns to robotic motion strategies.

Neurophysiological studies have shown that the natural movement of the human upper limbs can be decomposed into a large number of small movement units that can be combined in an orderly fashion to produce a variety of complex movement, which researchers call movement primitives (Giszter, 2015). In fact, research results from several fields has shown that human upper limb movement exhibits "primitive" properties at the level of brain motor cortex (Averbeck et al., 2002), kinematics (Rohrer et al., 2002), and dynamics (Mussa-Ivaldi and Bizzi, 2000). Therefore, the movement primitives can be regarded as the implicit embodiment of human motion characteristics, which cannot only explain the law governing upper limb movement and enhance the understanding of their own motion, but also serve as a carrier to transfer the movement law from the human upper limb to the humanoid robotic arm, so as to make its motion anthropomorphic.

Based on the human upper limb movement dataset, the researchers proposed a demonstration-learning-reconstruction method to extract the movement primitives. Firstly, they used human natural motion data as demonstration trajectories. Then, they constructed a learning model using statistical methods to encode them. Finally, they applied upper limb motion characteristics to the robotic arm motion to reconstruct similar behaviors. The most common learning models are Gaussian mixture model (GMM), Dynamic movement primitives (DMP), and hidden Markov model (HMM). Specifically, GMM has powerful coding and noise reduction capabilities and is often used to solve high-dimensional problems. Deng et al. (2020) proposed a strategy for learning human motor skills using GMM, which allowed robots to learn how to successfully perform fixed impedance-based tasks and achieve safe human-robot cooperation. DMP has strong adaptability and robustness. Lauretti et al. (2019) proposed a method to obtain joint space and Cartesian space anthropomorphic trajectories using DMP and extracted DMP parameters as motion characteristics to obtain obstacle avoidance trajectories via locally weighted regression, which was finally experimentally validated on a humanoid robotic arm LWR4+ (KUKA, Augsburg, Germany). HMM has strong predictive ability and can easily extract motion characteristics. Takano and Nakamura (2017) proposed a method for extracting motion data information using HMM, which could control the moments of all joints of a humanoid robot to achieve the desired contact force and overall motion. Furthermore, Zhang et al. (2020) proposed a new anthropomorphic motion control framework using GMM and DMP to learn the demonstration trajectories and generate the anthropomorphic motion trajectories, which was tested on a mobile service robot to prove its effectiveness.

The anthropomorphic motion generated by the above work are all simple reaching movement. There are also many studies that have reproduced complex movement. Pignat and Calinon (2017) used a hidden semi-Markov model (HSMM) to enable the robot to successfully assist humans in dressing. Koenig and Matarić (2016) used Bayesian networks to enable the robot to perform basic movement such as grasping and releasing. Mülling et al. (2013) and Calinon et al. (2010) developed table tennis robotic systems for anthropomorphic motion using mixture of motor primitives (MoMP), HMM and Gaussian mixture regression (GMR), respectively. Yi et al. (2022) developed an autonomous robotic grasping system using an imitation learning algorithm consisting of K-means clustering and DMP, which could be finely manipulated using a variety of machine learning methods, and proved its reliability through evaluation. There are also studies on improving individual algorithms or combining multiple algorithms to improve iterative efficiency and reproduction accuracy, such as task-parameterized GMM is used to learn the demonstration trajectory to obtain motion characteristics, which enables the robot to perform the dual-arm sweeping task smoothly (Silvério et al., 2015). However, the reference movement for demonstration learning relies on the richness of experimental data. When adding new sample data to the training model for training, it is common practice to retrain the original model after increasing the number of network layers or changing the structure, which consumes a lot of time. This problem is simplified by the broad learning system based on incremental learning principle (Huang and Zhang, 2020). In the broad learning system, even if new sample data is added, there is no need to retrain the existing structure and parameters even if new sample data is added. We only need to compute the added parameters and assign new computational weights to easily achieve incremental learning of input samples, characteristic nodes, and enhancement nodes.

Even as the dataset continues to grow, new questions also arise. Researchers expect that robots with human motor skills will also have the ability to understand and predict in the same way that humans do. Humans participate in interactions by predicting the behavior of others (Wenderoth et al., 2012), while the robot's motion

commands are issued by a controller, whose output commands are preset by a human input program, and the accuracy of the preset program commands affects the anthropomorphism of the movement trajectories to some extent. The anthropomorphic motion trajectories generated by demonstration learning are too dependent on the reference trajectory, which means that changes in the content of the demonstration may lead to different extracted movement primitives. Therefore, each trajectory iteration accumulates small prediction errors, which leads to the deformation of the robotic arm motion (Sasagawa et al., 2021). To overcome this problem and avoid the chance of the parameters of the upper limb model, Yang et al. (2021) combined the multiple characteristics of the human upper limb movement process, adopted the reward function, and used reinforcement learning to plan the anthropomorphic motion of the humanoid robotic arm, and verified the feasibility and validity of the robotic arm in anthropomorphic motion through experiments.

Furthermore, imitation-based motion planning algorithms commonly utilize motion datasets derived from demonstrative samples to create motion models. However, these models display limited generalization, thereby limiting their usability in unstructured scenarios. As a result, the motion variation of the upper limbs is compromised. Therefore, to enhance robots' capacity to mimic human-environment interaction, it is crucial to enhance the generalization of these models. The main factors affecting the generalization ability are the unknown environment and the targets. Learning reference inputs through DMP algorithm and adaptive optimal admittance control method can effectively improve the robot's ability to interact with unknown environment (Xue et al., 2022). Compared to other algorithms, the traditional DMP algorithm has excellent generalization and anti-interference capabilities (Gong et al., 2020). However, the limitation of this algorithm is that when the demonstration trajectory is learned, the trajectory characteristics represented by the basis functions are fixed. Even if the starting point and scaling factor are changed, the result is only a change in speed and the scaling of the trajectory, which cannot be applied to different complex tasks and environments. Although some studies have improved the DMP by adding constraints, the results are still unsatisfactory (Gams et al., 2014; Huang et al., 2019). Qian et al. (2020) proposed a hierarchical demonstration learning framework that combined symbolic and trajectory learning to improve a robot's ability to adapt to new tasks and environmental changes. Lu et al. (2023) combined DMP with neural networks and admittance control to incrementally update the nonlinear function by adding new basis functions and weights to mimic the new trajectory, and finally experimentally demonstrated that the generalization of the trajectory was improved. Averta et al. (2020) used functional principal component analysis (fPCA) to extract functional principal components/basis functions (describing the motion variance of each joint trajectory at the time level) from human upper limb movement data, and argued that a general upper limb motion trajectory can be described as an ordered combination of a set of functional principal components, and that an anthropomorphic motion trajectory could be generated by optimizing the weights of these functional principal components.

In order to quantify the variation of human movement, Gielniak et al. (2013) adopted variance as a variable in the algorithm when studying anthropomorphic motion planning, and used variance as a measure of the motion variation, and concluded through experiments that highly constrained movement or body parts have less variance (or motion variability), which is basically the same as the intuitive feeling of human movement. Table 3 gives an overview of 12 approaches to solve motion variation.

Most of the current methods to solve the problem of robot motion variation are demonstration learning. Although they can effectively reproduce human upper limb movement under specific environments and tasks, the generalization ability is weak and difficult to apply to complex scenarios. In addition, the data samples must be expanded to improve the accuracy of the motion, but the large number of operations severely affects the efficiency of the robot motion. Therefore, the study of motion variation from a statistical point of view alone remains deficient and needs to be synthesized in terms of the hypostasis of human movement.

4 Motion coordination

The human body is a complex bio-motor system, and each of its movement behaviors requires coordination inside and outside the body, that is, the ability of a system's various joints, components, or systems to work together and cooperate with each other in the execution of complex actions or task, which enables the system to achieve the efficient and precise completion of the task. In particular, the upper limbs play a very important role in human life (the function of the upper limbs accounts for about 60% of the whole body), and almost all daily activities require some coordination between the upper limbs (Guiard, 1987), and the level of coordination directly affects human movement ability (Freitas et al., 2016).

To successfully perform a daily activity, the human body requires a number of sensory organs to process information and control upper limb movement, a process whose mechanism is not fully understood. In neurophysiology, there is evidence that the central nervous system is responsible for the vast majority of human movement. When confronted with different external stimuli, humans are always able to respond appropriately, which relies heavily on human sensorimotor modeling (Wolpert and Ghahramani, 2000). According to the model, there is a relationship between sensory inputs and motor outputs in the human body, in which the particular patterns present are likely to be the criteria for the generation and control of movement by the central nervous system, which provides a physiological basis for anthropomorphic motion planning for robotic arms.

Some studies have designed mechanical musculoskeletal structures that mimic the human upper limbs based on the musculoskeletal kinesiology, and have used control strategies involving internal force kinematics (Tahara et al., 2006) to reproduce muscle activities as closely as possible in a biological motion pattern (Northrup et al., 2001), which provides an achievable platform for anthropomorphic motion planning. On this basis, how to provide the humanoid robotic arm with highly anthropomorphic motion ability becomes a challenge.

When people interact with the outside world, the whole process from contacting information to making a response is about 0.2–0.4 s (Otaki and Shibata, 2019). It remains an unsolved question how

TABLE 3 Approaches to solve motion variation.

Study	Task	Anthropomorphic criterion	Approach	Contribution
Calinon et al. (2010)	Hitting a ball with a table tennis racket	Movement primitives	HMM and GMR	Present and evaluate an approach to allow robots to acquire new skills
Mülling et al. (2013)	Striking movements in table tennis	Movement primitives	MoMP	Presented a framework that allows a robot to play table tennis with a human
Gielniak et al. (2013)	Mimicking performance	Spatiotemporal correspondence	Human-like and variance optimization	Present a quantitative metric for human-like motion
Koenig and Matarić (2016)	A set of basic actions	A series of actions with features	Bayesian networks	Presents a framework for lifelong robot task learning from demonstrations
Pignat and Calinon (2017)	Dressing task	Movement primitives	HSMM	Propose a method for efficient skill acquisition
Takano and Nakamura (2017)	Touching an object with the right hand	Synthesis of joint angle sequences	HMM	Propose a method for motion synthesis and force control
Lauretti et al. (2019)	Reaching and pouring task	Four performance indices	Hybrid Joint/Cartesian DMPs	100% in avoiding obstacles and high Cartesian accuracy
Deng et al. (2020)	Drawing specific lines	Movement primitives	GMM	Present a hierarchical control scheme for human-robot co-manipulation
Zhang et al. (2020)	Feeding meals to patients	Human activity recognition	Combine GMM with DMP	Propose a novel human-like control framework for the mobile medical service robot
Averta et al. (2020)	30 activities of daily living	A variety of movement parameters	fPCA	Embed synergies of human movements for robot motion generation
Yang et al. (2021)	Reaching motion	Feature variables of human arm	Reinforcement learning	Present a humanoid method, and verify humanization, feasibility, and effectiveness
Yi et al. (2022)	Grasping complex-shaped objects	Movement primitives	K-means clustering and DMP	Presents an autonomous grasping approach for complex-shaped objects

humans can easily coordinate multiple redundant DoFs of the body in a short period of time during movement. The causes of motion coordination are multifaceted and can stem from both intrinsic and extrinsic factors. The physiological basis of motion coordination is synergy, which is a key component throughout the entire motion process of the upper limbs and changes accordingly with different motion patterns. Motion coordination is specifically manifested as the precise control of the timing and spatial position of multi-degree-of-freedom movements during the movement process (temporal and spatial coordination), which is mainly dependent on the control of the nervous system. The internal neural control is further complemented by the coordination of the arms (inter-arm coordination) and body language (coordination of different limbs), which enables the coordinated movement of the limbs. Motion coordination of the upper limbs is a key component of the human motor system, which relies on the central nervous system and the cooperation of multiple muscles and joints, and involves fluidity, timing, and precision of movement, which is a challenge that is still not fully solved in the anthropomorphic motion planning system.

Classical neuromechanics suggests that the central nervous system relies on the interlocking of the muscular and skeletal systems to coordinate body movement, which is often called "synergy". Recent research has revealed the existence of synergies at three levels, including kinematics, muscle mechanics, and neural centers (Bruton and O'dwyer, 2018), and has been widely applied to robotic arms to reproduce reaching movement (Liu et al., 2018) and grasping movement (Ficuciello et al., 2014) of the upper limbs. During human movement, the nervous system dynamically adjusts the synergies by regulating the control strategy to control the coordinated movement of the limbs to meet the requirements of the task. Hierarchical theory states that human high-level motion control units focus on generating upper limb configurations during reaching movement, and that low-level motor units synergistically control the joints associated with the movement to ensure coordination of upper limbs (Gosselin-Kessiby et al., 2008; Herbort and Butz, 2010). Correspondingly, by investigating the role of different synergy components in the reaching movement, Tang et al. (2019) found that the high percentage synergy is related to the movement trend, while the low percentage synergy is related to the specific task movements. Different principal components have some effects on the movement trajectory and endpoint accuracy, and the synergies are dynamically adjusted with different tasks. At the same time, the expressions of synergies in different motion patterns vary. Zhao et al. (2022) extracted the synergies under different numbers of trials and different arrival directions in point-to-point reaching movement experiments and found that the synergies increased with the number of trials or the number of arrival directions. When the number of experiments or the number of arrival directions reached a threshold, the synergies did not change significantly. The researchers hypothesized that different training patterns (number of trials, target category) affected muscle activation modules, which in turn affected synergies.

The study of synergistic movement of upper limbs is based on the foundation that humans activate discrete motion modules to

perform biological activities through the cooperation and collaboration of different muscle groups to meet the needs of basic daily activities (Bizzi and Cheung, 2013). It is mainly categorized into three main components: synergistic control of nervous system (d'Avella, 2016), synergistic contraction of muscles (Pham et al., 2014; Tang et al., 2014), and synergistic movement of joints (Garcia-Rosas et al., 2018; Moiseev and Gorodnichev, 2022). The central nervous system receives information from the outside world as input, integrates and processes it to generate motor commands. The commands are transmitted and delivered, whose output is manifested as precise synergistic control of the relevant muscles and joints. The upper limb muscle groups take the received motor commands as input, then trigger the synergistic contraction of the corresponding muscles depending on the complexity of the commands, to produce the appropriate force to control skeletal movement. The synergistic contraction of muscles causes the attachment points on the corresponding bones to move, resulting in the simultaneous movement of multiple bones, which in turn causes synergistic movement of joints. The overall motion of the upper limbs is controlled by the motion of specific bones, whose specific path of motion is determined by the additional motion of specific joints. At the same time, the sensory and feedback mechanisms of the nervous system are able to provide timely information to the brain about the position, force, and movement status of the upper limbs, thus realizing more precise synergistic movement.

The study of synergistic movement of upper limbs is based on the foundation that humans activate discrete motor modules to perform biological activities through the cooperation and collaboration of different muscle groups to meet the needs of basic daily activities (Bizzi and Cheung, 2013). An important part of the synergistic movement of the upper limbs is the synergistic contraction of the muscles, which is accompanied by the synergistic movement of the muscles. Coscia et al. (2014) studied hand trajectories and shoulder and elbow angular displacement trajectories of an upper limb weight support in different horizontal planes, analyzed the synergy patterns of muscles, and found that modular organization activated by synergistic movement of muscle groups underlies upper limb reaching movement generation.

Synergistic movement of upper limbs also involve motion learning and memory processes. The human nervous system uses hundreds of millions of nerve cells to precisely regulate the body's more than 600 muscles, turning flexion, extension, rotation, and grasping into functions that can run in the background without thinking. Through constant practice and repetitive movement, the brain can gradually build up the appropriate neural pathways and patterns to form a memory of muscle coordination.

Theoretical perspectives related to neuroscience and motion control suggest that the central nervous system views the multiple Dofs of the upper limbs as a luxury tool rather than a burden of control. In motion control of the human body, it is not necessary for the nervous system, which is the endpoint, to control all DoFs, which can lead to a lack of stability in the system. In motion coordination, stability and coordination do not coexist. To resolve this contradiction, Scholz and Schöner (1999) skillfully combine stability and coordination by designing experiments using a dynamical systems approach to approximate control structures in joint space. They proposed the uncontrolled manifold (UCM) hypothesis to quantify the joint coordination of human movement. Togo et al. (2016) proposed a UCM reference feedback control method that incrementally generated a target UCM from a given target end-effector trajectory and combined it with the target joint in joint space to minimize the cost function with respect to the input joint torque and torque variation. They also quantitatively compared the results of simulation and measurement experiments for a target tracking task. Statistical results showed that the proposed method quantitatively reproduced the kinematics and dynamics properties of the upper limbs (end-effector posture, end-effector velocity, and joint torque, etc.).

In upper limb rehabilitation, temporal and spatial coordination serve as an important indicator of whether the human body has normal motion ability, which directly reflects the rehabilitation effect of patients with physical disabilities. In complex scenarios such as industrial and service, temporal and spatial coordination can reflect the degree of collaboration of multiple robotic arms and directly affect the efficiency of task completion (Zhao et al., 2021). Gielniak et al. (2013) used motion clarity as a measure of a robot's ability to understand human movement and engage in human-robot interaction, and used spatiotemporal coordination as a factor in synchronizing robotic arm movement with human movement in an anthropomorphic motion generation algorithm.

The aforementioned work is concerned with intra-arm coordination in single-arm movement, in addition to inter-arm coordination between dual-arm movement and coordination between the upper limbs and other parts of the body. Qu et al. (2019) constructed a learning model including PCA, GMM and GMR to extract the intra-arm and inter-arm coordination characteristics of the human upper limbs by analyzing the human bimanual motion data, derived the anthropomorphic coordination motion equations by combining the intra-arm and inter-arm coordination constraints, generated anthropomorphic trajectories of bimanual robots, and experimentally reproduced the anthropomorphic coordination motion, which could improve the human-robot interaction capability of the bimanual robots.

Furthermore, body language (gestures, body postures, facial expressions, etc.) is also an important part of conveying social information in human-computer interaction (Lütkebohle et al., 2010). Through body language, complemented by coordinated body movement to signal or imply goals, express emotions or intentions, and obtain status or feedback, human-computer interaction can be more natural and efficient. However, sometimes the information expected to be expressed by head movement is not perfect and the interacting objects cannot understand the full meaning, and then the auxiliary functions of other limbs become extremely important. Researchers have explored the role of coordination movement of different limbs (e.g., hand-eye coordination (Chao et al., 2018; Olson et al., 2020), head-eye coordination (Omrcen and Ude, 2010; Milighetti et al., 2011), neck-eye coordination (Rajruangrabin and Popa, 2010), etc.) in augmenting head movement at the level of information conveyance, as well as their planning and control schemes. Based on these studies, Zhang et al. (2015) proposed a new online generation method of anthropomorphic motion based on head-arm coordination, which considered not only the two-arm coordination motion, but also the head-arm coordination, and finally verified by computer simulation and physical experiments.

TABLE 4 Approaches to solve motion coordination.

Study	Task	Anthropomorphic criterion	Approach	Contribution
Rajruangrabin and Popa (2010)	Robot head human tracking	Eye-neck coordination	Visual feedback and optimization, reinforcement learning	Propose an optimization approach, combined with real-time visual feedback, to generate human-like motion
Milighetti et al. (2011)	Visual tracking of a moving target with unknown and arbitrary trajectory	Head-eye coordination	Adaptive Kalman Filter, trajectory tracking control	Proposed a gaze control scheme to achieve human-like joint motions
Coscia et al. (2014)	Reaching movements	Muscle synergies	Non-negative matrix factorization	Understand the effect of muscle coordination when performing upper extremity exercises
Zhang et al. (2015)	Tracking external targets and body parts	Head-arm coordination	A quadratic program-based method	Propose a novel head-arm-based human-like behavior generation scheme
Togo et al. (2016)	One-dimensional target-tracking task	Joint coordination	UCM	UCM reference feedback control can reproduce human-like joint coordination
Chao et al. (2018)	Saccade movements, hand spontaneous movements	Hand-eye coordination	Constructive neural networks	Build a reverse transformation from the robot actuators space to the robot visual space
Tang et al. (2019)	Reaching task	Kinematic synergies	PCA	Confirm that kinematic synergies can be used for exoskeleton motion planning
Qu et al. (2019)	Carrying and pouring	Intra-arm and inter-arm coordination	A learning model consisting of PCA, GMM and GMR	Propose a method based on human-arm coordination characteristics to enhance human-robot interaction ability
Zhao et al. (2022)	Point-to-point reaching movements	Muscle synergies	Non-negative matrix factorization	Promote applications of muscle synergies in clinical scenarios

Table 4 gives an overview of main approaches to solve motion coordination.

Although researchers have proposed various coordination algorithms to control the coordinated motion of the robotic arm, due to the limitation of the understanding of the human movement control mechanism, the researches on motion coordination can only reduce the motion errors of the robotic arm in most cases, and cannot make it eliminated. By further studying the human-robot interaction mechanism and assisting more accurate and sensitive sensor technology to provide better theoretical guidance for the robot's motion control strategy, it is possible to better optimize the coordination of the robot's anthropomorphic motion.

5 Future challenges

With the in-depth study of human movement function, wearable exoskeleton robots (Liu et al., 2018) and medical robots (Zhang et al., 2020) with anthropomorphic motion planning ability have gradually come into view. In the future, it is expected that more products will be introduced to meet human needs. However, in order to provide high-quality services and realize large-scale applications, the following challenges need to be addressed based on existing researches.

(1) Intelligence and autonomy enhancement. In unstructured scenarios such as homes and restaurants, to provide better service, robots should be more intelligent, make fast and accurate decisions, and take appropriate actions based on task requirements and real-time situations to improve work efficiency. At the same time, the full autonomy of humanoid robots allows them to take on heavy, dangerous or boring tasks, which enables humans to focus more on creative and advanced thinking. Unfortunately, existing humanoid robots are not yet able to be fully autonomous from humans. With continuous advances in artificial intelligence, sensor technology, control algorithms, and other fields, we can expect future robots to achieve a higher level of autonomy.

(2) Multimodal interaction and human-robot fusion. To enhance the personalized interaction experience, the robot should integrate multiple sensors such as visual, auditory, and haptic (Li G. et al., 2019) to comprehensively understand the user's behavioral patterns, accurately respond to the user's needs, and monitor the user's feedback. Through various forms of input and corresponding outputs, the multimodal interaction capability can realize a richer and more convenient human-computer interaction experience. However, current technologies cannot fully resolve the conflict between interaction efficiency and safety.

(3) Emotional interaction and emotional intelligence. Emotional interaction and emotional intelligence in humanoid robots enable them to better understand and respond to human emotional needs. Through emotional interaction, robots can communicate and interact emotionally with humans. Through emotional intelligence, robots can process and analyze emotional information and make corresponding intelligent decisions based on emotional information. The development of this technology will bring people more user-friendly and personalized robot services and support.

(4) Humanitarian and ethical considerations. The future development of humanoid robots should also focus on humanitarian and ethical considerations. Ethical guidelines

must be followed in the design and application process to ensure that robots behave in accordance with moral and social values and are able to contribute positively to human wellbeing and social development.

6 Conclusion

In this article, we reviewed representative anthropomorphic motion planning researches for multi-degree-of-freedom robotic arms. By in-depth analysis of human natural motion, we proposed a novel classification method that incorporated human movement laws into robot motion control based on physiology, and constructed a more complete anthropomorphic planning system to better address the problem of anthropomorphic motion planning. This classification encompasses the majority of current anthropomorphic motor planning research results. It not only summarizes and integrates existing research results but also provides an in-depth exploration and understanding of the deeper causes of human movement ability. This categorization method comprehensively and systematically examines the reasons for the formation of unique human movement abilities in three major aspects: motion patterns, individual variation, and functional control. Firstly, from a physiological perspective, the formation of natural human movement ability is inextricably linked to body composition. The flexibility provided by the redundancy of the upper limbs ensures that humans can accomplish various types of complex tasks. Therefore, motion redundancy is the primary issue addressed in anthropomorphic motion planning. Secondly, individual variation is also a significant factor affecting human movement abilities. Each individual possesses unique physical characteristics, exercise habits, and psychological states, which can influence movement performance. Therefore, it is crucial to consider individual variation when designing anthropomorphic movement plans. Motion variation is a significant challenge in this domain. Finally, functional control is essential for human movement ability. The nervous system plays a pivotal role in regulating daily life movement. In addition, in order to maintain balance during movement and to improve the accuracy and stability of movement execution, the motion coordination of the limbs is an important symbol that distinguishes human beings from non-living beings (robots) or human beings with impaired motor function (patients with limb disabilities). Therefore, motion coordination is an important criterion for robot motion to be anthropomorphic. During the development, researchers have moved from single anthropomorphic criterion to consider multiple criteria to ensure that motion is sufficiently anthropomorphic. In addition, each section of the article discusses in detail the various research approaches to understanding the anthropomorphism of movement and expresses appreciations for the value that these findings provide in the anthropomorphic planning system. The article also points out the current challenges faced by anthropomorphic motion planning and suggests possible trends for the future. Once these difficulties are overcome, humanoid robots with more advanced anthropomorphic motion planning abilities will be realized in real life, contributing to the improvement of human living standards for the benefits of the society.

Author contributions

XZ: Formal Analysis, Investigation, Methodology, Validation, Visualization, Writing–original draft, Writing–review and editing. YH: Conceptualization, Funding acquisition, Project administration, Resources, Supervision, Writing–original draft, Writing–review and editing. JL: Conceptualization, Funding acquisition, Project administration, Resources, Supervision, Writing–original draft, Writing–review and editing.

Funding

The author(s) declare that financial support was received for the research, authorship, and/or publication of this article. This research was funded by the National Key R&D Program of China (2020YFC2007800) granted to Huazhong University of Science and Technology and the National Natural Science Foundation of China (52005191, 32271082, and 52027806).

Conflict of interest

The authors declare that the research was conducted in the absence of any commercial or financial relationships that could be construed as a potential conflict of interest.

Publisher's note

All claims expressed in this article are solely those of the authors and do not necessarily represent those of their affiliated organizations, or those of the publisher, the editors and the reviewers. Any product that may be evaluated in this article, or claim that may be made by its manufacturer, is not guaranteed or endorsed by the publisher.

References

Albrecht, S., Ramirez-Amaro, K., Ruiz-Ugalde, F., Weikersdorfer, D., Leibold, M., Ulbrich, M., et al. (2011). "Imitating human reaching motions using physically inspired optimization principles," in 2011 11th IEEE-RAS International Conference on Humanoid Robots (Bled, Slovenia: IEEE), 602–607. doi:10.1109/humanoids.2011.6100856

Arimoto, S., and Sekimoto, M. (2006). "Human-like movements of robotic arms with redundant DOFs: virtual spring-damper hypothesis to tackle the Bernstein problem," in Proceedings of the 2006 IEEE International Conference on Robotics and Automation (Orlando, Florida, USA: IEEE), 1860–1866. doi:10.1109/robot.2006.1641977

Arkin, R. C., and Moshkina, L. (2014). "Affect in human-robot interaction," in *The oxford handbook of affective computing*. Editor R. Calvo (Oxford: Oxford University Press), 483–493.

Artemiadis, P. K., Katsiaris, P. T., and Kyriakopoulos, K. J. (2010). A biomimetic approach to inverse kinematics for a redundant robot arm. *Aut. Robots* 29 (3-4), 293–308. doi:10.1007/s10514-010-9196-x

Atkeson, C. G., and Hollerbach, J. M. (1985). Kinematic features of unrestrained vertical arm movements. *J. Neurosci.* 5 (9), 2318–2330. doi:10.1523/jneurosci.05-09-02318.1985

Averbeck, B. B., Chafee, M. V., Crowe, D. A., and Georgopoulos, A. P. (2002). Parallel processing of serial movements in prefrontal cortex. *Proc. Natl. Acad. Sci.* 99 (20), 13172–13177. doi:10.1073/pnas.162485599

Averta, G., Della Santina, C., Valenza, G., Bicchi, A., and Bianchi, M. (2020). Exploiting upper-limb functional principal components for human-like motion generation of anthropomorphic robots. *J. Neuroeng Rehabil.* 17 (1), 63. doi:10.1186/s12984-020-00680-8

Berman, S., and LiebermannFlash, D. G. T. (2008). Application of motor algebra to the analysis of human arm movements. *Robotica* 26 (4), 435–451. doi:10.1017/S0263574707003979

Berret, B., Chiovetto, E., Nori, F., and Pozzo, T. (2011). Evidence for composite cost functions in arm movement planning: an inverse optimal control approach. *PLoS Comput. Biol.* 7 (10), e1002183. doi:10.1371/journal.pcbi.1002183

BizziCheung, E. V. C. K. (2013). The neural origin of muscle synergies. *Front. Comput. Neurosci.* 7, 51. doi:10.3389/fncom.2013.00051

Bruton, M., and O'dwyer, N. (2018). Synergies in coordination: a comprehensive overview of neural, computational, and behavioral approaches. *J. Neurophysiology* 120 (6), 2761–2774. doi:10.1152/jn.00052.2018

Calinon, S., D'halluin, F., Sauser, E., Caldwell, D., and Billard, A. (2010). Learning and reproduction of gestures by imitation. *IEEE Robotics Automation Mag.* 17 (2), 44–54. doi:10.1109/mra.2010.936947

Chao, F., Zhu, Z., Lin, C.-M., Hu, H., Yang, L., Shang, C., et al. (2018). Enhanced robotic hand–eye coordination inspired from human-like behavioral patterns. *IEEE Trans. Cognitive Dev. Syst.* 10 (2), 384–396. doi:10.1109/tcds.2016.2620156

Coscia, M., Cheung, V. C. K., Tropea, P., Koenig, A., Monaco, V., Bennis, C., et al. (2014). . *J. NeuroEngineering Rehabilitation* 11 (1), 22. doi:10.1186/1743-0003-11-22

d'Avella, A. (2016). Modularity for motor control and motor learning. *Prog. Mot. Control* 957, 3–19. doi:10.1007/978-3-319-47313-0_1

Deng, M., Li, Z., Kang, Y., Chen, C. L. P., and Chu, X. (2020). A learning-based hierarchical control scheme for an exoskeleton robot in human–robot cooperative manipulation. *IEEE Trans. Cybern.* 50 (1), 112–125. doi:10.1109/tcyb.2018.2864784

Dragan, A., and Srinivasa, S. (2014). "Familiarization to robot motion," in Proceedings of the 2014 ACM/IEEE international conference on human-robot interaction (Bielefeld, Germany: IEEE), 366–373. doi:10.1145/2559636.2559674

Fang, C., Ding, X., Zhou, C., and Tsagarakis, N. (2019). A2ML: a general human-inspired motion language for anthropomorphic arms based on movement primitives. *Robotics Aut. Syst.* 111, 145–161. doi:10.1016/j.robot.2018.10.006

Ferrer, M. A., Diaz, M., Quintana, J. J., Carmona-Duarte, C., and Plamondon, R. (2023). Extending the kinematic theory of rapid movements with new primitives. *Pattern Recognit. Lett.* 167, 181–188. doi:10.1016/j.patrec.2023.02.021

Ficuciello, F., Palli, G., Melchiorri, C., and Siciliano, B. (2014). Postural synergies of the UB Hand IV for human-like grasping. *Robotics Aut. Syst.* 62 (4), 515–527. doi:10.1016/j.robot.2013.12.008

Fitts, P. M. (1954). The information capacity of the human motor system in controlling the amplitude of movement. *J. Exp. Psychol.* 47 (6), 381–391. doi:10.1037/h0055392

Flash, T., and Hogan, N. (1985). The coordination of arm movements: an experimentally confirmed mathematical model. *J. Neurosci.* 5 (7), 1688–1703. doi:10.1523/jneurosci.05-07-01688.1985

Flash, T., Meirovitch, Y., and Barliya, A. (2013). Models of human movement: trajectory planning and inverse kinematics studies. *Robotics Aut. Syst.* 61 (4), 330–339. doi:10.1016/j.robot.2012.09.020

Freitas, D. L., Lausen, B., Maia, J. a. R., Gouveia, É. R., Thomis, M., Lefevre, J., et al. (2016). Skeletal maturation, body size, and motor coordination in youth 11–14 years. *Med. Sci. Sports Exerc.* 48 (6), 1129–1135. doi:10.1249/mss.0000000000000873

Gams, A., Nemec, B., Ijspeert, A. J., and Ude, A. (2014). Coupling movement primitives: interaction with the environment and bimanual tasks. *IEEE Trans. Robotics* 30 (4), 816–830. doi:10.1109/tro.2014.2304775

Garcia-Rosas, R., Oetomo, D., Manzie, C., Tan, Y., and Choong, P. (2018). "On the relationship between human motor control performance and kinematic synergies in upper limb prosthetics," in 2018 40th Annual International Conference of the IEEE Engineering in Medicine and Biology Society (EMBC) (Honolulu, Hawaii, USA: IEEE), 3194–3197. doi:10.1109/EMBC.2018.8512992

Geoffroy, P., Mansard, N., Raison, M., Achiche, S., and Todorov, E. (2014). From inverse kinematics to optimal control. *Adv. Robot Kinemat.*, 409–418. doi:10.1007/978-3-319-06698-1_42

Gielniak, M. J., Liu, C. K., and Thomaz, A. L. (2013). Generating human-like motion for robots. *Int. J. Robotics Res.* 32 (11), 1275–1301. doi:10.1177/0278364913490533

Giszter, S. F. (2015). Motor primitives - new data and future questions. *Curr. Opin. Neurobiol.* 33, 156–165. doi:10.1016/j.conb.2015.04.004

Gong, S., Zhao, J., Zhang, Z., and Xie, B. (2020). Task motion planning for anthropomorphic arms based on human arm movement primitives. *Industrial Robot-The Int. J. Robotics Res. Appl.* 47 (5), 669–681. doi:10.1108/ir-12-2019-0261

Gosselin-Kessiby, N., Messier, J., and Kalaska, J. F. (2008). Evidence for automatic on-line adjustments of hand orientation during natural reaching movements to stationary targets. *J. Neurophysiology* 99 (4), 1653–1671. doi:10.1152/jn.00980.2007

Guiard, Y. (1987). Asymmetric division of labor in human skilled bimanual action: the kinematic chain as a model. *J. Mot. Behav.* 19 (4), 486–517. doi:10.1080/00222895.1987.10735426

Guigon, E., Baraduc, P., and Desmurget, M. (2007). Computational motor control: redundancy and invariance. *J. Neurophysiology* 97 (1), 331–347. doi:10.1152/jn.00290.2006

Herbort, O., and Butz, M. V. (2010). Planning and control of hand orientation in grasping movements. *Exp. Brain Res.* 202 (4), 867–878. doi:10.1007/s00221-010-2191-9

Hu, Y., Zhang, S., and Chen, Y. (2023). Trajectory planning method of 6-DOF modular manipulator based on polynomial interpolation. *Journal of Computational Methods in Sciences and Engineering* 23 (3), 1589–1600. doi:10.3233/JCM-226672

Huang, R., Cheng, H., Qiu, J., and Zhang, J. (2019). Learning physical human–robot interaction with coupled cooperative primitives for a lower exoskeleton. *IEEE Trans. Automation Sci. Eng.* 16 (4), 1566–1574. doi:10.1109/tase.2018.2886376

HuangZhang, H. T., Yang, C., and Chen, C. L. P. (2020). Motor learning and generalization using broad learning adaptive neural control. *IEEE Trans. Industrial Electron.* 67 (10), 8608–8617. doi:10.1109/tie.2019.2950853

Kang, T., Tillery, S. H., and He, J. (2003). "Determining natural arm configuration along reaching trajectory," in Proceedings of the 25th Annual lntemational Conference of the IEEE Engineering in Medicine and Biology Society (Cancun, Mexico: IEEE), 1444–1447. doi:10.1109/iembs.2003.1279599

Kavraki, L. E., Svestka, P., Latombe, J. C., and Overmars, M. H. (1996). Probabilistic roadmaps for path planning in high-dimensional configuration spaces. *IEEE Trans. Robotics Automation* 12 (4), 566–580. doi:10.1109/70.508439

Kiesler, S., Powers, A., Fussell, S. R., and Torrey, C. (2008). Anthropomorphic interactions with a robot and robot-like agent. *Soc. Cogn.* 26 (2), 169–181. doi:10.1521/soco.2008.26.2.169

Kim, H., Li, Z., Milutinovic, D., and Rosen, J. (2012). "Resolving the redundancy of a seven dof wearable robotic system based on kinematic and dynamic constraint," in 2012 IEEE International Conference on Robotics and Automation (Saint Paul, Minnesota, USA: IEEE), 305–310. doi:10.1109/icra.2012.6224830

Kim, S., Kim, C., and Park, J. H. (2006). "Human-like arm motion generation for humanoid robots using motion capture database," in Proceedings of the 2006 IEEE/RSJ International Conference on Intelligent Robots and Systems (Beijing, China: IEEE), 3486–3491. doi:10.1109/iros.2006.282591

KoenigMatarić, N. M. J., and Matarić, M. J. (2016). Robot life-long task learning from human demonstrations: a Bayesian approach. *Aut. Robots* 41 (5), 1173–1188. doi:10.1007/s10514-016-9601-1

Kuffner, J. J., and Lavalle, S. M. (2000). "RRT-connect: an efficient approach to single-query path planning," in Proceedings of the 2000 IEEE International Conference on Robotics and Automation (San Francisco, California, USA: IEEE), 995–1001. doi:10.1109/robot.2000.844730

Kühnlenz, B., Sosnowski, S., Buß, M., Wollherr, D., Kühnlenz, K., and Buss, M. (2013). Increasing helpfulness towards a robot by emotional adaption to the user. *Int. J. Soc. Robotics* 5 (4), 457–476. doi:10.1007/s12369-013-0182-2

Kulic, D., Venture, G., Yamane, K., Demircan, E., Mizuuchi, I., and Mombaur, K. (2016). Anthropomorphic movement analysis and synthesis: a survey of methods and applications. *IEEE Trans. Robotics* 32 (4), 776–795. doi:10.1109/tro.2016.2587744

Kuniyoshi, Y., Inaba, M., and Inoue, H. (1994). Learning by watching: extracting reusable task knowledge from visual observation of human performance. *IEEE Trans. robotics automation* 10 (6), 799–822. doi:10.1109/70.338535

Latash, M. L., Scholz, J. P., and Schöner, G. (2002). Motor control strategies revealed in the structure of motor variability. *Exerc. Sport Sci. Rev.* 30 (1), 26–31. doi:10.1097/00003677-200201000-00006

Lauretti, C., Cordella, F., and Zollo, L. (2019). A hybrid joint/cartesian DMP-based approach for obstacle avoidance of anthropomorphic assistive robots. *Int. J. Soc. Robotics* 11 (5), 783–796. doi:10.1007/s12369-019-00597-w

Lenzi, T., Lipsey, J., and Sensinger, J. W. (2016). The RIC arm - a small, anthropomorphic transhumeral prosthesis. *IEEE-ASME Trans. Mechatronics* 21 (6), 2660–2671. doi:10.1109/tmech.2016.2596104

Li, G., Fang, Q., Xu, T., Zhao, J., Cai, H., and Zhu, Y. (2019a). Inverse kinematic analysis and trajectory planning of a modular upper limb rehabilitation exoskeleton. *Technol. Health Care* 27 (S1), 123–132. doi:10.3233/THC-199012

Li, S., Han, K., He, P., Li, Z., Liu, Y., and Xiong, Y. (2022). Human-like redundancy resolution: an integrated inverse kinematics scheme for anthropomorphic manipulators with radial elbow offset. *Adv. Eng. Inf.* 54, 101812. doi:10.1016/j.aei.2022.101812

Li, Z., Chen, F., Bicchi, A., Sun, Y., and Fukuda, T. (2019b). Guest editorial neuro-robotics systems: sensing, cognition, learning, and control. *IEEE Trans. Cognitive Dev. Syst.* 11 (2), 145–147. doi:10.1109/tcds.2019.2915408

Li, Z., Zuo, W., and Li, S. (2020). Zeroing dynamics method for motion control of industrial upper-limb exoskeleton system with minimal potential energy modulation. *Measurement* 163, 107964. doi:10.1016/j.measurement.2020.107964

Liu, H.-Y., Wang, W.-J., Wang, R.-J., Tung, C.-W., Wang, P.-J., and Chang, I. P. (2012). Image recognition and force measurement application in the humanoid robot imitation. *IEEE Trans. Instrum. Meas.* 61 (1), 149–161. doi:10.1109/tim.2011.2161025

Liu, K., and Xiong, C. (2013). "A novel 10-DoF exoskeleton rehabilitation robot based on the postural synergies of upper extremity movements," in Intelligent Robotics and Applications: 6th International Conference, ICIRA 2013 (Busan, South Korea: IEEE), 363–372. doi:10.1007/978-3-642-40852-6_37

Liu, K., Xiong, C.-H., He, L., Chen, W.-B., and Huang, X.-L. (2018). Postural synergy based design of exoskeleton robot replicating human arm reaching movements. *Robotics Aut. Syst.* 99, 84–96. doi:10.1016/j.robot.2017.10.003

Liu, W., Chen, D., and Steil, J. (2016). Analytical inverse kinematics solver for anthropomorphic 7-DOF redundant manipulators with human-like configuration constraints. *J. Intelligent Robotic Syst.* 86 (1), 63–79. doi:10.1007/s10846-016-0449-6

Lu, Z., Wang, N., Li, Q., and Yang, C. (2023). A trajectory and force dual-incremental robot skill learning and generalization framework using improved dynamical movement primitives and adaptive neural network control. *Neurocomputing* 521, 146–159. doi:10.1016/j.neucom.2022.11.076

Lütkebohle, I., Hegel, F., Schulz, S., Hackel, M., Wrede, B., Wachsmuth, S., et al. (2010). "The bielefeld anthropomorphic robot head "flobi"," in 2010 IEEE International Conference on Robotics and Automation Anchorage Convention District (Anchorage, Alaska, USA: IEEE), 3384–3391. doi:10.1109/robot.2010.5509173

Milighetti, G., Vallone, L., and De Luca, A. (2011). "Adaptive predictive gaze control of a redundant humanoid robot head," in 2011 IEEE/RSJ International Conference on Intelligent Robots and Systems (San Francisco, California, USA: IEEE), 3192–3198. doi:10.1109/iros.2011.6094417

Minato, T., Shimada, M., Itakura, S., Lee, K., and Ishiguro, H. (2012). Evaluating the human likeness of an android by comparing gaze behaviors elicited by the android and a person. *Adv. Robot.* 20 (10), 1147–1163. doi:10.1163/156855306778522505

Moiseev, S. A., and Gorodnichev, R. M. (2022). Motor synergy structure variability in different intensity locomotions. *Hum. Physiol.* 48 (4), 370–380. doi:10.1134/s0362119722040089

Morasso, P. (1981). Spatial control of arm movements. *Exp. Brain Res.* 42 (2), 223–227. doi:10.1007/bf00236911

Mülling, K., Kober, J., and KroemerPeters, O. J. (2013). Learning to select and generalize striking movements in robot table tennis. *Int. J. Robotics Res.* 32 (3), 263–279. doi:10.1177/0278364912472380

Mussa-Ivaldi, F. A., and Bizzi, E. (2000). Motor learning through the combination of primitives. *Philos. Trans. R. Soc. Lond B Biol. Sci.* 355 (1404), 1755–1769. doi:10.1098/rstb.2000.0733

Nagahama, K., Demura, S., and Yamazaki, K. (2021). Robot learning of tool manipulation based on visual teaching with mitate expression. *Adv. Robot.* 35 (12), 741–755. doi:10.1080/01691864.2021.1914724

Northrup, S., Sarkar, N., and Kawamura, K. (2001). "Biologically-inspired control architecture for a humanoid robot," in Proceedings of the 2001 IEEE/RSJ International Conference on Intelligent Robots and Systems (Maui, Hawaii, USA: IEEE), 1100–1105. doi:10.1109/IROS.2001.976315

Ogawa, K., Narioka, K., and Hosoda, K. (2011). "Development of whole-body humanoid "Pneumat-BS" with pneumatic musculoskeletal system," in 2011 IEEE/RSJ International Conference on Intelligent Robots and Systems (San Francisco, California, USA: IEEE), 4838–4843. doi:10.1109/iros.2011.6095091

Olson, S., Abd, M., and Engeberg, E. D. (2020). Human-inspired robotic eye-hand coordination enables new communication channels between humans and robots. *Int. J. Soc. Robotics* 13 (5), 1033–1046. doi:10.1007/s12369-020-00693-2

Omrcen, D., and Ude, A. (2010). "Redundant control of a humanoid robot head with foveated vision for object tracking," in 2010 IEEE International Conference on Robotics and Automation Anchorage Convention District (Anchorage, Alaska, USA: IEEE), 4151–4156. doi:10.1109/robot.2010.5509515

Otaki, M., and Shibata, K. (2019). The effect of different visual stimuli on reaction times: a performance comparison of young and middle-aged people. *J. Phys. Ther. Sci.* 31 (3), 250–254. doi:10.1589/jpts.31.250

Paik, J. K., Shin, B. H., Bang, Y.-B., and Shim, Y.-B. (2012). Development of an anthropomorphic robotic arm and hand for interactive humanoids. *J. Bionic Eng.* 9 (2), 133–142. doi:10.1016/s1672-6529(11)60107-8

Pham, H., Ariga, Y., Tominaga, K., Oku, T., Nakayama, K., Uemura, M., et al. (2014). Extraction and implementation of muscle synergies in neuro-mechanical control of upper limb movement. *Adv. Robot.* 28 (11), 745–757. doi:10.1080/01691864.2013.876940

Pignat, E., and Calinon, S. (2017). Learning adaptive dressing assistance from human demonstration. *Robotics Aut. Syst.* 93, 61–75. doi:10.1016/j.robot.2017.03.017

Potkonjak, V., Tzafestas, S., Kostic, D., and Djordjevic, G. (2001). Human-like behavior of robot arms: general considerations and the handwriting task - Part I: mathematical description of human-like motion: distributed positioning and virtual fatigue. *Robotics Comput. Integr. Manuf.* 17 (4), 305–315. doi:10.1016/S0736-5845(01)00005-9

Qian, K., Liu, H., Valls Miro, J., Jing, X., and Zhou, B. (2020). Hierarchical and parameterized learning of pick-and-place manipulation from under-specified human demonstrations. *Adv. Robot.* 34 (13), 858–872. doi:10.1080/01691864.2020.1778523

Qu, J., Zhang, F., Wang, Y., and Fu, Y. (2019). Human-like coordination motion learning for a redundant dual-arm robot. *Robotics Computer-Integrated Manuf.* 57, 379–390. doi:10.1016/j.rcim.2018.12.017

Rajruangrabin, J., and Popa, D. O. (2010). Robot head motion control with an emphasis on realism of neck–eye coordination during object tracking. *J. Intelligent Robotic Syst.* 63 (2), 163–190. doi:10.1007/s10846-010-9468-x

Rohrer, B., Fasoli, S., Krebs, H. I., Hughes, R., Volpe, B., Frontera, W. R., et al. (2002). Movement smoothness changes during stroke recovery. *J. Neurosci.* 22 (18), 8297–8304. doi:10.1523/jneurosci.22-18-08297.2002

Sasagawa, A., Sakaino, S., and Tsuji, T. (2021). Motion generation using bilateral control-based imitation learning with autoregressive learning. *IEEE Access* 9, 20508–20520. doi:10.1109/access.2021.3054960

Scholz, J. P., and Schöner, G. (1999). The uncontrolled manifold concept: identifying control variables for a functional task. *Exp. Brain Res.* 126 (3), 289–306. doi:10.1007/s002210050738

Seraji, H. (1989). Configuration control of redundant manipulators: theory and implementation. *IEEE Trans. Robotics Automation* 5 (4), 472–490. doi:10.1109/70.88062

Shin, S. Y., and Kim, C. (2015). Human-like motion generation and control for humanoid's dual arm object manipulation. *IEEE Trans. Industrial Electron.* 62 (4), 2265–2276. doi:10.1109/tie.2014.2353017

Silvério, J., Rozo, L., Calinon, S., and Caldwell, D. G. (2015). "Learning bimanual end-effector poses from demonstrations using task-parameterized dynamical systems," in 2015 IEEE/RSJ International Conference on Intelligent Robots and Systems (IROS) (Hamburg, Germany: IEEE), 464–470. doi:10.1109/IROS.2015.7353413

Soechting, J. F., and Lacquaniti, F. (1981). Invariant characteristics of a pointing movement in man. *J. Neurosci.* 1 (7), 710–720. doi:10.1523/jneurosci.01-07-00710.1981

Soltani Zarrin, R., Zeiaee, A., Langari, R., Buchanan, J. J., and Robson, N. (2021). Towards autonomous ergonomic upper-limb exoskeletons: a computational approach for planning a human-like path. *Robotics Aut. Syst.* 145, 103843. doi:10.1016/j.robot.2021.103843

Soltani-Zarrin, R., Zeiaee, A., Langari, R., and Robson, N. (2017). "Reference path generation for upper-arm exoskeletons considering scapulohumeral rhythms," in 2017 International Conference on Rehabilitation Robotics (ICORR) (London, UK: IEEE), 753–758. doi:10.1109/icorr.2017.8009338

Su, H., Enayati, N., Vantadori, L., Spinoglio, A., Ferrigno, G., and De Momi, E. (2018). Online human-like redundancy optimization for tele-operated anthropomorphic manipulators. *Int. J. Adv. Robotic Syst.* 15 (6), 172988141881469. doi:10.1177/1729881418814695

Su, H., Qi, W., Yang, C., Aliverti, A., Ferrigno, G., and De Momi, E. (2019). Deep neural network approach in human-like redundancy optimization for anthropomorphic manipulators. *IEEE Access* 7, 124207–124216. doi:10.1109/access.2019.2937380

Tahara, K., Luo, Z.-W., and Arimoto, S. (2006). "On control mechanism of human-like reaching movements with musculo-skeletal redundancy," in Proceedings of the 2006 IEEE/RSJ International Conference on Intelligent Robots and Systems (Beijing, China: IEEE), 1402–1409. doi:10.1109/IROS.2006.281931

Taïx, M., Tran, M. T., Souères, P., and Guigon, E. (2013). Generating human-like reaching movements with a humanoid robot: a computational approach. *J. Comput. Sci.* 4 (4), 269–284. doi:10.1016/j.jocs.2012.08.001

Takano, W., and Nakamura, Y. (2017). Planning of goal-oriented motion from stochastic motion primitives and optimal controlling of joint torques in whole-body. *Robotics Aut. Syst.* 91, 226–233. doi:10.1016/j.robot.2017.01.013

Tang, L., Li, F., Cao, S., Zhang, X., and Chen, X. (2014). "Muscle synergy analysis for similar upper limb motion tasks," in 2014 36th Annual International Conference of the IEEE Engineering in Medicine and Biology Society (Chicago, Illinois, USA: IEEE), 3590–3593. doi:10.1109/EMBC.2014.6944399

Tang, S., Chen, L., Barsotti, M., Hu, L., Li, Y., Wu, X., et al. (2019). Kinematic synergy of multi-DoF movement in upper limb and its application for rehabilitation exoskeleton motion planning. *Front. Neurorobotics* 13, 99. doi:10.3389/fnbot.2019.00099

Tangpattanakul, P., and Artrit, P. (2009). "Minimum-time trajectory of robot manipulator using harmony search algorithm," in 2009 6th International Conference on Electrical Engineering/Electronics, Computer, Telecommunications and Information Technology (ECTI-CON) (Chonburi, Thailand: IEEE), 354–357. doi:10.1109/ecticon.2009.5137025

Taniai, Y., Naniwa, T., and Nishii, J. (2022). Optimal reaching trajectories based on feedforward control. *Biol. Cybern.* 116 (4), 517–526. doi:10.1007/s00422-022-00939-4

Todorov, E. (2004). Optimality principles in sensorimotor control. *Nat. Neurosci.* 7 (9), 907–915. doi:10.1038/nn1309

Todorov, E., and Jordan, M. I. (1998). Smoothness maximization along a predefined path accurately predicts the speed profiles of complex arm movements. *J. Neurophysiology* 80 (2), 696–714. doi:10.1152/jn.1998.80.2.696

Togo, S., Kagawa, T., and Uno, Y. (2016). Uncontrolled manifold reference feedback control of multi-joint robot arms. *Front. Comput. Neurosci.* 10, 69. doi:10.3389/fncom.2016.00069

Tommasino, P., and Campolo, D. (2017). Task-space separation principle: a force-field approach to motion planning for redundant manipulators. *Bioinspir Biomim.* 12 (2), 026003. doi:10.1088/1748-3190/aa5558

Von Zitzewitz, J., Boesch, P. M., Wolf, P., and Riener, R. (2013). Quantifying the human likeness of a humanoid robot. *Int. J. Soc. Robotics* 5 (2), 263–276. doi:10.1007/s12369-012-0177-4

Wada, Y., Kaneko, Y., Nakano, E., Osu, R., and Kawato, M. (2001). Quantitative examinations for multi joint arm trajectory planning-using a robust calculation algorithm of the minimum commanded torque change trajectory. *Neural Netw.* 14 (4-5), 381–393. doi:10.1016/s0893-6080(01)00026-0

Wang, H., Xu, H., Tian, Y., and Tang, H. (2020). α-Variable adaptive model free control of iReHave upper-limb exoskeleton. *Adv. Eng. Softw.* 148, 102872. doi:10.1016/j.advengsoft.2020.102872

Wei, Y., and Zhao, J. (2019). Designing human-like behaviors for anthropomorphic arm in humanoid robot NAO. *Robotica* 38 (7), 1205–1226. doi:10.1017/s026357471900136x

Wenderoth, N., Kupferberg, A., Huber, M., Helfer, B., Lenz, C., Knoll, A., et al. (2012). Moving just like you: motor interference depends on similar motility of agent and observer. *PLoS ONE* 7 (6), e39637. doi:10.1371/journal.pone.0039637

Wochner, I., Driess, D., Zimmermann, H., Haeufle, D. F. B., Toussaint, M., and Schmitt, S. (2020). Optimality principles in human point-to-manifold reaching accounting for muscle dynamics. *Front. Comput. Neurosci.* 14, 38. doi:10.3389/fncom.2020.00038

Wolpert, D. M., and Ghahramani, Z. (2000). Computational principles of movement neuroscience. *Nat. Neurosci.* 3 (11), 1212–1217. doi:10.1038/81497

Xia, J., Jiang, Z., Zhang, H., Zhu, R., and Tian, H. (2021). Dual fast marching tree algorithm for human-like motion planning of anthropomorphic arms with task constraints. *IEEE-ASME Trans. Mechatronics* 26 (5), 2803–2813. doi:10.1109/tmech.2020.3047476

Xie, B., Zhao, J., and Liu, Y. (2011). "Human-like motion planning for robotic arm system," in The 15th International Conference on Advanced Robotics (Tallinn, Estonia: IEEE), 88–93. doi:10.1109/icar.2011.6088543

Xue, X., Zuo, L., Wang, N., and Bueno, A. (2022). A robot human-like learning framework applied to unknown environment interaction. *Complexity* 2022, 1–10. doi:10.1155/2022/5648826

Yamane, K. (2020). Kinematic redundancy resolution for humanoid robots by human motion database. *IEEE Robotics Automation Lett.* 5 (4), 6948–6955. doi:10.1109/lra.2020.3026972

Yang, A., Chen, Y., Naeem, W., and FeiChen, M. L. (2021). Humanoid motion planning of robotic arm based on human arm action feature and reinforcement learning. *Mechatronics* 78, 102630. doi:10.1016/j.mechatronics.2021.102630

Yi, J.-B., Kim, J., Kang, T., Song, D., Park, J., and Yi, S.-J. (2022). Anthropomorphic grasping of complex-shaped objects using imitation learning. *Appl. Sci.* 12 (24), 12861. doi:10.3390/app122412861

Young, S. J., Pratt, J., and Chau, T. (2009). Target-directed movements at a comfortable pace: movement duration and fitts's law. *J. Mot. Behav.* 41 (4), 339–346. doi:10.3200/jmbr.41.4.339-346

Zacharias, F., Schlette, C., Schmidt, F., Borst, C., Rossmann, J., and Hirzinger, G. (2011). "Making planned paths look more human-like in humanoid robot manipulation planning," in 2011 IEEE International Conference on Robotics and Automation Shanghai International Conference Center (Shanghai, China: IEEE), 1192–1198. doi:10.1109/icra.2011.5979553

Zanchettin, A. M., Bascetta, L., and Rocco, P. (2013). Acceptability of robotic manipulators in shared working environments through human-like redundancy resolution. *Appl. Ergon.* 44 (6), 982–989. doi:10.1016/j.apergo.2013.03.028

Zanchettin, A. M., Rocco, P., Bascetta, L., Symeonidis, I., and Peldschus, S. (2011). "Kinematic analysis and synthesis of the human arm motion during a manipulation task," in 2011 IEEE International Conference on Robotics and Automation (ICRA) (Shanghai, China: IEEE), 2692–2697. doi:10.1109/icra.2011.5979654

Zhang, X., Li, J., Qi, W., Zhou, X., Hu, Y., Quan, H., et al. (2020). A novel human-like control framework for mobile medical service robot. *Complexity* 2020, 1–11. doi:10.1155/2020/2905841

Zhang, Z., Beck, A., and Magnenat-Thalmann, N. (2015). Human-like behavior generation based on head-arms model for robot tracking external targets and body parts. *IEEE Trans. Cybern.* 45 (8), 1390–1400. doi:10.1109/tcyb.2014.2351416

Zhao, K., Zhang, Z., and WenScano, H. A. (2022). Number of trials and data structure affect the number and components of muscle synergies in upper-limb reaching movements. *Physiol. Meas.* 43 (10), 105008. doi:10.1088/1361-6579/ac9773

Zhao, L., Zhao, J., and Liu, H. (2021). Solving the inverse kinematics problem of multiple redundant manipulators with collision avoidance in dynamic environments. *J. Intelligent Robotic Syst.* 101 (2), 30. doi:10.1007/s10846-020-01279-w

Zucker, M., Ratliff, N., Dragan, A. D., Pivtoraiko, M., Klingensmith, M., Dellin, C. M., et al. (2013). CHOMP: covariant Hamiltonian optimization for motion planning. *Int. J. robotics Res.* 32 (9-10), 1164–1193. doi:10.1177/0278364913488805

Zuher, F., and Romero, R. (2012). "Recognition of human motions for imitation and control of a humanoid robot," in 2012 Brazilian Robotics Symposium and Latin American Robotics Symposium (Fortaleza, Brazil: IEEE), 190–195. doi:10.1109/sbr-lars.2012.38

frontiers | Frontiers in Bioengineering and Biotechnology

TYPE Original Research
PUBLISHED 30 May 2024
DOI 10.3389/fbioe.2024.1385076

OPEN ACCESS

EDITED BY
Wujing Cao,
Chinese Academy of Sciences (CAS), China

REVIEWED BY
Wojciech Wolański,
Silesian University of Technology, Poland
Xiangxin Li,
Chinese Academy of Sciences (CAS), China

*CORRESPONDENCE
Jiejunyi Liang,
jiejunyiliang@gmail.com

†These authors have contributed equally to this work and share first authorship

RECEIVED 11 February 2024
ACCEPTED 10 May 2024
PUBLISHED 30 May 2024

CITATION
Liu Y, Luo Y, Xiao T and Liang J (2024), Non-back-drivable clutch based self-locking mechanism of prosthetic joint to improve manipulation stability.
Front. Bioeng. Biotechnol. 12:1385076.
doi: 10.3389/fbioe.2024.1385076

Non-back-drivable clutch based self-locking mechanism of prosthetic joint to improve manipulation stability

Yang Liu[1†], Yuhui Luo[2†], Ting Xiao[3] and Jiejunyi Liang[1*]

[1]State Key Laboratory of Intelligent Manufacturing Equipment and Technology, Huazhong University of Science and Technology, Wuhan, China, [2]School of Art, Soochow University, Suzhou, China, [3]Huazhong University of Science and Technology Hospital, Wuhan, China

During activities of daily living (ADLs), the wrist is mainly engaged in positioning and directing the hand. Researches have demonstrated that restoring wrist mobility can significantly enhance the manipulation ability, reduce body distortion caused by motion compensation, and improve the quality of life for amputees. However, most daily activities, particularly the delicate ones, place high demands on the ability of wrist to maintain a certain rotation angle, also known as non-back-drivable ability, which poses a challenge to the design of prosthetic wrists. To address this issue, various solutions have been proposed, including motor holding brakes, high reduction ratio reducers, and worm gears. However, the motor holding brake only functions after a power outage and cannot continuously prevent torque from the load end. The latter two solutions may alter the transmission ratio, resulting in reduced movement speed and transmission efficiency. Therefore, how to design a miniaturized non-back-drivable mechanism without changing the transmission ratio so that the forearm rotational freedom can be locked at any position for any duration is a problem to be solved in the research of prosthetic wrist designs. This paper presents a line-contact based non-back-drivable clutch (NBDC) that does not cause changes in the transmission ratio, ensuring the motion performance of the prosthetic limb. At the same time, it does not introduce additional friction in the forward transmission process, guaranteeing the overall efficiency. Most importantly, it only allows the torque transmitting from the motor to the load, prevents the load reversely from driving back even in a power failure condition, significantly improving the stability, safety, and comfort. Detailed kinematic and static analyses of the working process has been conducted, and transient dynamics simulation has been performed to verify its effectiveness. Through experiments, it is demonstrated that the self-locking torque of the output end could reach approximately 600 Nmm, and the unlocking torque of the input end is about 80 Nmm, which can be effectively integrated in prosthetic wrist rotation joints, contributing to the performance, safety and energy saving of prosthetic joint systems.

KEYWORDS

prosthesis joint, wrist, non-back-drivable-clutch, backlash, manipulation stability, transient dynamics

1 Introduction

The rotation of the human forearm relies on the ulna and radius turning from a parallel state to an intersecting state. The successful realization of this movement depends on the complete distal radioulnar joint (Neumann, 2016). However, transradial amputation is the most common form of upper limb amputation, which leads to the inevitable destruction of the distal radioulnar joint. As the degree of amputation increases, the rotation ability of the residual limb decreases sharply. Even with a prosthetic hand, the patient's ADLs are still greatly restricted due to the lack of the most important rotation function of the wrist. In this case, to achieve motion compensation, amputee's body would inevitably be distorted during manipulation scenarios, which would not only seriously affect the amputee's comfort, but also bring depression and anxiety to them (Bandara et al., 2014; Semasinghe et al., 2018; Billones et al., 2020). Moreover, it has been discovered that compared with further improving the performance of prosthetic hand, it is more effective to employ a prosthetic wrist to achieve a substantial overall improvement (Montagnani et al., 2015a; Deijs et al., 2016; Bajaj et al., 2019; Lee et al., 2021).

A survey of upper-limb prosthetic users showed that features such as lightweight, durability, and long duration of single charge (more than 12 h) are directly related to whether prosthetic products will be accepted (Mustafa et al., 2006), and among which, lightweight is the most important (Biddiss et al., 2007). Therefore, commercially available prosthetic wrists generally adopt designs those only have a single degree of freedom, retaining the most important rotational freedom to meet the lightweight needs. However, during manipulation tasks, the wrist plays a crucial role in precise positioning the prosthetic hand before the hand comes into contact with the target, and is heavily involved in maintaining stability of the target during the contact, which excessively requires the non-back-drivable ability of the rotating component. To address this issue, various solutions have been proposed, including motor holding brakes, high reduction ratio reducers, and worm gears. However, the motor holding brake only functions after a power outage and cannot continuously prevent torque from the load end (Ann et al., 2000). The latter two solutions may alter the transmission ratio, resulting in reduced movement speed and transmission efficiency. Therefore, how to design a miniaturized non-back-drivable mechanism without changing the transmission ratio so that the forearm rotational freedom can be locked at any position for any duration is a problem to be solved in the research of prosthetic wrists (Controzzi et al., 2010; Kimura et al., 2021; Shi et al., 2021), and is critical to the successful completion of the manipulation task (Gao et al., 2021). In most grasping actions which require to maintain the locking state for a long time, if the actuator lacks a self-locking mechanism, the external load will directly act on the drive motor and drive the prosthetic wrist in the opposite direction, resulting in not only an unstable wrist rotation angle, but also a potential hazard (Guo et al., 2020; Wei et al., 2023). This hazard would be exacerbated in the event of a power failure due to a depleted battery or circuit failure. The unlocked wrist joint will rotate freely under the action of the external load, posing a great danger to amputees. Therefore, prosthetic joints that take into account both miniaturization requirements and self-locking capabilities have become the main development trend, and the key component is the non-back-drivable clutch.

To be specific, the input end of the NBDC is the power system such as the drive motor, and the output end is connected to the hand and the external loads. When the input end receives a motion command and the motor starts to rotate, whether it is clockwise rotation or counterclockwise, as long as the initial torque is greater than the unlocking torque, the transmission system can be activated to achieve efficient power transmission. To the contrary, regardless of whether the external loads apply clockwise or counterclockwise torque to the NBDC, as long as it is within the maximum self-locking torque range, the mechanism will automatically enter the locking state, so that the external loads will not directly affect the drive motor. This feature gives the prosthetic joint the ability to maintain stable grasping at any position for a long time. It also possesses the ability to function without power supply during operation that does not need further rotating, extending the battery life to a certain extent. Therefore, designing advanced NBDC and continuously optimizing its self-locking performance can effectively improve the stability, safety, and endurance of prosthetic joints (Liu et al., 2022).

Researches focusing on how to improve NBDC performance have concluded five optimization directions (Chu et al., 2008; Controzzi et al., 2010; Controzzi et al., 2017; Montagnani et al., 2015b; Hu et al., 2021; Wu et al., 2023): (1) Low cost. In order to meet the large-scale production and implementation of self-locking mechanisms, the cost of related components need to reasonably controlled (Liu et al., 2021) while ensuring the performance and quality (Mota et al., 2023). (2) Simplicity (Zhang et al., 2023), including miniaturization (Ding et al., 2021) and ease of manufacturing and assembly (Controzzi et al., 2010). (3) Safety. Due to the sufficient interaction between humans and prosthetic limbs(Lu et al., 2021), safety is the primary concern in real practice (Hu et al., 2020). If the external load can reversely drive the prosthetic joints, it will cause secondary damage to the amputees. (4) Energy efficiency. How to improve the battery duration of a single charge has always been an important topic in the field of prosthetics (Cirelli et al., 2021; Okafor and Longe, 2022; He et al., 2023). If a single charge cannot satisfy an amputee's normal use for a day, it will greatly affect its acceptance. As a result, reducing the friction energy loss and inertia would be of great importance (Cirelli et al., 2021). (5) Robustness. As the external load is determined by the actual manipulation tasks, the nominal self-locking torque should be high enough to cover most daily working scenarios.

Focusing on the above five requirements, Marco Controzzi et al. (Controzzi et al., 2010; Controzzi et al., 2017) designed a cylinder-based NBDC and applied it in the SmartHand (Cipriani et al., 2010), enabling it to effectively generate strong gripping force under strict power and weight constraints. Compared with the traditional non-back-drivable mechanism based on worm gears (Kang et al., 2015), this clutch, based on a wedge structure, achieves higher transmission efficiency. Within the load range from 50 Nmm to 150 Nmm, the maximum efficiency of this mechanism is around 0.95. Jun-Uk Chu et al. embedded a self-locking mechanism in the prosthetic finger joint (Chu et al., 2008). The self-locking mechanism adopts a coil spring and cam ball structure to prevent the reverse force of the grasped object on the fingers. However, the springs and cams in this mechanism suffer significant wear during operation, which does not

meet the durability requirements of prosthetic devices. Qiqiang Hu et al. (Hu et al., 2021)were inspired by the ratchet spanner and employed an interlock to increase the grip strength of the fingers, enabling them to safely perform high loads and prolonged gripping tasks. However, when the ratchet mechanism is unlocking, it is always in a state of friction with the buckle and is prone to wear. At the same time, there is a certain amount of free travel in the self-locking process, resulting a small deviation at the load end. Xiaofeng Wu et al. (Wu et al., 2023) proposed a compact arc-groove self-locking mechanism with two linear springs embedded in the arc grooves, eliminating the need for additional mounting structures. The whole system is compact, small, and modular, enabling underdriven finger mechanisms to achieve adaptive gripping. However, the groove needs to be regularly filled with an appropriate amount of grease to reduce the impact of friction between the spring and the groove. Federico Montagnani et al. (Montagnani et al., 2015b) designed a non-back-drivable mechanism for miniaturized application scenarios such as finger joints. This mechanism can turn off the power after reaching a stable state, thereby avoiding accidental release of the grasped object, and absorbs the impact generated during grasping. However, this mechanism must also consider the corrosion of lubricants, etc., limiting its application in certain conditions. In summary, for the existing self-locking mechanisms, there are still unsolved problems such as not being able to lock instantly, excessive wear of the system under normal operating conditions, and the need to add grease to the mechanism in a timely manner.

In this study, in order to solve the above problems, a novel NBDC is proposed, which achieves self-locking based on the line-contact between the wedges and the fixed support, and can be applied in prosthetic wrists to realize rotational self-locking. The proposed mechanism consists of a fixed support, a wedge pedestal, four wedges, a pin pedestal and four pins, meriting low cost and simplicity in manufacture and assembly. As to the operating mechanism, it mainly contains three key states: (1) Self-locking state. No matter whether the output end, which is connected to the external loads, moves clockwise or counterclockwise, the loads cannot be transmitted back to the input end. (2) Intermediate state of unlocking. 7° of idle angle exists between unlock state and complete lock state. (3) Unlocking state. When the torque at the input end drives the pin to rotate more than 7° of idle angle and reach 14°, the driving force would be transmitted to the output end, and then the self-locking system start to rotate as a whole. Simulations and Experiments have been conducted and verified that the self-locking structure could resist a reverse torque of 600 Nmm from the output end, and only requires an unlocking torque about 80 Nmm at the input end, making it highly efficient for the implementation in prosthetic wrists or other rotating joints.

The main contributions of this paper are as follows:

(1) A non-back-drivable clutch with self-locking features is designed, which does not change the transmission ratio of the system and can ensure the motion speed of the rotating forearm under the premise of stable manipulation. (2) A wavy spring with suitable stiffness is designed to switch between unlocking and locking modes in the self-locking system, separating the wedges from the support in the unlocking state, reducing the friction and improving the efficiency. (3) Critical working conditions of the self-locking system are analyzed and verified through detailed kinematic analysis, static analysis, transient dynamic simulations and experiments, proving the performance of the proposed system that the self-locking ability reaches 600 Nmm.

The rest of this study is organized as follows. Section 2 introduces the overall design of the new NBDC mechanism, and calculates the theoretical performance of the mechanism through kinematic analysis, static analyses and transient dynamics analysis. Section 3 introduces the experimental platform construction and result analysis of NBDC. Section 4 introduces applications with NBDC embedded in a prosthetic wrist. Section 5 discusses the limitations of this research and possible improvements in the future. The final conclusions can be found in Section 6.

2 Materials and methods

The proposed NBDC based on line-contact self-locking mechanism mainly consists of a fixed support, four wedges, a wedge pedestal, four pins and a pin pedestal. The pin pedestal can be used as the connection to the input end, through which the power system such as the motor could be connected. Four pins are mounted along the circumference of the pin pedestal, the pin drives two sets of wedges to rotate, ultimately generating a self-locking state, an unlocking intermediate state and an unlocking state together with the fixed support (see in Figure 1). Each wedge set is composed of two opposite wedges, connected by a wavy spring in the middle. The shape of each set of wedges is mirror symmetrical. The groove below the wedge connects the pin, and the groove presents a “V” shape. The fixed support is connected to the work platform through bolts, and also connected to the pin pedestal through bearings and pins. Its function is to provide self-locking through the friction between its inner wall and the top arc surface of the wedge in self-locking stage, absorbing the impact from the output end. This clutch is embedded between the wrist rotation motor and the harmonic reducer in practice, with its input end connected to the output shaft of the motor and its output end connected to the harmonic reducer. The specific section view and exploded view of the NBDC mechanism are shown in Figures 2A, B, respectively.

2.1 Kinematic analysis

In order to clearly describe the operating mechanism of the proposed NBDC, the section views of five key states of the self-locking mechanism are depicted in detail in Figure 3. These section views are drawn along the middle of the axis with the spring neglected, showing the changes of the input end. These five states can be further divided into three categories, which are: (1) Self-locking, as shown in Figure 3A. In this state, the pin pedestal is at zero point, and the pins don’t contact the inner wall of the groove below the wedges. The torque from the output end cannot be transmitted to the input end whether the motion is clockwise nor counterclockwise, and at the same time, the length of the wavy spring is the longest. (2) Intermediate state of unlocking, as shown in Figures 3B, D. The input end drives the pins through the pin pedestal to rotate 7° around the rotation center. Among the four pins, two of them pressure to the inner wall of the groove under the wedge,

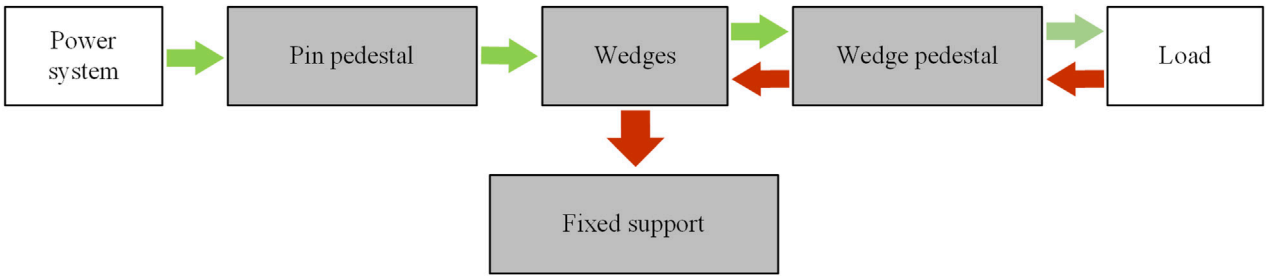

FIGURE 1
Driving mode (green arrow) and self-locking mode (red arrow) of the NBDC mechanism.

making it start to rotate. At the same time, the other two pins just reach the contacting point to the surface of the grooves of the above wedge. At this point, in the 2nd and 4th quadrants of Figures 3A, B gap forms between the edge of the wedges and the inner wall of the fixed support. Similarly, in the 1st and 3rd quadrants of Figures 3A, D gap also appears. (3) Unlocking state. The two pins that have been separated from the fixed support move in the groove during the rotation of 7°–14°, and finally reach the bottom of the groove. The other two pins drive their corresponding wedges to start moving, causing them to break away from the fixed support and eventually reach the bottom of the groove, as shown in the 1st and 3rd quadrants in Figure 3C and the 2nd and 4th quadrants in Figure 3E. Thereafter, the torque at the input end can be transmitted directly to the output, and the wavy spring is compressed to its shortest length. When there is no continuous torque input at the input end, the two springs will exert the stored elastic potential energy to press the wedges to the self-locking state again, back to Figure 3A, so that the torque of the external load will be blocked.

To investigate the influence of the angle change of the input end on the angle of the wedges in the three working states, kinematic analysis was carried out, taking the 1st and 4th quadrants as examples. As shown in Figure 4A, the inner diameter of the fixed support is R_{fix}, the radius of the pins is r_{pin}, the radius of the circle where the center of the pins is located is R_{pin}, the contact radius between the wedges and the flange bearing is r_{cam}, the radius of the circle where the center of the wedges is located is R_{cam}, and R_{pin}, R_{cam} have the same value. The angle between the pins is 45°, and the relative angle the pin pedestal rotates to the fixed support is θ_i. In the 1st quadrant, the center of the pins is P_1, the center of the wedges is C_1, and the action point of the connecting spring is S_1. In the 4th quadrant, the center of the pins is P_4, the center of the wedges is C_4, and the action point of the connecting wavy spring is S_4, as shown in Figure 4B.

Taking the counterclockwise movement of the input as an example, the positions of the centers of the pins in the 1st and 4th quadrants at any moment are shown in Eq. 1:

$$\begin{cases} \overrightarrow{OP_1} = R_{pin}[\cos(45° + \theta_i)\ \sin(45° + \theta_i)]^T \\ \overrightarrow{OP_4} = R_{pin}[\cos(315° + \theta_i)\ \sin(315° + \theta_i)]^T \end{cases} \quad (1)$$

The axis where the wedges are located are uniformly distributed along the center, the angle between them is 90°, and the specific position is related to the rotation angle θ_o of the output end of the wedge pedestal. The position of the center of the wedge in the 1st quadrant and the 4th quadrant are shown in Eq. 2:

$$\begin{cases} \overrightarrow{OC_1} = R_{cam}[\cos(45° + \theta_o)\ \sin(45° + \theta_o)]^T \\ \overrightarrow{OC_4} = R_{cam}[\cos(315° + \theta_o)\ \sin(315° + \theta_o)]^T \end{cases} \quad (2)$$

When the pin pedestal rotates $\theta_i < \theta_{iab}$, the stage changes from Figures 3A, B, and when the pin pedestal rotates $\theta_{iab} \le \theta_i < \theta_{iac}$, the stage changes from Figures 3B, C. The most important three topics of these two processes are: (1) The relationship between the rotation angle of the input θ_i, the rotation angles of the wedges in the 1st and 4th quadrants, and the wedge pedestal. (2) The changes in the distances between the 1st (4th) quadrant's wedge and the inner wall of the fixed support at the rotation angle θ_i; (3) The effective action length of the wavy spring changes according to the angle θ_i.

(1) According to the geometric relationship that the pin in the 4th quadrant is always tangent to the inner side of the groove of the wedge, it can be seen that the slope between the axis of the wedge and the axis of the pin satisfies the following Eq. 3:

$$k_{CP}^4 = \frac{y_P^4 - y_C^4}{x_P^4 - x_C^4} = \frac{R_{pin}\sin(315° + \theta_i) - R_{cam}\sin(315° + \theta_o)}{R_{pin}\cos(315° + \theta_i) - R_{cam}\cos(315° + \theta_o)} \quad (3)$$

Similarly, the slope between the axis of the wedge and the axis of the pin in the 1st quadrant satisfies Eq. 4:

$$k_{CP}^1 = \frac{y_P^1 - y_C^1}{x_P^1 - x_C^1} = \frac{R_{pin}\sin(45° + \theta_i) - R_{cam}\sin(45° + \theta_o)}{R_{pin}\cos(45° + \theta_i) - R_{cam}\cos(45° + \theta_o)} \quad (4)$$

The initial angle of the wedge in the 1st quadrant is θ_{camini}^1, that in the 4th quadrant is θ_{camini}^4, then relative rotation of the two wedges is Eq. 5:

$$\begin{cases} \theta_{cam}^1 = \arctan(k_{CP}^1) - \theta_{camini}^1 \\ \theta_{cam}^4 = \arctan(k_{CP}^4) - \theta_{camini}^4 \end{cases} \quad (5)$$

The relationship between the input rotation angle θ_i and the wedge rotation angle θ_{cam}^1, θ_{cam}^4 are shown in Figure 5A. When the input angle increases from 0° to 7°, the wedge in the 4th quadrant rotates counterclockwise, the 1st quadrant's wedge and wedge pedestal stay still. When the input angle increases from 7° to 14°, the wedge in the 4th quadrant continues to rotate counterclockwise, the wedge in the 1st quadrant rotates clockwise, and the wedge pedestal stays still. When the angle of the input continues to increase, the wedge no longer rotates relative to its axis, and the

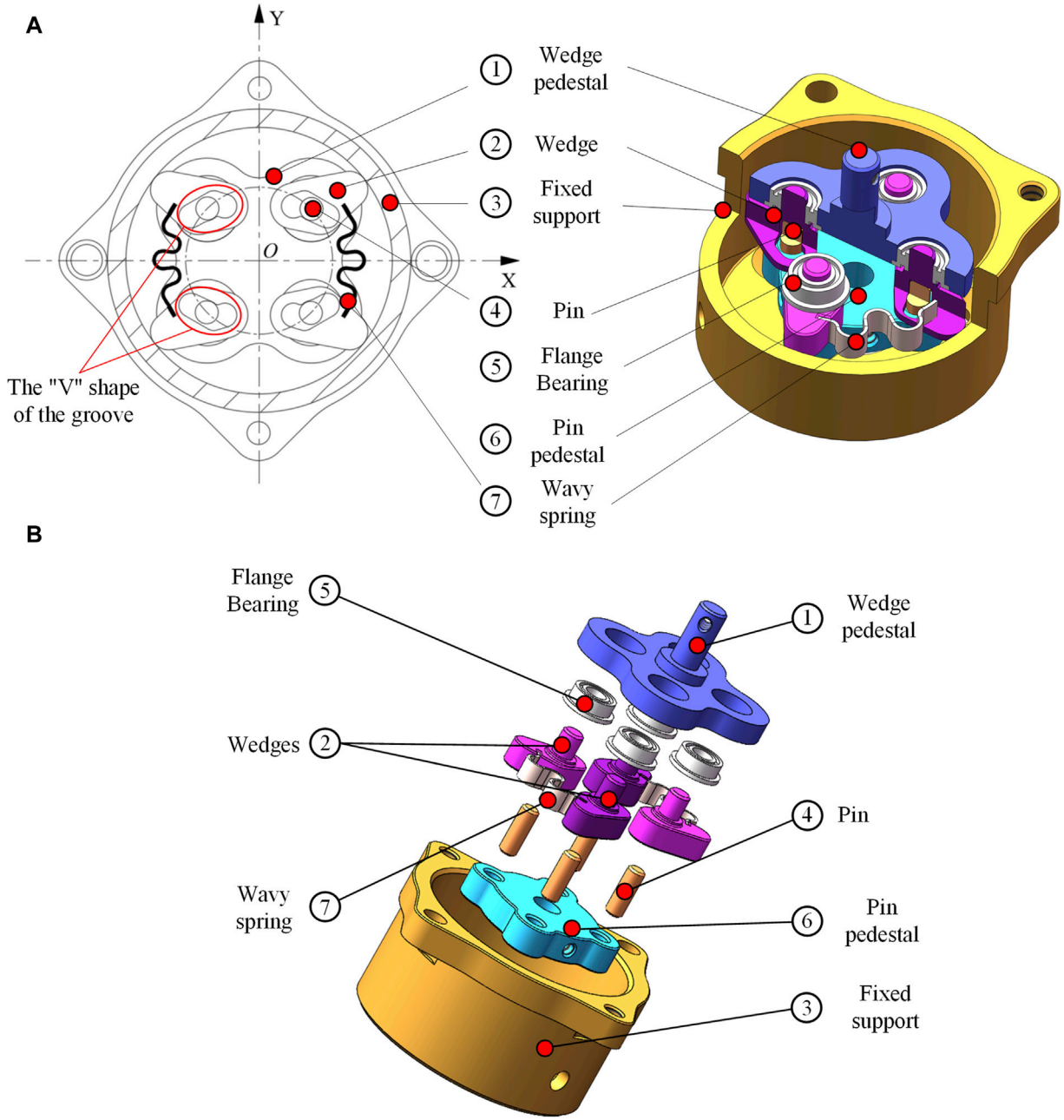

FIGURE 2
NBDC section view and exploded view. **(A)** Section view. **(B)** Exploded view.

angle of the wedge pedestal as the output end increases by the same amount as that of the input end.

(2) When the input end drives the pin pedestal to rotate, each set of wedges will gradually detach from the inner wall of the fixed support for a certain distance, and the nearest part between the wedges and the fixed support is a section of arc, the radius of which is r_{fillet}, and the distance from the center of the arc to the center of rotation of the wedges is $d_{cfillet}$. In the 1st quadrant, the initial angle of the line between the center of the arc and the center of the wedge is $\theta^1_{cfillet}$. In the 4th quadrant, the initial angle is $\theta^4_{cfillet}$. Therefore, the position of the centers of the arcs at the tips of the two wedges at any instant are in Eq. 6:

$$\begin{cases} \overrightarrow{OT_1} = \overrightarrow{OC_1} + d_{cfillet}\left[\cos\left(\theta^1_{cfillet} + \theta^1_{cam}\right) \ \sin\left(\theta^1_{cfillet} + \theta^1_{cam}\right)\right]^T \\ \overrightarrow{OT_4} = \overrightarrow{OC_4} + d_{cfillet}\left[\cos\left(\theta^4_{cfillet} + \theta^4_{cam}\right) \ \sin\left(\theta^4_{cfillet} + \theta^4_{cam}\right)\right]^T \end{cases} \tag{6}$$

The distance between the input angle θ_i and the distance between the 1st and 4th quadrants' wedges and the inner wall of the fixed support d^1_{cfix} and d^4_{cfix} satisfy Eq. 7:

$$\begin{cases} d^1_{cfix} = R_{fix} - \left\|\overrightarrow{OT_1}\right\| - r_{fillet} \\ d^4_{cfix} = R_{fix} - \left\|\overrightarrow{OT_4}\right\| - r_{fillet} \end{cases} \tag{7}$$

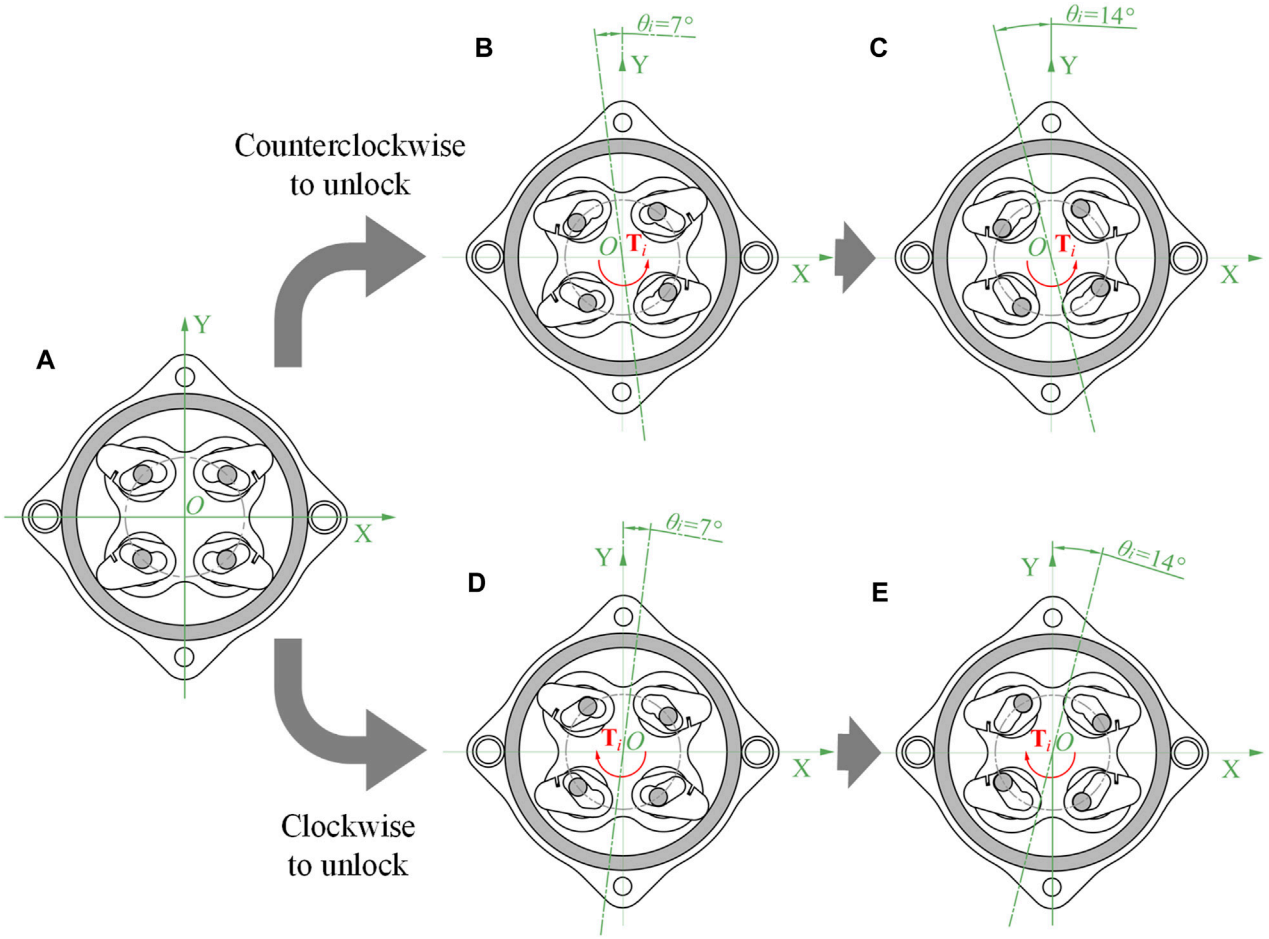

FIGURE 3
Five key states of the NBDC mechanism (spring not drawn). **(A)** Self-locking state. **(B)** Counterclockwise intermediate state of unlocking. **(C)** Counterclockwise unlocking state. **(D)** Clockwise intermediate state of unlocking. **(E)** Clockwise unlocking state.

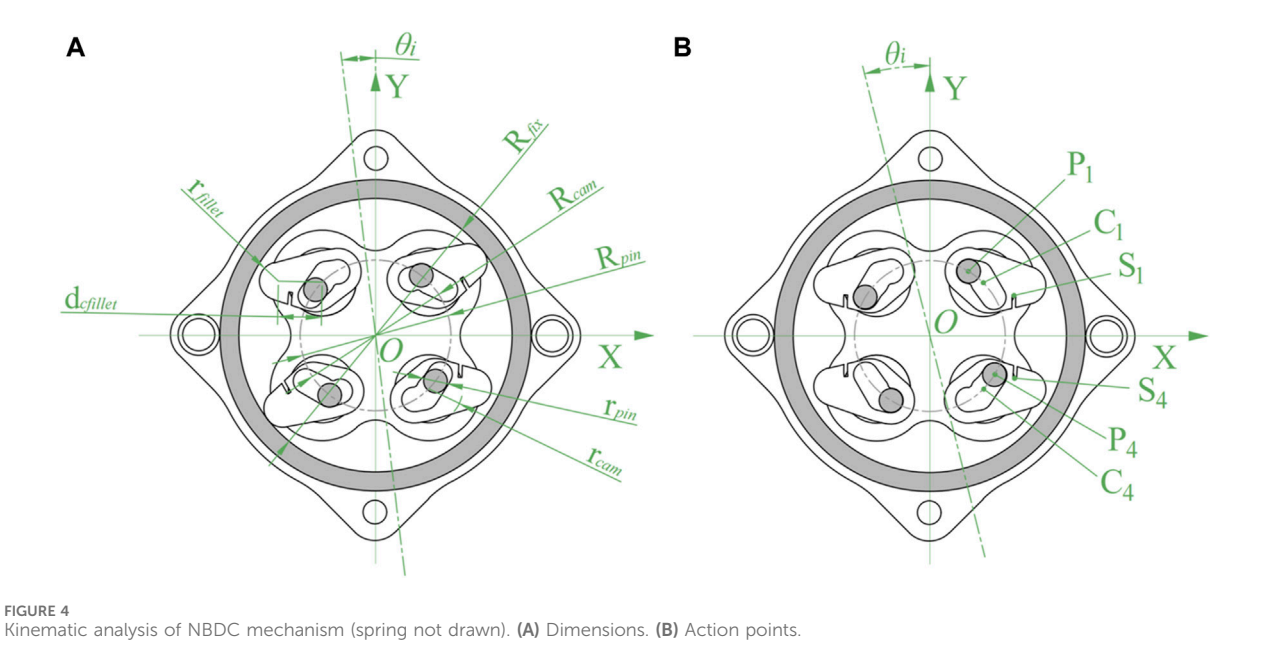

FIGURE 4
Kinematic analysis of NBDC mechanism (spring not drawn). **(A)** Dimensions. **(B)** Action points.

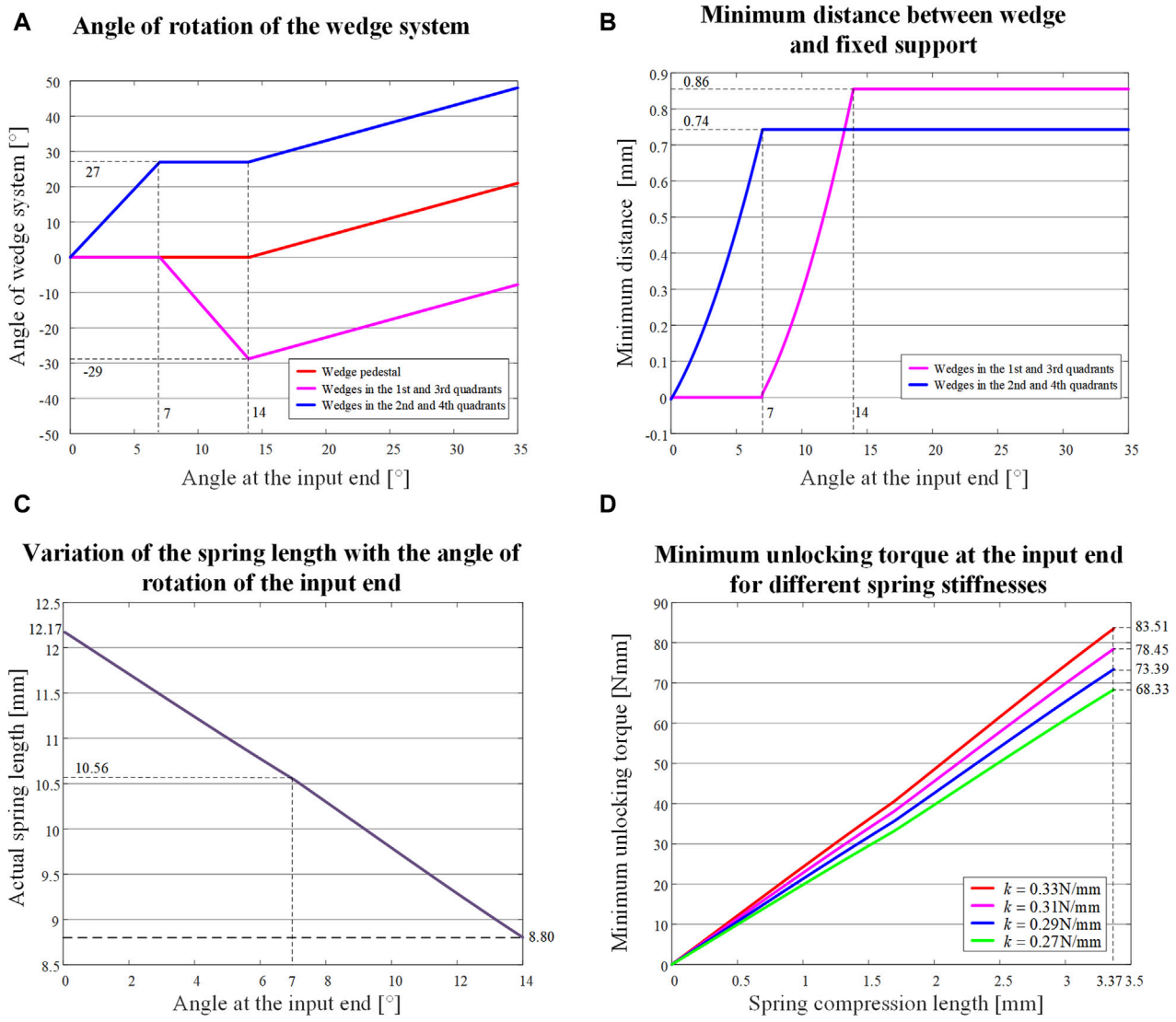

FIGURE 5
Variation of relevant parameters of the NBDC system with the angle of counterclockwise input. **(A)** Angle of the wedge and the wedge pedestal. **(B)** Minimum distance of the edge of the wedge from the inner wall of the fixed support. **(C)** Length of the spring. **(D)** Minimum unlocking torque of the input end with the compression length of the spring for different spring stiffnesses.

The input angle θ_i against the distance between the wedge and the inner wall of the fixed support is shown in Figure 5B. The maximum value of the minimum distance between the wedge and the inner wall of the fixed support in the 1st and 3rd quadrants is 0.86 mm, and the maximum value of the minimum distance between the wedge and the inner wall of the fixed support in the 2nd and 4th quadrants is 0.74 mm, which ensures that the relative motion in the unlocked state generates as little frictional wear as possible.

(3) During this process, the spring would be compressed to its shortest length. Taking the wavy spring between the wedges in the 1st and 4th quadrants as an example, the positions of the connection point between the spring and the two wedges at any time are shown in Eq. 8:

$$\begin{cases} \overrightarrow{OS_1} = \overrightarrow{OC_1} + d_{CS}\left[\cos\left(\theta_{CS}^1 + \theta_{cam}^1\right) \ \sin\left(\theta_{CS}^1 + \theta_{cam}^1\right)\right]^T \\ \overrightarrow{OS_4} = \overrightarrow{OC_4} + d_{CS}\left[\cos\left(\theta_{CS}^4 + \theta_{cam}^4\right) \ \sin\left(\theta_{CS}^4 + \theta_{cam}^4\right)\right]^T \end{cases} \tag{8}$$

where the distance from the connection point of the top of the wavy spring to the center of rotation of the wedge is d_{CS}, and the initial angles of the line connecting the connection point to the centers of rotation of the wedge in the 1st and 4th quadrants are θ_{CS}^1 and θ_{CS}^4. The length of the wavy spring can be calculated from the distance between the two connection points shown in Eq. 9:

$$L_s = \left\|\overrightarrow{OS_1} - \overrightarrow{OS_4}\right\| = \left\|\overrightarrow{S_4S_1}\right\| \tag{9}$$

The relationship of the input angel θ_i against the length of the spring L_s (the original length of the spring is L_{s0}) is shown in Figure 5C. As the input angle increases, the length of the wavy spring

is shortened from 12.17 mm to 10.56 mm in the first stage of 0°–7°, and further shortened from 10.56 mm to 8.80 mm in the second stage of 7°–14°, where the total shortage was 3.37 mm.

In the phase after Figure 3C, the pins no longer move with respect to the wedges, and the wedges no longer continue to rotate with respect to its own axis. The wedge pedestal at the output end follows the pin pedestal at the input end by the same angle $\theta_o = \theta_i - \theta_{iac}$.

2.2 Static analysis

The main function of the NBDC is to always remain locked when the load on the output end changes and to be able to unlock smoothly when power is supplied from the input end. In order to ensure the proper functioning of the mechanism, it is necessary to carry out force analysis for two different force conditions, which are torque $\mathbf{T}_i$ applied to the input end, and load torque $\mathbf{T}_o$ applied to the output end. When the self-locking requirements are met, the minimum friction coefficient between the wedge and the fixed support would be investigated, when the unlocking requirements are met, the reasonable stiffness of the wavy spring would be revealed.

2.2.1 Unlocking status analysis

Taking the counterclockwise input as an example, the initial state is the self-locking state shown in Figure 3A. When the system is subjected to counterclockwise input torque T_i, the pin pedestal drives the pins to rotate counterclockwise, i.e., C_i, $i = 1, 2, 3, 4$ rotates counterclockwise around the point O. In the 1st quadrant, the pin is not in contact with the groove of the wedge and can rotate freely. In the 4th quadrant, the pin is in contact with the groove of the wedge, generating a pressure $\mathbf{F}_{pin}^4$, which is given by the input torque $\mathbf{T}_i$ in Eq. 10:

$$\mathbf{T}_i = 2\left(\overrightarrow{OC_4} \times \mathbf{F}_{pin}^4\right) \tag{10}$$

The center of the pin P_4 is rotating along its trajectory, and the friction force $\mathbf{F}_T^4$ ($\mathbf{F}_T^4 = \mu_{cp} \cdot \mathbf{F}_{pin}^4$) is acting at the tangent point of the wedge Q_4 (moving along the inner wall of the groove of the wedge), μ_{cp} is the coefficient of friction between the surface of the pin and the inner surface of the groove of the wedge (when the pin is made of stainless steel, the wedge is made of 7,075 aluminum alloy, μ_{cp} = 0.4–0.7, take $\mu_{cp} = 0.6$). $\mathbf{F}_T^4$ exerts a torque $\overrightarrow{C_4Q_4} \times \mathbf{F}_T^4$ on the center of the wedge C_4. The wedge tends to rotate counterclockwise around the point C_4. We need to investigate whether friction exists at the point A_4, which is contacted between the wedge and the inner wall of the fixed support. The point T_4 is the center of the top arc of the wedge. Connect $\overrightarrow{C_4T_4}$ and extend it, intersecting the top arc of the wedge at point B_4. Since both $\overrightarrow{T_4B_4}$ and $\overrightarrow{T_4A_4}$ are arc radius, $\|\overrightarrow{T_4B_4}\| = \|\overrightarrow{T_4A_4}\|$. At the same time points C_4, T_4, A_4 are not collinear, therefore, Eq. 11 holds:

$$\begin{aligned}\left\|\overrightarrow{C_4B_4}\right\| &= \left\|\overrightarrow{C_4T_4} + \overrightarrow{T_4B_4}\right\| = \left\|\overrightarrow{C_4T_4}\right\| + \left\|\overrightarrow{T_4B_4}\right\| \\ &= \left\|\overrightarrow{C_4T_4}\right\| + \left\|\overrightarrow{T_4A_4}\right\| > \left\|\overrightarrow{C_4T_4} + \overrightarrow{T_4A_4}\right\| = \left\|\overrightarrow{C_4A_4}\right\|\end{aligned} \tag{11}$$

i.e., $\|\overrightarrow{C_4B_4}\| > \|\overrightarrow{C_4A_4}\|$ (identically $\|\overrightarrow{C_1B_1}\| > \|\overrightarrow{C_1A_1}\|$ in the 1st quadrant), and the distance from any point on the arc below point C_4 to point A_4 is less than $\|\overrightarrow{C_4A_4}\|$. Therefore, when the wedge is rotated counterclockwise, the top arc of the wedge is disengaged from the inner wall of the fixed support and there is no friction.

The spring between the two wedges $\|\overrightarrow{S_1S_4}\|$ is compressed and shortened due to the counterclockwise rotation of the wedges. In the 1st quadrant, the wedge tends to move counterclockwise due to the action of $\mathbf{F}_s^1$, but from the above derivation, $\|\overrightarrow{C_1B_1}\| > \|\overrightarrow{C_1A_1}\|$, so the wedge cannot rotate counterclockwise. As the spring deformation $\Delta s = L_s^{\theta_{iab}} - L_s^{0^\circ}$ becomes larger, $\mathbf{F}_s^4$ produces a clockwise torque $\overrightarrow{C_4S_4} \times \mathbf{F}_s^4$ in the 4th quadrant, where $\|\mathbf{F}_s^4\| = k \cdot |\Delta s| = k \cdot |(L_s^{\theta_{iab}} - L_s^{0^\circ})|$, k is the stiffness of the wavy spring. When the pin pedestal is rotated counterclockwise by 7°, as shown in Figure 3B, the pins in the 1st and 3rd quadrants start to contact the inner groove surface of their wedges, and the deformation of the springs reaches the maximum at this stage, at which time the total torque on the wedges in the 4th quadrant is $\mathbf{M}_{cam}^i$, shown in Eq. 12:

$$\mathbf{M}_{cam}^i = \overrightarrow{C_4Q_4} \times \mathbf{F}_T^4 + \overrightarrow{C_4S_4} \times \mathbf{F}_s^4 \tag{12}$$

Since the unlocking of the mechanism needs to keep the 4th quadrant wedge moving counterclockwise around the point C_4, specify the counterclockwise torque as positive and the clockwise torque as negative, it needs to satisfy Eq. 13:

$$\left\|\mathbf{M}_{cam}^4\right\| = \left\|\overrightarrow{C_4Q_4} \times \mathbf{F}_T^4\right\| - \left\|\overrightarrow{C_4S_4} \times \mathbf{F}_s^4\right\| > 0 \tag{13}$$

Substituting Eq. 10 into Eq. 13 yields Eq. 14:

$$\left\|\mathbf{F}_{pin}^4\right\| > \frac{k \cdot \left\|\overrightarrow{C_4S_4}\right\|}{\mu_{cp} \cdot r_{pin}} \cdot \left(L_s^{0^\circ} - L_s^{7^\circ}\right) \tag{14}$$

Define the angle between $\overrightarrow{OC_i}$ and $\mathbf{F}_{pin}^i$, $i = 1, 2, 3, 4$ as γ_{CP}^i, $\overrightarrow{OC_i}$ and $\mathbf{F}_s^i$, $i = 1, 2, 3, 4$ as γ_{CS}^i. In the process from Figures 3A, B, the variation of γ_{CP}^4 ranges from 17° to 0°, then $\mathbf{T}_i$ can be represented in Eq. 15:

$$\|\mathbf{T}_i\| = 2 \times \left(\left\|\overrightarrow{OC_4}\right\| \cdot \left\|\mathbf{F}_{pin}^4\right\| \cdot \sin\left(\gamma_{CP}^4\right)\right) \tag{15}$$

Substituting Eq. 15 into Eq. 14 yields Eq. 16:

$$\|\mathbf{T}_i\| > \frac{2k}{\mu_{cp}} \cdot \frac{R_{cam} \cdot d_{CS}}{r_{pin}} \cdot \left(L_s^{0^\circ} - L_s^{7^\circ}\right) \cdot \sin\left(\gamma_{CP}^4\right) \cdot \sin\left(\gamma_{CS}^4\right) \tag{16}$$

Due to $\sin(\gamma_{CP}^4) \cdot \sin(\gamma_{CS}^4) \le 1$, Eq. 17 can be got:

$$\left\|\mathbf{T}_{iab}^{cri}\right\| = \frac{2k}{\mu_{cp}} \cdot \frac{R_{cam} \cdot d_{CS}}{r_{pin}} \cdot \left(L_s^{0^\circ} - L_s^{7^\circ}\right) \tag{17}$$

The minimum unlocking torque at the input for the process from Figures 3A, B can be calculated as $\mathbf{T}_{iab}^{cri}$, and the magnitude of this value depends on the stiffness k of the wavy spring, provided that the dimensions of the structure and the material of the part are determined. The static analysis of this process is shown in Figure 6A.

When the input is in the intermediate state of counterclockwise unlocking, the pins in the 1st and 3rd quadrants are just touching the inner wall of the wedge grooves. At this point, the pins exert positive pressure on the inner wall only in the 1st and 3rd quadrants $\mathbf{F}_{pin}^1$ and $\mathbf{F}_{pin}^3$ (the $\mathbf{F}_{pin}^2$ and $\mathbf{F}_{pin}^4$ disappear in the 2nd and 4th quadrants because the pins' trajectory coincides with the groove trajectory).

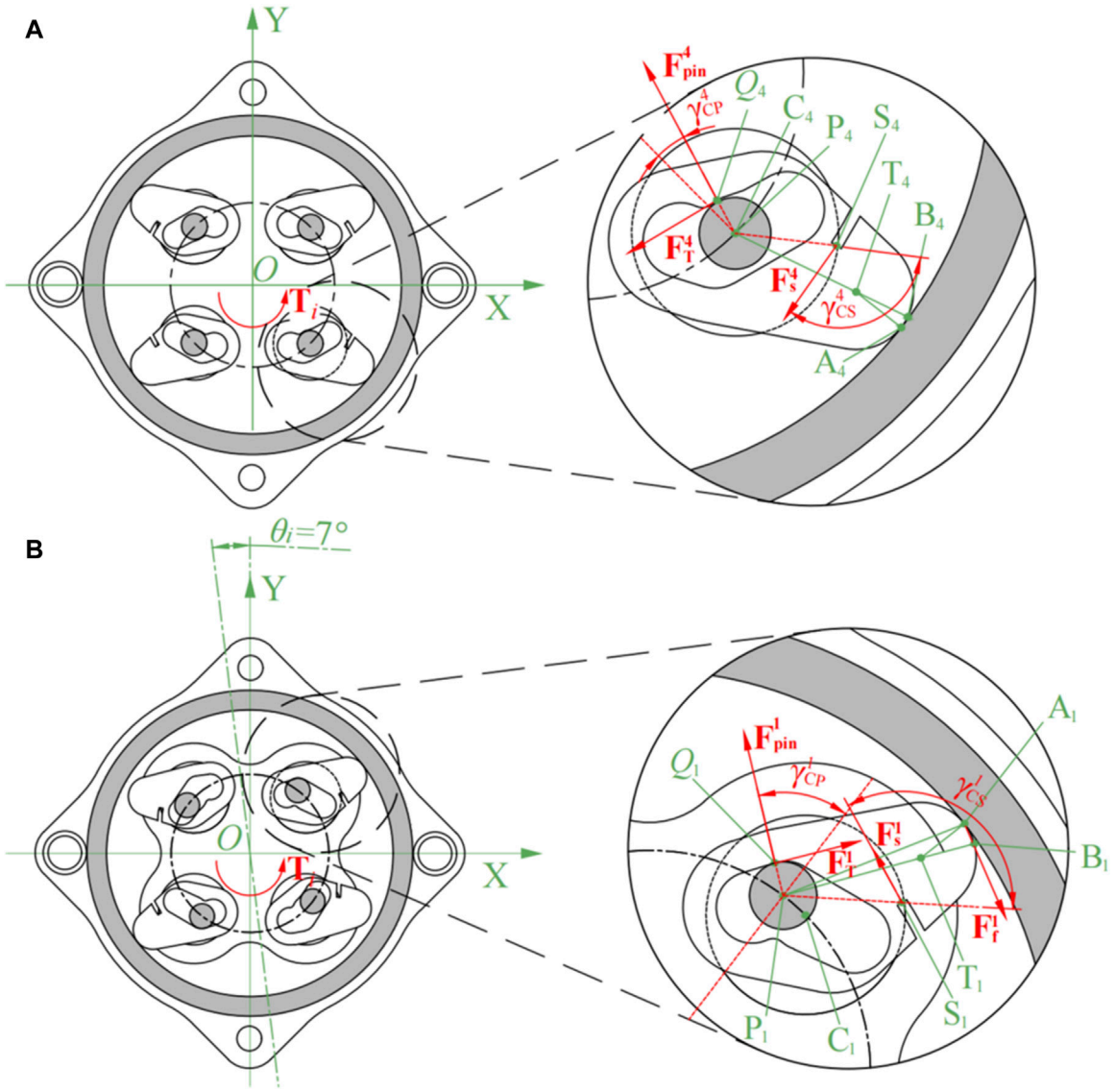

FIGURE 6
Mechanical analysis of the unlocking process (spring not drawn). **(A)** The initial counterclockwise rotate. **(B)** The input rotated 7° counterclockwise.

There is a tendency for the pins in the 1st and 3rd quadrants to slide counterclockwise, generating a corresponding friction force at the point of contact, and the wedges are subjected to a corresponding reverse friction force $\mathbf{F}^1_{\mathrm{T}}$ and $\mathbf{F}^3_{\mathrm{T}}$ ($\mathbf{F}^1_{\mathrm{T}} = \mu_{cp} \cdot \mathbf{F}^1_{pin}$; $\mathbf{F}^3_{\mathrm{T}} = \mu_{cp} \cdot \mathbf{F}^3_{pin}$). Due to the symmetry of the system, the input torque is $\mathbf{T}_i = 2(\overrightarrow{\mathrm{OC_i}} \times \mathbf{F}^1_{pin})$. Since $\|\overrightarrow{\mathrm{C_1B_1}}\| > \|\overrightarrow{\mathrm{C_1A_1}}\|$, when the wedge tends to rotate clockwise around the point $\mathrm{C_1}$, point A_1 detaches from the wall of the fixed support. At the same time, the distance from any point above it to the point $\mathrm{C_1}$ is smaller than $\|\overrightarrow{\mathrm{C_1A_1}}\|$, the friction $\mathbf{F}^1_f$ disappears. Smooth unlocking only requires the fulfilment of $\|\mathbf{M}^1_{cam}\| = \|\overrightarrow{\mathrm{C_1Q_1}} \times \mathbf{F}^1_{\mathrm{T}}\| - \|\overrightarrow{\mathrm{C_1S_1}} \times \mathbf{F}^1_s\| > 0$, as shown in Eq. 18:

$$\left\|\mathbf{F}^1_{pin}\right\| > \frac{k \cdot \mathrm{d_{CS}}}{\mu_{cp} \cdot \mathrm{r}_{pin}} \cdot \left(L^{0^\circ}_s - L^{7^\circ}_s\right) \cdot \sin\left(\gamma^1_{\mathrm{CS}}\right) \tag{18}$$

Owing to Eq. 19:

$$\|\mathbf{T}_i\| = \left\|2\left(\overrightarrow{\mathrm{OC_i}} \times \mathbf{F}^1_{pin}\right)\right\| = 2 \times \left(\mathrm{R}_{cam} \cdot \left\|\mathbf{F}^1_{pin}\right\| \cdot \sin\left(\gamma^1_{\mathrm{CP}}\right)\right) \tag{19}$$

Substituting Eq. 19 into Eq. 18 yields Eq. 20:

$$\|\mathbf{T}_i\| > \frac{2k}{\mu_{cp}} \cdot \frac{\mathrm{R}_{cam} \cdot \mathrm{d_{CS}} \cdot \left(L^{0^\circ}_s - L^{7^\circ}_s\right)}{\mathrm{r}_{pin}} \cdot \sin\left(\gamma^1_{\mathrm{CP}}\right) \cdot \sin\left(\gamma^1_{\mathrm{CS}}\right) \tag{20}$$

Due to $\sin\left(\gamma^1_{\mathrm{CP}}\right) \cdot \sin\left(\gamma^1_{\mathrm{CS}}\right) \leq 1$ and $L^{14^\circ}_s < L^{7^\circ}_s$, we have Eq. 21:

$$\left\|\mathbf{T}^{cri}_{iac}\right\| = \frac{2k}{\mu_{cp}} \cdot \frac{\mathrm{R}_{cam} \cdot \mathrm{d_{CS}} \cdot \left(L^{0^\circ}_s - L^{14^\circ}_s\right)}{\mathrm{r}_{pin}} \tag{21}$$

For smooth unlocking, the input torque should be at least $\mathbf{T}^{cri}_{iac}$ and $\|\mathbf{T}^{cri}_{iac}\| > \|\mathbf{T}^{cri}_{iab}\|$. Due to the symmetry of the mechanism, $\|\mathbf{T}^{cri}_{iac}\| = \|\mathbf{T}^{cri}_{iae}\|$, $\mathbf{T}^{cri}_{iae}$ is the minimum torque for clockwise unlocking of the input. Substituting the relevant parameters, the

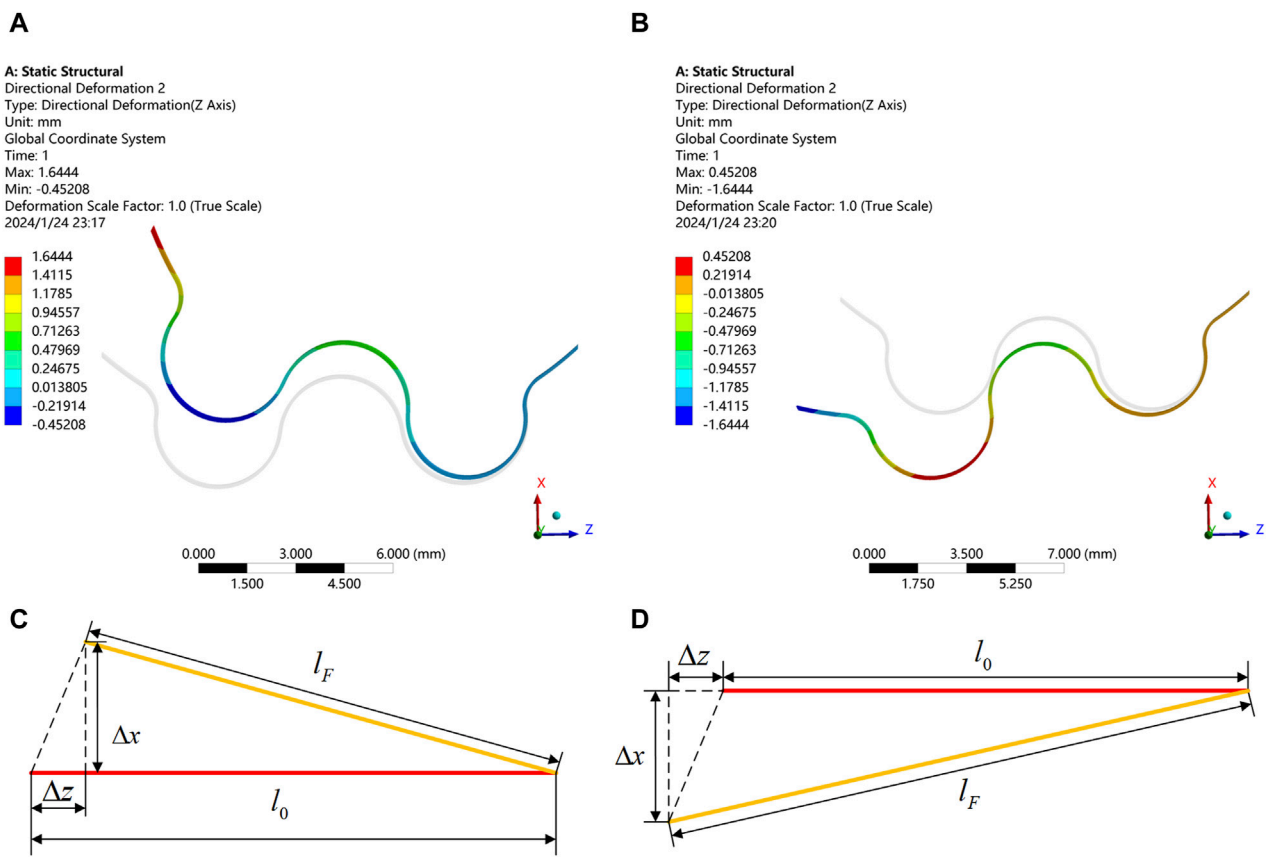

FIGURE 7
Static simulation of wavy spring in compression and tension. **(A)** Compression displacement of spring in Z-direction. **(B)** Tension displacement of spring in Z-direction. **(C)** Compression variation of spring in Z-direction. **(D)** Tension variation of spring in Z-direction.

relationship between the torque and the stiffness k (Nmm) of the wavy spring can be found as in Eq. 22:

$$\left\|\mathbf{T}_{iac}^{cri}\right\| = \left\|\mathbf{T}_{iae}^{cri}\right\| = k \cdot 253.06 \text{ (Nmm)} \tag{22}$$

After the aforementioned process, the pin pedestal continues to rotate counterclockwise by 7° as shown from Figures 3B, C, and the static analysis is shown in Figure 6B. In order to investigate the influence of the thickness and material on the stiffness of wavy spring, simulations were carried out using hydrostatic simulation software. The specific analytical settings for the wavy spring's thickness was 0.1 mm, and the material was 301 stainless steels. The horizontal direction was set to be the Z-axis. In Figure 7A, the right end of the wavy spring was fixed and a compression force of 0.5 N was applied to the left end of the wavy spring. In Figures 7A, B pulling force of 0.5 N was applied to the left end of the wavy spring with the right end fixed. It can be seen from Figures 7A, B that the wavy spring was both deformed by 1.6444 mm under the load of 0.5 N in either direction. To better convey the idea, the simplified the model in these two cases are shown in Figures 7C, D.

The stiffness of the spring is calculated with Eq. 23:

$$k = \frac{F}{\Delta z} = \frac{0.5}{1.6444} = 0.304 \text{ N/mm} \tag{23}$$

Substituting Eq. 22 into Eq. 23 yields Eq. 24:

$$\left\|\mathbf{T}_{iac}^{cri}\right\| = \left\|\mathbf{T}_{iae}^{cri}\right\| \approx 0.304 \times 253.06 = 76.95 \text{ Nmm} \tag{24}$$

When considering the spring manufacturing accuracy, the stiffness variation range is taken as 0.270–0.330 N/mm, the variation of the minimum unlocking torque of the system with the compression length of the spring is shown in Figure 5D. For smooth unlocking, the minimum unlocking torque should be around 65–85 Nmm.

2.2.2 Self-locking status analysis

When the input torque is less than the critical starting torque $\mathbf{T}_{iac}^{cri}$ or $\mathbf{T}_{iae}^{cri}$, the spring releases to drive the two wedges to contact the inner wall of the fixed support, at this point, the system enters the self-locking state. In this state, the output end applies force to the wedge through the wedge pedestal, and the mechanical analysis of the output end is shown in Figure 8.

Since the wedge pedestal provide the rotational torque through the flange bearings, the forces acting on each of the four wedges are $\mathbf{F}_{Nc}^{i}$, $i = 1, 2, 3, 4$, $\mathbf{T}_o = 2(\overrightarrow{OC_1} \times \mathbf{F}_{Nc}^{1} + \overrightarrow{OC_4} \times \mathbf{F}_{Nc}^{4})$. At the top of the wedge are reaction force $\mathbf{F}_{Nf}^{i}$, $i = 1, 2, 3, 4$ from the wall of the fixed support and the corresponding frictions are $\mathbf{F}_{f}^{i}$, $i = 1, 2, 3, 4$. In the 2nd and 4th quadrants, the combined force of $\mathbf{F}_{Nc}^{i}$, $\mathbf{F}_{Nf}^{i}$, $\mathbf{F}_{f}^{i}$, $i = 2, 4$, acts on points C_2 and C_4, so that the wedges tend to rotate counterclockwise with respect to their respective centers of rotation. Taking the 4th quadrant wedge as an example, when

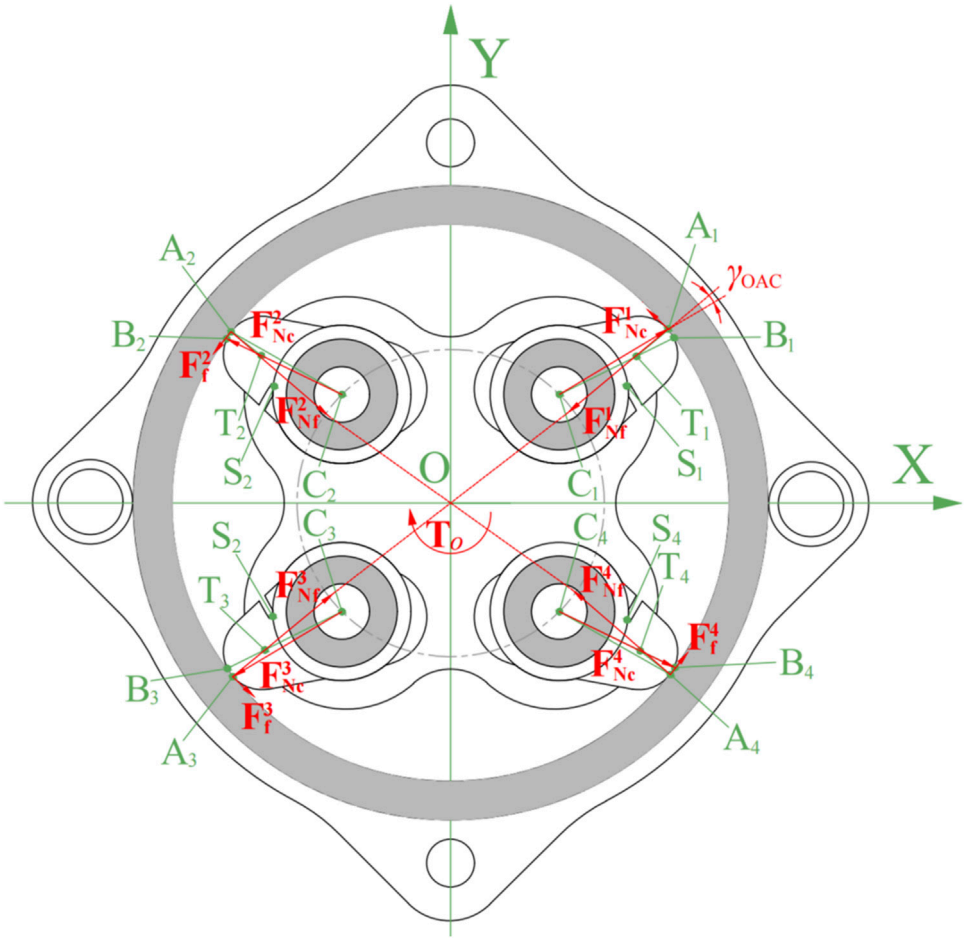

FIGURE 8
Static analysis of the system with counterclockwise loading torque at the output end under self-locking stage (spring not drawn).

the wedge is rotated by a certain angle, the wedge is no longer tangent to the fixed support wall, and $\mathbf{F}_{Nf}^{4}$ and $\mathbf{F}_{f}^{4}$ disappear, the wedge would return into a steady state. Assume the system reaches a self-locking state, the angle between $\overrightarrow{OA_1}$ and $\overrightarrow{C_1A_1}$ is γ_{OAC}, we get Eq. 25:

$$\begin{cases} \left\|\mathbf{F}_{Nf}^{1}\right\| = \left\|\mathbf{F}_{Nc}^{1}\right\| \cdot \cos\left(\gamma_{OAC}\right) \\ \left\|\mathbf{F}_{f}^{1}\right\| = \left\|\mathbf{F}_{Nc}^{1}\right\| \cdot \sin\left(\gamma_{OAC}\right) \end{cases} \tag{25}$$

At this point, friction $\|\mathbf{F}_f^1\|$ is less than maximum friction $\|\mathbf{F}_f^1\|_{\max} = \mu_{cf} \cdot \|\mathbf{F}_{Nf}^1\|$, i.e., $\|\mathbf{F}_f^1\| < \mu_{cf} \cdot \|\mathbf{F}_{Nf}^1\|$. Substitute into Eq. 25, and we can get Eq. 26:

$$\mu_{cf} > \tan\left(\gamma_{OAC}\right) \approx 0.158 \tag{26}$$

It can be seen that when the coefficient of friction between the wedge and the inner wall of the fixed support meets the requirements, regardless of the torque applied in any direction at the output end, it will cause instant self-locking. However, when the load torque is too large, causing excessive deformation of the curved surface at the top of the wedge, i.e., $\|C_iB_i\| \le \|C_iA_i\|$, the self-locking will fail, and this process would be demonstrated in the following simulations and experiments.

2.3 Transient dynamic simulations and analysis

In order to verify the accuracy of the above theoretical analysis, simulation work was also carried out. The platform was Workbench of ANSYS 2020R2, with the transient dynamics analysis module. The transient dynamics model can effectively analyze the impact of external shocks on the system. On the one hand, it can be verified whether the system can be unlocked when the input end is rotated in the self-locking state. On the other hand, the system self-locking performance of the output end under load can be verified. To reduce the complexity of the iteration without affecting the simulation results, the spring force was simplified to be the maximum force at the compression extreme. This is because the minimum unlocking moment of the system depends on the stiffness k of the wavy spring.

In order to verify the unlocking performance of the input end, the displacement and stress of the wedge when rotating by 7° and 14° in counterclockwise and clockwise were investigated, respectively. Figures 9A, E describe the counterclockwise and clockwise unlocking intermediate states (rotate by 7°) respectively, and the corresponding stress values are shown in Figures 9B, F. The stress maxima are basically the same, which are all lower than 50 MPa,

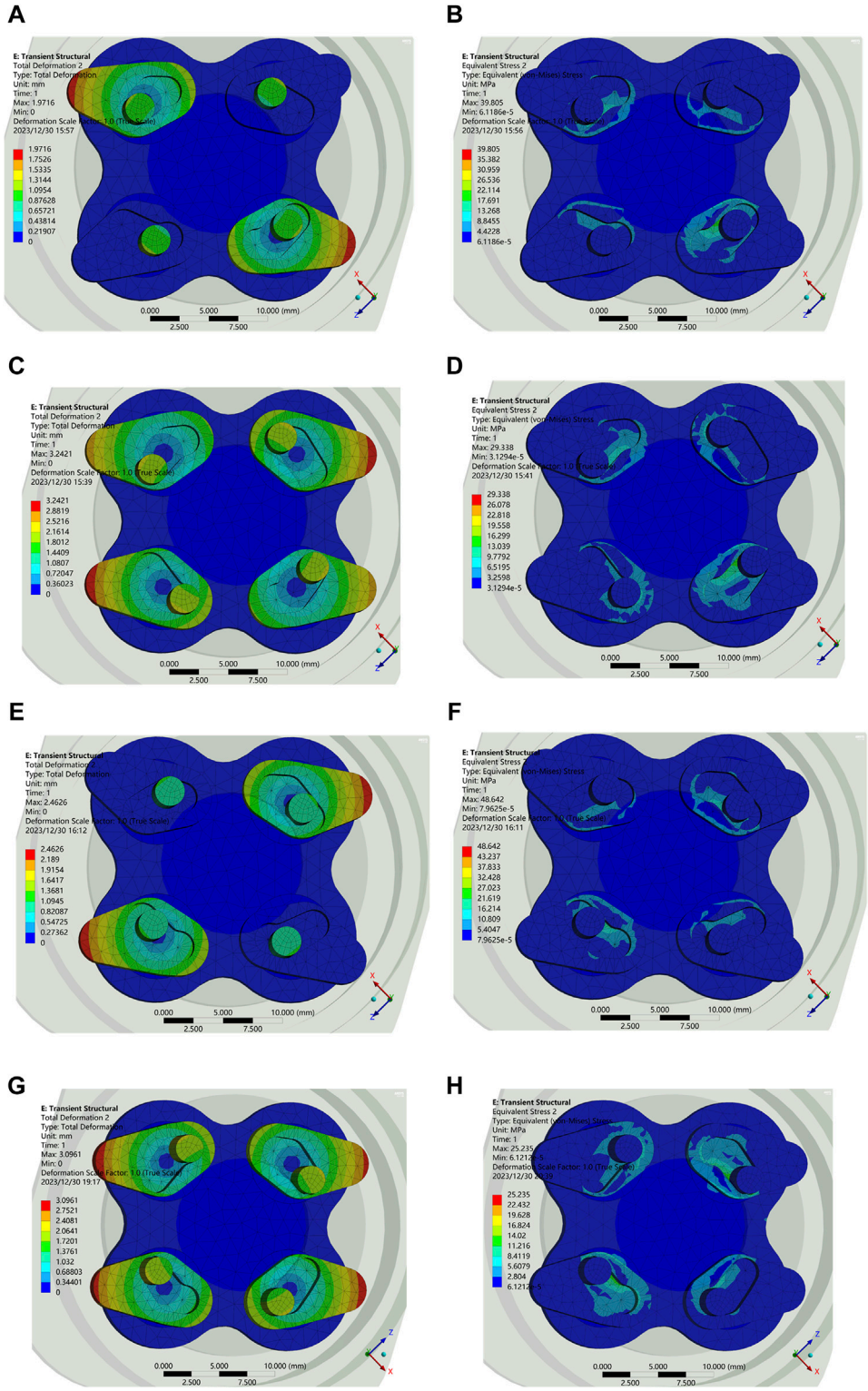

FIGURE 9
Displacement and stress. **(A)** Displacement at 7° counterclockwise. **(B)** Stress at 7° counterclockwise. **(C)** Displacement at 14° counterclockwise. **(D)** Stress at 14° counterclockwise. **(E)** Displacement at 7° clockwise. **(F)** Stress at 7° clockwise. **(G)** Displacement at 14° clockwise. **(H)** Stress at 14° clockwise.

within the nominal value of 7,075 aluminum alloy. The simulation results are consistent with the design in Figures 3B, D. Similarly, Figures 9C, G are the displacement for 14° counterclockwise and clockwise rotations of the input, and their corresponding stress diagrams are in Figures 9D, H, which is also in accordance with Figures 3C, E.

In order to verify the self-locking performance of the output end, the arc surface strain at the top of the wedge is set to be $\varepsilon = 0.2\%$,

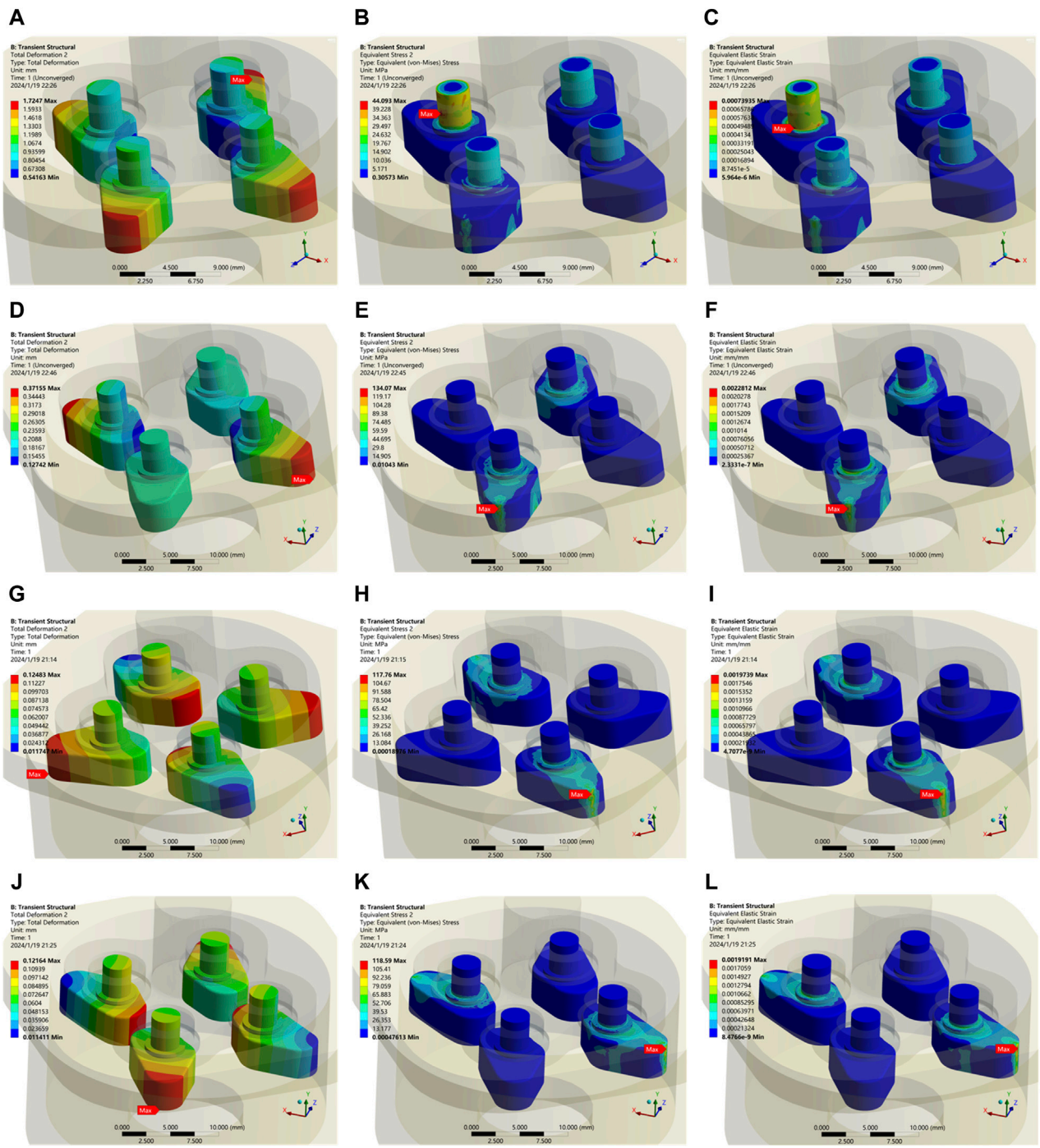

FIGURE 10
Transient dynamic analysis of the output end with applied load. **(A)** Self-locking failure with displacement of the wedge. **(B)** Stress in the wedge in self-locking failure. **(C)** Strain in the wedge in self-locking failure. **(D)** Displacement of the wedge in the state under μ_{cf} = 0.16, T_o = 600 Nmm. **(E)** Stress in the wedge under μ_{cf} = 0.16, T_o = 600 Nmm. **(F)** Displacement of the wedge under μ_{cf} = 0.16, T_o = 600 Nmm. **(G)** Displacement of the wedge under μ_{cf} = 0.25, T_o = 600 Nmm. **(H)** Stress in the wedge under μ_{cf} = 0.25, T_o = 600 Nmm. **(I)** Displacement of the wedge under μ_{cf} = 0.25, T_o = 600 Nmm. **(J)** Displacement of the wedge under μ_{cf} = 0.25, T_o = −600 Nmm. **(K)** Stress in the wedge under μ_{cf} = 0.25, T_o = −600 Nmm. **(L)** Displacement of the wedge under μ_{cf} = 0.25, T_o = −600 Nmm.

which is used as the boundary of self-locking failure (Karbalaei Akbari et al., 2013). The performance of clockwise and counterclockwise loads on the shaft of the wedge pedestal is verified respectively. The load was set from 100 Nmm to 800 Nmm with a step of 100 Nmm. When μ_{cf} = 0.15 and T_o = 100 Nmm, the self-locking experience a failure, and all four wedges are displaced, as shown in Figure 10A. The stress is concentrated at the cylindrical surface where the wedge is in contact with the flange bearing, and the maximum strain is also at 0.074%, as shown in Figures 10B, C, respectively. When μ_{cf} =

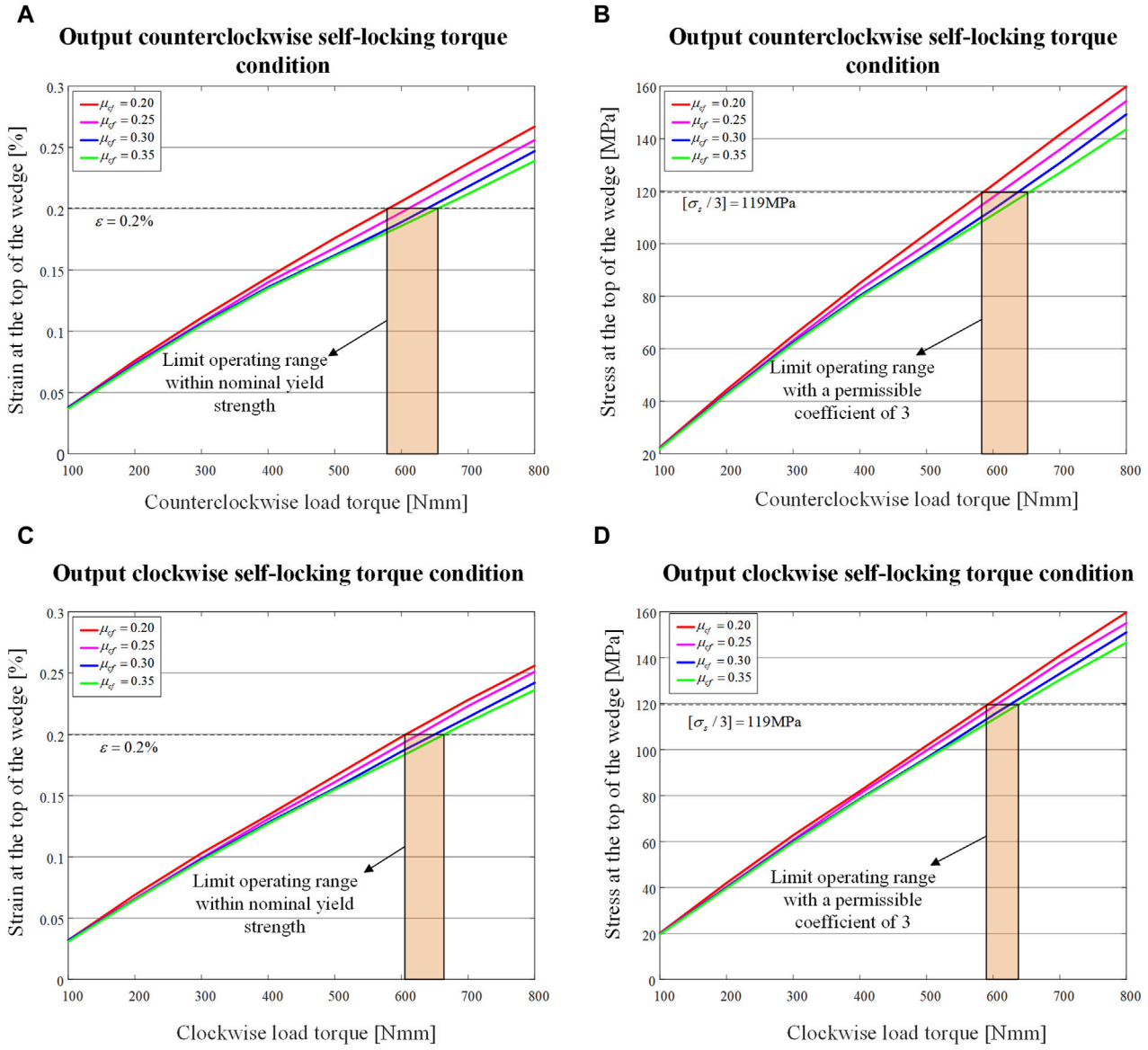

FIGURE 11
Maximum stress and maximum strain at the top of the wedge when load torque is applied to the output end for different values of μ_{cf}. **(A)** Maximum strain curve of the wedge when load torque is applied counterclockwise. **(B)** Maximum stress curve of the wedge when load torque is applied counterclockwise. **(C)** Maximum strain curve of the wedge when load torque is applied clockwise. **(D)** Maximum stress curve of the wedge when load torque is applied clockwise.

0.16 and $\mathbf{T}_o$ = 600 Nmm, the self-locking function well, justifying Eq. 26. However, at this point, the wedges in the 2nd and 4th quadrants complete the self-locking process, the maximum stress value is 134.07 MPa, the strain is 0.228% > 0.2%, as shown in Figures 10D–F, respectively. It can be concluded that μ_{cf} = 0.16 is not the ideal friction coefficient for the self-locking system.

For further investigation, the range of μ_{cf} is set to be from 0.20 to 0.35 with a step size of 0.05. When $\mathbf{T}_o$ = 600 Nmm (positive is counterclockwise, negative is clockwise) and μ_{cf} = 0.25, the corresponding displacements, stresses and strains are shown in Figures 10G–I, the displacement of the top of the wedges in the 2nd and 4th quadrants is 0.0117 mm, the system completes self-locking with a strain of 0.197% and a maximum stress of 117.76 MPa. When $\mathbf{T}_o$ = −600 Nmm and μ_{cf} = 0.25, the corresponding displacements, stresses and strains are shown in Figures 10J, K, L, the displacement of the top of the wedges in the 1st and 3rd quadrants is 0.0114 mm, the system completes self-locking with a strain of 0.192% and a maximum stress 118.59 MPa.

The maximum stress and strain at the top of the wedge for different values of μ_{cf} are plotted against the load are shown in Figure 11.

The overall trend is that as $\mathbf{T}_o$ increases, the stress at the top of the wedge increases linearly, and as μ_{cf} increases, the maximum stress tends to decrease. Excessively large μ_{cf} often causes wear problems when the system works for a long time, so μ_{cf} = 0.25 is the preferred value. Bounded by a strain of 0.2% at the nominal yield stress, the bi-directional self-locking torque at the load side of the system is about 600 Nmm (greater than this value also allows self-locking, but carries the risk of irreversible deformation of the wedge, which needs to be

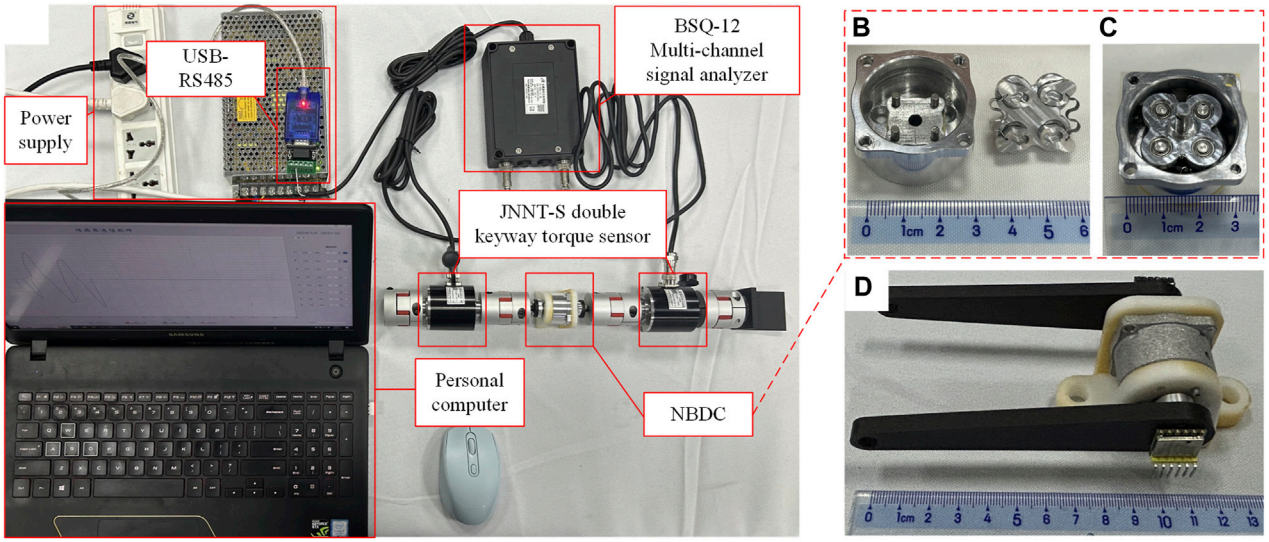

FIGURE 12
NBDC torque test experimental setup. **(A)** Experimental setup. **(B)** NBDC components. **(C)** Assembled NBDC. **(D)** NBDC unlocking test.

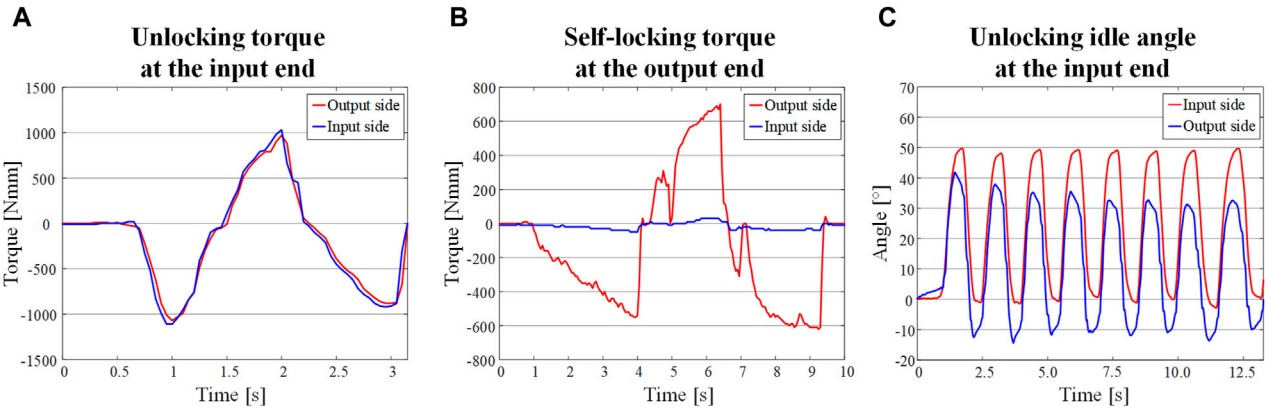

FIGURE 13
Unlocking and self-locking experiments of the NBDC. **(A)** Bidirectional unlocking torque change at the input end. **(B)** Self-locking torque change at the output end. **(C)** Unlocking idle angle at the input end.

verified experimentally). In the study by R Muraliraja et al. (Muraliraja et al., 2019), the ultimate yield stress of the 7,075 aluminum alloy is σ_s = 357 MPa. When the strain is 0.197%, close to the nominal yield strength of 0.2%, the stress is 117.76 MPa, which is about 1/3 of the ultimate yield stress, meaning that the safety allowable factor is 3, as indicated in the stress-torque diagram in Figures 11B, D.

By drawing a boundary line $[\sigma_s/3]$ = 119 MPa, it can be found that the extreme working range of the self-locking system under this boundary condition is basically consistent with the working range under the ε = 0.2% condition (see in Figures 11A, C).

3 Experimental analysis of NBDC

According to the previous analysis, a 3D model was established, and a prototype was assembled. The pin pedestal, wedge pedestal, wedges and fixed support are made of aluminum alloy (7,075 series), wavy springs were customized (stainless steel, 301 series, stiffness is around 0.30 N/mm), the four pins were selected as standard parts (stainless steel, 304 series, Φ 2.5 × 8), the four flange bearings are standard MF63ZZ 3 × 6 × 2.5 (bearing steel, 45#). The prototype is shown in Figures 12B, C, with a diameter of 33 mm and height of 15 mm, weighting 25.5 g.

The NBDC was positioned between two JNNT-S dual keyway torque transducers to test the unlocking torque from the input end and the maximum self-locking torque from the output end, which are shown in Figure 12A. The system configuration is as follows:

(1) The input end and output end were connected to the connecting flange through tightening screws, and then connected to the JNNT-S double keyway torque transducers through an elastic coupling (static torque

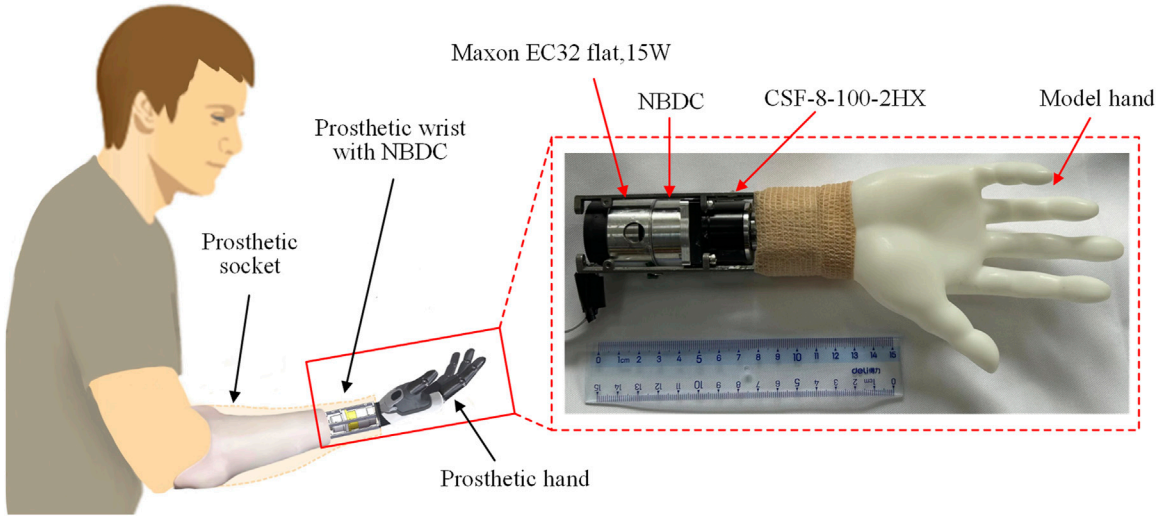

FIGURE 14
Schematic of the specific application of the NBDC mechanism to the prosthetic wrist.

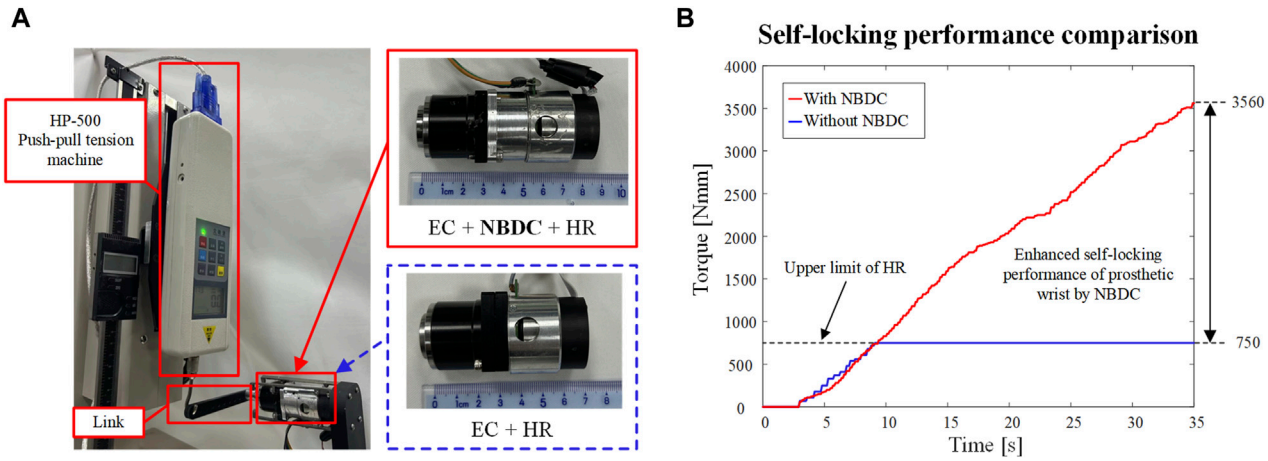

FIGURE 15
Experimental self-locking performance of NBDC in prosthetic wrist system. **(A)** The self-locking performance of the prosthetic wrist with and without the NBDC mechanism was tested separately. **(B)** Self-locking performance comparison.

transducer, movement range of 0°–180°, torque range of 0–20 Nm).

(2) JNNT-S double keyway torque transducer were connected to BSQ-12 multi-channel signal analyzer which connected to a computer via USB-RS485, outputting the synchronous torque of two transducers.

(3) Elastic coupling could eliminate the axis deviation of the overall transmission system, the transmission efficiency is 98%, which was negligible.

(4) By fixing the output end coupling, bidirectional torque could be transmitted to the input end, and the unlocking torque would be obtained through numerical analysis of the two sensors.

(5) By fixing the input end coupling, bidirectional torque could be exerted on the output end, and the maximum self-locking torque would be obtained through numerical analysis of the two sensors.

In order to test the bidirectional unlocking idle angle, a 10 cm long rocker was installed at the input end and the output end respectively to facilitate the experiment. The WT901164K angle sensors (sampling frequency is 2000 Hz) were placed at the center of the shafts to capture the angle changes of the two ports simultaneously, as shown in Figure 12D.

By applying torque to the input and output ends respectively, the corresponding response was recorded by the torque sensor. As shown in Figure 13A, when the input end is unlocked, the output torque lags the input torque change and the difference is within 80 Nmm. This value is the unlock torque of the system, which is basically the same as the theoretical value in Figure 5D. From the

TABLE 1 Mechanical requirements and wearability requirements for the NBDC mechanism.

Classification	Parameter	Unit	Value
Mechanical requirements	Required rotation angle	°	Not required
	Stiffness of the wavy spring	Nmm	0.27–0.33
	Unlocking torque of the input end	Nmm	65–80
	Maximum torque of the input end	Nmm	Not required
	Maximum torque of the output end	Nmm	Within 600
	μ_{cf}	—	More than 0.25
Wearability requirements	Height	mm	15
	Diameter	mm	33
	Weighting	g	25.5

results of transient dynamics, the self-locking torque of the system during normal operation is about 600 Nmm. When the load applied to the output is 600 Nmm, as shown Figure 13B, there is barely no torque response from the input end (less than 40 Nmm in both directions), which is consistent with the finite element simulation. The reason for the torque fluctuation at the input end is when the diagonal wedge self-locks, the other diagonal wedge rotates a slight angle, and during the rotation, the inner wall of the wedge groove transfers part of the force to the corresponding pin. The force is further transmitted to the torque sensor through the pin pedestal. This small torque will not cause back-driving phenomena at the input end. By rotating the rocker in both directions at the input end, it can be seen that the angular response of the output end is shifted by 14°, as shown in Figure 13C, which is consistent with design of the idle angle.

4 Applications with NBDC embedded in a prosthetic wrist

To better demonstrate how the proposed component could be used in practical applications, a prosthetic wrist with rotation function was built, integrating the proposed NBDC. There are three reasons for the chosen of the application scenario: (1) The rotational degree of freedom of the wrist is mostly used in practice (Seo et al., 2017). (2) The rotation of the wrist is prone to stay unchanged once reach the target angle (Neumann, 2016). (3) The physiological rotational movement of the human wrist comes from the rotation of the radius around the ulna, and the actual rotational movement occurs near the elbow joint. If the amputation was executed near the hand, the amputee would still retain some rotational function of the forearm and does not need a rotationally functional prosthetic wrist. Thus, the prosthetic wrist module with rotational freedom is suitable for amputees with amputations close to the elbow, providing ample space for the implementation of the prosthesis. Figure 14 illustrates the application scenario where the proposed locking component was integrated to a prosthetic wrist. The prosthetic wrist was attached to the amputee through a prosthetic socket, and the constituent components of the prosthesis from the socket to the hand were the driving motor, the self-locking component and the harmonic reducer respectively. The integrating of the proposed locking component would allow the transmission of the rotational motion of the motor to the load transparently, while the time-varying torque generated at the load side would be prevented from transmitting back by this component, which ensures the stability of the prosthetic joint and reduces the power consumption. The component, with a diameter of 33 mm and a length of 15 mm, weighting 25.5 g, could theoretically be integrated in series to any forearm joint except the hand without compromising the total weight and dimension, and thus has the potential to be widely used in prosthetic rotary joints.

Figure 15A illustrates the self-locking performance experiments of NBDC in a prosthetic wrist system, where the self-locking ability of the wrist joint was tested with and without NBDC, respectively, and the results are shown in Figure 15B. Since the harmonic reducer itself has certain self-locking capacity, the upper limit of the self-locking capacity of without the embedded NBDC component is 750 Nmm. By contrast, the self-locking capacity with the NBDC reaches 3560 Nmm in this experiment. It is worth pointing out that 3560 Nmm is not the upper limit of the system with the NBDC, but a safe experimental limit set to protect the harmonic reducer. From the calculation and analysis in Section 3, it can be seen that the theoretical upper limit could reach 600 × 100 = 60,000 Nmm under this condition. However, excessive loads would not occur in real application scenarios, and the improvement from 750 Nmm to 3560 Nmm could adequately demonstrate that the embedding of the NBDC mechanism could bring significant improvement in the self-locking performance of the rotary joint. The specific mechanical requirements and wearability requirements are summarized in Table 1.

5 Discussion

This paper designed a new type of NBDC mechanism, theoretically analyzed the self-locking conditions of the model and the influence of different friction coefficients on the self-locking performance, revealed that the friction coefficient μ_{cf} should be at least 0.16, as shown in Eq. 26, which was verified in a transient kinematic finite element simulation shown in Figure 10. The current locking torque of the mechanism is still not ideal, which

is mainly constrained by the materials of the two contact bodies. In this paper, 7,075 aluminum alloy is chosen due to the lightness, which is important for prosthetic wrists. If lightness is not the primary consideration, materials with higher yield strengths could be adopted to further increase the maximum locking torque. In the simulation for the performance of different μ_{cf}, as shown in Figure 11, a higher μ_{cf} is preferable to improve the locking torque, and the friction coefficient of the contact surfaces can be further improved by means of surface sandblasting, etc. However, the potential to improve the locking torque in this way is limited, so we chose $\mu_{cf} = 0.25$ as a representative case. In terms of the surface contact form, line contact is currently adopted in this study, which limits the performance to a certain extent, where further improvement could be expected by expanding the contact area. For the number of wedges, it is possible to follow M. Controzzi's research (Controzzi et al., 2017) by placing more wedges through dimensional optimization, further enhancing the self-locking performance. In terms of the idle angle, it only exists on the motor side, but not on the load side, which is to say, if the motor moves, it has to offset an idle angle before it starts to drive the load. The motion and force on the load side in any direction will not be transmitted to the motor side. In terms of the unlocking torque, the main constraint is the stiffness of the wavy spring. High stiffness will increase the unlocking torque and make it more difficult for the system to work properly. Low stiffness will potentially result in the failure of the spring or the inability to recover the self-locking state in the case of the maximum deformation. Therefore, the type of spring should be optimized in the future to reduce the unlocking torque of the system. During normal operation, driving from the motor requires a 14° idle rotation to trigger the unlocking state of the NBDC, which helps to reduce wear inside the mechanism, but would introduce a position error for the control system. Fortunately, this idle angle can be compensated by an external angle sensor.

6 Conclusion

In this paper, a novel NBDC is proposed, which can be applied in the forearm rotary motion joints of prosthetic wrists. It may save power to a certain extent under the premise of guaranteeing the safety and stability of manipulations. Detailed kinematic, static and transient dynamic analysis were carried out, and a prototype of the proposed design was assembled and tested to verify its self-locking and unlocking performance. Experimental results showed that the bidirectional self-locking torque of this NBDC for external load is about 600 Nmm, and the unlocking torque at the input end is about 80 Nmm. It is worth pointing out that connecting a reducer in series between the output end and the load can further expand the self-locking performance of the mechanism, thereby expanding its application scenarios.

Data availability statement

The original contributions presented in the study are included in the article/Supplementary material, further inquiries can be directed to the corresponding author.

Author contributions

YLi: Data curation, Formal Analysis, Investigation, Methodology, Project administration, Software, Writing–original draft, Writing–review and editing, Conceptualization, Validation. YLu: Formal Analysis, Investigation, Methodology, Project administration, Writing–original draft, Writing–review and editing, Data curation, Software, Validation. TX: Formal Analysis, Project administration, Supervision, Writing–original draft, Writing–review and editing. JL: Conceptualization, Formal Analysis, Methodology, Project administration, Writing–original draft, Writing–review and editing, Funding acquisition, Investigation, Resources, Supervision, Visualization.

Funding

The author(s) declare that financial support was received for the research, authorship, and/or publication of this article. This research was funded by the National Key R&D Program of China (2020YFC2007800) granted to Huazhong University of Science and Technology, and the National Natural Science Foundation of China (52005191 and 52027806).

Conflict of interest

The authors declare that the research was conducted in the absence of any commercial or financial relationships that could be construed as a potential conflict of interest.

Publisher's note

All claims expressed in this article are solely those of the authors and do not necessarily represent those of their affiliated organizations, or those of the publisher, the editors and the reviewers. Any product that may be evaluated in this article, or claim that may be made by its manufacturer, is not guaranteed or endorsed by the publisher.

References

Ann, N. K., Lin, W., and Ng, L. E. (2000). A new linear piezoelectric motor with self-lock feature. *Jpn. J. Appl. Phys.* 39, 1311–1313. doi:10.1143/jjap.39.l1311

Bajaj, N. M., Spiers, A. J., and Dollar, A. M. (2019). State of the art in artificial wrists: a review of prosthetic and robotic wrist design. *IEEE Trans. Robot.* 35, 261–277. doi:10.1109/tro.2018.2865890

Bandara, D. S. V., Gopura, R., Hemapala, K., and Kiguchi, K. (2014). "A multi-DoF anthropomorphic transradial prosthetic arm," in *5th IEEE RAS/EMBS international conference on biomedical robotics and biomechatronics*, 1039–1044. doi:10.1109/biorob.2014.6913917

Biddiss, E., Beaton, D., and Chau, T. (2007). Consumer design priorities for upper limb prosthetics. *Disabil. Rehabil. Assist. Technol.* 2, 346–357. doi:10.1080/17483100701714733

Billones, R. K. C., Lim, J. M., Cardenas, R., Manguerra, M. V., Vicerra, R. R. P., Bugtai, N. T., et al. (2020). "Prototyping a prosthetic arm for ulnar and radial deviation," in *2020 IEEE 12th international conference on humanoid, nanotechnology, information Technology, communication and control, environment, and management (HNICEM)*, 1–6. doi:10.1109/hnicem51456.2020.9400108

Chu, J.-U., Jung, D.-H., and Lee, Y.-J. (2008). "Design and control of a multifunction myoelectric hand with new adaptive grasping and self-locking mechanisms," in *2008 IEEE International conference on robotics and automation*, 743–748. doi:10.1109/robot.2008.4543294

Cipriani, C., Controzzi, M., and Carrozza, M. C. (2010). Objectives, criteria and methods for the design of the SmartHand transradial prosthesis. *Robotica* 28, 919–927. doi:10.1017/S0263574709990750

Cirelli, M., Giannini, O., Cera, M., Simoni, F.De, Valentini, P. P., and Pennestri, E. (2021). The mechanical efficiency of the Rzeppa transmission joint. *Mech. Mach. THEORY* 164, 104418. doi:10.1016/j.mechmachtheory.2021.104418

Controzzi, M., Bassi Luciani, L., and Montagnani, F. (2017). Unified approach to bi-directional non-back drivable roller clutch design. *Mech. Mach. Theory* 116, 433–450. doi:10.1016/j.mechmachtheory.2017.06.010

Controzzi, M., Cipriani, C., and Carrozza, M. C. (2010). Miniaturized non-back-drivable mechanism for robotic applications. *Mech. Mach. Theory* 45, 1395–1406. doi:10.1016/j.mechmachtheory.2010.05.008

Deijs, M., Bongers, R. M., Ringeling-van Leusen, N. D. M., and Van Der Sluis, C. K. (2016). Flexible and static wrist units in upper limb prosthesis users: functionality scores, user satisfaction and compensatory movements. *J. Neuroeng. Rehabil.* 13, 1–13. doi:10.1186/s12984-016-0130-0

Ding, H., Shi, Z., Hu, Y., Li, J., Yu, B., and Zhang, P. (2021). Lightweight design optimization for legs of bipedal humanoid robot. *Struct. Multidiscip. Optim.* 64, 2749–2762. doi:10.1007/s00158-021-02968-2

Gao, X., Zhang, S., Deng, J., and Liu, Y. (2021). Development of a small two-dimensional robotic spherical joint using a bonded-type piezoelectric actuator. *IEEE Trans. Ind. Electron.* 68, 724–733. doi:10.1109/TIE.2019.2959475

Guo, X.-Y., Li, W.-B., Gao, Q.-H., Yan, H., Fei, Y.-Q., and Zhang, W.-M. (2020). Self-locking mechanism for variable stiffness rigid-soft gripper. *SMART Mater. Struct.* 29, 035033. doi:10.1088/1361-665X/ab710f

He, B., Zhang, C., Cao, X., Li, G., and Xiong, X. (2023). An approach to recognizing the working cycle stage with small sample data for energy conservation. *J. Clean. Prod.* 414, 137771. doi:10.1016/j.jclepro.2023.137771

Hu, Q., Bai, Y., He, L., Cai, Q., Tang, S., Ma, G., et al. (2020). Intelligent framework for worker-machine safety assessment. *J. Constr. Eng. Manag.* 146. doi:10.1061/(ASCE)CO.1943-7862.0001801

Hu, Q., Huang, H., Dong, E., and Sun, D. (2021). A bioinspired composite finger with self-locking joints. *IEEE Robot. Autom. Lett.* 6, 1391–1398. doi:10.1109/LRA.2021.3056345

Kang, J., Seo, K., and Kim, K. (2015). Experimental investigation of friction noise in lead screw system under mode-coupling. *J. Mech. Sci. Technol.* 29, 5183–5188. doi:10.1007/s12206-015-1118-6

Karbalaei Akbari, M., Baharvandi, H. R., and Mirzaee, O. (2013). Fabrication of nano-sized Al2O3 reinforced casting aluminum composite focusing on preparation process of reinforcement powders and evaluation of its properties. *Compos. Part B Eng.* 55, 426–432. doi:10.1016/j.compositesb.2013.07.008

Kimura, A., Omura, L., Yoshioka, S., and Fukashiro, S. (2021). Identifying coordination between joint movements during a throwing task with multiple degrees of freedom. *Hum. Mov. Sci.* 77, 102799. doi:10.1016/j.humov.2021.102799

Lee, G., Hong, G. Y., and Choi, Y. (2021). Tendon-driven compliant prosthetic wrist consisting of three rows based on the concept of tensegrity structure. *IEEE Robot. Autom. Lett.* 6, 3956–3963. doi:10.1109/lra.2021.3067237

Liu, C., Tosun, T., and Yim, M. (2021). A low-cost, highly customizable solution for position estimation in modular robots. *J. Mech. Robot. ASME* 13. doi:10.1115/1.4050249

Liu, X.-F., Zhang, X.-Y., Cai, G.-P., and Chen, W.-J. (2022). Capturing a space target using a flexible space robot. *Appl. Sci.* 12, 984. doi:10.3390/app12030984

Lu, L., Jiang, C., Hu, G., Liu, J., and Yang, B. (2021). Flexible noncontact sensing for human-machine interaction. *Adv. Mater.* 33, e2100218. doi:10.1002/adma.202100218

Montagnani, F., Controzzi, M., and Cipriani, C. (2015a). Is it finger or wrist dexterity that is missing in current hand prostheses? *IEEE Trans. Neural Syst. Rehabil. Eng.* 23, 600–609. doi:10.1109/tnsre.2015.2398112

Montagnani, F., Controzzi, M., and Cipriani, C. (2015b). Non-back-drivable rotary mechanism with intrinsic compliance for robotic thumb abduction/adduction. *Adv. Robot.* 29, 561–571. doi:10.1080/01691864.2014.992957

Mota, B., Faria, P., and Ramos, C. (2023). Joint production and maintenance scheduling for total cost and machine overload reduction in manufacturing: a genetic algorithm approach. *IEEE ACCESS* 11, 98070–98081. doi:10.1109/ACCESS.2023.3312557

Muraliraja, R., Arunachalam, R., Al-Fori, I., Al-Maharbi, M., and Piya, S. (2019). Development of alumina reinforced aluminum metal matrix composite with enhanced compressive strength through squeeze casting process. *Proc. Inst. Mech. Eng. Part L J. Mater. Des. Appl.* 233, 146442071880951–314. doi:10.1177/1464420718809516

Mustafa, S. K., Yang, G., Yeo, S. H., Lin, W., and Pham, C. B. (2006). "Development of a bio-inspired wrist prosthesis," in *2006 IEEE conference on robotics* (Bangkok, Thailand: IEEE), 1–6.

Neumann, D. A. (2016) *Kinesiology of the musculoskeletal system-e-book: foundations for rehabilitation*. Elsevier Health Sciences.

Okafor, K. C., and Longe, O. M. (2022). WearROBOT: an energy conservative wearable obstacle detection robot with LP multi-commodity graph. *IEEE ACCESS* 10, 105843–105865. doi:10.1109/ACCESS.2022.3211319

Semasinghe, C. L., Ranaweera, R., Prasanna, J. L. B., Kandamby, H. M., Madusanka, D. G. K., and Gopura, R. (2018). HyPro: a multi-DoF hybrid-powered transradial robotic prosthesis. *J. Robot.* 2018, 1–15. doi:10.1155/2018/8491073

Seo, M., Kim, H., and Choi, Y. (2017). "Human mimetic forearm mechanism towards bionic arm," in *2017 international conference on rehabilitation robotics (ICORR)*, 2017, 1171–1176. doi:10.1109/ICORR.2017.8009408

Shi, Q., Gao, Z., Jia, G., Li, C., Huang, Q., Ishii, H., et al. (2021). Implementing rat-like motion for a small-sized biomimetic robot based on extraction of key movement joints. *IEEE Trans. Robot.* 37, 747–762. doi:10.1109/TRO.2020.3033705

Wei, T., Liu, W., Yang, W., Zeng, S., Yan, X., and Guo, J. (2023). Structural design and self-locking performance verification of the snap-fit spatial self-locking energy absorption system under the impact loading. *Int. J. CRASHWORTHINESS*, 1–16. doi:10.1080/13588265.2023.2253040

Wu, X., Hua, H., Zhao, C., Shi, N., and Wu, Z. (2023). A back-drivable rotational force actuator for adaptive grasping. *Actuators* 12, 267. doi:10.3390/act12070267

Zhang, G., Ma, S., Liu, J., Zeng, X., Kong, L., and Li, Y. (2023). Q-Whex: a simple and highly mobile quasi-wheeled hexapod robot. *J. F. Robot.* 40, 1444–1459. doi:10.1002/rob.22186

frontiers | Frontiers in Bioengineering and Biotechnology

TYPE Original Research
PUBLISHED 06 June 2024
DOI 10.3389/fbioe.2024.1392824

OPEN ACCESS

EDITED BY
Wujing Cao,
Chinese Academy of Sciences (CAS), China

REVIEWED BY
Hewei Wang,
Fudan University, China
Mohammad Dawood Rahimi,
Herat University, Afghanistan

*CORRESPONDENCE
Yilan Li,
liyilan1367@163.com

RECEIVED 28 February 2024
ACCEPTED 30 April 2024
PUBLISHED 06 June 2024

CITATION
Wang J, Ma J, Zhang Y, Tian Y, Wang X, Wang Y, Xiang D, Wang D, Huang K, Mao L, Zhang J, Fan H and Li Y (2024), The rehabilitation efficacy of diaphragmatic breathing combined with limb coordination training for lower limb lymphedema following gynecologic cancer surgery.
Front. Bioeng. Biotechnol. 12:1392824.
doi: 10.3389/fbioe.2024.1392824

The rehabilitation efficacy of diaphragmatic breathing combined with limb coordination training for lower limb lymphedema following gynecologic cancer surgery

Jingxin Wang[1], Jiahui Ma[1,2], Yujie Zhang[3], Yuan Tian[4], Xinxin Wang[1], Yu Wang[5], Dongquan Xiang[6], Daoyu Wang[7], Kun Huang[1], Luxi Mao[1], Jiaxin Zhang[1], Huixuan Fan[1] and Yilan Li[1]*

[1]Department of Rehabilitation Medicine, Zhengzhou Central Hospital Affiliated Zhengzhou University, Zhengzhou, China, [2]Xinxiang Medical University, Xinxiang, China, [3]Department of Geriatrics, The First Affiliated Hospital of Fujian Medical University, Fujian Key Laboratory of Molecular Neurology and Institute of Neuroscience, Fujian Medical University, Fuzhou, China, [4]Department of Ultrasound Medicine, Zhengzhou Central Hospital Affiliated Zhengzhou University, Zhengzhou, China, [5]Fuwai Central China Cardiovascular Hospital, Zhengzhou, China, [6]Senior Department of Orthopedics, The Fourth Medical Centre, Chinese PLA General Hospital, Beijing, China, [7]Academy for Engineering and Technology, Fudan University, Shanghai, China

Objective: To investigate the impact of diaphragmatic breathing combined with limb training on lower limb lymphedema following surgery for gynecological cancer.

Methods: From January 2022 to May 2022, 60 patients with lower limb lymphedema post-gynecologic cancer surgery were chosen. They were split into a control group (n = 30) and a treatment group (n = 30). The control group underwent complex decongestive therapy (CDT) for managing lower limb lymphedema after gynecologic cancer surgery, while the treatment group received diaphragmatic breathing combined with limb coordination training alongside CDT. Both groups completed a 4-week treatment regimen. The lower limb lymphedema symptoms were evaluated using the genital, lower limb, buttock, and abdomen (GCLQ) scores; bilateral lower limb circumference measurements; and anxiety and depression scores.

Results: Compared to sole CDT administration, individuals undergoing diaphragmatic breathing coupled with limb coordination training experienced notable reductions in scores for the self-perceived symptom assessment questionnaire (GCLQ), bilateral lower limb circumference, as well as anxiety and depression scores.

Conclusion: The incorporation of diaphragmatic breathing combined withalongside limb coordination training can accelerate and augment the efficacy of treating lower limb lymphedema post-gynecologic cancer surgery.

KEYWORDS

diaphragmatic breathing, coordination training, rehabilitation efficacy, lower limb lymphedema, gynecologic cancer surgery

1 Introduction

In recent years, the prevalence of lower limb lymphedema following gynecologic cancer surgery has steadily risen, mirroring the high occurrence of gynecologic malignancies, which ranges from 20% to 60% (Carlson et al., 2020). Common gynecologic cancers include cervical cancer, ovarian cancer, endometrial cancer, and vaginal cancer, among others. Surgical procedures often entail pelvic lymph node dissection, while varying degrees of chemotherapy and radiotherapy postoperatively can impair the lymphatic system responsible for draining lymphatic fluid from the lower limbs (Kalemikerakis et al., 2021; Zeng et al., 2021; Dokku et al., 2023; Patil et al., 2023). Moreover, postoperative factors such as obesity, insufficient physical activity, and unhealthy habits can impede lower limb lymphatic circulation, resulting in swelling, discomfort, and sensory disturbances in the lower extremities (Yildiz Kabak et al., 2021; Sudduth and Greene, 2022; Faerber, 2023). Severe cases may lead to complications such as cellulitis, acute infections, and can trigger anxiety, and depression, significantly impacying patients' quality of life and occupational functioning (Dessources et al., 2020; Tedeschi, 2023).

Previously, complex decongestive therapy (CDT) was extensively employed as a cornerstone treatment for lymphedema (Executive Committee of the International Society of Lymphology, 2020; Liu et al., 2021). CDT involves manual lymphatic drainage, skin care, compression bandaging, and physical exercise. However, its effectiveness is limited and requires sustained patient adherence. With the increasing diversity of patients and the expanding range of clinical interventions, numerous novel approaches are now being integrated into clinical practice (Thomas et al., 2020). Studies indicate that following standardized deep breathing (Douglass et al., 2020), there is a notable immediate reduction in limb volume and edema percentage, persisting for at least 30 min. Diaphragmatic breathing enhances respiratory muscle strength, endurance, and coordination, improves chest mobility, fortifies thoracic negative pressure capacity, and fosters deep blood and lymph circulation; thus, enhancing lymphatic flow (Fröhlich, 2021). Physical exercise regulates rhythmic compression of blood vessels and lymphatic systems, sustaining optimal muscle contraction strength to emulate a "muscle pump" effect, thereby aiding in augmenting lower limb lymphatic return and alleviating lymphedema (Hasenoehrl et al., 2020; Tendero-Ruiz et al., 2020; Saraswathi et al., 2021; Aguilera-Eguía et al., 2023).

The limb coordination training device LoopGO supports the gradual restoration of lower limb control, coordination, strength, joint range of motion, and other motor functions. In particular, it enhances patients' autonomy, and compliance, and promotes standardized and safe functional exercise. This study focused on gynecologic cancer surgery patients with lower limb dysfunction, and compared the effects of the LoopGO with those of conventional rehabilitation techniques. The aim of this study was to provide new rehabilitation measures for patients with gynecologic cancer surgery and lower limb dysfunction.

2 Materials and methods

2.1 General data

Sixty instances of lower limb lymphedema following after gynecologic cancer surgery treated at our facility between January and May 2022 were included in the study. Inclusion criteria involved: 1) a history of lymph node dissection due to gynecologic malignancy, confirmed both clinically and through imaging for lower limb lymphedema; 2) unilateral lower limb edema; 3) absence of deep vein thrombosis verified by color Doppler ultrasound; 4) capability to complete a 4-week treatment regimen; 5) voluntary participation with signed informed consent signed. Exclusion criteria consisted of: 1) patients with acute skin infections like cellulitis and erysipelas, deep vein thrombosis, or severe cardiac conditions; 2) patients with suspected or confirmed cancer recurrence or metastasis; 3) patients unable to adhere to the treatment requirements during the study period.

We initially collected 122 patients, but after applying inclusion and exclusion criteria and considering other factors such as attrition, only 60 patients were ultimately eligible for treatment and analysis. This study utilized a single-blind experimental design, with researchers aware of the group allocations while subjects remained unaware of whether they belonged to the experimental or control group. Patient numbering and random selection were employed to assign 30 individuals to the treatment group and the remaining to the control group. Prior to study commencement, all trial implementers underwent centralized training to familiarize themselves with the study's significance and procedures, participating only after passing the training assessment. Treatment was administered by certified rehabilitation therapists with extensive experience. No significant differences were observed between the two groups concerning age, disease type, postoperative edema duration, and other factor ($p > 0.05$), indicating their comparability. Please refer to Table 1. All procedures conducted in this study received approval from the Medical Ethics Committee of Zhengzhou Central Hospital (No. 202256).

2.2 Experiments design

2.2.1 Control group

Each patient in this group underwent CDT, which included the following (Schiltz et al., 2024): ① Manual Lymphatic Drainage (MLD): According to the Vodder method created by Dr. Vodder in the third edition of Foldi's Lymphology, lymph node activation and lymphatic drainage were performed at the required treatment sites, with 5-7 activations and drainages at each site. MLD was conducted once daily for 40 min each time. ② Pressure Therapy: This involves Intermittent Pneumatic Compression (IPC) and Bandaging Pressure Therapy. Using the Israeli Megoafek company's 24-cavity type III air wave pressure therapy machine, pressure therapy was applied to the patients' bilateral lower limbs and waist-abdomen areas before and after MLD. IPC mimics manual lymphatic drainage, reaching areas inaccessible to manual techniques, with a treatment intensity set at 55 mmHg, administered once daily for 40-min sessions. Following MLD and IPC treatment, bandaging pressure therapy is applied. Various widths of German Biaform low-stretch bandages (6-9 rolls) are applied in an "eight" pattern to exert pressure on the affected leg and foot once daily for 24 h, including overnight during sleep. ③ Skin care involves the uniform application of Vitamin E cream to the affected lower limb before and after bandaging removal to maintain soft and smooth skin. Daily skin cleansing and hygiene are vital, including cleaning or wiping the affected lower limb before each skin care session. ④ Edema exercise includes passive supine bilateral lower limb isometric training conducted once daily for 20 min following bandaging pressure. Each patient undergoes these treatments continuously for 4 weeks.

TABLE 1 General Information of the Two Patient Groups. [1]*t*-test; [2] Fisher's exact test.

	Control Group (*n* = 30)	Treatment Group (*n* = 30)	*p*-Value
Age (Years)	55.03 ± 9.74	54.1 ± 8.27	0.691[1)]
Cancer type			0.446[2)]
Cervical Cancer (Number of Cases)	20 (66.7%)	18 (60%)	
Endometrial Cancer (Number of Cases)	7 (23.3%)	10 (33.3%)	
Ovarian Cancer (Number of Cases)	3 (10%)	1 (3.3%)	
Fallopian Tube Cancer (Number of Cases)	0	1 (3.3%)	
Postoperative Edema Duration (Years)	5.33 ± 1.75	5.13 ± 1.87	0.604[1)]

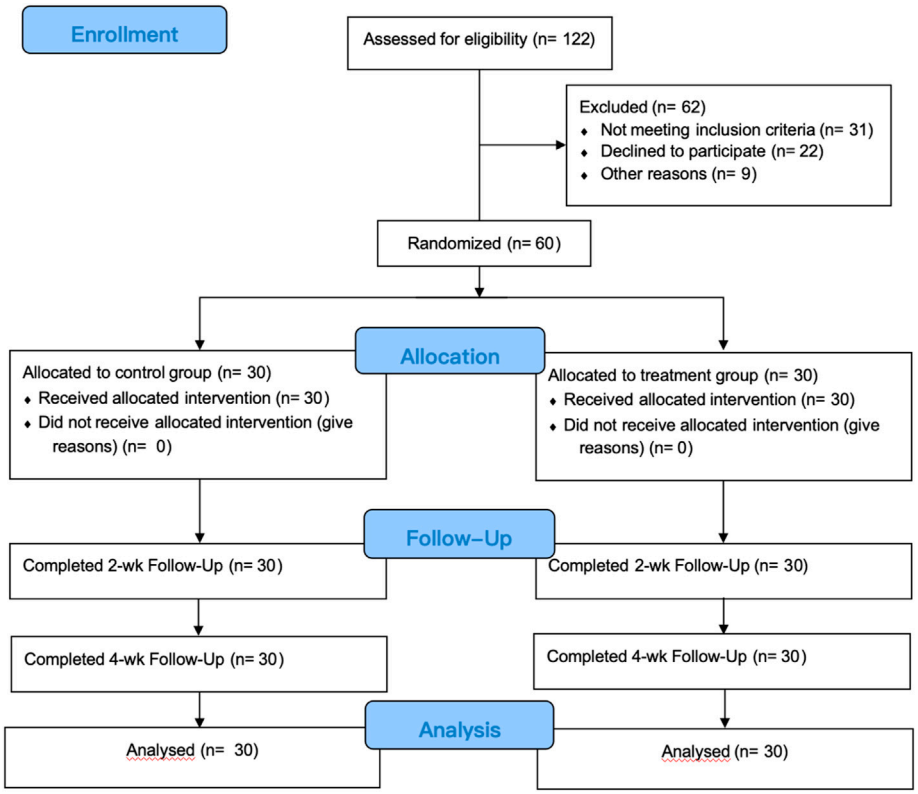

FIGURE 1
Flow chart of study implementation. Control group: received complex decongestive therapy; Treatment group: received complex Decongestive therapy, Diaphragmatic Breathing and Coordination Training.

2.2.2 Treatment group

In the treatment group, patients underwent diaphragmatic breathing along with limb coordination training, in contrast to the control group. Before starting CDT treatment, breathing training occurred with patients lying supine and knees bent. Therapists placed their hands on the patient's abdomen, offering resistance based on their ability to maintain diaphragmatic breathing. Meanwhile, patients were instructed to practice resistance diaphragmatic breathing while pursing their lips, inhaling through the nose, and exhaling slowly as if blowing out a candle. The inhalation-exhalation ratio remained at 1:2, with each group completing five breaths, totaling two sets before initiating CDT treatment. Each training session lasted for 10 min. Conversely, the control group continued normal breathing throughout this period.

Limb coordination training was initiated on the lower limb of the affected side after CDT treatment, using a limb coordination training device LoopGO (see Figure 2). The prototype of the limb coordination training device is shown in Figure 1. The LoopGO includes upper and lower limb training modules. We selected a multihead worm gear reducer as the power source for the upper limb training module. To achieve synchronous or asynchronous circular

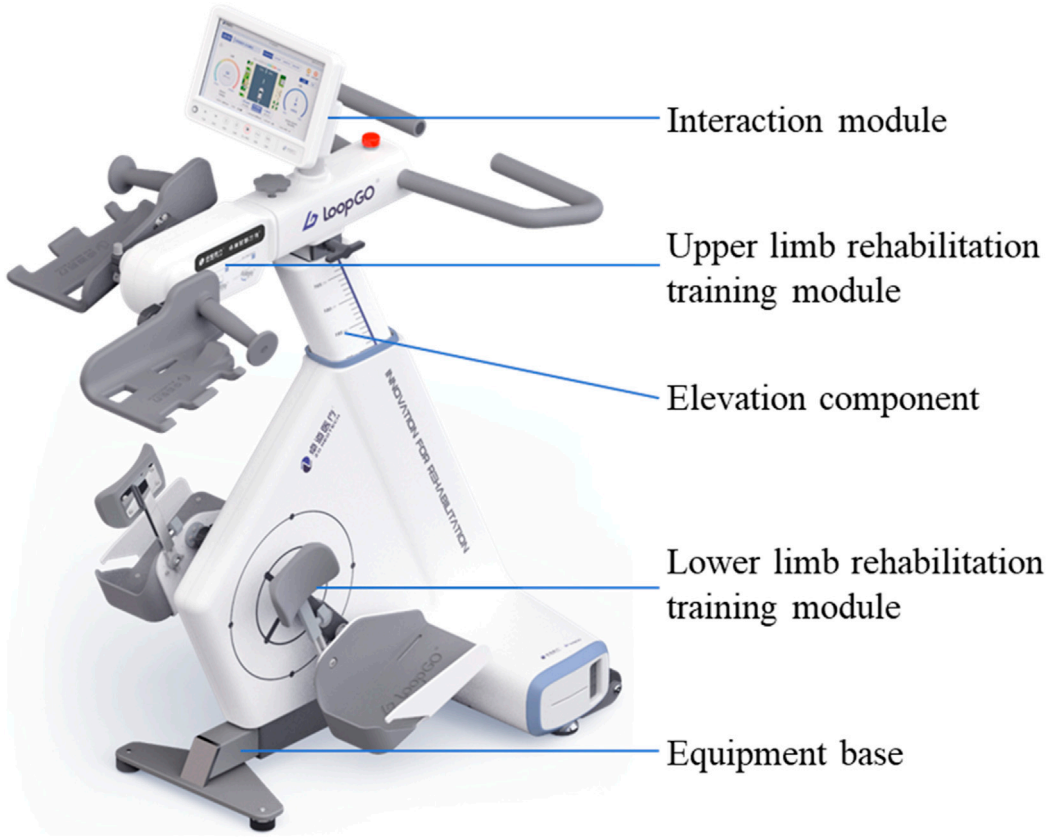

FIGURE 2
The prototype of the limb coordination training device.

motion with both hands securely fixed, the above mentioned worm gear reducer mentioned above should be a dual-output shaft reducer. The upper limb training module requires two crank components, a driving crank and a gripping crank. The gripping crank must rotate freely relative to the crank. Both crank components should be adaptable to mount in reverse or forward orientations on the output shafts positioned on both sides of the worm gear reducer. The lower limb training module has opted for a motor with an output end of a Φ16 mm multi-vee pulley as the power source. The motor, driven by a multi-vee belt, rotates a large-diameter turntable through speed reduction and torque amplification, ensuring that the maximum motion torque of the turntable is no less than 20 Nm.

The standard training program involved activating the lower limbs primarily. Patients were guided to sit and exert force with both legs together while maintaining a neutral body position. Each training session lasted for 20 min and was conducted once daily, consistently over a span of 4 weeks.

2.3 Evaluation standard

2.3.1 Lower limb lymphedema self-perceived symptom assessment questionnaire (GCLQ)

To assess the GCLQ scores (Carter et al., 2019) of the two groups before and after the 4-week intervention, we employed the Lower Limb Lymphedema Self-Perceived Symptom Assessment Questionnaire (GCLQ). This questionnaire was used to evaluate sensations associated with lower limb lymphedema experienced over the past 4 weeks. It comprises seven symptom clusters, including heaviness, overall edema, local swelling, sensory symptoms, pain, numbness, and limb function, totaling 20 items. Each item is rated on a scale of 0 to 1, where 0 indicates the absence and 1 indicates the presence of the symptom. A total score of ≥4 signifies the diagnosis of lower limb lymphedema. The questionnaire exhibits good sensitivity (92.86%) and specificity (83.33%) when the total score is ≥4.

2.3.2 Bilateral lower limb circumference measurement

The bilateral lower limb circumferences of the two groups of patients before and after the 4-week intervention were compared, and the circumferences of the ankles at the narrowest point cB, the widest point of the calf cC, and the root of the thigh cG on the affected side were measured with a tape measure.

2.3.3 Hospital anxiety and depression scale

Comparison of the Hospital Anxiety and Depression Scale (HADS) (Annunziata et al., 2020) scores before and after the 4-week intervention demonstrated significant changes. Originally introduced by Zigmond and Snaith in 1983, the HADS is predominantly used by healthcare professionals to assess anxiety and depression severity in hospitalized patients. It comprises

14 items, equally divided between depression and anxiety. Each item rates the frequency of symptoms over the past month on a 4-point scale, ranging from 0 to 3 points resulting in four severity levels. The maximum score for both anxiety and depression is 21 points, with higher scores indicating more severe symptoms. Scores are categorized as follows: 0–7 points (negative), 8–10 points (mild), 11–14 points (moderate), and 15–21 points (severe).

2.4 Statistical analysis

2.4.1 Sample size

We used G*Power (version 3.1) to estimate the sample size required to detect differences in the effects of group × time interactions on clinical outcomes (CCLQ score, circumference of the lower limbs, and HADS score). We mainly used F tests for specific analyses, and ANOVA: Repeated measures, and within-between interactions were used in the statistical test. By default, the effect size f is 0.25, the 2-sided significance level is 0.05 and the power is 95%. Based on this analysis, the target sample size was 54.

We organized the data and conducted statistical analyses using SPSS and Prism9. The final results are presented as the mean ± standard error of the mean (SEM). ANOVA was employed to assess the effect of different conditions on the treatment. Differences between pre-treatment, 2-week, and 4-week intervals were evaluated through two-sided paired t-tests. SPSS was utilized for analysis by Pearson Chi-square, Likelihood Ratio Chi-square or Fisher's exact test. Statistical significance was determined with a p-value of <0.05.

3 Results

3.1 Lower limb lymphedema self-perceived symptom assessment questionnaire (GCLQ)

For the control group, the GCLQ scores were 9.73 ± 0.69 at the initial state, 7.37 ± 0.77 2 weeks after treatment, and 6.20 ± 0.85 4 weeks after treatment. Meanwhile, for the treatment group, the GCLQ scores were 10.30 ± 1.02 at the initial state, 6.03 ± 0.72 2 weeks after treatment, and 3.00 ± 0.64 4 weeks after treatment. Two-way ANOVA was used to compare the changes in GCLQ scores between the two groups at different time points. The results indicated no significant difference between the two groups at the initial state ($p = 0.067$). As time progressed, both the 2-week and 4-week posttreatment scores were significantly lower than the initial scores for both groups. Furthermore, at both the 2 weeks after treatment and 4 weeks after treatment, the treatment group exhibited significantly lower scores than the control group ($p < 0.001$, see Figure 3).

3.2 Bilateral lower limb circumference measurement

The initial ankle circumference, measured at 2 weeks and 4 weeks after treatment in the control group, was 27.55 ± 0.51 cm, 25.82 ± 0.48 cm, and 24.81 ± 0.48 cm, respectively. In the treatment group, the initial ankle circumference, 2 weeks, and 4 weeks after treatment were 27.53 ± 0.50 cm, 25.33 ± 0.64 cm, and 23.34 ± 0.57 cm, respectively. A two-way ANOVA analysis compared changes in bilateral lower limb circumference of both lower limbs between the two groups at different time points. Initially, there was no significant difference between the two groups at the initial state ($p > 0.999$). However, as time progressed, both groups showed significantly lower measurements at 2 and 4 weeks after treatment compared to the initial state ($p < 0.001$). Additionally, at both 2 weeks after treatment ($p = 0.006$) and 4 weeks after treatment ($p < 0.001$), the treatment group exhibited significantly lower measurements compared to the control group (see Figure 4).

3.3 Hospital anxiety and depression scale

The HADS scores (Blumenthal et al., 2021) recorded at the initial state, 2 weeks after treatment, and 4 weeks after treatment in the control group were 16.87 ± 0.63, 15.17 ± 0.70, and 13.33 ± 0.71, respectively. Meanwhile, in the treatment group, the HADS scores at the initial state, 2 weeks after treatment, and 4 weeks after treatment were 17.10 ± 0.71, 13.43 ± 1.10, and 8.83 ± 0.75, respectively. Analysis using two way ANOVA analysis was conducted to compare the alterations in HADS scores between the two groups at various time points. The results indicated no significant difference between the two groups in the initial state ($p = 0.857$). As time progressed, both the 2-week and 4-week posttreatment scores were significantly lower than the initial scores for both groups. Furthermore, at both the 2 weeks after treatment and 4 weeks after treatment, the treatment group exhibited significantly lower scores than the control group ($p < 0.001$, see Figure 5).

4 Discussion

While studies on lower limb lymphedema post-gynecological cancer surgery are less abundant compared to those on secondary upper limb lymphedema, they demonstrate a consistent trend of progression and treatment challenges. Although early-stage lower limb lymphedema may temporarily improve after a night's rest, it typically advances as a progressive condition often disregarded by patients in its initial phases, leading to missed opportunities for optimal treatment. This progression can culminate in irreversible stages like skin fibrosis, elephantiasis, and severe complications such as skin infections, significantly impacting patients' daily lives, work, and mental well-being. Consequently, it imposes a considerable psychological burden and anxiety on affected individuals (Săvulescu et al., 2021; Baik et al., 2022; Lee et al., 2022).

During rest, lymphatic flow occurs at a slow pace, with interstitial fluid entering lymphatic capillaries to form lymph. Following a series of filtration and convergence processes, lymph proceeds to the thoracic duct or right lymphatic duct before eventually entering the bloodstream through the superior vena

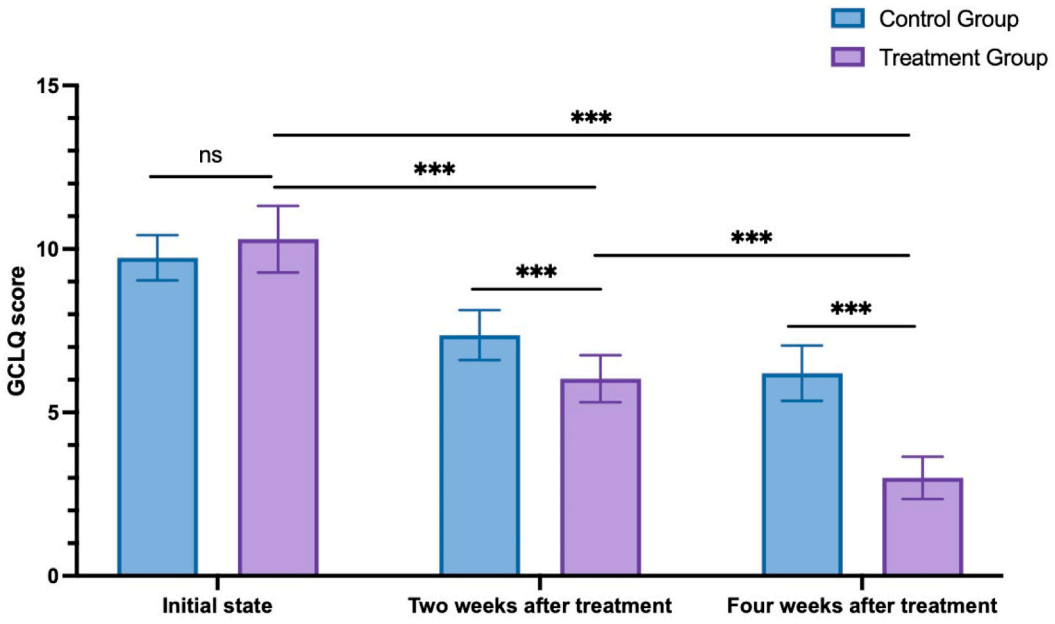

FIGURE 3
GCLQ score changes in the control group and treatment group. ns: non-significant; ***$p < 0.001$.

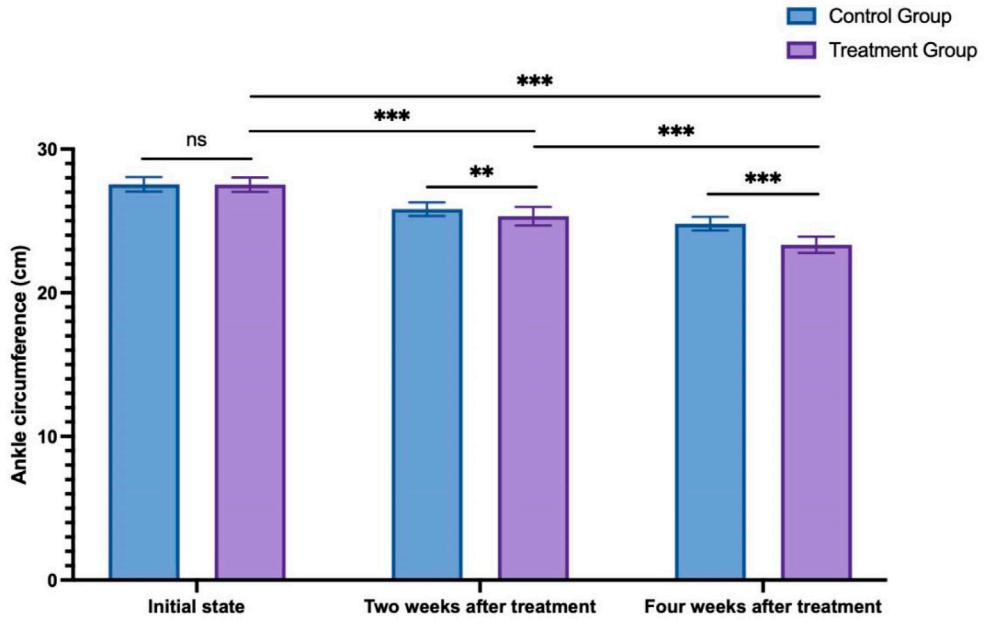

FIGURE 4
The change in ankle circumference between the control group and treatment group. ns: non-significant; **$p < 0.01$; ***$p < 0.001$.

cava system. Under normal physiological circumstances, there exists a dynamic equilibrium between lymphatic load and transport capacity. However, gynecologic cancer surgeries or treatments such as radiation and chemotherapy can disrupt normal lymphatic tissue, resulting in inadequate transport capacity, accumulation of interstitial fluid in the subcutaneous tissue, and the onset of lymphedema (Bartels et al., 2023; Daggez et al., 2023). Various factors contribute to the driving force behind lymphatic flow including muscle contractions, intrathoracic negative pressure, lymphatic pump, and arterial pulsation. During inspiration, the increased intrathoracic negative pressure promotes dilation of the thoracic duct, thereby facilitating lymphatic flow. Studies have demonstrated that in dogs subjected to excessive ventilation, thoracic duct flow increases, whereas it decreases when the

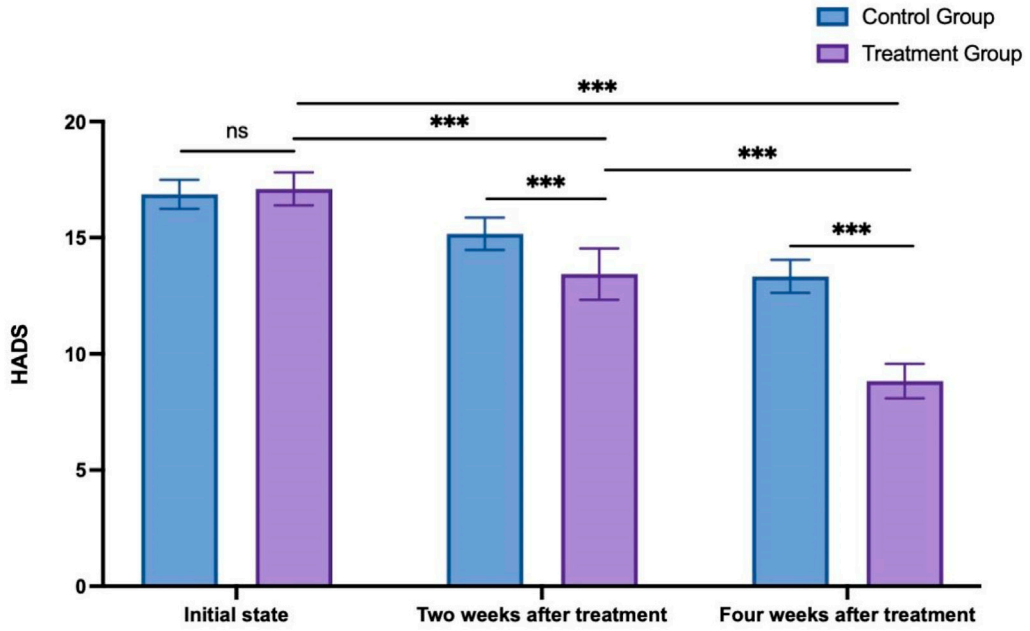

FIGURE 5
HADS score changes in the control group and treatment group. ns: non-significant; ***$p < 0.001$.

thoracic cavity is opened and intrathoracic pressure is reduced. Human trials conducted by Ajima revealed that 30 min of diaphragmatic breathing in a supine position effectively induced thoracic duct lymphatic drainage (Kawai et al., 2015). Furthermore, Ratnayake et al. (Ratnayake et al., 2018) observed that the pressure difference between the terminal lymphatic duct and the venous end varies with the respiratory cycle. Hence, respiratory movements can effectively facilitate gas exchange in the alveoli, diminish venous hypertension, and induce lymphatic fluid flow. In 2020, the International Society of Lymphology's consensus statement underscored the significance of integrating deep breathing training into self-management strategies for breast cancer-related lymphedema (BCRL) (Wang et al., 2023). Additionally, the Clinical Practice Guidelines (CPG) developed and released by the Oncology Section of the American Physical Therapy Association advocate for a range of measures, including deep breathing exercises, to ameliorate lymphedema while promoting relaxation and enhancing emotional well-being among patients (Campione et al., 2023).

Active exercise plays a crucial role in the rehabilitation of lymphedema, while resistance training involves engaging in rhythmic, multi-set weight or resistance exercises to stimulate muscle contraction (Zaborova et al., 2023). This stimulation augments muscle pressure, thereby facilitating lymphatic drainage, enhancing metabolic capacity, and alleviating lymphedema symptoms. Limb coordination training adjusts the training mode and intensity according to the patient's strength, thereby regulating the training intensity by modifying resistance levels. By exerting pressure on deep tissues, this training encourages muscle contractions and relaxation, effectively acting as a "muscle pump" to facilitate the return of lymphatic fluid.

The study results show that combining diaphragmatic breathing with limb coordination training can reduce lower limb lymphedema following gynecologic cancer surgery. This combination significantly enhances lower limb circumference, emotional well-being, and symptom perception compared to the control group. Thus, focusing on patients' breathing conditions and integrating complex decongestive therapy after respiratory training can improve rehabilitation outcomes when combined with limb coordination training.

The study has limitations. The sample size might restrict the generalizability of the findings, necessitating larger studies to endorse the conclusions. Additionally, the investigation focused solely on the 4-week treatment duration, warranting further exploration of the long-term effects of diaphragmatic breathing and limb coordination training.

5 Conclusion

In conclusion, diaphragmatic breathing exhibits superior effectiveness in treating lower limb lymphedema after gynecologic cancer surgery compared to traditional CDT therapy. Future clinical practice, should prioritize diaphragmatic breathing and limb coordination training. This approach is safe, yields visible outcomes, reduces treatment duration for patients, and warrants dissemination among therapists specializing in post-gynecologic cancer surgery lower limb lymphedema treatment.

Data availability statement

The raw data supporting the conclusion of this article will be made available by the authors, without undue reservation.

Ethics statement

The studies involving humans were approved by the Medical Ethics Committee of Zhengzhou Central Hospital. The studies were conducted in accordance with the local legislation and institutional requirements. The participants provided their written informed consent to participate in this study.

Author contributions

JW: Writing–original draft. JM: Formal Analysis, Writing–review and editing. YZ: Writing–review and editing. YT: Writing–review and editing. XW: Writing–review and editing. YW: Writing–review and editing. DX: Writing–review and editing. DW: Writing–review and editing. KH: Writing–review and editing. LM: Writing–review and editing. JZ: Writing–review and editing. HF: Writing–review and editing. YL: Writing–review and editing.

Funding

The author(s) declare that financial support was received for the research, authorship, and/or publication of this article. This research was funded by the Key Research and Promotion Project of Henan Province (Science and Technology Tackling Key Problems) Project, grant number 222102310657; Henan Province Medical Science and Technology Key Tackling Plan (Joint Construction) Project, grant number LHGJ20191057; Special Topic on Scientific Research of Traditional Chinese Medicine in Henan Province, grant number 2019ZY3011.

Conflict of interest

The authors declare that the research was conducted in the absence of any commercial or financial relationships that could be construed as a potential conflict of interest.

The reviewer HW declared a shared parent affiliation with the author DW to the handling editor at the time of review.

Publisher's note

References

Aguilera-Eguía, R. A., Gutiérrez-Arias, R., Zaror, C., and Seron, P. (2023). Effectiveness of physical exercise programmes in reducing complications associated with secondary lymphoedema to breast cancer: a protocol for an overview of systematic reviews. *BMJ Open* 13 (7), e071630. doi:10.1136/bmjopen-2023-071630

Annunziata, M. A., Muzzatti, B., Bidoli, E., Flaiban, C., Bomben, F., Piccinin, M., et al. (2020). Hospital anxiety and depression scale (HADS) accuracy in cancer patients. *Support Care Cancer* 28 (8), 3921–3926. doi:10.1007/s00520-019-05244-8

Baik, J. E., Park, H. J., Kataru, R. P., Savetsky, I. L., Ly, C. L., Shin, J., et al. (2022). TGF-β1 mediates pathologic changes of secondary lymphedema by promoting fibrosis and inflammation. *Clin. Transl. Med.* 12 (6), e758. doi:10.1002/ctm2.758

Bartels, S. A. L., Donker, M., Poncet, C., Sauvé, N., Straver, M. E., van de Velde, C. J., et al. (2023). Radiotherapy or surgery of the axilla after a positive sentinel node in breast cancer: 10-year results of the randomized controlled EORTC 10981-22023 AMAROS trial. *J. Clin. Oncol.* 41 (12), 2159–2165. doi:10.1200/jco.22.01565

Blumenthal, J. A., Babyak, M. A., Craighead, W. E., Davidson, J., Hinderliter, A., Hoffman, B., et al. (2021). The role of comorbid anxiety in exercise and depression trials: secondary analysis of the SMILE-II randomized clinical trial. *Depress. anxiety* 38, 124–133. doi:10.1002/da.23088

Campione, E., Wampler, M., Bolch, C. A., and Krzak, J. J. (2023). Barriers and facilitators to implementation of APTA's breast cancer-related lymphedema diagnosis and intervention clinical practice guidelines. *J. Cancer Surviv*. Published online October 18. doi:10.1007/s11764-023-01475-1

Carlson, J. W., Kauderer, J., Hutson, A., Carter, J., Armer, J., Lockwood, S., et al. (2020). GOG 244-The lymphedema and gynecologic cancer (LEG) study: incidence and risk factors in newly diagnosed patients. *Gynecol. Oncol.* 156 (2), 467–474. doi:10.1016/j.ygyno.2019.10.009

Carter, J., Huang, H. Q., Armer, J., Carlson, J. W., Lockwood, S., Nolte, S., et al. (2019). GOG 244 - the LymphEdema and Gynecologic cancer (LEG) study: the association between the gynecologic cancer lymphedema questionnaire (GCLQ) and lymphedema of the lower extremity (LLE). *Gynecol. Oncol.* 155 (3), 452–460. doi:10.1016/j.ygyno.2019.09.027

Daggez, M., Koyuncu, E. G., Kocabaş, R., and Yener, C. (2023). Prophylactic complex physiotherapy in gynecologic cancer survivors: patient-reported outcomes based on a lymphedema questionnaire. *Int. J. Gynecol. Cancer* 33 (12), 1928–1933. doi:10.1136/ijgc-2023-004811

Dessources, K., Aviki, E., and Leitao, M. M., Jr (2020). Lower extremity lymphedema in patients with gynecologic malignancies. *Int. J. Gynecol. Cancer* 30 (2), 252–260. doi:10.1136/ijgc-2019-001032

Dokku, K. S., Nair, A. S., Prasad Mantha, S. S., Naik, V., Saifuddin, M., and Rayani, B. (2023). A randomized controlled study to compare analgesic efficacy of sublingual buprenorphine and intravenous tramadol in patients undergoing mastectomy. *Med. Gas. Res.* 13 (3), 118–122. doi:10.4103/2045-9912.345170

Douglass, J., Mableson, H., Martindale, S., Jhara, S. T., Karim, M. J., Rahman, M. M., et al. (2020). Effect of an enhanced self-care protocol on lymphedema status among people affected by moderate to severe lower-limb lymphedema in Bangladesh, a cluster randomized controlled trial. *J. Clin. Med.* 9 (8), 2444. doi:10.3390/jcm9082444

Executive Committee of the International Society of Lymphology (2020). The diagnosis and treatment of peripheral lymphedema: 2020 consensus document of the international society of Lymphology. *Lymphology* 53 (1), 3–19. doi:10.2458/lymph.4649

Faerber, G. (2023). Adipositas und sekundäres Lymphödem [Obesity and secondary lymphedema]. *Dermatol. (Heidelb).* 74 (8), 588–593. doi:10.1007/s00105-023-05180-z

Fröhlich, E. (2021). Acute respiratory distress syndrome: focus on viral origin and role of pulmonary lymphatics. *Biomedicines* 9 (11), 1732. doi:10.3390/biomedicines9111732

Hasenoehrl, T., Keilani, M., Palma, S., and Crevenna, R. (2020). Resistance exercise and breast cancer related lymphedema - a systematic review update. *Disabil. Rehabil.* 42 (1), 26–35. doi:10.1080/09638288.2018.1514663

Kalemikerakis, I., Evaggelakou, A., Kavga, A., Vastardi, M., Konstantinidis, T., and Govina, O. (2021). Diagnosis, treatment and quality of life in patients with cancer-related lymphedema. *J. BUON* 26 (5), 1735–1741.

Kawai, Y., Ajima, K., Nagai, T., Yokoyama, Y., Kaidoh, M., Seto, E., et al. (2015). Abdominal respiration induces hemodilution and related reduction in ADH concentration of blood. *Lymphat. Res. Biol.* 13 (3), 202–207. doi:10.1089/lrb.2015.0017

Lee, S., Lee, D. G., and Kim, K. T. (2022). Temporal changes in subcutaneous fibrosis in patients with lower extremity lymphedema following surgery for gynecologic cancer: a computed tomography-based quantitative analysis. *Diagn. (Basel)* 12 (8), 1949. doi:10.3390/diagnostics12081949

Liu, F., Liu, N. F., Wang, L., Chen, J., Han, L., Yu, Z., et al. (2021). Treatment of secondary lower limb lymphedema after gynecologic cancer with complex decongestive therapy. *Lymphology* 54 (3), 122–132. doi:10.2458/lymph.4786

Patil, P., Dhulkhed, P. V., and Dhulkhed, V. K. (2023). Isobaric forms of ropivacaine vs. bupivacaine in lower abdominal surgeries: a hospital-based, prospective, comparative study. *Med. Gas. Res.* 13 (3), 123–127. doi:10.4103/2045-9912.359678

Ratnayake, C. B. B., Escott, A. B. J., Phillips, A. R. J., and Windsor, J. A. (2018). The anatomy and physiology of the terminal thoracic duct and ostial valve in health and disease: potential implications for intervention. *J. Anat.* 233 (1), 1–14. doi:10.1111/joa.12811

Saraswathi, V., Latha, S., Niraimathi, K., and Vidhubala, E. (2021). Managing lymphedema, increasing range of motion, and quality of life through yoga therapy among breast cancer survivors: a systematic review. *Int. J. Yoga* 14 (1), 3–17. doi:10.4103/ijoy.ijoy_73_19

Săvulescu, A. F., Cîrlan, C., Simionescu, A. A., Budrugeac, A. I., Stanciu, D., et al. (2021). Fibrosis associated with retroperitoneal abscess after multimodal treatment of cervical carcinoma - a case report and brief review of the literature. *Chir. (Bucur).* 116 (3), 361–367. doi:10.21614/chirurgia.116.3.361

Schiltz, D., Eibl, D., Mueller, K., Biermann, N., Prantl, L., and Taeger, C. D. (2024). Therapist versus machine-immediate effects of manual versus mechanical lymphatic drainage in patients with secondary lymphedema. *J. Clin. Med.* 13, 1277. doi:10.3390/jcm13051277

Sudduth, C. L., and Greene, A. K. (2022). Lymphedema and obesity. *Cold Spring Harb. Perspect. Med.* 12 (5), a041176. doi:10.1101/cshperspect.a041176

Tedeschi, R. (2023). Biomechanical alterations in lower limb lymphedema: implications for walking ability and rehabilitation. *Phlebology* 38 (8), 496–502. doi:10.1177/02683555231188236

Tendero-Ruiz, L., Palomo-Carrión, R., Megía-García-Carpintero, Á., Pérez-Nombela, S., López-Muñoz, P., and Bravo-Esteban, E. (2020). The effect of therapeutic exercise in the prevention of lymphoedema secondary to breast cancer: a systematic review. *Arch. Med. Sci.* 19 (6), 1684–1692. doi:10.5114/aoms.2020.101435

Thomas, C., Le, J. T., and Benson, E. (2020). Managing lymphedema in fracture care: current concepts and treatment principles. *J. Am. Acad. Orthop. Surg.* 28 (18), 737–741. doi:10.5435/jaaos-d-19-00722

Wang, L., Shi, Y. X., Wang, T. T., Chen, K. X., and Shang, S. M. (2023). Breast cancer-related lymphoedema and resistance exercise: an evidence-based review of guidelines, consensus statements and systematic reviews. *J. Clin. Nurs.* 32 (9-10), 2208–2227. doi:10.1111/jocn.16437

Yildiz Kabak, V., Gursen, C., Aytar, A., Akbayrak, T., and Duger, T. (2021). Physical activity level, exercise behavior, barriers, and preferences of patients with breast cancer-related lymphedema. *Support Care Cancer* 29 (7), 3593–3602. doi:10.1007/s00520-020-05858-3

Zaborova, V. A., Butenko, A. V., Shekhter, A. B., Fayzullin, A., Pekshev, A., Serejnikova, N., et al. (2023). Nitric oxide therapy is beneficial to rehabilitation in professional soccer players: clinical and experimental studies. *Med. Gas. Res.* 13 (3), 128–132. doi:10.4103/2045-9912.344983

Zeng, W., Wang, R., Ying, W., Xu, W., and Zhao, X. (2021). Impact on lower limb lymphedema of pelvic lymphadenectomy with external iliac lymph nodes left-opened distal lymphatics technique. *Int. Angiol.* 40 (2), 143–149. doi:10.23736/s0392-9590.20.04486-7

frontiers | Frontiers in Bioengineering and Biotechnology

TYPE Original Research
PUBLISHED 14 June 2024
DOI 10.3389/fbioe.2024.1334643

OPEN ACCESS

EDITED BY
Nicolás Navarro-Guerrero,
L3S Research Center, Germany

REVIEWED BY
Josip Josifovski,
Technical University of Munich, Germany
Junpei Zhong,
Hong Kong Polytechnic University, Hong Kong SAR, China

*CORRESPONDENCE
Wenwei Yu,
yuwill@faculty.chiba-u.jp

RECEIVED 07 November 2023
ACCEPTED 10 May 2024
PUBLISHED 14 June 2024

CITATION
Zhou Z, Lu Y, Tortós PE, Qin R, Kokubu S, Matsunaga F, Xie Q and Yu W (2024), Addressing data imbalance in Sim2Real: ImbalSim2Real scheme and its application in finger joint stiffness self-sensing for soft robot-assisted rehabilitation.
Front. Bioeng. Biotechnol. 12:1334643.
doi: 10.3389/fbioe.2024.1334643

Addressing data imbalance in Sim2Real: ImbalSim2Real scheme and its application in finger joint stiffness self-sensing for soft robot-assisted rehabilitation

Zhongchao Zhou[1], Yuxi Lu[1], Pablo Enrique Tortós[1], Ruian Qin[1], Shota Kokubu[1], Fuko Matsunaga[1], Qiaolian Xie[1,2] and Wenwei Yu[1,3]*

[1]Department of Medical System Engineering, Chiba University, Chiba, Japan, [2]Institute of Rehabilitation Engineering and Technology, University of Shanghai for Science and Technology, Shanghai, China, [3]Center for Frontier Medical Engineering, Chiba University, Chiba, Japan

The simulation-to-reality (sim2real) problem is a common issue when deploying simulation-trained models to real-world scenarios, especially given the extremely high imbalance between simulation and real-world data (scarce real-world data). Although the cycle-consistent generative adversarial network (CycleGAN) has demonstrated promise in addressing some sim2real issues, it encounters limitations in situations of data imbalance due to the lower capacity of the discriminator and the indeterminacy of learned sim2real mapping. To overcome such problems, we proposed the imbalanced Sim2Real scheme (ImbalSim2Real). Differing from CycleGAN, the ImbalSim2Real scheme segments the dataset into paired and unpaired data for two-fold training. The unpaired data incorporated discriminator-enhanced samples to further squash the solution space of the discriminator, for enhancing the discriminator's ability. For paired data, a term targeted regression loss was integrated to ensure specific and quantitative mapping and further minimize the solution space of the generator. The ImbalSim2Real scheme was validated through numerical experiments, demonstrating its superiority over conventional sim2real methods. In addition, as an application of the proposed ImbalSim2Real scheme, we designed a finger joint stiffness self-sensing framework, where the validation loss for estimating real-world finger joint stiffness was reduced by roughly 41% compared to the supervised learning method that was trained with scarce real-world data and by 56% relative to the CycleGAN trained with the imbalanced dataset. Our proposed scheme and framework have potential applicability to bio-signal estimation when facing an imbalanced sim2real problem.

KEYWORDS

imbalanced sim2real problem, scarce real-world data, CycleGAN, finger joint stiffness self-sensing technology, soft robot-assisted rehabilitation

1 Introduction

In the field of deep learning, it is a prevalent method to train the model within a simulated environment and afterward deploy it in real-world scenarios (Tobin et al., 2017). However, modeling discrepancies between the simulation and real-world domains make it difficult to replicate simulation results in the real world (Truong et al., 2021). The gap between simulation and real-world data is known as the simulation-to-reality (sim2real) problem (Hofer et al., 2021). Additionally, in certain fields like medicine and healthcare, the challenge is not only addressing the sim2real problem but also doing it in the context of data imbalance, especially with featured abundant simulation data and scarce real-world data. This phenomenon arises because obtaining real-world data is expensive and risky, and in some cases, even illegal or unethical (Abascal et al., 2021). Such challenges can be further characterized as the imbalanced sim2real problem. Further refinement arises in the imbalanced sim2real problem depending on the nature of the real-world domain. When the real-world domain is a categorical variable, the problem is identified as a classification-type imbalanced sim2real problem. Conversely, when the real-world domain is continuous, it presents a specific challenge known as the regression-type imbalanced sim2real problem (Han et al., 2022). The regression-type imbalanced sim2real problem is particularly difficult because regression is equivalent to having theoretically infinite categories, demanding greater efficacy and accuracy in the transformation process. To bridge the gap between simulated and real-world environments with imbalanced data, researchers have proposed some methods, which are mainly categorized into domain randomization and domain adaptation (Salvato et al., 2021). However, both methods encounter challenges when confronted with the regression-type imbalanced sim2real problem.

Starting with domain randomization, it entails randomizing the simulation model to a wide range of simulated environments (such as the parameters of the friction and contact models and possible delays in the actuation) during training (Muratore et al., 2022). By training in such varied environments, models have the potential to attain superior generalization capabilities in the real-world (Tobin et al., 2017). Domain randomization has the potential to address the regression-type imbalanced sim2real problem completely, avoiding the dependence on the real-world data. However, domain randomization can lead to significant computational costs because of the need for multiple simulations to account for all environmental variations (Josifovski et al., 2022). Despite the deployment of a multitude of simulation environments, domain randomization still cannot fully capture the complexities and natures of the real world (Zhao et al., 2020). Furthermore, while real-world data may be scarce, they are not entirely absent. Thus, exclusive reliance on domain randomization may lead to underutilizing the real-world data (Ding et al., 2020).

Conversely, domain adaptation aims to align the disparity between domains such that the trained model in simulation can be generalized into the real-world domain, which entails the training of models utilizing a combination of simulation and real-world data (Peng et al., 2022). Some researchers combined domain adaptation with imbalanced learning. Such methods can tackle the label shift problem encountered during the training and testing phases, which can ensure that models maintain robust classification performance even when the distributions of the training and test datasets diverge (Zhu et al., 2022; Ding et al., 2023). Other imbalanced domain adaption methods emphasize addressing imbalances that frequently arise among different categories for classification tasks, regardless of data count or distribution (Kuang et al., 2022).

However, current existing imbalanced domain adaptation learning almost exclusively focuses on classification issues, with scarce solutions addressing the regression-type sim2real problem. Moreover, most imbalanced domain adaptation methods address the issue of quantity imbalances in input data. Given the overarching context of sim2real, simulations serve as inputs and real-world data act as the corresponding outputs (as labels), while finding a source and target domains with balanced label space is usually arduous or even impossible (Farahani et al., 2021). Lastly, in situations with quantitative imbalances, the unpaired simulation and real-world data emerge as a significant constraint in harnessing this methodology. Thus, current domain adaptation techniques remain insufficient at addressing the regression-type imbalanced sim2real problem comprehensively.

Setting aside the imbalanced data factor, one methodology to address the sim2real challenge is the bidirectional unsupervised domain adaptation approaches, which entail the concurrent learning of both sim2real and real2sim mapping (Bhagat et al., 2019). Among these approaches, the cycle-consistent adversarial network (CycleGAN) stands out as one of the most notable approach (Zhu et al., 2017). The CycleGAN's prowess lies in its ability to manage the sim2real challenge even with unpaired training datasets. Furthermore, it has been verified that simultaneously tackling both sim2real and real2sim not only enhances the quality of the generated data but also exhibits considerable generalizability even faced with unseen data samples. Consequently, this facilitates a more effective transfer of knowledge between the two domains (Chen et al., 2022). The efficacy has shown in scenarios where both simulation and real-world data are abundant and balanced, as demonstrated in works such as Chen et al. (2022), Jianu et al. (2022), and Zhao et al. (2023), which contain 1,429, 2079, and 1980 simulation and real-world data, maintaining a 1:1 ratio, respectively. However, when dealing with the regression-type imbalanced sim2real problem, CycleGAN may have the following two problems, as shown in Figures 1A, B:

1. Scarce real-world data for training discriminator. As shown in Figure 1A, in the CycleGAN framework for sim2real tasks, both the ground truth real-world domain and transferred real-world domain are typically provided to the discriminator. However, scarce real-world data make the training of discriminator quite difficult as it is difficult to obtain the correct distribution of real-world data, culminating in the generator's incapacity to generate data that resemble real-world data.
2. Specific sim2real mapping issue. As shown in Figure 1B, while it is possible to learn a mapping from the simulation domain to the real-world domain with unpaired data using CycleGAN, it may not necessarily generate the desired specific mapping, causing the transferred real-world domain to deviate from the expectation (Harms et al., 2019). In other words, the structure of CycleGAN is capable of learning a domain transformation between simulation and real world represented by $G_{sim2real}$ (abbreviated as G_{s2r}) : $x^S \rightarrow \tilde{x}^{S\rightarrow R}$ and $G_{real2sim}$ (abbreviated

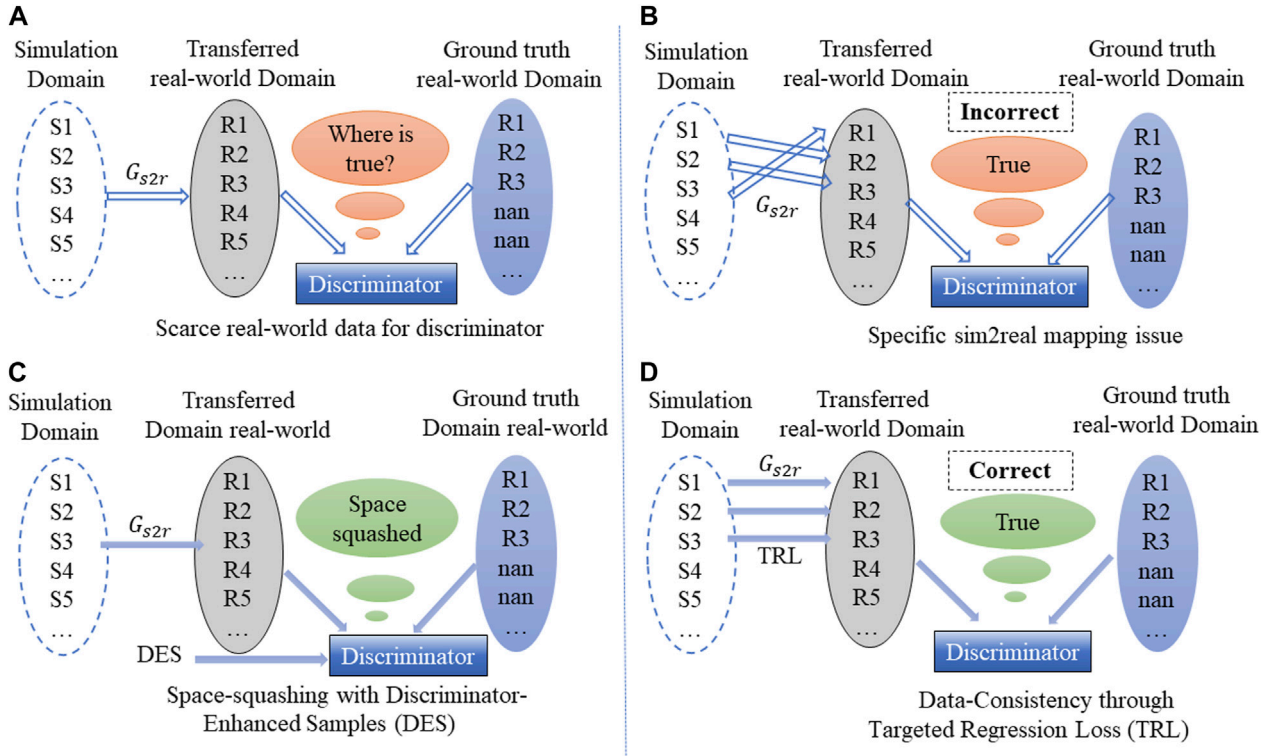

FIGURE 1
Current issues with CycleGAN when faced with the imbalanced sim2real problem and the potential solution. **(A)** Scarce real-world data for discriminator, **(B)** Specific sim2real mapping issue, **(C)** Space-squashing with DES, **(D)** Data-consistency through TRL.

as G_{r2s}) : $x^R \rightarrow \tilde{x}^{R\rightarrow S}$. Although we hope that $x^{S1} \rightarrow \tilde{x}^{S1\rightarrow R1}$ can be preserved, it potentially learns a domain transformation between *S1* and another real-world subdomain *R2* as well. Even though the discriminator may consider $\tilde{x}^{R1\ or\ R2\ or\ R3\ or\ \ldots}$ as "real," such mappings do not align with our expectation (Zhang et al., 2018; Xie et al., 2020). This predicament stems from the CycleGAN's inherent capability to ensure cycle consistency, e.g., $G_{r2s}\left(G_{s2r}\left(x^S\right)\right) = x^S$. It is possible to demonstrate that any bijective geometric transformation T, along with its inverse T^{-1}, can be applied to G_{s2r} and G_{r2s} such that ${G_{s2r}}' = G_{s2r} \circ T$ and ${G_{r2s}}' = G_{r2s} \circ T^{-1}$ and the transformed functions ${G_{r2s}}'\left({G_{s2r}}'\left(x^S\right)\right) = x^S$, is also cycle-consistent (here $\circ$ denotes the concatenation operation of two transformations). CycleGAN lacks the direct error between $G_{s2r}\left(x^S\right)$ and x^R or $G_{r2s}\left(x^R\right)$ and x^S, which introduce uncertainty and difficulty in achieving desired outputs task. Although the presence of abundant simulation and real-world data could somehow mitigate this issue, the results would be significantly affected when dealing with the quantitative regression-type sim2real problem with scarce real-world data.

To address the sim2real challenge with imbalanced paired–unpaired data, the imbalanced Sim2Real (ImbalSim2Real) scheme was proposed. Although the ImbalSim2Real scheme incorporates architectural components commonly found in models like the CycleGAN, such as G_{s2r} and G_{r2s}, as well as the discriminator for simulation data (abbreviated as D_{sim}) and discriminator for real-world data (abbreviated as D_{real}), it introduces several innovations tailored specifically to address the regression-type imbalanced sim2real problem.

Separate training: In the ImbalSim2Real scheme, in order to make full use of all real-world data, the dataset is segmented into paired and unpaired data, and two-fold training is performed.

Space squashing with discriminator-enhanced samples: The first-fold shifts attention to unpaired data. As shown in Figure 1C, to enhance the capability of the discriminator, the discriminator is space-squashed by providing additional discriminator-enhanced samples (DES). The strength of the discriminator plays a crucial role in the training of the generator as a stronger discriminator forces the generator to improve its ability to generate realistic samples (Schonfeld et al., 2020).

Data consistency through targeted regression loss: The second-fold training focuses on paired data. As shown in Figure 1D, to effectively utilize paired data and ensure a specific and quantitative mapping between the simulation domain and ground truth real-world domain, the second-fold training involves a data-consistency module, which is referred to as targeted regression loss (TRL). The update of G_{s2r} is not only confined to the discriminator but also has a direct correlation with the TRL, hence lowering the uncertainty and difficulties associated with obtaining desired outputs. Following the enhancement by the first-fold, the second-fold was used to further minimize the solution space of G_{s2r} for paired data in order to improve the accuracy of unpaired data generation.

As an application of the ImbalSim2Real scheme, we focus on the finger joint stiffness sensing problem, taken as a prime imbalanced sim2real problem in the soft robot-assisted rehabilitation scenario. Soft

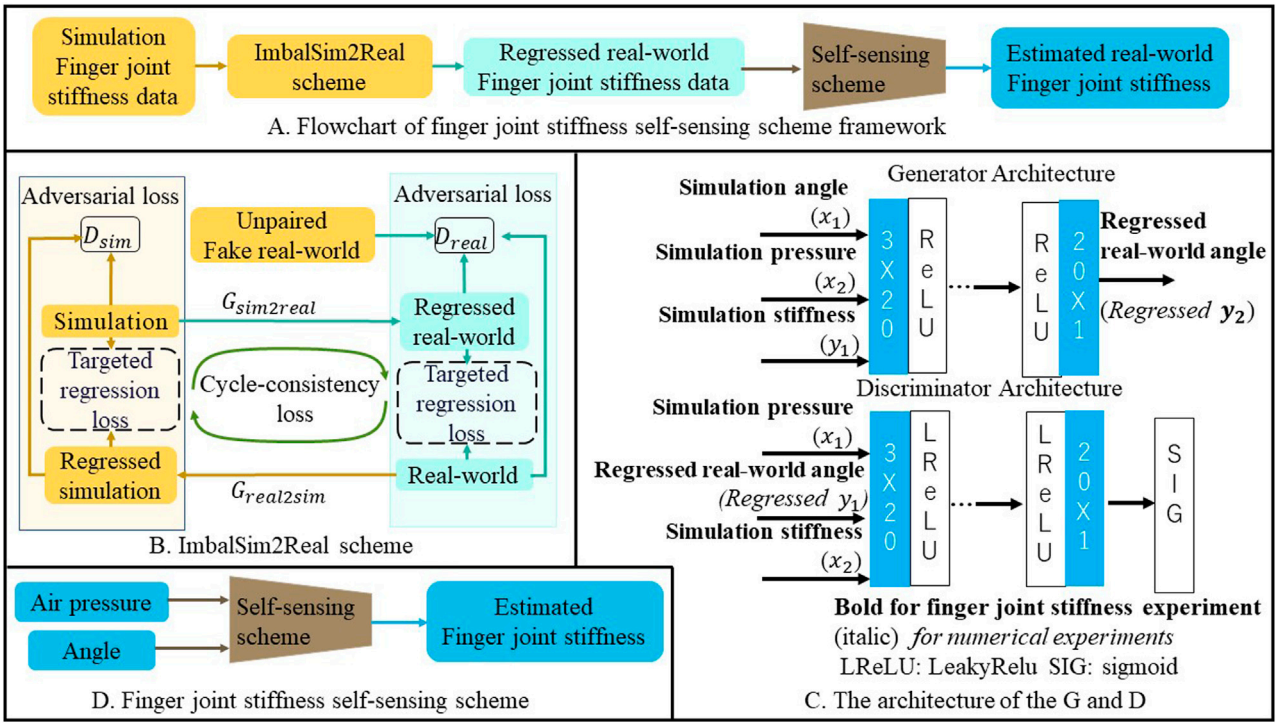

FIGURE 2
(A) A Flowchart of finger joint stiffness self-sensing scheme framework, **(B)** ImbalSim2Real scheme, **(C)** The architecture of the G and D, **(D)** Finger joint stiffness self-sensing scheme.

actuators have been applied in various healthcare fields, such as rehabilitation (Wang et al., 2021), surgery (Lu et al., 2023), and assistance (Zhou et al., 2022). In particular, Heung et al. analyzed the relationship between finger joint stiffness, soft actuator's angle, and air pressure, and hence developed an accurate analytic angle-pressure-finger joint stiffness model (Heung et al., 2020). However, this approach is based on the chamber structure of the soft actuator, which cannot be used with a model-unknown soft actuator because of its model dependency (Matsunaga et al., 2023). In spite of the lack of the literature, it is not difficult to conceive the possibility of estimating finger joint stiffness by training a neural network-based finger joint stiffness self-sensing scheme with the air pressure and angle of a soft actuator as inputs. We utilized a simulation-based model, notably COMSOL Multiphysics for data collection. The simulation data would be transformed into real-world data through the ImbalSim2Real scheme, thus augmenting the availability of real-world data, and then, generated real-world data could be used to train a finger joint stiffness self-sensing scheme.

Our contribution can be summarized as follows:

1. An ImbalSim2Real scheme was specifically proposed for the purpose of transferring simulation data to real-world data in regression tasks with an imbalanced dataset.
2. A finger joint stiffness self-sensing scheme was proposed, in which the finger joint stiffness can be estimated online without the need for the analytic model of the soft actuator.
3. The novel finger joint stiffness self-sensing framework which combined the self-sensing scheme with the ImbalSim2Real scheme was proposed. To the best of our knowledge, this is the first framework for the learning-based estimation of finger joint stiffness. Furthermore, this framework holds potential for the application in other experiments requiring the estimation of biological signals in real world.

This paper is structured as follows. In Section 2, the proposed framework is presented and discussed. Section 3 provides a detailed description of the numerical imbalanced domain transfer experiment and finger joint stiffness experiment. The results of the experiments are presented and analyzed in Section 4. Ablation studies are conducted in Section 5 to further validate the efficacy of the proposed ImbalSim2Real scheme. In Section 6, the implications and limitations of the proposed framework are discussed. Finally, in Section 7, the conclusion and directions for future research are outlined.

2 Methods

2.1 Finger joint stiffness self-sensing framework

The flowchart of the finger joint stiffness self-sensing framework is depicted in Figure 2A, comprising both the ImbalSim2Real scheme and the self-sensing scheme. The input to the framework constitutes the simulated finger joint stiffness-related data (air pressure and angle). The simulated finger joint stiffness-related data were first transferred into regressed real-world finger joint stiffness data by the ImbalSim2Real scheme shown in Figure 2B. The regressed real-world finger joint data were then utilized to train the

self-sensing scheme shown in Figure 2D, which could be applied to estimate real-world finger joint stiffness.

2.2 ImbalSim2Real scheme

As illustrated in Figure 2B, the ImbalSim2Real scheme comprises a generator G_{s2r} that generated real-world data from simulation data and G_{r2s} that generated simulation data based on real-world data (as mentioned before, the generated real-world data and generated simulation data were named regressed real-world data and regressed simulation data, respectively). A discriminator D_{real} is applied for judging real-world data or regressed real-world data, and a discriminator D_{sim} is applied for judging simulation data or regressed simulation data (all abbreviations for the symbols used are provided in Supplementary Material S1). The ImbalSim2Real scheme contained total three loss functions, namely, adversarial loss $\mathcal{L}_{GAN}$, targeted regression loss $\mathcal{L}_{TRL}$, and cycle-consistency loss $\mathcal{L}_{cyc}$. Given this diversity in loss mechanisms, the scheme employed a two-fold training approach.

2.2.1 Adversarial loss

In this study, $\mathcal{L}_{GAN}$ was divided into two parts, $\mathcal{L}_{GAN(s2r)}$ and $\mathcal{L}_{GAN(r2s)}$, respectively. The adversarial loss is defined by Zhu et al. (2017), which is expressed as follows:

$$\mathcal{L}_{GAN(s2r)}(G_{s2r}, D_{real}) = \mathbb{E}_{real\sim p_{data(real)}}[log\, D_{real}(real)] + \mathbb{E}_{sim\sim p_{data}(sim)} log\,((1 - D_{real}(G_{s2r}(sim))),$$

$$\mathcal{L}_{GAN(r2s)}(G_{r2m}, D_{sim}) = \mathbb{E}_{sim\sim p_{data(sim)}}[log\, D_{sim}(sim)] + \mathbb{E}_{real\sim p_{data}(real)} \log((1-D_{sim}(G_{r2s}(real)).$$

The real-world data conform to the distribution $p_{data}(real)$, where $real \sim p_{data(rea)}$ indicates that the real-world data are sampled from $p_{data}(real)$. Similarly, the simulation data conform to the distribution $p_{data}(sim)$, where $sim \sim p_{data(sim)}$ indicates that the simulation data are sampled from $p_{data}(sim)$. Although $\mathcal{L}_{GAN}$ was the same as the loss function of CycleGAN, the training data were different. Whether in CycleGAN or GAN, the generator is trained to maximize the probability of the discriminator making a mistake, and the discriminator is trained to correctly classify the samples as real or generated, while the generator and discriminator perform a min–max game. At the same time, a powerful discriminator encourages the generator to increase its capacity to produce realistic samples, which is a critical factor in the training of the generator.

For D_{sim}, because there is a large amount of true simulation data, D_{sim} can make good judgments and G_{r2s} can capture the simulation data distribution, regardless of the amount of real-world data. However, for D_{real}, it can judge poorly when there are just a few true real-world data. In order to improve the performance of D_{real}, a strategy of providing D_{real} with DES was proposed. By providing D_{real} with DES, the discriminator was exposed to a wider range of data. This squashed the solution space of the discriminator, which improved its ability to distinguish between real and fake samples, resulting in more accurate guidance to G_{s2r}. Due to the inherent disparities between simulation environments and real-world data, a bijective relationship existed between simulation data and real-world data, while these two sets of data remained independent of each other. Consequently, this results in data derived from simulations being totally distinct from real-world data. Therefore, $G_{r2s}(G_{s2r}(\text{simulation}))$ could be considered fake data for D_{real}. After convergence, the data equivalency between simulation and $G_{r2s}(G_{s2r}(\text{simulation}))$ would be established.

2.2.2 Targeted regression loss

Only $\mathcal{L}_{GAN}$ could hardly guarantee that the problem of mis-mapping would not arise for paired data. An example to illustrate the concept of the mis-mapping problem is shown herein. Consider two sets, X and Y, where each element in X has a corresponding element in Y based on a pre-defined mapping. Assume X = {1, 2, 3} and Y = {a, b, c}, with the mapping 1 → a, 2 → b, and 3 → c. When using the conventional GAN model to generate elements of Y from X, the generator may learn mappings such as 2 → a, 3 → b, and 1 → c, which do not only align with the specific desired mapping but also satisfies the GAN loss. In order to ensure data consistency, a specific loss term was introduced for paired simulation and real-world data, which can be expressed as

$$\mathcal{L}_{TRL(s2r)} = \frac{1}{n}\sum_{i=1}^{n}(G_{s2r}(sim_i) - real_i)^2,$$

$$\mathcal{L}_{TRL(r2s)} = \frac{1}{n}\sum_{i=1}^{n}(G_{r2s}(real_i) - sim_i)^2,$$

where i is the index of the data and n is the total amount of data. As depicted in Figure 2B, $\mathcal{L}_{TRL}$ was employed to ensure the consistency of the regressed real-world and its corresponding real-world data. Similarly, $\mathcal{L}_{TRL}$ could also be calculated when the real-world data were converted into regressed simulation data.

2.2.3 Cycle-consistency loss

To solve the problem of training generator with unpaired data from two domains while preserving cycle consistency, CycleGAN introduced $\mathcal{L}_{cyc}$, which was defined as L1 loss in Zhu et al. (2017). In this study, we modified it to L2 loss, which was more suitable for regression tasks.

$$\mathcal{L}_{cyc}(G_{s2r}, G_{r2s}) = \mathbb{E}_{x_{sim}\sim p_{data}(x_{sim})}[\|G_{r2s}(G_{s2r}(\text{sim})) - \text{sim}\|_2] + \mathbb{E}_{x_{real}\sim p_{data}(x_{real})}[\|G_{s2r}(G_{r2s}(\text{real})) - \text{real}\|_2].$$

2.2.4 Two-fold approach training

Due to the presence of both unpaired and paired data types, the proposed ImbalSim2Real scheme required a two-fold approach for training the generator. The first-fold approach employed $\mathcal{L}_{GAN} + \mathcal{L}_{cyc}$ as the loss function. This approach used all the available data, including both paired and unpaired data. The second-fold approach utilized only the paired data and employed the use of $\mathcal{L}_{TRL}$ as the loss function. The usage ratio of the first fold: second fold = 2:1.

2.3 Neural network implementation

As illustrated in Figure 2C, the generator utilizes a multilayer perceptron (MLP), consisting of 5 hidden layers with 20 nodes per layer, connected by an activation function ReLu and a linear layer.

TABLE 1 Functional relationships for three groups.

Group	y_1	y_2	Range x_2	Number of y_1	Number of y_2	Paired data	Have y_1 no y_2	Have y_2 no y_1
A	$x_1 x_2$	$x_1^3 + 2\sin(x_2)$	Random (10)	370	30	30	340	0
B	$x_1 x_2$	$\sqrt{x_2} - \sin(x_1) + \sqrt[3]{x_2} + {x_1}^4$	Random (20)	370	30	10	360	20
C	$x_1 + x_2$	$x_1 x_2 \sin(x_1) + ({x_2}^3 - x_2 \cos(x_1))$	Random (± 10)	350	50	20	330	30

The activation function of the discriminator is LeakyReLu. It is worth mentioning that the output layer of the discriminator in the code is a linear layer rather than a sigmoid layer, which is used for calculating the least squares based on the framework of least squares generative adversarial net (LSGAN) to mitigate the issue of vanishing gradients (Mao et al., 2017). The Adam optimization algorithm is selected as the optimizer for all schemes. The finger joint stiffness self-sensing scheme also utilizes an MLP with five hidden layers, each containing 20 nodes. The activation function is ReLu, the output layer is a linear layer, and L2 loss is employed as the cost function. Throughout the training of all schemes, the Adam optimization algorithm is utilized. All schemes were developed using Python 3.9.12 64-bits. The neural networks were developed using PyTorch 1.12.1 with CUDA 11.3 support for enhanced computational performance.

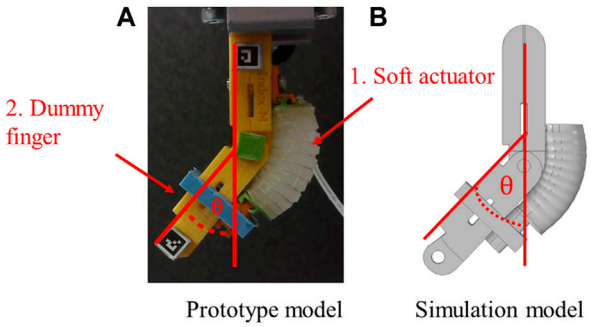

FIGURE 3
(A) Prototype model, **(B)** Simulation model.

3 Experiment setting

3.1 Numerical imbalanced domain transfer experiment setting

To investigate the capacity of the ImbalSim2Real scheme in addressing regression-type imbalanced sim2real problems with varying complexity domain transformations, three sets of numerical imbalanced domain transfer experiments (numerical experiments) were conducted between two domains: the source domain is represented by $y_1 = f_1(x_1, x_2)$ and the target domain is represented by $y_2 = f_2(x_1, x_2)$. The functional relationships and respective data amount of the three sets are detailed in Table 1.

Group A involves a mapping from a complex domain to another complex domain, group B involves a mapping from a complex domain to a simple domain, and group C involves a mapping from a simple domain to a complex domain (the complexities of the three sets of numerical experiments are depicted in the Supplementary Material S2). The x_1 in each group ranges from −1 to 1, with a step size of 0.1. For x_2, groups A, B, and C consist of random numbers drawn from a uniform distribution between (0, 10), (0, 20), and (−10,10) with four decimal places, respectively. All data were chosen randomly. Moreover, the number of data conformed to the following rules:

$$y_1\text{Number} = \text{Paired data} + \text{Have } y_1 \text{ no } y_2,$$
$$y_2\text{Number} = \text{Paired data} + \text{Have } y_2 \text{ no } y_1.$$

Each group underwent an initial training phase of 5,000 epochs at a learning rate of 1e-4, followed by 5,000 epochs with a learning rate of 1e-5. The trained ImbalSim2Real scheme was compared to a supervised learning method trained on only paired data.

3.2 Finger joint stiffness experiment setting

3.2.1 Data collection of finger joint stiffness data

In order to verify the effectiveness of the finger joint stiffness self-sensing framework, finger joint stiffness data in FEM software and real-world were collected.

The actuator's body (shown in Figure 3(A-1)) was made entirely of Dragon Skin 10 MEDIUM (Smooth-On, Inc., US), with Kevlar™ (DuPont, Inc., US) wrapped around it using a two-dimensional hitching technique. The dummy joint (Figure 3(A-2)) was designed and created using a 3D printer with 20% density PLA based on our earlier work (Kokubu and Yu, 2020). The dimensions were based on the average size of Japanese index fingers (Department of Defense Human Factors Engineering Technical Advisory Group, 2000). Moreover, to represent finger joint stiffness, a torsion spring was integrated into the joint.

For the stationary finite element simulation, COMSOL Multiphysics® was used, and all meshes were done using tetrahedral elements. Boundary load conditions were applied to simulate input air pressure and the hyperelastic behavior of the silicone sections, and a third-order Yeoh hyperelastic constitutive model was used, with the parameters obtained from the experimental data on Dragon skin in the Soft Robotics Materials Database Application (Marechal et al., 2021). The elastic band material, Smooth-on Sil 950, was modeled as a first-order Yeoh material model with C1 = 0.34 MPa (Labazanova et al., 2021) as it underwent less deformation than the actuator. To reduce

computation time, symmetry boundary conditions were applied. Additionally, gravity was added in all models. The model was configured for measuring the bending angle (θ) (see Figure 3) based on experiments designed in the previous work (Tarvainen et al., 2018; Kokubu and Yu, 2020). The dummy joint was also modeled using solid mechanics interface and hinge joint conditions.

3.2.2 Dataset preparation and training process setting

As shown in Figure 2C, the inputs of G_{s2r} are simulation angle, pressure, and stiffness values, while the output is the regressed real-world angle. It should be noted that the simulation and real-world pressure are the same, with a maximum air pressure of 100 kPa and an increment of 5 kPa per pressure level. The finger joint stiffness data in the simulation were 0.11, 0.15, 0.2, 0.5, 0.58, 0.7, 1.03, 1.19, 1.4, 1.70, and 2.12 Nmm/° and in real world, were 0.11, 0.58, 1.03, 1.19, and 2.11 Nmm/°. These values were selected based on the range of finger joint stiffness observed in individuals with spasticity and in healthy individuals (Matsunaga et al., 2023). Among them, 0.11, 1.19, and 2.12 Nmm/° were selected as the training dataset, and 0.58, 1.53, and 1.03 Nmm/° were selected as the validation dataset. Notably, 1.53 Nmm/° was absent from both the simulation and real-world training datasets. Each dataset was divided into two sets, Dataset_1 containing only paired data, specifically the data on the stiffness values of 0.11, 1.19, and 2.12 Nmm/°, and Dataset_2 containing all the available data. Datasets were run alternately during the training process.

The ImbalSim2Real scheme was trained for a total of 17,000 epochs with a learning rate of 1e-4, followed by 17,000 epochs with a learning rate of 1e-5. The ImbalSim2Real scheme was compared to the supervised learning method training by Dataset_1 and the original CycleGAN training by Dataset_2. Following the successful training of the ImbalSim2Real scheme, all simulation data were input into the trained scheme to obtain regressed real-world data, which were subsequently utilized to train the finger joint stiffness self-sensing scheme for a total of 10,000 epochs, with a learning rate of 1e-4.

For comparative purposes, two additional finger joint stiffness self-sensing schemes were developed and implemented. The first alternative scheme entailed replacing the trained ImbalSim2Real scheme with the trained original CycleGAN, following the same steps as previously outlined. The second alternative scheme employed a supervised learning method, utilizing only real-world finger joint stiffness data.

4 Results

4.1 Numerical imbalanced domain transfer experiment results

The results of the numerical experiment are shown in Table 2, which indicate that the proposed scheme outperforms the supervised learning method in terms of validation MSE (detailed results are provided in Supplementary Material S3). Specifically, the proposed scheme decreases the validation MSE in groups A, B, and C by 3.81, 5.21, and 29.56 times, respectively.

TABLE 2 Total validation MSE of the basic numerical experiment.

Group	Supervised	Proposed	Supervised/proposed
A	1,092.6	286.66	3.81
B	313.9	60.2	5.21
C	8606479	291122	29.56

4.2 Finger joint stiffness experiment results

4.2.1 Finger joint stiffness Imbalanced sim2real transfer results

The comparative analysis of training losses between the ImbalSim2Real scheme and the supervised learning method is illustrated in Figure 4A. The results demonstrate that both the supervised learning and the proposed ImbalSim2Real scheme achieve convergence, with the supervised learning method demonstrating a faster convergence speed. Moreover, as shown in Figures 4B–F, while the supervised learning method successfully transforms simulation data samples in the training dataset into real-world data, it is unable to perform such transformation when the simulation data samples are not in the training dataset. In contrast, the ImbalSim2Real scheme yields slightly poorer results for the data in the training dataset but better results for the data outside of the training dataset.

In addition, in cases where the finger joint stiffness values are 0.11, 0.58, and 1.03 Nmm/°, the angle values of simulation are smaller than the corresponding real-world values, but this is reversed for the stiffness values 1.19 and 2.12 Nmm/°. Since around 73% of the training dataset cases have simulation angles larger than their real-world counterparts, the supervised learning method tends to learn a pattern of reducing simulation angles for accurate real-world angle transformation. As a result, the resultant angle values for 0.58 and 1.03 Nmm/° are smaller than the corresponding angle values of simulation. On the other hand, the proposed ImbalSim2Real scheme is able to capture the true pattern of the real-world angles.

In order to quantitatively evaluate the efficacy of the ImbalSim2Real scheme, a success rate metric, defined by the proportion of regressed real-world angles falling within 10% of the true real-world angles, is used to gauge successful transformations. As shown in Table 3, the ImbalSim2Real method attains an overall success rate of 88%, which is considerably higher than 63% achieved by the supervised learning method and 41% by CycleGAN. Furthermore, in scenarios without applying any sim2real method, only 34% of the simulation data naturally align with the real-world data. Notably, for the data point of 1.03 Nmm/°, the simulation and real-world angles show close similarity in Figure 4D, and the supervised learning underestimates most angle values in simulation data in order to optimize the training loss. In contrast, the proposed scheme avoids this issue while maintaining data integrity. The results of the original CycleGAN demonstrate a relatively low success rate in transforming training data. In terms of generalizability, it performs somewhat better than supervised learning but is significantly less effective than the proposed ImbalSim2Real scheme.

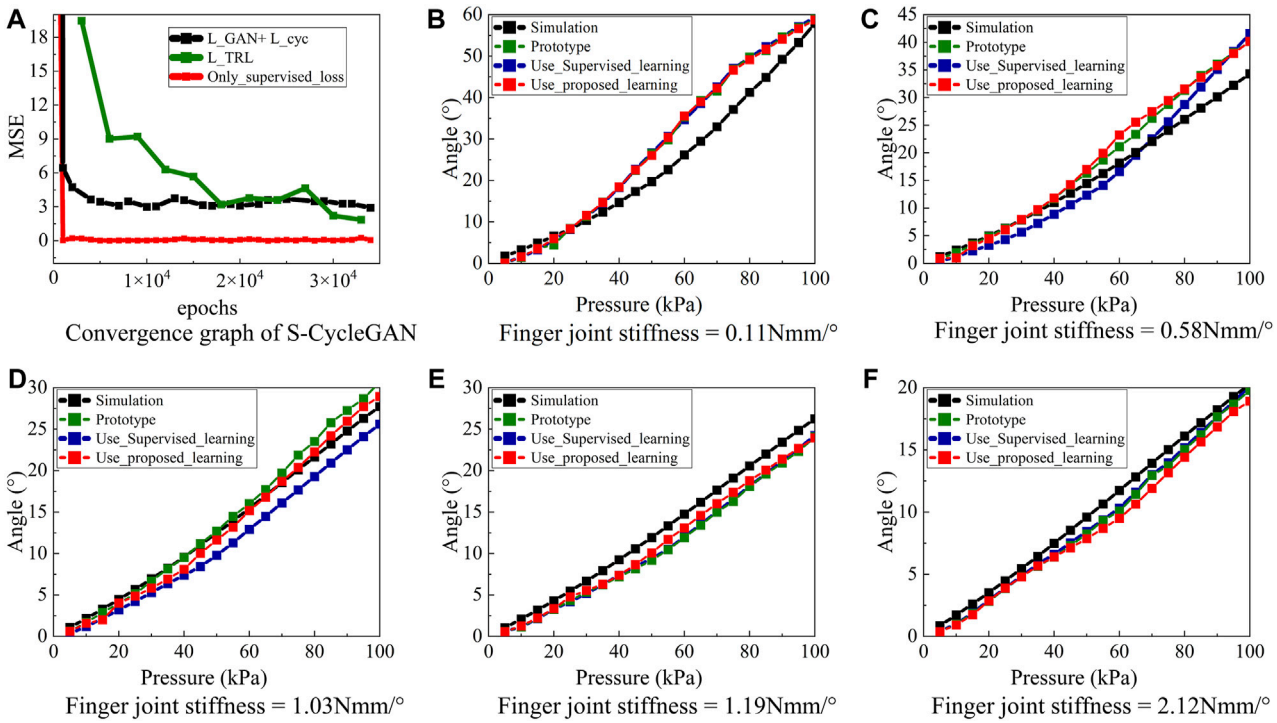

FIGURE 4
(A) Convergence graph, **(B)** Finger joint stiffness = 0.11 Nmm/°, **(C)** Finger joint stiffness = 0.58 Nmm/°, **(D)** Finger joint stiffness = 1.03 Nmm/°, **(E)** Finger joint stiffness = 1.19 Nmm/°.

TABLE 3 Successful rate for sim2real transfer for each method.

Stiffness value (Nmm/°)	0.11 (%)	0.58 (%)	1.03 (%)	1.19 (%)	2.12 (%)	Total (%)
Proposed	90	90	75	85	100	88
CycleGAN	40	30	10	80	45	41
Supervised	95	25	0	100	95	63
No transfer method	25	30	75	5	35	34

TABLE. 4 Results for finger joint stiffness estimation for each method (mean ± STD).

Stiffness value (Nmm/°)	1.53	0.11	0.58	1.03	1.19	2.12	Total MSE	Average MSE
Supervised learning	1.12 ± 0.49	0.16 ± 0.21	0.38 ± 0.14	0.61 ± 0.20	1.23 ± 0.17	2.06 ± 0.20	16.00	0.13
CycleGAN	0.96 ± 0.25	0.22 ± 0.27	0.40 ± 0.08	0.59 ± 0.07	1.14 ± 0.11	1.67 ± 0.28	19.60	0.16
Proposed framework	1.32 ± 0.16	0.19 ± 0.19	0.59 ± 0.06	1.06 ± 0.12	1.47 ± 0.18	1.78 ± 0.33	9.43	0.07[a]

[a]MSE of 0.15 Nmm/° reported in previous studies (Shi et al., 2020).

4.2.2 Finger joint stiffness self-sensing framework results

The results presented in Table 4 support a similar conclusion: the finger joint stiffness self-sensing scheme trained through the Imbalanced sim2real scheme reduces the estimation error by 41% compared to the supervised learning method trained on only real-world data. Additionally, when replacing the Imbalanced sim2real scheme with CycleGAN, the estimation error increases by 56%. Moreover, the proposed framework exhibits smaller standard deviation (STD) values, indicating a more stable output. When compared to the average MSE of 0.15 Nmm/° reported in previous studies (Shi et al., 2020), supervised learning achieved a similar performance, and the proposed scheme is even better, providing further evidence of its effectiveness as a model-independent method.

TABLE 5 Total validation MSE of group A for different methods.

	Proposed	Supervised	Fake-provided CycleGAN	Original CycleGAN	Original/fake-provided	Fake-provided/proposed	Original/proposed
MSE (unpaired)	284.8	1,092.2	468.3	1,244.8	2.65	1.64	4.37
MSE (paired)	1.9	0.381	29.7	28.6	0.96	15.63	15.05
Total	286.7	1,092.6	498.0	1,273.4	2.56	1.74	4.44

5 Ablation studies

To further assess the efficacy of the ImbalSim2Real scheme, ablation studies were conducted from three aspects: architectural differences, sensitivity to the ratio of paired *versus* unpaired data, and the impact of target domain data selection strategies.

5.1 Architectural analysis (via the group A dataset)

The ImbalSim2Real scheme was compared not only to the supervised learning method but also to the original CycleGAN and a variant of CycleGAN in which the discriminator only provided extra fake data without using a targeted regression loss (fake-provided CycleGAN).

The results in Table 5 reveal that the proposed ImbalSim2Real scheme has the smallest total validation MSE when converged. Meanwhile, Figure 5 presents 3D graphs of transformation (lower row) and projection diagrams (upper row) for different methods.

By comparing the $x_2 - y$ plane of the projection diagrams in Figures 5B, D, despite both the supervised learning and the original CycleGAN exhibiting the same level of large validation MSE, the reasons are different. In Figure 5B, the transferred domain points in the $x_2 - y$ plane are divergent when $x_2 > 5$. These points are considerably distant from the target domain points, thereby contributing to the large validation MSE. In contrast, the results of the original CycleGAN do not diverge. As shown in Figure 5D, in the $x_2 - y$ plane, the transferred data points cluster around the target domain points but do not align with them when $x_2 > 5$. The large amount of such data results in a relatively large validation MSE.

The validation MSE in the fake-provided CycleGAN is smaller than that of the original CycleGAN in Table 5, upon comparing Figures 5C, D (the iterative process of the fake-provided CycleGAN is provided in Supplementary Material S4). It is evident that the fake-provided CycleGAN exhibits superior performance in terms of the domain transformation, which appears more compressed and adherent to the target domain points and compares to that of the original CycleGAN. This can be ascribed to the augmented number of fake data supplied to D_{real}, which drives G_{s2r} to generate data points that more resemble the target domain distribution. Nonetheless, an unambiguous line (green dots form a line from $x_2 = 4$–6.5) can be discerned in the projection diagram (Figure 5C), indicating suboptimal or incomplete training of D_{real} in the corresponding region. Comparing the fake-provided CycleGAN method to the proposed scheme, it can be seen that the improvement in unpaired data is 1.54 times and that of paired data is 15.63 times.

5.2 Paired data sensitivity (via the group B dataset)

To investigate the significance of paired data for domain transformation and training convergence, we conducted experiments which maintained a constant total amount of y_2 data while controlling the ratio of paired data to unpaired y_2 data. Specifically, two ratios were considered, paired data: have y_2 no y_1 = 0:30 and 10:20. It should be noticed that the training process was performed 10 times for each ratio with 10,000 epochs.

The results in Table 6 indicate that when the data are entirely unpaired, the performance of the ImbalSim2Real scheme is significantly degraded. However, when the paired data points are introduced, the ImbalSim2Real scheme essentially converges to a similar state. Furthermore, we established a specific convergence success index, characterized as the validation MSE below 150, indicating convergence at the specific mapping. In the 0:30 case, due to the inability to use $\mathcal{L}_{TRL}$, only one group successfully converges at the specific mapping. For the remaining nine groups, although the training loss remains small, the validation loss is relatively large (additional results for different paired and unpaired ratios are provided in Supplementary Material S5).

5.3 Data selection analysis (via the group C dataset)

To verify the impact of the dispersion of target domain data (y_2 data) sampling on domain transformation, we performed experiments with extensive selection and intensive selection of y_2 data, respectively, while keeping the number of y_2 data and paired data constant (the specific details regarding the extent of the extensive and intensive selections are provided in Supplementary Material S6).

The results in Figure 6B demonstrate that when the source domain is exceedingly simple and the sampled target domain data can only represent a fraction of the distribution, the ImbalSim2Real scheme may learn a distribution that passes through this partial representation. On the other hand, Figures 6A, C indicate that more extensive sampling can better reflect the overall distribution, which is advantageous for the training process of the ImbalSim2Real scheme. Group C inherently involves a transformation from a

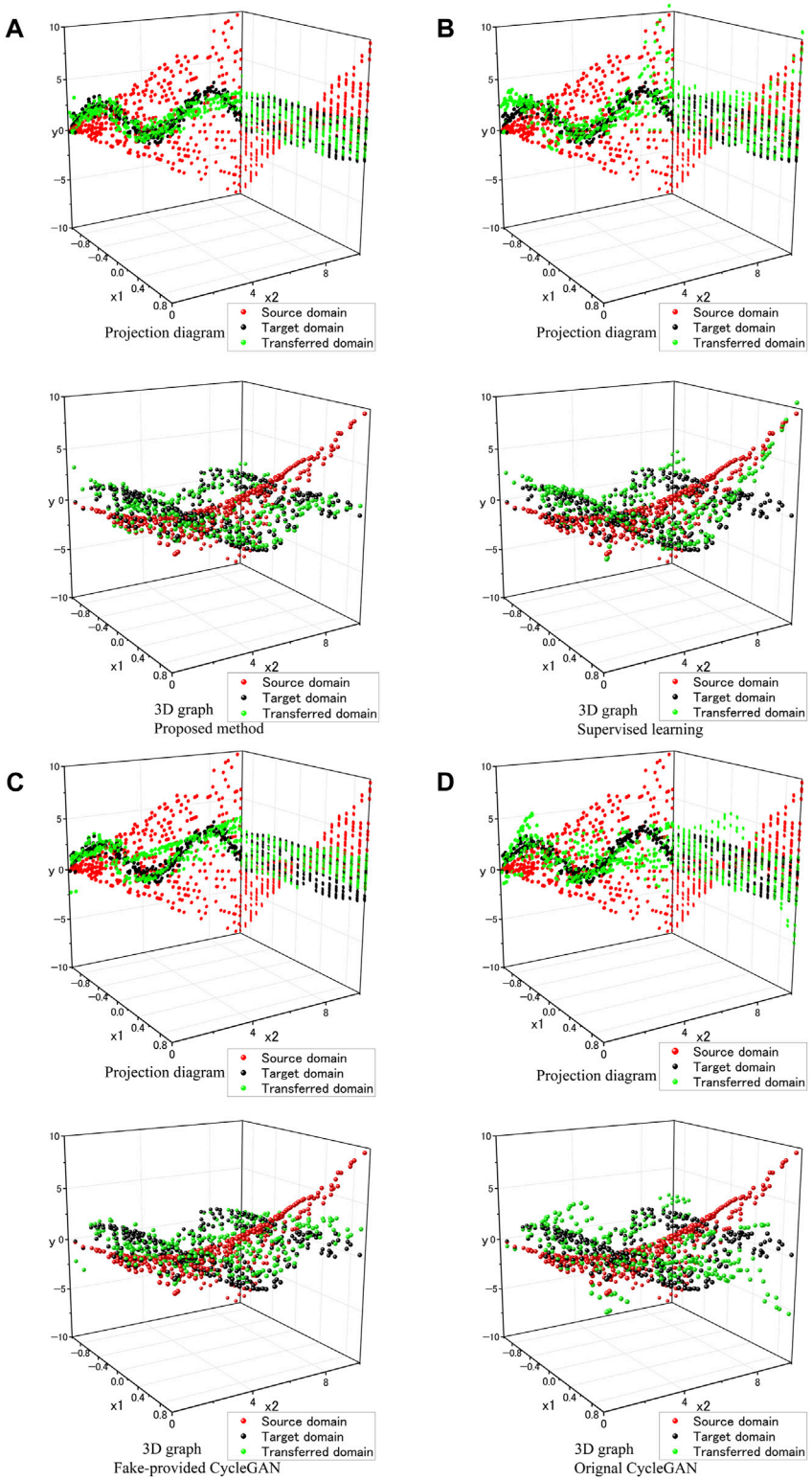

FIGURE 5
(A) Proposed method, **(B)** Supervised learning, **(C)** Fake-provided CycleGAN, **(D)** Original CycleGAN; each with upper: Projection diagram, lower: 3D graph.

simple domain. The excessively simple distribution of the source domain (only a red line in Figure 6) results in a limited supply of fake data for D_{real}, thereby limiting its capability to improve. In such cases, if the quality of the points collected by the source domain is poor, the learning effect of the uncollected points tends to be greatly reduced.

TABLE 6 Validation MSE of group B for different methods (paired: unpaired).

	0:30	20:10
10 times average	353,220.35	81.67
10 times variance	4.87e + 11	1,384.25
Specific convergence success index	10%	100%

6 Discussion

The problem of regression-type imbalanced sim2real poses a significant challenge when deploying simulation-trained models to real world, particularly in fields with limited real-world data, such as medicine and healthcare. In this paper, we proposed the ImbalSim2Real scheme and conducted detailed comparisons with the supervised learning and the original CycleGAN through numerical imbalanced domain transfer experiments, finger joint stiffness experiments, as well as ablation studies.

6.1 Compared to the supervised learning

In both the numerical imbalanced domain-transfer experiment and the finger joint stiffness experiment, the ImbalSim2Real scheme was compared with the supervised learning method. The findings in Tables 2, 3, 5 consistently demonstrate that, regardless of the type of the domain transfer problem (complex-to-simple domain, complex-to-complex domain, and simple-to-complex domain), the proposed ImbalSim2Real scheme achieves a smaller total validation MSE than the supervised learning method. More specifically, the supervised learning exhibits a smaller validation MSE for paired data (within the training dataset) while showing a larger MSE for unpaired data (outside the training dataset). Figure 5B indicates that such low generalization is because the supervised learning methods only rely on paired data, thus struggling to accurately capture the target domain distribution, especially in cases of limited data quantity. The supervised learning method's low data usage efficiency is the primary drawback when paired and unpaired data are included in the same training dataset. Additionally, as indicated in Figure 4A, the loss of the supervised learning method decreased rapidly, indicating a risk of overfitting, which also led to an increase in total validation MSE.

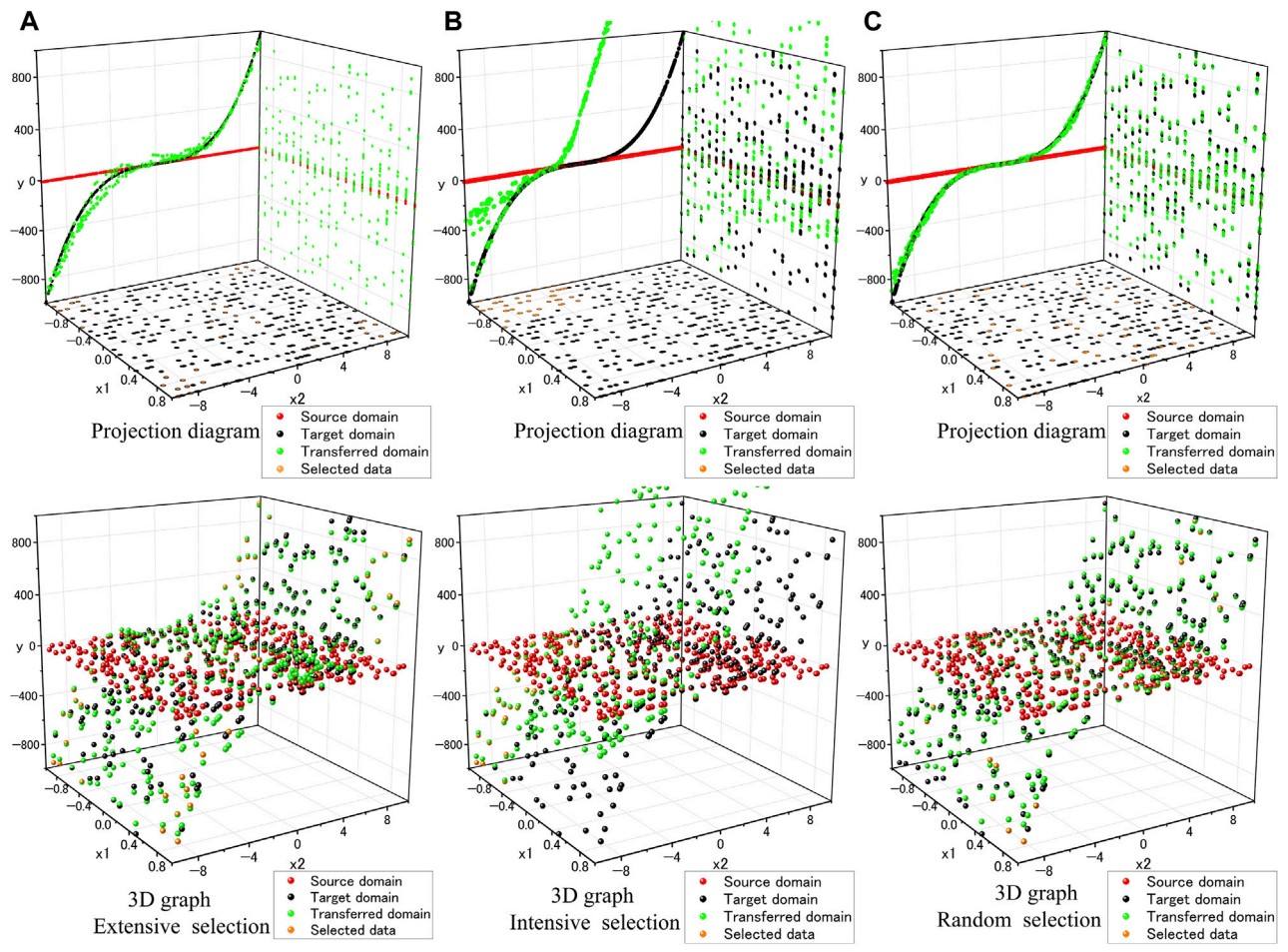

FIGURE 6
(A) Extensive selection, **(B)** Intensive selection **(C)** Random selection; each with upper: Projection diagram, lower: 3D graph.

6.2 Compared to the original CycleGAN

In both the numerical imbalanced domain-transfer experiment and the finger joint stiffness experiment, comparisons were also made between the ImbalSim2Real scheme and the CycleGAN, with detailed contrasts explored in the ablation studies. According to Figure 5D, the original CycleGAN can learn a subset of the target domain distribution but still exhibits a large validation MSE. This phenomenon can be attributed to two key factors, which are identified as the 'scarce real-world data for discriminator issue' and the 'specific sim2real mapping issue'.

To address the specific sim2real mapping issue, a specific mapping constraint $\mathcal{L}_{TRL}$ was introduced to the ImbalSim2Real scheme. The results in Tables 5, 6 validate the effectiveness of this approach. In contrast to the supervised learning method, CycleGAN relies solely on the distribution information of paired data while entirely neglecting to utilize the critical aspect of accurate mappings between the source and target domains. This results in CycleGAN's convergence being somewhat randomly achieved, which can be inferred through the convergence success index, as shown in Table 6. The ImbalSim2Real scheme combines the advantages of the supervised learning method and CycleGAN, effectively utilizing paired data through $\mathcal{L}_{TRL}$ and $\mathcal{L}_{GAN}$ while fully leveraging unpaired data via $\mathcal{L}_{GAN}$. Moreover, as shown in Figure 4A and Table 6, it is evident that not only is there no conflict between $\mathcal{L}_{TRL}$ and $\mathcal{L}_{GAN}$ + $\mathcal{L}_{cyc}$ but this combination also contributes to more stable and robust convergence. $\mathcal{L}_{TRL}$ represents a subset of the mapping sets that satisfies $\mathcal{L}_{GAN}$ + $\mathcal{L}_{cyc}$; thus, $\mathcal{L}_{TRL}$ is expected to accelerate the convergence of $\mathcal{L}_{GAN}$ + $\mathcal{L}_{cyc}$. Additionally, due to the alternating employment of $\mathcal{L}_{GAN}$ + $\mathcal{L}_{cyc}$ and $\mathcal{L}_{TRL}$ in the ImbalSim2Real scheme, $\mathcal{L}_{GAN}$ + $\mathcal{L}_{cyc}$ serves as a regularization term to prevent overfitting caused by $\mathcal{L}_{TRL}$. Although the significance of $\mathcal{L}_{TRL}$ and paired data was demonstrated in the paired data sensitivity experiment, the exact minimum proportion of paired data necessary for $\mathcal{L}_{TRL}$ to exhibit its effectiveness remained unestablished, which needs to be investigated in future work.

To address the scarce real-world data for the discriminator issue, we proposed D_{real} with additional DES. The effectiveness of this method is reflected in Table 5, where the validation MSE of the fake-provided CycleGAN is reduced by 2.65 times compared to the Original CycleGAN, even in the absence of $\mathcal{L}_{TRL}$. In instances, where there are paired data to guarantee that the data distribution has a specific limit, providing D_{real} with additional DES enables it to determine which data distribution is fake, thereby further prohibiting G_{s2r} from creating data comparable to the fake data distribution. This method cannot guarantee that the final G_{s2r} distribution would be correct, but it increases the likelihood of learning a proper distribution compared to not providing DES. Furthermore, it is well-known that the training of GAN-type models is heavily dependent on the quality of the training data. For the ImbalSim2Real scheme, the results of the data selection analysis experiment (Figure 6) also demonstrate that intensive (this can be considered low-quality since the term "intensive" suggests a reduced likelihood of capturing the majority of distribution information) target domain sampling yields much worse results than extensive or random (high-quality) target domain sampling. Additionally, as DES are from the source domain, high-quality source domain data can also enhance D_{real}'s performance. The appearance of an unambiguous line in Figure 5C substantiates this inference. A closer inspection of the source domain reveals the absence of sampling points in the region traversed by the unambiguous line within the $x_2 - y$ plane. This deficiency in the distribution of source domain sampling points adversely affects D_{real}'s training, reflecting in the observed anomaly. Similarly, the findings in Figure 6B also verify that when the source domain is inherently simple with limited information, providing additional DES did not yield effective results. Therefore, no matter whether there is an absence of certain source domain data or the source domain lacks complexity, both scenarios can lead to D_{real} incapable of making accurate judgments. The final ImbalSim2Real scheme only misidentifies a domain that contains subsets similar to a portion of the target domain as the true target domain.

In summary, the resolution of the sim2real challenge hinges critically on both the quality and quantity of data from the source domain, as well as from the target domain. In the realm of the imbalanced sim2real problem, the limitations on the quantity of target domain data necessitate the use of higher-quality data, such as paired data or those capable of representing distribution characteristics. In cases where high-quality sampling of the target domain data is not feasible, it becomes essential to utilize the available target domain data with high quality, which is the primary motivation behind introducing $\mathcal{L}_{TRL}$. Regarding the source domain data, while increasing its quantity, high-quality source domain sampling points are critical for the successful training of D_{real}. The ImbalSim2Real scheme effectively capitalizes on this characteristic, an aspect that is notably absent in the original CycleGAN architectures.

6.3 Application to the finger joint stiffness self-sensing framework

The proposed ImbalSim2Real scheme was used to resolve a practical issue in a model-independent finger joint stiffness self-sensing framework. The results of finger joint stiffness estimation in Table 4 demonstrate that the performance of the proposed framework is superior to the supervised learning method trained on a scarce real-world dataset and the original CycleGAN. However, the results of joint stiffness 1.19 and 2.12 Nmm/° are inferior to the supervised learning due to the following possible causes: first, during the training of the finger joint stiffness self-sensing scheme, real-world data are not used for training; instead, the training data consisted solely of regressed data, which included the values of 1.19 and 2.12mm/°. This implies that fine-tuning the trained model on real-world data may provide a potential solution to address this issue more effectively (real-world data fine-tuned results are provided in Supplementary Material S7). Second, 1.19 and 2.12 Nmm/° were the greatest values relative to the rest of the data; hence, their MSEs tend to be larger.

7 Conclusion

In this study, we proposed a novel ImbalSim2Real scheme. The proposed ImbalSim2Real scheme includes a targeted regression loss and augments fake data for enhanced domain transfer. This approach

effectively leverages both paired and unpaired data to achieve a specific regression-type domain transfer, even in situations with limited available real-world data. Furthermore, we presented a finger joint stiffness framework as an application of the proposed ImbalSim2Real scheme. With the proposed framework, the validation loss for estimating real-world finger joint stiffness was reduced by roughly 41% compared to the supervised learning method and by 56% relative to the CycleGAN trained on the imbalanced dataset. Future research should concentrate on further enhancing the training effect of D_{real} in the ImbalSim2Real scheme and investigating the potential applicability of the ImbalSim2Real scheme to high-dimensional datasets.

Data availability statement

The original contributions presented in the study are included in the article/Supplementary Material; further inquiries can be directed to the corresponding author.

Author contributions

ZZ: conceptualization, methodology, software, validation, writing–original draft, and writing–review and editing. YL: investigation and writing–review and editing. PT: investigation and writing–review and editing. RQ: investigation and writing–review and editing. SK: investigation and writing–review and editing. FM: investigation and writing–review and editing. QX: investigation and writing–review and editing. WY: conceptualization, funding acquisition, supervision, and writing–review and editing.

Funding

The authors declare that financial support was received for the research, authorship, and/or publication of this article. This work was partially supported by JST, the establishment of university fellowships toward the creation of science technology innovation, grant number JPMJFS2107, and Grant-in-Aid for Scientific Research (B), JSPS KAKENHI, grant number 22H03450.

Conflict of interest

The authors declare that the research was conducted in the absence of any commercial or financial relationships that could be construed as a potential conflict of interest.

Publisher's note

All claims expressed in this article are solely those of the authors and do not necessarily represent those of their affiliated organizations, or those of the publisher, the editors, and the reviewers. Any product that may be evaluated in this article, or claim that may be made by its manufacturer, is not guaranteed or endorsed by the publisher.

Supplementary material

The Supplementary Material for this article can be found online at: https://www.frontiersin.org/articles/10.3389/fbioe.2024.1334643/full#supplementary-material

References

Abascal, J. F. P. J., Ducros, N., Pronina, V., Rit, S., Rodesch, P. A., Broussaud, T., et al. (2021). Material decomposition in spectral ct using deep learning: a Sim2Real transfer approach. *IEEE Access* 9, 25632–25647. doi:10.1109/ACCESS.2021.3056150

Bhagat, S., Banerjee, H., Tse, Z. T. H., and Ren, H. (2019). Deep reinforcement learning for soft, flexible robots: brief review with impending challenges. *Robotics* 8, 1–36. doi:10.3390/robotics8010004

Chen, W., Xu, Y., Chen, Z., Zeng, P., Dang, R., Chen, R., et al. (2022). Bidirectional sim-to-real transfer for GelSight tactile sensors with CycleGAN. *IEEE Robot. Autom. Lett.* 7, 6187–6194. doi:10.1109/LRA.2022.3167064

Department of Defense Human Factors Engineering Technical Advisory Group (2000) *Human engineering design data digest*.

Ding, Y., Jia, M., Zhuang, J., Cao, Y., Zhao, X., and Lee, C. G. (2023). Deep imbalanced domain adaptation for transfer learning fault diagnosis of bearings under multiple working conditions. *Reliab. Eng. Syst. Saf.* 230, 108890. doi:10.1016/j.ress.2022.108890

Ding, Z., Lepora, N. F., and Johns, E. (2020). Sim-to-Real transfer for optical tactile sensing. *Proc. - IEEE Int. Conf. Robot. Autom.*, 1639–1645. doi:10.1109/ICRA40945.2020.9197512

Farahani, A., Voghoei, S., Rasheed, K., and Arabnia, H. R. (2021). "A brief review of domain adaptation," in *Advances in data science and information engineering*, 877–894. doi:10.1007/978-3-030-71704-9_65

Han, X., Zheng, H., and Zhou, M. (2022). CARD: classification and regression diffusion models. *Adv. Neural Inf. Process. Syst.* 35. doi:10.48550/arXiv.2206.07275

Harms, J., Lei, Y., Wang, T., Zhang, R., Zhou, J., Tang, X., et al. (2019). Paired cycle-GAN-based image correction for quantitative cone-beam computed tomography. *Med. Phys.* 46, 3998–4009. doi:10.1002/mp.13656

Heung, H. L., Tang, Z. Q., Shi, X. Q., Tong, K. Y., and Li, Z. (2020). Soft rehabilitation actuator with integrated post-stroke finger spasticity evaluation. *Front. Bioeng. Biotechnol.* 8, 1–10. doi:10.3389/fbioe.2020.00111

Hofer, S., Bekris, K., Handa, A., Gamboa, J. C., Mozifian, M., Golemo, F., et al. (2021). Sim2Real in Robotics and automation: applications and challenges. *IEEE Trans. Autom. Sci. Eng.* 18, 398–400. doi:10.1109/TASE.2021.3064065

Jianu, T., Gomes, D. F., and Luo, S. (2022). Reducing tactile Sim2Real domain gaps via deep texture generation networks. *Proc. - IEEE Int. Conf. Robot. Autom.*, 8305–8311. doi:10.1109/ICRA46639.2022.9811801

Josifovski, J., Malmir, M., Klarmann, N., Zagar, B. L., Navarro-Guerrero, N., and Knoll, A. (2022). Analysis of randomization effects on Sim2Real transfer in reinforcement learning for robotic manipulation tasks. *IEEE Int. Conf. Intell. Robot. Syst.*, 10193–10200. doi:10.1109/IROS47612.2022.9981951

Kokubu, S., and Yu, W. (2020). Developing a hybrid soft mechanism for assisting individualized flexion and extension of finger joints. *Proc. Annu. Int. Conf. IEEE Eng. Med. Biol. Soc. EMBS* 2020, 4873–4877. doi:10.1109/EMBC44109.2020.9176061

Kuang, J., Xu, G., Tao, T., and Wu, Q. (2022). Class-imbalance adversarial transfer learning network for cross-domain fault diagnosis with imbalanced data. *IEEE Trans. Instrum. Meas.* 71, 1–11. doi:10.1109/TIM.2021.3136175

Labazanova, L., Wu, Z., Gu, Z., and Navarro-Alarcon, D. (2021) "Bio-inspired design of artificial striated muscles composed of sarcomere-like contraction units," in *2021 20th int. Conf. Adv. Robot. ICAR 2021*, 370–377. doi:10.1109/ICAR53236.2021.9659330

Lu, Y., Zhou, Z., Kokubu, S., Qin, R., Vinocour, P. E. T., and Yu, W. (2023). Neural network-based active load-sensing scheme and stiffness adjustment for pneumatic soft actuators for minimally invasive surgery support. *Sensors* 23, 833. doi:10.3390/s23020833

Mao, X., Li, Q., Xie, H., Lau, R. Y. K., Wang, Z., and Smolley, S. P. (2017). "Least squares generative adversarial networks," in *Proceedings of the IEEE international conference on computer vision (ICCV)*, 2794–2802. doi:10.1080/0142569900110108

Marechal, L., Balland, P., Lindenroth, L., Petrou, F., Kontovounisios, C., and Bello, F. (2021). Toward a common framework and Database of materials for soft Robotics. *Soft Robot.* 8, 284–297. doi:10.1089/soro.2019.0115

Matsunaga, F., Kokubu, S., Tortos Vinocour, P. E., Ke, M. T., Hsueh, Y. H., Huang, S. Y., et al. (2023). Finger joint stiffness estimation with joint modular soft actuators for hand telerehabilitation. *Robotics* 12, 83. doi:10.3390/robotics12030083

Muratore, F., Ramos, F., Turk, G., Yu, W., Gienger, M., and Peters, J. (2022). Robot learning from randomized simulations: a review. *Front. Robot. AI* 9, 1–19. doi:10.3389/frobt.2022.799893

Peng, J., Huang, Y., Sun, W., Chen, N., Ning, Y., and Du, Q. (2022). Domain adaptation in remote sensing image classification: a survey. *IEEE J. Sel. Top. Appl. Earth Obs. Remote Sens.* 15, 9842–9859. doi:10.1109/JSTARS.2022.3220875

Salvato, E., Fenu, G., Medvet, E., and Pellegrino, F. A. (2021). Crossing the reality gap: a survey on sim-to-real transferability of robot controllers in reinforcement learning. *IEEE Access* 9, 153171–153187. doi:10.1109/ACCESS.2021.3126658

Schonfeld, E., Schiele, B., and Khoreva, A. (2020). A U-net based discriminator for generative adversarial networks. *Proc. IEEE Comput. Soc. Conf. Comput. Vis. Pattern Recognit.*, 8204–8213. doi:10.1109/CVPR42600.2020.00823

Shi, X. Q., Heung, H. L., Tang, Z. Q., Tong, K. Y., and Li, Z. (2020). Verification of finger joint stiffness estimation method with soft robotic actuator. *Front. Bioeng. Biotechnol.* 8, 1–12. doi:10.3389/fbioe.2020.592637

Tarvainen, T. V. J., Fernandez-Vargas, J., and Yu, W. (2018). New layouts of fiber reinforcements to enable full finger motion assist with pneumatic multi-chamber elastomer actuators. *Actuators* 7, 31–18. doi:10.3390/ACT7020031

Tobin, J., Fong, R., Ray, A., Schneider, J., Zaremba, W., and Abbeel, P. (2017). Domain randomization for transferring deep neural networks from simulation to the real world. *IEEE Int. Conf. Intell. Robot. Syst.*, 23–30. doi:10.1109/IROS.2017.8202133

Truong, J., Chernova, S., and Batra, D. (2021). Bi-directional domain adaptation for Sim2Real transfer of embodied navigation agents. *IEEE Robot. Autom. Lett.* 6, 2634–2641. doi:10.1109/LRA.2021.3062303

Wang, Y., Kokubu, S., Zhou, Z., Guo, X., Hsueh, Y. H., and Yu, W. (2021). Designing soft pneumatic actuators for thumb movements. *IEEE Robot. Autom. Lett.* 6, 8450–8457. doi:10.1109/LRA.2021.3105799

Xie, X., Chen, J., Li, Y., Shen, L., Ma, K., and Zheng, Y. (2020). Self-supervised CycleGAN for object-preserving image-to-image domain adaptation. *Lect. Notes Comput. Sci. Incl. Subser. Lect. Notes Artif. Intell. Lect. Notes Bioinforma. 12365 LNCS*, 498–513. doi:10.1007/978-3-030-58565-5_30

Zhang, Z., Yang, L., and Zheng, Y. (2018). Translating and segmenting multimodal medical volumes with cycle- and shape-consistency generative adversarial network. *Proc. IEEE Comput. Soc. Conf. Comput. Vis. Pattern Recognit.*, 9242–9251. doi:10.1109/CVPR.2018.00963

Zhao, W., Queralta, J. P., and Westerlund, T. (2020). Sim-to-Real transfer in deep reinforcement learning for Robotics: a survey. *2020 IEEE Symp. Ser. Comput. Intell. SSCI* 2020, 737–744. doi:10.1109/SSCI47803.2020.9308468

Zhao, Y., Jing, X., Qian, K., Gomes, D. F., and Luo, S. (2023). Skill generalization of tubular object manipulation with tactile sensing and Sim2Real learning. *Rob. Auton. Syst.* 160, 104321. doi:10.1016/j.robot.2022.104321

Zhou, Z., Kokubu, S., Wang, Y., Lu, Y., Tortos, P. E., and Yu, W. (2022). Optimization of spring constant of a pneumatic artificial muscle-spring driven antagonistic structure. *IEEE Robot. Autom. Lett.* 7, 5982–5989. doi:10.1109/lra.2022.3162021

Zhu, J.-Y., Efros, T. P., Isola, P., and Efros, A. A. (2017). Unpaired image-to-image translation using cycle-consistent adversarial networks. *Proc. IEEE Int. Conf. Comput. Vis.*, 183–202. doi:10.1109/iccv.2017.244

Zhu, Y., Wu, X., Li, Y., Qiang, J., and Yuan, Y. (2022). Self-adaptive imbalanced domain adaptation with deep sparse autoencoder. *IEEE Trans. Artif. Intell.* 4, 1293–1304. doi:10.1109/TAI.2022.3196813

frontiers | Frontiers in Bioengineering and Biotechnology

TYPE Original Research
PUBLISHED 20 June 2024
DOI 10.3389/fbioe.2024.1305837

OPEN ACCESS

EDITED BY
Wujing Cao,
Shenzhen Institute of Advanced Technology (CAS), China

REVIEWED BY
Wojciech Wolański,
Silesian University of Technology, Poland
Christian Liebsch,
Ulm University Medical Center, Germany

*CORRESPONDENCE
Jian Qiao,
qiaojj99065@163.com

RECEIVED 02 October 2023
ACCEPTED 03 June 2024
PUBLISHED 20 June 2024

CITATION
Kang J, Wu Y and Qiao J (2024), Numerical evaluation of spinal reconstruction using a 3D printed vertebral body replacement implant: effects of material anisotropy.
Front. Bioeng. Biotechnol. 12:1305837.
doi: 10.3389/fbioe.2024.1305837

Numerical evaluation of spinal reconstruction using a 3D printed vertebral body replacement implant: effects of material anisotropy

Jianfeng Kang, Yanlong Wu and Jian Qiao*

School of Mechatronic Engineering and Automation, Foshan University, Foshan, China

Background and objective: Artificial vertebral implants have been widely used for functional reconstruction of vertebral defects caused by tumors or trauma. However, the evaluation of their biomechanical properties often neglects the influence of material anisotropy derived from the host bone and implant's microstructures. Hence, this study aims to investigate the effect of material anisotropy on the safety and stability of vertebral reconstruction.

Material and methods: Two finite element models were developed to reflect the difference of material properties between linear elastic isotropy and nonlinear anisotropy. Their biomechanical evaluation was carried out under different load conditions including flexion, extension, lateral bending and axial rotation. These performances of two models with respect to safety and stability were analyzed and compared quantitatively based on the predicted von Mises stress, displacement and effective strain.

Results: The maximum von Mises stress of each component in both models was lower than the yield strength of respective material, while the predicted results of nonlinear anisotropic model were generally below to those of the linear elastic isotropic model. Furthermore, the maximum von Mises stress of natural vertebra and reconstructed system was decreased by 2–37 MPa and 20–61 MPa, respectively. The maximum reductions for the translation displacement of the artificial vertebral body implant and motion range of whole model were reached to 0.26 mm and 0.77°. The percentage of effective strain elements on the superior and inferior endplates adjacent to implant was diminished by up to 19.7% and 23.1%, respectively.

Conclusion: After comprehensive comparison, these results indicated that the finite element model with the assumption of linear elastic isotropy may underestimate the safety of the reconstruction system, while misdiagnose higher stability by overestimating the range of motion and bone growth capability.

KEYWORDS

spinal reconstruction, biomechanical properties, finite element analysis, linear elastic isotropy, nonlinear anisotropy

1 Introduction

Spinal column, regarded as the central axis of human skeleton system, possesses multiple functions of load-bearing, shock absorption, protection, and movement. Unfortunately, traumatic injury, congenital defects or surgical removal of tumors can result in large defects or absences of vertebrae that require clinical intervention if functional restoration is to be achieved. Currently, this combination of artificial vertebral body implants and different fixation strategies is usually used to accomplish vertebral replacement and functional reconstruction (Zhang and Guo, 2023). Moreover, some 3D printed patient-specific implants considering fully the differences of individualized defects and anatomical morphology, are also designed and applied to harvest better service performance in clinic (Hu et al., 2022; Palmquist et al., 2023). However, several postoperative complications still existed (Yoshioka et al., 2013), such as subsidence of implants, screw misplacement and pedicle breakage, degeneration of adjacent segments, etc. These risks are closely associated with the biomechanical properties of the spinal reconstruction system, and portend that further investigation for influence factors of biomechanical performance will provide a solid foundation for improving clinical outcomes.

The Wolff's law pointed out that host bones can adapt to satisfy functional response demands by changing their internal structure and external morphology. Under the action of complex physiological loads and motions, the hierarchical and porous structure of natural bone exhibits mechanical anisotropy, further providing excellent stress distribution and effectively maintaining a dynamic balance between bone formation and resorption. In this scenario, the anisotropic behaviour of mechanical properties for the cortical or cancellous bone in various vertebrae was investigated by using micro computed tomography (μCT) scanning analysis (Perilli et al., 2012), micro-scale finite element method (Goda and Ganghoffer, 2015), uniaxial loading tests (Yeni et al., 2022), nanoindentation test (Wolfram et al., 2010) and ultrasound measurements (Nicholson and Alkalay, 2007). These studies fully confirmed the significant anisotropy of mechanical properties for the host bone, such as the anisotropic degree of thoracic and lumbar vertebral segment reached to 1.47 ± 0.17 and 1.51 ± 0.21, respectively (Lochmüller et al., 2008). Great variability of mechanical properties was closely related to the anatomic location, orientation, and nonhomogeneous morphology (Hulme et al., 2007). However, the material properties of natural vertebrae in the process of biomechanical analysis were set as the linear elastic isotropy (Fan et al., 2021), or based on the mapping relationship of the grayscale-apparent density-modulus (Gong et al., 2022). Hence, it is indispensable and urgent to take full account of the influence of material anisotropy during the design and biomechanical evaluation of bone defect repair, so as to accurately reflect the service performance of the reconstructed system.

Artificial vertebral body implants constructed with a combination of solid and porous structures, can obtain integrated advantages of light weight, high strength and superior stability through the rational design of macro/microstructures and additive manufacturing technology (Kang et al., 2021), such as the 3D ACT vertebral body prosthesis from Beijing AKEC Medical Co., Ltd., the F3D corpectomy vertebral body replacement system from CoreLink LLC., etc. These certified implants were prepared using a variety of porous lattice types, controllable geometric parameters, as well as different powder bed fusion 3D printing technologies including selective laser melting and electron beam melting. Overall, the mechanical properties of porous lattices and their influencing factors have been extensively studied based on the homogenization theory, finite element analysis and experimental measurements, further better serving the design and modeling of 3D printed medical implants (Wang et al., 2017). Nevertheless, the anisotropy of mechanical properties for the implant's microstructure was notable and have been studied (Barba et al., 2019; Jia et al., 2023). In our previous study (Kang et al., 2020), the numerical method for modulus anisotropy of porous structures was developed to characterize the spatial distribution of elastic modulus and degree of anisotropy effectively. Despite multiple benefits attributed to the porosity design of medical implants, the anisotropic mechanical properties of porous structures should also be paid more attention and analyzed accurately in the evaluation of biomechanical performance.

The finite element method was widely used to explore the biomechanical performance of vertebral defect repair under various loading and activities conditions similar with *in vivo* environment (Dong et al., 2020; Dai et al., 2022; Mehboob, 2023). After the numerical calculation, the safety and stability of spinal reconstruction system can be evaluated quantitatively. However, the material properties of cancellous or cortical bone in the finite element analysis were frequently simplified as linear elastic isotropy (Dong et al., 2020; Kang et al., 2021). Directional dependent variation in mechanical properties for the implant's microstructure have not been fully considered (Wang et al., 2016). Overall, existing finite element models for the biomechanical analysis of vertebral reconstruction systems rarely take into account the effect of material anisotropy from host bone and implant's microstructure on their biomechanical properties, which may cause significant discrepancies between real service performance and design expectations.

Oriented to the clinical complications of vertebral body replacement, the study aims to understand the effect of material anisotropy of component materials on the biomechanical properties of spinal reconstruction. Hence, two finite element models considering anisotropic difference were developed to evaluate and compare the biomechanical properties under various loads conditions. This study not only reveals the influence of different material properties on biomechanical properties, but also provides an effective methodology for the design and performance evaluation of artificial vertebral implants.

2 Materials and methods

2.1 Reconstruction of geometrical models

According to the CT images of a 25-year-old male patient provided by Xijing Hospital (the First Affiliated Hospital of the Fourth Military Medical University, Shaanxi, China), malignant tumor location can be clearly observed in the second segment of the lumbar vertebra, accompanied by severe vertebral erosion symptoms, as shown in Figure 1A. Therein, the exported DICOM files with a slice thickness

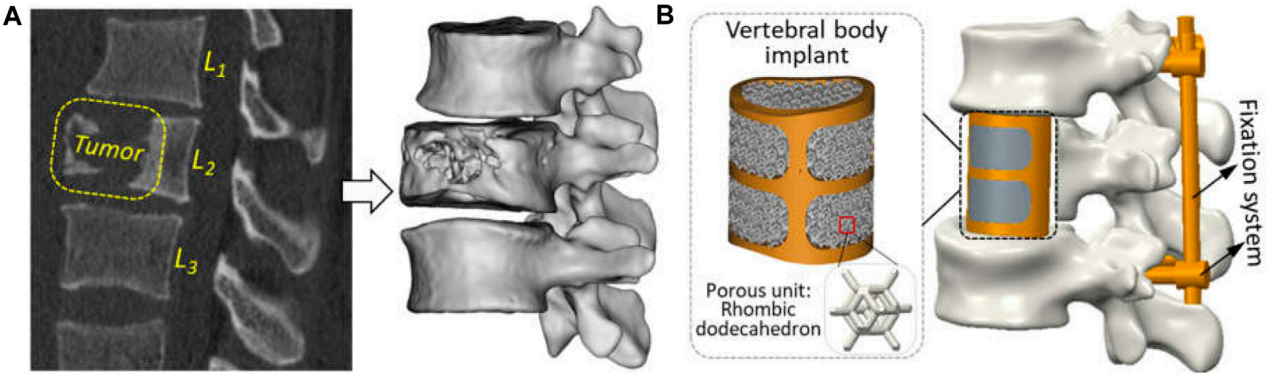

FIGURE 1
Reconstruction of geometric models for clinical treatment of vertebral defect: **(A)** tumor observation in the CT scanning image and three-dimensional geometric modeling; **(B)** vertebral replacement using by the artificial vertebral body implant and posterior fixation system.

of 0.625 mm and a pixel size of 0.35 mm ensured the reconstruction of three-dimension geometrical models for the spine and tumor. Briefly, the modeling process was to import CT images into the Mimics software (Version 17.0, Materialise, Inc., Leuven, Belgium), extracting the three-dimensional geometric model of target components separately by setting different gray thresholds, and then import the outputted STL files into the Geomagic Wrap software (Version 2017, 3D System, Inc., United States) for the operation of polygon smoothing and exact surfacing. Based on the patient's actual situation, the preoperative planning was determined to be complete resection of the tumor, attached locally to the vertebral segment and adjacent intervertebral discs. And then the repair of vertebral defect was designed with artificial vertebral body implant combining with posterior fixation system.

Under the guidance of clinical surgeons, numerical simulation of tumor resection was performed to measure some key characteristic parameters of the defect region, such as the height, transverse diameter, sagittal diameter, etc. Based on the aforementioned parameters, a patient-specific artificial vertebral body implant with solid beams and porous structure was designed. Since the design of vertebral body implant was investigated in previous studies (Shi et al., 2020), a traditional trussed vertebral implant with solid wall thickness of 2 mm was used directly. Its macro geometric shape adopts the orthogonal combination of transverse and longitudinal beam in the anterior and solid thin wall in the posterior. Based on existing studies (Shi et al., 2020; Kang et al., 2021), a rhombic dodecahedron unit with a length of 2 mm, a porosity of 80%, and a strut diameter of 0.3 mm possessed excellent bone-ingrowth capability and has been applied clinically. So, this porous lattice was used to fill inside vertebral implant. Additionally, the posterior fixation system, including pedicle screws ($\phi \times L$: 4 × 40 mm) and connecting rods ($\phi \times L$: 5 × 75 mm), were fabricated by traditional machining methods using Ti_6Al_4V material and used to further enhance the stability of reconstructed model.

2.2 Finite element modeling

Based on the above geometric model, the responding finite element model was developed in the Abaqus software (Version 6.14, Dassault Systems Inc., France). To evaluate the influence of material anisotropy on the biomechanical properties of vertebral body replacement, different material properties with linear elastic isotropic and nonlinear anisotropic features for each component of the reconstructed lumbar spine model were assigned as given in Table 1. The effective elastic modulus and yield strength of porous structure was measured by compression (Dong et al., 2020; Kang et al., 2021). For another, the modulus anisotropy of porous structures considering the irregular geometry after 3D-printing was analyzed by the numerical method developed of previous study (Kang et al., 2020). Besides, corresponding ligaments were integrated into the model through nonlinear springs to define the tension-only and incompressible behaviours (Kang et al., 2021), as shown in Table 2.

Each component was meshed using the Hypermesh software (Version 12.0, Altair Engineering, Inc., United States) and then imported into Abaqus software for a finite element analysis, as shown in Figure 2. According to existing studies (Kang et al., 2021) combined with the statistical measurements of the patient's CT image data, the triangular prism element (C3D6) with a layer of 0.4 mm thick was used to reflect the role of cortical bone. The C3D6 element can ensure good stress transfer at the interface between cortical bone and cancellous bone through the co-node feature. The cancellous bone and the remaining components were meshed using a tetrahedron element (C3D4). To remove the impacts of meshing size, a meshing sensitivity analysis was carried out under the conditions of meshing sizes of 0.5 mm, 1 mm and 2 mm. Less than a 5% relative difference was achieved across all sizes, thus 1 mm was selected. Overall, 782,804 elements were included for a complete model.

A "tie" constraint was set for the contact interface between the endplate and vertebral body implant, as well as between the pedicle screws and bone. Facet joint articulation at all levels was simulated as a finite sliding contact problem with frictionless property owing to the cartilaginous effect. These settings of contact mode were widely accepted in the studies (Dreischarf et al., 2014; Tsouknidas et al., 2015). Additionally, the boundary and loading conditions were shown in Figure 2. For the spinal finite element model, it is very common to fix the lower surface of the bottom vertebrae and apply load to the upper surface of the top vertebrae to simulate the human spinal daily activities (Cao et al., 2001; Vadapalli et al., 2006;

TABLE 1 Assignment of materials properties for each component.

Models	Components	Properties parameters	References
Linear elastic isotropic model	Cortical bone	E = 12 GPa; ν = 0.3	Lu et al. (2022)
	Cancellous bone	E = 100 MPa; ν = 0.2	Lu et al. (2022)
	Solid part of vertebral body implant	E = 110 GPa; ν = 0.3	Dong et al. (2020), Kang et al. (2021)
	Porous part of vertebral body implant	E = 800 MPa; ν = 0.3	Dong et al. (2020), Kang et al. (2021)
	Fixation system with Ti_6Al_4V material	E = 110 GPa; ν = 0.3	Dong et al. (2020), Kang et al. (2021)
Nonlinear anisotropic model	Cortical bone	C_{11} = 11.13, C_{22} = 11.13, C_{33} = 15.37 C_{44} = 6.92, C_{55} = 6.92, C_{66} = 5.89, C_{12} = 5.24, C_{23} = C_{13} = 6.15	Wolfram et al. (2010)
	Cancellous bone	C_{11} = 152, C_{22} = 152, C_{33} = 539, C_{44} = 1.8, C_{55} = 3.2, C_{66} = 3.2, C_{12} = 4.0, C_{23} = C_{13} = 11.0	Goda and Ganghoffer (2015)
	Porous part of vertebral body implant	C_{11} = C_{22} = C_{33} = 2.405, C_{44} = 1.705, C_{55} = 1.845, C_{66} = 3.538, C_{12} = C_{23} = C_{13} = 1.875	Kang et al. (2020)

TABLE 2 Materials properties of different ligaments in the finite element model.

Materials	Young's modulus (MPa)	Sectional area (mm^2)	Stiffness (N/mm)
Transverse ligament	10	1.8	0.9
Interspinous ligament	10	70	35
Ligamentum flavum	15	40	30
Capsular ligament	7.5	30	10
Supraspinous ligament	10	70	35
Posterior longitudinal ligament	10	20	10

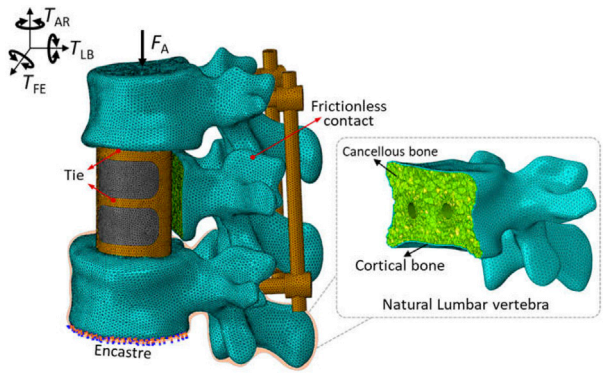

FIGURE 2
The basic setups of finite element model of artificial vertebral body replacement.

Dreischarf et al., 2014). The inferior endplate of vertebra L_3 was fully constrained, and a vertical load of 400 N and a moment of 10 Nm from different directions were applied on the upper surface of the L_1 segment to simulate flexion, extension, lateral bending and axial rotation according to normal vertebral activity (Wang et al., 2018).

2.3 Biomechanical evaluation

After finishing the numerical calculation, the von Mises stress, displacement and effective strain of each component were extracted to analyze the safety and stability of spinal reconstruction. The safety evaluation was carried out by comparing the maximum von Mises stress of each component with the yield strength of its own material. The initial stability of the reconstruction system was assessed by the translational and rotational displacement, and medium-long term stability by the effective strain to stimulate bone ingrowth. According to the bone's mechanostat (Frost, 2003), the effective strain range for maintaining bone balance and bone remodeling is 200–5,000 $\mu\varepsilon$, with the minimum effective strain threshold for remodeling being 200 $\mu\varepsilon$, modeling being 1,000 $\mu\varepsilon$, and pathologic microdamage being 3,000-5,000 $\mu\varepsilon$. Hence, the effective strain on the vertebral endplate adjacent to the implant was employed to reflect the potential of bone remodeling.

3 Results

3.1 Safety evaluation

The stress distribution and statistical analysis results of each component of the spinal reconstruction model under different load

10.3389/fbioe.2024.1305837

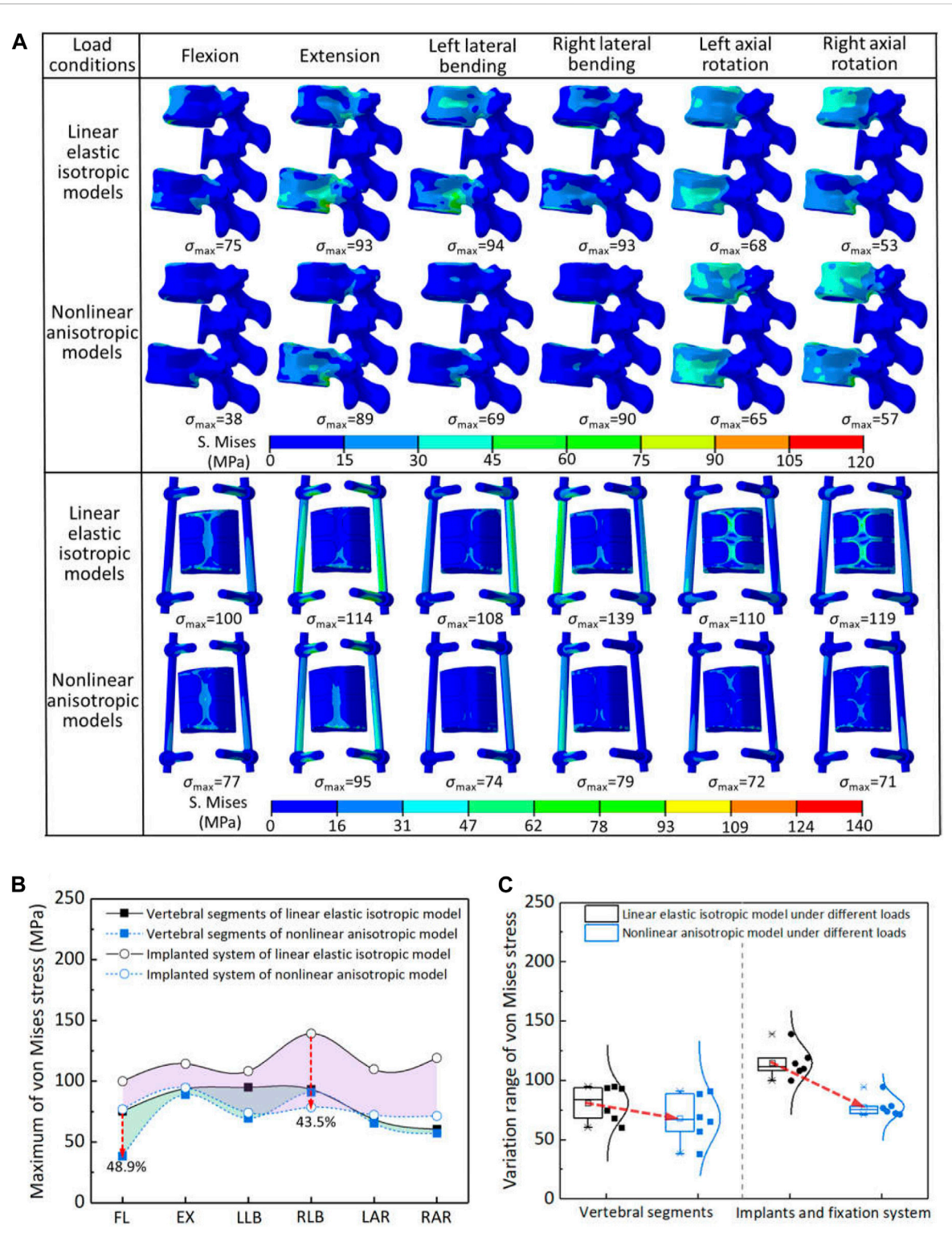

FIGURE 3
The von Mises stress results of two models under different load conditions: **(A)** the stress distribution of each component; **(B)** comparison of stress reduction between natural vertebra and reconstructed system (FL—flexion, EX—extension, LLB—left lateral bending, RLB—right lateral bending, LAR—left axial rotation, RAR—right axial rotation); **(C)** statistical analysis for the variation range of von Mises stress.

conditions were shown in Figure 3. For the linear elastic isotropic models, the variation range of the maximum von Mises stress for the natural vertebrae and reconstruction system (including the artificial vertebral implant and posterior fixation system) under all load conditions was 75–94 MPa and 100–139 MPa, respectively. Among them, the maximum von Mises stress of natural vertebrae during lateral bending and extension was higher than that of the remaining load, which was mainly located at the contact

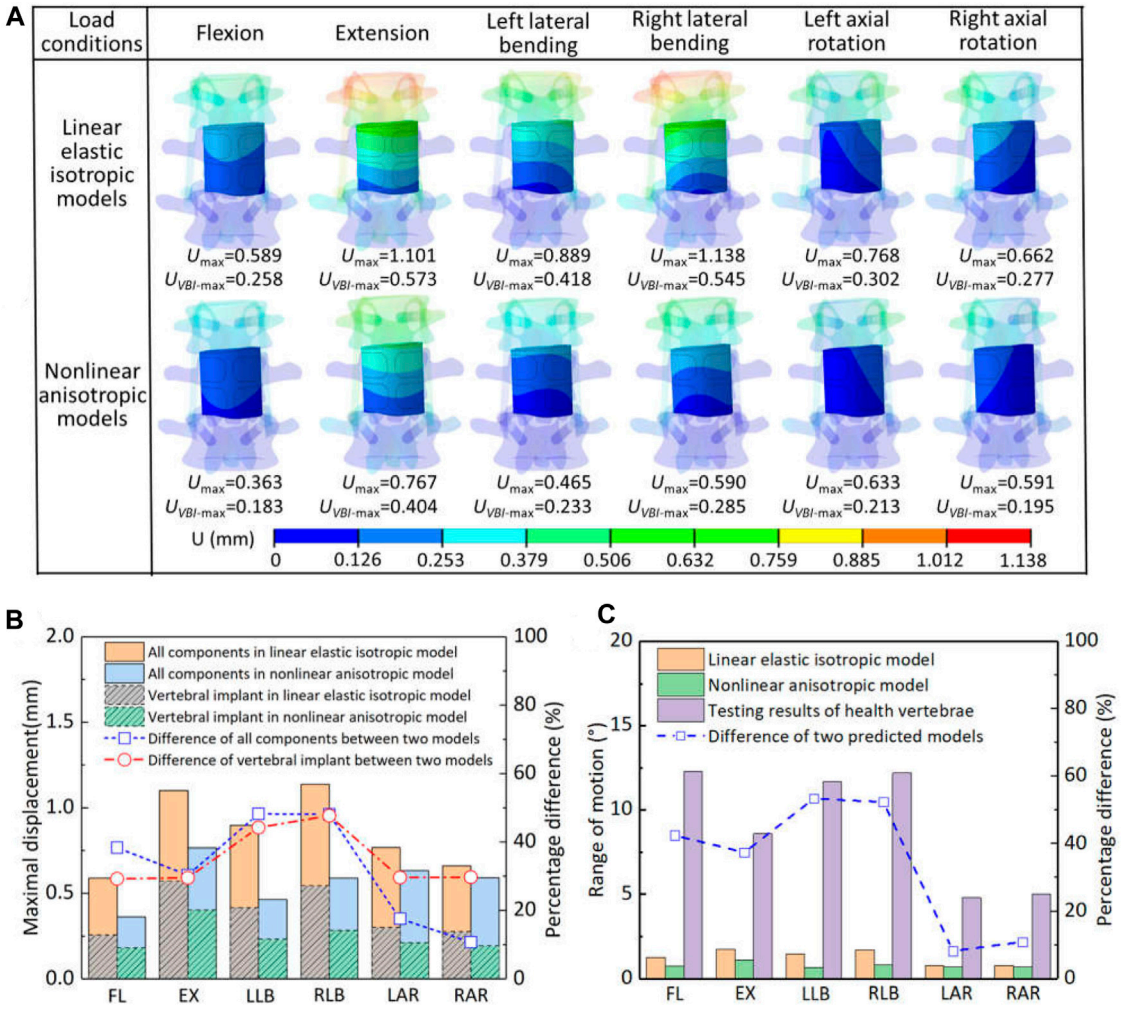

FIGURE 4
The displacement and range of motion for the two models under different load conditions: **(A)** the displacement distribution of artificial implant; **(B)** comparison of maximal displacement of all components and artificial implant in the two models; **(C)** comparison of the range of motion.

interface between the vertebral implant and adjacent endplates. The maximum von Mises stress of the reconstruction system was the highest under the right axial rotation, and it could be seen from the stress distribution that the truss structure of the artificial vertebral implant played an important load-bearing role. For the nonlinear anisotropic model, the maximum von Mises stress of natural vertebra and reconstructed system under all loading conditions was lower than that of the linear elastic isotropic model, which were 38–90 MPa and 71–95 MPa, respectively. The maximum von Mises stress of the natural vertebra was the highest in the right lateral bending and extension movements, while the reconstruction system was the highest in the extension movement. On the whole, taking the anisotropic properties of the host bone and microstructure of vertebral implant into account, the loading mode for generating the maximum von Mises stress was changed, and the maximum von Mises stress can be effectively reduced.

The maximum von Mises stress of natural vertebrae and reconstructed system were further quantitatively compared in the two models, as shown in Figure 3B,C. When considering anisotropy, the decrease percentage of the maximum von Mises stress for the natural vertebrae and reconstructed system under all loading conditions was 2.6%–48.9% and 17.3%–43.5%, respectively. The natural vertebrae were the most reduced in the flexion motion, while the reconstructed system was the right lateral bending. Overall, the maximum von Mises stress of all components in the two models was less than the yield strength of the materials. Therefore, according to the results of von Mises stress, it can be seen that the linear elastic isotropy setting may underestimate the safety of the reconstruction system. Namely, the safety of spinal reconstruction will be safer than the assumption of linear elastic isotropy.

3.2 Displacement of movement

The displacement distribution and range of motion for the spinal reconstruction model under different load conditions were shown in Figure 4. Overall, the displacement distribution trend of each component in the two models was similar, while the maximum displacement was different. For the linear elastic isotropic model, the maximum displacement under the right lateral bending was

10.3389/fbioe.2024.1305837

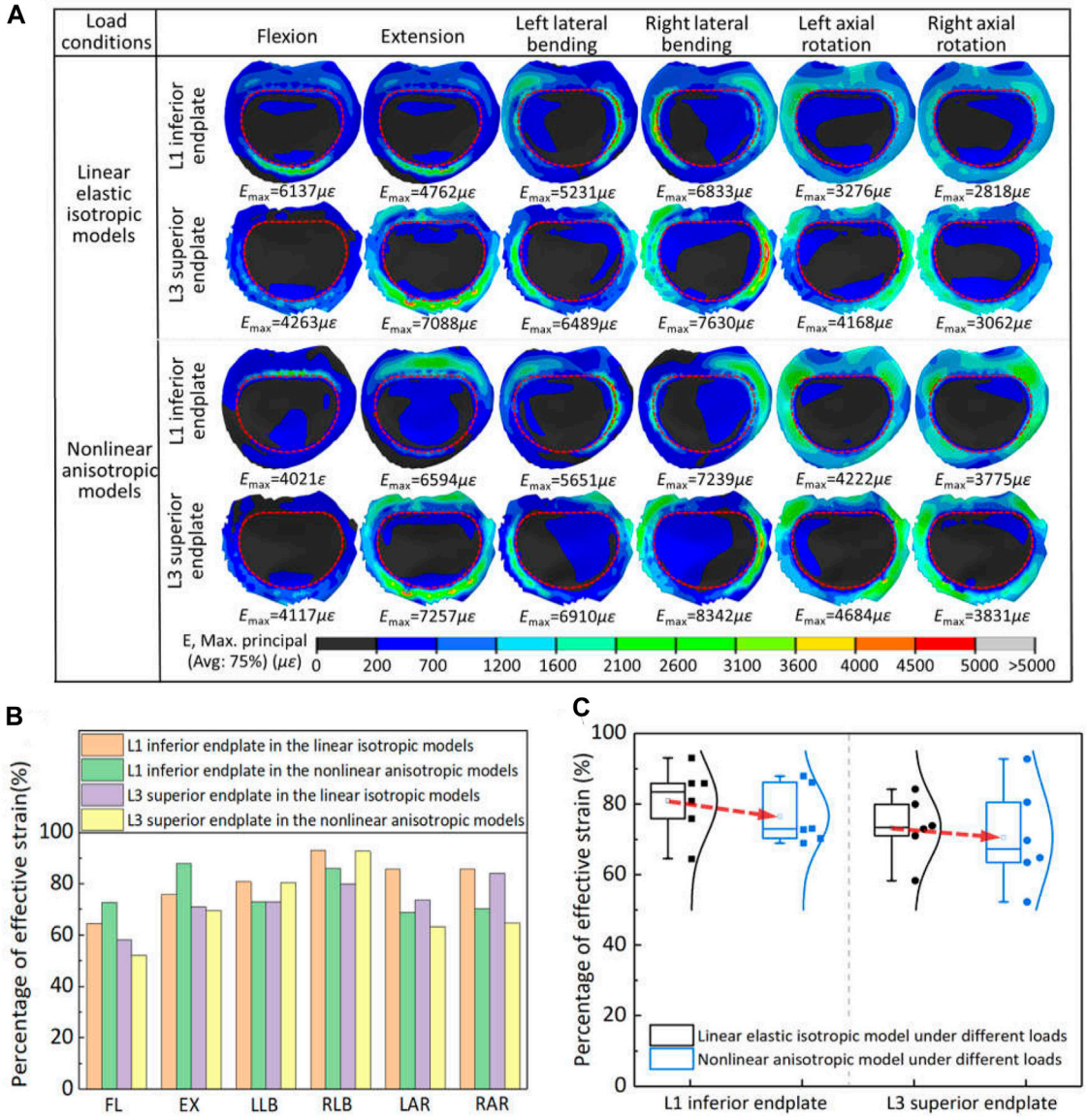

FIGURE 5
The effective strain results on the vertebral endplates adjacent to the artificial implant in two models: **(A)** the effective strain distribution of vertebral endplates; **(B)** comparison of percentage of effective strain in two models under different loads; **(C)** statistical analysis for the variation range of effective strain in the two models.

relatively larger than that of other motions, but the corresponding law was found in the extension for the nonlinear anisotropic model. In addition, the maximum displacements of all components and artificial vertebral implant in the two models were further analyzed, and it was found that the calculation results of the nonlinear anisotropic model were lower than those of the linear elastic isotropic model in the left and right lateral bending motion, with a reduction range of 44.3%–48.3%. The maximum displacement of artificial vertebral implant can account for half of the those of the whole model in flexion, extension and lateral bending motion, but the proportion decreases to 32.9%–41.8% for axial rotation motion. In addition, compared with the linear elastic isotropic model, the range of motion for the nonlinear anisotropic model decreased in the range of 8.2%–53.4%. With reference to the mobility of the normal human vertebrae (L_1—L_3), there was a significant reduction in overall mobility due to strong posterior fixation system, with an overall reduction of essentially 79.5%–94.2% in both models. Overall, from the results of displacement and range of motion, the artificial vertebral body implant has better initial stability when considering the anisotropic properties.

3.3 Bone remodeling capability

The effective strain distribution for bone growth stimulation and its statistical analysis on the vertebral endplates adjacent to the artificial implant in two models were shown in Figure 5. The maximum strain and distribution of vertebral endplate were

different under different load conditions due to different settings of material properties. Except for the flexion and extension, the maximum strain values for the inferior and superior vertebral endplates of the linearly elastic isotropic model were lower than those of the nonlinearly anisotropic model under all motion conditions, with increases ranging from 2.4% to 38.5%, and the maximum strain values occurred at roughly similar locations. But the flexion-extension motion showed the opposite tendency, with decreases of 34.5% and 3.4% respectively. Moreover, the maximum strain of L_1 inferior endplate changed from the anterior region to the posterior end. In addition, more strain values for maintaining bone balance were observed inside the contact surface between the vertebral endplate and the artificial vertebral implant, while effective strain values for stimulating bone growth were observed in the marginal area of the contact surface.

The percentage of effective strain elements on the inferior/superior vertebral endplate stimulating bone growth in the two models was further extracted for statistical analysis. For the axial rotation, the effective strains in the vertebral endplates of the linear elastic isotropic model were higher than those of the nonlinear anisotropic model, with a range of 14.1%–23.1%. For lateral bending and flexion-extension motion, the effective strains in the vertebral endplates may show a pattern of strain transfer or compensation. For example, the effective strains in the L_1 inferior endplate of the linear elastic isotropic model were lower than those of the nonlinear anisotropic model under the flexion-extension movements, but this pattern was reversed for the L_3 superior endplate. Finally, the proportion of strain units that effectively stimulated bone growth calculated by the linear elastic model was significantly higher than that calculated by the nonlinear anisotropic model, indicating that the setting of linear elastic isotropic material properties may overestimate the bone growth ability to some extent.

4 Discussion

Two finite element models for linear elastic isotropy and nonlinear anisotropy were developed to evaluate the effect of different material properties on the safety of vertebral reconstructed system. For above two models, the maximum von Mises stress of the natural vertebrae was 95 MPa and 90 MPa, respectively, and that of the reconstructed system was 139 MPa and 95 MPa. Among, the maximal stresses of these natural vertebrae were lower than the yield strength of material itself (104.9–114.3 MPa) (Haghshenas, 2017). Morover, the stress distribution of artificial vertebral body implant showed that the solid truss structure plays an important role in load-bearing aspect, and these maximal stresses under various loads were also below the reported fatigue strength of 3D printed solid samples (about 200–300 MPa) (Denti et al., 2019; Liu and Shin, 2019). Overall, the maximum von Mises stress calculated by both models for each component of the spinal reconstructive system was less than the yield strength of the material itself. However, the predicted results of the linear elastic model were higher than those of the nonlinear anisotropic model, which indicated the setting of linear elastic isotropy will overestimate the safety when compared with the anisotropic model.

After comparing the predicted results of two finite element models, it can be seen that the assignment of anisotropic properties not only changed the stress distribution pattern under different load conditions, but also effectively reduced the value of maximal stress. This variation was mainly attributed to the diversity in the spatial distribution of elastic modulus between natural vertebrae and implant's microstructure. From their anisotropic parameters in Table 1, the spatial surface of elastic modulus was plotted and variation ranges were statistically analyzed by normal distribution, as shown in Figure 6. For the cortical bone of natural vertebrae, the maximal and minimal modulus were located on the body diagonal direction and the axial direction with a variation of 7.78 GPa–15.79 GPa, and the percentages for below and above 12 GPa were roughly half. Especially for cancellous bone, the spatial distribution of elastic modulus varied significantly owing to the influence of porosity variety and sampling site. Despite large difference for the minimal and maximal value for the elastic modulus, nearly 90% was between 0.07 GPa and 0.1 GPa. In addition, for the porous structure of the artificial vertebral body implant, the spatial distribution of elastic modulus was closely related to the geometry of porous structure, which has been confirmed by previous studies (Kang et al., 2020). The rhombic dodecahedral porous structure belongs to centrosymmetric, resulting in predicted elastic modulus of 0.762 GPa in all three axial directions, which was close to the experimental measurement of 0.8 GPa (Dong et al., 2020). But the elastic modulus in the body diagonal direction was as high as 4.75 GPa and more than 75% was greater than 0.8 GPa. Hence, due to these discrepancy in spatial distribution of elastic modulus, it is necessary to fully consider and understand the influence of material anisotropy on the biomechanical properties of spinal reconstruction system.

Due to strong protection of the posterior fixation system, the maximum translational displacement of vertebral implant for two models under all load cases were 0.573 mm and 0.404 mm, respectively, which occurred in extension motion. Compared with the testing results of heath vertebrae at L_1—L_3 segments (Yamamoto et al., 1989), the predicted range of motion for two models decreased significantly, with a decrease of 79.5%–94.2%.In addition, some studies (Dong et al., 2020; Zhang and Guo, 2023) on reliability of different fixation strategies pointed out that posterior fixation system exhibited strong effect compared with other fixation methods. According to the spatial distribution difference of elastic modulus given in Figure 6, the response displacement generated under the actual load-bearing process was different. Overall, the predicted results of nonlinear anisotropic model were smaller than those of linear elastic model, which indicated the setting of linear elastic isotropy may overestimate the mobility of the reconstruction system.

Owing to the lack of human spine specimens, indirect validation of the finite element models was mainly performed by comparing the results of existing biomechanical experiment testing and numerical simulations. First, the finite element model of the intact lumbar segments was validated by the comparing the range of motion values from the reported experiment data in our previous study (Dong et al., 2020). These results showed that the predicted range of motion was in good agreement with the *in vitro* experimental data or numerical results. On the basis of the previous finite element model, the effect of material properties on biomechanical properties was evaluated in this study. Moreover, the predicted range of motion under the condition of flexion, extension and lateral bending (0.728 mm, 1.1 mm and 0.8 mm)

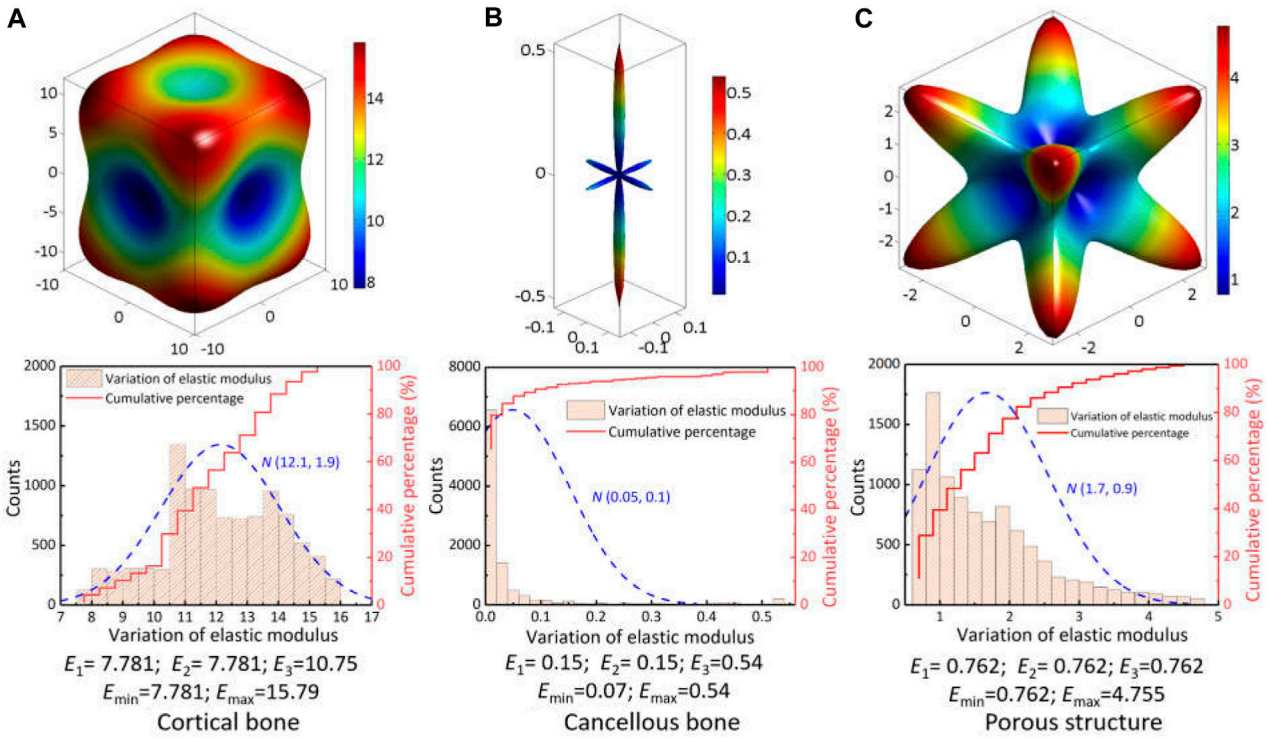

FIGURE 6
Spatial distribution of elastic modulus for the vertebral skeleton structures and implant's porous structure: **(A)** cortical bone; **(B)** cancellous bone; **(C)** porous structure.

was closer to the experimental results of corresponding motions (0.6 ± 0.37 mm, 1.56 ± 0.74 mm and 0.87 ± 0.55 mm) (Disch et al., 2008). However, it should be noted that the performance of artificial vertebral implants *in vivo* will be affected by a combination of factors (Dreischarf et al., 2014; Liebsch et al., 2020a; Liebsch et al., 2020b), such as geometrical morphology of different human vertebrae, the design and material of artificial vertebral implants, internal fixation systems and clinical implantation biases, etc. According to the single factor rule, this study can also effectively evaluate the influence of different material property on biomechanical performance to a certain extent.

Comparing further the calculation results of two models under the lateral bending and axial rotation in the left and right direction, it can be shown that the maximal von Mises stress (108 MPa) and maximal displacement (0.889 mm) under the left lateral bending were lower than that of the right lateral bending (139 MPa and 1.138 mm). Yet, both of the above results under the left and right axial rotation exhibited an opposite rule, namely, maximal von Mises stress located in the left axial rotation, maximal displacement within the right axial rotation. These differences have also been observed in existing studies (Dai et al., 2022; Hao et al., 2023), and were resulted from multiple factors, such as the asymmetry of natural vertebrae model in the sagittal plane, actual placement of artificial vertebral implant and posterior fixation system, the consideration of anisotropic materials properties, etc. Consequently, this also indicated it is necessary to take into account the loading effects along the left and right direction when the biomechanical evaluation of vertebral reconstruction.

It was found that the linear elastic model had a higher percentage than the anisotropic model with respect to the element units to stimulate bone ingrowth and maintain bone balance. Moreover, the consideration of anisotropic mechanical properties brought a regional transfer or compensation of the effective strain in the vertebral endplate adjacent to the artificial implant. These variations were mainly caused by the anisotropy of elastic modulus for different components. According to the spatial distribution and statistical analysis for the elastic modulus of porous structure in Figure 6C, it can be seen that the elastic modulus in most directions was greater than 0.8 GPa set in the linear elastic isotropic model, which resulted in the increasement of maximum strain as shown in Figure 5A. The response trend was consistent with existing study (Lu et al., 2022), in which the relationship between the elastic modulus of cage materials (0.1 GPa–110 GPa) and the biomechanical properties of transforaminal lumbar interbody fusion was developed. These differences of effective strain result implied that the setting of linear elastic isotropy may overestimate the bone remodeling potential to some extent.

Some limitations of this work must also be noted. The simplification treatment by using solid elements with equivalent mechanical properties instead of porous structures was widely applied in the finite element analysis. Nevertheless, many geometrical models of artificial vertebral body implants constructed by employing Boolean operations tend to form incomplete porous units on their contoured surfaces. So, this treatment still needs to be explored further due to the scale effect

and discrepancies in the mechanical properties of various incomplete porous units. In addition, the anisotropic property of this study mainly focused on the elastic deformation stage, actually the yield strength with directional dependence. Despite the choice of minimal yield strength in different directions to ensure overall safety, subsequent study also was carried out by introducing the anisotropic strength to develop more accurate evaluation method. Finally, since this study focused on the influence of anisotropy with finite element methods, there are still some problems that should be given sufficient attention, such as the asymmetry of geometric model, validation of material properties, lack of experimental testing to verify the analysis results.

5 Conclusion

In this study, the influence of material anisotropy derived from the skeleton structure of natural vertebrae and implant's microstructure on the biomechanical properties of spinal reconstruction system was investigated under various load conditions. The safety, initial and long-term stability for the spinal reconstruction system with linear elastic isotropy and nonlinear anisotropy were compared to better guide clinical repair. Through finite element analysis, the predicted results of nonlinear anisotropic model showed smaller maximum von Mises stress, lower translational and rotational displacement, less element percentage of effective strain compared with the linear elastic isotropic model. It can be concluded that the assumption of linear elastic isotropy in the biomechanical evaluation of spinal reconstruction system may underestimate the safety, while overestimating the initial and long-term stability as reflected by the displacement of movement and bone ingrowth capacity.

Data availability statement

The raw data supporting the conclusion of this article will be made available by the authors, without undue reservation.

Author contributions

JK: Conceptualization, Methodology, Software, Writing–original draft, Writing–review and editing. YW: Data curation, Methodology, Writing–review and editing. JQ: Conceptualization, Supervision, Writing–review and editing.

Funding

The author(s) declare that financial support was received for the research, authorship, and/or publication of this article. The work was supported by the Guangdong Basic and Applied Basic Research Foundation [2020A1515111127] and [2021A1515010399], the Fundamental Research Funds for the Foshan University.

Acknowledgments

We wish to thank Lei Shi from Xijing Hospital to provide imaging data.

Conflict of interest

The authors declare that the research was conducted in the absence of any commercial or financial relationships that could be construed as a potential conflict of interest.

Publisher's note

References

Barba, D., Alabort, E., and Reed, R. C. (2019). Synthetic bone: design by additive manufacturing. *Acta Biomater.* 97, 637–656. doi:10.1016/j.actbio.2019.07.049

Cao, K. D., Grimm, M. J., and Yang, K. H. (2001). Load sharing within a human lumbar vertebral body using the finite element method. *Spine (Phila Pa 1976)* 26 (12), E253–E260. doi:10.1097/00007632-200106150-00011

Dai, H., Liu, Y., Han, Q., Zhang, A., Chen, H., Qu, Y., et al. (2022). Biomechanical comparison between unilateral and bilateral percutaneous vertebroplasty for osteoporotic vertebral compression fractures: a finite element analysis. *Front. Bioeng. Biotechnol.* 10, 978917. doi:10.3389/fbioe.2022.978917

Denti, L., Bassoli, E., Gatto, A., Santecchia, E., and Mengucci, P. (2019). Fatigue life and microstructure of additive manufactured Ti6Al4V after different finishing processes. *Mater. Sci. Eng. A* 755, 1–9. doi:10.1016/j.msea.2019.03.119

Disch, A. C., Schaser, K. D., Melcher, I., Luzzati, A., Feraboli, F., and Schmoelz, W. (2008). *En bloc* spondylectomy reconstructions in a biomechanical *in-vitro* study. *Eur. Spine J.* 17, 715–725. doi:10.1007/s00586-008-0588-y

Dong, E., Shi, L., Kang, J., Li, D., Liu, B., Guo, Z., et al. (2020). Biomechanical characterization of vertebral body replacement *in situ*: effects of different fixation strategies. *Comput. Methods Programs Biomed.* 197, 105741. doi:10.1016/j.cmpb.2020.105741

Dreischarf, M., Zander, T., Shirazi-Adl, A., Puttlitz, C. M., Adam, C. J., Chen, C. S., et al. (2014). Comparison of eight published static finite element models of the intact lumbar spine: predictive power of models improves when combined together. *J. Biomech.* 47 (8), 1757–1766. doi:10.1016/j.jbiomech.2014.04.002

Fan, R., Liu, J., and Liu, J. (2021). Prediction of the natural frequencies of different degrees of degenerated human lumbar segments L2-L3 using dynamic finite element analysis. *Comput. Methods Programs Biomed.* 209, 106352. doi:10.1016/j.cmpb.2021.106352

Frost, H. M. (2003). Bone's mechanostat: a 2003 update. *Anat. Rec. A Discov. Mol. Cell Evol. Biol.* 275A (2), 1081–1101. doi:10.1002/ar.a.10119

Goda, I., and Ganghoffer, J.-F. (2015). Identification of couple-stress moduli of vertebral trabecular bone based on the 3D internal architectures. *J. Mech. Behav. Biomed. Mater* 51, 99–118. doi:10.1016/j.jmbbm.2015.06.036

Gong, X., Zhang, A., Han, Q., Wang, Y., Liu, Y., Jiao, J., et al. (2022). Biomechanical effects of individualized artificial titanium alloy lamina implantation after laminectomy: a finite element analysis. *Front. Bioeng. Biotechnol.* 10, 1019510. doi:10.3389/fbioe.2022.1019510

Haghshenas, M. (2017). Mechanical characteristics of biodegradable magnesium matrix composites: a review. *J. Magnesium Alloys* 5 (2), 189–201. doi:10.1016/j.jma.2017.05.001

Hao, J., Tang, X., Jiang, N., Wang, H., and Jiang, J. (2023). Biomechanical stability of oblique lateral interbody fusion combined with four types of internal fixations: finite element analysis. *Front. Bioeng. Biotechnol.* 11, 1260693. doi:10.3389/fbioe.2023.1260693

Hu, X., Kenan, S., Cheng, M., Cai, W., Huang, W., and Yan, W. (2022). 3D-Printed patient-customized artificial vertebral body for spinal reconstruction after total *en bloc* spondylectomy of complex multi-level spinal tumors. *Int. J. Bioprinting* 8 (3), 576. doi:10.18063/ijb.v8i3.576

Hulme, P. A., Boyd, S. K., and Ferguson, S. J. (2007). Regional variation in vertebral bone morphology and its contribution to vertebral fracture strength. *Bone* 41 (6), 946–957. doi:10.1016/j.bone.2007.08.019

Jia, Z., Xu, X., Zhu, D., and Zheng, Y. (2023). Design, printing, and engineering of regenerative biomaterials for personalized bone healthcare. *Prog. Mater. Sci.* 134, 101072. doi:10.1016/j.pmatsci.2023.101072

Kang, J., Dong, E., Li, D., Dong, S., Zhang, C., and Wang, L. (2020). Anisotropy characteristics of microstructures for bone substitutes and porous implants with application of additive manufacturing in orthopaedic. *Mater. Des.* 191, 108608. doi:10.1016/j.matdes.2020.108608

Kang, J., Dong, E., Li, X., Guo, Z., Shi, L., Li, D., et al. (2021). Topological design and biomechanical evaluation for 3D printed multi-segment artificial vertebral implants. *Mater Sci. Eng. C Mater Biol. Appl.* 127, 112250. doi:10.1016/j.msec.2021.112250

Liebsch, C., Aleinikov, V., Kerimbayev, T., Akshulakov, S., Kocak, T., Vogt, M., et al. (2020a). *In vitro* comparison of personalized 3D printed versus standard expandable titanium vertebral body replacement implants in the mid-thoracic spine using entire rib cage specimens. *Clin. Biomech.* 78, 105070. doi:10.1016/j.clinbiomech.2020.105070

Liebsch, C., Kocak, T., Aleinikov, V., Kerimbayev, T., Akshulakov, S., Jansen, J. U., et al. (2020b). Thoracic spinal stability and motion behavior are affected by the length of posterior instrumentation after vertebral body replacement, but not by the surgical approach type: an *in vitro* study with entire rib cage specimens. *Front. Bioeng. Biotechnol.* 8, 572. doi:10.3389/fbioe.2020.00572

Liu, S., and Shin, Y. C. (2019). Additive manufacturing of Ti6Al4V alloy: a review. *Mater. Des.* 164, 107552. doi:10.1016/j.matdes.2018.107552

Lochmüller, E. M., Pöschl, K., Würstlin, L., Matsuura, M., Müller, R., Link, T. M., et al. (2008). Does thoracic or lumbar spine bone architecture predict vertebral failure strength more accurately than density? *Osteoporos. Int.* 19 (4), 537–545. doi:10.1007/s00198-007-0478-x

Lu, T., Ren, J., Sun, Z., Zhang, J., Xu, K., Sun, L., et al. (2022). Relationship between the elastic modulus of the cage material and the biomechanical properties of transforaminal lumbar interbody fusion: a logarithmic regression analysis based on parametric finite element simulations. *Comput. Methods Programs Biomed.* 214, 106570. doi:10.1016/j.cmpb.2021.106570

Mehboob, H. (2023). Biomechanical performance evaluation of composite metamaterial implant with 3D printing approach for lumbar interbody fusion surgery: a finite element study. *Compos. Struct.* 303, 116379. doi:10.1016/j.compstruct.2022.116379

Nicholson, P. H. F., and Alkalay, R. (2007). Quantitative ultrasound predicts bone mineral density and failure load in human lumbar vertebrae. *Clin. Biomech.* 22 (6), 623–629. doi:10.1016/j.clinbiomech.2006.12.008

Palmquist, A., Jolic, M., Hryha, E., and Shah, F. A. (2023). Complex geometry and integrated macro-porosity: clinical applications of electron beam melting to fabricate bespoke bone-anchored implants. *Acta Biomater.* 156, 125–145. doi:10.1016/j.actbio.2022.06.002

Perilli, E., Briggs, A. M., Kantor, S., Codrington, J., Wark, J. D., Parkinson, I. H., et al. (2012). Failure strength of human vertebrae: prediction using bone mineral density measured by DXA and bone volume by micro-CT. *Bone* 50 (6), 1416–1425. doi:10.1016/j.bone.2012.03.002

Shi, L., Li, X., Li, X., Wang, L., Fu, J., Wang, Z., et al. (2020). Preliminary study on the a novel individualized 3D printing artificial vertebral body in spine reconstruction. *Chin. J. Orthopacdics* 40 (6), 335–343. doi:10.3760/cma.j.cn121113-20200303-00128

Tsouknidas, A., Sarigiannidis, S. O., Anagnostidis, K., Michailidis, N., and Ahuja, S. (2015). Assessment of stress patterns on a spinal motion segment in healthy versus osteoporotic bony models with or without disc degeneration: a finite element analysis. *Spine J.* 15 (3), S17–S22. doi:10.1016/j.spinee.2014.12.148

Vadapalli, S., Sairyo, K., Goel, V. K., Robon, M., Biyani, A., Khandha, A., et al. (2006). Biomechanical rationale for using polyetheretherketone (PEEK) spacers for lumbar interbody fusion-A finite element study. *Spine (Phila Pa 1976)* 31 (26), E992–E998. doi:10.1097/01.brs.0000250177.84168.ba

Wang, L., Kang, J., Shi, L., Fu, J., Li, D., Guo, Z., et al. (2018). Investigation into factors affecting the mechanical behaviours of a patient-specific vertebral body replacement. *Proc. Inst. Mech. Eng. H.* 232 (4), 378–387. doi:10.1177/0954411918754926

Wang, L., Kang, J., Sun, C., Li, D., Cao, Y., and Jin, Z. (2017). Mapping porous microstructures to yield desired mechanical properties for application in 3D printed bone scaffolds and orthopaedic implants. *Mater. Des.* 133, 62–68. doi:10.1016/j.matdes.2017.07.021

Wang, X., Xu, S., Zhou, S., Xu, W., Leary, M., Choong, P., et al. (2016). Topological design and additive manufacturing of porous metals for bone scaffolds and orthopaedic implants: a review. *Biomaterials* 83, 127–141. doi:10.1016/j.biomaterials.2016.01.012

Wolfram, U., Wilke, H.-J., and Zysset, P. K. (2010). Rehydration of vertebral trabecular bone: influences on its anisotropy, its stiffness and the indentation work with a view to age, gender and vertebral level. *Bone* 46 (2), 348–354. doi:10.1016/j.bone.2009.09.035

Yamamoto, I., Panjabi, M. M., Crisco, T., and Oxland, T. O. M. (1989). Three-dimensional movements of the whole lumbar spine and lumbosacral joint. *Spine* 14 (11), 1256–1260. doi:10.1097/00007632-198911000-00020

Yeni, Y. N., Dix, M. R., Xiao, A., and Oravec, D. J. (2022). Uniaxial compressive properties of human lumbar 1 vertebrae loaded beyond compaction and their relationship to cortical and cancellous microstructure, size and density properties. *J. Mech. Behav. Biomed. Mater.* 133, 105334. doi:10.1016/j.jmbbm.2022.105334

Yoshioka, K., Murakami, H., Demura, S., Kato, S., Kawahara, N., Tomita, K., et al. (2013). Clinical outcome of spinal reconstruction after total *en bloc* spondylectomy at 3 or more levels. *Spine (Phila Pa 1976)* 38 (24), E1511–E1516. doi:10.1097/BRS.0b013e3182a6427a

Zhang, D., and Guo, L. (2023). Effect of different fixation methods on biomechanical property of cervical vertebral body replacement and fusion. *Clin. Biomech.* 101, 105864. doi:10.1016/j.clinbiomech.2022.105864

frontiers | Frontiers in Bioengineering and Biotechnology

TYPE Original Research
PUBLISHED 26 June 2024
DOI 10.3389/fbioe.2024.1392448

OPEN ACCESS

EDITED BY
Wujing Cao,
Chinese Academy of Sciences (CAS), China

REVIEWED BY
Marco Parente,
University of Porto, Portugal
Yadong Mo,
Beijing University of Posts and Telecommunications (BUPT), China
Zw Z.,
University of Shanghai for Science and Technology, China

*CORRESPONDENCE
Liwei Jing,
lwjing2004@ccmu.edu.cn

RECEIVED 27 February 2024
ACCEPTED 04 June 2024
PUBLISHED 26 June 2024

CITATION
Wang R, Liu G, Jing L, Zhang J, Ye Y and Zhu H (2024), Quantifying the effects of five rehabilitation training methods on the ability of elderly men to control bowel movements: a finite element analysis study.
Front. Bioeng. Biotechnol. 12:1392448.
doi: 10.3389/fbioe.2024.1392448

Quantifying the effects of five rehabilitation training methods on the ability of elderly men to control bowel movements: a finite element analysis study

Rui Wang[1], Guangtian Liu[2], Liwei Jing[1]*, Jing Zhang[1], Yan Ye[1] and Haoran Zhu[1]

[1]School of Nursing, Capital Medical University, Beijing, China, [2]College of Nursing and Rehabilitation, North China University of Science and Technology, Hebei, China

Purpose: The study aims to develop a finite element model of the pelvic floor and thighs of elderly men to quantitatively assess the impact of different pelvic floor muscle trainings and the urinary and defecation control ability.

Methods: A finite element model of the pelvic floor and thighs of elderly men was constructed based on MRI and CT. Material properties of pelvic floor tissues were assigned through literature review, and the relative changes in waistline, retrovesical angle (RVA) and anorectad angulation (ARA) to quantitatively verify the effectiveness of the model. By changing the material properties of muscles, the study analyzed the muscle strengthening or impairment effects of the five types of rehabilitation training for four types of urination and defecation dysfunction. The changes in four outcome indicators, including the retrovesical angle, anorectad angulation, stress, and strain, were compared.

Results: This study indicates that ARA and RVA approached their normal ranges as material properties changed, indicating an enhancement in the urinary and defecation control ability, particularly through targeted exercises for the levator ani muscle, external anal sphincter, and pelvic floor muscles. This study also emphasizes the effectiveness of personalized rehabilitation programs including biofeedback, exercise training, electrical stimulation, magnetic stimulation, and vibration training and advocates for providing optimized rehabilitation training methods for elderly patients.

Discussion: Based on the results of computational biomechanics, this study provides foundational scientific insights and practical recommendations for rehabilitation training of the elderly's urinary and defecation control ability, thereby improving their quality of life. In addition, this study also provides new perspectives and potential applications of finite element analysis in elderly men, particularly in evaluating and designing targeted rehabilitation training.

KEYWORDS

elderly men, rehabilitation training, muscles, quantification, urinary and defecation control ability, finite element analysis

1 Introduction

In contemporary society, the aging of the population continues to intensify, and the health problems of the elderly have received increasing attention. The decline in muscle strength and diminished neurological control often experienced with age and frailty lead to conditions such as urinary incontinence, urinary retention, fecal incontinence and constipation (Talasz et al., 2018; Ma and Chen, 2020; Levaillant et al., 2023; Salari et al., 2023), significantly affecting life quality. The resultant emotional distress and increased dependency on caregivers (Bektas et al., 2023), which plays a vital role in determining the care dependence of the elderly and has an impact on social and economic development. It is becoming more and more prominent that how to effectively improve the urinary and defecation control ability of the elderly in the field of rehabilitation medicine.

For the elderly retaining partial urinary and defecation control ability, the five rehabilitation training methods of exercise training, magnetic stimulation, electrical stimulation, vibration stimulation and biofeedback, which are validated for enhancing the muscles strength in the pelvic floor, abdomen, back, and hips, thereby improving control bowel movements (Mazur-Bialy et al., 2020; Alouini et al., 2022). However, different rehabilitation training methods may have different effects on the urinary and defecation control ability, it is necessary to delineate the quantitative relationship between different rehabilitation training methods and urinary and defecation control ability and to understand the underlying mechanism to provide guidance for clinical rehabilitation practices. Finite element analysis (FEA), a critical computational tool, is considered a technique for simulating the mechanical properties of an object by dividing it into discrete elements and creating a numerical calculation model to represent its behavior (Chen et al., 2010). In recent years, it is widely used in the urethral support function (Peng et al., 2016), the occurrence of levator ani muscle injury and pelvic floor disease during vaginal delivery (Zhou et al., 2020), and the mechanical mechanism of posterior vaginal prolapse (Qiu, 2017). By establishing finite element models, it can simulate the biomechanical behavior of human tissues and organs and analyze the biomechanics of complex systems quantitatively. It is a method that provides a new idea for the evaluation of the effects of rehabilitation training (Yang et al., 2024). This approach underpins the development of models to simulate elderly men's pelvic floor structures, enhancing our understanding of urinary and defecation control ability mechanisms (Zhang and Yao, 2015).

This study aims to develop a finite element model to simulate five distinct rehabilitation training methods. By changing the values of material properties proportionally, the strengthening and impairment of muscle capacity are simulated. Meanwhile, the defecation ability of the elderly is reflected through the retrovesical angle (RVA) and anorectad angulation (ARA). By comparing the changes in defecation outcome indicators under various parameter settings, the mechanism and relationship between the rehabilitation training methods and urinary and defecation control ability is quantified. This provides precise and effective guidance for the rehabilitation training of the elderly, thereby improving their quality of life.

2 Methods

2.1 Participant

The implementation of this study complied with relevant ethical requirements (ethical approval number: Linyanshen [2023] No.079 and Z2024SY007). Our study has been registered in the Chinese Clinical Trial Registry Center (ChiCTR2400080749) and our research protocol has been published online (Wang et al., 2024). The pelvic floor medical imaging data collection participant is a 61-year-old Chinese old adult with a body mass index (BMI) of 25.4 kg/m^2, good physical health, normal daily living ability, normal cognitive ability, normal communication ability, and normal pelvic floor medical imaging data. The participant's bowel function was normal, and there was no history of defecation dysfunction or surgery. Participant signed informed consent forms before scanning medical images. During the scan, participant was placed in a supine position with his hands on top of head and legs together and straightened. Scanning started from the highest point of the participant's iliac crest, CT scan to the knee joint, and MRI scan to 1 cm of the perineum. Radiologists used a 64-slice spiral scanning dual-source CT machine produced by Siemens of Germany and a 3.0T magnetic resonance scanner produced by Philips of the Netherlands to scan, obtain pelvic floor scan data and store it in DICOM format. Among them, CT was scanned with a slice thickness of 0.5 mm and a resolution of 512 × 512, with a total of 598 images, as shown in Figure 1. Static MRI was scanned with 3D-PelvicVIEW-T2, TR 1250 ms, TE 151 ms, field of view 400 cm, continuous 1.0 mm slices Thickness-free volumetric scanning, a total of 400 images, as shown in Figure 2. After the static MRI scan, the participant was asked to perform resting maneuvers, Kegel maneuvers, relaxation maneuvers, and Valsalva maneuvers in order, and at the same time, dynamic MRI scans were performed. Dynamic MRI used the BTFE_Sag_Dyn sequence along the sagittal plane, with a slice thickness of 8 mm and a frame rate of 9–10 frames/s, with a total

FIGURE 1
CT image.

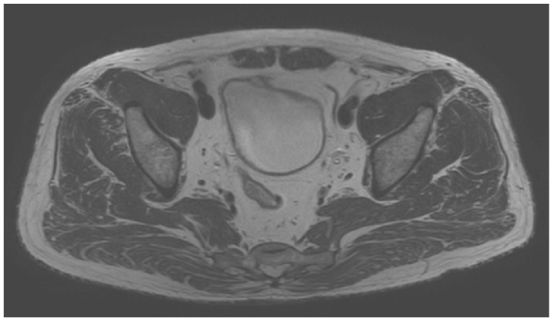

FIGURE 2
Static MRI image.

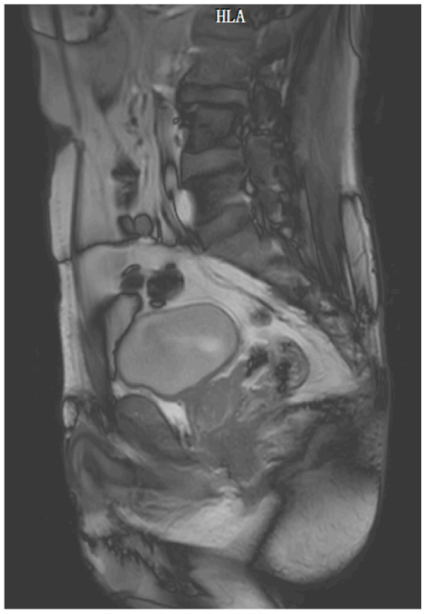

FIGURE 3
Dynamic MRI image.

of 150 images, as shown in Figure 3. For inclusion and exclusion criteria for the participant and the specific data collection methods, please refer to our previous research protocol (Wang et al., 2024).

A composite finite element model of the participant's pelvic floor, abdomen, back and hip was established through medical imaging data, in which the bone geometry model was through CT images and the soft tissue geometry model was through MRI images. First, the segmentation was performed under the guidance of experienced pelvic floor radiologists. We used the medical modeling software Mimics to reconstruct a relatively rough model, and then used the smoothing function in the Mimics software to beautify it, reduce the angle of points or edges, make the edges smoother, smooth the 3D image, and then the accurate model is imported into Ansys software for numerical simulation calculations.

2.2 Material properties

Since this study focuses on the mechanical analysis results of muscles related to urination and defecation, the material properties of the bladder, urethra, rectum, external anal sphincter, external urethral sphincter, and levator ani muscle were analyzed using Yeoh and Mooney-Rivlin hyperelastic structures. For simulation, Hooke linear elastic structures were used for other organs, muscles and fat of the pelvic floor, and viscoelastic structures of the standard linear solid model and hooke were used for the abdominal, back and hip muscles. The pelvis was modeled as a rigid body and fixed structure, considering that its stiffness is much higher than that of soft tissue and therefore its deformation is negligible under normal pelvic function. The finite element type is mainly tetrahedron, supplemented by hexahedron. When setting the material properties in the model, we retrieved existing material data in previous studies (Lee et al., 2005; Boubaker et al., 2009; Zhang et al., 2009; Rao et al., 2010; Venugopala Rao et al., 2010; Wein, 2011; Larson et al., 2012; Chen, 2014; Sichting et al., 2014; Brandão et al., 2015; Chen et al., 2015; Krcmar et al., 2015; Samavati et al., 2015; Sun, 2015; He, 2016; Ma et al., 2016; Peng et al., 2016; Silva et al., 2016; Dias et al., 2017; Li et al., 2017; Liu, 2017; Ricci et al., 2018; Guo et al., 2019; Li et al., 2019; Ma, 2019; Wu, 2019; Zhou et al., 2020; Xu et al., 2021; Xuan et al., 2021; Li, 2022; Yao et al., 2022; Zong, 2022), summarized the mechanical parameters recognized in the literature, and obtained the material properties of the research object in this study. Because the literature shows that there are differences in the mechanical performance characteristics of old and young pelvic soft tissues, and the material properties may change (Chantereau et al., 2014), we made appropriate adjustments on the of material properties, and we verified whether the data conditioning is appropriate by completing the verification steps of the finite element model, the specific parameters are shown in Table 1.

2.3 Constraint boundaries

The coordinates of the three-dimensional finite element model are set as follows: the x-axis is perpendicular to the sagittal plane of the human body, and the positive direction points to the left; the *y*-axis is perpendicular to the coronal plane of the human body, and the positive direction points backward; the *z*-axis is the longitudinal axis of the human body, and the positive direction points to the head. In the analysis of static structural mechanics, in order to simulate the in-body state of human defecation-related muscles as closely as possible, the bone is set as a rigid body and all nodes are fully constrained. We limited the translation and rotation of bones in the three axes of x, y and z. The tops of the rectus abdominis muscle, psoas major muscle, and erector spinae muscle are fixed. The contact condition between bones and muscles, bladder and prostate, prostate and colon were set to bind.

2.4 Model validity verification

In the finite element modeling process, it is very necessary to verify the validity of the finite element model. The methods of finite element model validation usually include geometric shape

TABLE 1 Material properties of various parts in the model.

No.	Anatomical element	Material constants		Structures	Constitutive models
		In the literature	After adjustment		
1	bladder	C_{10} = 0.071 C_{20} = 0.202 C_{30} = 0.048 (Chen et al., 2015; Li, 2022)	C_{10} = 0.061 C_{20} = 0.202 C_{30} = 0.048	hyperelastic structures (Venugopala Rao et al., 2010; Chen et al., 2015)	Yeoh (Chen et al., 2015; Li, 2022)
2	urethra		C_{10} = 0.071 C_{20} = 0.282 C_{30} = 0.048		
3	rectum	C_{10} = 0.088 C_{20} = 3.092 C_{30} = 2.871 (Li, 2022)	C_{10} = 0.082 C_{20} = 3.092 C_{30} = 2.871		
4	prostate	young's module 6 MPa (Boubaker et al., 2009; Samavati et al., 2015) Poisson's ratio 0.495 (Boubaker et al., 2009; Samavati et al., 2015)	young's module 5.8 MPa Poisson's ratio 0.495	linear elastic structures (Dias et al., 2017)	Hooke (Dias et al., 2017)
5	hipbone	young's module 15244 MPa (Sichting et al., 2014) Poisson's ratio 0.3 (Sichting et al., 2014; He, 2016; Peng et al., 2016; Ricci et al., 2018; Guo et al., 2019; Zong, 2022)	No change	rigid body (Brandão et al., 2015; Xu et al., 2021)	
6	sacrum	young's module 16262 MPa (Sichting et al., 2014) Poisson's ratio 0.3 (Sichting et al., 2014; He, 2016; Peng et al., 2016; Ricci et al., 2018; Guo et al., 2019; Zong, 2022)	No change		
7	coccyx	young's module 11000 MPa (Sichting et al., 2014) Poisson's ratio 0.3 (Sichting et al., 2014; He, 2016; Peng et al., 2016; Ricci et al., 2018; Guo et al., 2019; Zong, 2022)	No change		
8	femur	young's module 13500 MPa (Guo et al., 2019) Poisson's ratio 0.3 (Sichting et al., 2014; He, 2016; Peng et al., 2016; Ricci et al., 2018; Guo et al., 2019; Zong, 2022)	No change		
9	fat	young's module 0.05 MPa (Dias et al., 2017) Poisson's ratio 0.49 (Rao et al., 2010; Dias et al., 2017; Ma, 2019)	No change	linear elastic structures (Chen et al., 2010; Rao et al., 2010; Dias et al., 2017)	Hooke (Chen et al., 2010; Rao et al., 2010; Dias et al., 2017)
10	bulbospongiosus muscle	young's module 2.4 MPa (Zhang et al., 2009; Chen et al., 2010; Rao et al., 2010; Dias et al., 2017) Poisson's ratio 0.49 (Rao et al., 2010; Dias et al., 2017; Ma, 2019)	young's module 3.4 MPa Poisson's ratio 0.49		
11	ischiocavernous muscle				
12	superficial transverse perineal muscle, deep transverse perineal muscle				
13	external anal sphincter	C_{10} = 11.8 kPa C_{20} = 5.53e-3 kPa (Silva et al., 2016)	C_{10} = 12.8 kPa C_{20} = 5.53e-3 kPa	hyperelastic structures (Silva et al., 2016; Xuan et al., 2021)	Mooney-Rivlin (Silva et al., 2016)
14	external urethral sphincter				
15	coccygeal muscle	young's module 2.4 MPa (Zhang et al., 2009; Dias et al., 2017) Poisson's ratio 0.49 (Dias et al., 2017; Xu et al., 2021)	No change	linear elastic structures (Dias et al., 2017)	Hooke (Dias et al., 2017)
16	levator ani muscle, including pubococcygeus muscle, iliococcygeus muscle, puborectalis muscle	C_{10} = 2.5 KPa C_{20} = 0.625 KPa (Lee et al., 2005; Wu, 2019)	No change	hyperelastic structures (Krcmar et al., 2015)	Mooney-Rivlin (Wu, 2019)

(Continued on following page)

TABLE 1 (*Continued*) Material properties of various parts in the model.

No.	Anatomical element	Material constants		Structures	Constitutive models
		In the literature	After adjustment		
17	obturator internus muscle	young's module 0.95 MPa (Chen, 2014; Peng et al., 2016; Liu, 2017) Poisson's ratio 0.45 (Chen, 2014)	No change	viscoelastic materials	Hooke
18	rectus abdominis muscle	young's module 13.3 MPa (Sun, 2015) Poisson's ratio 0.45 (Chen, 2014)	No change	viscoelastic materials (Li et al., 2017)	Hooke
19	iliac muscle	young's module 19 MPa (Li et al., 2017) Poisson's ratio 0.45 (Chen, 2014)	No change		
20	psoas major muscle	young's module 13.3 MPa (Sun, 2015) Poisson's ratio 0.45 (Chen, 2014)	No change		
21	quadriceps femoris muscle				
22	tensor fascia lata muscle				
23	gluteus maximus muscle	young's module 19 MPa (Li et al., 2017) Poisson's ratio 0.45 (Chen, 2014)	No change		
24	gluteus medius muscle				
25	piriformis muscle				
26	hamstring muscles	young's module 13.3 MPa (Sun, 2015) Poisson's ratio 0.45 (Chen, 2014)	No change		
27	pubic muscle				
28	adductor longus muscle				
29	latissimus dorsi muscle				
30	erector spinae muscle				

validation, literature result validation, and experimental result validation (Peng et al., 2023). Peng et al. (2016) conducted a validation study by comparing pelvic floor configurations achieved in computer simulation results with dynamic MRI observations along the midsagittal plane at both rest and maximal Valsalva maneuvers, and we highly recognize this geometric form validation method. Due to the lack of literature results and experimental results of elderly pelvic floor, It is very difficult to verify using methods such as literature results verification and experimental results verification. Therefore, We will compare the Valsalva maneuvers of the elderly during dynamic MRI scanning with the Valsalva maneuvers of the pelvic floor simulated by the finite element model, and compare whether the variety of the three anatomical landmark points of the two are consistent.

The specific process of dynamic MRI scanning is detailed in our previous research protocol (Wang et al., 2024) and we completed the Valsalva maneuvers through simulation of the finite element model. The Valsalva simulation plan's loading site is the anterior abdominal wall, and in the resting state, E = 0.019 and the load is 0.5 kPa. At moderate tension, E = 0.241 and the load is 4.5 kPa. Under severe tension, E = 0.947 and the load is 5.0 kPa (Wu, 2019), and the direction of application is from the top of the anterior abdominal wall to the direction of the coccyx (Qiu, 2017). During model verification, the three anatomical landmarks include relative changes in waistline, changes in retrovesical angle (RVA) and changes in anorectad angulation (ARA). Among them, the RVA is the angle formed by the median sagittal plane of the bladder floor and the long axis of the urethra, and the ARA is the angle between the longitudinal axis of the anal canal and the posterior wall of the rectum above the levator ani muscle. These two angles are often measured in imaging data of the pelvic floor. Due to the lack of relevant research and guidelines specifying the scope of differences, we consulted relevant biomechanical experts and combined them with clinical situations. If the differences are within 10%, it will be considered that the model construction is more accurate.

2.5 Applied loads and simulation plans analysis

After completing the construction and verification of the finite element model, we will conduct specific finite element analysis under different simulation plans. Muscle elastic modulus refers to the ratio of deformation to the force applied on muscles and is a critical parameter for assessing muscle stiffness. Research has shown that rehabilitation exercises such as muscle contraction training and resistance movements can indirectly affect this modulus, resulting in decreased passive stiffness and increased muscle softness and flexibility (de Sousa et al., 2023). Since finite element analysis does not directly simulate rehabilitation training, we adapted simulation to reflect muscle capacity changes after rehabilitation training. So, we simulated a 25%, 50%, 75%, 100% strengthening in

TABLE 2 Simulation plans table.

No.	Simulated rehabilitation trainings	Loading site	Abdominal pressure (kPa)	Outcome indicators
1	anal sphincter training for fecal incontinence	external anal sphincter	0.6	ARA, stress, strain
2	transcutaneous electrical nerve stimulation for urinary retention	urethral sphincter	0.6	RVA, stress, strain
3	a. biofeedback for urinary incontinence b. biofeedback for urinary retention c. Exercise training for fecal incontinence-levator ani activities d. Exercise training for constipation-levator ani exercise	levator ani muscle	0.6	RVA, ARA, stress, strain
4	a. Exercise training for urinary incontinence b. Exercise training for urinary retention	levator ani muscle and urethral sphincter	0.6	RVA, stress, strain
5	a. Magnetic stimulation of constipation b. biofeedback of constipation c. Exercise training for constipation	levator ani muscle and external anal sphincter	0.6	ARA, stress, strain
6	a. Exercise training for urinary incontinence b. Electrical stimulation for urinary incontinence c. Magnetic stimulation for urinary incontinence d. biofeedback for urinary incontinence e. Vibrational stimulation for urinary incontinence f. Exercise training for urinary retention g. Magnetic stimulation for urinary retention h biofeedback for urinary retention i. Electrical stimulation for urinary retention j. Electrical stimulation for fecal incontinence-sacral nerve anterior root electrical stimulation k. biofeedback for fecal incontinence combined with pelvic floor muscle training l. Magnetic stimulation for fecal incontinence m. Exercise training for constipation-pelvic floor muscle training n. Tibial nerve electrical stimulation, sacral nerve electrical stimulation, and transcutaneous acupoint electrical stimulation for constipation o. Magnetic stimulation for constipation p. biofeedback for constipation q. Vibrational stimulation for constipation	pelvic floor muscles	0.6	RVA, ARA, stress, strain
7	magnetic stimulation for fecal incontinence-functional magnetic stimulation	pelvic floor muscles and rectus abdominis muscle and erector spinae muscle	0.6	ARA, stress, strain
8	exercise training for urinary incontinence-hip muscle exercises	pelvic floor muscles and hip muscles	0.6	RVA, stress, strain
9	exercise training for urinary incontinence-suspension exercise training	pelvic floor muscles and rectus abdominis muscle and hip muscles and erector spinae muscle	0.6	RVA, stress, strain

muscle capacity, a normal muscle capacity, a 25%, 50%, 75%, 95% impairment in muscle capacity. These adjustments were achieved by varying the material properties' correlation properties to 1.25x, 1.5x, 1.75x, 2x (for increases), 1x (for baseline), 0.75x, 0.5x, 0.25x, and 0.05x (for decreases), respectively.

Currently, there are five known rehabilitation training methods for improving bowel function including exercise training, biofeedback, electrical stimulation, magnetic stimulation, and vibrational stimulation. Table 2 lists the muscles based on the literature content corresponding to the five types of rehabilitation training for the four types of urination and defecation dysfunction. We found that the five rehabilitation training methods mainly enhance the elderly's urination and defecation abilities through muscle training, such as external anal sphincter, urethral sphincter, levator ani muscle, pelvic floor muscles, rectus abdominis muscle, hip muscles and erector spinae muscle. When performing finite element analysis, delete tissues and muscles that are weakly related to urination and defecation from the established finite element model, such as obturator internus muscle, skin, fat, pyramidal muscle, tensor fascia lata muscle, pubic muscle and latissimus dorsi muscle.

Regarding intra-abdominal pressure, a search of the literature shows that the resting intra-abdominal pressure is 0.4–0.64 kPa (Song et al., 2012), and the abdominal pressure in another literature was 0.665 kPa (Korkmaz and Rogg, 2007), so the abdominal pressure was selected as 0.6 kPa in our study. The main outcome measure of the study are RVA and ARA, which are well-known parameters for evaluating the control ablity of urination and defecation dysfunction (Guo et al., 2015; Zhou and Lai, 2021). The second outcome measure of the study are the von Mises

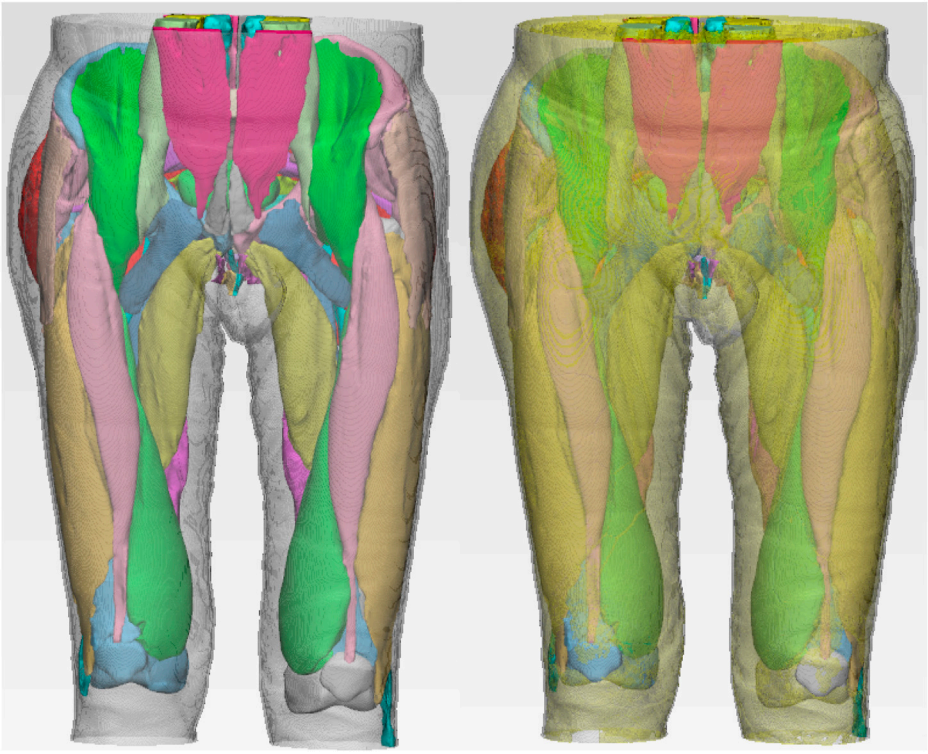

FIGURE 4
Finite element model of old adult.

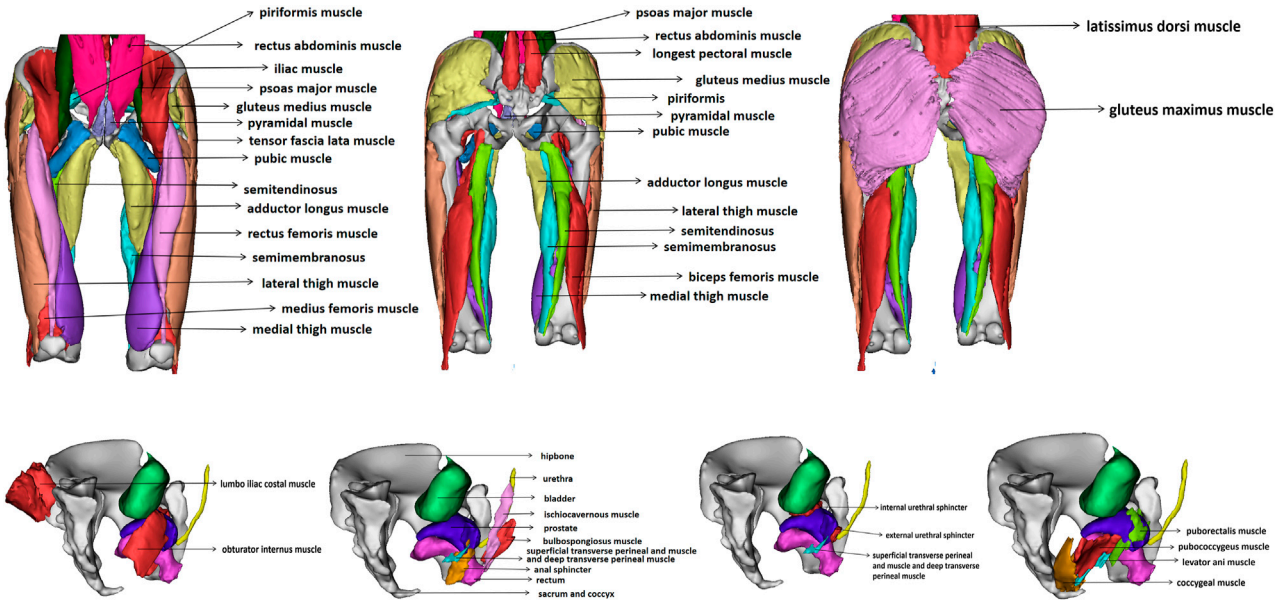

FIGURE 5
Annotation diagram of different muscle positions of the finite element model.

stress cloud map and strain region of the area in the finite element model of elderly men under different simulation plans. The simulation plans table is listed in Table 2. The first two columns list the test number and the simulated rehabilitation trainings, and the third column lists the loading site. The first to ninth simulation plans simulate the muscle strengthening or impairment effects of the five types of rehabilitation training for the four types of urination and defecation dysfunction.

FIGURE 6
Mesh division of the finite element model.

3 Results

3.1 Finite element model establishment

The finite element model includes the final three-dimensional pelvic floor model including organs including bladder, urethra, rectum and prostate, bones including hipbone, sacrum, coccyx and femur, pelvic floor muscles including bulbocavernosus muscle, ischiocavernosus muscle, superficial transverse perineal muscle, deep transverse perineal muscle, external anal sphincter, external urethral sphincter, coccygeal muscle, pubococcygeus muscle, iliococcygeus muscle, puborectalis muscle and obturator internal muscle, abdominal muscles including rectus abdominis muscle and pyramidal muscle, hip muscles including iliacus muscle, psoas major muscle, rectus femoris muscle, vastus lateralis muscle, vastus intermedius muscle, vastus medialis muscle, tensor fascia lata muscle, gluteus maximus muscle, gluteus medius muscle, piriformis muscle, semitendinosus muscle, semimembranosus muscle, biceps femoris muscle, pubic muscle and adductor longus muscle, back muscles including latissimus dorsi muscle, iliocostalis muscle, longissimus thoracis muscle, skin, fat, a total of 41 structures, 1188,251 nodes and 251,290 elements. Figure 4 shows the finite element model of old adult. Figure 5 is an annotation diagram of different muscle positions of the finite element model. Figure 6 shows the mesh division of the finite element model.

3.2 Verification of finite element model

We compared pelvic floor changes achieved along the midsagittal plane in computer simulations with imaging observations of Valsalva maneuvers in dynamic MRI. The results showed that the relative changes in waistline, RVA and ARA are within 3.51%, indicating a high consistency between the simulated situation constructed in the study and the actual pelvic floor situation of the elderly, as shown in Figure 7. The comparison of

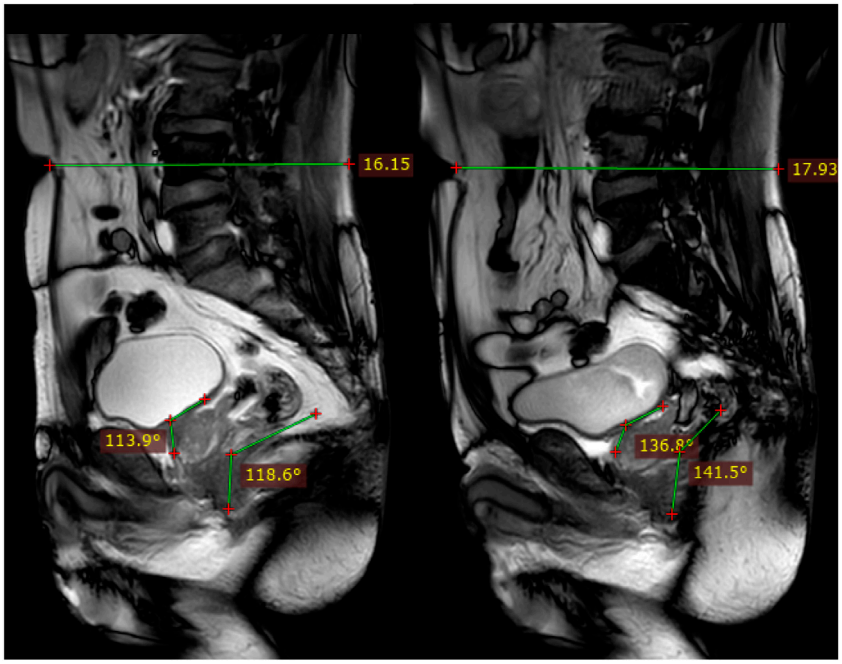

FIGURE 7
Schematic diagram of measuring relative changes in waistline, RVA, and ARA.

TABLE 3 Comparison of dynamic MRI and 3D model measurement results.

Validation indicators		Measurement results		Difference percentage
		Dynamic MRI	3D model	
Waistline	Before Valsalva	161.50 mm	165.72 mm	2.61%
	After Valsalva	179.30 mm	173.01 mm	3.51%
RVA	Before Valsalva	113.9°	115.58°	1.47%
	After Valsalva	136.8°	135.01°	1.31%
ARA	Before Valsalva	118.6°	118.08°	0.44%
	After Valsalva	141.5°	143.44°	1.37%

dynamic MRI and 3D model measurement results are shown in Table 3.

3.3 Finite element simulation plans analysis results

3.3.1 Results of changes in ARA and RVA with material properties

We analyzed the numerical changes of ARA and RVA in response to varying material properties respectively, illustrating how these changes correlate with the urinary and defecation abilities of elderly individuals. These relationships are depicted through changes in muscle strength associated with specific defecation and urinary rehabilitation training methods, as shown in Table 4 and 5. Figures 8, 9 present line graphs illustrating the angular responses (ARA and RVA) of five distinct muscle or muscle group combinations to variations in material properties. The x-axis quantifies the changes in material properties as multiplicative factors ranging from 0.05 to 2 times, while the *y*-axis displays the angular response values, with AVA ranging from 110° to 140°and RVA from 105° to 135°. Figure 8 illustrates that with the increase of material properties, the ARA consistently rises under simulation plans 1, 3, 5, 6, and 7. Conversely, as shown in Figure 9, the RVA diminishes with increasing in material properties under simulation plans 2, 3, 4, 6, 8, and 9. The variation in the slope of each line demonstrates the sensitivity of different muscle groups to changes in material properties.

3.3.2 Comparative analysis of simulated rehabilitation muscles for constipation and fecal incontinence

Simulation plans 3, 5, and 6 were designed to simulate the muscles strengthening and impairment effects on muscles implicated in constipation rehabilitation training. The muscles examined include levator ani muscle, levator ani muscle and external anal sphincter, and pelvic floor muscles. Comparative analysis of improvement of ARA across different simulations, if rehabilitation training gradually changes the material properties of muscles in elderly people from below normal to normal, the training effect of levator ani muscle is better than that of levator ani muscle, external anal sphincter, and pelvic floor muscles in sequence (Figures 10, 11). When the material properties of muscles gradually changes from greater than the normal value to the normal value, the training effect of levator ani muscle and external anal sphincter is better than levator ani muscle and pelvic floor muscles in sequence (Figures 12, 13).

Simulation plans 1, 3, 6, and 7 were designed to simulate the muscles strengthening and impairment effects of fecal incontinence rehabilitation training, among which the muscles included external anal sphincter, levator ani muscle, pelvic floor muscles, pelvic floor muscles and rectus abdominis muscle and erector spinae muscle. By comparing the improvement degree of ARA under different simulations, when rehabilitation training gradually changes the material properties of muscles in elderly people from less than normal to normal the training effect of levator ani muscle is better than that of pelvic floor muscles and rectus abdominis muscle and erector spinae muscle, pelvic floor muscles, and external anal sphincter, sequentially (Figures 10, 11). As the material properties of muscles gradually changes from approach normalcy from above-normal levels, the training effect of external anal sphincter is better than that of pelvic floor muscles and rectus abdominis muscle and erector spinae muscle, levator ani muscle, and pelvic floor muscles, respectively (Figures 14, 15).

It is noteworthy that regardless of muscle material properties in elderly people, training the levator ani muscle alone yields better outcomes than training it as part of the pelvic floor group for managing constipation and fecal incontinence in the elderly. Furthermore, regardless of the state of muscle material properties in the elderly, a comprehensive training approach that includes pelvic floor muscles, rectus abdominis, and erector spinae muscles proves more effective than focusing solely on the pelvic floor muscles in constipation and fecal incontinence rehabilitation trainings.

3.3.3 Comparative analysis of simulated rehabilitation muscles for urinary incontinence and urinary retention

Simulation plans 3, 4, 6, 8, and 9 were designed to simulate the muscles enhancement and impairment effects of urinary incontinence rehabilitation training. The targeted muscle groups included levator ani muscle, levator ani muscle and urethral sphincter, pelvic floor muscles, pelvic floor muscles and hip muscles, pelvic floor muscles and rectus abdominis muscle and hip muscles and erector spinae muscle. By comparing the degree of improvement in RVA under different simulations, it can be

TABLE 4 Numerical table of ARA changes with material properties.

Simulation plans	Muscles	Angle	Multiple of material properties									Changes in material properties		
			0.05 times	0.25 times	0.50 times	0.75 times	1.00 times	1.25 times	1.50 times	1.75 times	2.00 times	From 0.05 times to 1 times	From 1 times to 2 times	From 0.05 times to 2 times
No.1	external anal sphincter	ARA	113.66	115.34	117.82	119.18	121.58	124.29	127.75	131.47	133.72	7.92	12.14	20.06
No.3	levator ani muscle	ARA	110.79	111.81	117.63	121.59	125.20	126.95	128.48	130.45	134.58	14.41	9.38	23.79
No.5	levator ani muscle and external anal sphincter	ARA	116.02	116.78	120.42	123.78	127.34	130.33	132.57	134.86	137.93	11.32	10.59	21.91
No.6	pelvic floor muscles	ARA	122.06	123.03	125.33	127.73	130.40	132.08	134.47	136.57	138.16	8.34	7.76	16.1
No.7	pelvic floor muscles and rectus abdominis muscle and erector spinae muscle	ARA	117.39	117.88	120.48	124.29	126.61	128.51	131.14	133.64	136.22	9.22	9.61	18.83

TABLE 5 Numerical table of RVA changes with material properties.

Simulation plans	Muscles	Angle	Multiple of material properties									Changes in material properties		
			0.05 times	0.25 times	0.50 times	0.75 times	1.00 times	1.25 times	1.50 times	1.75 times	2.00 times	From 0.05 times to 1 times	From 1 times to 2 times	From 0.05 times to 2times
No.2	urethral sphincter	RVA	123.14	121.32	118.68	116.68	115.21	114.17	113.33	112.79	112.17	−7.93	−3.04	−10.97
No.3	levator ani muscle	RVA	125.20	124.47	122.56	119.53	116.79	115.79	114.49	113.54	112.64	−8.41	−4.15	−12.56
No.4	levator ani muscle and urethral sphincter	RVA	126.27	125.37	123.59	120.46	118.87	117.88	116.80	116.02	115.23	−7.4	−3.64	−11.04
No.6	pelvic floor muscles	RVA	126.54	125.71	124.02	121.94	120.68	119.21	117.58	116.82	116.38	−5.86	−4.3	−10.16
No.8	pelvic floor muscles and hip muscles	RVA	119.8	119.24	118.44	116.97	115.4	114.25	113.93	113.07	112.71	−4.4	−2.69	−7.09
No.9	pelvic floor muscles and rectus abdominis muscle and hip muscles and erector spinae muscle	RVA	119.89	118.64	116.69	115.22	113.36	111.58	110.64	109.57	109.17	−6.53	−4.19	−10.72

10.3389/fbioe.2024.1392448

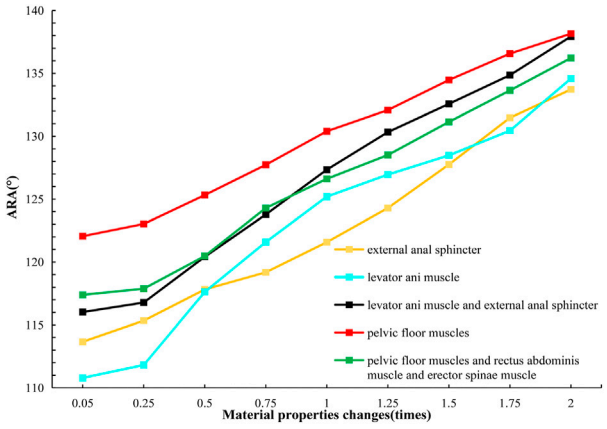

FIGURE 8
Curve chart of ARA changes with material properties.

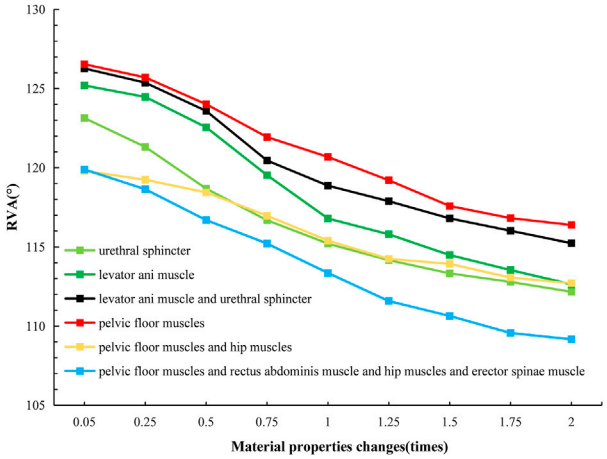

FIGURE 9
Curve chart of RVA changes with material properties.

indicated that rehabilitation training progressively changes the material properties of muscles in elderly people from less than normal to normal, the efficacy of training the levator ani muscle alone surpassed that of combined training with the urethral sphincter, and also outperformed the broader group training involving pelvic floor muscles and rectus abdominis muscle and hip muscles and erector spinae muscle, pelvic floor muscles, pelvic floor muscles and hip muscles, sequentially (Figures 10, 11). Furthermore, when the material properties of the muscles from greater than the normal value to the normal value, the training effectiveness of the pelvic floor muscles excelled over that of the pelvic floor muscles and rectus abdominis muscle and hip muscles and erector spinae muscls, levator ani muscles, levator ani muscles and urethral sphincter, and pelvic floor muscles and hip muscles in sequence (Figures 16, 17).

Simulation plans 2, 3, 4, and 6 were designed to simulate the muscles strengthening and impairment effects of urinary retention rehabilitation training. The muscles include urethral sphincter, levator ani muscle, levator ani muscle and urethral sphincter, and pelvic floor muscles. By comparing the degree of improvement in RVA under different simulations, it can be concluded that rehabilitation training gradually changes the material of muscles in elderly people from less than normal to normal, and the training's efficacy on levator ani muscle surpassed urethral sphincter alone and levator ani muscle combined with the urethral sphincter (Figures 10, 11). The training's efficacy on levator ani muscle and also exceeded training effects on pelvic floor muscles. In addition, when the material properties of the muscles gradually changes from greater than the normal value to the normal value, the effect of pelvic floor muscles is superior to those involving levator ani muscle alone, or levator ani muscle in combination with urethral sphincter, and urethral sphincter alone respectively (Figures 16, 17).

It should be noted that irrespective of the muscle material properties in the elderly, the training of the levator ani muscle alone demonstrates superior effectiveness over combined training with the urethral sphincter in managing urinary incontinence and retention. Furthermore, both individual and combined training of pelvic floor muscles with rectus abdominis muscles, hip muscles, erector spinae muscles provide more significant benefits compared to training that combines only the pelvic floor muscles with hip muscles.

Moreover, it was observed that alterations in the material properties of muscles from 0.05 to 0.25 times did not significantly impact the ARA. Similarly, when the muscle material properties ranged from 1.50 to 2.00 times, there was no significant change in the RVA.

4 Discussion

This study gathered muscles medical imaging from a elderly male to develop and verified a finite element model. This study explored the quantitative relationship between rehabilitation training methods on muscles and urinary and defecation dysfunction, ultimately elucidating the mechanism of improving urinary and defecation dysfunction. One of the advantages of finite element models is that they provide a cost-effective solution for studying complex biomechanical processes, such as rehabilitation training for bowel and bladder functions, without the need for extensive resources, specialists, or equipment. Additionally, these models enhance safety by eliminating the potential risks associated with human trials. Due to the consistent reproducibility of computations, finite element models are able to deliver highly repeatable results. Previous studies have developed some pelvic floor finite element models for the treatment of urinary incontinence, however that predominantly focused on young postpartum women (Hu and Pierre, 2019), leading to a gap in models suited for older men. Male and female pelvic floor anatomy are different, and aging individuals experience physiological changes including decreased muscle strength and changes in pelvic floor tissue relaxation and elasticity. Currently, there is a lack of finite element model of the pelvic floor for analyzing fecal incontinence, constipation, urinary incontinence and urinary retention in elderly men, therefore it is very necessary to construct a finite element model of the pelvic floor of elderly men to guide rehabilitation and treatment. In addition, our model also integrates additional muscular systems, such as those of the back, hip, and abdomen,

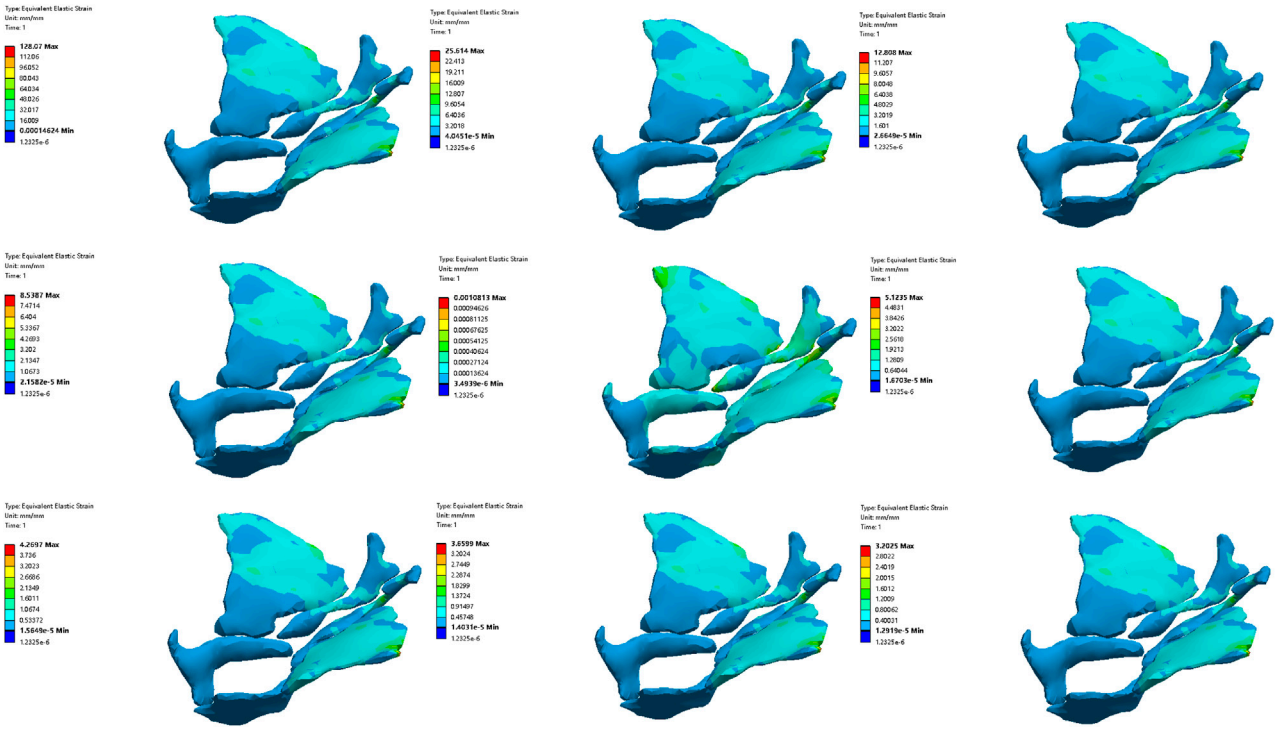

FIGURE 10
Strain diagram of levator ani muscle in simulation plan No.3.

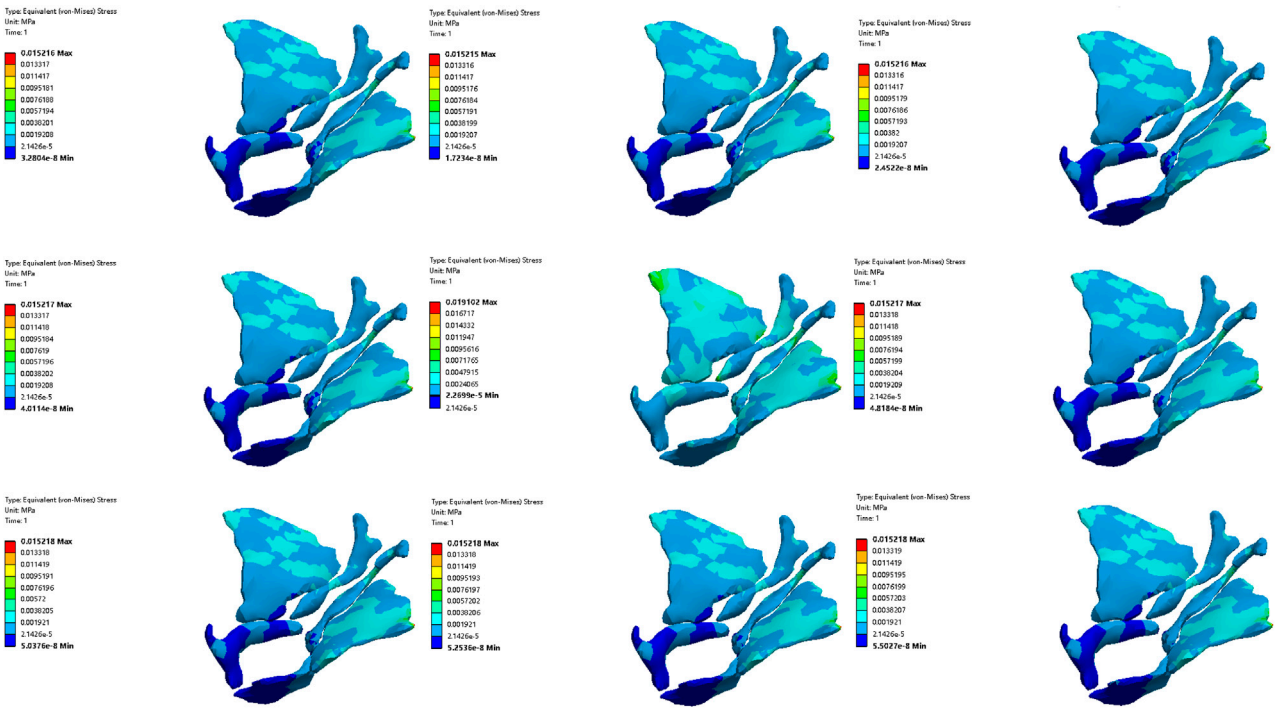

FIGURE 11
Stress diagram of levator ani muscle in simulation No.3.

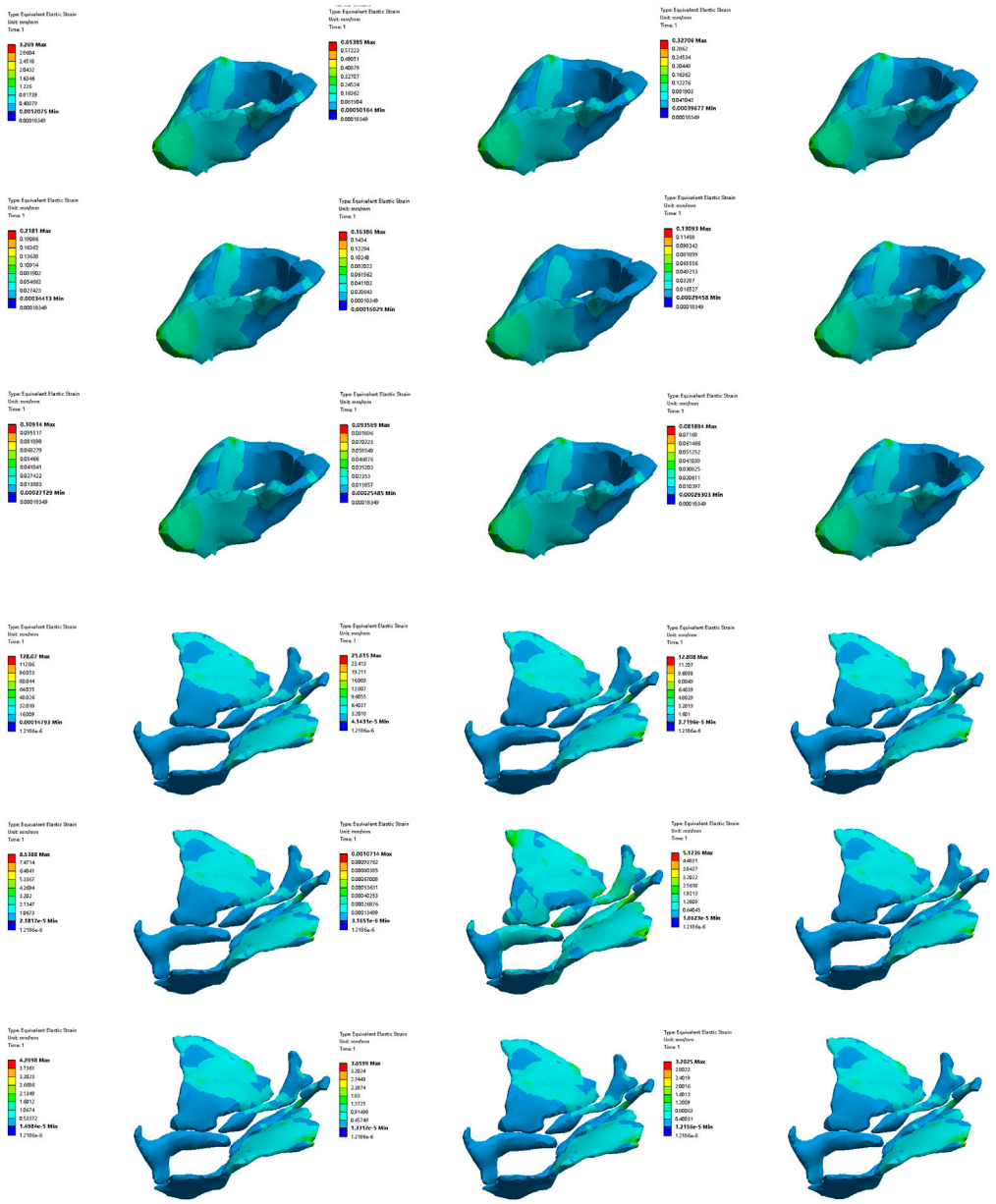

FIGURE 12
Strain diagram of levator ani muscle and external anal sphincter in simulation No.5.

which play significant roles in urination and defecation rehabilitation training and are often overlooked in existing models. This innovative approach is more conducive to simulating the rehabilitation training methods and measuring the quantitative relationship between five rehabilitation training methods and the urinary and defecation control ability of elderly men, which is also one of the innovative points of this study.

The primary structures that affect the ability to control bowel movements are mainly divided into three parts including pelvic floor muscles, core muscles and sacral nerves. Pelvic floor muscles are crucial for regulating urination, defecation, and maintaining vaginal contractions. Core muscles, encompassing the waist, abdomen, hips, and legs, serve as pivotal points for trunk movements, enhancing stability for the spine and pelvis, and increasing abdominal pressure. Sacral nerves play a vital role in managing the reflexes of the bladder, sphincters, and pelvic floor. In this study, we systematically investigatesd the impact of rehabilitation training on the urinary and defecation abilities of elderly by analyzing the angular changes of ARA and RVA in response to alterations in the material properties of involved muscles.

Regarding the changes in material properties of pelvic floor muscles in the elderly, it is observed that these tissues physiologically lose some elasticity due to aging, potentially reducing the Young's module of soft tissues (Bhattarai and Staat, 2018). Regular muscle training or other healthy habits in some elderly individuals may increase the Young's module, potentially reversing some age-related degenerative changes. It is important to note that changes in the

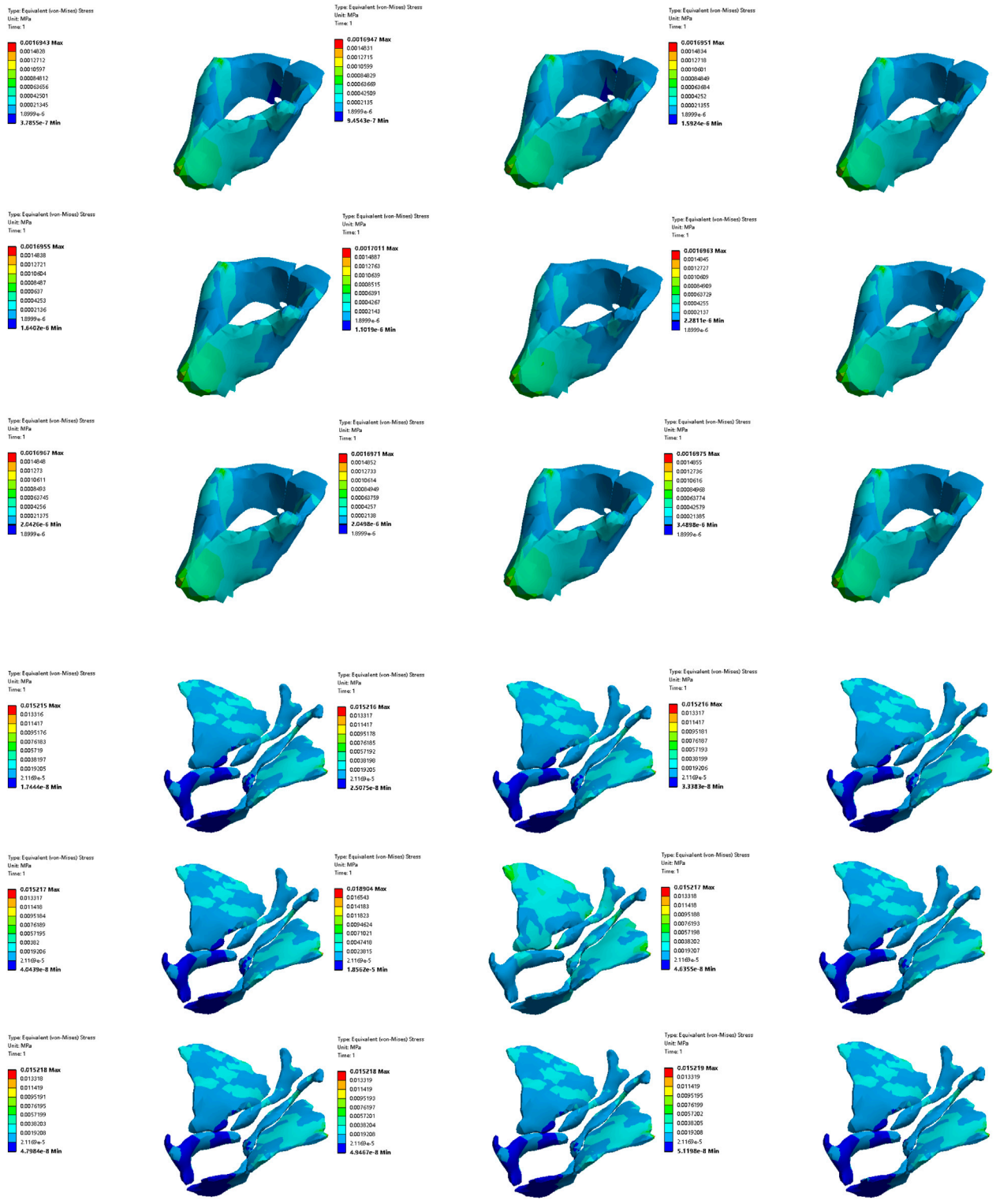

FIGURE 13
Stress diagram of levator ani muscle and external anal sphincter in simulation No.5.

Young's module of pelvic floor muscles in the elderly are not absolute. These changes depend on individual characteristics, natural aging, disease types, and cannot be universally generalized. Hence, our study simulated a range of material properties from 0.05 to 2 times to accommodate various simulation scenarios.

The normal range of ARA and RVA vary, and the variability in results could be attributed to the individual differences among

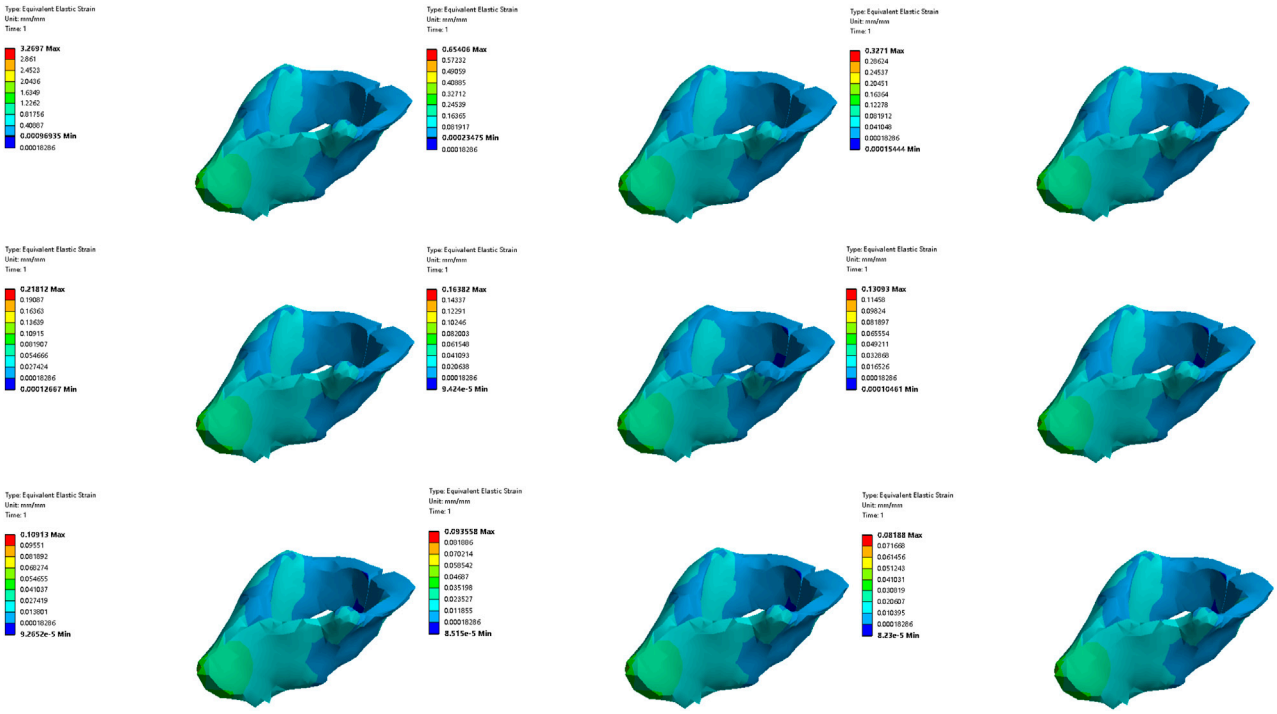

FIGURE 14
Strain diagram of external anal sphincter in simulation No.1.

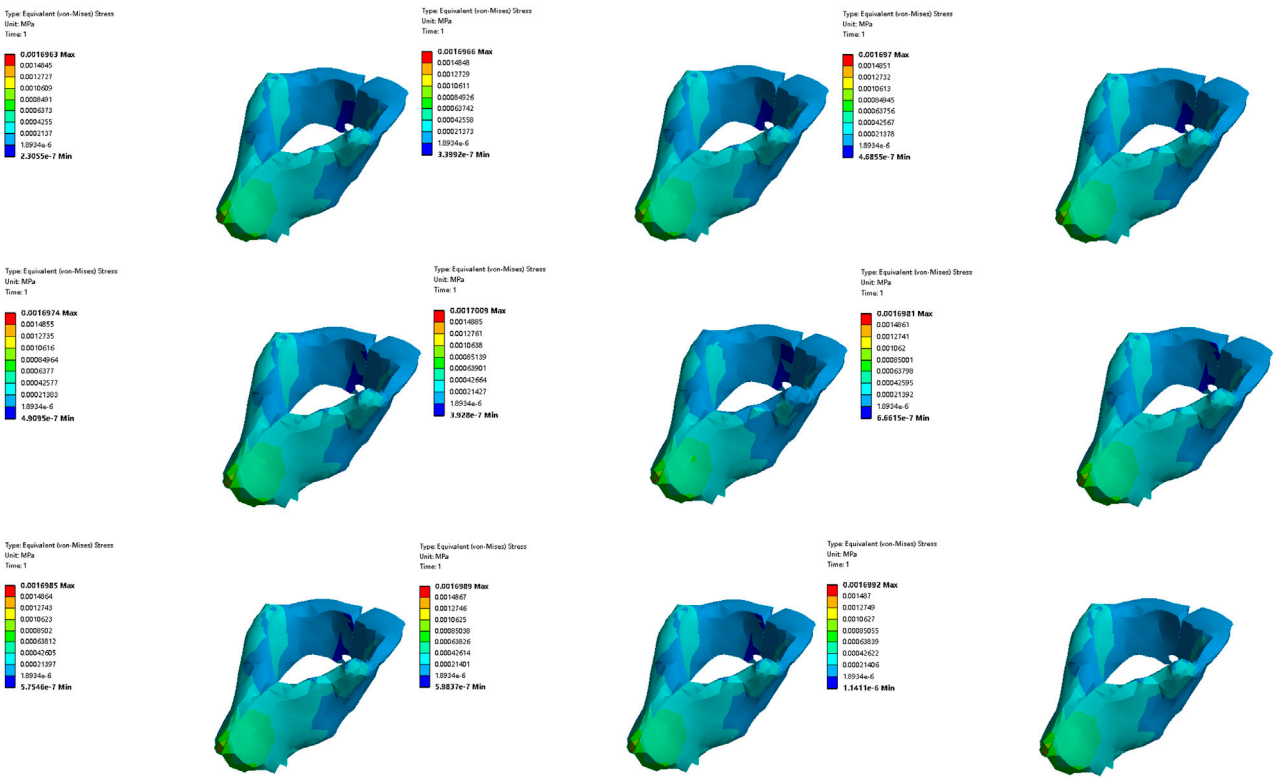

FIGURE 15
Stress diagram of external anal sphincter in simulation No.1.

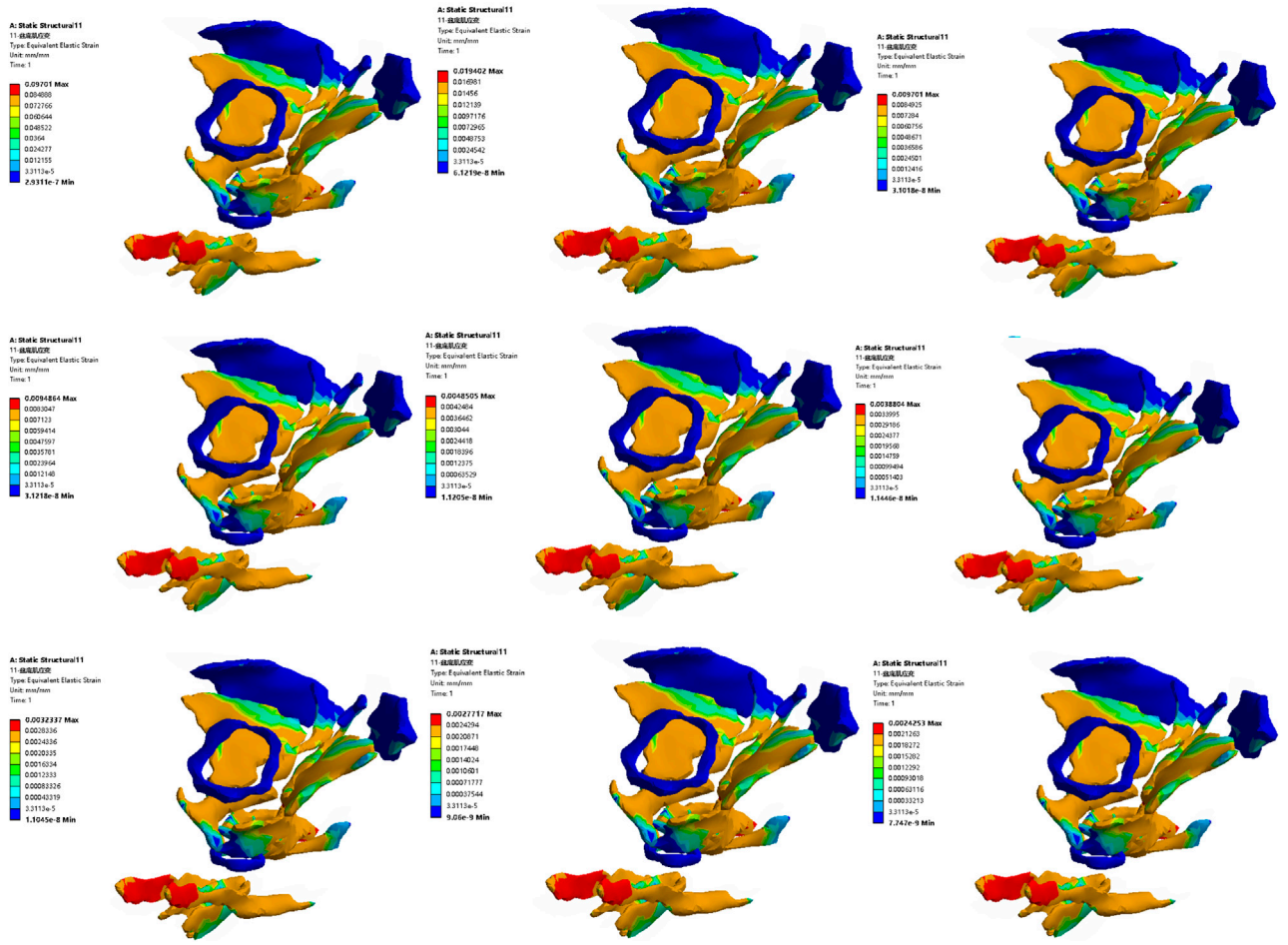

FIGURE 16
Stress diagram of external anal sphincter in simulation No.6.

assessors or the participants. According to literature (Xue, 1996; Mortele and Fairhurst, 2007; Colaiacomo et al., 2009; Bitti et al., 2014; Kobi et al., 2018; Zhou and Lai, 2021; The MR Group of the Radiology Branch of the Chinese Medical Association, 2022), the typical resting range of ARA is between 90° and 127°, while during defecation, it extends from 120° to 152.4°. The resting RVA spans from 90° to 120° (Liu et al., 2013). In cases of anterior pelvic dysfunction, RVA values can expand from the normal range of 90°–120°–160°–180°during the tension phases (Fielding et al., 2000). Some research also suggests that RVA for individuals with stress urinary incontinence may exceed 140° (Li and Yan, 2015). The results indicate that as the material properties of muscles or muscle groups change, ARA and RVA are gradually approaching the normal range. Therefore, theoretically, it can be posited that rehabilitation training methodologies including biofeedback, exercise training, electrical stimulation, magnetic stimulation, and vibration training may enhance the ability of elderly men to control bowel movements.

The responsiveness of different muscles to changes in ARA and RVA angles can be evaluated by comparing the slopes of each line in Tables 8 and 9. A higher slope indicates a greater responsiveness of that muscle or muscle combination to changes in ARA and RVA angles. Research findings indicate that individual training of specific muscle groups, particularly the levator ani muscle, proves more effective in treating disorders of both urination and defecation in the elderly compared to combined training with pelvic floor and urethral sphincter muscles. This could be due to the specific role that the levator ani muscle plays in supporting the pelvic organs and controlling the functions closely related to the bowel movements. While the specific research studies that the comparative effectiveness of isolated levator ani muscle training *versus* comprehensive pelvic floor muscle training might not be directly available, general principles of physical therapy and muscle rehabilitation suggest that targeted exercises can indeed improve the functionality of specific muscles more effectively than generalized training. A study reached a similar conclusion to ours, the study pointed out that with the increase of external load, the training effect on certain muscles significantly increases, while the training effect on other muscles is much smaller. The simulation results show that compared with pure weightlifting training, training based on optimal load orientation concept (OLOC) can significantly improve the training effect of specific muscles, and training methods targeting specific muscles maximize the training effect of target muscles (Song et al., 2018).

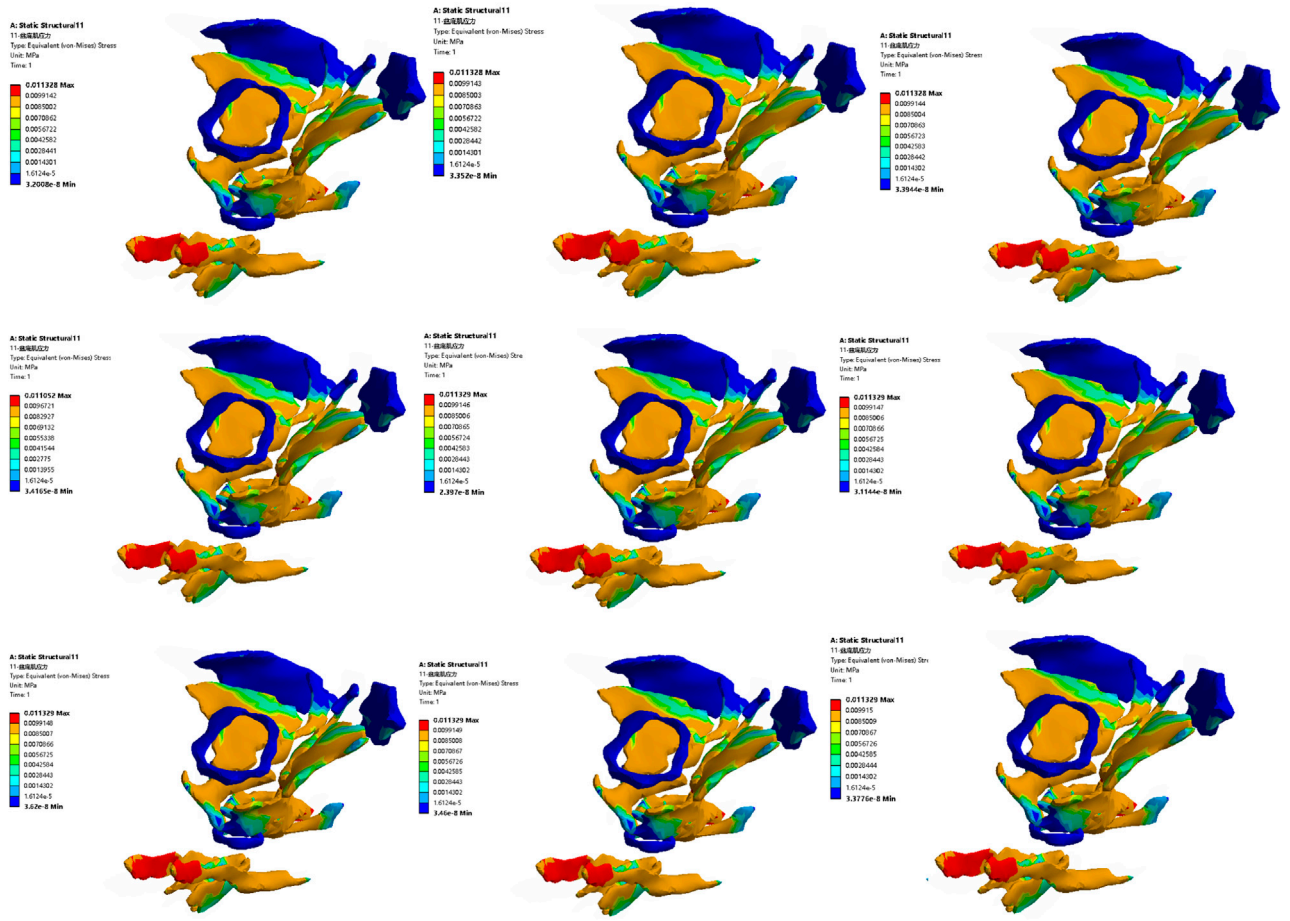

FIGURE 17
Stress diagram of pelvic floor muscles in simulation No.6.

In addition, research findings indicate that targeted muscle rehabilitation training for the levator ani muscle and anal external anal sphincter in cases of fecal dysfunction, and for the levator ani muscle and pelvic floor muscles in cases of urinary dysfunction, theoretically holds the greatest potential for significant improvement in the urinary and defecation control ability of the elderly. Previous studies (Zhou and Lai, 2021) have highlighted that the key factors influencing individual urinary and defecation control ability include the levator ani muscle, puborectalis muscle, and external anal sphincter, all of which are closely associated with fecal dysfunction. Abnormalities in the structure or function of these muscles lead to bowel control problems. This aligns with the conclusions of our research, which suggests that optimizing the function of the peri-anal muscle group is essential for improving urinary and defecation control ability. Furthermore, for urinary function, the pelvic floor muscles are the most critical source of support (Li and Lu, 2023), with the levator ani muscle playing a significant supportive role (Ashton-Miller and DeLancey, 2007). The literature (Zhou et al., 2020) pointed out that pelvic floor muscle exercise, mainly involving the levator ani muscle, is a method for treating pelvic floor dysfunction diseases. Pelvic floor muscles rehabilitation training, including Kegel exercises, pelvic floor muscle training, biofeedback training, electrical stimulation, and acupuncture, is commonly used in elderly males post-laparoscopic radical prostatectomy (Feng, 2022) and for managing lower urinary tract symptoms post-stroke (Tibaek et al., 2017).

In conclusion, these results are significant for understanding and treating muscle-related urination and defecation dysfunction. The findings emphasize the importance of personalized and targeted rehabilitation approaches in effectively addressing pelvic floor dysfunctions. Some studies (Okada et al., 2001; Tang et al., 2020) have employed shear wave elastography (SWE) to assess the biomechanical properties of pelvic floor muscles. Future research should further explore how specific rehabilitation training methods practically affect muscle material properties, aiming to adjust these properties through tailored exercises to improve bowel disorders in the elderly. When designing and implementing targeted rehabilitation training, it is recommended to advocate for personalized and dynamic treatment plans. Specifically, the response characteristics of different muscles under varying stress conditions should be considered, and training intensity and muscle group rehabilitation strategies should be adjusted based on the changes in muscle material properties to enhance the effectiveness of rehabilitation training for the elderly.

The study acknowledges several limitations. Firstly, due to constraints, this study was conducted on a single elderly male subject, and the results may not fully represent all elderly men. Secondly, the complexity of the human body necessitated the simplification of certain biomechanical processes. This includes a focus on specific muscle groups, such as the abdominal muscles specifically refer to the rectus abdominis, and the hip muscles specifically refer to the iliopsoas, quadriceps, gluteus maximus, hamstrings, gluteus medius, and adductor longus The back muscles were specifically the erector spinae, without incorporating ligament roles or all muscle combinations. Third, while the study provides insights into muscle functionality and its effects on rehabilitation outcomes, the results of this study are based on the relationship between muscles and ARA, RVA, and it does not a direct relationship between rehabilitation training methods and urinary and defecation control ability. This possibly leading to over-idealized conclusions. In actual rehabilitation training, it may not be possible to train a single muscle alone, and it is also difficult to achieve proportional changes in muscles. However, this research offers a methodological approach to explain the mechanism of urinary and defecation control ability and elucidates the potential mechanisms linking rehabilitation training methods with the urinary and defecation control ability in the elderly.

5 Conclusion

In conclusion, by constructing and verificating a finite element model the study demonstrates that rehabilitation training, including exercise training, electrical stimulation, magnetic stimulation, biofeedback, and vibration stimulation, can improve the urinary and defecation control ability of elderly men. Crucially, the research results highlights the pivotal role of the levator ani muscle, external anal sphincter, and pelvic floor muscles in the managing of urination and defecation dysfunction. Moreover, this study emphasizes the effectiveness of targeted rehabilitation training in restoring urinary and defecation control among the elderly, emphasizing the need to adjust muscle training intensity and method based on the individual's muscle material properties to optimize therapeutic outcomes.

Data availability statement

The raw data supporting the conclusion of this article will be made available by the authors, without undue reservation.

Ethics statement

The studies involving humans were approved by Ethics Committee of Xuanwu Hospital, Capital Medical University and Ethics Committee of Capital Medical University. The studies were conducted in accordance with the local legislation and institutional requirements. The participants provided their written informed consent to participate in this study. Written informed consent was obtained from the individual(s) for the publication of any potentially identifiable images or data included in this article.

Author contributions

RW: Data curation, Formal Analysis, Investigation, Methodology, Software, Validation, Writing–original draft, Writing–review and editing. GL: Formal Analysis, Methodology, Supervision, Validation, Writing–review and editing. LJ: Formal Analysis, Funding acquisition, Resources, Supervision, Writing–review and editing. JZ: Formal Analysis, Methodology, Supervision, Writing–review and editing. YY: Data curation, Writing–review and editing. HZ: Data curation, Writing–review and editing.

Funding

The author(s) declare that financial support was received for the research, authorship, and/or publication of this article. This study is supported by the National Key R&D (research and development) Program of China (grant 2022YFB4703300). Any opinions, findings, conclusions, or recommendations expressed in this material are those of the authors and do not necessarily reflect the views of National Key R&D Program of China.

Acknowledgments

Thanks to Zhu Ying from Peking University First Hospital, Wu Chunxue from Xuanwu Hospital of Capital Medical University, professor Qian Xiuqing from Biomedical Engineering College of Capital Medical University, Zhang Zhiyong from North China University of Science and Technology for their guidance and help in this research.

Conflict of interest

The authors declare that the research was conducted in the absence of any commercial or financial relationships that could be construed as a potential conflict of interest.

Publisher's note

References

Alouini, S., Memic, S., and Couillandre, A. (2022). Pelvic floor muscle training for urinary incontinence with or without biofeedback or electrostimulation in women: a systematic review. *Int. J. Environ. Res. Public Health* 19 (5), 2789. doi:10.3390/ijerph19052789

Ashton-Miller, J. A., and DeLancey, J. O. (2007). Functional anatomy of the female pelvic floor. *Ann. N. Y. Acad. Sci.* 1101, 266–296. doi:10.1196/annals.1389.034

Bektas, A. N., Unal, N., and Akpinar, C. (2023). Urinary incontinence in older adults: impact on caregiver burden. *J. Gerontol. Nurs.* 49 (4), 39–46. doi:10.3928/00989134-20230310-01

Bhattarai, A., and Staat, M. (2018). Modelling of soft connective tissues to investigate female pelvic floor dysfunctions. *Comput. Math. Methods Med.* 2018, 1–16. doi:10.1155/2018/9518076

Bitti, G. T., Argiolas, G. M., Ballicu, N., Caddeo, E., Cecconi, M., Demurtas, G., et al. (2014). Pelvic floor failure: MR imaging evaluation of anatomic and functional abnormalities. *Radiographics* 34 (2), 429–448. doi:10.1148/rg.342125050

Boubaker, M. B., Haboussi, M., Ganghoffer, J. F., and Aletti, P. (2009). Finite element simulation of interactions between pelvic organs: predictive model of the prostate motion in the context of radiotherapy. *J. Biomech.* 42 (12), 1862–1868. doi:10.1016/j.jbiomech.2009.05.022

Brandão, S., Parente, M., Mascarenhas, T., da Silva, A. R. G., Ramos, I., and Jorge, R. N. (2015). Biomechanical study on the bladder neck and urethral positions: simulation of impairment of the pelvic ligaments. *J. Biomech.* 48 (2), 217–223. doi:10.1016/j.jbiomech.2014.11.045

Chantereau, P., Brieu, M., Kammal, M., Farthmann, J., Gabriel, B., and Cosson, M. (2014). Mechanical properties of pelvic soft tissue of young women and impact of aging. *Int. Urogynecol J.* 25 (11), 1547–1553. doi:10.1007/s00192-014-2439-1

Chen, W., Yan, Z. H., and Wu, L. J. (2010). Finite element analysis of female pelvic floor anal elevator muscle. *Chin. J. Tissue Eng. Res. Clin. Rehabilitation* 14 (43), 8125–8128. doi:10.3969/j.issn.1673-8225.2010.43.036

Chen, Z. W., Joli, P., Feng, Z. Q., Rahim, M., Pirró, N., and Bellemare, M. E. (2015). Female patient-specific finite element modeling of pelvic organ prolapse (POP). *J. Biomech.* 48 (2), 238–245. doi:10.1016/j.jbiomech.2014.11.039

Colaiacomo, M. C., Masselli, G., Polettini, E., Lanciotti, S., Casciani, E., Bertini, L., et al. (2009). Dynamic MR imaging of the pelvic floor: a pictorial review. *Radiographics* 29 (3), e35. doi:10.1148/rg.e35

Chen, Q. Q. (2014). *A finite element studies of the different functions for the ligaments of the uterus in maintaining uterine in the normal position[D]*. Shanghai: Fudan University.

de Sousa, A. M. M., Cavalcante, J. G. T., Bottaro, M., Vieira, D. C. L., Babault, N., Geremia, J. M., et al. (2023). The influence of hip and knee joint angles on quadriceps muscle-tendon unit properties during maximal voluntary isometric contraction. *Int. J. Environ. Res. Public Health* 20 (5), 3947. Published 2023 Feb 23. doi:10.3390/ijerph20053947

Dias, N., Peng, Y., Khavari, R., Nakib, N. A., Sweet, R. M., Timm, G. W., et al. (2017). Pelvic floor dynamics during high-impact athletic activities: a computational modeling study. *Clin. Biomech. (Bristol, Avon)* 41, 20–27. doi:10.1016/j.clinbiomech.2016.11.003

Feng, Y. Y. (2022). *Application study of pelvic floor rehabilitation plan based on Cox health behavior interaction model in patients with urinary incontinence after laparoscopic radical prostatectomy[D]*. Jiangnan University. doi:10.27169/d.cnki.gwqgu.2022.002315

Fielding, J. R., Dumanli, H., Schreyer, A. G., et al. (2000). MR-based threedimentional modeling of the normal pelvic floor. *AJR* 174 (3), 567–660. doi:10.2214/ajr.174.3.1740657

Guo, E. F., Ma, L., Kan, Y. M., Zhang, S. H., Sun, M., Liu, Y., et al. (2015). The application value of transperineal ultrasound in female stress urinary incontinence. *Chin. J. Clin. Med. Imaging* 26 (03), 197–199.

Guo, P. N., Zhang, Z. Y., and Gao, Y. (2019). Design and Finite element analysis of customized pelvic prosthesis. *China J. Orthop. traumatology* 32 (06), 564–568. doi:10.3969/j.issn.1003-0034.2019.06.016

He, J. L. (2016). *Anatomy studies and finite element analysis for unstable posterior pelvic ring di sruptions treated with tension band pIate[D]*. Shandong University. doi:10.7666/d.Y3037037

Hu, J. S., and Pierre, E. F. (2019). Urinary incontinence in women: evaluation and management. *Am. Fam. Physician* 100 (6), 339–348.

Kobi, M., Flusberg, M., Paroder, V., and Chernyak, V. (2018). Practical guide to dynamic pelvic floor MRI. *J. Magn. Reson Imaging* 47 (5), 1155–1170. doi:10.1002/jmri.25998

Korkmaz, I., and Rogg, B. (2007). A simple fluid-mechanical model for the prediction of the stress-strain relation of the male urinary bladder. *J. Biomech.* 40 (3), 663–668. doi:10.1016/j.jbiomech.2006.02.014

Krcmar, M., Krofta, L., Urbankova, I., Reisl, J. F., Havelkova, L., and Hyncik, L. (2015). "Biomechanical properties of levator ani muscle used for virtual model of pelvic floor,". International Urogynecology Journal, S163–S164. SPRINGER LONDON LTD 236 GRAYS INN RD, 6TH FLOOR, LONDON WC1X 8HL, ENGLAND.

Larson, K. A., Luo, J., Guire, K. E., Chen, L., Ashton-Miller, J. A., and DeLancey, J. O. L. (2012). 3D analysis of cystoceles using magnetic resonanceimaging assessing midline, paravaginal, and apical defects. *Int. urogynecolog J.* 23 (3), 285–293. doi:10.1007/s00192-011-1586-x

Lee, S. L., Darzi, A., and Yang, G. Z. (2005). Subject specific finite element modelling of the levator ani. *Med. Image Comput. Assist. Interv.* 8 (Ptl), 360–367. doi:10.1007/11566465_45

Levaillant, M., Venara, A., Damon, H., Siproudhis, L., Brochard, C., and Hamel, J. F. (2023). Young women and elderly men at risk of severe faecal incontinence: results of a French nationwide database analysis: faecal incontinence in France. *Int. J. Colorectal Dis.* 38 (1), 131. doi:10.1007/s00384-023-04431-8

Li, D., and Lu, R. (2023). Research progress in pelvic floor ultrasound for assessing the morphology and function of levator ani muscle in women. *Zhong Nan Da Xue Xue Bao Yi Xue Ban.* 48 (8), 1267–1273. doi:10.11817/j.issn.1672-7347.2023.220577

Li, G., Tan, Z., Lv, X., and Ren, L. (2019). A computationally efficient finite element pedestrian model for head safety: development and validation. *Appl. Bionics Biomech.* 2019, 1–13. doi:10.1155/2019/4930803

Li, H. Y., Cui, Z. Y., Cui, S. H., Ruan, S. J., and He, L. J. (2017). Development and validation of a finite element model for a 6-year-old child pelvis. *Chin. J. Automot. Eng.* 7 (2), 100–105. doi:10.3969/j.issn.2095-1469.2017.02.04

Li, J. Q., and Yan, H. F. (2015). Clinical exploration of ultrasound measurement of bladder neck mobility and posterior angle of bladder urethra in the diagnosis of stress urinary incontinence in middle-aged and elderly women. *J. Changzhi Med. Coll.* 29 (04), 287–289. doi:10.3969/j.issn.1006-0588.2015.04.018

Li, S. (2022). *Computer simulation biomechanical research based on magnetic resonance imaging of female pelvic organ prolapse[D]*. Kunming Medical University. doi:10.27202/d.cnki.gkmyc.2022.000772

Liu, F. F., Xu, L., Ying, T., Tao, J. J., and Hu, B. (2013). The value of perineal ultrasound in the diagnosis of anterior pelvic dysfunction in women. *Chin. J. Ultrasound Imaging* 22 (12), 1063–1066. doi:10.3760/cma.j.issn.1004-4477.2013.12.016

Liu, X. (2017). *Finite element modeling of pelvic floor muscles in female patients with moderate to severe stress urinary incontinence and simulation stress analysis of storage and leakage state[D]*. Shanxi Medical University.

Ma, X. B., and Chen, C. X. (2020). The defecation status and its impact on physical and mental health of elderly people. *Chin. J. Gerontology* 40 (18), 3983–3986. doi:10.3969/j.issn.1005-9202.2020.18.053

Ma, X. X., Shi, S. Y., Xi, B., Chan, Y., Sun, X. L., Yang, X., et al. (2016). Stress distribution and deformation of uterosacral ligament and cardinal ligament under different working conditions simulated by the finite element model. *Chin. J. Obstet. Gynecol.* 51 (2), 14–19. doi:10.3760/cma.j.issn.0529-567X.2016.02.007

Ma, Z. J. (2019). *Study on the mechanism of pelvic vascular injury by lateral impact[D]*. Nanjing Medical University. doi:10.27249/d.cnki.gnjyu.2019.000006

Mazur-Bialy, A. I., Kołomańska-Bogucka, D., Nowakowski, C., and Tim, S. (2020). Urinary incontinence in women: modern methods of physiotherapy as a support for surgical treatment or independent therapy. *J. Clin. Med.* 9 (4), 1211. doi:10.3390/jcm9041211

Mortele, K. J., and Fairhurst, J. (2007). Dynamic MR defecography of the posterior compartment: indications, techniques and MRI features. *Eur. J. Radiol.* 61, 462–472. doi:10.1016/j.ejrad.2006.11.020

Okada, Y., Nakagawa, C., Shigeta, M., Nomura, Y., Inoue, E., Ichizuka, K., et al. (2001) 2024). Evaluation of levator ani muscle elasticity after vaginal delivery and cesarean section using shear wave elastography. *J. Med. Ultrason.* 51 (1), 95–101. doi:10.1007/s10396-023-01369-w

Peng, L., Duan, Z. L., Li, Z. Y., Li, J. H., Li, Y. H., Wang, S., et al. (2023). Research status and progress on the establishment and validation of finite element models for adolescent idiopathic scoliosis. *Chin. J. Tissue Eng. Res.* 27 (27), 4393–4400. doi:10.12307/2023.388

Peng, Y., Khavari, R., Nakib, N. A., Boone, T. B., and Zhang, Y. (2016). Assessment of urethral support using MRI-derived computational modeling of the female pelvis. *Int. Urogynecol J.* 27 (2), 205–212. doi:10.1007/s00192-015-2804-8

Qiu, Z. Y. (2017). *Finite element analysis and mechanical mechanism of posterior vaginal prolapsed based on MR imaging[D]*. Fujian Medical University. doi:10.27020/d.cnki.gfjyu.2017.000067

Rao, G. V., Rubod, C., Brieu, M., Bhatnagar, N., and Cosson, M. (2010). Experiments and FE modeling for the study of prolapsed in the pelvic system. *Comp. Meth Biomech. Biomed. Eng.* 13 (3), 349–357. doi:10.1080/10255840903251270

Ricci, P. L., Maas, S., Kelm, J., and Gerich, T. (2018). Finite element analysis of the pelvis including gait muscle forces: an investigation into the effect of rami fractures on load transmission. *J. Exp. Orthop.* 5 (1), 33. doi:10.1186/s40634-018-0151-7

Salari, N., Ghasemianrad, M., Ammari-Allahyari, M., Rasoulpoor, S., Shohaimi, S., and Mohammadi, M. (2023). Global prevalence of constipation in older adults: a

systematic review and meta-analysis. *Wien Klin. Wochenschr* 135 (15-16), 389–398. doi:10.1007/s00508-023-02156-w

Samavati, N., Mcgrath, D. M., Jewett, M. A., van der Kwast, T., Ménard, C., and Brock, K. K. (2015). Effect of material property heterogeneity on biomechanical modeling of prostate under deformation. *Phys. Med. Biol.* 60 (1), 195–209. doi:10.1088/0031-9155/60/1/195

Sichting, F., Rossol, J., Soisson, O., Stefan Klima, S., Milani, T., and Hammer, N. (2014). Pelvic belt effects on sacroiliac joint ligaments: a computational approach to understand therapeutic effects of pelvic belts. *Pain Physician* 17 (1), 43–51. doi:10.36076/ppj.2014/17/43

Silva, M., Brandão, S., Parente, M., Mascarenhas, T., and Natal Jorge, R. (2016). Establishing the biomechanical properties of the pelvic soft tissues through an inverse finite element analysis using magnetic resonance imaging. *Proc. Institution Mech. Eng. Part H J. Eng. Med.* 230 (4), 298–309. doi:10.1177/0954411916630571

Song, H. F., Huang, Y., Ni, C. X., Lei, L. L., Wang, X. Y., Liu, Z. C., et al. (2012). A finite element method for the simulation of levator ani muscle stress under different conditions. *Chin. J. Tissue Eng. Res.* 16 (26), 4852–4856. doi:10.3969/j.issn.1673-8225.2012.26.020

Song, Z., Nie, C., Li, S., Dario, P., and Dai, J. S. (2018). A muscle-specific rehabilitation training method based on muscle activation and the optimal load orientation concept. *Appl. Bionics Biomech.* 2018, 1–13. doi:10.1155/2018/2365983

Sun, T. J. (2015). *Abdominal impact and injury mechanism analysis of a six-year-old occupant based on finite element methods[D]*. Tianjin University of Science and Technology.

Talasz, H., Gosch, M., Kofler, M., and Lechleitner, M. (2018). Voiding disorders in geriatric patients: correlation with agerelated functional impairments. *Z Gerontol. Geriatr.* 51 (1), 67–73. doi:10.1007/s00391-016-1097-y

Tang, J. H., Zhong, C., Wen, W., Wu, R., Liu, Y., and Du, L. (2020). Quantifying levator ani muscle elasticity under normal and prolapse conditions by shear wave elastography: a preliminary study. *J. Ultrasound Med.* 39 (7), 1379–1388. doi:10.1002/jum.15232

The MR Group of the Radiology Branch of the Chinese Medical Association (2022). The MR Group of the Radiology Branch of the Chinese Medical Association MRI techniques and reporting standards for female pelvic floor functional disorders Chinese. *J. Radiology* 56 (1), 16–24. doi:10.3760/cma.j.cn112149-20210426-00412

Tibaek, S., Gard, G., Dehlendorff, C., Iversen, H. K., Biering-Soerensen, F., and Jensen, R. (2017). Is pelvic floor muscle training effective for men with poststroke lower urinary tract symptoms? A single-blinded randomized, controlled trial. *Am. J. Mens. Health* 11 (5), 1460–1471. doi:10.1177/1557988315610816

Venugopala Rao, G., Rubod, C., Brieu, M., Bhatnagar, N., and Cosson, M. (2010). Experiments and finite element modelling for the study of prolapse in the pelvic floor system. *Comput. Methods Biomech. Biomed. Engin* 13 (3), 349–357. doi:10.1080/10255840903251270

Wang, R., Liu, G., Jing, L., Zhang, J., Li, C., and Gong, L. (2024). Finite element analysis of pelvic floor biomechanical models to elucidate the mechanism for improving urination and defecation dysfunction in older adults: protocol for a model development and validation study. *JMIR Res. Protoc.* 13, e56333. doi:10.2196/56333

Wein, A. J. (2011). Re: FDA safety communication: update on serious complications associated with transvaginal placement of surgical mesh for pelvic organ prolapse. *J. Urology* 186 (6), 2328–2330. doi:10.1016/j.juro.2011.08.047

Wu, X. L. (2019). *Finite element analysis of biomechanics of injured levator ani muscle in female patients with moderate to severe SUI[D]*. Shanxi Medical University.

Xu, Z., Wu, Y., and Zhang, X. Q. (2021). *Finite element modeling method of female pelvic floor structure with mechanical simulation function*. China Patent: CN 113570723A 10.29.

Xuan, R., Yang, M., Gao, Y., Ren, S., Li, J., Yang, Z., et al. (2021). A simulation analysis of maternal pelvic floor muscle. *Int. J. Environ. Res. Public Health* 18 (20), 10821. doi:10.3390/ijerph182010821

Xue, J. L. (1996). Evaluation of anorectal angle in self-made and clinical application of the anus. *J. Pract. Med. Technol.* (05), 379–380.

Yang, M., Chen, C., Wang, Z., Long, J., Huang, R., Qi, W., et al. (2024). Finite element analysis of female pelvic organ prolapse mechanism: current landscape and future opportunities. *Front. Med. (Lausanne)* 11, 1342645. doi:10.3389/fmed.2024.1342645

Yao, T. Q., Qian, J. W., and Shen, J. H. (2022). *Refined reconstruction modeling and mechanical analysis method of female pelvic floor system under sagittal plane[P]*. China Patent: CN 114121290A, 2022.03.01.

Zhang, H., and Yao, L. Q. (2015). Research progress on the application of the finite element method in female pelvic floor functional disorders. *J. Chronic Dis.* 16 (01), 57–60. doi:10.16440/j.cnki.1674-8166.2015.01.018

Zhang, Y., Kim, S., Erdman, A. G., Roberts, K. P., and Timm, G. W. (2009). Feasibility of using a computer modeling approach to study SUI Induced by landing a jump. *Ann. Biomed. Eng.* 37 (7), 1425–1433. doi:10.1007/s10439-009-9705-2

Zhou, C. J., and Lai, S. L. (2021). Research progress on MRI evaluation of abnormal defecation control function. *Magn. Reson. Imaging* 12 (8), 114–117124. doi:10.12015/issn.1674-8034.2021.08.027

Zhou, L. X., Gu, X. L., and Du, H. L. (2020). Injury of levator ani muscles and occurrence of pelvic floor diseases during vaginal delivery based on finite element method. *J. Med. Biomechanic* 35 (06), 732–738. doi:10.16156/j.1004-7220.2020.06.013

Zong, J. K. (2022). *Finite element analysis of a novel anatomical plate for sacroiliac joint dislocation[D]*. Hebei Medical University.

Frontiers in
Bioengineering and Biotechnology

Accelerates the development of therapies, devices, and technologies to improve our lives

A multidisciplinary journal that accelerates the development of biological therapies, devices, processes and technologies to improve our lives by bridging the gap between discoveries and their application.

Discover the latest Research Topics

See more →

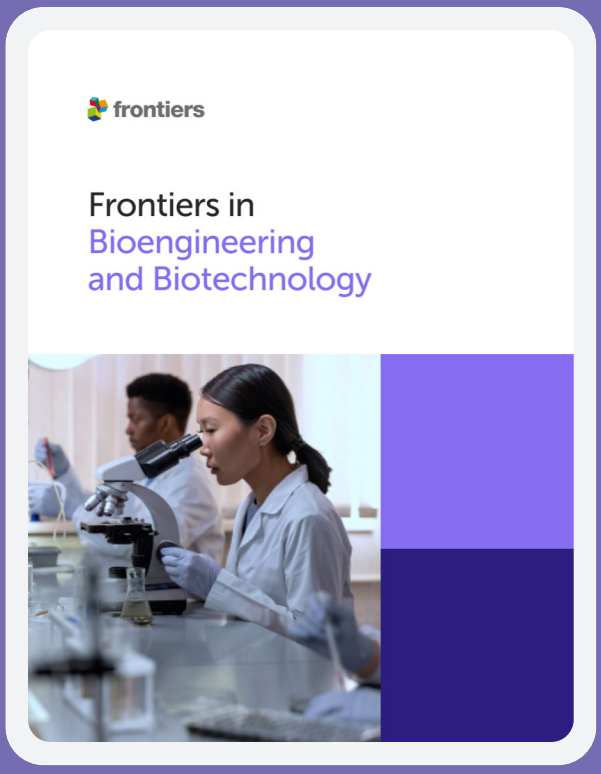

Frontiers

Avenue du Tribunal-Fédéral 34
1005 Lausanne, Switzerland
frontiersin.org

Contact us

+41 (0)21 510 17 00
frontiersin.org/about/contact